CORRÉLATIONS ÉLECTRONIQUES : DE LA MÉSO- À LA NANO-PHYSIQUE

ELECTRONIC CORRELATIONS: FROM MESO- TO NANO-PHYSICS

Sponsored by

- CNRS (*Centre National de la Recherche Scientifique*)
- CEA (*Commissariat à l'Énergie Atomique*)
- UE (*Union Européenne*)
- Région Rhône Alpes

XXXVIth Rencontres de Moriond
Les Arcs, Savoie, France – January 20-27, 2001

Electronic correlations: From meso- to nano-physics
Series: Moriond Workshops

ISBN 2-86883-570-8
© EDP Sciences, 2001

This work is subject to copyright. All rights are reserved, whether the whole or part of the material is concerned, specifically the rights of translation, reprinting, re-use of illustrations, recitation, broad-casting, reproduction on microfilms or in other ways, and storage in data banks. Duplication of this publication or parts thereof is only permitted under the provisions of the French Copyright Law of March 11, 1957. Violations fall under the prosecution act of the French Copyright Law.

Proceedings of the XXXVIth RENCONTRES DE MORIOND

Series: Moriond Workshops

Les Arcs, France *January 20-27, 2001*

ELECTRONIC CORRELATIONS: FROM MESO- TO NANO-PHYSICS

edited by

Thierry Martin
Gilles Montambaux
Jean Trân Thanh Vân

EDP SCIENCES

7 avenue du Hoggar, PA de Courtabœuf, B.P. 112, 91944 Les Ulis cedex A, France

XXXVIth Rencontres de Moriond

Electronic correlations: From meso- to nano-physics

were organized by:

J. Trân Thanh Vân (Orsay)

with the active collaboration of:

G. Glattli (Saclay)
T. Martin (Marseille)
G. Montambaux (Orsay)
B. Pannetier (Grenoble)
M. Sanquer (Grenoble)

International Advisory Committee:

H. Bouchiat (Orsay)
Y. Gefen (Weizman)
L. Glazman (Minneapolis)
D. Loss (Basel)
C. Marcus (Harvard)
M. Pepper (Cambridge)
J. Van Ruitenbeck (Leiden)

'2001 RENCONTRES DE MORIOND

The XXXVIth Rencontres de Moriond were held in Les Arcs 1800, Savoie, France.

The first meeting took place at Moriond in the French Alps in 1966. There, experimental as well as theoretical physicists not only shared their scientific preoccupations but also the household chores. The participants in the first meeting were mainly French physicists interested in electromagnetic interactions. In subsequent years, a session on high energy strong interactions was also added.

The main purpose of these meetings is to discuss recent developments in contemporary physics and also to promote effective collaboration between experimentalists and theorists in the field of elementary particle physics. By bringing together a relatively small number of participants, the meeting helps to develop better human relations as well as a more thorough and detailed discussion of the contributions.

This concern of research and experimentation of new channels of communication and dialogue which from the start animated the Moriond meetings, inspired us to organize a simultaneous meeting of biologists on Cell Differenciation (1980) and to create the Moriond Astrophysics Meeting (1981). In the same spirit, we have started a new series on Condensed Matter Physics in January 1994. Common meetings between biologists, astrophysicists, condensed matter physicists and high energy physicists are organized to study the implications of the advances of one field into the others. I hope that these conferences and lively discussions may give birth to new analytical methods or new mathematical languages.

At the XXXVIth Rencontres de Moriond in 2001, three physics sessions, one condensed matter session, one astrophysics session and one biology session were held:

* January 20-27	"Very high energy phenomena in the Universe"
	"Electronic correlations: From Meso- to Nanophysics"
* March 10-17	"Electroweak Interactions and Unified Theories"
	"Galaxy Clusters ang the High Redshift Universe observed in X-rays"
* March 17-24	"QCD and High Energy Hadronic Interactions"
	"Rencontre de Biologie – Méribel"

I thank the organizers of the XXXVIth Rencontres de Moriond:

- F.A. Aharonian, R. Ansari, J. Ballet, M. Boer, M. Boratav, B. Degrange, J. Dumarchez, F. Feinstein, G. Fontaine, G. Ghisellini, Y. Giraud-Héraud, F. Halzen, J.M. Hameury, G. Henri, F. Krennrich, M. Lemoine, C. Magneville and A. Watson, for the "Energy densities in the Universe" session,
- J. Bagger, A. Blondel, P. Fayet, J.-M. Frere, H. Frisch, L. Krauss, J.P. Lees, S. Loucatos, F. Montanet, L. Okun, L. Randall, G. Unal, D. Wood, and F. Zwirner for the "Electroweak Interactions and Unified Theories" session,

- N. Aghanim, J. Delabrouille, F. Durret, W. Forman, D.M. Neumann, and R. Teyssier,
- E. Auge, E. Berger, A. Capella, S. Catani, D. Denegri, B. Klima, L. Kluberg, G. Korchemsky, L. McLerran, L. Montanet, B. Pietrzyk, Chung-I Tan, and C. Voltolini, for the "QCD and High Energy Hadronic Interactions" session,
- B. Godelle, C. Robaglia, M. Sitbon, P. Sonigo, and K. Tran Thanh Van for the Biology meeting,

and the conference secretariat: C. Barthélemy, I. Cossin, D. Granger, Y. Guillaume, G. Hérent, M. Joguet, S. Lantz, H. Mauger, F.N. Oswald, Pham Duy Tu, A.M. Renault-Perrin, F. Warin, C. Wrzesinski, and V. Zorica.

I am also grateful to Mr. D. Schemann, Mr. Philippe Chevalier, Mr. Guillaume Delormas and Ms. Salima Telali who contributed through their hospitality and cooperation to the well-being of the participants enabling them to work in a relaxed atmosphere.

These Rencontres were sponsored by the European Union Training and Mobility of Researchers Program, the Centre National de la Recherche Scientifique (INSU, SPM and FP), the Institut National de Physique Nucléaire et de Physique des Particules (IN2P3-CNRS), the Commissariat à l'Énergie Atomique (DAPNIA), the Ministère de l'Enseignement Supérieur et de la Recherche (programme ACCES) and the National Science Foundation. I would like to express my thanks for their encouraging support.

I sincerely wish that a fruitful exchange and an efficient collaboration between the physicists, the astrophysicists and the biologists will arise from these Rencontres as from the previous ones.

J. Trân Thanh Vân

PRÉFACE

La physique quantique mésoscopique décrit les phénomènes de transport et les propriétés thermodynamiques des systèmes électroniques dont la taille typique est comprise entre les échelles microscopique et macroscopique, de sorte que la cohérence de phase est préservée. Durant la dernière décennie, ce domaine a connu une évolution rapide tant à cause d'avancées dans les procédés de fabrication, qu'à cause des problèmes théoriques qui s'y posent. La nanofabrication implique de nos jours des étapes de lithographie avancée, mais elle bénéficie aussi de la possibilité d'utiliser des nano-objets préexistants : les nanotubes de carbone et les molécules organiques ont rapproché la physique mésoscopique du monde nanoscopique.

Cette session est la quatrième des Rencontres de Moriond sur la physique mésoscopique. Lorsqu'on parcourt les programmes des rencontres précédentes, on constate l'évolution rapide des sujets et les progrès de cette thématique. *Effets d'interférence et effets coulombiens dans les petites structures électroniques (1994)* mit l'emphase sur le blocage de Coulomb. *Fermions corrélés et transport dans les systèmes mésoscopiques (1996)* aborda la physique des liquides de Luttinger, des structures hybrides contenant des supraconducteurs, ainsi que la compétition entre effets de désordre et d'interactions. *Physique quantique à l'échelle mésoscopique (1999)* présenta les premiers résultats expérimentaux sur ces prédictions, et introduisit la possibilité d'implémenter les opérations logiques quantiques en physique mésoscopique.

Cette nouvelle session s'est ouverte par des présentations sur le transport quantique à l'échelle nanométrique : le transport a travers des nano-objets tels que des molécules artificielles et des polymères conjugués, tant du point de vue théorique que du point de vue expérimental. Des sujets plus conventionnels ont suivi, comme l'effet Hall quantique, nous rappelant qu'il s'agit là d'un domaine très ouvert, puisque bien des résultats de mesure ne trouvent pas leur explication dans les théories existantes. La détermination de la charge effective des porteurs extraite de mesures de bruit continue d'intriguer, l'effet de leur statistique fractionnaire dans les mesures de transport n'a pas encore été observé. Une grande partie de cette conférence a été consacrée aux structures hybrides (métal normal, supraconducteur, ferromagnétique). Ces structures sont intéressantes tant par leur aspect fondamental de transport quantique, que qu'elles sont actuellement parmi les meilleurs candidats pour implémenter des opérations d'informatique quantique. Le rôle des interactions coulombiennes en deux dimensions, qui semble pertinent pour la description de la transition métal-isolant dans les hétérostructures semiconductrices, a été exposé sous plusieurs aspects et l'apport des sondes locales telles que la microscopie à champ proche a été mis en avant. D'autres thématiques plus familières figuraient déjà dans les sessions précédentes comme les points quantiques ou les courants permanents, où certains problèmes à caractère fondamental ne sont toujours pas compris. L'effet Kondo est maintenant observé dans les points quantiques fabriqués à partir de semiconducteurs et de nanotubes de carbone. Ce problème fondamental de corrélation électronique attire les deux communautés expérimentale et théorique. Les effets reliés au spin électronique dans le transport quantique sont en plein développement. Plusieurs expériences de transport sur les nanotubes de carbone – le nano objet par excellence – ont été présentées. Une autre nouveauté de cette rencontre fut l'apparition de systèmes mésoscopiques bosoniques. Au delà de leur caractère fondamental, ces travaux ont montré comment pousser les limites de fabrication et les conditions de mesure. Enfin la physique mésoscopique propose des situations modèles pour les ordinateurs quantiques. La question de la solidité d'un bit quantique supraconducteur a été abordée, et l'enchevêtrement des électrons proposé comme mécanisme pour propager l'information de façon fiable. La conférence s'est terminée par une session sur le problème central de la cohérence de phase en physique mésoscopique.

Cette Rencontre de Moriond peut prétendre avoir donné une « photo de famille » des aspects les plus récents de la physique mésoscopique et de leur rapprochement vers la nano-physique. Ce succès s'explique en partie par le fait que nous sommes en présence d'un domaine mûr qui, dans les dernières décennies, a attiré une masse critique de physiciens de la matière condensée. Mais il s'explique avant tout par la qualité scientifique des participants qui font vivre ce domaine très dynamique et compétitif de la physique. En particulier, nous tenons à remercier chaleureusement ceux d'entre eux qui ont accepté de nous donner une contribution écrite. Notons au passage que l'organisation des différentes contributions en sections peut parfois sembler arbitraire. Ceci est simplement du à l'extrême enchevêtrement des différents sujets abordés dans cette conférence.

Thierry Martin et Gilles Montambaux

FOREWORD

Quantum mesoscopic physics deals with phase coherent transport phenomena as well as thermodynamical properties of systems on a scale intermediate between the microscopic and the macroscopic level. Over the years, this field has enjoyed a rapid growth, due to breakthroughs in sample fabrication techniques, and also due to rather close interactions between experimentalists and theorists. Yet conventional fabrication techniques are no longer sufficient to make state of the art mesoscopic devices. Nowadays nano-fabrication involves sophisticated lithographic methods, and it also benefits from the availability of ready-made nanoscopic "objects": carbon nanotubes, as well as organic molecules, have allowed to bring this field of study closer to the nanoscopic limit.

This session is the fourth Rencontre de Moriond devoted to mesoscopic physics. Over the years, the scientific topics have evolved in a spectacular manner, as is already explicit in the titles of each conference. Coulomb and interference effects in small electronic structures (1994) addressed many aspects of the Coulomb blockade phenomenon. Correlated fermions and transport in mesoscopic systems (1996) dealt with the physics of Luttinger liquids, with hybrid superconducting structures and with the interplay between disorder and interaction. Quantum physics at the mesoscopic scale (1999) presented experimental evidence for these predictions, and announced the possibility of using mesoscopic devices in order to implement quantum logical operations.

The present meeting started with presentations on nano-scale quantum transport: transport through nano-objects such as artificial molecules and conjugated polymers, from the experimental and theoretical points of view. More conventional topics followed, such as the quantum Hall effect, notwithstanding the fact that it remains largely an open field, with many observed phenomena not accounted for by existing theoretical models. Measurements of effective charges extracted from noise measurements are still puzzling and the effect of fractional statistics in transport measurements has not yet been observed. A large portion of the meeting dealt with the state of the art investigations of hybrid normal-metal/superconductor/ferromagnet structures. These structures are relevant because of the fundamental aspects of quantum transport that they address, and because of their potential application for building quantum logic circuitry. The importance of Coulomb interaction in two dimensions, which seems relevant for the study of the metal insulator transition in semiconductor heterostructures, was presented from the bulk point of view, but also using local probes such as scanning tunneling microscope. Some of the presentations in mesoscopic physics sounded more familiar, because they concerned topics that had been considered in previous Rencontres: quantum dots, persistent currents, among others. Yet, it became apparent that many fundamental issues remain unexplored or not fully understood. The Kondo effect, now observed in semiconductor quantum dots as well as in carbon nanotube quantum dots is one of them. The fact that it constitutes a correlated electron problem in a mesoscopic setting gathers the interest of theorists and experimentalists alike. Spintronics regroups phenomena involving transport experiments through quantum dots or through magnetic heterostructures. Reports on transport experiments through carbon nanotubes – the archetype of a nano-object – were presented. A novelty of the meeting was a presentation on bosonic mesoscopic systems. The issue of quantum computing was approached from the point of view of nano-physics in condensed matter systems. The feasibility and robustness of a quantum bit was addressed, as well as the issue of how to preserve the information, using entangled pairs of electrons.

This Rencontre de Moriond may claim to have given a family portrait of the strategic issues in mesoscopic physics and in nanophysics. This success is due in part to the fact that we are dealing

now with a mature field, which has attracted a critical mass of condensed matter physicists over the ast decade. This success is also due for the most part to the participants, who are all active players n this competitive field of physics. In particular, we wish to thank those who went through the trouble of providing us with a written contribution. Note that the order of appearance of the manuscripts in this book may seem somewhat arbitrary in some cases. It merely reflects the close nteractions which exist between the different topics of mesoscopic physics.

Thierry Martin and Gilles Montambaux

CONTENTS

Préface VII
Foreword IX

I. Molecular Systems

Shell structure in nanowires of simple metals. *J. Van Ruitenbeek* 3
Kondo tunneling through a biased double quantum dot. *Y. Avishai* 11
Dynamical Coulomb blockade in quantum point contacts. *A. Levy Yeyati* 17
Electron transport in molecular wires mediated via polarons and solitons: coherent electron-phonon interaction. *H. Ness* 23
Statistics of quantum transport in metal nanowires with surface disorder. *J. Bürki* 27

II. Quantum Hall Effect

Elastic theory of quantum Hall stripes. *F. von Oppen* 33
Chiral and midgap edge electron states in the quasi-one-dimensional organic conductors (TMTSF)2X. *V.M. Yakovenko* 39
On-resonance and off-resonance tunneling at the fractional quantum Hall edge. *A.M. Chang* 41
Coherent control of fractional charges in quantum antidot devices. *V.J. Goldman* 51
Unpolarizable groud states in the fractional quantum Hall effect at n=2/3. *L.P. Lévy* 59
Fractional statistics and noise correlations in the FQHE. *I. Safi* 67
Shot noise in the FQHE: Strong backscattering by a weak impurity. *C. Glattli* 73

III. Shot Noise

The effect of interaction on shot noise in the quantum limit. *Y. Gefen* 85
Full counting statistics of electron transfer between superconductors. *Y.V. Nazarov* 93
Shot noise of series quantum point contacts. *S. Oberholzer* 99
The fermionic analog of the Hanbury-Brown and Twiss experiment with a superconductor. *J. Torrès* 103
Effect of incoherent scattering on shot noise correlations in the quantum Hall regime. *C. Texier* 107
Fractional exclusion statistics and shot noise in ballistic conductors. *G. Gomila* 111

IV. Hybrid Structures

Observing single electron tunneling events in a superconducting single electron transistor. *K. Lehnert* 117
Doubled shot noise in hybrid NS junctions. *M. Sanquer* 121
Subharmonic Shapiro steps in a mesoscopic S-N-S junction. *B. Pannetier* 127
Fermions and bosons in superconducting amorphous wires. *Y. Oreg* 133
Superposition of two mesoscopically distinct quantum states. *C. Bruder* 137
Coupling of two superconductors through a ferromagnet. SFS h-junctions and inner frustrated networks. *V.V. Ryazanov* 143
Magnon-assisted Andreev reflection in a ferromagnet-superconductor junction. *V. Falko* 147
Electron transport through semiconductor-superconductor junction in Integer Quantum Hall Effect. *N.M. Chtchelkatchev* 153
Local spectroscopy of a superconductor-normal metal junction. *H. Courtois* 159
Shot noise in incoherent superconducting/normal metal/superconducting junction. *F. Lefloch* 163

Quantum interference effects in isolated Josephson junction loops. *D. Ivanov* 167
Controlled decoherence due to a normal-metal superconductor proximity wire. *T. Martin* 171
Spatially resolved tunneling spectroscopy on normal nanostructures in contact with a superconductor. *M. Vinet* 175

V. Metal-Insulator Transition in 2D
On the relation between interband scattering and "metallic" behavior of two dimensional holes in GaAs/AlGaAs. *U. Sivan* 181
Microscopic structure of the metal-insulator transition in two dimensions. *A. Yacoby* 187
Fermi-liquid behaviour of 2D systems near the crossover from "metal" to "insulator". *A.K. Savchenko* 195
In-plane magnetization of electrons in a silicon inversion layer. *M. Reznikov* 201
Electrical conductivity of strongly interacting holes in 2D and 0D. *U. Gennser* 207
Oscillatory instability in short-gate GaAs MESFETs. *S.S. Safonov* 213
Mesoscopic Wigner crystallization in two dimensional lattice models. *J.-L. Pichard* 217
Percolation approach to the metal-insulator transition in two dimensions. *Y. Meir* 221
Diluted electron gas near the metal insulator transition in silicon inversion layers. *A.M. Finkel'stein* 225

VI. Quantum Coherence
Decoherence from vacuum fluctuations. *M. Büttiker* 231
Coulomb effects and electron transport through a coherent conductor. *A.D. Zaikin* 237
Quantum noise, detailed balance and Kubo formula in non equilibrium quantum systems. *Y. Imry* 243
Mesoscopic metallic rings out of equilibrium. *E. Kanzieper* 251
Experimental and theoretical investigations on Aharonov-Bohm cages. *D. Mailly, J. Vidal* 255
Persistent currents in mesoscopic connected rings. *L. Saminadayar* 263
Transport properties of one-dimensional trapped atomic gases. *H.P. Büchler* 267
Measurements of flux dependent screening in Aharonov-Bohm rings. *R. Deblock* 273
Localization and absence of Breit-Wigner form for Cauchy random band matrices. *K.M. Frahm* 279
Local density of states probed by single electron tunneling. *J. Könemann* 283
Correlations and fluctuations of a confined electron gas. *A. Monastra* 287
Does Berry phase exist for a system coupled to its environment? *R.S. Withney* 291

VII. Electronic Correlations
Influence of magnetic field on effective electron-electron interactions in a copper wire. *A. Anthore* 301
Quantum interference and Coulomb interaction in granulated metals. *K.B. Efetov* 309
Topological confinement of spins and charges: Spinons as p- jonctions. *S. Brazovski* 315
Discrete thermodynamic Bethe ansatz. *K. Imura* 319
Fast ground-state reordering from off-diagonal fluctuations of interaction. *P. Jacquod* 323
Excited states of the Cooper problem in a three-dimensional disordered system. *J. Lages* 329
Non-equilibrium tunneling effects of interacting Hubbard-Anderson impurities. *N.S. Maslova* 333
Theory of Fano resonance in STM spectroscopy of Kondo ions on metal surfaces. *O. Ujsàghy* 339

Dynamics of Coulomb-correlated electron-hole pairs in disordered semiconductor nanowires. *I. Varga* 34
Ballistic Hall response. *X. Zotos* 34

VIII. Quantum Dots
Phase evolution in a Kondo-correlated system. *M. Heiblum* 35
Multi-level Kondo regimes in a quantum dot. *S. De Franceschi* 36
Spin effects in quantum dots with steep potential walls. *K. Ensslin* 36
Time-reversal symmetry breaking by AC field: Effect of commensurability in the frequency domain. *V.E. Kravtsov* 37
Universal scrambling properties of wavefunctions and energy spectra in Coulomb blockade quantum dots. *F. Piéchon* 38
Comparision between one- and two-channel Kondo effects in mesoscopic systems. *A. Zawadowski* 38
Coulomb blockade and electron spin in quantum dots. *C. Marcus* 39
The g-factors of discrete levels in nanoparticles. *L.I. Glazman* 40
Shot noise of weak cotunneling current: Non-equilibrium fluctuation-dissipation theorem. *E.V. Sukhorukov* 41

IX. Nanotubes
Doping state of multi-wall carbon nanotube wires and quantum dots. *C. Schönenberger* 42
Electrostatic force microscopy of electronic transport in carbon nanotubes. *A. Bachtold* 42
1/f noise in carbon nanotubes. *H. Postma* 43
Tunneling into resistive multiwalled carbon nanotubes. *M. Paalanen* 43
Proximity-induced and intrinsic superconductivity in carbon nanotubes. *B. Reulet* 44
Transport phenomena in nanotube quantum dots from strong to weak confinement. *J. Nygard* 45
Low-noise electrometer made of multiwalled carbon nanotube. *L. Roschier* 45

X. Spin Injection and Magnetism
Two-component interference effect in one- and two-dimensional systems. *P. Streda* 46
Design of a semiconductor ferromagnet in artificial crystals. *H. Takayanagi* 46
Spin transport and spin injection in mesoscopic metal and semiconductor devices. *B.J. van Wees* 47
Channel blocking by a thin domain wall in ballistic ferromagnetic quantum wires. *D. Weinmann* 48
A phenomenological two-subband model for quantum point contacts: The 0.7 conductance anomaly and the associated thermopower. *H. Bruus* 48
Tunneling magnetoresistance in nanoscale F-N-F systems: Mesoscopic fluctuations. *G. Usaj* 49
Spin torque in a magnetic trilayer coupled to a superconductor. *X. Waintal* 49

XI. Quantum Computing
Resonant Cooper tunneling through a double superconducting island qubit. *P. Lafarge* 50
Engineering entanglement with Josephson qubits. *R. Fazio* 50
Cooper pair box coupled to a current-biased Josephson junction. *F.W.J. Hekking* 51
Dynamic of Andreev level qubits. *G. Wendin* 52
Electron spins for spintronics and quantum communication in quantum dots and wires. *D. Loss* 52

Correlated electron transport at multiple superconductor-ferromagnet interfaces. *D. Feinberg* 535
Generating entangled electron pairs from a superconductor. *G. Lesovik* 541
Electronic EPR-like experiments with superconductors. *R. Mélin* 547
Quantum computation with FQHE quasiparticles. *D.V. Averin* 551
Efficient quantum computing insensitive to phase errors. *B. Georgeot* 557

List of Participants 563

Index of Authors 569

MOLECULAR SYSTEMS

SHELL STRUCTURE IN NANOWIRES OF SIMPLE METALS

A.I. YANSON[1,2], I.K. YANSON[1,3], J.M. VAN RUITENBEEK[1]
[1] *Kamerlingh Onnes Laboratorium, Universiteit Leiden, Postbus 9504, NL 2300 RA Leiden, The Netherlands*

[2] *Present address: Dept. of Physics, 510 Clark Hall, Cornell University, Ithaca, NY 14853*

[3] *B. Verkin Institute for Low Temperature Physics and Engineering, National Academy of Sciences, 310164, Kharkiv, Ukraine*

By means of mechanically controllable break junctions the conductance traces for large numbers of contact breaking cycles have been recorded in the form of conductance histograms. For the alkali metals at moderate temperatures we observe periodic structures in the histograms that are interpreted in terms of self-selecting magic nanowire geometries of the metallic contacts. This is explained in analogy to the shell structure observed for metal clusters.

1 Introduction

We want to consider the relationship between electrical conductance and cohesion in metallic nanowires, formed during the controlled breaking of a clean metallic contact. Apart from their role in determining the electronic transport properties of the contacts, the quantization of the wave functions inside the contact also affects its cohesive energy. Several approaches to free electron models have been used to evaluate the contribution of conductance modes to cohesion at the atomic scale [1,2,3]. It has not yet been demonstrated how this quantum cohesion can be separated from other contributions to metallic bonding, and this requires further study. However, there is a related quantum effect on the cohesion for which we present the experimental evidence. This can be seen for alkali metal contacts at contact diameters well above those for which the quantization peaks in the conductance histograms are observed (see e.g. Krans *et al.* [4]), and for temperatures well above helium temperature. During the stretching of the contact under these conditions a nanowire is formed that shows a periodic structure of stable diameters. The periodic structure is closely related to the well-known magic number series for metal clusters.

2 Summary of shell effects in metal clusters

For those readers who are not familiar with the work on metal clusters we will start by briefly summarizing the main results. When a hot metal vapor is allowed to expand through a nozzle into vacuum in the presence of an inert carrier gas the metal atoms fuse together to form clusters of various sizes. The size distribution for these clusters can be measured using a mass spectrometer. In a seminal experiment Knight *et al.* [5] discovered that this distribution for sodium has not a smooth bell-type shape, as one might naively expect, but rather shows a series of so-called magic numbers. Those clusters that are composed of a number of atoms corresponding to one of these magic numbers are found to be exceptionally abundant. One finds peaks or discontinuities in the abundance spectrum at 8, 20, 40, 58, 70, 92,... atoms. The explanation for these numbers is based on a shockingly simple model. The clusters are regarded as spherically symmetric potential wells containing a number of free and independent electrons equal to the number of atoms forming the cluster (since we consider monovalent metals). For hard-wall boundary conditions the wave functions for the electrons are given by the product of the spherical harmonics $Y_{lm}(\theta,\phi)$, and the spherical Bessel functions, $j_l(\gamma_{nl}r/r_0)$, with r_0 the radius of the cluster. The ground state of the system is determined by the filling of the

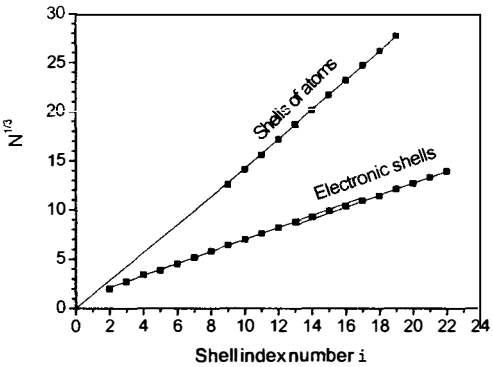


Figure 1: Cube root of the cluster magic numbers obtained from abundance spectra for Na, plotted against the index of the magic number. The data set labeled as 'Electronic shells' is taken from Pedersen *et al.*[6]. The break in the linear dependence signifies a phase shift in the points at a beat minimum due to the supershell structure. The data set labeled 'Atomic shells' is taken from Martin *et al.*[7] and is obtained for the largest clusters in a relatively cold cluster beam.

energy levels starting at the bottom. The levels are given by $E_{nlm} = \hbar^2\gamma_{nl}^2/2m_e r_0^2$, where m_e is the electron mass and γ_{nl} is the n^{th} zero of the l^{th} order Bessel function: $j_l(\gamma_{nl}) = 0$. The lowest energy level corresponds to the first zero of the $l = 0$ Bessel function, the only possible value for the quantum number m is 0, and including spin degeneracy two electrons can be accommodated in the lowest level. The next level is three-fold degenerate ($m = 0, \pm 1$) so that it is completed with a total number of 8 electrons in the cluster. For the monovalent metal considered in the experiment, this implies that also 8 atoms are required to allow filling the electronic shell, and so forth. The difference in the total energy of the cluster makes a larger jump each time a degenerate level is completed, and the energy gap to the next level needs to be bridged. This explains the stability of the filled-shell clusters, just as the stability of the noble gasses is explained by the filling of the electronic shells for the elements in the periodic table.

Thus the dominant structure in the experimental abundance spectrum can be understood by considering the clusters as smooth spheres filled with free and independent electrons. This interpretation in its simplest form works best for the alkali metals, for which the quasiparticle spectrum in the bulk metals is known to be well-approximated by a free and independent electron gas. Moreover, the outer s electron of the alkali metal atoms is weakly bound to the atom core and orbits at a rather large distance around the nucleus. This leads to a smoothening of atomic surface corrugation to such an extent that the electron distribution around a di-atomic molecule is not a dumbbell, as one would naively expect, but is rather more closely approximated by a spherical electron cloud.

When the magic numbers are indicated as N_i, with i an index giving the sequential number of the magic number, e.g. $N_1 = 2$, $N_2 = 8$, $N_3 = 20$ etc., then a plot of the cube root of the magic numbers against the index number shows a linear dependence, see Fig. 1. In other words, the magic numbers form a periodic series as a function of the cube root of the number of atoms in the cluster, which is proportional to the cluster radius. The explanation for this periodic appearance of the magic numbers is given in terms of the bunching of energy levels, which is conveniently described in a semi-classical approximation.

Indeed, the individual-level picture described above only works for the lowest quantum numbers. For larger quantum numbers we cannot even approximately identify the shells with individual quantum numbers. For these large quantum numbers, i.e. in the limit of large cluster sizes, it is instructive to approximate the true quantum properties of the clusters by a

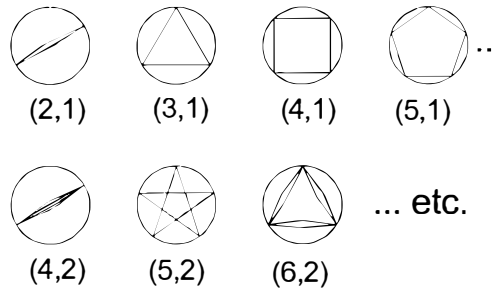


Figure 2: The lowest-order semi-classical trajectories for a particle inside a steep-walled spherical or cylindrical cavity. The orbits are labeled by two integers (p,t), where p is the number of vertices of the orbit and t is the winding number, i.e. the number of times the particle encircles the center before the orbit is closed.

semi-classical approximation. This makes use of the work on the distribution of the resonant modes in a cavity that has been discussed in terms of classical trajectories by Guzwiller [8] and by Balian and Bloch [9]. In this approximation the allowed orbits for the electrons inside a steep-walled potential well can be identified with the closed classical trajectories of the electron as it bounces back and forth between the walls. For a circular system the lowest order trajectories are given in Fig. 2. The allowed wave vectors are then obtained by applying the Bohr-Sommerfeld quantization condition for each closed trajectory. It is immediately obvious that for each solution at a given radius R of the system, a new solution will be found when the length of the trajectory is increased by a full electron wavelength. Therefore, the distribution of modes (as a function of R or as a function of wave vector k_{F}, or more generally as a function of $k_{\mathrm{F}}R$) has a periodic structure.

However, we do not have a single period, since each of the classical trajectories (Fig. 2) gives rise to it own periodicity. Taking the amplitude factors into account it can be shown that the dominant contributions to the level distribution for a spherical system come from the triangular and square orbits. The difference in the periods for the level distribution belonging to these two orbits gives rise to a beating pattern: in some range of $k_{\mathrm{F}}R$ the two orbits will give rise to levels that nearly coincide, thus amplifying the shell structure in this range. On the other hand at other ranges of $k_{\mathrm{F}}R$ the levels of the square orbits will fall in between the levels of the triangular orbit, thus smoothening out the shell effects. This beating pattern in the shell structure is known as supershell structure, and it has been observed for Na, Li and Ga metallic clusters [6,10,11]. The length of the triangular orbit is $3\sqrt{3}R$ while that of the square orbit is $4\sqrt{2}R$. The ratio of these two lengths is 1.09 from which we see that is requires about 11 periods of the individual oscillations to complete a beat of the combined pattern. For the metallic clusters one or two beat-minima have been observed, but nature does not provide enough chemical elements to observe supershell structure in the periodic table or in the stability pattern of the nuclei. For the simple, spherical, independent-electron quantum well system under consideration one can, of course, obtain all the quantum levels directly from the exact solutions of the Schrödinger equation. However, one cannot identify the periodic structure with any particular quantum numbers. The periodic structure of the levels, in other words the modulation in the density of levels, is a result of a bunching of individual levels. A bunch of levels together forms a wave packet that approximates the motion along the classical trajectories.

At still larger cluster sizes one observes a crossover to a new series of magic numbers, having a different periodicity, which is seen in the plot of Fig. 1 as a crossover to a new slope in the data points. The new series is a result of the filling of *geometric* shells of atoms, rather than electronic shells [12]. The clusters form regular facetted crystalline structures, which attain an

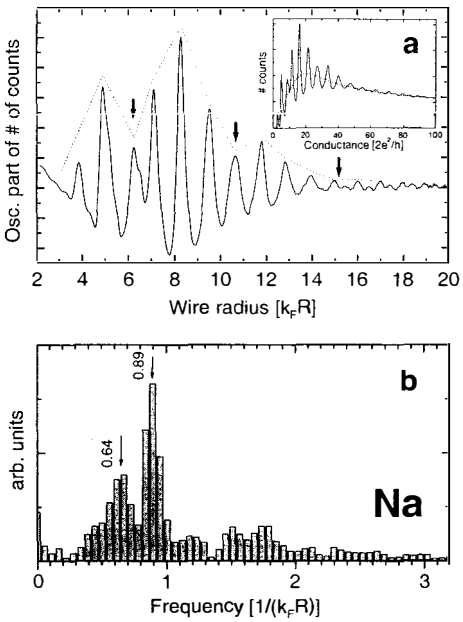


Figure 3: (a) Conductance histogram for sodium after subtraction of a smooth background. $T = 90\,\mathrm{K}$, bias voltage $V = 100\,\mathrm{mV}$, and the number of curves included in the histogram is 13 800. The original curve and the background are shown in the inset. The arrows indicate the positions of minimal amplitude, which are the nodes of the supershell structure. When taking the Fourier transform of the curve in (a) the spectrum in panel (b) is obtained, which shows two dominant frequency components. From Yanson *et al.* [18,21].

energy minimum each time a new layer of atoms filling all facets is completed. For some metals (e.g. Al and Ca) one observes additional structure due to the filling of partial atomic shells, corresponding to the completion of individual facets. The facet-completing sub-shell structure can in some cases be as strong as the full atomic shell structure.

3 Theory for electronic shell effects in nanowires

The shell effects discussed previously concerning atomic nuclei, the elements or metallic clusters, are all based on models of fermions that are completely confined inside symmetric potential wells. However, the same concepts can be applied to nanowires, for which one of the three dimensions is open and connected to infinitely long metallic leads. In this case there are no true gaps in the density of states, since the conductance modes have a continuous degree of freedom along the current direction. Nevertheless, a modulation of the density of levels is still present. At the points where a new mode (the bottom of a 1-dimensional subband) crosses the Fermi energy, the density of states shows a $1/\sqrt{E - E_n}$ singularity. By the same mechanism that leads to the shell structure for closed fermion systems the symmetry of the wire gives rise to a bunching of the singularities, and these bunches can be associated with the electronic shells in metal clusters. The resulting density-of-states oscillations have been analyzed for independent-electron models [1,2,13,14] and by local-density functional methods [15]. The fluctuations in the density of states result in local minima in the free energy for the nanowire, which in turn give rise to self-selecting magic wire configurations. As for metallic clusters, one can make a semi-classical expansion of the density of states and this was done by Yannouleas *et al.*[15] and in spirit of Balian and Bloch by

Höppler and Zwerger [14] and by Kassubek *et al.* [16]. The stable wire diameters predicted from this model are in fairly good agreement with the observed periodic peak structure in the histograms [17], as we will discuss below. The periodic pattern has again a supershell modulation due to the contribution of several types of orbits. The types of orbits are the same as for spherical clusters, Fig. 2, but the relative weight for each is different. The diametric orbit $(p, t) = (2, 1)$ has only a minor contribution to the structure in the density of states for clusters, while it is of comparable weight as the triangular and square orbits for a cylindrical system.

4 Observation of electronic shell effects in nanowires

The shell effects in nanowires have been observed most clearly for the alkali metals Li, Na, and K [17,18]. The experiments were performed using the Mechanically Controllable Break Junction (MCBJ) technique[4,19]. For atomic-size contacts at low temperatures the conductance histograms for the alkali metals show the characteristic series of conductance peaks at 1, 3, 5, and 6 times the conductance quantum, $G_0 = 2e^2/h$. As was discussed by Krans *et al.* [4], this observation strongly suggests that one forms nanowires of nearly-perfect circularly-symmetric shape while stretching the contact, and the conduction electrons behave nearly free-electron like. When the experiment is extended to higher conductance one observes a number of rather broad but reproducible peaks. These peaks become more pronounced as the temperature is raised to about 90 K and more of them become visible at still higher conductance, Fig. 3(a). The separation between the peaks grows for increasing conductance, but a regular periodic peak structure is obtained when plotting the spectrum as a function of the radius of the nanowire. The radius is obtained from the conductance by the semi-classical relation [20,14],

$$G = gG_0 \simeq G_0[(\frac{k_F R}{2})^2 - \frac{k_F R}{2} + \frac{1}{6} + \cdots]. \quad (1)$$

The values of $k_F R$ at the positions of the peaks in a histogram are plotted versus the index of the peaks in Fig. 4. The linear dependence illustrates the fact that the peaks in the histogram are found at regular intervals in the radius of the nanowire and this periodicity suggests an analogy with the shell structure observed for clusters. But it is more than an analogy: when we take the cluster magic numbers for the electronic shell structure from Fig. 1 and convert the number of atoms N_i into the cluster radius through $k_F R_i = 1.92 N_i^{1/3}$, appropriate for sodium, we obtain the black dots in Fig. 4. The close agreement between the two sets of data suggests an intimate relation between the cluster magic numbers and the peaks in the conductance histogram. Applying the semi-classical theory outlined in section 3 for shell structure in nanowires produces the open triangles in the figure. The agreement with the experimental points is quite good, especially in the beginning. The deviation for larger cluster sizes requires further study, but this may be due to approximations in the calculation, where hard wall boundaries have been assumed, and to ignoring contributions from electron trajectories beyond the lowest three.

The shell structure only clearly appears when the temperature is raised well above liquid helium temperature. This finds a natural interpretation within the framework of the shell effect. The shell structure makes the free energy for specific wire configurations favorable above the average. When a contact is stretched at very low temperatures, the shape and size of the contact evolves along a local energy minimum trajectory. Only when the system is exposed to large enough thermal fluctuations it can explore the various contact configurations in order to find the deeper minimum at the magic wire configurations. Also for metallic clusters temperature has a significent influence on the degree to which shell structure is expressed in the experiments[23].

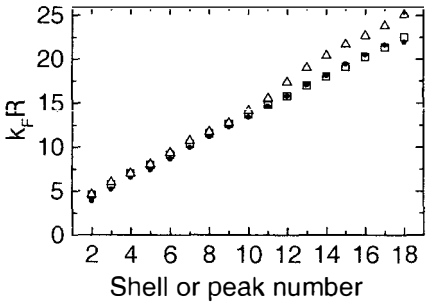


Figure 4: Radius of the nanowire at the positions of the maxima observed in histograms similar to the one in Fig. 3(a) versus peak number (□), where R is given in units k_F^{-1}. The radii at the peak positions are compared to the radii corresponding to the magic numbers for sodium metal clusters (•) [22] and to those expected from a semi-classical description for the fluctuations in the free energy for the nanowire (△) [15,14].

5 Supershell effects

On top of the shell structure a pronounced modulation due to supershell structure can be observed for metallic nanowires, as shown in the conductance histogram for Na in Fig. 3(a), for which the periods in the structure are made visible by taking a Fourier transform in Fig. 3(b). Similar results have been obtained for Li and K [18]. The modulation in the histogram peak amplitudes already suggests a beating pattern of two dominant frequencies, which is confirmed by the Fourier spectrum. The two peaks in the spectrum correspond very well to the ones found in the Fourier transform for the calculated free energy in a cylindrical nanowire [21]. When L is the length of a particular semi-classical orbit we can express it in units of the Fermi wavelength as L/λ_F. For the diametric orbit we then have $L/\lambda_F = 4R/\lambda_F = (2/\pi)(k_F R) \simeq 0.637(k_F R)$. This is just the frequency of the first peak in the Fourier spectrum. Similarly, we obtain for the triangular orbit $L/\lambda_F = 3\sqrt{3}R/\lambda_F \simeq 0.827(k_F R)$ and for the square orbit $L/\lambda_F = 4\sqrt{2}R/\lambda_F = \simeq 0.900(k_F R)$. We conclude that the first peak is due to the diametric orbit, which is prominent in the spectrum, in contrast to that for metallic clusters. The second peak is due to a combination of the triangular and the square orbits, which are not resolved here. The larger separation of the period of the diametric orbit from that of the trangular/square orbits results in a shorter beat-period compared to the situation for clusters, where the beat is due to interference of the square with the triangular orbits. As a result, for the nanowires the two main periods can be directly resolved in the Fourier transform.

6 Geometric shell effects

Beyond a certain diameter a new periodic structure was encountered in the conductance histograms for Na, K and Cs, which points at a transition from electronic shell effect to atomic shell structure, in close analogy to what has been observed for the clusters [18,24]. The position of the transition region between the two periodic features depends strongly on experimental parameters such as the sample temperature, the voltage bias and the depth of indentation, and shifts to smaller diameters when the metal is found further down the first column of the periodic table of the elements. The new oscillating phenomenon has approximately a three times smaller period than that for the electronic shell structure. The points for the electronic shell effect in sodium nanowires plotted in Fig. 4 have a slope of 0.56 ± 0.01. Beyond the cross-over (not shown in the figure) the points obey a linear relation with a much smaller slope of 0.223 ± 0.001. By varying the experimental conditions one can greatly extend the conductance range over which

this electronic shell structure is observed, while the slope always agrees with the periodicity expected for this effect. As an interpretation for the new periodic structure it is proposed that geometric shell closing takes over, where the dominant effect comes from a wire atomic arrangement with only close-packed surfaces. For a bcc stacking a hexagonal wire with exclusively [110] facets can be formed with its axis along [111], and the observed periodicity agrees with that expected for the successive filling of these facets.

7 Conclusion

Electronic and atomic shell structure have been observed for the alkali metals Li, Na, K and Cs. From shell effects observed for metal clusters one may infer that shell effects in nanowires may be observable in other metals as well. In view of the much higher melting point for some of the favorable candidates (Au, Al, ...) observation of such effects will probably require experiments under UHV conditions at elevated temperatures.

References

1. C.A. Stafford, D. Baeriswyl, and J. Bürki, *Phys. Rev. Lett.* **79**, 2863 (1997).
2. J.M. van Ruitenbeek, M.H. Devoret, D. Esteve, and C. Urbina, *Phys. Rev.* B **56**, 12566 (1997).
3. C. Yannouleas and U. Landman, *J. Phys. Chem.* B **101**, 5780 (1997).
4. J.M. Krans, J.M. van Ruitenbeek, V.V. Fisun, I.K. Yanson, and L.J. de Jongh, *Nature* **375**, 767 (1995).
5. W.D. Knight, K. Clemenger, W.A. de Heer, W.A. Saunders, M.Y. Chou, and M.L. Cohen, *Phys. Rev. Lett.* **24**, 2141 (1984).
6. J. Pedersen, S. Bjørnholm, J. Borggreen, K. Hansen, T.P. Martin, and H.D. Rasmussen, *Nature* **353**, 733 (1991).
7. T.P. Martin, T. Bergmann, H. Göhlich, and T. Lange, *Z. Phys.* D **19**, 25 (1991).
8. M.C. Guzwiller, *J. Math. Phys.* **12**, 343 (1971).
9. R. Balian and C. Bloch, *Ann. Phys. (N.Y.)* **69**, 76 (1972).
10. C. Bréchignac, Ph. Cahuzac, M. de Frutos, J.Ph. Roux, and K. Bowen in *Physics and chemistry of finite systems: from clusters to crystals*, eds. P. Jena, S.N. Khanna, and B.K. Rao (Kluwer Academic Publishers, Dordrecht, 1992).
11. M. Pellarin, E. Cottancin, B. Baguenard, J. Lermé, J.L. Vialle, and M. Broyer, *Phys. Rev.* B **52**, 16807 (1995).
12. T.P. Martin, *Phys. Rep.* **273**, 199 (1996).
13. F. Kassubek, C.A. Stafford, and H. Grabert, *Phys. Rev.* B **59**, 7560 (1999).
14. C. Höppler and W. Zwerger, *Phys. Rev.* B **59**, R7849 (1999).
15. C. Yannouleas, E.N. Bogachek, and U. Landman, *Phys. Rev.* B **57**, 4872 (1998).
16. F. Kassubek, C.A. Stafford, H. Grabert, and R.E. Goldstein, *Nonlinearity* **14**, 167 (2001).
17. A.I. Yanson, I.K. Yanson, and J.M. van Ruitenbeek, *Nature* **400**, 144 (1999).
18. A.I. Yanson, *PhD thesis*, Universiteit Leiden, The Netherlands, (2001).
19. J.M. van Ruitenbeek in *Mesoscopic Electron Transport*, eds. L.L. Sohn, L.P. Kouwenhoven, and G. Schön, (Kluwer Academic Publishers, Dordrecht, 1997).
20. J.A. Torres, J.I. Pascual, and J.J. Sáenz, *Phys. Rev.* B **49**, 16581 (1994).
21. A.I. Yanson, I.K. Yanson, and J.M. van Ruitenbeek, *Phys. Rev. Lett.* **84**, 5832 (2000).
22. T.P. Martin, S. Bjørnholm, J. Borggreen, C. Bréchignac, Ph. Cahuzac, K. Hansen, and J. Pedersen, *Chem. Phys. lett.* **186**, 53 (1991).
23. W.A. de Heer. *Rev. Mod. Phys.* **65**, 611 (1993).
24. A.I. Yanson, I.K. Yanson, and J.M. van Ruitenbeek, *to be published*, (2001).

KONDO TUNNELING THROUGH A BIASED DOUBLE QUANTUM DOT

YSHAI AVISHAI and KONSTANTIN KIKOIN
Ilse Katz Center for Nanotechnology, Ben-Gurion University of the Negev, 84105 Beer-Sheva, Israel

Abstract

Electron tunneling through a system formed by two coupled quantum dots in a parallel geometry is considered within a generalized Anderson model. The dots are assumed to have nearly equal radii but different (and tunable) gate voltages. In the absence of tunneling to and from the leads, the isolated two-dot system (with two electrons in it) resembles an hydrogen molecule within the Heitler London approximation. In particular, it has a singlet ground state and low lying excited triplet state. When tunneling is switched on, and when the gate voltages are properly tuned the ground state becomes a triplet and singlet and triplet states are intermixed. In the region where charge fluctuations are suppressed, the pertinent antiferromagnectic exchange interaction has the form $(J^T\mathbf{S} + J^{ST}\mathbf{P})\cdot\mathbf{s}$. It is written in terms of the electron spin $\mathbf{s}$, the double dot spin 1 operator $\mathbf{S}$ and an additional vector operator $\mathbf{P}$. The operators $\mathbf{S}$ and $\mathbf{P}$ generate the algebra o_4 of a spin rotator. The related Kondo effect is similar to that of a vertical quantum dot, discussed and analyzed recently.

1 Introduction

Experimental discovery of resonance Kondo tunneling through quantum dots under strong Coulomb blockade[1] is an impressive recent result in the physics of nanostructures. The observation of Kondo-like zero bias anomaly in the tunneling current through planar GaAs/GaAlAs quantum dot (QD) with odd electron occupation and a net spin $S = 1/2$ confirmed earlier theoretical predictions [2]. A natural question then arose whether the Kondo tunneling is possible when the number of electrons in the dot is even, so that the nominal spin of an isolated QD is zero. Some experimental data were consistent with the occurrence of Kondo resonance also in that case[3]. Of course, the simple reason for Kondo scattering in this case is the triplet ground state which can be realized provided the exchange interaction compensates the energy δ_e of excitation of one electron from the last doubly occupied state. Another compensation mechanism is the Zeeman splitting of excited triplet state in external in-plane magnetic field B [4,5]. In this case Kondo resonance in electron tunneling should be observed at a specific value of Zeeman energy $E_Z = g\mu_b B = \delta_e$. Unlike the conventional Kondo mechanism, this effect arises under a condition of broken rotational invariance in spin space, and the tunneling induced singlet-triplet mixing is shown to be the source of Kondo-like resonance. The experimental observation of Kondo tunneling in even Coulomb blockade windows at $B = 1.36$ T in QD formed in nanotube [6] confirmed these theoretical predictions.

Another interesting possibility of realization of Kondo tunneling in QD with even electron occupation arises when the low-energy part of its spectrum consists of spin singlet, spin triplet and singlet charge transfer exciton [7]. It was shown in the above paper that such spectrum arises in double quantum dots (DQD) provided this kind of nanostructure consists of two wells of different depth and the tunneling is allowed only through the "shallow" well with larger radius and smaller Coulomb charging energy Q. In this case, the singlet-triplet crossover is an *intrinsic* property of nanoobject in a contact with metallic leads, which arises even at zero magnetic field. This artificial molecule has a natural prototype: the low-energy part of the electron spectrum of complex molecules in which a rare-earth ion is secluded in a carbon cage has the above mentioned structure provided the covalent chemical bonds exist between the f-electron of a rare-earth ion and p-electrons of carbon cage. Cerocene $Ce(C_8H_8)_2$ is a known example of such double-shell molecule[8]. Being adsorbed on a metallic substrate this molecule is expected to demonstrate the Kondo-type behavior.

12

2 Effective spin hamiltonian for biased DQD

In the present research we study the tunneling through DQD formed by two dots of nearly equal radii in a parallel geometry (Fig.1) with two separate gates generating voltages $V_g^{l,r}$. Such setups were fabricated several years ago [9]. If only one of the tunnel channels (say, left)

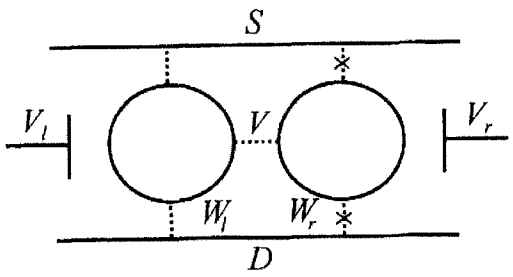


Figure 1: Double quantum dot in a parallel geometry.

between the dot and the lead is open (the inter-dot tunneling $V = 0$, the tunnel coupling between the right dot and the leads $W_r = 0$), we are left with the "electrometer" configuration when the tunneling through the left well is controlled by the charge state in the right well. The Coulomb blockade windows between the resonances in the Coulomb energy of the dot $\mathcal{E}_{\nu_r,\nu_l}(V_g^r, V_g^l)$ form a honeycomb pattern where the vertices connect the windows with charge configurations $(\nu_r, \nu_l), (\nu_r, \nu_l - 1), (\nu_r + 1, \nu_l - 1)$. The lines $\mathcal{E}_{\nu_l,\nu_r} \approx \mathcal{E}_{\nu_l+1\nu_r}$, are the regions where the Coulomb resonance induced by V_g^r allows tunneling through the left dot [9].

We consider the tunneling through DQD where the source – drain current is allowed only through the left dot, but the tunnel coupling with the right dot controls the spin degrees of freedom of the DQD. The case of DQD occupied by two electrons in its ground state is studied assuming that both left and right dots are neutral at $\nu_r = \nu_l = 1$. Then the isolated DQD under strong Coulomb blockade conditions reminds, in some respect, the hydrogen molecule in the Heitler-London approximation. This system is described by a generalized Anderson tunneling Hamiltonian

$$\begin{aligned} H &= \sum_{i=l,r}\sum_{\sigma}\epsilon_i n_{i\sigma} + V\sum_{i\neq j} d_{i\sigma}^{\dagger} d_{j\sigma} + \frac{1}{2}\sum_i Q_i n_i(n_i - 1) \\ &+ \sum_{k\sigma\alpha}\varepsilon_{k\sigma\alpha} c_{k\sigma\alpha}^{\dagger} c_{k\sigma\alpha} + \sum_{k\sigma}\left(W_l c_{k\sigma}^{\dagger} d_{l\sigma} + H.c.\right) \end{aligned} \tag{1}$$

Here the quantized energy levels of electrons in the dots $\epsilon_i = \varepsilon_i + V_g^i$ are biased by the gate voltages, the Coulomb blockade energies are assumed to be the same for both dots, $Q_l = Q_r = Q$, $\varepsilon_{k\sigma\alpha}$ are the band energies of the electrons in the leads, $\alpha = s, d$ stands for electrons from the source and drain electrodes, $c_{k\sigma} = 2^{-1/2}(c_{k\sigma,s} + c_{k\sigma,d})$, $W_{ki} = W_{k\alpha,i}/(W_{ks,i}^2 + W_{kd,i}^2)^{1/2}$.

We are interested in the case when the artificial Heitler-London molecule is strongly biased by the gate voltages so that $\mathcal{E}_{2,2} - \mathcal{E}_{1,2} \gg \mathcal{E}_{1,2} - \mathcal{E}_{1,1}$, but still $\beta \equiv V/(\mathcal{E}_{1,2} - \mathcal{E}_{1,1}) \ll 1$ (Fig.2). In this case the dot Hamiltonian (first three terms in eq. (1)) may be easily diagonalized, and the lowest three levels are

$$E_S = \epsilon_l + \epsilon_r - 2\beta V, \quad E_T = \epsilon_l + \epsilon_r, \quad E_R = 2\varepsilon_r + Q + 2\beta V \tag{2}$$

The small parameter is $\beta = V/(Q - \epsilon_l + \epsilon_r)$ expressed in terms of the coupling parameters entering the Hamiltonian (1) (see Fig.2). The gate voltage $V_g^l - V_g^r$ is applied in such a way that the spin and charge degrees of freedom are nearly separate in isolated DQD, i.e. the

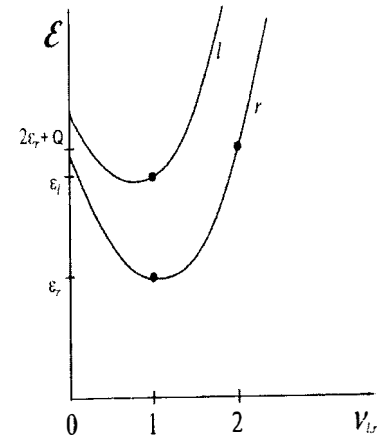


Figure 2: Electrostatic energy of the right (r) and left (l) dot as a function of electron occupation numbers ν_r and ν_l.

energy of charge transfer exciton $E_R - E_S = Q - \epsilon_l + \epsilon_r + 4\beta V$ substantially exceeds the energy of spin exciton $E_T - E_S = 2\beta V$.

If the tunnel coupling between the DQD and the metallic leads is also small, $W_l/(E_R - E_S) \ll 1$, only the singlet-triplet excitations are involved in forming the tunnel transparency of the left dot. In spite of the occurrence of singlet ground state, the Kondo-like processes involving the triplet exciton are possible, and one can expect the corresponding anomalies provided the characteristic Kondo temperature T_K is comparable with the energy $2\beta V$ of singlet-triplet excitation in DQD [7]. To study the low-energy anomalies we use the Haldane-Anderson renormalization group (RG) approach [10]. According to this method the Hamiltonian (1) diagonalized in accordance with (2) is rescaled by absorbing the high-energy excitations of order D_0 (where D_0 is the width of conduction band) in the renormalized parameters of this Hamiltonian at reduced $D = D_0 - \delta D$. It is known that one can neglect renormalization of the tunneling constant W_l in comparison with rescaling of the energy levels E_S and E_T. The scaling equations are

$$dE_\Lambda/d\ln D = \Gamma_\Lambda/\pi, \tag{3}$$

where $\Lambda = S, T$. The tunnel coupling constants $\Gamma_\Lambda = \pi\rho_0|\langle 0|c_{k\sigma}d_{k\sigma'}|W_l|\Lambda\rangle|^2$ are *different* for singlet and triplet states because the singlet exciton (ρ_0 is the density of states in the leads). In other words, the doubly occupied right dot state $|ex_r\rangle = d^\dagger_{r\uparrow}d^\dagger_{r\downarrow}|0\rangle$ is admixed to the bare singlet $|s\rangle = \frac{1}{\sqrt{2}}\sum_\sigma \sigma d^\dagger_{l\sigma}d^\dagger_{r\bar{\sigma}}|0\rangle$ by inter-dot tunneling, whereas the triplet states $|t_0\rangle = \frac{1}{\sqrt{2}}\sum_\sigma d^\dagger_{l\sigma}d^\dagger_{r\bar{\sigma}}|0\rangle$, $|t_\sigma\rangle = d^\dagger_{l\sigma}d^\dagger_{r\sigma}|0\rangle$ are not affected by this tunneling,

$$|S\rangle = (1-\beta^2)|s\rangle + \sqrt{2}\beta|ex_r\rangle,\ |T0\rangle = |t_0\rangle,\ |T\pm\rangle = |t_\pm\rangle. \tag{4}$$

As a result $\Gamma_S/\Gamma_T = 1 - 2\beta^2 < 1$. Due to this relation the scaling trajectories $E_\Lambda(D)$ determined by the scaling invariants for eq. (3) may intersect at a point D_c estimated as

$$\frac{\Gamma_T - \Gamma_S}{\pi}\ln\frac{\pi D_0}{D_c} = E_T(D_0) - E_S(D_0) \equiv \delta_0. \tag{5}$$

According to numerical calculations of Ref. [7], this level crossing can occur either before or after the crossover to a Schrieffer-Wolff regime when the one-electron energies $E_{\mathbf{\Lambda}}(D) - E_{1b}$ exceed the half-width of reduced continuum band, $\bar{D} \sim |E_{\mathbf{\Lambda}}(\bar{D}) - E_{1b}|$. In both cases the charge degrees of freedom are quenched for the excitation energy within the interval $-\bar{D} < \varepsilon < \bar{D}$. Then, integrating out the residual charge excitations (tunneling transitions to the states with one and three electrons in the DQD) one comes to an effective Hamiltonian including only spin degrees of freedom,

$$\tilde{H} = \sum_{\Lambda=S,T} \bar{E}_\Lambda X^{\Lambda\Lambda} + \sum_{\langle k\rangle\sigma} \epsilon_k c^\dagger_{k\sigma} c_{k\sigma} + \sum_{\mathbf{\Lambda\Lambda'}\lambda} \sum_{kk'\sigma\sigma'} J^{\Lambda\Lambda'} X^{\mathbf{\Lambda\Lambda'}} c^\dagger_{k\sigma} c_{k'\sigma'} \tag{6}$$

where $\bar{E}_\Lambda = E_\Lambda(\bar{D})$, $J^{\Lambda\Lambda'} \approx 2\sqrt{|\Gamma_\Lambda \Gamma_{\Lambda'}|}/(\varepsilon_F - \bar{\epsilon}_l)$, $X^{\mathbf{\Lambda\Lambda'}} = |\Lambda\rangle\langle\mathbf{\Lambda'}|$ is a configuration change operator, $\bar{\epsilon}_l = \epsilon_l(\bar{D})$ includes the above RG operation, $\langle \boldsymbol{k}\rangle$ are the states inside the reduced conduction band.

Unlike conventional Schrieffer-Wolff Hamiltonian for a local spin that arises as a result of RG procedure [10], the effective Hamiltonian (6) contains also the singlet term with renormalized energy $\bar{E}_S$ and the effective interaction with coupling constant J^{ST} intermixing singlet and triplet states of DQD. The coupling constants are connected by the relations $J^S = \alpha^2 J^T$, $J^{ST} = \alpha J^T$ $(\alpha = 1 - \beta^2)$. This means that the Heitler-London type DQD possesses the symmetry of a ***spin rotator***, i.e. that its algebra o_4 is described by two vectors $\mathbf{S}$ and $\mathbf{P}$ with spherical components

$$\begin{aligned} &S^+ = \sqrt{2}\left(X^{10} + X^{0,-1}\right),\ S^- = \sqrt{2}\left(X^{01} + X^{-1,0}\right),\ S_z = X^{11} - X^{-1,-1}, \\ &P^+ = \sqrt{2}\left(X^{1S} - X^{S,-1}\right),\ P^- = \sqrt{2}\left(X^{S1} - X^{-1,S}\right),\ P_z = -\left(X^{0S} + X^{S0}\right) \end{aligned} \tag{7}$$

obeying the commutation relations

$$[S_j, S_k] = ie_{jkl}S_l,\ [P_j, P_k] = ie_{jkl}S_l,\ [P_j, S_k] = ie_{jkl}P_l$$

$(j, k, l$ are Cartesian coordinates). These vectors are orthogonal, $\mathbf{S}\cdot\mathbf{P} = 0$, and the Casimir operator is $\mathbf{S}^2 + \mathbf{P}^2 = 3$. In terms of these operators the interaction term in the effective Hamiltonian acquires a symmetric form,

$$\tilde{H}_{int} = J^T(\mathbf{S}\cdot\mathbf{s}) + J^{ST}(\mathbf{P}\cdot\mathbf{s}) + \frac{J_T}{2}\sum_{\mu\sigma} X^{\mu\mu} n_\sigma, \tag{8}$$

where the local electron operators are defined as

$$n_\sigma = c^\dagger_\sigma c_\sigma = \sum_{kk'} c^\dagger_{k\sigma} c_{k\sigma},\ \ \mathbf{s} = 2^{-1/2}\sum_{kk'}\sum_{\sigma\sigma'} c^\dagger_{k\sigma}\hat{\tau} c_{k'\sigma'}.$$

($\hat{\tau}$ is the Pauli matrix).

3 Kondo tunneling

If the inequality $\bar{D} < D_c$ is satisfied, the triplet becomes the lowest state of the DQD, i.e., $\bar{\delta} = \bar{E}_T - \bar{E}_S < 0$, and a Kondo screening for $S = 1$ should emerge. However, the Anderson-type scaling equations for the parameters $J(D)$ involve both J^T and J^{ST}. In dimensionless variables $j_1 = \rho_0 J^T, j_2 = \rho_0 J^{ST}, d = \rho_0 D$ these equations are written as

$$dj_1/d\ln d = -\left[(j_1)^2 + (j_2)^2\right],\ \ dj_2/d\ln d = -2j_1 j_2. \tag{9}$$

Such quasi degeneracy of triplet and singlet states was discussed previously in relation to the physics of tunneling through vertical quantum dots [11], planar QD occupied by even number of electrons [5] and strongly asymmetric DQD containing two dots of essentially different radii [7]. In the first two cases the singlet-triplet degeneracy is induced by an external magnetic field, while in the third case the asymmetry is an intrinsic property of the DQD. In the case under consideration here, the desired asymmetry is induced by the asymmetric

gate voltage. Analysis of the scaling equations (9) shows that both **S** and **P** operators are involved in anomalous Kondo scattering in a case when $\bar{\delta} < T_K$. Then the scaling equations (9) are reduced to a single equation for the reduced exchange parameter $j_+ = j_1 + j_2$

$$dj_+/d\ln D = -(j_+)^2 \tag{10}$$

with a fixed point at $j_+ = \infty$ and the Kondo temperature $T_{K0} = \bar{D}\exp(-1/j_+)$. This is a Kondo temperature of a spin rotator, having the rotational symmetry $SO(4)$. The spin symmetry of DQD is reduced together with the Kondo temperature in the case $\bar{\delta} \gg T_K$. Then the singlet-triplet coupling j_2 is quenched at energies $D \sim \bar{\delta}$, so the low-energy spectrum is determined by the $S = 1$ triplet state. The Kondo temperature at large $\bar{\delta}$ is a function of $\bar{\delta}$ which obeys the law $T_K/T_{K0} = (T_{K0}/\bar{\delta})^{\lambda}$, where λ is a universal numerical constant [5].

The Kondo-type zero bias anomaly in conductance arises when $\bar{\delta} < 0$ and the DQD is in a state with S=1. It growth with temperature as $G \sim \ln^{-2}[T/T_K(\bar{\delta})]$ for $|\bar{\delta}| \gg T \gg T_K(\bar{\delta})$ and as $G \sim \ln^{-2}[T/T_{K0}]$ for $T \gg T_{K0} \gg \bar{\delta}$. At $T \to 0$ the conductance tends to the unitarity limit $G_0 = 2e^2/\pi\hbar$.

Thus one arrives at the following picture of rearrangement of the low-energy spectrum of DQD occupied by two electrons in a parallel geometry (Fig.1) under external bias. In a symmetric case $V_g^l = V_g^r$ the isolated system possesses an axial symmetry and a singlet ground state (Heitler-London type artificial molecule). Its spin spectrum consists of singlet-triplet excitations, and the singlet state is stabilized by the indirect exchange energy $E_T - E_S = V^2/Q$ (Fig. 3a). Two singlet charge excitons (even and odd) corresponding to symmetric and asymmetric combination of the polar states $d_{i\uparrow}^{\dagger} d_{i\downarrow}^{\dagger}|0\rangle$ $(i = l, r)$ are separated by a large energy gap Q from the spin exciton. The level renormalization (3) is the same for the singlet and triplet states because the charge transfer excitations are axially symmetric in this case. The only possibility to open a Kondo channel is achievable by a trivial switching off the interdot tunneling ($V \to 0$). Then the singlet-triplet gap also tends to zero, and when it becomes less than T_K for the left dot, the latter behaves as conventional $S = 1/2$ QD with odd occupation. The axial symmetry is broken when $V_g^l - V_g^r > 0$, and the "right" exciton E_R then softens (Fig. 3b). The system acquires the symmetry of a spin rotator described

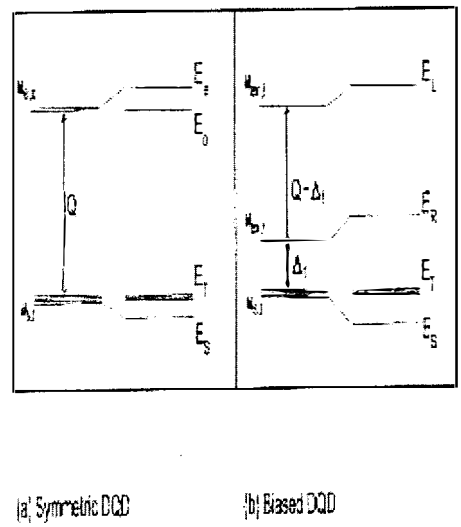


Figure 3: Electron levels of double quantum dot at zero (a) and non-zero (b) value of $V_g^r - V_g^l$.

by the semi-simple Lie group $SO(4)$ with triplet exciton mixed with the singlet ground state

due to the tunneling interaction with the leads. When the condition (5) and the inequality $\tilde{D} < D_c$ are valid, the ground state of DQD becomes a triplet and it behaves as an underscreened $S = 1$ Kondo center with zero bias anomaly of the conductance. Thus, the charge excitations in the right dot that is not involved directly in the source-drain tunneling can drive the spin excitations in the left dot and induce the Kondo resonance in a DQD with even occupation.

4 References

1. D. Goldhaber-Gordon *et.al.,* Phys. Rev. Lett. **81**, 5225 (1998); S.M. Cronenwett *et al.,*, Science, **281**, 540 (1998); F. Simmel *et al.,* Phys. Rev. Lett. **83**, 804 (1999).
2. L.I. Glazman and M.E. Raikh, JETP Lett. **47**, 452, (1988); T.K. Ng and P.A. Lee, Phys. Rev. Lett., **61**, 1768 (1988).
3. L.P. Rokhinson, et al., Phys. Rev. B **60**, 16319 (2000); J. Schmid, et al., Phys. Rev. Lett. **84**, 5824 (2000).
4. M. Pustilnik, Y. Avishai and K. Kikoin, Phys. Rev. Lett. **84**, 1756 (2000).
5. M. Pustilnik and L. Glazman, Phys. Rev. Lett. **85**, 2993 (2000); cond-mat/0102458.
6. J. Nygård, D.H. Cobden and P.E. Lindelof, Nature **408**, 342 (2000).
7. K. Kikoin and Y. Avishai, Phys. Rev. Lett. **86**, 2090 (2001).
8. W. Liu et al, J. Chem. Phys. **107**, 3584 (1997).
9. L.W. Molenkamp et al, Phys. Rev. Lett. **75**, 4282 (1995); F. Hofmann et al, Phys. Rev. B**51**, 13872 (1995).
10. A.C. Hewson, *The Kondo Problem to Heavy Fermions* (Cambridge University Press, Cambridge) 1993
11. D. Giuliano and A. Tagliacozzo, Phys. Rev. Lett. **84**, 4677 (2000); M. Eto and Yu.V. Nazarov, Phys. Rev. Lett. **85**, 1306 (2000).

DYNAMICAL COULOMB BLOCKADE IN QUANTUM POINT CONTACTS

R. CRON[2], E. VECINO[1], M.H. DEVORET[2], D. ESTEVE[2], P. JOYEZ[2], A. LEVY YEYATI[1], A. MARTIN-RODERO[1] AND C. URBINA[2]

The influence of the electromagnetic environment on the current-voltage characteristic of a quantum point contacts is studied both theoretical and experimentally. We use a scattering approach to describe the coupling of the electron states with the environmental modes. In the weak blockade regime the Coulomb blockade is found to be directly related to current fluctuations in the contact, vanishing at perfect transmission in the same way as shot noise. For the experimental test we use aluminum atomic contacts embedded in a well characterized electromagnetic environment. The preliminary results seem to support the theoretical predictions

1 Introduction

A fundamental issue in nanoelectronics is the understanding of the quantum circuit rules. For example, what is the total conductance of the series arrangement of a nanoscale element, having by itself a certain IV characteristics, with a macroscopic impedance? In the case of an ultrasmall tunnel junction it is well known that the conductance of the series circuit is suppressed at sufficiently low voltage and temperature [1,2]. This phenomenon, called environmental or dynamical Coulomb blockade has been extensively studied in various systems [3]. The aim of the present work is to investigate, both theoretically and experimentally, how this phenomenon is modified when the tunnel junction is replaced by a point contact with a reduced number of conduction channels, whose transmissions can take an arbitrary value between zero and one.

In a recent work [4], we have shown that environmental Coulomb blockade in a single channel contact is directly connected to the current fluctuations in the contact itself using the Keldysh perturbation theory for non-equilibrium situations. We found in particular that Coulomb blockade vanishes at perfect transmission in the same way as shot noise. In the present work we show that the same results can be obtained using a simpler scattering approach, and we present a preliminary experimental test of these predictions obtained on atomic-size contacts. Atomic-size contacts are indeed well-suited for that purpose because they can have a small number of conduction channels whose transmissions can be accurately determined from the current-voltage characteristic in the superconducting state.

The paper is organised as follows: In section II we present the scattering formalism for a quantum point contact (QPC) coupled to an electromagnetic environment characterized by a generic impedance $Z(\omega)$. In section III we calculate the correction to the current-voltage characteristic due to the coupling with the environment in the weak blockade regime ($Z < 1/G_0$, where $G_0 = 2e^2/h$) and give explicit results for the ohmic case. Finally, we present in section IV our experimental results and compare them to the predictions.

2 The scattering approach

In Ref. [4] the contact was described by a Hamiltonian with a single hopping term connecting both electrodes, which allowed to introduce the coupling with the environment as in the case of tunnel junctions [1]. The current voltage characteristic of the coupled system was then calculated. It was argued that the validity of the result was not restricted to the particular model used to describe the contact. In the present work, we follow the usual approach to describe the QPC in terms of scattering states [5]. We assume that the QPC is connected to the left and right electrodes through perfect leads with the same number of modes M below de Fermi energy. Let us call $\hat{a}^{\dagger}_{m\sigma,\mu}(E)$ and $\hat{b}^{\dagger}_{m\sigma,\mu}(E)$ the creation operator for an electron in an incoming or an outgoing scattering state on mode m with spin σ at lead μ ($\mu \equiv L, R$) with energy E. These two set of operators are

connected by the QPC scattering matrix, through the relation $\hat{b}_{m\sigma,\mu}(E) = \sum_{n,\nu} s_{nm,\mu\nu}(E)\hat{a}_{n\sigma,\nu}$. The current operator on lead μ is then given by [5]

$$\hat{I}_{\mu}(t) = \frac{e}{h}\sum_{m,\sigma}\int d\epsilon_1 d\epsilon_2 e^{i(\epsilon_1-\epsilon_2)t/\hbar}\left[\hat{a}^{\dagger}_{m\sigma,\mu}(\epsilon_1)\hat{a}_{m\sigma,\mu}(\epsilon_2) - \hat{b}^{\dagger}_{m\sigma,\mu}(\epsilon_1)\hat{b}_{m\sigma,\mu}(\epsilon_2)\right]. \quad (1)$$

This expression can be written completely in terms of $\hat{a}$ operators by means of the scattering matrix. For the sake of simplicity we shall concentrate in the case of a single channel contact with transmission τ (the generalization to the multichannel case is straightforward). The current operator $\hat{I}(t) = \hat{I}_L(t) = -\hat{I}_R(t)$, in terms of the incoming states adopts the form

$$\begin{aligned}\hat{I}(t) &= \frac{e}{h}\sum_{\sigma}\int d\epsilon_1 d\epsilon_2 e^{i(\epsilon_1-\epsilon_2)t/\hbar}\left\{\tau\left[\hat{a}^{\dagger}_{\sigma,L}(\epsilon_1)\hat{a}_{\sigma,L}(\epsilon_2) - \hat{a}^{\dagger}_{\sigma,R}(\epsilon_1)\hat{a}_{\sigma,R}(\epsilon_2)\right]\right. \\ &\left. + i\sqrt{\tau(1-\tau)}\left[\hat{a}^{\dagger}_{\sigma,R}(\epsilon_1)\hat{a}_{\sigma,L}(\epsilon_2) - \hat{a}^{\dagger}_{\sigma,L}(\epsilon_1)\hat{a}_{\sigma,R}(\epsilon_2)\right]\right\}. \quad (2)\end{aligned}$$

Let us now discuss the coupling to the environmental modes. We can associate a fluctuating vector potential $\mathbf{A}(r,t)$ to the electromagnetic modes in the environment. This potential modifies the Hamiltonian for the electrons in the QPC through the kinetic term by the replacement of the momentum $\vec{p}$ by $\mathbf{p} - \frac{e}{c}\mathbf{A}$. We are not interested in the detailed spatial behaviour of $\mathbf{A}$ (which would require a detailed knowledge of the contact geometry). Instead, the only relevant feature is that the phase given by $\delta\phi(x) = \frac{e}{c\hbar}\int^x dx'\mathbf{A}(x')$, varies from zero to a finite value ϕ_0 when traversing the contact region, which is usually modeled by just a step function (in a tight-binding Hamiltonian description this corresponds to the phase factors in the hopping elements). The scattering matrix is modified by the presence of the vector potential through a phase factor $e^{i\phi_0}$ affecting the transmission amplitudes. Up to second order in $\mathbf{A}$ we thus obtain

$$\delta\hat{H}_{QPC} = \frac{\hbar}{e}\left[\phi_0\hat{I} + \frac{\phi_0^2}{2}\left(\frac{\partial\hat{I}}{\partial\phi_0}\right)_{\phi_0=0}\right], \quad (3)$$

where we have used the Hamilton equation $\hat{I} = \frac{e}{\hbar}\frac{\partial\hat{H}_{QPC}}{\partial\phi_0}$. The derivative in the second order term has the expression

$$\left(\frac{\partial\hat{I}}{\partial\phi_0}\right)_{\phi_0=0} = -\frac{c}{h}\sum_{\sigma}\int d\epsilon_1 d\epsilon_2 e^{i(\epsilon_1-\epsilon_2)t/\hbar}\sqrt{\tau(1-\tau)}\left[\hat{a}^{\dagger}_{\sigma,R}(\epsilon_1)\hat{a}_{\sigma,L}(\epsilon_2) + \hat{a}^{\dagger}_{\sigma,L}(\epsilon_1)\hat{a}_{\sigma,R}(\epsilon_2)\right]. \quad (4)$$

It is important to point out that the current operator itself is modified due to the presence of the fluctuating field

$$\delta\hat{I} = \phi_0\left(\frac{\partial\hat{I}}{\partial\phi_0}\right)_{\phi_0=0} + \frac{\phi_0^2}{2}\left(\frac{\partial^2\hat{I}}{\partial\phi_0^2}\right)_{\phi_0=0}. \quad (5)$$

In order to take into account quantum fluctuations due to the environment we now consider ϕ_0 as a quantum operator $\hat{\phi}_0$, whose dynamics is determined by a Hamiltonian $\hat{H}_{env}$, which represents the environment as a set of harmonic oscillators [2].

3 *IV* curve in the weak blockade regime

The simplest but still meaningful limit to be analyzed is the weak blockade regime in which the environment impedance Z is small compared to $1/G_0$ and the coupling to the environment can

be treated in a perturbative way. The correction to the current up to the second order in the fluctuating phase ϕ_0 can be obtained using the following expression

$$\begin{aligned}\delta I &= <\delta\hat{I}> + \frac{1}{i\hbar}\int_0^\infty dt <\left[\hat{I}(t)+\delta\hat{I}(t), \delta\hat{H}_{QPC}(0)\right]> \\ &\quad -\frac{1}{\hbar^2}\int_0^\infty dt_1 \int_0^{t_1} dt_2 <\left[\left[\hat{I}(t_1), \delta\hat{H}_{QPC}(t_2)\right], \delta\hat{H}_{QPC}(0)\right]> . \end{aligned} \tag{6}$$

The term $<\delta\hat{I}>$ clearly vanishes. The evaluation of the remaining expression requires the calculation of the commutators $\left[\hat{I}(t_1), \hat{I}(t_2)\right]$. Using expression (2) one can show that

$$\begin{aligned}\left[\hat{I}(t_1), \hat{I}(t_2)\right] &= \left(\frac{e}{\hbar}\right)^2 \sum_\sigma \int d\epsilon_1 \int d\epsilon_2 \left[\int d\epsilon_3 e^{i(t_1-t_2)\epsilon_3/\hbar}\tau\right]\left(e^{-i\epsilon_1 t_1 + i\epsilon_2 t_2} - e^{i\epsilon_2 t_1 - i\epsilon_1 t_2}\right) \\ &\quad \times \left[\hat{a}^\dagger_{\sigma,R}(\epsilon_1)\hat{a}_{\sigma,R}(\epsilon_2) + \hat{a}^\dagger_{\sigma,L}(\epsilon_1)\hat{a}_{\sigma,L}(\epsilon_2)\right] . \end{aligned} \tag{7}$$

Thus, when the energy dependence of the transmission is neglected, the integration over ϵ_3 can be performed trivially and the commutator in (7) vanishes. It remains to evaluate the second term in (6). A straightforward calculation leads then to

$$\delta I = \tau(1-\tau)\frac{e}{h^2}\int_{-\infty}^{\infty} dt J(t) \int d\epsilon_1 d\epsilon_2 e^{-i(\epsilon_1-\epsilon_2)t/\hbar}\left[f_R(\epsilon_1)\left(1-f_L(\epsilon_2)\right) - f_L(\epsilon_1)\left(1-f_R(\epsilon_2)\right)\right], \tag{8}$$

where $f_{L,R}(\epsilon)$ denotes the Fermi function on the left and right electrodes and $J(t)$ is the phase correlation function given by

$$J(t) = <\hat{\phi}_0(t)\hat{\phi}_0(0)> - <\hat{\phi}_0^2> . \tag{9}$$

The result (8) is completely equivalent to the one obtained in Ref. [4] for the case of a single channel contact with energy independent transmission. As stated in [4] this expression establishes a close relationship between environmental Coulomb blockade and shot noise [6].

In order to obtain more specific results the relation between the phase correlation function $J(t)$ and the environment impedance $Z(\omega)$ is needed. This is given by [2]

$$J(t) = G_0 \int d\omega \frac{\mathrm{Re}Z(\omega)}{\omega}\frac{e^{i\omega t}-1}{1-e^{-\beta\hbar\omega}}. \tag{10}$$

From Eq. (8) one can then obtain the relative reduction of the differential conductance at finite temperature

$$\frac{\delta G}{G} = 2(1-\tau)\int_0^{+\infty} \frac{dt}{\hbar\beta}\frac{\pi t}{\hbar\beta}\mathrm{Im}J(t)\cos\frac{eVt}{\hbar}\mathrm{csch}^2\frac{\pi t}{\hbar\beta}, \tag{11}$$

where $\beta = 1/k_B T$. Notice that this result is equivalent to the corresponding one for a tunnel junction in series with an impedance [7] except for the extra Fano factor $1-\tau$. For practical applications, a particularly relevant case is that of an ohmic environment in which $Z(\omega)$ is determined by the series resistance R in paralel with the capacitance of the contact itself, i.e. $Z(\omega) = R/(1+i\omega RC)$. In this case $\mathrm{Im}J(t) = 2\pi RG_0\left(e^{-t/RC}-1\right)$ is independent of temperature and the evaluation of (11) is straightforward.

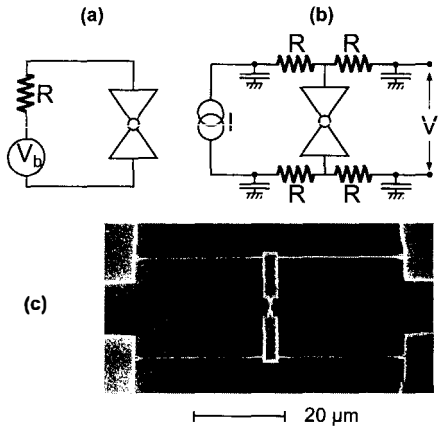


Figure 1: (a) Principle of the experiment : an atomic contact (right symbol) is placed in series with a pure resistor. (b) Actual implementation : the differential conductance of the atomic contact is measured using in a 4-point setup, each lead including a resistor and a large shunt capacitor (~100 pF) to ground. The equivalent circuit impedance as seen from the atomic contact closely matches that of (a) at all relevant frequencies, with $R = 920\ \Omega$. (c) Electron micrograph showing details of the sample. The atomic contact is formed at the constriction in the center of the picture, and the four resistors are the narrow strips connecting the atomic contact to the rest of the circuit (see text for fabrication details).

4 Comparison with existing experimental results

We now present a preliminary experimental test of the above predictions, obtained on atomic-size contacts. It is by now well established that atomic-size constrictions between two metallic electrodes accommodate a small number of conduction channels with distributed transmissions that can be precisely determined using the non-linearities caused by multiple Andreev reflections on the I-V characteristic in the superconducting state [9]. Actually, atomic size contacts are a nearly ideal test-bed for mesoscopic models that express transport quantities in terms of channel transmissions. They have already been used to test the predictions on shot noise in the normal [12] and superconducting state [12], and on the supercurrent [10].

To check our predictions on dynamical Coulomb blockade we have embedded an atomic contact in an electromagnetic environment essentially equivalent to a pure ohmic resistor of the order of 1 kΩ (see Figure 1). The atomic contact is inserted in a circuit consisting of four nominally identical resistors which allow a four-point measurement of the differential conductance of the contact while maintaining the desired impedance owing to large capacitors which close the circuit at all frequencies relevant to the experiment. The fabrication process is similar to that described in [11], making use of e-beam lithography and shadow mask evaporation. The material chosen for both the atomic contact and the resistors is aluminum. The resistors are made of 25 μm-long, thin (12 nm) and narrow (200 nm) strips evaporated at right angle; the remaining part of the circuit, much thicker (150 nm), is evaporated at angles of $\pm 40°$ so that the parasitic images of the resistors lay on the side of the resist mask and are removed during lift-off.

The sample is then mounted in a controlled-bending mechanical setup [11] and cooled down to mK temperatures. Contacts of various conductances are established by progressively bending the elastic substrate. Once established, the contacts remain stable for days and can withstand thermal cycling to 1.5 K and magnetic field cycling between normal and superconducting states. The channel content of a contact is obtained from the best fit of its I-V characteristic [9] in the superconducting state to the sum of the contributions of independent channels. Note however

that in the superconducting state the resistors have zero resistance at dc but a finite one above twice the gap frequency [8]. This residual resistance is expected to slightly modify the shape of the I-V characteristic, in a way which is however not yet quantitatively known. The induced distortion of the I-Vs makes the channel decomposition of the contacts less accurate than in previous experiments.

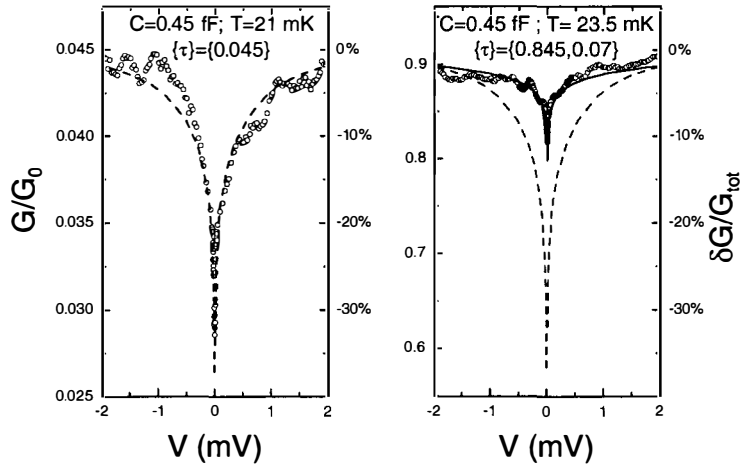


Figure 2: Measured differential conductance curves of two atomic contacts (symbols referred to the left axes, G_0 being the conductance quantum), and comparison with the predictions for the dynamic Coulomb blockade (lines, right axes, relative reduction of the conductance). Dashed lines are the predictions for the tunnel case [2] and the full line is the prediction of the present work (Eq. (11)), summing the contributions of the two channels of the contact. The wiggles and asymmetry appearing on the experimental curves are reproducible conductance fluctuations due to interference effects depending on the detailed arrangement of the atoms in the vicinity of the contact. On the left pannel, the contact consists of a single weakly transmitting channel, and it is well described by the standard theory of DCB valid for tunnel contacts, as expected. On the right pannel, the contact has a well transmitting channel with $\tau = 0.835$. In this case, the relative reduction of conductance is much less than in the tunnel case and in agreement with the predictions of Eq. (11).

In order to measure the dynamic Coulomb blockade, the sample is then placed in its normal state by applying a magnetic field of 0.2 T perpendicular to the plane of the sample. We have checked that in this field, aluminum thin films are in the normal state. The differential conductance of the contact is measured using a lock-in technique, slowly sweeping the dc bias. In Fig. 2 we show traces of these measurements for two different contacts. As expected, the standard theory of DCB in the tunnel regime applies well to the contact on the left panel which had a single channel with weak transmission of 4.5%. On the other hand, for the contact of the right panel, for which one channel had a transmission of $\simeq 0.83$, the relative amplitude of the dip in the differential conductance is markedly reduced compared to the weak transmission case (dashed line). A good qualitative agreement is recovered (full line) if one uses the results of the present work, summing the contributions of both channels calculated using Eq. (11). The comparison presented here involves two adjustable parameters. The first one is the capacitance of the atomic contact, taken as $C = 0.45$ fF for both contacts. This value closely corresponds to the geometric capacitance of the two banks of the atomic contact to the metallic substrate. The second parameter is the total conductance of the contact, *i.e.* the sum of all

channel transmissions. This adjustment is needed, because in the present experiment the total conductance cannot be obtained by measuring the differential conductance at large voltage due to the asymmetry appearing in the conductance curve on a large scale. The total conductance is adjusted by tuning the transmission of the most transmitting channel, on which the uncertainty of the value obtained by fitting the I-V is the greatest. We find that the adjustment needed (~2.5% for the right pannel contact) is compatible with the estimated uncertainty on the channel transmission.

The preliminary experimental data shown here thus seem to support the theoretical results presented above. Before drawing definitive conclusions one would need to check the temperature dependence predicted by Eq. (11), and to investigate contacts with other channel distributions.

Acknowledgments

This work was partially supported by BNM and MAE through PICASSO and the Spanish CICyT under contract PB97-0044.

References

1. M.H. Devoret et al., Phys. Rev. Lett. **64**, 1824 (1990); S.M. Girvin et al., Phys. Rev. Lett. **64**, 3183 (1990).
2. G.-L. Ingold and Yu.V. Nazarov in *Single Charge Tunneling*, edited by H. Grabert and M.N. Devoret (Plenum Press, New York, 1992).
3. A.N. Cleland, J.M. Schmidt and J. Clarke, Phys. Rev. Lett. 64, 1565 (1990); T. Holst, et al., Phys. Rev. Lett. **73**, 3455 (1994).
4. A. Levy Yeyati, A. Martin-Rodero, D. Esteve and C. Urbina, cond-mat/0102178.
5. M. Büttiker, Phys. Rev. B, **46**, 12485 (1992).
6. Coulomb blockade in a coherent conductor due to its own resistance has been recently addressed by D.S. Golubev and A.D. Zaikin, cond-mat/0010493. For this situation both theories yield similar results.
7. P. Joyez and D. Esteve, Phys. Rev. B. 56,1848 (1997).
8. M. Tinkham, Introduction to Superconductivity, Mc Graw-Hill.
9. E. Scheer et al. Phys. Rev. Lett. 78, 3535 (1997); E. Scheer et al., Nature 394, 154 (1998).
10. M. F. Goffman et al. Phys. Rev. Lett. 85, 170 (2000).
11. J. M. Ruitenbeek et al., Rev. Sci. Instr. 67, 108 (1996).
12. R. Cron, M. F. Goffman, D. Esteve and C. Urbina, Phys. Rev. Lett. 86 4104 (2001)

ELECTRON TRANSPORT IN MOLECULAR WIRES MEDIATED VIA POLARONS AND SOLITONS: COHERENT ELECTRON-PHONON INTERACTION

H. NESS, A.J. FISHER
Department of Physics and Astronomy, University College London, Gower Street, London WC1E 6BT, U.K.

We consider electron transport through one-dimensional molecular wires connected to two metallic electrodes. The molecules have a substantial band gap (gap between the Highest Occupied Molecular Orbital - HOMO and the Lowest Unoccupied Molecular Orbital - LUMO) arising from a Peierls transition due to strong electron-phonon interactions. At small biais, charge carriers can propagate from one electrode to the other by tunneling through the molecule's HOMO-LUMO gap. Owing to the electron-phonon coupling, polarons can be formed in the molecule, even in the tunneling regime. Polaron formation and propagation enhance the transmission through the molecule, especially in the tunneling regime. The presence of a midgap state due to other types of defect in the molecule, such as pre-existing solitons also affects the transport properties. We briefly discuss the effects of polaron-soliton interaction on the transport properties of the wires.

1 Introduction

With the recent developments in nanofabrication, the measurement of electron transport properties in mesoscopic physics can now be achieved on atomic/molecular-scale entities. The reduction from meso-scale down to nano-scale is a promising step toward miniaturization for new electronic devices based on atomic/molecular-scale wires. Such wires might be formed, for example, from individual organic molecules [1,2] or from atomic-scale structures produced on surfaces by atomic manipulation [3]. In such one-dimensional-like systems, the coupling between an electron and its environment (lattice vibration for instance) is strong, particularly if one focuses on the instability of one-dimensional metals towards Peierls distortion at low temperatures. Such a distortion is associated with the opening of a band-gap in an infinite system. In finite size molecular wires, one observes a substantial gap between the HOMO and the LUMO of the molecule; these electronic states are also strongly coupled to distortions of the atomic positions in the wire. When the wire is connected to electron reservoirs, for small applied bias electrons can propagate coherently through the wire within the HOMO-LUMO gap. This transport process involves a transient charging of the molecule which is expected to lead to similar behaviour to permanent charging due to doping. In particular, the induced lattice deformation (polaron formation for instance) should be similar for permanent charging (doping) or for transient charging (transport). However, since the transport occurs via tunneling, the conductance or electron transmission will be strongly dependent on any alteration of the gap due to induced lattice distortions. We therefore investigate the effects of the coupling between an injected tunneling electron and the lattice vibrations on the transport properties of one-dimensional molecular wires, by treating both the electron and phonon degrees of freedom on the quantum level.

2 Model systems

The model used for the molecular wire and the method used to calculate the electronic transport through the wire have already been described in detail elsewhere [4]. Below we briefly recall the main aspects of the method. The model for the molecular wire includes delocalized π-electrons along a one-dimensional chain which interact with quantum phonons. The electronic Hamiltonian is expressed in the basis set of the one-electron eigenstates (labelled by n) of the isolated molecule and the electron-phonon (*e-ph*) coupling is linear in the phonon displacements.

The Hamiltonian of the molecular wire is

$$H = \sum_n \epsilon_n c_n^\dagger c_n + \sum_\lambda \hbar\omega_\lambda a_\lambda^\dagger a_\lambda + \sum_{\lambda,n,m} \gamma_{\lambda nm}(a_\lambda^\dagger + a_\lambda) c_n^\dagger c_m, \quad (1)$$

where $c_n^\dagger$ (c_n) creates (annihilates) an electron in the n-th electronic state with energy ϵ_n and $a_\lambda^\dagger$ (a_λ) creates (annihilates) a quantum of energy $\hbar\omega_\lambda$ in the eigenmode of vibration λ of the isolated molecule. The values for the parameters are calculated from the ground state of the neutral isolated molecule. The molecule is taken to be the Su-Schrieffer-Heeger (SSH) model for a trans-polyacetylene molecular chain containing N monomers [5]. The vibrational eigenmodes V_λ and eigenvalues $\hbar\omega_\lambda$ of the molecule are calculated within the harmonic approximation for the atomic displacements [4,6].

In order to calculate the transport properties of the molecular wire, the left and right ends of the molecule are connected to metallic leads via hopping integrals $v_{L,R}$ respectively. The leads are modeled by one-dimensional semi-infinite rigid tight-binding chains with on-site energy $\epsilon_{L,R}$ and inter-site hopping matrix elements $\beta_{L,R}$. The transport through the system is tackled by mapping the many body (one-electron/many-bosons) problem onto a single electron problem with many channels [4,7,8]. Each channel represents a different scattering process for which the electron has exchanged a certain amount of energy with the phonon modes.

The scattering states for a single incoming charge carrier are expanded onto the eigenstates $|i, \{n_\lambda\}\rangle = c_i^\dagger \prod_\lambda (a_\lambda^\dagger)^{n_\lambda}/\sqrt{n_\lambda!}\,|0\rangle$, of the non-interacting *e-ph* system, where $|0\rangle$ is the vacuum state. The vacuum state $|0\rangle$ represents the neutral ground state of the whole system, with a definite number of electrons in each part of the system (the leads and molecule). The electronic states considered correspond to adding a single electron to this neutral state; the added electron can be anywhere in the system (in the left lead, the right lead, or the molecule) and interacts with phonons only inside the molecule.

We have shown that the problem is solved once the value of the scattering wave-functions $|\alpha\rangle$ inside the wire are known [4]. Such wave-functions are obtained by propagating the source term $|s\rangle$ (incoming electron or hole from the left or right lead) by use of the effective *e-ph* Green's function $G(E)$ inside the wire, $|\alpha(E)\rangle = G(E)|s(E)\rangle$, where G is given by $G(E) = (E - H - \Sigma_L(E) - \Sigma_R(E))^{-1}$. H is the molecular wire Hamiltonian defined in Eq. (1), and $\Sigma_{L,R}$ are complex potentials arising from embedding the molecular wire spectrum into the continuum of electronic states associated with the left and right leads, respectively. Once the solution of the linear system $|\alpha\rangle = G|s\rangle$ is obtained for each energy E, one can get the reflection and transmission coefficients for all the channels, and hence the partial and total currents flowing through the device. One can also calculate the expection values $\langle f[\{c_i\},\{a_\lambda\}]\rangle = \langle\alpha(E)|f[\{c_i\},\{a_\lambda\}]|\alpha(E)\rangle$ of any correlation functions $f[\{c_i\},\{a_\lambda\}]$ between the electron and phonon degrees of freedom.

Starting with an initial phonon distribution $b = \{m_\lambda\} = \{0\}$ taken to be the limit of low temperatures (all phonon modes are initially in the ground state) and an initial electron energy $\epsilon_{in} = \epsilon_L + 2\beta_L \cos k_b^L(E)$ for an incoming wave from the left lead, the transmission coefficients [4] for the different outgoing channels can be written in the following usual form [9] :

$$T_{ab}(\epsilon_{fi}, \epsilon_{in}) = 4\,\frac{v_L^2}{\beta_L}\sin k_b^L(\epsilon_{in})\,\frac{v_R^2}{\beta_R}\sin k_a^R(\epsilon_{fi})\;|\langle N|G_{ab}(E)|1\rangle|^2\;, \quad (2)$$

where $a = \{n_\lambda\}$ is the phonon configuration after scattering, and $\epsilon_{fi} = \epsilon_R + 2\beta_R \cos k_a^R(E)$ is the final energy of the transmitted electron, $\langle N|G_{ab}(E)|1\rangle$ is the matrix element of the Green's function defined previously taken between the left side $i = 1$ and the right side $i = N$ of the molecule, and between the phonon distributions before (b) and after (a) scattering. For the energy conservative system considered here, there exists a relation between the different energies introduced in Eq. (2): $E = \epsilon_{in} + \sum_\lambda m_\lambda\hbar\omega_\lambda = \epsilon_{fi} + \sum_\lambda n_\lambda\hbar\omega_\lambda$. Note that, in the limit of low

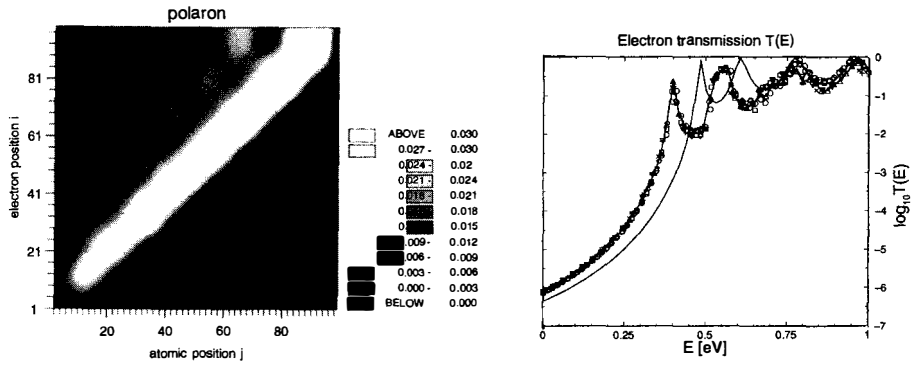


Figure 1: *(Left)* Dimerization pattern $d_j^{[i]}$ (in Å) for a $N = 100$ chain length for the different electron position i in the wire (injection energy at midgap $E = 0.0$). *(Right)* Effective total transmission $T(E) = \sum_a T_{ab}(\epsilon_{fi}, \epsilon_{in})$, with *e-ph* coupling (solid line with symbols), without *e-ph* coupling (solid line).

temperatures, the injection energy equals the total energy $\epsilon_{in} = E$. Finally note also that the factors $v_{L,R}^2/\beta_{L,R} \sin k_{b,a}^{L,R}$ are related to the imaginary parts of the embedding potentials $\Sigma_{L,R}$ respectively.

3 Results

Within the SSH model used to describe the molecular wire, the condition for having a finite band gap at zero temperature corresponds to a system that contains an even number N of monomers. For odd-numbered chains, the molecules still have double (short) bonds anchored at their ends. In this case, the alternation between short (double) and long (single) bonds from one end of the molecule to the other can only be accommodated by introducing a phase breaking in the bond alternation pattern inside the molecular wire. Then a topologic defect (called a soliton) occurs in the middle of the chain. The soliton corresponds to a domain wall between two domains having two different phases of the bond alternation pattern. A electron state is associated with the soliton which, in the SSH model, is located exactly at midgap owing to charge-conjugation symmetry.

First, we consider the lattice deformation induced by the tunneling electron in a even-numbered chain. We calculate the correlation function $\delta_\lambda^{[i]}$ between the electron density $P_i = c_i^\dagger c_i$ on the site i and the associated displacement $\Delta_\lambda = (a_\lambda + a_\lambda^\dagger)\sqrt{\hbar/2M\omega_\lambda}$ of the phonon mode λ as $\delta_\lambda^{[i]} = \langle P_i^\dagger \Delta_\lambda P_i \rangle / \langle P_i \rangle$. We can then define the atomic displacement $u_j^{[i]} = \sum_\lambda \delta_\lambda^{[i]} V_\lambda(j)$ on site j due to the displaced phonon modes when the electron "is found" on site i. The corresponding dimerization pattern $d_j^{[i]} = (-1)^j (u_{j+1}^{[i]} - 2u_j^{[i]} + u_{j-1}^{[i]})$ is shown on Fig. 1 for a $N = 100$ chain length. The induced lattice deformations are always located around the injected electron. This shows that the transport in such molecular wires involves the formation and propagation of "quasiparticles" consisting of the charge-carrier (electron or hole) surrounded by its phonon cloud (in the present case an electron polaron). The formation of such a polaron produces an effective reduction of the apparent HOMO-LUMO gap. This gap reduction is associated with an increase of the electron transmission in the tunneling regime as can be seen on the left graph in Fig. 1.

Now let us briefly discuss the case where a soliton defect is initially present in the molecule. For an injection energy $E = 0$ at mid-gap, due to *e-ph* coupling, the soliton defect becomes more "delocalized" and its width is modified while the electron propagates through the system.

With increasing energy E towards the edge of the valence band, one observes, in parallel with the soliton delocalization and deformation, the formation of a polaron. For electron positions i around the middle of the chain, the polaron and soliton defects interact strongly together. Such behaviour modifies the electron transmission as follows: (i) the delocalization and deformation of the soliton broaden the resonance peak at mid-gap (in the absence of *e-ph* coupling, such a peak is extremely narrow because the associated soliton state is very localized in the middle of the chain), (ii) for larger E, the formation of the polaron effectively reduces the apparent gap and a polaron resonance peak appears inside the original HOMO-LUMO gap (as shown on Fig. 1). This effective gap reduction increases the transmission in the tunneling regime.

4 Conclusion

These results demonstrate the complexity of electron transport through molecular wires. Due to the electron-phonon coupling, polarons can be formed inside the molecule. Polaron propagation is the main mechanism of transport through perfectly dimerized (semiconducting) molecules. The formation and propagation of virtual polarons induce an effective reduction of the HOMO-LUMO gap and therefore a strong increase of the electron transmission in the tunneling regime. The presence of a mid-gap state associated with a soliton defect in the middle of the molecule involves different mechanisms for the transport in the wire. For electron injection energy around the mid-gap state, the delocalization and deformation of the soliton is the main mechanism associated to the electron transfer. For electron injection above the mid-gap, the transport is then associated with more complicated mechanisms involving the interaction of both a polaron and the soliton. In all the cases examined, the effective reduction of the HOMO-LUMO gap due to the polaron formation, the delocalization/deformation of the soliton and the polaron-soliton interaction increases the transmission in the tunneling regime. Our results are generally applicable to other classes of one-dimensional atomic-scale wires which present strong *e-ph* coupling [10].

Acknowledgments

We acknowledge financial support from the U.K. EPSRC (Grant GR/M09193).

References

1. H. Park *et al.*, *Nature* **407**, 57 (2000); C. Kergueris *et al.*, *Phys. Rev.* B **59**, 12505 (1999); M.A. Reed *et al.*, *Science* **278**, 252 (1997).
2. L.C. Venema *et al.*, *Science* **283**, 52 (1999); M. Bockrath *et al.*, *Science* **275**, 1922 (1997); S.J. Tans *et al.*, *Nature* **393**, 49 (1998); D. Porath *et al.*, *Nature* **403**, 635 (2000).
3. T. Hitosugi *et al.*, *Phys. Rev. Lett.* **82**, 4034 (1999); T.C. Shen *et al.*, *Science* **268**, 1590 (1995).
4. H. Ness, S.A. Shevlin and A.J. Fisher, *Phys. Rev.* B **63**, 125422 (2001).
5. W.P. Su, J.R. Schrieffer, and A.J. Heeger, *Phys. Rev.* B **28**, 1138 (1983); A.J. Heeger *et al.*, *Rev. Mod. Phys.* **60**, 781 (1988).
6. K.A. Chao and Y. Wang, *J. Phys.* C **18**, L1127 (1985).
7. J. Bonča and S.A. Trugman, *Phys. Rev. Lett.* **75**, 2566 (1995); *Phys. Rev. Lett.* **79**, 4874 (1997).
8. H. Ness and A.J. Fisher, *Phys. Rev. Lett.* **83**, 452 (1999).
9. F. Sols, *Ann. Phys.* **214**, 386 (1992).
10. D.R. Bowler and A.J. Fisher, *Phys. Rev.* B **63**, 035310 (2001).

Statistics of quantum transport in metal nanowires with surface disorder

Jérôme Bürki[1], Charles A. Stafford[2]
[1] *Lyman Lab of Physics, Harvard University, Cambridge MA 02138, USA*

[2] *Department of Physics, University of Arizona, 1118 E. 4th St., Tucson AZ 85721, USA*

Experimental conductance histograms built from several thousand successive breakings of sodium nanowires [1,2] exhibit peaks up to rather high conductance values ($\sim 100 \times 2e^2/h$). In this paper, we present results from a disordered free-electron model of a metallic nanowire, which was previously successful in describing both conductance histograms and shot noise measurements in gold nanocontacts with much lower conductances.[3] We find in particular that, with a modification of the model of disorder, the conductance histogram can be understood as an interplay of conductance quantization and disorder for low conductances ($G \lesssim 10 \times 2e^2/h$), while peaks corresponding to higher conductance are actually a combination of several "quantized conductance peaks". We also predict a saturation of the shot noise at high conductance to about 1/10 of its classical value $2e\bar{I}$.

1 Introduction

Recent experiments by Yanson *et al.* [1,2] measuring conductance histograms for sodium nanocontacts have revealed the persistance of well-defined conductance peaks up to rather high conductance values, of order $100G_0$, where $G_0 = 2e^2/h$ is the quantum of conductance. A semi-classical calculation of Kassubek *et al.* [4] provided a description of the histograms in terms of the stability of nanowires of certain radii, but the shift of the experimental peaks with respect to quantized conductance values makes it difficult to identify a peak with a particular quantized conductance. We therefore solve in this paper a free-electron model [5] of a metallic nanowire that includes disorder [3] and allows for a more quantitative identification of the peaks, as well as the calculation of other quantities such as shot noise.

The sequence of conductance peaks observed [1,2] at low temperature ($1, 3, 5, 6, \ldots \times G_0$) is suggestive of cylindrical symmetry. We therefore use a three-dimensional model of a cylindrical wire with a constriction, presented in section 2. The extension of the recursive Green's function numerical method [3] to three-dimensional contacts is discussed in section 3. Finally, the results are presented and discussed in section 4.

2 Model

As in previous papers,[3,5] we use a free-electron model of a metallic nanowire. The nanowire is taken to be an infinite cylinder of radius R with a finite deformable part representing the contact, defined by the function $r(z) = R_{min} + (R - R_{min})\left[3u^2 - 3u^4 + u^6\right]_{u=2z/L}$, where R_{min} is determined at each step of the elongation L such that the volume of the contact is kept constant. Independent electrons are confined within the wire by hard-wall boundary conditions and the Fermi energy of the electron gas is taken to be the bulk sodium Fermi energy, namely $\varepsilon_F = 3.23eV$. All calculation are made at zero temperature.

The bulk model of disorder used previously to model gold nanocontacts [3] is problematic for sodium because of the larger size [1,2] of the contacts: A disorder resistance of a few hundred Ohms is necessary to shift the lower conductance peaks back onto quantized values, corresponding to a conductance of less than $100G_0$. If the disorder resistance is to be constant during elongation of the contact, which is the case with bulk disorder, it would be impossible to measure a conductance larger than this value, which is clearly not the case.[1] We therefore need a model of disorder whose resistance decreases with increasing conductance of the contact.

The material used in experiments being of very high purity, the main source of backscattering is likely to be surface roughness [6] or surface defects. We therefore introduce the following model of surface disorder: (i) As previously,[3] we use δ-function impurities of fixed strength W and random positions; (ii) The initial positions of the impurities are restricted to a length L_{dis} of the conductor that includes the constriction, and within a distance d of the surface of the wire (i.e. $R - d \leqslant r \leqslant R$, r being the radial coordinate of the impurity); (iii) During elongation of the contact, the distance of the impurity to the surface is kept constant, while its longitudinal position is changed such that the linear density of impurities is constant along the wire.

With this model, the resistance due to impurities will increase as the minimal cross-section area decreases. The thickness d of the disordered shell is chosen on physical grounds to be essentially one atomic layer, or $k_F d = 3$. We want to emphasize that this surface disorder model is likely to be a better model for gold as well, but all conductance histograms published for gold [7] were restricted to conductances lower than $10G_0$, in which regime both models give similar results.

3 Method

In principle, the recursive Green's function method used in our earlier paper [3] can be extended without further complication to a three-dimensional model such as considered in this work. In practice, however, one would need a very fine discretization of space in order to reproduce the correct degeneracies of the transverse energy levels, making the computation intractable, especially for the larger contacts we want to consider. Instead, we discretize only the longitudinal coordinate z after the change of coordinates that brings the constriction back to a cylinder, and use a basis of transverse eigenstates of the "free" problem (i.e. without a constriction or disorder) to get a matrix representation of the Hamiltonian of a slice. In order to have a finite matrix, we introduce an energy cutoff, which is chosen such that the number of states considered is of the order of twice the number of open channels. Except for this change of basis and the use of a three-dimensional model, the method is a straightforward generalization of our previous work.[3] Once the transmission matrix $t(\varepsilon_F)$ at the Fermi energy has been obtained from the Green's function,[3] the conductance G and shot noise S_I at zero temperature are computed using the Landauer-type formulae

$$G = \frac{2e^2}{h} \mathrm{Tr}\left(t^\dagger t\right), \qquad S_I = 2e\bar{I} \frac{\mathrm{Tr}\left[t^\dagger t\left(1 - t^\dagger t\right)\right]}{\mathrm{Tr}\left(t^\dagger t\right)}. \tag{1}$$

In order to generate a histogram of conductance, we compute the conductance as a function of elongation for a given configuration of disorder, divide the conductance axis in intervals of size $\Delta G = 0.1 G_0$ and count the number of points in each interval. We repeat this for 300 configurations of disorder, averaging at the same time on the geometry of the contact by using different initial lengths L_0 for the constriction ($5 \leqslant k_F L_0 \leqslant 25$). We then smoothen the histogram by taking an average over three bins with relative weights 1, 2, 1, similarly to what is done in the experiments.[1] We can also resolve individual "quantized" conductance peaks by restricting the elongation to intervals corresponding to a fixed number of open channels of the clean adiabatic wire. As to the shot noise, we average its value at a given conductance, using the same set of data as for the histogram.

4 Results

4.1 Conductance histogram

Following the procedure described above, we generated the histogram of Fig. 1(a). The first two peaks, near G_0 and $3G_0$, can be thought of as individual quantized conductance peaks, broadened and shifted downward slightly by disorder. However, the third peak is a mixture of $5G_0$ and $6G_0$, and higher peaks are typically even more complicated admixtures. In Fig. 1(b), the peak near $28G_0$ is shown, along with its decomposition in terms of individual quantized components; one sees that it is actually composed of many individual peaks. The peaks in the conductance histogram are thus generically not ascribable to individual quantized conductance channels, but rather represent a gross shell structure.[1,2] One notes that the agreement with the experimental results of Yanson *et al.*[1,2] is reasonable for conductances lower than $30G_0$, except for the one peak around $7G_0$, which seems to be out of place, and which will be discussed later. For larger conductance, the peaks start to be out of phase with the experimental peaks, which might have several causes: First of all, the disorder present in the experimental nanowires might be stronger or weaker than that in our model. Secondly, our calculation is made at zero

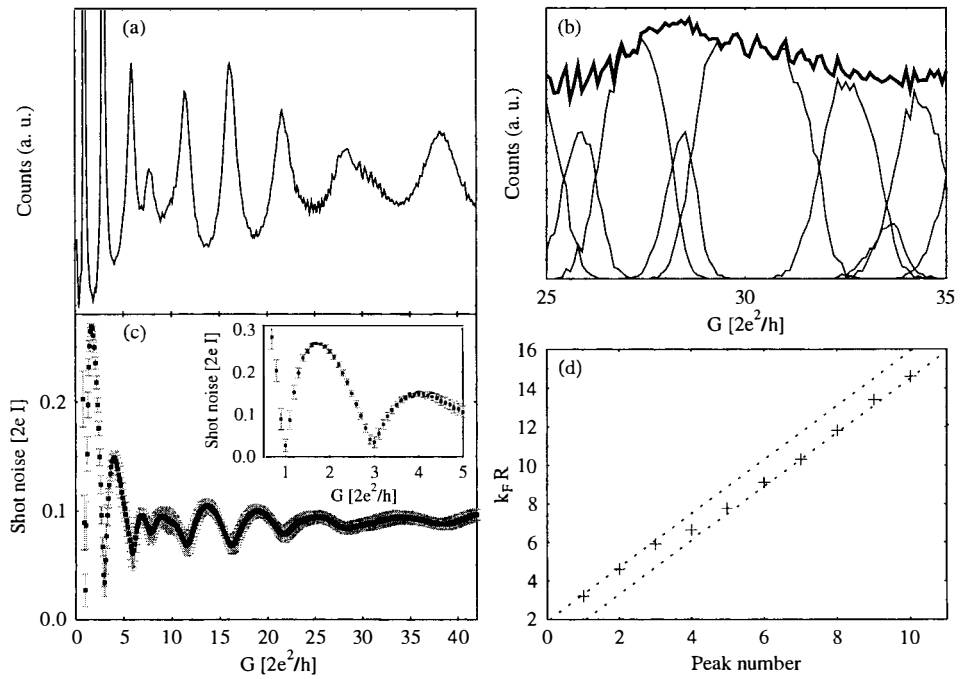


Figure 1: (a) Conductance histogram built from 300 disorder configurations. (b) Blowup of the eighth peak of the histogram (thick line). The thiner lines represent contributions to the histogram from individual "quantized" conductance peaks. (c) Average shot noise of the contact (squares) together with the standard deviation (bars) as a function of the conductance of the contact; the inset blows up the graph at small conductances. (d) Relation between the radius of the wire and the peak number (crosses); the dotted lines are a guide to the eye.

temperature, while the experiment is made around $90K$, where surface diffusion of atoms allows the contact to find more stable configurations, so that those peaks might reflect the stability of the contact, rather than quantum transport effects.

Coming back to the peak near $7G_0$, the discrepancy of its position and its relative weakness suggests that it might actually disappear if a larger amount of disorder was used. In that case, the higher conductance peaks would be shifted further downward, and would presumably correspond to lower experimental peaks. This hypothesis is supported by Fig. 1(d), which shows the radius of the wire, as obtained from the Sharvin formula $G_s = (k_F R/2)^2 (1 - 2/k_F R)$, as a function of the peak number. As is suggested by the two dotted lines, corresponding to a shift of the peak number by one, the linear relation between the radius and the peak number would be better if the fourth peak, which is the peak in question, were removed. The hypothesis of stronger disorder, currently under investigation, seems promising.

4.2 Shot noise

The shot noise, computed as described in Sec. 3, is shown in Fig. 1(c). It shows a strong suppression at low quantized-conductance values and weaker minima corresponding to higher peaks in the conductance histogram, as could be expected from our previous results on gold nanocontacts.[3] At larger conductance values, we observe a saturation of the shot noise at about 1/10 of the classical value $2e\bar{I}$, in contrast to a random-matrix prediction by Beenakker and Melsen [8] of a suppression factor of 1/3 in a disordered nanowire. Part of this discrepancy may come from the difference in disorder (surface versus bulk), but even our results for gold, which used a model much more similar to the one of Ref. [8], showed a saturation value that was about one half of the random-matrix prediction. The reason for this discrepancy is not fully understood, but it may indicate that tunneling through the nanocontact, which is neglected in the model of Ref. [8], plays an essential role in the shot noise in the saturation region, just as it does in the ballistic region at small conductance.

5 Conclusions

We have presented a model of surface disorder in a free-electron nanowire whose numerical solution, using a variation of the Green's function technique presented in our previous paper,[3] helps understand conductance histograms obtained experimentally for sodium nanowires, and provides a prediction for what the shot noise of such wires should look like. Our results show a discrepancy for the saturation value of the shot noise compared to random matrix theory [8] that is so far not understood.

Acknowledgments

JB was supported by a fellowship of the Swiss National Science Foundation. CAS was supported by NSF Grant DMR0072703.

References

1. A. I. Yanson, I. K. Yanson, and Jan M. van Ruitenbeek, *Nature* **400**, 144 (1999).
2. A. I. Yanson, I. K. Yanson, and J. M. van Ruitenbeek, *Phys. Rev. Lett.* **84**, 5832 (2000).
3. J. Bürki, C. A. Stafford, X. Zotos, and D. Baeriswyl, *Phys. Rev. B* **60**, 5000 (1999); J. Bürki and C. A. Stafford, *Phys. Rev. Lett.* **83**, 3342 (1999).
4. F. Kassubek, C. A. Stafford, H. Grabert, and R. E. Goldstein, *Nonlinearity* **14**, 167 (2001).
5. C. A. Stafford, D. Baeriswyl, and J. Bürki, *Phys. Rev. Lett.* **79**, 2863 (1997).
6. A. M. Bratkovsky and S. N. Rashkeev, Phys. Rev. B **53**, 13074 (1996).
7. J. L. Costa-Krämer, N. García, and H. Olin, *Phys. Rev. B* **55**, 12910 (1997).
8. C. W. J. Beenakker and J. A. Melsen, *Phys. Rev. B* **50**, 2450 (1994).

QUANTUM HALL EFFECT

Elastic theory of quantum Hall stripes

Felix von Oppen[1] and Stefan Scheidl[2]

[1] *Institut für Theoretische Physik, Freie Universität Berlin, Arnimallee 14, D-14195 Berlin, Germany*
[2] *Institut für Theoretische Physik, Universität zu Köln, Zülpicher Str. 77, D-50937 Köln, Germany*

The recently discovered striped phases in the Quantum Hall system are closely analogous in terms of symmetry to liquid-crystal systems, giving rise to terminology such as Quantum Hall smectics or Quantum Hall nematics. This analogy can be exploited to develop an elastic theory of the striped phases. Here we briefly summarize some recent results obtained by this approach, with an emphasis on the effects of disorder.

1 Introduction

Recent experiments[1] discovered that the resistivity develops a pronounced anisotropy in quantum Hall systems near half filling of higher Landau levels (Landau level filling factor $\nu \geq \frac{9}{2}$). This observation suggests that the ground state at these filling factors breaks orientational symmetry. It is believed that this is a manifestation of the formation of striped quantum Hall states whose existence had previously been predicted based on Hartree-Fock (HF) calculations[2] (for a recent review, see Ref. [3]. The existence of striped states in higher Landau levels has also been supported by exact numerical diagonalization studies[4] and by the experimental confirmation[1] of some explicit predictions[5,6] for their transport properties.

The HF calculations lead to a ground state near half filling of higher Landau levels which is a unidirectional charge density wave (CDW) whose period a is of the order of the cyclotron radius.[7] In addition to orientational order, this state also breaks translational symmetry in one direction. Fradkin and Kivelson[8] pointed out that this is analogous in terms of symmetries to smectic liquid crystals and termed this state a quantum Hall smectic state.

It is well known that HF overestimates the degree of ordering of a system. In particular, quantum or thermal fluctuations and disorder might destroy the full smectic order of the CDW. The analogy with liquid-crystal systems suggests that one can study the stability of the CDW state within the framework of an effective elastic theory. The elastic theory of the smectic quantum Hall state is closely analogous to those of conventional smectic liquid crystals. Caution has to be exercised when considering the dynamics within the elastic theory: Here, the chiral nature of the quantum Hall system leads to differences compared to the liquid crystal case.

In this article, we summarize recent results on striped quantum Hall states obtained within the framework of the elastic-theory approach. After a brief introduction to the elastic theory, we first discuss the effects of quantum[5] and thermal fluctuations.[9] In the remainder of the paper, we focus on the effects of disorder on the structural properties of the striped states,[10] addressing the following questions: Firstly, the interpretation of the experiments in terms of striped quantum Hall states requires that their orientational order is not destroyed by disorder. This is not obvious as disorder often leads to *qualitatively* stronger distortions than quantum and thermal fluctuations. Indeed, we find that disorder does destroy long-range orientational order in a model *without* a force aligning the stripes along a preferred direction! We give strong evidence that even a rather weak alignment field suffices to recover orientational order. By contrast, we find that translational order is always lost at long length scales. Secondly, we obtain structural information about the stripe pattern at intermediate length scales. These results should be relevant to experimental techniques such as surface acoustic waves or local probes.

2 Elastic theory

The Hartree-Fock striped state is characterized by alternating stripes of filling factor N and $N+1$. The low-energy excitations of this state are internal edge excitations associated with each stripe of filling factor $N+1$. More precisely, each stripe supports two counterpropagating gapless modes, one on each side. By exciting these internal edge modes, the stripes can both fluctuate in width and in position. It turns out that in the framework of elastic theory, the stripe width is a massive mode.

Thus, at low energies, the relevant massless excitations are fluctuations of the displacement field $u(\mathbf{r},\tau)$ associated with translational symmetry breaking[5,3] and defined as the phase of the charge-density modulation $\rho(\mathbf{r},\tau) = \rho_0 \cos[k(r_\parallel + u(\mathbf{r},\tau))]$. The position vector $\mathbf{r} = \mathbf{r}_\parallel + \mathbf{r}_\perp$ is represented by its components parallel and perpendicular to the CDW wave vector $\mathbf{k}$ which is related to the wave length a via $k = 2\pi/a$. (This definition, though perhaps slightly confusing, is standard in liquid crystal physics.) The degrees of translational and orientational order are described, respectively, by the correlation functions

$$f(\mathbf{r}) = \langle [u(\mathbf{r}') - u(\mathbf{r}'+\mathbf{r})]^2 \rangle, \tag{1}$$

$$g(\mathbf{r}) = \langle [\nabla'_\perp u(\mathbf{r}') - \nabla'_\perp u(\mathbf{r}'+\mathbf{r})]^2 \rangle. \tag{2}$$

The elastic free energy is of the smectic form[5]

$$E(\tau) = \frac{1}{2}\int_{\mathbf{r}} \left[B_\parallel \left(\nabla_\parallel u + \frac{1}{2}(\nabla_\perp u)^2 + \frac{C}{2} \right)^2 + K(\nabla_\perp^2 u)^2 + B_\perp (\nabla_\perp u)^2 \right]. \tag{3}$$

The constant C is determined by the requirement $\langle \nabla_\parallel u \rangle = 0$ which fixes the CDW wave length. The compression modulus $B_\parallel$ and the bending modulus K are related by $B_\parallel = 4k^2 K$. [11] For $B_\perp = 0$, this free energy is rotation invariant due to the anharmonic terms.[11] We have included a crystal field with tilt modulus $B_\perp$ which accounts for the presence of an *alignment force* orienting the stripe pattern along a preferred direction. Experiments suggest that this alignment force is quite weak, $B_\perp \ll B_\parallel$. The presence of the tilt modulus leads to an important (transverse) length scale in the problem, defined by $q_s = (B_\perp/K)^{1/2}$. For $q_\perp \gg q_s$, the bending energy of the stripes dominates over the tilt energy while for $q_\perp \ll q_s$, the tilt energy dominates.

The chiral nature of quantum Hall systems leads to peculiar dynamics of quantum Hall smectics as described by the elastic action[5] (β is the inverse temperature)

$$S_{\rm el}[u] = \frac{1}{\beta}\sum_\omega \sum_{\mathbf{q}} M \frac{\omega^2}{q_\perp^2} |u(\mathbf{q},\omega)|^2 + \int_0^{\beta\hbar} d\tau\, E(\tau). \tag{4}$$

Here M is a dynamic coefficient and $E(\tau)$ denotes the elastic free energy. The inverse powers of the transverse wave vector $q_\perp$ in the dynamic term are *specific* to quantum Hall smectics. This pecularity is crucial when considering the effects of quantum fluctuations at zero temperature in the quantum Hall system. We note that the elastic theory has recently been derived from the Hartree-Fock theory, providing explicit results for the elastic constants entering into Eq. (4).[12]

3 Thermal and quantum fluctuations

We first study the effects of thermal fluctuations in the absence of an alignment field, i.e. $B_\perp = 0$. Then, it is an immediate consequence of this elastic free energy that dislocations cost only a finite energy.[13] Thus there will be a finite density of dislocations at any non-zero temperature and the stripes should be broken down to stripe segments. This is expected to destroy translational long-range order but preserve quasi-long-range orientational order of the remaining stripe segments. Thus, the smectic order predicted by the HF approximation is

preserved only at zero temperature. At non-zero temperatures, the system is analogous in terms of symmetries to a 2d nematic liquid crystal.

As the temperature increases the system should undergo a Kosterlitz-Thouless transition from the nematic phase to an isotropic phase in which the orientational order of the stripe segments disappears. Nevertheless, short-range stripe ordering should still persist up to the presumably much higher Hartree-Fock transition temperature $T_c^{\rm HF}$.

Recently, Wexler and Dorsey[9] have made a quantitative study of this scenario and find that their estimates for the Kosterlitz-Thouless transition temperature are in reasonable agreement with the temperatures at which the anisotropy starts to appear in the experiments.

MacDonald and Fisher[5] have studied the stability of the CDW against quantum fluctuations within the framework of the elastic theory. They find that quantum fluctuations are not strong enough to destroy the smectic order predicted by the HF approximation. This result is specific to quantum Hall smectics as it crucially relies on the slow dynamics at long wavelengths implied by Eq. (4). The anomlous hydrodynamics of the striped quantum Hall states has been studied based on the elastic theory by Fogler and Vinokur.[14]

4 Effects of disorder

Various kinds of disorder may affect the quantum Hall stripes, including the disorder potential originating from the ionized impurities in the dopant layer and large-scale inhomogeneities of the sample. Here we focus on the effects of the short-range disorder since the large-scale disorder is difficult to model. Thus, our results provide a lower bound on the effects of impurities.

We model the short-range disorder within the framework of elastic theory by including a disorder potential $U(\mathbf{r})$ in the action via $S_{{\rm imp},V} = \int_{\mathbf{r},\tau} U(\mathbf{r})\rho(\mathbf{r},\tau)$. It can be rewritten as $S_{{\rm imp},V} = (\rho_0/2)\int_{\mathbf{r},\tau}[V(\mathbf{r})e^{iku(\mathbf{r},\tau)} + {\rm c.c.}]$, where V is effectively locally correlated, $\langle V(\mathbf{r})V^*(\mathbf{r}')\rangle \simeq W\delta(\mathbf{r}-\mathbf{r}')$, even for long-range-correlated impurity potentials $U(\mathbf{r})$ because of the oscillatory nature of the charge density $\rho(\mathbf{r},\tau)$. The effective disorder strength W is given by $W \simeq \langle U(-\mathbf{k})U(\mathbf{k})\rangle$. For quantitative estimates, we employ the impurity potential created by the ionized impurities (of areal density $n_{\rm imp}$) in the spacer layer which dominates the transport properties of two-dimensional electron systems (2DES). For uncorrelated impurity positions, the disorder potential experienced by the electrons in the 2DES has $W = e^2 n_{\rm imp} v_d^2(k)$. Here, $v_d(q) = 2\pi e^{-qd}/\epsilon(q)q$ is the screened Coulomb interaction, $\epsilon(q)$ the dielectric function, and d the distance of the impurity layer from the 2DES.

While the bare action contains only the point disorder $U(\mathbf{r})$, the action of the renormalization group (RG) generates a second type of disorder. This effective disorder corresponds to a random tilting force acting on the stripe pattern and is described by the additional term $S_{{\rm imp},h} = \int_{\mathbf{r},\tau} h(\mathbf{r})\nabla_\perp u(\mathbf{r},\tau)$ in the action with a local correlator $\langle h(\mathbf{r})h(\mathbf{r}')\rangle = \Delta_h\delta(\mathbf{r}-\mathbf{r}')$.

We proceed in a standard fashion by averaging the free energy over disorder using the replica trick which leads to the impurity-averaged replicated partition function

$$\langle Z^n\rangle = \int \prod_\alpha [du_\alpha] \exp\Big\{ -\frac{1}{\hbar}\sum_\alpha S_{\rm el}[u_\alpha] + \frac{1}{2\hbar^2}\int_{\mathbf{r},\tau,\tau'}\sum_{\alpha,\beta}\Big[\Delta_h(\nabla_\perp u_\alpha(\mathbf{r},\tau))(\nabla_\perp u_\beta(\mathbf{r},\tau')) + \Delta_V\cos[k(u_\alpha(\mathbf{r},\tau) - u_\beta(\mathbf{r},\tau'))]\Big]\Big\}. \quad (5)$$

Here, $\Delta_V = (1/2)\rho_0^2 W$ (Δ_h) is the strength of the point (tilt) disorder.

Within a perturbative treatment of the action in Eq. (5) (with $\Delta_h = 0$ and neglecting dislocations), one finds that $f(\mathbf{r})$ is infrared divergent for any nonzero $\mathbf{r}$, irrespectively of whether the tilt modulus $B_\perp$ vanishes or not. Because of the multistability of the disorder potential,

perturbation theory breaks down on scales where $f \geq a^2$,[15] i.e. *on all finite scales.* We have performed a RG calculation which properly accounts for the multistability by a significant downward renormalization of the disorder strength on large scales.

Despite the divergence, the perturbative expression determines the characteristic transverse scale q_V, below which the renormalization sets in. To this end, we demand $f(q_V^{-1}\mathbf{e}_\perp) \sim a^2$ with the provision that the integral over $q_\perp$ in the perturbative expression for f be self-consistently restricted to $q_\perp \geq q_V$. In the *weak-disorder regime* $q_V \ll q_s$, this gives $q_V = [\Delta_V/\Delta_V^c]^{1/2} q_s$, while in the *strong-disorder regime* $q_V \gg q_s$ one obtains $q_V = [\Delta_V/\Delta_V^c]^{1/5} q_s$. The disorder strength separating these two limits is given by $\Delta_V^c = 4\pi B_\parallel^{1/2} B_\perp^{5/2}/k^4 K$.

Our further analysis builds on previous RG studies for classical smectics,[11,16] adapting them to two dimensions where disorder is known to play a peculiar role.[17,18] As the approach neglects topological defects such as dislocations, the results are valid only up to the scale $L_\perp^{\text{disloc}}$ where dislocations start to appear. This length will be estimated below. We find that the nonlinear terms in the bare elastic action Eq. (4) lead to quantitatively small corrections only which will be ignored below. Deriving and solving the RG flow equations, we obtain explicit results for the correlation functions f and g. Our results are summarized in Fig. 1.

In the *weak-disorder regime* $q_V \ll q_s$ or $\Delta_V \ll \Delta_V^c$, we find for the translational order in the soft (perpendicular) direction

$$f(\mathbf{r}_\perp) \sim \frac{1}{k^2} \begin{cases} (q_V r_\perp)^2 \ln(q_s/q_V), & r_\perp \ll q_s^{-1}, \\ (q_V r_\perp)^2 \ln(1/q_V r_\perp), & q_s^{-1} \ll r_\perp \ll q_V^{-1}, \\ \ln^2(q_V r_\perp), & r_\perp \gg q_V^{-1}. \end{cases} \tag{6}$$

As opposed to the perturbative result, f is now finite for any finite $r_\perp$ and we can identify a correlation length $\xi_\perp^{\text{trans}}$ for the translational order by $f(\xi_\perp^{\text{trans}}) = a^2$ and find $\xi_\perp^{\text{trans}} \sim q_V^{-1}$. The slow $\ln^2$ increase of f in the regime $r_\perp \gg \xi_\perp^{\text{trans}}$, typical of two-dimensional disordered systems,[17] implies that the system exhibits "quasi"-long-range translational order, with power-law Bragg peaks with logarithmically varying powers. The orientational correlation function g remains finite, $g(\mathbf{r}_\perp) \sim (q_V/k)^2 \ln(q_s/q_V) \ll 1$, for arbitrarily large lengths $r_\perp \gg q_V^{-1}$. Hence the correlation length $\xi_\perp^{\text{orient}}$ for orientational order, defined by $g(\xi_\perp^{\text{orient}}) = 1$, is infinitely large.

For stronger disorder, we enter the *strong-disorder regime* $q_V \gg q_s$ or $\Delta_V \gg \Delta_V^c$ where

$$f(\mathbf{r}_\perp) \sim \frac{1}{k^2} \begin{cases} (q_V/q_s)^3 (q_s r_\perp)^2, & r_\perp \ll q_s^{-1}, \\ (q_V/q_s)^3 \ln(q_s r_\perp), & q_s^{-1} \ll r_\perp \ll q_h^{-1}, \\ \ln^2(q_s r_\perp), & r_\perp \gg q_h^{-1}. \end{cases} \tag{7}$$

In this case, the $\ln^2$ regime typically sets in only at extremely large length scales $r_\perp \gg q_h^{-1}$ with $q_h = q_s \exp[-(q_V/q_s)^3]$ so that we can restrict attention to the ln regime. At first sight, this seems to suggest the presence of quasi-long-range translational order in this case. While this is formally true, the corresponding singularities in the structure factor are extremely weak due to the large prefactor $(q_V/q_s)^3$ and for practical purposes, there is only short-range translational order with correlation length $\xi_\perp^{\text{trans}} = (q_s/q_V)^{1/2} q_V^{-1}$. As expected, translational order is significantly reduced compared to the weak-disorder regime. The degree of orientational order is also reduced, since $g(\mathbf{r}_\perp) \sim (q_V/k)^2 (q_V/q_s)$ for $r_\perp \gg q_s^{-1}$. Nevertheless, $\xi_\perp^{\text{orient}} = \infty$ as long as $q_V^3 \ll k^2 q_s$. Otherwise, for extremely strong disorder, $\xi_\perp^{\text{orient}} \sim k^2/q_V^3$.

It is important to note that in the absence of an alignment force ($B_\perp = 0$) orienting the stripes along a preferred direction, disorder destroys translational order and leads to short-range orientational order, even when neglecting dislocations. In fact, for $B_\perp = 0$, one has $q_s = 0$ so that one is always in the strong-disorder regime. Thus, from the expression for $g(r_\perp)$ in the strong-disorder regime, we find that g diverges on large scales for $q_s \to 0$. Thus the CDW can induce a resistivity anisotropy only if an alignment field is present. By contrast, in the presence

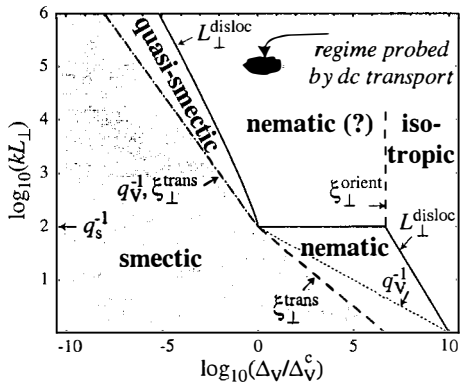


Figure 1: Illustration of regimes in dependence of disorder strength Δ_V and (transverse) length scale $L_\perp$ for $q_s = 0.01k$ as is typical for experiments. Here, $\xi_\perp^{\rm trans}$ and $\xi_\perp^{\rm orient}$ denote the correlation lengths for translational and orientational order, respectively. Dislocations appear on the scale $L_\perp^{\rm disloc}$. Renormalization of the disorder strength sets in for lengths beyond q_V^{-1}. All lengths are measured in units of the CDW wavelength $a = 2\pi/k$. In the smectic regime, both translational and orientational order are well preserved. In the weak disorder case $\Delta_V \ll \Delta_V^c$, this is followed by a quasi-smectic regime with quasi-long-range translational order. In the strong-disorder limit, $\Delta_V \gg \Delta_V^c$, a nematic regime follows in which translational order is effectively short ranged. Strictly speaking, our analysis based on elastic theory is not valid for $L_\perp \gg L_\perp^{\rm disloc}$. Nevertheless, since in the absence of dislocations, orientational order would be long ranged in this region except for extremely strong disorder, nematic order is likely to persist even beyond $L_\perp^{\rm disloc}$. dc transport measurements on macroscopic samples probe the regime in the indicated area.

of such an alignment field, g is smaller than unity asymptotically, i.e., orientational order is well preserved, as long as $q_s \gg q_V(q_V/k)^2$. Satisfying this condition requires an alignment field $B_\perp \gg Kk^2(q_V/k)^6$. Note that q_V decreases with decreasing disorder strength and that $q_V \sim 10^{-2}k$ is typical for experiments. Thus, in this case a $B_\perp$ smaller than Kk^2 by about twelve orders of magnitude is sufficient for orientational order.

As mentioned already, our results are valid up to the lengthscale $L_\perp^{\rm disloc}$, at which dislocations appear. Based on energetic considerations,[10] we find that disorder always induces a finite density of dislocations. We estimate for the weak-disorder regime that $L_\perp^{\rm disloc} \sim q_V^{-1} \exp[c \ln^{2/3}(q_s/q_V)]$ with c a constant of order one. In the *strong-disorder limit*, we find $L_\perp^{\rm disloc} \sim q_s^{-1} \min[1, k^2 q_s/q_V^3]$. Thus, within a finite range of disorder strengths, $\Delta_V^c \ll \Delta_V \ll (k/q_s)^{10/3}\Delta_V^c$ or $q_s^3 \ll q_V^3 \ll k^2 q_s$, $L_\perp^{\rm disloc}$ saturates at q_s^{-1}, before it shrinks further, coinciding with $\xi_\perp^{\rm orient}$.

Our results therefore lead to the following overall picture, as summarized in Fig. 1. In the weak-disorder limit we have a sequence of transverse length scales $q_s^{-1} \ll q_V^{-1} \simeq \xi_\perp^{\rm trans} \ll L_\perp^{\rm disloc}$. On short scales $L_\perp \ll q_V^{-1}$, the system looks like a *smectic* with pronounced translational order ($f \ll a^2$) and no free dislocations. On intermediate scales $q_V^{-1} \ll L_\perp \ll L_\perp^{\rm disloc}$, there are still no free dislocations. However, $f \gg a^2$ and f increases logarithmically, displaying quasi-long-range order, whence we call this regime *quasi-smectic*. For $L_\perp \gg L_\perp^{\rm disloc}$ dislocations appear and destroy translational order.

In the strong-disorder regime, the sequence of scales is $\xi_\perp^{\rm trans} \ll q_V^{-1} \ll L_\perp^{\rm disloc} \leq q_s$. Good translational order survives only for $L_\perp \ll \xi_\perp^{\rm trans}$. Beyond this scale, translational order is rapidly lost as f increases as a power law with $f \gg 1$. On the other hand, orientational order is still retained, $g \ll 1$. Hence, we cross over from a *smectic* regime for $L_\perp \ll \xi_\perp^{\rm trans}$ to a *nematic* regime for $L_\perp \gg \xi_\perp^{\rm trans}$.

Neglecting dislocations, one finds $g \ll 1$ (i.e. $\xi_\perp^{\rm orient} = \infty$) on all scales and thus well-pronounced orientational long-range order both in the weak-disorder regime and in the strong-

disorder regime unless the disorder becomes extremely strong, $\Delta_V \gg (k/q_s)^{10/3}\Delta_V^c \gg \Delta_V^c$. In view of this fact, it is rather plausible to expect that orientational order also survives for length scales larger than $L_\perp^{\rm dislоc}$, even in the presence of dislocations. On this basis, we labeled the corresponding region in Fig. 1 (to the left of the vertical dashed line) as a nematic regime. However, in the absence of an alignment field ($B_\perp = 0$), the system is in the extreme limit of strong disorder and orientational order is short ranged, $g(\mathbf{r}_\perp) \sim r_\perp$.

For typical experimental samples,[1] we estimate $q_s \sim q_V \sim 0.01k$, indicating that they are located in the crossover region between the weak- and strong-disorder regimes (cf. Fig. 1). This implies that translational order in the transverse direction is preserved for only about 100 wavelengths of the CDW while orientational order is more robust. As argued above, it is quite plausible to expect that in this parameter regime orientational order persists well beyond the length $L_\perp^{\rm disloc}$ where dislocations start to appear. This is in agreement with the experimental observation of anisotropies in dc transport. We emphasize again that orientational order *requires* the presence of a weak alignment field orienting the stripes along a preferred direction. Such a field, albeit rather weak, presumably exists in the experimental samples as indicated by the observation that the stripe pattern consistently aligns along certain crystallographic axes.[1]

The regimes at smaller lengths may be accessible to surface acoustic waves experiments and should form the basis of a theory of the transport properties of quantum Hall smectics.

Acknowledgments

This work was partly supported by the DFG through SP "Quanten-Hall-Systeme" and SFB 341.

References

1. M. P. Lilly *et al.*, Phys. Rev. Lett. **82**, 394 (1999); R. R. Du *et al.*, Solid State Comm. **109**, 389 (1999); J. P. Eisenstein *et al.*, cond-mat/0003405.
2. M. M. Fogler, A. A. Koulakov, and B. I. Shklovskii, Phys. Rev. B **54**, 1853 (1996); R. Moessner and J. T. Chalker, Phys. Rev. B **54**, 5006 (1996).
3. F. von Oppen, B. I. Halperin, and A. Stern, cond-mat/0002087.
4. E. H. Rezayi, F. D. M. Haldane, and K. Yang, Phys. Rev. Lett. **83**, 1219 (1999).
5. A. H. MacDonald and M. P. A. Fisher, Phys. Rev. B **61**, 5724 (2000).
6. F. von Oppen, B.I. Halperin, and A. Stern, Phys. Rev. Lett. **84**, 2937 (2000).
7. In principle, the CDW is unstable with respect to charge ordering along the stripes at extremely low temperatures.[5] Presumably this ordering is destroyed by minute impurity concentrations even at zero temperature. Thus we will ignore this complication.
8. E. Fradkin and S. A. Kivelson, Phys. Rev. B **59**, 8065 (1999).
9. C. Wexler and A.T. Dorsy, cond-mat/0009096.
10. S. Scheidl and F. von Oppen, cond-mat0007442 (to appear in Europhys. Lett.); and to be published.
11. G. Grinstein, and R. A. Pelcovits, Phys. Rev. A **26**, 915 (1982).
12. A. Lopatnikova, S.H. Simon, B.I. Halperin, and X.-G. Wen, cond-mat/0105079.
13. D.R. Nelson, in *Phase Transitions and Critical Phenomena*, ed. by C. Domb and J.L. Lebowitz, (Academic Press, London, 1983).
14. M. M. Fogler and V. M. Vinokur, Phys. Rev. Lett. **84**, 5828 (2000).
15. H. Fukuyama and P. A. Lee, Phys. Rev. B **17**,535 (1978); P. A. Lee and T. M. Rice, Phys. Rev. B **19**, 3970, (1979); A. I. Larkin, Sov. Phys. JETP **31**, 784 (1970).
16. L. Radzihovsky and J. Toner, Phys. Rev. B **60**, 206 (1999).
17. J. Villain and J. F. Fernandez, Z. Phys. B **54**, 139 (1984).
18. For a recent review, see T. Nattermann and S. Scheidl, Adv. Phys. **49**, 607 (2000).

CHIRAL AND MIDGAP EDGE ELECTRON STATES IN THE QUASI-ONE-DIMENSIONAL ORGANIC CONDUCTORS $(TMTSF)_2X$

VICTOR M. YAKOVENKO, K. SENGUPTA, H.-J. KWON, I. ŽUTIĆ, AND S. DAS SARMA
Department of Physics and Center for Superconductivity Research, University of Maryland, College Park, Maryland 20742-4111, USA

In Ref. [1], we develop a microscopic picture of the electron states localized at the edges perpendicular to the chains in the Bechgaard salts in the quantum Hall regime. In a magnetic-field-induced spin-density-wave state (FISDW) characterized by an integer N, there exist N branches of chiral gapless edge excitations. Localization length is much longer and velocity much lower for these states than for the edge states parallel to the chains. We calculate the contribution of these states to the specific heat and propose a time-of-flight experiment to probe the propagating edge modes directly.

In Ref. [2], we show that the singlet s-, d- and triplet p-wave pairing symmetries in quasi-one-dimensional organic superconductors can be experimentally discriminated by probing the Andreev bound states at the sample edges. These states have the energy in the middle of the superconducting gap and manifest themselves as a zero-bias peak in tunneling conductance into the corresponding edge. Their existence is related to the sign change of the pairing potential around the Fermi surface. We present an exact self-consistent solution of the edge problem showing the presence of the midgap states for p_x-wave superconductivity. The spins of the edge state respond paramagnetically to a magnetic field parallel to the vector $\mathbf{d}$ that characterizes triplet pairing.

References

1. K. Sengupta, Hyok-Jon Kwon, and V. M. Yakovenko, *Phys. Rev. Lett.* **86**, 1094 (2001).
2. K. Sengupta, I. Žutić, H.-J. Kwon, V. M. Yakovenko, and S. Das Sarma, *Phys. Rev. B* **63**, 144531 (2001).

ON-RESONANCE AND OFF-RESONANCE TUNNELING AT THE FRACTIONAL QUANTUM HALL EDGE

ALBERT M. CHANG
Department of Physics, Purdue University, West Lafayette, IN 47907

Luttinger liquid represents one of the most experimentally accessible *non-Fermi* liquid systems available. Unlike conventional metals for which the electron-electron interaction can be taken into account within the Fermi liquid picture, in 1-dimensional systems interaction gives rise to a new type of correlated metallic matter known as the Tomonaga-Luttinger liquid (TLL). The most unusual feature of this TLL is the existence of a power law tunneling density of states. The 1-d edge of the fractional quantum Hall liquid represents a particularly clean example of a Chiral Luttinger liquid. We present clear-cut evidence of power law behaviors in the electron tunneling transport measurements in both *on-resonance* and *off-resonance* tunneling. In particular we present strong evidence for: 1) the discovery of an area *non-preserving* resonant tunneling peak under voltage bias, never before observed in nature, and 2) power-law current-voltage (I-V) characteristics as well as temperature dependence of the low bias conductance for off-resonance tunneling, including the presence of a plateau in the power law exponent near the value of 3, as the Laudau filling factor is varied.

1 Introduction

The low energy properties of conventional metals are well described by the Fermi liquid picture when electron interaction is taken into account wherein long-lived, Fermionic quasi-particles (holes) comprise the low energy excitations as the energy approaches zero. In contrast, non-Fermi liquid metallic systems are often distinguished by the *absence* of a single particle pole in the single particle spectral function replaced instead by power law dependences yielding a power law density of states for the tunneling of electrons and a suppression of tunneling at zero energy. The chiral Luttinger liquid at the fractional quantum Hall edge represents an extremely clean example of a non-Fermi liquid,[1,2,3,4,5,6,7,8,9,10,11] resulting from the quasi-one-dimensionality and inherent strong correlations. In this paper we present evidence from both on-resonance[12] and off-resonance tunneling[13] which clearly demonstrate unusual tunneling properties associated with this power-law tunneling density of states.

2 Sample Characteristics

The experiments were performed on samples grown by the Cleaved-Edge-Overgrowth technique.[14] Using this technique we produce devices in which a tall, thin $Al_{0.1}Ga_{0.9}As$ barrier separates the structurally atomically sharp edge of the 2DEG, confined within a quantum well, from a heavily doped n+ GaAs bulk metal layer. The sharp edge is created by in-situ cleaving along the (011) direction followed by a regrowth of the thin barrier, a 150$\AA$ region of undoped GaAs, and the heavily doped n+GaAs metal on this (011) plane perpendicular to the conventional (100) growth plane. The barrier thickness is of order 50-125 $\AA$ while its height rises 70meV above the 2DEG chemical potential far exceeding the 2DEG Fermi energy of $< 3.6meV$. This tall, thin barrier has proven essential by enabling access to a significant range of dynamic range in the tunneling bias voltage without concomitant distortions of the barrier shape. The detailed sample characteristics are as follows. Sampes 1 (R in figs. 1 and 2) and 2 comprise the first set and possess an identical 2DEG but differ in the subsequent Cleaved-Edge-Overgrowth. The 2DEG is of density $1.08\text{x}10^{11}\text{cm}^{-2}$ and mobility $3\text{x}10^{6}\text{cm}^{2}/\text{Vs}$. Sample 3 has a 2DEG density of $0.61\text{x}10^{11}\text{cm}^{-2}$ and a mobility of $8\text{x}10^{5}\text{cm}^{2}/\text{Vs}$. The $Al_{0.1}Ga_{0.9}As$ barrier thickness for samples 1, 2, and 3 are 90$\AA$, 125$\AA$, and 50$\AA$, respectively. Judging from the quantum Hall characteristics, these samples are of higher quality than those which previously exhibited $\alpha \sim 1/\nu$ behavior.[4] The n+ GaAs is

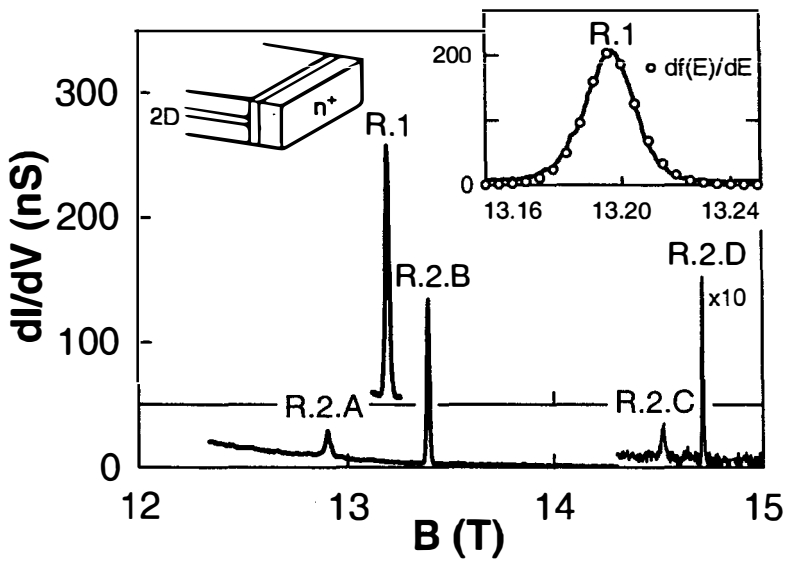


Figure 1: Conductance resonance for Sample R.1, and R.2. Inset, right: R.1 plotted with expanded scale against a derivative Fermi function. Device inset, left.

doped to $1.4 - 2\text{x}10^{18}\text{cm}^{-3}$ carrier density yielding a chemical potential of 65-83meV from the GaAs band bottom (70-88meV from the impurity band bottom), while the chemical potential of the 2DEG is approximately 25meV (15meV) above band bottom for samples 1 and 2 (3). Charge redistribution can take place across the barrier due to this chemical potential imbalance. The actual density profile will also depend on whether residual silicon dopants penetrate into the 150Å undoped GaAs buffer layer during the regrowth process. For each sample, two separate contacts are made one to the 2DEG and the other to the n+GaAs metal.

3 On-Resonance Tunneling

First we focus on the on-resonance tunneling behavior. Ideally a simple measurement of the resonance lineshape can theoretically resolve the character of the leads (2DEG or n+GaAs leads) [15,16,17,6], but in practice the subtle difference between a Fermi-liquid (FL) and Luttinger-liquid (LL) resonance lineshape is beyond the resolution of experiments to date[18]. One must therefore introduce an external energy scale, e.g. temperature, to probe the character of the resonance. Here we demonstrate another energy scale besides temperature that can reveal non-Fermi liquid behavior, namely an external voltage bias.

To measure conductance, we applied an 8 μV AC square wave to the sample and measured the resulting AC current with a lockin amplifier while sweeping the magnetic field, B (Fig. 1). Since the exact density profile at the edge is uncertain due to surface reconstruction we refer to all filling factors as ν_{bulk}. For sample R, we label the first and second cooldowns as R.1 and R.2, and for multiple resonances we append an additional suffix (R.2.A, R.2.B, etc.). Sample R.1 showed the strongest resonance at ν_{bulk}=0.338 as can be seen in Fig. 1. For the second

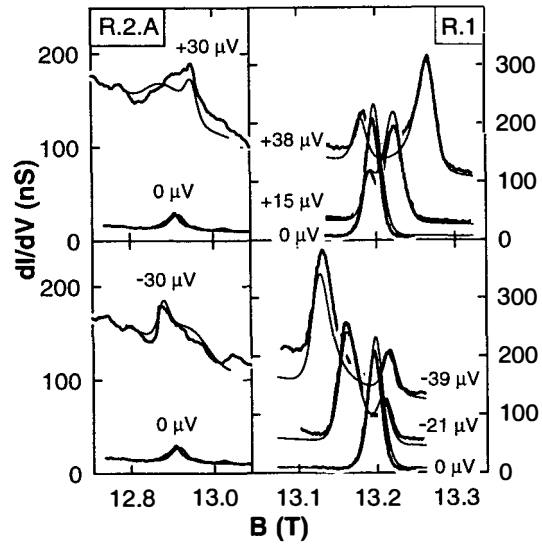


Figure 2: dI/dV vs. B at fixed DC bias for resonances R.2.A and R.1: data (thin lines), and fit (heavy lines).

cooldown R.2, we see four resonances at $\nu_{\rm bulk} = 0.346$, 0.333, 0.307, and 0.303 from left to right, respectively.

To measure bias dependence, a fixed DC bias was added to the AC square wave and differential conductance was measured as a function of B sweep (Fig. 2). Our sign convention refers to electrically grounding the 2D and applying the signed voltage to the n^+ electrode. With bias the background conductance increases due to the power law density of states. Starting with R.1 (Fig. 2 right), the peak splits under bias into atwo peaks of different height with a separation in B proportional to the applied voltage. The total area subtended by the two peaks above the background conductance increases only slightly. The bias dependence of resonance peak R.2.A (Fig. 2, left), instead of splitting, this peak broadens into a lopsided single peak that leans to the right for positive bias and to the left for negative bias. Most notably, the area subtended by the resonance relative to the background conductance increases by a factor of $\sim$6 under the application of a 30 μV DC bias, an altogether different qualitative behavior than R.1.

To understand this behavior requires comparing the *relative* coupling strength of the resonance to the two leads with the notation of $\Gamma_{\rm FL}$ as the tunnel coupling strength from the resonant state to the n^+ lead, and $\Gamma_{\rm QH}$ to the quantum Hall edge. Since the strongest peak is a factor of 100 smaller than the perfect resonant conductance, $e^2/3h$, overall the resonance is in the weakly coupled limit . The tunnel conductance will be determined entirely by the *weakly-coupled lead.* We begin by discussing the limiting case where the strongly coupled lead combines with the resonance to act as a delta function at the resonance energy E_r. Under bias V, a current I_r results from the weakly coupling Γ to the density of states in the remaining lead [with $f(E) = (e^{E/kT} + 1)^{-1}$]:

$$I_r(E_r) \;=\; \Gamma \frac{e}{h} \frac{dn}{dE}(E_r) \times \Big\{ [1 - f(E_r)] f(E_r - eV)$$

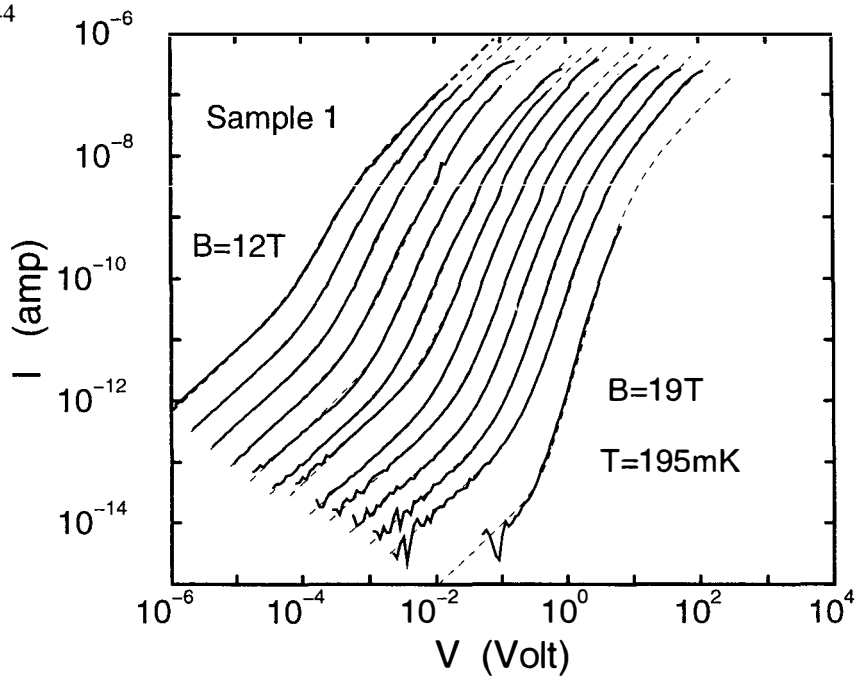


Figure 3: Log-log plot of the I-V characteristics (solid lines) for electron tunneling from the FQH edge into the bulk doped n+ GaAs in sample 1 at various magnetic fields from 12T to 19T in steps of 0.5T, 18T and 18.5T excluded. Corresponding filling factors vary from 2.69 to 4.26. Dashed lines represent best fits to Eq. 4. Successive curves are shifted by 0.3 units (a factor of 2) in the x-direction for clarity.

$$-f(E_r)[1-f(E_r-eV)]\Big\} \tag{1}$$

The real space position of the resonance in the tunnel junction causes the resonance energy, E_r, to depend on bias. Assuming the resonance is bound to the local band structure inside the barrier with energy E_0, and defining the lever arm parameter λ as the fraction of the applied bias that falls to the weakly coupled side of the resonance yields:

$$E_r(V,B) = \lambda eV + \beta B + E_0 \tag{2}$$

Eq. (1) and (2) and differentiation with respect to V yields the differential conductance:

$$\begin{aligned}\frac{dI_r}{dV}(E_r) &= \Gamma\frac{e^2}{h}\Big[\lambda\frac{d^2n}{dE^2}(E_r)\{\cdots\} - \lambda\frac{dn}{dE}(E_r)f'(E_r) \\ &\quad -(1-\lambda)\frac{dn}{dE}(E_r)f'(E_r-eV)\Big]\end{aligned} \tag{3}$$

where the expression in braces $\{\cdots\}$ is the same as that in Eq. 1.

In the *Fermi-liquid coupled* (FLC) limit, $\Gamma_{\rm FL} << \Gamma_{\rm QH}$, the Fermi-liquid density of states enters. Neglecting the first term in Eq. 3 relative to the others since for a FL $\frac{d^2n}{dE^2} << \frac{dn}{dE}f'(E)$ at low temperatures and approximating the density of states by $\frac{dn}{dE} = n_0$, the second term in Eq. 3 produces a peak weighted by λ when the resonance is aligned with the n^+ chemical potential, while the third term produces a peak weighted by $(1-\lambda)$ when the resonance is aligned with the chemical potential of the FQHE edge. These behaviors are qualitatively similar to the data in Fig. 2. In the contrasting *quantum Hall coupled* (QHC) limit $\Gamma_{\rm QH} << \Gamma_{\rm FL}$, the

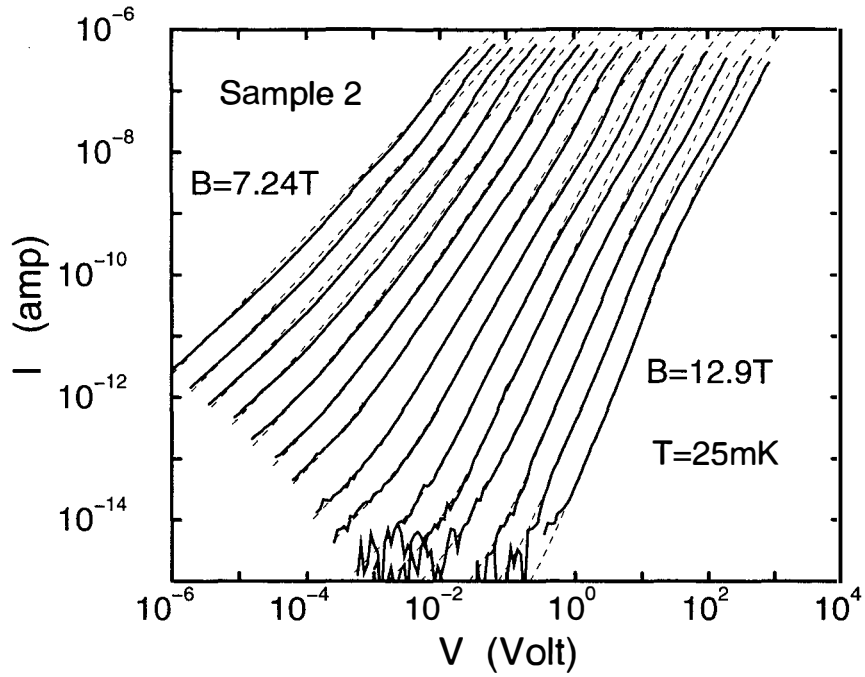


Figure 4: Log-log plot of I-V characteristics (solid lines) for sample 2 at B=7.24, 7.5, 7.76, 8.02, 8.28, 8.53, 8.79, 9.31, 9.83, 10.34, 10.86, 11.38, 11.9, 12.4, and 12.9T, ($1.611 < 1/\nu < 3$). Dashed lines represent best fits. Note x-shifts for clarity.

power law density of states enters. Here the resonance peak from the second term in Eq. 3 is completely suppressed because the density of states $\frac{dn}{dE}(E_r)|_{E_r=0} = E_r^{\alpha-1} = 0$, vanishes when the resonance is aligned with the FQHE chemical potential. We expect only a *single peak* from the third term when E_r is aligned with the n^+ chemical potential. The first term in Eq. 3, now contributes a conductance proportional to the derivative of the density of states $\frac{d^2n}{dE^2}$ between the two resonance centers. For $\alpha = 3$ at a 1/3 FQHE edge, this additional conductance goes as $\frac{dI}{dV} \sim E_r^{\alpha-2} \sim E_r$, a contribution that rises linearly with B as it approaches the single resonance peak, seen clearly in Fig. 2, left. More quantitatively, a fit of the data can be obtained by adopting the resonance formalism of Chamon and Wen[16] for sequential tunneling between biased chiral Luttinger liquids, keeping the Luttinger parameter of one channel at g = 1/3 and changing the parameter of the other channel to g = 1 to represent a Fermi liquid. The resulting fitting parameters are shown in Table 1.

4 Off-Resonance Tunneling

Next we discuss the behavior for off-resonance tunneling. Previous results have shown that the observed power law in the tunneling I-V characteristics are of extraordinary quality and can span $4\frac{1}{2}$ decades in current and $1\frac{1}{2}$ decades in excitation voltage, a dynamic range far surpassing other promising Luttinger liquid systems. Moeoever it was found that the power law behavior is not restricted to incompressible FQH fluids at special rational filling factors and is in fact present for general filling factors with the exponent, α, varying roughly as $1/\nu$ for $1/\nu > 1.3$.[3,4] The observed stands in direct contrast to theoretical expectations of step-like plateau features in α versus $1/\nu$,[2,19] (more precisely Hall resistivity,ρ_{xy},) and has presented a significant puzzle. Because the $\nu = 1/3$ FQH fluid possesses the largest gap and is robust, evidence for plateauing in the exponent is of critical importance.

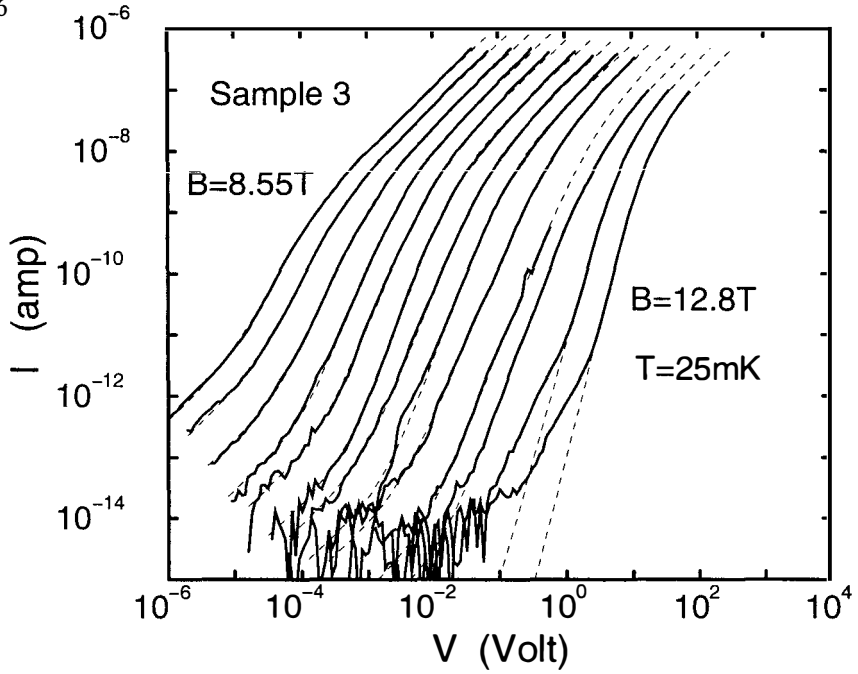


Figure 5: Log-log plot of I-V characteristics (solid lines) for sample 3 at B=8.55, 8.75, 9.15, 9.58, 10., 10.4, 10.8, 11.2, 11.6, 12.0, 12.2, 12.4, 12.8T, ($3.605 < 1/\nu < 5.082$). Dashed lines represent best fits. Note x-shifts for clarity.

Here we report clear observation of a plateau feature for the α versus $1/\nu$ dependence with an α value close to 3. Characterizing the α versus $1/\nu$ plot by the slope, $S \equiv d\alpha/d(1/\nu)$, in the first set of samples S exhibits an abrupt change from 1.15 ± 0.3 reflecting a roughly $\alpha \sim 1/\nu$ dependence to 0.15 ± 0.15 as $1/\nu$ increases beyond 2.76, constituting a reduction of more than a factor of seven in S. This plateau region of reduced slope extends from $1/\nu = 2.76$ to 3.33 before reverting to a value of ~ 1.05 above $1/\nu = 3.33$. Similarly in a second set S abruptly reduces from 0.33 ± 0.3 for $1/\nu < 4.12$ to -0.14 ± 0.18 for $4.12 < 1/\nu < 4.76$ before increasing rapidly, e.g. $S > 1.5$ for $1/\nu > 4.76$. In both sets of data the plateau region is centered about a value for α of 2.7, slightly below 3.

In figures 3-5 we presents log-log plots of the tunneling I-V characteristics between the 2DEG and the n+ GaAs bulk metal (solid curves) for samples 1, 2, and 3, respectively, in a wide range of magnetic fields/filling factors in order to deduce the behavior of the power law exponent, α, as a function of $1/\nu$. Successive curves are shifted in the positive direction on the horizontal axis by 0.3 units (a factor of 2) for clarity and curves for which sufficient dynamic range is available to yield a meaningful exponent are included. The dashed curves represent best fits to data as described below. Ideally, an I-V curve consists of 3 regimes: a) a low voltage bias regime with a linear I-V where the thermal energy, kT, dominates over the voltage bias energy, eV, ($eV \leq 2\pi kT$),[2,1] b) an intermediate voltage bias regime ($2\pi kT \leq eV \leq T_S$) exhibiting the important power law I-V behavior,[2,1,20] and c) a high bias saturation regime ($eV > kT_S$) in which I-V approaches linearity again and where the tunneling conductance saturates to the 2 terminal conductance of the 2DEG as the tunnel barrier becomes transparent. Here T_S represents a cross-over temperature with kT_S the cross-over energy above which saturation takes place. [20] In fact essentially all data for samples 1 and 3 exhibit this generic behavior while noting that the thermally dominated low voltage bias, linear regime (a) is visible only when it is above the noise floor ($\sim 4fA$).

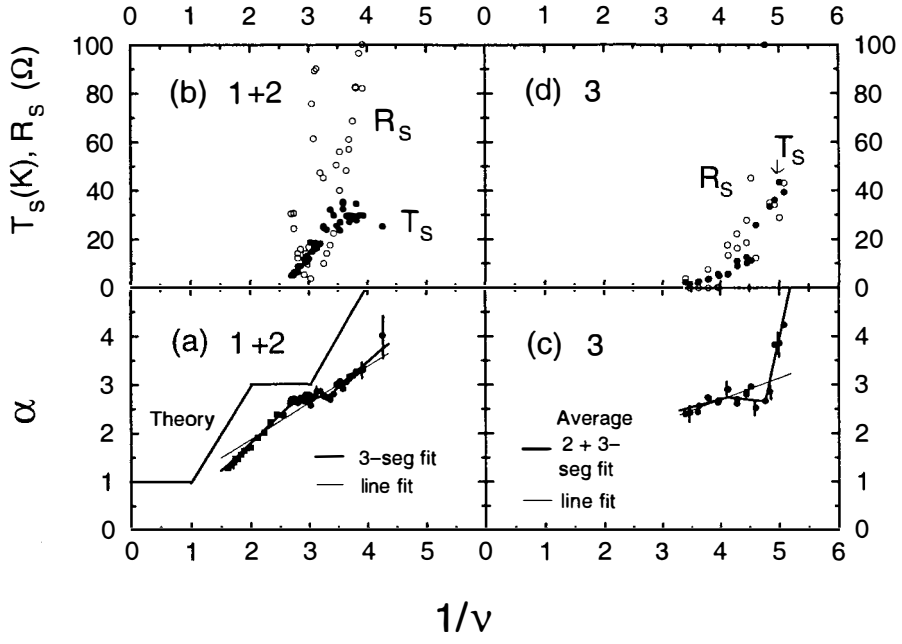


Figure 6: The power law exponent, α, for sample 1 and 2, versus $1/\nu$, in (a), for sample 3 in (c). Representative error bars are as shown and solid curves are as labeled. The parameters T_S and R_s are summarized in panels (b) and (d).

To establish the presence of a plateau feature in the exponent, α, we extract α in a systematic way by fitting the entire I-V range containing the three bias regimes to the Chamon-Fradkin expression for the tunnel current, I, at voltage bias, V, with the notation $\beta = \alpha - 1, r = \frac{2\pi T}{T_S}$:

$$I = \int_0^V \nu \frac{e^2}{h} \left(1 - \frac{e^{-\frac{1}{2}r^\beta}}{\left[\frac{\left(\frac{V'}{rT_S}\right)^\beta}{\Gamma^2\left(\frac{\alpha+1}{2}\right)} \left(1 - e^{-\frac{\beta}{2}r^\beta}\right) + 1 \right]^{\frac{\alpha}{\beta}}} \right) dV' \qquad (4)$$

which represents a universal scaling formula for tunneling into a Luttinger liquid with exponent, α, in conjunction with the constraint that $V_a = V + IR_s$ where V_a is the voltage applied on the device across contacts and R_s a 2DEG series resistance. Since the temperature is known, 3 parameters are need: α, T_S, and a 2DEG series resistance R_s. For samples 1 and 3, a full fit over the entire range of I-V can be accomplished. The fitted I-V curves are plotted as dashed lines. As evidenced by the near complete overlap of the fit and data in a majority of the traces, excellent fits are achieved. For sample 2, the absence of a true saturation regime precludes a full fit and the fitting is only performed within the low and intermediate bias regimes containing the linear and power law dependences.

Figure 6 summarizes the fitting parameters α, T_S, and R_s deduced for the two sets of samples versus $1/\nu$. Results for samples 1 and 2 containing identical 2DEG are presented together. We focus our attention on α in panels (a) and (c). To establish unequivocally the presence of a plateau we first fit our data to curves containing a) three line segments where the middle exhibits a reduced slope, b) two line segments, and c) a single straight lines, indexed by 3, 2,

Parameters for lever arm model.				
	R.1 (FLC)	R.2.A (QHC)	R.2.B (FLC)	
λ'	0.20	0.30	0.20	Lever arm
β	$+0.43\frac{\text{meV}}{\text{T}}$	$-0.26\frac{\text{meV}}{\text{T}}$	$+0.59\frac{\text{meV}}{\text{T}}$	dE_r/dB
Γ_{FL}	1.3	1.0	1.0	Coupling to n^+
Γ_{QH}	19.7	3.5	14.0	Coupling to QH edge
	$\times 1.5 \pm .1$	$\times 6 \pm 1$	$\times 1.7 \pm .1$	Area Increase - Data
	($\times$ 1.54)	($\times$ 5.9)	($\times$ 1.58)	(Area Increase - Fit)
	39μeV	30μeV	30μeV	at bias voltage

and 1, respectively. We next apply the statistical F-test on the resulting χ^2's. We find the 3-segment fit to be superior and are able to reject the competing 1- and 2-segment fits with a confidence exceeding 99%.

It is worthwhile to note that in both sample sets, the value of α is centered about a value of 2.7 below 3. Based on topological considerations, theory has traditionally predicted an exponent, α, of exactly 3 for short ranged electron-electron interaction. However, recently exact numerical diagonalization[21] as well as calculations based on composite Fermion edge-state wavefunctions[22] are indicating that for realistic interactions of either the 3-d Coulomb type or Yukawa type with screening distance of order the magnetic length, l_o, the exponent is no longer universal and takes on a value in the 2.6-2.75 range in agreement with experiment. These new developments suggest that the edge dynamics in the fractional quantum Hall regime may be more complex than previously thought and potentially will lead to further discoveries of more novel and interesting physics.

Acknowledgement

A.M.C. would like to thank Virginia Pang-Ying Yeh Chang for her many contributions. He gratefully acknowledges the contributions of his collaborators L.N. Pfeiffer, K.W. West, M. Grayson, D.C. Tsui, M.K. Wu, and C.C. Chi, and also wishes to acknowledge stimulating conversations with M. Fisher, E. Fradkin, B. Halperin, C. Kane, L. Levitov, and X.-G. Wen. Work at Purdue supported by NSF Grant #DMR-9801760. Work at Tsing-Hua University supported by the Taiwan National Science Council.

References

1. X.G. Wen, Phys. Rev. **B43**, 11025 (1991); Phys. Rev. Lett. **64**, 2206 (1990); Phys. Rev **B44**, 5708 (1991), Int. Jour. Mod. Phys. B **6**, 1711 (1992).
2. C.L. Kane, and M.P.A. Fisher, Phys. Rev. **B46**, 15233 (1992); Phys. Rev. Lett. **68**, 1220 (1992), Phys. Rev. **B51**, 13449 (1995).
3. A.M. Chang, L.N. Pfeiffer, and K.W. West, Phys. Rev. Lett. **77**, 2538 (1996); Physica **B249-251**, 383 (1998).
4. M. Grayson et al., Phys. Rev. Lett. **80**, 1062 (1998).
5. P. Fendley et al., Phys. Rev. Lett. **74**, 3005 (1995).
6. K. Moon et al., Phys. Rev. Lett. **71**, 4381 (1993).
7. K. Imura and N. Nagaosa, Phys. Rev. **B55**, 7690 (1977).
8. W.J. Zheng and Yue Yu, Phys. Rev. Lett. **79**, 3242 (1997).

9. J.M. Luttinger, J. Math. Phys. **4**, 1154 (1963); S. Tomonaga, Prog. Theor. P hys. (Kyoto) **5**, 544 (1950).
10. F.D.M. Haldane, J. Phys. **C14**, 2585 (1981); and Phys. Rev. Lett. **47**, 1840 (1981).
11. U. Zuelicke, and A.H. MacDonald, Phys. Rev. **B54**, R8349 (1996).
12. M. Grayson, D.C. Tsui, L.N. Pfeiffer, K.W. West, and A.M. Chang, Phys. Rev. Lett. **86**, 2645 (2001)
13. A.M. Chang, M.K. Wu, C.C. Chi, L.N. Pfeiffer, and K. W. West, Phys. Rev. Lett. **86**, 143 (2001).
14. L.N. Pfeiffer et al., Appl. Phys. Lett. **56**, 1697 (1990).
15. C. L. Kane and M. P. A. Fisher, Phys. Rev. **B 46**, 15233 (1992).
16. C. Chamon and X. G. Wen, Phys. Rev. Lett. **70**, 2605 (1993).
17. A. Furusaki and N. Nagoaosa, Phys. Rev. **B 47** 3827 (1993); A. Furusaki, Phys. Rev. **B 57** 7141 (1998).
18. F. P. Milliken, C. P. Umbach and R. A. Webb, Solid State Comm. **97**, 309 (1996).
19. A.V. Shytov et al., Phys. Rev. Lett. **80**, 141 (1998).
20. C. Chamon and E. Fradkin, Phys. Rev. **B56**, 2012 (1997).
21. V.J. Goldman, and E.V. Tsiper, cond-mat/0101221 and to appear in Phys. Rev. Lett ., June 25 (2001).
22. Sudhansu S. Mandal, and J.K. Jain, cond-mat/0103630.

COHERENT CONTROL OF FRACTIONAL CHARGES IN QUANTUM ANTIDOT DEVICES

V. J. GOLDMAN[1]
[1] *Department of Physics, State University of New York, Stony Brook, NY 11794-3800, U.S.A.*

I review the basic physics of quantum antidots in the quantum Hall regime. Recent experiments have demonstrated invariance of charge of antidot-bound Laughlin quasiparticles, and their coherence in a quantum antidot "molecule". Thus we conclude, based on our experimental results, that it is possible to control and manipulate fractional quasiparticles localized on quantum antidots in a manner similar to electrons in quantum dots. An objective of future research is to study the possibility of using the controlled transport of fractional quasiparticles in multiple antidots to perform topological quantum logic operations.

1 Introduction

A quantum antidot (QAD) electrometer has been used in the first direct observation of the fractionally quantized electric charge of Laughlin quasiparticles.[1] In a parallel development, topological computation with Abelian and non-Abelian quasiparticles of two-dimensional interacting electron systems has been suggested as a way of implementing intrinsically fault-tolerant quantum computation.[2] Topological computation employs a fractional statistical phase created by the transfer of one quasiparticle of the system around another to perform quantum logic. Such a phase is fixed by the topological properties of the system wavefunction and should be insensitive to environment-induced perturbations of the quasiparticle dynamics. The most thoroughly studied and realistic example of a two-dimensional system with fractional statistics of quasiparticles is provided by incompressible electron liquids of the fractional quantum Hall (FQH) effect. [3]

A review of the basic physics of quantum antidots in the $i = 1$ and $f = 1/3$ QH states is followed by an account of recent experiments demonstrating invariance of quasiparticle charge on the integer $i = 1, 2$ and fractional $f = 1/3$ quantum Hall plateaus extending over a filling factor range of at least 27%.[4] In these experiments the Laughlin quasiparticle charge has been found to be $e^* = e/3 \pm 1.2\%$ independent of temperature, tunneling current and conductance in a wide range of experimental parameters. The experimental determination of the $e/3$ quasiparticle coherence time has demonstrated a coherently coupled quantum antidot "molecule".[5] Thus we conclude, based on our experimental results, which imply robustness of Laughlin quasiparticles localized on QADs, that it is possible to control and manipulate fractional quasiparticles in a manner similar to electrons in quantum dots.

The objective of future research is to study possibility of using the controlled transport of FQH quasiparticles in structures with multiple antidots to perform quantum logic operations.[6] The most important question to be answered by the future work is to what extent the topological nature of the statistical phase of fractionally charged quasiparticles helps to alleviate the decoherence problem in quantum computation. The future research should result in a detailed understanding of topological quantum computation and should clarify issues relevant to its eventual practical implementation using FQH systems.

2 Quasiparticles in the Quantum Hall Effect

The most conspicuous aspect of the quantum Hall effect[3] (QHE) is the constancy of the Hall conductance over a finite range of the filling factor ν. Indeed, this property defines the phenomenon of QHE; the *quantized* value of the Hall conductance σ_{xy} of a particular QH state in units of $\frac{e^2}{h}$ is a principal quantum number of that QH state, $f = \sigma_{xy} h/e^2$, called "exact filling". Specifically,

the electric charge of the quasiparticles is expected to be determined by the relevant quantum numbers, including f, and thus is not expected to vary on a QH plateau when ν is varied from the exact filling [7,8]. The exactness of quantization of the Hall conductance is understood as a consequence of the gauge invariance of electromagnetic field and the exact quantization of the charge of electrons [7]. On a plateau the charge of quasiparticles localized in the *interior* of a two dimensional electron system (2DES) is well defined [9]. In the case of the integer QH plateau at exact filling $f = i$ ($i = 1, 2, \ldots$) the quasielectrons are simply electrons in the Landau level $i+1$, and the quasiholes are the holes in the i-th level. It is easy to understand the properties of FQH quasiparticles using composite fermions [10]. In the case of the FQH plateau at $f = \frac{i^*}{2pi^*+1}$ quasielectrons are composite fermions (an electron binding $2p$ vortices) in the "Landau level" $i^* + 1$ of composite fermions, and the quasiholes are the holes in the i^*-th level. It has been predicted theoretically [11,12] that the electric charge of these quasiparticles is $q = \frac{e}{2pi^*+1}$. This fascinating fractional quantization of electric charge is a fundamental property of the strongly correlated FQH fluid.

However, the above-described "orthodox" theory has been questioned from two different directions. Jain has argued that since fractional quasiparticles and quasiholes are extended composite objects, their properties, and in particular charge, are not well defined away from exact filling, when their density is high and "they can certainly not be assigned a well defined charge or statistics" [13]. Even more recently, experiments measuring shot noise power in QH constrictions without antidots have been reported; these experiments, interpreted as a measurement of Laughlin quasiparticle charge, show variations of q by factors of up to three and even six depending on all: filling factor, two-terminal conductance, applied current and temperature [14]. If the charge of quasiparticles is not a well-defined and invariant quantum number throughout a plateau, then the "orthodox" theoretical proof of the exactness of quantization of σ_{xy} in the QHE [7,8] would *require* that there were corresponding large corrections to the Hall conductance too. Otherwise, if σ_{xy} is quantized exactly in some limit, with only exponentially small corrections, as numerous experiments show, the validity of the "orthodox" theory is under suspicion and additional theory is required to explain exact quantization of the Hall conductance even when the charge of quasiparticles is not well defined.

Although six years have passed since the first direct observation of $\frac{1}{3}e$ particles in quantum antidot (QAD) electrometer experiments [1], one crucial aspect of the theory remained untested: the invariance of charge at ν far from exact filling. In this paper we review experiments performed on the integer $i = 1, 2$ and fractional $f = \frac{1}{3}$ QH plateaus which extend over a filling factor ν range of 27% to 45%. The charge of the QAD-bound Laughlin quasiparticles has been measured to be constant, independent of ν over the entire plateau extent, with relative accuracy of $\pm 1.2\%$ and absolute accuracy of 4%. In addition, we observe no variation of the quasiparticle charge upon variation of temperature, tunneling conductance or applied current in the experimentally accessible range.

3 Quantum Antidot Electrometer

The QAD electrometer [1,15] is illustrated in Fig. 1. The antidot is defined lithographically in a constriction between two front gates in a 2DES. The antidot and the front gates create depletion potential hills in the 2DES plane and, in quantizing magnetic field B, the QHE edge channels are formed following equipotentials where the electron density n is such that $\nu = hn/eB$ is equal to integer i or fractional f exact filling. The edge channels on the periphery of the 2DES have a continuous energy spectrum, while the particle states of the edge channel circling the antidot are quantized by the Aharonov-Bohm condition that the state ψ_m with angular momentum $\hbar m$, in each Landau level, encloses $m\phi_0 = m\frac{h}{e}$ magnetic flux. In other words, the semiclassical area of the state ψ_m is $S_m = m\phi_0/B$. The electrometer application is made possible by a large,

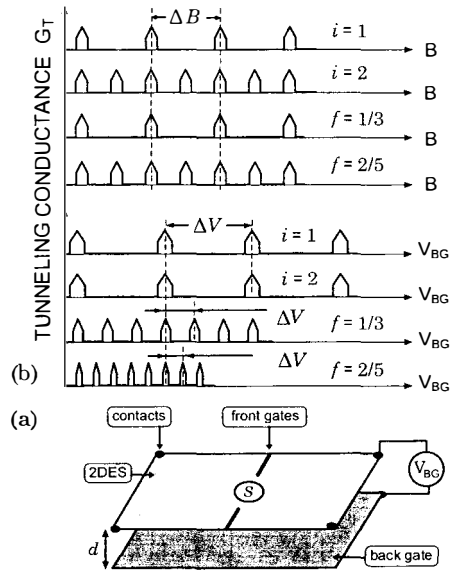


Figure 1: (a) Schematic of the quantum antidot electrometer. (b) Idealized summary of experimental observations. There is one G_T peak on the $i = 1$ and $f = \frac{1}{3}$ plateaus, and two peaks on the $i = 2$ and $f = \frac{2}{5}$ plateaus observed per period ΔB, with the back gate voltage held constant $V_{BG} = 0$. ΔB gives the size of the QAD: $S = \phi_0/\Delta B$. The same G_T peaks are also observed when a small perpendicular electric field V_{BG}/d is applied to 2DES by biasing the back gate. The period ΔV_{BG} then directly gives the charge q of the QAD-bound particles, in Coulombs, via $q = (\epsilon\epsilon_0\phi_0/d)(\Delta V_{BG}/\Delta B)$.

global "back gate" on the opposite side of the insulating GaAs substrate of thickness d. This gate forms a parallel plate capacitor with the 2D electrons.

When the constriction is on a quantum Hall plateau, particles can tunnel resonantly via the QAD-bound states giving rise to quasiperiodic tunneling conductance G_T peaks [16], see Fig. 1. A peak in G_T occurs when a QAD-bound state crosses the chemical potential and thus marks the change of QAD occupation by one particle. The experimental fact that the G_T peaks are observed implies that the charge induced in the QAD is quantized, that it comes in discrete particles occupying the antidot-bound states; the G_T peaks mark the change of the population of the QAD by one particle per peak. Measuring G_T as a function of B gives the area of the QAD-bound state through which the tunneling occurs, $S = \phi_0/\Delta B$, where ΔB is the quasiperiod in magnetic field. On the $\nu \approx i$ plateau there are i peaks per ΔB because i Landau levels are occupied. The above discussion is easy to generalize for $f = \frac{i^*}{2pi^*+1}$ FQH plateaus by considering "Landau levels" of composite fermions.

First, we neglect the small ($\sim 10\%$) change of the QAD area S upon change of B. The charge of the QAD-bound particles is then determined directly from the separation of the same G_T peaks as a function of the back gate voltage V_{BG}, Fig. 2. The back gate produces uniform electric field $E_\perp = V_{BG}/d$ which induces a small change of $\epsilon\epsilon_0 E_\perp$ in the 2DES charge density.[17] Classical electrostatics states [18] that the charge induced in the QAD is exactly equal to the 2D charge density induced far from the QAD times the area of the QAD, $\epsilon\epsilon_0 E_\perp S$. The classical correction due to finite size of the antidot is very small: $S/\pi d^2 \sim 10^{-6}$. The quantum capacitance correction due to finite compressibility of 2DES [19,20] is very small too: $\sim 10^{-5}$. Thus, the charge of one particle q is directly given by the electric field needed to attract one more particle in the area S: $q = \epsilon\epsilon_0 S\Delta V_{BG}/d$, where ΔV_{BG} is the change of the global gate voltage between two

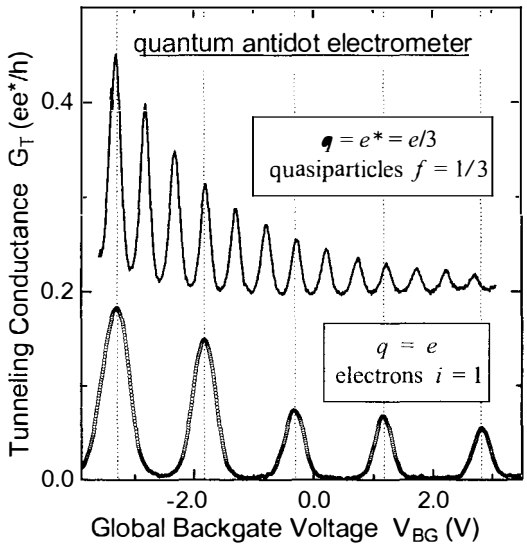


Figure 2: In the experiment G_T peaks occur each time the occupation of the antidot changes by one particle, an electron for IQHE and a Laughlin quasielectron for the $f = \frac{1}{3}$ FQHE. The measured charge q of the particle is directly proportional to V_{BG}: it takes the same electric field V_{BG}/d to attract three $e/3$ quasiparticles as one electron. The upper G_T curve is offset vertically by $0.2e^2/3h$.

consecutive conductance peaks.[21] An absolute and more accurate determination of q uses direct measurement of area $S = \phi_0/\Delta B$ for each QH plateau, as described in Sect. 5.

4 Resonant Tunneling Experiments

We use low disorder GaAs heterojunction material where 2DES (density 1×10^{11} cm^{-2} and mobility 2×10^{6} cm$^2/Vs$) is prepared by exposure to red light at 4.2 K. The antidot-in-a-constriction geometry (somewhat different from that of Refs.[1,15]) was defined by electron beam lithography on a pre-etched mesa with Ohmic contacts. After ≈150 nm of chemical etching, Au/Ti front gate metalization was deposited in the etched trenches. Samples were mounted on sapphire substrates with In metal which serves as the global back gate. All data presented in this paper were taken at 12 mK bath temperature with sample immersed in ^{3}He - ^{4}He mixture. Extensive cold filtering cuts the electromagnetic background incident on the sample to 5×10^{-17} W, which allows us to achieve a record low effective electron temperature of 18 mK reported for a mesoscopic sample [22,5].

Figures 3 and 4 show the directly measured four-terminal R_{xx} *vs.* B data for two QAD plateaus: $i = 1$ and $f = \frac{1}{3}$. We use ν to denote the filling factor in the constriction region. The front gates are biased negatively in order to bring the edges closer to the antidot to increase the amplitude of the tunneling peaks to a measurable level. This results in ν being smaller than ν_B in the rest of the sample ("the bulk"). A QHE sample with two ν_B regions separated by a lower ν region, if no tunneling occurs, has $R_{xx} = R_L \approx R_{xy}(\nu) - R_{xy}(\nu_B)$. The equality is exact if both ν and ν_B are on a plateau, where the Hall resistances of all regions aquire quantized values. Thus, several R_L plateaus (neglecting tunneling peaks) are seen in Figs. 3 and 4. The tunneling peaks are superimposed on the smooth R_L background, and we calculate G_T as described previously [15,22]. In some data we observe both R_{xx} peaks for $\nu < i$ ("back scattering") and dips for $\nu > i$ ("forward scattering") [16,23]. Details of this behavior were presented elsewhere.

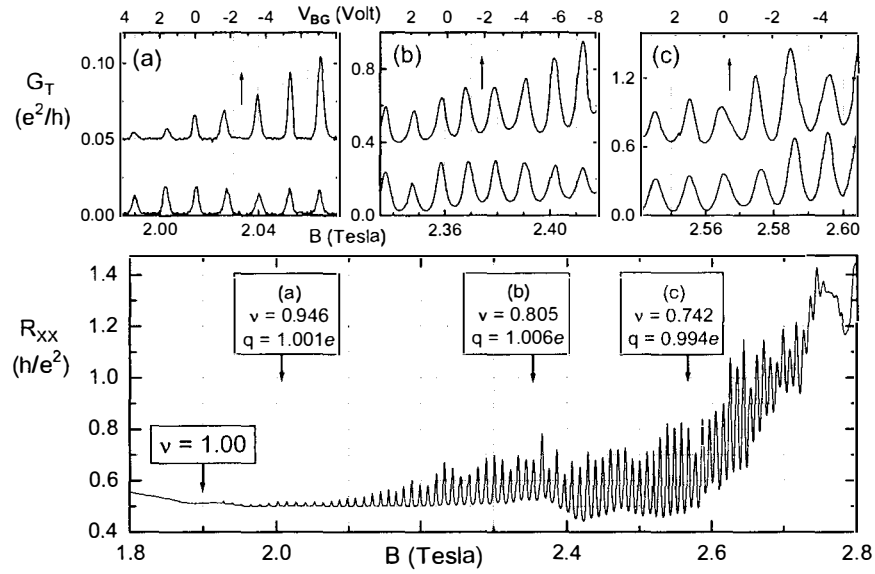


Figure 3: R_{xx} *vs.* magnetic field B for the antidot filling ν on the $i = 1$ plateau. The upper panels (a) - (c) give the tunneling conductance measured both as a function of B (back gate voltage $V_{BG} = 0$), and as a function of V_{BG} (B is held constant). The G_T *vs.* V_{BG} curves in panels (a) - (c) are offset vertically.

5 Quasiparticle Charge

At several ν on each plateau we took high resolution B-sweeps at $V_{BG} = 0$, and, having put the superconducting magnet in the persistent current mode to fix B, we took corresponding sweeps of V_{BG}. This constitutes an accurate measurement of QAD-bound quasiparticle charge, as described in Sect. 3. Representative G_T *vs.* B and V_{BG} data are shown in the upper panels of Figs. 3 and 4. Note that the negative V_{BG} axis direction corresponds to the increasing B. This is so because increasing B results in incremental depopulation of QAD, independent of the sign of the particle charge: the states ψ_m move closer to the center of the QAD, that is, states move above the chemical potential and become unoccupied. Negative V_{BG} depopulates the QAD if the charge of the particles is negative. Thus the QAD electrometer measures not only the magnitude of q, but also its sign.

As discussed in Sect. 3, the charge of one QAD-bound particle q is directly given by the electric field needed to attract one more particle in the area S: $q = \epsilon\epsilon_0 S\Delta V_{BG}/d$, where ΔV_{BG} is the change of the global gate voltage between two consecutive conductance peaks [1,15]. The magnitude of the charge q of the QAD-bound particles is then given by

$$q = \frac{\epsilon\epsilon_0\phi_0}{d} \cdot \frac{\Delta V_{BG}}{\Delta B} \quad \text{in Coulombs,} \tag{1}$$

using the low-temperature GaAs dielectric constant $\epsilon = 12.74$ [24] and the measured thickness of the sample $d \approx 0.430$ mm. The average of the eleven values obtained for the $i = 1, 2$ plateaus $\langle q \rangle_{\text{integer}} = 0.9651e$ is off by 3.5%, more than the standard deviation of $0.0070e$ for the combined data [25], and similar to the results from another electrometer device reported in Refs. [1,15]. We then *normalize* values of q by setting $\langle q \rangle_{\text{integer}} = e$. Thus determined q are shown for (a) - (c) data in Figs. 3 and 4, and summarized in Fig. 5. The striking feature of the data of Fig. 5 is that the values of q are constant to a relative accuracy of at least $\pm 1.2\%$ throughout the plateau

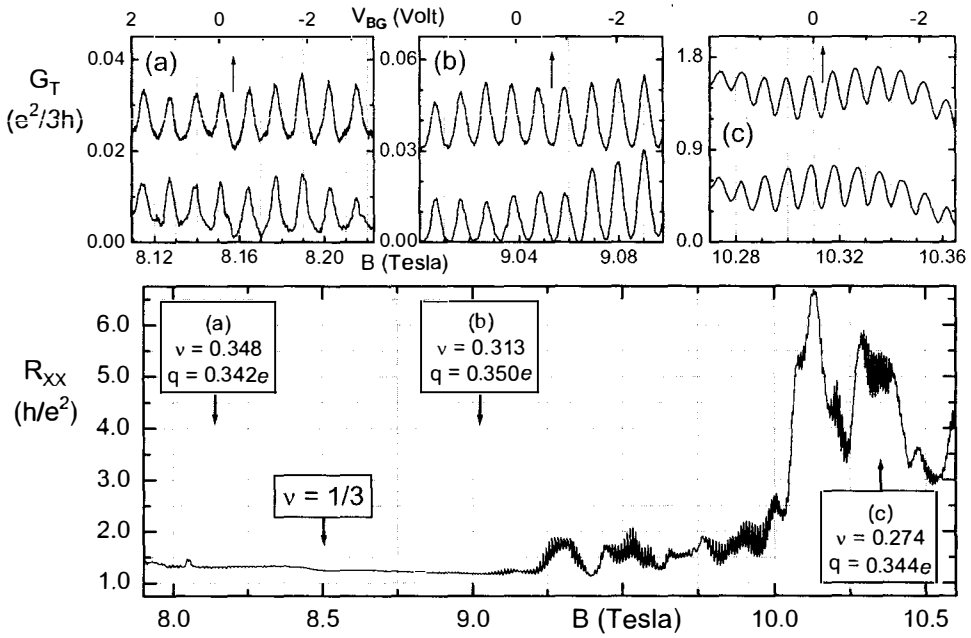


Figure 4: R_{xx} *vs.* magnetic field B for the antidot filling ν on the $f = \frac{1}{3}$ plateau. The upper panels (a) - (c) give the tunneling conductance measured both as a function of B (back gate voltage $V_{BG} = 0$), and as a function of V_{BG} (B is held constant). The G_T *vs.* V_{BG} curves in panels (a) - (c) are offset vertically.

regions where it was possible to measure the particle charge. The range of ν is about 45% for the $i = 2$ plateau, 27% for the $i = 1$ plateau (the combined normalized ν/i range is 57%), and also 27% for the $f = \frac{1}{3}$ plateau.

For $\nu = 0.274$ on the $f = \frac{1}{3}$ plateau (inset (c) in Fig. 4), the density of quasiholes is $3(1 - 3\nu) \approx 0.53n$; that is, on the average there is one quasihole per two 2D electrons. The average separation between these quasiholes is $7\ell_0$, where ℓ_0 is the magnetic length. Given that $23\ell_0^2$ is the average area per electron, and that the characteristic"radius" of an $e/3$ quasihole[3] is $\sqrt{6\pi}\ell_0 \approx 4\ell_0$, we conclude that under these conditions the quasiholes do overlap; yet, as our data show, their charge is still well-defined, being quantized to at least 3%. Thus Laughlin quasiparticles at low energies do behave as just particles. We should add that FQH quasiparticles are the elementary charged excitations of the FQH condensate, a distinct state of matter that is necessarily separated from all noninteracting electron states by a phase transition. Therefore, FQH quasiparticles are composite objects vastly different from electrons, and are *not* adiabatic images of electrons as are quasiparticle excitations of metals and band insulators (such as the IQHE states).

We also note that the tunneling current $I_t \approx IG_T/\sigma_{xy}$ is proportional to G_T and thus varies much for peaks of different amplitude. Here I is the applied current used to measure R_{xx}; the $f = \frac{1}{3}$ plateau data of Fig. 4 was taken with $I = 50$ pA, and we have measured $\Delta V_{BG}/\Delta B$ with I up to 1 nA, which, combined with the variation in *peak* G_T by a factor of ≈ 100 gives the range of 5×10^{-13} A $\leq I_t \leq 2\times10^{-10}$ A. Furthermore, $\Delta V_{BG}/\Delta B$ has been measured in the temperature range 12 mK $\leq T \leq$ 70 mK [20,22]. Under these conditions we observe no change in the value of $q = e/3$ within our experimental accuracy of a few percent. These results are in stark disagreement with recent reports of experiments [14]measuring shot noise power in QH

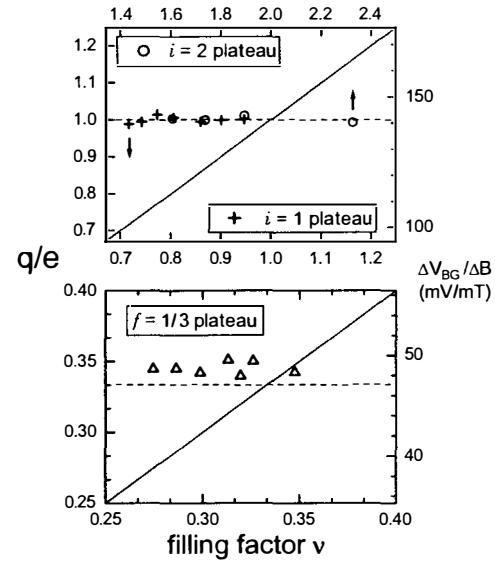


Figure 5: Summary of the measured QAD-bound quasiparticle charge q in units of e. The horizontal dashed lines give the values e and $e/3$. The solid lines have the unit slope $\propto \nu$.

constrictions without antidots, which, interpreted as a measurement of charge, show variations of q by factors of up to three and even six depending on all: ν, I_t, G_T and T.

Thus, based on our experimental results, we conclude that the charge of the bulk quasiparticles is indeed a well defined quantum number characterizing a particular QHE state.

6 Conclusions

"Topological" quantum computation with FQH quasiparticles has been suggested as a possible physical realization of intrinsically fault-tolerant quantum computation. Our recent experiments have demonstrated invariance of charge of antidot-bound Laughlin quasiparticles, and their coherence in a quantum antidot "molecule". Thus we conclude, based on our experimental results, that it is possible to control and manipulate fractional quasiparticles localized on quantum antidots, which opens an experimental possibility of a fault-tolerant quantum computation with anyons.

Acknowledgments

Parts of this work were done in collaboration with D. V. Averin, I. Karakurt, J. Liu, I. J. Maasilta and A. Zaslavsky. This work was supported by the US NSF and the US ARO.

References

1. V. J. Goldman and B. Su, Science **267**, 1010 (1995).
2. S. Lloyd, *"Quantum computation with Abelian anyons"*, quant-ph/ 0004010 and references therein.
3. For reviews see: *The Quantum Hall Effect*, 2nd Ed. (ed. by R. E. Prange and S. M. Girvin) Springer, NY (1990); *Perspectives in Quantum Hall Effects*, (ed. by S. Das Sarma and

A. Pinczuk) Wiley, NY (1997); S. M. Girvin, *The Quantum Hall Effect*, Les Houches Lecture Notes (1998); V. J. Goldman, Physica B **280**, 372 (2000).
4. V. J. Goldman, I. Karakurt, J. Liu, and A. Zaslavsky, Phys. Rev. B **64**, 0853XX-1 (2001).
5. I. J. Maasilta and V. J. Goldman, Phys. Rev. Lett. **84**, 1776 (2000).
6. D. V. Averin and V. J. Goldman, to be published.
7. R. B. Laughlin, Phys. Rev. B **23**, 5632 (1981).
8. B. I. Halperin, Phys. Rev. B **25**, 2185 (1982).
9. The excitation spectrum of QH edge channels is gapless, thus excitations of arbitrary charge can be created; see X.-G. Wen, Intl. J. Mod. Phys. B **6**, 1711 (1992). These edge excitations are a sort of 1D charge density fluctuations in the direction transverse to the edge, and generally are not Laughlin quasiparticles. A weakly coupled QAD serves as a "charge filter" for interedge tunneling.
10. J. K. Jain and V. J. Goldman, Phys. Rev. B **45**, 1255 (1992).
11. R. B. Laughlin, Phys. Rev. Lett. **50**, 1395 (1983).
12. F. D. M. Haldane, Phys. Rev. Lett. **51**, 605 (1983); B. I. Halperin, Phys. Rev. Lett. **52**, 1583 (1984).
13. J. K. Jain, Adv. Phys. **41**, 105 (1992); J. K. Jain, in "*Rerspectives in Quantum Hall Effects*", Ref. 3.
14. D. Glattli *et al.*, Physica E **6**, 22 (2000); T. Griffiths *et al.*, Phys. Rev. Lett. **85**, 3919 (2000).
15. V. J. Goldman, Physica E **1**, 15 (1997); mesurement of $e/5$ quasiparticles in the $q = e/5$ data are given in V. J. Goldman, Surf. Sci. **362**, 1 (1996).
16. J. K. Jain and S. A. Kivelson, Phys. Rev. Lett. **60**, 1542 (1988).
17. Even on a QHE plateau it is possible to change 2DES density in the "incompressible" interior with a gate so long as it is done slowly on the time scale of $\tau = RC \approx \epsilon\epsilon_0 L^2/(d\sigma_{xx})$, where L is the size of 2DES, because of finite diagonal conductivity σ_{xx} at a finite temperature.
18. L. D. Landau and E. M. Lifshitz, *Electrodynamics of Continuous Media*, Chap. 1, Sect. 3.
19. A. L. Efros, Solid State. Commun. **65**, 1281 (1988).
20. I. J. Maasilta and V. J. Goldman, Phys. Rev. B **57**, R4273 (1998).
21. A small front gate that *defines* the antidot (as in J. Franklin *et al.*, Surf. Sci. **361/362**, 17 (1996)) clearly does not produce a uniform $E_\perp$.
22. I. J. Maasilta and V. J. Goldman, Phys. Rev. B **55**, 4081 (1997).
23. C. J. B. Ford *et al.*, Phys. Rev. B **49**, 17456 (1994).
24. G. A. Samara, Phys. Rev. B **27**, 3494 (1983).
25. Unintentional impurities near the antidot can change their charge state as B or V_{BG} are swept. Such events, often reproducible, cause "phase slips" of the G_T peaks; we exclude such data from the charge analysis.

Unpolarizable ground states in the fractional quantum Hall effect at $\nu = 2/3$

N. Freytag[1], Y. Tokunaga[1], M. Horvatić[1], C. Berthier[1,2], M. Shayegan[3], L. P. Lévy[1,4]

[1] *Grenoble High Magnetic Field Laboratory, MPI-FKF and CNRS, B.P.166, F-38042 Grenoble Cedex 9*

[2] *Laboratoire de Spectrométrie Physique, Université J. Fourier, B.P. 87, F-38402 St. Martin d'Hères*

[3] *Department of Electrical Engineering, Princeton University, Princeton N.J. 08544*

[4] *Institut Universitaire de France and Université J. Fourier, B.P. 41, F-38402 St. Martin d'Hères, France,* email:levy@grenet.fr

There are now clear evidences[1,2] that the two-dimensional electron gas in the lowest Landau level becomes fully polarized only when the Zeeman energy is sufficiently large. The relative strength of the Zeeman (Δ_Z) to the Coulomb energy (Δ_Z) is measured with the parameter $\eta = \Delta_Z/\Delta_C$ which may be varied by tilting the two-dimensional electron gas with respect to the total magnetic field $\vec{B}$, keeping the normal component to the sample constant. At $\nu = 2/3$, a remarkable behavior of the electron spin polarization is observed as a function of η through the NMR ^{71}Ga Knight-shift in two GaAs/GaAlAs multiple quantum wells samples. The polarization jumps abruptly from $P = 1$ to another value of P close to 3/4, as η is decreased below $\eta_c = 0.0185$. Activation studies show that the fully and three-quarter polarized states are gapped with comparable values of the activation energy. This is strong evidence that the partially polarized state at this fraction is also incompressible.

1 Introduction

It is now established[1,2] that the two-dimensional electron gas is not always fully polarized in the lowest Landau level. Several theoretical approaches have been used to find the possible polarization of fractional quantum Hall (FQH) states[4,6]. A very simple picture can be derived from the Composite Fermion (CF) model of the fractional quantum Hall effect which maps each state onto an integer quantum Hall state using a series of polarization preserving transformations. In this picture, the possible polarizations of FQH states are the polarizations of filled Landau levels which may be realized as a function of Zeeman energy. The following table summarizes the possible spin-configurations of the filled parent integer states and their mapping onto the corresponding daughter fractional states. The transformation $\mathcal{D}$ attaches two flux quanta per electron and maps the integer state ν to the fractional state $\nu^* = \nu/(2\nu + 1)$. $\mathcal{R}$ reverses the magnetic field direction, mapping ν into $-\nu$. The combination $\mathcal{DR}$ maps ν into $\nu^* = \nu/(2\nu - 1)$, and is often referred to as an anti-parallel flux attachment. Finally the charge conjugation symmetry, including spin degrees of freedom, maps ν^* into $2 - \nu^*$. The Landau level translation operator $\mathcal{L}$ shifts ν into $\nu + 1$ adding a fully spin polarized level with either $\uparrow$ or $\downarrow$ spin.

ν	$\mathcal{P}$ {conf }	$\mathcal{P}$ {conf }	$\mathcal{P}$ {conf }	ν_{CF} $[\mathcal{D}]$	ν_{CF} $[\mathcal{DR}]$	ν_{CF} $[\mathcal{L}_{\uparrow,\downarrow}^{-1}\mathcal{CD}]$
1	1 $\{\uparrow\}$	-	-	1/3	-	2/3
2	0 $\{\uparrow,\downarrow\}$	1 $\{\uparrow,\uparrow\}$	-	2/5	2/3	3/5
3	1/3 $\{\uparrow,\downarrow,\uparrow\}$	1 $\{\uparrow,\uparrow,\uparrow\}$	-	3/7	3/5	4/7
4	0 $\{\uparrow,\downarrow,\uparrow,\downarrow\}$	1/2 $\{\uparrow,\uparrow,\uparrow,\downarrow\}$	1 $\{\uparrow,\uparrow,\uparrow,\uparrow\}$	4/9	4/7	5/9
5	1/5 $\{\uparrow,\downarrow,\uparrow,\downarrow,\uparrow\}$	3/5 $\{\uparrow,\downarrow,\uparrow,\uparrow,\uparrow\}$	1 $\{\uparrow,\uparrow,\uparrow,\uparrow,\uparrow\}$	5/11	5/9	7/11

Table 1: Possible polarization of integer and fractional quantum Hall states for arbitrary Zeeman energy. The spin configurations of filled Landau bands are represented by arrows. The transformations $\mathcal{R}$, $\mathcal{D}$, $\mathcal{C}$ $\mathcal{L}_{\uparrow,\downarrow}$ mapping integer to fractional QH states are defined in the text.

The result of all these transformations, projected in the lowest Landau level, are completely filled CF spin-levels. They are gapped states, homogenous in space, *i.e.* their wavefunctions are

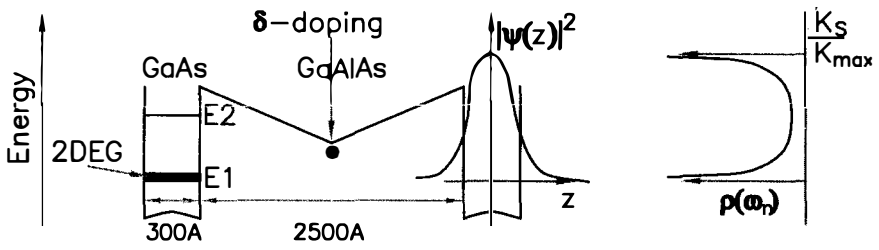


Figure 1: Left: schematic bandstructure of the GaAs/GaAlAs multilayer-sample M280 (resp. M242). 300Å (resp. 250Å) wide GaAs quantum wells are separated by 2500Å (resp. 1850Å) GaAlAs barriers. Electrons are transferred from the $\delta-$doped layer into the lowest electrical subband of the quantum wells. Right: the profile of the electron charge density $|\psi(z)|^2$ in the wells determines the spectral weight of the well-nuclei $\rho_n(z)$ shifted by a Knight shift K_s relative to the maximum shift K_s^{max} in the middle of the wells.

invariant under spatial transformations in the lowest Landau level.

Varying the Zeeman energy, transitions between different polarized ground states can be induced. In the integer regime, a transition between two $\nu = 2$ spin states has been observed in a tilted field magneto-transport experiment in a GaInP/InP heterostructure[7] and at $\nu = 4$ in a hole-doped GaAlAs/GaAs[8] heterojunction.

In the fractional regime, theoretical[5,6] studies have focused on $\nu = 2/3$ where a phase transition from unpolarized to fully polarized state is predicted at a critical value η_c of the ratio between Zeeman to Coulomb energy $\eta = \Delta_Z/\Delta_C$.

This transition has also been observed experimentally in magneto-transport[9,10] and magneto-optical[11,12,13] studies of the 2D electron-gas at a critical value $\eta_c \approx 0.01$. In the NMR studies presented here, experimentally accessible values for η using the tilted field technique always exceed 0.014, where the system should always be fully polarized according to these earlier studies. From the data presented in Fig. 3, we see this is not the case: at low magnetic fields, the polarization at $\nu = 2/3$ is clearly less than one. This observation stresses the importance of *direct* experimental observations of the electron spin-polarization, which is carried out in this study using Nuclear Magnetic Resonance (NMR).

2 NMR and spin polarization in quantum wells

The two multi-layer samples used in this NMR study are schematically represented in Fig. 1. The 100 MBE grown layers are 300Å (resp. 250Å) wide GaAs quantum wells separated from each other by much thicker $Al_xGa_{1-x}As$ barriers. The 2D mobile electrons are confined in the quantum wells, with a wavefunction extent perpendicular to the wells mostly determined by the well width. The electron densities and mobilities of the two samples M280 and M242 are respectively $8.5 \cdot 10^{10}\mathrm{cm}^{-2}$ $[\mu = 7 \cdot 10^5\mathrm{cm}^2/(\mathrm{V{\cdot}sec})]$ $1.4 \cdot 10^{11}\mathrm{cm}^{-2}$ $[\mu = 3 \cdot 10^5\mathrm{cm}^2/(\mathrm{V{\cdot}sec})]$.

The spins of the mobile electrons interact with the ^{71}Ga nuclei in the wells mostly through the Fermi-contact interaction $H_{\mathrm{hyp}} = \frac{8\pi\hbar^2|\gamma_e|\gamma_n}{3}\sum_{i,j}\mathcal{I}_j \cdot \mathcal{S}_i|\psi(R_j)|^2$. Hence, the Knight shift of the nuclei in the wells depends on the local electronic spin polarization as well as the density profile $n_e(z) \propto |\psi(z)|^2$ of the electrons in the wells. A convenient parameterization of the local ^{71}Ga Knight shift is

$$K_s(z) = \mathcal{C}n_e(z)\mathcal{P}(\vec{R}, \nu, T), \tag{1}$$

where $\mathcal{C}$ is a constant which may be extracted from the experiment when the electron gas is known to be fully polarized (at the ferromagnetic filling factor $\nu = 1/3$, with the largest field and the lowest temperature accessible). The intrinsic NMR lineshape, in absence of broadening

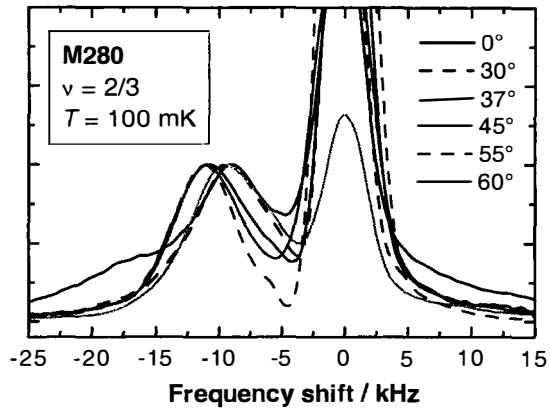


Figure 2: The spectra for sample M280 corresponding to points in figure 3 are shown. The signal amplitude is normalized to the quantum well's signal.

and diffusion processes, is proportional to the density of nuclei with a given value of K_s. In other words, the intrinsic lineshape is $L(\omega_n = K_s) \propto \frac{dz}{dn_e}(K_s)$. For an electronic density profile $n_e \propto |\psi(z)|^2 = \cos^2(z)$, this intrinsic lineshape $L(\omega) \propto 1/\sqrt{\omega(K_s^{\max} - \omega)}$ has two singularities: one at the unshifted NMR line ($\omega = 0$) and the second at the maximum shift ($\omega = K_s^{\max}$) felt by the nuclei in the wells centers. In real samples, dipolar interactions broaden the observed NMR lines: typical spectra at $\nu = 2/3$ for different Zeeman energies are shown in Fig. 2. These actual lineshapes can be fitted qualitatively after a convolution of $L(\omega)$ with a Gaussian broadening function and adding an additional contribution from the nuclei in the barriers which are unshifted and contribute to the $\omega = 0$ peak. Experimentally, the NMR lineshape is measured after driving the nuclear polarization to zero everywhere using an appropriate pulse sequence and waiting for the nuclear polarization to recover in the well. Recovery time in the barriers being close to an order of magnitude larger, it is possible to measure NMR spectra dominated by the quantum well contributions.

The spectral position of the NMR line in the quantum wells is a good measure of the electronic spin polarization $\mathcal{P}$ which is experimentally determined as $\mathcal{P} = \frac{K_s}{K_s(\mathcal{P}=1)}$. This quantity can be studied as a function of Zeeman energy, using the tilted field technique: tilting the sample by an angle θ with respect to the external field while keeping the normal component of the field $B_\perp$ constant, the Zeeman field $H_Z \propto \frac{\mu_0 B_\perp}{\cos\theta}$ can be increased at fixed filling factor ν. Tables 2 and 3 give the values of Zeeman energy and its ratio to the Coulomb energy η at filling factor $\nu = 2/3$ for both samples M280 and M242.

θ	0°	30°	37°	45°	55°	60°
B	5.325 T	6.15 T	6.67 T	7.53 T	9.28 T	10.65 T
Δ_Z	1.6 K	1.8 K	2.0 K	2.3 K	2.8 K	3.2 K
$\eta = \frac{\Delta_Z}{\Delta_C}$	0.0138	0.0160	0.0173	0.0196	0.0241	0.0277

Table 2: Total magnetic field, Zeeman energy and ratio $\eta = \Delta_Z/\Delta_C$ for sample M280 at $\nu = 2/3$.

θ	0°	14°	20°	30°	40°	47°
B	8.55 T	8.81 T	9.10 T	10.24 T	11.16 T	13.01 T
Δ_Z	2.6 K	2.7 K	2.8 K	3.1 K	3.5 K	3.9 K
$\eta = \frac{\Delta_Z}{\Delta_C}$	0.0175	0.0181	0.0187	0.0206	0.0229	0.0262

Table 3: Total magnetic field, Zeeman energy and ratio $\eta = \Delta_Z/\Delta_C$ for sample M242 at $\nu = 2/3$.

3 Spin polarization as a function of η

The dependence of the electron spin polarization on $\eta = \frac{\Delta_Z}{\Delta_C}$ at filling factor $\nu = 2/3$ is shown in Fig. 3 for both samples M280 and M242. In contrast to the full polarization expected in this range of values for η, a Zeeman energy induced phase transition is observed from a *partially* polarized ground-state with an average $\mathcal{P} \approx \frac{3}{4}$ to a *fully* polarized ground-state above the *same* critical value $\eta_c \approx 0.0185$ for both samples (the total magnetic fields at this critical point are $B_c^{M280} = 6.9$ T and $B_c^{M242} = 8.8$ T according to table 2 and 3). The transition from one ground-state to the other is very sharp, in a range of η of about 3%. Such a sharp jump in spin-polarization suggests a first-order phase transition. The accuracy in the polarization measurement is determined by the precision at which the NMR line center can be determined: from Fig. 2, where the spectra corresponding to the data for M280 Fig. 3 are shown, we see the error on the line's position is less than 0.1 kHz. It is instructive to contrast the polarization dependence of Fig. 3 with the dependence observed at filling factor $\nu = 1/2$: at $\nu = 1/2$, $\mathcal{P}$ increases linearly with η until $\eta_c = 0.022$ where saturation ($\mathcal{P} = 1$) is reached. Except for the discontinuous jump of $\mathcal{P}_{2/3}(\eta)$ at $\eta_c = 0.0185$, the overall values of $\mathcal{P}$ are generally consistent at both filling factors, and are in particular significantly less than 1 when $\eta < 0.02$.

Numerical studies of the $\nu = 2/3$ state have found so-far either a fully or an unpolarized ground-state [5,6]. As shown in the introduction, the composite fermion model has only two possible polarization $\mathcal{P} = 0$ and $\mathcal{P} = 1$ at $\nu = 2/3$. Within this picture a partial polarization $\mathcal{P} \approx 3/4$ *cannot* be constructed from filled composite fermion "Landau levels", but have to be considered as an inhomogenous mixture of $\mathcal{P} = 1$ and $\mathcal{P} = 0$ states. Possible constructions of inhomogenous CF-states are discussed at the end of the paper.

This value of the polarization is hard to investigate by exact diagonalization on a small system unless at least $8 \cdot k$ electrons are included. This exceeds the limit of existing state-of-the-art calculations already for $k > 2$. Recently Apalkov *et al.* [14] found in a narrow range of η transitions from an unpolarized to half polarized followed by fully polarized ground-state, on a 12 electrons-system.

There are other pieces of evidence for partially polarized QH phases at $\nu = 2/3$. Using optical methods, Kukushkin *et al.* [11,13] have observed partially polarized ground-state at $\nu = 2/3$ with $\mathcal{P} = 1/2$ at $\eta \approx 0.008$. In their measurement the polarization rises smoothly from $\mathcal{P} = 0$ at

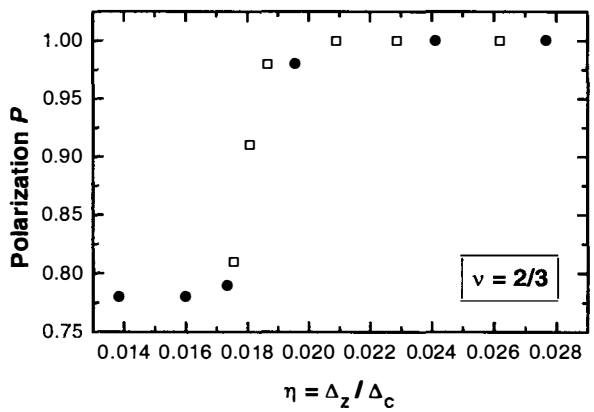


Figure 3: The phase transition in the $\nu = 2/3$ state observed through the dependence of the spin polarization on the ratio of Zeeman and Coulomb energies $\eta = \frac{\Delta_Z}{\Delta_C}$ for sample M280 (•) and M242 (□) at temperatures below 100 mK. η was changed by tilting the angle θ between the magnetic field direction and the normal to the 2D plane.

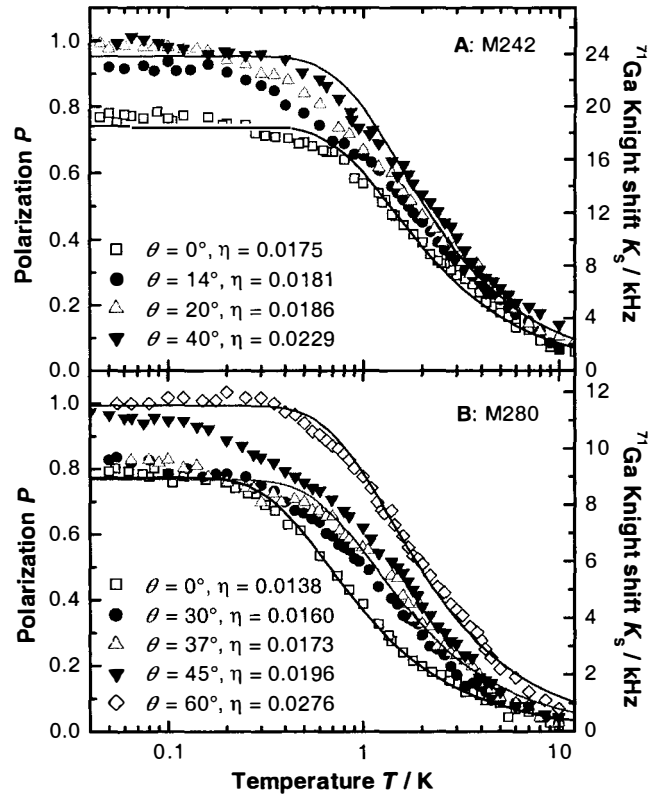


Figure 4: The temperature dependence of the spin polarization at $\nu = 2/3$ for Sample M242 (A) and M280 (B) at various tilt angles θ. The magnetic field is given by $5.325/\cos\theta$ T for M280 and $8.55/\cos\theta$ T for M242. The solid lines are least square fits of a two level model to the data of the same color.

$\eta < 0.007$ to $\mathcal{P} = 1$ for $\eta > 0.01$ with a narrow plateau at half polarization. In contrast, tilted field transport measurements on electron doped samples at $\nu = 2/3$ are displaying a deep minimum of the thermal activation gap at $\eta \approx 0.01$. This indirect measurement was interpreted as a transition from unpolarized to fully polarized states $\mathcal{P} = 0 \rightarrow \mathcal{P} = 1$ [9,10]. In our samples, where $\eta(\theta = 0°) \geq 0.0138$, the transport gap at $\nu = 2/3$ monotonically increases with increasing Zeeman energy, even across the transition at η_c: The charge gap is always finite at η_c.

4 Thermal activation at exactly $\nu = 2/3$

The temperature dependence of the polarization at $\nu = 2/3$ for both samples at various tilt-angles is presented in Fig. 4. The measurement has been performed under five different tilt angles $\theta = 0°$, 30°, 37°, 45°, and 60° for sample M280, and four different tilt angles $\theta = 0°$, 14°, 20°, and 40° for sample M242. The corresponding parameters are given in table 2 and 3, respectively.

Assuming the partition function factorizes into a spin-independent and a spin-dependent part, a two-level model composed by the ground state and the first spin excited state may be

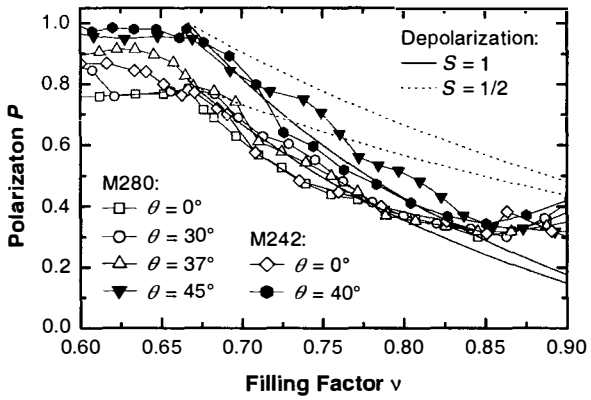


Figure 5: The filling factor dependence of the polarization for samples M280 (blue) and M242 (black) at $T = 100$ mK and various tilt angles θ. Solid symbols correspond to full polarization at $\nu = 2/3$ (M280: $\theta = 45°$ and M242: $\theta = 40°$) and open symbols (M280: $\theta = 0°$, 30°, 37° and M242: $\theta = 0°$) to partial polarization; thin lines are guide to the eye. The solid (dotted) lines simulate a depolarization of *two* (one) spin flips, $\Delta m_S = -2$, ($\Delta m_S = -1$) per removed flux quantum.

used to fit the polarization at low temperature. This yields a temperature dependence

$$\mathcal{P}(B,T) = \mathcal{P}_0(B) \cdot \tanh\left(\frac{\Delta}{4k_B T}\right), \tag{2}$$

where the gap $\Delta = g^*\mu_B B$ (g^* is the enhanced g-factor) is the splitting between the spin-up and spin-down components. Away from the transition ($\eta \not\approx \eta_c$), this fit describes correctly the data (M280: $\eta = 0.0138$, 0.0276 and M242: $\eta = 0.0229$). This model defines a thermally activated spin-gap Δ which varies smoothly across the transition at η_c from 2 K to 5 K. Such a dependence rules out a simple "level crossing transition" between two magnetic ground-states, where Δ should collapse at the transition, or at least be strongly reduced. This spin-gap appears to scale linearly with Zeeman energy $\Delta = (1.54 \pm 0.04)\,\Delta_Z$, with an exchange enhancement of the order of 50%. This Zeeman gap appears to be the main parameter in the problem, since it is possible to rescale *all* the data from Fig. 4 in a single graph by plotting $\frac{\mathcal{P}(T)}{\mathcal{P}(T=0)}$ as a function of the effective temperature $T^* = \frac{T}{\Delta_Z}$. This gives a strong argument, that the spin-flip gap probed by thermal activation is *proportional* to the total applied magnetic field.

Very close or at the transition ($\eta \approx \eta_c$), this two-level model fails to describe the temperature dependence of $\mathcal{P}$: the saturation value $\mathcal{P}_0$ of $\mathcal{P}$ is only reached at very low T , while $\mathcal{P}$ is reduced at intermediate temperatures. This may be a consequence of a coexistence region between two phases with different polarizations expected for a first-order transition.

5 The charged excitations around $\nu = 2/3$

In Fig. 5, the filling factor dependence of the spin polarization is shown for both samples and various tilt angles. The most surprising observation is the strong depolarization measured above filling factor $\nu = 2/3$, whether the polarization at $\nu = 2/3$ is full or partial. The data below and above the transition represented in Fig. 5 as open and filled symbols respectively, can be overlayed for both samples. This spin depolarization can be well reproduced over a wide range of ν if we assume *two* spin flips per removed flux quantum. This is shown by solid lines in Fig. 5. For comparison, a depolarization corresponding to a single spin flip per flux quantum is also shown in dotted lines, clearly out of the observed behavior.

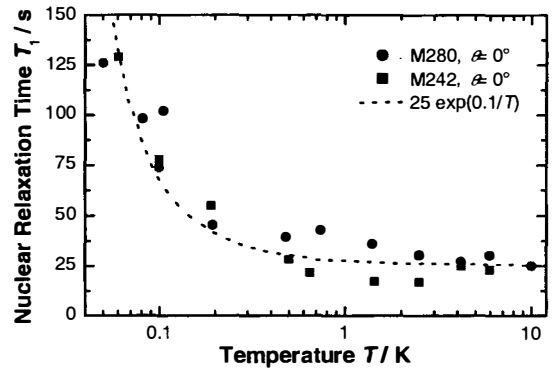


Figure 6: The temperature dependence of the nuclear spin-lattice relaxation time for Sample M242 (□) and M280 (•) for untilted field ($\theta = 0°$). The solid line is a fit to the data displaying a gap of ≈ 100 mK.

For filling factors lower than $\nu = 2/3$, the behavior of $\mathcal{P}(\nu)$ is radically different; the polarization remains *constant* for $\nu < 2/3$, for both full and partial polarization. The exception to this behavior are only the data sets (M280: $\theta = 37°$, M242: $\theta = 0°$) *at* the transition $\eta \approx \eta_c$, where polarization increases from partial towards full polarization when ν is reduced below 2/3.

In a 2/3-FQH state, 2/3 of the $\frac{\phi}{\phi_0}$ available orbital states are occupied by electrons, *i.e.* there are precisely 3 flux quanta per 2 electrons. If the magnetic field is slightly decreased or increased, the filling factor will be slightly higher or lower than $\nu = 2/3$, but the lowest energy ground-state will remain to be the same 2/3-FQH state, now containing the quasi-holes or quasi-particles corresponding to the "extra" or "missing" flux quanta. These quasi-particle excitations at 2/3 carry a charge of $\frac{e}{3}$. Hence a quasi-particle requires an additional flux of $\frac{1}{3} \cdot \frac{3}{2}\phi_0 = \frac{1}{2}\phi_0$, meaning that *two* quasi-particles are added for each additional flux quantum ϕ_0. This pair of quasiparticles will have a total spin of $\mathcal{S} = 1$ or 0 but never $\mathcal{S} = \frac{1}{2}$.

The same conclusion can be derived from the composite fermion picture, where the $\nu = 2/3$ state is mapped from the $\nu = 2$ state. Increasing the field, *i.e.* injecting additional flux quanta, increases the degeneracy of the Landau levels. The quasi-holes added in this way are preferentially placed into the same, *spin-aligned* CF-LLs: this does not modify the polarization of the system, as is experimentally observed *below* $\nu = 2/3$. Decreasing the field is equivalent to adding quasi-particles to the filled CF-LLs. For each flux quantum ϕ_0, there is one quasi-particle per CF-LL and at $\nu = 2/3$ there are two occupied CF-LLs. If both quasi-particles occupy *spin-reversed* CF-LLs, this accounts for a depolarization of two reversed spins per additional ϕ_0, as is observed *above* $\nu = 2/3$.

6 Spin dynamics at exactly $\nu = 2/3$

For untilted samples, we also measured the nuclear spin-lattice relaxation time T_1, shown in Fig. 6, as a function of temperature. T_1 has a weakly activated behavior with an effective spin-gap of the order of 100 mK. When the samples are tilted to angles corresponding to a η larger than η_c ($\mathcal{P}_0 = 1$), T_1 increased by more than one order of magnitude making it impossible to perform an accurate measurement. This behavior can be qualitatively understood if we note that when all electrons are polarized at low T, the gap corresponding to electronic spin flips is of the order of $\Delta \approx 3$ K, and there is no other relaxation channel, leading to very slow relaxation at low T. On the other hand, when the electronic ground state is not fully polarized, reversed spins are present in the wave-function and local longitudinal spin fluctuations are possible without

any cost in Zeeman energy. If the hyperfine coupling tensor has non-diagonal matrix elements, longitudinal and transverse spin-fluctuations contribute to the spin lattice relaxation. This provides additional relaxation channels, enhancing the T_1 processes. Hence, the gap measured in a (dynamic) T_1 measurement can be far lower than the gap measured by (static) thermal activation.

7 Conclusions

The polarization at filling factor $\nu = 2/3$ changes abruptly from 1 to $\mathcal{P} \approx 3/4$ when decreasing the Zeeman energy. This phase transition appears to be first order. The partially polarized state has a finite spin and charge gapped and is therefore "unpolarizable" and "incompressible". Such a state is completely unexpected within the present understanding of the fractional quantum Hall effect, for which $\mathcal{P} = 0$ and 1 are the only possible polarization at $\nu = 2/3$. The simplest way to accommodate for a partial polarization at this filling factor is to invoke spatially inhomogenous states. The nature of excitations above and below $\nu = 2/3$ suggest that the entities which are modulated in space are made of pairs of spin-states. Simple pair wavefunctions have been proposed early on by Halperin[15]. A few spin-density states can be built up along these lines. Another approach using composite fermions was suggested by Murthy[17] for filling factor $\nu = 2/5$. In addition, it is also possible to build various valence bond similar to the ground state of the two-dimensional Shastry-Sutherland model[16].

In conclusion, this NMR study has revealed a new phase transition between ground states with different spin-polarizations at $\nu = 2/3$. Whereas the quasi-hole excitations for $\nu < 2/3$ are spin aligned, the quasi-particle excitations for $\nu > 2/3$ are found to be spin-reversed, leading to a rapid depolarization above $\nu = 2/3$.

References

1. A.E. Dementyev, N.N. Kuzma, P. Khankelwal, S.E. Barrett, L. Pfeiffer and K.W. West, *Phys. Rev. Lett.* **83**, 5074 (1999).
2. S. Melinte, N. Freytag, M. Horvatic, C. Berthier, L.P. Lévy, V. Bayot and M. Shayegan, *Phys. Rev. Lett.* **84**, 354 (2000).
3. S. Melinte, private communication.
4. X.G. Wu, G. Deb and J.K. Jain, *Phys. Rev. Lett.* **71**, 153 (1993).
5. T. Chakraborty, *Surf. Sci.* **229**, 16 (1990).
6. T. Chakraborty and P. Pietilinen, *Phys. Rev. Lett.* **76**, 4018 (1996).
7. S. Koch, R.J. Haug, K. von Klitzing and M. Razeghi, *Phys. Rev.* B **47**, 4048 (1993).
8. A.J. Daneshvar, C.J.B. Ford, M.Y. Simmons, A.V. Khaetskii, A.R. Hamilton, M. Pepper and D.A. Ritchie, *Phys. Rev. Lett.* **79**, 4449 (1997).
9. J.P. Eisenstein, H.L. Stormer, L.N. Pfeiffer and K.W. West, *Phys. Rev.* B **42**, 7910 (1990).
10. L.W. Engel, S.W. Hwang, T. Sajoto, D.C. Tsui and M. Shayegan, *Phys. Rev.* B **45**, 3418 (1992).
11. I.V. Kukushkin, K. von Klitzing and K. Eberl, *Phys. Rev. Lett.* **82**, 3665 (1999).
12. I.V. Kukushkin, K. von Klitzing and K. Eberl, *Phys. Rev.* B **60**, 2554 (1999).
13. I.V. Kukushkin, J.H. Smet, K. van Klitzing and K. Eberl, *Phys. Rev. Lett.* **85**, 3688 (2000).
14. V.M. Apalkov, T. Chakraborty, P. Pietilinen and K. Nielmel, *Phys. Rev. Lett.* **86**, 1311 (2001).
15. B.I. Halperin *Helvetica Physica Acta*, **56**, 75 (1983).
16. B.S. Shastry and B. Sutherland *Physica* B **108**, 1069 (1981).
17. G. Murthy, *Phys. Rev. Lett.* **84**, 350 (2000).

FRACTIONAL STATISTICS AND NOISE CORRELATIONS IN THE FQHE

I. SAFI[1], P. DEVILLARD[1,2], T. MARTIN[1,3]
[1] *Centre de Physique Théorique, Case 907 Luminy, 13288 Marseille Cedex 9, France*

[2] *Université de Provence, 13331 Marseille Cedex 03, France*

[3] *Université de la Méditerranée, 13288 Marseille Cedex 9, France*

A microscopic theory of current partition in fractional quantum Hall liquids, described by chiral Luttinger liquids, is developed to compute the noise correlations, using the Keldysh technique. In this Hanbury-Brown and Twiss geometry, at Laughlin filling factors $\nu = 1/m$, the real time noise correlator exhibits oscillations which persist over larger time scales than that of an uncorrelated Hall fluid. The zero frequency noise correlations are negative at filling factor $1/3$ as for bare electrons (anti-bunching), but are strongly reduced in amplitude. These correlations become positive (bunching) for $\nu \leq 1/5$, suggesting a tendency towards bosonic behavior.

1 Introduction

The purpose of this talk is to discuss the relevance of "multi–terminal" noise correlations to probe the (unconventional) statistics of the carriers in mesoscopic devices. Transport experiments in the fractional quantum Hall effect (FQHE)[1] have provided a direct measurement of the fractional charge of the quasi-particles[2,3] associated with these correlated electron fluids. The discussion has centered on the charge of the quasiparticles[4,5], rather than the statistics. On the other hand, noise correlation experiments[6,7] in branched mesoscopic devices, i.e. fermion analogs of the Hanbury–Brown and Twiss experiments for photons[8], have detected the negative noise correlations predicted by theory[9]. So far in the FQHE, the measurement of the noise reduction [2] – smaller than that of fermions – constitutes the only hint that the statistic is not fermionic.

Here, it is suggested that the statistics of the underlying excitations of the FQHE can be monitored via a Hanbury–Brown experiment where quasiparticles emitted from one edge and tunneling through the correlated Hall fluid are collected into two receiving edges (see Fig. 1). This constitutes a mesoscopic analogue of a collision process which involves many quasi-particles, and therefore provides a direct probe of their underlying statistics. The Luttinger edge state theory [?] is used to compute the current and noise with the Keldysh technique. The analytic results for the noise in this partition experiment show that: a) upon increasing the magnetic field from the integer quantum Hall effect (IQHE) to filling factor $1/3$, the (negative) correlations are strongly reduced in amplitude; b) these correlations change sign and are positive at $\nu \leq 1/5$. This work attempts to go further than a recent proposal where statistics and scattering properties were dissociated[10], which correlations are fermionic[11].

The suggested geometry is depicted in Fig. 1: it requires *three* edges (two of which are assumed to be decoupled), in contrast to previous noise correlation measurements[2,6] in the IQHE and in the FQHE where a single constriction controlled the transmission between two edge states. There, negative noise correlations between the receiving ends of two edge states (inset Fig 1a) are the consequence of a noiseless injecting channel together with current conservation, for arbitrary ν. On the other hand, removing excitations from one edge state and redistributing them to two other edges (Fig.1) is clearly relevant for uncovering the bunching/anti-bunching properties of quasi-particles. This setup can be considered as a detector of partition noise between edge 1 and 3, but in the presence of a "noisy" injecting current (due to backscattering between 2 and 3).

The edge modes running along each gate, characterized by chiral bosonic fields ϕ_l ($l = 1, 2, 3$) are described by a Hamiltonian $H_0 = (v_F\hbar/4\pi)\sum_{l=1,2,3}\int ds(\partial_s\phi_l)^2$ with s the curvilinear

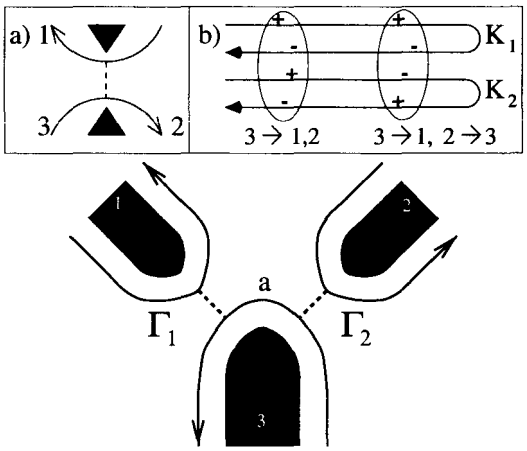


Figure 1: Hanbury-Brown and Twiss geometry: 3 metallic gates (grey) define 3 edge states, with 2 tunneling paths separated by a and with tunneling amplitudes Γ_1 and Γ_2. Insets: a) Correlation experiment in a 2-edge quantum Hall bar with a constriction. b) Charge configurations on the two Keldysh contours K_1 and K_2 which contribute to the $\omega = 0$ noise correlations at finite (left and right) and at zero (left only) temperature.

abscissa, and with a current $v_F\sqrt{\nu}\partial_s\phi_l/2\pi$, which is conserved in the absence of scattering (v_F is the Fermi velocity). ϕ_l satisfy the commutation relation $[\phi_l(s), \phi_{l'}(s')] = i\pi\delta_{ll'}sgn(s-s')$ [12]. The quasi-particle operators are expressed as $\psi_l^\dagger(s) = (2\pi\alpha)^{-1/2}F_l e^{ik_F s}e^{i\sqrt{\nu}\phi_l(s)}$, where α is a cutoff. Both the above commutation relation and the (unitary) Klein factors F_l guarantee fractional exchange statistics provided that:

$$F_l F_{l'} = e^{-i\pi p_{ll'}\nu}F_{l'}F_l \tag{1}$$

with 3 possible statistical phases $p_{ll'} = -p_{l'l} = \pm(1-\delta_{ll'})$. In particular, this insures that the fields ψ_l anti-commute for $\nu = 1$ and commute for $\nu \to 0$.

Tunneling of quasi-particles occurs at two locations $s = \pm a/2$ on edge 3, and at $s = 0$ on edges 1 and 2. A non-equilibrium situation is achieved by imposing a bias $\hbar\omega_l/e^* = -\partial\chi_l/\partial t$ ($l = 1, 2$) between 3 and l, where χ_l denotes the gauge parameter which appears in the tunneling Hamiltonian $H_B = H_{B1} + H_{B2}$, with:

$$H_{Bl} = \Gamma_l e^{-ie^*\chi_l/\hbar c}\psi_l^\dagger(0)\psi_3\left((-1)^l a/2\right) + H.c.\ . \tag{2}$$

H_{B1} and H_{B2} are required to commute [13], which imposes the constraint $p_{12} + p_{23} + p_{31} = 1$ on the statistical phases of Eq. (1).

2 Perturbation theory

Non-equilibrium averages are extracted from the Keldysh partition function. The perturbation theory is analogous to the Coulomb gas models which have been proposed to study transport in Luttinger models[5]. Here two contours K_l ($l = 1, 2$) contain m_l (even) charges ($\pm$) which account for the quasi-particle transfer to/from edge 3 to l at time t_{lk} attached to the upper/lower branch of K_l. Expanding the exponential, the partition function reads:

$$Z_K = \sum_{m_1,m_2=0}^{\infty}\left(\frac{-i}{\hbar}\right)^{m_1+m_2}\sum_c\int\frac{dt_{11}...dt_{1m_1}dt_{21}...dt_{2m_2}}{m_1!m_2!}$$
$$\times\langle T_K H_{B1}(t_{11})...H_{B1}(t_{1m_1})H_{B2}(t_{21})...H_{B2}(t_{2m_2})\rangle_c\ . \tag{3}$$

where the subscript $\mathcal{C}$ identifies charge configurations. Relevant charge configurations which contribute to lowest order to the noise correlations are depicted in Fig. 1b): charge neutrality is imposed on each contour. The terms in the nonequilibrium average Eq. (3) can in general be decoupled into four contributions: one Keldysh ordered product of bosonic fields for each edge, which dynamics are specified by the Green's function of the chiral boson fields[15] $G_{\eta\eta'}(s,t)$ (with contour branch labels $\eta,\eta' = \pm$), and a fourth contribution which arises from the Klein factors, which have no dynamics of their own, yet which are essential in order to specify the tunneling operators.

The quasi-particle current operator between leads 3 and $l = 1,2$ is $I_l = -c\,\partial H_B/\partial\chi_l$. The symmetrized real time current–current correlator between edges 1 and 2 which is used to compute the noise contains two time arguments, which are assigned to different branches of the Keldysh contour (thus the notation $\chi_l^{\eta}(t)$ below). Performing functional derivatives on Z_K,

$$S_{12}(t-t') = -(\hbar c)^2 \sum_{\eta=\pm} \frac{\delta^2 Z_K}{\delta\chi_1^{\eta}(t)\delta\chi_2^{-\eta}(t')}\Big|_{\omega_{1,2}=\omega_0}\,, \tag{4}$$

assuming equal biases on 1 and 2. The leading term in Eq. (4) is of fourth order in the tunneling amplitudes, corresponding to $m_1 = m_2 = 2$ in Eq. (3), in contrast to the leading contribution to the individual currents and noises (second order "dipole" contributions). Zero temperature, $a = 0$, and a symmetric bias $\omega_{1,2} = \omega_0$ are chosen in order to enhance statistical signatures. Experimentally this implies that the two tunneling paths lie within a few Fermi wave-lengths from each other. The overlap between quasiparticles in edge 3 is then more prominent. Here, only $\eta_2 = -\eta_1 = 1$ is retained because first, it provides the large time behavior and second, it corresponds to the contribution of the zero frequency noise correlations (to be computed later on). Using the explicit expressions of the Green's function at equal abscissa, $G_{\eta\eta'}(t) = -\ln[1 + it(\eta\theta(t) - \eta'\theta(-t))/\tau_0]$ and rescaling the times by the short time cutoff $\tau_0 \sim \alpha/v_F$, this contribution reads:

$$\begin{aligned} S_{12}^{--++}(t) = -4\frac{|e^*\tau_0\Gamma_1\Gamma_2|^2}{(\hbar\alpha)^4} Re \int_{-\infty}^{\infty} dt_1 \int_{-\infty}^{\infty} dt_2 \sum_{\epsilon=\pm} \epsilon \\ \times \cos\left[\omega_0(t_1+\epsilon t_2)\right] (1-it_1)^{-2\nu} (1+it_2)^{-2\nu} (1-it)^{\epsilon\nu} \\ \times \left[1+i(t+t_2-t_1)\right]^{\epsilon\nu} (1+i|t+t_2|)^{-\epsilon\nu} (1-i|t_1-t|)^{-\epsilon\nu} \\ \times \exp\left(i\epsilon\frac{\pi}{2}\nu\left[sgn(t+t_2) - sgn(t-t_1)\right]\right). \end{aligned} \tag{5}$$

A leading contribution to $S_{12}^{--++}(t)$ is plotted in Fig. 2, as well as the excess noise at $\nu = 1$ for comparison. The latter oscillates with a frequency ω_0, and decays as t^{-2}. $S_{12}^{--++}(t)$ scales as $|\omega_0|^{4\nu-2} f(\omega_0 t)$, with $f(x)$ an oscillatory function which decays at least as $x^{-2\nu}$, thus a slower decay than that of electrons. At large times, the frequency of the oscillations stabilizes as $\omega_0 = e^*V/\hbar$.

3 Zero–frequency correlations

The result in Eq. (5) is now integrated over t after subtracting the average current products: $\tilde{S}_{12}(\omega) \equiv \int dt\, e^{-i\omega t}[S_{12}(t) - 2\langle I_1\rangle\langle I_2\rangle]$. The sign and magnitude of the $\omega = 0$ correlations tell us the tendency for the quasiparticle to exhibit bunching or antibunching. Turning now to the charge configurations of Fig. 1b, at zero temperature only $\epsilon = -1$ in $\tilde{S}_{12}(0)$ contributes, which gives the information that an "exclusion principle" prohibits the excitations to be transfered from the collectors to the emitter. The zero frequency noise correlations have the general form:

$$\tilde{S}_{12}(0) = (e^{*2}|\omega_0|/\pi) T_1^r T_2^r R(\nu) \tag{6}$$

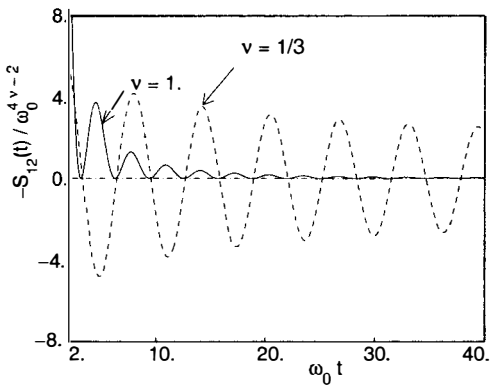


Figure 2: Contribution to the real time correlator $S_{12}^{-+}(t)$, for bias $\omega_0 = e^*V/\hbar$, normalized to $|\tau_0\Gamma_1\Gamma_2|^2|\omega_0|^{4\nu-2}$ for a filling factor $\nu = 1/3$ (dashed line). $2\langle I_1\rangle\langle I_2\rangle$ has been subtracted. The exact *excess* noise at $\nu = 1$: $S_{12}^{ex}(t) \propto \sin^2(\omega_0 t/2)/t^2$ (full line), keeping all η configurations, is plotted for comparison.

where the renormalized transmission probabilities are $T_l^r = (\tau_0|\omega_0|)^{2\nu-2}\left[\tau_0\Gamma_l/\hbar\alpha\right]^2/\Gamma(2\iota\nu)$, and the dimensionless function $R(\nu)$ characterizes the statistical correlations. At $\nu = 1$, it is shown explicitly that $R(1) = -1$ using contour integration, so that $\tilde{S}_{12}$ coincides exactly with the scattering theory result[9]. This issue represents a crucial test of the implementation of the Klein factors. Moreover, for arbitrary ν, $R(\nu)$ could in principle be directly measured in an experiment. Indeed one can rescale the noise correlation $\tilde{S}_{12}$ by the individual shot noises $\tilde{S}_l \simeq 2e^*\langle I_l\rangle$ or equivalently (at this order) by the individual currents: $R(\nu) = |\omega_0|\tilde{S}_{12}/[4\pi\langle I_1\rangle\langle I_2\rangle]$.

A central result of this letter is the analytical expression for the function $R(\nu)$ in Eq. (6). It is obtained by performing a change of variables of the 3 time integrals in $\tilde{S}_{12}(0)$, neglecting the short-time cutoff in the diagonal elements of the Keldysh Green's function in Eq. (5). This procedure is consistent with the limit of small biases which is assumed here $|\omega_0|\tau_0 \ll 1$, but strictly speaking it is valid in the range $1/2 < \nu \leq 1$. One then obtains the asymptotic series:

$$R(\nu) = \frac{-\sin(\pi\nu)\Gamma^2(2\nu)}{2\sqrt{\pi}\Gamma(2\nu-1)\Gamma(2\iota\nu-1/2)\Gamma(-\nu)} \sum_{n=0}^{\infty} \frac{\Gamma(n-\nu)\Gamma(n+1-\nu)\Gamma(\nu+n-1/2)}{n!\Gamma(n+\nu)\Gamma(n+3/2-\nu)}, \tag{7}$$

which converges as $n^{-\nu-2}$. Here, $\iota\nu$ can be treated as a continuous variable, whereas it has a physical meaning when it is a Laughlin fraction $1/m$ (m odd). At first glance the only physical filling factor which one can reach with this series is $\nu = 1$. Yet, it is possible to extend $R(\nu)$ to the range $[0, 1/2]$: the zero frequency noise correlations do not contain any true divergence (it would require the introduction of an infrared cutoff with a physical origin), but the integration method which is used here breaks down at $\nu = 1/2$, a feature which can already be seen in computing the average product $\langle I_1\rangle\langle I_2\rangle$ in a similar manner (although $\langle I_1\rangle$ converges for all ν). It is still possible to extract a meaningful result for $\tilde{S}_{12}$ from this integration procedure: $R(\iota\nu)$ having no poles in [1/2, 1], it can be analytically continued to the interval $[0, 1/2]$. Indeed, note that the terms of the series of Eq. (7) are still well defined for $\nu < 1/2$).

The continuation procedure could be jeopardized if other tunneling operators generated by the renormalization group (RG) procedure happened to be more relevant at $\nu = 1/2$. Consider a higher order tunneling operator $V_{\vec{n}}e^{i\sqrt{\nu}\vec{n}.\vec{\phi}}$, where $\vec{n} = (n_1, n_2, n_3)$ (n_l integer) satisfies quasi-particle conservation $\sum_{l=1}^{3} n_l = 0$ and $\vec{\phi} = (\phi_1, \phi_2, \phi_3)$ contains the fields of the three edges. The

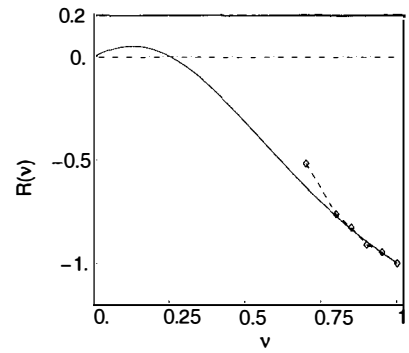


Figure 3: Normalized $\omega = 0$ correlations $R(\nu)$, plotted with the analytic expression of Eq. (7) for arbitrary ν, and compared to the direct numerical calculation for $0.7 \leq \nu \leq 1$ (lozenges)

RG flow is then :

$$\frac{dV_{\vec{n}}}{dl} = \left(1 - \frac{\nu}{2}\sum_{l=1}^{3} n_l^2\right) V_{\vec{n}} \ . \tag{8}$$

The bare tunneling terms are relevant at $\nu < 1$, and always dominates all other $V_{\vec{n}}$, which become relevant below $\nu = 1/3$ at most.

For $\nu \simeq 1$, a check is obtained by direct numerical integration of $S_{12}(t)$. The comparison between the series solution of Eq. (7) and the numerical data shows a fair agreement for $0.7 \leq \nu \leq 1$.

4 Conclusion:

Starting from the IQHE and decreasing ν (Fig. 3), the noise correlations between the two collector edges are reduced in amplitude at any $\nu = 1/m$. When a quasi-particle is detected, in 1, one is less likely to observe a depletion of quasi-particles in 2 than in the case of noninteracting fermions. The reduction of the (normalized) noise correlations constitutes a direct prediction of the statistical features associated with fractional quasiparticles in transport experiments, and should be detectable at $\nu = 1/3$.

At $\nu = 1/4$, $\tilde{S}_{12}$ vanishes and becomes positive for lower physical filling factors $(1/5, 1/7, ...)$, which is reminiscent of bosons bunching up together. Positive correlations have been predicted in superconductor–normal metal junctions [11], and bosonic behavior was attributed to the presence of Cooper pairs – effective bosons – leaking on the normal side. Here the positive correlations can be either attributed to the fact that the fractional statistics are bosonic at $\nu \to 0$, or to the eventual presence of composite bosons resulting from attachment of an odd number of flux tubes [16]. On the one hand, one is dealing with a fermionic system where *large* negative correlations are the norm. On the other hand, the presence of an external magnetic field and the (resulting) collective modes of the edge excitations favor bosonic behavior. The competition between these two tendencies yields a statistical signature which is close to zero – analogous to the noise correlations of "classical" particles. Independent of this sign issue, for $\nu \leq 1/3$, the amplitude of the normalized correlations is strongly reduced and this effect could be checked experimentally for Laughlin fractions. The tendency for the noise correlation ratio to be reduced compared to its non interacting value is consistent with the existing data for two-terminal devices [2], as a connection exists between the two types of measurements [9,11]. There, shot noise suppression was

observed to be weaker than that of bare electrons, which then multiplies the shot noise by $1-T$ [9,17], the reflection amplitude. However, a qualitative analysis of noise reduction in this situation is rendered difficult because of the nonlinear current–voltage characteristics. In contrast, an HBT experiment constitutes a direct and crucial test of the Luttinger liquid models used to describe the edge excitations in the FQHE, as it addresses the role of fractional statistics in transport experiments. These experiments could also probe hierachical fractions of the FQHE, as well as non-chiral Luttinger systems such as carbon nanotubes.

References

1. R. B. Laughlin, Rev. Mod. Phys. **71**, 863 (1999); H.L. Stormer, *ibid*, 875 (1999).
2. L. Saminadayar, D. C. Glattli, Y. Jin, and B. Etienne, Phys. Rev. Lett. **79**, 2526 (1997).
3. R. de-Picciotto *et al.*, Nature **389**, 162 (1997).
4. C. L. Kane and M. P. A. Fisher, Phys. Rev. Lett. **72**, 724 (1994); P. Fendley, A. W. W. Ludwig, and H. Saleur, *ibid.* **75**, 2196 (1995).
5. C. de C. Chamon, D. E. Freed, and X. G. Wen, Phys. Rev. B **51**, 2363 (1995-II).
6. M. Henny *et al.*, Science **296**, 284 (1999).
7. W. Oliver *et al.*, Science **296**, 299 (1999).
8. Hanbury-Brown and Q. R. Twiss, Nature **177**, 27 (1956).
9. T. Martin and R. Landauer, Phys. Rev. B **45**, 1742 (1992); M. Büttiker, Phys. Rev. Lett. **65**, 2901 (1990); Phys. Rev. B **46**, 12485 (1992).
10. S. Isakov, T. Martin, and S. Ouvry, Phys. Rev. Lett. **83**, 580 (1999).
11. J. Torrès and T. Martin, Eur. Phys. J. B **12**, 319 (1999).
12. M. Geller and D. Loss, Phys. Rev. B **56**, 9692 (1997).
13. C. Nayak *et al.*, Phys. Rev. B **59**, 15694 (1999).
14. I. Safi, P. Devillard and T. Martin, *in preparation.*
15. C. Chamon and D. Freed, Phys. Rev. B **60**, 1842 (1999).
16. S. C. Zang *et al.*, Phys. Rev. Lett. **62**, 82 (1988); S. M. Girvin and A. H. MacDonald, *ibid.* **58**, 1252 (1987).
17. M. Reznikov *et al.*, Phys. Rev. Lett. **75**, 3340 (1995); A. Kumar *et al.*, *ibid.* **76**, 2778 (1996).

SHOT NOISE IN THE FQHE: STRONG BACKSCATTERING BY A WEAK IMPURITY

D. C. Glattli[1], V. Rodriguez[1], P. Roche[1], Y. Jin[2], B. Etienne[2].
[1] *Service de Physique de l'Etat Condensé, CEA Saclay, 91191 Gif-sur-Yvette, France*

[2] *Laboratoire de Microstructures et Microélectronique, CNRS B.P. 107, F-92225 Bagneux, France*

We present shot noise measurements in the Fractional Quantum Hall regime at $\nu = 1/3$. The fractional edge channels which carry the current at the two opposite boundaries of a quantum Hall sample are weakly coupled by an artificial impurity, namely a Quantum Point Contact. The coupling gives rise to a current between the two edge channels and the random transfer of the charges gives rise to fluctuations of the current. For low voltages at low temperature, the chiral Luttinger liquid models suggest a renormalization of the coupling strength leading to strong backscattering even when the bare coupling is weak. They predict a noise power proportional to the *transmitted current* I and to the electronic charge e. However, at vey low temperature, our shot noise measurements show a surprising enhancement of the shot noise which is doubled. This phenomenon has been observed in two samples and for various filling factor ν_{bulk} in the leads. .

1 Introduction

The random transfer of carriers through a conductor whose contacts are biased by a potential difference V generates a fundamental noise called shot noise. This is a non-equilibrium noise different from the equilibrium noise generated by thermal fluctuations. At low frequency, the current fluctuations in a frequency bandwidth Δf $\left\langle (\Delta I)^2 \right\rangle = S_I \Delta f$ are characterized by the frequency independent spectral density $S_I = 2FqI$, where F is a Fano factor characterizing the statistics, q is the carriers charge, and I the average current. When the conditions for poissonian statistics are realized, $F = 1$, the simultaneous measurements of S_I and I give a direct determination of the carrier charge. Although measuring current noise is more difficult than simply measuring conductance, recent experimental progress have been made and noise measurements have reached a high level of reliability. This has lead to the first determination of the fractional carrier charge $q = e/3$ and $e/5$ of the Fractional Quantum Hall (FQH) [1,2] effect and to the observation of $2e$ and ne carrier charges in mesoscopic normal-superconducting (N-S) and S-N-S devices [3]. Here, we presents results for which we have applied the noise measurement technique to characterize the carriers at the edge of a FQH system in a regime were an integer charge e is expected. The results reported here show that a *doubling* of the charge is instead currently observed. This unexpected observation, associated with a study of the non-linear IV characteristics, rises important questions about our understanding of transport in the FQH regime.

A two-dimensional electron gas (2DEG) under high perpendicular magnetic field B shows the integer quantum Hall effect and then the FQH effect due to Landau level formation and to interactions. These regimes occur when the Landau level filling factor $\nu = n_s/n_\Phi$ is integer or fractional respectively (n_s and n_Φ are the electron and flux quantum h/e densities) The Landau levels are characterized by the formation an energy gap in the electronic excitations in the bulk making the system insulator for longitudinal transport but perfect conductor for the transverse Hall current. As a result the current is concentrated at the boundaries of the sample and flows following gapless edge channels which form ideal one dimensional chiral conductors. In the FQH regime the chiral modes are believed to share common properties with one dimensional systems with short range interaction called Tomonaga-Luttinger Liquids (TLL) and they are called Chiral TLL (χ-TLL)[4]. Here the fractional filling ν plays the role of the Luttinger parameter g. A one dimension TLL is intermediate between a conductor with Fermi liquid properties and

a one dimensional crystal. In particular the positional or temporal electron correlation show a slow algebraic decay. As a consequence a single impurity has a tendency to pin the correlated electrons and gives rises to a vanishing conductance at low temperature : $G \sim (T/T_B)^\alpha$ where T_B characterizes the unrenormalized strength of the impurity. A similar result is expected for the counter propagating fractional edges coupled by an impurity and theories predict a simple relation between α and ν. The physical separation of the upper and lower edge modes counter propagating at the boundaries (equivalent to the k_F and $-k_F$ modes in 1D TLL) suppresses unintentional backscattering and thus provides an ideal situation for experiments The FQH edge channels can be studied by two different approaches : either by tunneling electrons from an external contact into an edge channel through an insulating barrier or by looking at the internal tunneling of quasiparticles between two opposite edge modes through the correlated fractional quantum Hall fluid. In the first case, the simplest χ-TLL theories predict a the tunneling exponent $\alpha = 1/\nu - 1$ for a Laughlin filling factor $\nu = 1/(2k+1)$ [4]. In this simple situation this can be qualitatively understood as resulting from electron *charge fractionalization.* For example if an electron is injected to a 1/3 fractional edge channel with an energy in the range $[eV, eV + d(eV)]$ above the Fermi energy, the number of possible ways to generate three quasiparticles $e/3$ is, according to energy conservation, $\sim (eV)^2 d(eV)$. As a result, the differential conductance dI/dV should vary as V^2 ($\alpha = 2$). For Jain's filling factors $\nu = 2p/(2kp+1)$, the predictions are : $\alpha = 2k-1$ for $p > 1$ and $\alpha = 2k - 1/|p|$ for $p \leq -1$ [5,6,7,8]. Experiments performed in this regime show that the tunneling current between the Fermi liquid reservoir and the FQH edges show a power law variation with voltage in aggreement with the χ-TLL predictions but the exponents are somewhat different than expected. At $\nu = 1/3$, remarkable experiments by A. Chang *et al.* [9] showed a power law close to 2 when measuring the tunneling form a metallic contact to the edge of a 2D electron gas (2DEG). Experiments for lower magnetic fields[10] showed a unexpected variation of α nearly linearly decreasing with ν. Indeed specific details, including long range interaction and bulk dissipation, spoil the universality of the tunneling exponents predicted in idealized models [11]. In the second case, where internal tunneling between two fractional regions is provided by the strong impurity potential of a controllable artificial impurity, a Quantum Point Contact QPC, the tunneling exponents are expected to be doubled compared to the previous case. Here also only a qualitative experimental agreement is found with the theory, as shown below. Experiments using QPCs have been done at $\nu = 1/3$ to check these predictions. In [12] the predicted T^4 temperature variation of the conductance was observed in a limited range of temperature, but this was not clearly confirmed by other groups [13,14].The specific details of the dynamics of the modes close to the QPC can be even more relevant than in the first case and the scaling limit allowing a determination of α is more difficult to reach[15,16,17]. Regarding shot noise, the tunneling through an insulating barrier, first case, or via a strong impurity potential, second case, is associated with random transfer of uncorrelated charge e with poissonian statistics with $S_I = 2eI$ [18,19,20]. We will show below that when the QPC potential is very strong, i.e. pinch-off, this is experimentally observed. However if the QPC potential is weak but the conductance is strongly reduced by the interaction a doubled, and sometime higher shot noise is observed as shown below.

In this regime, an interesting issue is wether the strong backscattering regime resulting from the renormalization at low temperature of a *weak* impurity potential is equivalent to the strong backscattering regime with exist at all temperature in the case of a *strong* impurity potential. In the last case the system is cut into two parts and single electron charges tunnel via an insulating region. In the first case the fractionally charged quasiparticle observed for weak backscattering at large voltage should condense into electrons at low voltage and lead to a strong backscattering regime. χ-TLL models predict tunneling exponents α identical the case of a strong impurity potential and a shot noise corresponding to possonian tunneling of charge e. However, there is still a debate on the nature of this strong backscattering regime [21]. In the case where the bare

weak coupling contains higher order terms than the $2k_F$ term (a highly probable situation in real experiments), these terms are considered as non-relevant but at finite temperature the irrelevant terms may be not negligible [22]. Finally,the long range Coulomb interaction, more effective at low energy as it is less efficiently screened, can strongly change the results.

In the following we will concentrate on this regime and will present results combining non-equilibrium measurements of the differential conductance and measurements of the current noise.

2 The samples and the measurement setup

Two GaAs/AlGaAs samples, called I and II, having similar characteristics have been measured. The two dimensional electron gas (2DEG) have electronic density $n_s \lesssim 10^{11} cm^{-2}$ and mobility of $\mu \simeq 10^6 cm^2 V^{-1} s^{-1}$. At the center of each wide mm size Hall bar, the QPC used to couple opposite edge states, is made using two TiAu gates with $\simeq$280nm lithographic aperture. Because the Luttinger liquid features expected for fractional edges are very sensitive to electromagnetic environment at very low temperature, the samples are mounted in a metallic box with special care regarding filtering. Lossy coaxial leads connecting the box to hoter parts of the external circuit ($\geq$ K) have a radiofrequency absorption (33dB$\times\sqrt{f_{[GHz]}}$ from 0.1GHz to 1THz) calculated and measured to prevent external radiation to change the electronic temperature [23]. By using this experimental scheme and also by screening the whole cryostat from microphonic and radiofrequency perturbations, the electronic temperature T_e in high magnetic field was found able to reach the base temperature T =19mK. This was checked in the FQHE regime, by comparing the equilibrium current noise with the Johnson-Nyquist noise formulas (1% agreement) and by looking at the differential conductance scaling law $G(V,T) = G(0,T)f(eV/2\pi k_B T)$, see below, which was obeyed down to the lowest temperature.

Conductance and noise are measured using the setup shown in fig.1. A current source injects a current I_0 in contact 1. Under Hall quantization in the mesa, filling factor ν_{bulk}, the potential V_1 of contact 1, also called the drain source voltage V, is $V_1 \equiv V = \nu_{bulk}^{-1}(h/e^2)I_0$. The coupling between upper and lower edges induced by the QPC splits the injected current $I_0 = I + I_B$ into transmitted and backscattered currents I and I_B. Each current returns to ground via contact 3 or 6 and is measured through voltages $V_2 = \nu_{bulk}^{-1}(h/e^2)I$ and $V_5 = \nu_{bulk}^{-1}(h/e^2)I_B$ respectively. adding a small $\simeq$ 113Hz AC current to I_0 the differential conductances $G = dI/dV$ or $G_B = dI_B/dV$ can be measured. The voltages and their fluctuations are measured using two identical ultra low noise amplifiers (6fA/$\sqrt{Hz}$ current and 1.2nV/$\sqrt{Hz}$ voltage noise). The amplifiers either detect the same signal, V_2 in setup a1 and V_5 in setup a2, or are used in a "Hanbury Brown and Twiss" (HB&T) configuration, setup b and measure both voltages. For noise measurements, a fast-Fourier transform signal analyzer calculates the cross correlation of the output voltages. Referred to amplifier inputs, the set-ups can measure:

$$S_{V_2V_2} = (h/\nu_{bulk}e^2)^2(S_{II} + S^A_{I_N} + \nu_{bulk}(e^2/h)4k_BT) + (dI/dV)^2 S^C_{I_N} \quad (1)$$

$$S_{V_5V_5} = (h/\nu_{bulk}e^2)^2(S_{I_BI_B} + S^A_{I_N} + \nu_{bulk}(e^2/h)4k_BT) + (dI_B/dV)^2 S^C_{I_N} \quad (2)$$

$$S_{V_2V_5} = (h/\nu_{bulk}e^2)^2 S_{II_B} + (dI/dV)(dI_B/dV)S^C_{I_N} \quad (3)$$

for a1, a2 and b respectively. S_{AB} denotes the spectral density $\int_0^\infty d\tau \cos(2\pi f\tau)\,\langle \delta A(0)\delta B(\tau)\rangle$ of fluctuations of the observables A and B. S_{II}, $S_{I_BI_B}$ and S_{II_B} denotes autocorrelation and cross-correlation of the physical *excess* current noise (i.e. total noise minus thermal equilibrium noise) of the carriers partitioned at the QPC. $S^A_{I_N}$ is the sum of the current noise of the two amplifiers and $S^C_{I_N}$ the noise of the current source. $S^A_{I_N}$ and $S^C_{I_N}$ are accurately known and stable over weeks. It is remarkable that in this configuration we are only sensitive to the

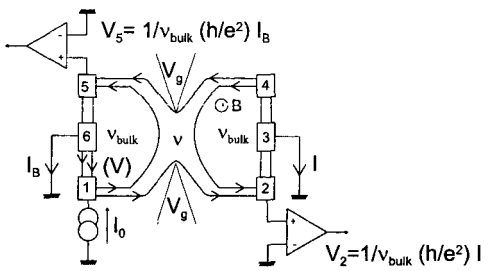


Figure 1: schematic view of the measurement set-up for the HB&T configuration (set-up b). In set-up a1and a2 the two amplifiers are connected in parallel on a single contact (contact 2 or 5 respectively).

excess noise and that the thermal noise contribution does not depend on the differential conductance. To understand the physical part of equation (1) : $S_{II} + S^A_{I_N} + \nu_{bulk}(e^2/h)4k_BT$, it is interesting to compare it with what we would expect in the same measurement configuration for a non interacting Fermi liquid. If we were measuring the ordinary partition shot noise of uncorrelated electrons crossing a barrier of transmission t, the excess partition noise would be $S_{II} = 2eI(1-t)(\coth(eV/2k_BT) - 2k_BT/eV)$. The temperature dependent term in the expression of S_V corresponds to the Johnson-Nyquist voltage noise $4k_BT3h/e^2$ of contact 2 whose resistance is $3h/e^2$. This thermal noise contribution does not depend on dI/dV because the thermal voltage fluctuations observed in contact (2) correspond to the sum of the thermal current fluctuations emitted by contact (2) plus the thermal current fluctuations emitted by contacts (1) and (4), one with a weight equal to the transmission and the second with a weight equal to the reflection (in the case of fermions the three contributions would be respectively : $2k_BTe^2/3h$, $t2k_BTe^2/3h$ and $(1-t)2k_BTe^2/3h$ [24]). For equation (3) the absence of thermal contribution in the cross-correlation $-S_{I,I_B}$ is remarkable, and also experimentally useful. We have made a very accurate experimental check of this property.

Amplifier gains and circuit components are know within 0.8%. Systematic equilibrium thermal noise measurements from 20mK to 300mK at $\nu = 1/3$ allowed us to check the noise calibrations with high accuracy in the frequency range 3 to 6kHz providing 1% absolute calibration. Fermionic (QHE regime) or super-Fermionic (FQHE regime) correlations between electrons implies that I_0 is noiseless [24]. This forces current fluctuations to be perfectly anticorrelated. Using setup b the equalities $S_{II} = S_{I_BI_B} = -S_{II_B}(\equiv S_I)$ were indeed accurately checked. For short notation, S_I will denote the excess noise in the following.

3 Non-linear transport at ν=1/3

Before presenting the results on shot noise, we describe below the non-linearities in the transport observed at $\nu = 1/3$. These non-linearities are not specific of the particular sample used here but are also observed in samples with different geometries, mobilities or densities.

Fig.2(a) shows the low temperature differential conductance dI/dV versus gate voltage V_g for various bias voltages V and Fig.2(b) the zero voltage conductance versus V_g for different temperatures at bulk filling factor $\nu = 1/3$. The striking features of Fig.2 are – 1) the similarity between both graphs : finite bias voltages and finite temperatures produce similar effects on the conductance; – 2) the insulating behavior at low energy (temperature or voltage). Both features qualitatively agree with the χLL prediction that the weakest impurity, here the artificial impurity realized with a QPC, leads to an insulating regime at low energy due to a renormalization by the interaction of the potential which couples the opposite edge channels. Similar features are observed with filling factor 1/3 at the QPC and filling factor 1/2 or 2/3, in the bulk. We would

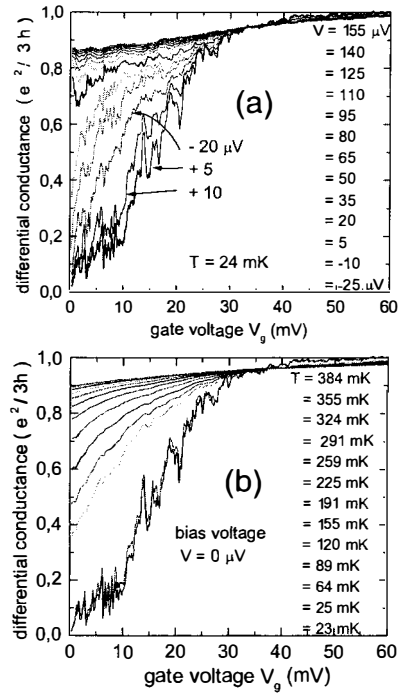


Figure 2: (a) differential conductance versus gate voltage for different bias voltages at bulk filling factor $\nu = 1/3$ and fixed temperature. V varies from -25 to $155\mu V$ using $15\mu V$ increments. For a given V_g the differential conductance monotonically increases with V; (b) zero bias voltage conductance versus gate voltage for different temperatures. For a given V_g the conductance increases with T.

like to emphasize the non-trivial origin of the non-linear conduction. Indeed, the lower the bias voltage and the temperature, the stronger are the non-linearities. A change of the coupling with bias would give non-linear conduction at large bias rather than at low bias. Such trivial effect is therefore not the dominant effect. It is also important to note that the nearly zero conductance found at low voltage and temperature does not correspond to the pinch-off regime which would occur for gate voltages around -400mV. The high T and large V saturation of the conductance at the lowest gate voltage shown in Fig.2 for $V_g = 0$mV is around 0.85-0.9 $(e^2/3h)$ and indicates that the density at the middle of the QPC is at most 10-15% smaller than the bulk density. From this we can infer that the QPC only *weakly perturbs* the quantum Hall fluid. The insulating behavior and the non-linearities are thus *fundamental properties* of the fractional quantum Hall state.

Fig.3(a) displays the differential conductance versus bias for a series of fixed gate voltages at $T = 24$mK. For small V_g, a rapid increase of the conductance with bias is followed by a slow variation toward an asymptotic value. The cross-over between the two regimes illustrates the transition from strong to weak backscattering. For larger V_g only the weak backscattering regime is observed. Again, the shape of the curves qualitatively agree with the prediction of χLL models, but not in the very details. To be more quantitative we have plotted in Fig.3(b) a series of differential conductance traces normalized to the zero bias conductance versus $eV/2\pi k_B T$ and taken at different temperatures for the same $V_g = 2.07$mV. All traces merge rather well

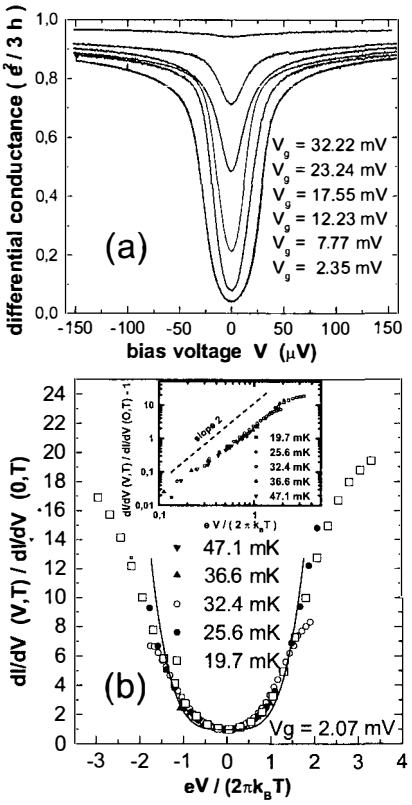


Figure 3: (a) differential conductance versus bias voltage for different gate voltages. The curve with the lower $V = 0$ conductance corresponds to $V_g = 2.35mV$; (b) differential conductance curves normalized to their zero bias conductance plotted versus the reduced variable $eV/2\pi k_B T$. The data are taken at $V_g = 2.07mV$ and for different temperatures. The solid curves correspond to the χLL prediction. Inset : a log-log plot shows the V^2 variation of dI/dV.

together to give a unique curve except for few departures from it at large bias. This means that $eV/2\pi k_B T$ is a good parameter to describe the conductance at fixed coupling as suggested by χLL models. In particular the conductance is doubled for $eV \simeq 2\pi k_B T$. The inset shows however a power law variation with exponent 2 in contrast with the χLL exponent 4. The χLL prediction $dI/dV(V,T) = dI/dV(0,T)(1 + \frac{-1+2/\nu}{\Gamma(\nu)^2}\left(\frac{eV}{2\pi T}\right)^{-2+2/\nu})$ for $\nu = 1/3$ is plotted as the solid curve of Fig.3(b). There is a clear discrepancy with the experimental curves although the predicted values are not far from the data. We found that similarly all traces of Fig.2(a) start as V^2 and a power 4 is not observed. More details will be given elsewhere.

To summarize this first part devoted to the characterization of transport, we have found *qualitative* agreement with the χLL picture. Combining these results with previous studies [12,13,14], it seems that to find a quantitative agreement with experiments using QPC probably requires modifications of the χLL models: – 1) long range intra-edge interactions: for $V < 50\mu$V, using a typical 10^7cm.s^{-1} drift velocity, the χLL boson modes have wavelengths $>100\mu$m and screening by the QPC gates is ineffective. This would give I-V curves intermediate between

χLL and dynamic Coulomb blockade predictions. The coupling of the 1/3 fractional edge with extra propagating modes is highly probable has the samples have a smoothly decreasing density at the edge and reconstruction occurs [?]; – 2) χLL models only consider a sharp δ potential coupling the edges, while the QPC potential is smooth and slightly lowers the electron density. A local variation of the Luttinger liquid parameter in the coupling region should be included; – 3) It is likely that spin is important: spin reversed quasi-particles may be created together with ordinary Laughlin quasi-particles when the filling factor deviates from 1/3. A possible spin texture at the edge may affect the χLL predictions. Finally the small random potential fluctuations added to the QPC potential and a possible change of coupling with bias have to be considered even though they probably do not give the most relevant contributions.

After the characterization of the transport, we now discuss another χLL prediction about shot noise when renormalization of the coupling leads to strong backscattering.

4 Shot noise in the strong backscattering regime

χLL models predict that in the large bias voltage limit the backscattered current $I_B = I_0 - I$ vanishes and shot noise experiments would observe the Poissonian noise of quasiparticles with fractional charge $e/3$ at $\nu = 1/3$ [19,20,18]. Indeed two experiments, one measuring the autocorrelation $S_I = \langle \Delta I^2 \rangle / \Delta f$ of the total current fluctuations with $\nu_{bulk} = 1/3$ [2] and the other one measuring the anticorrelated fluctuations of the transmitted and backscattered current $S_{I,I_B} = -\langle \Delta I_B \Delta I \rangle / \Delta f$ with $\nu_{QPC} = 1/3$ and $\nu_{bulk} = 2/3$ [1], have found the predicted noise power $\simeq 2(e/3)I_B$ when $I_B \ll I_0$. Here we focus on another remarkable χLL prediction that for a very weak coupling, the insulating regime occurring at sufficiently low V and T will make the quasiparticles *condense* into electrons [18,20,25]. A poissonian shot noise $S_I \simeq 2eI$ would result when $I \ll I_0$, a result which may look trivial as the common belief is that this regime becomes similar to the tunneling in the pinch-off regime. However, we emphasize that *there is no tunnel barrier* and that we are far from the pinch-off regime as shown in the first part. Instead we are considering a weak coupling potential whose effect is fundamentally enhanced by the interaction.

Fig.4 (a to c) shows the non-linear variation with bias voltage V of the differential conductance dI/dV, the current I, and the excess shot noise S_I observed in sample I, setup a1, with $\nu = \nu_{bulk} = 1/3$ at low temperature when a very weak QPC potential couples opposite edges. Although the coupling is weak (at T =200mK and 350mK, the $V = 0$ conductance increases to 0.8 and 0.9 $e^2/3h$), the interactions quickly lead to a strong backscattering regime at low temperature (conductance below 0.25 $e^2/3h$ for T <50mK). These typical non-linear features have been already discussed above. In (d) the excess noise shows a striking *linear* variation with current I, characteristic of shot noise, which strongly contrasts with the *non-linear* variation with V displayed in (c). The experimental data are compared with the excess noise expected for the poissonian transfer of charges $q = e$ (dashed curves) and $q = 2e$ (solid curves) through the QPC : $2q|I|\left(\coth(qV/2k_BT) - 2k_BT/qV\right)$. In this strong backscattering regime, i.e. I is $\ll I_0$, the poissonian noise prediction of charge e, with $S_I = 2eI$, is nearly observed for the first two traces of figure (d) but the traces at lower temperature ($T \leq 32$mK) show a sharp transition toward super-poissonian shot noise at low current with $S_I \simeq 2(2e)I$. This unexpected *doubling of shot noise* has been observed in the strong backscattering regime for various (weak) coupling and measurement conditions providing the zero bias conductance is small.

In the following we will show that the super-poissonian shot noise observed is robust upon varying several parameters. Figure 5 (a-c) shows various examples. In (a), same sample and same $\nu_{bulk} = \nu = 1/3$, after thermal cycling to change the measurement setup (setup b) the doubling of noise is still observed. The phenomenon is thus robust to thermal cycling and does not depend on the measurement procedure (here the HB&T configuration provides extremely reliable noise measurement conditions). A slightly less weak coupling is used but the temperature

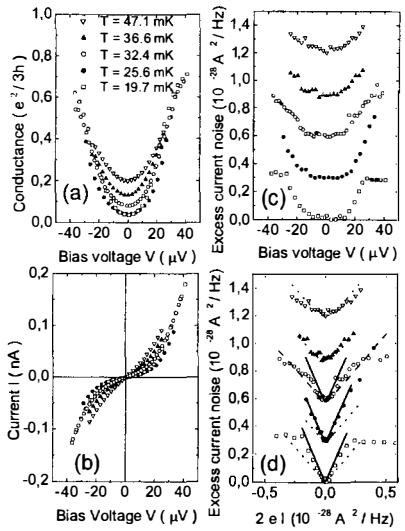


Figure 4: (a-c) differential conductance, current and excess shot noise versus voltage for four temperatures using set-up a1, sample I; (d) excess noise versus current in units of 2eI. The dashed and solid lines show comparison with e and $2e$ shot noise (no adjustable parameter. Noise traces at different temperatures are shifted by a same amount for clarity.

(43mK) is larger than the temperature for which the doubling occurred in the previous data (32mK). If the doubling of shot noise was related to a fundamental change of the ground state excitations, the phenomenon would occur at a definite temperature. We may conclude that the phenomenon is related to the physics of the backscattering. Does the doubling of noise is robust upon changing the bulk filling factor? Figure 5 (b) and (c) show that this is the case. Similar backscattering conditions are used but $\nu_{bulk} = 2/5$ and $= 2/3$ for (b) and (c) respectively while the filling factor $\nu = 1/3$ is kept at the vincinity of the QPC. As in addition, sample II has been used in (c) we have a check that the shot noise doubling is not sample specific. Is the noise pure shot noise? It is known that sometimes a large noise may result from an extra noise due to impurity fluctuations around the QPC. Such extra noise would vary like I^2 and show a $1/f$ frequency dependence. On the contrary, our data show linear variation with I and the inset in figure 5(c) shows that the noise is frequency independent (white) over two octaves. We can thus conclude that *pure shot noise* is observed. Finally, it is interesting to look at the shot noise close to pinch-off when the QPC is so strong that a nearly insulating tunnel barrier is formed at any relevant energy scale. In that case, FQHE correlations are expected to be locally suppressed and shot noise of charge e should be recovered. The noise measurements taken in this regime do indeed show poissonian noise of charge e (figure 5 (d)).

We have yet no explanation for such an observation. We believe that the physics is related to the backscattering mechanism. If we look carefully to the shot noise traces it seems that at very low current the noise starts as $2eI$ but very quickly jumps to $2(2e)I$. For very low temperature and for very small conductance (but still far from the pinch-off regime) we also have observed shot noise even higher than $S_I = 2(2e)I$. Superpoissonian noise has been predicted when resonant tunneling and leads to multivalued I(V) characteristics [26]. Although we have to keep in mind such possible process, the phenomenon observed here seems not related to transmission resonances and exact doubling of noise is not expected in this model. A possible track would be to consider, in the frame of Luttinger liquid models, the so-called non relevant contribution

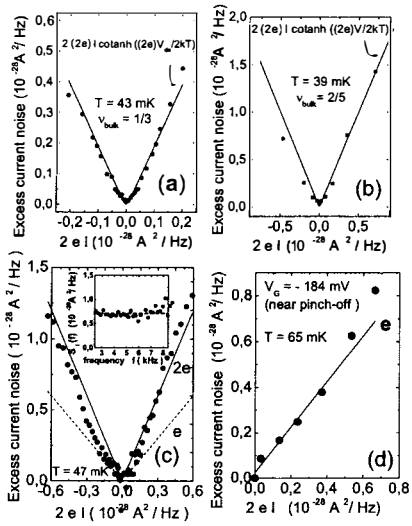


Figure 5: Shot noise observed in different conditions : (a) sample I, $\nu_{bulk} = \nu = 1/3$, coupling slightly less weak than in fig.4 but higher T=43mK, set-up b; (b) sample I, $\nu_{bulk} = 2/5$, $\nu = 1/3$, set-up b, T=39mK; (c) sample II, $\nu_{bulk} = 2/3$, $\nu = 1/3$, set-up a2. The inset shows that the noise is white; (d) near pinch-off, sample I, shot noise of charge e is recovered.

which transfer multiple charges [27,22]. Indeed, at finite bias or temperature, multiple electron process could compete with single electron process and in this temperature regime although the zero bias conductance is rather low compare to $e^2/3h$ the scaling limit is perhaps not reached . Another track would be to consider the effect of spin reversed excitation for ν below 1/3 which perhaps may favor spin singlet tunneling. In any case our results show that the physics of impurity tunneling in the FQHE regime is far from being understood.

5 Conclusion

In conclusion, we have shown that the χLL features, i.e. non-linear conduction and appearance of a strong backscattering regime for a weak impurity potential weak are qualitatively observed in transport experiments using QPC at bulk filling factor 1/3. We have found that at low temperature and low drain source voltage the conductance drops to very small value, even for extremely weak QPC potential, reflecting the renormalization of the coupling strength predicted by the χLL models. The agreement with the theoretical predictions is only quantitative and in particular the predicted power law dependance of the conductance with the bias voltage are not observed. Shot noise measurements shown that, at low voltage and temperature, the current noise is linear with current reflecting the poissonian transfer of charges trough the QPC. However, while a poissonian noise of charge e is expected in this regime, the *shot noise is found super poissonian* with an effective charge $2e$ and sometimes even higher. The phenomenon is observed in two samples for a filling factor $\nu \lesssim 1/3$ at the QPC and for various bulk filling factors $\nu_B = 1/3,\ 2/5,\ 2/3$ far in the leads.

We acknowledge useful discussions with Th. Martin, V. Pasquier, H. Saleur, I. Safi and N. Sandler.

References

1. L. Saminadayar, D.C. Glattli, Y. Jin, and B; Etienne, con-mat/9706307, Phys. Rev. Lett. **79** (1997) 2526.
2. R. de-Picciotto *et al.*, con-mat/9707289; Nature **389** (1997) 162.
3. for a review on shot noise see : Y. M. Blanter and M. Buettiker, Phys. Reports vol **336** (2000) 1-166.
4. X.G. Wen, Phys. Rev. Lett. **64** (1990) 2206.
5. X.G. Wen and A. Zee, Phys. Rev **B46,** (1992) 2246
6. A. Lopez and E. Fradkin, Phys. Rev **B51**, (1995) 4347
7. C. L. Kane and M. P. A. Fisher Phys. Rev. **B 51**, 13449 (1995)
8. K. Imura, Europhysics Lett. **47**, (1999) 233.
9. A. M. Chang, L. N. Pfeiffer, K. W. West, Phys. Rev. Lett. **77** (1996) 2538.
10. M. Grayson, D.C. Tsui, L.N. Pfeiffer, K.W. West, and A.M. Chang, Phys. Rev. Lett, **80** (1998) 1062.
11. A.V. Shytov, L.S. Levitov and B.I. Halperin, Phys. Rev. Lett., **68** (1992) 141.
12. F.P. Milliken, C. P. Umbach, and R.A. Webb, Solid State Commun. **97** (1995) 309.
13. P.J. Turley, D.P. Druist, E.G. Gwinn, K. Maranowski, K. Campmann, A.C. Gossard, Physica B **249-251**, (1998) 410.
14. Masato Ando, Akira Endo, Shingo Katsumoto, Yasuhiro Iye, Physica B **249-251**, (1998) 427.
15. K. Moon and S. M. Girvin, Phys. Rev. B **54** (1996) 4448.
16. B. Rosenow and B.I. Halperin, condmat/0106071.
17. Y. Oreg and A.M. Finkel'stein Phys. Rev. Lett. **74**, (1995) 3368 ; Phys. Rev. Lett. 76, (1996) 4282.
18. C.L. Kane and M.P.A. Fisher, Phys. Rev. Lett. **72** (1994) 724
19. C. de C. Chamon, D.E. Freed, and X.G. Wen, Phys.Rev. B **51** (1995) 2363.
20. P. Fendley, A.W.W. Ludwig, and H. Saleur, Phys. Rev. Lett. **75** (1995) 2196.
21. Y. Oreg and A.M. Fonkel'stein, condmat/9709037.
22. R. Egger, A. Kommink, and H. Saleur, condmat/9904314
23. D.C. Gattli *et al.*, J. Appl. Phys. **81** (1997) 7350.
24. see for example : Th. Martin and R. Landauer, Phys. Rev. B **45**, (1992) 1742; Physica B **175** (1991) 167and M. Büttiker, Phys. Rev. B **46** (1992) 12485.
25. P. Fendley and H. Saleur, Phys. Rev B **54** (1996) 10845.
26. Ya. M. Blanter and M. Buettiker, Phys. Rev B **59** (1999) 10217.
27. C.L. Kane and M.P.A. Fisher, Phys. Rev. B **46** (1992) 15233.

SHOT NOISE

The Effect of Interaction on Shot Noise in The Quantum Limit

D.B. Gutman and Yuval Gefen
Department of Condensed Matter Physics, The Weizmann Institute of Science 76100, Rehovot, Israel

We calculate the current and the current noise in a diffusive micro-bridge in the presence of electron-electron interactions. Out of equilibrium the fluctuation-dissipation theorem (FDT) does not apply, hence these two quantities are not simply related to each other. For a two-dimensional electron gas (2DEG) we obtain logarithmic singularities in the low frequency limit. PACS Nos. 71.10.Ay, 71.23.An, 73.50.Td

1 Introduction

The physics of non-equilibrium mesoscopic systems has been the subject of extensive theoretical and experimental research for more than a decade[1,2,3]. The first step[4,5,6,7] was the understanding that Fermi statistics has a dramatic effect on the noise in the quantum limit. Employing various methods (e.g. semiclassical approximations [5] the Landauer scattering states approach [5,6,7] and diagrammatic Keldysh techniques [8]) it has been recognized that the zero frequency [9] zero temperature noise vanishes in the limit of perfect transparency, while the conductance remains finite. For a multichannel geometry one obtains

$$S(0) = \frac{e^2}{\pi\hbar}\sum_n T_n(1-T_n)eV \ , \tag{1}$$

where $\{T_n\}$ are the channel transparencies and V is the voltage drop across the junction under consideration. This result may be used when discussing disordered conductors. Upon averaging over an ensemble of coherent diffusive systems (the size of which is smaller than any of the inelastic, dephasing and localization lengths), one obtains a universal 1/3 reduction from the traditional expression for shot-noise [10], $S = e < I >$ (the expectation value with respect to the effective action, denoted by <> , includes configuration averaging).

While the physics of non-interacting electrons (especially when disorder averaging is involved) turns out to be quite universal, this is not the case when electron-electron interactions are present. Nevertheless, when the dynamics of the electrons is classical, rendering quantum mechanical interference effects negligible, one may resort to the physically appealing kinetic equation technique, or more specifically, employ the Kogan-Shulman [11] approach. Under such conditions it is possible to define an effective single-particle distribution function which fluctuates in time and space. The characteristics of this distribution function , which affect the noise, depend on non-universal factors such as the external screening [12,13], the geometrical details of the contacts[14] and the various inelastic processes rates[2,15] . One may then consider two limiting cases, namely the short and the long energy relaxation length. Correspondingly, and depending on the frequency range , one may obtain different suppression factors (see e.g.[15,16]), or even a noise spectrum which depends on the spatial coordinate[12]. The dependence of the shot noise on both Fermi statistics and on the value of the discrete elementary charge has become manifest through experiments on fractional quantum Hall systems, where electron-electron interaction redefine the quasi-particle charge [17].

Apart from the later effect, electron-electron interactions may introduce further non-trivial signatures. For interacting systems *at equilibrium* this has been studied by Altshuler and Aronov [18], who found small albeit singular (in the temperature) corrections to the linear conductivity (hence, by FDT, to the equilibrium noise). These corrections to the noise are the result of an interplay between disorder and interaction, and depend on the coherence of the electrons. One might expect an analogous type of physics out of equilibrium. Pursuing the study of the effect

of interactions *beyond* the scope of the kinetic equation and well into the quantum regime is the main focus of the present work.

2 Results

We consider here a high mobility disordered metallic bridge, whose *Ohmic* conductance is G_{Ohm}. This bridge is connected to two ideal leads , each merging adiabatically onto a respective reservoir. The reservoirs are assumed to be at equilibrium with chemical potentials differing by eV. The linear dimensions of the bridge are all larger than the elastic mean free path , l, yet much shorter than the inelastic length, l_{in}. As the problem is technically challenging, we resort to a model calculation ,taking the interaction to be short-ranged. Considering a low electron-electron collision rate, one may assume the temperature T to be constant throughout the system [19]. It is now convenient to define $\zeta = \max\{eV, T\}$; $g_{\square}$ will denote the dimensionless conductance per square, $\hbar\nu D$, where ν is the single electron density-of-states and D is the diffusivity. Our main result concerns the zero frequency noise which is written as

$$S = S_{\bullet} + \delta S \ , \tag{2}$$

where the interaction corrections to the zero frequency noise are given by

$$\delta S = \frac{G_{Ohm}}{6\pi^2 g}\left[2T\ln\left(\frac{\zeta\tau}{\hbar}\right) + eV\coth\left(\frac{eV}{2T}\right)\left(\ln\left(\frac{\zeta\tau}{\hbar}\right) + \ln\left(\frac{T\tau}{\hbar}\right)\right)\right]. \tag{3}$$

This result should be compared with the corresponding correction to the conductance. We have obtained

$$\delta G_{Ohm} = \frac{G_{Ohm}}{2\pi^2 g}\ln\left(\frac{\zeta\tau}{\hbar}\right) \ . \tag{4}$$

At equilibrium , as long as FDT is applicable, the interaction correction to the current noise may be cast as a correction to the Ohmic part of the conductance [18] . Our results , Eqs.(3) and (4), demonstrate that out of equilibrium this is not any more the case: while corrections to the conductance are determined by the larger of the temperature and the applied voltage, the most singular correction to the noise involves a temperature-dominated logarithmic singularity.

3 The Approach

We now present a brief description of our derivation. Full account of the analysis is presented elsewhre[20] We took notice of the work of Kamenev and Andreev [21] , who had addressed the physics of disordered interacting electron gas by deriving a sigma-model description [22] defined on a Keldysh contour (see also Ref. [23]). In their work [21] the interaction has been accounted for by expanding around an (approximate) interaction-dominated saddle point , obtained through gauge transformation. Here we pursue the Kamenev-Andreev approach further, to include non-equilibrium effects [20].

Our starting point is the Lagrangian density

$$\hat{\mathcal{L}} = \overline{\Psi}[\hat{G}_0^{-1} - U_{dis}]\Psi - \overline{\Psi}\overline{\Psi}\hat{V}\Psi\Psi \ . \tag{5}$$

Here $\hat{V}$ represents the electron-electron interaction ; the Schrödinger operator of an electron of mass m in the presence of a vector potential a is given by

$$\hat{G}_0^{-1} = i\hbar\frac{\partial}{\partial t} + \frac{\hbar^2}{2m}(\nabla - a)^2 + \mu \ . \tag{6}$$

All energies are measured from the chemical potential μ. The action now contains an integral over space and an integral in time over the Keldysh contour . Such a representation is particularly convenient for averaging over disorder, as the generating functional $Z[a]$ is identically equal to 1 when the external sources on the forward and backward paths are equal.

Next , one averages over the δ-correlated disorder. We then perform a Hubbard-Stratonovich transformation, introducing the bosonic fields Q and Φ which decouple the non-local-in-time term (generated by disorder averaging) and the non-local-in-space term (produced by the Coulomb interaction) respectively. In terms of the bosonic matrix field Q and Φ the action now reads

$$iS[\hat{Q},\hat{\Phi}] = i\mathrm{Tr}\{\Phi^T \mathrm{V}^{-1}\gamma_2\Phi\} - \frac{\pi\nu}{4\tau}\mathrm{Tr}\{\hat{Q}^2\} + \mathrm{Tr}\ln\left[\hat{G}_0^{-1} + \frac{i\hat{Q}\sigma_3}{2\tau} + \hat{\phi}_\alpha\hat{\gamma}^\alpha\right]. \tag{7}$$

Unlike the original treatment of Ref.[21], we presently try to avoid the overwhelming task of finding an interaction-gauged saddle-point solution out of equilibrium . Instead, we consider here short-ranged interaction which , we believe, captures the essentials of the problem at hand:

$$\hat{\mathrm{V}}(x - x') = \Gamma\delta(x - x') . \tag{8}$$

Hereafter Γ is assumed to be small ($\Gamma\nu \ll 1$). For weak disorder ($\epsilon_F\tau \gg 1$,τ being the elastic mean free time) it is possible to separate the slow and fast degrees of freedom . Expanding around the *noninteracting* saddle point yields the following effective action

$$iS = i\Gamma^{-1}\mathrm{Tr}\{\Phi^T\gamma_2\Phi\} - \frac{\pi\nu}{4}\mathrm{Tr}\{D(\nabla Q)^2 - 4i(\phi_\alpha\gamma^\alpha + \hat{\epsilon})Q\} , \tag{9}$$

with the usual non-linear constraint $Q^2 = 1$. Here $\Phi^T = (\phi_1, \phi_2)$ and

$$\gamma_1 = \begin{pmatrix} 1 & 0 \\ 0 & 1 \end{pmatrix}, \ \gamma_2 = \begin{pmatrix} 0 & 1 \\ 1 & 0 \end{pmatrix} . \tag{10}$$

Within this model one may calculate the correlation function of the fluctuations of the electric potential

$$\langle\phi_i(r,\omega)\phi_j(r',-\omega)\rangle = -i\Gamma\delta(r - r')\gamma_2^{i,j} . \tag{11}$$

Let us first consider the non-interacting scenario , stressing a few points that were implicit in previous works [24,8]. The gapless fluctuations of Q around the saddle point are conveniently parameterized as

$$\begin{aligned} &Q = \Lambda\exp(W) , \\ &\Lambda W + W\Lambda = 0 . \end{aligned} \tag{12}$$

To satisfy the non-linear constraint on Q and , at the same time , conform to Eq. (12), one may use the representation

$$W_{x,\epsilon,\epsilon'} = \begin{pmatrix} F_{x,\epsilon}\bar{w}_{x,\epsilon,\epsilon'} & -w_{x,\epsilon,\epsilon'} + F_{x,\epsilon}\bar{w}_{x,\epsilon,\epsilon'}F_{x,\epsilon'} \\ -\bar{w}_{x,\epsilon,\epsilon'} & -\bar{w}_{x,\epsilon,\epsilon'}F_{x,\epsilon'} \end{pmatrix} , \tag{13}$$

where the fields $\omega, \bar{\omega}$ are unconstrained. Expanding the action to second order in the soft modes yields for the free part of the action

$$iS[W] = iS^0[W] + iS^1[W] + iS^2[W] . \tag{14}$$

The zeroth order term vanishes at the saddle point. The linear part in W should vanish as well, yielding an equation for F which, together with the appropriate boundary conditions, determines F uniquely The quadratic part of the action is equal to

$$iS^2[W] = \frac{\pi\nu}{2}\Big[\bar{w}_{x,\epsilon,\epsilon'}[-D\nabla^2 + i(\epsilon - \epsilon')]w_{x,\epsilon',\epsilon} - D\nabla F_{x,\epsilon}\bar{w}_{x,\epsilon,\epsilon'}\nabla F_{x,\epsilon'}\bar{w}_{x,\epsilon',\epsilon}\Big] . \quad (15)$$

The last term in (15) is responsible for equilibration along the longitudinal coordinate; it is absent at equilibrium.

Turning our attention now to the diffusive constriction geometry, we specifically consider the slow energy relaxation time limit. The distribution function is then readily calculated [24,21]. One may next evaluate various correlation functions for this system out of equilibrium. For our unconstrained Gaussian action, Eq. (15), they can be written in terms of the diffusion propogator [25]

$$\begin{aligned}
&\langle w(x,\epsilon_1,\epsilon_2)\bar{w}(x',\epsilon_3,\epsilon_4)\rangle = 2\delta_{\epsilon_1,\epsilon_4}\delta_{\epsilon_2,\epsilon_3}\mathrm{D}(x,x',\epsilon_1-\epsilon_2)\\
&\langle w(x,\epsilon_1,\epsilon_2)w(x',\epsilon_3,\epsilon_3)\rangle = -\delta_{\epsilon_1,\epsilon_4}\delta_{\epsilon_2,\epsilon_3}2\pi\nu D\\
&\mathrm{D}_{\epsilon_1-\epsilon_2,x,x_1}\nabla F_{\epsilon_2,x_1}\otimes\nabla F_{\epsilon_1,x_1}\mathrm{D}_{\epsilon_2-\epsilon_1,x_1,x'} .
\end{aligned} \quad (16)$$

Employing the above building blocks we may calculate the symmetrized current-current correlation function

$$\mathrm{S}(t,x,t',x') = \frac{1}{2}[\langle\langle\hat{I}(t,x)\hat{I}(t',x') + \hat{I}(t',x')\hat{I}(t,x)\rangle\rangle] . \quad (17)$$

Under stationary conditions it is a function of the difference of its arguments. Relying on the identity $Z[a_+, a_- = 0] = 1$ (where the indices refer to the symmetric ("classical") and the antisymmetric ("quantal") combinations over the Keldysh branches) , we express S as

$$\mathrm{S}(x,t;x',t') = -\frac{e^2}{4}\frac{\delta^2 Z[a]}{\delta a_2(x,t)\delta a_2(x',t')} . \quad (18)$$

After functional differentiation one obtains the following equation

$$\mathrm{S}_{x,t;x',t'} = \frac{e^2\pi\nu D}{4}\left\langle \mathrm{I}^D_{x,t,t}\delta_{x,x'} - \frac{\pi\nu D}{2}\mathrm{M}_{x,t}\mathrm{M}_{x',t'}\right\rangle - \langle\mathrm{I}\rangle^2, \quad (19)$$

where we have introduced the notation

$$\begin{aligned}
\mathrm{I}^D_{x,t} &= \mathrm{Tr}\Big\{Q_{x,t,t'}\gamma_2 Q_{x',t',t}\gamma_2 - Q_{x,t,t'}Q_{x',t',t}\Big\}\delta_{x,x'}\\
\mathrm{M}_{x,t} &= \mathrm{Tr}\Big\{(Q_{x,t,t_1}\nabla Q_{x,t_1,t} - (\nabla Q_{x,t,t_1})Q_{x,t_1,t})\gamma_2\Big\} .
\end{aligned} \quad (20)$$

Expanding Eq. (19) to first order in $1/g$ and to zeroth order in Γ , we recover the results of the direct diagrammatic analysis of this problem [8]. The extra power of g in the second term (a non-local part) cancels with $\langle\mathrm{I}\rangle^2$. At high frequencies, dynamical fluctuations of the local density are feasible, leading to the dependence of the noise on the the spatial coordinates; this is not anymore the case at low frequencies, $\omega \ll E_{Th}$, which is a direct consequence of particle conservation. In this limit S is given as a sum of three equilibrium spectral functions [27]

$$\mathrm{S}_0(\omega) = \frac{1}{6}[4\mathrm{S}^{eq}(\omega) + \mathrm{S}^{eq}(\omega + eV) + \mathrm{S}^{eq}(\omega - eV)] , \quad (21)$$

as has been found earlier [5].

4 The Effect Of e-e Interaction

So far we have considered the leading part of the current noise. Now on we discuss corrections due to e-e interactions. We note that under the conditions specified above, the non-equilibrium quasi-particle distribution function is essentially of a (temperature and interaction smeared) double-step form. We first evaluate the interaction correction to the stationary value of electron current, $\delta \mathrm{I}^{ee}$. Employing the relation

$$I = \frac{-e}{2i}\frac{\delta Z[a]}{\delta a_2} , \tag{22}$$

and using the action (Eq. 9), we obtain

$$\delta \mathrm{I}^{ee} = \frac{e\pi\nu D(i\pi\nu)^2}{4}\langle \mathrm{M}\,\mathrm{Tr}\{\phi_\alpha\gamma^\alpha Q\}\mathrm{Tr}\{\phi_\beta\gamma^\beta Q\}\rangle_0 . \tag{23}$$

Employing the rules of Eq.16 , this leads to

$$\delta \mathrm{I}^{ee} = \langle \mathrm{I}\rangle \frac{\Gamma\nu}{2(2\pi)^2 g}\ln\left(\frac{\zeta\tau}{\hbar}\right) . \tag{24}$$

Let us turn now to the calculation of the interaction correction to the current noise. To this end one evaluates Eq. (19), employing the interaction dependent action, Eq. (21) . In first order in the interaction we obtain

$$\delta \mathrm{S}^{ee}(0) = \frac{e^2\pi\nu D}{4}\Big\langle [I^D_{x,t,t'}\delta_{x,x'} - \frac{\pi\nu D}{2}M_{x,t}M_{x',t'}]$$
$$\mathrm{Tr}\{\phi_\alpha\gamma^\alpha Q\}\mathrm{Tr}\{\phi_\beta\gamma^\beta Q\}\Big\rangle . \tag{25}$$

To proceed , we first carry out the averaging over the fields ϕ in Eq. (25) employing Eq. (11) . This leads to a Γ dependent expression written solely in terms of the matrices Q. We then expand in the fields $\omega, \bar{\omega}$ and perform contractions according to the rules of Eq.(16). For frequencies smaller than the Thouless frequency , the current-current correlation function does not depend on the choice of the cross-section : integration over the spatial coordinates will lead to the suppression of space-derivative terms. We finally obtain

$$\delta S^{ee} = \frac{G\Gamma\nu}{12\pi^2 g}\left[2T\ln\left(\frac{\zeta\tau}{\hbar}\right) + eV\coth\left(\frac{eV}{2T}\right)\left(\ln\left(\frac{\zeta\tau}{\hbar}\right) + \ln\left(\frac{T\tau}{\hbar}\right)\right)\right]. \tag{26}$$

The derivation of Eqs. (24) and (26) involves some controlled approximations. The use of a short range interaction (assumed to be small, $\Gamma\nu \ll 1$) renders them model dependent.

To establish a relation with the "real" screened Coulomb interaction, we further propose the following heuristic picture: we argue that the correct prefactor in the expression for $\delta \mathrm{I}^{ee}$ should not depend strongly on either the temperature or the voltage ; hence it can be restored based on equilibrium calculations [18] ,

$$\delta \mathrm{I}^{ee} = \langle \mathrm{I}\rangle \frac{1}{2\pi^2 g}\ln\left(\frac{\zeta\tau}{\hbar}\right) . \tag{27}$$

Comparing Eqs.(24) and (27) we are able to express Γ in terms of the model-independent parameters of the problem , which leads to Eq.(4). This mapping will be employed for the expression for the noise as well, leading to Eq. 3. Hereafter we have assumed $\zeta \gg E_{Th}$, which is readily satisfied for macroscopic samples. We note that both the voltage and the temperature

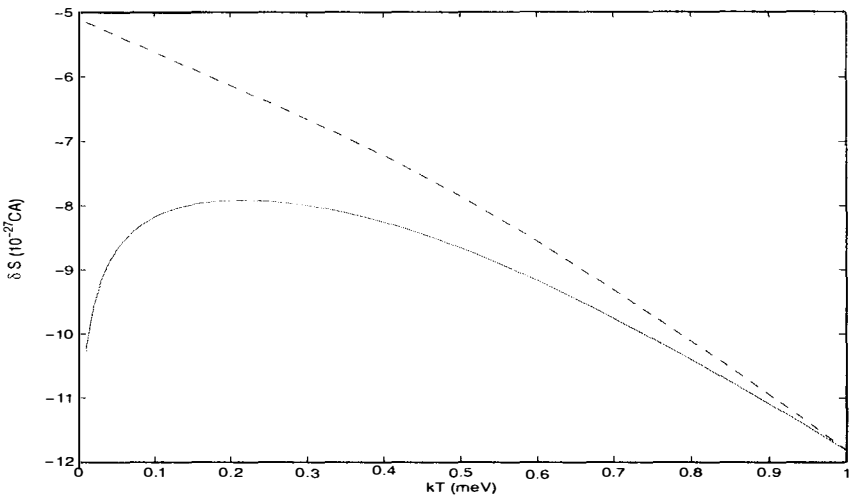


Figure 1: Interaction correction to the noise (solid line) and the "naive expectation" (dashed line), see text for definitions.

may serve as cut-offs for the logarithmic singularity. For $T \gg eV$ the singularity is governed by T, resulting in the Altshuler-Aronov correction to the conductance.

Considering the asymptotic high temperature behavior of Eq.(3), one notes that the equilibrium part is dominant. By the FDT Eq. (3) is related to the Altshuler-Aronov correction to the conductance [18] , which is obtained from Eq. (4) by substituting $\zeta = T$:

$$\delta \mathrm{S} = \frac{G_{Ohm}}{\pi^2 g} T \ln\left(\frac{T\tau}{\hbar}\right), \tag{28}$$

or, alternatively, it is related to the correction to the mean current, Eq.(27).

In the large voltage limit, current fluctuations are dominated by the bias dependent shot noise. Note, though, that the interaction corrections to it are still determined by the *temperature*,

$$\delta \mathrm{S} = \frac{G_{Ohm}}{6\pi^2 g} e|V| \ln\left(\frac{T\tau}{\hbar}\right) . \tag{29}$$

The FDT breaks down manifestly , and the results for the current (Eq. 27) and for the current noise (Eq. 29) are no longer related to each other in a simple way. Moreover, the interaction correction to the current noise is larger (for large bias) than the corresponding correction to the mean current. On a qualitative level we note that within a classical picture,the electron-electron interaction may indeed lead to strong suppression of current fluctuations without affecting the mean current much, in agreement with our quantitative analysis. In other words, the relation between the mean current and the noise , $S \sim eI$, which is valid for Poisson-like processes, is no longer applicable. While we have presented here specific expressions for the interaction corrections in two dimensions, we do expect effects of similar nature to take place at other dimensions as well.

5 Experimental Relevance

From the experimental point of view and for standard range of parameters, the effect we predict here is quite small (i.e., the logarithm of the ratio between the voltage and the temperature dominated corrections is typically close to unity. However, the incipient logarithmic singularity found here may, in principle, be spotted by carefully scanning the temperature dependence of the noise. Moreover, one can push the temperature and the voltage to values where the effect is particularly enhanced. Fig[1] presents a comparison of the corrections to the zero frequency current noise derived here (solid line) with a "naive" prediction (dashed line). The latter refers to using a standard expression for the shot noise, where we insert the non-equilibrium interaction corrections for G_{Ohm}. Here our two-dimensional metallic film is assumed to have a square geometry. Its conductance measured in units of quantum conductance is taken to be $G_{Ohm} = 10\frac{e^2}{\hbar}$, and the value of the elastic mean free time is chosen to be $\tau = 10^-2\frac{1}{meV}$. The applied bias $V = 1meV$ and the temperature varies in the range $0.001\text{meV} < kT < 1\text{meV}$. As the temperature decreases, the discrepancy between the "naive expectation" and the correct result becomes increasingly pronounced.

Acknowledgments

We acknowledge discussions with A.M. Finkelstein, A. Kamenev, D.E. Khmel'nitskii, L.S. Levitov, A.D. Mirlin, M. Rokni, B.Z. Spivak and useful input on expermintal aspects from D. Prober, M. Reznikov and R. Schoelkopf. Y.G. acknowledges the hospitality of and the interaction with B.L. Altshuler at Princeton/NEC. This work was supported by the U.S.-Israel Binational Science Foundation, the DIP Foundation, the Israel Academy of Sciences and Humanities-Centers of Excellence Program, and by the German-Israeli Foundation (GIF).

1. Sh. Kogan *Electronic Noise and Fluctuations in Solids* , Cambridge Press (1996) .
2. Ya. M. Blanter, M. Büttiker *Physics Reports* **336**, 2, (2000) .
3. M.J.M. de Jong and C.W.J. Beenakker in a *Mesoscopic Electron Transport*, **NATO ASI** Series E, Vol 345, Kluwer Academic Publishers, Dordrecht, (1997).
4. R. Landauer, 1989, *private communication.*
5. V.A. Khlus *JETP* **66** , 6 (1987) .
6. G. Lesovik *JETP* Lett., **49** , 592 (1989).
7. M. Büttiker *Phys. Rev. Lett* **65** , 2901 (1990) .
8. B.L. Altshuler, L. S. Levitov and A. Yu. Yakovetz *JETP Lett.* **59**, 12 (1994) .
9. One should also keep in mind that this type of analysis is applicable only in the case when shot or Nyquist noise are dominant, and it is justified to neglect $1/f$ noise, i.e. the "zero frequency" is assumed to be finite.
10. C.W. Beenakker and M. Büttiker *Phys. Rev. B* **46**, 1889 (1992).
11. Sh.M. Shulman A.Ya. Kogan *JETP* **29** , 3 (1969) .
12. K.E. Nagaev *Phys. Rev. B* **57**, 4628 (1998) .
13. K.E. Nagaev *Phys. Rev. B* **62**, 5066 (2000) .
14. Y. Naveh, D.V. Averin and K.K. Likharev . *Phys. Rev. B* **59**, 2848, (1999);Y. Naveh, A.N. Korotkova and K.K. Likharev *Phys. Rev. B (RC)* **60**, **2169** (1999) .
15. K.E. Nagaev *Phys. Rev. B* **52**, 4740, (1995) .
16. A. H. Steinbach J. M. Martinis and M. H. Devoret em Phys. Rev. Lett. **76**. 3806 (1996); M. Henny, S. Oberholzer, C. Strunk, and C. Schnenberger *Phys. Rev. B* **59**, 2871 (1999).
17. R de-Piccioto, M. Reznikov, M. Heiblum, V. Umansky, G. Bunin, D. Mahalu *Nature* **389**, 6647 (1997), L. Saminadayar, D. C. Glattli, Y. Jin, B. Etienne . *Phys.Rev. Lett.* **79**, 2526 (1997) .

18. B.L. Altshuler and A.G. Aronov in *"Electron-Electron Interaction in Disordered Systems"*, Elsevier Science Publishers B.V., Nort-Holand, New-York (1985) .
19. By this we do not imply that the system is at equilibrium.On the contrary, the distribution function of the electron gas is a weighted sum of two Fermi-Dirac functions, with different chemical potentials but the same underlying T.
20. D.B. Gutman Y. Gefen , *cond-mat/0102134*
21. A. Kamenev, A. Andreev *Phys. Rev. B* **60**, 2218 (1999).
22. A.M. Finkelstein *"Electron Liquid in disordered Conductors"* Sov. Sci. Rev. A. Phys. 14 Harwood Academic Publishers, GmbH, London (1990) .
23. C. Chamon, A.W. Ludwig, C. Nayak *Phys. Rev. B* **60**, 2239 (1999) .
24. K.E. Nagaev *Phys. Let. A* **169**, 103 (1992) .
25. The diffusion propagator D is defined through $\left(-i\omega + D\nabla^2\right) \mathrm{D}(\omega, r, r') = \frac{1}{\pi\nu}\delta(r-r')$, with the appropriate boundary conditions.
26. In order for the diffusion approximation for the kinetic equation to be valid , deviations from equilibrium should be small, i.e. the energy gain between two consecutive elastic scattering is small in comparison with the Fermi energy ($(eU/\epsilon_F)(l/L) \ll 1$) .
27. The subscript 0 refers to averaging with respect to the non-interacting action.

Full counting statistics of electron transfer between superconductors

Yu. V. Nazarov[1], W. Belzig[1,2]

Department of Applied Physics and Delft Institute of Microelectronics and Submicrontechnology, Delft University of Technology, Lorentzweg 1, 2628 CJ Delft, The Netherlands

[2] *Department of Physics and Astronomy, University of Basel, Klingelbergstr. 82, CH-4056 Basel, Switzerland*

We present an extension of the Keldysh-Green's function method, which allows to calculate the full distribution of transmitted particles through a mesoscopic (super-)conductor. The method is applied to the statistics of supercurrent in short contacts. If the current is carried by Andreev bound states the distribution corresponds to switching between long trains of electrons going in opposite directions. For weak (gapless) superconductors or tunnel junctions we find that at low temperatures the distribution has negative "probabilities". Accounting for the quantum mechanical nature of the electron counting device shows that these negative values can indeed be measured.

1 Introduction

Coherent charge transfer between superconductors (S), supercurrent, is essentially an quantum-mechanical process. Although superconducting junctions are commonly used, the statistical properties of the charge transfer involved into the supercurrent are not yet completely understood. In view of recent attempts to use the coherence of superconductors to build quantum bits[1], it is necessary to reveal the basic limitations on this coherence (if there are any). Additionally, the problem of the statistics of transferred charge in a quantum process is of fundamental interest. It is related to the understanding of the measurement process and the interpretation of its outcome.

Recently the current noise exhibited in SNS junctions, where N is a diffusive normal metal, was addressed experimentally.[2] The experimental results show a giant excess noise in the low temperature and voltage regime in those samples, in which at the same temperature a coherent coupling through the normal metal was measured. This is in accordance with theoretical predictions for the shot noise in short contacts.[3] This may hint to the importance of an understanding of the statistical properties of the supercurrent in such junctions. The equilibrium noise properties have been studied in[4] and[5]. Further experimental progress in the fabrication of controllable single-channel junctions is to be expected in the near future. This will shed more light on the fundamental statistical properties of charge transfer between

An understanding of the statistics of the charge transfer process can be found by the so called *full counting statistics* (FCS), originally introduced to calculate the distribution of transmitted charge through a contact between normal metals[6]. This theory allows to find the cumulant generating function (CGF) $S(\chi)$, from which the distribution of transmitted charge follows via $P(N) = \int d\chi \exp(-S(\chi) - iN\chi)$. It is tempting (and has been done so far) to interpret $P(N)$ as the probability that N charges have been transferred through the contact during the time of observation. We will show below that this interpretation is strict only for normal constrictions. For superconducting constrictions (with phase difference ϕ) $P(N,\phi)$ can also take also negative values, which hampers such interpretation. This is related to the fact that the phase and number of charges transferred can be regarded as canonically conjugated variables. Still $P(N,\phi)$ provides a complete description of all charge transfer processes and can be extracted from the results of measurements.

2 Model and Method

The most powerful and general method of calculating transport properties of mesoscopic conductors is the nonequilibrium Green's function approach (see [7]). It was shown in [8] that this approach can be generalized to access FCS. In this Letter we extend the approach to superconductors. This allows to obtain the FCS of an arbitrary mesoscopic conductor at all temperatures and voltages. The CGF is derived for a contact which is fully characterized by an ensemble of transmission eigenvalues $\{T_n\}$. We evaluate the FCS of supercurrent in two generic cases. First, we find the distribution of transmitted charge of a single channel contact between two gapped superconductors. Here the current is carried by phase dependent Andreev bound states and, as shown by our analysis, conforms with the switching picture.[5] The two bound states carrying current in opposite directions are alternately occupied and charges are transfered in 'long trains', which reflects the coherent nature of the supercurrent. In the second case we calculate the CGF of a contact between two weak superconductors. The resulting CGF corresponds to the tunnel limit for gapped superconductors and can be related to the effective Keldysh action of a Josephson junction discussed in detail in Ref.[9]. The standard interpretation[6] of the CGF leads in the low temperature regime to negative "probabilities" $P(N,\phi)$. Negative values of $P(N,\phi)$ occur because of an attempt to interpret the quantum mechanical phenomenon of supercurrent with classical means. If we account for the quantum mechanical nature of the measuring device, we can resolve the paradox and specify how $P(N,\phi)$ can be measured.

To study FCS, we consider a mesoscopic conductor placed between two reservoirs. The counting field χ is introduced on an arbitrary cross section in one of the reservoirs and couples to the operator of current through that cross section. The counting field choosen in this way can be incorporated into the boundary condition imposed by the reservoir onto the mesoscopic conductor.[10] That is, the reservoir Green's function effectively takes the form

$$\check{G}_1(\chi,\phi) = e^{\frac{i}{2}\chi\check{\tau}_K}\check{G}_1(\phi)e^{-\frac{i}{2}\chi\check{\tau}_K} \ . \tag{1}$$

Here $\check{G}_1(\phi)$ is the reservoir Green's function at superconducting phase ϕ in the absence of the counting field and $\check{\tau}_K = \hat{\sigma}_3\bar{\tau}_3$ a matrix in Keldysh(ˆ)-Nambu(¯) space. Now the counting field is included into the boundary condition for the Keldysh-Nambu matrix Green's functions provided by the left reservoir. Inside the system of interest the transport properties are described by quasiclassical Eilenberger equations.[11] It is important that $\check{G}(\chi,\phi)$ still obeys the quasiclassical normalization condition $\check{G}^2(\chi,\phi) = \check{1}$.

In certain cases the action $S(\chi,\phi)$ can be found quite generally. One example is a constriction shorter than the coherence length, which is fully characterized by a set of transmission eigenvalues $\{T_n\}$. The matrix current was derived in [10] and is given by

$$\check{I}(\chi,\phi) = \frac{1}{2\pi}\sum_n \int dE \frac{T_n\left[\check{G}_1(\chi,\phi),\check{G}_2\right]}{4+T_n\left(\{\check{G}_1(\chi,\phi),\check{G}_2\}-2\right)} \ . \tag{2}$$

The action can then be found from the relation $(\partial/\partial\chi)S(\chi,\phi) = -it_0\mathrm{Tr}(\check{\tau}_K\check{I}(\chi,\phi))$. We obtain

$$S(\chi,\phi) = \frac{-t_0}{2\pi}\int dE \mathrm{Tr}\ln\left[4+T_n\left(\{\check{G}_1(\chi,\phi),\check{G}_2\}-2\right)\right] \ . \tag{3}$$

Eq. (3) is very general. It contains the statistical properties of all types of superconducting constrictions. For instance the FCS of an SN-contact [12] can easily be obtained from (3).

3 Equilibrium Noise in Superconducting Point Contact

In the rest of the paper we will study equilibrium noise and statistics of systems with two superconducting contacts in two different limits. We limit the discussion to a single channel of

transmission T_1 and identical reservoirs at equilibrium. To be specific, we consider the Green's functions of the reservoirs

$$\check{G}_S = \frac{1}{2}\begin{pmatrix} \bar{R}+\bar{A}+(\bar{R}-\hat{A})h & (\bar{A}-\bar{R})(1-h) \\ (\bar{A}-\bar{R})(1+h) & \bar{R}+\bar{A}-(\bar{R}-\bar{A})h \end{pmatrix}. \tag{4}$$

Here $\bar{R}(\bar{A})\,(E)$ are retarded and advanced Green's functions of the banks and $h(E) = \tanh(E/2T)$ accounts for the equilibrium distribution at a temperature T. The phase difference ϕ is introduced by setting $\check{G}_1(\phi) = \exp(i\phi\bar{\tau}_3/2)\check{G}_S\exp(-i\phi\bar{\tau}_3/2)$ and $\check{G}_2 = \check{G}_S$. Advanced and retarded functions in (4) possess the structure $\bar{R}(\bar{A}) = g_{R,A}\bar{\tau}_3 + f_{R,A}\bar{\tau}_1$ fulfilling the normalization condition $f^2+g^2=1$.

The trace in the action can be evaluated and we obtain the main result of this paper

$$S(\chi,\phi) = \frac{-t}{\pi}\int dE \ln\left[1+\sum_{n=-2}^{2}\frac{A_n(\phi)}{Q(\phi)}\left(e^{in\chi}-1\right)\right]. \tag{5}$$

Introducing $q = (1-g_R g_A)(1-h^2) + f_R f_A(1+h^2)$ the coefficients may be written as

$$A_{\pm 2} = \frac{T_1^2}{64}q^2, \tag{6}$$

$$A_{\pm 1} = \frac{T_1}{4}q - \frac{T_1^2}{16}q\left[q - 4f_R f_A \sin^2\frac{\phi}{2}\right] + \frac{T_1}{8}\left[(f_R+f_A)h\cos\frac{\phi}{2} \mp i(f_R-f_A)\sin\frac{\phi}{2}\right]^2, \tag{7}$$

$$Q = \left[1-T_1 f_R^2\sin^2\left(\frac{\phi}{2}\right)\right]\left[1-T_1 f_A^2\sin^2\left(\frac{\phi}{2}\right)\right]. \tag{8}$$

The interpretation of the different terms is analogous to that given in [12]. A coefficient $A_{\pm n}$ is related to events in which a charge n is transfered to the right(left). The presence of terms, which describe charge transfers of 2e, is a consequence of superconducting correlations. The interpretation as probabilities stems from the comparison with the case of Poissonian statistics (see [6]). As we will discuss below this interpretation only makes sense for normal metals.

Considering only the phase independent terms demonstrates an interesting feature of (5)-(8). These terms can be factorized into

$$\left[1+\frac{T_1 q}{8}\left(e^{i\chi}-1\right)+\frac{T_1 q}{8}\left(e^{-i\chi}-1\right)\right]^2. \tag{9}$$

The processes described by this expression consist of two independent statistical events, which we can identify with electron and hole transfers. The phase dependent terms inhibit this factorization and lead to correlations between electrons and holes, as expected in superconductors. The denominator Q, common to all coefficients, has roots for energies, at which Andreev bound states exist. Consequently the statistical properties are dominated by the charge transfer through Andreev bound states. The corresponding "probabilities" can be very large, in particular, larger than 1. Thus, we can not interpret the coefficients (6)-(8) as probabilities anymore. To find the statistics of the charge transfer, we have to specify the system further.

4 Gapped superconductors

If the two leads are gaped like BCS superconductors the spectral function are given by $f_{R,A} = i\Delta/((E\pm i\delta)^2-\Delta^2)^{1/2}$ and $g_{R,A}$ follows from normalization. Here Δ is the pair potential and δ the

a broadening parameter, which accounts for the finite lifetime of the Andreev bound states. The supercurrent is solely carried by Andreev bound states with energies $\pm\Delta(1 - T_1 \sin^2 \phi/2)^{1/2} \equiv \pm E_B(\phi)$. The importance of these bound states can be seen from the coefficient Q (8). It may become zero and will thus produce singularities in the action.[13] The broadening δ shifts the singularities of Q into the complex plane and allows an expansion of the coefficients in Eq. (6)-(8) close to that energy. Performing the energy integration the action results in

$$S(\chi, \phi) = -2t\delta\sqrt{1 - I_1^2(\phi)\chi^2/4\delta^2 - i\chi\bar{I}_1(\phi)/\delta}\,, \tag{10}$$

where $I_1(\phi) = \Delta^2 T_1 \sin(\phi)/2E_B(\phi)$ is the supercurrent carried by one bound state and $\bar{I}_1(\phi) = I_1(\phi)\tanh(E_B/2T)$ is the average current through the contact. In deriving (10) we have also assumed that $\chi \ll 1$. This corresponds to a restriction to "long trains" of electrons transfered, and the discreteness of the electron transfer plays no role here. Fast switching events become less probable at low temperatures and are neglected here. In the saddle point approximation at low temperatures $\gamma \equiv 1/\cosh(E_B/2T) \ll 1$ we find for the current distribution

$$P(j, \phi) \sim \begin{cases} \gamma^{-1} e^{2\delta t\left(\gamma\sqrt{1-j^2(\phi)} - j(\phi)\sqrt{1-\gamma^2}\right)} & , \ |j(\phi)| \leq 1 \\ 0 & , \ |j(\phi)| > 1 \end{cases} . \tag{11}$$

Here, we have expressed the transfered charge in terms of the current normalized to the zero temperature supercurrent: $j(\phi) = I/I_1(\phi)$. The current is related to the particle number by $N = It_0$. At zero temperature Eq. (11) approaches $P(j, \phi) \to \delta(j - 1)$, which follows from a direct calculation. Thus, at zero temperature the current is noiseless and the distribution at finite temperature is in accordance with the picture of switching between Andreev states which carry current in opposite directions.

Let us finally comment on the limits under which the previous result is valid. In the energy integration it was assumed that the bound states are well defined. For small transmission the distance of the bound state to the gap edge is $\approx T_1\Delta$. Thus, to have well defined bound states we have to require $\delta < T_1\Delta$. Similarly for a high transmissive contact and a small the phase difference we require $\phi \sim I/I_c > \delta/\Delta$. The statistics beyond these limits is similar to what is discussed in the following.

5 Tunnel junction/gapless superconductors

Let us now consider the supercurrent statistics between two weak superconductors, where the Green's functions can be expanded in Δ for all energies. One can see that this is equivalent to the tunneling limit, that is an expansion in $\{T_n\} \ll 1$. Expanding the action (3) to lowest order and using that the counting rotation can be written as $\exp(i\chi\check{\tau}_K) = \frac{1}{2}\left[e^{i\chi/2}(1 - \check{\tau}_K) + e^{-i\chi/2}(1 + \check{\tau}_K)\right]$ we find

$$S = -t\left[iI_s(\phi)\sin\chi + P_s(\phi)\left(\cos\chi - 1\right)\right] . \tag{12}$$

Supercurrent $I_s(\phi)$ and noise $P_s(\phi)$ are given by

$$I_s(\phi) = -\frac{G}{8}\int dE \mathrm{Tr}\left\{\bar{\tau}_3\left[\bar{R}_1(\phi), \bar{R}_2\right] - (R \leftrightarrow A)\right\} h \tag{13}$$

$$P_s(\phi) = -\frac{G}{8}\int dE \mathrm{Tr}\left\{\bar{\tau}_3\bar{A}_1(\phi)\bar{\tau}_3\bar{R}_2 + (R \leftrightarrow A)\right\}(1 - h^2) \tag{14}$$

G being total conductance of the contact. The equivalence of this result to the limit of gapless superconductors follows from an expansion of (3)-(8) to orders f^2.

6 Interpretation of the results

Eq. (14) shows that P_s vanishes at zero temperature, whereas I_s vanishes at T_c. Therefore, there is some crossover temperature below which $P_s < I_s$. In this limit the action possesses no saddle point anymore and by expansion in powers of $\exp(i\chi)$ it follows, that $P(N,\phi)$ becomes negative. Obviously this questions the direct interpretation of $P(N,\phi)$ as a probability. Thus, we are forced to have a closer look on what $P(N,\phi)$ actually is.

To clarify, we present a short summary of recent results [14] concerning the interpretation of $P(N,\phi)$. We assume a simple model of a measuring device: a capacitor of infinite capacitance that stores the charge passed through the constriction. The exact quantum mechanical treatment of this device involves its density matrix $\rho(q,q')$, q being the charge stored.

We find the relation between initial and final density matrices of the device. This can be most conveniently expressed in terms of the density matrix in Wigner representation, $\rho(x,q)$, x being canonical conjugate of q. It reads

$$\rho_f(x,q) = \sum_N P(N,\phi - x)\rho_i(x,q-N)\,, \tag{15}$$

so that $P(N,\phi)$ fully characterizes the quantum mechanical behavior of the capacitor. For a normal constriction $P(N,\phi)$ does not depend on ϕ. In this case the quantum mechanics becomes excessive, since we can rewrite Eq. (15) directly in terms of charge distributions $\Pi(q) \equiv \int dx\rho(x,p)$,

$$\Pi_f(q) = \sum_N P(N)\Pi_i(q-N)\,. \tag{16}$$

Therefore, $P(N)$ can be interpreted as *classical* probability. For a superconducting constriction quantum mechanics is essential and the resulting charge distribution depends on details of ρ_i. For instance, if one sets $\rho(q,q')$ to $\delta(q)\delta(q')$ the probabilities $\Pi_f(q)$ do not depend on ϕ:

$$\Pi_f(q) = \sum_N \delta(q-N)\int d\phi P(N,\phi)\,. \tag{17}$$

A similar result for a simple Josephson junction model was cited in [9]. A more general choice of ρ_i preserves the ϕ-dependence. One can summarize the situation by saying that N and ϕ are related to canonically conjugated variables q and x, that hampers their simultaneous measurement.

Since $\rho(x,p)$ are not positive in general, the $P(N,\phi)$ do not have to be positive. It might seem that these "negative probabilities" can not be measured. Fortunately, it is not so. To understand this, let us see how one would measure $P(N)$ in the *classical* case. The only exact way is to make use of Eq. (16). One thus measures $\Pi_{i,f}$ separately and then obtains $P(N)$ from a deconvolution procedure: the Fourier transform of P is the ratio of Fourier transforms of Π's. Our main result is that the same deconvolution procedure can be applied to Eq. (15). In [14] it is shown, that for a wide class of initial density matrices the deconvolution gives $P(N,\phi)$ in the limit $t_0 \to \infty$. This allows one to characterize and measure $P(N,\phi)$, whatever sign it has.

7 Conclusions

In conclusion we have studied the statistical properties of supercurrent in short constrictions. An extension of the Keldysh technique to account for full counting statistics of systems containing superconductors was developed. In the case of the supercurrent through a short constriction (point contact or tunnel junction) the cumulant generating function can be found quite generally. It shows that charge transfer occurs in units of e and $2e$, which largely enhanced probabilities in the case of contacts with large transmission. The charge transfer occurs in long trains of electrons passing through the contact in either direction, which is a signature of the coherent nature of the

supercurrent. The relative probability of trains in the two directions is determined by the thermal occupation and the switching rate between them by the broadening parameter in the bulk of the superconductors. For tunnel junctions or point contacts between gapless superconductors we find the occurrence of negative values of $P(N, \phi)$, which questions the interpretation as a probability. Accounting for the full time evolution of an (idealized) measuring device, we have shown that these negative values can indeed be observed.

Acknowledgments

We acknoledge fruitful discussions with C. W. J. Beenakker, M. Kinderman and L. S. Levitov. W.B. was financially supported by the "Stichting voor Fundamenteel Onderzoek der Materie" (FOM) and the "Alexander von Humboldt-Stiftung".

References

1. A. Shnirman, Z. Hermon, and G. Schön, Phys. Rev. Lett. **79**, 2371 (1997); J. E. Mooij *et al.*, Science **285**, 1036 (1999); L. B. Ioffe *et al.*, Nature **398**, 679 (1999).
2. T. Hoss *et al.*, Phys. Rev. B **62**, 4079 (2000).
3. J. C. Cuevas, A. Martín-Rodero, and A. Levy Yeyati, Phys. Rev. Lett. **82**, 4086 (1999); Y. Naveh and D. V. Averin, *ibid.*, 4090.
4. A. Martín-Rodero, A. Levy Yeyati, and F. J. García-Vidal, Phys. Rev. B **53**, R8891 (1996).
5. D. Averin and H. T. Imam, Phys. Rev. Lett. **76**, 3814 (1996).
6. L. S. Levitov, H. W. Lee, and G. B. Lesovik, Journ. Math. Phys. **37**, 10 (1996).
7. J. Rammer and H. Smith, Rev. Mod. Phys. **58**, 323 (1986).
8. Yu. V. Nazarov, Ann. Phys. (Leipzig) **8** Spec. Issue, SI-193 (1999).
9. G. Schön and A. D. Zaikin, Phys. Rep. **198**, 237 (1990).
10. Yu. V. Nazarov, Superlattices Microst. **25**, 1221 (1999).
11. G. Eilenberger, Z. Phys. **214**, 195 (1968); A. I. Larkin and Yu. N. Ovchinnikov, Sov. Phys. JETP **26**, 1200 (1968); K. D. Usadel, Phys. Rev. Lett. **25**, 507 (1970).
12. B. A. Muzykantskii and D. E. Khmelnitzkii, Phys. Rev. B **50**, 3982 (1994).
13. It is interesting to note that in the limit $\delta \to 0$ the action has poles for energies $E_B^2(\chi) = \Delta^2 \left(1 - T \sin^2 \left(\frac{\phi \pm \chi}{2}\right)\right)$. The counting field therefore couples directly to the phase sensitivity of the Andreev bound states.
14. M. Kindermann and Yu.V. Nazarov (unpublished).

SHOT NOISE OF SERIES QUANTUM POINT CONTACTS

S. OBERHOLZER[1], E. V. SUKHORUKOV[2], C. STRUNK[3], C. SCHÖNENBERGER[1]
[1] *University of Basel, Klingelbergstr. 82, CH-4056 Basel, Switzerland*

[2] *University of Florida, Gainesville, Florida 32611-8440, USA*

[3] *University of Regensburg, D-93040 Regensburg, Germany*

Shot noise of series quantum point contacts forming a sequence of cavities in a two dimensional electron gas are studied theoretically and experimentally. Noise in such a structure originates from local scattering at the point contacts as well as from chaotic motion of the electrons in the cavities. The observed shot noise allows to distinguish between noise of the point contacts and noise from the cavities in reasonable agreement with theoretical predicitons.

1 Introduction

Shot noise is a non-equilibrium type of electrical current noise directly resulting from random transfer of discrete charge quanta [1]. For Poissonian transfer of single electrons the spectral density of the current fluctuations is $S_{Poisson} = 2e|I|$. Correlations imposed by fermionic statistics or Coulomb interaction may change shot noise from $S_{Poisson}$ which is expressed by the Fano factor F defined as $F \equiv S/S_{Poisson}$. As an example, a one mode quantum wire with an intermediate barrier of transmission probability T has a Fano factor of $F = 1 - T$. Thus, for $T > 0$ shot noise is suppressed below its full Poissonian value. In various mesoscopic systems universal Fano factors have been found such as $F = 1/3$ in metallic diffusive wires [2,3] or $F = 1/4$ in chaotic cavities [4,5,6]. This paper is devoted to the crossover between shot noise of a single scatterer with $F = 1 - T$ to the diffusive regime with a large number of scatterers for wich F is $1/3$. Experimentally, this can be investigated measuring shot noise of several quantum point contacts (QPC), which model impurity scattering in a diffusive wire.

2 Theory

Shot noise for a sequence of N planar tunnel barriers has been calculated by de Jong and Beenakker within a semiclassical description based on the Boltzmann-Langevin approach [7]. For equal transmission probabilities $T_{1,2...N} = T$ the Fano factor F reaches $1/3$ with increasing barrier number ($N \to \infty$) for any value of the transparency $T \in [0, 1]$. Hence, in this description a diffusive conductor can be modeled as the continuum limit of a series of tunnel barriers. However, the calculation in Ref. [7] is only valid for one-dimensional transport since it neglects transverse motion of the electrons in between the barriers. It is therefore not appropriate to describe our physical system consisting of a series of quantum point contacts. Here, we consider the case that there are cavities between the barriers in which the electrons scatter chaotically leading to additional cavity noise [4,5].

In general, the fluctuations in the total current through a system as shown in Fig. 1 can be written as [5]

$$\delta I = \delta I_n^S + G_n(\delta V_{n-1} - \delta V_n), \quad n = 1, \ldots N \tag{1}$$

using the fact that the total current is conserved. $G_n = G_0 \sum_k T_{kn}$ ($G_0 = 2e^2/h$) is the conductance of the n-th barrier and δV_n the voltage fluctuations inside the n-th cavity. δI_n^S are the "Poissonian" current fluctuations of a single QPC [8]:

$$\langle \delta I_n^S \delta I_m^S \rangle = S_n \delta_{nm} \quad \text{with} \tag{2}$$

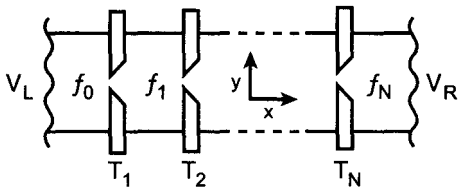


Figure 1: Schematic of the considered system: N quantum point contacts forming a series of cavities. $f_{n=0\ldots N}$ denote the distribution functions of the electrons. In such a system shot noise arises due to quantum diffraction inside the cavity as well as to partitioning at the contacts.

$$S_n = 2G_0 \sum_k \int d\epsilon \Big[T_{kn} f_{n-1}(1-f_{n-1}) + T_{kn} f_n (1-f_n) + T_{kn}(1-T_{kn})(f_{n-1}-f_n)^2 \Big]. \quad (3)$$

Summing Eq. 1 over n while assuming equal conductances $G_n = G$ the total noise power follows as

$$S \equiv \langle \delta I^2 \rangle = \frac{1}{N^2} \sum_{n,m=1}^{N} \langle \delta I_n^S \delta I_m^S \rangle = \frac{1}{N^2} \sum_{n=1}^{N} S_n, \quad (4)$$

where we assumed $\delta V_1 = \delta V_N = 0$, i.e. no fluctuations in the potential of the perfect metallic leads.

2.1 Non-interacting electrons

The distribution function f_n of the n-th cavity follows from the conservation of numbers of electrons in each energy interval[5]

$$f_n(\epsilon) = \left(\frac{N-n}{N} \right) f_L(\epsilon) + \frac{n}{N} f_R(\epsilon), \quad (5)$$

with $f_L(\epsilon) = f_F(\epsilon, eV_L, \theta)$ and $f_R(\epsilon) = f_F(\epsilon, eV_R, \theta)$ the equilibrium Fermi function in the left and right reservoir, respectively. θ denotes the bath temperature. For simplicity we consider in the following only one propagating mode and introduce the backscattering parameter $\mathcal{R}_n \equiv 1 - T_n = \mathcal{R}$ assumed to be the same for all barriers. Substituting the distribution function f_n from Eq. 5 into Eq. 3, the total noise of N point contacts in series follows from Eq. 4. In the zero temperature limit we obtain for the Fano factor

$$F \equiv \frac{S}{2e|I|} = \left(\frac{1}{3} + \frac{\mathcal{R}}{N^2} - \frac{1}{3N^2} \right). \quad (6)$$

For a single QPC ($N = 1$) F equals the backscattering parameter $\mathcal{R} = 1 - T$ as expected. For $N = 2$ we have a single cavity which is separated from the leads by two QPCs and for ideal contacts ($\mathcal{R} = 0$) the Fano factor is $1/4$. If the QPCs are in tunneling regime ($\mathcal{R} \approx 1$) noise is dominated by the QPCs and the dynamics inside the cavity play no role. The Poissonian voltage noise of the two contacts adds up resulting in a Fano factor $1/2$. In the intermediate regime $F = \frac{1}{4}(1 + \mathcal{R})$. Increasing the number of QPCs ($N \to \infty$) the Fanofactor F reaches $1/3$ *independent* of $\mathcal{R} = 1 - T$ as for the calculation in Ref. [7].

In Fig. 2(a) we compare our result of Eq. 6 with the result for one-dimensional tunnel-barriers. For point contacts with low transparencies ($T = 0.1$) the results are very similar because in this case noise is dominated by the contacts. But for high transparencies ($T = 0.9$) the calculation including noise of cavities (Eq. 6) shows that shot noise increases much faster with the number of QPCs N in contrast to the linear model of de Jong and Beenakker [7].

2.2 Interacting electrons

In case of strong electron-electron interaction in the cavities the distribution function inside the n-th cavity $f_n(\epsilon, \theta)$ equals a Fermi function $f_F(eV_n, \theta_n)$ at an elevated electron temperature θ_n.

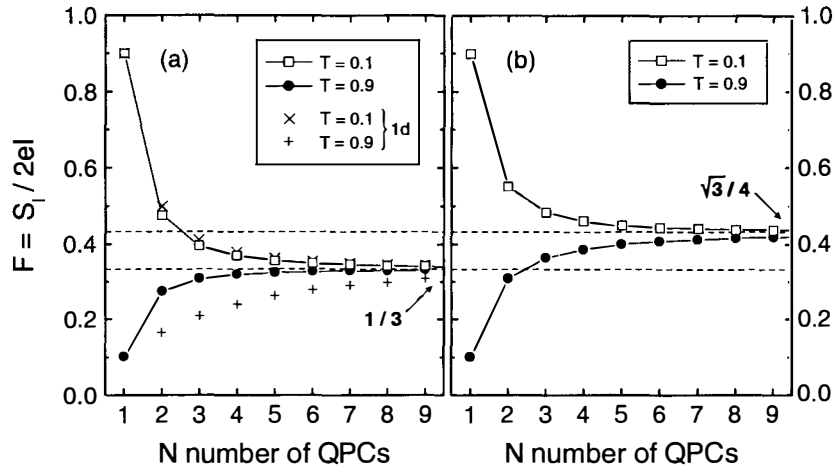


Figure 2: Shot noise normalized to the Poissonian limit $2e|I|$ as a function of the number of QPCs N in series for cold (a) and hot electrons (b) at zero bath temperature. The crosses $(\times, +)$ in the left plot correspond to a calculation of de Jong and Beenakker for one-dimensional transport, not including the noise arising from chaotic motion of the carriers in the cavities between the barriers.

$V_n = V(1 - n/N)$ is the potential in the n-th cavity with $V = V_L - V_R$ the potential difference between left and right reservoir. The electron temperature θ_n follows from energy balance equation using the Wiedemann-Franz law [9]:

$$\theta_n^2 = \theta^2 + \frac{3n(N-n)}{N^2}\left(\frac{eV}{\pi k_B}\right)^2. \tag{7}$$

Using Eq. 3 and 4 the noise power for hot electrons can be calculated numerically. Results are shown in Fig. 2(b). In the continuum limit ($N \to \infty$) the Fano factor F equals $\sqrt{3}/4$ as for a diffusive wire with electron heating [10,11].

3 Experimental

Experimentally, a series of up to four QPCs is defined by split gates across a Hall bar in a two dimensional electron gas (2 DEG) forming at the interface of a standard GaAs/GaAlAs-heterojunction (Fig. 3(a)). In the experiment, we used only up to three QPCs because one of the four did not show proper conduction quantization. Voltage fluctuations across the series of QPCs are detected using a crosscorrelation technique with two identical low-noise amplifiers. A spectrum analyzer calculates the crosscorrelation of the two amplified signals. Voltage noise is measured as a function of current for one to three QPCs in series with fixed transmission probabilities. The transmission of a single point contact can be independently adjusted measuring its conductance $G = G_0 \sum_k T_k$. The spectral density of the voltage fluctuations are averaged over a frequency bandwith of 1 kHz at ~8 kHz. For experimental details, see Ref. [3,6].

4 Results and discussion

In Fig. 3(b) the Fano factor $F \equiv S/2e|I|$ extracted from the shot noise measurements is plotted as a function of the number of point contacts. The black dots correspond to experimental data obtained for a transmission probability $T = 0.9$ of the single QPCs. The dashed line is

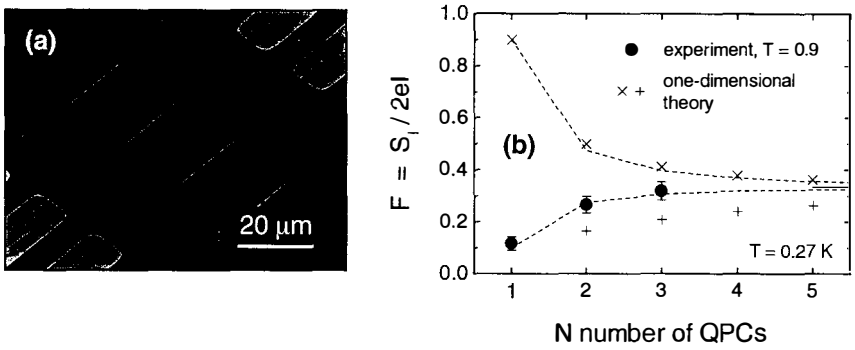


Figure 3: (a) Scanning electron microscope picture of the measured device. The Fermi energy of the 2 DEG is 94 K and the elastic mean free path $l_e \approx 7$ μm. (b) The black points are experimental data for one mode transmitted at the point contacts with probability 0.9. The dashed line are theoretical predictions including cavity noise for non-interacting electrons. The crosses correspond to the one-dimensional model of de Jong and Beenakker.

the prediction of Eq. 6, whereas the crosses correspond to the one-dimensional calculation of Ref. [7]. For $N = 1$ shot noise is strongly suppressed compared to $S_{Poisson} = 2e|I|$, as expected for a single QPC with high transmission probability [12]. When N goes from 1 to 3 shot noise becomes larger. Because in our system we not only have partition noise at the contacts, but also additional cavity noise the Fano factor indeed increases much faster with increasing number of the contacts N compared to the prediction of the one-dimensional theory. Since the cavities are huge compared to the mean free path of the electrons the electrons stay relatively long in the cavity so that they might inelastically scatter from each other. However, the uncertainties of the experimental data do not allow to distuinguish between the cold- and hot-electron regime.

Acknowledgments

This work was supported by the Swiss National Science Foundation. Discussions with F. Rohlfing are gratefully acknowledged.

References

1. For a recent review, see: Ya. M. Blanter and M. Büttiker, "Shot Noise in Mesoscopic Conductors", Phys. Rep. **336**, 1 (2000).
2. C. W. J. Beenakker and M. Büttiker, Phys. Rev. B **51**, 1889 (1992).
3. M. Henny, S. Oberholzer, C. Strunk, and C. Schönenberger, Phys. Rev. B, **59**, 2871 (1999).
4. R. A. Jalabert, J.-L. Pichard and C. W. J. Beenakker, Europhys. Lett. **27**, 255 (1994).
5. Ya. M. Blanter and E. V. Sukhorukov, Phys. Rev. Lett. **84**, 1280 (2000).
6. S. Oberholzer *et al.*, Phys. Rev. Lett. **86**, 2114 (2001).
7. M. J. M. de Jong and C. W. J. Beenakker, Phys. Rev. B **51**, 16867 (1995).
8. G. B. Lesovik, JETP Lett. **49**, 592 (1989), M. Büttiker, Phys. Rev. Lett. **65**, 2901 (1990).
9. E. V. Sukhorukov and D. Loss, Phys. Rev. B **59**, 13054 (1999).
10. K. E. Nagaev, Phys. Rev. B **52**, 4740 (1995).
11. A. H. Steinbach, J. M. Martinis, and M. H. Devoret, Phys. Rev. Lett. **76**, 2778 (1996).
12. A. Kumar *et al.*, Phys. Rev. Lett. **76**, 2778 (1996).

THE FERMIONIC ANALOG OF THE HANBURY-BROWN AND TWISS EXPERIMENT WITH A SUPERCONDUCTOR

JULIEN TORRÈS[1], THIERRY MARTIN[1]
[1] *Centre de Physique Théorique, Luminy Case 907, F-13288 Marseille Cedex 9, France*

The noise correlations are studied in a new analog of the Hanbury-Brown and Twiss experiment for fermions: a superconductor connected to two normal leads. Noise correlations are found to be either negative (fermionic) or positive (bosonic), depending on the transmission of the beam splitter.

1 Introduction

Noise and noise correlations have proven to be a very useful tool in mesoscopic physics. Noise measures the time fluctuations of the current around its average value. It contains more information than the conductance. In general, at zero temperature, shot noise is proportional to the average current and to the effective charge of the carriers in the system. An recent application of this particular point has been achieved by the direct measurement of the fractional charge in a quantum Hall liquid [1,2]. On the other hand, noise correlations give information about the statistical nature of the carriers. Hanbury-Brown and Twiss-type experiments [3] consist in the measurement of the correlations between two partial beams originating from the same initial beam of particles. This yields a different sign for bosons and for fermions [4,5].

In a multi-terminal device, shot noise in a given lead, or noise correlations between two terminals are defined as the Fourier transform of the current-current correlation function:

$$S_{ij}(\omega) = \lim_{T\to+\infty} \frac{2}{T} \int_{-T/2}^{T/2} dt \int_{-\infty}^{+\infty} dt' e^{i\omega t'} \Big(\langle I_i(t) I_j(t+t') \rangle - \langle I_i \rangle \langle I_j \rangle \Big) \ . \qquad (1)$$

When $i = j$, $S_{ii}(\omega)$ corresponds to the noise in the terminal i, whereas if i and j are different, $S_{ij}(0)$ represents the zero frequency noise correlations between lead i and lead j.

The first result [3] about noise correlations for photons described an interferometer to measure the size of a radio star. This experiment was followed by another one using a coherent light source, where a beam was partitioned by a splitter into a reflected and a transmitted part. Intensity correlations between reflected and transmitted beams were found to be positive. Particles in a beam of bosons tend to cluster together (bunching), so the probability to detect simultaneously two photons (one in each beam) is non-zero, and therefore correlations are positive. On the other hand, two indistinguishable fermions exclude each other because of Pauli principle (anti-bunching), and thus, reflected and transmitted beams are anti-correlated [4,5].

More recently, two analogs to the original Hanbury-Brown and Twiss experiment, using electrons propagating in semiconductors were achieved. The system considered is a three terminals device where the first two leads are supposed to be at the same chemical potential: $\mu_1 = \mu_2$. The bias (or the voltage) is defined as $eV = \mu_3 - \mu_{1,2}$. With these assumptions, it is possible to show from the definition (1) that the correlations between terminal 1 and 2 are $S_{12} = -(4e^2/h)eV\ T_{13}T_{23}$, with T_{ij} the probability of transmission from terminal i to terminal j. Thus, negative correlations were expected, and were experimentally verified [6,7,8].

2 The Hanbury-Brown and Twiss experiment with a superconductor

2.1 Model

Here a superconductor is introduced just next to the beam splitter (figure 1, left). Transport in normal metal-superconducting junctions involves Andreev reflection [9]: an incoming electron is

reflected as a hole at the boundary. The remaining charge $2e$ is absorbed by the superconductor via a Cooper pair. While Cooper pairs are not strictly bosons, an arbitrary number of these can exist in the same momentum state, so bosonic statistics could be detected in such a system. Thus the possibility for *positive* noise correlations cannot be ruled out. Below, it is shown that the sign of the noise correlations depends on the transparency of the beam splitter.

The Bogolubov-de Gennes [10] approach to inhomogeneous superconductivity is the adapted formalism to treat electrons and holes on the same footing. Performing the Bogolubov transformation and going to an energy representation, the annihilation operator of a particle with spin σ ($\sigma = \pm 1$) at the position x in the terminal i $\psi_{i,\sigma}(x)$ can be written as:

$$\psi_{i,\sigma}(x) = \frac{1}{\sqrt{2\pi\hbar v_F}} \sum_j \sum_\beta \int_0^{+\infty} dE \left(u_{ij\beta}(x) c_{j\beta\sigma}(E) - \sigma v^*_{ij\beta}(x) c^+_{j\beta-\sigma}(E) \right) . \qquad (2)$$

States $u_{ij\beta}$ and $v_{ij\beta}$ are solution of the Bogolubov-de Gennes equations, and they are given by:

$$u_{ij\beta}(x) = \delta_{i,j}\delta_{e,\beta} e^{ik_F x} + s_{ije\beta} e^{-ik_F x} , \qquad (3)$$

$$v_{ij\beta}(x) = \delta_{i,j}\delta_{h,\beta} e^{-ik_F x} + s_{ijh\beta} e^{ik_F x} . \qquad (4)$$

$u_{ij\beta}$ ($v_{ij\beta}$) corresponds to the wave function of a electron (a hole) scattered in terminal i, due to a quasi-particle of type β (electron or hole, $\beta = e, h$) which was incoming from lead j. The current and the average current are calculated with the operators (2). Then, using the definition (1) the zero-frequency limit for noise correlations between terminals i and j yields [11,12,13,14,15]:

$$S_{ij}(0) = \frac{e^2\hbar^2}{m^2 v_F^2} \frac{1}{2\pi\hbar} \int_0^{+\infty} dE \sum_{m,n} f_m(E)(1 - f_n(E)) |A_{imjn}(E,E) + B^*_{imjn}(E,E)|^2 , \qquad (5)$$

with the matrix elements $A_{imjn}(E,E',t) = u_{jn}(E',t)\partial_x u^*_{im}(E,t) - u^*_{im}(E,t)\partial_x u_{jn}(E',t)$ and $B_{imjn}(E,E',t) = v^*_{jn}(E',t)\partial_x v_{im}(E,t) - v_{im}(E,t)\partial_x v^*_{jn}(E',t)$.

The device is composed of two normal leads (1 and 2 see figure 1, left) linked by a semi-transparent beam splitter (BS) and connected to a superconductor. The incoming states are related to the outgoing states by the scattering matrix of the system (S matrix). From Eq. (5) and in the limit of zero temperature, it is possible to express the correlations in terms of the elements of the S matrix:

$$\begin{aligned} S_{12}(0) = \frac{4e^2}{h} \int_0^{eV} dE \Big[& \sum_{i,j=1,2} \left(s^*_{1iee} s_{1jeh} - s^*_{1ihe} s_{1jhh} \right) \left(s^*_{2jeh} s_{2iee} - s^*_{2jhh} s_{2ihe} \right) \\ & + \sum_{i=1,2\,;\,\alpha=e,h} \left(s^*_{1iee} s_{14e\alpha} - s^*_{1ihe} s_{14h\alpha} \right) \left(s^*_{24e\alpha} s_{2iee} - s^*_{24h\alpha} s_{2ihe} \right) \Big] . \end{aligned} \qquad (6)$$

The sign of Eq. (6) depends on the specific form of the S matrix, which can be established by combining the S matrices of the beam splitter and of the N-S junction (between 3 and 4). Thus, two simple models are proposed, where the beam splitter is dissociated from the N-S junction. In both models, the beam splitter is described by a S matrix S_{BS} which gives the outgoing states as a function of incoming ones. The expression of the electronic part S_{BS_e} of the S matrix is identical to that of Ref. [16,17]. S_{BS_e} depends only on a single parameter ε which monitors the transparency of the splitter. For example if $\varepsilon = 0$ no transmission occurs from region (1) or (2) to region (3). Note that the splitter does not couple electrons and holes. Thus, the expression of the S matrix for holes is the same, as no magnetic field is assumed to be present here.

2.2 Small biases: Andreev regime

When the applied bias is much smaller than the gap ($eV \ll \Delta$), Andreev reflection between is the dominant transport process. Thus, the scattering matrix of the N-S junction S_{NS} only

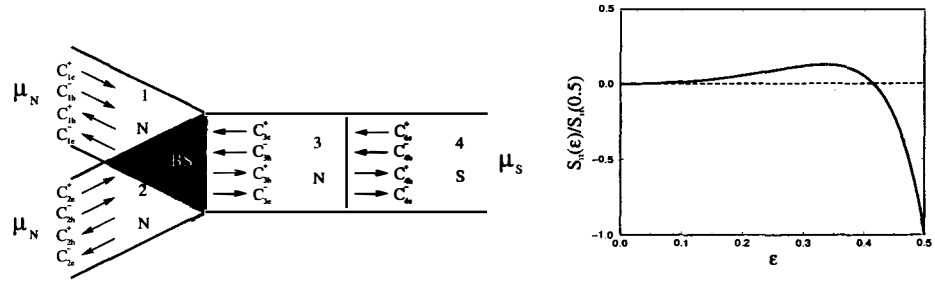


Figure 1: Left: two normal leads (1 and 2) are linked by a semi-transparent beam splitter (BS) and connected to a superconductor (4) via a normal region (3). Right: noise correlations between the two normal reservoirs of the device, as a function of transmission of the beam splitter, showing both positive and negative correlations.

converts electrons into holes, and vice versa. Combining S_{BS} and S_{NS} using the analogy with a Fabry-Perrot interferometer, one obtains the scattering matrix of the whole system which does not depend on the energy in this regime. Therefore the integral (6) can be performed:

$$S_{12}(0) = \frac{4e^2}{h} eV \frac{\varepsilon^2}{2(1-\varepsilon)^4} \left(-\varepsilon^2 - 2\varepsilon + 1\right) . \tag{7}$$

Noise correlations vanish at $\varepsilon = 0$, when conductors 1 and 2 are equivalent to a two-terminal device decoupled from the superconductor. A plot of S_{12} (normalized to the noise in 1 (or 2) at $\varepsilon = 1/2$) as a function of ε (figure 1) indicates that the correlations are positive (bosonic) for $0 < \varepsilon < \sqrt{2} - 1$ and negative (fermionic) for $\sqrt{2} - 1 < \epsilon < 1/2$. At maximal transmission into the normal leads ($\epsilon = 1/2$), the correlations give the negative minimal value: electrons and holes propagate independently into the normal terminals, signature of a purely fermionic system. Decreasing the transmission ε allows to balance the contribution of Andreev reflection with that of normal transport. Expression (7) predicts maximal correlations at $\epsilon = 1/3$.

2.3 Larger biases

If the applied bias is greater than the gap, transmission of quasi-particles from the normal side to the superconductor is allowed, and the elements of the S matrix now depend on the energy. The BTK model[18] is chosen, since it allows a complete description of the N-S junction with a minimal number of parameters. A delta function potential barrier $V(x) = \hbar v_F Z \delta(x)$ is introduced at the N-S boundary. Z is the height (transparency) of the barrier. With this model, the S matrix of the N-S junction is computed. Then it is combined with the same matrix beam splitter.

A numerical calculation of noise correlations is performed with the help of Eq. (6). If one considers a high transparency barrier ($Z = 0.1$) and a small bias, one finds a good agreement with previous analytical results (figure 2, left). The more the bias is increased, the weaker the positive correlations are. If the voltage is large enough (beyond the gap) positive correlations are completely destroyed. As in the analogy with the normal-normal junction, Andreev reflection contribute only for a small part to the transport, and the system loses its bosonic features.

Intermediate transparencies are now considered ($Z = 1$, figure 2, right), and a different behavior is obtained. For weak biases, noise correlations remain positive over the whole range of ε. It is possible to find an appropriate value (for example $eV = 0.95\Delta$) in order to observe oscillations between positive and negative values of the correlations. Positive correlations in fermionic systems with a superconductor are thus *enhanced* by the barrier opacity. Nevertheless, at the same time, for opaque barriers, the absolute magnitude of S_1 and S_{12} becomes rather

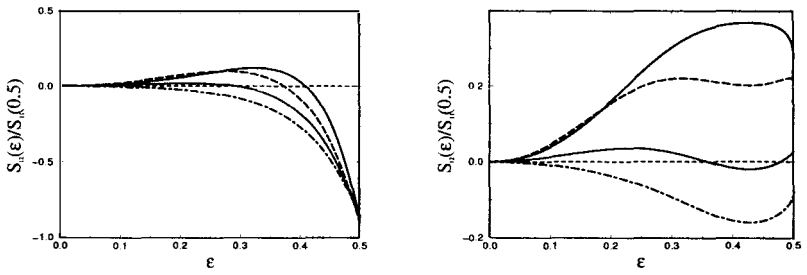


Figure 2: Left: noise correlations using an N-S boundary modeled by BTK for a high transparency barrier ($Z = 0.1$). From top to bottom, $eV/\Delta = 0.5, 0.95, 1.2, 1.8$. Right: noise correlations using an N-S boundary modeled by BTK for intermediate transparency: $Z = 1$ (same biases as in Fig. 2).

small, which limits the possibility of an experimental check in this regime. If the bias is increased further, correlations again become negative over the whole range of ε.

3 Conclusion

The noise correlations have been shown to have either a negative or a positive sign in the same device. Therefore, such a *fermionic* system can exhibit a "*bosonic*" behavior. Other works reported positive correlations in fermionic systems, the one in a N-S junction weakly coupled to a contact [19], and the other in the edge states of the fractional quantum Hall effect [20]. Recent experiments in the "normal" fermionic Hanbury-Brown and Twiss analog [6,7,8] were performed successfully, and these experiments could possibly be extended to the case presented here.

References

1. L. Saminadayar, D. C. Glattli, Y. Jin, and B. Etienne, Phys. Rev. Lett. **79**, 2526 (1997).
2. R. de-Picciotto *et al.*, Nature **389**, 162 (1997).
3. R. Hanbury-Brown and R. Q. Twiss, Nature **177**, 27 (1956).
4. Th. Martin and R. Landauer, Phys. Rev. B **45**, 1742 (1992).
5. M. Büttiker, Phys. Rev. B **45**, 3807 (1992).
6. M. Henny *et al.*, Science **284**, 296 (1999).
7. S. Oberholzer *et al.*, Physica E **6**, 314 (2000).
8. W. D. Oliver, J. Kim, R. C. Liu et Y. Yamamoto, Science **284**, 299 (1999).
9. A. F. Andreev, J. Exp. Theor. Phys. **46**, 1823 (1964) [Sov. Phys. JETP **19**, 1228 (1964)].
10. N. N. Bogolubov, V. V. Tolmachev and D. V. Shirkov, *A New Method in the Theory of Superconductivity* (Consultant Bureau, New York, 1959); P. G. de Gennes, *Superconductivity of Metals and Alloys*, (Addison Wesley, 1966, 1989).
11. Th. Martin, Phys. Lett. A **220**, 137 (1996).
12. M. P. Anantram and S. Datta, Phys. Rev. B **53**, 16390 (1996).
13. J. Torrès and T. Martin, Eur. Phys. J. B **12**, 319 (1999).
14. J. Torrès, T. Martin and G. B. Lesovik, Phys. Rev. B **63**, 134517 (2001).
15. Ya. M. Blanter and M. Büttiker, Phys. Rep. **336**, 1-2 (2000).
16. Y. Gefen, Y. Imry and M. Ya. Azbel, Phys. Rev. Lett. **52**, 129 (1984).
17. M. Büttiker, Y. Imry and M. Ya. Azbel, Phys. Rev. A, **30**, 1982 (1984).
18. G. E. Blonder, M. Tinkham and T. M. Klapwijk, Phys. Rev. B **25**, 4515 (1982).
19. T. Gramespacher and M. Büttiker, Phys. Rev. B **61**, 8125 (2000).
20. C. Texier and M. Büttiker, Phys. Rev. B **62**, 7454 (2000).

EFFECT OF INCOHERENT SCATTERING ON SHOT NOISE CORRELATIONS IN THE QUANTUM HALL REGIME

CHRISTOPHE TEXIER[1,2] and MARKUS BÜTTIKER[3]

[1] *Laboratoire de Physique Théorique et Modèles Statistiques. Université Paris-Sud, Bât. 100. F-91405 Orsay Cedex. France.*

[2] *Laboratoire de Physique des Solides. Université Paris-Sud, Bât. 510. F-91405 Orsay Cedex. France.*

[3] *Département de Physique Théorique. Université de Genève. 24, quai Ernest Ansermet. CH-1211 Genève 4. Switzerland.*

We have studied the effect of incoherent scattering in a Hanbury Brown and Twiss situation with electrons in edge states of a three-terminal conductor submitted to a strong perpendicular magnetic field. The modelization of incoherent scattering is performed by introducing an additional voltage probe through which the current is kept equal to zero which causes voltage fluctuations at this probe. It is shown that inelastic scattering can lead in this framework to positive correlations, whereas correlations remain always negative for quasi-elastic scattering.

1 Introduction

The effect of incoherent scattering on transport and noise in mesoscopic structures has been of interest in a number of previous works (for review see [1,2]). In our work [3] we examine how it affects the noise correlation in a 3-terminal structure in the Integer Quantum Hall regime.

To demonstrate the reality of edge states [4] (despite their small contribution to the overall density of states) the possibility of creating a non-equilibrium population [5] has been crucial. Several experiments have investigated the equilibration of edge states selectively populated with the help of various contacts by transport measurements[6,7,8,9]. A natural problem is to investigate the effect of inter-edge state scattering on the noise on such structures.

Recently, Hanbury Brown and Twiss (HBT) experiments studying current correlations using partially degenerate stream of fermions were performed [10,11], starting from the idea [12] of using the edge states in a conductor submitted to a strong magnetic field. A Y-structure is discussed in Ref. [13] and a HBT experiment without a magnetic field has also been realized [14]. Here we are interested in the experimental arrangement of Oberholzer *et al.* [11] which is depicted in figure 1, with the only difference that the magnetic field, in this experiment, was adjusted in such a way that only one spin-degenerate edge state (filling factor $\nu = 2$) carries the current, and not two, as it is represented on the figure. Contact 1, which is at a potential eV above the potentials of the two other contacts, acts as a carrier source and contacts 2 and 3 as detectors for the beams of electrons. The incident beam is splitted at two quantum point contacts (QPC) which can be tuned by applied voltages. In the following we will denote by T_1 and $R_1 = 1 - T_1$ the transmission and reflection coefficients at QPC at contact 1, and introduce T_3 and R_3 for QPC at contact 3. The quantity of interest in this experiment, revealing statistical properties of the carriers, is the correlation $S_{23} = \langle \Delta I_2 \Delta I_3 \rangle$ between the current at the two contacts. To be precise the noise spectrum is defined as $S_{\alpha\beta}(\omega) 2\pi\delta(\omega+\omega') = \langle \Delta\hat{I}_\alpha(\omega)\Delta\hat{I}_\beta(\omega') + \Delta\hat{I}_\beta(\omega')\Delta\hat{I}_\alpha(\omega)\rangle$ with $\Delta\hat{I}_\alpha(\omega) = \hat{I}_\alpha(\omega) - \langle\hat{I}_\alpha(\omega)\rangle$, where $\hat{I}_\alpha(\omega)$ is the Fourier transform of the current operator at contact α. (For a recent presentation of the formalism and notations, see Ref. [2]). The zero frequency limit will be denoted: $S_{\alpha\beta} = S_{\alpha\beta}(\omega = 0)$. Following the scattering approach, we construct the scattering matrix for the system to calculate the noise correlation [15,2]:

$$S_{\alpha\beta} = \frac{2e^2}{h} \int \mathrm{d}E \sum_{\gamma,\lambda} \mathrm{Tr}\left\{ A^\alpha_{\gamma\lambda} A^\beta_{\lambda\gamma} \right\} f_\gamma (1 - f_\lambda) \,, \tag{1}$$

where f_α is the Fermi-Dirac distribution at the contact α; we consider the case of zero temperature. The matrices A's are related to the on-shell s-matrix: $A^\alpha_{\gamma\lambda} = \delta_{\alpha\gamma}\delta_{\alpha\lambda} - s^\dagger_{\alpha\gamma}(E)s_{\alpha\lambda}(E)$.

After having constructed the s-matrix for the arrangement of figure 1 with one edge state we can compute the correlations between the currents at contacts 2 and 3, which is eventually found to be[11]:

$$S_{23} = -\frac{2e^2}{h}|eV|R_3T_3T_1^2\,. \tag{2}$$

The R_3T_3 factor is the usual partition factor due to the separation of the electron beam at QPC 3. The T_1^2 term is due to the fact that the processes leading to correlations between contacts 2 and 3 involve two electrons transmitted through the QPC 1, which happens with probability T_1^2. Compared to the initial experiment by Henny ***et al.*** [10] the experiment by Oberholzer ***et al.*** [11] introduces fluctuations in the incident beam and thus the current correlations are not determined already from current conservation alone.

In the following we will be interested in the case where the distance between the QPC's is long so that incoherent processes may occur along this edge. If only one edge state is populated, phase breaking processes are of little interest since S_{23} measures in this case quantum-statistical properties of the carriers revealed by the separation of the beam at QPC 3, and what happens before this separation is of little importance. In contrast, when several edge states are populated, inter-edge state scattering along one boundary may cause a redistribution of the carriers between the edge states and thus modify the noise properties of each channel. This is the situation that has interested us[3]. We will not take into account the spin degeneracy which only would multiply the conductances and the noise by a factor 2.

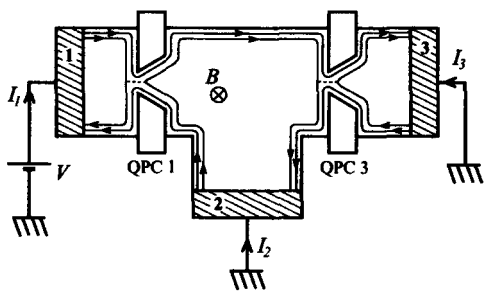


Figure 1: Experimental arrangement of[11]. The two edge states are populated at contact 1. One of those channels is perfectly transmitted the other being partially transmitted at QPC 1. The transmission may be tuned by an applied gate voltage. QPC 3 splits the partially degenerate beam and distributes the current to contacts 2 and 3 where it is measured. Without inter-edge state scattering, the perfectly transmitted channel does not manifest itself on the correlations.

2 Coherent inter-edge state scattering

To describe coherent scattering between edge states we introduce the probability ε that an electron, starting in one of the two channels, is scattered into the other edge state when it travels between the two QPC's. After having constructed the s-matrix, formula (1) gives[3]:

$$S_{23}^{\rm coh} = -\frac{2e^2}{h}|eV|R_3\Big[(1-\varepsilon)^2T_3T_1^2 + \varepsilon^2T_3 + \varepsilon(1-\varepsilon)(1-2R_3T_1+T_1^2)\Big]\,. \tag{3}$$

Let us now discuss two limiting cases. If $\varepsilon = 0$ (no inter-edge state elastic scattering) we fall back to the previous situation (2) since the outer edge state is noiseless. Another interesting

case occurs for $T_3 = 0$ (see figure 3). Then the two edge states are perfectly separated at QPC 3. The first edge state flows towards contact 3 whereas the second goes to contact 2. This situation is particularly interesting since it allows us to study separately the noise spectrum of each edge state after having travelled along the upper edge of the conductor. In the absence of scattering between edge states, the currents remain uncorrelated, whereas if redistribution of charges occurs between edge states, it may induce correlations. For coherent scattering, we find: $S_{23}^{\rm coh} = -\frac{2e^2}{h}|eV|\varepsilon(1-\varepsilon)R_1^2$. The only separation of the beam that can cause correlations occurs along the edge with usual partition factor $\varepsilon(1-\varepsilon)$; the factor R_1^2 ensures that, if the currents in the two channels are noiseless before exchanging carriers along the upper edge, they remain noiseless and uncorrelated.

3 Incoherent inter-edge state scattering

We modelize the presence of incoherent scattering by adding a fictitious contact at the edge along which incoherent scattering is expected to occur [16,1,2]. Let us remark that the only place where it can have some influence on the correlations S_{23} is the edge between the two QPC's where we have introduced it (see figure 2). Since the current is obviously conserved along the edge, we have to impose that the current I_4 through this contact is zero at any time. The consequence is that the potential μ_4 at this probe is fluctuating.

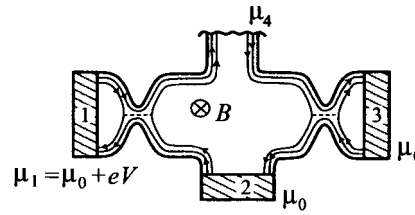


Figure 2: Modelization of phase breaking processes along the upper edge: introduction of a fictitious contact.

We consider two models of incoherent scattering: (*i*) a model of inelastic scattering [16] which is defined by imposing that the total current through the fictitious contact vanishes $I_4 = 0$ and that the average distribution function at this contact is a Fermi distribution. (*ii*) A model of quasi-elastic scattering [1] where not only the total current $I_4 = \int {\rm d}E\, j_4(E)$ vanishes but moreover the contribution to the current of the states of energy E vanishes $j_4(E) = 0$; it follows that the average distribution function at contact 4 is not the equilibrium Fermi distribution.

In both models the fact that I_4 vanishes on average gives information on the average distribution function at the fictitious contact and imposing that the fluctuations vanish also, $\Delta I_4 = 0$, relates the intrinsic fluctuations of the current to the potential fluctuations $\delta\mu_4$.

Finally we obtain the following results (for details on the derivation, see [3]), for the quasi-elastic case:

$$S_{23}^{\rm qe} = -\frac{e^2}{h}|eV|\frac{R_3}{4}\Big[2T_3(1+T_1)^2 + (1+T_3)R_1^2\Big]\,, \tag{4}$$

and for the inelastic case:

$$S_{23}^{\rm in} = -\frac{e^2}{h}|eV|\frac{R_3}{2}\Big[2T_3(1+T_1) - (1+T_3)R_1T_1\Big] \tag{5}$$

leading to the possibility of positive correlations (let us recall that correlations in the presence of coherent scattering only are always negative due to the fermionic nature of carriers [15]). If $T_3 = 0$, we get $S_{23}^{\rm in} = +\frac{e^2}{h}|eV|\frac{R_1T_1}{2}$. This result means that this modelization of inelastic scattering gives the possibility for a fluctuation of the potential μ_4 to inject in a correlated way in the two channels some current.

Note that the occurence of positive correlation $S_{23}^{\rm in}$ might be destroyed by two factors[3]: (i) large transmission T_3, (ii) temperature effects since we should recover at temperature $kT \gg |eV|$ the fluctuation-dissipation theorem.

On table 1 we summarize the various results for the noise correlations obtained for $T_3 = 0$ (see figure 3). To compare the coherent case with the incoherent cases, we set $\varepsilon = 1/2$ since the two models of incoherent scattering equilibrate the current in the two channels.

Nature of scattering	$\tilde{S}_{23}$	$\tilde{S}_{22}$	$\tilde{S}_{33}$
no scattering	0	$2R_1T_1$	0
coherent ($\varepsilon = 1/2$)	$-\frac{R_1^2}{2}$	$\frac{1+T_1}{2}R_1$	$\frac{1+T_1}{2}R_1$
quasi-elastic	$-\frac{R_1^2}{4}$	$\frac{1+3T_1}{2}\frac{R_1}{2}$	$\frac{1+3T_1}{2}\frac{R_1}{2}$
inelastic	$+\frac{R_1T_1}{2}$	$\frac{R_1T_1}{2}$	$\frac{R_1T_1}{2}$

Table 1: Noise and correlation for $T_3 = 0$ depending on the nature of inter-edge state scattering. $S_{\alpha\beta} = \frac{e^2}{h}|eV|\tilde{S}_{\alpha\beta}$.

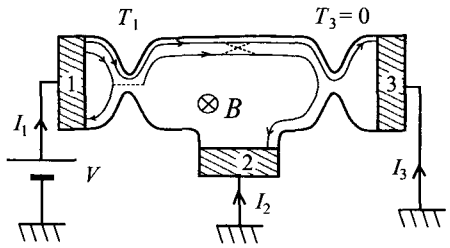


Figure 3: Flow of the average current when $T_3 = 0$.

4 Conclusion

Transport measurements[6,7,8] have provided information on the presence of inter-edge state scattering. Here we have shown that the study of noise correlation may give some information, not only on the existence, but moreover on the nature of inter-edge state scattering: if $T_3 = 0$, in the absence of inter-edge state scattering the correlation S_{23} vanishes, for elastic scattering and for quasi-elastic scattering it is negative and for inelastic scattering it is positive.

Acknowlegments

Interest in the topic of this work was stimulated by a question of B. J. van Wees. We acknowledge Ya. M. Blanter and A. M. Martin for very interesting discussions. This work was supported by the Swiss National Science Foundation and by the TMR Network Dynamics of Nanostructures.

References

1. M. J. M. de Jong and C. W. J. Beenakker, Physica A **230**, 219 (1996).
2. Ya. M. Blanter and M. Büttiker, Phys. Rep. **336**, 1 (2000).
3. C. Texier and M. Büttiker, Phys. Rev. B **62**, 7454 (2000).
4. B. I. Halperin, Phys. Rev. B **25**, 2185 (1982).
5. M. Büttiker, Phys. Rev. B **38**, 9375 (1988).
6. B. J. van Wees *et al.*, Phys. Rev. B **39**, 8066 (1989).
7. S. Komiyama, H. Hirai, S. Sasa, and T. Fujii, Solid State Commun. **73**, 91 (1990).
8. B. W. Alphenaar *et al.*, Phys. Rev. Lett. **64**, 677 (1990).
9. G. Müller *et al.*, Phys. Rev. B **45**, 3932 (1992).
10. M. Henny *et al.*, Science **284**, 296 (1999).
11. S. Oberholzer *et al.*, Physica E **6**, 314 (2000).
12. M. Büttiker, Phys. Rev. Lett. **65**, 2901 (1990).
13. Th. Martin and R. Landauer, Phys. Rev. B **45**, 1742 (1992).
14. W. D. Oliver *et al.*, Science **284**, 299 (1999).
15. M. Büttiker, Phys. Rev. B **46**, 12485 (1992).
16. M. Büttiker, Phys. Rev. B **33**, 3020 (1986).

FRACTIONAL EXCLUSION STATISTICS AND SHOT NOISE IN BALLISTIC CONDUCTORS

G. GOMILA[1,2], L. REGGIANI[2]
[1]*Departament de Física Aplicada, Universitat Politècnica de Catalunya*
Av. Dr. Marañon, 44, E-08028, Barcelona, Spain

[2]*INFM and Dipartimento di Ingengeria dell'Innovazione, Università di Lecce*
Via Arnesano s/n, I-73100, Lecce, Italy

We have studied the noise properties of ballistic conductors with carriers satisfying fractional exclusion statistics. We have found that the noise properties of weakly degenerate systems under current saturation conditions depend upon the statistical parameter g, displaying suppressed shot noise for $1/2 \leq g \leq 1$, and enhanced shot noise for $0 < g < 1/2$, according to the atractive or repulsive nature of the carriers exclusion statistics.

1 Introduction

Exclusons are quasiparticles obeying fractional exclusion statistics (FES). Introduced by Haldane [1] as a phenomenological description of excitations with statistical properties intermediate between fermions and bosons, the concept of **FES** has shown to be applicable to several physical models, like: elementary excitations for strongly correlated particles in one dimension and two dimensions, anyons, and quasi-particle excitations in the fractional quantum Hall effect.

The noise properties of systems of exclusons have received only a minor consideration in the literature. A significative attempt to this subject was presented recently,[2] where a generalization of the first quantized Landauer approach to conductance and noise was proposed for these quasiparticles. The application of the formalism to the case of strongly degenerate systems revealed that the effects of carriers statistics on the noise properties is only appreciated in the transition region between thermal and shot noise. Surprisingly enough, the shot noise suppression factor was found to be independent of the particle statistics. Thus, no evidence of the *attractive* or *repulsive* nature of the different statistics was expected.

The aim of this contribution is to show that the noise properties of ballistic conductors can depend strongly on the statistics of the carriers, thus sedding new light on the attractive or repulsive nature of FES.

2 System under study

We consider a standard two terminal experiment where two reservoirs are adiabatically interconnected by a one-dimensional channel with the following assumptions. (i) The channel is ballistic and perfectly coupled with the reservoirs acting as ideal contacts so that no reflections take place at the interfaces. (ii) Each reservoir is in quasi-equilibrium at a temperature T, and electrochemical potential ϕ. (iii) All the band bending occurs in the channel and the relative position of the conduction band and the electrochemical potential does not change in the contacts, i.e. the chemical potential μ is independent of the applied bias. (iv) The charge of the carriers, q, is taken to be independent of carrier statistics. To include the combined effect of fractional charge and fractional statistics one only needs to substitute q by ge in the final results. (v) The carriers are assumed to form a generalized gas of particles satisfying FES, with an equilibrium distribution function, $f_g(\varepsilon - \mu)$, given by the implicit equation [3]

$$(1 - g f_g(z))^g \, (1 + (1 - g) f_g(z))^{1-g} = f_g(z) e^{\frac{z}{k_B T}}, \tag{1}$$

where ε is the carrier energy and k_B the Boltzmann constant. Here, g is the statistical parameter with the limiting values $g = 1$ and $g = 0$ corresponding to the Fermi-Dirac and Bose-Einstein statistics, respectively.

3 Transport properties

Under the conditions that long range coulomb interaction can be neglected,[4] the average current flowing through a ballistic one dimensional channel can be written as:[2,5]

$$I = (2s+1)\frac{q}{h}\int_0^{+\infty}[f_g(\varepsilon-\mu) - f_g(\varepsilon+qV-\mu)]\,d\varepsilon, \tag{2}$$

where s is the spin factor, h the Planck constant and use is made that $\phi_2 - \phi_1 = qV$. For FES one can integrate the current equation obtaining the $I-V$ characteristics in explicit form as

$$I = I_0 \ln\left(\frac{1+(1-g)f_g(-\mu)}{1-gf_g(-\mu)}\right) - \ln\left(\frac{1+(1-g)f_g(qV-\mu)}{1-gf_g(qV-\mu)}\right). \tag{3}$$

Here, $I_0 = (2s+1)\frac{q}{h}k_BT = G_0\frac{k_BT}{q}$, with $G_0 = (2s+1)\frac{q^2}{h}$. The differential conductance can be easily calculated from the previous expression thus giving[2,5,6]

$$G = \frac{dI}{dV} = G_0\int_0^{+\infty}\left[-f_g'(\varepsilon+qV-\mu)\right]d\varepsilon = G_0 f_g(qV-\mu). \tag{4}$$

At equilibrium one simply has $G^{eq} = G_0 f_g(-\mu)$.

A main feature of the $I-V$ characteristics is the occurrence of current saturation conditions. This current saturation condition appears when: (i) all carriers injected from the contact at higher voltage are collected by the opposite contact and, (ii) all carriers injected from the contact at lower voltage return back to the same contact. Under saturation conditions the current is given by:

$$I_s = (2s+1)\frac{q}{h}\int_0^{+\infty} f(\varepsilon-\mu)d\varepsilon = I_0 \ln\left(\frac{1+(1-g)f_g(-\mu)}{1-gf_g(-\mu)}\right). \tag{5}$$

We anticipate that the current saturation condition plays a determinant role in evidencing the effects of the statistics on the noise properties of the system.

4 Noise properties

In the present structure current fluctuations originate solely from the randomness of carrier injection from the contacts. The carrier injection into the ballistic region must be, of course, consistent with the statistics of the quasi-particles. For the case of contacts at equilibrium, this consistency is satisfied by assuming that the low frequency current spectral density in the energy range $(\varepsilon, \varepsilon+d\varepsilon)$, is given by $s_I(\varepsilon-\mu)d\varepsilon$, with[2,7]

$$s_I(\varepsilon-\mu) = 2G_0k_BT\frac{\partial f_g(\varepsilon-\mu)}{\partial\mu}. \tag{6}$$

The current fluctuations are then computed as:[2]

$$S_I = \int_0^{+\infty}[s_I(\varepsilon-\mu) + s_I(\varepsilon+qV-\mu)]\,d\varepsilon, \tag{7}$$

where we have used that the channel is perfectly ballistic and transmitting and that the effects of the long range Coulomb interaction can be neglected. After substituting Eq.(6) into Eq.(7), one obtains

$$S_I = 2G_0k_BT\,[f_g(-\mu) + f_g(qV-\mu)] = 2k_BT(G^{eq}+G). \tag{8}$$

We note that, independently of carriers statistics, at thermal equilibrium one always has $S_I^{eq} = 4k_BTG^{eq}$,thus recovering Nyquist theorem, as it should be.

Under current saturation conditions one can neglect in Eq.(8) the contribution from one of the contacts and obtain

$$S_I^s = 2G_0k_BTf(-\mu) = \frac{2G_0k_BT}{g + [exp(I_s/I_0) - 1]^{-1}}. \tag{9}$$

Here, in the second equality we have used Eq.(5). The above expression give S_I^s as a function of I_s, q (through G_0 and I_0) and g, and can be used to obtain direct information on the carriers statistics from noise analysis.

A convenient figure of merit for these noise studies is the Fano factor γ defined as $\gamma = S_I/2qI$. For the system under consideration, and under current saturation conditions, the Fano factor reads

$$\gamma_s = \frac{f_g(-\mu)}{\ln\left(\frac{1+(1-g)f_g(-\mu)}{1-gf_g(-\mu)}\right)} = \frac{I_0/I_s}{g + [exp(I_s/I_0) - 1]^{-1}}, \tag{10}$$

where we have used Eqs. (5) and (9).

5 Effects of carriers statistics on the noise properties

Now we are in a position to analyze the effects of the carriers statistics on the noise properties of ballistic conductors. To this end we will consider different degenerancy conditions and restrict ourselves to the current saturation regim.

When the injection of carriers occurs under strongly degenerate conditions (i.e., $\mu/k_BT > 3$, $I_s/I_0 \gg 1$) we obtain from Eqs.(9) and (10):

$$(S_I^s)^{\text{deg}} = 2q\left(\frac{k_BT}{\mu}\right)I_s; \qquad (\gamma_s)^{\text{deg}} = \frac{k_BT}{\mu}. \tag{11}$$

This result correspond to suppressed shot noise, since the Fano factor is always below one. Notice that the Fano factor is independent of the carrier statistics.

Furthermore, under non-degenerate conditions (i.e $\mu/k_BT < -3$, $I_s/I_0 \ll 1$) we can approximate Eqs. (9) and (10) by

$$(S_I^s)^{\text{non-deg}} = 2qI_s; \qquad (\gamma_s)^{\text{non-deg}} = 1, \tag{12}$$

thus recovering full shot noise. This result is a direct consequence of the fact that the distribution function for non-degenerate conditions is the Maxwell-Boltzmann one. In this limit the results are, again, independent of the carriers statistics.

In the transition region between weakly and strongly degenerate conditions (i.e., $|\mu| < 3k_BT$) one must use the full expressions given in Eqs.(9) and (10). Figure 1 reports the Fano factor under current saturation conditions as a function of the chemical potential, as obtained from Eq.(10), with the values of the distribution function being computed from Eq.(1). Here, the Fano factor is found to depend significantly on the carriers statistics. In particular, in the transition region $|\mu| < 3k_BT$ the "attractive" or "repulsive" nature of the exclusion statistics becomes manifest by the fact that the Fano factor takes values larger (for $0 < g < 1/2$) or smaller (for $1/2 \leq g \leq 1$) than one, respectively.

6 Conclusions

We have studied the noise properties of perfect ballistic, one-dimensional channels with carriers satisfying FES. We have found that the attractive or repulsive nature of the carriers statistics can

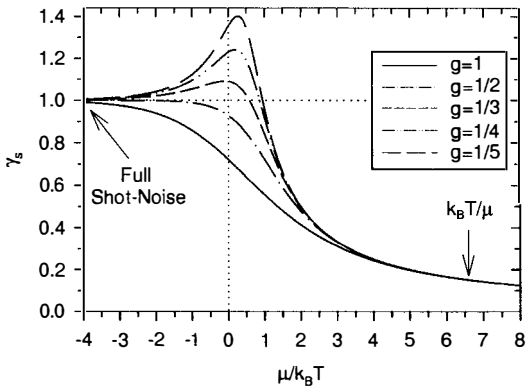


Figure 1: Fano factor of the ballistic conductor under current saturation conditions as a function of the chemical potential for different exclusion statistics.

be really appreciated only in the case of systems which are under weakly degenerate conditions. Then, under current saturation conditions the Fano factor is found to display enhanced shot noise ($\gamma_s > 1$), or suppressed shot noise ($\gamma_s < 1$) depending on whether the statistical parameter is in the range $0 < g < 1/2$, or in the range, $1/2 \leq g \leq 1$, respectively. These results show that for particles with $0 < g < 1/2$ the statistics tends to bunch the carriers, while for particles with $1/2 \leq g \leq 1$ it tends to antibunch them.

In the remaining range of degenerancy we have found that the effects of the statistics on the noise properties are less pronounced. In particular, for both strongly degenerate and non-degenerate conditions the Fano facto is found to be independent on the statistics of the carriers under saturation current conditions. [8]

Acknowledgments

This research has been supported by a Marie Curie Fellowship of the European Community programme Improving Human Research Potential under contract number HPMF-CT-1999-00140, and by the DURSI of the Generalitat de Catalunya.

References

1. F.D.M. Haldane, Phys. Rev. Lett. **67**, 937 (1991).
2. S.B. Isakov, T. Martin and S. Ouvry, Phys. Rev. Lett. **83**, 580 (1999).
3. A. Dasnières de Veigy, S. Ouvry, Phys. Rev. Lett. **72**, 600 (1994); S. Isakov, Mod. Phys. Lett. B **8**, 319 (1994); Y.S. Wu, Phys. Rev. Lett. **73**, 922 (1994).
4. G. Gomila and L. Reggiani, Semicond. Sci. Technol. **15**, 829 (2000).
5. L.G.C. Rego and G. Kirczenow, Phys. Rev. B **59**, 13080 (1999).
6. I.V. Krive and E.R. Mucciolo, Phys. Rev. B **60**, 1429 (1999).
7. A. Greiner, L. Reggiani and T. Kuhn, Physica B **272**, 75 (1999).
8. G. Gomila and L. Reggiani, Phys. Rev. B (scheduled issue 15 April) 2001.

HYBRID STRUCTURES

Observing single electron tunneling events in a superconducting single electron transistor

K. W. Lehnert[1], P. Wahlgren[2], Per Delsing[2], R. J. Schoelkopf[1]
[1] *Yale University, Department of Applied Physics, New Haven CT 06511, USA*

[2] *Department of Microelectronics and Nanoscience, Chalmers University of Technology, Göteborg Sweden*

We measure in real time the addition or subtraction of individual electrons from the island of a superconducting single electron transistor (SSET). By measuring the microwave conductance of an SSET, we are able to observe both the preference for the island to have an even number of quasiparticle excitations and the rate at which the island changes between even and odd numbers of quasiparticles excitations. The microwave measurements have sufficient bandwidth and sensitivity to resolve the individual parity switching events.

1 Introduction

Although the processes which control transport through an SSET occur at gigahertz rates, the SSET is generally probed with only 1 kilohertz of bandwidth. Typically, a long cable connects the high impedance SSET to an amplifier, as the SSET must be cooled to millikelvin temperatures but the amplifier cannot be. The high impedance of the SSET and large cable capacitance act to limit the measurement bandwidth to about 1 kilohertz.

These slow measurements reveal the time average behavior of the SSET and accurately characterize its equilibrium or steady state properties. Inaccessible to these measurements are the dynamics of SSET. In particular, the transport in an SSET is a mixture of Cooper-pair tunneling and quasiparticle tunneling. The existence of occasional quasiparticle tunneling events conceals or poisons the signatures of Cooper-pair tunneling in the time averaged behavior. While the thermodynamics of this quasiparticle poisoning has been studied extensively, little is known about the kinetics [4].

1.1 The RF-SET

This RC-time limitation can be overcome by embedding the SSET in an LC resonant circuit, which acts as an impedance transformer, and measuring the damping of the resonance by the SSET [1]. This is the same circuit that forms the radio-frequency single electron transistor (RF-SET) electrometer (Fig. 1).

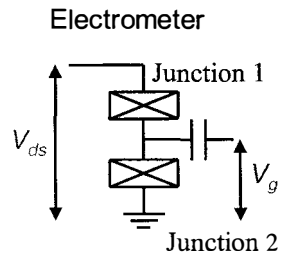


Figure 1: Circuit diagram of the SSET. The SSET is composed of an aluminum island coupled capacitively to a gate with capacitance C_g and through a pair of aluminum oxide tunnel junctions (labeled 1 and 2) to two leads, the drain and source. Current through the SSET flows between the drain and source and is controlled by both the drain-source voltage V_{ds} and the gate voltage V_g.

The SSET is probed by applying a small carrier signal at the circuit's resonance frequency and measuring the amount of the carrier power that is reflected from the resonator. In these experiments the carrier's amplitude is small so that the reflected power is a simply related to the differential conductance of the SSET.

1.2 Parity in an SSET

In the absence of tunneling and quasiparticle excitations, the eigenstates of the SSET island are states of definite Cooper-pair number. The energies of these states form a family of parabolas as a function of V_g (Fig. 2). At special points in gate voltage these parabolic bands cross, indictating that states with different numbers of Cooper-pairs have the same energy. The tunneling of Cooper-pairs across the junctions lifts this degeneracy. At these special points in gate voltage, the supercurrent that flows from source to drain is maximal. The supercurrent is a minimum halfway between a pair of degeneracy points where the electrostatic energy required to add a Cooper-pair is maximal [3].

With the addition of a single quasiparticle to the island, the state of the island is described by a new set of parabolic bands, shifted in gate voltage by one electron and up in energy an amount known as the even-odd free energy difference $\tilde{\Delta}$. For and ideal BCS superconductor

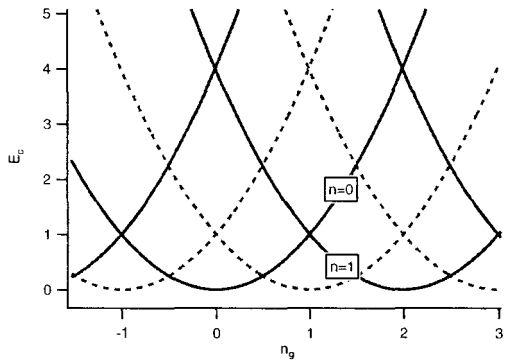


Figure 2: The electrostatic energy of an SSET as a function of $n_g = C_g V_g/e$ and labeled by n, the number of excess Cooper pairs on the island. The solid lines represent even states with no quasiparticle exications, the dashed lines represent odd states with a single quasiparticle on the island. The y-axis scale is in units of E_c, the electrostatic energy required to an additional electron to the island. In this figure $\tilde{\Delta}$ is zero.

at zero temperature $\tilde{\Delta} = \Delta$ the BCS gap parameter. Because the quasiparticle may occupy many states of the island, $\tilde{\Delta}$ is approximately linearly suppressed with increasing temperature reaching zero between 250 and 300 mK, depending on the island's volume. These thermodynamic arguments cannot describe the rate at which the island reaches equilibrium; they do not contain predictions for the kinetics of the island [4].

2 Results

We measure the reflected power from an SSET with source-drain resistance of 30 kΩ and $E_c =$ 91 μeV in a dilution refrigerator cable of achieving temperatures below 20 mK. The SSET is embedded in an LC resonant circuit with resonant frequency of 225 MHz. The sample is held in a light tight box, where all of the dc leads are filtered by passing fine wire through epoxy-impregnated metal powder. The single microwave lead connecting the SSET to a microwave

amplifier at 4 K is filtered with a reflective low pass filter, rejecting above 750 MHz, and coaxial cables which have been modified to be lossy above 10 GHz.

By measuring the reflected power as a function of the V_g and V_{ds} we are able to calibrate V_g in units of electrons on the gate capacitor and V_{ds} in units of E_c/e (See S. L. Pohlen [2] for a description of interpreting these charging diagrams). Here we present data at $V_{ds} = 0$.

Below 250 mK, the average of many measurements of reflected power versus V_g at $V_{ds} = 0$ shows a series of dips one at every integer n_g. We surmise that these dips correspond to the absorption of microwave energy as the carrier repeatedly switches the SSET off of and back onto the superconducting branch of the $I-V$. Power absorbed in each such cycle will be proportional to the critical current I_c^2. Therefore the quantity plotted in figure 3a is proportional to $(1 - I_c)$.

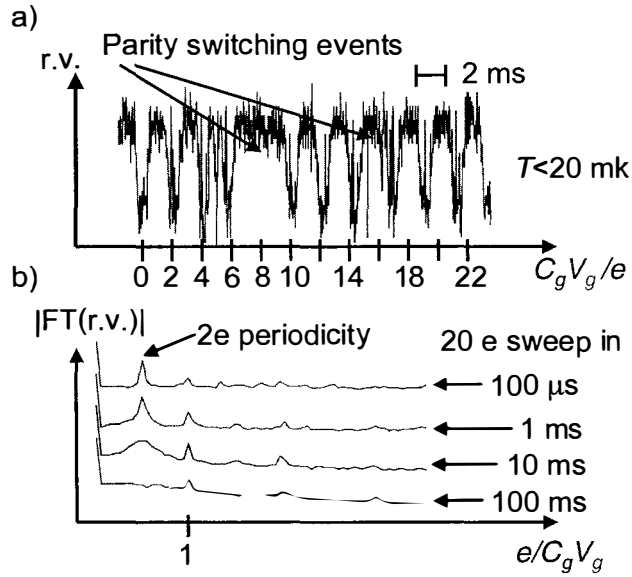


Figure 3: a.) The square root of the reflected power (r.v) as a function of gate voltage. V_g is swept at a rate of 1 e/ms. The predominant pattern corresponding to supercurrent every two electrons is occasionally broken by a parity switching event. Note that the Supercurrent dips on the left side of the trace occur at even integer values of C_gV_g/e, the dips on the right side occur on the odd integers. b.) The average of the power spectra of many 2e sweeps for four different sweep rates. The Y-axis zeros have been shifted. Note the clear transition from 2e-periodicity to e-periodicity at around 10 ms.

In figure 3 the observed supercurrent is periodic in 2e electrons but contains occasional 1e shifts in the 2e periodic pattern. We identify these events with parity changes, the addition or subtraction of a single quasiparticle from the island. Our measurement technique provides sufficient bandwidth and sensitivity to observe these single electron tunneling events as they happen, approximately once every 10 ms (Another group has observed the these slow parity changes in the histograms of switching current distributions [7]).

As the temperature is increased the rate of parity switching changes less than a factor of two until 250 mK. At this temperature the pattern becomes e-periodic for even the fastest sweep rate in figure 3c. The dips in reflected power occur not at the integer values of n_g but at half integer values, indicating that the SSET island changes its parity before the gate can be swept to the true degeneracy point(Fig. 2). The fastest gate sweep rate used, 0.2 e/μs, therefore sets

a upper limit on the parity switching time of 2.5 μs.

3 Discussion

Our SSET never displayed any preference for even parity states over odd parity states at zero source-drain bias. The thermodynamic arguments [4] can fail either because some rare process, probably photons with energy greater than 2Δ, occasionally break Cooper-pairs [5], or the island of the superconductor does not have a perfect BCS density of states [6]. Nonetheless, below 250 mK the 2e-periodic supercurrent is concealed by interleaving two different 2e-periodic patterns shifted by 1e at a rate slow compared to the bandwidth of our measurements. This is consistent with a picture of parity changes arising from rare events, either the breaking of Cooper-pairs, or the occupation of some discrete state in the BCS gap. If these rare events are still more frequent than the SSET island's spontaneous return to its parity ground state, the island will spend as much time in the odd as the even parity states.

Above 250 mK the rate of parity switching increases at least 2500 times. At a temperature around 250 mK, depending on the islands volume, an the SSET island will have on average one thermally excited quasiparticle [4], implying that $\tilde{\Delta} = 0$. One can estimate the time for a single quasiparticle to leave the 250 mK SSET island as a time between 0.1 and 1 μs [5], consistent with our observed upper limit.

4 Conclusion

We have measured the microwave reflectance of an SSET configured as an RF-SET. When we study the SSET over times less than 10 ms the SSET has 2e-periodic supercurrent. At temperatures below 250 mK, we are able observe individual parity switching events that correspond to single electron tunneling events. Above 250 ms we show that the rate is at least once per 2 μs. These results are the direct observation of the processes that were believed to destroy 2e periodicity in time averaged measurements of SSET's [5]. They also demonstrate fast charge measurements, vital to charge based quantum computing proposals.

Acknowledgments

The authors acknowledge many useful discussions with M. H. Devoret. This work was supported in part by the National Security Agency (NSA) and Advanced Research and Development Activity (ARDA) under Army Research Office (ARO) contract number DAAD19-99-1-0346.

References

1. R. J. Schoelkopf *et al.*, Science **280**, 1238 (1998).
2. S. L. Pohlen, The Superconducting Single Electron Transistor, Ph.D. disseration, Harvard University, (1999).
3. P. Joyez, Le Transistor a une Paire de Cooper: un Systeme Quantique Macroscopique, Ph.D. disseration, University of Paris, (1995).
4. M. T. Tuominen *et al.*, *Phys. Rev. Lett.* **69**, 1997 (1992).
5. J. M. Hergenrother *et al.*, *Phys. Rev. Lett.* **72**, 1742 (1994a). J. M. Hergenrother, Parity Effect and Charge Transport in the Single-Electron Transistor, Ph.D. dissertation, Harvard University, (1995).
6. P. Lafarge *et al.*, *Phys. Rev. Lett.* **70**, 994 (1993).
7. V. Bouchiat, Quantum fluctuations of the charge in single electron and single Cooper pair devices, Ph.D. disseration, University of Paris, (1997).

DOUBLED SHOT NOISE IN HYBRID NS JUNCTIONS

X. Jehl[1], M. Sanquer[1], R. Calemczuk[1] and D. Mailly[2]
[1] *DRFMC-SPSMS, CEA-Grenoble, F-38054 Grenoble cedex 9, France*

[1] *Laboratoire de Photonique et de Nanostructures, CNRS-LPN, F-92225 Bagneux, France*

Abstract

We measured the current fluctuations in short normal-metal/superconductor junctions, and observed the predicted doubled shot noise at voltages below the superconducting gap due to the effective charge $2e$ transferred by the Andreev reflection processes. The data show a very good agreement with the semiclassical theory on all the bias range, demonstrating that doubling is insensitive to phase coherence.

1 Introduction

In hybrid junctions between a normal metal (N) and a superconductor (S), the energy gap Δ in the excitation spectrum of the superconductor forbids transport of unpaired electrons at low voltages V. Although the proximity-induced superconductivity in an NS bilayer is known since more than 30 years [1], the detailed treatment of mesoscopic NS contacts is more recent. In a pioneering work on ballistic NS constrictions, Khlus [2] recognized how the shot noise is modified both by the Andreev reflection at the S interface and by the Pauli exclusion principe in the N electrode. The Andreev process describes the retroreflection of an incident electron as a hole at the NS boundary, and the subsequent transmission of a Cooper pair in the superconducting condensate at the Fermi energy E_F. This second order process therefore transfers elementary charge bundles of $2e$ (e is the charge of the electron). The shot noise, which is sensitive to the charge of the carriers, is therefore doubled in NS junctions.

NS interfaces can be implemented in various kinds of samples. Beyond the simplest case of a single NS contact, SNS and multi-terminal geometries have been studied. In SNS the transport can be dramatically modified by the Josephson coupling and the Multiple Andreev Reflections (MAR) between the superconducting reservoirs. Long SNS structures can behave like two NS junctions incoherently coupled and exhibit enhanced shot noise due to incoherent MAR as well as shot noise reduction due to electron interaction [3]. In the other limit of a very short N region, MAR are coherent. The divergence of the effective charge at low voltages has been observed [4], and recently the increase of the transmitted charge versus voltage has been monitored in superconducting atomic point contacts [5].

The doubling of shot noise in diffusive NS junction was first predicted in the phase coherent transport framework, using a scattering approach [6] (valid only at zero temperature) and a wave packet approach [7]. These predictions only describe the low voltage regime. Recently Nagaev and Büttiker gave a semiclassical description of the diffusive NS junction which recovers the coherent transport results at low voltages but extends up to voltages above the gap [8]. Here we compare these theories to our experimental data.

2 Theory

2.1 Phase coherent transport

We first recall some basic results for a coherent normal conductor characterized by a scattering matrix $\mathbf{t}$. The Landauer formula gives the 2-wire conductance G_N (including the contact resistance [9]) at zero temperature and small applied voltage:

$$G_N = G_0 \mathrm{Tr}(\mathbf{t}\mathbf{t}^+) = G_0 \sum_{n=1}^{N} T_n \qquad (1)$$

where $G_0 = \frac{2e^2}{h}$ and T_n ($n = 1..N$) are the transmission coefficients. The expression for the low frequency shot noise power P_N reads [10,11]:

$$P_N = 2e|V|G_0 \sum_{n=1}^{N} T_n(1 - T_n) \tag{2}$$

From this equation, channels perfectly transmitting or reflecting give no contribution to the shot noise, as expected from the Pauli principle (the occupation number of such states does not fluctuate). This feature has been verified in quantum point contacts in a two-dimensionnal electron gas [12,13].

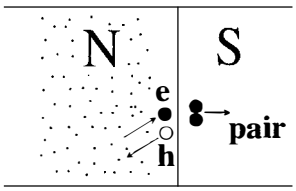
In a disordered normal metal the distribution of the T_n is not uniform but bimodal: most channels are nearly open or closed [14]. With this particular distribution the shot noise is reduced [15] by a factor $\frac{1}{3}$ below its Poisson value $2eI$: $P_N = \frac{1}{3}2eI$. This factor has been observed experimentally [16,17].

If one electrode is superconducting, equations 1 and 2 become ($T, V = 0$):

$$G_{NS} = 2G_0 \sum_{n=1}^{N} \frac{{T_n}^2}{(2 - T_n)^2} \tag{3}$$

$$P_{NS} = 2e|V|G_0 \sum_{n=1} N \frac{16{T_n}^2(1 - T_n)}{(2 - T_n)^4} \tag{4}$$

The conductance is no longer a linear function of the T_n, but due to the bimodal distribution, one obtains $< G_{NS} >=< G_N >$. This striking property was observed as a "reentrance" of the resistance of NS samples at very low temperature: below an energy related to the Thouless energy the resistance increases as temperature is lowered [18]. This effect is strongly related to the diffusive nature of the normal region: a ballistic NS contact will instead exhibit a doubling of its conductance [19].



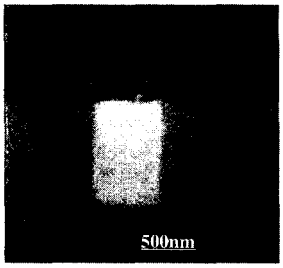


Figure 1: **(a)** Model for a diffusive NS junction of length L. The disordered region of length L and the NS interface are spatially separated. **(b)** Scanning electron microscope image of the sample showing the superconducting niobium (Nb) and normal copper (Cu) reservoirs with a Cu finger overlapping the Nb defining the junction.

Now when the bimodal distribution of the T_n for diffusive systems is used with equation 4, one gets both the $\frac{1}{3}$ due to the disorder and a doubling interpreted as a doubled charge $2e$ transferred by each Andreev reflection process:

$$P_{NS} = 2 \times (\frac{1}{3}2eI) \tag{5}$$

Electron interactions, with other electrons or with phonons, cannot be included in this appoach. Also the role of phase coherence is unclear; the same diffusive $\frac{1}{3}$ factor was obtained by a semiclassical approach neglecting coherence [20].

2.2 Semiclassical approach

The semiclassical approach ignores the phase of the electron wavefunction and allows to treat the case of strong electron-electron and electron-phonon interactions. Therefore its predictions for diffusive metals are valid over a larger range of temperature and length.

First the distribution function $f(x)$ (which connects the two Fermi-Dirac equilibrium functions of the two reservoirs shifted by eV) along the wire is calculated. The Langevin method on the Boltzmann equation provides an expression for the shot noise based on $f(x)$:

$$P = \frac{4}{LR} \int f(x;E)(1 - f(x;E))dxdE \qquad (6)$$

For a normal diffusive conductor in absence of inelastic interactions the same factor $\frac{1}{3}$ is found than with the coherent transport [20]. In presence of electron-electron interaction an increase over the $\frac{1}{3}$ factor is found: the shot noise reaches $\frac{\sqrt{3}}{4} 2eI$. In terms of an effective electron temperature this is interpreted as an overheating of the electron bath and has been studied experimentally [16,17]. When electron-phonon interaction is strong the electrons can efficiently release their energy by emitting phonons and stay at the temperature fixed by the reservoirs. In this regime, which corresponds to which of a macroscopic resistor, the shot noise vanishes.

Recently Nagaev and Büttiker extended the semiclassical approach to the diffusive NS case. The distribution function of the carriers is carefully computed and used with equation 6 to obtain [8]:

$$\begin{aligned} P_{NS} &= 4\frac{kT}{R}\left\{\frac{2}{3} + \frac{1}{3}\frac{eV}{kT}\coth\left(\frac{eV}{kT}\right) + \frac{1}{6}\left[\tanh\left(\frac{\Delta + eV}{2kT}\right) + \tanh\left(\frac{\Delta - eV}{2kT}\right) - 2\tanh\left(\frac{\Delta}{2kT}\right)\right]\right. \\ &+ \left.\frac{1}{6}\left[\coth\left(\frac{eV}{2kT}\right) - 2\coth\left(\frac{eV}{kT}\right)\right]\ln\left[\frac{\exp(\Delta/kT) + \exp(eV/kT)}{\exp(\Delta/kT) + \exp(-eV/kT)}\right]\right\} \end{aligned} \qquad (7)$$

This expression reduces for $T = 0$ and $V \neq 0$ to:

$$P_{NS} = \frac{4}{3}\frac{e|V|}{R} + \frac{2}{3}\theta(e|V| - \Delta)\frac{\Delta - e|v|}{R} \qquad (8)$$

For voltages below Δ the shot noise is doubled. This extends the coherent predictions to regimes where phase coherence is destroyed. Also, because heat transport through an NS interface is very inefficient [21], only the normal reservoir can heat sink the electron gas and the interacting electron shot noise is also doubled. Above Δ the shot noise recovers the value for a normal contact with a voltage independent excess noise. This equation permits a direct comparison with experimental data over the whole bias range and with no adjustable parameter since both the gap Δ and the $I(V)$ characteristics can be recorded independently.

3 Experimental data

3.1 Sample and transport characterization

The experimental detection of doubled shot noise in diffusive NS junction was obtained independently and simulteanously by our group [22] and Kozhevnikov at al.[23] who measured the high frequency regime of the shot noise, in the GHz range. The Andreev reflection being a two-particle process, the subgap current through a NS contact is proportionnal to the square of the barrier transmission. In order to get a sizeable current a very clean interface is necessary. The samples were niobium (S) and copper (N) contacts made by electron beam lithography at CNRS-LPN. The Nb electrode is defined by SF_6 reactive ion etching on a $500\,nm$ thick Nb film through an Al mask, which is subsequently removed. The $100\,nm$ thick Cu electrode is Joule evaporated and lift-off leaves a 800×500 Cu finger on the top of the niobium (fig. 1). The good transparency is obtained by a $500\,V$ argon etching of the niobium just before the copper deposition. The Nb film is superconducting below $8.3\,K$ and the Cu film has a sheet resistance $R_\square = 0.15\,\Omega$ at T$= 1.4\,K$, resulting in a diffusion constant $D \simeq 2 \times 10^{-2}\,m^2 s^{-1}$ or an elastic scattering length $\ell \simeq 40\,nm$. Conductance measurements were performed down to very low temperatures to characterize the junctions. The differential resistance (fig. 2a) displays oscillations above the critical current and a dip around zero voltage. This dip is a signature of the good NS interface: superconductivity is induced by the niobium into the copper, resulting in a lower resistance at zero voltage. At $1.35\,K$ a $0.6\,mV$ voltage destroys this effect, and the differential resistance reaches a plateau before

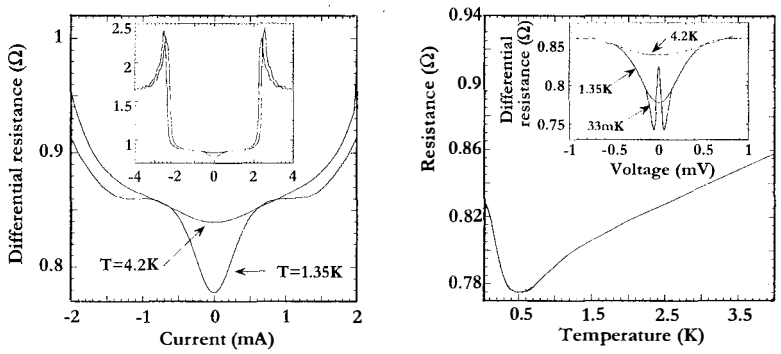


Figure 2: (a) Differential resistance dV/dI in ohms as a function of the mean bias current I in mA, at T = 4.2 and 1.35 K. When lowering the temperature the superconductivity induced in copper is enhanced at low voltage; this results in a dip around zero bias, indicating that the NS interface is excellent. Inset: above the critical current of $\approx 2.4\,mA$ the Nb film switches into the normal state. (b) Resistance versus temperature : at T = 0.5 K the resistance reaches a minimum and increases again at lower temperature. Inset shows another signature of this re-entrance effect : at very low temperature (33 mK) a peak appears in the differential resistance at a finite voltage V_0 where $eV_0 \simeq k_B T_0$, which is superimposed on the resistance dip due to the proximity effect.

increasing irreversibly up to the critical current (fig. 2a). The resistance versus temperature is presented in figure 2b. Its value in the kelvin range is about 0.8 Ω, and decreases with decreasing temperature following the $\delta R \propto T^{-\frac{1}{2}}$ prediction for the standard proximity effect. Below $T_0 = 0.55\,K$ this behaviour changes to a sharp increase as the temperature decreases (fig. 2b). This corresponds to the previously introduced reentrance effect, which predicts that at zero temperature the conductance of N and NS disordered contacts are equal. The reentrance is observed down to $33\,mK$. In the differential resistance it appears as a peak superimposed to the bottom of the dip (fig. 2). T_0 is related to the diffusion time τ_D of the quasiparticles in the sample: $k_B T_0 \approx \hbar/\tau_D$. From $T_0 = 550\,mK$ we deduce $\tau_D = 14\,ps$ comparable to the actual size of our sample. Previous measurements of the Fermi distribution function in copper wires[24] have shown that electrons in a $1.5\,\mu m$ long wire, with a diffusion time of $350\,ps$, are in the non-interacting regime for an applied voltage $V = 0.2\,mV$. In our sample, τ_D is indeed much smaller than any estimate of τ_{ee}, thus ensuring that even for the largest bias currents the carriers diffusing through the junction are out of equilibrium. For 2D films, $\hbar/\tau_{ee} = (e^2/h) k_B T R_\square \ln(h/2e^2 R_\square)$[25]. This gives $\tau_{ee} \simeq 100\,ns$ for T = 1K. In $45\,nm$ thick copper films, a typical energy relaxation time is $1\,ns$ (T=1K)[26].

3.2 Noise measurements

The low resistance inherent to a short NS contact is not adapted to the usual noise measurement scheme, consisting in voltage noise measurements by two independent low noise amplifiers and computation of the cross correlation. For higher resistances several samples can be put in series, but for a sub-ohmic resistance, a direct measurement of the current noise is the preferred choice. The thermal noise of 0.8 Ω at 1 K is of the order of $10\,pA/\sqrt{Hz}$. The total noise resulting from this thermal noise plus the full Poisson shot noise with a bias current of 1.5 mA is roughly $20\,pA/\sqrt{Hz}$. This picoamp sensitivity is reached with a dc-SQUID operating at $T = 4.2\,K$. Getting away from the thermal regime at about 1 K in such low resistors requires the use of quite high bias currents, in the mA range. For this purpose a resistance bridge probed by the SQUID has been developped[27].

The noise data are presented in figures 3 and 4. Together with the data we plot 3 different fits. Two of them correspond to a single ($e^* = e$) and double ($e^* = 2e$) charge shot noise on

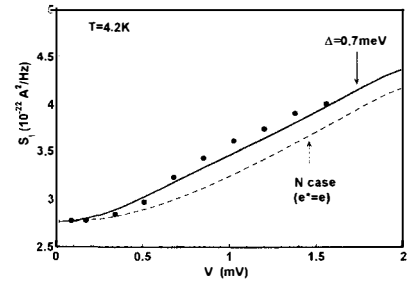


Figure 3: Shot noise at 4.2 K compared to the semiclassical theory with $\Delta = 0.7\,meV$ (solid line), and to the noise of a normal contact (dashed line). The measured noise lies in between the normal and doubled values, as qualitatively expected in the high temperature regime where kT is not negligible compared to Δ.

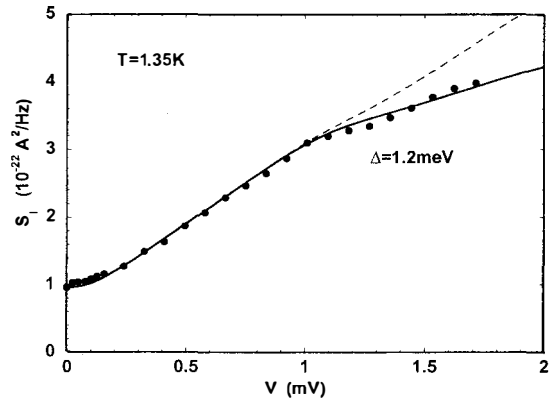


Figure 4: Shot noise measurements (dots) in an NS (Cu-Nb) junction compared to the predictions (solid line) from the semiclassical theory with the superconducting gap Δ as only parameter. For $V < \Delta$ the predicted doubled shot noise is confirmed experimentally. The dashed line simulates a doubled shot noise above Δ to quantitatively emphasize the difference with the normal case. For $V > \Delta$ an excellent quantitative agreement with the theory is found for the first time.

all the bias range added to the thermal noise:

$$P_{NS} = \frac{2}{3}\left[\frac{4k_B\mathrm{T}}{R_d} + e^{\star} I \coth\left(\frac{e^{\star}V}{2k_B\mathrm{T}}\right)\right] \tag{9}$$

This formula contains no free parameters apart from the charge of the carriers $e^{\star}$. The values of I, V and $R_d = dV/dI$ are taken from the data shown in figure 2. This formula is strictly established for $e^{\star} = e$, and might in principle change for $e^{\star} = 2e$, but in a single channel case the exact calculation results only in a small correction [7]. As expected, both at 4.2 and 1.35 K the experimental noise is greater than the single charge noise, because the superconducting reservoir enhances the effective transmitted charge. Also one can note that at 1.35 K and above a bias current 1.2 mA the slope of the data is similar to the $\frac{1}{3} \times 2e$ slope of a normal diffusive contact. The prediction for $e^{\star} = 2e$ in equation 9 is in very good agreement with the measured noise at 1.35 K, confirming the predicted doubled shot noise [22]. Moreover the exact doubling is observed on a larger range than the validity range of the phase coherent theories. From the reentrance measurements it is clear that phase coherence is destroyed above $I_\phi \approx 0.5\,mV$, though doubling is observed up to 1.2 mA. This experimental suggestion that the doubling doesn't require phase coherence has been confirmed by comparison with the semiclassical theory [28].

The fit from the semiclassical theory (equation 7) is in very good agreement with our data on all the bias range, with no free parameter. The value for the gap 1.2 meV is very closed to the measured value in similar films. At 4.2 K one can try to fit the data with a reasonnable gap value of 0.7 meV, but because at $\Delta \approx 2k_BT$, in this high temperature regime electron-like excitations might be involved in the transport, violating the basic assumption that only Andreev reflections can account for the transport at $V < \Delta$. In that case one expects an effective charge between e and $2e$, and a noise between the doubled and normal case, in accordance with the data [22]. A quantitative comparison between the data at 4.2 K and the semiclassical theory cannot yield definitive conclusions because it takes place in the high temperature regime where $kT \approx \Delta$.

4 Conclusion

We have shown with low frequency current noise measurements that the current noise in a short diffusive NS junction at temperatures well below the superconducting critical temperature corresponds to the shot noise from carriers with twice the fundamental electron charge. The doubling of the charge in NS junctions enlightens a subtile aspect of proximity induced superconductivity: while the zero temperature conductance of the junction does not depend on whether the emitter is superconducting or not [29], the shot noise is doubled. The excellent agreement with the semiclassical theory for doubled shot noise up to the gap confirms that phase coherence is not necessary to observe the effect. Above the gap the shot noise is found to recover the value for a normal contact with a voltage-independent excess noise, in quantitative agreement with the theory.

References

1. G. Deutscher & P.G. deGennes in *Superconductivity*, ed. R.D. Parks (Dekker, 1969).
2. V.A. Khlus, Sov. Phys. JETP **66**, 1243 (1987).
3. C. Hoffmann *et al.*, this volume.
4. P. Dieleman, *et al.*, Phys. Rev. Lett. **79**, 3486-3489 (1997).
5. R. Cron *et al.*, Phys. Rev. Lett. **86**, 4104 (2001).
6. M. J. M. deJong & C. W. J. Beenakker, Phys. Rev. B **49**, 16070 (1994).
7. T. Martin, Phys. Lett. A **220**, 137 (1996).
8. K. E Nagaev & M. Büttiker, Phys. Rev. B **63**, 81301 (2001).
9. R. de Picciotto *et al.*, Nature **411**, 51 (2001).
10. G. B. Lesovik, JETP Letters **49**, 593, (1989).
11. M. Büttiker, Phys. Rev. Lett. **65**, 2901 (1990).
12. M. Reznikov *et al.*, Phys. Rev. Lett. **75**, 3340 (1995).
13. A. Kumar *et al.*, Phys. Rev. Lett. **76**, 2778 (1996).
14. O. N. Dorokhov, Sol. Stat. Comm. **51**, 381 (1984).
15. C. W. J. Beenakker & M. Büttiker, Phys. Rev. B **46**, 1889 (1992).
16. A. H. Steinbach *et al.*, *Phys. Rev. Lett.* **76**, 3806-3809 (1996).
17. M. Henny *et al.*, *Phys. Rev. B* **59**, 2871-2880 (1999).
18. B. Pannetier & H. Courtois, J. Low Temp. Phys. **118**, 599 (2000).
19. G. E. Blonder *et al.*, Phys. Rev. B **25**, 4515 (1982).
20. K. E. Nagaev, Phys. Lett. A **169**, 103 (1992).
21. A. F. Andreev, *Sov. Phys. JETP* **19**, 1228-1231 (1964).
22. X. Jehl *et al.*, Nature **405**, 50 (2000).
23. A.A. Kozhevnikov *et al.*, J. Low Temp. Phys. **118**, 671 (2000).
24. H. Pothier *et al.*, Phys. Rev. Lett. **79** , 3490-3493 (1997).
25. B. L. Altshuler & A. G. Aronov in *Electron-Electron Interaction in Disordered Systems* (eds Efros, A. L. & Pollak, M., North-Holland, Amsterdam, 1985).
26. A.B. Gougam *et al.*, J. Low Temp. Phys. **118**, 447 (2000).
27. X. Jehl *et al.*, Rev. Sci. Inst. **70**, 2711-2714 (1999).
28. X. Jehl & M. Sanquer, Phys. Rev. B **63**, 52511 (2001).
29. S. N. Artemenko *et al.*, Sol. Stat. Comm. **30**, 771 (1979).

SUBHARMONIC SHAPIRO STEPS IN A MESOSCOPIC S-N-S JUNCTION

P. Dubos, O. Buisson, H. Courtois and B. Pannetier
Centre de Recherches sur les Très Basses Températures, C.N.R.S.,
associé à l'Université Joseph Fourier,
25, Av. des Martyrs, 38042 Grenoble, France

We report on microwave irradiation experiments on high quality niobium-copper-niobium mesoscopic junctions at high temperatures when the *d.c.* Josephson coupling is strongly suppressed. The physical parameters correspond to the long junction limit where the Thouless energy ϵ_c is much smaller than the superconducting gap. Experiments are performed under low voltage conditions $eV \approx \hbar\Omega < \epsilon_c < k_BT$. We observe, in addition to the ordinary Shapiro steps, a series of subharmonic steps which persist at the highest temperatures.

Josephson effect arises when two superconducting bodies are weakly coupled. In the generic superconductor-insulator-superconductor (S-I-S) junction orginally considered by Josephson[1], the coupling is due to the tunneling of Cooper pairs through a thin dielectric barrier with thickness in the nanometer range. In the case of a superconductor - normal metal - superconductor (S-N-S) junction [2], the coherent transfer of Cooper pairs is possible through a micrometer size metallic coupling region. The Andreev reflection at the superconductor metal interfaces and the phase-coherent transport in the normal metal are two important ingredients of this proximity effect.

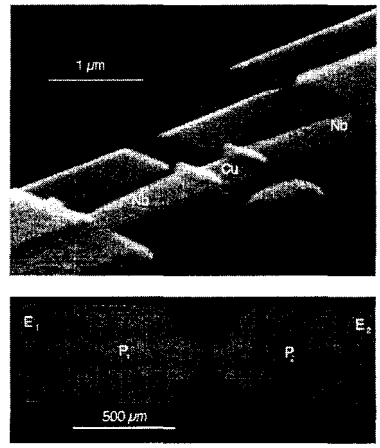


Figure 1: Top : Scanning electron micrograph of the niobium-cooper-niobium junction (oblique view). The length and width of the copper island are respectively $0.8\mu m$ and $0.53\mu m$. Bottom : Large scale view of the contact pads. The outer electrodes designed for injection of the microwave current are capacitively coupled to the inner electrodes. The SNS junction, located at the center is not visible at this scale.

In this report we consider long diffusive junctions where the length L of the normal metal is such that the diffusion time $\tau_D = L^2/D$ exceeds the microscopic characteristic time $\hbar/\Delta$ of the superconducting state. Here D is the normal metal diffusion length and Δ the superconducting gap of the electrodes. In this regime, the characteristic energy scale is not the superconducting gap but the smaller Thouless energy $\epsilon_c = \hbar/\tau_D$, controlled by the diffusion time of single electrons across the normal metal. We have investigated the *a.c.* Josephson effect by probing the response of a S-N-S junction to a microwave excitation. The length L of the normal metal is smaller than the phase memory length L_ϕ. The main result is the observation of subharmonic Shapiro steps

at low microwave frequency in the phase-coherent regime $eV < \epsilon_c$. This observation strongly suggests that the *a.c.* Josephson effect can persist at high temperature in mesocopic diffusive SNS junctions. The corresponding *a.c.* coupling mechanism thus differs from the *d.c.* coupling.

The response of a superconducting junction to a microwave excitation is a well known test for the Josephson coupling. Shapiro steps result from the locking of the Josephson oscillation to the external microwave frequency Ω. In standard S-I-S junctions, the Shapiro steps appear in the current voltage characteristics as a serie of well-defined plateaus at voltages given by the relation $V = \hbar\Omega/2e$ and its multiples[3]. The step amplitudes are well characterized in terms of simple Bessel function of the microwave amplitude. In addition to these so-called integer steps, subharmonic steps can also take place in some special situations : i) In junctions having a non-sinusoidal current-phase relationship, the finite amplitude harmonics $\sin m\phi$ give rise to a locking at fractions Ω/m of the microwave frequency. Such a situation can be expected in long superconducting bridges[2,4] and in ballistic contacts[5]; ii) In underdamped Josephson junctions a transition to chaos has been considered at large microwave amplitude[6]. This situation, met in low-dissipative junctions in which the junction capacity is dominant, is analogous to the problem of the *a.c.* driven pendulum. A very rich structure also attributed to subharmonic mode locking was observed in charge density wave materials under radiofrequency irradiation[7].

The present work deals with overdamped single S-N-S junctions (class i) where the current-phase relationship is expected to be purely sinusoidal in the temperature range of the experiments. Accordingly, our observation of subharmonic structures is totally unexpected.

We fabricated niobium-copper-niobium junctions (see Fig.1) with the following choice of sample parameters and experimental conditions :

- diffusive normal metal. The mean free path is much smaller than the normal metal length. The corresponding diffusion coefficient of the measured sample is D =230 cm^2/sec.
- high transparency superconducting normal interfaces. This was achieved by in-situ preparation of the samples in a UHV chamber using shadow evaporation with thermostable stencil masks[9].
- long junction regime : The choice of superconducting niobium electrodes ($\Delta = 1300\ \mu eV$) and their separation $L \approx 0.8\mu m$ ensure the condition $\epsilon_c \ll \Delta$. For the measured sample, $\epsilon_c = 24\mu eV$.
- coherent regime : The experiments were restricted to very low voltages $eV < \epsilon_c$. For electrons within ϵ_c of the Fermi energy, the dynamic phase acquired during diffusion accross the normal metal is small, thus insuring long range coherence[10].
- non-equilibrium electrons in the normal metal : Because of the absence of normal reservoir and as result of the Andreev reflection, the copper island is a "closed" system which traps the subgap electrons. The electron distribution can only relax *via* inelastic processes.
- Negligible thermal fluctuations at all operating temperatures. This was achieved by using a large junction conductance, *i.e.* wide normal bridge. Sample resistance was 0.17 Ω.

We measured the differential resistance *vs* *d.c.* bias current in presence of a low amplitude microwave irradiation. The microwave current was injected through the capacitor formed by the gap between specially designed contact pads as shown in Fig. 1, lower part. Fig. 2 left shows the current-voltage characteristics at moderate microwave power ($-10\ dBm$), frequency $4\ GHz$ and temperature $T = 4K$. One observes the integer Shapiro steps corresponding exactly to the locking at the Josephson frequency $V = \hbar\Omega/2e$ and its first harmonic. In addition, one also observes steps 1/2 and 3/2. Subharmonic steps at higher order fractions $n\hbar\Omega/2me$ (not shown) were also observed on the differential resistance curves[11] up to $m = 6$. Fig. 2 right shows

the differential resistance *vs* voltage at microwave frequency 6 GHz and low power -20 dBm. Apart from the main dip labelled 1 one can observe the dips at 1/2 and 1/3 of the fundamental step voltage. Because of the high temperature and the small microwave amplitude the dips do not reach the zero resistance value. The smeared shape of the dips can be fitted in the vicinity of the steps with a RSJ model with thermal broadening[2]. From a detailed analysis[11] of the -20 dBm data we could determine both the ac microwave amplitude and the step amplitude. We found a microwave current $I_{ac} \approx 10\mu A$, i.e. about one tenth of the bias current.

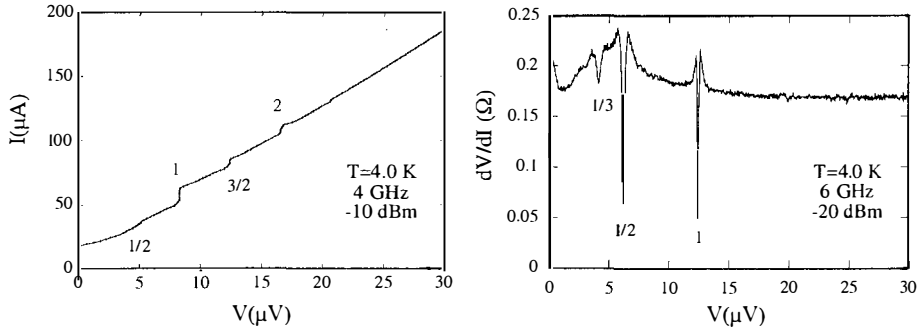


Figure 2: Left : Current voltage characteristics at $4K$ in presence of a moderate (-10 dBm) microwave power at frequency 4 GHz. Integer Shapiro steps (1 and 2) appear at voltages 8.28 and 16.56 μV. Subharmonic steps are also visible with smaller amplitudes. Right : Differential resistance *vs* current bias at 4 K in presence of a low power microwave excitation at frequency 6 GHz. In addition to the integer step (dip at 12.42 μeV), subharmonic steps as indicated by the dips at 1/2 and 1/3, are clearly visible at 6.21 and 4.18 μV

As shown in Fig. 3, the amplitude of the step 1 (labelled $Ic_{eff,1}$) is suppressed as the temperature increases[12] and follows the same temperature dependence as that of the *d.c* critical current I_c. This behavior agrees with the standard theoretical predictions. At 4 K the 1 and 1/2 dips have similar amplitudes. At 6 K the 1/2 step exceeds the fundamental Shapiro step by about one order of magnitude. While the integer steps can be well understood in terms of the ordinary Josephson coupling[3], the very existence and the behaviour of the subharmonic steps are new and surprising. As mentioned above, a non-sinusoidal current-phase relationship can be expected in a long diffusive S-N-S junction at very low temperature[4]. The presence of harmonics $\sin n\chi$ could therefore give rise to $1/n$ steps at low temperature. However, it can be shown that, in long junctions, the weight of the harmonic terms is rapidly suppressed as the temperature is increased[9]. For example, when $k_BT > 5\epsilon_c$ ($2K$ in our samples) the second harmonic contributes to less than 2% of the total current. Therefore, our observations which are performed at $T > 2.5K$ cannot be explained by the *d.c.* current-phase relationship.

Our results are supported by similar observation recently reported by K. Lehnert et *al.*[14] in a different system. These authors observed the 1/2 Shapiro step at high temperature in a InAs-based hybrid structure. Although the latter experiment was carried out in the clean limit, as opposed to the diffusive metallic regime of our experiment, it also reveals some novel aspect of the Josephson coupling in long junctions. The Josephson coupling with a $\sin 2\chi$ current phase relationship was considered by N. Argaman[15] in a phenomenological model involving the dynamic non-equilibrium electron distribution. This model accounts qualitatively for the existence of the 1/2 step and its slow decay at high temperature and could presumably account for the other subharmonic steps observed in the present work. However, the relaxation time approximation of this phenomenological model may occult some important physical aspects of the dynamics of the quantum transport in the normal metal island.

In particular, the connection between the $\sin n\chi$ term and coherent multiple Andreev reflec-

tion (MAR) is still missing. It is worth noticing that the key ingredients of our observation are the high transparency of the N-S barrier and the smallness of the electron characteristic energies ($eV \approx \hbar\Omega \leq \epsilon_c$). Both provide favorable conditions for the occurrence of coherent multiple Andreev reflections. In contrast to the standard signatures of MAR at energies $eV = \Delta/n$ in the I-V characteristics, here the relevant energy scale is the microwave photon energy $\hbar\Omega$. This energy is two orders of magnitude smaller than the superconducting energy gap and falls within the Thouless coherent energy window of the proximity effect[10]. Our observations can therefore be viewed as a signature of the coherent transfer of multiple charges accross the normal metal.

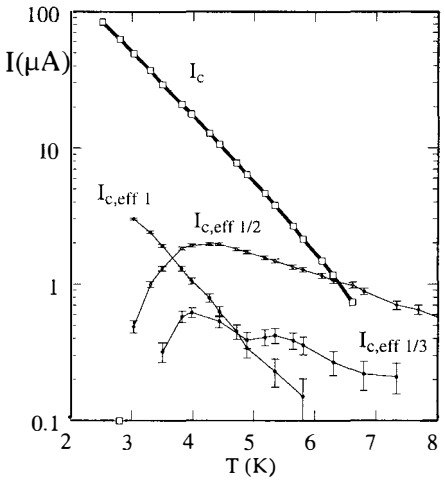


Figure 3: Temperature dependence of the amplitude of the first integer $I_{c,eff1}$ and the main subharmonic steps $I_{c,eff1/2}$ and $I_{c,eff1/3}$. For comparison is shown the measured temperature dependence of the *dc* critical current I_c measured on the same sample. The striking result is the persistence of the subharmonic steps (1/2, 1/3) at high temperature when the *d.c.* Josephson coupling is suppressed.

In conclusion, we have presented a clear experimental observation of subharmonic Shapiro steps in diffusive S-N-S junctions. The phenomena is observed in the high temperature and low energy regime $eV < \epsilon_c < k_BT$ where the ordinary Josephson coupling is suppressed. These new observations calls for a complete theoretical analysis of the time-dependent processes in mesoscopic diffusive proximity systems.

Acknowledgements

We acknowledge fruitful discussions with F. Hekking, F. Wilhelm, A. Zaikin, M. Büttiker, Y. Blanter, K. Lehnert and A. Levy-Yoeyati. We are grateful to B. Camarota for her help in the experiment. This work was partially support by EU TMR contract "Dynamics of superconducting nanoscircuits".

References

1. B.D. Josephson, *Phys. Letters*, **1**, 251 (1962)
2. K. Likharev, *Rev. Mod. Phys.* **51**, 101 (1979) ; K. Likharev, *Dynamics of Josephson Junctions and Circuits*, Ed. Gordon and Breach Sciences Publishers (1991).
3. M. Tinkham, *Introduction to superconductivity*, Ed. Mac Graw Hill, second edition (1996).

4. I.O. Kulik and A.N. Omel'yanchuk, *J. Low Temp. Phys.* **4**, 142 (1978); see also discussion in Ref[9].
5. D.Averin and A. Bardas, *Phys. Rev. Lett.* **75**, 1831 (1995).
6. P. Bak, *Solid State Comm.* **51**, 231 (1984)
7. P. Monceau, J. Richard and M. Renard, *Phys. Rev. Lett.* **45**, 43 (1980); G. Grüner, *Density Waves in Solids* , Ed. Addison-Wesley Publishing Company (1994).
8. P. Dubos, P. Charlat, Th. Crozes, P. Paniez and B. Pannetier, *J. Vac. Sci. Technol.* B **18**, 122 (2000).
9. P. Dubos, H. Courtois, B. Pannetier, F.K. Wilhelm, A.D. Zaikin and G. Schön, *Phys. Rev.* **B63**, 64502 (2001).
10. H. Courtois, Ph. Gandit, D. Mailly and B. Pannetier, Phys. Rev. Lett. **76**, 130 (1996).
11. P. Dubos, O. Buisson, H. Courtois and B. Pannetier, unpublished.
12. The existence of Shapiro-like steps at high temperatures has been discussed recently by A. Volkov and H. Takayanagi[13]. This effect involves the integer steps is expected in a four terminal configuration under current injection from normal reservoir. It cannot be observed in our two terminal S-N-S junction.
13. A.P. Volkov and H. Takayanagi, *Phys. Rev. Lett.* **76**, 4026 (1996).
14. K. W. Lehnert, N. Argaman, H. R. Blank, K. C. Wong, S. J. Allen, E. L. Hu, and H. Kroemer, Phys. Rev. Lett. **82**, 1265 (1999)
15. N. Argaman, *Superlattices and Microstructures* **25**, 861 (1999).

Fermions and Bosons in Superconducting Amorphous Wires

YUVAL OREG[1] and EUGENE DEMLER[2]
[1] *Department of condensed matter physics, Weizmann Institute of Science, Rehovot 76100*
[2] *Lyman Laboratory of Physics, Harvard University, Cambridge MA 02138 USA*

We discuss the destruction of superconductivity in quasi-one-dimensional systems due to the interplay between disorder and Coulomb repulsion. We argue that to understand the behavior of the system one has to study both fermionic and bosonic mechanisms of suppression of superconductivity. The former describes reduction in the mean field critical temperature T_c, while the latter refers to thermal and quantum fluctuations in the order parameter. A change in parameters such as wire width and disorder strength significantly affects both mechanisms.

1 Introduction

The combination of disorder and Coulomb repulsion suppresses superconductivity in low dimensional samples, and may destroy it completely. Advanced technics for fabrication of superconducting wires allow a detailed experimental study [1,2,3] of this destruction.

Does R_N, the normal-state-resistance of the wire at high temperature, determine the destruction of superconductivity on it own? Or do parameters such as the amount of disorder, the width of the wire, its length, the introduction of a magnetic field, and the environment have additional effects, beside their direct effect on R_N? Can they lead to a transition in the ground state properties of the system at zero temperature, and to a qualitative change in the whole structure of the wire resistance curve as a function of the temperature T?

We argue below, that to understand the answers to these questions we have to follow both the physics of the electrons above the mean field T_c, and of the Cooper pairs (bosons) below it.

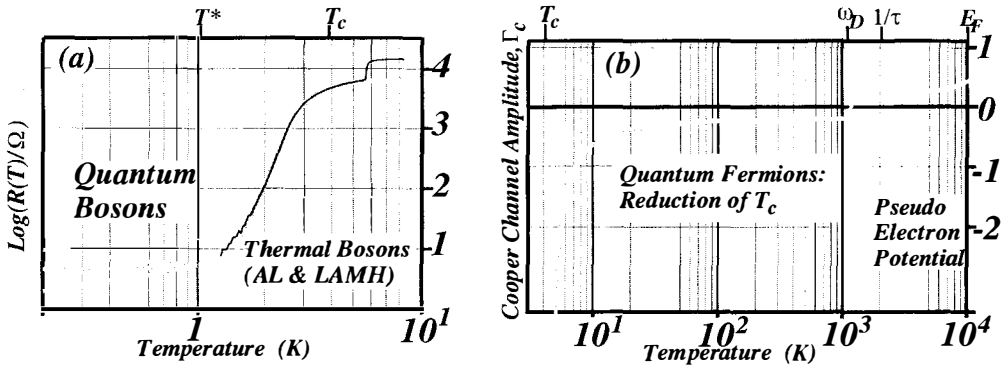


Figure 1: Theories of fermions and bosons, abbr. are explained in the text, notice the log scale of the temperature.

To follow the interplay between bosons and fermions we plot schematically the evolution of the resistance R (Fig. 1a), and of the vertex part of the Cooper channel amplitude, Γ_c (Fig. 1b), as T decreases. At T_c the superconducting instability occurs and Γ_c diverges. [4] It is useful to imagine a flow in the renormalization-group sense, and find the influence of disorder on it.

Let us first discuss Γ_c. Between the fermi energy E_F and the inverse of the mean free time between elastic collisions τ, Fermi-liquid parameters are established. In this temperature range the amplitude Γ_c describes the mutual Coulomb repulsion between electrons in the Cooper channel. In this region it is reduced by a logarithmic factor $\propto \log(E_F\tau)$, known as the Anderson-Morel-Tolmachev log, or *pseudo-electron potential* log. [5] Below $1/\tau$ the electrons' motion becomes diffusive, "dresses" the mutual Coulomb repulsion between them, and enhances

it. Hence, the pseudo-electron logarithmic reduction is less effective.[6,7,8] At the Debye frequency[a] $\omega_D < 1/\tau$ we also have to include the attraction due to phonons. At yet lower T, Γ_c decreases until it diverges at T_c. Below ω_D the dynamically dressed Coulomb repulsion changes the whole evolution of Γ_c and reduces T_c. It appears that the dynamic change of the interaction in the Cooper channel arises from frequencies larger than T, we therefore use the phrase *quantum fermions* in Fig. 1b.[b]

Now we move on to discuss $R(T)$ (Fig 1a). Close to, but above T_c we can still describe the system by fermions and discuss Cooper pair fluctuations that enhance the conductance (the Aslamazov-Larkin (AL) correction).[9] Alternatively we can describe the system by fluctuations of a bosonic field (the complex-order-parameter) with zero average.[10] Below T_c the magnitude of the order parameter develops and it is more appropriate to describe the system in terms of an effective bosonic theory - the time dependant Ginzburg-Landau theory. Langer, Ambegaakor, McCumber and Halperin (LAMH) [11] discuss the way thermal activation of phase slips in the order parameter influence the resistance of the system below T_c.

At $T \ll T_c$ the amplitude of the order parameter is well developed and thermal activations of phase slips are very rare. One then has to consider. the quantized nature of the phase slips, at frequencies larger than T.[12] A variety of phase-only-models were suggested to describe the behavior of the system at low temperatures. We emphasize that the parameters in these models depend on fermionic physics which in turn depends on external parameters.

The resistance increases with the number of phase slips. Coupling to a dissipative environment increases the action of a single phase slip and can reduce their number, see for example Ref.[13,14]. The three curves in Fig. 1a at low T indicate the possible ways the resistance curve can behave: for strong coupling to a dissipative environment the number of phase slips (and hence resistivity) decreases when T decreases, and vice versa for weak coupling to the environment. The middle curve schematically describes a possible intermediate case.

For the most part the literature discusses the bosonic or the fermionic mechanisms separately. Larkin[15] addresses the necessity to discuss both of them together in the case of two dimensional systems. Here we suggest a scheme that combines fermionic and bosonic physics in quasi-1D.

2 Comparison with experiment

The reduction of T_c due to the enhanced Coulomb repulsion in dirty wires may be written, in terms of parameters that are experimentally accessible, as[6,7,8]

$$T_c = T_c^0 \exp\left[-b(4R_q)/R_\xi + O\left((R_q/R_\xi)^2\right)\right], \qquad (1)$$

where T_c^0 is the temperature where Γ_c diverges in the absence of disorder, $R_q = 2\pi\hbar/(2e)^2 \approx 6.453k\Omega$ is the quantum resistance, $R_\xi = \rho\xi/A$ is the resistance for a wire of coherence length ξ, and A is the wire cross section. In the 1D limit where $\xi \gg \sqrt{A}$ the number $b = \sqrt{A}\Sigma_2/(\xi\pi)$ is $O(1)$ and depends weakly on T_c^0 and on A. In the intermediate region, where $\xi \sim \sqrt{A}$, b is very sensitive to microscopic parameters and boundary conditions.[8] Notice that the factor $4R_q$ in Eq. (1) suggests that we are dealing with the effects of fermions. The sum (over certain diffusion propagators) Σ_2, is defined precisely in Ref.[7]. To get a good estimate for T_c-reduction, we need to find b accurately since T_c depends on it exponentially, and to include effects of higher orders of R_q/R_ξ. This was performed for a few examples,[7,8] by a solution of an integral equation, .

In Fig. 2 we plot experimental results taken from Ref.[1] in comparison with our theory. We use the expressions in Ref. [10] to plot the theoretical resistance curves (gray) based on LAMH-

[a]The case $\omega_D > 1/\tau$ can be discussed as well but to make the discussion simpler we assume $1/\tau > \omega_D$.

[b]Below $1/\tau$ there are also corrections to the system properties due to weak localization and interaction effects. For weak disorder, however, they are small compared to the correction to Γ_c and therefore we neglect them.

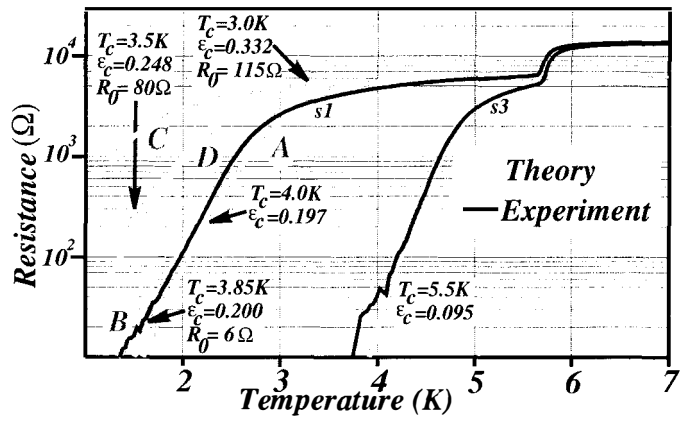


Figure 2: Comparison between theory and experiments. [16]

theory [11] ($T < T_c$), with the AL correction ($T > T_c$). LAMH-theory gives:

$$R(T) = R_N\, 2^{1/4}\sqrt{\pi}\alpha_0\, |\epsilon/\epsilon_c|^{9/4} \exp\left(-(4\sqrt{2}/3)\, |\epsilon/\epsilon_c|^{3/2}\right), \qquad (2)$$

with $\alpha_0 \propto T_c\tau$, $\epsilon_c^{3/2} \propto 1/A, \epsilon \propto T - T_c$. To fit the experimental curves we use the two fitting parameters that enter LAMH-theory, namely the critical temperature T_c and the transition width ϵ_c. The agreement between theory and experiment appears to be good, and our fitting procedure is sensitive to T_c and ϵ_c. Indeed, when we plot a curve where ϵ_c and T_c deviate by less than 10% from the best fitting parameters (A in Fig. 2) it is far from the experimental curve $s1$.

At low T the experimental results deviate from the curve calculated from the thermal-bosonic-LAMH-theory combined with the quantum fermions T_c-reduction (B in Fig. 2). For $s1$ the deviation occurs below $R \approx 10\Omega$. This could be related to quantum phase slips. [2] We note that even for a perfect superconducting wire one should include the contact resistance in "two-probe measurements". [12] A rough estimate of the contact resistance for sample $s1$ in Ref. [1] shows that $R_{\rm contact} \approx R_q/(A/\lambda_F^2) \approx 11\Omega$ (we take $A \approx 50nm^2$ and $\lambda_F \approx 0.3nm$). In Fig. 2 the tail of the theoretical curve that fits $s1$ splits into two (near the point mark by B). One curve corresponds to LAMH theory and in the second we add a resistance R_0 in series. We choose $R_0 = 6\Omega$ to best fit the experiment. Since the phase slip core action is exponentially small in A and $R_{\rm contact} \propto 1/A$ we expect the former to be more relevant to R_0 for relatively narrow wires.

In addition, we show a curve that corresponds to a narrow long wire, so that R_N is similar to those in $s1$ and $s3$ (curves C and D) . Since the cross section A is smaller both the T_c-reduction is stronger and the contact resistance is higher. In particular note that, as Ref. [2] suggests, an addition of R_0 in series to LAMH expressions does not predict a negative curvature for $\log R(T)$ for all values of T. Due to the T_c-reduction $R(T)$ at $T \sim 1.5K$ is very sensitive to wire width.

Fig. 1 indicates that fermions determine T_c, and thermal activation of bosonic phase slips determines the resistance through the LAMH theory. The quantum bosons physics should be relevant at low T. Thus, in contrast to the previous theoretical [13] calculations and experimental [1] results, we do not expect R_N to be the only parameter that determines the quantum transition.

While preparing this manuscript we have learned of a wider set of experiments on superconducting wires of different lengths and cross sections. [2] They show, indeed, as was also observed in Ref. [3], that long wires become superconducting even when their resistance is much higher than the quantum resistance. [2] A bosonic theory [13] explains some features of this behavior. We believe, however, that to fully understand the nature of the phase transition in superconducting

wires one should consider the combined effects of fermionic and bosonic mechanisms.

3 Conclusions.

We studied the interplay between fermions and bosons in superconducting wires. We argued that the disorder enhanced repulsion between the electrons – the quantum physics of fermions - reduces T_c in dirty wires, with larger reduction for narrower wires. This quantum physics of fermions controls the parameters of the effective bosonic physics (both classical and quantum). A modification in wire width affect the low temperature behavior directly through the core energy of quantum phase slips and the contact resistance, and indirectly through the extra reduction of T_c via the fermions mechanism. We showed that when analyzing the available experimental data it is important to include the reduction of T_c together with quantum phase slips. The contact resistance in two-probe-measurements may not be neglected in some cases.

Acknowledgements

It is a pleasure thank Daniel S. Fisher. B. I. Halperin, A. Stern and R. A. Smith for valuable suggestions and C. N. Lau, N. Markovic, M. Bockrath, A. Bezeryadin and M. Tinkham for enlightening conversations and for allowing us to plot parts of their data in this manuscript.

References

1. A. Bezryadin, C. N. Lau, and M. Tinkham. *Nature*, 44:971, 2000.
2. C. N. Lau *et al.* Preprint, May 2001.
3. M. Kociak *et al.* *Phys. Rev. Lett.*, 86:2416, 2001.
4. For a precise definition of Γ_c see A. A. Abrikosov, L. P. Gorkov and I. E. Dzyaloshinski. *Methods of Quantum Field Theory in Statistical Physics* Sec. 33.3 Prentice-Hall, 1963.
5. P. Morel and P. W. Anderson. *Phys. Rev*, 125:1263, 1962.
6. A. M. Finkel'stein. *Physica* **B**, 197:636, 1994.
7. Yuval Oreg and Alexander M. Finkel'stein. *Phys. Rev. Lett.*, 83:191, 1999.
8. R. A. Smith, B. S. Handy, and Vinay Ambegaokar. *Phys. Rev.* **B**, 63:94513, 2001.
9. L. G.Aslamazov and A. I. Larkin. *Sov. Phys – Solid State*, 10:875, 1968.
10. J. R. Tucker and B. I. Halperin. *Phys. Rev.* **B**, 3:3768, 1971.
11. LAMH Theory: **J**. S. Langer and Vinay Ambegaokar *Phys. Rev.* 164:498, 1967 and D. E. McCumber and B. I. Halperin *Phys. Rev.* 1:1054, 1970.
12. M. Tinkham. *Introduction to Superconductivity*, page 293. McGraw-Hill, 1996.
13. Andrei D. Zaikin, et al. *Phys. Rev. Lett.*, 78:1552, 1997. see also cond-mat/0012104.
14. Eugene Demler, Yuval Oreg, and Daniel S. Fisher. Preprint 2001.
15. A. I. Larkin, *Ann. Phys. (Leipzig)* 8:SI-785, 1999.
16. The theory does not address the knee in the experimental data at $5.5K$ which is related to the superconducting phase transition in the two dimensional leads.

SUPERPOSITION OF TWO MESOSCOPICALLY DISTINCT QUANTUM STATES

FLORIAN MARQUARDT[1], C. BRUDER[1]
[1] *Departement Physik und Astronomie, Universität Basel, Klingelbergstrasse 82, CH-4056 Basel, Switzerland*

We consider a system of two superconducting islands, each of which is coupled to a bulk superconductor via Josephson tunneling. One of the islands represents a "Cooper-pair box", i.e. it is an effective two-level system. The other island has a smaller charging energy and approximates a harmonic oscillator. A capacitive interaction between the islands results in a dependence of the oscillator frequency on the quantum state of the box. Placing the latter in a coherent superposition of its eigenstates and exciting coherent oscillations in the large island will lead to a phase-shift of these oscillations depending on the box quantum state, thereby producing a coherent superposition of two "mesoscopically distinct" quantum states in the large island.

1 Introduction

Recently, the possibility to study coherent quantum dynamics in solid-state systems has attracted a lot of interest. In particular, experiments in superconducting circuits [1] have demonstrated this possibility using a "Cooper-pair box" that consists of a small capacitance superconducting island coupled to a bulk superconductor via Josephson tunneling. Due to the small capacitance, there can be only zero or one excess Cooper pair on the island, which leads to an effective two-level description of the system (at appropriate values of the external bias voltage). Such two-level systems have been suggested as building blocks of a quantum computer (see [2,3], and [4] for a recent review). However, it is clear that realizing such a quantum computer with even a modest number of qubits will prove exceedingly difficult and progress will be made only in small steps. A first step in this direction will consist in the coupling of two such Cooper-pair boxes.

In this paper, we consider theoretically a related problem [5]: the capacitive coupling to a larger superconducting island which has a comparatively small charging energy, see Fig. 1. Its dynamics will involve more charge states and would approach that of a harmonic oscillator in the limit $E_J/E_C \to \infty$, where E_J and E_C denote the Josephson coupling energy and the charging energy of the large island, respectively. This suggests a rough analogy to the case of a two-level atom interacting with a single mode of the quantized electromagnetic field. Such a system has been explored experimentally in the field of cavity quantum electrodynamics. In particular, it has been used to entangle the two-level atom's state with a coherent state of the field harmonic oscillator, thereby creating a kind of "Schrödinger cat" state, in which the phase of the coherent oscillations depends on the quantum state of the two-level system.[6] Therefore, the quantum superposition of two different microscopic states has been carried over to a superposition of two mesoscopically distinct states. This has also been considered as a model system for studying both the measurement process and decoherence by coupling the "mesoscopic" system to the external states of the environment (decay of the cavity mode). Although a kind of Schrödinger cat state has been proposed theoretically before in the context of a single Josephson junction, using quite a different mechanism,[7] it did not feature the entanglement of a "microscopic" with a "mesoscopic" system.

The key ingredient of such a system is making the harmonic oscillator frequency dependent on the quantum state of the two-level system. For the superconducting island, this would mean a dependence of E_J (or E_C) on the state of a two-level system, which can be done in principle by replacing the Josephson junction by a SQUID threaded by the flux of the "phase

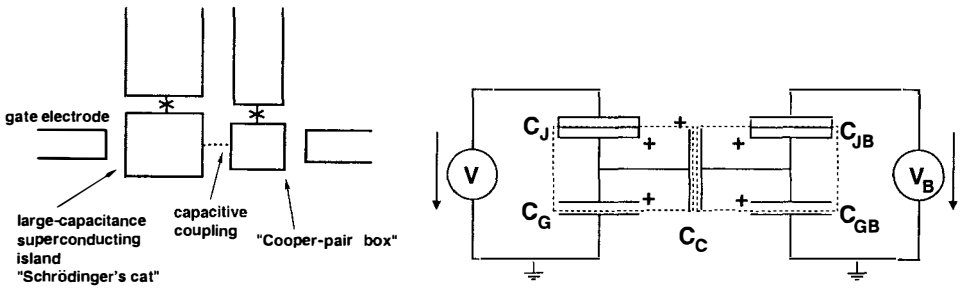


Figure 1: Left side: Schematic diagram of the proposed experimental setup. The crosses denote Josephson junctions between each of the islands and the corresponding bulk superconductor. All other couplings are purely capacitive. Right side: Circuit diagram. The two superconducting islands correspond to the regions marked by dashed rectangles. The junction and gate capacitances are C_J and C_G for the larger island and C_{JB}, C_{GB} for the "box". The coupling capacitance is denoted by C_C and the gate voltages are V and V_B.

qubit" (proposed by Mooij *et al.* [8]). In the present work, we will consider another possibility, suggested by the analogy to the two-level atom, which changes the cavity mode frequency by an off-resonant (dispersive) coupling between the two. In the setting of the two capacitively coupled islands, this can be realized by detuning the oscillation frequency of the "large island" and the Josephson frequency of the Cooper-pair box. It is also necessary to operate the box at the degeneracy point, where the charging energies of the two states (with and without one excess Cooper pair) coincide and where the eigenstates are superpositions of the two charge states. Since the capacitive coupling is diagonal in the charge basis, it will be non-diagonal in the eigenbasis of the box, which will be essential for the proposed realization of a state-dependent frequency of the larger island.

2 The model

The Hamiltonian consists of the charging energies and Josephson coupling energies of both islands separately and an additional interaction term representing the purely capacitive coupling between the charges on both islands:

$$\begin{aligned} \hat{H} = & - E_{JB}\cos(\hat{\phi}_B) + E_{CB}(\hat{N}_B - N_{GB})^2 \\ & - E_J\cos(\hat{\phi}) + E_C(\hat{N} - N_G)^2 \\ & + E_{CC}\hat{N}(\hat{N}_B - \frac{1}{2}) \,, \end{aligned} \tag{1}$$

where the three lines refer to the Cooper-pair box, the large island ("oscillator") and the interaction, respectively.

Here, $\hat{N}$ and $\hat{N}_B$ are the operators corresponding to the number of excess Cooper pairs on the large and small islands, respectively, while $\hat{\phi}$ and $\hat{\phi}_B$ are the corresponding canonically conjugate phases. Gate voltages applied to both islands independently introduce offsets of N_G and N_{GB} for the charging energies. The Josephson coupling energies are given by E_J, E_{JB}, and the charging energy for a single Cooper pair is E_C or E_{CB}. The strength of the interaction between the charges on both islands, resulting from the mutual capacitive coupling, is given by E_{CC}. The offset of $-1/2$ in the interaction energy is introduced for convenience and could be compensated by a shift of the gate charge in N_G. Expressions relating these parameters to the the capacitances and gate voltages are given in the appendix of:[5]

The charging energy of the Cooper-pair box is assumed to be so large that it is permissible to neglect all charge states except for the two lowest-lying ones. Initially, the Cooper-pair box is prepared in an equal superposition of its two energy eigenstates by switching the gate offset N_{GB} to the degeneracy point $N_{GB} = 1/2$, starting at a value which is sufficiently far away from this point. The gate offset of the large island is first set to a value $N_G \gg 1$, which is then quickly switched to zero. We are interested in analyzing the subsequent quantum dynamics of the entire system which will turn out to entangle the box states with two states of the large island that can be "mesoscopically distinct".

3 Approximation through a harmonic oscillator

In the limit $E_J/E_C \gg 1$, the width δN of the ground state of the large island is much larger than one. Therefore, we can treat the charge variable $\hat{N}$ as continuous and arrive at the model of a harmonic oscillator coupled to a two-level system ("Jaynes-Cummings model" in quantum optics). Choosing $\sqrt{2E_JE_C}$ as unit of energy, we obtain the dimensionless Hamiltonian

$$\hat{H}_O = \frac{(\hat{q} - q_G)^2}{2} + \frac{\hat{p}^2}{2} + \frac{\omega_B}{2}\hat{\sigma}_z + \sqrt{2}g\hat{q}\hat{\sigma}_x \,, \tag{2}$$

where $\hat{q}$ corresponds to the scaled charge variable (now taken to be continuous), $\hat{p}$ is its canonically conjugate momentum ($\hbar$ has been set to 1), $\hat{\sigma}_z$ and $\hat{\sigma}_x$ act on the two-level-system whose Hamiltonian is diagonal in the z-basis with an energy difference of ω_B, and g is a dimensionless measure of the coupling strength:

$$\hat{q} \equiv \left(\frac{E_J}{2E_C}\right)^{-1/4} \hat{N} \tag{3}$$

$$\omega_B \equiv \frac{E_{JB}}{\sqrt{2E_JE_C}} \tag{4}$$

$$g \equiv \frac{E_{CC}}{4(2E_JE_C^3)^{1/4}} \,. \tag{5}$$

Note that the coupling term $\sim \hat{\sigma}_x$ between the charges on both islands is non-diagonal in the eigenbasis of the two-level system, since at the degeneracy point $N_{GB} = 1/2$ the eigenstates are equally weighted superpositions of the two charge states.

In the context of Josephson junctions, the Jaynes-Cummings model has been studied previously for the coupling to a single mode of the quantized electromagnetic field [9] and to a superconducting resonator circuit.[10]

Without the interaction, the eigenstates of $\hat{H}_O$ can be labeled $|\pm, n\rangle$ ($n = 0, 1, 2, \ldots$), where n refers to the eigenstates of the harmonic oscillator and $-$ and $+$ stand for the ground state and excited state of the two-level system. The energies are given by

$$\epsilon_{\pm,n} = n + \frac{1}{2} \pm \frac{\omega_B}{2} \,. \tag{6}$$

For a harmonic oscillator, switching the gate voltage (and thereby the offset q_G of the harmonic oscillator potential) excites coherent oscillations of amplitude q_G in the variable $\hat{q}$. The effect of the coupling to the two-level-system is to shift the frequency of the coherent oscillations by an amount that depends on the state of the two-level-system. This can be analyzed most easily within the rotating-wave approximation to the Jaynes-Cummings model, where only the coupling between the almost degenerate states $|+, n\rangle$ and $|-, n+1\rangle$ is taken into account and the Hamiltonian is diagonalized within these two-dimensional subspaces. This is permissible as long as both the detuning $\delta\omega \equiv 1 - \omega_B$ between oscillator and two-level system and the coupling between them are much smaller than the frequency of the oscillator ($\delta\omega \ll 1$ and $g\sqrt{n} \ll 1$).

For the particular case of weak coupling considered here, $g\sqrt{n} \ll \delta\omega$, the most important effect on the quantum dynamics is due to the small shift in energy levels, given by:

$$\delta\epsilon_{-,n+1} = -\delta\epsilon_{+,n} \approx \frac{g^2(n+1)}{\delta\omega} \ . \tag{7}$$

There is no shift for the state $|-,0\rangle$ in this approximation. In the following, we will only take into account the energy shift, which leads to a slow change of the phase over the course of many oscillations. We will neglect the small change in the eigenstates, which is of order $g\sqrt{n}\delta\omega^{-1}$. It is unimportant for the present discussion, as it does not lead to such a phase shift growing in time.

An initial product state $\Psi_{\pm}(0) = |\pm\rangle \otimes |\alpha\rangle$ consisting of one of the two eigenstates $|\pm\rangle$ of the two-level-system and an oscillator coherent state

$$|\alpha\rangle \equiv e^{-\frac{|\alpha|^2}{2}} \sum_{n\geq 0} \frac{\alpha^n}{\sqrt{n!}} |n\rangle \tag{8}$$

will evolve into

$$\Psi_{\pm}(t) \approx \exp\left(-i\varphi_{\pm}(t)\right) \cdot |\pm\rangle \otimes |\alpha_{\pm}(t)\rangle \ , \tag{9}$$

where the global phase of the wave function is given by $\varphi_{\pm}(t)$, whereas the time-evolved complex phase for the coherent oscillation is $\alpha_{\pm}(t)$:

$$\varphi_{+}(t) = \left(\frac{1+\omega_B}{2} - \frac{g^2}{\delta\omega}\right) t \tag{10}$$

$$\varphi_{-}(t) = \frac{1-\omega_B}{2} t \tag{11}$$

$$\alpha_{\pm}(t) = \alpha \exp\left(-i\left(1 \mp \frac{g^2}{\delta\omega}\right) t\right) \ . \tag{12}$$

Therefore, a phase difference $2g^2t/\delta\omega$ develops between the two coherent states. Starting with the initial condition

$$\Psi(0) = \frac{1}{\sqrt{2}} \left(|+\rangle + |-\rangle\right) \otimes |\alpha\rangle \ , \tag{13}$$

the system will, after a time on the order of $\delta\omega/g^2$, evolve into a superposition of two different coherent states of the harmonic oscillator. They will be "mesoscopically distinct", provided the amplitude of the coherent oscillations is larger than the width of the wave packet, i.e. the width of the ground state (which is ≈ 1 in these dimensionless variables). These states are entangled with the states of the two-level-system. In this way, a "Schrödinger cat state" has been produced.

In [5], we have investigated numerically how this scenario changes when we go back to the original system of a superconducting island with a large but finite ratio E_J/E_C, instead of the ideal harmonic oscillator considered up to now in the rotating-wave approximation.

4 Possible experimental realization

Initially, both the "box" and the harmonic oscillator have to be prepared in their ground states, which depend on the gate voltages applied to the two islands. The gate-voltage of the box should be chosen sufficiently far away from the degeneracy point such that its ground state is a charge state. A nonvanishing gate-voltage must be applied to the large island, so that the corresponding gate charge N_G is (preferably much) larger than 1. At $t = 0$, N_G is switched to

zero, on a time scale which is short compared to the oscillation period. This will start coherent oscillations of a frequency close to $\sqrt{2E_JE_C}$. Similarly, the box gate charge N_{GB} must be switched to (or near) the value of $1/2$ corresponding to the degeneracy point, so that its old ground state now becomes a superposition of the two new energy eigenstates (with equal weights in the case of $N_{GB} = 1/2$). The subsequent time evolution of the entire system will lead to the entangled "Schrödinger cat"-like state described above. After a time of the order of $t \approx \delta\omega/g^2$, i.e. $t \approx (\hbar E_C (1 - E_{JB}/\sqrt{2E_JE_C})) \cdot E_{CC}^{-2}$, when the desired state has been produced, it is to be measured. To this end, it is preferable to "freeze" the charge dynamics both of the box and the oscillator. For the case of the box, this can be done by switching the box gate charge N_{GB} back to zero. The Josephson coupling E_J of the oscillator could be set to zero if the junction connecting the large island and the corresponding bulk superconductor (marked by C_J in Fig. 1) is replaced by a dc-SQUID ring, whose effective E_J depends on the flux threading the ring and vanishes for $\Phi = \Phi_0/2$.

In the following, we will discuss possible measurement procedures that can check for the successful production of the entangled state. The probability P of having no excess Cooper pair on the box can be measured like in Nakamura's experiment [1] as an average current which flows during repeated identical preparations, without the need for measurements of single-electron events or current correlations.

As a function of preparation time, P initially oscillates between 0 and 1, since the box starts in an equal superposition of its new energy eigenstates at the degeneracy point. After some time, the coupling to the large island gradually leads to entanglement of the box eigenstates with the coherent oscillator states. Since the frequency of the oscillation depends on the box eigenstate, the phases of the two oscillator states become distinct. Therefore, the overlap of these states becomes zero, so that the reduced density matrix of the box describes an equal mixture of the two charge states. This suppresses the observed oscillations in the probability P. In the ideal case (at least), one may observe a revival of these oscillations, once the accumulated phase difference reaches the value of 2π. This would distinguish coherent dynamics from decay due to uncontrolled decoherence processes.

Concerning the possible values of the charge number on the large island (the "oscillator"), the preparation described so far always leads to a superposition of coherent states (Gaussian wave packets) of the form $e^{i\varphi}|\alpha_+(t)\rangle + |\alpha_-(t)\rangle$ for both possible values of the box charge number (with different phases φ). Both the average charge number $< \hat{N} >$ and the fluctuations of the charge $< \delta\hat{N}^2 >$ on the large island (measured without regard to the box charge) therefore depend sensitively on the center-of-mass positions of the coherent states (i.e. on the arguments of the complex numbers $\alpha_\pm$). In particular, when both wave packets reach the two turning points at opposite sides of the oscillator potential at the same time, the perfect "Schrödinger cat state" has been produced and the fluctuation in the charge number is at a maximum while the average charge is zero. A Nakamura-like experiment could be used to measure this, if, in addition to observing the current, its fluctuations are measured as well.

Further information on the entangled state can be gathered by performing a rotation on the Cooper-pair box "qubit" before reading out the charge states. After freezing the dynamics of the large island, one may use either a microwave Rabi pulse or an adiabatic change of the box gate charge to map the previous energy eigenstates $|\pm\rangle$ (which are coupled to the oscillator coherent states) onto charge states $|0\rangle$ and $|1\rangle$. This procedure introduces correlations between the charge states of the box and the oscillator, such that each of the box charge states corresponds to a different coherent state of the island. These correlations could be measured directly once a single-electron readout device [11] can be coupled to each of the islands, performing a projection-like measurement of both charges. Alternatively, one could average over many identical preparations and observe the fluctuations in the sum and difference of the currents emanating from both islands. A measurement of this type has been performed in the experimental realization of the

Hanbury-Brown-Twiss effect for fermions.[12]

Is it possible to choose the experimental parameters such that the experiment described above could be performed? Assuming a temperature of 5mK, we can choose the charging energy of the large island to be $E_C = 10$mK, and the Josephson energy of the order of $E_J = 50E_C = 0.5$K. The latter is smaller than the gap of Al used in Nakamura's experiment. Possible parameters of the box are $E_{JB} = 10E_C = 100$mK and $E_{CB} = 1$K. Note that the size of E_{CB} does not matter unless it is too small (compared with E_{JB}), since in that case the approximation of a two-level system is no longer justified. The charging energy connected with the capacitive coupling is $E_{CC} = 0.1E_C = 1$mK. This value is smaller than the thermal energy. However, this does not rule out experimental realization, since the influence of thermal fluctuations on the dynamics depends on the strength of the coupling to the environment and the duration of the experiment.

In conclusion, we have analyzed the model of two capacitively coupled superconducting islands, one of which can be considered to be a two-level system and the other one an approximation to a harmonic oscillator, whose oscillation frequency depends on the state of the two-level system. Placing the former in a coherent superposition and the latter in an oscillation of the average charge number will result in a time evolution that leads to mesoscopically different states of the large superconducting island (so that its wave function is peaked at different values of the charge number). A measurement of the resulting "Schrödinger cat" state could be realized using the method employed in [1], possibly coupled with correlation measurements, or single-electron readout devices.

References

1. Y. Nakamura, Y. A. Pashkin, and J. S. Tsai, Nature **398**, 786 (1999).
2. A. Shnirman, G. Schön, and Z. Hermon, Phys. Rev. Lett. **79**, 2371 (1997).
3. D. V. Averin, Solid State Commun. **105**, 659 (1998).
4. Yu. Makhlin, G. Schön, and A. Shnirman, Rev. Mod. Phys. **73**, 357 (2001).
5. F. Marquardt and C. Bruder, Phys. Rev. B **63** 054514 (2001).
6. M. Brune *et al.*, Phys. Rev. Lett. **77**, 4887 (1996).
7. C. C. Gerry, Phys. Rev. B **57**, 7474 (1998).
8. J. E. Mooij *et al.*, Science **285**, 1036 (1999).
9. A. A. Odintsov and A. Vourdas, Europhys. Lett. **34**, 385 (1996).
10. O. Buisson and F.W.J. Hekking, cond-mat/0008275.
11. A. Shnirman and G. Schön, Phys. Rev. B **57**, 15400 (1998).
12. M. Henny *et al.*, Science **284**, 296 (1999); S. Oberholzer *et al.*, Physica E **6**, 314 (2000).

COUPLING OF TWO SUPERCONDUCTORS TROUGH A FERROMAGNET. SFS π-JUNCTIONS AND INNER FRUSTRATED NETWORKS

VALERY V. RYAZANOV[1], VLADIMIR A. OBOZNOV[1], ALEXANDER YU. RUSANOV[1], ALEXANDER V. VERETENNIKOV[1], ALEXANDER A. GOLUBOV[2], JAN AARTS[3]

[1] *Institute of Solid State Physics, Russian Academy of Sciences, Chernogolovka, 142432, Russia*

[2] *University of Twente, P.O.Box 217, 7500 AE Enschede, the Netherlands*

[3] *Kamerlingh Onnes Laboratory, Leiden University, P.O. Box 9504, 2300 RA Leiden, the Netherlands*

We report an observation of the crossover of the superconductor- ferromagnet-superconductor (SFS) junctions to the π-state which manifests itself in reentrant superconducting behavior of the critical supercurrent temperature dependence of the junctions as well as in the half-period shift of the external magnetic field dependence of the transport critical current in the triangular SFS arrays. Latter is associated with the appearance of spontaneous supercurrents in the triangular π-junction array at zero external field, with the ground state degenerated with respect to the two possible current flow directions. In conventional Josephson arrays this state can be observed only by imposing frustrating external field equal to a half-integer number of magnetic quanta per cell.

1 π-state of the Josephson SFS junction

In recent years considerable attention has been given to possible realization of 'π-contacts', i.e. weakly coupled junctions formed in superconducting and superfluid systems which demonstrate π-shift of macroscopic phase difference in the ground state [1,2,3,4,5]. The π-state in a superconductor-ferromagnet-superconductor (SFS) junction arises due to an oscillating (sign-reversal) behaviour of superconducting order parameter induced in the ferromagnet close to the SF-interface [2,6]. The spatial variation of the order parameter in the ferromagnet arises as a response of the Cooper pair to the energy difference between the two spin directions in ferromagnet. In the regime of high exchange energy $E_{ex} \gg k_B T$, the order parameter decay length ξ_{F1} is given by $(\hbar D/E_{ex})^{1/2}$, where D is the electron diffusion coefficient in the ferromagnet, while the order parameter oscillation period $2\pi\xi_{F2}$ is equal to $2\pi(\hbar D/E_{ex})^{1/2}$. Due to the oscillations, different signs of the order parameter can occur at the two banks of the SFS junction when the F-layer thickness d_F is of the order of half a period. This is the so-called π-phase state, which competes for existence with the ordinary 0-phase state. We showed in [7] that in the case of weak exchange energy $E_{ex} \geq k_B T$, when the thermal and exchange energy make comparable contributions to the pair decay process, the general expression for the complex coherence length in dirty ferromagnet is the following:

$$\xi_F = \left(\frac{\hbar D}{2(\pi k_B T + i E_{ex})} \right)^{1/2}, \tag{1}$$

The imaginary part

$$\xi_{F2} = \sqrt{\frac{\hbar D}{((\pi k_B T)^2 + E_{ex}^2)^{1/2} - \pi k_B T}}, \tag{2}$$

defines the order parameter oscillation wavelength $2\pi\xi_{F2}$ that decreases with decrease of temperature. This allows observation of the SFS junction transition to the π-state as temperature decreases down to $T = T_\pi$, when the half-wave of the oscillations, $\pi\xi_{F2}$, becomes close to the ferromagnetic interlayer thickness, d_F. The transition from the 0-phase state to the π-state in a single SFS junction leads to a zero-crossing temperature dependence of the critical current or, more truly, to a sharp cusp in the $I_c(T)$ dependence with vanishing of I_c amplitude at $T = T_\pi$

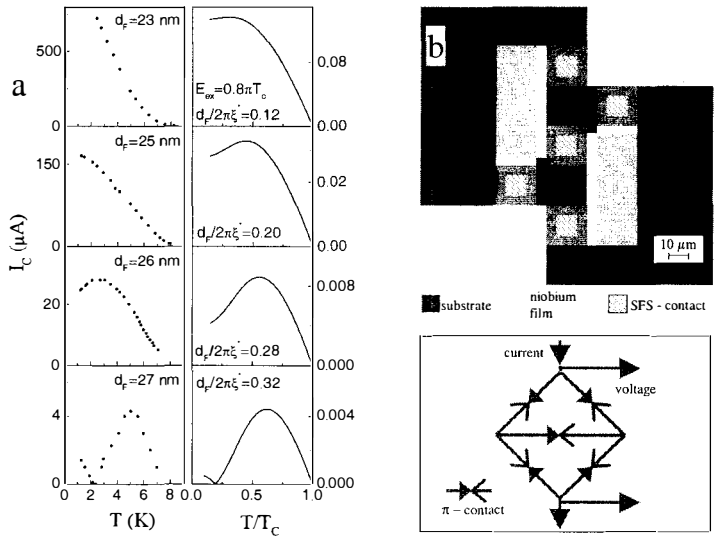


Figure 1: a. Left: critical current I_c as a function of temperature for $Nb - Cu_{0.48}Ni_{0.52} - Nb$ junctions with different F-layer thicknesses between 23 nm and 27 nm as indicated. Right: model calculations of the temperature dependence of the critical current in an SFS junction for $E_{ex} = 0.9\pi T_c$ and various ratios of d_F/ξ^*, where $\xi^* = \sqrt{\hbar D/(2\pi k_B T_c)}$. b. Real (upper) and schematic (low) pictures of the network of five SFS junctions $Nb - Cu_{0.46}Ni_{0.54} - Nb$ (d_F = 19 nm), which was used in the phase-sensitive experiment.

(due to an obvious fact that only the absolute value of a critical current can be observed in a single junction). The junctions we studied consisted of superconducting Nb (S) banks with an interlayer of a ferromagnetic $Cu_{1-x}Ni_x$ alloy (F). The onset of ferromagnetism in these alloys is around $x = 0.44$; above this concentration the Ni magnetic moment increases with about 0.01 $\mu_B/at.\%$ Ni, which allows precise tuning of the magnetism. Shown in Fig. 1a (left) is a series of measurements for junctions with $Cu_{0.48}Ni_{0.52}$ interlayer of different thicknesses in the range 23 nm to 27 nm. (At this concentration the ferromagnetic transition temperature T_{Curie} is about 20 K to 30 K.) At 23 nm only positive curvature is visible, an inflection point is observed for 25 nm, a maximum for 26 nm, and the full cusp at 27 nm. Fig. 1a (right)shows a set of calculations based on the formalism of the quasiclassical Usadel equations, with reasonable parameters for E_{ex} and d_F/ξ^*_F, where $\xi^*_F = (\hbar D/(2\pi k_B T))^{1/2}$, demonstrating how the crossover moves into the measurement window upon increasing the F-layer thickness.

2 Triangular arrays of SFS junctions. Direct observation of the π-shift

Several experimental phase-sensitive methods of direct detection of the π-state transition were suggested [1,3]. The signature of the π-state could be the appearance of a spontaneous magnetic flux equal to half of the flux quantum, $\Phi_0/2$, in a high-inductance superconducting loop containing a π-contact. Josephson π-junction was first predicted in [1] and it was shown there that the state with a spontaneous flux could be realized in such a one-contact interferometer only if $2\pi LI_c \geq \Phi_0$, where L is the loop inductance and I_c is the contact critical current. For our purposes it was more convenient to use weakly-inductive interferometers with $2\pi LI_c \ll \Phi_0$. In such a case the signature of the transition to the π-state would be the shift of the external flux Φ dependence of the transport critical current $I_m(\Phi)$ for a two-contact interferometer made of Josephson 0- and π-contacts of nearly equal critical currents. However, it was found to be very

difficult to fabricate 0- and π-junctions with close Josephson critical currents. Therefore we actually used slightly more complicated intrinsically frustrated structure consisting of five identical SFS junctions arranged into two loops (shown in Fig.1b). All five $Nb - Cu_{0.46}Ni_{0.54} - Nb$ junctions in the array had areas 10×10 μm^2 and junction critical currents I_c=0.3 μA at T=4.2 K. The $Cu_{0.46}Ni_{0.54}$ alloy with T_{Curie} about 100 K was used as a F-interlayer. The SFS junctions with the F-layer thickness of d_F = 19 nm demonstrate transition to the π-state at T_π=2.2 K. Above this temperature (0-state) the $I_m(H)$ pattern for the investigated array is the same as the one predicted in [8,9] for a two-cell interferometer (see Fig.2a, upper). Periodical maximal peaks are observed at external fields corresponding to an integer number of the flux quanta per cell, i.e. integer frustration parameters $f = \Phi/\Phi_0$. Also small peaks can be seen at half-integer values of the frustration parameter f. These secondary peaks result from the phase interference over the outer loop of the net structure, which is twice the unit cell, so a half-integer f leads to an integer number of flux quanta inside the outer loop. At temperatures below T_π (in the π-state) the $I_m(H)$ pattern was found to be shifted by exactly half a period (Fig.2a, low). Upon neglect of the additional minor peaks at half-integer frustrations the behaviour of this five-loop π-junction interferometer resembles that of the two-contact 0-π-interferometer. At $f = 0$ and other integer values there is a current close to the junction critical current, I_c, flowing in the outer double loop of the array. The current induces the extra phase shift $2 \times \pi/2$ in each cell and compensates for the odd number of π-shifts in them. The maximal array transport supercurrent, I_m, is close to zero at H=0 because the array is initially in the spontaneous fully frustrated state. The external magnetic flux equal to half-integer quanta per cell produces the necessary phase shift of π in each cell in the absence of any circular currents in the structure, therefore I_m reaches maxima only at half-integer frustration parameters. Due to the contribution of the outer double-cell contour of the net structure, $I_m(H = 0)$ is not zero in the π-state but is determined by the amplitude of the small peak, as it seen in Fig.2a,low. The $I_m(T)$ dependence at $H = 0$, shown in Fig.2b,upper, mimics the $I_c(T)$ dependence for single junctions and demonstrates sharp cusp at the temperature T_π of the transition into the π-state. However one should keep in mind that the left and right (below and above T_π) branches of the $I_m(H = 0, T)$ dependence are intrinsically asymmetric: while the high-temperature branch corresponds to the temperature dependence of the doubled junction critical current, the low-temperature branch corresponds to the dependence on temperature of the small peak amplitude only. Fig.2b,low shows the maximal peaks positions before and after the $0 - \pi$ transition and demonstrates the sharpness of this transition.

'Self-frustrated' superconducting networks with π-junctions could be usefull for the realization of the superconducting quantum bit [10]. Originally, the suggested superconducting 'phase' qubits were based on magnetic-frustrated superconducting networks [11]. Those systems are not isolated from environment and are estimated to have shorter coherence time with respect to qubits using a π-junction [10]. Another possible application of π-junctions are related to the development of superconducting 'complementary' electronics [12] based on the analogy to complementary metal-oxide-semiconductor (CMOS) logic family.

Acknowledgments

The authors would like to thank M.V. Feigel'man for the helpful discussion and N. S. Stepakov for the technical assistance. The work was supported by the Russian Ministry of Science project ('Electron States'), by RFBR Grant N 01-02-17581, INTAS Grant N 97-1940, by Swiss National Research Foundation Project NFSF N7SUPJ062253.00, and by Grant No. 047-005-001 from the Netherlands Organization for Scientific Research (NWO).

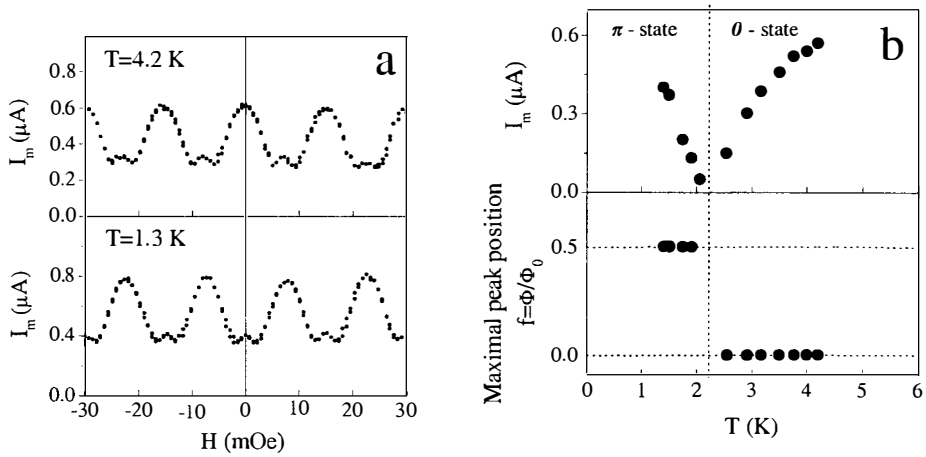


Figure 2: a. Magnetic field dependences of the critical transport current for the structure depicted in Fig.1b at temperature above (upper) and below (low) T_π. b. Upper: Temperature dependence of the critical transport current for the structure depicted in Fig.1b in the absence of applied magnetic field; Low: Temperature dependence (jump) of the position of the maximal peak on the curves $I_m(H)$.

References

1. L.N. Bulaevskij, V.V. Kuzij, and A.A. Sobyanin, JETP Lett. **25**, 290 (1977).
2. A.V. Andreev, A.I. Buzdin, and R.M. Osgood, *Phys. Rev.* B **43**, 10124 (1991).
3. D.J. Van Harlingen, Rev. Mod. Phys. **67**, 515 (1995).
4. J.A. Baselmans, A.F. Morpurgo, B.J. van Wees, and T.M. Klapwijk, Nature **397**, 43 (1999).
5. O. Avenel, Yu. Mukharsky, and E. Varoquaux, Nature **397**, 484 (1999).
6. A.I. Buzdin, B. Vujichich, and M.Yu. Kupriyanov, Sov. Phys. JETP **74**, 124 (1992).
7. V.V. Ryazanov, V.A. Oboznov, A.Yu. Rusanov, A.V. Veretennikov, A.A. Golubov, and J. Aarts, *Phys. Rev. Lett.* **86**, 2427 (2001).
8. Tsang Von-Tien, T. Van Duzer, J. Appl. Phys. **46**, 4573 (1975).
9. K.K. Likharev, *Dymamics of Josephson junctions and circuits*, Ch.8 (Gordon and Breach science publisher, 1986).
10. G. Blatter, V.B. Geshkenbein, and L.B. Ioffe, *Phys. Rev.* B **63**, 174511 (2001).
11. J.E. Mooij, T.P. Orlando, L. Levitov, L. Tian, C.H. van der Wal, and S. Lloyd, Science **285**, 1036 (1999).
12. E. Terzioglu, M.R. Beasley, IEEE Trans. Appl. Superc. **8**, 48 (1998).

MAGNON-ASSISTED ANDREEV REFLECTION IN A FERROMAGNET-SUPERCONDUCTOR JUNCTION

VLADIMIR I FAL'KO, GRIGORIY TKACHOV, EDWARD McCANN
Department of Physics, Lancaster University, Lancaster, LA1 4YB, United Kingdom

We study subgap transport in a ferromagnet-superconductor junction at low temperature due to Andreev reflection. The mismatch of spin polarized current in the ferromagnet and spinless current in the superconductor results in an additional contact resistance which can be reduced by magnon emission in the ferromagnet. Using the s-f model and focusing on half-metallic ferromagnets, we calculate the corresponding nonlinear contribution to the current which is asymmetric with respect to the sign of the bias voltage and is related to the density of states of magnons in the ferromagnet.

Spin polarized transport is a subject of intense research, motivated largely by the possibility of developing a form of electronics which utilizes the spin polarization of carriers[1]. Ferromagnetic (F) metals have more carriers of one spin polarization (known as majority carriers) present at the Fermi energy E_F than of the inverse polarization (minority carriers). Of particular interest are so called half-metals where the splitting Γ between the majority and minority conduction bands is greater than E_F measured from the bottom of the majority band. In such a material only majority carriers are present at the Fermi energy and electric current in it is completely spin polarized. An F-F junction with antiparallel spin polarizations has a larger contact resistance than a junction with parallel polarizations due to a mismatch of spin currents at the interface, leading to tunneling magnetoresistance in F-F junctions[2,3] and giant magnetoresistance in multilayer structures[4,5]. Spin current mismatch may also affect the conductance of a ferromagnet-superconductor junction[6,7,8,9]. At low temperatures and small bias voltage, current flows through the interface due to Andreev reflection[10] whereby particles in the ferromagnetic region with excitation energies ϵ smaller than the superconducting gap energy Δ are reflected from the interface as holes. Since subgap transport in the superconductor (S) is mediated by spinless Cooper pairs the spin current is zero in the superconductor in contrast to the ferromagnet.

Spin relaxation processes[1,11], such as spin-orbit scattering at impurities or magnon emission, can reduce the spin current mismatch. In a given junction, spin-orbit scattering (which is an elastic process) would reduce the value of the additional contact resistance [9,12] whereas the inelastic process of magnon emission would manifest itself as a modification of the form of the $I(V)$ characteristics. Nonlinear $I(V)$ characteristics due to magnon-assisted tunneling between two ferromagnets have already been studied both theoretically[13] and experimentally[14] with a view to relate the second derivative of the current to the density of states of magnons $\Omega(\omega)$ as $d^2I/dV^2 \propto \Omega(eV)$. In the present work we analyze the role of magnon emission in the formation of the subgap $I(V)$ characteristics, $eV < \Delta$, of a ferromagnet-superconductor junction with emphasis given to half-metallic ferromagnets. Microscopically, the relevant process involves the transfer of a singlet pair of electrons from the superconductor to the ferromagnet where one of them forms an intermediate state at an energy below the bottom of the conduction band for minority electrons. Then, this latter electron can emit a magnon in the ferromagnet which will carry away excess spin allowing the electron to incorporate itself into the majority conduction band. The s-f model[15,16] is employed to describe a ferromagnet assuming that electrical conduction and magnetism are caused by different groups of electrons which interact via s-f exchange.

To anticipate a little, due to magnon-assisted Andreev reflection at zero temperature, the $I(V)$ characteristics of an F-S junction for $eV < \Delta$ acquire an additional contribution which is

specified by the differential of the nonlinear differential conductance,

$$\frac{d^2I}{dV^2} = \frac{evG_A}{S}\left\{\frac{\Omega(2eV)}{\left[1+\frac{(2eV-\omega_0)W}{\Gamma\omega_m}\right]^2\left[1-\left(\frac{eV}{\Delta}\right)^2\right]} + \int_0^{2eV}\frac{\Omega(\epsilon)\left[F\left(\frac{eV}{\Delta}\right)-F\left(\frac{\epsilon-eV}{\Delta}\right)\right]\frac{d\epsilon}{2\Delta}}{\left[1+\frac{(\epsilon-\omega_0)W}{\Gamma\omega_m}\right]^2}\right\}. \quad (1)$$

Here $F(x) = x/(1-x^2)^2$, ω_m is the magnon bandwidth and ω_0 is the anisotropy energy responsible for a gap in the magnon density of states [$\Omega(\omega)$ is non-zero for $\omega_0 < \omega < \omega_m$ and zero otherwise][17]. The factor of two in $\Omega(2eV)$ arises because an elementary Andreev reflection process involves a net transfer of charge $2e$ across the biased junction. The conductance G_A incorporates tunneling parameters relevant for the Andreev process and it is defined explicitly later. W is the conduction band width of electrons, v is the volume of a unit cell, and $\Gamma = 2\mathcal{J}S$ is the conduction electron band splitting where S is the spin of the local moments, and $\mathcal{J}$ is the s-f exchange constant.

The nonlinear contribution to the current, Eq. (1), is asymmetric with respect to bias voltage V. It is zero for negative bias and finite for $V > \omega_0/(2e)$. This feature can be expained using the sketch in Fig 1 which illustrates the tunneling process between an S electrode on the left hand side and an F electrode on the right for (a) $V > 0$ and (b) $V < 0$. We have adopted the convention that positive (negative) voltage results in a Fermi energy E_F in the ferromagnet that is lower (higher) by energy $|eV|$ than the Fermi energy E_S in the superconductor. For $V > 0$, Fig 1(a), Andreev reflection results in the injection of both a majority (spin 'up') and a minority (spin 'down') electron into the ferromagnet. One of these electrons has an energy ϵ above the Fermi energy in the superconductor E_S, the other has an energy ϵ below E_S. With respect to the Fermi energy in the ferromagnet E_F these energies are $eV + \epsilon$ and $eV - \epsilon$, respectively, which are both above E_F because of the need to move into unoccupied states in the ferromagnet, $\epsilon \leq eV$. At zero temperature $T = 0$ the core spins are all aligned in the majority, up direction and, if $E_F \ll \Gamma$, then only spin up conduction electrons are present at E_F in the ferromagnet. A dynamic process which allows a spin down electron to enter the ferromagnet is shown schematically in Fig 1(a). The spin down electron tunnels from the superconductor into a virtual, intermediate spin down state above E_F, then it emits a magnon and incorporates itself into an empty state in the majority conduction band. In Fig 1(a) the magnon is depicted as a flip in the spin of one of the localized magnetic moments.

On the other hand, for $V < 0$, Fig 1(b), Andreev reflection would result in the injection of a spin up and a spin down electron from the ferromagnet into the superconductor with energies ϵ above and below E_S. With respect to the Fermi energy in the ferromagnet E_F these energies are $-|eV| + \epsilon$ and $-|eV| - \epsilon$, respectively, which are both below E_F because of the need to have initially occupied states in the ferromagnet, $\epsilon \leq |eV|$. As stated above, there are no spin down states at these energies near E_F. Since a spin up electron cannot emit a magnon (left side of Fig 1(b)), due to conservation of total spin in the exchange interaction, the only possibility would be that a spin up electron in the ferromagnet would absorb a magnon to form an intermediate spin down state before tunneling into the superconductor. However there are no thermally excited magnons at $T = 0$ in the initial state of the ferromagnet (right side of Fig 1(b)) so it is impossible for magnon-assisted Andreev reflection to contribute to current formation in negatively biased junctions.

To calculate the current across an F-S junction, we use the transfer Hamiltonian method and the nonequilibrium Keldysh technique[18,19] to express the current in terms of the tunneling density of states in the metallic ferromagnet which will be determined using the s-f model. We will generalize an approach[19] developed for normal-superconductor junctions to the case of an F-S junction. We consider a point contact geometry which consists of a narrow constriction

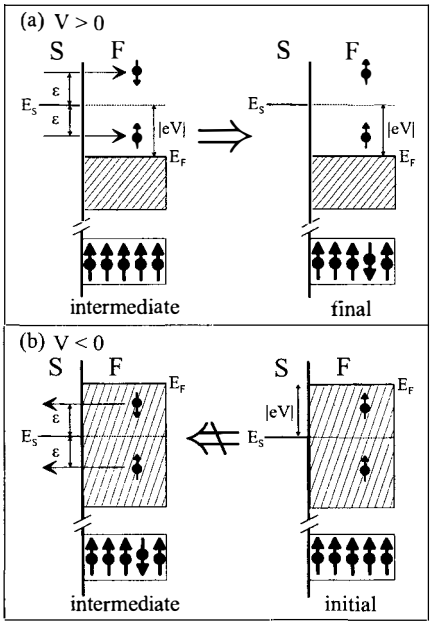


Figure 1: Schematic of the tunneling process between a superconducting electrode on the left hand side and a ferromagnetic electrode on the right for (a) $V > 0$ and (b) $V < 0$. For (a) $V > 0$ a down spin electron tunneling into the ferromagnet may emit a magnon and incorporate itself into the majority conduction band. For (b) $V < 0$ no spin flip process is possible at $T = 0$ because in the initial state (right) there are no thermal magnons for an up spin electron to absorb. See text for details

between S and F electrodes and we use the total Hamiltonian of the system in the form of

$$\begin{aligned} H &= H_S + H_F + H_T, \\ H_T &= \sum_{\alpha} \left(t\, c^{\dagger}_{S,\alpha} c_{F,\alpha} + t^{*}\, c^{\dagger}_{F,\alpha} c_{S,\alpha} \right), \end{aligned}$$

in all calculations paying attention to the spin index $\alpha = \{\uparrow, \downarrow\}$. In the tunneling Hamiltonian H_T, t describes the transfer of an electron from S to F. We assume that t is independent of energy and that spin is conserved upon electron transfer across the interface.

Assuming that the voltage drop V occurs across the point contact and both electrodes are almost in equilibrium, for a given distribution and density of states in the reservoirs, the current can be calculated as the mean value of the current operator, $I = (ie/\hbar) \sum_{\alpha} (t \langle c^{\dagger}_{S,\alpha} c_{F,\alpha} \rangle - t^{*} \langle c^{\dagger}_{F,\alpha} c_{S,\alpha} \rangle)$. The averages in this equation may be expressed in terms of nonequilibrium Keldysh Greens functions $\hat{G}^{+-}$ and it is convenient for the case of a superconducting electrode to use the 2×2 Nambu representation[19]. After some algebra we arrive at the following expression for the current

$$\begin{aligned} I(V) &= \frac{e}{\hbar} 4\pi^2 |t|^4 \int_{-\infty}^{\infty} d\epsilon \left| \hat{G}^{R}_{S,12}(\epsilon) \right|^2 [f(\epsilon - eV) - f(\epsilon + eV)] \\ &\quad \times [\rho_{\uparrow}(E_F + \epsilon + eV)\rho_{\downarrow}(E_F - \epsilon + eV) + \rho_{\downarrow}(E_F + \epsilon + eV)\rho_{\uparrow}(E_F - \epsilon + eV)]. \quad (2) \end{aligned}$$

This expression describes the current due to Andreev reflection of electrons at the F-S interface. The gap-full spectrum of quasi-particles in the superconductor is taken into account in the

off-diagonal element of the retarded Greens function $\hat{G}^R_{S,12}$ and the energy ϵ is measured with respect to the Fermi energy E_S in the superconductor.

In Eq. (2), $\rho_\alpha(E)$ is the tunneling density of states of spin state α in the ferromagnet. For $\Gamma \gg \{E_F, eV\}$ and in the absence of spin waves, $\rho_\downarrow(E)$ is zero in a half metal at energies close to the chemical potentials of the electrodes and $I(V) = 0$. However, as explained above, $\rho_\downarrow(E)$ is nonzero for $E > E_F + \omega_0$ because of the dynamical process of magnon-assisted tunneling. The tunneling density of states $\rho_\downarrow(E)$ is determined using the s-f model[15,16] with the following Hamiltonian

$$\begin{aligned} H_F &= H_0 + H_J + H_{ex}, \\ H_0 &= \sum_{\langle ij\rangle\sigma} t_{ij} c^\dagger_{i\alpha} c_{j\alpha} \equiv \sum_{k\alpha} \epsilon_k c^\dagger_{k\alpha} c_{k\alpha}, \\ H_J &= -J \sum_{\langle ij\rangle} \mathbf{S_i}.\mathbf{S_j} - \omega_0 \sum_i S^z_i, \\ H_{ex} &= -\mathcal{J} \sum_{j\alpha\beta} (\sigma_{\alpha\beta}.\mathbf{S_j})\, c^\dagger_{j\alpha} c_{j,\beta}, \end{aligned}$$

where H_0 deals with conduction band electrons, H_J is the Heisenberg Hamiltonian of the localized moments and H_{ex} takes into account the s-f intra-atomic exchange. We will consider weak, ferromagnetic s-f coupling $0 < \mathcal{J}S < W$, thus excluding the case corresponding to double exchange $\mathcal{J}S \gg W$.

The conduction electron single particle Greens function and energy spectrum have been studied in the limit of zero temperature both for zero conduction band filling[15] and finite filling[16]. In the regime $\{eV, \omega_0\} \ll E_F \ll \Gamma \ll W$ the minority electron density of states is

$$\rho_\downarrow(E) \approx \frac{v\Gamma^2}{2SL^d} \sum_{k'} \sum_q \frac{[1 - f(k')]\, \delta\left(\epsilon_{k'} - E + \omega_q\right)}{\left(\epsilon_{k'+q} - E + \Gamma\right)^2}, \tag{3}$$

where the energy E is measured from the bottom of the spin up conduction band and L^d is the volume of the system. A similar expression, with $2S = 1$, was also obtained for itinerant ferromagnets using the Hubbard model[20]. The energy in the denominator of Eq. (3), $\epsilon_{k'+q} - E + \Gamma$, is related to the inverse lifetime of an electron in the virtual state, the delta function in the numerator accounts for energy conservation of the entire process and the factor $[1 - f(k')]$ indicates that this process is a dissipative one and only involves unoccupied final (spin up) states. Therefore the minority density of states is finite for energies $E > E_F + \omega_0$ only. At $T = 0$, in our regime of interest, spin waves do not affect the majority density of states $\rho_\uparrow(E) \approx N(E)$, where $N(E)$ is the bare electron density of states arising from the Hamiltonian H_0. We have neglected interactions between conduction electrons so that the dominant effect of finite filling is the requirement to obey Fermi statistics.

The dispersion of magnons in a ferromagnet is quadratic at low frequencies, $\omega_q = Dq^2 + \omega_0$ where $D = 2JS^2a^2$ and a is the lattice constant. For simplicity, we shall also use the Debye approximation for a broader range of energies of the magnon spectrum by introducing a cutoff of the parabolic magnon dispersion at $\omega_m \approx D(6\pi^2/v)^{2/3}$ since, for $\Delta \ll \omega_m$, such a simplification does not influence the final results. We also use a parabolic approximation for free electrons in a conduction band and find that, for a three dimensional ferromagnetic metal and $E \approx E_F$,

$$\rho_\downarrow(E) \approx \frac{vN(E)}{2S} \int_0^{E-E_F} \frac{\Omega(\omega)\, d\omega}{\left[1 + \left(\frac{W}{\Gamma}\right) \frac{\omega - \omega_0}{\omega_m}\right]^2}, \tag{4}$$

$$\Omega(\omega) = \frac{\sqrt{\omega - \omega_0}}{4\pi^2 D^{3/2}} \quad ; \qquad \omega_0 < \omega < \omega_m. \tag{5}$$

We use Eq. (2) to calculate the current due to Andreev reflection for low bias voltage $eV < \Delta$, taking into account the lowest order in the tunneling matrix elements, $|t|^4$. In a BCS superconductor the off-diagonal Greens function is $\hat{G}^R_{S,12}(\epsilon) \approx \pi N(E_S)/\sqrt{1-(\epsilon/\Delta)^2}$ for $\epsilon < \Delta$, where $N(E_S)$ is the density of states in the normal state near the Fermi energy. Note that if the ferromagnet were to be replaced by a normal metal where the density of states at E_F is $N(E_F)$ for both spin channels, the current at low bias would be $I = VG_A$ with conductance $G_A \approx (e^2/h)16\pi^4 |t|^4 N^2(E_F)N^2(E_S)$. As we assume $eV \ll E_F$, $\rho_\uparrow \approx N(E_F)$, and Eq. (2) for an F-S junction can be simplified, by shifting the energy variable, into

$$I(V) \approx \frac{G_A}{2eN(E_F)} \int_0^{2eV} \frac{d\epsilon\, \rho_\downarrow(E_F+\epsilon)}{\left[1-\left(\frac{eV-\epsilon}{\Delta}\right)^2\right]}. \tag{6}$$

Using $\rho_\downarrow(E_F+\epsilon)$ from Eq. (4), we find for $eV < \Delta \ll \omega_m \Gamma/W$ that[17]

$$\begin{aligned} I(V) \approx\ & \frac{v\,\Delta\, G_A}{24e\pi^2 S D^{3/2}} \theta(2eV-\omega_0) \Bigg\{ -2\Delta\sqrt{2eV-\omega_0} + \\ & + (\Delta - eV + \omega_0)^{3/2} \arctan\left(\sqrt{\frac{2eV-\omega_0}{\Delta - eV + \omega_0}}\right) \\ & + (\Delta + eV - \omega_0)^{3/2} \operatorname{arctanh}\left(\sqrt{\frac{2\mathrm{eV}-\omega_0}{\Delta + \mathrm{eV} - \omega_0}}\right) \Bigg\}. \end{aligned}$$

The $I(V)$ characteristics obtained yield the relation between the magnon density of states and d^2I/dV^2 shown in Eq. (1). For small voltages $eV \ll \Delta$, the current may be simplified further as

$$I(V) \approx \frac{v\, G_A}{60e\pi^2 S D^{3/2}} (2eV - \omega_0)^{5/2}\, \theta(2eV-\omega_0), \tag{7}$$

and $d^2I/dV^2 \propto \Omega(2eV)$. The factor $\theta(2eV-\omega_0)$ emphasises the absence of a contribution to the current from magnon-assisted Andreev reflection for negative bias. At zero temperature, the $I(V)$ characteristics are asymmetric, which can be used to extract magnon-assisted Andreev reflection in an F-S junction involving a ferromagnet with electrons of both polarizations present at E_F. Note that at $T > \omega_0$, the absorption of thermal magnons would allow for a similar contribution to the current at $V < 0$.

To summarise, spin current mismatch in an F-S junction at subgap voltages may be lifted by magnon-assisted tunneling resulting in nonlinear $I(V)$ characteristics related to the magnon density of states. Such features are typical not only for junctions between ferromagnets and BCS superconductors, but also for HiTc materials, since subgap transport through any spin singlet superconductor would be affected by spin current mismatch at the F-S interface. For a matching pair of materials, with the Curie temperature of the ferromagnet similar to the transition temperature of the HiTc material, the Andreev reflection process could be used to probe the whole magnon spectrum.

Acknowledgments

The authors thank N. R. Cooper, D. M. Edwards, C. J. Lambert, and Yu. V. Nazarov for discussions. This work was supported by EPSRC, with partial travel support from NATO and COST.

References

1. G. A. Prinz, *Physics Today*, April, 58 (1995). *Science* **282**, 1660 (1998), and Refs. therein.
2. M. Julliere, *Phys. Lett.* **54A**, 225 (1975).
3. J. S. Moodera, T. H. Kim, C. Tanaka, and C. H. de Groot, *Philos. Mag.* **B 80**, 195 (2000).
4. M. N. Baibich, J. M. Broto, A. Fert, N. Van Dau, F. Petroff, P. Eitenne, G. Creuzet, A. Friederich, and J. Chazelas, *Phys. Rev. Lett.* **61**, 2472 (1988). G. Binasch, P. Grünberg, F. Saurenbach, and W. Zinn, *Phys. Rev.* **B 39**, 4828 (1989).
5. W. P. Pratt Jr., S. F. Lee, J. M. Slaughter, R. Loloee, P. A. Schroeder, and J. Bass, *Phys. Rev. Lett.* **66**, 3060 (1991). S. F. Lee, W. P. Pratt Jr., R. Loloee, P. A. Schroeder, and J. Bass, *Phys. Rev.* **B 46**, 548 (1992).
6. M. J. M. de Jong and C. W. J. Beenakker, *Phys. Rev. Lett.* **74**, 1657 (1995).
7. V. I. Fal'ko, A. F. Volkov, and C. J. Lambert, *Phys. Rev.* **B 60**, 15394 (1999). E. McCann, V. I. Fal'ko, A. F. Volkov, and C. J. Lambert, *Phys. Rev.* **B 62**, 6015 (2000).
8. F. J. Jedema, B. J. van Wees, B. H. Hoving, A. T. Filip, and T. M. Klapwijk, *Phys. Rev.* **B 60**, 16549 (1999).
9. V. I. Fal'ko, C. J. Lambert, and A. F. Volkov, *Pis'ma v ZhETF* **69**, 497 (1999) [*JETP Letters* **69**, 532 (1999)].
10. A. F. Andreev, *Zh. Exp. Teor. Fiz.* **46**, 1823 (1964) [*Sov. Phys. JETP* **19**, 1228 (1964)].
11. M. Johnson and R. H. Silsbee, *Phys. Rev. Lett.* **55**, 1790 (1985).
12. D. V. Baxter, S. D. Steenwyk, J. Bass, and W. P. Pratt Jr., *J. Appl. Phys.* **85**, 4545 (1999).
13. A. M. Bratkovsky, *Appl. Phys. Letts.* **72**, 2334 (1998). F. Guinea, cond-mat/9712075.
14. D. C. Tsui, R. E. Dietz, and L. R. Walker, *Phys. Rev. Lett.* **27**, 1729 (1971). J. S. Moodera, J. Nowak, and R. J. M. van de Veerdonk, *Phys. Rev. Lett.* **80**, 2941 (1998).
15. B. S. Shastry and D. C. Mattis, *Phys. Rev.* **B 24**, 5340 (1981). S. R. Allan and D. M. Edwards, *J. Phys. C: Solid State Phys.* **15**, 2151 (1982).
16. R. B. Woolsey and R. M. White, *Phys. Rev.* **B 1**, 4474 (1970). M. I. Auslender and V. Y. Irkhin, *J. Phys. C: Solid State Phys.* **18**, 3533 (1985).
17. Strictly speaking, the condition $eV < \Delta$ should be replaced by $eV < \Delta\sqrt{1-\pi^2|t|^2N^2(E_F)}$ where we consider $\pi^2|t|^2N^2(E_F) \ll 1$.
18. C. Caroli, R. Combescot, P. Nozieres, and D. Saint-James, *J. Phys. C* **4**, 916 (1971).
19. J. C. Cuevas, A. Martín-Rodero, and A. Levy Yeyati, *Phys. Rev.* **B 54**, 7366 (1996).
20. D. M. Edwards and J. A. Hertz, *J. Phys. F: Metal Phys.* **3**, 2191 (1973).

Electron transport through Semiconductor-Superconductor junction in Integer Quantum Hall regime

N.M. Chtchelkatchev[1],
[1]*L.D.Landau Institute for Theoretical Physics RAS, 117940 Moscow, Russia*

The conductance of 2DEG-Normal metal contacts is known to exhibit universal quantization in the Integer Quantum Hall regime. In this note we compute the conductance G of a 2DEG-Superconductor (S) structure in a high magnetic field. When the cyclotron diameter in 2DEG becomes larger than the width of the 2DEG-S surface then G becomes nonmonotonous function of the filling factor ν due to the Aharonov–Bohm type interference of electron- and hole-like quasiparticles. At certain parameters of the junction the conductance oscillates with filling factor ν.

In recent years, the study of hybrid systems consisting of superconductors in contact with normal metals in strong magnetic field has attracted considerable interest [1] - [5]. Investigation of physical phenomena in S-2DEG devices in high magnetic field may help to establish a link between mesoscopic superconductivity and quantum - Hall physics. It was found experimentally [1] that zero-bias conductance G of a ballistic S - 2DEG - S junction in Integer Quantum Hall (IQH) regime exhibits quantization under variation of magnetic field. The quantum of G was not equal to a universal value in this experiment, as for instance in IQH or in a quantum point contact [7], but it was an oscillating function of the field H. Numerical simulations [4], [5] showed that the conductance of a 2DEG-S contact in IQH regime is a nonmonotonous function of the filling factor ν; there is nonuniversal quantization of G when 2DEG-S boundary is perfect [6]; at specific range of magnetic field $G(\nu)$ oscillates. A phenomenological theory of the conductance oscillations was suggested in [5]. But, it is still unclear when the conductance becomes sensitive to H, why it exhibits oscillations, how one can analytically describe $G(H)$. The analytical form of $G(\nu)$ is found in this paper. It is shown that the conductance becomes sensitive to H when $2R_c \gtrsim L$, where R_c is a cyclotron radius in 2DEG, L characterizes the length of the 2DEG-S boundary; nonlinearities of $G(\nu)$ result from Aharonov–Bohm type interference of quasiparticles at the boundary.

We consider a junction consisting of a superconductor, 2DEG and a normal conductor segments (see Fig.1). Magnetic field H is applied along z direction, perpendicular to the plain of 2DEG. It is supposed that quasiparticle transport is ballistic (the mean free path of an electron $l_{tr} \gg L$, where L is the length of the 2DEG-S boundary). The current I is supposed to flow between normal (N) and superconducting (S) terminals (the voltage V is applied between them). The conductance $G(H, L) = I/V, V \to 0$ is studied in the paper.

Following [8], we shall describe transport properties of the junction in terms of electron and hole quasiparticle scattering states, which satisfy Bogoliubov-de Gennes (BdG) equations. Then the conductance

$$G = \left.\frac{\partial I}{\partial V}\right|_{V\to 0} = \frac{2e^2}{h}\sum_{l_o,n_i} R_{he,l_o n_i} = \frac{4e^2}{h}\mathcal{R}, \qquad (1)$$

where $R_{he,l_o n_i}$ is probability of Andreev reflection of an electron with the energy $E = 0$ (with the respect to E_f) incident on the superconductor in the channel with quantum number n_i to a hole going from the superconductor in the channel l_o. Before explicit calculation of G, we shall discuss on a qualitative level how G should depend on H. When H is small ($R_c \ll L$) then $R_{he,l_o n_i} \simeq R_{he}\delta_{l_o,n_i}$, with R_{he} weakly depending on H. So,

$$\mathcal{R} \simeq R_{he}N,\ N = Lp_f/2\pi. \qquad (2)$$

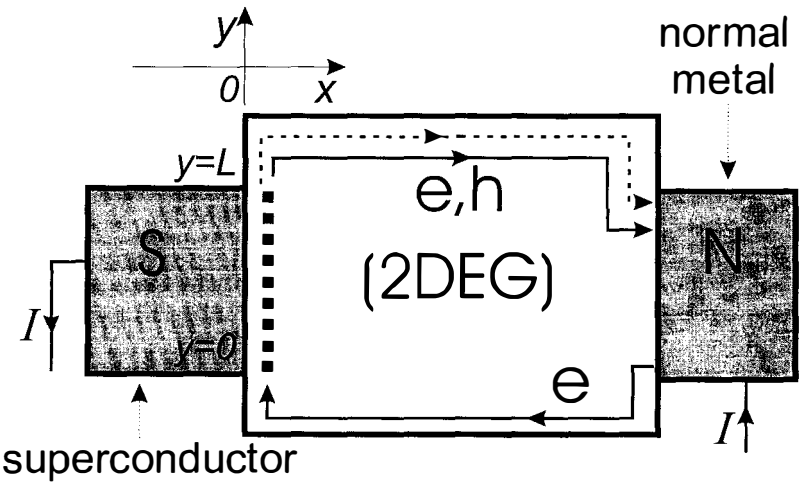


Figure 1: The device, which we investigate, consists of a superconductor, 2DEG and a normal conductor. An electron injected from the normal conductor in IQH regime goes through an edge state to the superconductor, reflects into a hole and an electron which return to the normal contact through the other edge states.

If $2R_c \gtrsim L$, quasiparticles reflected from the superconductor (S) due to normal and Andreev reflection of the electron return to S again due to bending of the trajectories by magnetic field. Then $G(H)$ dependence is not weak. We shall investigate the conductance using semiclassical approximation when $\nu \gg 1$. An electron (hole) quasiparticle in 2DEG can be viewed in semiclassics as a beam of rays (in a similar way propagation of light is described by beams of rays in classical optics [9]). Trajectories of the quasiparticle rays can be found from the equations of classical mechanics. If $R_c \gg L$ ($\nu \ll L/\lambda_f$), the edge states at 2DEG do not overlap. Then the quantum numbers n_o, l_i (1) of the incident electron and reflected hole correspond to the edge states. Reflection of an electron from the superconductor is schematically shown in Fig.1. The electron ray (Fig.2) reflects into electron and hole rays from S at y_0. These rays reflect into

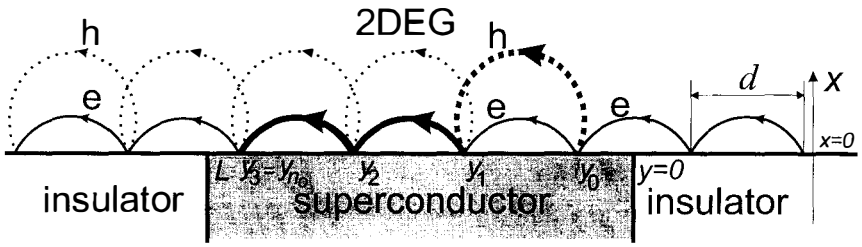


Figure 2: A quasiparticle wave in quasiclassical approximation can be treated as a beam of rays. The figure displays reflection of a ray (solid curve), corresponding to an electron injected from N, from the superconductor. Dashed curves correspond to hole rays.

other hole and electron rays at y_1. So, two hole and two electron rays propagate between y_2 and y_3. Then eight hole rays come from S to N propagating along the same hole path beginning at y_3. One can approximate the probability P of this hole path by the expression:

$$P(y_0, n_i, n_o) \simeq \left| r_{he} r_{ee} r_{ee} r_{ee} e^{3iS_e - i3\pi/2} + r_{hh} r_{he} r_{ee} r_{ee} e^{iS_h + 2iS_e - i\pi/2} + \ldots \right|^2, \qquad (3)$$

where r_{ba} is the amplitude of reflection of a quasiparticle a into a quasiparticle b from the superconductor. $S_{e(h)}$ is the quasiclassical action of an electron (hole) taken along the part of the trajectory connecting adjacent points of reflection. Then $R_{eh,l_on} \simeq \langle P(y_0)\rangle \delta_{n_i,l_0}$, where the average is taken over $0 < y_0 < d(n_i)$, with d being the length of the quasiparticle "jump" along the edge of 2DEG (see Fig. 2). Expression (3) includes interference terms which depend on $S_e - S_h$. As $S_e - S_h = 2\pi(\nu - 1/2)$, one can expect the conductance to be a nonlinear function of ν due to the interference terms. The nature of this nonlinearity indeed resembles Aharonov–Bohm effect, as it was supposed in [5], where the conductance oscillates with H because vector potential changes phases of electrons going from source to drain along different paths. It will be seen below that at certain conditions S-2DEG conductance oscillates with ν.

Semiclassical estimates used above supposed that there is spin degeneracy; $T, eV = 0$; diffraction is small: difference of hole and electron momentum at $E > 0$ was neglected. This approximation is valid when $\max\{T, |eV|, g\mu_B H\}/\mu \ll \lambda_F/L$, where λ_F is Fermi wavelength in 2DEG. Calculation of the conductance below also supposes these conditions to be satisfied.

The conductance of 2DEG-S structure will be calculated below as a semiclassical asymptotic ($\nu \gg 1$) of (1). If the S-2DEG surface is flat then the approach of [8], [10] gives an idea how one can express $R_{eh,ln}$ via semiclassical asymptotic of greens functions of BdG equations. Doing this calculation we confirm, that above naive estimates of G really lead to semiclassical asymptotic of the conductance:

$$\mathcal{R} = \sum_{n_i} \int_0^{d(n_i)} \left\{ \rho(n_i, y_0) \left| \sum_a t_a \exp\left(iS_a - i\frac{\pi}{2}\mu_a \right) \right|^2 \right\} dy_0, \tag{4}$$

where n_i is the index of an edge state of an electron incident on the superconductor, $d(n_i)$ is the length of a quasiparticle jump; t_a is the probability amplitude for the classical quasiparticle trajectory from $y = y_0$ to $y = y_{n_o}$ – the coordinate of the last reflection from the superconductor. The amplitude t_a is a product of Andreev and normal reflection amplitudes; S_a is the action taken from y_0 – the coordinate of the first quasiparticle reflection to y_{n_o} – the coordinate of the last reflection (see Fig. 2); μ_a is Maslov index of the trajectory. For example, $t_a = r_{he} r_{ee} r_{eh} r_{he}$ and $S_a = S_h + 2S_e$ for the trajectory distinguished by a thick line in Fig. 2. Summation over a means the sum over all paths connecting y_0 with y_{n_o} at 2DEG-S boundary. The wight function $\rho(n_i, y_0)$, where $\int_0^d \rho(n_i, y_0) dy_0 = 1$, generally depends on the shape of 2DEG-S contact. If 2DEG spreads over the region $x > 0$, $y > 2R_c + L$, $y < -2R_c$, as it is in Fig. 2, then $\rho = 1/d$. Formula (4) is a central result of the paper.

The sum over trajectories in (4) could be converted into an analytical expression:

$$G = \frac{4e^2}{h} \sum_{n_i} \sum_s P_s \frac{R_{eh} \sin^2(s \arccos(\sqrt{R_{ee}} \cos(\Omega)))}{1 - R_{ee} \cos^2(\Omega)}, \tag{5}$$

where $\Omega = \pi\nu + \theta - 2\lambda p_\perp$; $\theta = arg(r_{ee})$ is the phase of the amplitude of electron – electron reflection from the superconductor, $R_{ee} = |r_{ee}|^2$; $p_\perp = p_\perp(n_i)$ is the perpendicular component of momentum of a quasiparticle when it reflects from the superconductor; λ is equal to the penetration length of the superconductor; $\nu = E_f/(\hbar w_c) - 1/2$. Function P_s is the probability to have s reflections from the surface of the superconductor. When $\rho = 1/d$ this function could be expressed through the maximum number of jumps $g = [L/d]$ over the S-2DEG surface, where $[\ldots]$ denotes the integer part:

$$P_s = \begin{cases} \frac{L - gd}{d} & \text{if } s = g + 1, \\ 1 - \frac{L - gd}{d} & \text{if } s = g, \\ 0 & \text{otherwise.} \end{cases} \tag{6}$$

Expressions (4-5) are the central result of the paper; they show how the conductance depends on magnetic field and parameters of the contact. At small magnetic field (5) reduces to (2). If $2R_c \gtrsim L$, it follows from (5) that the conductance becomes sensitive to H. Few limiting cases of (5) will be considered below in this regime. The Aharonov–Bohm type conductance oscillations are the most interesting property of $G(\nu)$. It follows from (5) that oscillations are visible when $\lambda/L \ll R_c^2/L^2$ and $R_{eh} \lesssim 1/2$. A typical contact where S terminal is prepared with superconductor of first type, 2DEG formed in GaAs, has $\lambda \sim \lambda_F \backsim 10^{-6}cm$, $L \sim 10^{-3}cm$. It follows from given above conditions that if $R_c \sim L$, oscillations can be seen in the contact. (These oscillations were numerically investigated in [4], [5]. It was checked that there is consistence between the theory presented in our paper and the numerical calculations.) When $R_{ee} \ll 1$ the conductance shows steps. It is interesting to investigate the regime $R_{eh} \ll 1$, $L/R_c \gg 1$. Then functional dependence $G(\nu)$ resembles light intensity distribution $I(\delta)$ seen in optics with Lummer - Gerike interferometer[9]. If one considers s as the number of beams in the interferometer, $\delta = 2\Omega$ as the phase difference between successive beams. The probability R_{he} will correspond to the transmission probability through the mirror of the interferometer. Examination of quasiparticle trajectories in (4), which give the main contribution to the conductance, shows that they are similar to trajectories of light beams in the interferometer.

Fig. 3 illustrates how the conductance depends on the magnetic field according to (5). One

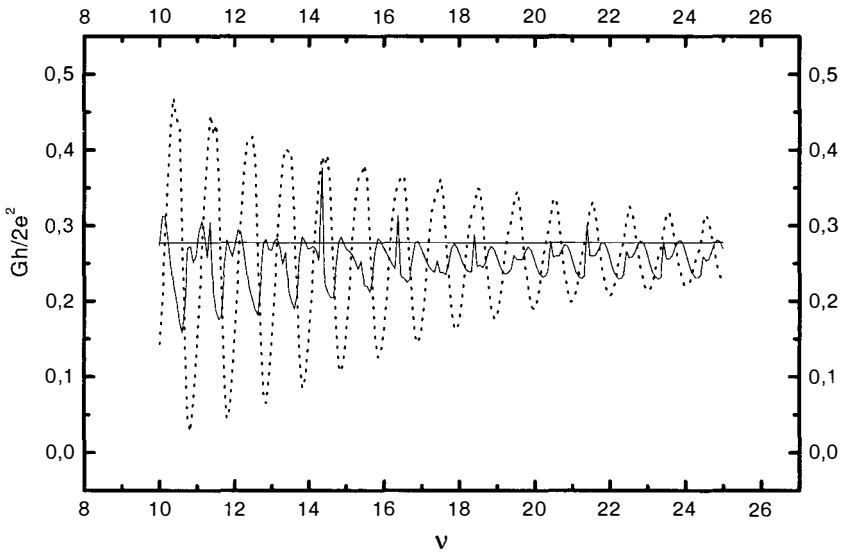


Figure 3: The curve drawn with the solid line represents the conductance for $\lambda L = 3$, with dots – for $\lambda L = 1$. The curves drawn in the figure approach $G(H = 0)$ (2) for large ν.

curve corresponds to $\lambda p_f = 1$ (dots), another – $\lambda p_f = 3$ (solid line). The solid line parallel to the X axes represents the conductance (2). If $2R_c \lesssim L$ the conductance oscillates because of quasiparticle interference, but when ν becomes larger ($2R_c \gtrsim L$) then interference phenomena become less probable and the conductance approaches (2). The graph also illustrates that increasing the ratio λ/L leads to smearing of the oscillations. The following parameters of the contact were used: $Lp_f = 80$, $Z = 5$. Parameter Z [11] characterizes normal scattering from the superconductor due to Shottki barriers, differences of the effective masses in 2DEG, S and

so on. Amplitudes r_{ee}, r_{eh} of normal and Andreev reflection from the superconductor were calculated for zero magnetic field by matching quasiparticle wave functions in 2DEG to the wave functions in S. This procedure is true while $(\lambda/R_c)^2 \ll 1$, where R_c is a cyclotron radius in the superconductor. Magnetic fields used for making the plot satisfy this condition. The ratio Δ_0/E_f were equal to 0.02, with the gap $\Delta(x) = \Delta_0$ in the superconductor and zero in 2DEG.

It seems to be important to determine how a disorder at S-2DEG surface can influence on $G(\nu)$. The disorder could be represented by the roughness of the surface, impurities and so on. Disorder at the surface can induce fluctuations of S_a, t_a in (4), break the interference of quasiparticles. We will characterize disorder by mean free path l_{tr} of electron elastic scattering on impurities, by mean square root deviations $\delta n = \sqrt{\langle(\mathbf{n} - \mathbf{n_0})^2\rangle}$ of the normal unit vector to S-2DEG boundary from the direction $\mathbf{n_0}$ of the X axes, where $\langle(\mathbf{n} - \mathbf{n_0})^2\rangle = \int_0^L dy(\mathbf{n}(y) - \mathbf{n_0})^2/L$. Then one can deduce that formula (5) is correct if $R_c \ll l_{tr}$ and $\delta n \ll \min\{l_H^2/L\lambda, 1/p_f L\}$.

When the surface of the superconductor is diffusive, i.e. $\delta n \gtrsim \max\{1/\lambda p_f, 1/\nu\}$ or $l_{tr} \lesssim R_c$, then there would be no interference between different paths in (4). One can estimate the reflection probability in this regime neglecting interference terms in (5). Then

$$\mathcal{R} \backsimeq \sum_{n_i} \int_0^{d(n_i)} dy_0 \sum_a |t_a|^2/d(n_i) \tag{7}$$

The number of quasiparticle reflections from the surface of the superconductor would be about $s_0 = [L/2R_c]$ then

$$G = \frac{4e^2}{h}\mathcal{R} \backsimeq [\nu]\frac{4e^2}{\hbar}\langle R_{eh}\rangle(1 - 2\langle R_{eh}\rangle)^{1-s_0/2}U_{s_0}(\langle R_{ee}\rangle)/\sqrt{1 - 2\langle R_{eh}\rangle}, \tag{8}$$

where $U_s(x) = \sin(s\arccos(x))/\sin(\arccos(x))$ is the Chebishev polinomial of the second kind [12]. When $s_0 \to \infty$ then the conductance (8) will approach $[\nu]2e^2/h$.

One can suppose that the deviations from ideal conductance quantization (with the universal step $2e^2/h$) observed in the experiment [1] originate from the interference of quasiparticles studied above. The S-2DEG boundary of the device used in [1] was hardly flat, so contributions from harmonics with large s (see eq. 5) should be suppressed. Then it is reasonable to approximate the conductance G by $(2e^2/h)f(\nu)(1 + a\cos(\pi\nu + \varphi_0))$, where $a \ll 1$ characterizes disorder at the surface, φ_0 is a phase - shift, $f(\nu) \sim [\nu]$ describes the shape of the "quantum" of the conductance. It was checked that this formula is a good fit to the experimental data.

Acknowledgments

We thank G.B.Lesovik, M.V.Feigelman, Yu.V.Nazarov, A.Ioselevich, A.Shytov for helpful discussions. It is to Lesoviks interest that this article owes its appearance. This work was supported by the Russian Foundation for Basic Research, project no. 00-02-16617. The author is grateful to Swiss National Foundation and to The Netherlands Organization for Scientific Research (NWO) for support provided in the course of Dutch-Russian collaboration.

References

1. H.Takayanagi, T.Akazaki, *Physica (Amsterdam)* **249-251B**, 462 (1998).
2. T.D.Moore, D.A.Williams, *Phys. Rev.* B **59**, 7308 (1999)
3. H.Hoppe, U.Zülike, and G.Schön, *Phys. Rev. Lett.* **84**, 1804 (2000).
4. Y.Takagaki, *Phys. Rev.* B **57**, 4009 (1998).
5. Y.Asano, *Phys. Rev.* B **61**, 1732 (2000); Y.Asano, T.Yuito, *Phys. Rev.* B **62**, 7477 (2000).

6. We say that S-2DEG boundary is "perfect" when the probability of Andreev reflection of an electron or hole quasiparticle with zero energy and momentum directed perpindicular to the surface is close to unity.
7. L.I.Glazman, G.B.Lesovik, D.E.Khmelnitskii *et al., Pisma Zh. Eksp. Teor. Fiz.* **48**, 218 (1998)[*JETP Lett.* **48**, 238 (1988)].
8. C.J.Lambert, *J. Phys.: Condens. Matter* **3**, 6579(1991); Y.Takane and H.Ebisawa, *J. Phys. Soc. Jpn.* **61**, 1685 (1992).
9. M.Born, E.Wolf, "Principles of optics", Pergamon Press, 1986, p. 341.
10. H.Baranger, D.DiVincentzo, R.Jalabert, *et al*, *Phys. Rev.* B **44**, 10637 (1991).
K.Richter, "Semiclassical theory of mesoscopic quantum systems", Springer-Verlag Berlin Heidelberg, 2000, (Springer tracts in modern physics; Vol. 161), pp. 63-68.
11. G.E.Blonder, M.Tinkham, and T.M.Klapwijk, *Phys. Rev.* B **25**, 4515 (1982).
12. I.S.Gradshtein, I.M.Ryzhik, "Table of integrals, series, and products", Academic Press, Inc, 1980.

LOCAL SPECTROSCOPY OF A SUPERCONDUCTOR-NORMAL METAL JUNCTION

H. Courtois, N. Moussy, V. Chandrasekhar*, and B. Pannetier
CRTBT-CNRS, in convention with Université Joseph Fourier, 25 Av. des Martyrs, Grenoble, France

At the junction with a superconductor, a normal metal acquires superconducting-like properties. The induced superconducting correlations show up as a spatially-dependent modification of the density of states. We measured the local density of states in Nb-Au heterostructures with the help of a very-low temperature (60 mK) Scanning Tunneling Microscope. On the superconducting dots, we obtain a fully-developed gap but with a reduced amplitude because of the inverse proximity effect. In the normal metal, we observe a pseudo-gap of decreasing width as the distance to the interface is increased. We compared our experimental results to the prediction of the quasiclassical theory.

1 Introduction

In the recent years, there have been a noticeable renewed interest in the proximity effect appearing at the junction between a Normal metal (N) and a Superconductor (S). In particular, the transport properties of the normal metal part were shown to exhibit a striking energy dependence with a long range persistence.[1] Another aspect of the proximity effect is the local modification of the energy spectrum. The local density of states was measured in the vicinity of a N-S junction with the help of submicron planar tunnel junctions.[2] A more local study is welcome in order to overcome the unavoidable spatial averaging of such conventional experiments. Indeed, the Scanning Tunneling Microscopy (STM) in the spectroscopy mode enables one to measure the very local density of states under the tip. Due to the technical complexity of (very-)low-temperature STM, the local study of mesoscopic superconductor is still in its infancy.

Our very low temperature STM works at 60 mK in a dilution refrigerator. It features both the atomic resolution and a large scanning range of $6 \times 6\,\mu\mathrm{m}^2$ at low temperature. Fig. 1 shows the spectroscopy data of a plain Nb-Au bilayer. The normal metal Au layer was made thin enough (10 nm) so that the density of states at the surface should be very close to the one of the bulk superconducting (50 nm) Nb. We compared this spectrum to a BCS spectrum with a thermal averaging. In order to fit the data, we have to introduce a smearing of the theoretical curve over 36 μeV, which corresponds to an effective temperature of 210 mK. A similar experiment on an Al film exhibited the same behavior.[3] These fits were performed without any inelastic scattering parameter.

Here, we report on local spectroscopy measurements we performed on artificial N-S hybrid structures. Compared to previous studies, we have been able to reach the very-low temperature regime ($T < 1$ K). This ensures a much improved energy resolution of the density of states measurement and therefore the possibility to probe the proximity effect on a larger length scale with a better insight. We observed spectra with a fully-developed gap in the regions where a normal metal layer caps the superconductor film. Close to the N-S interface, a clear proximity effect is observed, both on the normal metal side and on the superconductor side of the interface. Our experimental results are compatible with the expectations of the quasiclassical theory based on the Usadel equations.

2 The experiment

Our samples were made by successive in-situ evaporation of Nb (Superconducting below about 9 K) and Au (Normal metal). First, the Si sample substrate was introduced in the UHV chamber with a patterned Si membrane clamped on it. This 5 μm-thick Si membrane was previously

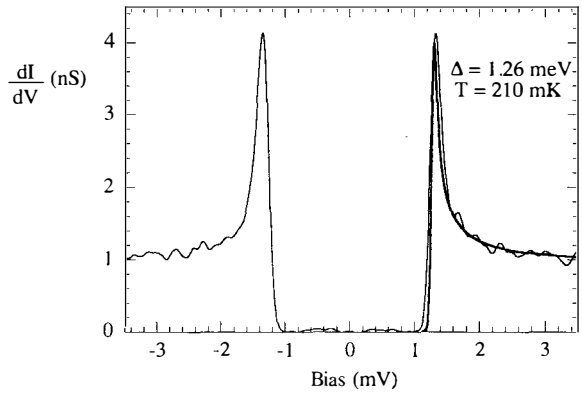


Figure 1: Tunnel spectrum measured at the surface of a 50 nm Nb-10 nm Au bilayer together with a thermally-smeared (T = 210 mK) BCS density of states for $Delta_{Nb}$ = 1.26 meV (right part).

patterned by e-beam lithography and deep Reactive Ion Etching. An array of holes with a periodicity of 4 μm and a diameter of about 1.1 μm were drilled throughout the membrane. During Nb evaporation, the Si membrane acts as a mechanical mask, so that only dots of Nb are deposited on the substrate. After the deposition of 40 nm of Nb, the mask was removed in-situ with the help of a manipulator. An uniform layer of 20 nm of Au was afterwards deposited. The pressure was below 5.10^{-8} mbar during the few minutes between the two evaporations. This ensures a highly transparent Nb-Au interface. We will concentrate here on one of the two Nb-Au samples we studied.

Fig. 2b shows an STM image of the sample at 60 mK. Two Nb dots are clearly visible. The relief of the Nb dots is rather smooth. This is due to both the thickness of the mask and the residual distance between the substrate and the mask. This smooth relief is a drawback in terms of geometry simplicity but an advantage for STM imaging. We performed several series of spectroscopies, as a function of distance from a Nb dot, by traveling along one line. During each series, the displacement speed was reduced to 10 nm/s and the scanning direction was kept fixed in order to reduce the piezo-electric hysteresis. Fig. 3a shows a representative selection of spectra taken on a single line. The surface profile of the same line is shown in Fig. 2a. Labeled arrows indicate the position of the measured spectrum.

In the center of the Nb island (curve a), the density of states exhibits a clear gap similar to a BCS behavior. Compared to the bulk Nb gap value $\Delta_{Nb} \simeq 1.3$ meV, the measured gap is significantly reduced. This is due to the presence of the Au layer on top of the Nb dot. As we move away from the Nb dot center (curves b to d), the density of states first continues to exhibit a fully-developed but reduced gap. This remains approximately true up to close to the location e, which shows a clear pseudo-gap : the density of states goes approximately linearly to zero at the Fermi level. As the tip is moved further away from the interface (spectra f to j), the pseudo-gap width is reduced. We have been able to observe a pseudo-gap behavior in the density of states spectra over about 300 nm.

3 Discussion

The proximity effect in diffusive metals can be described by the quasiclassical theory based on the Usadel equations.[4,5,6] In this work, we benefited from the numerical code developed by W. Belzig et al.[5]. This code solves numerically the Usadel equation and calculates the local density of states in a quasi-1D N-S junction. In order to analyze easily our experimental results, we

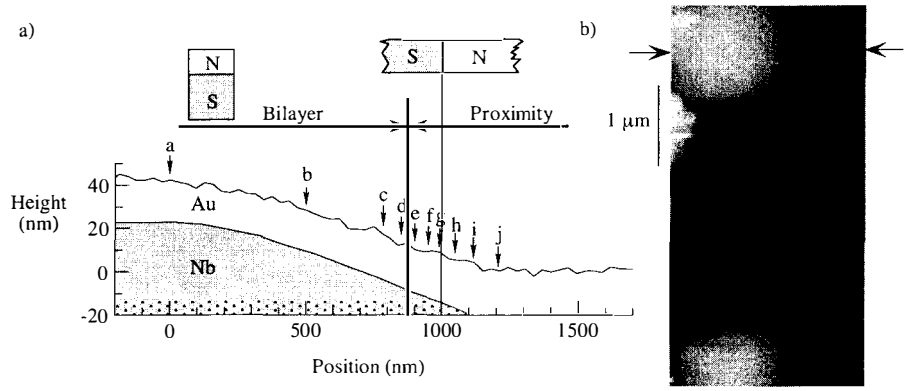


Figure 2: a : Profile of the sample surface extracted from image b) together with a schematics of the sample geometry. This (horizontal) line is indicated by the two arrows. Note that the vertical scale has been expanded by a factor of about 10 compared to the horizontal one. The locations where the spectra of Fig. 3 were measured are indicated, as well as the domains of application of the two geometry modelizations. In the "Bilayer" region, the sample is modeled by a (vertical) N-S bilayer ; the thickness of Nb being given by the measured profile. In the "Proximity" region, the sample is modeled by a (horizontal) N-S region. From the fitting procedure, we deduced that the first $6nm$ of the Nb layer (shadowed region) are not superconducting. b : $2.6 \times 5\,\mu m^2$ STM image at 60 mK. Two Nb dots are visible.

modeled the different parts of our structures as quasi-1D junctions. On the Nb dot, we locally model the sample as an uniform bilayer of Nb and Au, see Figure 2a. Note that the vertical magnification by a factor of about 10 may make the reader underestimate the validity of this approach. In this region labeled "Bilayer", see Fig. 2a, a mini-gap in the energy spectrum is expected, and indeed observed. In the remaining region labeled "Proximity", we model our sample by a horizontal N-S junction with an interface position determined by the comparison with the theory. In this region, a pseudo-gap is obtained, as expected.

Let us first consider the "Bilayer" region. The sample is locally modeled as a quasi-1D N-S junction with a constant length of N metal (the 20 nm thickness of the N layer) and a locally varying length of S metal (measured in the experiment). From the fitting procedure, we found a good agreement between experiment and theory with a Nb gap $\Delta = 0.82$ meV. This value is significantly smaller than the Nb bulk value, which we attribute to the special conditions of Nb evaporation. Fig. 3b shows the calculated curves for locations a to d in the "Bilayer" region, taking into account the *measured* thickness of the Nb layer. In these curves as well as in the other ones, we introduced an effective temperature T = 210 mK in order to account for the experimental accuracy.

At the peripherals of the Nb dot, the measured spectra (curve e and beyond) show a filling of the density of states near the Fermi level and a peak shape that are not compatible with a bilayer model. This pseudo-gap behavior is the signature of the proximity effect in a N-S junction with a long normal metal N. In this "Proximity" region (curves f to j), we described the sample as a single N-S junction extending laterally. In order to describe successfully the data, we had to put a reduced gap value $\Delta' = 0.29$ meV. Compared to the value in the bilayer region, this reduced value can be understood as the effective gap of the Nb-Au dot treated as a whole. The experimental curves e to j were fitted within this model. In this procedure, the position of the tip was a free parameter. The main fitting criteria was the density of states peak position.

The whole set of adjusted curves is shown in Fig. 3b. We assumed a perfect interface transparency and no inelastic or spin-flip scattering. Both in the "Bilayer" and the "Proximity"

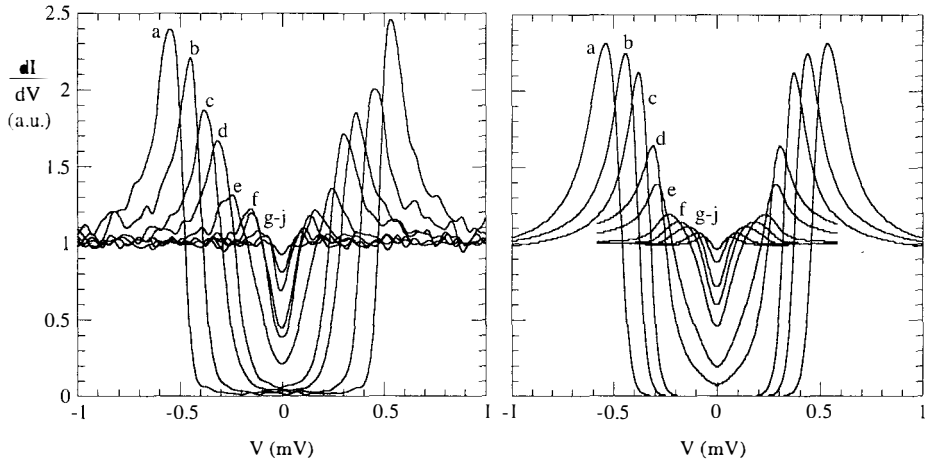


Figure 3: Left : Experimental spectra measured on locations a to j. Right : calculated curves using the Usadel equations (see text).

regions, both the mini- or pseudo-gap amplitudes and the overall spectra shapes are well described. In the "Proximity" region, the fit-derived position of each spectrum is consistent with the experimental position.

In conclusion, we have been able to probe the local density of states in the vicinity of a N-S junction at very low temperature. On the superconductor side of the junction, we observed a strong inverse proximity effect, with a density of states strongly modified compared to the BCS spectrum. On the normal metal side, we observed a pseudo-gap of decreasing amplitude as the tip is moved away from the N-S interface. The experimental data compares favorably with the spectra calculated from the Usadel equations, assuming a very simple geometrical model of our complex sample geometry.

Acknowledgments

We gratefully thank W. Belzig for the use of his numerical code. We acknowledge the help of T. Fournier and T. Crozes for the Si membrane technique. We benefited from discussions within the TMR network "Dynamics of Superconducting Nanocircuits". This work is supported by the French Ministry of Education and Research under an "ACI Nanostructures" contract. V. C. acknowledges the hospitality of the University Joseph Fourier.

References

*on leave from Northwestern University, Evanston (Illinois), USA

1. B. Pannetier and H. Courtois, J. of Low Temp. Phys. **118**, 599 (2000).
2. S. Guéron, H. Pothier, N. O. Birge, D. Estève, and M. H. Devoret, Phys. Rev. Lett. **77**, 3025 (1996)
3. N. Moussy, H. Courtois and B. Pannetier, Rev. of Sci. Instrum. **72**, 128 (2001).
4. A. A. Golubov and M. Yu. Kupriyanov, J. of Low Temp. Phys. **61**, 83 (1988).
5. W. Belzig, C. Bruder and G. Schön, Phys. Rev. B **54**, 9443 (1994).
6. S. Pilgram, W. Belzig and C. Bruder, Phys. Rev. B **62**, 12462 (2001).

Shot noise in incoherent Superconducting / Normal metal / Superconducting S/N/S junction

F. Lefloch[1], C. Hoffmann[1] and M. Sanquer[1]
[1] *CEA/Grenoble, Département de Recherche Fondamentale sur la Matière Condensée*
Service de Physique Statistique, Magnétisme et Supraconductivité
17, Avenue des martyrs, 38054 Grenoble cedex 09 - France
flefloch@cea.fr

We compare experimental results of noise in two Superconducting / Normal metal / Superconducting S/N/S heterostructures of different geometries. We show that the measured noise is enhanced due to incoherent Multiple Andreev Reflections. When the normal metal is confined within the two superconducting electrodes, we find that the excess noise is consistent with the semi-classical predictions. However, when the normal metal is not restricted to some area between the two S/N interfaces, the power can be evacuated away from the normal link and the excess noise is reduced.

1 Introduction

When a Superconductor / Normal metal / Superconductor S/N/S junction is driven out-of equilibrium, Multiple Andreev Reflections (MAR) occurs [1, 2]. During this process, a hole (electron) that is reflected at a first S/N interface can again be reflected as an electron (hole) at the second S/N interface. At every passage across the junction, the quasiparticules gain an energy equals to eV (V is the voltage applied across the junction). When the number of Andreev reflections is sufficient for the total energy gain to reach the superconducting gap, the quasiparticules escape the from the S/N/S well. In short S/N/S junctions, the trajectories between the two superconductors are coherent. In this situation, the junctions carry a Josephson current and sometimes show subgap structures. In long junctions at non zero temperature, the finite single quasiparticule phase coherence length L_Φ and/or the electron-hole coherence length $L_{T,V} \simeq \sqrt{\hbar D/max(eV, k_B T)}$ becomes smaller than the actual size L of the junction and the Josephson oscillations are strongly suppressed. In this case the proximity effect is restricted to a small region close to the two S/N interfaces and the I-V characteristic is almost linear and do not show any subgap structures. Nevertheless, recent calculations by Bezuglyi et al.[1] predict that some features of incoherent MAR in diffusive S/N/S junctions can be observed in the current noise. They find that the noise is that of normal quasiparticules $S_I = 1/3\, 2eI$ plus some excess noise due to incoherent MAR $S_{I,exc} = 4\Delta/3R$. These calculations, performed within the semi-classical approach, estimate the distribution function in the diffusive normal metal N. One possible interpretation of their result is that, because of the Andreev thermal resistance, the quasiparticules "heat" up to the superconducting gap leading to an excess noise. From an experimental point of view, besides shot noise measurements [3, 4], traces of incoherent MAR have been obtained recently by F. Pierre et al. [5], by measuring directly the distribution function in long diffusive Ag/Al based S/N/S junction.
In this paper, we compare current noise measurements performed on two different types of S/N/S junctions. In a first experiment, the junction is made of a piece of normal diffusive metal of length $L \simeq 0.9\,\mu m$ (Aluminum above its critical temperature) which is confined between two superconducting reservoirs. In a recent publication X. Jehl et al.[6] showed that the current noise of this junction is enhanced due to Multiple Andreev reflections. We shall see that, at least for the lowest temperature $T = 2.5\,K$, these results are consistent with recent theoretical calculations of Bezuglyi et al.[1]. In a second experiment, the two superconducting electrodes lay on top of an quasi-infinite normal metal plane facing each other with a distance in between of $L \simeq 1.7\,\mu m$. We show that in the first sample (sample#1), the effective temperature reached by

the quasiparticules trapped in the S/N/S well is higher than in the second one (sample#2). This is not only because sample#1 is shorter than sample#2 but also because heat can be evacuated by conduction electrons perpendicularly to the junction in the second case.

2 Sample#1 : Confined geometry

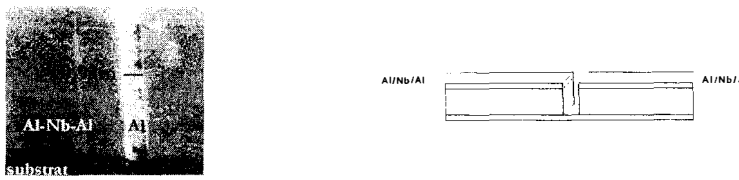


Figure 1: Scanning electron microscope image and a schematic description of the sample used in this first experiment (sample#1)

Figure 1 is a scanning electron microscope image and a schematic description of the sample used in this first experiment (sample#1). First an Al/Nb/Al trilayer deposited in the same sputtering machine, is etched to defined a bridge $200\,\mu m$ long and $40\,\mu m$ wide. Then, the upper two layers of aluminum and niobium are etched to create a gap in the superconducting electrodes and the remaining aluminum defined the normal metal bridge of this S/N/S junction. Because of the nature of the normal metal, experiments have been performed only down to $2.5\ K$, otherwise the aluminum bridge becomes superconducting. We also consider that the aluminum layer underneath the niobium contacts is already superconducting by proximity effect. Therefore, the normal metal is confined between two superconducting reservoirs. In order to be as close as possible to the theoretical situation, we shall focus only in the lowest temperature $T = 2.5\,K$ at which, we consider that electron-phonon interaction is negligible and that the electron-electron interaction length is larger than the length of the normal bridge.

Figure 2 shows the current noise of sample#1 as a function of the voltage across the junction at various temperatures. The noise has been measured with a DC-Squid based resistance bridge[7]. As mentionned by Jehl et al.[6], the amplitude of the noise is larger than what one could expect from a carrier flow of charge e (e being the electron charge) in a diffusive metal. In a semi-classical approach, Bezuglyi et al.[1] predicted a voltage dependence of the noise given by :

$$S_I = \frac{2}{3R}(eV + 2\Delta) \tag{1}$$

The relation is valid at zero temperature and can be extended to non-zero temperatures as long as the Johnson-Nyquist noise is smaller than the incoherent MAR induced excess noise. The solid line in figure 2 corresponds to equation 1 with $R = R_N = 0.35\,\Omega$ and $\Delta = 1.15\,meV$. The gap value is very consistent with that of niobium but suprisingly a much better fit is obtained by using a constant value for the resistance in equation 1 rather than the actual voltage dependance of the differential resistance. This point is, so far, not well understood but is probably not a coincidence. In figure 2, we see that deviations from equation 1 occurs at a voltage around $0.8\ V$. Such a deviation is expected when the total length travelled by the quasiparticules (alternatively a quasi-electron and a quasi-hole) during Multiple Andreev Reflection reaches the electron-electron interaction length. This is therefore obtained when :

$$N_A L = (\frac{2\Delta}{eV} + 1)L \sim L_{ee}(\Delta) \tag{2}$$

where N_A is the number of Andreev reflection for the quasiparticules to reach the gap and $L_{ee}(\Delta)$ the electron-electron interaction length taken at the gap energy. With $V = 0.8\,mV$ we get $L_{ee} \simeq 3\,\mu m$ which is a reasonable value[8].

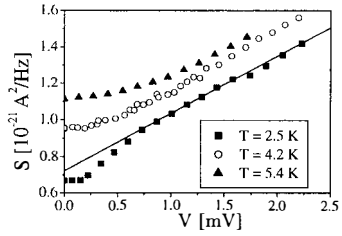


Figure 2: Current noise of sample#1 as a function of the applied voltage. The solid line is a fit using equation 1.

3 Sample#2 : Infinite plane geometry

In this second part, we discuss noise results obtained in the sample#2 shown in figure 3. For this sample, the two niobium superconducting contacts lay on top of a infinite copper plane. The distance between the superconducting electrodes $L = 1.7\mu m$ is much larger than the thermal length L_T even at the lowest temperature we have reached $T = 1.35\,K$. Therefore, sample#2 do not show any Josephson current in the temperature range considered.

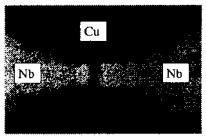


Figure 3: Picture of sample#2. The niobium electrodes are $120\,nm$ thick and the infinite cooper plane $80\,nm$

Figure 4 shows the current noise, measured with the same experimental set-up than for sample#1, as a function of the applied voltage. The results are again compared to theoretical prediction for S/N/S contacts (dashed line). We see that the noise stays lower than the expected response. In terms of effective temperature, it means than the quasiparticules are colder than expected. This can be understood by the specific geometry of the sample. Indeed, some power can be evacuated perpendicularly to the junction by conduction electrons [9]. This behavior is re-enforced by the fact that the distance between the superconducting electrodes is rather large. In that case, the time the quasiparticules need to travel from one side to another may be long enough to allow interaction between electrons.

The right scale in Figure 4 shows the effective temperature of the quasiparticules extracted from the noise using :

$$T_{eff} = \frac{S_I R_d}{4k_B} \tag{3}$$

where R_d is the differential resistance of the contact which is almost constant in our case.

4 Conclusion

We have compared the current noise of S/N/S contacts in two different geometries. In both cases, we observed excess noise that reveals the strong out-of-equilibrium characteristic of the distribution function of the quasiparticules between the two superconducting reservoirs. We found that, as expected, the "effective temperature" of the quasiparticules is higher when the normal metal is confined between the two superconducting reservoirs (sample#1) than in the case where some power can be evacuated perpendicularly to the junction (sample#2). Moreover, we showed that some of the results can be interpreted within a semi-classical description.

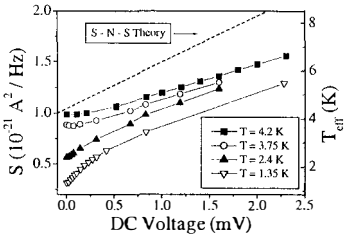


Figure 4: Current noise of sample#2 as a function of the applied voltage.

References

1. E. V. Bezuglyi et al, *Phys. Rev.* B **63**, 100501 (2001) and *Phys. Rev.* B **62**, 14439 (2000)
2. J. C. Cuevas et al, *Phys. Rev. Lett.* **82**, 4086 (1999)
3. P. Dieleman et al, *Phys. Rev. Lett.* **76**, 3486 (1997)
4. T. Hoss et al, *Phys. Rev.* B **62**, 4079 (2000)
5. F. Pierre et al, *Phys. Rev. Lett.* **86**, 1078 (2001)
6. X. Jehl et al, *Phys. Rev. Lett.* **83**, 1660 (1999)
7. X. Jehl et al, *Rev. Sci. Instr.* **70**, 2711 (1999)
8. B. L. Altshuler et al, *Sov. Sci. A***9**, 223 (1987)
9. F. C. Wellstood et al, *Phys. Rev.* B **49**, 5942 (1994)

QUANTUM INTERFERENCE EFFECTS IN ISOLATED JOSEPHSON JUNCTION LOOPS

D. A. IVANOV[1], L. B. IOFFE[2], V. B. GESHKENBEIN[1], G. BLATTER[1]
[1] *Theoretische Physik, ETH-Hönggerberg, CH-8093 Zürich, Switzerland*
[2] *Center for Materials Theory, Physics Department, Rutgers University, Piscataway, NJ 08854 USA*

For small-size Josephson junctions, the superconducting phase across the link is a periodic quantum variable. Isolated Josephson junction arrays thus exhibit pronounced quantum interference effects arising from paths with different winding numbers (Aharonov–Casher effects). These interference effects have strong implications for the excitation spectrum of the array which are relevant in applications of superconducting junction arrays for quantum computing. The interference is most pronounced in arrays composed of identical junctions and possessing geometric symmetries; they may be controlled by either external gate potentials or by adding/removing charge to/from the array. Here we consider a loop of N identical junctions encircling one half superconducting quantum of magnetic flux. In this system, the ground state is found to be non-degenerate if the total number of Cooper pairs on the array is divisible by N, and doubly degenerate otherwise (after the stray charges are compensated by the gate voltages).

Josephson junction arrays are excellent tools for exploring quantum-mechanical phenomena in a wide range of parameter space.[1] The charge and phase on each island provide a set of conjugate quantum variables, allowing for dual descriptions of the array either in terms of charges (Cooper pairs) hopping between the islands or in terms of vortices hopping between the plaquets of the array.[2] This opens the door for the set up and manipulation of interesting quantum interference effects in Josephson junction arrays: in a magnetic field, charges pick up additional Aharonov–Bohm phases and hence the properties of the array depend on the field strength. In the dual language, vortices moving around islands gain phases proportional to the average charges on the islands (Aharonov–Casher phases).[3,4] These features have recently been used in various proposals for solid state implementations of qubits for quantum computing, based on either the charge[5] or phase[6,7,8] degree of freedom in Josephson junction arrays.

In the present paper we study an interference effect in an isolated Josephson junction array which interpolates between those dual descriptions in terms of charges and vortices. Namely, we study the dependence of the quantum-mechanical spectrum of an isolated Josephson-junction array on its total charge. We shall see below that this dependence is most pronounced when the array has geometric symmetries, in which case the degeneracy of the ground state depends on the charge on the array. We consider one of the simplest examples of Josephson-junction arrays with geometric symmetries: the symmetric loop of $N \geq 3$ identical Josephson junctions pierced by one-half superconducting flux quantum of magnetic field (Fig. 1a). Similar designs have been employed for phase qubits,[6,7,8] with half-quantum flux penetrating the loop implying a double degeneracy of the Josephson energy of the loop [in the original qubit design the loop has been made asymmetric in order to suppress the interference of different tunneling paths[6,8]]. We neglect the inductance of the loop and assume sufficiently low temperature to freeze out the quasiparticles on the islands. Then the loop may be described by the Hamiltonian

$$H = \frac{1}{2}\sum_{ij} Q_i (C^{-1})_{ij} Q_j + \sum_i V_i Q_i + \sum_i U_i(\varphi_{i+1} - \varphi_i - a_{i,i+1}), \qquad (1)$$

where φ_i are the phases on the islands, $Q_i \equiv -i\partial/\partial\varphi_i$ are the charge operators conjugate to φ_i (we measure Q in units of $2e$ from now on), $(C^{-1})_{ij}$ is the inverse capacitance matrix, V_i are the gate voltages applied to the islands, U_i are the Josephson energies of the junctions, and $a_{i,i+1}$ is the electromagnetic vector potential induced by the external magnetic field. The symmetry

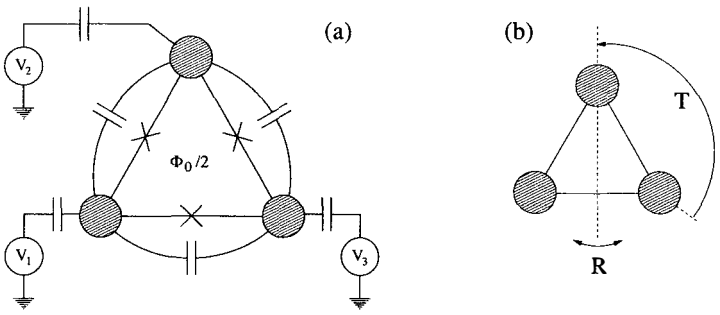


Figure 1: **(a)** The symmetric Josephson-junction loop (with $N = 3$). The N islands are connected by Josephson junctions and capacitively coupled to each other and to the ground. The loop is placed in an external magnetic field providing one half superconducting magnetic flux through the loop. **(b)** Geometric symmetries of the loop consist of cyclic permutations T and of reflections R.

of the loop requires $(C^{-1})_{ij} = (C^{-1})_{i+k,j+k}$ for the Coulomb term and equality of all Josephson terms $U_i(\varphi)$. This implies that the loop is invariant under circular permutation of the islands. Also, if the flux through the loop is exactly one half flux quantum, the loop is invariant under 'flips' changing the orientation of the loop.

This Hamiltonian acts on the wave functions $\Psi(\varphi_1, \ldots, \varphi_N)$ which are assumed to be periodic in their variables:

$$\Psi(\varphi_1, \ldots, \varphi_i + 2\pi, \ldots, \varphi_N) = \Psi(\varphi_1, \ldots, \varphi_i, \ldots, \varphi_N). \tag{2}$$

In general, the boundary conditions (2) may contain arbitrary phase shifts $e^{i\theta_i}$ incorporating the effect of background charges. The phase shifts may be manipulated by the gate voltages V_i and compensated through appropriate fine tuning (this is equivalent to adjusting the zero positions of the gate voltages). We assume that such a tuning is performed once in the beginning of the experiment and later measure the gate voltages relative to these reference values. Experimentally, a similar fine tuning has been done recently in the system with two islands.[9] In our system, the tuning may be performed, for example, by maximizing the gap above the ground state (see below).

The total charge on the loop is conserved (the corresponding operator $Q = \sum_i Q_i$ commutes with the Hamiltonian), and we may split the Hilbert space into the subspaces with fixed values of the total charge Q, implying the transformation rule

$$\Psi(\varphi_1 + \delta\varphi, \ldots, \varphi_N + \delta\varphi) = e^{i\delta\varphi Q}\Psi(\varphi_1, \ldots, \varphi_N). \tag{3}$$

From the symmetry of the loop, it easily follows that its energy spectrum depends periodically on Q with the period N (measured in units of $2e$ as the number of Cooper pairs). A more detailed consideration shows that, under the boundary conditions Eq. 2, the ground state is non-degenerate for Q divisible by N and doubly degenerate otherwise. This can be most easily understood in the two limiting cases: in the phase-dominated limit with the Josephson energy in the Hamiltonian Eq. 1 much bigger than the charging energy, and in the opposite charge-dominated limit.

In the phase-dominated limit, the low-energy states of the qubit are determined by the classical minima of the Josephson energy, with a weak quantum tunneling between them (due to the charging energy). The particular form of the Josephson energy $U(\varphi)$ is not important for our discussion, with the only requirement that the energy profile must have two degenerate minima when the loop is frustrated by half a quantum of magnetic flux (in particular, for $N \geq 3$,

the cosine form $U(\varphi) = -E_J \cos(\varphi)$ satisfies this condition). Each of these two minima contains a continuous family of points generated by the overall shift of all phases by an arbitrary value $\delta\varphi$. This extra degree of freedom may be excluded using the transformation rule Eq. 3, and the total charge Q then enters the boundary conditions on the reduced wave function depending only on the phase differences. Between the two minima of the Josephson energy, there exist N equivalent quasiclassical tunneling trajectories, with different winding numbers of the phases on the islands. The relative phases of these quasiclassical trajectories may be obtained from the boundary conditions and produce the following final result for the splitting of the two minima:

$$\Delta = \Delta_0 \left| 1 + e^{2\pi i q_1} + e^{2\pi i (q_1+q_2)} + \ldots + e^{2\pi i (q_1+\ldots+q_{N-1})} \right|, \tag{4}$$

where Δ_0 is the absolute value of the quasiclassical tunneling amplitude and q_i are the average values of the electric charges on the islands. This result is valid for arbitrary values of the voltages V_i in the Hamiltonian Eq. 1. One can see that the maximal splitting is attained when all charges q_i are integers. This may be used to calibrate the gate voltages V_i (or, equivalently, to set the boundary conditions Eq. 2).

In the opposite limit of big charging energy, we specify to the case of tunnel Josephson junctions with the cosine form of the Josephson energy $U(\varphi) = -E_J \cos(\varphi)$. In the charge representation,[10] this Josephson energy maps onto nearest-neighbor hopping of bosons (Cooper pairs). Considering for simplicity the diagonal matrix $(C^{-1})_{ij}$ (i.e., ignoring capacitances of the junctions), this problem reduces to that of Q hard-core bosons (the hard-core condition being enforced by the large charging energy) on the circle of N cites (with the anti-periodic boundary conditions). It can be solved by mapping onto free fermions, with the appropriate shift of the boundary conditions. The boundary conditions for fermions are periodic for even Q and anti-periodic for odd Q. This results in a non-degenerate ground state for Q divisible by N (with the splitting of the two lowest levels of order E_J/N) and a doubly degenerate ground state otherwise. Turning on the junction capacitance makes the particles (Cooper pairs) repel each other, and they tend to arrange in configurations with maximal separation between them. By explicitly studying such configurations for N up to 5, we find that our conclusion about the ground state degeneracy remains valid. From the symmetry analysis described below, it follows that the ground-state degeneracy remains unchanged in a finite range of values of the junction capacitances.

The ground state degeneracy may be established from the dimensions of the corresponding irreducible representations of the symmetry group. The geometric symmetry group of the symmetric loop is the dihedral group D_N generated by cyclic permutations T and reflections ('flips') R (Fig. 1b). The half-quantum magnetic flux through the loop results in the central extension of this group by the central element Z, with the set of defining relations

$$Z^N = T^N = (TR)^2 = 1, \quad R^2 = Z^{-1}, \quad ZR = RZ, \quad ZT = TZ. \tag{5}$$

In the sector with charge Q, the central element Z takes value $\exp(2\pi i Q/N)$. From constructing the character table of this group and explicitly analyzing the representations corresponding to the two lowest states in the charge-dominated and phase-dominated limits, we find that these representations coincide in the two limits and that the ground state degeneracy (for Q not divisible by N) is a consequence of symmetry. It therefore should persist in a finite range of parameters near these two limits. Unless level-crossings with states of different symmetries occur in the intermediate parameter range, these degeneracies persist for arbitrary ratios of Josephson and charging energies. We indeed verified the absence of such level crossings (by means of exact diagonalization) for $N = 3$ and $N = 4$ for the case of a diagonal capacitance matrix $(C^{-1})_{ij}$.

A side result of our symmetry analysis is that for N even and Q odd all levels (not only the ground state) are doubly degenerate.

Experimentally, the dependence of the level splitting on the gate voltages and on the total charge may be detected with the help of a SQUID, in a setup similar to the experiment of van der Wal et al.[11] The magnetic response of the loop depends strongly on the splitting of the ground state: at large splitting, the system is rigid with a zero average current in the loop; at zero splitting, the loop easily develops a magnetic moment in response to the external field. At the first stage of the experiment, the gate voltage dependence of the splitting should be measured; this also allows to compensate for background charges.[9] At a second stage, the dependence on the total charge on the loop may be measured by feeding Cooper pairs to the loop from an electrode connected to one of the islands via a high-resistance tunnel junction. Cooper pairs should be transferred between the electrode and the loop one by one by simultaneously shifting all gate voltages, without changing the relative potentials of the islands.

Acknowledgments

We thank M. Feigelman and O. Hallatschek for helpful discussions, and M. Troyer for providing the exact diagonalization code. We thank the Swiss National Fonds for financial support. L. I. thanks ETH Zürich for hospitality.

References

1. R.S. Newrock *et al.*, *Solid State Physics* **54**, 263 (2000) and references therein.
2. Ya.M. Blanter, R. Fazio, and G. Schön, *Duality in Josephson junction arrays*, cond-mat/9701223.
3. Y. Aharonov and A. Casher, *Phys. Rev. Lett.* **53**, 319 (1984).
4. W.J. Elion *et al.*, *Phys. Rev. Lett.* **71**, 2311 (1993).
5. A. Shnirman, G. Schön, and Z. Hermon, *Phys. Rev. Lett.* **79**, 2371 (1997).
6. T.P. Orlando *et al.*, *Phys. Rev.* B **60**, 15398 (1999).
7. L. B. Ioffe *et al.*, *Nature* **398**, 679 (1999).
8. G. Blatter, V.B. Geshkenbein, and L.B. Ioffe, *Engineering superconducting phase qubits*, cond-mat/9912163.
9. C.H. van der Wal and J.E. Mooij, *J. Superconduct.* **12**, 807 (1999).
10. P. Lafarge, M. Matters, and J.E. Mooij, *Phys. Rev.* B **54**, 7380 (1996).
11. C.H. van der Wal *et al.*, *Science* **290**, 773 (2000).
12. A.O. Barut and R. Raszka, *Theory of group representations and applications* (World Scientific, Singapore, 1986).

CONTROLLED DECOHERENCE DUE TO A NORMAL–METAL SUPERCONDUCTOR PROXIMITY WIRE

R. GUYON[1], T. MARTIN[1], G. LESOVIK[1,2]
[1] *Centre de Physique Théorique, Université de la Méditerranée, Luminy Case 907, F–13288 Marseille Cedex 9, France*

[2] *L. D. Landau Institute for Theoretical Physics, 117940 Moscow , Russia*

The decoherence rate of a quantum dot coupled to a fluctuating environment described by a normal–metal superconductor junction is considered. Below and above the gap, at zero temperature the density correlator contains spatial oscillations at half of the Fermi wave length on the normal side. As the bias crosses the superconducting gap, the opening of new scattering channels enhances the decoherence rate dramatically, suggesting the possibility of tuning the decoherence rate in a controllable manner.

1 Introduction

The problem of decoherence and dephasing in a mesoscopic system has been addressed in several recent works [1,2,3]. Here, the decoherence rate is computed for the situation where the discrete level (the dot) is coupled electrostatically to the fluctuating charges of a normal metal–superconductor junction with an arbitrary bias. Specifically, in both the Andreev [4] and the sub–gap regime, the decoherence rate depends crucially on the range of the potential which couples the dot to its environment: when this range is lowered below the Fermi wavelength, oscillatory terms in the density–density correlator contribute substantially to the decoherence rate. Even more stunning is the behavior of the decoherence rate as the voltage bias crosses the gap. The opening of new scattering channels accounts for an additional charge noise, and thus provokes a sharp increase in this rate. In principle, this could allow to tune the system from a "quantum" behavior to a "classical" behavior in a controllable manner. The computation of the decoherence rate in the present work, which typically involves the calculation of a density–density correlator in the limit of zero frequency, uses as a starting point known results for the finite frequency current noise[5,6], rather than a direct computation of the density fluctuations.

In contrast, here one is interested both in ultra–small junctions and in the transition to the above–gap regime. Moreover, decoherence also occurs for an "ideal" NS junction, the superconducting–normal metal analog of an adiabatic point contact [7]. In all of the above, spatial oscillations of the density–density correlations are shown to occur, and to enter the computation of the decoherence rate. To our knowledge these oscillations have not been described in previous work.

2 Dephasing mechanism and NS junction

The device is depicted in Fig. 1 (see caption). The system is described by a Hamiltonian which characterized the dot, the NS junction and the coupling between the two:

$$H_C = c^\dagger c \int dx U(x) \psi^\dagger(x) \psi(x) \tag{1}$$

where $\psi(x)$ and c ($\psi^\dagger(x)$ and $c^\dagger$) are fermion creation and annihilation operators in the NS junction and in the dot. The potential $U(x)$ depends on the location of the charges in the NS junction. Later on, different ranges will be specified for $U(x)$ in order to observe their consequence on the decoherence rate.

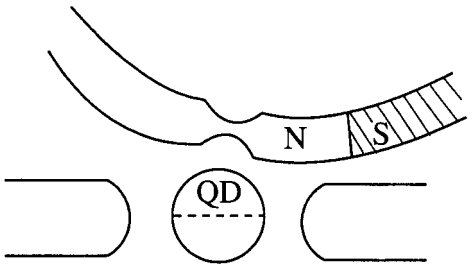


Figure 1: A quantum dot (QD), which contains a sharp level, is connected to two semi-infinite leads (lower half of the figure). In its vicinity, a fluctuating current flows through a nanoscopic (single channel), normal metal–superconductor junction (upper half). Broadening of the level occurs in the presence of an electrostatic coupling between the dot and the normal side of the NS wire.

In the presence of the fluctuating current in the proximity NS wire, the dot Greens function acquires a non–oscillatory component: $G(t) \propto e^{-t/\tau_\phi} e^{-i\epsilon_0 t/\hbar}$ where τ_ϕ is the decoherence time. The following result for the decoherence rate neglects the back–effect of the dot on the NS junction [3]:

$$\frac{1}{\tau_\phi} = \frac{1}{2\hbar^2} \int\int\int_{-\infty}^{+\infty} dx_1\, dx_2\, dt\, U(x_1)U(x_2) \times \langle\langle \rho(x_1,t)\rho(x_2,0) + \rho(x_2,0)\rho(x_1,t)\rangle\rangle \qquad (2)$$

The main issue to compute this rate is to specify the density–density correlator using the property that electrons and holes on the normal side, and possibly quasi–particles on the superconducting side, are scattered at the NS junction. The scattering matrix specifies the amplitudes of the transmitted/reflected particles : It specifies the asymptotic behavior of the electron and hole wave functions away from the junction [5,8,9].

3 Current and density fluctuations

The statistical average of the current–current operator is obtained by performing the Bogolubov transformation [10] on the current operator. For the decoherence time, it is necessary to keep the two current locations x_1 and x_2 separate.

The continuity equation allows to relate the current operator to the density operator as it holds in second quantized form:

$$\langle\langle \rho(x_1,\omega)\rho(x_2,-\omega)\rangle\rangle = \int_{-\infty}^{+\infty} \frac{dt}{\omega^2} e^{i\omega t} \times \partial_{x_1}\partial_{x_2}\langle\langle I(0)I(t)\rangle\rangle \qquad (3)$$

At zero temperature ($\omega > 0$) the only interval which survives is the one specified by the Fermi functions $f_e(\epsilon)(1 - f_h(\epsilon - \omega))$. At low frequencies, and $k_B\Theta = 0$, the double integral in energy is eV and the correlator becomes:

$$\langle\langle \rho(x_1,\omega)\rho(x_2,-\omega)\rangle\rangle_{A,\omega=0} = \frac{2e^3V|s_{eh}|^2}{\pi^2\hbar v_F^2} \times [|s_{ee}|^2 + s_{ee}^* e^{2ik_F x_2} + s_{ee} e^{-2ik_F x_1} + e^{2ik_F(x_2-x_1)}] \qquad (4)$$

The low frequency density–density correlator has an oscillatory spatial dependence with wavelength $\lambda_F/2$, which contribute to Eq. (1) when $U(x)$ is short ranged. The decoherence rate

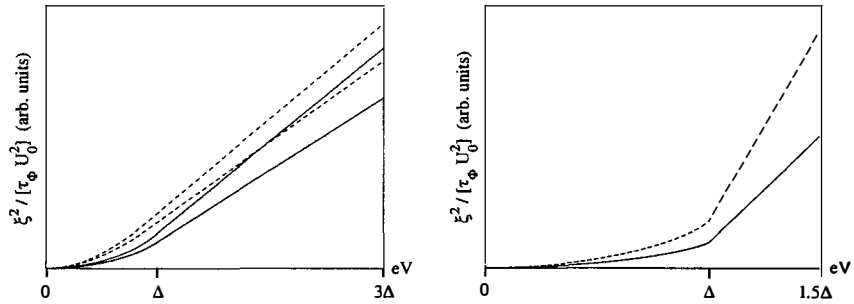


Figure 2: Left: Decoherence rate $\xi^2[\tau_\phi U_0^2]^{-1}$ as a function of bias voltage in the Andreev and sub-gap regime, for barrier transparencies ($Z = mV_B/\hbar^2 k_F$) : $Z = 0.1$ (dashed line), at $\xi = 0.15\lambda_F$ (top) and at $\xi = 10\lambda_F$ (bottom); $Z = 1.0$ (full line) at $\xi = 10\lambda_F$ (top) and at $\xi = 0.15\lambda_F$ (bottom). Right: Same for opaque barriers ($Z = 10.$): $\xi = 10\lambda_F$ (dashed line), and $\xi = 0.15\lambda_F$ (full line).

in the Andreev regime gives :

$$\begin{aligned}\frac{1}{\tau_\Phi^A} &= \lim_{\omega\to 0}\frac{e^2}{\hbar^3 v_F^2}\int_0^{+\infty} d\varepsilon f_e(\epsilon)(1-f_h(\epsilon-\omega))\Theta(\epsilon-\omega)\\ &\times[s_{he}^*(s'_{hh}\tilde{U}(0)+\tilde{U}(-2k_F)) - s'_{eh}(s_{he}^*\tilde{U}(0)+\tilde{U}(-2k_F))]\\ &\times[s_{he}(s'^*_{hh}\tilde{U}(0)+\tilde{U}(2k_F)) - s'^*_{eh}(s_{ee}\tilde{U}(0)+\tilde{U}(2k_F))],\end{aligned} \tag{5}$$

where prime denotes quantities at $\epsilon-\omega$ and $\tilde{U}(q)$ is the Fourier transform of $U(x)$.

4 Decoherence rate at arbitrary bias

The calculation proceeds in a similar way as in the Andreev limit, except that processes involving quasi-particle emission from the superconductor now contribute :

$$\begin{aligned}\frac{1}{\tau_\Phi} - \frac{1}{\tau_\Phi^A} = \frac{e^2}{\hbar^3 v_F^2}\int_0^{eV} d\varepsilon\Big\{ &\\ &(s_{NShe}s^*_{NNhe}\tilde{U}(0)+s_{NSee}(\tilde{U}(-2k_F)+s^*_{NNee}\tilde{U}(0)))\\ &\quad\times(s^*_{NShe}s_{NNhe}\tilde{U}(0)+s^*_{NSee}(\tilde{U}(2k_F)+s_{NNee}\tilde{U}(0)))\\ &+(s_{NShh}s^*_{NNhe}\tilde{U}(0)-s_{NSeh}(\tilde{U}(-2k_F)s^*_{NNee}\tilde{U}(0)))\\ &\quad\times(s^*_{NShh}s_{NNhe}\tilde{U}(0)-s^*_{NSeh}(\tilde{U}(2k_F)+s_{NNee}\tilde{U}(0)))\Big\}\end{aligned} \tag{6}$$

The results are now illustrated by plotting the decoherence rate as a function of bias voltage, for different values of the potential range ξ. A model with a minimal set of parameters, the BTK model [11], is chosen, with a delta function barrier $V(x) = V_B\delta(x)$ and a step-wise pair potential $\Delta(x) = \Delta\Theta(x)$.The scattering matrix elements of this model are known[6].

For high to intermediate barrier transparencies, the decoherence rate is plotted in Fig. 2 (Left). This rate is normalized to the interaction strength squared $(U_0/\xi)^2$, which allows to plot the curves corresponding to $Z = 0.1$ and $Z = 1.0$ on the same scale. In addition, results are illustrated for two values of the range ξ for comparison: $\xi = 10\lambda_F$ corresponds to a range where the negative exponentials in the density-density correlator can be neglected; on the opposite, for $\xi = 0.15\lambda_F$ these exponentials give a significant contribution.

The results plotted in Fig. 2 (Left) show that the relative magnitude of these (normalized) decoherence rates depends in a non trivial manner on the potential range ξ: for intermediate barriers ($Z = 1.0$) the oscillatory terms in the density–density correlator tend to reduce $\xi^2[\tau_\phi U_0^2]^{-1}$, while for high transparency barriers, they increase the decoherence rate. In addition, for $eV \sim 1.9\Delta$ the curves for $\xi = 10\lambda_F$ corresponding to intermediate and weak barriers cross, and the rate corresponding to $Z = 1.0$ is larger beyond this.

Opaque barriers ($Z = 10.$) are considered in Fig. 2 (Right). For both potential ranges $\xi = 10\lambda_F$ and $\xi = 0.15\lambda_F$, τ_Φ^{-1} displays a clear cusp as the bias crosses the gap. This cusp corresponds to the opening of new scattering channels – electron and hole quasi–particle transfer from the normal metal to the superconductor – which gave previously a gradual change – and no obvious crossover region – for higher transparencies (Fig. 2 , Left): here, the crossover region is confined in a very small interval with a width lesser than a few percent of Δ. Above the gap, the linear dependence on the bias is recovered.

5 Conclusion

We have thus extended decoherence time estimates to the situation where both Cooper pairs and quasi–particles are transmitted in the proximity wire. This rate rises sharply as the voltage bias is increased above the superconducting gap, especially for opaque barriers (Fig. 2, Right), because of additional scattering channels. Consider a quantum bit (qubit), implemented by a quantum dot apparatus: the coupling to a neighboring NS junction can render the system classical (besides the tunneling processes in and out of the dot) or quantum in a perfectly controllable manner. Decoherence, reduced abruptly by lowering the voltage bias below the gap, could be used to determine when the quantum evolution of the qubit is supposed to start.

References

1. E. Buks *et al.*, Nature (London) **391**, 871 (1998).
2. D. Sprinzak, E. Buks, M. Heiblum and H. Shtrikman, Phys. Rev. Lett. **84**, 5820 (2000).
3. Y. Levinson, EuroPhys. Lett. **39**, 299 (1997); I.L. Aleiner, N.S. Wingreen and Y. Meir, Phys. Rev. Lett. **79**, 3740 (1997); Y. Levinson, Phys. Rev. B **61**, 4 748 (2000).
4. A. A. Kozhevnikov, R. J. Shoelkopf and D. E. Prober, Phys. Rev. Lett. **84**, 3398 (2000).
5. G. B. Lesovik, T. Martin and J. Torrès, Phys. Rev. B **60**, 11935 (1999).
6. J. Torrès, T. Martin and G. B. Lesovik, cond-mat 0004489.
7. G. Lesovik, JETP Letters **70**, 208 (1999).
8. M. J. M. de Jong and C. W. J. Beenakker, Phys. Rev. B **49**, 16070 (1994); B. A. Muzykantskii and D. E. Khmelnitskii, *ibid.* **50**, 3982 (1994); Th. Martin, Phys. Lett. A **220**, 137 (1996). .
9. M. P. Anantram and S. Datta, Phys. Rev. B **53**, 16 390 (1996). Phys. Rev. B **25**, 4515 (1982).
10. N. N. Bogolubov, V. V. Tolmachev and D. V. Shirkov, *A New Method in the Theory of Superconductivity* (Consultant Bureau, New York, 1959); P. G. de Gennes, *Superconductivity of Metals and Alloys*, (Addison Wesley, 1966, 1989).
11. G. E. Blonder, M. Tinkham and T. M. Klapwijk, Phys. Rev. B **25**, 4515 (1982).

SPATIALLY RESOLVED TUNNELING SPECTROSCOPY ON NORMAL NANOSTRUCTURES IN CONTACT WITH A SUPERCONDUCTOR

MAUD VINET, CLAUDE CHAPELIER, FRANCOIS LEFLOCH
Département de Recherche Fondamentale sur la Matière Condensée, CEA-Grenoble, 17 av des martyrs, 38054 F-Grenoble Cedex 9

We investigated the local density of states (LDOS) of a normal metal (N) in good electrical contact with a superconductor (S) as a function of the distance x to the NS interface. We used a low temperature scanning tunneling microscope (STM) to record simultaneously $dI/dV(V,x)$ curves and the topographic profile. Nearby the NS interface, all the spectra show a dip near the Fermi energy but depending on the geometry, we can distinguish different behaviors.

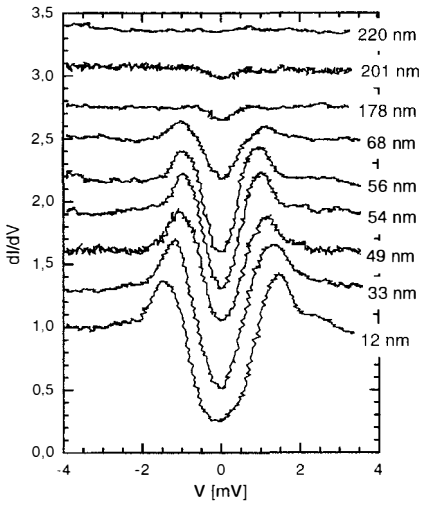
- First, when the characteristic size of the normal metal L is much larger than the coherence length $\xi_N = \sqrt{\hbar D_N/2\Delta}$, the spectral extension of the dip decreases from Δ at the NS interface to zero at distances $x \gg \xi_N$.
- Second, in normal ridges where L is comparable to ξ_N, the apparent gap in the LDOS is space-independent. Its spectral extension depends on the Thouless energy.

Recent advances in nanofabrication renewed the interest in the proximity effect between a superconductor and a metal normal, especially at the mesoscopic scale when the characteristic size L of the normal metal becomes smaller than the thermal length $L_T = \sqrt{\hbar D_N/2\pi k_B T}$ (D_N is the diffusion constant in the normal metal). The predictions made on the LDOS in N depend on whether the normal metal is infinite or not.[1,2] Experimentally, one have to compare L and ξ_N where L is the size of the normal metal and $\xi_N = \sqrt{\hbar D_N/2\Delta}$ its coherence length (Δ is the superconducting gap).[2] Guéron *et al.* tested the theory in the infinite case using nanofabricated tunnel junctions to measure the DOS $n(E,x)$ at three distinct positions along a normal wire in contact with a superconductor.[3] On a much smaller scale, STM was used to study the proximity effect in ballistic N metals (*i.e.* $L \ll \xi_N, l_N$).[4,5]

We report measurements of the LDOS by scanning tunneling spectroscopy on Nb/Au proximity junctions. We are able to spatially resolve the LDOS in the normal metal as a function of the distance x to the NS interface (x can vary from zero to several coherence lengths with a resolution of a few nanometers). Moreover we can discriminate between the two situations: $L \leq \xi_N$ and $L \gg \xi_N$ within the same sample.

Tunneling spectra are obtained by a lock-in detection technique with a $77\,\mu$V peak-to-peak modulation voltage of the bias at 1 kHz. We measure the differential conductance dI/dV versus V while holding the STM tip at a fixed height above each position $\mathbf{r}$. This provides a local probe of the LDOS $n(eV,\mathbf{r})$. The energetic resolution is determined by the thermal broadening at 1.5 K. Each curve is a single acquisition process with no additional averaging. The dI/dV curves and the topography are measured during the same line scan allowing us to correlate them precisely. Data are normalized to the conductance at high voltage ($V > \Delta$) with the *same* coefficient for all the curves. The typical tunneling resistance is $10^7\,\Omega$.

The sample consists of a 50 nm thick pattern of juxtaposed strips, $1\,\mu$m wide and $250\,\mu$m long, of Au and Nb in good electrical contact, see right part of Fig. 1.[6] Transport measurements of thin films provided the mean free path l and coherence length of gold, $l_N \simeq 22$ nm and $\xi_N \simeq 53$ nm, and of niobium, $l_S \simeq 6$ nm and $\xi_S = \sqrt{\hbar D_S/2\Delta} \simeq 27$ nm. Moreover, as seen on the right of Fig.1, Au forms ridges on each side of the Nb strips whose typical dimension is a few tens of nanometers. They are in electrical contact with Nb but poorly connected to the rest of Au. Indeed we observe BCS-like $dI/dV(V)$ curves in between the Au ridges and the Au strips which indicates the presence of bare Nb. At this place, the spectra can be fitted using a BCS model and



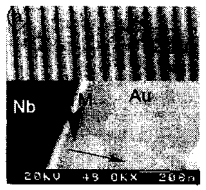


Figure 1: On the left, spectra taken at 1.5 K at different positions above the wide strip of gold. The distance x to the NS interface corresponding to each curve is indicated on the right. The curves have been evenly shifted for clarity. The pseudogap decreases from Δ at the NS interface to 0 at distances larger than 220 nm (upper curve). On the right, (a) Optical microscope picture of the sample. It consists of a 50-nm-thick pattern of self-aligned strips 1 μm wide and 250 μm long of gold and niobium. (b) Scanning electon photography of the sample displaying the small ridge which lie on each side of the gold strip. During one acquisition, the spectra are taken along a line perpendicular to the interface to measure the evolution of the local density of states as a function of the distance to the NS interface.

a phenomenological parameter Γ_{in}.[7] The calculation provides a superconducting gap $\Delta = 1.15$ meV and $\Gamma_{in} = 0.07\Delta$. In contrast spectra taken above Au either over the ridges or the strips can not be fitted using this model. The transition from these two types of spectra allows us to infer the position of the NS interface.

In order to describe our results we need to take into account coherence effects of the quasi-particles inside the normal metal. In the framework of the quasi-classical Green's function formalism, induced correlations between electrons of opposite spin in the normal metal are described by a complex angle $\theta(E, \mathbf{r})$.[2] The LDOS of the quasi-particles n is related to θ by $n(E, \mathbf{r}) = n_0 Re[\cos\theta(E, \mathbf{r})]$. In the dirty limit and in zero magnetic field, $\theta(E, \mathbf{r})$ obeys the 1D-diffusion Usadel equation:[3]

$$\frac{\hbar D}{2}\frac{\partial^2\theta}{\partial x^2} + [iE - \Gamma_{in} - 2\Gamma_{sf}\cos\theta]\sin\theta + \Delta(x)\cos\theta = 0, \qquad (1)$$

where Γ_{sf} and Γ_{in} are the spin-flip and the inelastic scattering rates respectively, $\Delta(x)$ the pair potential. The order parameter is space dependent and obeys a self-consistent equation.[1,2] However, for the sake of simplicity we assume no pair potential in the normal metal ($\Delta_N = 0$) whereas we take Δ equals to its bulk value everywhere in the superconductor. Conditions of continuity, $\theta_{x=0^-} = \theta_{x=0+}$ and spectral current conservation $\sigma_S(\frac{\partial\theta}{\partial x})_{x=0^-} = \sigma_N(\frac{\partial\theta}{\partial x})_{x=0+}$ are imposed at the NS interface which is valid in the case of a perfect electrical contact. This assumption is justified by the careful cleaning of the Nb surface prior to the normal films deposition. However the presence of Ti complicates a lot the actual interface description. We therefore choose to introduce an effective conductivity $\sigma_{N\text{eff}}$ instead of the gold one σ_N.

When $L \gg \xi_N$, the normal metal can be considered as semi-infinite and one recovers the N density of states far away from the superconductor. The boundary condition of eq.(1) on the N side is then $\theta(E, \infty) = \theta_N = 0$. This situation corresponds experimentally to the 1 μm wide strip of Au. In the first set of experiments we scanned above its surface and measured the LDOS as a function of the distance x to the NS interface, located within ± 5 nm. The spectra were taken along the same line perpendicular to the interface. The space dependent

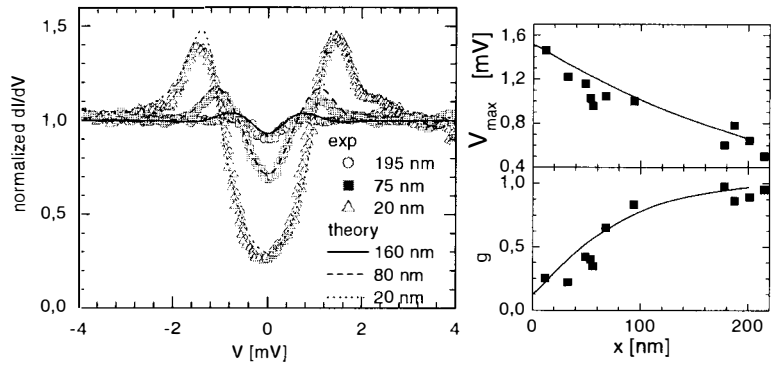


Figure 2: Comparison between theory and experiment. On the left, three measured spectra taken at 20, 75, and 195 nm from the interface are compared to calculated ones at 20, 80, and 160 nm. On the right, the upper curve represents the bias of the peak V_{max} and the lower one represents the normalized zero-bias conductance g as a function to the distance x to the NS interface. The solid lines correspond to the fit.

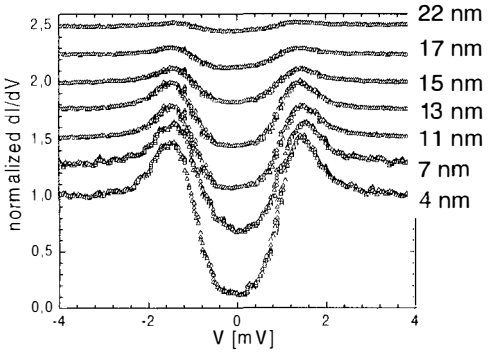
LDOS is plotted in Fig. 1 for x ranging from 12 to 220 nm. We observe a dip around the Fermi energy in $G_V(x) = dI/dV(V,x)$ whose energetic extension decreases as we move away from the superconductor. A zero density of states at the Fermi level is never observed due to pair breaking mechanisms such as spin-flip and inelastic scattering which cannot be neglected at 1.5 K.

We compare our measurements to the convolution of the LDOS calculated from eq. (1) with a Fermi-Dirac distribution. For the superconducting part, we used the value of Δ and Γ_{in} given by the BCS fit above Nb. For the normal part, the rates Γ_{in}, Γ_{sf}, the coherence length ξ_N and the ratio $\sigma_S/\sigma_{N\text{eff}}$ are taken as adjustable parameters. As can be seen on the right, the experimental spectra (points) obtained at distances x=20, 75, 195 nm are very similar to the calculated ones (lines) at distances 20, 80 and 160 nm with $\sigma_S/\sigma_{N\text{eff}} = 4$ and $\xi_N = 70$ nm. For all the spectra, we extracted the bias, V_{max}, of the peak in G_V(upper curve) and the normalized zero bias conductance $g = G_{V=0}/G_{V=4mV}$ (lower curve) as a function of x and compared them to the fits (solid lines). The shape an the spatial evolution of the spectra are well reproduced. Moreover the fits are sensitive in different ways to the two scattering rates. This difference is blurred by the temperature and we can not exclude a possible mixture of the two mechanisms from our calculations. Yet we are able to deduce the spin-flip as the main decohering mechanism and a spin-flip time $\tau_{sf} = \hbar/\Gamma_{sf} = 4$ ps in good agreement with recent experiments.[9]

In the second step of experiments, we have investigated the LDOS over two small ridges of Au which are lying over Nb. The NS interface is now horizontal. Due to the initial slope of their edges, when moving the STM tip horizontally we can change the distance to the NS interface (see on the left of Fig. 3). Therefore we obtain the actual spatial dependence of the LDOS $n(E,x)$ of a normal system with a fixed dimension L.

In this configuration, we find that the spectra show a dip in the DOS. the position of the peaks on each side of this dip is related to the height of the ridge. For a ridge of 20 nm height, we observe that the maximum is located at 1.5 meV (see Fig. 3) whereas in a ridge of height 50 nm, the position of the peak is 0.95 meV.

Theoretically, in a finite diffusive geometry, *i.e.* when $L \simeq \xi_N \gg l_N$, the N side boundary condition of eq. (1) is $\frac{\partial\theta}{\partial x}(E, x = L) = 0$ and a minigap E_g is predicted to appear in the LDOS. E_g is related to the Thouless energy $E_{Th} = \hbar D_N/L^2$. [2] In the smaller ridge, $E_{Th} = 18$ meV$\gg \Delta$, the minigap is limited by the superconducting one. On the contrary,



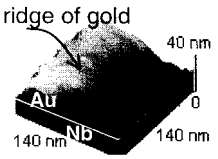


Figure 3: On the right, $140\times140\times140$ nm^3 topographic STM pictures of a gold ridge lying above a niobium strip. On the left, spectra taken between 4 and 22 nm far away from the NS interface above the 22 nm high ridge of gold The curves have been evenly shifted for clarity.

in the bigger ridge, $E_{Th} = 2.8$ meV that yields to a minigap E_g=0.53 meV. Although we measure the position of the peaks and not E_g, our results are consistent with a size dependent minigap. However, because of the uncontroled fabrication of the Au ridges fluctuations of the NS interface transparency might also affect the value of E_g.

In conclusion, we have probed the proximity effect in two different systems. First, we have investigated the LDOS of a semi-infinite normal metal and found space dependent energy spectra as a function of the distance to the NS interface. This behaviour is qualitatively and quantitatively in very good agreement with the pseudo-gap model predicted by the theory of non-equilibrium superconductivity. We have also investigated the local density of states in a confined geometry. In this case we have found a spectral structure which can be related to the Thouless energy.

References

1. C. Bruder, Superconducting Rev. **1**, 261 (1996). A.F. Volkov *et al.*, Physica C **210**, 21-34, (1993). A.A. Golubov, Phys. Rev. B **55**, 1123 (1997).
2. W. Belzig *et al.*, Phys. Rev. B **54**, 9443 (1996).
3. S. Guéron *et al.*, Phys. Rev. Lett. **77**, 3025 (1996).
4. S.H. Tessmer *et al.*, Phys. Rev. Lett. **70**, 3135 (1993);*ibid* Phys. Rev. Lett **77**, 924 (1996).
5. A.D. Truscott *et al.*, Phys. Rev. Lett. **83**, 1014 (1999).
6. For details on the fabrication, see M. Vinet *et al.*, Phys. Rev. B **63**, 165420 (2001).
7. R.C. Dynes *et al.*, Phys. Rev. Lett. **41**, 1509 (1978).
8. K.D. Usadel, Phys. Rev. Lett. **25**, 507 (1970).
9. A.B. Gougam *et al.*, Low Temp. Phys. **118**, 447 (2000).

METAL-INSULATOR TRANSITION IN 2D

ON THE RELATION BETWEEN INTERBAND SCATTERING AND "METALLIC" BEHAVIOR OF TWO DIMENSIONAL HOLES IN GaAs/AlGaAs

Uri Sivan[1], Yuval Yaish[1], Oleg Prus[1], Shye Shapira[2], Ido Ussishkin[3], Evgeny Buchstab[1], Gidi Ben Yoseph[1], and Ady Stern[3]

[1]*Dep. of Physics and Solid State Institute, Technion-IIT, Haifa 32000, Israel.*
[2]*Cavendish Laboratory, Madingly Road, Cambridge CB3 OHE, United Kingdom.*
[3]*Dep. of Condensed Matter Physics, Weizmann Institute of Science, Rehovot 76100, Israel*

The "metallic" regime of holes in GaAs/AlGaAs heterostructures corresponds to densities where two spin split bands exist at a zero magnetic field. Using Landau fan diagrams and weak field magnetoresistance curves we extract the carrier density in each band and the interband scattering rates. The measured inelastic rates depend Arrheniusly on temperature with activation energy similar to that characterizing the longitudinal resistance. The "metallic" characteristics, namely, the resistance increase with temperature, is hence traced to the activation of inelastic interband scattering.

The scaling theory of localization[1] suggests that all states of a non-interacting two-dimensional electron layer are localized for any finite amount of disorder. Non-interacting two dimensional electron gas (2DEG) is hence believed to be insulating in the sense that its resistance always diverges as the temperature, T, approaches zero. This trend is opposite to that characteristic of most 3D metals where for $T \to 0$, the resistance becomes smaller and eventually saturates to a finite value. The insulating nature of 2D systems has been observed in many experiments[2,3] and was a generally accepted dogma until a few years ago, Kravchenko *et al.*[4] discovered that in silicon based high mobility 2DEG at high enough carrier densities, the resistance decreases as $T \to 0$ ("metallic" behavior). The same samples, at lower densities, displayed insulating characteristics and the crossover from positive to negative variation of the resistance with temperature was soon identified as a novel metal-insulator transition.

Since the discovery of Kravchenko *et al.* qualitatively similar dependencies of the resistance upon temperature were observed in two dimensional hole gas (2DHG) in GaAs/AlGaAs heterostructures[5,6,7], SiGe quantum wells[8,9], InAs quantum wells[10] as well as other silicon samples[11]. While the nature of the insulating phase may be roughly understood, the physics of the metallic phase remains obscure. Some suggestions based on the combined role of disorder and Coulomb interaction have been made but no clear picture emerged.

A mere reduction of the resistance with temperature does not necessarily imply delocalization. Within a Drude-like framework it may result from an appropriate temperature dependence of the carrier density, or as suggested by Altshuler and Maslov[12], by a temperature dependent scattering time. The specific mechanism proposed in that reference has been challenged due to the unrealistic impurity concentration needed to account for the magnitude of the effect as well as its specificity to certain systems.

Here we provide experimental evidence that indeed suppression of scattering with decreasing T is responsible for the metallic characteristics of 2DHG in GaAs/AlGaAs

heterostructures. The scattering mechanism, interband Coulomb scattering between two spin-orbit split bands, is very different from the one proposed by Altshuler and Maslov[12]. The correlation between the existence of two conducting bands and "metallic" behavior was first put forward by Pudalov[13]. It has recently been convincingly substantiated by Papadakis *et al.*[14]. We find the same correlation but go beyond that and prove that the characteristic dependence upon temperature, $\rho_{xx}(T)=\rho_{xx}(0)+\alpha\exp(-T_0/T)$ (T_0 and α are some constants) follows from a similar dependence of the intra and interband inelastic scattering rates upon temperature.

Spin-orbit split bands in GaAs/AlGaAs heterostructures have been extensively studied both theoretically[15,16] and experimentally[17,18]. The two bands are degenerate up to a certain energy where they split and acquire very different effective masses. Thus, above a threshold density, current is carried by two bands as reflected in slope variation in the corresponding Landau fan diagram[17] or in the appearance of a second frequency in Shubnikov de Haas measurements[18]. Using either method, the hole densities in the two bands, p_1, p_2 can be extracted[18] and fig. 1 depicts them as a function of the total density, p_{total}. For a total density below $1.6\times10^{11}\,cm^{-2}$ the bands are degenerate. For higher densities they split and for a total density above $2.8\times10^{11}\,cm^{-2}$ practically all additional carriers go to the heavier and less mobile band. The inset to fig. 1 depicts a characteristic Shubnikov - de Haas curve and demonstrates the existence of two sets of oscillations corresponding to the two bands. The data were taken using a high mobility ($330{,}000\,cm^2/V\cdot s$ at $100\,mK$) 2DHG with both front and back gates.

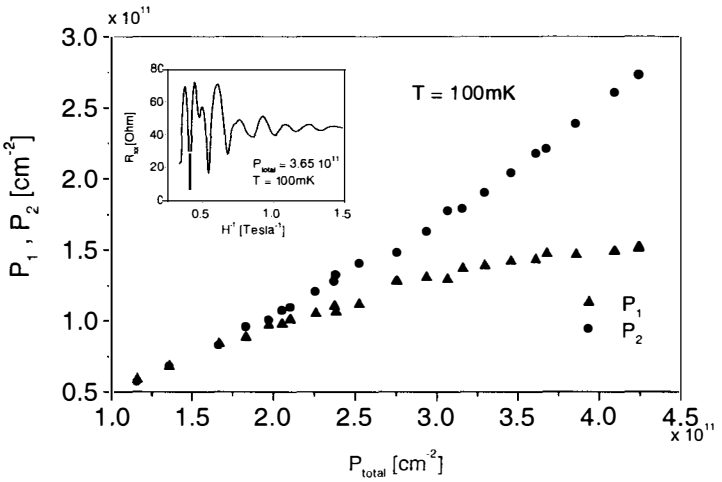


Fig. 1 – Carrier density in the two spin-orbit split bands vs. total carrier density. Inset – typical Shubnikov – de Haas trace used to extract the two carrier densities.

The simultaneous transport of two types of carriers with different mobilities and densities is also manifested in our system by a weak field classical positive

magnetoresistance[19]. A set of resistance curves for $p_{total} = 4.25\times10^{11}\,cm^{-2}$, $p_1 = 1.52\times10^{11}\,cm^{-2}$, $p_2 = 2.73\times10^{11}\,cm^{-2}$ and different temperatures is depicted in the inset to fig. 2. Measurements as a function of density show that the positive magnetoresistance at weak fields appears when the total density exceeds the split off density, namely, when the two bands acquire different masses and mobility. It then grows larger with density, as the bands deviate further. The Lorentzian shaped magnetoresistance expected from two band transport is obtained by subtracting the weak parabolic negative magnetoresistance attributed to Coulomb interactions[20] from the full magnetoresistance curve. The resulting two-band contribution to the magnetoresistance is depicted in fig. 2. Note the excellent agreement with the predicted Lorentzian shape. Below $T \approx 0.6K$ the resistance is practically independent of T while for temperatures above $\approx 2K$ the Lorentzian is hardly visible. The suppression of the classical two band magnetoresistance results from interband scattering. At low temperatures this scattering is mainly elastic. As the temperature is increased, inelastic scattering commences, the drift velocities of carriers in the two bands gradually approach each other, and the magnetoresistance is consequently diminished.

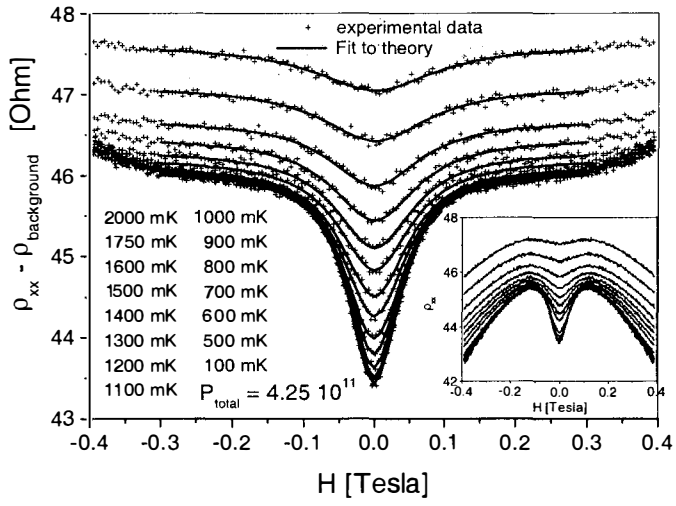


Fig. 2 – Classical two band magnetoresistance after subtraction of the interaction contribution. The solid lines correspond to the theory given by eq. 2. Inset – Full magnetoresistance curves. The parabolic negative magnetoresistance results from Coulomb interaction in the diffuson channel.

The data presented in figs. 1 and 2 can be used to extract the interband scattering rates. To that end, the standard two band transport formulae should be generalized to include interband scattering. The starting point is coupled Drude equations for transport in the two bands[7]

$$\begin{bmatrix} \varepsilon_x \\ \varepsilon_y \\ \varepsilon_x \\ \varepsilon_y \end{bmatrix} = \begin{bmatrix} S_1 & -HR_1 & Q & 0 \\ HR_1 & S_1 & 0 & Q \\ Q & 0 & S_2 & -HR_2 \\ 0 & Q & HR_2 & S_2 \end{bmatrix} \begin{bmatrix} J_{1x} \\ J_{1y} \\ J_{2x} \\ J_{2y} \end{bmatrix}. \qquad (1)$$

Setting $J_{1y} = J_{2y} = 0$ one obtains for the longitudinal resistance

$$\rho_{xx}(H) \equiv \frac{\varepsilon_x}{J_{1x} + J_{2x}} = \rho_{xx}(H \to \infty) + \frac{L}{1 + (H/W)^2} \qquad (2)$$

$$\rho_{xx}(H \to \infty) = \frac{R_2^2 S_1 + R_1^2 S_2 - 2QR_1R_2}{(R_1 + R_2)^2}; \quad W = \frac{S_1 + S_2 + 2Q}{R_1 + R_2}$$

$$L = -\frac{[R_1(S_2 + Q) - R_2(S_1 + Q)]^2}{(S_1 + S_2 + 2Q)(R_1 + R_2)^2}.$$

Here, ε and H are the electric and magnetic fields, respectively, R_1, R_2 are the corresponding Hall coefficients, and J_1, J_2 are the current densities in the two bands. The diagonal conductances, S_1, S_2 pertain to scattering (elastic and inelastic) within each band while Q accounts for interband scattering. The latter processes include carrier transfer from one band to the other as well as drag-like processes where one particle from one band scatters off a particle in the other band and both carriers maintain their bands.

As the temperature is increased, interband scattering is enhanced, S_1, S_2, Q grow, and the Lorentzian broadens and reduced in height, in agreement with the experimental data. The hole densities in the two bands, and hence R_1, R_2 are known from fig. 1. Fitting the data depicted in fig. 2 to eq. 2, one obtains $\rho_{xx}(H \to \infty)$, W, and L which are in turn used to extract S_1, S_2, and Q as a function of temperature and density. The Shubnikov-de Haas oscillations combined with the low field magnetoresistance, hence provide a unique opportunity to directly measure inter and intraband scattering. The results of such analysis are shown in fig. 3 where S_1, S_2, Q and $\rho_{xx}(H = 0)$ are depicted vs. T for the same total density as in fig. 2. At low temperatures, all these quantities saturate to some residual values which we attribute to inter and intraband elastic scattering. As the temperature is increased, inelastic scattering commences and these quantities grow.

The remarkable and central result of our work is the observation that the inelastic scattering rates follow the same temperature dependence as $\rho_{xx}(H = 0)$, namely, $S_i(T) = S_i(0) + \alpha \exp(-T_0/T)$; $Q(T) = Q(0) + \exp(-T_0/T)$ where $S_i(0), Q(0)$ are due to elastic scattering. Remarkably, the characteristic temperature, T_0, is almost identical for all these quantities, including $\rho_{xx}(H = 0)$! For S_1 and S_2 we find $T_0 = 5K$, for Q, $T_0 = 4.8K$, and for $\rho_{xx}(H = 0)$, $T_0 = 4.3K$.

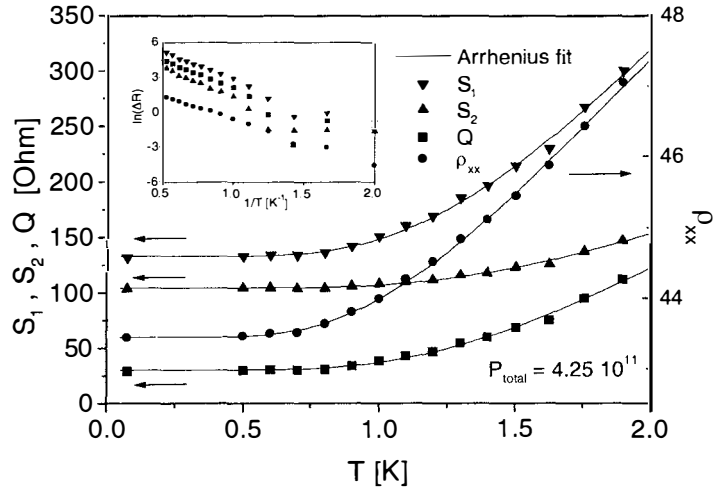


Fig. 3 – The various resistance matrix elements and ρ_{xx} vs. temperature. Inset – the same in a log vs. $1/T$ plot. The similarity in temperature dependence of the various matrix elements and the longitudinal resistance implies that ρ_{xx} increases with T due to inelastic interband scattering.

Similar correlations are found for different total densities in the "metallic" regime. Our results hence strongly suggest that the universal Arrhenius temperature dependence of the resistance in the "metallic" regime merely reflects the increase of inelastic scattering with temperature and probably have nothing to do with phase transition into a delocalized state.

As expected, the light band (#1) is more susceptible to scattering and hence $\alpha(S_1) > \alpha(S_2)$. Note the inelastic contributions to S_1 and Q at $T = 2K$ are larger than their elastic counterparts. Moreover, they are all larger than ρ_{xx}, indicating the two bands are strongly coupled by scattering. Eventually, for $T > 2K$ the coupling equilibrates the two drift velocities and the classical magnetoresistance is fully suppressed. However, the resistance, ρ_{xx}, continues to grow. The latter growth results from inelastic interband scattering that affects the resistance even when the bands are already strongly coupled. In fact, in some of the data published in the literature, the Arrhenius dependence of the resistance is not accompanied by the Lorentzian magnetoresistance, probably indicating strong interband scattering.

In Summary. We have shown experimentally that the "metallic" behavior of the resistance of holes in GaAs/AlGaAs heterostructure results from inelastic scattering between two spin-orbit split bands. The measured low T scattering rates between electrons in the two bands depend Arrheniusly on temperature with practically the same activation energy as the longitudinal resistance. The absence of a substantial power law contribution to the inelastic scattering remains to be explained.

Acknowledgements
Research was partially supported by the Israeli Science Foundation, the Binational Science Foundation Israel-US, and by DIP. Discussions with M. Reznikov are gratefully acknowledged.

References

[1]E. Abrahams *et al.*, *Phys. Rev. Lett.* **42**, 673 (1979).
[2] D. J. Bishop *et al.*, *Phys. Rev. Lett.* **44**, 5737 (1980).
[3]M. J. Uren *et al.*, *J. Phys. C: Solid State Phys.* **14**, 5737 (1981).
[4] S. V. Kravchenko *et al.*, *Phys. Rev.* **B50**, 8039 (1994).
[5] Y. Hanin *et al.*, *Phys. Rev. Lett.* **80**, 1288 (1998).
[6] M. Y. simmons *et al.*, *Phys. Rev. Lett.* **80**, 1292 (1998).
[7] Y. Yaish *et al.*, *Phys. Rev. Lett.* **84**, 4954 (2000).
[8] P. T. Koleridge *et al.*, *Phys. Rev.* **B56**, R12764 (1997).
[9]J. Lam *et al.*, *Phys. Rev.* **B56**, R12741 (1997).
[10] S. J. Papadakis and M. Shayegan, *Phys. Rev.* **B57**, R15068 (1998).
[11] D. Popovic *et al.*, *Phys. Rev. Lett.* **79**, 1543 (1997).
[12] B. L. Altshuler and D. Maslov, *Phys. Rev. Lett.* **82**, 145 (1999).
[13]V. M. Pudalov, *Pis'ma Zh. Eksp. Teor. Fiz.* **66**, 168 (1997) [*JETP Lett.* **66**, 175 (1997)].
[14] S. J. Papadakis *et al.*, *Science* **283**, 2056 (1999).
[15] D. A. Broido and L. J. Sham, *Phys. Rev.* **B31**, 888 (1985).
[16] U. Ekenberg and M. Altarelli, *Phys. Rev.* **B32**, 3721 (1985).
[17]H. L. Stormer *et al.*, *Phys. Rev. Lett.* **51**, 126 (1983).
[18] J. P. Lu *et al.*, *Phys. Rev. Lett.* **81**, 1282 (1998).
[19] N. W. Ashcroft and D. D. Mermin, *Solid State Physics*, Harcourt Brace College Publishers (1976), p. 240.
[20] M. A. Paalanen *et al.*, *Phys. Rev. Lett.* **51**, 2226 (1983); K. K. Choi et al., *Phys. Rev.* **B33**, 8216 (1986).

Microscopic Structure of the Metal-Insulator Transition in Two-Dimensions[a]

S. Ilani, A. Yacoby, D. Mahalu and Hadas Shtrikman
Braun Center for Submicron Research, Dept. of Condensed Matter Physics, Weizmann Institute of Science, Rehovot 76100, Israel.

A single electron transistor is used as a local electrostatic probe to study the underlying spatial structure of the metal-insulator transition in two dimensions. The measurements show that as we approach the transition from the metallic side, a new phase emerges that consists of weakly coupled fragments of the two-dimensional system. These fragments consist of localized charge that coexists with the surrounding metallic phase. As the density is lowered into the insulating phase, the number of fragments increases on account of the disappearing metallic phase. The measurements reveal that the metal-insulator transition is a result of the microscopic restructuring that occurs in the system.

The ground state of electronic systems is found to change from metallic to insulating with increasing disorder. Disorder localizes the electronic wave functions and limits their ability to screen mutual Coulomb interactions. By reducing the density of carriers in such systems, both the effects of disorder and Coulomb interactions increase, thereby driving the system from metallic to insulating. Until recently, a metal-insulator transition (MIT) was believed to exist only in three-dimensional systems, as only insulating behavior was predicted in lower dimensions [1]. However, recent transport experiments have revealed the same phenomena in two-dimensional (2D) systems [2,3]. Despite extensive knowledge gained in recent experiments on the macroscopic characteristics of the 2D MIT phenomena, its microscopic properties remain unknown. We report on local compressibility measurements that unravel the microscopic structure that underlies the MIT in 2D.

Compressibility reflects the ability of an electronic system to screen external charges. When an external charge is brought in close proximity to the surface of a metal, mobile electrons accumulate in its vicinity to screen it. A system that cannot redistribute its charge is, hence, incompressible. The electronic compressibility, therefore, provides a primary tool to understand the type of ground state that is formed by electrons. We used a single electron transistor (SET) to measure the local compressibility of a two-dimensional hole gas (2DHG) across the MIT. We use GaAs/AlGaAs samples having a 2DHG formed 400nm beneath the surface. An additional 400nm of AlGaAs barrier material separates the 2DHG from a back gate, which enables us to tune the density of holes across the MIT [4]. The 2DHG is accumulated solely by the back gate, and no intentional doping is present in the structure. The transport properties of these structures have been studied extensively, and a clear MIT phenomenology is observed [5]. An aluminum SET positioned on the surface of the structure is used to measure the local chemical potential [6,7,8], μ, as well as the local compressibility, $\kappa = n^{-2}[\delta n/\delta\mu]$ (n being the average density of holes), at dilution fridge temperatures (50mK).

Looking at the behavior of μ as a function of the hole density (Fig. 1A), it seems that starting from the metallic side, μ increases as the density is lowered - a behavior that corresponds to negative compressibility [9,10]. This behavior persists down to the critical density, n_c, which is determined by transport measurements [11]. When the density is further lowered, μ starts to decrease rapidly, indicating a positive and vanishing compressibility. As was described in previous works [4,12], this change of sign of the compressibility constitutes the macroscopic thermodynamic signature of the MIT [13]. However, in our previous structures [4], charge traps have limited our ability to determine the microscopic properties, and only the macroscopic thermodynamic behavior was determined. Here, we used a structure design in which the 2D carriers are accumulated

[a] Reprinted with permission from Science, **292**, 1354(2001). Copyright ©2001 American Association for the Advancement of Science.

using a gate (MOSFET principle) and not by intentional doping. This allows us to avoid the presence of charge traps and as a result enabled us to resolve the microscopic evolution of the MIT.

The microscopic behavior emerges as an intricate fine structure in the compressibility that is superimposed on the average macroscopic behavior. Two generic types of microscopic structures are apparent in the measured signal (Fig. 1). The larger structure is a staircase decrease of μ on the insulator side (arrows in Fig. 1A). However, a much finer structure appears when we directly measure the derivative of μ with respect to the back-gate voltage, $\delta\mu/\delta V_{BG}$ (Fig. 1B). This structure assumes the form of very sharp spikes that are superimposed on a smooth background. Because the back gate voltage controls the average density, $\delta\mu/\delta V_{BG}$ is a direct measure of the local inverse compressibility, $n^2\delta\mu/\delta n$. The emergent spikes in $\delta\mu/\delta V_{BG}$ are the main focus of this work, as they correspond to microscopic processes that happen in the 2DHG near the MIT and their spectrum captures the fingerprint of these processes. These spikes commence already in the metallic phase, where a relatively sparse spectrum of negative spikes

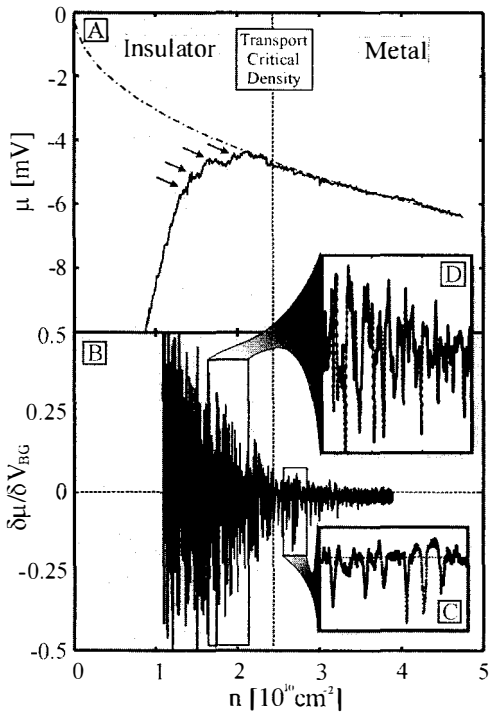


Figure 1: (A) Density dependence of the local chemical potential, μ, across the MIT. To measure this quantity, we deposited a metallic single electron transistor (SET) 400nm above the 2DHG. By monitoring the current through the SET, we can deduce the local electrostatic potential, which directly determines the local , given that the sample is in equilibrium [4]. A transport measurement on the same device determines the MIT critical density, n_c (dashed line). Above this density, $\mu(n)$ follows the prediction of the Hartree-Fock theory multiplied by 1.8 (dashed-dotted line). A rich reproducible microscopic structure is observed when we measure the derivative with respect to the back gate voltage, $\delta\mu/\delta V_{BG}$, using AC-lockin techniques (B). This structure assumes the form of sharp spikes (a prototype spike is marked in gray), which emerge already on the metallic side (C) but becomes more dense and intense as the system crosses to the insulator side (D). Identical features of the spikes spectrum have been observed in measurements of several other devices. In each of these devices, a different spike spectrum was observed, being a fingerprint of the specific local disorder.

is observed (Fig. 1C). As the density is lowered across the transition, this spectrum becomes richer - both the number of spikes and their amplitudes increase substantially (Fig. 1D). Once deep in the insulating side, the spectrum is made up of many positive and negative overlapping spikes. The appearance of spikes superimposed on the continuous $\delta\mu/\delta V_{BG}$ signal already hints at the presence of a new phase that develops as we approach the MIT.

A spike in the local compressibility signifies a discrete screening event. Such a process is rather unexpected if one assumes that the 2DHG can smoothly redistribute its charge. However, within various theories of the MIT, there are several fundamental processes that might break the smooth screening capability on the microscopic level. One set of theories [1,14,15] suggests that strongly localized states must appear near the apparent MIT. Each such state can either be empty or hold a single electron. In this scenario the sharp transition between the two situations will cause an abrupt jump in the local μ and a spike in $\delta\mu/\delta V_{BG}$. Another set of theories [16,17] claim that the MIT results from percolation in the electron liquid. In this scenario, puddles of charge are formed in the percolation landscape. The puddles can be charged only discretely - one electron at a time - which results in having only a discrete set of back gate voltages where the system is compressible. Because in both scenarios the system is incompressible between the discrete charging events, the spikes in $\delta\mu/\delta V_{BG}$ are expected to be superimposed on an incompressible background ($\delta\mu/\delta V_{BG} = 1$). This is not observed experimentally (Fig. 1C), where the observed background has very high compressibility ($\delta\mu/\delta V_{BG} \ll 1$). This suggests the coexistence of two phases: one with continuous response producing the compressible background and one with discrete response producing the spikes - namely, a two-liquid behavior. One can see (Fig. 1D) that as the system deepens into the insulating regime the background $\delta\mu/\delta V_{BG}$ increases toward the incompressible value ($\delta\mu/\delta V_{BG} = 1$), whereas the number of spikes and their amplitudes increase. This behavior demonstrates that as the density of holes is reduced, the discrete phase grows at the expense of the coexisting compressible phase.

The above models are only suggestive candidates for the nature of the discrete phase and clearly, more complicated models, such as electron crystallization [18,19,20,21,22,23], should also be considered. However, the essential feature that all the possible descriptions would share is the local reorganization of charge, a necessary condition for the appearance of spikes. This locality implies that the onset of spikes must be accompanied by a spatial structure. We now demonstrate how this spatial structure is resolved experimentally even with a detector that is fixed at a single point. The idea is to use the SET not only as an electrometer but also as a top gate. In contrast to the back gate, which affects the density uniformly in space, the top gate influences the density in a manner proportional to the distance from its edge. A spike in Fig. 1 occurs when a charging event crosses the Fermi energy. This happens at a certain local density. Changing the back gate voltage by δV_{BG} shifts this event from the Fermi energy. However, one can restore the local density and hence shift the event back to the Fermi energy by applying a compensating top gate voltage δV_{TG}. The further away the event is from the SET, the larger is δV_{TG} that is required in order to shift it back. Each charging event is, therefore, characterized by a "charging line" in the plane of $[V_{BG}, V_{TG}]$ (Fig. 2). The slope of the charging line, $s = -\frac{\delta V_{TG}}{\delta V_{BG}}$, determines the position of the event in the 2DHG: An event happening just below the SET would have the smallest slope, $s_{\min}$. The further away the event is from the SET, the more vertical its slope will be [25].

Figure 2 shows how the overlapping spectrum of Fig. 1D disentangles into separate events, each having a different slope and amplitude. The span of slopes reflects the different positions of the events in the 2DHG. The smallest slope observed is $s_{\min}^{\exp} = 2.26$, which corresponds to an event that occurs just under the SET [25]. The largest slope observed, $s_{\max}^{\exp} = 6.9$, corresponds to an event occurring $1.1\mu m$ away from the SET and defines the measurement horizon. This horizon is in good agreement with what is expected for a SET situated $400nm$ above the 2DHG. A clear correlation can be seen between the position of an event and its amplitude - the closer

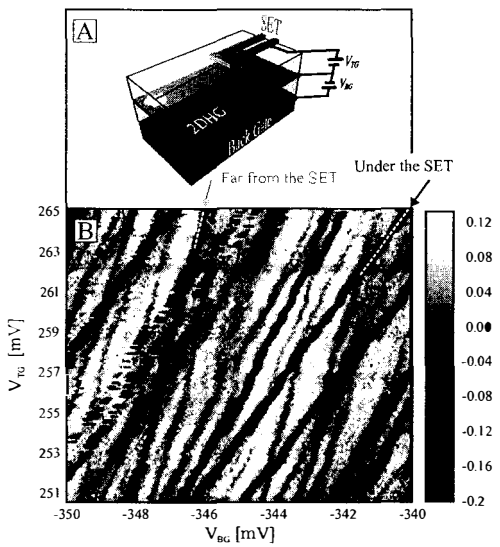


Figure 2: (A) Scheme of the measurement circuit, which is used to identify the position of events within the 2DHG. (B) Color map representing the measured value of the derivative $\delta\mu/\delta V_{BG}$ as function of the back-gate voltage, V_{BG}, and top-gate voltage, V_{TG}. Each discrete event in the 2DHG gives rise to a line in this plot whose slope reflects the distance of the event from the SET (see text). Arrows mark the lines that correspond to two typical events, one that occurs directly under the SET and one that occurs far from the SET.

it is to the SET, the stronger it appears. As the slopes can be measured rather accurately, we are able to position the events within the 2DHG with an accuracy of up to ~$20nm$.

Our microscopic measurements, therefore, reveal that as the density of holes approaches the critical density from the metallic side, the 2DHG fragments into localized charge configurations that are distributed in space. The rather abrupt appearance of these events near n_c suggests that this fragmentation is the microscopic signature of the MIT. However, their simultaneous appearance in large numbers masks our ability to determine their size, mutual interactions, and the quantum mechanical probability for charge tunneling among the different configurations. To unravel these properties, we use the SET (top gate) to form a density gradient in its vicinity. As we increase the bulk density using the back gate, we reduce it locally using the SET top gate. This maintains the local density under the SET at a constant value and generates a density gradient surrounding the SET. Because the spikes appear only at densities that are comparable to or smaller than n_c, we can continuously reduce the area from which the spikes appear and hence their number.

The result of such a measurement is shown in Fig. 3. We plot our result in a coordinate system that is rotated to reflect the independent control over the density under the SET, n_{local}, and far away from the SET, n_{bulk}. In this plot, horizontal charging lines correspond to events that occur very far from the SET, and vertical charging lines correspond to local events, occurring directly under the SET. As we go from the bottom of the figure to its top, we continuously evolve from a homogenous system, namely, $n_{bulk} = n_{local}$, to a system with a large density gradient, $n_{bulk} \gg n_{local}$. Noticeably, distant events (horizontal lines) are affected by n_{bulk}, and as this density exceeds n_c, most of them disappear rather abruptly, reflecting once more the fragmentation of the 2D system at the MIT. At the top of the scan, we are, therefore, left with only a few local charging events (vertical lines), which allow us to focus on the nature of the interactions between them. The coupling among the different charge configurations is

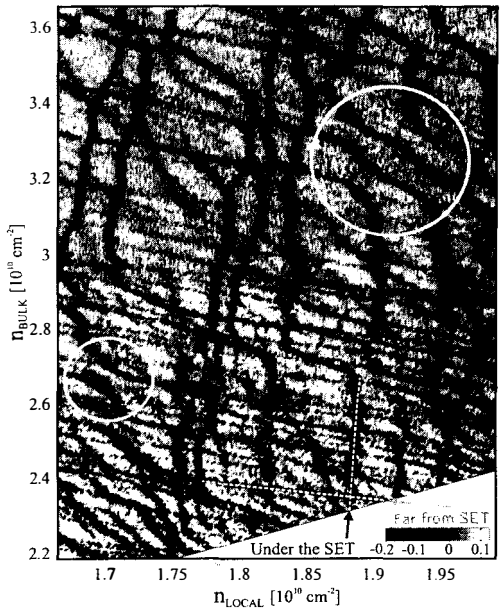


Figure 3: Evolution of discrete events in response to an induced density gradient. Here, as in Fig. 2, the derivative $\delta\mu/\delta V_{BG}$ is measured as function of V_{BG} and V_{TG}; however, now substantially higher voltages are applied so the density profile in the 2DHG is modified. The coordinate system is rotated with respect to Fig. 2: The horizontal axis corresponds to the density just below the SET, n_{local}, and the vertical axis corresponds to the density far away from the SET, n_{bulk}. In this coordinate system, vertical (horizontal) charging lines correspond to local (distant) charging events. The circles mark avoided crossing between the charging lines that demonstrate the existence of tunneling amplitude between relatively distant charge configurations.

apparent where the corresponding charging lines cross. Many encounters of avoided crossings are apparent, implying the existence of tunneling between the corresponding events. Encircled in this figure are large tunneling gaps that connect configurations whose spatial separation exceeds $1\mu m$. As only nearly overlapping configurations are mixed by tunneling (which is otherwise exponentially suppressed), this suggests that certain configurations extend more than $1\mu m$ in space - an order of magnitude more than the electron wavelength at this density.

As we go slightly deeper into the insulating side the crossing of charging lines assumes a new form, which reflects the Coulomb interactions between events (Fig. 4). Here the slopes of the charging lines flip abruptly at two separate corners that are interconnected by a new charging segment. A typical vertex is drawn at the top of the figure. The black/gray charging lines correspond to charging of two events that are depicted by black and gray. Together with the new charging segment, they separate the four possible configurations of the two sites. The two sites can be charged with the use of the back gate in three different cycles, marked in Fig. 4 as A, B, and C. In cycle A, the gray charging line is crossed before the black charging line, and, therefore, the gray site is charged before the black site. Because the black and gray charge configurations repel electrostatically, when the gray site is charged after the black site, as in cycle B, its energy is pushed upward. This is manifested in the parallel shift of the gray line to higher back gate voltages. Cycle C forms the most complicated charging sequence. It starts with the charging of the gray site, followed by an abrupt reorganization of the system in which the charge jumps from the gray site to the black site and finally a recharging of the gray site. The observed reorganization of charges signifies the importance of interactions in the ground

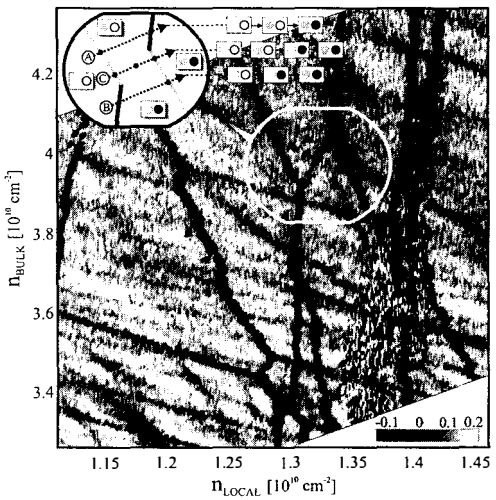


Figure 4: Measured electrostatic interaction between events. This scan is similar to that in Fig. 3 but is done for local densities that are deeper in the insulator side. In this region, many encounters between charging lines assume a new form of crossing, which reflects the electrostatic interactions between events. The inset describes schematically a typical vertex. The colors of the charging lines (black/gray) associate them with the corresponding charging sites. The dashed lines labeled A, B, and C describe three different charging cycles of the two sites as function of the back gate voltage.

state of the system near the MIT - a charging event will always be dressed by the reorganization of the system in nearby sites [26].

Acknowledgments

We benefited from discussions with M. Brodsky, A. M. Finkel'stein, Y. Imry, Y. Meir, A. Stern, C. M. Varma, and N. B. Zhitenev. This work was supported by the MINERVA Foundation, Germany.

References

1. E. Abrahams, P. W. Anderson, D. C. Licciardello, and T. V. Ramakrishnan, Phys. Rev. Lett. **42**, 673 (1979).
2. S. V. Kravchenko, G. V. Kravchenko, J. E. Furneaux, V. M. Pudalov, and M. D'Iorio, Phys. Rev. B **50**, 8039 (1994).
3. For a comprehensive review of the MIT in 2D, see E. Abrahams, S. V. Kravchenko, and M. P. Sarachik, Rev. Mod. Phys. **73**, 251 (2001).
4. S. Ilani, A. Yacoby, D. Mahalu, and H. Shtrikman, Phys. Rev. Lett. **84**, 3133 (2000).
5. Y. Hanein, U. Meirav, D. Shahar, C. C. Li, D. C. Tsui, and H. Shtrikman, Phys. Rev. Lett. **80**, 1288 (1998).
6. M. J. Yoo, T. A. Fulton, H. F. Hess, R. L. Willett, L. N. Dunkleberger, R. J. Chichester, L. N. Pfeiffer, and K. W. West, Science **276**, 579 (1997).
7. Y. Y. Wei, J. Weis, K. V. Klitzing, and K. Eberl, Phys. Rev. Lett. **81**, 1674 (1998).
8. N. B. Zhitenev, T. A. Fulton, A. Yacoby, H. F. Hess, L. N. Pfeiffer, and K. W. West, Nature **404**, 473 (2000).
9. J. P. Eisenstein, L. N. Pfeiffer, and K. W. West, Phys. Rev. Lett. **68**, 674 (1992).

10. S. Shapira, U. Sivan, P. M. Solomon, E. Buchstab, M. Tischler, and G. B. Yoseph, Phys. Rev. Lett. **77**, 3181 (1996).
11. The critical density was determined by simultaneous measurement on the same device, with the same technique as in [4].
12. S. C. Dultz and H. W. Jiang, Phys. Rev. Lett. **84**, 4689 (2000).
13. A possible explanation of this behavior, which relates it to effects of disorder, has been given by Si and Varma [Q. Si and C. M. Varma, Phys. Rev. Lett. **81**, 4951 (1998)].
14. B. L. Altshuler, D. L. Maslov, and V. P. Pudalov, cond-mat **0003032**,(2000).
15. A. L. Efros and B. I. Shklovskii, J. Phys. C **8**, L49 (1975).
16. S. He and X. C. Xie, Phys. Rev. Lett. **80**, 3324 (1998).
17. Y. Meir, Phys. Rev. Lett. **83**, 3506 (1999).
18. An electron crystal, which is suggested by several theories [19,20,21,22,23] to appear at the MIT, might produce both continuos and discrete behaviors. Generally, the crystal deforms continuously to screen an external potential, producing a continuous response. However, occasionally, electrons collectively reorganize around pinning centers [24], causing an abrupt reduction of energy and hence a spike in $\delta\mu/\delta V_{BG}$. In this scenario, a single spike corresponds to a many-electron charging event, rather than a single-electron charging, as in previous scenarios.
19. B. Tanatar and D. M. Ceperley, Phys. Rev. B **39**, 5005 (1989).
20. S. T. Chui and B. Tanatar, Phys. Rev. Lett. **74**, 458 (1995).
21. G. Benenti, W. Xavier, and J. L. Pichard, Phys. Rev. Lett. **83**, 1826 (1999).
22. S. Chakravarty, S. Kivelson, C. Nayak, and K. Voelker, Philos. Mag. B **79**, 859 (1999).
23. J. Yoon, C. C. Li, D. Shahar, D. C. Tsui, M. Shayegan, Phys. Rev. Lett. **82**, 1744 (1999).
24. I. M. Ruzin, S. Marianer, B. I. Shklovskii, Phys. Rev. B **46**, 3999 (1992).
25. The value of $s_{\min}$ could be estimated from the ratio of capacitances between the 2DHG and the top and back gates to be $s_{\min} = 2.3$.
26. M. Pollak and M. Ortuno, in *Electron-Electron Interactions In Disordered Systems*, Vol. 10 of *Modern Problems in Condensed Matter Sciences*, edited by A. L. Efros and M. Pollak (North-Holland, Amsterdam, 1985), pp. 287–408.

FERMI-LIQUID BEHAVIOUR OF 2D SYSTEMS NEAR THE CROSSOVER FROM 'METAL' TO 'INSULATOR'

A.K.SAVCHENKO[1], Y.Y.PROSKURYAKOV[1], S.S.SAFONOV[1], S.H.ROSHKO[1], M. PEPPER[2], M.Y.SIMMONS[2], D.A.RITCHIE[2], A.G.POGOSOV[1,3], Z.D.KVON[3]

[1]*School of Physics, University of Exeter, Stocker Road, Exeter, EX4 4QL, U.K.*

[2]*Cavendish Laboratory, University of Cambridge, Madingley Road, Cambridge CB3 0HE, U.K.*

[3]*Institute of Semiconductor Physics, Siberian Branch Russian Academy of Sciences, 630090 Novosibirsk, Russia*

We study the applicability of the Fermi-liquid description to the crossover from 'metallic', $dR/dT > 0$, to 'insulating', $dR/dT < 0$, behaviour of the 2DHG and 2DEG. For a low-density 2DHG, we have seen that the negative magnetoresistance near the crossover is described by weak localisation even when the interaction parameter approaches $r_s \sim 30$, with the dephasing rate dominated by hole-hole scattering in the regime of a clean Fermi-liquid. Experiments on a 2DEG in *vicinal* Si MOSFETs have revealed that the crossover has a classical origin and is caused by a narrow impurity band at the interface.

1 Introduction

Opinions about the origin of the unexpected in 2D change, with increasing carrier density p, of the temperature dependence from 'insulating' ($d\rho/dT < 0$) to 'metallic' ($d\rho/dT > 0$), are polarised. This crossover has been seen in low-density clean 2D systems where the ratio of the Coulomb to Fermi energies $r_s = U/E_F \propto m^*/p^{1/2}$ is large [1]. Thus it was suggested that interactions play a significant role and the Fermi-liquid approach is not valid [2]. At the same time, there are several models where the crossover is explained conventionally [3,4].

In this work we examine the behaviour near the crossover of two 2D systems: a) holes in GaAs/AlGaAs, and b) electrons in Si transistor structures. On 2DHG structures, where the crossover occurs at a large value of r_s, we study the magnetoresistance and analyse it in terms of weak localisation (WL). As the WL theory has been derived for $r_s \ll 1$ [5], it provides a good test for a Fermi-liquid and also presents information about the interactions between the carriers. There have already been indications that WL and weak hole-hole interaction (HHI) effects do not show anomalies up to $r_s \sim 10 - 14$ [6,7]. As our structures have higher mobility and lower densities ($p = 1.17 \times 10^{10}$ cm^{-2}, $r_s \sim 29$), we expected to see deviations from Fermi-liquid behavior.

All previous studies of the crossover in the 2DEG in Si MOSFETs were performed on electrons on the (100) Si surface. To see whether the crossover depends on the surface orientation, we have studied the 2DEG on a *vicinal* Si surface, which is slightly tilted to the (100) plane.

2 Magnetoresistance of the 2DHG near the crossover

The experiments have been performed on a heterostructure with a peak mobility of $\mu_p = 6.5 \times 10^5$ cm^{2}V^{-1}s^{-1} at $T = 45$ mK, formed on a (311)A GaAs substrate, where the 2DHG is separated from the Si doped layer by a 500Å spacer. The hole density is varied by the front gate voltage in the range of r_s from 10 to 29 (with effective mass m^* taken as 0.38 m_0).

Fig. 1a shows a typical temperature dependence of the longitudinal resistivity. In the crossover region, where r_s varies from 23 to 29, negative perpendicular magnetoresistance (NMR) is seen, Fig. 1b, which increases with decreasing p (determined from the Shubnikov-de Haas

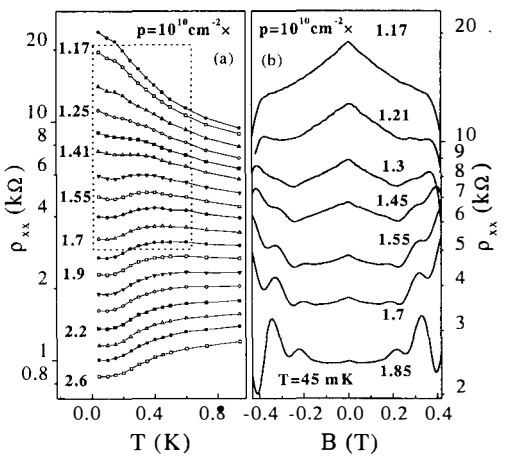


Figure 1: (a) Temperature dependence of the resistivity at different hole densities. The dashed box encloses the range of NMR study. (b) NMR at $T = 45$ mK, for different hole densities.

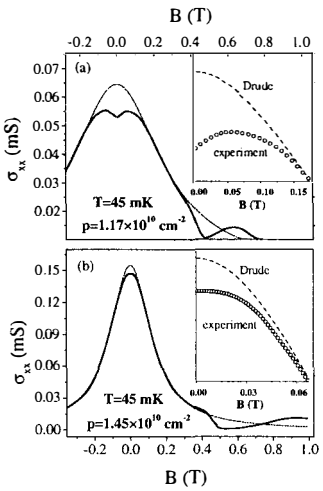


Figure 2: (a,b) Experimental conductivity $\sigma_{xx}(B)$ shown together with Drude conductivity (the insets present zoomed-in regions).

(SdH) effect). The SdH oscillations are seen on both sides of the crossover, which is a clear indication of the presence of the Fermi surface in the whole range of hole densities.

Analysis of the WL magnetoresistance in high-mobility structures is not straightforward. The conventional theory is based on the diffusion approximations and restricted by the range of magnetic fields $B < B_{tr}$, where $B_{tr} = \hbar/4De\tau$ is the 'transport' magnetic field, D is diffusion coefficient and τ is momentum relaxation time. Physically, this means that no negative magnetoresistance is expected for $B > B_{tr}$ when the magnetic length L_B becomes smaller than the mean free path l. In our samples B_{tr} ranges from 0.003 to 0.08 T, however the NMR is seen up to $B \sim 0.2$ T where SdH oscillations start. The theory of WL for $B > B_{tr}$ has also been developed [8], although no experimental test of it has yet been performed. Theories of WL discuss the positive magnetoconductivity $\triangle\sigma^{WL}(B) = \delta\sigma_{xx}(T,B) - \delta\sigma_{xx}(T,0)$, where $\delta\sigma_{xx}(T,B)$ is a negative correction to the classical (Drude) conductivity. To analyse $\triangle\sigma^{WL}(B)$ in a high-mobility system, one should take into account the magnetic field dependence of the Drude conductivity itself: $\sigma^{D}_{xx}(B) = \sigma_{\blacksquare}/(1 + (\mu B)^2)$.

Figure 2 shows the total conductivity as a function of magnetic field obtained by inversion of the resistivity tensor, $\sigma^{tot}_{xx}(B) = (1/\rho_{xx})/(1 + \rho^2_{xy}/\rho^2_{xx})$. The dotted lines are plotted using the classical expression with $\mu B = \rho_{xy}(B)\sigma_{\blacksquare}$. The zero-field Drude conductivity $\sigma_{\blacksquare}$ is found as an adjustable parameter to make the best fit in the higher field region of $\sigma^{tot}_{xx}(B)$ where WL is expected to be totally suppressed. The difference between the solid and dotted lines gives the WL correction $\delta\sigma_{xx}(T,B)$.

We analyse the WL magnetoconductivity using theory [8] which is valid for an arbitrary ratio B/B_{tr}, provided $\tau < \tau_\varphi$ is satisfied:

$$\Delta\sigma^{WL}(B) = \frac{-e^2}{\pi\hbar(1+\gamma)^2}\left[\sum_{n=0}^{N}\left(\frac{b\cdot\psi_n^3(b)}{1+\gamma-\psi_n(b)}\right) - \ln\frac{1+\gamma}{\gamma}\right], \qquad (1)$$

where $\gamma = \tau/\tau_\varphi$, τ_φ is the dephasing time, $b = \frac{1}{(1+\gamma)^2}\frac{B}{B_{tr}}$, $\psi_n(b) = \int_0^\infty d\xi \cdot e^{-\xi - b\xi^2/4} L_n(b\xi^2/2)$, and L_n are the Laguerre polynomials. In Fig. 3a we show representative data, plotted against

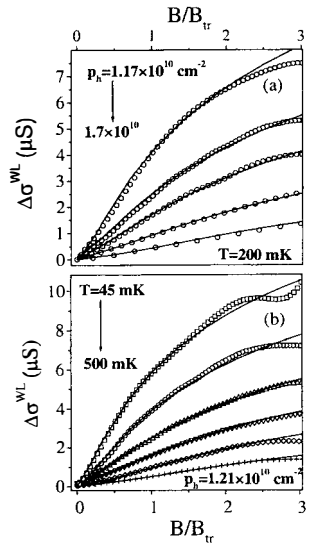


Figure 3: Magnetoconductivity $\Delta\sigma_{xx}^{WL}$ as a function of dimensionless magnetic field ($B_{tr} = \hbar/4De\tau$), for different densities (a) and temperatures (b). Solid lines are fit to Eq. (1).

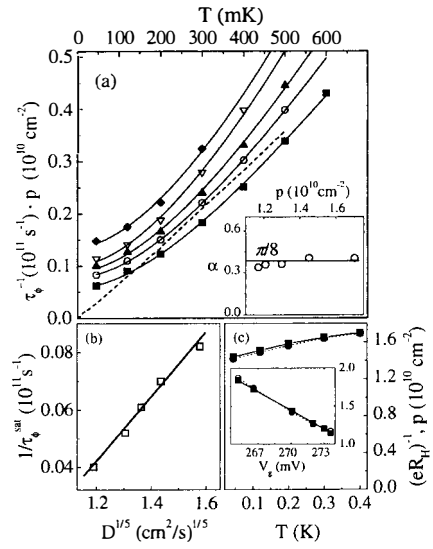


Figure 4: (a) Temperature dependence of the dephasing rate at different gate voltages, p =1.17 - 1.7×10^{10} cm^{-2} (top). Solid lines are fits to Eq. (2). (b) The saturation value of the dephasing rate at $T = 0$ against diffusion coefficient. (c) Comparison of the hole densities determined from the Hall coefficient and SdH effect.

dimensionless magnetic field B/B_{tr}, with B_{tr} found as $(4\pi\hbar\mu\sigma_\square/e^2)^{-1}$. Solid lines in Fig. 3 are obtained from Eq. (1), where γ is used as an adjustable parameter. The obtained γ-values range from 0.04 to 0.4, with an error less than 10%, and satisfy the condition $\tau < \tau_\varphi$.

Further evidence for the existence of a Fermi-liquid comes from the temperature dependence of the dephasing rate $\tau_\varphi^{-1}(T)$. Estimations show that the contribution to $\tau_\varphi^{-1}(T)$ from electron-phonon scattering is negligible. According to the Fermi-liquid theory[9,5], the dephasing rate due to electron-electron scattering is dominated either by a linear or quadratic term, depending on the parameter $k_BT\tau/\hbar$:

$$\tau_\varphi^{-1}\cdot p = \frac{m^*}{\pi\hbar^3}\left[\alpha k_B^2T^2\ln\left(\frac{4E_F}{k_BT}\right)\right], \qquad k_BT\tau/\hbar \gg 1 \tag{2}$$

$$\tau_\varphi^{-1}\cdot p = \frac{m^*}{\pi\hbar^3}\left[k_BT\frac{\hbar}{2\tau}\ln\left(\frac{2E_F\tau}{\hbar}\right)\right], \qquad k_BT\tau/\hbar \ll 1 \tag{3}$$

where $\alpha = \pi/8$ [9]. The quadratic term, Eq. (2), is due to Landau-Baber scattering in a clean Fermi-liquid associated with collisions with large momentum transfer, and the linear term, Eq. (3), corresponds to interactions with small energy transfer in a disordered conductor. (To take into account a slight ($\sim$ 10%) increase of the hole density with T in the sample, we analyse the product $\tau_\varphi^{-1}\cdot p$, with density p directly measured at each temperature by the SdH effect.) We have established that in the entire range of p and T, the data are well described by the quadratic term with a zero-temperature saturation value $1/\tau_\varphi^{sat}$ added. Coefficient α, found as an adjustable parameter, agrees within 20% accuracy with the value $\pi/8$, inset to Fig. 4a. The results show that the linear term is suppressed by more than an order of magnitude, its value estimated using Eq. (3) for $p = 1.3\times10^{10}$ cm^{-2} is shown in Fig. 4a as a straight line.

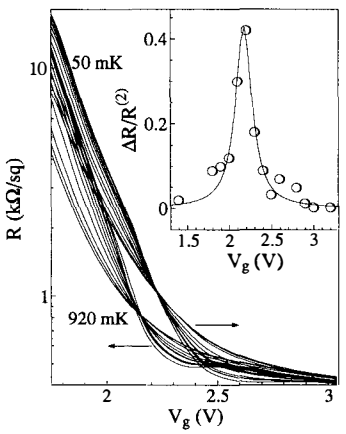


Figure 5: Resistance as a function of the gate voltage for sample Si-4.1 at $T = 50 - 920$ mK. The arrows show different directions of the V_g sweeps. Inset: the resistance difference for the two sweep directions.

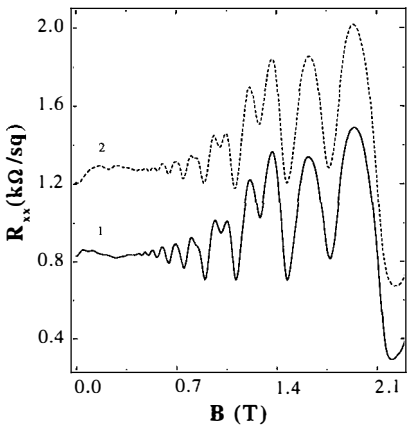


Figure 6: SdH oscillations measured at $V_g = 2.2V$, after it was approached from two opposite directions: 1 - $V_g = 0.5V$, 2 - $V_g = 9.5V$; $T = 50$ mK.

Usually, WL in a disordered system is accompanied by the HHI effect, seen as a quantum correction to the conductivity and Hall coefficient. At small r_s, the two corrections are related as $\delta R_H(T)/R_H = -2\delta\sigma(T)/\sigma$ [5]. In Fig. 4c the Hall coefficient is presented as $(R_H e)^{-1}$ for different temperatures (solid squares) and it agrees, within 2%, with the hole density measured by the SdH effect. We suggest that the suppression of the temperature dependence $\delta R_H(T)$, when compared with the estimated value [5], is linked to the observed absence of the linear term in the dephasing rate.

Let us briefly discuss the saturation of τ_φ^{-1}. In our case, the effect has one characteristic feature - the saturation becomes more pronounced with increasing p. This excludes overheating as its origin and agrees qualitatively with the suggestion that it can be related to an external noise, Fig. 4b. According to Ref. (10), the expected saturation is then $1/\tau_\varphi^{sat} \simeq D^{1/5}(\Omega e E_{ac})^{2/5}$, where Ω is the radiation frequency and E_{ac} is amplitude of an external ac field.

3 Impurity scattering as the origin of the crossover in the 2DEG on vicinal Si

The vicinal samples used in this work are MOSFETs fabricated on a surface which is tilted from the (100) surface around the [011] direction by an angle of 9.5°. The samples have a peak mobility of $2 \times 10^4\ cm^2/Vs$ at $T = 4.2$ K. The oxide thickness is 120 nm.

Fig. 5 shows the resistance as a function of V_g for vicinal sample Si-4.1 in the temperature range below 1 K, with the crossover near $\rho_{xx} \sim 1$ kOhm $\sim 0.04 \times h/e^2$. At $T \leq 4.2$ K two distinct groups of curves are seen for opposite directions of V_g-sweep. We have performed an experiment at T=50 mK where a particular V_g is approached, by a jump, from two opposite points: $V_g^{(1)} = 0.5$ V and $V_g^{(2)} = 9$ V. After an initially rapid change, the resistance comes practically to saturation, and the measurements of the quasi-equilibrium values $R^{(1)}(V_g)$ and $R^{(2)}(V_g)$ have revealed a difference $\Delta R = \mid R^{(1)} - R^{(2)} \mid$ presented in Fig. 5, inset. The hysteresis shows a peak exactly in between the two crossover points. At the same time, the Shubnikov-de Haas measurements show that electron densities $n^{(1)}(V_g)$ and $n^{(2)}(V_g)$ are equal, within an accuracy of a few percent, Fig. 6. This implies that the difference ΔR is caused by the difference in the mobility of the 2DEG.

We suggest that the crossover is caused by an impurity band at the Si/Si-oxide interface which is similar to that considered in Ref. (3). It scatters electrons when it is positively charged and the number N_+ of ionised impurities in it decreases with rising Fermi level in the 2DEG. The hysteresis is due to a slow electron exchange between the 2DEG and the IB which are separated by a barrier. The hysteresis peak appears in the energy range of the IB, and from its width the IB extent can be estimated: $W \leq 0.3$ meV.

Let us discuss how the IB scattering of 2D electrons produces a crossover. When the Fermi level F is in the upper part of the IB, increasing temperature gives a decrease of the IB electron occupancy and an increase in the number of ionised scatterers N_+, and hence an increase in the resistance of the 2DEG. The change in the sign of dR/dT occurs when the Fermi level is close to the IB centre, and with its further decrease the resistance shows 'insulating' behaviour, as N_+ decreases with T.

Fig. 7 shows the temperature dependence of the resistance $R^{(2)}$, presented as $\mu^{-1}(T)$, near the crossover at $n_c \simeq 4.18 \times 10^{11}\ cm^{-2}$, in the range T=50 mK –4 K. Assuming the IB to be centered at the level $E_i$the mobility is given by $\mu^{-1}(T) \propto N_+ \propto 1/\left(1+\exp\frac{F-E_i}{k_BT}\right)$. To calculate the IB contribution, we have subtracted the value of μ^{-1} at $V_g = 2.4$ V when the IB is full. The value $F - E_i$ is calculated from the known electron density and the Fermi energy. In this analysis the IB is taken as a step with width $W \simeq 0.08$ meV found as an adjustable parameter. Using the formula for the mobility due to ionised impurity scattering [11] we estimate the total concentration of scatterers in the IB: $N_+^{(1)} = 0.34 \times 10^{11}\ cm^{-2}$ and $N_+^{(2)} = 0.23 \times 10^{11}\ cm^{-2}$.

The 'insulator' in the range $R = 0.9 - 1.2$ kOhm , Fig. 8, corresponds to a metallic 2DEG with a well defined Fermi surface. One can see that the low-temperature crossover at $R \sim 1$ kOhm exists only in a narrow range of temperatures, and $R(T)$ has in general a complicated, non-monotonic character. A strong 'insulator' at $V_g < 2$ V cannot be explained by the simple model of IB as it can only give a resistance decrease by factor of two when T is increased. This insulator cannot occur due to the electron localisation of a quantum nature because of the low sample resistance, but can be a result of electron localisation due to classical percolation. The inset in Fig. 8 shows the variation of the slope of $R(T)$ using an exponential fit in the range $T \sim 1.5 - 7$ K. The estimated activation energy $\Delta = E_c - F$ is seen to increase linearly with decreasing Fermi level and it extrapolates to zero at the mobility edge E_c corresponding to $n = 3.74 \times 10^{11}\ cm^{-2}$.

Let us briefly discuss $R\,(T)$ with increasing temperature. At higher T, another crossover in dR/dT is seen at $\rho_{xx} \sim 3$ kOhm. We note that in the temperature range $T > 4$ K the system experiences a transition from degenerate to nondegenerate state. The variation of the Fermi temperature T_F corresponds to shift of the hump in Fig. 8. All main features of the model [4,11] for the temperature dependent ionised impurity scattering are seen in the high-temperature crossover.

4 Conclusion

We have shown that the negative magnetoresistance of a high-mobility low-density hole gas can be described by weak localisation theory on both sides of the 'metal'-to-'insulator' crossover, including the density with $r_s \sim 30$. The Fermi-liquid character of the 2DHG is also supported by the behaviour of the dephasing rate, where the domination of the Landau-Baber term is seen. The weak localisation description of the magnetoresistance of such a strongly interacting system is a surprising result, which requires further elucidation. The observed suppression of weak hole-hole interactions in the dephasing rate and the Hall coefficient also deserves further attention.

Our results on a 2DEG in a vicinal Si MOSFET show that the crossover occurs at much lower resistance than that for electrons in (100)Si studied earlier. We have been able to explain

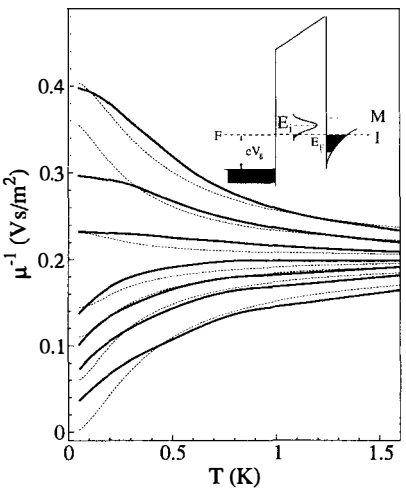


Figure 7: Temperature dependence of the mobility near the crossover at different electron densities,$n = 4.08 - 4.32 \times 10^{11}\ cm^{-2}$ and $V_g = 2.1 - 2.24$ V, from top to bottom. Dashed lines show the theoretical fit.

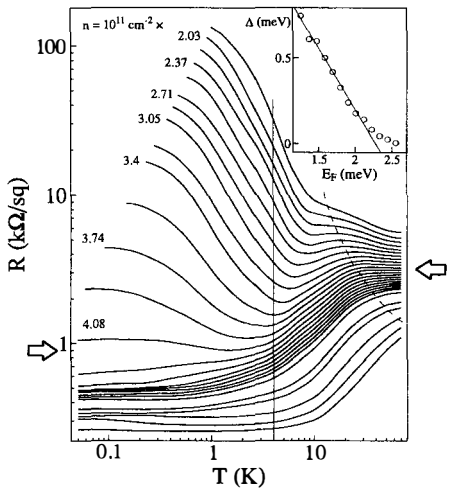


Figure 8: $R(T)$ in the full range of temperatures. Low- and high-T crossovers are indicated by the arrows. Dashed line shows the Fermi temperature T_F .

most of the unusual features of $R(T)$ in this system by the electron scattering caused by a narrow impurity band.

Acknowledgments

We are grateful to B. L. Altshuler and D. L. Maslov for stimulating discussions, EPSRC and ORS award fund for financial support.

References

1. S.V. Kravchenko *et al*, *Phys. Rev.* B **50**, 8039 (1994); M. Y. Simmons *et al*, *Phys. Rev. Lett.* **80**, 1292 (1998); Y. Hanein *et al*, *Phys. Rev. Lett.* **80**, 1288 (1998); P. T. Coleridge *et al*, *Phys. Rev.* B **56**, R12764 (1997).
2. V. Dobrosavljevic *et al*, *Phys. Rev. Lett.* **79**, 455 (1997); S. He and X. C. Xie, *Phys. Rev. Lett.* **80**, 3324 (1998); Q. Si and C. M. Varma, *Phys. Rev. Lett.* **81**, 4951 (1998).
3. B. L. Altshuler and D. L. Maslov, *Phys. Rev. Lett.* **82**, 145 (1999).
4. S. Das Sarma and E. H. Hwang, *Phys. Rev. Lett.* **83**, 164 (1999); Y. Meir, *Phys. Rev. Lett.* **83**, 3506 (1999); Y. Yaish *et al*, *Phys. Rev. Lett.* **84**, 4954 (2000).
5. B. L. Altshuler and A. G. Aronov, in *Electron-Electron Interaction in Disordered Systems*, edited by A. L. Efros and M. Pollak (North Holland, Amsterdam, 1985).
6. M. Y. Simmons *et al*, *Phys. Rev. Lett.* **84**, 2489 (2000).
7. V. Senz *et al*, *Phys. Rev. Lett.* **85**, 4357 (2000).
8. H.-P. Wittman and A. Schmid, *J. Low Temp. Phys.* **69**, 131 (1987).
9. M. Reizer and J. W. Wilkins, *Phys. Rev.* B **55**, R7363 (1997).
10. I. L. Aleiner *et al*, *Wave Random Media* **9**, 201 (1999) [cond-mat/9808053].
11. A. Gold and V. T. Dolgopolov, *Phys. Rev.* B **33**, 1076 (1986).

In-plane Magnetization of Electrons in a Silicon Inversion Layer

M. REZNIKOV[1], O. PRUS[1], Y. YAISH[1], , U. SIVAN[1], V. PUDALOV[2]
[1]*Dep. of Physics and Solid State Institute, Technion-IIT, Haifa 32000, Israel*

[2]*P. N. Lebedev Physics Institute, 119991 Moscow, Russia*

Abstract

The in-plane magnetization of 2D electrons in a silicon inversion layer is measured. The g-factor is found to be strongly enhanced compared with free electrons, especially at low densities and temperatures. No signs of a ferromagnetic instability is observed for r_s values as high as 7.2.

Introduction

Since the Stoner instability due to Coulomb interaction between conduction electrons was first predicted [1], the possibility of ferromagnetic ordering of conduction electrons in metals has been studied extensively. The interaction strength is usually characterized by the dimensionless parameter $r_s = a/a_0$, namely, the ratio between the radius a of a circle enclosing one particle on the average and the Bohr radius, a_0. In two dimensions $a = (\pi n)^{-1/2}$, where n is the electron density. For systems with no valley degeneracy, r_s is also given by the ratio between the characteristic inter particle coulomb interaction $E_c = e^2/\kappa a$ and the Fermi energy, E_F (κ is the host dielectric constant). For electrons on the (100) surface of silicon $E_c/E_F = 2r_s$ due to the two fold valley degeneracy. As the system density decreases, r_s grows indicating growing importance of interactions between electrons. In a clean system the interaction is expected to lead to a ferromagnetic instability [1,2]. Analytic calculations of the free energy of strongly interacting electrons are not available. Calculations in the Hartree-Fock approximation predict a ferromagnetic instability at $r_s \sim 2$, in sharp contrast with all experimental observations. However, it is well known that the Hartree-Fock approximation fails at large r_s values, since it neglects all correlations beyond the Pauli principle. Numerical calculations by Tanatar and Ceperley[3] show that at zero temperature the system polarizes at $r_s \approx 37$, namely, very close to the predicted Wigner crystallization. For smaller r_s values, the 2D system is paramagnetic with an enhanced susceptibility, χ, compared with the Pauli susceptibility, χ_0, of noninteracting electrons. Besides an estimate in Ref. [3] there are no rigorous calculations of χ at zero temperature, let alone at finite ones.

The interest in the magnetic properties of 2D electrons was renewed in the mid 90th following the observation of a large, unexpected resistance drop with cooling in Si inversion layers[4,5] as well as in other 2D systems (for a review see, e.g. [6]). The resistance drop was interpreted as a novel metallic phase in two dimensions and therefore drew considerable attention. The observed resistance drop is suppressed by a few Tesla [7,8] in-plane magnetic field, indicating a relation between the resistance drop and spin polarization.

Several studies of the spin susceptibility of 2D electrons in silicon structures were reported. The most direct ones are based on the analysis of Shubnikov-de Haas oscillations in a tilted magnetic field [9,10,11,12]. In these experiments, the in-plane magnetic field component results in a different population of the two spin subbands, which manifests itself in beating of the Shubnikov-de Haas oscillations as a function of the perpendicular

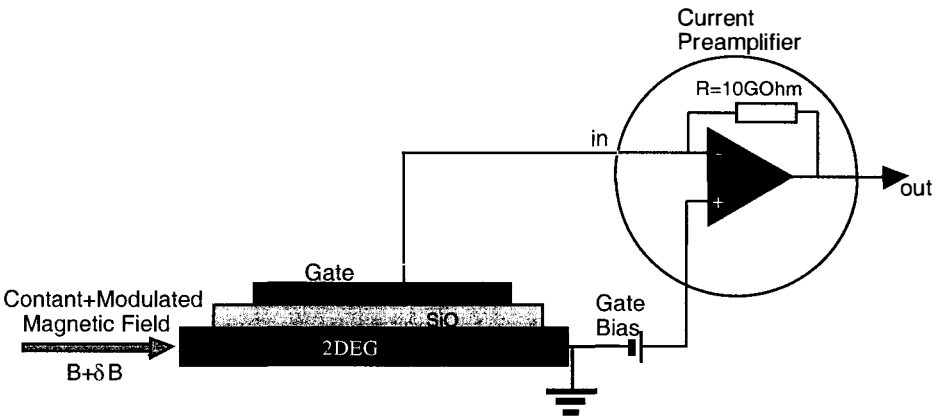


Figure 1: Magnetization measurement setup

magnetic field component. These experiments find a substantial increase of the effective Landé g factor with increasing r_s (decreasing density). This method yields reliable results for the metallic phase, but requires relatively large magnetic fields ($\omega_c\tau \approx 1$) and low temperatures $T \ll \hbar\omega_c$. Thus, the most interesting critical region of concentrations and low magnetic fields, in which the metallic behavior transforms to an insulating one, is inaccessible by this technique. In addition, Shubnikov-de Haas oscillations may not probe the magnetic moments of the localized electrons, which cam be present in the critical region.

The in-plane magnetoresistance was analyzed in several papers [13,14] trying to extract the effective Landé g factor for densities at which Shubnikov-de Haas oscillations cannot be observed. The analysis is based on the assumption that the magnetoresistance saturates as a function of in-plane magnetic field when the electron spins are polarized. This assumption was justified in [10,11] for magnetic fields where both Shubnikov-de Haas and magnetoresistance saturation can be observed, and then extrapolated in Ref. [13,14] to lower magnetic fields. The effective g-factor found this way further increases with decreasing carrier concentration towards the "critical" density, n_c, that separates the metallic and insulating like temperature dependencies. Based on this observation, in [13] a quantum phase transition was suggested to occur close to the "critical" density and [14] suggested a ferromagnetic instability.

Experimental setup

Trying to directly measure the spin susceptibility at low densities and weak magnetic fields we have developed a novel experimental scheme for measuring the variation of the chemical potential with magnetic field. The method facilitates measurements in samples containing as few as $\approx 5 \times 10^9$ electrons, much below the minimal number of particles measured by torque magnetometery or NMR. The experimental setup is presented in Fig. 1.

Modulation of the parallel magnetic field at a frequency ω induces a chemical potential

modulation which, in turn, produces an ac current, δI, flowing from the gate to the 2DEG channel. The current is given by

$$\delta I = i\omega C \delta B \frac{\partial \mu}{\partial B}, \tag{1}$$

where δB is the magnetic field modulation and C is the gate capacitance relative to the channel. Measuring the induced current and knowing the capacitance, $\partial\mu/\partial B$ is extracted. Using one of Maxwell's relations

$$\frac{\partial M}{\partial n} = -\frac{\partial \mu}{\partial B} \tag{2}$$

we then obtain $\partial M/\partial n$ which is later integrated with respect to n to yield the magnetization, $M(B,n)$. The magnetic susceptibility, χ, and effective g-factor can be calculated from the slope of $M(B,n)$ versus B at small fields.

While the principle is simple, the experiment is very demanding since the current induced by the field modulation is typically of the order of 10^{-15} A while the spurious signal due to the emf induced in all wire loops by the ac magnetic field, and even more so, the emf induced by mechanical vibrations of the sample in the strong dc magnetic field, are potentially orders of magnitude larger. To eliminate these spurious signals we have minimized all loops and rebuilt the sample holder several times to achieve high enough mechanical rigidity. This way we were able to drive the mechanical resonances to frequencies considerably higher than the field modulation frequency and hence were able to suppress the mechanical vibrations.

The samples were similar to those used in Ref.[4,5]. They consisted 5 mm long, 0.8 mm wide Hall bars with 2.5 mm separation between the potential probes. The oxide was 200 nm thick leading to a $C = 740$ pF device capacitance. In-plane alternating magnetic field of typically 100-300 Gauss (rms) and $f = \omega/2\pi = 5 \div 20$ Hz frequency was applied parallel to the dc external field produced by the main coil. A home-made preamplifier with ~ 2 fA$/\sqrt{\text{Hz}}$ current noise was used to measure the current and bias the gate (see Fig. 1).

Results and discussion

Typical experimental results, together with the expected $\partial M/\partial n$ are shown in Fig. 2. Due to the constant density of states the paramagnetzation, M_p, of noninteracting 2D electrons at zero temperature is proportional to n in the fully polarized regime and constant at fields for which both spin subbands are populated. Consequently, $\partial M_p/\partial n = \mu_B$ at low densities, when electrons are spin polarized, and vanishes at higher densities. Interactions renormalize the effective g-factor, thus reducing the magnetic field required for full polarization of the system and giving rise to non vanishing contribution into $\partial M_p/\partial n$ at higher densities. The result obtained using an interpolation formula[12] for the product of the renormalized g-factor and the effective mass is depicted in Fig. 2 by the dotted curve. The substantial difference between the measured curve and the calculated one[12] is attributed to the subband diamagnetic shift due to electron confinement in the direction perpendicular to the 2D plane by the magnetic field. The level shift is easily calculated for zero density. Calculation of the diamagnetic contribution at finite densities is much harder and less reliable. To separate the spin paramagnetic contribution from the orbital

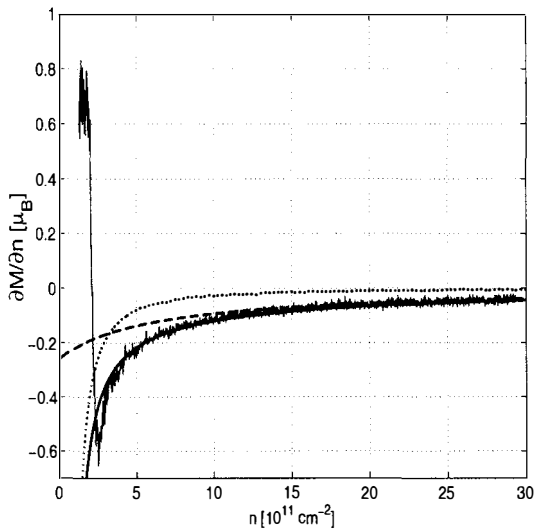


Figure 2: Noisy curve - typical experimental results for B=9 T and T=0.1 K. Dotted curve - paramagnetic contribution $\partial M_p/\partial n$ from Ref. [12]. Dashed curve - fitted diamagnetic contribution. Solid curve- fitted diamagnetic plus paramagnetic contributions.

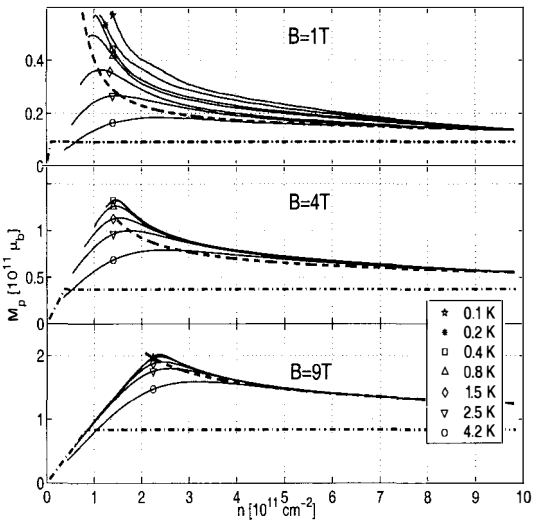


Figure 3: Spin contribution, M_p, to the magnetization at different magnetic fields for several temperatures. The dashed line is obtained using Ref.[12] and the dash-dotted line is the zero temperature, noninteracting result.

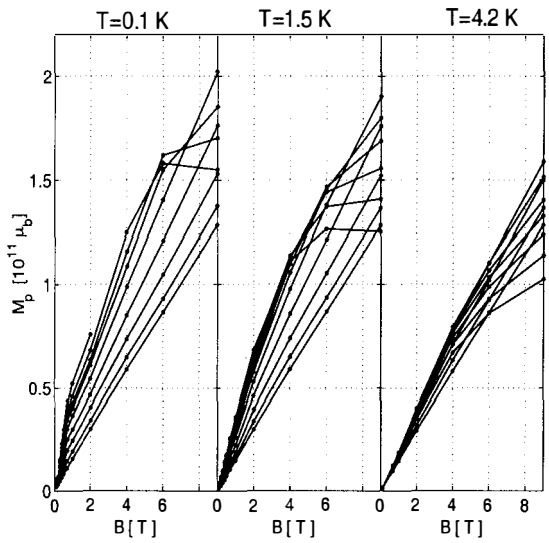


Figure 4: Spin contribution, M_p, to the magnetization at various densities $n = 1.32, 1.50, 1.68, 1.86, 2.04, 2.40, 3.21, 4.64, 6.61, 8.58 \times 10^{11}$ cm^{-2} for different temperatures. Some points at low densities in high magnetic field are absent due to the large sample resistance. The low field slope increases with decreasing density indicating enhanced susceptibility. Data points are obtained by integration from $n = 10^{12}$ cm^{-2}. The lines serve as guides to the eye.

diamagnetism we adopted the following procedure: at zero density the diamagnetic contribution can be calculated accurately by solving a triangular well with an image potential in a parallel magnetic field. At high densities we assume a paramagnetic contribution equal to that reported in Ref.[12] and tune the diamagnetic contribution such that the sum of these contributions matches our measured total $\partial M/\partial n$. Having now the high density tail of the diamagnetic contribution, as well as its value at zero density, we interpolate between the two limits to obtain the diamagnetic contribution in the whole density range. We then subtract the diamagnetic contribution from the measured $\partial M/\partial n$ to obtain the derivative of the *paramagnetic* contribution with respect to density, $\partial M_p/\partial n$. Although the above procedure is heuristic, there is very little freedom in interpolating between the zero density point and the high density diamagnetic tail, and the extracted paramagnetic contribution should hence be rather accurate.

Having subtracted the diamagnetic contribution, we assume a given magnetization at some large density, say 10^{12} cm^{-2}, for which the g-factor is reliably known [10,12], and integrate the remaining paramagnetic contribution with respect to density to obtain the magnetization due to spin polarization, M_p, at lower densities. The results for the $M_p = \mu_B(n\uparrow - n\downarrow)$, at different magnetic fields and densities are shown in Figs. 3,4.

It is important to mention that up to intermediate temperatures, 1.5 K in Fig. 4, all curves for which the magnetization M_p saturates with increasing magnetic field ($n < 1.68 \times 10^{11}$ cm^{-2}), give $M_p \approx n\mu_B$ to better than 10% accuracy . This fact justifies our procedure for subtracting the diamagnetic contribution.

Several qualitative results should be emphasized.

(a) The degree of spin polarization found here is consistently higher than the ones

reported in Ref. [10,12]. The difference grows larger at lower densities and temperatures. Since the polarization reported in Ref. [10,12] is temperature independent, we propose that the difference is due to states, possibly localized, that do not contribute to the Shubnikov-de Haas oscillations but do contribute to our thermodynamic magnetization.

(b) As seen from Fig. 4, the degree of polarization at low densities, close to the critical density, is strongly nonlinear with respect to the magnetic field. A g-factor is hence correctly defined by measuring the polarization at small enough magnetic fields, typically below 0.5 T. These fields are inaccessible to Shubnikov-de Haas measurements due to the low $\omega_c\tau$.

(c) At the lowest accessible density, $n = 1.32 \times 10^{11}\mathrm{cm}^{-2}$, which is close to n_c, the susceptibility χ approaches 8 times the Pauli susceptibility for noninteracting electrons. The susceptibility is though finite, indicating the absence of ferromagnetic ordering.

Acknowledgements

We have benefited from numerous discussions with A. Finkelstein, A. Kamenev, A. Stern, and B. Altshuler. This work was supported by the ISF, DIP, and INTAS grants.

1. E.C. Stoner, Rept. Prog. Phys. **11**, 43 (1947).
2. See, for example S. Doniach and E.H. Sondheimer, *Green's functions for Solid State Physicists* (W.A. Benjamin, Reading, MA, 1974).
3. B. Tanatar and D.C. Ceperley, Phys. Rev. B, **39**, 5005 (1989).
4. S. V. Kravchenko, G. V. Kravchenko, J. E. Furneaux, V. M. Pudalov, M. D'Iorio, *Phys. Rev. B* **50**, 8039 (1994), cond-mat/9405082.
5. S. V. Kravchenko, W. E. Mason, G. E. Bowker, J. E. Furneaux, V. M. Pudalov, M. D'Iorio, Phys. Rev. B **51**, 7038 (1995), cond-mat/9412103.
6. E. Abrahams, S. V. Kravchenko, M. P. Sarachik, *Rev. Mod. Phys.* **73**, 251 (2001), cond-mat/0006055.
7. Pudalov, V. M., G. Brunthaler, A. Prinz, and G. Bauer, JETP Lett. **65**, 932 (1997).
8. Simonian, D., S. V. Kravchenko, M. P. Sarachik, and V. M. Pudalov, Phys. Rev. Lett. **79**, 2304 (1997).
9. F. F. Fang and P. J. Stiles, Phys. Rev. **174**, 823 (1968).
10. T. Okamoto, K. Hosoya, S. Kawaji, and A. Yagi, Phys. Rev. Lett. **82**, 3875 (1999).
11. S. Vitkalov, H. Zheng, K. Mertes, M. Sarachik, T. Klapwijk, Phys. Rev. Lett. **85**, 2164 (2000).
12. V. M. Pudalov, M. Gershenson, H. Kojima, N. Butch, E. M. Dizhur, G. Brunthaler, A. Prinz, G. Bauer, cond-mat/0105081.
13. S. Vitkalov, H. Zheng, K. Mertes, M. Sarachik, T. Klapwijk, Phys. Rev. Lett. **87**, 086401 (2001).
14. A. A. Shaskin, A. V. Kravchenko, V. T. Dolgopolov, T. M. Kapwijk, Phys. Rev. Lett. **87**, 86801 (2001).

ELECTRICAL CONDUCTIVITY OF STRONGLY INTERACTING HOLES IN 2D AND 0D

U. Dötsch [1], V. Senz[2], U. Gennser[1 2], T. Heinzel[3], T. Ihn[3], S. Lüscher[3], K. Ensslin[3], G. Dehlinger[1], C. David[1], and D. Grützmacher[1].

[1] *Paul Scherrer Institute, CH-5232 Villigen PSI, Switzerland*

[2] *Laboratoire de Microstructures et de Microelectronique - CNRS, 196, Ave. Henri Ravera, F-92220 Bagneux, France*

[3] *Solid State Laboratory, ETH Zürich, CH-8093 Zürich, Switzerland*

Electronic transport through low-dimensional p-SiGe systems with high ratio r_s between the Coulomb energy of the carriers and their Fermi energy has been investigated. The magnetoresistance and Hall effect at low magnetic fields allow us to understand the 2D behavior in terms of weak localisation, impurity scattering and screening. The Coulomb blockade spectra of the 0D system are dominated by disorder as well as by Coulomb interaction.

1 Introduction

The interplay between electronic interactions and disorder has an important history within 2-dimensional physics. One of its early successes was the experimental verification of weak localization theory,[1] demonstrating that as long as the electron-electron interactions do not dominate over the kinetic energy, the conductance in zero or low magnetic Œelds can be described within a Fermi liquid theory, implying localized states at $B = 0$ and su ciently low temperatures. However, with the work by S. V. Kravchenko, et al.,[2] the question of the zero-Œeld behavior of 2-dimensional systems has attracted renewed attention, as it seemed that electron-electron interaction could indeed result in non-Fermi liquid behavior. During the last 5 years, a number of systems have been presented, for which it is not *a priori* given that they can be understood by the traditional perturbation approach.

The springing issue at hand has been whether strong electron-electron interactions can lead to a 2D metallic state, in contrast to the case of weak interactions. The existence of a true metallic state has been inferred from, e.g., the metallic-like temperature dependence of the resistivity of Si-MOSFETs below a critical carrier density n_c;[2] and their apparent temperature independence over two orders of magnitude at n_c;[3] the similar (but weaker) temperature dependence of other 2D gases;[4 5 6] the increase of the resistivity with an order of magnitude in a moderate (1 T) magnetic field parallel to the 2D layer;[8] and an order of magnitude lower weak localization observed in p-GaAs compared to theory.[9] However, in a number of investigations it has also been shown that samples presumably exhibiting a metallic behavior, in actual fact can be well described by the physics of a Fermi liquid. The observed positive temperature dependence of the resistivity has, in the various types of samples, been attributed to screening of electron-electron and electron-impurity scattering,[10 11] scattering on spin-orbit split bands,[12] and scattering on an impurity band at the oxide-semiconductor interface of a Si MOSFET.[13] Thus, the evidence from different experiments and groups seem conflicting, and it is essential to review the results of different 2D systems, to asses what is the current understanding (or lack thereof) of the combination of large electronic interactions and disorder.

Customarily the parameter r_s, the ratio between the Coulomb energy of the carriers at their average separation, $E_{e\text{-}e}$, and their Fermi energy, E_F, is taken as a measure of the importance of Coulomb interactions. For a 2D gas r_s is proportional to m^* and inversely proportional to n_s. In Fig. 1 it is shown for four different 2D systems, as a function of their carrier density. To reach a value of $r_s >> 1$ for a normal 2D electron gas in a GaAs quantum well, it is necessary to achieve

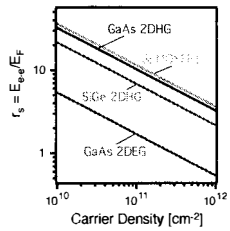


Figure 1: r_s as a function of carrier density for four typical 2D systems.

a carrier density an order of magnitude smaller than that of typical GaAs or SiGe hole gases or Si MOSFET electron gases. However, at sufficiently low densities the resistivity is $>> h\ e^2$, due to strong localization as the wave functions is localized around valleys in the disorder potential. The systems of interest are therefore those for which the density can be reduced sufficiently to obtain values of r_s exceeding 1, and for which the resistivity still is $\leq h\ e^2$.

2D hole gases (2 DHGs) are very interesting systems for this purpose, in lieu of the generally high effective masses in the valence bands ($m^*_{SiGe} \approx 0\ 25m_0, m^*_{GaAs} \approx 0\ 3m_0 - 0\ 4m_0$). Here we will show results from investigations of such a hole gas, confined in a $Si_{0\ 85}Ge_{0\ 15}$ quantum well, both of the transport through a macroscopic, gated sample, and of a top-gate defined SiGe dot. Both the 2D system and the 0 D system indicate a transport dominated by disorder rather than electron electron interactions, in spite of high r_s values, around 5.

2 SiGe 2 Dimensional Hole Gas

The samples employed in this study were grown by molecular beam epitaxy, and comprise a modulation doped 200 A $Si_{0\ 85}Ge_{0\ 15}$ layer where the 2 DHG is formed, sandwiched between undoped Si layers. Conventional, macroscopic Hall bars were gated with a Ti/Al Schottky gate. For more details see Ref. 7. Transport measurements, using both AC and DC measurement techniques, were carried out at temperatures between 190 mK and 15 K.

The sheet carrier density in the ungated device was 4.3×10^{11} cm $^{-2}$. The gate allowed tuning the density between 1.1 - 2.6 $\times$ 10^{11} cm $^{-2}$. This implies a Fermi energy below 2 meV for all densities explored, compared with the separation of the first (heavy hole) and second (light hole) subband separation of ca. 25 meV. The hole mobility in these structures increases with carrier concentration from 1000 cm^2/Vs at the lowest to 7800 cm^2/Vs at the highest density, similar to other p-SiGe structures.[15] The ratio of the Drude scattering time τ_e and the quantum lifetime τ_q extracted from Shubnikov-de Haas oscillations is close to one, indicating that transport is dominated by a short range scattering potential. This agrees with earlier studies, that large angle scattering at interface charges dominates the mobility in such structures.[14 15]

The temperature dependence of the resistivity is found to have a positive slope for high carrier densities, whereas it is negative for low carrier densities. The behavior changes from metallic to insulating at a density n_c corresponding to $r_s \approx 6$. This is qualitatively similar to the comportment of Si MOSFETs,[2] GaAs 2 DHGs,[4 16] and similar SiGe 2 DHGs,[6] although the temperature dependence in the metallic region is much less pronounced than for the MOSFETs. We show that the $\rho(T)$ curves for densities above n_c do not deviate from the expected T-dependence of a Fermi liquid with linear screening. Three effects are considered: (1) weak localization, (2) electronelectron scattering, and (3) screening of impurity scattering. The weak localization produces a negative temperature dependence, as the phase coherence length decreases for increasing temperatures, with fewer back-scattering paths contributing to the resistivity. Also the correc-

tion to the resistivity due to electron-electron scattering relies on phase coherence. Whereas the small momentum transfers of exchange scattering have a temperature behavior similar to that of weak localization, the Hartree term has a delocalizing in uence. In the case of the large angle impurity scattering present in our samples, the number of states available for this mechanism increases with temperature, resulting in a positive temperature dependence of ρ. In addition, the scattering between different energy bands may also lead to a positive temperature dependence, with an activation energy equal to the energy separation of the bands.[12] In the present investigation such an activated behavior in the metallic region is not observed.

Measurements in moderate magnetic fields make it possible to determine independently the strength of all these scattering mechanisms except for the impurity scattering. The weak localization shows up in the magnetoresistance, as the magnetic field destroys the quantum interference of back scattered paths. It can also allow a quantitative measure of any interband scattering, which is seen as a positive magnetoresistance at the lowest fields. Fig. 2a shows the conductivity as a function of a small magnetic field, $|B| \leq 0.1T$, for a series of temperatures and a carrier density of 2.6×10^{11} cm^{-2}. The sample has a metallic behavior for this density, as deduced from the temperature dependence of the resistance at $B = 0$. The positive magnetoconductance is a typical signature of weak localization. The temperature dependence of the conductivity minimum is overpowered by the much stronger background conductivity. The magnetic field dependence is fitted with the theory developed in Ref. 17 for p-type 2D hole gases which takes the valence band structure into account and includes the effect of heavy-light hole mixing. We find that the spin-orbit coupling is negligible. The phase-breaking time τ_ϕ is proportional to T^{-1}, and increases with decreasing hole concentration, as expected from theory.

The interaction corrections to the conductivity have been extracted from the temperature dependence of the Hall resistance at small magnetic fields.[18] They are predicted to obey [19] $\delta\sigma_I = -\sigma\delta R_H/2R_H = e^2/(2\pi\hbar^2)(1 - 3F^*/4)ln(kT\tau_e/\hbar)$, where $R_H = d\rho_{xy}/dB$ is the Hall constant. Figure 2b shows the change in Hall slope for two different temperatures. The $\delta\sigma_I$ determined from δR_H in this way in the metallic regime is found to be negative, corresponding to $F^* = 0.91$, in agreement with Ref. 14 and indicating the importance of the exchange contribution to the screening.

In Fig. 2c the weak localization and interaction corrections have been subtracted from the measured conductivity for a hole density 2.6×10^{11} cm^{-2}; the remaining part is assumed to be the Drude conductivity. A remarkably linear behavior is observed. For dominant large-angle impurity scattering ($q \approx 2k_F$) it has been shown that the Drude conductivity is $\sigma_D(T) = \sigma_D(0)\,[1 - C(p)T/T_F] + \mathcal{O}\,[(T/T_F)^{3/2}]$.[20] The linear term stems from the T-dependence of the dielectric function, $\varepsilon(q, T)$, especially important for large angle scattering. It is a direct consequence of electron-electron interactions causing a temperature dependent polarizability of the 2D hole gas. For charged interface impurity scattering $C(p) = 2.8$ for the hole density of the trace shown in Fig. 2b, in very good agreement with the experimental value $C = 3.1$ extracted from the slope of σ_D in the figure. Similar agreement has been found for all densities in the metallic regime. This demonstrates that temperature dependent screening can indeed explain the metallic temperature dependence of the resistivity in our p-SiGe system, in spite of the value $r_s > 1$. For the insulating region, where $k_F l < 1$, the treatment is not expected to hold, and one rather expects to have a strong localization.

3 Single Hole Transistor

In order to further explore the conduction mechanism in the pSiGe system, we have fabricated single-hole transistors using top gate electrodes on the same type of 2D hole gas as described in section 2. Coulomb blockade (CB) oscillations in disordered quantum dots with high r_s values have attracted theoretical interest.[22] An additional important feature is the large g-factor

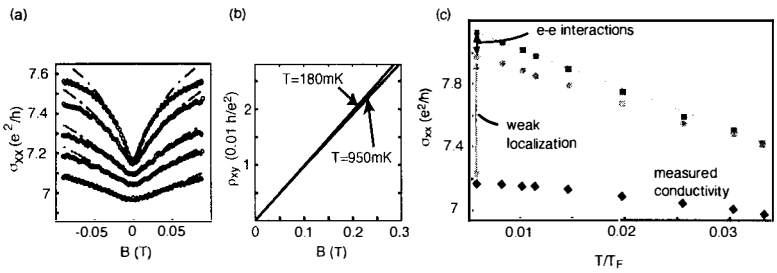


Figure 2: (a) Magnetic field dependence of the conductivity, for different temperatures from 170 mK (top trace) to 940 mK (bottom trace). The solid lines are fit with weak localization theory. (b) Hall resistivity for two different temperatures, used to extract the interaction correction to the conductivity. (c) Zero-field contributions to the conductivity. From the measured curve (T) (bottom, diamonds), the weak localization contribution is first subtracted, arriving to the curve marked by circles, and the interaction corrections, leaving the bare Drude conductivity $\sigma_D(T)$. All measurements shown are in the metallic phase, for $p = 2.6 \times 10^{11}$ cm^{-2} .

of SiGe, $g_{eff} \approx 6.7$. A similar SiGe 2 DHG structure as in section 2 was used for these experiments (ungated carrier density, $p = 3.6 \times 10^{11}$ cm^{-2}; elastic mean free path, $l = 100$ nm). 10 nm Ti / 20 nm Al top gates were patterned by electron beam lithography and thermal evaporation. Details of the process can be found elsewhere.[23] In Fig. 3 the island geometry is shown. Three split gate electrodes (point contact gates pc1, pc2, as well as the center gates cg) define the dot with a lithographic size of 500 nm × 800 nm. DC voltages V_{sd} are applied between source and drain, and the current is measured with a resolution of 500 fA. The leakage current of the gates was kept well below 10 pA for the whole voltage range explored. Two different quantum dots of identical geometry have been studied during several cool downs, all leading to similar results. Split gates pc1 and pc2 are used to adjust the coupling of the island to source and drain. Due to the small elastic mean free path, conductance quantization in the point contacts is not observed. At sufficiently large split gate voltages V_{pc1} and V_{pc2} Coulomb blockade oscillations are observed as a function of the center gate voltage V_{cg} (Fig. 3). Comparing fits of the measured resonances describing a thermally smeared CB peak in the multilevel transport regime or Lorentzian homogeneously broadened levels, the former gives a significantly better fit. From measurements of the Coulomb diamonds a lever arm $\eta = 0.68$ eV/V is obtained.[23] The total capacitance of the dot is estimated to be 170 aF, and the average level spacing $\approx 8\mu eV$.[23] The effective hole temperature T_h is used as a fit parameter, and is found to be between 390 - 570 mK, depending on the peak. This temperature is significantly higher than the lowest bath temperatures, and also saturates for source-drain voltages below 120 μV.

For higher bath temperatures not only are the CB oscillations smeared out, but a general increase in the background conductance is observed. Since neither the conductance of the individual tunnel barriers nor the leakage current increases with T in the range explored, this increase of G stems form the island itself, and indicates a thermally enhanced transport through the island. Reasonable fits with an Efros-Shlovskii hopping model can be made, giving a characteristic temperature of 0.55 K. However, because of the limited temperature range, it is not possible to rule out other possible hopping mechanisms.

Only very small variations of the resonance positions ($\approx 100\mu$eV) are observed in a magnetic field, $0 \leq B \leq 8$T. This is much smaller than the cyclotron energy of the unpatterned 2 DHG at 8 T (≈ 3.6 meV), and can be explained by holes being localized in the disorder potential of the device, in agreement with the picture of hopping conductance indicated by the temperature dependence. The peak conductance shows a large modulation with a 1/B periodicity, demonstrating the importance of tunneling in from (out of) edge states in the emitter (collector) to

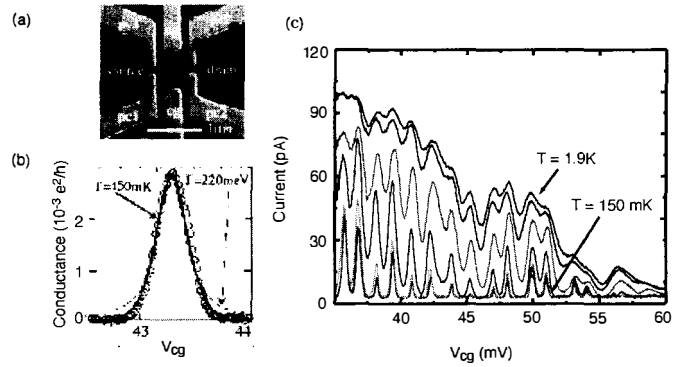


Figure 3: (a) Scanning electron micrograph of the gate geometry used for the single electron transistor. The gates appear as bright areas. (b) Conductance peak taken under source-drain voltage V_{sd} = 100μV (open circles) and T = 90 mK, fitted to Lorentzian (dashed line), and a thermally broadened CB resonance (full line). Coulomb blockade spectra for temperatures 150 mK-1.9 K.

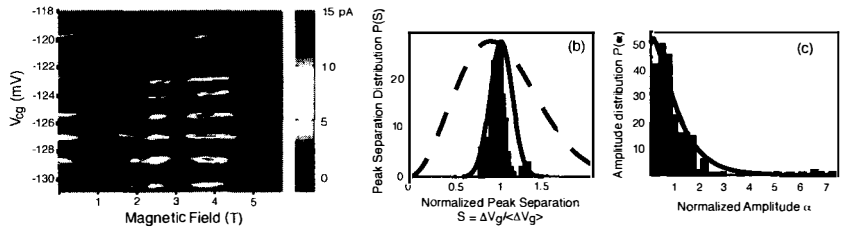


Figure 4: (a) Grey scale plot of the source-drain current as a function of gate voltage and magnetic field, at T = 90 mK. (The dark areas within the white dots around 4 T correspond to high current). (b) Histogram of the normalized variation of nearest neighbor peak separation, for a magnetic field 0.05 T≤ B ≤ 1.95 T, sample rate (50 mT)$^{-1}$, and T = 100 mK. Full line: Gaussian fit $P(S) = 28exp(-35(S-1)^2)$, dashed line: GUE distribution $P(S) = (32S^2/\pi^2)exp(-4S^2/\pi)$. (c) Histogram of the normalized peak amplitude a for the same T, field and sampling as in a. Full line: function $P(\alpha) = C2\alpha[K_0(\alpha) + K_1(\alpha)]e^{-\alpha}$, with C = 25 as a fit parameter.

(from) the disordered dot.

Finally, we have investigated the statistics of the resonance peak variation (Fig. 5). The fluctuations of the peak positions are expected to be statistically independent for a change in the magnetic field of more than one flux quantum through the dot, which for a dot radius of 200 nm corresponds to ΔB = 30 mT. A sampling of spectra has been made for 0.05 T ≤ B ≤ 1.95 T with ΔB = 50 mT and for 2.5 T ≤ B ≤ 4.5 T with ΔB = 100 mT for two different single hole transistors. Very similar results where obtained for the two samples. In Fig. 4b the distribution of the normalized voltage difference between nearest neighbor peak positions, $S = \Delta V_g / <\Delta V_g>$, is shown for the low field sampling. The width of the distribution is about 1/4 of what is expected from the GUE distribution predicted by random matrix theory. A much better fit is obtained by a Gaussian distribution $P(S) = A\ exp(-b(S-1)^2)$, with A = 28 and b = 35, as indicated by the figure. A similar fit (A = 19 b = 25) is obtained for the higher B field range. Such a distribution has been found in earlier investigations [24,25] and seems to be in qualitative agreement with the exact diagonalization calculations, which suggest that the interaction can reduce the spin-flip energy sufficiently to destroy the GUE distribution.[26] The distribution of the normalized peak amplitude a is shown in Fig. 4b for the same sampling as in Fig. 4a. A good fit is obtained with $P(\alpha) = 2\alpha[K_0(\alpha) + K_1(\alpha)]e^{-\alpha}$, with K_0 and K_1 modified

Bessel functions, in agreement with random matrix theory.

4 Conclusion

The behavior of a p-SiGe 2 DHG with $r_s < 1$ is found to be in good agreement with the theory of temperature dependent screening for systems in which large angle scattering dominates. A quasi-0D p-SiGe system shows a behavior dominated by the disorder in the sample. In the Coulomb blockade regime its level statistics is in agreement with a Gaussian distribution.

Financial support from ETH Zürich and the Schweizerischer Nationalfonds is acknowledged.

1. E. Abrahams, *et al.*, Phys. Rev. Lett. **42**, 673 (1979).
2. S.V. Kravchenko *et al.*, Phys. Rev. B **50**, 8039 (1994).
3. S. V. Kravchenko and T. M. Klapwijk, cond-mat/9909458 (1999).
4. Y. Hanein *et al.*, Phys. Rev. Lett. **80**, 1288 (1998); J. Yoon *et al.*, Phys. Rev. Lett. **82**, 1744 (1999).
5. Y. Hanein *et al.*, Phys. Rev. B **58**, R13338 (1998).
6. P.T. Coleridge, *et al.*, Phys. Rev. B **56**, R12764 (1997).
7. V. Senz *et al.*, Ann. Phys. (Leipzig) **8**, SI 237 (1999).
8. D. Simonian, S. V. Kravchenko, M. P. Sarachik, and V. M. Pudalov Phys. Rev. Lett. **79**, 2304 (1997).
9. A. P. Mills *et al.*, cond-mat/010120.
10. V. Senz *et al.*, Phys. Rev. Lett. **85**, 4357 (2000).
11. A.R. Hamilton, M.Y. Simmons, M. Pepper, and D.A. Ritchie, cond-mat/0003295.
12. Y. Yaish *et al.*, Phys. Rev. Lett. **84**, 4954 (2000).
13. S. S. Safonov *et al.*, Phys. Rev. Lett **86**, 272 (2001).
14. C.J. Emeleus *et al.*, J. Appl. Phys. **73**, 3852 (1993).
15. T.E. Whall, Appl. Surf. Sci. **102**, 221 (1996).
16. A. R. Hamilton, *et al.*, Phys. Rev. Lett. **82**, 1542 (1999).
17. N.S. Averkiev, L.E. Golub, and G.E. Pikus, JETP **86**, 780 (1998).
18. D.A. Poole, M. Pepper, and R.W. Glew, J. Phys. **C14**, L995 (1981).
19. B.L. Altshuler and A.G. Aronov, Electron-Electron Interaction In Disordered Conductors, editors A.L. Efros and M. Pollak, Elsevier Science Publishers B.V., 1985.
20. A. Gold and V.T. Dolgopolov, Phys. Rev. B **33**, 1076 (1986).
21. M.Y. Simmons *et al.*, Phys. Rev. Lett. **84**, 2489 (2000).
22. P. N. Walker, G. Montambaux, and Y. Gefen, in XXXIVth Rencontres de Moriond: Quantum Physics at Mesoscopic Scale, ed. C. Glattli, M. Sanquer, and J. Tran Thnanh Van (EDP Sciences, France 2000).
23. U. Dötsch *et al.*, Appl. Phys. Lett. 78, 341 (2001).
24. F. Simmel *et al.*, Phys. Rev. B **59**, R10441 (1999); F. Simmel, T. Heinzel, and D. A. Wharam, Europhys. Lett. **38**, 123 (1997).
25. S. R. Patel *et al.*, Phys. Rev. Lett. **80**, 4522 (1998).
26. R. Berkovits, Phys. Rev. Lett **81**, 2128 (1998).

OSCILLATORY INSTABILITY IN SHORT-GATE GAAS MESFETS

S. S. SAFONOV[1], A. K. SAVCHENKO[1], W. R. TRIBE[2] and E. H. LINFIELD[2]
[1]*School of Physics, University of Exeter, Stocker Road, Exeter, EX4 4QL, UK*

[2]*Cavendish Laboratory, University of Cambridge, Madingley Road, Cambridge, CB3 0HE, UK*

In a short ($\sim 0.4\mu$m) n-GaAs MESFET, we have observed S-shaped I-V characteristics in the low-temperature insulating regime of conduction. S-shaped I-V gives rise to stochastic and periodic oscillations, which are due to dynamic behaviour of current filaments in the potential barrier. We discuss the origin of the S-type I-V in terms of the model where the instability occurs as an interplay between tunnelling current and thermionic current over the barrier.

1 Introduction

Instability and S-shaped I-V characteristics have been found in various semiconductor devices[1,2]. In the regime of instability such devices usually show similar behaviour including chaotic and periodic voltage (current) oscillations. In spite of this similarity, the mechanisms of the formation of negative differential conductance (NDC) in the I-V can be very different in different systems. There are two main mechanisms which are responsible for instability in semiconductor devices: low temperature impact ionization[2] and overheating instability[3].

In this work we study current and voltage instability observed in a short-gate n-GaAs MESFET in the insulating regime of conduction[4,5]. In Ref. (4) this instability has been seen as random telegraph noise (RTN) or hysteresis in I-V in the voltage-controlled regime, which is due to S-type I-V observed in the current-controlled regime[5]. However, the microscopic origin of the S-type I-V still remains unclear. Here, a study of the voltage fluctuation spectrum has revealed not only stochastic jumps but also periodic oscillations, which occur exactly in the middle of the S-shaped region. This is considered as an indication of the formation of a conducting filament in the barrier. We discuss the microscopic nature of the S-type I-V, in terms of several mechanisms, and suggest that the most probable onecan be based on the theoretical model by Wacker and Scholl, Ref. (3).

2 Sample

Our experiments have been performed on an n-GaAs MESFET with doping $N_D = 10^{17}$ cm^{-3}. The length of the gate in the current direction is $0.4\,\mu$m and the width is 4 μm, Fig. 1, top. By changing the negative gate voltage V_g, the height of the potential barrier between the source and drain with localized states in it, is varied, Fig. 1, bottom. The I-V characteristics have been measured using both voltage- and current-controlled regimes, in the temperature range from 50 mK to 4.2 K, and in perpendicular magnetic field up to 14 T.

3 Experimental Results

3.1 Voltage-controlled regime

Fig. 2 shows I-V characteristics of sample 6T21 at different V_g with two steps in I-V for $V_g = -1.05$ V. At $V_g = -1.15$ V, the hysteresis starts appearing for voltage sweeps in 'up' and 'down' directions. Similarly to Ref. (4), we have found that, at the position of each step, RTN exists.

We have investigated the effect of V_g on the 'equal' time of RTN, τ_0, which is realised at the middle of the step. The existence of an optimal V_g at which τ_0 is at its maximum is clearly seen

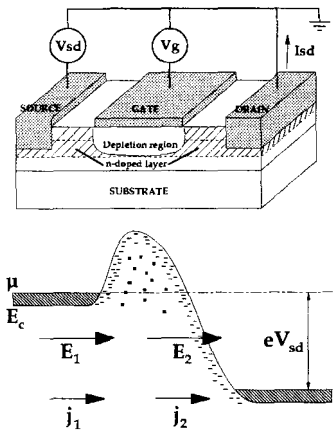


Figure 1: Top: Schematic diagram of a MESFET showing the region of electron depletion where the barrier is formed. Bottom: Energy band diagram of the channel in the insulating regime.

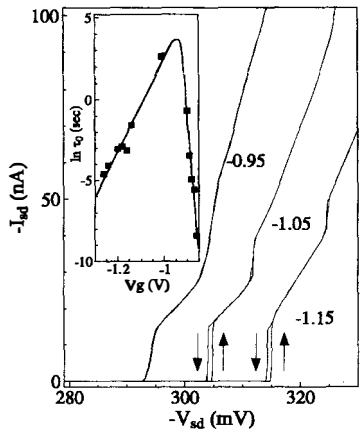


Figure 2: Typical I-V curves for three values of gate voltage measured at $T = 50$ mK, $B = 8$ T in the voltage-controlled regime. The $V_g = -1.05$ V and 1.15 V curves have been offset in the x-direction by 80 mV and 160 mV, respectively. The arrows show the direction of the source-drain bias sweep. Inset: Value of the equal time τ_0 for RTN at a step in I-V as a function of gate voltage, $T = 50$ mK and $B = 0$ T.

in Fig. 2, inset. This is in agreement with Ref. (4), although in our case a very slow switching time is observed resulting in hysteresis in I-V. A perpendicular applied magnetic field generally decreases the frequency of RTN.

3.2 Current-controlled regime

We have also measured the I-V characteristics in the current-controlled regime, where the current is supplied by a variable source of current. In the region of bistability, we have observed an S-type NDC, Fig. 3. Similar to the voltage-controlled regime, the I-V characteristics at a fixed current exhibit random jumps of voltage. The variation of the switching time with V_g is now different from that in the voltage-controlled regime. At the optimal V_g the switchings of the voltage are faster than those at any other V_g . In Fig. 3 one can see that at an optimal V_g the mean times of random switchings are so small that our apparatus is not able to resolve them and a smooth I-V with NDC appears. As shown in Fig. 3, inset, the region of bistability in the voltage-controlled regime (seen as a hysteresis loop) coincides with the NDC region measured in the current-controlled regime.

Detailed study showed that the shape of the NDC region in I-V can be rather complex and changes with V_g. At a particular V_g, the I-V characteristic has a vertical part, parallel to the current axis, Fig. 4a.

Let us discuss noise properties in the instability regime. In the region of bistability a Lorentzian spectrum is seen, corresponding to RTN. It is seen in Fig. 4b that its magnitude varies non-monotonically with current, reaching its maximum value at the boundaries of the vertical part of I-V. Noticeably, on top of the Lorentzian, a distinct peak in the spectrum appears when the current sweeps through the vertical part of I-V. The frequency of these oscillations changes when one varies the current through the vertical part, Fig. 4c. In the centre of the vertical part, the frequency of the peak has its maximum equal to 150 Hz.

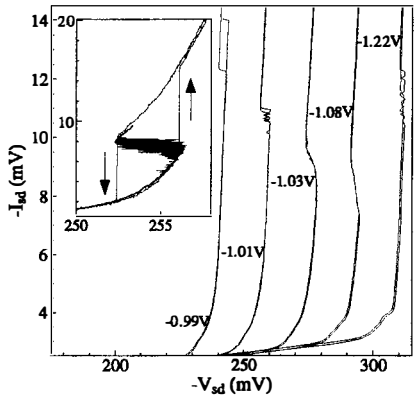


Figure 3: I-V for different V_g in the current-controlled regime at $T = 50$ mK. The $V_g = -1.08$ V and 1.22 V curves have been shifted in the x-direction by 28 mV and 142 mV, respectively. Inset: the I-V curve for $V_g = -1$ V at $T = 50$ mK in both voltage- and current-controlled regimes. The arrows show the directions of the source-drain voltage sweep in the voltage-controlled regime.

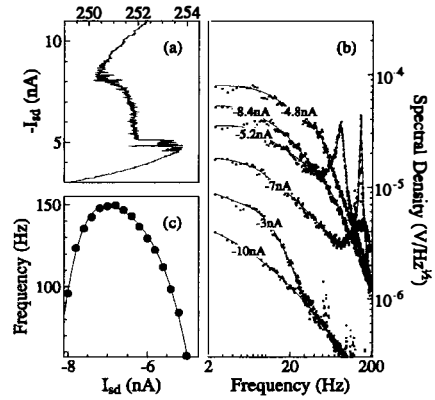


Figure 4: a) Filament-like S-type I-V at $T = 4.2$ K and $V_g = -1.02$ V. b) Spectral density of voltage noise for different currents through the barrier, $V_g = -1.02$ V and $T = 4.2$ K. c) Frequency position of the noise peak as a function of the source-drain current in the current-controlled regime.

4 Discussion

First of all, let us consider two possible microscopic models of S-type current-voltage characteristics: a) impact ionization and b) heating of current carriers.

4.1 Impact ionization

In strong electric fields an electron can acquire a large enough energy to excite another electron from an impurity to the conduction band. One can consider two possible scenarios in our case: multiplication of carriers occurs in 1) the barrier and 2) in the doped contacts.

1) Assuming that the total source-drain voltage is applied to the barrier, i.e. the contact resistance is much smaller that the resistance of the barrier, we estimate the electric field in the barrier as $E \sim 2 \times 10^3$ V/cm. At the same time, due to extremely high donor concentration, the energy acquired by an electron on the mean free path of $l \sim 200\mathring{A}$ is only 10μeV. Also, the number of donors along the barrier length is around 10-30 which is not enough to produce a dramatic increase in electron concentration. It is worth noting that this electric field is much stronger than that in the experiments on impact ionization [2] where $E \sim 10$ V/cm. In our case there can be no electrons on shallow donors: in a strong field all electrons trapped inside the barrier could have tunnelled to the right contact.

2) Current-voltage instabilities due to impurity breakdown at low temperature in n-type GaAs have been intensively studied [2], although in these studies low-doped systems are usually used. Our samples are made of heavily doped n-GaAs where electrons are provided to the conduction band by the overlap of electron wave functions on donors. Also, the strong and non-monotonic dependence of the effects (Figs. 2, inset and 3) on the gate voltage indicates that the region under the gate indeed plays a significant role in the dynamics of instability.

From the above arguments one can conclude that it is unlikely that impact ionization is the origin of non-linearity in our short barrier samples with heavily doped contacts.

4.2 Heating of electrons

This process seems to be more appropriate in our case. We can suggest a simple model based on theory Ref. (3). Source-drain electric field applied to the structure breaks into two parts: before the barrier, E_1, and after the barrier, E_2, with the corresponding currents in these regions j_1 and j_2, Fig. 1, bottom. At small electric field, when there is no current through the barrier, E_1 is much smaller than E_2. (The difference in electric fields is related to an extra negative charge on the left side of the barrier.) An increase of electric field increases tunnelling (or hopping) through the barrier. As soon as the current appears in the system, electric fields start changing: E_1 increases, while E_2 decreases. With increasing E_1, electrons in the left contact gain more energy from the electric field and are able to overcome the barrier without tunnelling. This enhances the current j_2 and further increases E_1, so that an electron avalanche occurs, which is the basis for the existence of S-type characteristics. With a rapid development of the electron avalanche over the barrier, the system does not need an initial voltage to support the current, hence, there is a drop of voltage with increasing current. At a fixed voltage, the system exhibits jumps between two current states: tunnelling or hopping (low state) and thermionic current over the barrier (high state).

However, further consideration is needed to show the applicability of this model to our system and to find the physical parameters responsible for its non-linear behaviour. It would be interesting to find out the reason for extremely low-frequency oscillations and non-monotonic variation of the frequency with V_g and I_{sd} (Figs. 2 and 4c).

5 Conclusion

We have observed an S-shaped I-V characteristic in a short-gate n-GaAs MESFET in the insulation regime of conductance and discussed its origin in terms of several possible mechanisms of instability. A suggestion has been made that the model of the instability can be based on the competition between the tunnelling and the thermionic currents.

Acknowledgments

We are grateful to D. H. Cobden, Sh. M. Kogan, M. Polak, S. H. Roshko, and A. F. Volkov for useful discussions.

References

1. M. P. Shaw, V. V. Mitin, E. Scholl, and H. L. Grubin, The Physics of Instabilities in Solid State Electron Devices, Plenum, New York, 1992.
2. E. Scholl, *Phys. Rev. B* **34**, 1395 (1986); A. Brandl and W. Prettl, *Phys. Rev. Lett.* **66**, 3044 (1991).
3. A. Wacker and E. Scholl, *Appl. Phys. Lett.* **59**, 1702 (1991); A. Wacker and E. Scholl, *Semocond. Sci. Technol.* **7**, 1456 (1992); A. Wacker and E. Scholl, *Semicond. Sci. Technol.* **9**, 592 (1994).
4. A. K. Savchenko *et. al.*, Proceedings of the 5th International Conference on Hopping and Related Phenomena, eds: C. J. Adkins, A. R. Long, J. A. McInnes, World Scientific, 41 (1994), A. Woolfe, PhD. dissertation, University of Cambridge, 1995.
5. S. S. Safonov, A. K. Savchenko, W. R. Tribe, and E. H. Linfield, *Phys. Stat. Sol. (b)* **218**, 145 (2000).
6. Sh. Kogan, Electronic Noise and Fluctuations in Solids, Cambridge University Press, Cambridge 1996.

MESOSCOPIC WIGNER CRYSTALLIZATION IN TWO DIMENSIONAL LATTICE MODELS

JEAN-LOUIS PICHARD[1], GEORGIOS KATOMERIS[1,2], FRANCK SELVA[1]
[1] *Service de Physique de l'Etat Condensé, CEA - Saclay, 91191 Gif sur Yvette cedex, France*

[2] *Department of Physics, University of Ioannina, Greece*

The quantum-classical crossover from the Fermi liquid towards the Wigner solid is numerically revisited, considering small square lattice models where electrons interact via a Coulomb U/r potential. The studies of models without disorder and spin and including disorder and spin show that the electron solid is formed in two stages, giving rise to an intriguing solid-liquid regime at intermediate couplings.

1 Lattice model

We consider N electrons on $L \times L$ square lattice with periodic boundary conditions (BCs). The Hamiltonian reads

$$\mathcal{H} = \sum_{i,\sigma}(-t\sum_{i'} c^{\dagger}_{i',\sigma}c_{i,\sigma} + v_i n_{i,\sigma}) + \frac{U}{2}\sum_{\substack{i,i'\\ i\neq i'}} \frac{n_{i,\sigma}n_{i',\sigma'}}{|i-i'|} + 2U\sum_i n_{i,\uparrow}n_{i,\downarrow}, \quad (1)$$

where $c_{i,\sigma}$ ($c^{\dagger}_{i,\sigma}$) destroys (creates) an electron of spin σ at the site i and $n_{i,\sigma} = c^{\dagger}_{i,\sigma}c_{i,\sigma}$. The first terms describe the kinetic energy ($\propto -t$) and the random substrate energy (potentials v_i uniformly distributed inside $[-W/2, W/2]$). The interaction consists of a $U/|i-i'|$ Coulomb repulsion plus a $2U$ Hubbard repulsion. $|i-i'|$ is the smallest distance between the sites i and i' on a square lattice with periodic BCs. In our model, the Coulomb energy to kinetic energy ratio $r_s = U/(2t\sqrt{\pi n_e})$ for a filling factor $n_e = N/L^2$.

$\mathcal{S}$ and $\mathcal{S}_z$ are the total spin and its component along an arbitrary direction z. $\mathcal{H}$ can be written in a block-diagonal form, with $N+1$ blocks where $S_z = -N/2, \ldots, N/2$ respectively. Assuming $N = 4$ and $L = 6$, the three blocks with $S_z \geq 0$ are diagonalized using Lanczos algorithm to obtain the minimum eigenenergy $E_0(S_z)$ of each block.

2 Spinless fermions without disorder

We begin by studying[1] the ground state (GS) of the block $\mathcal{H}(S_z = 2)$ when $W = 0$. When $U = 0$, the states are N_H plane wave Slater determinants (SDs) $\prod_{p=1}^{4} d^{\dagger}_{k(p)}|0>$, where $d^{\dagger}_{k(p)}$ creates a particle in a state of momentum $k(p) = 2\pi(p_x, p_y)/L$ and $|0>$ is the vacuum state. The low energy eigenstates are given by: (A) 4 degenerate ground states (GSs) $|K_0(\beta)>$ ($\beta = 1, \ldots, 4$) of energy $E_0(U=0) = -13t$ and of momenta $K_0 \neq 0$; (B) 25 first excitations of energy $E_1(U=0) = -12t$. (C) 64 second excitations $|K_2(\alpha)>$ of energy $E_2(U=0) = -11t$; (D) 180 third excitations $|K_3(\alpha)>$ of energy $E_3(U=0) = -10t$ and (E) 384 fourth excitations of energy $E_4(U=0) = -9t$. We define the 20 plane wave SDs useful to partly describe the intermediate GS. They are given by 4 plane wave SDs $|K_1(\beta)>$ of energy $-12t$ where the particles have energies $-4t, -3t, -3t, -2t$ respectively, and by 16 plane waves SDs $|K_4(\delta)>$ of energy $-9t$ where the particles have energies $-4t, -3t, -2t, 0t$ (first set of 8 SDs) and $-3t, -3t, -2t, -t$ (second set of 8 other SDs) respectively. Those 20 SDs are directly coupled by the pairwise interaction and their momenta are zero ($K = \sum_{p=1}^{4} k(p) = 0$).

When $t = 0$, the states are N_H Slater determinants $c^{\dagger}_i c^{\dagger}_j c^{\dagger}_k c^{\dagger}_l|0>$ built out from the site orbitals. The low energy states are the following site SDs: (A) 9 squares $|S_0(I)>$ ($I = 1, \ldots, 9$)

of side $a = 3$ and of energy $E_0(t = 0) \approx 1.80U$; (B) 36 parallelograms $|S_1(I) >$ of sides $(3, \sqrt{10})$ and of energy $\approx 1.85U$; (C) 36 other parallelograms $|S_2(I) >$ of sides $(\sqrt{10}, \sqrt{10})$ and of energy $\approx 1.97U$ and (D) 144 deformed squares $|S_3(I) >$ obtained by moving a single site of a square $|S_I >$ by one lattice spacing and of energy $\approx 2U$.

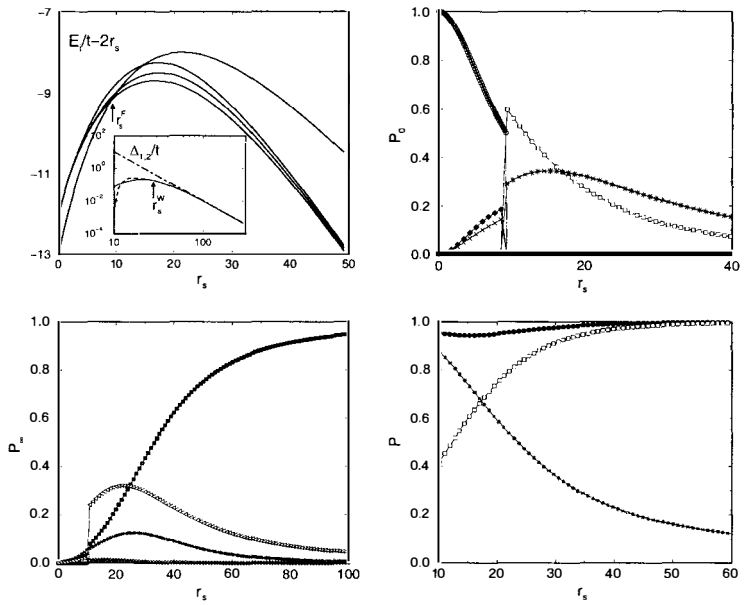


Figure 1: UPPER LEFT: Low energy part of the spectrum exhibiting a GS level crossing at r_s^F. Inset: two first level spacings Δ_1/t (dashed) and Δ_2/t (dotted) which become equal at r_s^W and the perturbative result $\Delta_1/t = \Delta_2/t \approx 10392/r_s^3$ valid when $r_s \to \infty$ (dot-dashed). UPPER RIGHT: GS projections $P_0(r_s)$ onto a few plane wave SDs, given by the $4|K_0(\beta) >$ (empty circle), the $4\ |K_1(\beta) >$ (empty square), the $64\ |K_1(\alpha) >$ (filled diamond), the $180\ |K_2(\alpha) >$ (×), the $16\ |K_4(\delta) >$ (asterisk) respectively. LOWER LEFT: GS projection $P_{\circ\bullet}(r_s)$ onto a few site SDs, given by the 9 squares $|S_0(I) >$ (filled square), the 36 parallelograms $|S_1(I) >$ (asterisk), the 36 parallelograms $|S_2(I) >$ (diamond), and the 144 deformed squares $|S_3(I) >$ (left triangle) respectively. LOWER RIGHT: GS projection $P_0^t(r_s)$ (asterisk) and $P_{\circ\bullet}^t(r_s)$ (empty square) and total GS projection P (filled circle) onto the re-orthonormalized basis using the low energy eigenvectors of the two limiting bases.

For the first low energy states, the crossover from the $U = 0$ eigenbasis towards the $t = 0$ eigenbasis is shown in Fig. 1 (upper left) when one increases the ratio r_s. If we follow the 4 GSs $E_0(r_s = 0)$ $(K_0 \neq 0)$, one can see a first level crossing at $r_s^F \approx 9.3$ with a non degenerate state $(K_0 = 0)$ which becomes the GS above r_s^F, followed by two other crossings with two other sets of 4 states with $K_I \neq 0$. When r_s is large, 9 states coming from $E_1(r_s = 0)$ have a smaller energy than the 4 states coming from $E_0(r_s = 0)$. The degeneracies ordered by increasing energy become $(1, 4, 4, 4, \ldots)$ instead of $(4, 25, 64, \ldots)$ for $r_s = 0$. These 9 low energy states give the 9 square molecules $|S_0(I) >$ when $r_s \to \infty$. When r_s^{-1} is very small, the first 9 states correspond to a solid molecule free to move on a restricted 3×3 lattice, with an effective hopping term $T \propto t r_s^{-3}$. This gives 9 states of kinetic energy given by $-2T(\cos K_l(I) + \cos K_t(I))$ with $K_l(I) = 2\pi p_l/3$ and $K_t(I) = 2\pi p_t/3$ $(p_{l,t} = 1, 2, 3)$. This structure with degeneracies $1, 4, 4$ respectively and two equal energy spacings Δ_1 and Δ_2 appears (inset of Fig. 1 upper left) when r_s is larger than the crystallization threshold $r_s^W \approx 28$. The two characteristic thresholds r_s^F (level crossing) and r_s^W (9 first states having the structure of the spectrum of a single solid molecule free to move on a

3×3 square lattice) can also be detected by other methods given in Ref. [1].

To understand further the nature of the intermediate GS between r_s^F and r_s^W, we have projected the GS wave functions $|\Psi_0(r_s)>$ over the low energy eigenvectors of the two eigenbases valid for $U/t = 0$ and for $t/U = 0$ respectively. Let us begin with the $U = 0$ eigenbasis. Below r_s^F, each of the 4 GSs $|\Psi_0^\alpha(r_s)>$ with $K_0 \neq 0$ has still a large projection $P_0(r_s, 0) = \sum_{\beta=1}^{4} | < \Psi_0^\alpha(r_s)|K_0(\beta) > |^2$ over the 4 non interacting GSs. There is no projection over the 25 first excitations and smaller projections $P_0(r_s, 2)$ and $P_0(r_s, 3)$ over the 64 second and 180 third excitations of the non interacting system. Above r_s^F, the non degenerate GS with $K_0 = 0$ has a large projection

$$P_0(r_s, 1) = \sum_{\beta=1}^{4} | < \Psi_0(r_s)|K_1(\beta) > |^2 \tag{2}$$

which is equally distributed over the 4 excitations $|K_1(\beta)>$ of momentum $K_1 = 0$ and a second significant contribution

$$P_0(r_s, 4) = \sum_{\delta=1}^{16} | < \Psi_0(r_s)|K_4(\delta) > |^2 \tag{3}$$

given by its projection onto the 16 mentionned plane wave SDs $|K_4(\delta)>$ of energy $-9t$. Above r_s^F, its projections onto the 4 $|K_0(\beta)>$, the 21 other first excitations and the second and third excitations of the non interacting system are zero or extremely negligible. The total GS projection $P_0^t(r_s) = P_0(r_s, 1) + P_0(r_s, 4)$ onto the 4 $|K_1(\beta)>$ and 16 $|K_4(\delta)>$ is given in Fig. 1 (lower right) when $r_s > r_s^F$. This shows us that a large part of the system remains an excited liquid above r_s^F.

We now study the GS projections P_∞ onto the $t = 0$ eigenbasis. The GS projection

$$P_\infty(r_s, 0) = \sum_{I=1}^{9} | < \Psi_0^\alpha(r_s)|S_0(I) > |^2 \tag{4}$$

onto the 9 square site SDs $|S_0(I)>$ is given in Fig. 1 (lower left), together with the GS projection $P_\infty(r_s, J)$ onto the site SDs corresponding to the J^{th} degenerate low energy excitations of the $t = 0$ system. The total GS projection $P_\infty^t(r_s) = \sum_{p=0}^{3} P_\infty(r_s, p)$ onto the 9 squares $|S_0(I)>$, the 36 parallelograms $|S_1(I)>$, the 36 other parallelograms $|S_2(I)>$ and the 144 deformed squares $|S_3(I)>$ is given in Fig. 1 (lower right) when $r_s > r_s^F$. This shows us that the ground state begins to be a floppy solid also above r_s^F.

The site SDs and plane wave SDs are not orthonormal. After re-orthonormalization, the total projection P of $|\Psi_0(r_s)>$ over the subspace spanned by the 4 $|K_1(\beta)>$ and 16 $|K_4(\delta)>$ and 225 site SDs of lower electrostatic energies are given in Fig. 1 (lower right), showing that $|\Psi_0(r_s)>$ is almost entirely located inside this very small part of a huge Hilbert space for intermediate r_s, spanned by low energy SDs of different nature, and adapted to describe a solid entangled with an excited liquid.

3 Magnetization and polarization energies in presence of a random substrate

We now consider weakly disordered samples when the spin degrees of freedom are included [2]. Their role and the consequences of an applied parallel magnetic field which aligns only the spins without inducing orbital effects, have been the subject of Ref. [2]. The study of a statistical ensemble of samples with $W = 5$, $N = 4$ and $L = 6$ provides complementary signatures of a particular intermediate behavior. Let us note M the fraction of clusters with $S = 1$ at $B = 0$, $Q_2 = E_0(S_z = 2) - E_0(S_z = 0)$ and $Q_1 = E_0(S_z = 1) - E_0(S_z = 0)$ the Zeeman energies necessary to yield $S = 2$ and $S = 1$ respectively for a cluster with $S = 0$.

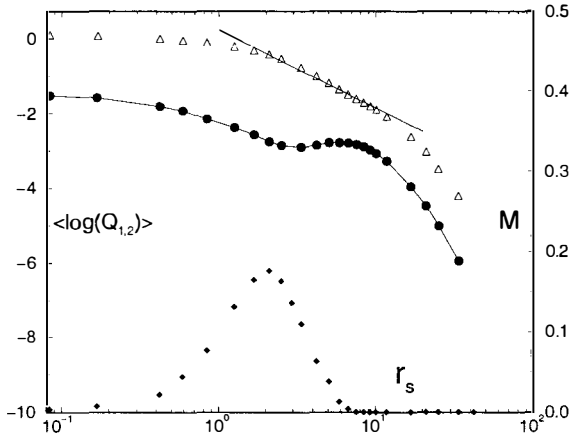


Figure 2: As a function of r_s, fraction M of clusters with $S = 1$ at $B = 0$ (filled diamond, right scale), partial $< \log Q_1 >$ (filled circle, left scale) and total $< \log Q_2 >$ (empty triangle, left scale) energies required to polarize $S = 0$ clusters to $S = 1$ and $S = 2$ respectively. The straight line corresponds to $0.25 - 2 \log r_s$.

In Fig. 2, M is given as a function of r_s. One can see a first threshold at $r_s \approx 0.35$ where the interaction can drive $S = 1$ in certain samples. Above a second threshold r_s^{FS}, M regularly decreases to reach a zero value at a third threshold $r_s^{WS} \approx 9$ where an antiferromagnetic square molecule is formed. The ensemble averages $< \log Q_1 >$ and $< \log Q_2 >$ (without taking into account the $S = 1$ spontaneously magnetized clusters) define the typical fields B necessary to yield $S = 1$ or $S = 2$ in a $S = 0$ cluster. In Fig. 2, one can see an intermediate regime again for $r_s^{FS} < r_s < r_s^{WS}$ where $< \log Q_1 >$ becomes roughly independent of r_s, while $Q_2 \propto r_s^{-2}$.

4 Conclusion

One concludes that mesoscopic Wigner crystallization proceeds in two stages. In a clean system, a minimal description of the intermediate GS requires to combine the low energy states of the two limiting eigenbases. In this sense, the intermediate GS is neither solid, nor liquid, but rather the quantum superposition of those two states of matter. This is strongly reminiscent of the conjecture proposed by Andreev and Lifshitz [3] for the quantum melting of a solid. A path integral Monte Carlo approach [4] has recently shown that a few electrons confined in a harmonic trap crystallize also in two stages, firstly via a radial ordering of electrons on shells and secondly via the freezing of the intershell rotation. As one can see, a two stage crystallization is not only characteristic of a mesoscopic harmonic trap, but also occurs in a mesoscopic $2d$ torus. To add a random substrate defavors the liquid state. The magnetization gives also the signature of an intermediate regime where Stoner ferromagnetism is defavored by Wigner antiferromagnetism.

References

1. G. Katomeris and J.-L. Pichard, cond-mat/0012213, submitted to *Phys. Rev. Lett.*.
2. F. Selva and J.-L. Pichard, cond-mat/0012015, submitted to *Europhys. Lett.*.
3. A. F. Andreev and I. M. Lifshitz, *JETP* **29**, 1107 (1969).
4. A. V. Filinov, M. Bonitz and Yu. E. Lozovik, *Phys. Rev. Lett.* **86**, 3851 (2001).

Percolation approach to the metal-insulator transition in two dimensions

Yigal Meir[1]

[1] *Department of Physics, Ben-Gurion University, Beer Sheva 84105, ISRAEL*

A simple non-interacting-electron model, combining local quantum tunneling via quantum point contacts and global classical percolation, in introduced in order to describe the observed "metal-insulator transition" in two dimensions. [1] It is shown that many features of the experiments, such as the exponential dependence of the resistance on temperature on the metallic side, the linear dependence of the exponent on density, the e^2/h scale of the critical resistance, the quenching of the metallic phase by a parallel magnetic field and the non-monotonic dependence of the critical density on a perpendicular magnetic field, can be naturally explained by the model.

1 Background and introduction of the model

The surprising experimental observation of a metal-insulator transition in two dimensions,[2] in contradiction with the predictions of single-parameter scaling theory for noninteracting electrons, has been a subject of extensive investigation in recent years. In this work[1] I proposed a simple non-interacting electron model, combining local quantum tunneling and global classical percolation, to explain several features of the experimental observations. At low electron or hole densities the potential fluctuations due to the disorder cannot be screened and they define density puddles. These puddles are connected via saddle points, or quantum points contacts (QPCs). It is now established that even at low temperatures and for open puddles (or quantum dots), the dephasing time may be shorter than the escape time from the puddle.[3] Thus it is assumed that between tunneling events through the QPCs dephasing takes place, and the conductance of the system will be determined by adding classically these quantum resistors. Each saddle point is characterized by its critical energy ϵ_c, such that the transmission through it is given by $T(\epsilon) = \Theta(\epsilon - \epsilon_c)$. (I assume that the energy scale over which the transmission changes from zero to unity is smaller than the other relevant energy scales, to avoid additional parameters). Then the conductance through a QPC is given by the Landauer formula,

$$\begin{aligned} G(\mu,T) &= \frac{2e^2}{h}\int d\epsilon \left(-\frac{\partial f_{FD}(\epsilon)}{\partial \epsilon}\right) T(\epsilon) \\ &= \frac{2e^2}{h}\frac{1}{1+\exp[(\epsilon_c-\mu)/kT]}, \end{aligned} \tag{1}$$

where μ is the chemical potential, and f_{FD} is the Fermi-Dirac distribution function.

The system is now composed of classical resistors, where the resistance of each one of them is given by (1), with random QPC energies. At low temperatures the resistors can be divided into two groups, the conducting ones ($\epsilon_c < \mu$), whose conductance is about $2e^2/h$, and the insulating ones ($\epsilon_c > \mu$), whose conductance is nearly zero. Thus the distribution of the conductances will be a two-peak distribution, where the weight of each peak will be determined mainly by density (or chemical potential) and the position of the conducting peaks will be determined mainly by temperature. Since most properties of such a percolating network are insensitive to details of this distribution, I replace it by a two-delta function distribution, namely replace the network by a network comprising of two types of conductors and calculate the conductance for such two-species percolation mixture, using its known scaling form near the percolation threshold is well known.[4,5]

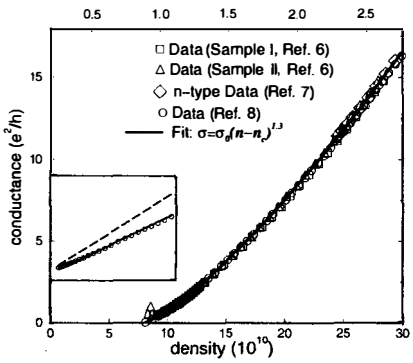


Figure 1: Comparison of the lowest temperature data of [6] (triangles and squares) and of [7] (circles) and of [8] (diamonds) to the prediction of percolation theory (solid line). Inset: Logarithmic derivative of the data [6] which gives a line whose slope is inverse of the critical exponent. The percolation prediction ($t \simeq 1.3$) is given by the solid line. For comparison a $t = 1$ slope is also shown (broken line).

2 "Zero" temperature

At low enough temperatures, the conductors have either zero conductance or a conductance equal to $2e^2/h$. If the dephasing time is still finite at these temperatures, one has a random-resistor network, which exhibits a second-order percolation transition.[5] In Fig. 1 I fit the lowest-temperature experimental data of [7,8,6] to the expected critical dependence. Clearly, the agreement with the classical percolation prediction is excellent. Such as agreement with the classical percolation critical behavior may serve as an additional experimental indication that the dephasing is still finite at the lowest available experimental temperatures.

In the inset I plot the experimental data[6] for $1/(d\log\sigma/d\log n)$, which, if indeed $\sigma \sim (n-n_c)^t$, is given by $(n-n_c)/t$. The data indeed fits on a straight line, with a slope given by $1/t \simeq 1/1.3$, the known value of this exponent. For comparison a straight line with a slope of unity is also depicted, in order to demonstrate that a critical exponent of unity cannot fit the data.

3 Temperature dependence of the resistance

As temperature increases, the Fermi-Dirac distribution is broadened. Consequently the conductance of the of the transparent quantum point contacts ($\epsilon_c < \mu$) decreases exponentially (towards half its value), while that of the insulating ones increases. Thus we expect to see rather dramatic effects as a function of temperature. As temperature is lowered, systems with slightly different resistance at high temperatures will diverge exponentially with decreasing temperatures. The resistance of systems on the metallic side ($n > n_c$) will saturate at zero temperature, while that of insulating samples will diverge, in agreement with the general shape of the experimental curves. Close to the transition, on the metallic side, as temperature decreases, the conductance of the insulating part decreases significantly, and its contribution to the total conductance is dramatically reduced. Since the critical percolation cluster is very ramified (in fact of fractal dimension), the contribution of the insulating part of the system dominates at high temperatures, and the increase of its resistance with decreasing temperature leads to an increase of the resistance as temperature is lowered, even on the metallic side. At low enough temperatures, however, when the resistance of the insulating part of the network becomes high enough, its contribution to the total conductance becomes negligible. Then the total resistance is domi-

nated by the percolating conducting network, and thus the overall resistance will decrease with decreasing temperature. This leads to a nonmonotonic temperature dependence on the metallic side of the critical point, which was indeed observed experimentally.

4 Parallel magnetic fields

The effect of a parallel magnetic field on the overall conductance is determined by the way it affects the individual points contacts. The effect of a parallel field on transport through a single QPC has been studied in detail. [9] These experimental and theoretical studies demonstrated that the threshold density where the QPC opens up *increases* parabolically with the in-plane magnetic field. This effect was attributed to coupling of the in-plane motion to the strong confinement in the vertical direction, leading to an increase in the confining enrgy. Writing, for simplicity, the three dimensional Hamiltonian that describes free motion in two-dimensions and a harmonic confining potential in the third (z) direction, with a magnetic field pointing in the x-direction

$$\mathcal{H} = \frac{p_x^2}{2m} + \frac{(p_y + eBz)^2}{2m} + \frac{p_z^2}{2m} + \frac{1}{2}m\omega_0^2 z^2 \quad , \tag{2}$$

it is straightforward to see that the bottom of the 2d band shifts from $\hbar\omega_0/2$ to $\hbar\sqrt{\omega_0^2 + \omega_c^2}/2$, with $\omega_c \equiv eB/mc$, leading to a corresponding decrease in the kinetic energy of all electrons. Thus the effective critical Fermi energy, or density, becomes larger. In other words, for a given density or chemical potential, if the system at zero field is on the metallic side, i.e. if the Fermi momentum is above the critical momentum (or kinetic energy) allowing percolation through the system, a parallel field will lower that energy towards the critical energy, eventually crossing the critical point and leading to an insulating behavior.

The above discussion allows a quantitative prediction of the effective critical energy in a parallel field. On the metallic side the resistance increases rapidly as the magnetic field brings the critical point closer to the chemical potential and then an abrupt change of behavior as the system enters the insulating regime. As was mentioned above, the critical point in the density – magnetic field plane shifts towards higher densities with increasing magnetic field. Yoon et al.[10] have also measured the dependence of the critical field on density, which can be readily deduced from the above argument,

$$H_c = m^* c/e\sqrt{\Delta(H)^2 + 2\hbar\omega_0\Delta(H)}, \tag{3}$$

where $\Delta(H) \equiv \epsilon_c(H) - \epsilon_c(H=0)$. The comparison of the prediction of this simple equation to the data is depicted in Fig. 2 for two samples cut from the same wafer. The fitting parameters are the zero-field critical point, that can be read directly from the data, the gate capacitance - the rate at which the Fermi energy changes with density, and the confining energy in the perpendicular direction, $\hbar\omega_0$. It is encouraging to note that while the critical energy, which is determined by the disorder realization, and the gate capacitance, which is determined by the geometry, are different for the two samples, both sets of data can be fitted by the same value of the perpendicular confining energy, which ought to be the same for the two samples, and turns out to be $\hbar\omega_0 \simeq 0.8meV$, leading to an extension of the wavefunction in the perpendicular direction of the order of 11 nm. Consequently, it seems that the effects of parallel fields can be understood without employing the electron spin.

To conclude, a semi-classical model, combining local quantum transport and global classical percolation was employed to explain the observed metal-insulator transition. The model attributes the transition to the finite dephasing length in these temperatures. As temperature is lowered even further, and the dephasing length becomes larger than the puddle size, quantum localization effects should kick in, and eventually these systems will eventually becomes Anderson insulators.

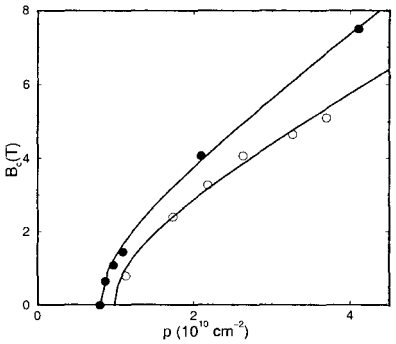


Figure 2: Comparison of the measured density dependence of the critical magnetic field[10] (circles) to the prediction of the theory (Eq.3, solid lines). The two data sets are two different samples cut from the same wafer, and can be fitted using the same value of the perpendicular confining energy.

Acknowledgments

This work was supported by THE ISRAEL SCIENCE FOUNDATION - Centers of Excellence Program, and by the German Ministry of Science.

References

1. Y. Meir, *Phys. Rev. Lett.* **83**, 3506 (1999); Y. Meir, *Phys. Rev.* **B 61**, 16470 (2000); Y. Meir, *Phys. Rev.* **B 63**, 073108 (2000).
2. E. Abrahams, S. V. Kravchenko amd M. P. Sarachik, Rev. Mod. Phys. **73**, 251 (2001).
3. See, e,.g., D. P. Pivin et al., *Phys. Rev. Lett.* **82**, 4687 (1999).
4. A. L. Efros and B. I. Shklovskii, Phys. Stat. Sol. **B76**, 475 (1976); A. Bunde et al., J. Phys. **A 18**, L137 (1985).
5. For a review of pecolation theory see, for example, D. Stauffer and A. Aharaony, *Introduction to Percolation Theory* (Taylor & Francis, London, 1992).
6. Y. Yaish and el., *Phys. Rev. Lett.* **84**, 4954 (2000).
7. Y. Hanein et al., *Phys. Rev. Lett.* **80**, 1288 (1998).
8. Y. Hanein et al., *Phys. Rev.* **B58**, R13338 (1998).
9. See, e.g. T. P. Smith et al., *Phys. Rev. Lett.* **61**, 585 (1988).
10. J. Yoon et al., *Phys. Rev. Lett.* **84**, 4421 (2000).

DILUTE ELECTRON GAS NEAR THE METAL INSULATOR TRANSITION IN SILICON INVERSION LAYERS.

ALEXANDER PUNNOOSE and ALEXANDER M. FINKEL'STEIN
Department of Condensed Matter Physics, Weizmann Institute of Science, Rehovot, 76100, Israel

In recent years systematic experimental studies of the temperature dependence of the resistivity in a variety of dilute, ultra clean two dimensional electron/hole systems have revived the fundamental question of localization or, alternatively, the existence of a metal-insulator transition in the presence of strong electron-electron interactions in two dimensions. We argue that under the extreme conditions of ultra clean systems not only is the electron-electron interaction very strong but the role of other system specific properties are also enhanced. In particular, we emphasize the role of valleys in determining the transport properties of the dilute electron gas in silicon inversion layers (Si-MOSFETs). It is shown that for a high quality sample the temperature behavior of the resistivity in the region close to the critical region of the metal-insulator transition is well described by a renormalization group analysis of the interplay of interaction and disorder if the electron band is assumed to have two distinct valleys. The decrease in the resistivity up to five times has been captured in the correct temperature interval by this analysis, without involving any adjustable parameters. The considerable variance in the data obtained from different Si-MOSFET samples is attributed to the sample dependent scattering rate across the two valleys, presenting thereby with a possible explanation for the absence of universal behavior in Si-MOSFET samples of different quality.

The resistivity, $R_\Box(T)$, of high mobility two dimensional (2D) electron/hole systems is seen to exhibit a noticeable drop as the temperature is reduced [1,2]. (For an extensive bibliography, see Ref. 3.) The drop appears to be completely quenched when a magnetic field is applied parallel to the plane [4]. This anomalously strong positive magnetoresistance points to the importance of the electron-electron (e-e) interaction in this phenomenon. Indeed, the high quality of the samples allows measurements to be made at very low carrier densities corresponding to $r_s \gtrsim 10$, where $r_s = E_{e\text{-}e}/E_{\rm F}$ is the ratio of the Coulomb energy to Fermi energy.

The most pronounced anomaly has been reported in the cleanest (001) Si-MOSFET samples, where a steep drop in $R_\Box(T)$ of up to five to six times has been observed. In Fig. 1 the temperature dependence of the resistivity for different densities in a Si-MOSFET sample with a very high peak mobility has been reproduced [5]. The insulating region, where the resistivity increases with decreasing temperature, is labeled as **I** in Fig. 1. The range of densities where the resistivity depends non-monotonically on temperature is labeled as $\mathbf{C}^*$ in Fig. 1. (For the specific sample used in Fig. 1, this region covers electron densities in the range $0.8 \times 10^{11} < n < 1 \times 10^{11}{\rm cm}^{-2}$.) A narrow range of densities in between these two regions, can be considered as the critical region **C**. The region where no clear maximum in the resistivity is observed (unlike $\mathbf{C}^*$) is labeled as **M** in Fig. 1. The region $\mathbf{C}^*$ is the subject of interest here.

Since the maximum of the resistivity in the region $\mathbf{C}^*$ is comparable to $\sim \hbar/e^2$, the transport mean free path time, τ, of the electrons here is such that $\hbar/\tau \lesssim E_{\rm F}$. The maximum together with the steep decrease in $R_\Box(T)$ occurs at low temperatures well below the Fermi energy (see Fig. 1). Therefore, the indications are that the non-monotonic behavior of the resistivity in the region $\mathbf{C}^*$ is a manifestation of the physics of strongly interacting electrons that are in the diffusive regime: $T < \hbar/\tau \lesssim E_{\rm F}$.

In the region **M** in Fig. 1 a naive estimate for τ can be extracted from the Drude expression for the resistivity, $\hbar/\tau = 4(e^2/\hbar)R_\Box(T=0)E_{\rm F}$. This estimate gives values for $\hbar/\tau$ that are well below the Fermi energy, while the steep drop in the resistivity develops at temperatures that are comparable to or larger than $\hbar/\tau$. This implies that the anomalies in the region **M** occur in the temperature range $\hbar/\tau \lesssim T < E_{\rm F}$, and their origin may be attributed to a strong temperature dependence of the single particle mean free path time $\tau(T)$ [6]. On the contrary,

the situation in the region $\mathbf{C}^*$ is quite different since the anomalies here are in the temperature range $T < \hbar/\tau \lesssim E_F$ where disorder quenches the effects of thermal smearing on $\tau(T)$.

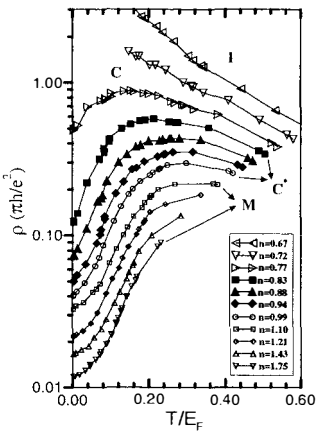


Figure. 1: *Resistivity of a high mobility Si-MOSFET sample for various densities as a function of temperature. The electron densities, n, are defined in units of* $10^{11}\,cm^{-2}$. *Data are reproduced from Fig. 1(a) of Ref. 5.* **I** *labels the insulating region, and* **C** *labels the critical region.* $\mathbf{C}^*$ *is the region near the critical region where a clear maximum is observed in the temperature dependence of the resistivity and is the region that is studied in the text.* **M** *labels the region further away from the critical region where such a maximum is not observed.*

These considerations lead us to the conclusion that the anomalous decrease in the resistivity in the two regions, $\mathbf{C}^*$ and **M**, may have different origins and are hence best studied separately.

Since considerable variance is seen even in the data obtained from different samples of similar origin, for a quantitative understanding of the temperature dependence of the resistivity some system specific non-universal mechanism should be necessarily invoked. The conduction band of the electrons in a (001) Si-MOSFET surface has two almost degenerate valleys [7]. Here, the sensitivity of the transport properties to the scattering rate across the two valleys is presented as a possible explanation for the absence of this universality.

To understand the temperature dependence of $R_\Box(T)$ in the case of two valleys, we study the interplay of the appropriate collective modes. These modes describe fluctuations of the local density of particles, spin, and in addition the fluctuations involving electron states from different valleys. Altogether there are $4 \times 4 = 16$ electron-hole states that break up into one singlet and fifteen multiplet states. In the case of strong intervalley scattering, however, the modes that are made of states from different valleys acquire a gap proportional to $\hbar/\tau_\perp$. At temperatures comparable to the rate of the intervalley scattering, $\hbar/\tau_\perp$, a crossover occurs between a band with two distinct valleys and a band where the two valleys are effectively unified due to the intervalley scattering. We believe that in a typical sample the value of $\hbar/\tau_\perp$ falls within the temperature interval in which measurements are made. Hence due to the crossover at $T \sim \hbar/\tau_\perp$ the resistivity $R_\Box(T)$ will be non-universal. Only in an ultra clean sample, where the intervalley scattering is very weak and the two valleys are well separated, should a universal behavior hold.

In 2D the leading divergences are logarithmic and the RG equation describing the evolution of the resistivity in the case of two distinct valleys, *i.e.*, when $T > \hbar/\tau_\perp$, can be easily generalized from the previous studies in the absence of valleys [8,9]:

$$\frac{d\rho}{d\xi} = \rho^2 \left[2 + 1 - 15 \left(\frac{1+\gamma_2}{\gamma_2} \ln(1+\gamma_2) - 1 \right) \right] . \qquad (1)$$

Here $\xi = -\ln(T\tau)$ and the dimensionless parameter $\rho = (e^2/\pi h) R_\Box$. In the square brackets the first term corresponds to the weak localization correction (cooperons) while the second term is the contribution of the singlet density mode which due to the long ranged nature of the Coulomb interaction is universal [10]. The last term describes the contribution of the 15 multiplet modes. γ_2 is the Fermi liquid amplitude that controls the *e-e* interaction in all the multiplet

channels, normalized by the density of states for a single spin and valley species. Due to the increase of the number of the multiplet modes in the case of two valleys, the last term that favors antilocalization noticeably increases compared to the single valley case. The resulting flow of $\rho(\xi)$ becomes antilocalizing when γ_2 is greater than the value $\gamma_2^* = 0.45$, while in the case of a single valley $\gamma_2^* = 2.04$. The reduction of γ_2^* from 2.04 to 0.45 makes it easier in the case of two valleys to reach the stage where the resistivity starts to decrease.

In 2D the amplitude γ_2 also experiences logarithmic corrections due to the disorder[8,9]. The equation describing the RG evolution of γ_2 is the same for both one and two valleys:

$$\frac{d\gamma_2}{d\xi} = \rho \frac{(1+\gamma_2)^2}{2} . \tag{2}$$

As the temperature is lowered γ_2 increases monotonically, and when it increases beyond the value γ_2^* the resistivity will pass through a maximum. Although the initial values of ρ and γ_2 are not universal, the flow of ρ can be described by a universal function $R(\eta)$[8]:

$$\rho = \rho_{\max} R(\eta) \text{ and } \eta = \rho_{\max} \ln(T_{\max}/T) , \tag{3}$$

where $T_{\max}$ is the temperature at which ρ reaches its maximum value $\rho_{\max}$, *i.e.*, $\gamma_2(T_{\max}) = \gamma_2^*$. For the case of two valleys, the function $R(\eta)$ is found here by numerically integrating Eq. 1 and Eq. 2 with the boundary conditions: $\rho(\xi = 0) = \rho_{\max} = 1$ and $\gamma_2(\xi = 0) = \gamma_2^* = 0.45$.

Thus, if the experimental data of the resistivity are scaled according to Eq. 3, the data should collapse on the function $R(\eta)$. This analysis has certain limitations, however. The RG equations have been derived in the lowest order in ρ and therefore cannot be applied in the critical region **C** where $\rho \gtrsim 1$. On the other hand, for $\rho \ll 1$ exponentially small temperatures are needed for changes in the resistivity to become noticeable. In addition, some other mechanism operating in the region **M** may mask the small logarithmic corrections when $\rho \ll 1$. For these reasons, only curves in the region $\mathbf{C}^*$ with maximum ρ ranging from $\rho_{\max} \approx 0.3$ to $\rho_{\max} \approx 0.6$ have been used to test the RG analysis. The result is presented in Fig. 2. The decrease in the resistivity up to five times together with its saturation has been captured in the correct temperature interval by this analysis without any adjustable parameters.

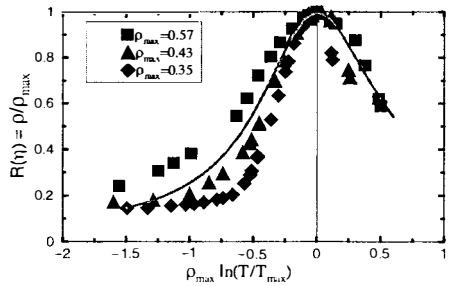


Figure. 2: *The data corresponding to* $n = 0.83, 0.88,$ *and* $0.94 \times 10^{11} cm^{-2}$ *in Fig. 1 are scaled according to Eq. 3. The solid line corresponds to the solution of the renormalization group Eqs. 1 and 2; no adjustable parameters have been used in this fit.*

In low mobility samples, where a description in terms of an effective single valley is relevant, the large value for $\gamma_2^* = 2.04$ makes it difficult for the non-monotonicity to be observed. Then, to scale the amplitude γ_2 till the value γ_2^* will, for $\rho \ll 1$, demand exponentially small temperatures. On the other hand, for ρ near the critical region the resistivity flows rapidly to such large values that the system instead of passing through the maximum becomes insulating.

The strong magnetoresistance in a parallel magnetic field can be also understood by the reduction of the number of diffusion modes that contribute to the antilocalizing corrections[11]. Here, the Zeeman splitting induces a gap in the propagators of the diffusion modes that are made of states with different spin projections. In a very strong magnetic field when the electrons are completely polarized, the system becomes identical to one with no valleys with the original

valleys acting as fictitious spin projections. The difference in the resistivity of two- and one-valley systems, which is large at low enough temperatures, will be recovered as the magnetic field is applied resulting in a very strong positive magnetoresistance.

Information about the rate of the intervalley scattering can be obtained from the measurements in a weak perpendicular magnetic field. The results of these measurements [12], which yield a negative magnetoresistance, have been fitted with a standard expression [13] containing the Digamma function, Ψ. For the prefactor α in this expression, the theory predicts: $\alpha = 1$ in the absence of the intervalley scattering and $\alpha = 0.5$ in the case of strong intervalley scattering [14]. The experimental situation for the sample used in Fig. 1 (but after some age degradation, however) remains uncertain. The optimal fit gives values for α between 0.6 and 0.8, with a tendency to be larger when the density decreases [12]. We consider the fact that α is noticeably larger than 0.5 as an indication that the intervalley scattering is not too strong in the system at low density.

In conclusion, we have demonstrated that in an ultra clean (100) Si-MOSFET the temperature behavior of the resistivity in the region $\mathbf{C}^*$ is well described by the RG analysis of the interplay of the *e-e* interaction and disorder when the electron band has two distinct valleys. We have argued that it is not the large value of r_s that makes the physics of the region not far from the transition in high mobility MOSFET samples so different from that in lower mobility samples, but the difference in their number of effective valleys.

We have benefited greatly from numerous discussions with V. M. Pudalov. This work was supported by the German Ministry of Science (DIP) and INTAS. A. P. acknowledges the support of the Feinberg Graduate School of the WIS.

1. S. V. Kravchenko *et al.*, *Phys. Rev.* B **50**, 8039 (1994).
2. S. V. Kravchenko *et al.*, *Phys. Rev.* B **51**, 7038 (1995).
3. E. Abrahams, S. V. Kravchenko, M. P. Sarachik, *Rev. Mod. Phys.* **73**, 251 (2001).
4. D. Simonian *et al.*, *Phys. Rev. Lett.* **79**, 2304 (1997); V. M. Pudalov, G. Brunthaler, A. Prinz, G. Bauer, *JETP Lett.* **65**, 932 (1997).
5. V. M. Pudalov, G. Brunthaler, A. Prinz, G. Bauer, *Physica* E **3**, 79 (1998).
6. F. Stern, *Phys. Rev. Lett.* **44**, 1469 (1980); A. Gold, V. T. Dolgopolov, *Phys. Rev.* B **33**, 1076 (1986); S. Das Sarma, *Phys. Rev.* B **33**, 5401 (1986).
7. T. Ando, A. B. Fowler, F. Stern, F., *Rev. Mod. Phys.* **54**, 437 (1982).
8. A. M. Finkel'stein, *Sov. Phys. JETP* **57**, 97 (1983); *Z. Phys.* B **56**, 189 (1984); *Sov. Sci. Rev. A. Phys.* **14(2)**, 1 (1990).
9. C. Castellani *et al.*, *Phys. Rev.* B **30**, 1596 (1984).
10. B. L. Altshuler, A. G. Aronov, in *Electron-Electron Interactions in Disordered Systems*, A. L. Efros, M. Pollack, Eds. (North-Holland, Amsterdam, 1985), pp. 1-153.
11. P. A. Lee, T. V. Ramakrishnan, *Phys. Rev.* B **26**, 4009 (1982); C. Castellani, C. Di Castro, P. A. Lee, *Phys. Rev.* B **57**, R9381 (1998).
12. G. Brunthaler *et al.*, Preprint cond-mat/0007230 at ⟨http://xxx.lanl.gov⟩ (2000).
13. B. L. Altshuler, D. E. Khmelnitskii, A. I. Larkin, P. A. Lee, *Phys. Rev.* B **22**, 5142 (1980).
14. H. Fukuyama, *J. Phys. Soc. Jpn.* **50**, 3562 (1981).

QUANTUM COHERENCE

DECOHERENCE FROM VACUUM FLUCTUATIONS

MARKUS BÜTTIKER
Département de Physique Théorique, Université de Genève, CH-1211 Genève 4, Switzerland

Vacuum fluctuations are a source of irreversibility and decoherence. We investigate the persistent current and its fluctuations in a ring with an in-line quantum dot with an Aharonov-Bohm flux through the hole of the ring. The Coulomb blockade leads to persistent current peaks at values of the gate voltage at which two charge states of the dot have the same free energy. We couple the structure to an external circuit and investigate the effect of the zero-temperature (vacuum fluctuations) on the ground state of the ring. We find that the ground state of the ring undergoes a crossover from a state with an average persistent current much larger than the (time-dependent) mean squared fluctuations to a state with a small average persistent current and large mean squared fluctuations. We discuss the spectral density of charge fluctuations and discuss diffusion rates for angle variables characterizing the ground state in Bloch representation.

1 Introduction

In this work we are interested in the coherence properties of the ground state of a mesoscopic system coupled to an environment. In the zero-temperature limit, the only source of decoherence are then provided by vacuum fluctuations. The work is motivated by a recent discussion in the mesoscopic physics community which largely insists that dephasing rates tend to zero (typically with some power law) as a function of temperature and that there is therefore no dephasing in the zero-temperature limit. For references to this discussion we direct the reader to Ref. [1] .

A key argument is that in the zero-temperature limit a system can not excite a bath by giving away an energy quantum nor can a bath in the zero-temperature limit give an energy quantum to the system. This view holds that dephasing is necessarily associated with an energy transfer (a real transition) and since this is impossible there is in the zero-temperature limit no dephasing. However, this argument rests on the assumption that the system and the bath are in their ground state which they assume in the absence of any coupling. In the ground state of the system + bath, even at absolute zero, the energy of the small system fluctuates [2,3] and the ground state of the small system is not a pure state.

To illustrate this we investigate a simple mesoscopic system, a quantum dot with its leads formed into a ring [2], as shown in Fig. 1. Such a ring, when the coupling between the dot and the arms of the ring is sufficiently weak, exhibits Coloumb blockade peaks in the persistent current at gate voltages which equalize the free energy of the N-th and $N+1$-th charge state of the dot. We couple this system capacitively to an external circuit with ohmic resistance R and investigate the persistent current near a resonance. At absolute zero temperature the gate voltage fluctuates due to vacuum fluctuations of the resistor. We show that the ground state of this system is not a pure coherent state. In the two state limit, the system shown in Fig. 1 maps onto the spin boson problem: for this system there exits a large literature [4,5]. We emphasize that the work presented here is not directly related to weak localization but considers the persistent current (a ground state property).

2 Coulomb Blockade Peaks of the Persistent Current

Consider the system shown in Fig. 1. The arm of the ring contains electrons in levels with energy E_{am} and the dot contains electrons in levels with energy E_{dn}. First let us for a moment neglect tunneling. Let F_N be the free energy for the case that there are N electrons in the dot and M electrons in the arm. The transfer of an electron from the arm to the dot gives a free

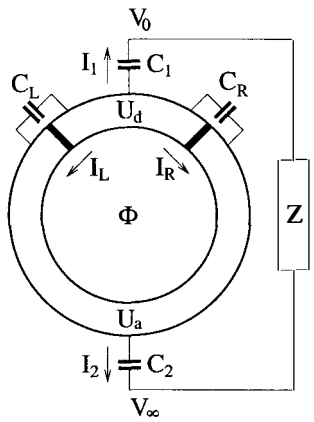


Figure 1: Ring with an in-line dot subject to a flux Φ and capacitively coupled to an external impedance Z.

energy F_{N+1}. The difference of these two free energies is

$$\hbar\epsilon_0 = F_{N+1} - F_N = E_{d(N+1)} - E_{aM} + \frac{e^2(N+1/2-C_0V_e)}{C}. \quad (1)$$

Here the first two terms arise from the difference in kinetic energies. The third term results from the charging energy of the dot. $C_0^{-1} = C_i^{-1} + C_e^{-1}$ is the series capacitance of the internal capacitance $C_i = C_L + C_R$ and the external capacitance $C_e^{-1} = C_1^{-1} + C_2^{-1}$. The total capacitance is $C = C_i + C_e$. Tunneling through the barriers connecting the dot and the arm is described by amplitudes t_L and t_R and depends on the Aharonov-Bohm flux Φ in the following way [6],

$$\frac{\hbar\Delta_0}{2} = \left(t_L^2 + t_R^2 \pm 2t_L t_R \cos\frac{2\pi\Phi}{\Phi_0}\right)^{1/2}, \quad (2)$$

where $\Phi_0 = hc/e$ is the single electron flux quantum. The sign depends on the number of electrons in the dot and arm: it is positive if the total number is odd, and it is negative if the total number is even. The voltage across the system is $V = V_0 - V_\infty$. The Hamiltonian consists of the system part H_0, the coupling H_c and the bath H_B with

$$H_0 = \frac{\hbar\epsilon_0}{2}\sigma_z - \frac{\hbar\Delta_0}{2}\sigma_x, \quad H_c = \frac{C_0}{C_i}\frac{eV}{2}\sigma_z. \quad (3)$$

H_0 has eigenstates with energies

$$E_\mp = \mp\frac{\hbar}{2}\sqrt{\epsilon_0^2 + \Delta_0^2} \equiv \mp\frac{\hbar\Omega_0}{2}. \quad (4)$$

In the presence of a flux Φ the ground state of the ring-dot system (see Fig. 1) permits a persistent current which is [6]

$$< I >= -c\frac{dE_-}{d\Phi} = \mp e\frac{4\pi t_L t_R}{\Omega_0}\sin(2\pi\Phi/\Phi_0). \quad (5)$$

The equilibrium current is a pure quantum effect: only electrons whose wave functions are sufficiently coherent to reach around the loop contribute to the persistent current. Thus the persistent current is a measure of the coherence of the ground state. At resonance $\epsilon = 0$ the

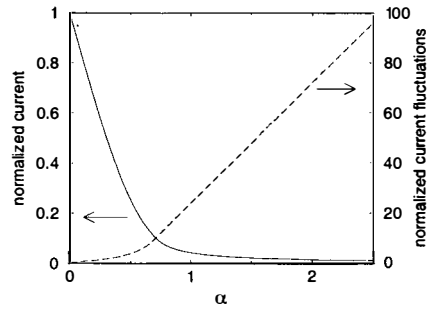


Figure 2: The persistent current $< I >$ at resonance $\epsilon = 0$ for a symmetric ring (solid line) and the fluctuations of the circulating current $(< (I(t) - < I(t) >)^2 >)^{1/2} / < I >$ (dashed line) as a function of the coupling parameter α. The average persistent current is in units of the persistent current at $\alpha = 0$. The fluctuations are normalized by the average current. The parameters are $\omega_c = 25\Delta_0$. After [2].

current is of the order of et with t a transmission amplitude and it decreases and becomes of the order of et^2/ϵ as we move away from resonance.

In the two-level limit of interest here the transmission amplitudes t_L and t_R are taken to be very small compared to the level spacing in the dot and in the arm. For larger transmission amplitudes the system without a bath will already exhibit a Kondo effect [7,8,9]. A completely equivalent model consists of a superconducting electron box [10] which can be opened to admit an Aharonov-Bohm flux [11,12].

We are interested in the effect of the bath on the persistent current. With the bath included our two-level system becomes a spin-boson problem [4,5]. Cedraschi, Ponomarenko and the author [2,13] used known solutions based on a Bethe ansatz and perturbation theory (for the anisotropic Kondo model) to provide an answer. For the symmetric case $t_L = t_R$, $C_L = C_R$, the average current is shown in Fig. 2 as a function of the coupling parameter

$$\alpha \equiv \frac{R}{R_K}\left(\frac{C_0}{C_i}\right)^2, \quad \Gamma \equiv \pi\alpha\frac{\Delta_0^2}{\Omega_0} \tag{6}$$

with $R_K \equiv h/e^2$ the quantum of resistance. We have also introduced the relaxation rate Γ which as will be shown governs the zero-temperature decoherence of the system. The persistent current is in units of the current for $\alpha = 0$. In addition Ref. [2] also investigated the (instantaneous) fluctuations of the equilibrium current away from its average, $(< (I(t) - < I(t) >)^2 >)^{1/2}$ shown in Fig. 2 in units of the average current $< I(t, \alpha) >$. With increasing resistance we have thus a *cross over* from a state with a well defined persistent current (small mean-squared fluctuations) to a fluctuation dominated state in which the mean-squared fluctuations of the persistent current are much larger than the average persistent current. For the derivation we refer the reader to Refs. [2] and [13]. Here we pursue a discussion based on Langevin equations [14]. This approach is valid only for weak coupling constants $\alpha \ll 1$ but has the benefit of being simple.

We want to find the time evolution of a state $\psi(t)$ of the two-level system in the presence of the bath. We write the state of the two-level system

$$\psi = e^{i\chi/2}\begin{pmatrix}\cos\frac{\theta}{2}\, e^{i\varphi/2} \\ \sin\frac{\theta}{2}\, e^{-i\varphi/2}\end{pmatrix}, \tag{7}$$

with θ, φ and χ real. This is the most general form of a normalized complex vector in two dimensions. In terms of θ, φ and the global phase χ, the time dependent Schrödinger equation reads

$$\dot{\varphi} \;=\; -\varepsilon_0 - \delta\varepsilon(t) - \Delta_0 \cot\theta \cos\varphi, \tag{8}$$

$$\dot{\theta} = -\Delta_0 \sin\varphi, \tag{9}$$

$$\dot{\chi} = \Delta_0 \frac{\cos\varphi}{\sin\theta}. \tag{10}$$

Here $\delta\varepsilon(t) = (e/h)(C_0/C_i)V(t)$ arises from the gate voltage fluctuations. As shown by Eq. (10) the dynamics of the phase χ is completely determined by the dynamics of the phases θ and φ and has no back-effect on the evolution of θ and φ. While χ is irrelevant for expectation values, like the persistent current or the charge on the dot, it plays an important role, in the discussion of phase diffusion times.

To close the system of equations, we have to find the voltage which drops across the system. The charge transfer between the dot and its arms permits a displacement current through the system which we have to include to find the voltage fluctuations. The charge operator on the dot for our problem is $\hat{Q}_d = (1/2)(\sigma_z + 1)$. Its quantum mechanical expectation value is $Q_d = \langle\psi(t)|\hat{Q}_d|\psi(t)\rangle = e\cos^2(\theta/2)$. The displacement current is proportional to the time-derivative of this charge, $\dot{Q}_d = -\frac{e}{2}\sin\theta\,\dot{\theta}$ multiplied by a ratio of capacitances which has to be found from circuit analysis [14]. We find that the total current through the system is now given by $C_0\dot{V} - (C_0/C_i)(e/2)\sin\theta\,\dot{\theta}$. Using this result we find from conservation all currents that the fluctuating voltage across the system is determined by

$$V = -C_0 R\,\dot{V} - R\frac{C_0}{C_i}\frac{e}{2}\sin\theta\,\dot{\theta} + RI_N(t). \tag{11}$$

Eqs. (8, 9) and (11) form a closed system of equations in which the external circuit is incorporated in terms of an ohmic resistor R in parallel with a fluctuating current $I_N(t)$ with spectral density $S_{II}(\omega) = (\hbar\omega/R)coth(\hbar\omega/2kT)$. In the next section, we investigate Eqs. (8, 9) and (11) to find the effect of zero-point fluctuations on the persistent current of the ring.

3 Fluctuations around the ground state

In the absence of the noise term $I_N(t)$, the stationary states of the system of differential equations, Eqs. (8, 9) and (11) are given by $\varphi \equiv \varphi_0$, with $\varphi_0 = 0$ or $\varphi_0 = \pi$ and $\theta \equiv \theta_0$, with $\cot\theta_0 = \pm\frac{\varepsilon_0}{\Delta_0}$. The lower sign applies for $\varphi_0 = 0$. This is the *ground state* for the ring-dot system at fixed $\varepsilon(t) \equiv \varepsilon_0$, and the upper sign holds for $\varphi_0 = \pi$. The energy of the ground state is $-\hbar\Omega_0/2$, thus the global phase is $\chi_0(t) = \Omega_0 t$. We also introduce the "classical" relaxation time $\tau_{RC} \equiv RC_0$.

Now, we switch on the noise $I_N(t)$. We seek $\varphi(t), \theta(t)$, $\chi(t)$ and $V(t)$ in linear order in the noise current $I_N(t)$. We expand $\varphi(t)$ and $\theta(t)$ to first order around the ground state, $\varphi = 0$ and $\theta = \theta_0$. For $\delta\varphi(t) = \varphi(t) - \varphi_0$, $\delta\theta(t) = \theta(t) - \theta_0$, etc., we find in Fourier space,

$$-i\omega\delta\varphi = -\delta\varepsilon + \frac{\Omega_0^2}{\Delta_0}\delta\theta, \tag{12}$$

$$-i\omega\delta\theta = -\Delta_0\,\delta\varphi, \tag{13}$$

$$-i\omega\,\delta\varepsilon = \frac{1}{\tau_{RC}}\left[-\delta\varepsilon - \Gamma\,\delta\varphi + \frac{e}{\hbar}R\frac{C_0}{C_i}I_N\right], \tag{14}$$

$$-i\omega\delta\chi = \Omega_0\frac{\varepsilon_0}{\Delta_0}\delta\theta. \tag{15}$$

Here we have also expanded the global phase $\chi(t)$ around its evolution in the ground state $\chi_0(t) = \Omega_0 t$, and define $\delta\chi(t) = \chi(t) - \chi_0(t)$. We note that there is no effect of the global shift in energy, $\hbar\nu(t)$, as it is quadratic in the voltage δV, and we are only interested in effects up to linear order in δV.

4 Mapping onto a harmonic oscillator

Let us assume that the charge relaxation time of the external circuit τ_{RC} is very short compared to the dynamics of the two-level system $\tau_{RC} \ll \Omega_0$. Eliminating $\delta\theta$ with the help of Eq. (13) and $\delta\varepsilon$ with the help of Eq. (14) we find

$$(\omega^2 - i\omega\Gamma - \Omega_0^2)\,\delta\theta = \Delta_0 \frac{e}{\hbar}\frac{C_0}{C_i} R I_N. \tag{16}$$

Thus we have mapped the dynamics of the fluctuations away from the ground state of this two-level system on the quantum Langevin equation of a damped harmonic oscillator. $\delta\theta$ plays the role of the charge, $\delta\varphi$ the role of the current and Γ (defined in Eq. (6)) takes the role of the friction constant. The spectral density $S_{\theta\theta}(\omega)$ is just that of the coordinate of the harmonic oscillator,

$$S_{\theta\theta}(\omega) = \frac{2\pi\,\alpha\,\Delta_0^2\,|\omega|}{\left[(\omega^2 - \Omega_0^2)^2 + \Gamma^2\omega^2\right]}. \tag{17}$$

In the literature it is often the correlation function of σ_z which is of interest. We have $< \psi|\sigma_z|\psi >= \cos(\theta)$ and thus for the fluctuations away from the average $\Delta < \psi|\sigma_z|\psi >= -\sin(\theta_0)\delta\theta$. Since $\sin(\theta_0) = \Delta_0/\Omega_0$, we find in the zero-temperature limit $S_{\sigma_z\sigma_z}(\omega) = (\Delta_0^2/\Omega_0^2)S_{\theta\theta}(\omega)$. This result agrees with an expression given by Weiss and Wollensak [15] and Görlich et al. [16] who have used an entirely different approach. For non-zero temperatures Weiss and Wollensak find in addition a Debye peak around zero-frequency. The essential point is that the peaks are broadened with a relaxation rate Γ. Using Eqs. (13) and (14) we obtain similarly the spectral densities $S_{\varphi\varphi}(\omega)$, $S_{\chi\chi}(\omega)$ and cross-correlations like $S_{\theta\varphi}(\omega)$.

5 Suppression of the Persistent Current

Let us next examine the reduction of the persistent current using the approach outlined above. We consider only the case of a symmetric ring $t_R = t_L \equiv t$ and $C_R = C_L$ (see Fig. 1). The persistent current is the quantum and statistical average of the operator $\hat{I}_c = \mathcal{J}\sigma_x$ where $\mathcal{J}$ is given by $\mathcal{J} = \hbar c\frac{\partial\Delta_0}{\partial\Phi}$. In general, in the non-symmetric case, the operator for the persistent current depends also on the capacitances (see Appendix B of Ref. [14]). The quantum mechanical expectation value of the persistent current for the state given in Eq. (7) reads $I(t) \equiv \langle\psi(t)|\hat{I}_c|\psi(t)\rangle = \frac{1}{2}\mathrm{Re}\,(\mathcal{J}\sin\theta\, e^{-i\varphi})$. We are interested in the *statistically averaged* persistent current $\langle I(t)\rangle$. Therefore, we have to calculate the correlator $\langle\sin\theta\, e^{-i\varphi}\rangle$. Taking into account that for a harmonic oscillator the fluctuations are Gaussian, we find $\langle\sin\theta e^{-i\varphi}\rangle = \langle\sin\theta\rangle\langle e^{-i\varphi}\rangle$. and $\langle e^{-i\varphi(t)}\rangle = e^{-i\varphi_0}\langle e^{-i\delta\varphi(t)}\rangle = \langle\exp(-\delta\varphi^2(t)/2)\rangle$, where we have used that $\varphi_0 = 0$. In the weak coupling limit, and in the extreme quantum limit, $T = 0$, we find for the time averaged mean-squared fluctuations to leading order in Γ,

$$\langle\delta\varphi^2(t)\rangle = \int_0^{\omega_c}\frac{d\omega}{\pi}S_{\varphi\varphi}(\omega) = \frac{\Omega_0}{\Delta_0^2}[2\Gamma\ln\frac{\omega_c}{\Omega_0} - \Gamma + \pi\Omega_0] \approx 2\alpha\ln\frac{\omega_c}{\Omega_0}. \tag{18}$$

Here we have assumed that the cut-off frequency is so large that the logarithmic term dominates. In the limit $\omega_c \gg \Omega_0$, we can neglect $\langle\delta\theta^2(t)\rangle$ against $\langle\delta\varphi^2(t)\rangle$. We insert $\langle\delta\varphi^2(t)\rangle$ and $\sin\theta_0 = \Delta_0/\Omega_0$ into $\langle\sin\theta\, e^{-i\varphi}\rangle$, and find a noise averaged persistent current in the ring given by

$$\langle I(t)\rangle = -\frac{\hbar c}{2}\frac{\partial\Delta_0}{\partial\Phi}\frac{\Delta_0}{\Omega_0}\left(\frac{\Omega_0}{\omega_c}\right)^{\alpha}. \tag{19}$$

The weak coupling limit corresponds to $\alpha \ll 1$. The power law for the persistent current obtained in Eq. (19), as well as the exponent α, Eq. (6) coincide in this limit with the result obtained by Cedraschi et al. [2] using a Bethe ansatz solution. We next characterize the fluctuations of the ring-dot subsystem in more detail.

6 Phase Diffusion Times

Due to the vacuum fluctuations the ground state of the two-level system is a dynamic state. To see this we project the actual state of the system on the *ground state* $\psi_- = (\cos\theta_0/2, \sin\theta_0/2)$, with eigenvalue $-\hbar\Omega_0/2$, and the *excited state* $\psi_+ = (-\sin\theta_0/2, \cos\theta_0/2)$ with eigenvalue $\hbar\Omega_0/2$ of the isolated system. Instead of the wave function $\psi(t)$ it is more convenient to consider $\psi_R(t) \equiv \exp(i\hat{H}_0 t/\hbar)\psi(t)$. To first order in $\delta\varepsilon$, we find for the wave function $\psi_R(t) = (1 + ic_-)\psi_- + c_+\psi_+ e^{i\Omega_0 t}$ with

$$c_- = \frac{\delta\chi(t)}{2} - \frac{\varepsilon_0}{\Omega_0}\frac{\delta\varphi(t)}{2}, \quad c_+ = \left[\frac{\delta\theta(t)}{2} - i\frac{\Delta_0}{\Omega_0}\frac{\delta\varphi(t)}{2}\right] e^{i\Omega_0 t}. \tag{20}$$

Expressing the fluctuations of the angle variables in terms of their fluctuation spectra, we find $\left\langle |c_\mp(t) - c_\mp(0)|^2 \right\rangle = t/\tau_\mp$ with diffusion times [14]

$$\tau_- = \frac{\hbar}{2\pi\alpha kT}\frac{\Omega_0^2}{\varepsilon_0^2}, \quad \tau_+ = \frac{1}{\Gamma}\tanh\frac{\hbar\Omega_0}{2kT}. \tag{21}$$

Note that τ_- depends on the detuning ε_0. In particular, at resonance $\varepsilon_0 = 0$, the phase diffusion time τ_- diverges for any temperature. The long time behavior of τ_+, is determined by frequencies near Ω_0. Eq. (21) holds for finite temperatures as well as in the quantum limit. In the low-temperature or quantum limit, however, τ_+ *saturates* to a value $1/\Gamma$. Thus at short and intermediate times the ground state is not a coherent state but exhibits diffusion. The dephasing rate [15,16,17] is one-half of the sum of the two rates $1/\tau_\mp$.

References

1. D. Natelson, et al., Phys. Rev. Lett. **78**, 1821 (2001).
2. P. Cedraschi, V. V. Ponomarenko, and M. Büttiker, Phys. Rev. Lett. **84**, 346 (2000).
3. K. Nagaev, G. Seelig and M. Büttiker, (unpublished).
4. A. J. Leggett, et al., Rev. Mod. Phys. **59**, 1 (1987).
5. U. Weiss, *Quantum Dissipative Systems*, (Word Scientific, 2000).
6. M. Büttiker and C. A. Stafford, Phys. Rev. Lett. **76**, 495 (1996).
7. H.-P. Eckle, H. Johannesson, and C. A. Stafford, J. Low Temp. Phys. **118**, 475 (2000). cond-mat/0010101
8. K. Kang and S.-C. Shin, Phys. Rev. Lett. **85**, 5619 (2000).
9. I. Affleck and P. Simon, Phys. Rev. Lett. **86**, 2854 (2001); P. Simon, I. Affleck, cond-mat/0103175 .
10. V. Bouchiat, et al., J. of Superconductivity, **12**, 789 (1999).
11. J. E. Moji et al, Science **285**, 1036 (1999). L. Tian, et al., in "Quantum Mesoscopic Phenomena and Mesoscopic Devices in Microelectronics", edited by I. O. Kulik and R. Ellialtioglu, (Kluwer, Netherlands, 2000). p. 429.
12. Y. Makhlin, G. Schön, and A. Shnirman, in "Quantum Physics at Mesoscopic Scale" edited by D.C. Glattli, M. Sanquer and J. Tran Thanh Van (EDP Sciences, Les Ulis, 2000). p. 113
13. P. Cedraschi and M. Büttiker, Annals of Physics, **289**, 1 - 23 (2001).
14. P. Cedraschi and M. Büttiker, Phys. Rev. B **63**, 165312 (2001).
15. U. Weiss and M. Wollensak, Phys. Rev. Lett. **62**, 1663 (1989).
16. R. Görlich, M. Sassetti, and U. Weiss, Europhys. Lett. **10**, 507 (1989).
17. M. Grifoni, E. Paladino and U. Weiss, Eur. Phys. J. B**10**, 719 (1999).

COULOMB EFFECTS AND ELECTRON TRANSPORT THROUGH A COHERENT CONDUCTOR

A.D. ZAIKIN[1,2], D.S. GOLUBEV[2,3]
[1] *Forschungszentrum Karlsruhe, Institut für Nanotechnologie, D-76021 Karlsruhe, Germany*

[2] *I.E.Tamm Department of Theoretical Physics, P.N.Lebedev Physics Institute, Leninskii pr. 53, 117924 Moscow, Russia*

[3] *Institut für Theoretische Festkörperphysik, Universität Karlsruhe, D-76128 Karlsruhe, Germany*

We analyze electron transport through relatively short coherent conductors in the presence of Coulomb interaction. We evaluate the current-voltage characteristics of such conductors taking into account the effect of an external environment. Within our model, at large conductances and low T the conductance is suppressed by a universal factor which depends only on the type of the conductor. We also argue that at $T = 0$ the system "scatterer+shunt" can be either an insulator or a metal depending on whether its total resistance is larger or smaller than $R_Q = h/e^2 \approx 25.8$ kΩ. In a metallic phase the Coulomb gap is fully suppressed by quantum fluctuations.

1 Introduction

Discrete nature of the electron charge plays a crucial role in various phenomena in mesoscopic physics, causing, for instance, Coulomb blockade of electron tunneling in metallic junctions [1,2,3] and shot noise in mesoscopic conductors [4]. It is of particular importance to understand how an interplay of charge discreteness, Coulomb interaction and coherent scattering may affect electron transport in disordered conductors at sufficiently low temperatures.

Recently we argued [5] that the interaction term in the current-voltage characteristics of a (relatively short) coherent conductor is controlled by the parameter

$$\beta = \frac{\sum_n T_n(1-T_n)}{\sum_n T_n}, \tag{1}$$

which is already well known in the theory of shot noise [4]. Here T_n are the transmissions of conducting modes. A similar conclusion was also reached in Ref. 6 in the limit of a single conducting mode, in which case the parameter (1) reduces to $\beta = 1 - T_1$.

In this paper we extend our previous results [5] by considering the effect of an external environment on quantum transport through a coherent scatterer in the presence of Coulomb interaction.

2 Quasiclassical Langevin equation

As in Ref. 5 we will consider electron transport through an arbitrary coherent scatterer between two big reservoirs. The scatterer conductance without interactions is defined by the standard Landauer formula $1/R = (2e^2/h)\sum_n T_n$. Phase and energy relaxation are only allowed in the reservoirs and not during scattering, i.e. the scatterer is shorter than both dephasing and inelastic relaxation lengths L_φ and L_{in}. Coulomb effects in the scatterer region are described by an effective capacitance C. We also assume that the scatterer is attached to an external voltage source V_x via a linear impedance $Z_S(\omega)$.

In the limit of sufficiently large energies and/or at large scatterer conductances $g = R_Q/R \gg 1$ it is convenient to describe the system by means of the quasiclassical Langevin equation approach. This equation can be derived from the real time path integral technique [7,8,9]. For a coherent conductor to be considered here this derivation was performed in Ref. 5. The effect of

a linear external impedance can be incorporated in the same way as it was done for the case of tunnel junctions [9]. Combining the results [5,9] one arrives at the following Langevin equation

$$\frac{C}{e}\ddot{\varphi}+\frac{1}{eR}\dot{\varphi}+\int \hat{Z}_S^{-1}(t-t')\frac{\dot{\varphi}(t')}{e}dt'-\frac{V_x}{Z_S(0)}=\xi_1\cos\varphi+\xi_2\sin\varphi+\xi_3+\xi_S. \tag{2}$$

Here $\dot{\varphi}(t)/e=V(t)$ is the fluctuating voltage across the conductor. Eq. (2) is sufficient provided eV and T are smaller than the typical inverse traversal time $1/\tau_{trav}$ (e.g. the Thouless energy in the case of diffusive conductors). Below we will mainly address the limit $RC>\tau_{trav}$, however some of our results should remain valid in the opposite case as well. The terms in the right-hand side of (2) account for the current noise. They are defined by the correlators

$$\langle|\xi_1|^2_\omega\rangle=\langle|\xi_2|^2_\omega\rangle=\frac{\beta}{R}\omega\coth\frac{\omega}{2T},\qquad \langle|\xi_3|^2_\omega\rangle=\frac{1-\beta}{R}\omega\coth\frac{\omega}{2T}, \tag{3}$$

$$\langle|\xi_s|^2_\omega\rangle=\mathrm{Re}\left(\frac{\omega}{Z_S(\omega)}\right)\coth\frac{\omega}{2T}. \tag{4}$$

If we set $\varphi(t)=eV_xt$ and define the total fluctuating current $\delta I(t)=\xi_1\cos eV_xt+\xi_2\sin eV_xt+\xi_3$, we will immediately reproduce the standart result [10,4]:

$$\langle|\delta I|^2_\omega\rangle=\frac{1}{R_Q}\left\{2\omega\coth\frac{\omega}{2T}\sum_n T_n^2+\left[\sum_\pm(\omega\pm eV_x)\coth\frac{\omega\pm eV_x}{2T}\right]\sum_n T_n(1-T_n)\right\}. \tag{5}$$

The $I-V$ curve for a conductor can be obtained by averaging eq. (2) over noise. We find

$$IR=V-\langle[\xi_1\cos\varphi+\xi_2\sin\varphi]\rangle. \tag{6}$$

The last term in eq. (2) describes the effect of Coulomb interaction. We note that this term depends only on the two stochastic variables ξ_1 and ξ_2. Since the correlation functions for both these variables (3) are proportional to the parameter β, the magnitude of the whole interaction term in (6) should scale with the same parameter. Thus, the result (6) takes the form

$$R\frac{dI}{dV}=1-\beta f(V,T), \tag{7}$$

where $f(V,T)$ is the universal function which depends on R and $Z_S(\omega)$. This function was already evaluated in the case of tunnel junctions [9]. Defining $1/Z(\omega)=1/R-i\omega C+1/Z_S(\omega)$ and proceeding perturbatively in $\mathrm{Re}Z$, at $T\to 0$ one finds (cf., e.g., Refs. 9 and 6)

$$\frac{d^2I}{dV^2}=\frac{e^2\beta}{\pi RV}\mathrm{Re}[Z(eV)]. \tag{8}$$

In a special case of a linear Ohmic environment $Z_S(\omega)\simeq R_S$ we find

$$f(V,T) = \frac{e}{\pi}\int_0^{+\infty}dt\,\frac{(\pi T)^2}{\sinh^2(\pi Tt)}\mathrm{e}^{-F(t)}(1-\mathrm{e}^{-\frac{t}{R_0C}})\sin[eVt], \tag{9}$$

$$F(t) = -\frac{1}{g_0^2}\int_{-\infty}^{+\infty}dt'\frac{(\pi T)^2}{\sinh^2(\pi Tt')}\left(\beta g\cos[eVt']+(1-\beta)g+g_S\right) \times\left[|t'-t|-|t'|+R_0C\left(\mathrm{e}^{-|t'-t|/R_0C}-\mathrm{e}^{-|t'|/R_0C}\right)\right]. \tag{10}$$

where $g_0\equiv R_Q/R_0=g+g_S$ and $g_S=R_Q/R_S$. Eqs. (9), (10) work well provided either $g_0\gg 1$ or $\max(T,eV)\gg E_C$. In the limit $g_0\gg 1$ and $\max(eV,T)\gg g_0E_C\exp(-g_0/2)$ one can set $\exp(-F(t))\simeq 1$. Then eqs. (7), (9) yield the result

$$I=\frac{V}{R}-e\beta T\mathrm{Im}\left[w\Psi\left(1+\frac{w}{2}\right)-iv\Psi\left(1+\frac{iv}{2}\right)\right]. \tag{11}$$

where $\Psi(x)$ is the digamma function, $w = u + iv$, $u = g_0 E_C/\pi^2 T$ and $v = eV/\pi T$. At $T \to 0$ from (11) we obtain

$$R\frac{dI}{dV} = 1 - \frac{\beta}{g_0}\ln\left(1 + \frac{1}{(eVR_0C)^2}\right), \tag{12}$$

while in the limit $eV/E_C \gg \max(1,g)$ we find $RI = V - \beta e/2C$. At $V \to 0$ from (11) we get

$$f(0,T) = \frac{2}{g_0}\left[\gamma + 1 + \ln\left(\frac{g_0 E_C}{2\pi^2 T}\right)\right], \quad \gamma \simeq 0.577. \tag{13}$$

The above logarithmic dependencies on eV and T should also hold for $R_0C < \tau_{trav}$, in which case in eqs. (12) and (13) with the logarithmic accuracy one can set $g_0 E_C \to 1/\tau_{trav}$.

At very low temperatures and voltages $\max(T, eV) < g_0 E_C \exp(-g_0/2)$ the interaction correction to the conductance of a coherent scatterer *saturates* at a universal value which does not depend on the interaction but only on the transmission distribution. This result follows immediately from Eqs. (9), (10). Evaluating (10) at long times we find $F(t) \simeq (2/g_0)(\ln(t/R_0C) + \gamma)$ and performing the integral in (9), in the leading order in $\beta/g_0 \ll 1$ we obtain

$$G = \frac{1-\beta}{R} = \frac{2e^2}{h}\sum_n T_n^2, \tag{14}$$

This formula successfully reproduces a complete Coulomb blockade of tunneling $G \to 0$ in the limit $\beta \to 1$ (tunnel junctions), demonstrates the absence of it for ballistic scatterers ($\beta \to 0$), and yields suppression of the Landauer conductance by the factor 2/3 for diffusive conductors.

3 Comparison with experiments

In order to compare our theoretical results with recent experiments we will use the data reported recently by two groups [11,12].

Weber *et al.* [11] experimentally investigated the $I-V$ curve of a short ($L \sim 90$ nm $\ll L_\varphi, L_{in}$) diffusive conductor fabricated as a bridge between two big metallic reservoirs. Even though the conductance of this bridge was large $g \approx 2000$ the Coulomb blockade effect on the $I-V$ curve was clearly visible becoming more pronounced with decreasing temperature, see Fig. 3 of Ref. 11. It was observed that the experimental data [11] were well described by the formula

$$G(V,T) = G(0,T_0) + A\ln(T/T_0) + A\Phi(eV/T), \tag{15}$$

where A was determined to be $A \approx (0.4 \div 0.7) \times R_Q^{-1}$ depending on the sample and $\Phi(eV/T)$ was found to be a universal function of eV/T which tends to zero at $V \to 0$. The logarithmic dependence of $G(0,T)$ on temperature (15) agrees with our eqs. (7), (13). Both the function $\Phi(eV/T)$ and the value A can easily be evaluated within our theory. Making use of eq. (11) in the experimentally relevant interval of temperatures and voltages we obtain $A = 2\beta/R_Q$ and

$$\Phi(eV/T) = \mathrm{Re}\left[\Psi\left(1 + i\frac{eV}{2\pi T}\right) + \gamma + i\frac{eV}{2\pi T}\Psi'\left(1 + i\frac{eV}{2\pi T}\right)\right]. \tag{16}$$

The function (16) is plotted in Fig. 1 together with the experimental data [11] for the sample No. 1. One observes a very good agreement between theory and experiment except at high voltages where heating effects become dominant. From the same comparison for the sample No. 1 one finds $\beta \approx 0.25$ slightly smaller than the value $\beta = 1/3$ expected in a diffusive limit.

In another experiment Krupenin *et al.* [12] studied the $I-V$ curves of Cr resistors fabricated in the form of 2d strips and also clearly observed Coulomb blockade effects. The $\sim 1\mu$m long samples [12] were not diffusive (their resistances were too large to be described by the Drude

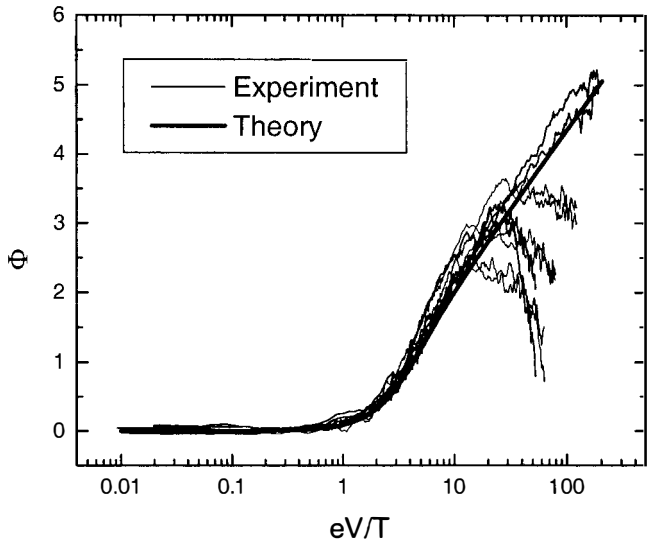


Figure 1: The function (16) plotted together with the experimental data [11] for the sample No 1. Different experimental curves correspond to different temperatures.

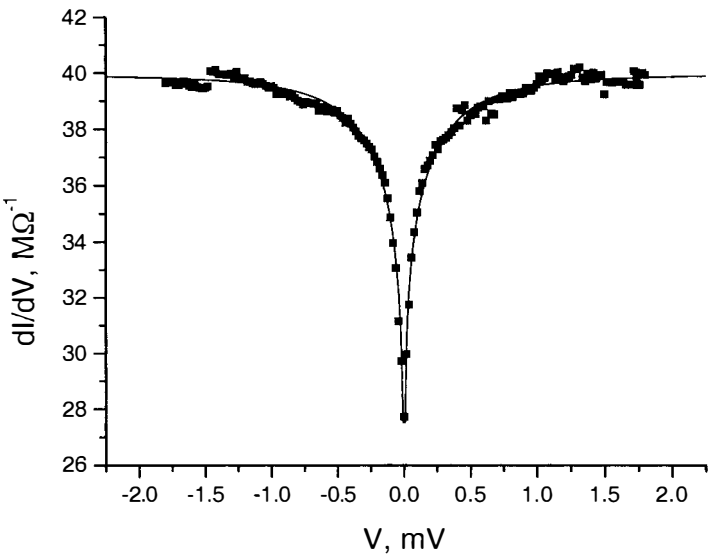


Figure 2: Eq. (12) plotted together with the experimental data [12] for the sample 1 with $R \approx 2.5$ KΩ per square.

formula) and most likely had a granular structure. For our comparison we will adopt the model of a granular array with grains connected via short coherent scatterers with some average value of the parameter β. For the sample [12] with the resistance 2.5 kΩ per square one can estimate the

average conductance of one scatterer as $g \approx 10$. Again, a very good agreement between theory and experiment is observed, see Fig. 2. From the best fit one can extract the value $\beta \approx 0.35$.

A relatively low value of the scatterer conductance $g \approx 10$ reached in the experiments [12] also allows to enter the regime $\max(T, eV) < gE_C \exp(-g/2)$, where the conductance was predicted to saturate at the level (14). According to this prediction the ratio between the values of G measured in the limits of low and high voltages should approach $1 - \beta$. From the data [12] we extract $\beta \approx 0.31$. This value is close to one found from the fit in Fig. 2. Thus the data [12] clearly support both our theoretical predictions (12) and (14). It is also interesting that both estimates give the values of β very close to $\beta = 1/3$ which one would expect for diffusive scatterers.

Finally, we notice that the results of recent conductance measurements [13] on multi-wall carbon nanotubes, with typical lengths of order L_φ or shorter, are also consistent with the logarithmic dependence predicted in eq. (12). Further experimental work on the subject would be highly desirable.

4 Instantons and metal-insulator phase transition

Under which conditions does the result (14) remain valid? One of them was already formulated above: $g_0 \gg 1$, i.e. either g or g_S should be much larger than one. In this case the conductance G saturates at the value (14) for $\max(eV, T) < g_0 E_C \exp(-g_0/2)$. In order to establish another important limitation for the result (14) let us recall that, even though our quasiclassical Langevin equation approach does account for nonlinear in φ effects, this approach may nevertheless become insufficient at very low energies even for $g_0 \gg 1$ because it does not include *instantons* [14], i.e. nontrivial saddle points for the exact effective action.

An important part of the instanton analysis was carried out by Nazarov [15] who derived the renormalized Coulomb energy $\tilde{E}_C$ for a general coherent conductor within the exponential accuracy. The result [15] can be written in the form $\tilde{E}_C \propto E_C \exp(-ag)$. One can also go beyond the exponential accuracy and estimate the pre-exponent in the expression for $\tilde{E}_C$. This was done in Ref. 16. Without going into details here, we only quote the result [16]

$$\tilde{E}_C / E_C \sim \left[\prod_n R_n\right] \ln \left[\prod_n R_n^{-1}\right] \sim ag \exp(-ag). \tag{17}$$

This formula is valid for $ag \gg 1$, i.e. either at large conductances $g \gg 1$ or, if $g \sim 1$, for very small values R_n implying $a \gg 1$.

The quantity $\tilde{E}_C$ (17) plays the role of an effective Coulomb gap in our problem. At $T < \tilde{E}_C$ our Langevin equation analysis is insufficient and, hence, eq. (14) becomes inaccurate. In this regime the conductance decreases with T and the system is an insulator at $T = 0$.

Let us now take into account the effect of an external linear Ohmic environment $Z_S \simeq R_S$. In this case quantum fluctuations of the charge in the shunt resistor will affect the Coulomb gap $\tilde{E}_C$ and – as we shall see – may even lead to its total suppression provided R_S is sufficiently low.

In order to proceed we will follow the analysis [14,16]. Treating the charge q as a quantum variable [2] and integrating out the phase φ one can map our problem onto that of a linearly damped quantum particle q in a periodic potential. This is a well-known problem [17,2] which can be treated, e.g., by means of the renormalization group (RG) technique. Successively reducing the high frequency cutoff ω_c and integrating out charges with higher frequencies one arrives at the standard RG equations [17]. After trivial manipulations these equations can be rewritten directly in terms of the combination $ag = \sum_n \ln R_n^{-1}$. One obtains [16]

$$d(ag)/d(\ln \omega_c) = (1 - g_\Sigma)(1 + 1/ag), \qquad dg_\Sigma/d(\ln \omega_c) = 0, \tag{18}$$

where $g_\Sigma = gg_S/g_0$ is the total dimensionless conductance. Eqs. (18) are valid as long as $ag \gg 1$. One observes that for $g_\Sigma < 1$ the quantity ag *decreases* in the course of renormalization. Hence,

in that case the Coulomb gap remains nonzero, the charge q is localized and the system is an insulator at $T = 0$. The effective Coulomb gap $\tilde{E}_C$ can be defined as the energy scale at which the renormalized value ag becomes of order one. Then from (18) one finds

$$\tilde{E}_C \sim E_C[ag\exp(-ag)]^{\frac{1}{1-g_\Sigma}} . \tag{19}$$

On the other hand, for $g_\Sigma > 1$ the combination ag always scales to *larger* values. In this case the Coulomb gap is fully suppressed by quantum fluctuations, $\tilde{E}_C = 0$, the charge q is delocalized and the conductance remains nonzero (14) even at $T = 0$. This is a metallic phase. A quantum phase transition between the insulating and metallic phases occurs at $g_\Sigma = 1$.

Finally, let us briefly discuss possible implications of our results for recent experiments [18] which strongly indicate the presence of a metal-insulator phase transition in various 2d disordered systems. One can consider a (sufficiently small) coherent scatterer with the dimensionless conductance g viewing all other scatterers in the system as an effective environment with the conductance g_S. *Assuming* this environment to be Ohmic at sufficiently low frequencies, one immediately arrives at the conclusion about the presence of a quantum metal-insulator phase transition at g_Σ=1. In 2d systems one has $g \sim g_S \sim g_0 \sim g_\Sigma$. Therefore in such systems this phase transition should be expected at conductances $\sim 1/R_Q$, exactly as it was observed in many experiments [18]. Local properties of the insulating and metallic phases are expected to be very different. In the insulating phase charges should be localized around inhomogeneities (puddles) due to Coulomb blockade, while in the metallic phase the Coulomb gap is suppressed and the charge distribution should be much more uniform. These expectations are fully consistent with experimental observations [19]. Thus, there might be a direct relation between the experimental results [18,19] and the old problem of a dissipative quantum phase transition [17].

References

1. D.V. Averin and K.K. Likharev, in *Mesoscopic Phenomena in Solids*, edited by B.L. Altshuler, P.A. Lee, and R.A. Webb (Elsevier, Amsterdam, 1991), p. 173.
2. G. Schön and A.D. Zaikin, *Phys. Rep.* **198**, 237 (1990).
3. *Single Charge Tunneling*, edited by H. Grabert and M.H. Devoret, NATO ASI Series B, vol. 294 (Plenum, New York, 1992).
4. Ya.M. Blanter and M. Büttiker, *Phys. Rep.* **336**, 1 (2000).
5. D.S. Golubev and A.D. Zaikin, *Phys. Rev. Lett.* (to be published); cond-mat/0010493.
6. A. Levy Yeyati, A. Martin-Rodero, D. Esteve, and C. Urbina, cond-mat/0102178.
7. A. Schmid, *J. Low Temp. Phys.* **49**, 609 (1982).
8. U. Eckern, G. Schön and V. Ambegaokar, *Phys. Rev.* B **30**, 6419 (1984).
9. D.S. Golubev and A.D. Zaikin, *Phys. Rev.* B **46**, 10903 (1992).
10. V.A. Khlus, *Sov. Phys. JETP* **66**, 1243 (1987).
11. H. Weber, R. Häussler, H. von Löhneysen, and J. Kroha, *Phys. Rev.* B **63**, 165426 (2001).
12. V.A. Krupenin *et al.*, cond-mat/0011427.
13. R. Tarkiainen *et al.*, to be published.
14. S.V. Panyukov and A.D. Zaikin, *Phys. Rev. Lett.* **67**, 3168 (1991).
15. Yu.V. Nazarov, *Phys. Rev. Lett.* **82**, 1245 (1999).
16. D.S. Golubev and A.D. Zaikin, cond-mat/0104310.
17. A. Schmid, *Phys. Rev. Lett.* **51**, 1506 (1983); S.A. Bulgadaev, *JETP Lett.* **39**, 315 (1984); F. Guinea, V. Hakim, and A. Muramatsu, *Phys. Rev. Lett.*, **54**, 263 (1985); M.P.A. Fisher and W. Zwerger, *Phys. Rev.* B **32**, 6190 (1985).
18. E. Abrahams, S. V. Kravchenko, M. P. Sarachik, *Rev. Mod. Phys.* **73**, 251 (2001).
19. S. Ilani *et al. Phys. Rev. Lett.* **84**, 3133 (2000); A. Yacoby (private communication).

QUANTUM NOISE, DETAILED BALANCE AND KUBO FORMULA IN NONEQUILIBRIUM QUANTUM SYSTEMS

U.GAVISH ,Y. IMRY, Y. LEVINSON
Department of Condensed Matter Physics, Weizmann Institute of Science, Rehovot, 76100, Israel

Current quantum noise can be pictured as a sum over transitions through which the electronic system exchanges energy with its environment. We formulate this picture and use it to show which type of current correlators are measurable, and in what measurement the zero point fluctuations will play a role (the answer to the latter is as expected: only if the detector excites the system.) Using the above picture, we calculate and give physical interpretation of the finite-frequency finite-temperature current noise in a noninteracting Landauer-type system, where the chemical potentials of terminals 1 and 2 are $\mu + eV/2$ and $\mu - eV/2$ respectively, and derive a detailed-balance condition for this nonequilibrium system. Finally, we derive a generalized form of the Kubo formula for a wide class of interacting nonequilibrium systems, relating the *differential* conductivity to the current noise.

1 Introduction

A general expression for the current correlators is derived below: it is a sum over transitions between pairs of energy levels. This expression is very similar to the one obtained by Van Hove [1] in the framework of neutron scattering theory. Using this sum over transitions we will identify the positive and negative frequency part of the correlator as having distinct, well-defined, separately-measurable, physical interpretations, namely: the emission and absorption spectra. This picture will enable us to analyze in what type of measurement the zero-point fluctuations will have an effect on the measured spectrum. It will also enable us to derive a detailed balance relation out of equilibrium for a Landauer-type system which consists of a point scatterer connected through two one-dimensional single-channel conducting arms, to two terminals whose chemical potentials differ. This condition keeps the system in a stationary nonequilibrium state. Finally, a Kubo formula for the differential conductivity is derived for a wide class of systems out of equilbrium, and is verified analytically for the above Landauer-type case.

2 General Formulation for the Quantum noise.

Consider the current correlator for a stationary system (i.e. with no dependence on t'),

$$C(t) \equiv \langle \hat{J}(t')\hat{J}(t'+t)\rangle \equiv \sum_i P_i \langle i|\hat{J}(0)\hat{J}(t)|i\rangle, \tag{1}$$

of a quantum system ("antenna"), characterized by a density matrix which is diagonal in the eigenstate basis. $|i\rangle$ are the eigenstates of the antenna with energies E_i and populations P_i. $\hat{J}$ is a space average [2] of the time-dependent current operator in the Heisenberg representation, $\hat{j}(x,t) = \exp(i\hat{H}t/\hbar)\hat{j}\exp(-i\hat{H}t/\hbar)$, where $\hat{H}$ is the Hamiltonian of the antenna, taken to be time independent, but otherwise very general, *including interactions*.

If the (stationary) system were describable classically, then one would have $C(t) = C(-t)$ and it would be clear what the time-dependent current fluctuations were: the average-over-realizations of the product of the values of the current at different times. However, in the quantum case the operators $\hat{j}(t)$ for different times do not commute. Therefore the quantum correlator can not, in general, be given this simple interpretation. Actually, in the quantum case $C(t)$ is in general *complex* and not symmetric, but just satisfies: $C(t) = C(-t)^*$, which means that *it is not a directly measurable quantity* in the sense that the product of the (real) current values that appear, say, on some ampermeter screen at different times does not give $C(t)$. Its

Fourier transform (to which we shall also refer, for brevity, as the correlator):

$$S(\omega) \equiv \int_{-\infty}^{\infty} e^{i\omega t} \langle |\hat{J}(0)\hat{J}(t)| \rangle dt, \tag{2}$$

is also nonsymmetric, $S(\omega) \neq S(-\omega)$, although it is obviously real (see eq.(3)). This can be seen[1] by inserting the identity operator $\sum_f |f\rangle\langle f|$ in eq.(2) and performing the time-integration, which yields:

$$S(\omega) = 2\pi\hbar \sum_{if} P_i |\langle f|\hat{J}|i\rangle|^2 \delta(E_i - E_f - \hbar\omega). \tag{3}$$

This expression is not symmetric with respect to ω since P_i usually decreases with E_i.

$S(\omega)$ has the following important physical significance. If the system is coupled, through a small term which is linear in $\hat{J}(t)$, to a second system (see examples below), then, by the Fermi golden rule, $S(\omega)$ is proportional to the transition rate between the initial state $|i\rangle$ and the final state $|f\rangle$, for which $E_i - E_f = \hbar\omega$. Therefore, for $\omega > 0$ it is proportional to the emission rate and for $\omega < 0$ it is proportional to the absorption rate[3].

For example, if the second system is the free EM field, then $S(\omega > 0)$ is proportional to the energy emission rate[3,4] into the vacuum state of this field (i.e. the state of the EM field with occupation number $N_\omega = 0$), and for $\omega < 0$ it is proportional to the energy absorption rate from an EM field with a given photon, i.e., with $N_{|\omega|} = 1$. Another example is provided by a system which is coupled to a measuring device[5,6,7,8] (e.g., a resonant circuit). Then $S(\omega)$ is proportional to the energy transfer rate between the system and the measuring-device: The terms with $E_i > E_f$ describe transitions in which an energy of $\hbar\omega = E_i - E_f > 0$ is transferred from the system to the measuring device, while terms with $E_f > E_i$ describe transitions in which an energy of $-\hbar\omega = E_f - E_i > 0$ is transferred from the measuring device to the system. When $\omega > 0$, only the first type of terms will remain and $S(\omega)$ will be the emission spectrum while $S(-\omega)$ will be the absorption spectrum. Thus, the two branches of $S(\omega)$ yield two physically interesting and separately-measurable quantities.

In the case when the antenna is in equilibrium at a temperature T and time-reversal symmetry holds, one finds the detailed balance relation[1]

$$S(\omega) = S(-\omega)e^{-\hbar\omega/k_B T}. \tag{4}$$

This detailed balance relation ensures that the system remains in equilibrium, by taking care that the asymmetry $S(\omega) \neq S(-\omega)$, i.e., the difference between the upward transitions (absorption) and the downward ones (emission) is compensated by the difference between the higher and lower thermal occupations. In section 3 the above relation is generalized for a particular nonequilibrium system, where it serves to keep the latter in its nonequilibrium, though stationary, state. From eq.(4) one sees that only for low frequencies $\hbar|\omega| \ll k_B T$, will the classical symmetry, $S(\omega) = S(-\omega)$, hold. In the time domain this means that the classical symmetry, $C(t) = C(-t)$, becomes valid only for late times $|t| \gg \hbar/k_B T$.

The customary way to treat the quantum case is[5,9] to consider the symmetrized correlator $C_S(t' - t) \equiv (1/2)\langle \hat{j}(t)\hat{j}(t') + \hat{j}(t')\hat{j}(t) \rangle$, which is real and symmetric like the classical one. However, for a wide class of noise detection schemes and in particular for a detector in its ground-state $C_S(t)$ is *not*, the measured correlator, since it contains the zero-point fluctuations. For example, if the antenna is in equilibrium at a temperature T, it follows from the fluctuation-dissipation theorem[9] that for $\omega > 0$ one has $S_S(\omega) \sim [N_T(\omega) + (1/2)]\omega$, where $S_S(\omega)$ is the Fourier transform of $C_S(t)$ and $N_T(\omega) = [exp(\omega/k_B T) - 1]^{-1}$ is the Planck function. This means that $S_S(\omega) \neq 0$ even when $T = 0$, and the antenna is in its ground state. Since being in the ground state the antenna can not radiate energy, $S_S(\omega)$ can not be considered as the correlator measured by detecting the radiation[11].

To conclude, the measured quantity will generally not contain the emission and absorption in a symmetric combination. This was shown for particular situations of quantum noise measurement in electronic transport [5,8,6,11] as well as in quantum optics [10,11,12]. The more physical correlator (and its power spectrum) is the one without symmetrization. Its transform is given by a sum over transitions - downward ones in the case of positive frequency, and upward ones in the case of negative frequency. Each of these two branches has its own distinct physical significance, the emission and absorption spectrum, that may in principle be detected separately.

3 Shot Noise

We now consider current fluctuations [13,14] for the Landauer model. A point-like elastic scatterer is connected through two ideal single-channel conducting ballistic arms to two Fermion reservoirs, 1, and 2, with chemical potentials $\mu + eV/2$ and $\mu - eV/2$ respectively. V is the voltage, and it is assumed that $eV, \hbar\omega, k_BT \ll \mu$. We consider non-interacting electrons and ignore spin. The single-particle scattering-states with energy $\epsilon_n = \hbar^2k^2/2m$, which corresponds to a wave that is incoming on arm $\alpha = 1, 2$, partially reflected back into it and partially transmitted into the other arms, is: $\varphi_n(x_\gamma) = L^{-1/2}[\delta_{\alpha\gamma}e^{-ikx_\gamma} + s_{\gamma\alpha}(k)e^{ikx_\gamma}]$. Here $n \equiv (\alpha, k)$ with $k > 0$; $\alpha, \gamma = 1, 2$, L is a normalization length, m the electron mass and x_γ the distance of a point on arm γ from the scatterer. $s_{\alpha\gamma}$ is the element of the unitary scattering matrix, and it is assumed to be energy independent unless otherwise stated. To specify that a state φ_n comes from terminal α, we shall write $n \in \alpha$. The current operator on arm α is

$$\hat{j}(x_\alpha) = -(ie\hbar/2m)\sum_{nn'}\hat{a}_n^\dagger\hat{a}_{n'}\varphi_n^*\nabla_\beta\varphi_{n'} + h.c.,$$

where $\hat{a}_n$ and $\hat{a}_n^\dagger$ are the annihilation and creation operators of the φ's.

We assume that the *measured* current is the average

$$\hat{J}(t) \equiv \frac{1}{L_0}\int_{L_0} dx_2\hat{j}(x_2) \tag{5}$$

over a segment L_0 far away from the scatterer which satisfies: $L_0k_F \gg 1$ and $\omega L_0m/(\hbar k_F) \ll 1$, where $k_F \equiv \sqrt{2m\mu}$, and ω is the frequency of the measured noise which is assumed to satisfy $\omega \ll \mu$. These conditions ensure that the correlators are independent of the length and position of the segment L_0,; i.e, it has no spatial dependence, which is not addressed in experiments.

To describe the current noise consider the correlator, given by eq. (3) We emphasize again that at least for some types of noise detection, it is eq. (2) and *not* its symmetrized version, which gives the measured noise if the detector is cold enough, i.e., when excitation of the system by the detector is unlikely so that the absorption is negligible. The states $|i\rangle$ are given according to the Landauer picture by the eigenstates of the system (i.e., Slater determinants) labelled by specifying a set $\{n_i\}$ of the occupied single-particle states (the scattering states φ_n emanating from the two reservoirs):

$$|i\rangle \equiv |\{n_i\}\rangle = \prod_{n_i}\hat{a}_{n_i}^\dagger|vacuum\rangle, \tag{6}$$

and the corresponding probabilities (for a more general derivation see Ref. [16]) are:

$$P_i \equiv \frac{1}{Z_1}exp[-\beta\sum_{n\in 1}(\epsilon_{n_i} - (\mu + eV/2))n_i] \times \frac{1}{Z_2}exp[-\beta\sum_{n\in 2}(\epsilon_{n_i} - (\mu - eV/2))n_i], \tag{7}$$

where $\beta \equiv (k_B T)^{-1}$ and

$$Z_\alpha \equiv \sum_{\{n_i\}} exp[-\beta \sum_{n\in\alpha} n_i(\epsilon_{n_i} - (\mu - eV(-1)^\alpha/2))]$$

$\alpha = 1, 2$. The probabilities P_i correspond to a situation in which the occupations in the gas in the one-dimensional system are determined by grand-canonical probabilities that depend on the chemical potential and the temperature of the terminals that supply the electrons to the system. From eqs.(7) and (6) it follows that at zero temperature $P_i = 0$ for any i except for one state, which we name a *cold transport state* which is given by:

$$|cold\ \ transport\rangle \equiv \prod_{\substack{n\in 1;\epsilon_n \le \mu + eV/2 \\ n\in 2;\ \epsilon_n \le \mu - eV/2}} \hat{a}_n^\dagger |vacuum\rangle, \tag{8}$$

In this cold transport state all the φ_n's are occupied up to an energy $\mu - eV/2$ if $n \in 2$ and up to $\mu + eV/2$ ($eV \ll \mu$) if $n \in 1$ (see fig. 1). Therefore, this state, although it is the stationary state with the lowest energy among those that are made possible by the two terminals, is not a ground state, and since it carries current, it is not even an equilibrium state.

In the sum in eq.(3), the non-diagonal matrix element $\langle i|\hat{J}(0)|f\rangle$ is nonzero only if $|f\rangle$ differs from $|i\rangle$ by moving one particle from an occupied state, φ_n, to a previously unoccupied state, $\varphi_{n'}$, i.e., $|f\rangle$ is of the form $\hat{a}_{n'}^\dagger \hat{a}_n |i\rangle$ (up to a fermionic factor of ± 1, that will play no role below.) The diagonal elements $\langle i|\hat{J}(0)|i\rangle$ appear in a term $\sim \delta(\hbar\omega)$. In what follows we consider only $\omega \neq 0$ and therefore neglect this term. In experiments the integration in eq.(2) is limited by the sampling time of the experiment, T_s, and as a result $\delta(\hbar\omega)$ is smoothed into a peak with a width of $\simeq \hbar/T_s$ which means that the condition $\omega \neq 0$ actually means $\omega T_s \gg 1$. We therefore have:

$$S(\omega) = 2\pi\hbar \sum_i P_i \sum_{nn'} |J^i_{nn'}|^2 \delta(\epsilon_n - \epsilon_{n'} - \hbar\omega). \tag{9}$$

where $J^i_{nn'} \equiv \langle i|\hat{J}(0)\hat{a}_{n'}^\dagger \hat{a}_n|i\rangle$, and where now the summation over n and n' is over all *single-particle* states φ_n and $\varphi_{n'}$ (with *single-particle* energies ϵ_n and $\epsilon_{n'}$) which are occupied and unoccupied, respectively, in $|i\rangle$. Now we divide the summation in eq. (9) into four partial sums, according to the four possible types of transitions: two auto-terminal ones and two cross-terminal ones (shown in fig. 1 for $\omega < 0$ in the cold transport state):

$$S(\omega) = \sum_{\alpha,\gamma=1,2} S_{\alpha\to\gamma}(\omega), \tag{10}$$

where $S_{\alpha\to\gamma}(\omega)$ contains only the transitions from states with $n \in \alpha$ to states $n \in \gamma$. Explicitly:

$$S_{\alpha\to\gamma}(\omega) = 2\pi\hbar \sum_i P_i \sum_{n\in\alpha,\ n'\in\gamma} |J^i_{nn'}|^2 \delta(\epsilon_n - \epsilon_{n'} - \hbar\omega) \tag{11}$$

Each of these four sums can be evaluated separately by calculating the current matrix elements in eq.(9), transforming the sums over k and k' (which are implicit in the sums over n and n') into integrals, performing the summation over i according to Eqs. (6) and (7), and integrating using the condition $\hbar\omega, eV, k_B T \ll \mu$ and the unitarity of the scattering matrix, $\sum_\gamma s_{\alpha\gamma} s^*_{\beta\gamma} = \delta_{\alpha\beta}$. The final results are:

$$S_{1\to 2}(\omega) = \frac{e^2 \tilde{T}(1-\tilde{T})}{h} \frac{\hbar\omega - eV}{e^{\beta(\hbar\omega - eV)} - 1} \tag{12}$$

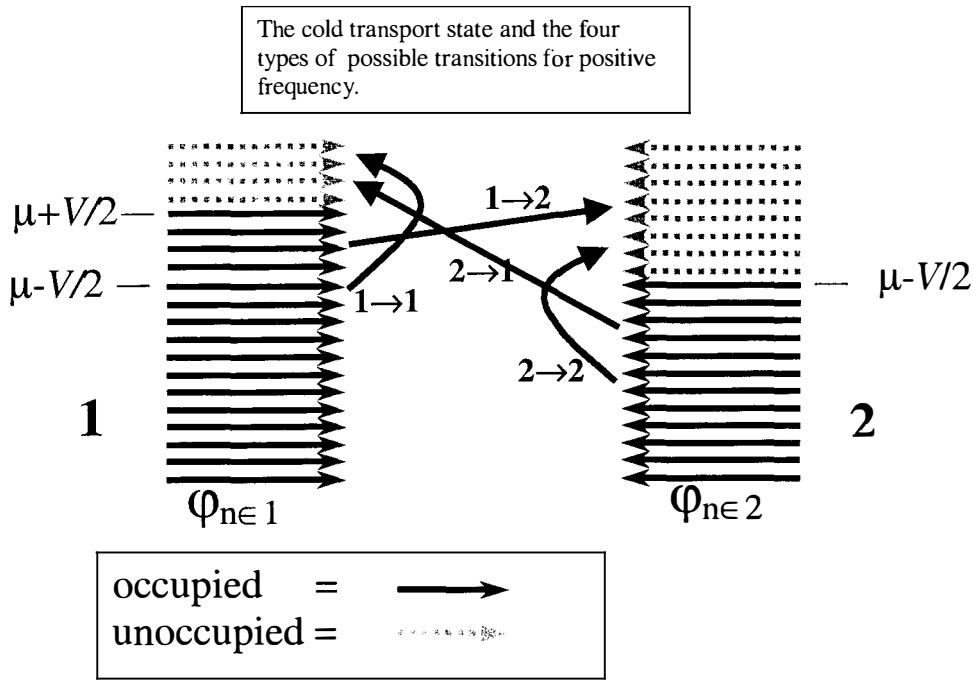


Figure 1: The Landauer model, states and transitions.

$$S_{2\to1}(\omega) = \frac{e^2\tilde{T}(1-\tilde{T})}{h}\frac{\hbar\omega + eV}{e^{\beta(\hbar\omega+eV)}-1} \tag{13}$$

$$S_{1\to1}(\omega) = S_{2\to2}(\omega) = \frac{e^2\tilde{T}^2}{h}\frac{\hbar\omega}{e^{\beta\hbar\omega}-1}. \tag{14}$$

Where, $\tilde{T} \equiv |s_{21}|^2$ is the transmission from arm 1 to 2. Substitution in eq.(10) yields:

$$S(\omega) = \frac{e^2\tilde{T}(1-\tilde{T})}{h}[F(\hbar\omega - eV) + F(\hbar\omega + eV)] + \frac{2e^2\tilde{T}^2}{h}F(\hbar\omega) \tag{15}$$

where $F(x) \equiv x(e^{\beta x}-1)^{-1}$. Eq. (15) is the non-symmetrized power spectrum, at finite frequency (positive or negative), voltage and temperature. It has been previously obtained by Aguado and Kouwenhoven [8] (they use an opposite convention for the sign of ω). Eq. (15) is consistent with the zero-temperature limit, i.e., the cold transport case, that was obtained by Lesovik and Loosen [5]. Unlike the symmetrized version that was derived by Yang [14] and de Jong and Beenakker [17], here $S(\omega) \neq S(-\omega)$.

Since the system is not in equilibrium, the detailed-balance condition eq.(4) is not satisfied, however, a modified version of it does exists. To obtain it, note that Eqs.(7) and (11), or (12),(13) and (14) imply:

$$S_{1\to1}(\omega) = S_{1\to1}(-\omega)e^{-\beta\hbar\omega}, \quad S_{2\to2}(\omega) = S_{2\to2}(-\omega)e^{-\beta\hbar\omega} \tag{16}$$

$$S_{1\to2}(\omega) = S_{2\to1}(-\omega)e^{-\beta\hbar\omega+\beta eV}, \quad S_{2\to1}(\omega) = S_{1\to2}(-\omega)e^{-\beta\hbar\omega-\beta eV}$$

In equilibrium, $eV = 0$ and the last two relations have the form of first two and then, by eq.(10), the ordinary detailed-balance relation, eq. (4) is recovered. The finite voltage creates a nonequilibrium but stationary state which is maintained by virtue of more complicated detailed-balance relations between upward and downward transitions, given by the above four equations. In particular these relations imply that $S(-\omega) \neq 0$ even at zero temperature which is not surprising since in the cold transport state, eq. (8), downward transitions are possible from occupied states with $n \in 1$ within the energy window $[\mu - eV/2, \mu + eV/2]$ into the empty states with $n \in 2$ and within the same energy window. That is, emission is possible.

Another conclusion arising from the above four equations is that in order to recover the classical symmetry $S(\omega) = S(-\omega)$, the condition $\hbar|\omega| \ll k_B T$ is not longer enough and should be replaced by: $eV + \hbar|\omega| \ll k_B T$.

4 Kubo Formula for Nonequilibrium Systems

Here we would like to make another application of the point of view of section 2. We again allow [14,18] for the antenna a large class of nonequilibrium situations - all those in which the density matrix is diagonal in the eigenstate basis (and it therefore commutes with the Hamiltonian). This may include electron-electron interactions and the possibility that $\langle \hat{j}(t) \rangle \neq 0$.

A useful example to have in mind is a Landauer-type transport system of section 3, which has a two-terminal linear conductance, per spin channel, of

$$G = \frac{e^2}{2\pi\hbar}\tilde{T}. \tag{17}$$

We use the explicit exact expression of eq.3 for the current power-spectrum $S(\omega)$. As emphasized in section 2, its important physical significance is that it gives [4,3] the emission rate into the vacuum (i.e. the state of the EM field where all $N_\omega = 0$) for $\omega > 0$ and the absorption rate for $\omega < 0$ and an EM field with one photon, $N_{|\omega|} = 1$.

We first take the (possibly D.C. driven) "antenna" to be in a given (usually the lowest) state consistent with the external driving (this will be valid, for example, when the reservoirs that feed the antenna are at $T = 0$ and there is either no coupling with any additional thermal bath, or when that coupling is with a bath at $T \to 0$, and no appreciable heating by the D.C. current has taken place. In the latter case, some tendency toward equilibrating the chemical potentials of the left- and right- moving electrons may occur, with a reduction of the D.C. current, which is of no particular concern to us). In the case of the Landauer-type system of section 3, this lowest state is the cold transport one, defined in eq. 8. The energy absorption rate, $R_a(\omega)$, by the antenna from a *classical field* (with $N_\omega \gg 1$ photons and a negligible spontaneous component of the emitted radiation) with a frequency $\omega > 0$ is given via the usual treatment [4] by:

$$R_a(\omega) = \omega|A(\omega)|^2 S(-\omega)/(\hbar c^2). \tag{18}$$

The emission rate, $R_e(\omega)$ is given by

$$R_e(\omega) = \omega|A(\omega)|^2 S(\omega)/(\hbar c^2). \tag{19}$$

The *net* absorption rate, $R_{a,net}(\omega)$ is given by the difference between eqs. (18) and (19). It is also given, writing the infinitesimal "tickling" electric field as $E(\omega) = iA(\omega)\omega/c$, by

$$R_{a,net}(\omega) = -2G_d(\omega)(\omega/c)^2|A(\omega)|^2, \tag{20}$$

where the volume of the system is defined as unity.

$G_d(\omega)$ is the differential ac conductance. It is defined as the in-phase (dissipative) linear response (A.C. current) to the tickling A.C. field at frequency ω. A finite D.C. current which in turn flows in response to the finite applied D.C. voltage [21] V, is allowed.

Using eqs. 18, 19 and 20, we reach our principal conclusion that *the antisymmetric part of the current noise in our nonequilibrium system (i.e. typically including quantum shot-noise [13]) is related to the differential ac conductance $G_d(\omega)$ at the same frequency ω.*

$$S(-\omega) - S(\omega) = 2\hbar\omega G_d(\omega), \qquad (\omega \geq 0), \tag{21}$$

Eq. 21 is the simple but nontrivial generalization of the Kubo formula [19] for the current-carrying, nonequilibrium, case. The antisymmetric combination appearing on the LHS corresponds to the Fourier transform of the commutator of the Heisenberg current operators at different times. A similar expression was obtained by Lesovik and Loosen [5] and by Lesovik [20]. Here we have interpreted it physically and put it in a general context

It is straightforward to generalize the above treatment to the case where the antenna is not at its lowest possible state, but has a density matrix (assumed to be diagonal in the eigenstates' basis) which allows the population of a number of states. The general form of the result of the *net* absorption rate is still valid. *Therefore, our principal result, eq. 21, is unchanged.*

We now verify the above results with the example of the Landauer-type model, of section 3. From eq. (15) and (17) it follows that:

$$S(-\omega) - S(\omega) = e^2 \frac{\tilde{T}}{\pi}\omega = 2\hbar\omega G, \tag{22}$$

in agreement with the generalized Kubo formula, eq. 21. To consider a more general case we now relax the assumption that the scattering matrix is energy independent and assume instead that the scale on which it changes is of the order of eV, and that $eV \gg \hbar\omega$. We emphasize that the energy dependence of the scattering matrix must be evaluated including the self-consistent changes in the potential of the scatterer due to the voltage V. A similar derivation to the one that led to eq. (15) and (22) now gives:

$$S(-\omega) - S(\omega) = e^2 \frac{1}{2\pi}\omega(1 - R^2(\mu - eV/2) + \tilde{T}^2(\mu + eV/2)) \tag{23}$$

where $R = 1 - \tilde{T}$. Approximating $\tilde{T}(\epsilon) = \tilde{T}(\mu - eV/2) + \lambda(\epsilon - \mu + eV/2) + O(V^2)$, one has:

$$S(-\omega) - S(\omega) = e^2 \frac{\tilde{T}}{\pi}\omega(1 + \lambda eV), \tag{24}$$

where $\tilde{T} = \tilde{T}(\mu - eV/2)$. This, together with eq.21, is a new prediction for the low, but finite frequency [21] dynamic conductivity, which may be different from the slope of the DC I-V characteristics.

The generalization of the above to the case of many transport channels, along the lines of the usual theories of quantum shot-noise [13,14], is straightforward. One uses the representation where the transmission part of the scattering matrix is diagonal. The results are expressed in terms of the transmission eigenvalues.

When the field probing the system has a finite number, N_ω, of photons, the net flow of energy, including the spontaneous process, from the system to the field is [5,6]:

$$R_M(\omega) = S(\omega)(N_\omega + 1) - N_\omega S(-\omega). \tag{25}$$

Using eq.15 for the quantum shot-noise, and taking $G_d = G$, we see that the spontaneous term is unimportant for $N_\omega \gg eV(1 - \tilde{T})/\hbar\omega$. In the opposite limit the sample just emits noise into the "cold detector".

Acknowledgements

This research was supported by the German-Israeli Foundation (GIF), the Israel Science Foundation, and the Israeli Ministry of Science and the French Ministry of Research and Technology. Instructive discussions with the late R. Landauer, and with D. Cohen, C. Glattli, M. Heiblum, J. Kurchan, R. de Picciotto and A. Stern are gratefully acknowledged. Some of this work was done while UG and YI were visiting the Ecole Normale Superieure in Paris, they thank S. Haroche and M. Voos for their hospitality and the Chaires Internationales Blaise Pascal for support.

References

1. L. van Hove, Phys. Rev **95**, 249 (1954).
2. The relevant quantity is often the space average, because of the excellent dipole approximation. An example[4] is a system whose size is much smaller than the radiation wave-length, coupled to the EM field. In section 3, the space averaging is taken only on the portion of the antenna which is assumed to interact with the measuring device.
3. The transition rate contains the properties of the system with which energy is exchanged. E.g, a factor A^2 for the EM field (eqs. 18 and 19). Due to the factor[4] of $1/\omega$ in A^2, $S(\omega)$ and the energy emission rate times the photon number have the same ω-dependence.
4. G. Baym, *Lectures on Quantum Mechanics*, pp. 271-276, Addison-Wesley (1993).
5. G.B. Lesovik and R. Loosen, JETP Lett., **65**, 269 (1997).
6. U. Gavish, Y. Levinson, and Y. Imry, Phys. Rev. **B RC**, R10637 (2000).
7. Y. Levinson and Y. Imry, in Proc. of the Nato ASI "Mesoscope 99" in Ankara/Antalya, Kluwer 1999.
8. R. Aguado and L. P. Kouwenhoven, Phys. Rev. Lett., **84**, 1986 (2000); C.W.J. Beenakker and H. Schomerus, Phys. Rev. Lett., **86**, 700 (2001).
9. L.D. Landau and E.M. Lifshitz, Statistical Physics, § 118, 124, 125; Pergamon, Oxford,1980.
10. M. Lax, Phys. Rev. 145, 110-129 (1966)
11. C. W. Gardiner, *Quantum Noise*, Springer Verlag, Berlin (1991), chapter 1.
12. E.g., R.J. Glauber, in *Quantum Optics and Electronics*, C. DeWitt, A. Blandin, and C. Cohen-Tannoudji (Eds.), Les Houches Summer School (1964), p.63, Gordon and Breach.
13. V.A. Khlus, JETP **66**, 1243 (1987); G.B. Lesovik, JETP Lett., **49**, 592 (1989), M. Büttiker, Phys. Rev. B **46**,12485 (1992).
14. S.-R. Eric Yang, solid state communications, **81**, 375, (1992).
15. Y. Imry, *Introduction to Mesoscopic Physics*, Oxford University Press (1997).
16. S. Hershfield, Phys. Rev. Lett. **70**, 2134 (1993).
17. M. J. M. de Jong and C. W. J. Beenakker, in *Mesoscopic Electron Transport,* edited by L. L. Sohn, L. P. Kouwenhoven, and G. Schön (Kluwer, The Netherlands, 1997).
18. R. M. More, J. A. Harte, G. B. Zimmerman, S. B. Libby, F. R. Graziani, K. B. Foumier and T. Kato, Non-LTE Linear Response Theory, Report UCRL-JC-129348.
19. R. Kubo, J. Phys. Soc. Japan, **12**, 570 (1957); **17**, 975, (1962). We refer to the result in Eq. 21 as a generalized Kubo formula. The term Fluctuation-Dissipation Theorem (FDT) is often reserved for the corresponding relationship between the linear response function and the *symmetrized* correlator. We are not using that correlator and believe that the truly fundamental relationship (generalized here to nonequilibrium systems) is the one between the differential linear response function and the *antisymmetrized* correlator.
20. G.B. Lesovik, Uspekhi **41**, 145 (1998).
21. The dissipated power is the time-averaged product of the driving field and the resulting current. If one of those is D.C. and the other has finite ω, the average power vanishes.

MESOSCOPIC METALLIC RINGS OUT OF EQUILIBRIUM

E. KANZIEPER[1], V. I. YUDSON[2], V. E. KRAVTSOV[3]
[1] *Hitachi Cambridge Laboratory, Madingley Road, Cambridge CB3 0HE, United Kingdom*

[2] *Centre for Frontier Science, Chiba University, 1-33 Yayoi-cho, Inage-ku, Chiba 263-8522, Japan and Institute for Spectroscopy, Troitsk, Moscow r-n, 142090, Russia*

[3] *The Abdus Salam International Centre for Theoretical Physics, P. O. Box 586, 34100 Trieste, Italy and Landau Institute for Theoretical Physics, 2 Kosygina Street, 117940 Moscow, Russia*

We demonstrate that real-time impurity diagrammatic technique is capable of describing the heating effect in disordered conductors. A novel diagrammatic element, the *loose diffuson*, responsible for catching the effect is identified. Equivalence of such a diagrammatic technique to a solution of a kinetic equation for a nonequlibrium electron energy distribution function is claimed for a particular problem of persistent currents fluctuations under ac pump.

1 Persistent currents in and out of equilibrium

An isolated normal-metal ring threaded by a constant magnetic flux ϕ carries dissipationless persistent currents [1]. For a given impurity configuration, the Aharonov-Bohm (AB) flux affects boundary conditions for the wavefunction of a single electron traveling along the ring thereby requiring any physical observable to be a periodic function of ϕ with a fundamental period $\phi_0 = h/e$, the flux quantum ($c = 1$). In particular, the flux dependence of the free energy F implies existence of the *equilibrium* persistent current, $I_{\rm PC} = -\partial F/\partial\phi = 2\sum_n[\partial E_n/\partial\phi]n(E_n)$. Here $\{E_n\}$ is the single electron spectrum, $n(E)$ is the Fermi occupation probability. The factor 2 accounts for spin degeneracy.

If the grand-canonical ensemble averaging is meant, the chemical potential in each sample is kept fixed and the average current is vanishingly small [2]. However, valuable sample-to-sample fluctuations of persistent currents are still allowed. Quantitatively, they are described by statistics of squared amplitudes $\langle I_n^2\rangle$ of n-th flux harmonics, $\langle I_{\rm PC}^2\rangle = \sum_{n=1}^{\infty}\langle I_n^2\rangle \sin^2(2\pi n\phi/\phi_0)$. One has [3]

$$\langle I_n^2\rangle = -4e^2n^2\left(\frac{\tau_{\rm D}}{\pi}\right)^{1/2}\int_0^\infty \frac{d\tau}{\tau^{3/2}}e^{-n^2\tau_{\rm D}/(4\tau)}\hat{f}^2(\tau), \qquad (1)$$

where $\hat{f}(\tau) = iT/\sinh(\pi\tau T)$, T is the equilibrium temperature, and $\tau_{\rm D}$ is the diffusion time.

In the present communication, we report on our studies [3] of fluctuation properties of persistent currents in the grand-canonical ensemble *out of equilibrium*. Throughout the paper, we think of a nonequilibrium setup consisting of a system of mesoscopic rings connected to the electron reservoir through the passive lead and pierced by a weak constant AB flux ϕ. In addition, at time $t = 0$, prior to which the system is assumed to be in the thermodynamic equilibrium, the rings are subject to the irradiation by external spatially homogeneous *circular* ac electric field $\mathbf{E}(t) = -\partial\mathbf{A}/\partial t$, where $\mathbf{A}(t)$ is a time dependent vector potential along the azimuthal direction.

2 Effects of ac field and structure of current expansion

The ac field causes two basic effects: the electron dephasing (decoherence) and the heating of the electron gas. As far as the decoherence is concerned, it can regularly be studied by analysing [3] the way in which the diffuson and the cooperon propagators get affected by external ac field. Below, we shall concentrate on the heating effect only.

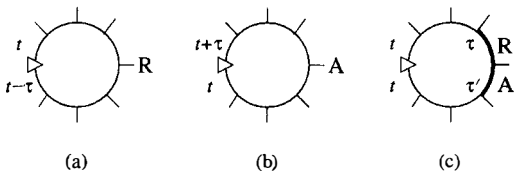


Figure 1: Graphic representation of the field-induced current $I(t)$ in the time domain: retarded (a), advanced (b), and retarded-advanced (c) electron loops. Shown in bold is the retarded-advanced junction, see text. The triangle and the arcs stand for $\hat{\mathbf{j}}$ and the ac-field free electron Green functions $G_0^{\mathrm{R(A)}}$, respectively. Emanating rays depict the electron-field interaction $\mathcal{H}_{e-f}$.

Theoretical descrition of both effects requires going beyond the linear response theory. For this reason, we are interested in essentially nonlinear in ac pumping field effects. The most straightforward way to derive the current expansion to all orders in the electron-field interaction $\mathcal{H}_{e-f} = -(\hat{\mathbf{j}}\,\mathbf{A})$, $\hat{\mathbf{j}}$ being the current operator, is to appeal to the Keldysh matrix technique. Treating the applied ac field as a *classical* field, we arrive at the formal expansion [3]

$$I(t) = i\sum_{p=0}^{\infty}\sum_{l=0}^{p}\mathrm{Tr}\left[\hat{\mathbf{j}}_\alpha\left\{G_0^{\mathrm{R}}(\hat{\mathbf{j}}\mathbf{A})\right\}^l G_0^{\mathrm{K}}\left\{(\hat{\mathbf{j}}\mathbf{A})G_0^{\mathrm{A}}\right\}^{p-l}\right](t,t). \tag{2}$$

Here, the subscript 0 marks the ac field-free electron Green function, $G_0^{\mathrm{K}}(E) = f(E)[G_0^{\mathrm{R}}(E) - G_0^{\mathrm{A}}(E)]$ is the 'bare' (equilibrium) Keldysh function, and $f(E) = \tanh(E/2T)$.

The expansion for the field induced current $I(t) = I_1(t) + I_2(t)$ can be brought into the compact form

$$I_1(t) = i\int d\tau \hat{f}(\tau)\mathrm{Tr}\left\{\hat{\mathbf{j}}\left[G^{\mathrm{R}}(t,t-\tau) - G^{\mathrm{A}}(t+\tau,t)\right]\right\}, \tag{3}$$

$$I_2(t) = i\int d\tau \int d\tau' \hat{f}(\tau-\tau')\left[\mathbf{A}_\alpha(\tau) - \mathbf{A}_\alpha(\tau')\right]\mathrm{Tr}\left\{\hat{\mathbf{j}}G^{\mathrm{R}}(t,\tau)\hat{\mathbf{j}}_\alpha G^{\mathrm{A}}(\tau',t)\right\}, \tag{4}$$

where $G^{\mathrm{R(A)}}$ is exact retarded (advanced) electron Green function. These two equations hold for a given impurity configuration.

The first contribution, I_1, can graphically be depicted by a difference between the retarded and the advanced electron loops [Figs. 1(a) and 1(b)], each consisting of either retarded or advanced (ac-field free) Green functions G_0. The second contribution, I_2, is given by the retarded-advanced loop, Fig. 1(c). Its distinctive feature, that can be traced back to a causal nature of the system response to the perturbation by ac field, lies in existence of only one electron-field vertex where the chain of retarded Green functions changes to the chain of advanced ones. This part of the loop, referred to as the *retarded-advanced junction*, is essentially nonlocal in the time domain and is given by

$$\int d\tau_1 \int d\tau_2 G^{\mathrm{R}}(\tau,\tau_1)\hat{f}(\tau_1-\tau_2)\hat{\mathbf{j}}_\alpha\left[\mathbf{A}_\alpha(\tau_1) - \mathbf{A}_\alpha(\tau_2)\right]G^{\mathrm{A}}(\tau_2,\tau'), \tag{5}$$

see Eq. (4). In absence of ac pumping, I_1 equals the equilibrium persistent current I_{PC} while I_2 vanishes identically.

3 Fluctuations of persistent currents out of equilibrium: heating effect

The analytic structure of the retarded-advanced junction leads, after disorder averaging, to an unusual object, the *loose diffuson*. Indeed, the retarded-advanced junction [Fig. 2(a)], taken

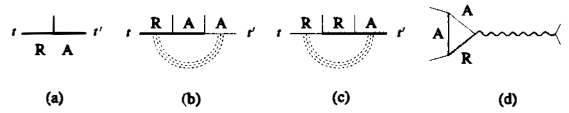


Figure 2: The retarded-advanced junction (a), and its averaging [(b) and (c)] resulting in the loose diffuson (d) that ends up with either RAA or RRA triangle. Dashed lines in (b) and (c) denote the ac-field regularised diffuson. Equation (6) holds for $t \to t + \tau/2$ and $t' \to t - \tau/2$.

together with one of the adjacent electron-field vertices [Figs. 2(b) and 2(c)], can be isolated off from the rest of the diagram by performing the disorder averaging as is shown in Figs. 2(b) and 2(c) to result in the *loose diffuson* shown in Fig. 2(d).

Using conventional contraction rules and explicit form of the ac filed dependent diffuson, one derives[3] that the loose diffuson is given by $\hat{f}(\tau)\Lambda_\tau(t)$ with

$$\Lambda_\tau(t) = D\int_{-\infty}^{t} d\xi\,[\mathbf{A}(\tau+\xi)-\mathbf{A}(\xi)]^2\, e^{-\gamma(t-\xi)} \exp\left\{-D\int_{\xi}^{t} d\xi'\,[\mathbf{A}(\tau+\xi')-\mathbf{A}(\xi')]^2\right\}, \qquad (6)$$

and γ being the electron escape rate to external reservoir via the passive lead.

The out-of-equilibrium fluctuations of persistent currents are given by an average of the pairwise product of three electron loops shown in Fig. 1. Two types of diagrams are available. The first set of diagrams arises from the cross-product of the retarded and the advanced loops. Two skeleton diagrams of this type are depicted in Figs. 3(a) and 4(a). These two diagrams, referred to as the *parental* diagrams and evaluated under the simplifying condition of large temperatures, $T \gg 1/\tau_\phi, \gamma$ (τ_ϕ is the total dephasing rate), yield the well-known result for the *equilibrium* fluctuations of persistent currents, Eq. (1).

However, there also exists another set of diagrams originating from the product of two electron loops, at least one of which is the retarded-advanced electron loop. These diagrams, referred to as the *daughter* diagrams, contain at most two loose diffusons and are shown in Figs. 3(b), 3(c), 4(b), 4(c), and 4(d).

We claim that the *diagrams with loose diffusons describe the heating effect.* To prove this explicitly, we proceed in two steps. (i) First, we evaluate the contributions of both the parental and the daughter diagrams to persistent currents fluctuations under the simplifying condition of large temperatures (see above). The resulting expression

$$\langle I_n^2(t)\rangle = -4e^2n^2\left(\frac{\tau_D}{\pi}\right)^{1/2}\int_0^\infty \frac{d\tau}{\tau^{3/2}} e^{-n^2\tau_D/(4\tau)}\hat{f}^2(\tau)\,[1-\Lambda_\tau(t)]^2 \qquad (7)$$

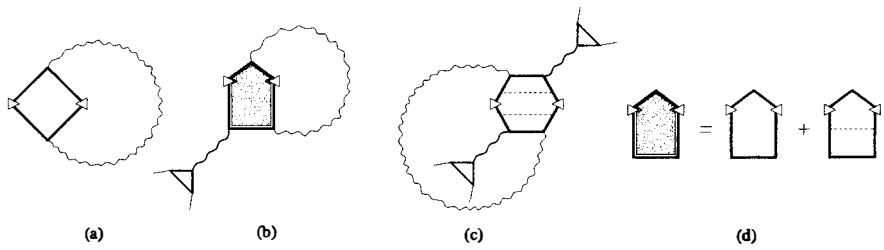


Figure 3: Local single-loop parental (a) and daughter [(b) and (c)] diagrams contributing to the nonequilibrium fluctuations of persistent currents. The three diagrams arise disorder average of $\langle I_1 I_1\rangle$, $\langle I_1 I_2\rangle$ and $\langle I_2 I_2\rangle$, respectively. Hikami box of the diagram (b) is detailed in (d).

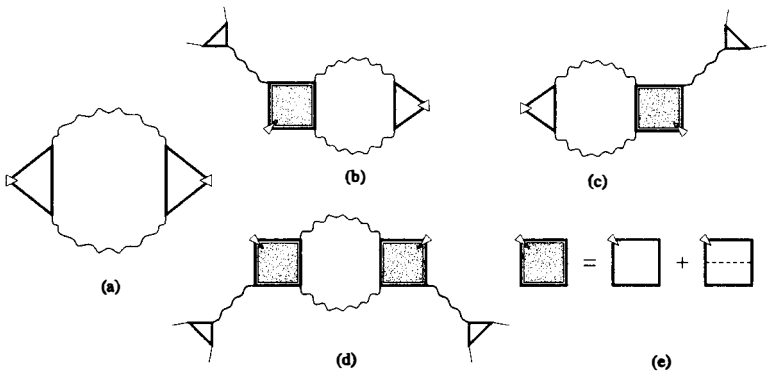


Figure 4: Nonlocal single-loop parental (a) and daughter [(b) – (d)] diagrams contributing to the nonequilibrium fluctuations of persistent currents. The four diagrams are associated with the averages $\langle I_1 I_1 \rangle$, $\langle I_1 I_2 \rangle$, $\langle I_2 I_1 \rangle$ and $\langle I_2 I_2 \rangle$, respectively. Hikami box of the diagrams (b) – (d) is detailed in (e).

is remarkable: It copies the structure of Eq. (1) for persistent currents fluctuations in equilibrium. The only (though important) difference is that the Fourier transform $\hat{f}(\tau)$ of the electron energy distribution function gets renormalised in accordance with the pattern

$$\hat{f}(\tau) \mapsto \hat{f}(\tau)[1 - \Lambda_\tau(t)]. \tag{8}$$

This clearly suggests that $\hat{f}(\tau)[1 - \Lambda_\tau(t)]$ should be interpreted as (a Fourier transform of) the *effective* electron distribution function renormalised due to the electron interaction with the pumping ac field. (ii) To corroborate the guess, we have explicitly verified [3] that solution to a kinetic equation for diffusive electrons in external ac field does coincide with the one extracted from the above mentioned interpretation [Eq. (8)] of Eq. (7) that has been obtained by taking into account the diagrams with loose diffusons. This coincidence completes the proof of our main statement.

4 Conclusions

We have shown that the real-time impurity diagrammatic technique does catch the heating effect in disordered conductors under ac pumping without a need for explicit solving a kinetic equation. It turns out that entire information about heating is encoded in the diagrams of a new class which contain the loose diffusons as a compulsory element. As a closing remark, let us stress that the above renormalisation, Eq. (8), of the electron distribution function is *not* a must, and there are observables which are insensitive to the heating of the electron gas. The formalism we launched is capable of automatic distinguishing between them. The reader is referred to the tutorial paper [3] for further details.

References

1. M. Büttiker, Y. Imry, and R. Landauer, Phys. Lett. A **96**, 365 (1983).
2. B. L. Altshuler, Y. Gefen, and Y. Imry, Phys. Rev. Lett. **66**, 88 (1991); H.-F. Cheung, E. K. Riedel, and Y. Gefen, Phys. Rev. Lett. **62**, 587 (1989).
3. V. I. Yudson, E. Kanzieper, and V. E. Kravtsov, Limits of the dynamical approach to the nonlinear response of mesoscopic systems, eprint cond-mat/0012200, to appear in Phys. Rev. B (2001).

EXPERIMENTAL AND THEORETICAL INVESTIGATIONS ON AHARONOV-BOHM CAGES

C. NAUD[1] , G. FAINI[1], D. MAILLY[1]
J. VIDAL[2], B. DOUÇOT[3], G. MONTAMBAUX[4]
A. WIECK[5], D. REUTER[5]
[1] *Laboratoire de Photonique et de Nanostructures*
196, avenue Henri Ravéra BP 26 F-92222 Bagneux cedex France
[2] *Groupe de Physique des Solides, CNRS UMR 7588, Université Paris 6 et 7*
2 place Jussieu, F-75251 Paris cedex 05 France
[3] *Laboratoire de Physique de la Matière Condensée, CNRS UMR 8551, Ecole Normale Supérieure*
24 rue Lhomond, F-75231 Paris cedex 05 France
[4] *Laboratoire de Physique des Solides, CNRS UMR 8502, Université Paris Sud*
Bât 510, F-91405 Orsay France
[5] *Lehrstuhl für Angewandte Festkoerperphysik Ruhr-Universität Bochum NB 03 / 58 Universitätsstrasse*
150 D-44780 BOCHUM Germany

Aharonov-Bohm oscillations have been observed in a lattice formed by a two dimensional paving of hexagonal tiles. This observation is in good agreement with a recent theoretical calculation of the energy spectrum of this so called $\mathcal{T}_3$ lattice. We have investigated the low temperature magnetotransport of the $\mathcal{T}_3$ lattice realized in the GaAlAs/GaAs system. Using an additional electrostatic gate, we have studied the influence of the channel number on the oscillations amplitude. Finally, the role of the disorder on the strength of the localization is discussed.

1 Introduction

The spectral properties of an electron in a periodic lattice in the presence of a magnetic field are of particular interest. Indeed, the frustration between the spatial periodicity and the one induced by the magnetic field gives rise to spectacular energy spectra versus the reduced flux $f = \phi/\phi_0$, where ϕ is the magnetic flux per elementary cell and ϕ_0 is the flux quantum. A well-known example is the Hofstadter butterfly [1]. Recently, the study of a bipartite two-dimensional rhombus tiling, named $\mathcal{T}_3$, (shown in figure 1) has attracted a lot of attention [2]. For $f = 1/2$, its energy spectrum is reduced to three degenerate discrete levels (see figure 2). The whole lattice is then similar to a unique super-atom with localized electrons. This behavior is very different from the case of the square lattice where for any rational value of the reduced flux the energy spectrum is continuous. This localization for the $\mathcal{T}_3$ lattice can be easily understood in terms of the Aharonov-Bohm (AB) effect. Indeed, in order to propagate through the lattice, an electron must travel through AB loops. For $f = 1/2$ interferences are destructive and the electron is then confined in a so-called AB cage. This tight-binding calculation has received an experimental confirmation in the temperature dependence of the critical current of a superconducting network in the $\mathcal{T}_3$ geometry. In addition, the unusual nature of the state at half flux quantum has been revealed by a strong reduction of the critical current and by a very disordered vortex pattern through decoration experiments [3, 4].

The first experimental evidence of AB cages in a normal metal network tailored in a high mobility two dimensionnal electron gas (2DEG) has been recently reported [5]. The low temperature magnetoresistance measurements show clear h/e oscillations in arrays of 2500 cells. Experiments performed on square lattices of similar size do not show such a behavior. This is a strong indication that the cage effect predicted for a tight binding network persists for a networks of wires. Such persistence was also expected from theoretical calculations of the Landauer conductance in such structures (see section 3). The temperature dependence of the h/e peak amplitude of the Fourier transform for both the $\mathcal{T}_3$ lattice and the single rhombus have been measured. For a sin-

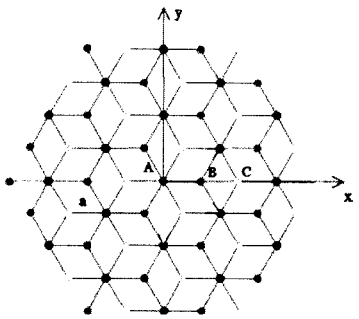


Figure 1: $\mathcal{T}_3$ lattice

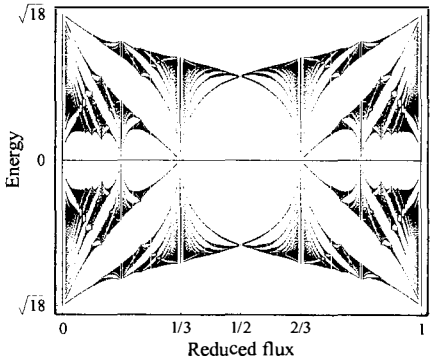


Figure 2: energy spectrum of a $\mathcal{T}_3$ lattice versus reduced flux

gle loop the amplitude of the AB signal is expected to follow a $T^{-1/2}$ law as long as the size of the loop L is smaller than the phase coherence length L_Φ, because of temperature smearing. When the temperature is such that $L > L_\Phi$ the AB signal falls down exponentially [6]. Thus, the size of a cage being larger than that of a single loop, one expects a cutoff temperature significantly smaller for the $\mathcal{T}_3$ as compared to the one for a single rhombus. The experimental results show that this critical temperature is around $1K$ for a rhombus whereas it is below 100 mK for the $\mathcal{T}_3$. If one assumes a $T^{-1/3}$ temperature dependence for L_Φ in GaAlAs/GaAs systems [7], the ratio of the measured critical lengths is 2.7, in good agreement with the geometrical dimensions yielding a ratio of 3. More strikingly, at high magnetic field, $h/2e$ oscillations appear whose amplitude can be much larger than the h/e signal. Such an amplitude dismisses a simple interpretation in terms of harmonics generation. Moreover, the temperature dependence of the $h/2e$ oscillations is similar to that of the h/e one. This indicates that the characteristic lengths associated with the two periodicities are alike and this rules out any interpretation in terms of harmonics. One may also think of Aronov-Altshuler-Spivak (AAS) oscillations when dealing with an $h/2e$ signal. But, due to the aspect ratio of the sample, the AAS signal should vanish for high magnetic fields. Thus, any explanation in terms of AAS would imply that a high magnetic field induces the squeezing of the wires leading to an array of one dimensionnal leads. A second explanation for the frequency doubling could be the electron-electron interactions which could induce charge doubling. Up to now the origin of this $h/2e$ peak at high magnetic fields remains unclear.

In the present paper we report on new experiments on the cage effect. These experiments in an other type of sample confirm both the existence of the cage effects and the systematic presence of the frequency doubling for high magnetic fields. We have realised $\mathcal{T}_3$ lattices on a GaAlAs/GaAs heterostructure on which electrostatics gates have been deposited in order to control the number of channels per wire. The fabrication process and the experimental results concerning these devices are introduced in section 2. Finally, in section 3 we present theoretical calculations concerning the influence of the disorder on the cage effect together with experimental results on networks made of silver.

2 Cage effect versus the number of channels

2.1 Realization of the gated samples

This work is carried out on high-mobility 2DEG heterojunction material with an initial mobility of 3×10^6 cm^2 V^{-1} s^{-1} and a carrier density of 3.7×10^{11} cm^{-2} which give a Fermi wavelength

λ_F = 41 nm and an elastic mean free path l_e = 12 μm. Figure 3 shows the experimental procedure to realize the electrostatic gate. A 200 nm thick insulator resist is first deposited on

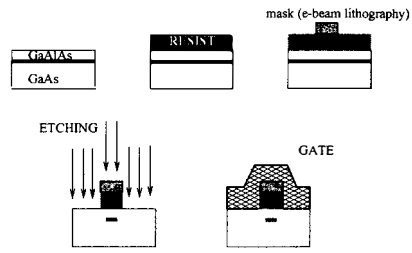


Figure 3: Step by step process for the realisation of the gated samples

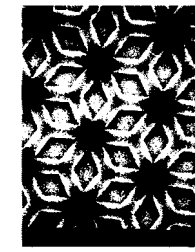


Figure 4: Electron microscope view of the aluminium mask used to etch the 2DEG. The nominal width of the wires defining the network is 0.4 μm whereas their length is about 1 μm

the top of the sample. We use then electron beam lithography and a lift-off technique to pattern the $\mathcal{T}_3$ lattice with an aluminium mask (figure 4). Reactive ion etching removes the resist from the unprotected regions. Then, etching using argon ions transfers the pattern into the 2DEG. Due to the lateral depletion resulting from the etching process, the effective electrical width is considerably smaller than the wire width mask. The metal of the gate is then evaporated onto the whole surface. As a result, the gate is in intimate contact with the regions where the 2DEG has been destroyed whereas the thick resist layer considerably reduces the influence of the gate on the gas beneath the wires. As a consequence, using this approach, we reduce the gate action on the electron density and favour a pinching of the wires making the lattice.

2.2 Characterization of the samples

In figure 5, we present the magnetoresistance of the $\mathcal{T}_3$ network for several gate voltage values. The measurements are performed at 50 mK. From the Shubnikov-de-Haas oscillations we can extract the electron density versus the gate voltage. In the low magnetic field regime we clearly

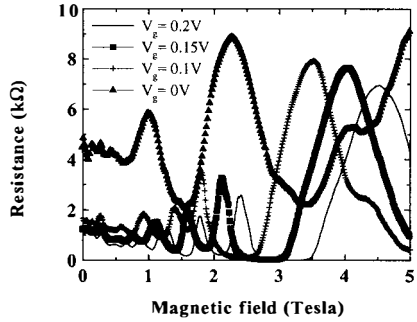


Figure 5: Magnetoresistance of a $\mathcal{T}_3$ lattice versus the gate voltage showing Shubnikov-de-Haas oscillations

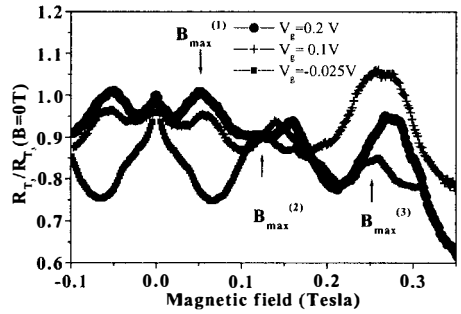


Figure 6: Same as figure 5 but in the low magnetic field range dominated by the classical boundary scattering effects

observe large features which depend on the gate voltage (indicated by arrows in figure 6). These features appear already at a temperature of 4K and are almost temperature independent down to 50 mK, indicating a classical effect. In 2DEG systems, the mean free path at low temperature

can be much larger than the width of the wire and the electrons are frequently scattered by the boundaries. Using a quasi-classical description, Ziman[8] considers the scattering of electrons by a rough boundary. The conclusions agree with our intuitive expectations : when the wavelength of the incident electron is much smaller than the average boundary roughness, the electron is strongly scattered in all directions. In the opposite case, when the Fermi wavelength is much larger, the incident electron undergoes specular reflections. These scatterings at the boundaries[9] lead naturally to the concept of the boundary scattering length, l_b, which is the average distance an electron can travel along a wire before a diffusive scattering event takes place. Then, the effective mean free path l_{eff} is such that $\frac{1}{l_{eff}} = \frac{1}{l_{trans}} + \frac{1}{l_b}$ where l_{trans} is the transport mean free path. As long as $l_{trans} \gg l_b$, boundary scattering dominates the momentum relaxation. The boundary scattering rate can be "tuned" using a magnetic field perpendicular to the wire. At zero or low magnetic field, electrons with a large component of momentum parallel to the boundaries contribute significantly to the conductivity. However, as the magnetic field increases, more and more electrons are forced to interact with the edges and random scattering reduces the effective mean free path l_{eff}. Thus, the resistivity increases and subsequently saturates at some maximum value when the cyclotron radius is approximatively twice the wire width[9]:

$$W = 0.55 \times r_c(B_{max}) = 0.55 \times \frac{\sqrt{2\pi\hbar^2 n_s}}{eB_{max}} \quad (1)$$

Any further increase of the magnetic field will now lead to a drop of the resistivity since the probability for an electron to be backscattered by the edges is reduced. In figure 6 we observe 3 maxima corresponding to the 3 magnetic field values denoted $B^{(1)}_{max}$, $B^{(2)}_{max}$ and $B^{(3)}_{max}$. These maxima correspond to three different widths we can identify in our samples: the width of the wires connecting the nodes and the diameter of the cavities formed at the sixfold coordinated and the threefold coordinated lattice sites. Using equation 1 we can deduce the real dimension of the electron path. The channel number can be deduced from the comparison between the Fermi wavelength and the wire width ($N = \frac{W^{(3)}}{\lambda_F/2}$).

These results are reported in the following table :

Gate voltage	n_s $10^{11}cm^{-2}$	$B^{(1)}_{max}$ (Tesla)	$W^{(1)}$ (μm)	$B^{(2)}_{max}$ (Tesla)	$W^{(2)}$ (μm)	$B^{(3)}_{max}$ (Tesla)	$W^{(3)}$ (μm)	N
$V_g = 0.2V$	1.48	0.052	0.67	0.159	0.219	0.274	0.127	3
$V_g = 0.15V$	1.32	0.052	0.63	0.154	0.219	0.268	0.123	3
$V_g = 0.1V$	1.17	0.056	0.56	0.140	0.221	0.262	0.118	3
$V_g = 0.05V$	0.9	hard to	locate	0.137	0.199	0.270	0.101	2
$V_g = 0V$	0.83	hard to	locate	0.122	0.213	0.256	0.101	2

The identification of $W^{(3)}$ to the wire width gives reasonable numerical values. Nevertheless, the values obtained for the cavities diameters are overestimated, which is not surprising since this wire model is not really adapted to the particular shape of the junctions.

2.3 Resistance oscillations versus the channel number

The unexpected frequency doubling leads us to define two magnetic field regimes : a *low field* regime (between 0.4T and 1.2T) where we observe only h/e oscillations and a *high field* regime (from 1.2T to 2T) where the $h/2e$ oscillations appear in addition to the h/e component. We substract a polynomial fit of the global magnetoresistance to the experimental points in order to extract the oscillations. This resulting signal is then Fourier transformed. Let us now discuss the influence of the gate voltage on the oscillations in both regimes. In figures 7 and 8, we have plotted the Fourier transform peak magnitude against the channel number. In the low field

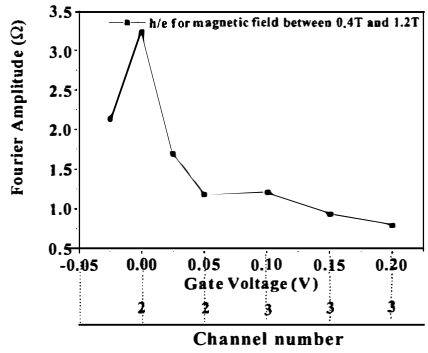


Figure 7: Variation of the h/e peak amplitude of the Fourier transform versus the channel number for the **low magnetic field regime**

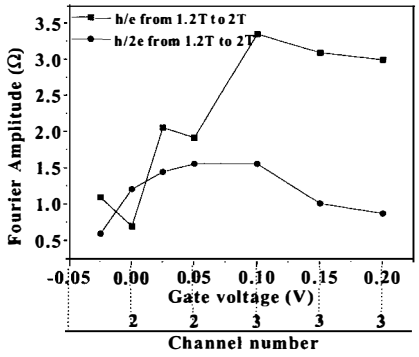


Figure 8: Variation of the h/e and $h/2e$ peak amplitudes of the Fourier transform versus the channel number for the **high magnetic field regime**

regime the AB amplitude clearly increases with decreasing the electrical wire width. This is in agreement with the work of M. Büttiker *et al.* on a simple loop [10]. Essentially, their calculation shows that if N is the channel number, the h/e signal results from N^2 uncorrelated contributions whose stochastic averaging gives rise to a decrease of the AB oscillation amplitude like $1/N$. Note that in our experiments the amplitude of the Fourier transform falls down at a critical gate voltage (about $0V$ corresponding to a channel number close to 2). This may be due to the wire pinch-off induced by the gate. As a result, the cutting of some wires suppresses the cage effect and consequently reduces the h/e signal. In the high field regime, we observe a different behavior between the h/e and the $h/2e$ components. The h/e amplitude decreases monotonously with the reduction of the channel number. On the other hand, the $h/2e$ oscillations seem to have a constant magnitude versus the gate voltage. This fact suggests a different mechanism to explain the two periodicities in this high field regime. More surprisingly, the h/e signal itself behaves in an opposite manner in the two regimes: whereas, as discussed above, the AB amplitude at low field has the expected channel number dependence, in the high field regime the h/e signal increases with N. This leads us to raise the hypothesis that we are dealing with different physical phenomena in the two magnetic field regimes. Up to now the origin of the $h/2e$ peak at high magnetic fields and, more, the different behavior of h/e signal versus channel number for the two magnetic field regime remain unclear.

3 The effect of disorder

3.1 Theoretical calculations

In this section, we discuss the influence of an elastic disorder on the periodicity of the Aharonov-Bohm oscillations in the $\mathcal{T}_3$ lattice. In order to simplify this analysis, we consider that there exists only one conduction channel. Of course this hypothesis is somehow unrealistic but it allows us to get a partial answer to this problem. The technical details can be found in ref. 11.

From a theoretical point of view, there are several ways to introduce disorder in a system. For instance, one can consider a random scattering matrix on each bond of the network or at each node. We can also put some additionnal dead-end bonds of random lengths to mimick the dephasing due to impurities. Here, we adopt another point of view by changing the length of each quantum path. One way to do this practically, is to make a random modulation Δl of each bond of length l without modifying the phase factor due to the magnetic field. Indeed, since each bond is considered as strictly one-dimensional, the circulation of the vector potential along

one link is not affected by reflections of the wavepacket on this link. Thus, in the Landauer-like transmission formalism that we have used, we only include these length fluctuations in the quantity kl which is the main parameter of our study [11]. In the following, we focus on the transmission properties of a piece of the $\mathcal{T}_3$ lattice and we compare it to a piece of the square lattice (see Fig. 9).

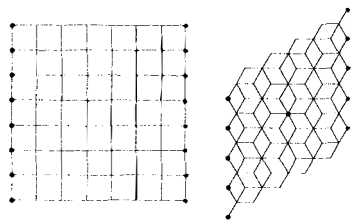


Figure 9: A piece of the square lattice (left) and of the $\mathcal{T}_3$ network (right). Black (respectively grey) dots represent the connections to the input (respectively output) channels. The central black dot is the input channel chosen for the bulk injection.

In the pure case ($\Delta l = 0$) the transmission coefficient T depends on the wave vector k of the incoming wave function and on the reduced flux f. We have displayed in Fig 10, the averaged transmission coefficient for $kl \in [0, 2\pi]$. One clearly observes some peaks for rationnal f (extended Bloch-like eigenstates) reminiscent of the butterfly-like structure of the energy spectrum. Due to the existence of the AB cages, the transmission coefficient is minimum at $f = 1/2$ for the $\mathcal{T}_3$ network but it does not strictly vanish. This is due to the existence of dispersive edges states [12] that are able to carry current even for $f = 1/2$. Nevertheless, when one injects the current in the bulk of the sample, we obtain $T = 0$ for $f = 1/2$ as expected. Note that for both systems, the signal is anharmonic but is periodic with period ϕ_0 leading to a h/e periodicity for the magneto-resistance.

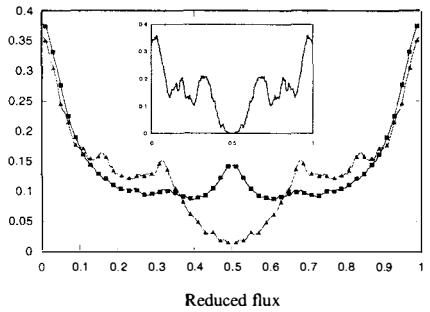


Figure 10: Averaged transmission coefficient as a function of the reduced flux for the square lattice (square) and for the $\mathcal{T}_3$ network (triangle). Inset : Averaged transmission coefficient for the $\mathcal{T}_3$ network with a single input channel in the bulk the network

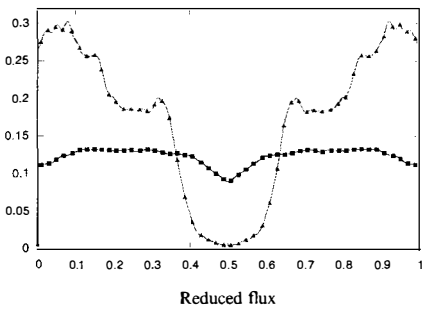


Figure 11: Transmission coefficient averaged over 50 configurations of disorder for $kl = \pi/3$ and $k\Delta l = 1.47$ as a function of the reduced flux.

The main question is to know how this periodicity is modified when we introduce the disorder. It is clear that if the disorder is very strong ($k\Delta l \simeq \pi$), there is no phase coherent transmission and we expect a vanishing transmission after averaging over disorder. Consequently, there might be interesting phenomenon for weak enough disorder. We emphasize that the notion of weak and strong disorder is related to the product $k\Delta l$ and thus depends on k. We have shown in figure 11 the effect of disorder on the transmission coefficient as a function of the magnetic flux.

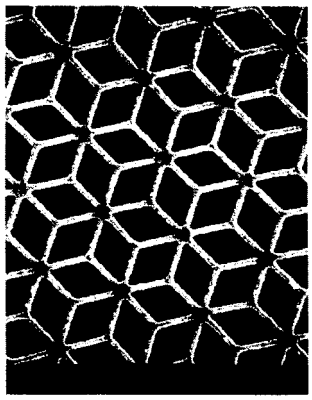


Figure 12: Electron microscope view of a silver $\mathcal{T}_3$ lattice. The width of the wires is about 50 nm and the wire length is 0.4 μm

It is clearly seen that for the square network, the periodicity is no longer ϕ_0 but $\phi_0/2$. This new periodicity is simply due to phase coherent pairs of time-reversed trajectories according to the weak-localization picture. The most striking feature is that for the $\mathcal{T}_3$ lattice, the transmission coefficient remains ϕ_0-periodic with a large amplitude. This strongly suggests that the cage effect (which locks the phase of the oscillations) survives for this strength of disorder. Physically, it means that a strong dephasing is required to destroyd the completely destructive quantum interferences responsible of the AB cages. In addition, note that, for this energy, the signal of the $\mathcal{T}_3$ lattice transmission coefficient is about 10 times larger than the one of the square network. In ref. 12 we report on other energy of the incoming wavepacket where we find always the same type of feature.

3.2 Experimental investigations

The theoretical calculations show that the cage effect is expected to be robust against a moderate amount of elastic disorder. The lattices realized in the GaAlAs/GaAs system gives an experimental evidence of this properties and while clear h/e oscillations have been observed for the $\mathcal{T}_3$ lattices, the experiments performed on square lattices do not show such a behaviour. The influence of a stronger disorder has been also investigated using networks in metallic systems. Actually the elastic mean free path is significantly smaller in metallic network and the transport is diffusive. To secure a phase coherence on a whole AB cage, the geometrical dimensions of the metallic $\mathcal{T}_3$ lattice have been reduced and imply that one flux quantum Φ_0 per unit cell corresponds now to a magnetic field of 300 Gauss. An example of a silver $\mathcal{T}_3$ network is shown in figure 12. The fabrication consists in the lift-off of the metal on the top of a silicon substrat which will be insulating at low temperature.

Up to now no h/e signal has been detected within a sensitivity of $\frac{\Delta R}{R} \sim 10^{-4}$. These preliminary investigations seems to show that a strong disorder destroyed the cage effect. Such a behavior can be theoretically obtained using the Landauer formalism. In fact, for both square and $\mathcal{T}_3$ networks, the $h/2e$ periodicity becomes quickly dominant from a critical value of the relevant parameter $k\Delta l$ which depends on the system size and converges to zero for infinite lattice[11]. Nevertheless due to the small resistance of the samples at zero magnetic field ($R(B = 0T) = 50\Omega$) the expected amplitude of the h/e oscillations is relatively small and at the present time we carry on the measurements with a better sensibility.

4 Conclusions

Localisation phenomenom induced by the magnetic field on the $\mathcal{T}_3$ topology has been confirmed in the GaAlAs/GaAs system. The frequency doubling in the high magnetic field regim is systematically observed and displays a different behavior versus the channel number compared to the fundamental period. This work on the cage effect in the $\mathcal{T}_3$ topology is being pursued with the experimental investigation of the role of the disorder in metallic samples. A generalization of the transmission calculation to a multichannel case is also in progress in order to understand the frequency doubling origin.

References

1. D. R. Hofstader, *Phys. Rev.* B.**14**, 2239 (1976)
2. J. Vidal, R. Mosseri and B. Douçot, *Phys. Rev. Lett.***81**, 5888 (1998)
3. C. C. Abilio, P. Butaud, Th. Fournier, and B. Pannetier, **J**. Vidal, S. Tedesco and B. Dalzotto, *Phys. Rev. Lett.***83**, 5102 (1999)
4. E. Serret *et al.*in preparation
5. C. Naud, G. Faini, D. Mailly *Phys. Rev. Lett.***86**, 5104 (2001)
6. F. P. Milliken, S. Wasburn, C. P. Umbach, R. B. Laibowitz, and R. A. Webb, *Phys. Rev.* B.**36**, 4465 (1987)
7. T. J. Thornton, M. Pepper, H. Ahmed, D. Andrews and G. **J**. Davies, *Phys. Rev. Lett.***56**, 1198 (1986)
8. J. M. Ziman, *Electrons and phonons* Chapter 11, Oxford Univ. Press UK (1960)
9. T. J. Thornton, M. L. Roukes, A. Scherer, B. P.Van der Gaag, Coherence in Mesoscopic Systeme Edited by B. Kramer Plenum Press (New York and London), series B : Physics Vol. **254**, 153 (1990)
10. M. Büttiker, Y. Imry, R. Landauer and S. Spinhas, *Phys. Rev.* B.**31**, 6207 (1985)
11. J. Vidal, G. Montambaux, and B. Douçot, *Phys. Rev.* B.**62**, R16294 (2000)
12. J. Vidal, P. Butaud, B. Douçot, and R. Mosseri, to be published in *Phys. Rev.* B.

Persistent Currents in Mesoscopic Connected Rings

L. Saminadayar[1,2], W. Rabaud[1], D. Mailly[3], K. Hasselbach[1], A. Benoît[1],
A. Wieck[4], D. Reuter[4] and B. Etienne[3]

[1] *Centre de Recherches sur les Très Basses Températures, B.P. 166X, F-38042 Grenoble Cedex 9, France*

[2] *Université Joseph Fourier, B.P. 53, F-38041 Grenoble Cedex 9, France*

[3] *Laboratoire de Photonique et Nanostructures, B.P. 107, F-92225 Bagneux Cedex, France*

[4] *Lehrstuhl für Angewandte Festkörperphysik, Ruhr-Universität Bochum, Universitätsstrasse 150, D-44780 Bochum, Germany*

Abstract

Since the first experiments on persistent currents in mesoscopic rings, much attention has been paid to the understanding of thermodynamic properties of isolated mesoscopic systems. In this paper, we report on the first observation of persistent currents in a sample much larger than l_ϕ, namely, a line of mesoscopic connected rings. Furthemore, we compare our result with measurements of persistent currents in the same but isolated rings. We find that *the amplitude of the persistent currents is not significantly modified when connecting or disconnecting the rings.*

1 Introduction

Persistent currents in mesoscopic rings is one of the most sriking consequences of the quantum coherence of the electronic wave function. These are due to the boundary conditions imposed by the magnetic flux enclosed by the ring[1,2] that imposes the electronic wave function to be periodic with flux with periodicity $\Phi_0 = h/e$. This leads to a persistent, non-dissipative current given by $I(\Phi) = -\partial\mathcal{F}(\Phi)/\partial\Phi$, where $\mathcal{F}$ is the free energy[2]. Both the sign and the amplitude of the current depend on the number of electrons in the ring and the microscopic disorder configuration. However, an order of magnitude of the current for a single, isolated ring can be characterized by its typical value $I_{typ} = \sqrt{\langle I^2 \rangle}$, $\langle\,\rangle$ denoting the average over disorder configurations. It is given[3,4] by $I_{typ} = 1.56\ I_0\ l_e/L$. In this formula, $I_0 = e\,v_F/L$ where v_F is the Fermi velocity and L the perimeter of the ring, and l_e is the elastic mean free path: the current varies as the inverse of the diffusion time $\tau_D = L^2/D$ where $D = v_F\,l_e$ is the diffusion constant.

A couple of experiments have clearly proved the existence of persistent currents, both in metallic systems[5,7,6] as well as semiconductor systems[8,9,10]. However, all these experiments have been performed on isolated systems, single ring or array of isolated rings, always smaller than the phase coherence length l_ϕ. Recently, some theoretical predictions[11] have suggested that persistent currents should also be observed in an array of *connected* rings, even if its total size is much larger than l_ϕ. Moreover, the amplitude of the persistent current should be only weakly reduced as compared to its value in the same but isolated rings.

In this paper, we report on the first observation of persistent currents in a system much larger than l_ϕ, namely, a line of connected rings[12]. The rings are made from GaAs/GaAlAs heterostructure, and a new on-chip multiloop μ-SQUID gradiometer has been developped to measure the magnetic response of the sample.

2 Sample

The sample (see fig.2) consists in a line of 16 GaAs/GaAlAs connecetd rings. The heterojunction was grown using molecular beam epitaxy: at $4.2\,K$ in the dark, the two dimensional electron gas (2DEG) at the heterointerface has an electron density of $5.2 \times 10^{11}\,cm^{-2}$ and a mobility of $0.8 \times 10^6\,cm^2\,V^{-1}\,s^{-1}$. This yields a Fermi velocity $v_F = 3.16 \times 10^5\,m\,s^{-1}$ and a Fermi wavelength $\lambda_F = 35\,nm$. Weak localisation and conductance measurements give an elastic mean free path of $l_e \approx 8\,\mu m$ and a phase coherence length of $l_\phi \approx 20\,\mu m$. Lithographic

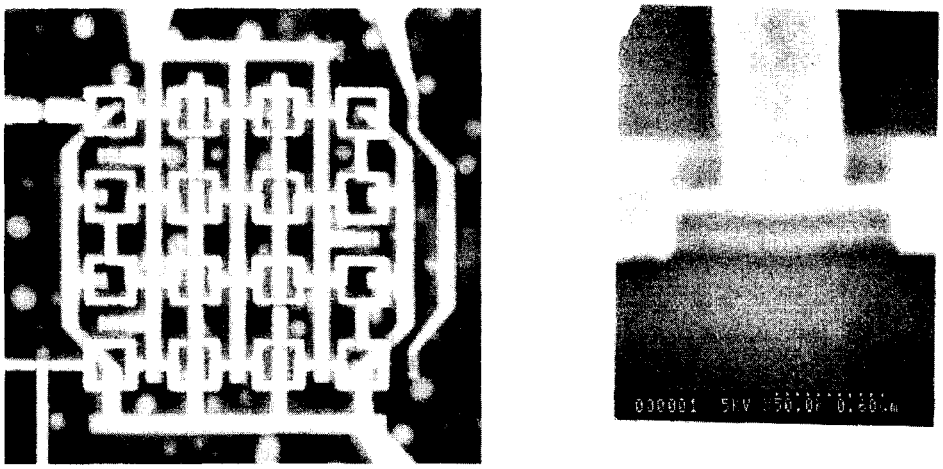


Figure 1: Left: Optical photograph of our sample: one can distinguish the μ-SQUID and the three gates. Right: SEM picture of the microbridges.

operations were performed using e-beam lithography on polymethyl methacrylate (PMMA) resist. The rings, actually squares of internal side length $2\,\mu m$, external side length $4\,\mu m$ and mean perimeter $L = 12\,\mu m$, connected by $2\,\mu m$ long arms, are fabricated by ion milling with an aluminium mask and connected to AuGeNi ohmic contacts in a two-probe geometry. Considering the depletion length ($\approx 100\,nm$), the actual width of the arms of the rings is $W = 0.8\,\mu m$. Three Schottky gates were deposited on the top of the rings: the first one cuts the arms of the rings, and allows to suppress persistent currents an thus to measure the noise level of the experimental setup. The second gate was deposited on the two outgoing wires and made possible the insulation of the rings from the ohmic contacts; the last one was placed on each arm joining two rings, allowing the measurement of isolated rings. A calibration loop with the same dimensions as one ring was patterned in order to calibrate our experimental setup. Gates and calibration loop were obtained by liftoff of $10\,nm$ titanium and $50\,nm$ gold films. The device was then covered with a $60\,nm$ insulating layer.

The next step is the fabrication of the aluminium gradiometer, designed as two counterwound loop. It has exactly the same shape as the rings, allowing a perfect coupling between the rings and the μ-SQUID[9,13]. The first level was deposited on top of the rings and of the calibration loop. Then a new insulating layer was deposited and the gradiometer was completed with the other half. The two Dayem micro-bridge Josephson junctions, $300\,nm \times 20\,nm \times 30\,nm$, were lithographically defined at this second stage: such a microbridge junction technique allows to avoid the complicated fabrication of tunnel jonctions[13]. The contact between the two aluminium levels was then obtained by covering them with aluminium pads deposited after an ion bombardment cleaning.

3 Experimental setup

The critical current of the μ-SQUID is measured using dedicated electronics which ramps a dc current until the μ-SQUID's critical current is attained[13]. The current is then reset, and the value of the critical current sent to a computer. This cycle is repeated periodically at $5\,kHz$, and the measured flux resolution of our gradiometer is then $\approx 5 \times 10^{-4}\,\Phi_0/\sqrt{Hz}$. The gain of the setup is calibrated by sending a dc current trough the calibration loop. Fig.2 shows a typical histogram of our μ-SQUID.

The procedure to measure persistent currents is the following: critical current of the

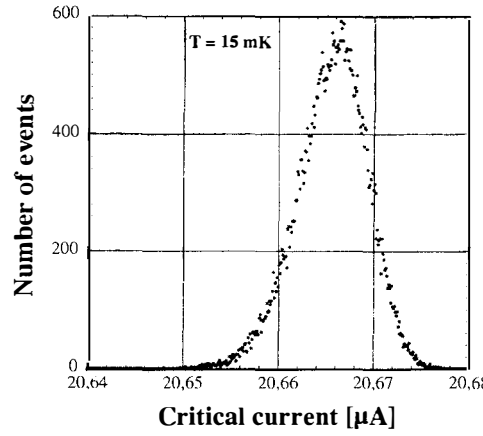


Figure 2: Typical switching histogram of our μ-SQUID at a temperature of 15 mK. The value of the critical current depends on the size of the microbridges.

μ-SQUID is measured as a function of magnetic field, successively for "opened" and "closed" rings ($-561\,mV$ applied on the gate when measuring opened rings, which gives the reference signal). The signal of persistent currents is then extracted by Fast Fourier Transform (FFT) of the difference between measurements with closed and opened rings, whereas the noise was obtained by FFT of the difference between two identical measurements, either with closed or opened rings.

4 Results

Fig.3 shows a typical power spectrum of the persistent currents. The peak in the "signal" curve within the Φ_0 frequency range, absent from the "noise" curve, is a clear signature of persistent currents in our line of connected rings. As in previous experiments[9], the amplitude of the signal varies due to relaxation processes in the GaAlAs layer. However, this instability allows to perform statistics over disorder configurations, and thus to measure the typical current. We followed this procedure over a sample of $\approx$ 1000 spectra, and obtained for our line of connected rings a typical current of $0.40 \pm 0.08\,nA$ per ring[12]. This value has to be compared with the theoretical value $0.58 \times 1.56\,(I_0/\sqrt{N_R})\,(l_e/L) \approx 0.63\,nA$ per ring, $r = 0.58$ being the reduction factor predicted for the same line of connected rings[11,14]. By applying $-540\,mV$ on the gate we isolated the rings and performed the same experiment as for connected rings. We also observed an h/e periodic signal, corresponding to persistent currents in the rings of $0.35 \pm 0.07\,nA$ per ring, to be compared with the theoretical value $1.56\,(I_0/\sqrt{N_R})\,(l_e/L) \approx 1.09\,nA$ per ring. From these two measurements we can calculate a ratio $I_{connected}/I_{isolated} \approx 1.2 \pm 0.5$.

Such a ratio of order unity is the most striking result of our experiment: persistent currents are not affected by the connection between the rings. Again, we would like to stress that the total size of the line of rings is much larger than l_ϕ: in that sense, it is a truly macroscopic object. By extension, our experiment suggests that persistent currents could be observed in other macroscopic samples, e.g. a two dimensional metallic film[14].

In conclusion, we have observed persistent currents in a line of connected rings, whose total size is much larger than the phase coherence length. The amplitude of this current has been found to be similar to the amplitude of the current in the same but disconnected rings. This suggests that persistent currents could be observed in a macroscopic two dimensional sample.

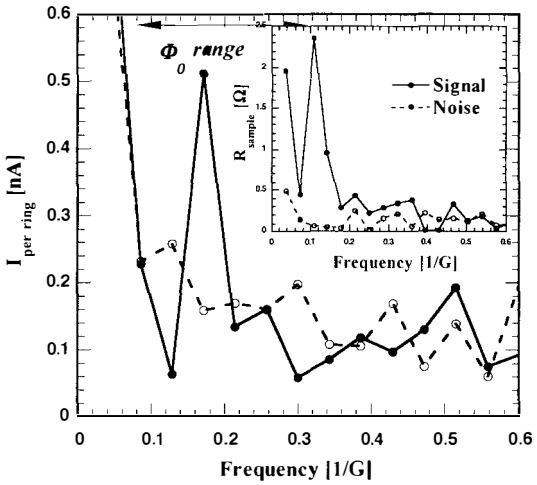


Figure 3: Typical power spectrum of the magnetization due to persistent currents in a line of 16 connected rings at 20 mK. Inset shows the power spectrum of the Aharonov-Bohm conductance oscillations in the same sample.

Acknowledgments

We would like to dedicate this article to the memory of P. Butaud. Fruitful discussions with G. Montambaux, M. Pascaud, H. Bouchiat and V. Chandeasekhar are acknowledged. We thank J. L. Bret, G. Simiand, J. F. Pini and H. Rodenas for technical help.

References

1. N. Byers and C. N. Yang, *Phys. Rev. Lett.* **7**, 46 (1961).
2. M. Büttiker, Y. Imry and R. Landauer, *Phys. Rev. Lett.* **96A**, 365 (1983).
3. H. F. Cheung, E. K. Riedel and Y. Gefen, *Phys. Rev. Lett.* **62**, 587 (1989); N. Argaman, Y. Imry and U. Smilansky, *Phys. Rev.* B **47**, 4440 (1993); E. K. Riedel and F. von Oppen, *Phys. Rev. Lett.* **47**, 15449 (1993).
4. G. Montambaux, in *Quantum Fluctuations*, S. Reynaud, E. Giacobino and J. Zinn-Justin eds., Amsterdam (1997) and references therein.
5. L. P. Lévy, G. Dolan, J. Dunsmuir and H. Bouchiat, *Phys. Rev. Lett.* **64**, 2074 (1990).
6. V. Chandrasekhar, R. A. Webb, M. J. Brady, M. B. Ketchen, W. J. Gallagher and A. Kleinsasser, *Phys. Rev. Lett.* **67**, 3578 (1991).
7. E. M. Q. Jariwala, P. Mohanty, M. B. Ketchen and R. A. Webb, *Phys. Rev. Lett.* **86**, 1594 (2001).
8. B. Reulet, M. Ramin, H. Bouchiat and D. Mailly,*Phys. Rev. Lett.* **75**, 124 (1995); Y. Noat, H. Bouchiat, B. Reulet and D. Mailly, *Phys. Rev. Lett.* **80**, 4955 (1998).
9. D. Mailly, C. Chapelier and A. Benoît, *Phys. Rev. Lett.* **70**, 2020 (1993).
10. L. P. Lévy, D. H. Reich, L. Pfeiffer and K. West, *Physica* (Amsterdam) **189B**, 204 (1993).
11. M. Pascaud and G. Montambaux, *Phys. Rev. Lett.* **82**, 4512 (1999).
12. W. Rabaud, L. Saminadayar, D. Mailly, K. Hasselbach, A. Benoit and B. Etienne, *Phys. Rev. Lett.* **86**, 3124 (2001).
13. K. Hasselbach, C. Veauvy and D. Mailly, *Physica* (Amsterdam) **332C**, 140 (2000).
14. G. Montambaux, private communication.

Transport properties of one dimensional trapped atomic gases

H.P. Büchler[1], V.B. Geshkenbein[1,2], and G. Blatter[1]
[1] *Theoretische Physik, ETH-Hönggerberg, CH-8093 Zürich, Switzerland*
[2] *Landau Institute for Theoretical Physics, 117940 Moscow, Russia.*

We study the transport properties of trapped one dimensional bosonic atom gases/liquids in the presence of strong quantum fluctuations. Driving the condensate with a moving defect we find that the new non-superfluid ground state exhibits Bloch oscillations in the chemical potential. These 'Bloch oscillations' describe the individual tunneling of atoms through the defect and thus are a consequence of particle quantization.

Trapped (quasi-) one dimensional atomic gases at ultra-cold temperatures have attracted much interest [1,2,3,4] as they exhibit specific phenomena not encountered in their two and three dimensional counterparts. Their nature is conveniently described in terms of the dimensionless parameter $\gamma^{-1} = n\hbar^2/mg$, where n and m denote the (one dimensional) atom density and mass, respectively, and g is the coupling constant of the repulsive interparticle interaction. Small and large values of γ correspond to weakly and strongly interacting bosons: for weakly interacting gases quantum fluctuations are suppressed and a mean field description via the Gross-Pitaevskii equation holds. In the strongly interacting situation ($\gamma \to \infty$) the influence of quantum fluctuations increases and the 1D Fermion-Boson duality becomes manifest with important consequences for the phase coherence [1] and the density profile.[2] The requirements for this so called Tonks-Girardeau limit have been discussed by Olshanii,[2] and its experimental realization defines an active field in current research.[5]

Recently, new types of experiments involving a moving laser beam perturbing a three dimensional condensate of sodium atoms enable the investigation of superfluid flow in Bose-Einstein condensates.[6] In this report, we study the transport properties of trapped one dimensional (1D) bosons in the presence of strong quantum fluctuations across such a moving impurity. We find that quantum fluctuations destroy the superfluid flow across the impurity, and the new ground state exhibits 'Bloch oscillations' in the chemical potential difference across the moving impurity. The physical origin of these oscillations is found in the particle quantization: the moving impurity enhances the particle density in front, producing a chemical potential difference across the impurity, which in turn is released each time an atom tunnels through the impurity.

A convenient starting point describing the low energy physics of trapped 1D atomic gases is the imaginary time action for the phase $\phi(x,\tau)$ of the bosonic field $\psi \propto \exp[i\phi]$,[7]

$$\mathcal{S}_0 = \frac{K\hbar}{2\pi}\int_0^{\hbar\beta} d\tau \int dx \left[c_s\,(\partial_x\phi)^2 + \frac{1}{c_s}\,(\partial_\tau\phi)^2\right], \qquad (1)$$

describing sound modes with velocity c_s to be cut-off at high energies Λ. For weak interaction, $\gamma \ll 1$, the sound velocity $c_s = \sqrt{ng/m}$, the dimensionless parameter $K = \pi/\sqrt{\gamma}$, and the cut-off $\Lambda = ng$ derive from the Gross-Pitaevskii equation; quantum fluctuations are suppressed in this limit. Increasing the interaction, quantum fluctuations renormalize the sound velocity c_s and the dimensionless parameter K in the low energy action (1): strongly interacting bosons with a contact potential $g\delta(x)$ are described by $K \approx 1 + 4/\gamma$ while $c_sK = \pi n\hbar/m$ remains unrenormalized (note that $K \to 1$ in the strong coupling or Tonks-Girardeau limit $\gamma \to \infty$; parameters $K < 1$ might be realized for bosons with long range interactions [7]). In Eq. (1) we assume a flat trapping potential along the longitudinal direction. A weak longitudinal trapping potential can be accounted for by space dependent parameters $K(x)$ and $c_s(x)$; the resulting deformation of the excitation spectrum will not change the main results presented below.

The transport properties of the (quasi-) condensate can be probed with a moving laser beam [6] which we describe by a (strong) impurity potential $V_{\rm imp}(x,t) = g_{\rm imp}\delta(x - vt)$ with $g_{\rm imp} > g$,

suppressing the particle density locally. In the weakly interacting limit we can integrate the Gross-Pitaevskii equation over the impurity region and derive a Josephson term coupling the left and right parts of the atom gas (the 'leads') [8,9],

$$V(\varphi) = E_J\left[1-\cos\varphi(\tau)\right] - \hbar n v \varphi, \tag{2}$$

with $E_J = (K/\pi) n g^2/g_{\rm imp}$, to be renormalized in the presence of large interactions. The second term drives the phase difference φ across the impurity. Next, we integrate over the phase dynamics (1) in the leads. The finite size of the system provides us with boundary conditions at the end of the tube. Here, we chose the hard wall approximation $\partial_x\phi(-L/2,\tau) = \partial_x\phi(L/2,\tau) = 0$ (note that a change of the topology to a ring geometry with periodic boundary conditions fundamentally affects the results [9]). The effective action for the phase difference φ across the impurity takes the form

$$\mathcal{S} = \frac{\hbar K}{4\pi}\int\frac{d\omega}{2\pi}\omega\tanh\frac{\omega L}{2c_s}|\varphi(\omega)|^2 + \int d\tau V\left[\varphi(\tau)\right]. \tag{3}$$

At high frequencies $\omega > 2c_s/L$, the kernel $\omega\tanh(\omega L/2c_s)$ reduces to the ohmic damping kernel $|\omega|$ describing the excitation of sound modes within the leads and provides us with the characteristic time scale $\tau_c = K\hbar/\pi E_J$, while at low frequencies $\omega < 2c_s/L$, the finite size of the tube introduces a smooth low frequency cut-off in the form $(L/2c_s)\omega^2$ (this is easily derived assuming a rigid wave function $\phi(x,\tau) = \varphi(\tau)\left[1/2 - \bullet(x)\right]$ within the leads [8]). The low frequency action reduces to that of a massive particle in a periodic potential

$$\mathcal{S} = \int d\tau\left\{\frac{\hbar^2}{E_L}\frac{(\partial_\tau\varphi)^2}{2} - i\hbar\left(\partial_\tau\varphi\right)\,\mathcal{N}(-i\tau) + E_J\left[1-\cos\varphi\right] + \mathcal{L}_>\right\}, \tag{4}$$

with the 'charging' energy $E_L = 4\pi\hbar c_s/KL$. The additional term $\mathcal{L}_>$ accounts for high frequency contributions $\omega > 2c_s/L$ and includes the remaining dissipative kernel in (3). The second term describes the drive of the system after subtraction of a total derivative $i\partial_\tau\left[\hbar\varphi\mathcal{N}(-i\tau)\right]$ with $\mathcal{N}(t) = nvt + \mathcal{N}_0$. This manipulation corresponds to a gauge transformation for a particle in an electric field where the static scalar potential $\sim nv\varphi$ is replaced by a time dependent vector potential $\sim \mathcal{N}(t)$ with $\mathcal{N}_0$ the 'gauge freedom'.

In the following, we study the quantum mechanical ground state properties (at fixed position of the impurity characterized by $\mathcal{N}_0$) and the response (finite velocity v of the impurity) of the system. We first neglect the high frequency contribution $\mathcal{L}_>$; this approximation is valid for short systems where the plasma frequency $\omega_p = \sqrt{E_J E_L}/\hbar$ is smaller than the energy of the first sound mode in the leads, i.e., $\omega_p < c_s/L$. The modifications due to $\mathcal{L}_>$ in long systems will be discussed in a second step. Applying canonical quantization $[p,\varphi] = (\hbar/i)$ with p the conjugate variable to the phase φ, i.e., $p = -i\hbar\partial_\varphi$, the Hamiltonian of the system (3) reduces to

$$H(t) = \frac{E_L}{2\hbar^2}\left[\frac{\hbar}{i}\frac{\partial}{\partial\varphi} + \hbar\mathcal{N}(t)\right]^2 + E_J\left[1-\cos\varphi\right]. \tag{5}$$

A crucial element entering the analysis is the nature of the quantum variable φ: in many applications, excitations of modes in the environment allow to distinguish between states φ and $\varphi + 2\pi j$ with $j \in \mathbf{Z}$, i.e., the phase is an extended variable $\varphi \in \mathbf{R}$.[10] Here, such a description is inappropriate as the ohmic damping kernel in (3) is cut-off at low frequencies and the phase φ is a compact variable $\varphi \in [0, 2\pi)$. The discrete sound modes in the leads described via $\mathcal{L}_>$ give rise to additional degrees of freedom.

The system described by (5) is equivalent to a massive charged particle on a 1D ring threaded by a time dependent magnetic flux and subject to a potential. Within the adiabatic limit $v \to 0$,

we can treat the 'quasinumber' $\mathcal{N}(t)$ as a constant, and solve the time independent Schrödinger equation

$$H(\mathcal{N})\, u_{j\mathcal{N}}(\varphi) = \epsilon_j(\mathcal{N})\, u_{j\mathcal{N}}(\varphi) \tag{6}$$

with periodic boundary conditions $u_{j\mathcal{N}}(\varphi) = u_{j\mathcal{N}}(\varphi + 2\pi)$. Removing the 'quasinumber' $\mathcal{N}$ via the transformation $u_{j\mathcal{N}}(\varphi) = \exp(-i\mathcal{N}\varphi) v_{j\mathcal{N}}(\varphi)$ reduces the problem to calculating the Bloch functions $v_j(\mathcal{N})$ in a periodic potential $E_J[1-\cos(\varphi)]$

$$\begin{aligned} H(0)\, v_{j\mathcal{N}}(\varphi) &= \epsilon_j(\mathcal{N}) v_{j\mathcal{N}}(\varphi), \\ v_{j\mathcal{N}}(\varphi + 2\pi) &= e^{2\pi i \mathcal{N}} v_{j\mathcal{N}}(\varphi), \end{aligned} \tag{7}$$

where the 'quasinumber' $\mathcal{N}$ is analogous to the 'quasimomentum' in the usual formulation of the Bloch problem with the lattice constant 2π. Varying the 'quasinumber' $\mathcal{N}$ we map out the Bloch bands $\epsilon_j(\mathcal{N})$ (note that the Born-von Kármán unit cell is identical to the period of the potential, hence the 'quasinumber' $\mathcal{N}$ selects one state within the band).

The ground state energy is $\epsilon_0(\mathcal{N}_0)$ and the 'quasinumber' $\mathcal{N}_0$ introduced before as a gauge freedom describes the position of the impurity: in general we have a particle inbalance in the leads due to particle quantization producing a finite chemical potential difference $\Delta\mu$ across the impurity. This difference in the chemical potential across the impurity in the ground state $u_{0,\mathcal{N}}$ is determined by the usual derivative

$$\Delta\mu = \langle \partial_{\mathcal{N}} H \rangle = \partial_{\mathcal{N}} \epsilon_0(\mathcal{N}). \tag{8}$$

The time evolution due to the drive v provides us with

$$\partial_t \mathcal{N} = nv \tag{9}$$

and leads to 'Bloch oscillations' in the chemical potential difference $\Delta\mu = \partial_{\mathcal{N}}\epsilon_0[\mathcal{N}(t)]$. These oscillations are due to the accumulation of particles in front of the impurity, the latter allowing only discrete particles to tunnel. Each 'Umklapp' process describes a particle tunneling through the impurity. The behavior of the tube then is dual to that of the classic Josephson junction, as is easily seen when replacing $\mathcal{N}$ by the phase drop Φ and $\Delta\mu$ by the supercurrent I: the relations (8) and (9) are equivalent to Josephson's famous relations $I = I_c \sin\Phi$ and $\partial_t \Phi = 2eV/\hbar$ with I_c and V the critical current and voltage across the junction. In the following, we will focus on the tight binding limit with $E_J/E_L = (K^2 4\pi^2) L/c_s\tau_c \gg 1$. Then, the lowest energy band becomes

$$\epsilon_0(\mathcal{N}) = -W\cos 2\pi\mathcal{N} \tag{10}$$

with the hopping amplitude calculated within the instanton approximation

$$W \sim \frac{\hbar}{\tau_c}\frac{L}{c_s\tau_c}\exp\left(-K\sqrt{L/c_s\tau_c}\right). \tag{11}$$

The breakdown of the adiabatic approximation is the relevant mechanism for the disappearance of 'Bloch oscillations': for driving forces nv larger than the band gap $\Delta = \sqrt{E_L E_J}$ transitions to higher bands, known as 'Zener tunneling',[11] become relevant and describe the accumulation of particles in front of the impurity, i.e., the absence of 'Umklapp' processes quenches the tunneling. The flow *across* the impurity then does not match the flow of particles *towards* the impurity, producing a steady increase in the chemical potential difference $\Delta\mu$. On the other hand, for high temperatures $T > \Delta$ thermal fluctuations lead to transitions into higher bands which quenches the coherent evolution of the wave function necessary for the 'Bloch oscillations'.

Next, we discuss the influence of the discrete sound modes in the leads which are described by $\mathcal{L}_>$. They become relevant for long tubes with $\omega_p > c_s/L$. While the presence of 'Bloch

oscillations' at low temperatures and low drives remains unaffected, the discrete sound modes introduces quantitative modifications: First, for long tubes the tight binding analysis is always justified and the lowest energy band is determined by (10). However, virtual excitations of sound modes during tunneling of the phase renormalize the hopping amplitude to

$$W \sim \frac{\hbar}{\tau_c}\left(\frac{\pi c_s \tau_c}{2L}\right)^K . \tag{12}$$

Second, the tunneling of the phase can be divided in two classes: diagonal transitions without excitation of sound modes in the leads leave the phase compact at low temperature and low driving forces, while nondiagonal transitions where the number of excited sound modes in the leads is changed leads to a non-compact phase variable (note that in this case the initial and final state can be distinguished by counting the number of excited sound modes).

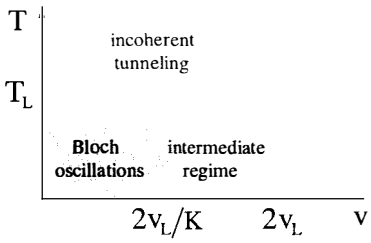


Figure 1: Response: for low driving forces $v < 2v_L/K$ and low temperatures $T < T_L$ the physics is determined by 'Bloch oscillations' with a band width W and a compact phase φ (dark region), while at high temperatures $T > T_L$ or high drives $v > 2v_L$ the response is characterized by incoherent tunneling with a rate Γ and an extended phase φ. For temperatures $T < T_L$ we have an intermediate regime for $2v_L/K < v < 2v_L$ where the 'Bloch oscillations' compete with the nondiagonal transitions (light region).

At zero temperature but finite driving force v, the nondiagonal transitions become relevant for velocities $v > 2v_L/K$ with $v_L = \pi\hbar/Lm$. Then, we enter a non-trivial intermediate regime where the physics of Bloch oscillations competes with the nondiagonal transitions involving the discrete sound modes in the leads. The situation simplifies for larger drives $v > 2v_L$: all processes are fast involving frequencies $\omega > c_s/L$ and the damping term in (4) dominates over the inertia. Nondiagonal transitions dominate in this regime, and we recover the physics of the infinitely long system: the tunneling of the phase is incoherent with a finite quantum nucleation rate producing a dissipative response[12,9] and the states φ and $\varphi \pm 2\pi$ are distinguishable, i.e., the phase φ becomes extended. On the other hand, at zero driving force $v = 0$ but finite temperature T the breakdown of 'Bloch oscillations' appears at the crossover temperature $T_L = 2\hbar c_s/L$. For $T < T_L$, corrections to the band width W due to the finite temperature are exponentially small at low temperatures, $W(T) = W[1 - 4K \exp(-\pi\hbar c_s/LT)]$, but strongly suppress the band width when approaching the crossover temperature T_L. At high temperatures $T > T_L$ all processes are fast and we recover the physics of the infinitely long wire with a linear response determined by the thermally activated quantum nucleation of phase slips,[12,9] the finite size of the system becoming irrelevant. A sketch of the boundaries in the $v - T$ diagram separating the Bloch type physics at small v, T from the intermediate and the incoherent tunneling regime is shown in Fig. 1.

In conclusion, we find that the superfluid transport present in three dimensional Bose-Einstein condensates is strongly affected by confining the atomic gas into a one dimensional trap with the new non-superfluid ground state exhibiting 'Bloch oscillations' in the chemical potential difference across the impurity.

1. D.S. Petrov, G.V. Shlyapnikov, and J.T.M. Walraven, Phys. Rev. Lett. **85**, 3745 (2000).

2. M. Olshanii, Phys. Rev. Lett. **81**, 938 (1998), see also V. Dunjko *et al.*, cond-mat/0103085.
3. E.B. Kolomeisky *et al.*, Phys. Rev. Lett. **85**, 1146 (2000).
4. M.D. Girardeau and E.M. Wright, Phys. Rev. Lett. **84**, 5239 (2000).
5. A. Görlitz et al., cond-mat/0104549. R. Folman et al., Phys. Rev. Lett. **84**, 4749 (2000); J. Reichel, W. Hänsel, and T.W. Hänsch, Phys. Rev. Lett. **83**, 3398 (1999).
6. C. Raman et al., Phys. Rev. Lett. **83**, 2502 (1999).
7. E.H. Lieb and W. Liniger, Phys. Rev. **130**, 1605 (1963); K.B. Efetov and A.I. Larkin, Sov. Phys. JETP **42**, 390 (1975); F.D.M. Haldane, Phys. Rev. Lett. **47**, 1840 (1981); V.N. Popov, *Functional Integrals in Quantum Field Theory and Statstical Physics* (D. Reidel Publishing Company, 1983).
8. S. Giovanazzi, A. Smerzi, and S. Fantoni, Phys. Rev. Lett. **84**, 4521 (2000).
9. H.P. Büchler, V.B. Geshkenbein, and G. Blatter (to be published).
10. G. Schön and A.D. Zaikin, Phys. Rep. **198**, 237 (1990).
11. K. K. Likharev and A. B. Zorin, J. Low. Temp. Phys. **59**, 347 (1985).
12. U. Weiss and H. Grabert, Phys. Lett. **108A**, 63 (1985).

Measurements of flux dependent screening in Aharonov-Bohm rings

R. Deblock[1], Y. Noat[1], H. Bouchiat[1], B. Reulet[1] and D. Mailly[2]
[1] *Laboratoire de Physique des Solides, Associé au CNRS, Bâtiment 510, Université Paris-Sud, 91405, Orsay, France.*

[2] *CNRS Laboratoire de Microstructure et Microélectronique, 196 avenue Ravera, 92220, Bagneux, France.*

In order to investigate the effect of electronic phase coherence on screening we have measured the flux dependent polarizability of isolated mesoscopic rings at 350 MHz. At low temperature (below 100 mK) the non-dissipative part of the polarizability exhibits flux oscillations with a period of half a flux quantum in a ring. The sign and amplitude of the effect are in good agreement with recent theoretical predictions for isolated rings at finite frequency. The observed positive magneto-polarizability corresponds to an enhancement of screening when time reversal symmetry is broken.

1 Introduction

When an electric field $\mathbf{E}$ is applied to an isolated metallic sample, electron screening gives rise to an induced dipole $\mathbf{d}$. In the linear response regime :

$$\mathbf{d} = \alpha \mathbf{E} \tag{1}$$

where α is the electric polarizability. For a sample of typical size a much larger than the Thomas-Fermi screening length λ_s, α is essentially determined by geometry, with a negative correction of the order of λ_s/a [1]. The measurement of α gives information on the way electrons screen an external electric field. At the mesoscopic scale, when phase coherence through the sample is achieved (*i.e.* the phase coherence length is of the same order as the typical size of the system) electronic properties are sensitive to the phase of the electronic wave functions, which can be tuned by an Aharonov-Bohm flux in a ring geometry [2]. It has been recently suggested that screening of an electric field may be sensitive to this phase coherence, leading to a flux dependent mesoscopic correction to polarizability [3,4,5]. In particular the polarizability of an Aharonov-Bohm ring is expected to exhibit oscillations as a function of the magnetic flux.

We have inferred the electrical response of an array of rings from the flux dependence of the capacitance C, placed underneath the rings, of an RF superconducting micro-resonator[6,7]. This experiment has been checked to be only sensitive to the electrical response of the rings [8]. C is modified by the non dissipative response α' of the rings :

$$\frac{\delta C}{C} = k N_s \alpha' \tag{2}$$

where N_s is the number of rings coupled to the resonator and k the electric coupling coefficient between a ring and the capacitance, which only depends on geometry. Since the resonance frequency $f = 1/(2\pi\sqrt{LC})$, with L the inductance of the resonator, the change in C shifts the resonance frequency :

$$\frac{\delta f}{f} = -\frac{1}{2} k N_s \alpha'(\omega) \tag{3}$$

In order to measure δf , the RF frequency is modulated at 100 kHz. Using lock-in detection, the reflected signal from the resonator at the modulated RF frequency is measured and used to lock the experimental setup on the resonance frequency. The feedback signal is then proportional to the variation of f. We are careful to inject sufficiently low power ($\approx 10pW$) so as not to heat the sample. The signal is measured as a function of magnetic field. To improve accuracy,

the derivative of the signal is also detected by modulating at 30 Hz a magnetic field of 1 Gauss amplitude. Our precision with this setup is $\delta f/f = 10^{-8}$.

The rings are etched in a high-mobility GaAs-AlGaAs heterojunction. Etching strongly decreases the conductivity of the rings, but the nominal conductivity is recovered by illuminating the sample with an infrared diode [9]. We have checked this on a connected sample. The characteristics of the rings, deduced from transport measurements on wires of the same width etched in the same heterojunction, are the following : at nominal electronic density ($n_e = 3.10^{11}\mathrm{cm}^{-2}$) the mean free path $l_e = 3\mu$m, the etched width is 0.5 μm whereas the effective width $W = 0.2\,\mu$m (estimated from weak localization experiments [18]) is much smaller due to depletion, the coherence length is $L_\Phi = 6.5\,\mu$m and the effective perimeter $L = 5.2\,\mu$m. The rings are thus ballistic in the transverse direction and diffusive longitudinally. The mean level spacing $\Delta = h^2/(2\pi mWL) \simeq 80$ mK $\simeq 1.66$ GHz and the Thouless energy $E_c = hD/L^2 = 450$ mK, with D the diffusion coefficient and m the effective mass of electrons. The Thomas-Fermi screening length is $\lambda_s = \pi a^\star/2 = 16$ nm, with $a^\star$ the effective Bohr radius. There are $N = 10^5$ rings on one sample. The resonator is made by optical lithography in niobium on a sapphire substrate. The length of the capacitance is $l = 20.5$ cm and the inductance is 5 cm long. It has a single resonance frequency $f_0 = 385$ MHz and a quality factor of 10 000. The distance between the capacitance and the inductance is 300 μm. A 0.9 μm thick mylar film is inserted between the detector and the ring substrate in order to reduce inhomogeneities of the magnetic field due to the Meissner effect in the vicinity of the superconducting resonator. The quality factor of the system constituted by the resonator and the rings is reduced to 3000, due to dielectric losses in the heterojunction.

2 Flux dependent polarisability

The derivative of the resonance frequency of the resonator with the rings is shown on figure 1 (a). This signal is a straight line, on top of which small oscillations are superimposed. The straight line is due to the field dependence of the penetration length in niobium, which constitutes the resonator. This behaviour has been verified to be the same with or without the rings. The oscillating behaviour is on the other hand attributed to the flux dependent electric response of the rings. To extract this response the base line is subtracted (figure 1 (b)). The signal obtained exhibits clear oscillations. Note their anharmonicity as well as the existence of an aperiodic signal. This behaviour is illustrated by the Fourier transform of the data (figure 1 (c)) : there is a peak corresponding to the oscillating behaviour. In order to focus on this signal, which is the expected signature of phase coherence, an numerical high pass filter with a cut-off frequency of 0.05 G^{-1} (corresponding to the arrow on figure 1 (c)) is applied and the signal is then numerically integrated in order to have the frequency shift due to the rings (figure 1 (d)). This shift is proportional to the variation of polarisability versus magnetic field according to formula 3. The aperiodic signal has been also studied [7].

2.1 Magneto-polarisability

The frequency shift due to the rings is periodic with a period of approximately 12.5 G. From the Fourier transform (figure 1 (c)) the period of the oscillation is deduced to be consistent with half a flux quantum $\Phi_0/2 = h/2e$ in a ring with no signature of Φ_0 periodicity, as expected for an Aharonov - Bohm effect averaged over many rings [10]. The sign of frequency shift is negative at low magnetic field which means according to formula 3 that the magneto-polarisability is positive , i.e. $\alpha'(H) - \alpha'(0) > 0$ at low magnetic field. The screening is thus better when time reversal symmetry is broken by magnetic field. The scale of the signal is given by the amplitude of the first oscillation. From figure 1 (d) we deduced $\delta_\Phi f/f = (f(3.13\mathrm{G}) - f(0))/f = -2.5\,10^{-7}$.

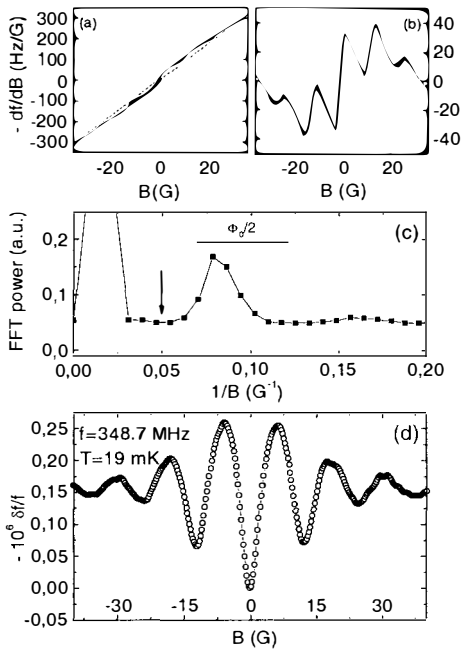


Figure 1: (a) Derivative of the resonance frequency of the resonator with the rings versus magnetic field at illumination time 870 s. (b) Signal obtained by subtracting the base line due to the resonator from previous data. (c) Fourier transform of signal (b). The vertical arrow indicates the cut-off frequency used for high pass filtering the signal. (d) Frequency shift due to the rings obtained after integration of the high pass filtered signal of (b).

Note that this value means detecting a frequency shift of 100Hz on a frequency of 350 MHz. It leads to the typical value of the magneto-polarisability $\delta_\Phi \alpha' / \alpha_{1D} = 5\,10^{-4} \pm 2.3\,10^{-4}$, $\alpha_{1D} = \epsilon_0 \pi^2 R^3 / \ln(R/W)$ is the calculated polarisability of a quasi one dimensional (quasi-1D) circular ring of radius R.

2.2 Theoretical predictions

Our experiment shows that there is a flux correction to the polarisability of the rings, which is *positive* at low field. Let's now compared this result to recent theoretical predictions. To do so let's first point out that because we are using a ring geometry we are going alternatively from a situation where the system presents time reversal symmetry (at flux value of $\Phi = n\Phi_0/2$, with $n \in \mathbb{Z}$) to the case where time reversal symmetry is broken by magnetic field. In the Random Matrix Theory (RMT) the first case corresponds to Gaussian Orthogonal Ensemble (GOE) whereas the second is related to the Gaussian Unitary Ensemble (GUE). As theories of magnetopolarisability essentially evaluate the variation of polarisability between GOE and GUE, we need a quantity which is related to this difference of statistical ensemble. We define such a quantity for a physical property A by $\delta_\Phi A = A(\Phi_0/4) - A(0)$.

The polarisability of small metallic grains was studied using RMT first by Gor'kov and Eliashberg [11] .The sensitivity of the electrostatic properties of mesoscopic systems to quantum coherence has been emphasized by Büttiker for connected geometries [12]. The phase coherent

correction to the polarisability of isolated systems was recently theoretically investigated. Efetov found that it is possible to relate self consistently this correction to the flux dependence of the screened potential [3]. Two recent work has calculated this effect in the diffusive regime using linear response formalism (Noat *et al.*) [4,13] or supersymmetry techniques (Blanter and Mirlin [5,14]).

In the grand canonical ensemble (GCE) the chemical potential in each rings is supposed to be constant. It describes a situation where the rings are connected to a reservoir of particules. *A priori* this is not the case in the experiment where the rings are isolated but as the theory is simpler in GCE we recall first the result in this statistical ensemble. No flux dependence for the polarisability is predicted if the RF pulsation ω is much smaller than the inverse relaxation time γ. However when $\omega \gg \gamma$ the magnetopolarisability is related to the flux dependence of the diagonal matrix element of the screened potential :

$$\delta_\Phi \alpha'_{GCE} = -\frac{2e^2}{E^2\Delta}\delta_\Phi \left(< |F_{\alpha\alpha}|^2 >_\mu \right) \tag{4}$$

$< |F_{\alpha\alpha}|^2 >_\mu$ is the disorder average square of the diagonal matrix element of the screened potential F at energy μ, the mean chemical potential of the rings. E is the applied electric field. We note ψ_α the eigenstates of the unperturbed system. This matrix element is then given by :

$$< |F_{\alpha\alpha}|^2 >_\mu = \int d\mathbf{r_1} \int d\mathbf{r_2} F(\mathbf{r_1}) F(\mathbf{r_2}) < |\psi_\alpha(\mathbf{r_1})\psi_\alpha(\mathbf{r_2})|^2 >_\mu \tag{5}$$

From this expression it appears that the magnetopolarisability is related to the difference of correlation function of the eigenstates with and without time reversal symmetry. This correlation function has been computed in the diffusive regime within a supermatrix σ-model approach [15,16]:

$$V^2 < |\psi_\alpha(\mathbf{r_1})\psi_\alpha(\mathbf{r_2})|^2 >_\mu = [1 + 2k_d(r)]\,[1 + 2\Pi_D(\mathbf{r_1}, \mathbf{r_2})] \quad (GOE) \tag{6}$$

$$V^2 < |\psi_\alpha(\mathbf{r_1})\psi_\alpha(\mathbf{r_2})|^2 >_\mu = [1 + k_d(r)]\,[1 + \Pi_D(\mathbf{r_1}, \mathbf{r_2})] \quad (GUE) \tag{7}$$

with V the volume of the sample, $k_d(r)$ a short range function which decays on the length scale of the mean free path and $\Pi_D(\mathbf{r_1}, \mathbf{r_2})$ the diffusion propagator. The correction due to the short range term $k_d(r)$ has been shown to be negligible [5]. By considering only the diffusion term the magnetopolarisability is given by :

$$\delta_\Phi \alpha'_{GCE} = \frac{2e^2}{E^2\Delta V^2} \int d\mathbf{r_1} \int d\mathbf{r_2} F(\mathbf{r_1}) F(\mathbf{r_2}) \Pi_D(\mathbf{r_1}, \mathbf{r_2}) \tag{8}$$

Note that this derivation of the magnetopolarisability is equivalent to the one used by Noat *et al* [4] based on the following RMT argument :

$$\delta_\Phi \left(< |F_{\alpha\alpha}|^2 > \right) \approx -\frac{1}{2} < |F_{\alpha\alpha}|^2 >_{GOE} \tag{9}$$

Indeed using autocorrelation function of wavefunction one can demonstrate this relation using the fact that :

$$\int \mathbf{dr} F(\mathbf{r}) = 0 \tag{10}$$

due to symmetry properties of the screened potential. The calculation of the magnetopolarisability using formula 8 for the case of a quasi-1D ring leads to :

$$\frac{\delta_\Phi \alpha'_{GCE}}{\alpha_{1D}} = \epsilon f(\frac{L}{W}) \frac{\lambda_s}{W} \frac{\Delta}{E_c} \tag{11}$$

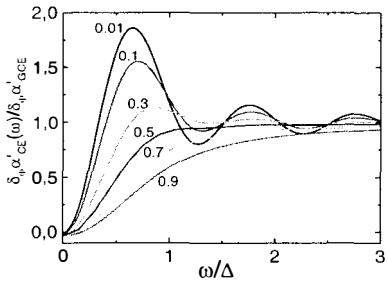


Figure 2: Calculated evaluation of $\delta_\Phi \alpha'_{CE}(\omega)/\delta_\Phi \alpha'_{GCE}$ at different value of the parameter γ/Δ. Note that the value of magnetopolarisability is zero at zero whatever the level broadening.

$f(x)$ is a function related to the geometry and the dimension of the sample [7]. Using this expression we have $\delta\alpha'_{GCE}/\alpha_{1D} = 1.2\,10^{-3}$. These results are valid in the regime $\omega \ll \Delta$.

In our experiment the rings are isolated, the number of electrons in each rings is supposed to be constant, so that the result of the canonical ensemble (CE) should apply. At T=0 and zero frequency the flux dependent correction to polarisability is found to be zero. However at finite frequency, we can recover the value of GCE. A recent work by Blanter and Mirlin takes frequency into account and leads to a canonical expression for the magneto-polarisability which is of the order of the result in the GCE when ω is of the order of Δ [14]. Following their reasoning but taking into account the level broadening γ we can write :

$$\delta_\Phi \alpha'_{CE}(\omega) = \delta_\Phi \alpha'_{GCE} F(\omega) \tag{12}$$

with $F(\omega)$ a function which depends only on the statistic of energy levels :

$$F(\omega) = 1 + \int_0^\infty d\epsilon \frac{1}{\epsilon} \left(\frac{\epsilon(\epsilon+\omega)+\gamma^2}{(\epsilon+\omega)^2+\gamma^2} + \frac{\epsilon(\epsilon-\omega)+\gamma^2}{(\epsilon-\omega)^2+\gamma^2} \right) \left[\delta_\Phi R_2(\epsilon) + \int_0^\epsilon d\epsilon_1 \delta_\Phi R_3(\epsilon, \epsilon_1) \right] \tag{13}$$

$R_2(\epsilon)$ and $R_3(\epsilon, \epsilon_1)$ are respectively the two and three levels correlation function, known from RMT [17]. By evaluating this expression versus frequency at different value of level broadening we get the results shown on figure 2. The behaviour at low value of the level broadening is in qualitative agreement with result of reference [14]. In particular the magnetopolarisability is found to be zero at zero frequency (in our calculation the value of $\delta_\Phi \alpha'_{CE}(\omega = 0)$ is at least 25 time smaller than $\delta_\Phi \alpha'_{GCE}$). In our case $\omega/\Delta = 0.2$, the CE magnetopolarisability is equal at most to 50 % of the GCE value (in the limit of small level broadening). As a consequence the expected value for $\delta_\Phi \alpha'_{CE}/\alpha_{1D}$ is then $6\,10^{-4}$ which is of the same order of magnitude than the experimental value. The result of the experiment is thus consistent with isolated rings at finite frequency. Note that the measurement is not sufficiently accurate so as to give an estimate of the level broadening by comparing the experimental result with the curves of figure 2. A very interesting extension of the experiment would be to study the magnetopolarisability at different frequencies in order to test the theoretical predictions. However in our setup changing frequency means changing the resonator. Moreover scanning a frequency range of two or three Δ would imply to change drastically the geometry of our resonator. At this stage, with our setup, this investigation is not possible.

3 Conclusion

We have presented measurements of electric response of Aharonov-Bohm etched in a 2DEG. The rings presents a flux dependent correction to screening. This correction is positive in low field which means that screening is enhanced when time reversal symmetry is broken by a magnetic field. The sign of the effect is consistent with theory for isolated rings at finite frequency. The value of magnetopolarisability is $\delta_\Phi \alpha^{'}/\alpha_{1D} = 5\,10^{-4} \pm 2.3\,10^{-4}$, with $\alpha_{1D} = \epsilon_0 \pi^2 R^3/\ln(R/W)$ the calculated polarisability of a quasi one dimensional (quasi-1D) circular ring of radius R.

Acknowledgments

We thank B. Etienne for the fabrication of the heterojunction. We acknowledge fruitful discussions with L.P. Lévy, Ya.M. Blanter and G. Montambaux and technical help of M. Nardone.

References

1. S. Strässler, M.J. Rice and P. Wyder, Phys. Rev. B **6**, 2575 (1972); M.J. Rice, W. R. Schneider and S. Strässler, Phys. Rev. B **8**, 474 (1973).
2. See, e.g., *Mesoscopic Phenomena in Solids* edited by B.L. Altshuler, P.A. Lee and R.A. Webb (Elsevier, Amsterdam, 1991); Y. Imry, *Introduction to Mesoscopic Physics* Oxford UP, New York, 1997.
3. K.B. Efetov, Phys. Rev. Lett. **76**, 1908 (1996).
4. Y. Noat, B. Reulet and H. Bouchiat, Europhys. Lett. **36**(9), pp. 701-706 (1996).
5. Ya.M. Blanter and A.D. Mirlin, Phys. Rev. B **57**, 4566 (1998).
6. R. Deblock, Y. Noat, H. Bouchiat, B. Reulet and D.Mailly, Phys. Rev. Lett. **84**(23), 5379 (2000).
7. R. Deblock *et al*, *to be published.*
8. This separation between magnetic and electric response has been checked by deposition of a paramagnetic system (DPPH) alternatively on the capacitive and inductive part of the resonator. A magnetic spin resonance signal was only observed when DPPH was on the inductive part.
9. For each illumination a current of $10\mu A$ is run through the diode during roughly 4 minutes. Then measurement is done at least one hour after the illumination in order to ensure good stability of the sample. Curves presented here correspond to illumination 0 (no illumination) to illumination 8 (2000 s of light). An upper value of the estimated illumination power coupled to the sample is 600 photons/s with a wavelength of 766 nm.
10. J.P. Carini, K.A. Muttalib and S.R. Nagel, Phys. Rev. Lett. **53**, 102 (1984); A. Kamenev and Y. Gefen, Phys. Rev. B **49**, 14474 (1994).
11. L.P. Gor'kov and G.M. Eliashberg, Sov. Phys.-JETP **21**, 940 (1965).
12. M. Büttiker, Phys. Scr. **54**,104 (1994). M. Büttiker and C.A. Stafford, Phys. Rev. Lett. **76**, 495 (1996).
13. Y. Noat *at al*, *to be published.*
14. Ya.M. Blanter and A.D. Mirlin, Phys. Rev. B **63** 113315 (2001).
15. Ya.M. Blanter and A.D. Mirlin, Phys. Rev. B **53**, 12601 (1996).
16. A.D. Mirlin, Physics-Reports. **326**(5-6), 259-382 (2000).
17. M.L. Mehta, *Random Matrices and the Statistical Theory of Energy Levels* (New York, Academic Press, 1967).
18. B. Reulet, H. Bouchiat and D. Mailly, Europhys. Lett. **31**(5-6), pp. 305-310 (1995).

LOCALIZATION AND ABSENCE OF BREIT-WIGNER FORM FOR CAUCHY RANDOM BAND MATRICES

KLAUS M. FRAHM
Laboratoire de Physique Quantique, UMR 5626 du CNRS,
Université Paul Sabatier, F-31062 Toulouse Cedex 4, France

We analytically calculate the local density of states for Cauchy random band matrices with strongly fluctuating diagonal elements. The Breit-Wigner form for ordinary band matrices is replaced by a Levy distribution of index $\mu = 1/2$ and the characteristic energy scale α is strongly enhanced as compared to the Breit-Wigner width. The unperturbed eigenstates decay according to the non-exponential law $\propto e^{-\sqrt{\alpha t}}$. We also discuss the localization length for this type of band matrices.

1 Introduction and Model

Band matrices with random elements appear in a varity of physical problems in the context of quantum chaos and localization.[1,2,3,4,5] A detailed analytical investigation of the properties of such matrices was performed by Fyodorov and Mirlin[3] using Efetov's supersymmetry technique.[4] Later, motivated by the localization problem of two interacting particles, Shepelyansky introduced and studied random band matrices superimposed with strongly fluctuating diagonal matrix elements.[6] Subsequent work on this type of matrices [7] showed the existence of the *Breit-Wigner regime* where the eigenstates have a very peaked structure inside an eventual localization domaine.

In all these cases the matrix elements were drawn from a regular, typically gaussian, distribution with finite variance. In the present work, we extend these band matrix ensembles [6,7] to the case of Cauchy distributed matrix elements. In an early work, Lloyd [8] already introduced and studied a model with diagonal Cauchy distributed disorder. A detailed study of the level statistics of full random matrices [9] with elements drawn from the more general Levy distribution [10] was performed by Cizeau and Bouchaud. Band matrix ensembles with Cauchy distributed matrix elements were recently argued to be relevant and studied numerically in the context of the localization problem of two interacting particles.[11,12] In this work, we present analytical results concerning the wave function properties for a model which differs from that of Cizeau et al. [9] by two important features: it concerns a banded and not full matrix, and its diagonal elements are typically much larger than the off-diagonal coupling elements.

Actually, we think that this case is of particular interest for a generic disordered fermionic many particle problem [13] where non-interacting eigenstates are coupled by quasi-random two-particle interaction matrix elements. There is an interesting and subtle regime [14] where the effective two-particle level spacing is smaller than the typical interaction matrix element while typical eigenstates are nevertheless composed of many non-interacting eigenstates. In this regime, we can diagonalize the problem for two particles by perturbation theory and apply the corresponding unitary transformation to the full many-particle Hamiltonian. This provides a new type of random matrix with residual three-body interaction matrix elements typically given by perturbative expressions with denominators, containing independent random non-interacting energy differences. Iterating this procedure one also obtains higher order contributions. Flambaum et al. [15] have argued that such denominators give effective distributions for these matrix elements characterized by long tails with the same power law as the Cauchy distribution. Even though the real situation is more complicated, this argument indeed shows the relevance of Cauchy random matrix ensembles.

The model we consider is a random band matrix of dimension $N \times N$ and of width $b \gg 1$ whose matrix elements are of the form $H_{kl} = \eta_k \, \delta_{kl} + U_{kl}$ with $U_{kl} = 0$ if $k = l$ or $|k - l| > b$.

These matrix elements are statistically independent and distributed according to a Cauchy distribution $p_a(x) \equiv \pi^{-1} a/(a^2+x^2)$ where the width a is given in terms of two parameters W and U_0 via $a \equiv W/\pi$ for η_k and $a \equiv U_0$ for U_{kl}. In this paper, we consider the orthogonal symmetry class where H is real symmetric. The generalization to the other symmetry classes is straightforward. We will furthermore concentrate on the case where U_0 is sufficiently large to avoid a simple perturbative situation but still so small that the total density of states will essentially be dominated by the unperturbed diagonal elements only.

For ordinary band matrices [7] with a finite variance of U_{jk}, this case corresponds to the Breit-Wigner regime where the eigenstates are in addition to an eventual space localization also localized in the (unperturbed) energy space, i. e. only the sites j with $|E-\eta_j| \lesssim \Gamma$ essentially contribute to an eigenstate of energy E where $\Gamma \approx 2\pi(2b)\langle|U_{jk}|^2\rangle/W \ll W$ is the Breit-Wigner width. This can be seen in the local density of states at site j which is a Lorentzian in $(E-\eta_j)$ of width [7] $\Gamma/2$.

2 Local Density of States

We first calculate the average local density of states, $\rho_j(E) = -\frac{1}{\pi}\,\mathrm{Im}\langle (E+i0-H)^{-1}_{jj}\rangle_j$, for the Cauchy band matrix ensemble. The average $\langle\cdots\rangle_j$ is taken with respect to all random matrix elements except the diagonal element η_j at the site j under consideration. As in the original Lloyd model [8] the average over the other diagonal elements η_k, $k \neq j$ can be exactly performed by replacing in the definition of the Green function these elements according to: $\eta_k + i\,0 \to i\,W/\pi$. Using a general algebraic identity for the block inverse of a matrix, we obtain

$$\rho_j(E) = -\frac{1}{\pi}\,\mathrm{Im}\left\langle \frac{1}{E+i0-\eta_j+i\Gamma_j(U)/2}\right\rangle_U \quad , \quad \Gamma_j(U) = 2i \sum_{k,l(\neq j)} U_{jk}\,\tilde{G}^{(+)}_{kl}\,U_{lj}\;, \qquad (1)$$

where $\langle\cdots\rangle_U$ denotes the average over U_{jk} only, and $\tilde{G}^{(+)} = (E+i\,W/\pi-\tilde{U})^{-1}$ with $\tilde{U}$ being the $(N-1)\times(N-1)$-matrix obtained from U after elimination of the j-th row and j-th column. Eq. (1) reproduces the Lorentzian Breit-Wigner form of width $\mathrm{Re}[\Gamma_j(U)]/2$ for a given realization of the coupling matrix U. For ordinary band matrices this width is a self-averaging quantity and the further U-average does not modify the Breit-Wigner form. However, for the case of Cauchy band matrices $\Gamma_j(U)$ is strongly fluctuating and the U-average will considerably modify the Breit-Wigner form. Now, we consider the limit $|E| \ll W$ and we neglect $\tilde{U}$ in the definition of $\tilde{G}^{(+)}$ which is possible for the regime we consider. Using, $\tilde{G}^{(+)} \approx (-i\,\pi/W)\mathbb{1}_N$, we obtain

$$\rho_j(E) = \frac{1}{\pi}\,\mathrm{Im}\left\{ i\int_0^\infty dt\; e^{i\,t(E-\eta_j)}\;\left[\phi\left(\frac{2\pi\,U_0^2\,t}{W}\right)\right]^{2b}\right\} \quad , \quad \phi(z) \equiv \frac{1}{\pi}\int_{-\infty}^{\infty} du\,\frac{1}{1+u^2}\;e^{-zu^2/2} \qquad (2)$$

where $\phi(z)$ is a function of $z \geq 0$. In the limit $b \gg 1$, the integral (2) is dominated by the behavior at small t. Using the approximation $\ln\phi(z) \approx -\sqrt{\frac{2}{\pi}\,z} + \mathcal{O}(z)$, we obtain

$$\rho_j(E) = \frac{1}{\alpha}L_{1/2}\left(\frac{E-\eta_j}{\alpha}\right) \quad , \quad \alpha = \frac{16\,U_0^2\,b^2}{W} \quad , \quad L_\mu(s) = \frac{1}{2\pi}\int_{-\infty}^{\infty} dt\; e^{its-|t|^\mu}\;. \qquad (3)$$

Here $L_\mu(s)$ represents a Levy distribution of index [10] μ with the behavior $L_\mu(s) \propto s^{-1-\mu}$ for $|s| \gg 1$. The expressions (3) provide the first important results for the Cauchy band matrix ensembles. They show that the local density of states is still a peaked function of $(E-\eta_j)$ but with two important modifications. First, the Lorentzian Breit-Wigner form is replaced by the Levy distribution $L_{1/2}$, and second, the characteristic energy scale behaves as $\alpha \approx (4/\pi)\,b\,\Gamma \gg \Gamma$ where Γ is the Breit-Wigner width for ordinary band matrices (with a finite variance $\langle U_{jk}^2\rangle \equiv U_0^2$).

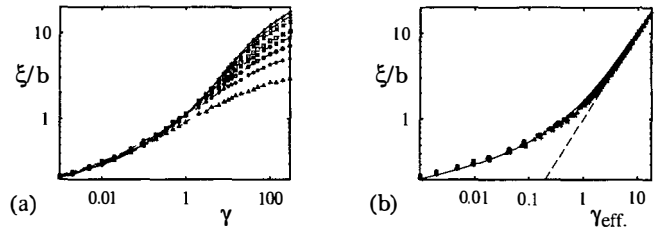


Figure 1: (a) The ratio ξ/b as a function of γ (see sec. 3 for notations). The different curves correspond to the values $b = 10, 20, 30, 40, 50, 70, 85, 100$ with $b = 10$ for the lowest curve. (b) The ratio ξ/b as a function of the effective parameter $\gamma_{\text{eff.}}$ defined in eq. (5). The data points are numerical values, the dashed line corresponds to the limit $\xi/b \approx \gamma_{\text{eff.}}$ for $\gamma_{\text{eff.}} \gg 1$ and the full line is the scaling curve (5).

We mention that the approximation to neglect the contribution of $\tilde{U}$ in $\tilde{G}^{(+)}$ is valid for $\alpha \ll W$, i. e. $U_0\, b \ll W$.

The first modification has an important implication for the time-evolution of a state $|\psi(t)>$ initially localized at one site, $|\psi(0)>=|j>$. Then, the average of the amplitude $<\psi(t)|j>$ obeys a non-exponential decay law of the form $\propto e^{-\sqrt{\alpha t}}$ instead of $\propto e^{-\Gamma t/2}$. This type of behavior was for instance recently found in the context of many-body effects in cold Rydberg atoms.[16] We conclude that it is a very general feature due to the long tail distribution of residual interaction matrix elements in many-body problems.[15]

The second modification concerning the large enhancement of the characteristic energy scale can be qualitatively understood by the fact that for a given realization of U the sum in eq. (1) is essentially determined by the typical maximal value $2bU_0$ of the $2b$ different matrix elements U_{jk}.

It is pretty obvious to generalize eqs. (3) to the case where the matrix elements U_{jk} are drawn from the more general Levy distribution $U_0^{-1}\, L_\mu(U_{jk}/U_0)$. In this case, we have to replace in (3) $L_{1/2}$ by $L_{\mu/2}$ and the characteristic energy scale is enhanced according to: $\alpha \sim b^{2/\mu-1}\,\Gamma$.

3 Localization Length

It is also possible to calculate analytically [17] the localization length ξ of the Cauchy band matrix ensemble by mapping it onto a supersymmetric one-dimensional non-linear σ model.[4] Here, we only present the result: [17]

$$\xi = \frac{2\pi\, b^4\, U_0^2}{W^2} = b\,\gamma \quad , \quad \gamma \equiv \frac{\pi}{16}\left(\frac{\alpha}{\Delta}\right) \tag{4}$$

where the dimensionless parameter γ counts the number of well coupled levels inside a strip of typical length $b \gg 1$, $\Delta = W/2b$ is the effective level spacing of such a strip, and α is the characteristic energy scale for the local density of states (3). (For the more general case of Levy distributed U_{jk}, we find: $\xi \sim b^{2+2/\mu}\, U_0^2/W^2$.) The relation (4) compares to $\xi \sim b\,(\Gamma/\Delta)$ for the case of ordinary band matrices.[7,12] However, it contradicts the expression $\xi \sim b\sqrt{\gamma}$ which was with proper translation of notations previously obtained [12] from a similar Cauchy band matrix model by numerical calculations. We attribute this to the extreme numerical difficulty to access the regime $1 \ll \gamma \ll b$ where we expect (4) to be valid. For $\gamma \lesssim 1$ we enter the perturbative regime with $\xi \sim b/\ln(\gamma^{-1})$ while for $\gamma \gtrsim b$ the localization length is likely to saturate at $\xi \sim b^2$. To verify this picture, we have therefore also numerically determined the localization length by the recursive Green function method for $0.001 \le \gamma \le 300$ and $10 \le b \le 100$. Fig. 1(a) shows the ratio ξ/b as a function of γ. At first sight, it is indeed very difficult to verify the analytical

result (4) and a direct numerical fit (e. g. for $b = 100$ and $2 \leq \gamma \leq 30$) gives the power law $\xi/b \approx \gamma^{0.6}$ rather than $\xi/b \approx \gamma$. To understand this, we note that the number of well mixed levels inside one bandwidth obviously saturates at b for $\gamma > b$. It appears therefore reasonable to replace in (4) γ by an effective value $\gamma_{\text{eff.}}$ that interpolates between γ and b. Actually, we find that our numerical data can be well approximated by the scaling curve (see Fig. 1(b))

$$\frac{\xi}{b} \approx \frac{1.5}{\ln(1 + 1.5/\gamma_{\text{eff.}})} \ , \ \gamma_{\text{eff.}} \equiv \frac{\gamma}{[1 + \sqrt{3.2\,(\gamma/b)}\,]^2} \tag{5}$$

which reproduces the perturbative limit for $\gamma \ll 1$, the analytical result (4) for $1 \ll \gamma \ll b$ and the behavior $\xi \sim b^2$ for $\gamma \gg b$. Note that eq. (5) provides for the case $\gamma/b \ll 1$ relative large corrections of order $\sqrt{\gamma/b}$ explaining the numerical difficulties to clearly identify this regime.

In summary, we have obtained analytical results for the local density of states and the localization length for Cauchy random band matrices. We find that the Breit-Wigner form is replaced by a Levy distribution with index $\mu = 1/2$ and that the Breit-Wigner width Γ for ordinary band matrices is replaced by a new enhanced energy scale $\alpha \sim b\,\Gamma$. This energy scale also determines the localization length $\xi \sim b\,(\alpha/\Delta)$.

References

1. G. Casati, I. Guarnery, F. M. Israilev and R. Scharf, *Phys. Rev. Lett.* **64**, 5 (1990); R. Scharf *J. Phys.* A **22**, 4223 (1989); B. V. Chirikov, F. M. Israilev, and D. L. Shepelyansky, *Physica* **33D**, 77 (1988).
2. S. Iida, H. A. Weidenmüller, and J. A. Zuk, *Ann. Phys.* (NY) **200**, 219 (1990).
3. Y. V. Fyodorov and A. D. Mirlin, *Phys. Rev. Lett.* **67**, 2405 (1991); ibid. **69**, 1093 (1992); ibid. **71**, 412 (1993); A. D. Mirlin and Y. V. Fyodorov, *J. Phys.* A: Math. Gen. **26**, L551 (1993).
4. K. B. Efetov, *Supersymmetry in Disorder and Chaos*, Cambridge University Press (1997).
5. T. Guhr, A. Müller-Groeling, and H. A. Weidenmüller, *Phys. Rep.* **299**, 189 (1998).
6. D. L. Shepelyansky, *Phys. Rev. Lett.* **73**, 2607 (1994).
7. P. Jacquod and D. L. Shepelyansky, *Phys. Rev. Lett.* **75**, 3501 (1995); Y. V. Fyodorov and A. D. Mirlin, *Phys. Rev.* B **52**, R11580 (1995); K. Frahm and A. Müller–Groeling, *Europhys. Lett.* **32**, 385 (1995).
8. P. Lloyd, *J. Phys.* C: *Solid St. Phys.* **2**, 1717 (1969).
9. P. Cizeau, and J. P. Bouchaud, *Phys. Rev.* E **50**, 1810 (1994).
10. J. P. Bouchaud and A. Georges, *Phys. Rep.* **195**, 127 (1990).
11. F. von Oppen, T. Wettig, and J. Müller, *Phys. Rev. Lett.* **76**, 491 (1996).
12. D. L. Shepelyansky, Proceedings of les Rencontres de Moriond 1996 on "Correlated Fermions and Transport in Mesoscopic Systems", edited by T. Martin, G. Montambaux and J. Trân Thanh Vân, 201 (1996).
13. B. L. Altshuler, Yu. Gefen, A. Kamenev and L.S. Levitov, *Phys. Rev. Lett.* **78**, 2803 (1997); P. Jacquod and D. L. Shepelyansky, *Phys. Rev. Lett.* **79**, 1837 (1997); A. D. Mirlin and Y. V. Fyodorov, *Phys. Rev.* B **56**, 13393 (1997); C. Mejía-Monasterio, J. Richert, T. Rupp and H. A. Weidenmüller, *Phys. Rev. Lett.* **81**, 5189 (1998); X. Leyronas, P. G. Silvestrov and C. W. J. Beenakker, *Phys. Rev. Lett.* **84**, 3414 (2000).
14. B. Georgeot and D. L. Shepelyansky, *Phys. Rev. Lett.* **79**, 4365 (1997).
15. V. V. Flambaum, A. A. Gribakina, G. F. Gribakin and M. G. Kozlov, *Phys. Rev.* A **50**, 267 (1994); V. V. Flambaum, A. A. Gribakina, G. F. Gribakin and I. V. Ponomarev, *Physica* D **131**, 205 (1999).
16. V. M. Akulin, F. de Tomasi, I. Mourachko and P. Pillet, *Physica* D **131**, 125 (1999).
17. K. M. Frahm, *preprint* cond-mat/0101431 (2001).

Local density of states probed by single electron tunneling

J. KÖNEMANN[1], P. KÖNIG[1], T. SCHMIDT[1], E. McCANN[2], V. I. FAL'KO[2], R. J. HAUG[1]
[1] *Universität Hannover, Institut f. Festkörperphysik, Appelstrasse 2, 30167 Hannover, Germany*

[2] *School of Physics & Chemistry, Lancaster University, LA1 4YB Lancaster, United Kingdom*

Mesoscopic fluctuations of the local density of states (LDOS) in a highly degenerate semiconductor are studied by single electron tunneling through a discrete localized state. A damping of the amplitude of the LDOS fluctuations with increasing voltage is observed. We attribute this damping to inelastic processes in the emitter. From this inelastic broadening of our spectrometer the quasi-particle relaxation is evaluated.

1 Introduction

The local electronic structure of highly disordered systems, e.g. the statistics of single-particle wave functions in the diffusive transport regime manifests itself in mesoscopic fluctuations of low-temperature transport properties [1]. The local density of states (LDOS) fully reflects this electronic structure, so that it was proposed as an ideal experimentally accessible quantity [2]. Impurity assisted tunneling through resonant double-barrier structures [3,4] has turned out to be an appropriate tool to directly image the LDOS and thus reveal the local electronic structure [5]. The impurity state as a spectrometer with high spatial and energy resolution probes the LDOS as a function of excitation energy measured from the Fermi energy of the emitter of our device [6]. The basic idea of resonant LDOS spectroscopy is illustrated in the inset of Fig. 1. The low-bias

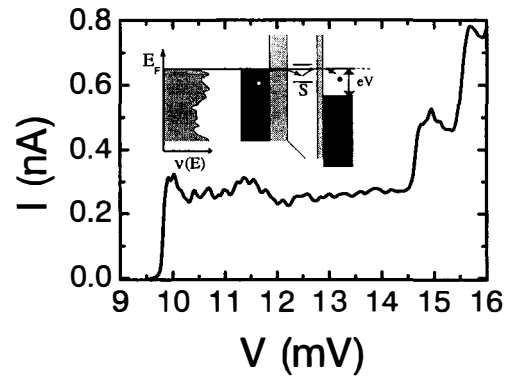


Figure 1: I-V characteristics for a typical magnetic field, on top of the current plateaus LDOS fluctuations. Inset: Schematical picture of LDOS spectroscopy.

part of a typical I-V characteristic, which has the well-known stair-like shape is shown in Fig. 1. Each step in I marks the tunneling through another localized state. An oscillatory fine structure can clearly be seen on top of each current plateau. This structure directly images the LDOS fluctuations. Due to the strong barrier asymmetry the tunneling current is dominated by the thick tunneling barrier adjacent to the emitter. The current is directly related to the mesoscopic fluctuations of the emitter LDOS ν, and thus $I \propto \nu$.

2 Sample and experimental method

Our sample is a highly asymmetric double barrier resonant tunneling heterostructure grown by molecular beam epitaxy on n^+-type GaAs substrate. The heterostructure consists of a 10 nm wide undoped GaAs quantum well sandwiched between two $Al_{0.3}Ga_{0.7}As$-tunneling barriers of 5 and 8 nm width. The contacts are formed with 300 nm thick GaAs layers highly doped with Si to $4.0 \cdot 10^{17}$ cm^{-3} and separated from the active region by 7 nm thick undoped GaAs spacer layers. We performed DC measurements of the I-V characteristics of our device in a dilution refrigerator at 20 mK.

For our experimental analysis we concentrated on the differential conductance $G = dI/dV$. In Fig. 2 (a) a typical G-V characteristic is presented. Three major peaks at 9.8 mV, 14.6 mV and

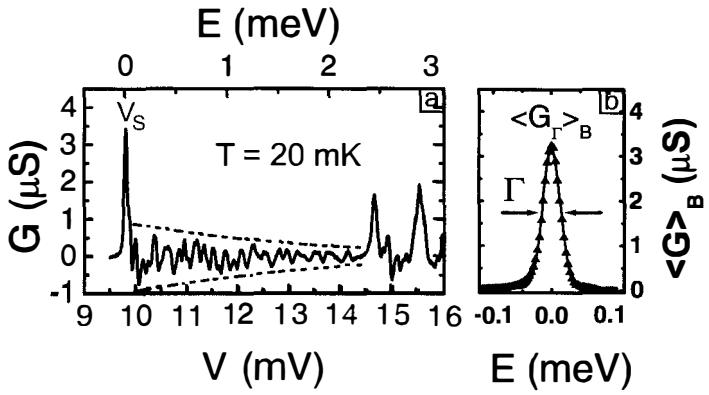


Figure 2: (a) G-V characteristics for typical B field: decay of LDOS fluctuations.(b) B-averaged main peak: spectrometer width Γ.

15.4 mV can be clearly distinguished. These peaks are attributed to three different localized states. From magnetic field measurements of the peak positions the states are identified as impurity states of the GaAs quantum well. The first peak position corresponds to the resonance situation, when the emitter Fermi energy E_F aligns with the resonant level energy E_S. By varying the bias voltage V, the spectrometer S is shifted to lower energies E relative to E_F and scans the LDOS of occupied emitter states. The differential conductance fluctuations

$$\delta G \propto \delta \frac{d\nu}{dE} \tag{1}$$

visualize the energy variations of the LDOS fluctuations. The main feature in Fig. 2(a) is the damping of the amplitude of LDOS fluctuations with increasing E. This is analyzed statistically in the following. Fig. 2(b) demonstrates the energy resolution $\Gamma = 36$ μeV of our spectrometer, which is estimated from the FWHM value of the main peak, averaged over a statistical ensemble of G-V curves between $B = 0 \ldots 1$ T.

3 Analysis

In Fig. 3 the peak value G_Γ is shown as a function of magnetic field B. The resonance conductance G_Γ refers to the coupling of the impurity state to the thick left emitter barrier. Furthermore G_Γ parameterizes the $G - V$ characteristics and will be used to normalize the amplitude of the LDOS fluctuations.At low magnetic fields the peak value G_Γ remains nearly constant. It is reduced to half of its value at $B = 0$ T around $B \approx 3$ T. This coincides with the observation of

Zeeman splitting of the main peak, like it was reported in a previous experiment[7]. The splitting of the main peak at around $B = 3$ T can be clearly resolved in the inset of Fig. 3. The dips in G_Γ, seen in Fig. 3 at $B \approx 4.5$ T and $B \approx 11.5$ T may be related to Landau quantization of the emitter.

In the following we want to analyze quantitatively the decay of LDOS fluctuation with increas-

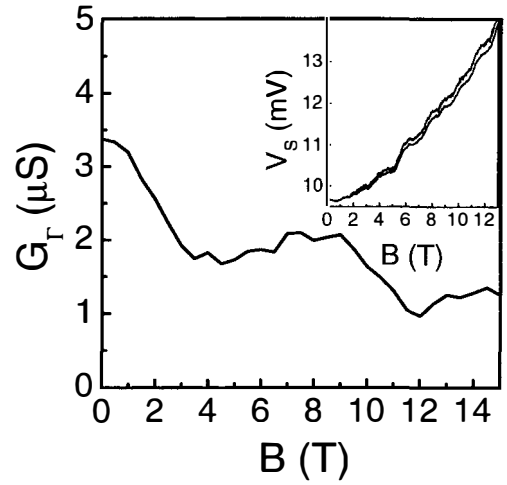


Figure 3: Resonance conductance G_Γ versus magnetic field B. Inset: Peak position V_S versus magnetic field B.

ing E. The energy $E = e\alpha(V - V_S)$ is the excitation energy of a quasi-hole left from the tunneling process of a single electron from an emitter state to the impurity state S. The accessible energy range of our experiment is given by the voltage difference of the first two main peaks in Fig. 2 (a). We calculated the variance of the differential conductance

$$\left\langle \delta G^2 \right\rangle_B = \left\langle (G(B) - \langle G \rangle_B)^2 \right\rangle_B \tag{2}$$

in dependence on E. The quantity $\langle \delta G^2 \rangle_B$ is a direct measure of the amplitude of the LDOS fluctuations averaged over a considerable number of different realizations of disorder with the experimental parameter B. Fig. 4 shows the sharp and monotonic drop of the amplitude of the LDOS fluctuations. This decrease is caused by the increase of the correlation energy $E_C = \Gamma + \hbar\gamma$ of the LDOS fine structure in G with increasing E. Here, γ represents the relaxation rate of inelastic processes in the emitter, when a quasi-hole relaxes to the Fermi energy. Such inelasticity leads to a smearing of the spectrometer[8], so that the relaxation rate γ for larger V dominates the effective spectrometer width. In this way inelastic broadening of states in the emitter leads to a decay of the amplitude of the LDOS fluctuations. Quantitatively one can write this relation as[9]

$$\left\langle \delta G^2 \right\rangle_B = \frac{1}{2} \cdot \frac{G_\Gamma^2}{\nu L R^2 (E_C/\Gamma)^3} \tag{3}$$

$$= \frac{G_N^2}{(E_C/\Gamma)^3}, \tag{4}$$

with L being the height, R the diameter of the diode, ν the density of states of the emitter, and G_N the corresponding differential conductance close to the Fermi energy. From this formula

we are able to extract the dependence of the quasi-particle relaxation rate γ on the excitation energy E in a diffusive system.

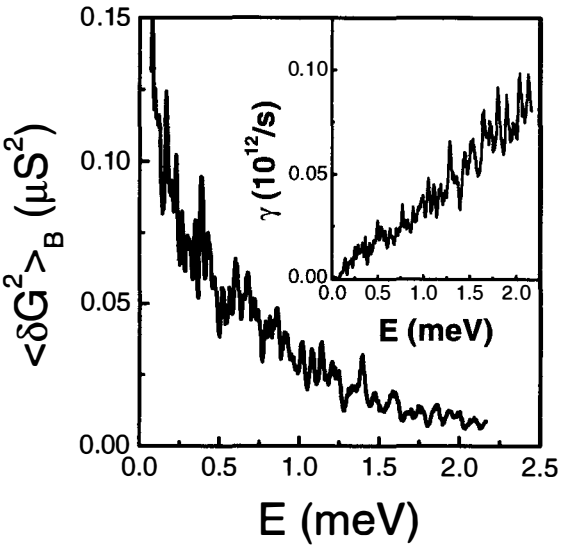


Figure 4: $\langle \delta G^2 \rangle_B$ versus excitation energy E. Inset: quasi-particle relaxation rate, extracted from $\langle \delta G^2 \rangle_B$.

4 Summary

In conclusion, we have used single electron tunneling via localized states to perform spectroscopy of the fluctuations of the local density of states in the emitter of a resonant tunneling device. Due to our high spectrometer resolution we were able to resolve the inelastic broadening of the emitter states. We have presented a direct measure of the quasi-particle relaxation rate.

References

1. I. V. Lerner, *Phys. Lett. A.* **133**, 253 (1988).
2. I. V. Lerner and M. E. Raikh,*Phys. Rev. B.* **45**, 14036 (1992).
3. M. W. Dellow, P. H. Beton, C. J. G. M. Langerak, T. J. Foster, P. C. Main, L. Eaves, M. Henini, S. P. Beaumont, C. D. W. Wilkinson, *Phys. Rev. Lett.* **68**, 1754 (1992).
4. P. Gueret, N. Blanc, R. Germann, and H. Rothuizen, *Phys. Rev. Lett.* **68**, 1896 (1992).
5. J. P. Holder, A. K. Savchenko, V. I. Fal'ko, B. Joualt, G. Faini, F. Laruelle, and E. Bedel, *Phys. Rev. Lett.* **84**, 1563 (2000).
6. T. Schmidt, P. König, E. McCann, V. I. Fal'ko, and R. J. Haug *Phys. Rev. Lett.* **86**, 276 (2001).
7. M. R. Deshpande, J. W. Sleight, M. A. Reed, R. G. Wheeler, R. J. Matyi, *Phys. Rev. Lett.* **76**, 1328 (1996).
8. U. Sivan, F. P. Milliken, K. Milkove, S. Rishton, Y. Lee, J. M. Hong, V. Boegli, D. Kern, and M. Defranza, *Europhys. Lett.* **25**, 605 (1994).
9. J. Könemann, P. König, T. Schmidt, E. McCann, V. I. Fal'ko, and R. J. Haug, *cond-mat/0105025.*

STATISTICS OF THE MESOSCOPIC THERMODYNAMIC FLUCTUATIONS

P. LEBOEUF, A. G. MONASTRA
Laboratoire de Physique Théorique et Modèles Statistiques, Bât. 100, 91405 Orsay Cedex, France

We investigate the probability distribution of the quantum fluctuations of thermodynamic functions of finite, ballistic, phase-coherent Fermi gases. Based on a semiclassical approximation, the fluctuations are expressed in terms of sums involving the classical periodic orbits of the single-particle dynamics. Depending on the chaotic or integrable nature of the underlying classical dynamics, we find two main classes of functions. The first class is made of thermodynamic functions whose corresponding distributions are system dependent non-universal functions, even at zero temperature. Explicit convergent expressions to compute all the moments in terms of the shortest classical periodic orbits are found in this case. Examples belonging to this class are the energy and the compressibility of the gas. The second class of functions is made of quantities whose distribution, at sufficiently low temperatures, are usually non-Gaussian functions determined only by the local statistical properties of the single-particle energy levels. The latter are universal and described by a Poisson statistics for a regular dynamics and by random matrix ensembles in the chaotic case. Examples in this class are the entropy, the specific heat and, for chaotic dynamics, those of the particle number in systems with fixed chemical potential. As the temperature is raised the universality characteristic of this latter class is lost. The dependence on temperature and on number of particles of the fluctuations is explicitly computed in all cases, and the different relevant energy scales displayed.

When the size of a system diminishes its properties become very sensitive to the variations of a control parameter. These finite-size quantum effects are due to the sensitivity of the wave functions on the parameters, and are a manifestation of the discrete nature of the energy spectrum created by the spatial confinement. To be experimentally observable, the temperature should be low enough to avoid the thermal smoothing. Our purpose is to compute the probability distribution of these quantum ("mesoscopic") fluctuations for the different thermodynamic functions of a confined Fermi gas as a function of temperature, and to display the most relevant parameter and energy scales involved. We summarize here some of the results reported in more detailed elsewhere[1].

Self-consistent theories which admit almost independent motion of quasiparticles and give rise to Fermi gases constitute a basic tool to describe fermionic many-body systems. Well known examples are independent-particle models in nuclear physics and, within a mean-field theory for the valence electrons, the jellium model for the electronic properties of metals and of simple alkali metal clusters. One of the most spectacular predictions of mean-field theories is the occurrence of shell effects in the energy of the fermion gas as a function of the number of particles, which produces magic numbers and deformations in nuclei and metallic particles [2,3]. When the potential has some symmetries, the quantum fluctuations describe the bunching of the single-particle energy levels in shells. From a semiclassical point of view [4,5], the shell and super-shell structures are interpreted as modulations in the single-particle density of states produced by some simple families of classical periodic orbits. The phase-space structure of these families is very regular, and it is this high regularity which is at the origin of the observed strong quantum modulations.

Similar quantum fluctuations are present in all equilibrium thermodynamic functions describing the many-body system. Their typical magnitude for some thermodynamic functions as well as many of their physical applications were discussed in the past, in particular in nuclear and atomic physics, and in different branches of condensed matter physics (see for example [2,3,6], and references therein). In general the nature of the fluctuations strongly depend on the underlying classical single-particle dynamics, and it is one of our goals to explicitly investigate

this dependence.

There are two main features of the single particle dynamics that determine the thermodynamic quantum fluctuations of the gas. On the one hand, the universality of the spectral fluctuations on local scales, i.e. in the range of the mean level spacing δ between single particle levels. This universality depends on the integrable or chaotic nature of the single-particle dynamics, but not on the details of the system. The second ingredient are the long range modulations of the spectrum (shells) produced by the shortest periodic orbits on a scale $E_c = \hbar/\tau_{min}$, with τ_{min} the period of the shortest periodic orbit of the single–particle classical dynamics. Typically $E_c \gg \delta$. These long range modulations are system-dependent, since the short orbits are. The amplitude of this effect also depends on the nature of the dynamics. If the classical motion is regular, symmetries are present and shell effects due to periodic orbits are important. On the contrary, if the corresponding classical motion is chaotic, the long-range modulations will have, compared to the regular case, a smaller amplitude.

Our main goal is to provide a full characterization of the probability distribution of the fluctuations of the different thermodynamic functions[1]. We also investigate their autocorrelation as a function of an external parameter x. We concentrate in the fluctuations of equilibrium properties of *ballistic* Fermi systems (i.e. with no disorder present in the potential) whose mean-field single particle motion is either regular or fully chaotic. Schematically we have in mind a mean-field potential which is almost flat in the interior and rises at the surface, like the Woods-Saxon potential in nuclear physics or the static homogeneous potential produced by the ionic background in the jellium model. Under these conditions, and in particular in the extreme case of a sharp boundary, the nature of the classical dynamics is determined by the shape of the cavity and by the external fields acting on the system. We ignore physical effects related to the spin degree of freedom, and we moreover assume that the inelastic processes can be neglected, namely the coherence length is much larger than the system size.

In a semiclassical approximation [7,4,8], the fluctuating part of any thermodynamic function can be written in the form[1]

$$\tilde{\Phi}(x,\mu,T) = 2\,\mathcal{C}\sum_{p}\sum_{r=1}^{\infty}\mathcal{A}_{p,r}(x,\mu,T)\cos\left[r S_p(x,\mu)/\hbar + \nu_{p,r}\right]\ , \qquad (1)$$

where the sum is over all the periodic orbits p of the classical single–particle motion and of its repetitions r. All the periodic orbits are computed at energy $E = \mu$, with μ the chemical potential. The constant coefficient $\mathcal{C}$ includes all the terms not depending on the periodic orbit, S_p are the actions, and $\nu_{p,r}$ the Maslov indices. The coefficient $\mathcal{C}$, as well as the functional form of the orbit-dependent prefactor $\mathcal{A}_{p,r}$, depend on the thermodynamic function considered. The periodic orbits are determined by the shape of the confining potential. The temperature enters as a multiplicative factor in $\mathcal{A}_{p,r}(x,\mu,T)$, which acts as an exponential cut off for orbits whose period is much longer than the inverse temperature [9]. At zero temperature, a priori all orbits contribute.

The study of the probability distribution of the fluctuations is based on Eq. (1). Once the periodic orbits are known, this expression allows to explicitly compute the quantum oscillatory contribution to a given thermodynamic function in a particular system. We are interested, however, in a statistical analysis valid for a generic system rather than in an explicit computation of the oscillations for a particular one. The picture that emerges from our analysis is very rich. We find that the probability distribution of the fluctuations strongly depends on the quantity considered and on the nature of the underlying single–particle classical dynamics.

The fluctuations of some thermodynamic functions, like the energy, the compressibility, or the force of the gas against a deformation of the shape of the confining potential, are dominated at any temperature by the long range modulations of the single–particle spectrum produced by the short periodic orbits. As a consequence, the probability distribution of the associated

quantum fluctuations is a non-universal, non-Gaussian asymmetric function. Its moments are determined by the shortest periodic orbits of the system, irrespective of the regular or irregular character of the dynamics. We have obtained explicit convergent expressions to compute all the moments. The repetitions of the orbits are found to play an important role since their interference produce, in particular, non–vanishing odd moments and therefore the asymmetry of the distributions. At zero temperature, the typical fluctuations of the gas (i.e., the width of the probability distributions) are always found to be much larger than the corresponding local fluctuations of the single–particle levels. For example, the typical fluctuations of the response of the gas (derivative of the grand potential with respect to the external parameter) is $\sqrt{g} = \sqrt{E_c/\delta}$ times larger than those of the single–particle levels located at Fermi energy, irrespective of the integrable or chaotic nature of the dynamics. Other amplifying factors are found for other thermodynamic functions, like the energy. Due to the dominance of the long–range single–particle modulations, the probability distributions are found to be, for these functions, relatively insensitive to temperature variations up to temperatures of order E_c. At higher temperatures the typical size of the fluctuations decay exponentially. The autocorrelation functions present moreover long range correlations.

There is a second class of thermodynamic functions, illustrated by quantities like the number of particles for systems with fixed chemical potential when the underlying classical dynamics is chaotic, and the fluctuations of the entropy and those of the specific heat for regular and chaotic motion. For these functions the quantum fluctuations are, at temperatures much smaller than E_c, dominated by the fluctuations of the single–particle levels on a scale δ. The latter fall in two different universality classes [10]. The first one, valid for integrable systems, is determined by local Poisson statistics, while in the chaotic case local fluctuations obeying random matrix theory apply (with subclasses depending on the presence or not of time reversal symmetry). In this low–temperature regime, the corresponding probability distributions of the thermodynamic fluctuations are found to be in general non-Gaussian, with the exception of the fluctuations of the number of particles for systems with fixed chemical potential in chaotic systems where it is conjectured to be Gaussian. They are very sensitive to temperature variations. For temperatures of order δ they considerably change as the temperature is raised, but they always remain in the corresponding universality class. For example, in the case of the entropy the width of the distribution grows linearly with temperature for temperatures much smaller than δ, irrespective of the nature of the single–particle dynamics. However, for higher temperatures the behavior strongly depends on the regular or chaotic character of the motion. The maximum size of the typical value of the entropy fluctuations is of order k_B in chaotic systems, and this maximum is reached for temperatures of order δ. Whereas in integrable systems the entropy fluctuations grow up to values $g\ k_B$. This maximum is reached at much higher temperatures compared to the chaotic case, of order E_c. For temperatures of order E_c the universality of the probability distributions of the quantum fluctuations in this class is lost. At those temperatures the short orbits become dominant, producing system–dependent distributions like for the first class of functions described above. In this high–temperature regime the moments of the distributions can be computed from periodic orbit theory using the shortest ones. At still higher temperatures the fluctuations are exponentially suppressed.

There are several distinct applications of the present results. Among them, we mentioned the study of the electronic contribution to the mechanical force measured in experiments where metallic nanocontacts are pulled, and the fluctuations of the total energy of nuclei as a function of the number of nucleons. Progress made in both directions will be published elsewhere. In a related work, the distribution of the energy of a Fermi gas whose single–particle energy levels are given by the imaginary part of the complex zeros of the Riemann zeta function was recently investigated [11]. This artificial fermionic system was named "the Riemannium". Aside its mathematical interest, it also serves as an explicit and important test of our results relating

the probability distribution of thermodynamic functions to periodic orbit theory. The concept of periodic orbit enters here because there exist strong connexions between the quantum theory of chaotic systems and the complex zeros of the Riemann zeta function interpreted as spectral eigenvalues. A high precision agreement was found between the numerical results and our analytical computation of the moments of the probability distribution of the grand potential of the Riemannium based on Eq.(1). Other numerical tests of Fermi gases contained in rectangular and Sinai–type cavities were done[1]. These two geometries produce regular and chaotic single–particle motions, respectively. The results confirm the validity of our results in the different temperature regimes.

Acknowledgments

The LPTMS is a "Unité de recherche de l'Université de Paris XI associée au CNRS".

1. P. Leboeuf and A. G. Monastra, *Phys. Rev. B* **62** (2000) 12617; preprint LPTMS, submitted for publication.
2. A. Bohr and B. R. Mottelson, *Nuclear Structure* (Benjamin, Reading, MS, 1975), Vol.II.
3. M. Brack, *Rev. Mod. Phys.* **65** (1993) 677.
4. R. Balian and C. Bloch, *Ann. Phys.* (N.Y.) **69** (1972) 76.
5. V. M. Strutinsky and A. G. Magner, *Sov. J. Part. Nucl.* **7** (1976) 138.
6. Y. Imry, *Introduction to Mesoscopic Physics* (Oxford University Press, New York, 1997).
7. M. C. Gutzwiller, *Chaos in Classical and Quantum Mechanics*, Springer, New York, 1990.
8. M. V. Berry and M. Tabor, *J. Phys. A* **10** (1977) 371.
9. K. Richter, D. Ullmo and R. Jalabert, *Phys. Rep.* **276** (1996) 1.
10. O. Bohigas, M.-J. Giannoni, and C. Schmit, *Phys. Rev. Lett.* **52** (1984) 1.
11. P. Leboeuf, A. G. Monastra and O. Bohigas, *Reg. Chaot. Dyn.* **6** (2001) 205.

DOES BERRY PHASE EXIST FOR A SYSTEM COUPLED TO ITS ENVIRONMENT?

Robert S. Whitney[1], Yuval Gefen[1]
[1] *Department of Condensed Matter Physics, Weizmann Institute of Science, Rehovot 76100, Israel.*

Berry phase was originally defined for systems whose states are separated by finite energy gaps. One might naively expect that a system without a gap cannot have a Berry phase. Despite this we ask whether a Berry phase can be observed in a system which has a continuous spectrum because its coupling to the environment has broadened its energy levels. We find that, contrary to the above naive expectation, there are conditions under which the Berry phase is observable. However it is modified by the presence of the environment and no longer has a simple geometric interpretation. The model system we consider is a spin-half in a slowly rotating magnetic field, with the spin also coupled to a Ohmic environment of harmonic oscillators (spin-boson model). Here we discuss the high-temperature limit of this model. We then interpret our results in terms of a spin under the influence of a classical stochastic field.

1 Motivation and Summary

Originally Berry phase [1] was defined for systems whose states were separated by finite energy gaps. Here we ask whether a Berry phase can be observed in a system whose spectrum is continuous, more specifically: a system which is not completely isolated from its environment. All real systems are coupled, at least weakly, to their environment and as a result never have a truly discrete energy level spectrum. The naive argument would be that, since the spectrum of the system does not have a gap, the parameters in the Hamiltonian could never be varied slowly enough to be considered adiabatic. This in turn would mean one could not observe a Berry phase in such a system. If this were the case one could never observe a Berry phase.

The above argument must be too naive: experiments have been carried out which do observe the Berry phase, both directly and indirectly [2,3,4]. We therefore take a simple model in which a quantum system which exhibits a Berry phase is coupled to many other quantum degrees of freedom. We then ask two questions. Firstly, under what conditions can the Berry phase be observed? Secondly, is the observed Berry phase the same as that of the isolated system, and if not is it still geometric in nature? While others have investigated systems with Berry phases coupled to other degrees of freedom [5,6,7], we believe we are the first to explicitly ask these two questions.

We should make it clear that we distinguish between the system and the environment in the following way. *The system* is something which we have experimental control over. Thus we can prepare the system in any state we like and choose all parameters in the Hamiltonian under which it evolves. *The environment* consists of all the degrees of freedom over which we have little experimental control. Usually the most we can do to the environment is to ensure the universe (system + environment) is in thermal equilibrium, with a temperature T. If we are able to take T to zero, then we can prepare the universe in its ground state. However to measure a Berry phase, we must devise a procedure for measuring the phase evolution of this state and getting rid of the dynamic part of the phase. Most such procedures involve the mixing of a large number of eigenstates (of the universe), and hence will lead to dephasing as is discussed below [8]. This implies that the extremely interesting recent work of Avron and Elgart [7] — on adiabatic evolution of eigenstates of models similar to ours — is not directly relevant to our work.

We choose to investigate a spin-half which is coupled to both a magnetic field and an environment. When isolated from its environment, this spin exhibits a Berry phase if we slowly rotate the magnetic field around a closed loop. We model the environment as a bath of harmonic oscillators coupled to the spin. This model has been chosen for its simplicity, despite this

it is relevant to recent suggestions for using Berry phases to control the qubits in a quantum computer[9,10]. This is of interest because the coupling to the environment is significant for most physical realisations of qubits. While we make no attempt to accurately model the real coupling between the qubit and its environment, we believe our results give an indication of what to expect in the real system.

In this article we concentrate on the case where the frequencies of the oscillators have been chosen so that the *bath is Ohmic*[11], and these oscillators are initially at a *high-temperature*. We find that coupling the spin-half to this type of environment causes four effects. (i) Exponential decay to a state in which the spin is thermalised with the bath, the time-scale associated with this is the spin flip time, T_1. (ii) Exponential decay of observables containing phase information, the time-scale associated with this is the dephasing time, T_2. (iii) A Lamb shift[12] of the energy-levels of the spin by an amount, δE. (iv) A modification to the Berry phase, $\delta\Phi_{\rm Berry}$. All four of these effects go like the second power of the coupling between the spin and its environment, the functional form of the results are given in Eq. (4). Of these (ii) and (iv) are of most interest to us. Effect (ii) tells us when we can measure the Berry (or any other) phase, while effect (iv) tells us what the Berry phase we measure will be.

Effect (ii) means that one cannot perform an arbitrarily long experiment to measure a phase. Even the most sensitive experiment will not be able to measure the phase if the time of the experiment is much larger than T_2, because of the exponential decay of the observables containing the phase information. This constraint on the time of the experiment is particularly relevant for Berry phase experiments, since they must be carried out over long times to ensure adiabaticity. So what is the Berry phase for an experiment in which the parameters of the Hamiltonian are taken around a closed loop in a finite time, $t_{\rm period}$? The Berry phase is the component of the phase which is independent of $t_{\rm period}$. Other contributions to the total phase are the dynamic phase which scales linearly with with $t_{\rm period}$, and non-adiabatic contributions which are proportional to $t_{\rm period}$ to some negative power. Clever experiments (see Section 3) can remove the dynamic phase but not the non-adiabatic contributions. One can argue that the Berry phase is present even for very fast experiments, it is just that then it is masked by the non-adiabatic contributions to the phase. For the Berry phase to be accurately measured it must be much larger than the non-adiabatic contributions to the total phase. This can only be achieved by carrying out the experiment slowly enough.

Let us assume that during an experiment on a spin-half in a magnetic field, $\boldsymbol{B}(t)$, we slowly change the direction of the field while keeping its magnitude fixed. Then at all times the energy gap between the up and down state is $g\mu B$, where $B = |\boldsymbol{B}(t)|$ is time-independent, g is the Landé g-factor, and $\mu \equiv \frac{e\hbar}{2mc}$ is the Bohr magneton. In this case the non-adiabatic contribution to the phase accumulated over a time, t, is of order $\hbar/(g\mu Bt)$. To measure the Berry phase — which is of order one — the non-adiabatic contributions to the total phase must be much less than one. Thus the time of the experiment should satisfy $t_{\rm period} \gg \hbar/(g\mu B)$. If dephasing occurs on a time-scale T_2 then we cannot measure the total phase for times larger than T_2. Unless $g\mu BT_2/\hbar \gg 1$ the non-adiabatic contributions to the total phase in an experiment which takes time T_2 will not be small enough for us to accurately measure the Berry phase.

Now that we understand the conditions under which we can measure the Berry phase, we ask if the Berry phase is purely geometric. The answer is no. Effect (iv) tells us that in general there are environment-induced contributions to the Berry phase which are not geometric in nature. Remember we are choosing to define the Berry phase as any contribution to the total phase which is independent of the time, $t_{\rm period}$, that it takes to vary the parameters of the system Hamiltonian around a closed loop. Is this non-geometric contribution to the Berry phase observable? It can be very large, but only if the coupling to the environment is large, in which case the experiment dephases quickly. Then a Berry phase measurement carried out before the system dephases will have significant non-adiabatic contributions to the total phase which may

mask $\delta\Phi_{\rm Berry}$. Therefore the environment-induced contribution to the Berry phase can only be observed if

$$\delta\Phi_{\rm Berry} \gtrsim \frac{\hbar}{g\mu B T_2}. \tag{1}$$

Only then is $\delta\Phi_{\rm Berry}$ of the same order or larger than the non-adiabatic corrections to the phase that occur when the experiment is carried out in a time $t_{\rm period} \sim T_2$. If we look at the functional form of T_2 and $\delta\Phi_{\rm Berry}$ in (4) we see that there are a wide range of parameters for which $\delta\Phi_{\rm Berry} \sim \frac{\hbar}{g\mu B T_2}$. In this parameter range the environment-inducted correction to the Berry phase is just about observable in an experiment which takes a time $t_{\rm period} \sim T_2$.

The remainder of this article is arranged as follows. In Section 2 we discuss the model and summarise our results for a high-temperature Ohmic bath. Then in Section 4 we describe the high-temperature Ohmic environment as a randomly-fluctuating magnetic field, and thus develop a more intuitive understanding of one limit of this model. To do this we first give a brief summary of Berry phase for an isolated spin (Section 3).

2 The model and high-temperature results

We will discuss the details of the derivation of the results elsewhere [8]; here we give a very brief overview of the derivation. We start with the following Hamiltonian,

$$\mathcal{H} = -\frac{g\mu}{2}\boldsymbol{B}(t)\cdot\hat{\boldsymbol{\sigma}} - \frac{g\mu}{2}\sum_i C\hat{q}_i\hat{\sigma}_z + \sum_i\left[\frac{\hat{p}_i^2}{2m} + \frac{m\Omega_i^2\hat{q}_i^2}{2}\right]. \tag{2}$$

It is a spin-boson model [13] with a time-dependent field, $\boldsymbol{B}(t)$. We consider an Ohmic bath of oscillators with an upper frequency cut-off, $\Omega_{\rm max}$, thus

$$\sum_i (\cdots)_{\Omega_i} = \alpha\int_0^\infty {\rm d}\Omega\ \Omega^2 {\rm e}^{-\Omega/\Omega_{\rm max}}(\cdots)_\Omega \tag{3}$$

We write the spin operators as operators on a two fermionic system $\sigma_z = f_1^\dagger f_1 - f_2^\dagger f_2$, $\sigma_+ = f_1^\dagger f_2$ and $\sigma_- = f_2^\dagger f_1$, we then write the Feynman propagator for the system as a coherent-states path integral in which the fermionic degrees of freedom represented by Grassman variables. We integrate out the oscillators exactly [14,11]. The effective action of the resulting path integral contains a term which is quartic in the fermionic degrees of freedom and couples the state of the spin at time t_1 to the state of the spin at time t_2. We carry out a perturbation expansion of this quartic term. We then use the fact that for an Ohmic bath the coupling between the spin state at t_1 and t_2 is dominated by $t_1 - t_2 \sim \Omega_{\rm max}^{-1}$. Thus in the limit where the time of the experiment $t \gg \Omega_{\rm max}^{-1}$, the perturbation expansion is dominated by a certain class of diagrams that we can sum to all orders.

Here we only discuss results for a *high-temperature* Ohmic environment. By high-temperature we mean that $k_{\rm B}T \gg \hbar\Omega_{\rm max}$, other limits are discussed in reference 8. For concreteness we take the case where the field $\boldsymbol{B}(t) = B\,(\hat{\boldsymbol{x}}\sin\theta\cos\omega t + \hat{\boldsymbol{y}}\sin\theta\sin\omega t + \hat{\boldsymbol{z}}\cos\theta)$ in an experiment which takes a time $t_{\rm period} = 2\pi/\omega$. The results — written in terms of the dimensionless coupling between the spin and the oscillators $\tilde{C} = g\mu C\,(\alpha/m\hbar)^{1/2}$ — are as follows,

$$\begin{aligned}
\frac{1}{T_1} &= \frac{\pi\tilde{C}^2(k_{\rm B}T)}{2\hbar}{\rm e}^{-\gamma}\sin^2\theta & \frac{1}{T_2} &= \frac{\pi\tilde{C}^2(k_{\rm B}T)}{4\hbar}\left(2\cos^2\theta + {\rm e}^{-\gamma}\sin^2\theta\right)\\
\frac{\delta E}{\hbar} &= \frac{\tilde{C}^2(k_{\rm B}T)}{4\hbar}f(\gamma)\sin^2\theta & \delta\Phi_{\rm Berry} &= \frac{\pi\tilde{C}^2(k_{\rm B}T)}{2\hbar\Omega_{\rm max}}f'(\gamma)\sin^2\theta\cos\theta
\end{aligned} \tag{4}$$

where $\gamma = g\mu B/\hbar\Omega_{\rm max}$. The function $f(x) = {\rm e}^x{\rm Ei}(-x) - {\rm e}^{-x}{\rm Ei}(x)$ where we define ${\rm Ei}(x)$ as the principal-value of the Exponential integral, $\int_{-x}^{\infty}{\rm d}t{\rm e}^{-t}/t$. Hence $f'(x) \equiv \frac{\rm d}{{\rm d}x}f(x) = {\rm e}^x{\rm Ei}(x) + {\rm e}^{-x}{\rm Ei}(-x)$.

3 Berry phase for an isolated spin : Rotating reference frame trick

Consider a spin-half coupled to a magnetic field, $\boldsymbol{B}(t)$, via the Hamiltonian,

$$\mathcal{H} = -\frac{g\mu}{2}\boldsymbol{B}(t)\cdot\hat{\boldsymbol{\sigma}} \tag{5}$$

Now imagine that the magnetic field rotates with angular velocity, $\boldsymbol{\omega}(t)$, so that $\frac{\mathrm{d}}{\mathrm{d}t}\boldsymbol{B}(t) = \boldsymbol{\omega}(t)\times\boldsymbol{B}(t)$. We can go to a reference frame which rotates with the $\boldsymbol{B}$-field. In this new non-inertial frame the spin experiences a pseudo-field, as well as the time-independent field $\boldsymbol{B}' = \boldsymbol{B}(0)$. The pseudo-field is simply $-\hbar\boldsymbol{\omega}(t)/g\mu$. Thus all the time-dependence in the problem has been moved from $\boldsymbol{B}$ to $\boldsymbol{\omega}$. In the rotating frame the Hamiltonian is

$$\mathcal{H}' = -\frac{g\mu}{2}\left[\boldsymbol{B}' - \frac{\hbar}{g\mu}\boldsymbol{\omega}(t)\right]\cdot\hat{\boldsymbol{\sigma}}. \tag{6}$$

Note that if we transform the initial state to the rotating frame, evolve it using $\mathcal{H}'$, then transform back to the non-rotating frame, we end up with a final state $|\psi'_f\rangle$. Careful analysis shows that the true final state is actually $|\psi_f\rangle = \mathrm{e}^{\mathrm{i}\phi\hat{\sigma}_z}|\psi'_f\rangle$, however in all cases we will consider ϕ is a multiple of π. The resulting sign difference between $|\psi_f\rangle$ and $|\psi'_f\rangle$ will be of no consequence and can be ignored.

The power of transforming to the rotating frame becomes clear if we consider a rotation of the $\boldsymbol{B}$-field for which $\boldsymbol{\omega}$ is time-independent. Then the transformation turns a time-dependent problem into a time-independent one. The time-independent problem can then be solved by working in the basis where $\mathcal{H}'$ is diagonal.

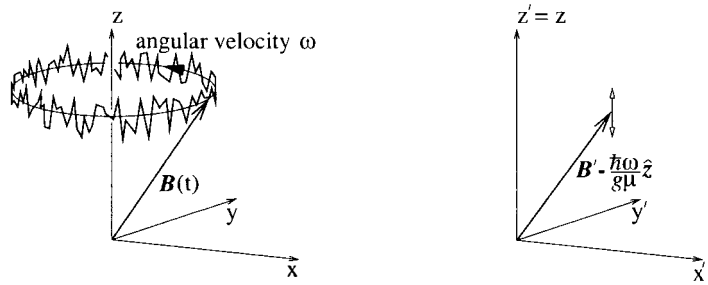
We consider the following experiment to measure the Berry phase. We start with a $\boldsymbol{B}$-field, $\boldsymbol{B}(0) = B\left(\hat{\boldsymbol{x}}\sin\theta + \hat{\boldsymbol{z}}\cos\theta\right)$, which we then rotate with angular velocity $\boldsymbol{\omega} = \hat{\boldsymbol{z}}\omega$ for a time $t_{\mathrm{period}} = 2\pi/\omega$. In the limit $\omega \to 0$, the component of the spin-state which is initially up relative to $\boldsymbol{B}(0)$ acquires a phase $\Phi = \frac{1}{2}\Theta + \int_0^{t_{\mathrm{period}}} E_\uparrow(t)\mathrm{d}t$, while the state which is initially down acquires a phase equal to $-\Phi$. The first term in Φ is the Berry phase (for a spin-half), $\Phi_{\mathrm{Berry}} = \frac{1}{2}\Theta$, where $\Theta = 2\pi\left(1-\cos\theta\right)$ is the solid-angle enclosed by the path the $\boldsymbol{B}$-field takes in the non-rotating frame. The second term is the dynamic phase, $\Phi_{\mathrm{dyn}} = \int_0^{t_{\mathrm{period}}} E_\uparrow(t)\mathrm{d}t$, where $E_\uparrow(t) = \frac{1}{2}g\mu B$ is the energy of the instantaneous eigenstate at time t.

We are in the adiabatic limit, which means that the dynamic phase is much larger than the Berry phase. If we wish to carry out an experiment which yields the Berry phase, rather than the sum of the Berry and dynamic phases, then we can eliminate the dynamic phase using the following spin-echo technique [9]. We (a) adiabatically rotate the $\boldsymbol{B}$-field around a closed loop, then (b) flip the spin, (c) rotate the field in the opposite direction round the same closed loop, and (d) flip the spin again. By flip the spin, we mean $|\uparrow\rangle \leftrightarrow |\downarrow\rangle$ where the up and down states are defined relative to the direction of $\boldsymbol{B}$-field at that time. This can be achieved by applying a fast π-pulse in a direction perpendicular to the $\boldsymbol{B}$-field. When we do (a)-(d) the Berry phases of the first and second loop add up, while the dynamic phases cancel. Thus the phase acquired by the spin is purely dependent on the Berry phase round the loop.

Thus we will consider a field, $\boldsymbol{B}(t)$, which rotates with angular velocity $\boldsymbol{\omega} = \hat{\boldsymbol{z}}\omega$ for $0 < t < t_{\mathrm{period}}$ (where $t_{\mathrm{period}} = 2\pi/\omega$) and $\boldsymbol{\omega} = -\hat{\boldsymbol{z}}\omega$ for $t_{\mathrm{period}} < t < 2t_{\mathrm{period}}$, with a spin flip at time t_{period} and time $2t_{\mathrm{period}}$. Then the probability of an initial state $|u_0, v_0\rangle = u_0|\uparrow\rangle + v_0|\downarrow\rangle$ ending up in a state $|u, v\rangle$ at time $2t_{\mathrm{period}}$ is

$$\begin{aligned} P\left(|u,v\rangle, 2t_{\mathrm{period}}; |u_0,v_0\rangle\right) &= \left|\langle u,v|\hat{\sigma_x}\exp\left[\mathrm{i}\Phi(-\omega)\hat{\sigma}_z\right]\hat{\sigma_x}\exp\left[\mathrm{i}\Phi(\omega)\hat{\sigma}_z\right]|u_0,v_0\rangle\right|^2 \\ &= u^*uu_0^*u_0 + v^*uv_0^*u_0\mathrm{e}^{\mathrm{i}4\Phi_{\mathrm{Berry}}} + u^*vu_0^*v_0\mathrm{e}^{-\mathrm{i}4\Phi_{\mathrm{Berry}}} + v^*vv_0^*v_0 \end{aligned} \tag{7}$$

where all spin-states are defined relative to the axis of the field $\boldsymbol{B}(0)$.



(a) Lab (unprimed) frame (b) Rotating (primed) frame

Figure 1: Here we show the magnetic field discussed in Section 4, in both the laboratory frame (a) and the rotating frame (b). The smooth line in (a) is the time-dependence of the field, $\boldsymbol{B}(t)$, while the irregular line represent the total field, $(\boldsymbol{B}(t) + \hat{\boldsymbol{z}}K(t))$. It fluctuates wildly because $K(t)$ fluctuates randomly with time. In the rotating frame (b) both the field $\boldsymbol{B}'$ and the pseudo-field $(-\hat{\boldsymbol{z}}\hbar\omega/g\mu)$ are time-independent, while the field $K(t)$ fluctates. The vertical double-ended arrow represent the fluctuations of the total field, $(\boldsymbol{B}' - \hat{\boldsymbol{z}}\hbar\omega/g\mu + \hat{\boldsymbol{z}}K(t))$.

4 Berry phase and decoherence in a randomly fluctuating magnetic field

A spin in an experimentally controlled magnetic field $\boldsymbol{B}(t)$ with a z-axis coupling to a high-temperature Ohmic bath of oscillators is equivalent to the spin in a field $\boldsymbol{B}(t) + \boldsymbol{K}(t)$ where $\boldsymbol{K}(t) = \hat{\boldsymbol{z}}K(t)$ is a randomly-fluctuating field [11]. The Hamiltonian for this model is simply $\mathcal{H} = -\frac{g\mu}{2}\left[\boldsymbol{B}(t) + \hat{\boldsymbol{z}}K(t)\right] \cdot \hat{\boldsymbol{\sigma}}$. If there is an upper cut-off on the frequencies of the oscillator, $\Omega_{\max}$, then $K(t)$ is Gaussianly distributed and uncorrelated for times longer than $\Omega_{\max}^{-1}$. Thus on time-scales much greater than $\Omega_{\max}^{-1}$ we can average over $K(t)$ using,

$$\langle \cdots \rangle = \frac{\int \left[\prod_{j=0}^{N-1} \mathrm{d}K_j\right] (\cdots) \exp\left[-\frac{\epsilon}{2\kappa^2}\sum_{j=0}^{N-1} K_j^2\right]}{\int \left[\prod_{j=0}^{N-1} \mathrm{d}K_j\right] \exp\left[-\frac{\epsilon}{2\kappa^2}\sum_{j=0}^{N-1} K_j^2\right]} \tag{8}$$

where $K_j \equiv K(j\epsilon)$ and the period of each time-slice $\epsilon = t/N$. We require that ϵ is of the order or larger than $\Omega_{\max}^{-1}$. This random-field model is equivalent to the Ohmic high-temperature bath of oscillators with

$$\kappa^2 = \frac{\alpha\pi C^2(k_{\mathrm{B}}T)}{m} = \frac{\pi\hbar\tilde{C}^2(k_{\mathrm{B}}T)}{g^2\mu^2}. \tag{9}$$

In general this equivalence does not aid our calculations. However there is one limit for which the random-field interpretation enables us to derive the results in a much simpler and more intuitive manner. This is the limit in which $\Omega_{\max} \ll g\mu B/\hbar$. Then the spin in the random field model can adiabatically follow the field $\boldsymbol{B}(t) + \hat{\boldsymbol{z}}K(t)$, because $K(t)$ varies smoothly on time-scales of order $\Omega_{\max}^{-1} \gg \hbar/(g\mu B)$. The exact requirement for the spin to adiabatically follow the field is that at all times

$$\frac{\mathrm{d}}{\mathrm{d}t}\left[\frac{\boldsymbol{B}(t) + \hat{\boldsymbol{z}}K(t)}{|\boldsymbol{B}(t) + \hat{\boldsymbol{z}}K(t)|}\right] \ll \frac{g\mu}{\hbar}\left|\boldsymbol{B}(t) + \hat{\boldsymbol{z}}K(t)\right|. \tag{10}$$

We assume that fluctuations in K are given by $\langle K^2\rangle^{1/2} \sim \kappa\Omega_{\max}^{1/2}$ for time-scales greater than $\Omega_{\max}^{-1}$, while K varies smoothly on time-scales shorter than that. If $B \gg \langle K^2\rangle^{1/2}$ then we do not need any detailed information on the dynamics of K on these short time-scales. We will restrict ourselves to the limit where $B \gg \langle K^2\rangle^{1/2}$ and $B \gg \hbar\Omega_{\max}/g\mu$. Hence the adiabaticity condition, Eq. (10), is reduced to $\kappa\Omega_{\max}^{3/2}/B^2 \ll 1$, which is automatically fulfilled in this limit.

The limit defined by these approximations is easy to work in because it is only in this limit that we are allowed to take the adiabatic limit first and then do the averaging.

If we consider the same time-dependence for $\boldsymbol{B}(t)$ as we did for the isolated spin, then we can simplify the problem significantly by going to the reference frame which rotates with $\boldsymbol{B}(t)$, see Fig. 1. Remember that in the non-rotating frame $K(t)$ fluctuates in the $\hat{\boldsymbol{z}}$-direction. Thus it unaffected by going to the rotating frame, in other words $\boldsymbol{K}'(t)$ as $\boldsymbol{K}(t)$. In the frame which rotates with angular velocity $\boldsymbol{\omega} = \pm\hat{\boldsymbol{z}}\omega$ the total phase acquired in time, $t_{\rm period}$, is simply the dynamic phase in this rotating frame,

$$\Phi(\pm\omega) = \frac{g\mu}{2\hbar}\int_0^{t_{\rm period}} \left|\boldsymbol{B}' \mp (\hbar/g\mu)\hat{\boldsymbol{z}}\omega + \hat{\boldsymbol{z}}K(t)\right| {\rm d}t \tag{11}$$

The path of $(\boldsymbol{B}(0) \mp (\hbar/g\mu)\hat{\boldsymbol{z}}\omega + \hat{\boldsymbol{z}}K(t))$ encloses no area in the rotating frame, so there is no Berry phase in this frame. It is important to remember that this does not mean there is no Berry phase in the laboratory frame. We have already seen this for the case where $\hat{\boldsymbol{z}}K(t) = 0$. Then there is no Berry phase in the rotating frame, but there is in the laboratory frame (as shown in Section 3). To identify the Berry phase we must first ensure $\omega = 2\pi/t_{\rm period}$, the Berry phase will then be the $t_{\rm period}$-independent component of the total phase.

We now wish to calculate the averaged propagation probability for evolution under the time-dependent $\boldsymbol{B}$-field described in Section 3. Before averaging the propagation probability is given by (7) with the phase $4\Phi_{\rm Berry}$ replaced by $2\left[\Phi(\omega) - \Phi(-\omega)\right]$, where $\Phi(\pm\omega)$ are given in (11). We can then average using (8). While in general carrying out the averaging is difficult, it is straightforward in the limit we are considering — $B \gg \langle K^2\rangle^{1/2}$ and $B \gg \hbar\Omega_{\rm max}/g\mu$. We will time-slice the propagator, writing the integral over time in the exponent as a sum of N time-slices each of which takes a time $\epsilon = t/N$. We use (8) to average the propagation probability, by evaluating a few Gaussian integrals. We find the random fluctuations of $K(t)$ cause the phase to acquire an imaginary part and an extra real part. The former causes an exponential decay of all in terms containing phase information. The latter means that the phase which is observed is different from the $K(t) = 0$ case. We extract the contributions to the Berry phase by finding the parts of the total phase which which are independent of $t_{\rm period}$. Similarly the contribution to the dynamic phase is the part of the total phase which scales linearly with $t_{\rm period}$. We then interpret the κ-dependent contribution to the dynamic phase as being a Lamb shift of the energy levels. In the language introduced in Section 1,

$$\begin{aligned}
\frac{1}{T_1} &= 0 & \frac{1}{T_2} &= \frac{1}{2}\left(\frac{g\mu\kappa}{\hbar}\right)^2\cos^2\theta \\
\frac{\delta E}{\hbar} &= \frac{1}{\#}\frac{g\mu\kappa^2\Omega_{\rm max}}{2\hbar B}\sin^2\theta & \delta\Phi_{\rm Berry} &= \frac{1}{\#}\frac{\pi\kappa^2\Omega_{\rm max}}{2B^2}\sin^2\theta\cos\theta.
\end{aligned} \tag{12}$$

where $\# = \epsilon\Omega_{\rm max}$ is a integer larger than one but still of order one. This means that the results are not independent of our choice of time-slicing for the averaging. This is not surprising since there is a time-scale ($\Omega_{\rm max}$) below which the field $K(t)$ is highly-correlated. This calculation is not sophisticated enough to tell us what # should be. However we can compare (12) with (4) using (9) and the large-x expansion of the Exponential integral, ${\rm Ei}(x) = -{\rm e}^x\left(x^{-1} + x^{-2} + \cdots\right)$. In this case we see the two sets of results agree completely if we set $\# = \pi$.

This derivation makes it very clear that $T_1 \to \infty$ in this limit because slow fluctuations of the field can dephase but not flip the spin. It also shows — in a more transparent manner than the calculation discussed in Section 2 — that the environment can modify the dynamic and Berry phases.

Acknowledgments

We gratefully acknowledge useful discussions with Qian Niu, Rosario Fazio and Frank Wilhelm. The research was supported by the U.S.-Israel Binational Science Foundation (BSF), by the Minerva Foundation, by the Israel Science Foundation – Center of Excellence, and by the German-Israel Foundation (GIF).

References

1. M.V. Berry, Proc. R. Soc. Lond. **392**, 45 (1984).
2. See references in the following review letter J. Anandan, J. Christian and K. Wanelik,Am. J. Phys. **65**, 180 (1997).
3. See for example D.J. Thouless, *Topological quantum numbers in non-relativistic physics* (World Scientific, Singapore, 1998).
4. P. Ao and D.J. Thouless, Phys. Rev. Lett. **70**, 2158 (1993). X.-M. Zhu, E. Brändström, and B. Sundqvist, Phys. Rev. Lett. **78**, 122 (1997).
5. F. Gaitan, Phys. Rev. A **58**, 1665 (1998).
6. P. Ao and X.-M. Zhu, Phys. Rev. B **60**, 6850 (1999).
7. J.E. Avron and A. Elgart, Phys. Rev. A **58**, 4300 (1998); Comm. Mat. Phys. **203**, 445 (1999).
8. R.S. Whitney and Y. Gefen - to be published.
9. J.A. Jones, V. Vedral, A. Ekert and G. Castagnoli, Nature **403**, 869 (2000). A. Ekert, M. Ericsson, P. Hayden, H. Inamori, J.A. Jones, D.K.L.Oi and V. Vedral , J. Mod. Opt. **47**, 2501 (2000).
10. G. Falci, R. Fazio, G.M. Palma, J. Siewert and V. Vedral, Nature **407**, 355 (2000).
11. A.O. Caldiera and A.J. Leggett, Physica **121A**, 587 (1983); Ann. Phys. **149**, 374 (1983).
12. See for example S.S. Schweber, *An Introduction to Relativistic Quantum Field Theory* (Row Peterson, Evanston, 1961).
13. A.J. Leggett, S. Chakravarty, A.T. Dorsey, M.P.A. Fisher, A. Garg and W. Zwerger, Rev. Mod. Phys. **59**, 1 (1987), and references therein.
14. R.P. Feynman and F.L. Vernon, Ann. Phys. **24**, 118 (1963).

ELECTRONIC CORRELATIONS

INFLUENCE OF MAGNETIC FIELD ON EFFECTIVE ELECTRON-ELECTRON INTERACTIONS IN A COPPER WIRE

A. Anthore, F. Pierre*, H. Pothier, D. Esteve, and M. H. Devoret
Service de Physique de l'Etat Condensé, Commissariat à l'Energie Atomique, Saclay, F-91191 Gif-sur-Yvette, France
(Present address: Michigan State University, East Lansing, MI 48824, USA)*

We have measured in a copper wire the energy exchange rate between quasiparticles as a function of the applied magnetic field. We find that the effective electron-electron interaction is strongly modified by the magnetic field, suggesting that magnetic impurities play a role on the interaction processes.

In metallic wires, electron-electron interactions lead to quasi-elastic scattering, which modifies the electron phase-coherence time, and to inelastic scattering, which redistributes energy between electrons. Several recent experiments have shown that these properties can be sample-dependent [1,2]. We have found furthermore that the low-temperature saturation of the phase-coherence time τ_φ of quasiparticles, observed in several experiments, is correlated with an anomalous dependence on the exchanged energy ε of $K(\varepsilon)$, a function proportional to the averaged squared interaction between two quasiparticles. The theoretical predictions, for pure Coulomb interactions [3], $\tau_\varphi \propto T^{-2/3}$ and $K(\varepsilon) \propto \varepsilon^{-3/2}$, were observed in silver wires [4], whereas a "saturating" τ_φ and $K(\varepsilon) \propto \varepsilon^{-2}$ were systematically found in copper wires [5,6]. In gold wires in which the presence of a large concentration of magnetic impurities ($\sim$ 50 ppm of iron) could be assessed, $K(\varepsilon)$ was also found to behave as ε^{-2}, with a particulary large prefactor [7]. On the theoretical side, it was recently understood that scattering by magnetic impurities, which limits the phase coherence time on a large range of temperature, can also provide another channel for energy exchange between quasiparticles [8,9,10]. In order to probe if magnetic impurities indeed play a role in copper wires, we have measured the magnetic field dependence of the energy exchange rate.

1 Measurement set-up

1.1 Principle of the experiment

In order to measure the energy exchange rates between quasiparticles, we have determined the local electron energy distribution function $f(x, E)$ in a stationary out-of-equilibrium situation [5], as described in Fig. 1. A mesoscopic metallic wire is placed between two large electrodes implementing Landauer reservoirs. In the absence of interactions, the population of quasiparticles at a given energy interpolates linearly between the distribution functions in the contacts, leading, if $k_B T \ll eU$, to a double-step-shaped distribution function. In the opposite "hot electron" regime, *i.e.* when the typical interaction time is much shorter than the diffusion time $\tau_D = L^2/D$, equilibrium is reached locally at each position along the wire: the energy distribution function $f(x, E)$ is a Fermi function, with a temperature dependent on the position along the wire [11,12]. Our experiments focus on the intermediate regime, in which interactions lead to a significant redistribution of the energy between quasiparticles, but not to a complete thermalization.

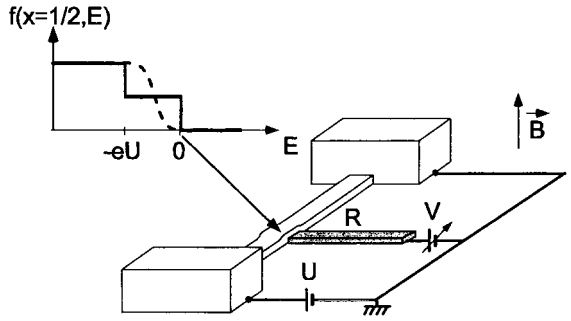


Figure 1: Experimental layout: A metallic wire of length L is connected to large reservoir electrodes, biased at potentials 0 and U. In the absence of interactions, the distribution function in the middle of the wire displays a step with height 1/2 for energies between $-eU$ and 0 (solid curve). When interactions are strong enough to thermalize electrons, the distribution function is a Fermi function (dashed curve). In the experiment, the distribution function is obtained from the differential conductance $\frac{dI}{dV}(V)$ of the tunnel junction formed by the wire and a reference resistive electrode placed underneath.

In previous experiments[4,5], the distribution function was infered from the differential conductance $\frac{dI}{dV}(V)$ of a tunnel junction between the wire and a superconducting probe electrode. Here the probe electrode, also fabricated with a superconducting metal (Aluminum), was designed as a long (25 μm), narrow (150 nm) and thin (12 nm) wire in order to present an appreciable resistance ($\sim$ 1 kΩ) in the normal state. In zero-magnetic field, the probe electrode was superconducting and the distribution function could be obtained as in the earlier experiments. In a magnetic field larger than 0.15 T, the probe electrode was normal and resistive. In this regime, dynamical Coulomb blockade of tunneling through the junction resulting from this "environmental" resistance[13] can be exploited as a quasiparticle energy probe. The relationship between the differential conductance of the junction $\frac{dI}{dV}(V)$ and the distribution function in the wire $f(E)$ is then:

$$\frac{dI}{dV}(V) = \frac{1}{R_T}\int dE\ f(E)\ \int d\varepsilon\ P(\varepsilon)\ \frac{\partial}{\partial E}((f_{\rm ref}(E+eV+\varepsilon) - f_{\rm ref}(E+eV-\varepsilon)) \qquad (1)$$

where R_T is the tunnel resistance of the junction, $f_{\rm ref}(E)$ the distribution function in the resistive electrode, assumed to be a Fermi function at temperature $T_{\rm ref}$, and $P(\varepsilon)$ the probability for an electron to tunnel through the barrier while giving the environnement the energy ε:

$$P(\varepsilon) = \int dt\ \exp[i\varepsilon t/\hbar]\ \exp J(t)$$

with

$$J(t) = 2\int_0^\infty \frac{d\omega}{\omega}\ \frac{{\rm Re}[Z_{\rm env}(\omega)]}{R_K}\ \frac{\exp[-i\omega t]-1}{1-\exp[-\hbar\omega/k_BT]}$$

where $R_K = \frac{h}{e^2} \approx 25.8$ kΩ, $Z_{\rm env}$ and T are the environmental impedance and temperature. In our set-up, the environment consists of the parallel combination of the capacitance C of the junction and the resistance R of the probe electrode.

In order to evaluate the sensitivity of this novel technique, we show in Fig. 2 the calculated differential conductance for characteristics of the environment close to the experimental ones and for two distribution functions in the wire: a Fermi function, as expected at $U = 0$, and a typical double-step function for $U = 0.3$ mV. The zero-bias conductance dip splits into a double-dip for a double-step distribution function. In the experiment, we invert the transformation shown in Fig. 2 and determine the unknown $f(E)$ from the measured $\frac{dI}{dV}(V)$.

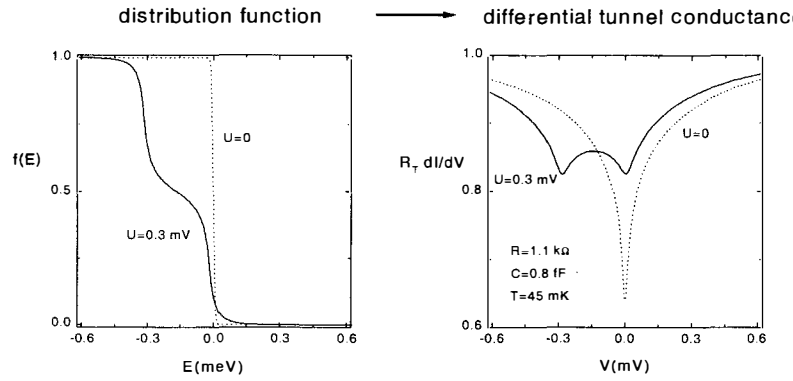


Figure 2: Computer-generated distribution functions at $U = 0$ and at $U = 0.3$ mV, with $kT = 0.004$ meV (left panel), and corresponding calculated differential conductance of the probe junction (right panel) for characteristics of the environment close to the experimental ones.

1.2 Experimental techniques

The sample was fabricated in a single pump-down, using three-angle shadow-mask technique through a PMMA suspended mask patterned using e-beam lithography. The substrate was thermally oxidized silicon. We first deposited a 12 nm-thick aluminum film defining the probe finger. It was then oxidized, in order to obtain the tunnel barrier. The wire and the reservoirs were obtained by the subsequent evaporation from a 99.999 % purity copper target, at a pressure of 10^{-6} mb, at a deposition rate of 1 nm/s. The thickness and width of the wire are 45 nm and 105 nm. The reservoirs are 400 nm-thick, with an area of about 1 mm^2. From the low temperature wire resistance $R = 29.5\ \Omega$, we deduced from Einstein's relation, assuming a rectangular cross-section, the diffusion constant $D = 90$ cm^2/s and the diffusion time $\tau_D = 2.8$ ns. The sample was mounted in a copper box thermally anchored to the mixing chamber of a dilution refrigerator. Measurements were performed at 25 mK. Electrical connections were made through filtered coaxial lines[14].

Measurements proceed as follows. In a first step, the voltage U is set to zero. The measured differential conductance of the tunnel junction $\frac{dI}{dV}(V)$, shown in Fig. 3, was found to be independent of the magnetic field at $B > 0.15$ T, a value at which all traces of superconductivity in the probe electrode are washed out. From the fit of $\frac{dI}{dV}(V)$ with Eq. 1, assuming $f(E) = f_{\rm ref}(E)$ and $T_{\rm ref} = T$, we deduce the tunnel junction conductance $R_{\rm T}^{-1} = 23\ \mu$S, the resistance of the probe electrode $R = 1.1$ kΩ, the tunnel junction capacitance $C = 0.8$ fF, and the temperature $T = 68$ mK. This excess temperature compared to the temperature of the mixing chamber of the dilution refrigerator (25 mK), might be due to an oversimplification of the environmental impedance, or to external noise. This question still has to be settled.

In a second step, the voltage U is set to a finite value. We fit the measured $\frac{dI}{dV}(V)$ with the calculated differential conductance using Eq. 1. The function $P(\varepsilon)$ is calculated with the environmental characteristics (R, C, T) determined at $U = 0$ and the fit parameters are the values of $f(E)$ at fourty regularly spaced energy values between $-eU - 0.1$ meV and 0.1 meV. Note that setting the temperature $T_{\rm ref}$ of the Fermi function $f_{\rm ref}(E)$ in the probe electrode also to 68 mK causing numerical instabilities, the data shown here were obtained with $T_{\rm ref} = 0$.

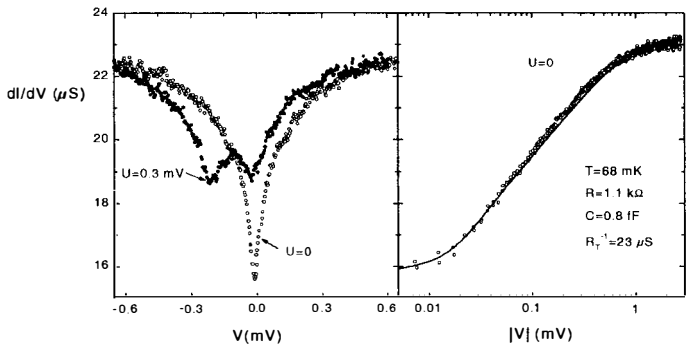


Figure 3: Left panel: Measured differential conductance at $B = 0.8$ T for $U = 0$ (open symbols) and $U = 0.3$ mV (black symbols). Right panel: Data at $U = 0$ reploted on a log-scale, together with the best fit with Eq. 1 (solid line) obtained with $R_T^{-1} = 23$ μS, $R = 1.1$ kΩ, $C = 0.8$ fF, and $T = 68$ mK.

2 Experimental results

2.1 Distribution functions

We show in Fig. 4 the distribution functions for two bias-voltages $U = 0.1$ mV and $U = 0.3$ mV and for magnetic fields varying from 0.16 T to 2 T. Also shown with dotted lines are the zero-magnetic field curves, obtained with the probe in the superconducting state.

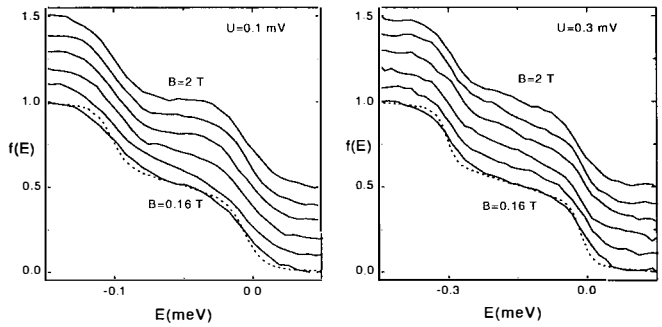


Figure 4: Measured distribution functions in the middle of the 5 μm-long copper wire. Solid line, from bottom to top: $B = 0.16$, 0.4, 0.8, 1.2, 1.6, and 2 T. Distribution functions are shifted vertically by steps of 0.1. Dotted line: Measured distribution function at $B = 0$, obtained with the probe in the superconducting state.

In zero-magnetic field, we find that $f(E)$ only depends on E/eU. Such a scaling property was found in all previous experiments on copper wires[5,6]. In a magnetic field, scaling does not hold any more. Besides, the evolution of $f(E)$ with the magnetic field is voltage-dependent: at $U = 0.1$ mV, the plateau of the measured distribution functions near $f(E) = 0.5$ first gets steeper with the magnetic field up to 0.4 T, then flattens and is finally horizontal at $B = 2$ T; at $U = 0.3$ mV, it gets steeper as the magnetic field increases up to $B = 1.6$ T, then flattens again.

The excess rounding of the steps in a magnetic field compared to the zero-magnetic field data might be due to the choice $T_{\rm ref} = 0$ in the deconvolution procedure, to an oversimplification of

the environmental impedance, to external noise, or, more fundamentally, to an increased energy exchange rate at low energies.

In the next section, we quantify the dependence of the interaction on B and U.

2.2 Energy exchange rates

The distribution function can be calculated by solving the stationary Boltzmann equation in the diffusive regime[12,15]:

$$\frac{1}{\tau_D}\frac{\partial^2 f(x,E)}{\partial x^2} + \mathcal{I}^{\rm in}_{\rm coll}(x,E,\{f\}) - \mathcal{I}^{\rm out}_{\rm coll}(x,E,\{f\}) = 0 \tag{2}$$

where $\mathcal{I}^{\rm in}_{\rm coll}(x,E,\{f\})$ and $\mathcal{I}^{\rm out}_{\rm coll}(x,E,\{f\})$ are the rates at which quasiparticles are scattered in and out of a state at energy E by inelastic processes. Assuming that the dominant inelastic process is a two-quasiparticle interaction which is local on the scale of variations of the distribution function,

$$\mathcal{I}^{\rm in}_{\rm coll}(x,E,\{f\}) = \int {\rm d}\varepsilon {\rm d}E' K(\varepsilon)\, f^x_{E+\varepsilon}(1-f^x_E) f^x_{E'}(1-f^x_{E'-\varepsilon}) \tag{3}$$

where the shorthand f^x_E stands for $f(x,E)$. The out-collision term $\mathcal{I}^{\rm out}_{\rm coll}$ has a similar form. The kernel function $K(\varepsilon)$ is proportional to the averaged squared interaction between two quasiparticles exchanging an energy ε. We have neglected the possible dependence of $K(\varepsilon)$ on the energies of the initial and final states and on the position along the wire. The theory of Coulomb interactions in disordered wires predicts $K(\varepsilon) \propto \varepsilon^{-3/2}$. However, in copper wires, at zero-magnetic field, the scaling property implies, by a simple change of variables in Eq. 2, that $U^2 K(\varepsilon)$ is a function of ε/eU only[16]. If futhermore $K(\varepsilon)$ does not depend on U, one obtains $K(\varepsilon) = \gamma/\varepsilon^2$, with γ a typical interaction rate, independent of U.

We have found that the curves $f(E)$ measured in a magnetic field could also be reasonably fitted assuming $K(\varepsilon) = \gamma(U,B)/\varepsilon^2$ where $\gamma(U,B)$ is now a fit parameter for each curve. It is only in zero-magnetic field that $\gamma(U,0)$ is independant of U. We show in Fig. 5 the evolution of this effective intensity $\gamma(U,B)$ with the bias voltage and the magnetic field, in a grayscale plot. One observes that the typical interaction rate has a non-monotonous behaviour with B. It increases roughly from $B=0$ to $B \approx \frac{eU}{4.3\mu_B}$ then decreases again. The zero-magnetic-field value $\gamma(U,0) = 0.52$ ns^{-1} is recovered near $B \approx \frac{eU}{2\mu_B}$ (see straight line on Fig. 5).

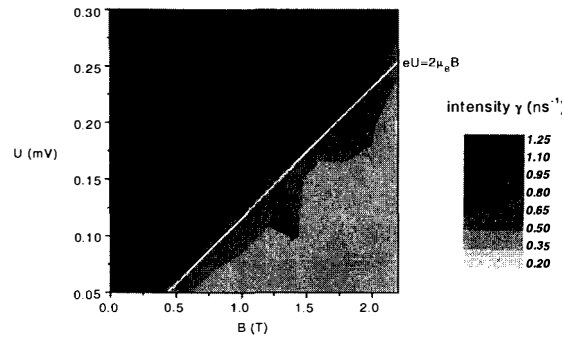


Figure 5: Evolution of the interaction intensity γ with the magnetic field B and the bias voltage U obtained from a fit assuming $K(\varepsilon) = \gamma/\varepsilon^2$. The straight line is $eU = 2\mu_B B$.

3 Magnetic-impurity-mediated energy exchange between electrons

Kaminski and Glazman have proposed a second order process associated with magnetic impurities in which energy is exchanged between quasiparticles [8]. In the top of Fig. 6, we describe this second-order process in the situation where, due to Zeeman effect, the spin-up and the spin-down states of the magnetic impurities are split by the energy $g\mu_B B$. For simplicity, the impurities are assumed to be spin 1/2; g is the gyromagnetic factor of the impurities. In Fig. 6, the initial polarisation of the impurity is assumed to correspond to its lowest-energy state. The energy of the intermediate state is then $-\varepsilon + g\mu_B B$, so that the rate of this process of second order in perturbation is proportional to $(-\varepsilon + g\mu_B B)^{-2}$. At $B = 0$, one obtains $K(\varepsilon) \propto \varepsilon^{-2}$.

On the other hand, in a magnetic field, inelastic scattering also occurs in the first order process: the energy $\pm g\mu_B B$ is exchanged directly between an electron and a magnetic impurity (see Fig. 6, bottom). The magnetic impurities then behaves as two-level systems, the occupation of the two states being determined self-consistently, at each position along ther wire, by the coupling to the quasiparticles [4]. This process could explain why the interaction rate γ first increases with magnetic field.

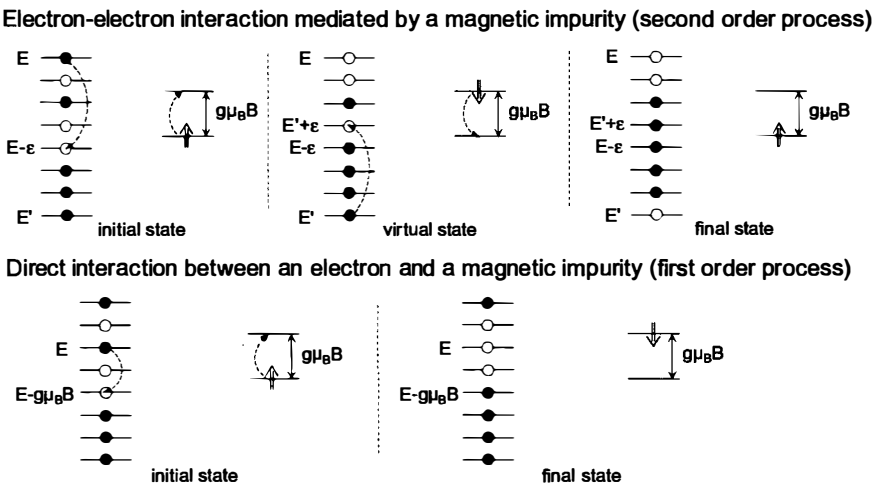


Figure 6: Description of the processes of redistribution of energy between quasiparticles mediated by magnetic impurity. In each panel, the left ladder represents the energy spectrum of the quasiparticles and the two states on the right side represent the energy levels of the spin-up and spin-down state of a magnetic impurity. Top: The second order process implies two electrons and the spin of a magnetic impurity. Bottom: The first order process directly exchanges $g\mu_B B$ between an electron and the spin of a magnetic impurity.

If the splitting $g\mu_B B$ becomes larger than eU, starting from an occupied electron-state at energy E, the state of energy $E - g\mu_B B$ is occupied. Then, due to Pauli principle, the rate for first order processes vanishes, and the magnetic impurities remain in their ground state. The rate of the second-order processes also vanishes at large magnetic fields because of the $g\mu_B B$ term in its denominator and of the Pauli constraint $\varepsilon \lesssim eU$. This explains the decrease of the interaction rate at $B \approx \frac{eU}{g\mu_B}$.

A quantitative description of these processes, taking into account the renormalisation of the coupling between quasiparticles and magnetic impurities due to Kondo effect, is under progress [17].

In conclusion, we have found that the anomalous energy exchange rate between quasiparticles in copper wire strongly depends on magnetic field. The magnetic field and bias-voltage dependence of the intensity of the interaction are in qualitative agreement with a magnetic-impurity-mediated interaction. The nature of the magnetic impurities is not known, but measurements of the phase-coherence time give evidence that the copper oxyde might play a role[18].

Acknowledgments

We are grateful to G. Göppert, H. Grabert, T. Giamarchi and A. Georges for useful discussions and comments, P. Joyez for permanent assistance, and P.F. Orfila for technical support. This work was partially supported by the Bureau National de Métrologie.

References

1. S. Wind, M.J. Rooks, V. Chandrasekhar, and D.E. Prober, Phys. Rev. Lett. **57**, 633 (1986); P.M. Echternach, M.E. Gershenson, H.M. Bozler, A.L. Bogdanov and B. Nilsson, *Phys. Rev.* **B 48**, 11516 (1993); P. Mohanty, E.M.Q. Jariwala and R.A. Webb, *Phys. Rev. Lett.* **78**, 3366 (1997).
2. A.B. Gougam, F. Pierre, H. Pothier, D. Esteve, and N.O. Birge, *J. Low Temp. Phys.* **118**, 447 (2000).
3. For a review, see B.L. Altshuler and A.G. Aronov, in *Electron-Electron Interactions in Disordered Systems,* Ed. A.L. Efros and M. Pollak (Elsevier Science Publishers B.V., 1985).
4. F. Pierre, H. Pothier, D. Esteve, and M. H. Devoret, *J. Low Temp. Phys.* **118**, 437 (2000)
5. H. Pothier, S. Guéron, Norman O. Birge, D. Esteve, and M. H. Devoret, *Phys. Rev. Lett.* **79**, 3490 (1997).
6. F. Pierre, thesis, Université Paris 6, Paris, 2000.
7. F. Pierre, H. Pothier, D. Esteve, M. H. Devoret, A. B. Gougam, and Norman O. Birge, Proceedings of the NATO Advanced Research Workshop on *Size Dependent Magnetic Scattering*, Ed. V. Chandrasekhar and C. Van Haesendonck (2001). (cond-mat/0012038)
8. A. Kaminski and L. I. Glazman, *Phys. Rev. Lett.* **86**, 2400 (2001).
9. G. Göppert and H. Grabert, *Phys. Rev.* **B 64**, 033301 (2001).
10. J. Kroha and A. Zawadowski, cond-mat/0104151.
11. A. H. Steinbach, J. M. Martinis, and M. H. Devoret, *Phys. Rev. Lett.* **76**, 3806 (1996).
12. V. I. Kozub and A. M. Rudin, *Phys. Rev.* **B 52**, 7853 (1995).
13. For a review, see G.-L. Ingold and Yu. Nazarov, in *Single Charge Tunneling,* Ed. H. Grabert and M. H. Devoret (Plenum Press, New York, 1992).
14. D. Vion, P.F. Orfila, P. Joyez, D. Esteve, and M. H. Devoret, *J. Appl. Phys.* **77**, 2519 (1995).
15. K.E. Nagaev, *Phys. Lett. A* **169**, 103 (1992); *Phys. Rev.* **B 52**, 4740 (1995).
16. H. Pothier, S. Guéron, Norman O. Birge, D. Esteve, and M. H. Devoret, *Z. Phys.* **B 104**, 178 (1997).
17. G. Göppert, private communication.
18. J. Vranken, C. Van Haesendonck, and Y. Bruynseraede, *Phys. Rev.* **B 37**, 8502 (1988).

QUANTUM INTERFERENCE AND COULOMB INTERACTION IN GRANULATED METALS

K.B. EFETOV[1], I.S. BELOBORODOV[1], A. ALTLAND[1], F.W.J. HEKKING[2]
[1] *Theoretische Physik III, Ruhr-Universität Bochum*

[2] *CNRS-CRTBT and UniversitéJoseph Fourter, 38042 Grenoble Cedex 9, France*

We study electronic properties of an array of small metallic grains connected by tunnel junctions. Such an array serves as a model for a granular metal. Previous theoretical studies of junction arrays were based on models of quantum dissipation which did not take into account the diffusive motion of electrons within the grains. We demonstrate that these models break down at sufficiently low temperatures: for a correct description of the screening properties of a granular metal at low energies the diffusive nature of the electronic motion within the grains is crucial. We present both a diagrammatic and a functional integral approach to analyse the properties of junction arrays. In particular, a new effective action is obtained which enables us to describe the array at arbitrary temperature. In the low temperature limit, our theory yields the correct, dynamically screened Coulomb interaction of a normal metal, whereas at high temperatures the standard description in terms of quantum dissipation is recovered.

1 Introduction

A considerable attention has been devoted recently to study of disordered bulk metals with electron-electron interactions [1,2,3] from the one hand and arrays of normal metallic grains connected by tunnel junctions [4] from the other. The Coulomb interaction plays a very important role in both types of system and many non-trivial physical effects occur due to it. In disordered metals, *e.g.*, the Coulomb interaction results in quantum corrections to conductivity and reduces the density of states, a phenomenon known as zero bias anomaly. Qualitatively similar effects were predicted and studied experimentally [5,7,6,8] for arrays of tunnel junctions in the normal state, where a sufficiently strong Coulomb interaction can suppress the conductivity (Coulomb blockade of tunneling).

In spite of the similarities in the physical behavior of disordered metals and normal arrays of tunnel junctions, completely different approaches are used for the theoretical description of these respective systems. As concerns disordered metals with interaction, either diagrammatic methods [1] or non-linear σ-models [9,10,11] are employed. The starting point of these theories is a model of a weakly disordered bulk metal. On the other hand, for the description of Coulomb blockade effects in a junction array or a granular material, a completely different approach based on the theory of Ambegaokar, Eckern and Schön (AES) [12] is commonly used.

We suggest a scheme unifying these two approaches and demonstrate that the previous theories describe the same granulated system in different temperature regimes. We consider a granular normal metal with Coulomb interaction between electrons that may lead Coulomb blockade effects. We assume that the macroscopic dimensionless conductance g_T of the granular metal is large, which enables us to develop a perturbative theory with g_T^{-1} as the small parameter. Within this theory, physical quantities can be calculated at arbitrary temperatures. The diagrammatic analysis is supplemented by the derivation of a σ-model that can be considerably simplified provided one does not take into account weak localization effects.

2 The model

We consider a d-dimensional array of normal metallic grains coupled to each other. It is assumed that there can be impurities inside them as well as on their surface. The mean level spacing in

a single grain is equal to $\delta = (\nu V)^{-1}$. However, the shapes of the grains need not considerably differ from each other and we assume for simplicity that the grains are arranged in a cubic lattice. The electrons can hop from grain to grain; moreover, they interact with each other. We are interested only in the long range part of the Coulomb interaction. In such a formulation the spin of the electrons is not important.

Under these assumptions the electron motion can be conveniently described by a functional integral of the type

$$\int \exp\left(-S[\psi]\right) \mathcal{D}\psi,$$

with an action $S[\psi]$ that can be written in the form

$$S[\psi] = S_{\mathrm{g}}[\psi] + S_{\mathrm{t}}[\psi] + S_{\mathrm{c}}[\psi]. \tag{1}$$

The action $S_{\mathrm{g}}[\psi]$ in Eq. (1) describes the electron motion within the grains and we write it in the form

$$S_{\mathrm{g}}[\psi] = \sum_i \int_0^\beta d\tau d\tau \psi_i^*(\tau, r) \left(\partial_\tau - \mu + \hat{H}_i\right) \psi_i(\tau, r), \tag{2}$$

where $\psi_i(\tau, r)$ is a fermion field in grain i at imaginary time τ and coordinate r (ψ^* is its complex conjugate), μ is the chemical potential, and $\beta = T^{-1}$ is the inverse temperature.

The operator $\hat{H}_i$ in Eq. (2) includes both the kinetic energy and scattering by impurities. The action $S_{\mathrm{t}}[\psi]$ stands for tunneling between the grains,

$$S_{\mathrm{t}}[\psi] = \sum_{ij} \int_0^\beta d\tau \psi_i^*(\tau) t_{ij} \psi_j(\tau), \tag{3}$$

and $S_{\mathrm{c}}[\psi]$ describes the charging of the grains

$$S_{\mathrm{c}}[\psi] = \frac{e^2}{2} \sum_{ij} \int_0^\beta d\tau n_i(\tau) C_{ij}^{-1} n_j(\tau), \tag{4}$$

where

$$n_i(\tau) = \int dr \psi_i^*(\tau, r) \psi_i(\tau, r)$$

is the density field in grain i, e is the electron charge, and C_{ij} is the capacitance matrix.

A convenient way to calculate physical quantities of interest is to decouple the term $S_{\mathrm{c}}[\psi]$ by a Gaussian integration over auxiliary fields $V_i(\tau)$ and introduce the phases $\dot{\phi}_i(\tau) = V_i(\tau)$. Making the transformation [14]

$$\psi_i(\tau) \to \psi_i(\tau) \exp\left(-i\phi_i(\tau)\right) \tag{5}$$

one reduces the calculation of physical quantities to the computation of a functional integral of the form

$$\int \exp\left(-S_0[\psi] - S_1[\psi, \phi] - S_2[\phi]\right) \mathcal{D}\psi \mathcal{D}\phi, \tag{6}$$

where

$$S_0[\psi] = \sum_i \int_0^\beta d\tau \psi_i^*(\tau) \left(\partial_\tau - \mu + \hat{H}_i\right) \psi_i(\tau), \tag{7}$$

$$S_1[\psi, \phi] = \sum_{ij} \int_0^\beta d\tau t_{ij} \psi_i^*(\tau) \psi_j(\tau) \exp\left(i\phi_{ij}(\tau)\right), \tag{8}$$

$$S_2[\phi] = \int_0^\beta d\tau \sum_{ij} \frac{C_{ij}}{2e^2} \frac{d\phi_i(\tau)}{d\tau} \frac{d\phi_j(\tau)}{d\tau}, \tag{9}$$

and $\phi_{ij}(\tau) = \phi_i(\tau) - \phi_j(\tau)$.

Disorder is still present in the operators $\hat{H}_i$ but the mean free path within the grains is assumed to be large, $lk_0 \gg 1$, where k_0 is the Fermi momentum. In this limit, the macroscopic conductivity is determined mainly by the tunneling conductance g_T,

$$g_T = \pi/(2e^2 R_T) = 2\pi^2 t^2 \nu^2 \approx 6.45 k\Omega / R_T \tag{10}$$

where R_T is the tunneling resistance.

3 Perturbation theory

A functional integral formulation was used in Ref.[12] to treat the quantum dynamics of a Josephson junction. The action derived in that work (AES action) was used later in the context of a normal tunnel junction[4]. The AES action can be obtained from Eqs. (6- 9). First, one should average the Green function G_0 corresponding to the action $S_0[\psi]$, Eq. (7), over impurities in the first Born approximation. After that one should make a cumulant expansion in the term $S_1[\psi, \phi]$, Eq. (8). Keeping only the second order of the expansion and assuming for simplicity that the capacitance matrix C_{ij} is diagonal one arrives at the AES action $S_{\rm AES}[\phi]$[12],

$$S_{\rm AES}[\phi] = \frac{1}{4E_c} \sum_i \int_0^\beta d\tau \left(\frac{d\phi_i}{d\tau}\right)^2 + \frac{g_T}{2} \sum_{i,j} \int_0^\beta d\tau d\tau' \alpha(\tau - \tau') \left(1 - \cos\left(\phi_{ij}(\tau) - \phi_{ij}(\tau')\right)\right), \tag{11}$$

where

$$\alpha(\tau - \tau') = \frac{T^2}{\sin^2 \pi T(\tau - \tau')}. \tag{12}$$

In Eq. (11), E_c is the charging energy $E_c = e^2/2C_{ii}$. The second term in Eq. (11) contains the sum over neighboring grains and t is the tunneling energy between them. In the limit of small phase fluctuations we can expand the second term in Eq. (11) in ϕ_{ij}. In the Fourier representation one obtains

$$S[\phi] = \frac{1}{2} \sum_{\mathbf{k}} T \sum_{\omega_n} \left(\frac{\omega_n^2}{2E_c} + \frac{4g_T}{\pi} |\omega_n| \sum_a (1 - \cos \mathbf{k}\mathbf{d}_a) \right) |\phi_{\omega_n}(\mathbf{k})|^2, \tag{13}$$

where $\mathbf{d}_a$, $a = x, y, z$ are vectors connecting the centers of the neighboring grains and ω_n are the Matsubara frequencies. The phase-phase correlation function

$$\Pi_{\rm AES}(\omega_n, \mathbf{k}) = T \langle \phi_{\omega_n}(\mathbf{k}) \phi^*_{\omega_n}(\mathbf{k}) \rangle$$

can be immediately calculated using Eq. (13) and we obtain

$$\Pi_{\rm AES}(\omega_n, \mathbf{k}) = \frac{4E_c}{\omega_n^2 + \frac{8}{\pi} g_T E_c |\omega_n| \sum_a (1 - \cos \mathbf{k}\mathbf{d}_a)}. \tag{14}$$

It is clear from general principles that, in the limit of small frequencies and wave vectors k, the network considered should correspond to a bulk normal metal, where one should have the propagator corresponding to a screened Coulomb interaction. However, the limit $\omega,\ k \to 0$ in Eq. (14) does not reproduce the screened Coulomb interaction.

In order to resolve this discrepancy we carry out an expansion in t_{ij} and demonstrate that keeping only the second order, which led us to Eq. (11) is not sufficient and that, in the limit of small frequencies or temperatures, one should sum up an infinite class of diagrams. These diagrams have a simple structure. Expanding in both the tunneling, the phases ϕ_{ij} and impurity

concentration one finds that the main contribution comes from diagrams that have a ladder structure. These diagrams contain only non-intersecting impurity lines and one can recognize the well-known diffusons.

In the present paper we consider the limit of sufficiently small grains, such that all relevant energies like temperature T, frequency ω, tunneling energy t, etc. are much smaller than the Thouless energy $E_T = \pi^2 D_0/R^2$,where D_0 is the diffusion coefficient of a single grain and R is the radius of the grain. In this limit the spectrum of the diffuson in a single grain is zero-dimensional. Coupling between the grains leads to a dependence on quasi-momentum $\mathbf{k}$ and can be accounted for by writing a geometric series for the function D describing the diffuson. As a result we obtain

$$D(\omega_n, \mathbf{k}) = \frac{2\pi\nu}{|\omega_n| + (2/\pi) g_T \delta \sum_{a=1}^{3} (1 - \cos k_a d)}. \tag{15}$$

This is a lattice version of the diffusion propagator. Many-diffuson contributions can be neglected provided the tunneling conductance g_T, Eq. (10), is large, $g_T \gg 1$, which means that we are far from the Anderson metal-insulator transition.

The averaging over the impurities and summation of the ladder diagrams allows to obtain the phase correlation function $\Pi(\omega_n, \mathbf{k})$ that should be written instead of $\Pi_{\mathrm{AES}}(\omega_n, \mathbf{k})$, Eq. (14). The result of the calculation is

$$\Pi(\omega_n, \mathbf{k}) = \frac{4E_c/\omega_n^2}{1 + 4E_c \frac{(2/\pi) g_T \sum_a (1 - \cos k_a d)}{|\omega_n| + (2/\pi) g_T \delta \sum_a (1 - \cos k_a d)}}. \tag{16}$$

Using the relation between the phase ϕ and the voltage V we derive an equation for the effective Coulomb interaction

$$V_{eff}(\omega_n, \mathbf{k}) = \omega_n^2 \Pi(\omega_n, \mathbf{k}). \tag{17}$$

The limit of small k in Eq. (17) coresponds to a screened Coulomb interaction of a bulk metal. Comparing Eq. (16) with Eq. (14) we see that the "quantum dissipation" model corresponds to the limit $T \gg g_T \delta$. Thus, we conclude that, when calculating physical quantities, the main contribution is due to small k only in the limit $T \ll g_T \delta$. Provided this inequality is satisfied, the properties of the tunnel junction array are equivalent to the properties of a weakly disordered bulk metal with Coulomb interaction.

Calculations were performed in this section using a diagrammatic expansion in the lowest order in the field ϕ. On the other hand, the AES free energy functional, Eq. (11), is written for arbitrary values of ϕ. One can generalize Eq. (17) to arbitrary values of ϕ writing a simplified version of a replica σ-model and using a non-trivial saddle point.

4 Effective action

We derive the effective action using the replica σ-model approach for interacting systems [3,9]. Although there are difficulties in using the replica σ-models for non-perturbative calculations, our goal is more modest and the final results obtained in the limit $g_T \gg 1$ neglecting all weak localization corrections will not depend on replica indices at all.

A proper σ-model for bulk systems with interaction has been derived in Refs. [3,9]. A generalization of the σ-model of Ref. [3,9] to granular metals can bee made without difficulties following Ref. [13], where a σ-model was written for a granular metal without interaction. Decoupling the Coulomb interaction by an auxiliary field V we obtain the variable ϕ. This variable appears

in addition to matrices Q in the σ-model. The final result for the free energy $F[Q,\phi]$ can be written as

$$F[Q,\phi] = F_2[\phi] + F_\omega + F_{\rm T}[Q,\phi], \tag{18}$$

$$F_2[\phi] = \frac{1}{2e^2}\sum_{i,j}\int {\rm tr} C_{ij}\frac{\partial\phi_i(\tau)}{\partial\tau}\frac{\partial\phi_j(\tau)}{\partial\tau}d\tau, \tag{19}$$

$$F_\omega[Q] = \frac{\pi}{\delta}\sum_i\int {\rm tr}(\hat{\omega}_\tau Q_i(\tau,\tau))d\tau, \tag{20}$$

$$F_{\rm T}[Q,\phi] = -\frac{g_T}{4}\sum_{i,j}\int {\rm tr}\left(e^{i\phi_{ij}(\tau)}Q_i(\tau,\tau')\,e^{-i\phi_{ij}(\tau')}Q_j(\tau',\tau)\right)d\tau d\tau', \tag{21}$$

where $\phi_{ij}(\tau) = \phi_i(\tau) - \phi_j(\tau)$. The field ϕ is diagonal in the replica indices, while the matrix $Q(\tau,\tau')$ is a $2r\times 2r$ (r is the number of replicas) matrix with the constraints

$$\int Q(\tau,\tau'')\,Q(\tau'',\tau')\,d\tau'' = \delta(\tau-\tau'),\quad {\rm tr}Q(\tau,\tau) = 0. \tag{22}$$

The limiting cases of the free energy $F[Q,\phi]$, Eqs. (18-22) are rather simple. Without electron-electron interaction the phase difference between neighboring grains equals zero $\phi_{ij}=0$. Such an action for granular metals corresponds to that derived within the supersymmetry scheme by one of the authors [13]. The second limiting case is achieved at sufficiently high temperatures. In this limit disorder is not important and the matrix Q does not fluctuate, being equal to the value Λ given by

$$\Lambda_{\tau,\tau'} = \frac{iT}{\sin T\pi(\tau-\tau')} \tag{23}$$

Inserting $Q=\Lambda$ into Eqs. (18-21) we reproduce immediately the AES action, Eq. (11) (in fact we obtain the r times replicated AES functional but only one replica field is important for us).

At not too high a temperature, a non-trivial behavior can be obtained even if the disorder is weak and all effects related to weak localization can be neglected. The limit of weak disorder enables us to neglect fluctuations of Q at given ϕ and take its value from a saddle-point equation. We thus reduce the computation of the functional integral with the free energy functional to the solution of a saddle-point equation, substituting the solution into the free energy $F[Q,\phi]$, Eqs. (18-21), and calculating a functional integral with the reduced free energy $\bar{F}[\phi]$

$$\bar{F}[\phi] = F[\bar{Q},\phi] \tag{24}$$

where $\bar{Q}$ is the solution of the saddle-point equation for a given ϕ.

Minimizing the functional $F[Q,\phi]$, Eqs. (18-21), with the constraints, Eqs. (22), we obtain the following equation

$$\frac{g_T}{2}\sum_j\int[e^{i\phi_{ij}(\tau)}\bar{Q}_i(\tau,\tau'')\,e^{-\phi_{ij}(\tau'')},\bar{Q}_j(\tau'',\tau')]d\tau'' + \frac{\pi}{\delta}[\bar{Q}_i(\tau,\tau),\hat{\omega})] = 0, \tag{25}$$

where the summation over j is performed over the nearest neighbors of i. In the commutator $[.,.]$ one should exchange properly the times when changing the order of the functions. In general, Eq. (25), can be solved only numerically but, in the limit $g_T \gg 1$, everything can be done analytically and one comes to Eq. (17) describing the screened Coulomb interaction of a normal metal.

With the explicit expression for the dynamically screened Coulomb interaction $V_{\rm eff}$ Eq. (17) we can calculate all physical quantities of interest. As an example, one can consider corrections to the conductivity and density of states that are known for bulk metals [1]. Since at small momenta the effective Coulomb interaction for granular materials, Eq. (17), agrees with the expression for a bulk metal, the corrections will have the same temperature dependence at low temperatures as those in Ref. [1].

5 Conclusion

In this paper we constructed a theory which describes arrays of tunnel junctions or granular metals, taking into account the effect of quantum interference. We considered the limit of large conductance $g_T \gg 1$. We demonstrated that at low temperatures $T < g_T\delta$ the disorder is very important and the motion of electrons is diffusive. It was shown that the so-called dissipation phenomenon corresponds to the screened Coulomb interaction at high temperatures. A field theoretical formulation to describe granular metals at arbitrary temperatures was given. Using the replica sigma-model, we derived a general action which, in the limit of large grains, yields the known AES [12] action. In the opposite limit we reproduce the known results for bulk metals. There is a number of experiments that could correspond to our theoretical prediction. For more detail one should read the original paper [15]

Acknowledgments

A support of the Graduiertenkolleg 384 and the Sonderforschungsbereich 237 is appreciated.

References

1. B.L. Altshuler and A.G. Aronov, in *Electron-Electron Interaction in Disordered Systems*, edited by A.L. Efros and M. Pollak, (North-Holland, Amsterdam, 1985).
2. P.A. Lee and T.V. Ramakrishnan, Rev. Mod. Phys. **57**, 287 (1985).
3. A.M. Finkelstein, *Electron Liquid in Disordered Conductors*, Vol. 14 of Soviet Scientific Reviews, ed. I.M. Khalatnikov, Harwood Academic Publishers, GmbH, London, 1990.
4. G. Schön and A.D. Zaikin, Phys. Rep. **198**, 237 (1990).
5. J.E. Mooij *et al.*, Phys. Rev. Lett. **65**, 645 (1990).
6. R. Yamada *et al.*, J. Phys. Soc. Jpn. **62**, 2229 (1993)
7. T.S. Tighe *et al.*, Phys. Rev. B **47**, 1145 (1993).
8. S. Kobayashi, A. Kanda, and R. Yamada, Jpn. J. Appl. Phys. **34**, 4548 (1995).
9. A.M. Finkelstein, Sov. Phys. JETP **57**, 97 (1983).
10. A. Kamenev and A. Andreev, Phys. Rev. B **60**, 2218 (1999).
11. C. Chamon, A.W.W. Ludwig, and C. Nayak, Phys. Rev. B **60**, 2239 (1999).
12. V. Ambegaokar, U. Eckern, and G. Schön, Phys. Rev. Lett. **48**, 1745 (1982).
13. K. B. Efetov, *Supersymmetry in Disoder and Chaos*, Cambridge University Press,(1997).
14. A. Kamenev, and Y. Gefen, Phys. Rev. B **54**, 5428 (1996).
15. I.S. Beloborodov, K.B. Efctov, A.Altland, F.W.J. Hekking, Phys.Rev.B 63, 115109 (2001)

Topological Confinement of Spins and Charges: Spinons as $\pi-$ junctions

S. Brazovskii [1,2]

[1] *Laboratoire de Physique Théorique et de s Modèles Statistiques, CNRS, Bât.100, Université Paris-Sud, 91405 Orsay cedex, France; http://ipnweb.in2p3.fr/ lptms/membres/brazov/ , brazov@ipno.in2p3.fr*

[2] *L.D. Landau Institute, Moscow, Russia.*

Topologically nontrivial states, the solitons, emerge as elementary excitations in $1D$ electronic systems. In a quasi $1D$ material the topological requirements originate the spin- or charge-roton like excitations with charge- or spin- kinks localized in the core. They result from the spin-charge recombination due to confinement and the combined symmetry. The rotons possess semi-integer winding numbers which may be relevant to configurations discussed in connection to quantum computing schemes. Practically important is the case of the spinon functioning as the single electronic $\pi-$ junction in a quasi $1D$ superconducting material.

1 Introduction to solitons.

Topological defects: solitons, vortices, anyons, etc., are discussed currently, see [1], in connection to new trends in physics of quantum devices, see [2]. Closest to applications and particularly addressed at this conference [3] are the $\pi-$ junctions which, linking two superconductors, provide degeneracy of their states with phase differences equal to 0 and 2π. The final goal of this publication is to show that in quasi one-dimensional ($1D$) superconductors the $\pi-$ junctions are produced already at the single electronic level extendible to a finite spin polarization. The effect results from reconciliation of the spin and the charge which have been separated at the single chain level. The charge and the spin of the single electron reconfine as soon as $2D$ or $3D$ long range correlations are established due to interchain coupling. The phenomenon is much more general taking place, in other respects, also in such a common system as the Charge Density Waves -CDWs and in such a popular system as the doped antiferromagnet or the Spin Density Wave as its quasi $1D$ version [4]. Actually in this article we shall consider firstly and in greater details the CDW which is an object a bit distant to the Moriond community. The applications to superconductors will become apparent afterwards. We shall concentrate on effects of interchain coupling $D > 1$: confinement, topological constraints, combined symmetry, spin-charge recombination. A short review and basic references on history of solitons and related topics in correlated electronic systems can be found in [4].

Solitons in superconducting wires were considered very early [6], within the macroscopic regime of the Ginzburg - Landau theory, for the phase slips problem. Closer to our goals is the microscopic solution for solitonic lattice in quasi $1D$ superconductors [7] at the Zeeman magnetic field. This successful of results from theory of CDWs, see [8], to superconductors provides also a link of pair breaking effects in these different systems. The solitonic structures in qasi $1D$ superconductors appear as a $1D$ version of the well known FFLO (Fulde, Ferrel, Larkin, Ovchinnikov) inhomogeneous state near the pair breaking limit. Being very weak in $3D$, this effect becomes quite pronounced in systems with nested Fermi surfaces which is the case of the $1D$ limit. To extend physics of solitons to the higher D world, the most important problem one faces is the effect of *confinement* (S.B. 1980): as topological objects connecting degenerate vacuums, the solitons at $D > 1$ acquire an infinite energy unless they reduce or compensate their topological charges. The problem is generic to solitons but it becomes particularly interesting at the single electronic level where the spin-charge reconfinement appears as the result of topological constraints. The topological effects of $D > 1$ ordering reconfines the charge and the spin *locally* while still with essentially different distributions. Nevertheless *integrally* one of the two is screened again, being transferred to the collective mode, so that in kinetics the massive particles carry only either

charge or spin as in $1D$, see the review [9].

2 Confinement and combined excitations.

2.1 The classical commensurate CDW: confinement of phase solitons and of kinks.

The CDWs were always considered as the most natural electronic systems to observe solitons. We shall devote to them some more attention because the CDWs also became the subject of studies in mesoscopics [10]. Being a case of spontaneous symmetry breaking, the CDW order parameter $O_{cdw} \sim \Delta \cos[\mathbf{Qr} + \varphi]$ possesses a manifold of degenerate ground states. For the $M-$fold commensurate CDW the energy $\sim \cos[M\varphi]$ reduces the allowed positions to multiples of $2\pi/M$, $M > 1$. Connecting trajectories $\varphi \rightarrow \varphi \pm 2\pi/M$ are phase solitons, or "$\varphi-$ particles" after Bishop *et al.* Particularly important is the case $M = 2$ for which solitons are clearly observed e.g. in polyacethelene [5] or in organic Mott insulators [11].

Above the $3D$ or $2D$ transition temperature T_c, the symmetry is not broken and solitons are allowed to exist as elementary particles. But in the symmetry broken phase at $T < T_c$, any local deformation must return the configuration to the same (modulo 2π for the phase) state. Otherwise the interchain interaction energy (with the linear density $F \sim \langle \Delta_0 \Delta_n \cos[\varphi_0 - \varphi_n] \rangle$ is lost when the effective phase $\varphi_0 + \pi sign(\Delta_0)$ at the soliton bearing chain $n = 0$ acquires a finite (and $\neq 2\pi$) increment with respect to the neighboring chain values φ_n. The $1D$ allowed solitons do not satisfy this condition which originates a constant *confinement force* F between them, hence the infinitely growing confinement energy $F|x|$. E.g. for $M = 2$ the kinks should be bound in pairs or aggregate into macroscopic complexes with a particular role plaid by Coulomb interactions [12].

Especially interesting is the more complicated case of *coexisting discrete and continuous symmetries*. As a result of their interference the topolological charge of solitons originated by the discrete symmetry can be compensated by gapless degrees of freedom originated by the continuous one. This scenario we shall discuss through the rest of the article.

2.2 The incommensurate CDW: confinement of Amplitude Solitons with phase wings.

Difference of ground states with even and odd numbers of particles is a common issue in mesoscopics. In CDWs it also shows up in a spectacular way. Thus any pair of electrons or holes is accommodated to the extended ground states for which overall phase difference becomes $\pm 2\pi$. Phase increments are produced by phase slips which provide the spectral flow [13] from the upper $+\Delta_0$ to the lower $-\Delta_0$ rims of the single particle gap. The phase slip requires the amplitude $\Delta(x,t)$ to pass through zero, at which moment the complex order parameter has a shape of the amplitude soliton (AS, the kink $\Delta(x = -\infty) \leftrightarrow -\Delta(x = \infty)$. Curiously, this instantaneous configuration becomes the stationary ground state for the case when only one electron is added to the system or when the total spin polarization is controlled to be nonzero, see Figure 1. The AS carries the singly occupied mid-gap state, thus having a spin $1/2$ but its charge is compensated to zero by local dilatation of singlet vacuum states [8,9].

As a nontrivial topological object (O_{cdw} does not map onto itself) the pure AS is prohibited in $D > 1$ environment. Nevertheless it becomes allowed even their if it acquires phase tails with the total increment $\delta\varphi = \pi$, see Figure 2. The length of these tails ξ_φ is determined by the weak interchain coupling, thus $\xi_\varphi \gg \xi_0$. As in $1D$, the sign of Δ changes within the scale ξ_0 but further on, at the scale ξ_φ, the factor $\cos[Qx + \varphi]$ also changes the sign thus leaving the product in O_{cdw} to be invariant. As a result the 3D allowed particle is formed with the AS core ξ_0 carrying the spin and the two phase $\pi/2$ twisting wings stretched over ξ_φ, each carrying the charge $e/2$.

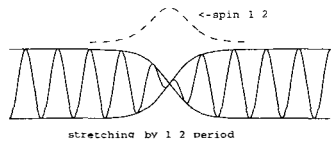


Figure 1: Amplitude soliton in the IC CDW

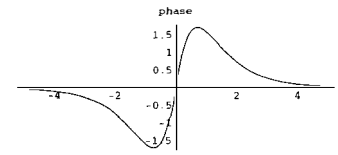


Figure 2: Phase tails adapting the AS.

2.3 Spin-Gap cases: the quantum CDW and the superconductivity.

We shall omit from consideration the case of repulsion which is relevant to the case of the incommensurate Spin Density Wave or to a hole within the antiferromagnetic media which is important for doped Mott insulators. These cases were emphasized in previous publications [4]. Here we shall concentrate upon systems with attraction which originate the gap and the discrete degeneracy in the spin channel. Firstly we shall generalize the description of the CDW solitons to the quantum model. Secondly we shall use the accumulated experience to arrive at our final goal: the spin carrier in the SC media.

$1D$ electronic systems are efficiently treated within the boson representation, see [15] for a review. The variables can be chosen as φ which is the analog of the CDW phase and θ which is the angle of the $SU2$ spin rotation. These phases are normalized in such a way that their increments divided by π count the electronic charge and spin.

For the incommensurate electronic systems the Lagrangian can be written as

$$\mathcal{L}_{atr} \sim \{C_1(\partial\theta)^2 + V\cos(2\theta)\} + C_2(\partial\varphi)^2\,;\; C_1, C_2 = cnst$$

where V is the backward exchange scattering and $(\partial f)^2 = (\partial_t f)^2 - (\partial_x f)^2$. Elementary excitations at $1D$ are the *spinon* as a soliton $\theta = 0 \rightarrow \theta = \pm\pi$, hence carrying the spin $\pm 1/2$, and the gapless charge sound in φ. It is important to recall the alternative description in terms of conjugated phases. We shall need only the one for the charge channel which is the standard gauge phase χ of the superconductivity. φ and χ are related (Efetov and Larkin 79) since their derivatives determine the same quantity - the current j: $\partial_t\varphi/\pi = j \sim \partial_x\chi$. The term $C_2(\partial\varphi)^2$ is duel to $\tilde{C}_2(\partial\chi)^2$ with $\tilde{C}_2 \sim 1/C_2$

The Quantum CDW and the Singlet Superconductivity.

The CDW order parameter is $O_{cdw} \sim \exp[i(Qx+\varphi)]\cos\theta$ The spin operator $\cos\theta$ stands for what was the amplitude in the quasi- classical description and at presence of the spinon it changes the sign as it was for Δ. Hence for the CDW ordered phase in a quasi $1D$ system the allowed configuration must be composed with two components: the spin soliton $\theta \rightarrow \theta + \pi$ and the phase wings $\varphi \rightarrow \varphi + \pi$ where the charge $e = 1$ is concentrated. Beyond the low dimensionality, a general view is: *the spinon as a soliton bound to the semi-integer dislocation loop.*

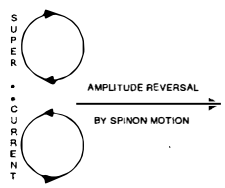


Figure 3. Motion of the topologically combined excitation in a spin-gap media. The string of the amplitude reversal of the order parameter created by the spinon is cured by the semi- vortex pair (the loop in $3D$) of the phase circulation. For the CDW case the curls are displacements contours for the half integer dislocation pair. For the superconductivity the curls are lines of electric currents circulating through the normal core carrying the unpaired spin.

For the Singlet Superconductivity the order parameter is $O_{sc} \sim \exp[i\chi]\cos\theta$. In $D > 1$ the elementary spin excitation is composed with the *spin soliton* $\theta \rightarrow \theta + \pi$ supplied with *current*

wings $\chi \to \chi + \pi$. The quasi $1D$ interpretation is that the *spinon works as a Josephson* $\pi-$ *junction* in the superconducting wire. The $2D$ view is a pair of superconducting $\pi-$ vortices sharing the common core where the unpaired spin is localized. The $3D$ view is a half flux vortex loop which collapse is prevented by the spin confined in its center.

The solitonic nature of the spinon in the quasi $1D$ picture corresponds to the string of reversed sign of the order parameter left behind in the course of the spinon motion. The spin soliton becomes an elementary fragment of the stripe pattern near the pair breaking limit (FFLO phase). The π wings along the line of the spinon motion become the persistent current.

For this combined particle the electronic quantum numbers are reconfined (while with different scales of localization). But integrally over the cross-section the local electric current induced by the spinon is compensated exactly by the back-flows at distant chains. This is a general property of the vortex dipole configuration constructed above. Finally, the soliton as a state of the coherent media will not carry a current and itself will not be driven by a homogeneous electric field.

Our conclusions have been derived for weakly interacting SC or CDW chains. Since The results are symmetrically and topologically characterized, they can be extrapolated to isotropic systems with strong coupling where a clear microscopical derivation is not available. Here the hypothesis is that instead of normal carries excited or injected above the gap, the lowest states are the symmetry broken ones described above as semiroton - spinon complex. This construction can be processed from another side considering a vortex configuration bound to an unpaired electron. Without assistance of the quasi one-dimensionality, a short coherence length is required to leave only a small number of intragap levels in the vortex core.

The existence of complex spin excitations is ultimately related to robustness of the FFLO phase at finite spin polarization. It must withstand a fragmentation due to quantum or thermal melting. Then any termination point of one stripe within the regular pattern (the dislocation) will be accompanied by the phase semiroton in accordance with the quasi $1D$ picture.

References

1. A.Yu Kitaev, **quant-ph**/9707021; D.A. Ivanov, this volume and **cond-mat**/0005069
2. D. Esteve, this volume
3. V.V. Ryazanov, et al, this volume and **cond-mat**/0008364,0103240.
4. S. Brazovskii, **cond-mat**/0006355; N. Kirova, **cond-mat**/0004313
5. Physics Today, **53**, #12, 19 (2000).
6. J.S. Langer and V. Ambegaokar, Phys. Rev. **164**,498 (1967).
7. A. Buzdin et al , Sov. Phys. JETP **66, 422** (1987); Physics Letters, **A225**, 341 (1997); Physica C, **316**, 89 (1999).
8. S. Brazovskii and N. Kirova, *Sov. Sci. Reviews.*, I.M. Khalatnikov ed., **A5**, Harwood Ac. Publ., 1984.
9. S. Brazovskii, in *Modern Problems in Condensed Matter Science*, v. **25**, p. 425 (Elsevier Sci. Publ., Amsterdam,1990).
10. H.S.J. van der Zant *et al*, J. de Physique IV, **9** (1999) Pr10 -157.
11. P. Monceau, F. Ya. Nad, S. Brazovskii, Phys. Rev. Lett. **86**, 4080 (2001)
12. S. Teber *et al*, J. Phys.: Condens. Matter **13**, 4015 (2001).
13. V. Yakovenko, this volume.
14. S. Brazovskii and S. Matveenko, Sov. Phys.: JETP, **72**, 492, 860 (1991).
15. V.J. Emery in *Highly Conducting One-dimensional Solids*, Plenum Press, NY

Discrete Thermodynamic Bethe Ansatz

Michel Bergère[1], Ken-Ichiro Imura[2,3], Stéphane Ouvry[2]
[1] *Spht, CEA-Saclay,* [2] *LPTMS, Université Paris-Sud,* [3] *LPS, Université Paris-Sud*

Discrete thermodynamic Bethe ansatz (TBA) equations for models with discrete spectrum are proposed. We illustrate our construction in the case of Calogero model in a harmonic well (Calogero-Moser model). We found the discrete 2-body TBA function which yields the exact N-body Calogero-Moser thermodynamics. The same logic applies for the Calogero model in a periodic box (Calogero-Sutherland model), provided that a global shift of bare quantum numbers is made in order to maintain a symmetric repartition of the dressed quantum numbers around zero.

It has been known for a long time that the spectrum of the Calogero model [1], defined as particles on an infinite line interacting via $\alpha(\alpha-1)/(x_i-x_j)^2$ 2-body interactions, can be found [2] by the Bethe ansatz (BA) which assumes periodic boundary conditions, and that its thermodynamics can be obtained, in the thermodynamic limit, by the thermodynamic Bethe ansatz (TBA). [3] The Calogero model realizes microscopically fractional exclusion statistics. [4,5] It is however not necessary to rely on the BA (or the TBA) to get the Calogero spectrum (or its thermodynamics). Indeed, the Calogero model is exactly solvable either by confining the particles in a harmonic well of frequency ω: the Calogero-Moser (CM) model [6] with discretized harmonic well quantum numbers and energies, or by confining the particles in a periodic box of length L: the Calogero-Sutherland (CS) model [7] with discretized momenta and energies. Both parameters ω and L can be considered as long distance regulators.

Starting from the BA spectrum, and following Yang and Yang footsteps [3], one can compute à la TBA the thermodynamics of the Calogero model in the thermodynamic limit $L\to\infty$. The thermodynamical potential $\ln\Xi$ -where $\Xi=\sum_{N=0}^{\infty}z^N Z_N$ is the grand partition function- ends up to be that of a free Fermi gas, but in terms of a 1-body dressed energy $\epsilon(k)$ which is related to the 1-body bare energy $k^2/2$ through the ϕ-function:

$$\log\Xi = \frac{L}{2\pi}\int_{-\infty}^{\infty}dk\log\left[1+ze^{-\beta\epsilon(k)}\right], \tag{1}$$

$$\epsilon(k) = \frac{k^2}{2}-\frac{L}{2\pi\beta}\int_{-\infty}^{\infty}dk'\phi(k,k')\log\left[1+ze^{-\beta\epsilon(k')}\right], \tag{2}$$

$$\phi(k,k') = \frac{2\pi}{L}(1-\alpha)\delta(k-k'). \tag{3}$$

The function $\phi(k,k')$, intimately related to the two-body scattering angle, encodes, if one thinks in terms of statistics, the statistical exclusion between two quantum states, here in the same energy level. Note that if one denotes $y(k)=1+ze^{-\beta\epsilon(k)}$, which can be regarded, in view of (1), as the grand partition function at momentum k, then (2) can be rewitten as [8,9]

$$y(k)-ze^{-\beta\epsilon_o(k)}y(k)^{1-\alpha}=1. \tag{4}$$

Now we might ask the following question: are the TBA equations (1,2) specific to the thermodynamic limit with continuous momenta and energies, or can they also describe the thermodynamic of the Calogero model in a harmonic well or in a periodic box with discretized energies? In other words, can we find a discretized version of the function $\phi(k,k')$ in (3) such that the harmonic well or periodic box thermodynamics narrow down to a set of defining equations analogous to (1,2)? We will show that the thermodynamic of the CM model can indeed be rewritten "à la TBA" in terms of a discretized function ϕ which will encode the statistical Calogero exclusion between different discrete harmonic energy levels and which will, as it should,

reproduce, in the thermodynamic limit $\omega \to 0$, $\phi(k-k')$ in (3). We will also argue that the same logic applies for the CS case, provided that a global shift of the bare quantum numbers is made in order to maintain a symmetric repartition of the dressed quantum numbers around zero.

In the case of a discrete one-body spectrum, the TBA equations (1,2) should rewrite as

$$\log \Xi = \sum_n \log\left[1 + ze^{-\beta\epsilon(n)}\right], \tag{5}$$

$$\epsilon(n) = \epsilon_0(n) - \frac{1}{\beta}\sum_{n'} \phi_{n,n'} \log\left[1 + ze^{-\beta\epsilon(n')}\right], \tag{6}$$

where the summation over n or n' should be taken over all possible non-negative (either positive, negative or null) integers in the case of CM (CS) model. Eq. (5,6) are just the discretized versions of (1,2). The one-body bare energy $\epsilon_0(n)$ is given by $\epsilon_0(n) = \omega(n+1/2)$ $\left(\epsilon_0(n) = \frac{1}{2}\left(\frac{2\pi}{L}\right)^2 n^2\right)$ in the case of CM (CS) model.

In eq. (6), $\phi_{n,n'}$ has to be understood as acting on the 1-body bare energy. i.e., as acting on the power series in z obtained from (6): $y(n) = 1 + z\exp[-\beta\epsilon(n)] = 1 + \sum_{N=1}^{\infty} y_N(n) z^N$. [a]

In order that the 2-body partition function or the TBA cluster coefficients obtained in this way [b] match against the exact Z_2 and b_2, the ϕ-function should be defined as

$$\phi_{n_1,n_2} = P_{n_1,n_2}(\alpha) - P_{n_1,n_2}(1) = P_{n_1,n_2}(\alpha) - f_{n_1,n_2}, \tag{9}$$

where $P_{n_1,n_2}(\alpha) = \sum_{\tilde{n}_2 \geq 0} \delta(n_1 + \tilde{n}_2 + \alpha, n_2)$ projects the independant quantum numbers $n_1, n_2 \geq 0$ onto the quantum numbers which, not surprisingly, obey exclusion statistics. More precisely,

[a] Lowest order terms of $y_N(n)$ $(N = 1, 2, \cdots)$ are given as

$$\begin{aligned}
y_1(n_1) &= e^{-\beta\epsilon_0(n_1)}, \quad y_2(n_1) = \sum_{n_2} \phi_{n_1,n_2} e^{-\beta[\epsilon_0(n_1)+\epsilon_0(n_2)]}, \\
y_3(n_1) &= \sum_{n_2,n_3} [\phi_{n_1,n_2}\phi_{n_2,n_3} + \frac{\phi_{n_1,n_2}\phi_{n_1,n_3}}{2} - \frac{\phi_{n_1,n_2}\delta_{n_2,n_3}}{2}] e^{-\beta[\epsilon_0(n_1)+\epsilon_0(n_2)+\epsilon_0(n_3)]}, \\
y_4(n_1) &= \sum_{n_2,n_3,n_4} \Big[\phi_{n_1,n_2}\phi_{n_2,n_3}\phi_{n_3,n_4} + \frac{\phi_{n_1,n_2}\phi_{n_2,n_3}\phi_{n_2,n_4} + \phi_{n_1,n_2}\phi_{n_1,n_3}\phi_{n_2,n_4} + \phi_{n_1,n_2}\phi_{n_1,n_3}\phi_{n_3,n_4}}{2} \\
&+ \frac{\phi_{n_1,n_2}\phi_{n_1,n_3}\phi_{n_1,n_4}}{6} - \phi_{n_1,n_2}\phi_{n_2,n_3}\left[\frac{\delta_{n_3,n_4}}{2} + \delta_{n_2,n_4}\right] - \phi_{n_1,n_2}\phi_{n_1,n_3}\frac{\delta_{n_3,n_4} + \delta_{n_2,n_4}}{4} \\
&+ \frac{\phi_{n_1,n_2}\delta_{n_2,n_3,n_4}}{3}\Big] e^{-\beta[\epsilon_0(n_1)+\epsilon_0(n_2)+\epsilon_0(n_3)+\epsilon_0(n_4)]},
\end{aligned} \tag{7}$$

where the summations should be taken for all possible independant integers.

[b] In order to find the ϕ-function we expand the grand partition function $\Xi = \prod_n y(n)$ in powers of z as

$$\begin{aligned}
Z_1 &= \sum_n y_1(n) = \sum_{n_1} \exp[-\beta\epsilon_0(n_1)], \\
Z_2 &= \sum_n y_2(n) + \sum_{n_1<n_2} y_1(n_1)y_1(n_2), = \sum_{n_1,n_2} [\phi_{n_1,n_2} + f_{n_1,n_2}] \exp[-\beta\{\epsilon_0(n_1) + \epsilon_0(n_2)\}], \\
Z_3 &= \sum_n y_3(n) + \sum_{n_1<n_2} [y_2(n_1)y_1(n_2) + y_1(n_1)y_2(n_2)] + \sum_{n_1<n_2<n_3} y_1(n_1)y_1(n_2)y_1(n_3) \\
&= \sum_{n_1,n_2,n_3} \left[\phi_{n_1,n_2}\phi_{n_2,n_3} + \frac{\phi_{n_1,n_2}\phi_{n_1,n_3}}{2} - \frac{\phi_{n_1,n_2}\delta_{n_2,n_3}}{2} + f_{n_1,n_2}[\phi_{n_1,n_3} + \phi_{n_2,n_3}] + f_{n_1,n_2,n_3}\right] \\
&\times \exp[-\beta\{\epsilon_0(n_1) + \epsilon_0(n_2) + \epsilon_0(n_3)\}],
\end{aligned} \tag{8}$$

where $f_{n_1,n_2,\cdots,n_p}$ is defined s.t. it restricts the independent summation over $n_1, n_2, \cdots, n_p$ onto fermionic quantum numbers: $f_{n_1,n_2,\cdots,n_p} = 1$ when $n_1 < n_2 < \cdots < n_p$, and 0 otherwise. Equivalently one can also expand the thermodynamic potential in terms of the TBA cluster coefficients as $\log\Xi = \sum_{N=1}^{\infty} b_N z^N$.

when $P_{n_1,n_2}(\alpha)$ is applied, e.g., to $\exp[-\beta\epsilon_0(n_2)]$ it replaces n_2 by $n_1+\tilde{n}_2+\alpha$ with n_1 fixed, where $\tilde{n}_2 \geq 0$. It implies in particular that $P_{n_1,n_2}(0)$ ($P_{n_1,n_2}(1)$) projects $n_1, n_2 \geq 0$ onto bosonic (fermionic) quantum numbers. In the thermodynamic limit, which means in a harmonic well: $\omega \to 0, n \to \infty$ with $(n+1/2)\omega \to k^2/2$, $\sum_{n_2} \phi_{n_1,n_2} e^{-\beta[\epsilon_0(n_1)+\epsilon_0(n_2)]} \to (1-\alpha)e^{-\beta k^2}$ i.e., $\phi_{n_1,n_2} \to \phi(k,k')$, as it should. For the CM model this ϕ-function indeed reproduces the exact Z_2 and b_2 obtained from the exact spectrum. Note that (9) implies that the N-body partition function Z_N obtained from (8) has, in the case of CM model, the simple factorized form

$$Z_N = \sum_{n_1,\cdots,n_N} P_{n_1,n_2}(\alpha) P_{n_2,n_3}(\alpha) \cdots P_{n_{N-1},n_N}(\alpha) \exp\left[-\beta \sum_{i=1}^{N} \epsilon_0(n_i)\right], \tag{10}$$

where $P_{n_1,n_2}(\alpha)P_{n_2,n_3}(\alpha)\cdots P_{n_{N-1},n_N}$ projects independant quantum numbers $n_1, n_2, \cdots, n_N$ to dressed quantum numbers s.t. $n_i \to n_{i-1} + \tilde{n}_i + \alpha(i-1) - \alpha(N-1)/2$, where $i = 1, 2, \cdots, N$, $\tilde{n}_i \geq 0$. Eq. (10) is indeed identical to the exact N-body partition function of the CM model.

One can understand on more general grounds this result by noticing that (9) allows to rewrite (6) as

$$y(n) - ze^{-\beta\epsilon_0(n)} \frac{\prod_{\tilde{n}=0}^{\infty} y(n+\tilde{n}+\alpha)}{\prod_{\tilde{n}=0}^{\infty} y(n+\tilde{n}+1)} = 1, \tag{11}$$

which can be viewed as the discretized version of (4). Going one step further one obtains

$$\prod_{\tilde{n}=0}^{\infty} y(n+\tilde{n}) = \prod_{\tilde{n}=0}^{\infty} y(n+\tilde{n}+1) + ze^{-\beta\epsilon_0(n)} \prod_{\tilde{n}=0}^{\infty} y(n_1+\tilde{n}+\alpha). \tag{12}$$

This equation can be interpreted as a grand partition function by saying that either the first particle is in the state at energy $\epsilon_0(n)$ and then the next one is at energy $\epsilon_0(n+\alpha)$ or it is at energy $\epsilon_0(n+1)$ and the n-th level is vacant. By applying recursively this procedure, one verifies that eq. (12) is a grand partition function of a system with N-body spectrum $E_N = \sum_{i=1}^{N} \epsilon_0(n_i + \alpha(i-1))$, where $n \leq n_1 \leq n_2 \leq \ldots \leq n_N$. Hence in the CM case eq. (12), taken at $n = 0$, is identical to the grand partition function of the CM model with N-body spectrum

$$E_N = \omega \sum_{i=1}^{N} [n_i + \alpha(i-1)] + \frac{1}{2} N\omega, \tag{13}$$

where $0 \leq n_1 \leq n_2 \leq \ldots$, expressed in terms of dressed quantum numbers $n_i \to n_i + \alpha(i-1) = n_{i-1} + \tilde{n}_i + \alpha(i-1)$ with $\tilde{n}_i \geq 0$, which in the two-body case $n_1 \to n_1, n_2 \to n_1 + \tilde{n}_2 + \alpha$ amounts to the the action of the projector $P_{n_1,n_2}(\alpha)$ on the a priori two independent quantum numbers $0 \leq n_1, n_2$.

Let us now focus on the CS model. One still has (5,6), but now the one-body dressed energy $\epsilon(n)$ should be defined in terms of the 1D one-body spectrum in a periodic box: $\epsilon_0(n) = \frac{1}{2}\left(\frac{2\pi}{L}\right)^2 n^2$. If one looks at the N-body CS spectrum

$$E_N = \frac{1}{2}\left(\frac{2\pi}{L}\right)^2 \sum_{i=1}^{N} \left[n_i + \alpha(i-1) - \alpha\frac{N-1}{2}\right]^2, \tag{14}$$

where $n_1 \leq n_2 \leq \ldots \leq n_N$, one finds that the dressed quantum numbers $n_i \to n_i + \alpha(i-1) - \alpha(N-1)/2 = n_{i-1} + \tilde{n}_i + \alpha(i-1) - \alpha(N-1)/2$ with $\tilde{n}_i \geq 0$, which in the two-body case read $n_1 \to n_1 - \alpha/2, n_2 \to n_1 + \tilde{n}_2 + \alpha/2$, amount to the the action of the CM projector $P_{n_1,n_2}(\alpha)$ on the a priori two independent quantum numbers n_1, n_2, up to the global N-body shift $n_i \to n_i - \alpha(N-1)/2$. So if one takes the same ϕ-function as in the CM case, one obtains the correct CS N-body partition function, if the above mentionned global shift is also made.

We have shown how the CM thermodynamics can be rewritten in terms of discrete TBA equations. In the CS model, the same TBA equations were shown to be operative, up to a global shift of the bosonic quantum numbers. One may naturally ask whether the discrete TBA equations can also be applied to the models such as the Lieb-Liniger model[10] in a harmonic well. Since the Lieb-Liniger model shares common features with the Calogero model -BA solvability, TBA thermodynamics in the thermodynamic limit, intermediate statistics- it might also have, when considered in a harmonic well, a discrete TBA thermodynamics. We have illustrated this point of view by proposing discrete TBA equations for the harmonic Lieb-Liniger model in analogy with the Calogero-Moser TBA thermodynamics. [11] However the groundstate energy shows deviations from this TBA framework at second order in perturbation theory.

References

1. F. Calogero, J. Math. Phys. **10**, 2191 (1969); ibid. **12**, 419 (1971).
2. for a recent review on the subject and references see A. P. Polychronakos, in Les Houches Lecture Notes, Session LXIX, "Topological Aspects of Low-dimensional Systems" (1998) Ed. Springer; see also V. E. Korepin et al, "Quantum Inverse scattering method and correlation functions" (1993) Cambridge monographs on mathematical physics.
3. C. N. Yang and C.P. Yang, J. Math. Phys. **10**, 1115 (1969).
4. S. B. Isakov, Int. J. Mod. Phys. **A9**, 2563 (1994).
5. D. Bernard, in les Houches Lecture Notes, Session LXII (1994), Ed. North Holland; D. Bernard and Y.S. Wu, in Proc. 6th Nankai Workshop, eds. M.L. Ge and Y.S. Wu, World Scientific (1995).
6. J. Moser, Adv. Math. **16**, 1 (1975).
7. B. Sutherland, J. Math. Phys. **12**, 246(1971); ibid. 251 (1971); Phys. Rev. **A4**, 2019 (1971); ibid. **A5**, 1372 (1972).
8. A. Dasnières de Veigy and S. Ouvry, Phys. Rev. Lett. **72**, 600 (1994).
9. Y.-S. Wu, Phys. Rev. Lett. **73**, 922 (1994); S. B. Isakov, Mod. Phys. Lett. **B8**, 319 (1994).
10. E. H. Lieb and W. Liniger, Phys. Rev. **130**, 1605 (1963).
11. M. Bergère, K.-I. Imura and S. Ouvry, cond-mat/0104107, to appear in Nucl. Phys. **B** [FS].

Fast Ground-State Reordering from Off-Diagonal Fluctuations of Interaction

Philippe Jacquod
Department of Applied Physics, P. O. Box 208284, Yale University, New Haven, CT 06520-8284, U.S.A.
Instituut-Lorentz, Universiteit Leiden P.O. Box 9506, 2300 RA Leiden, The Netherlands

It is shown that off-diagonal fluctuations of interaction lead to the breakdown of perturbation theory in the immediate vicinity of the ground-state of a fermionic system at a rate inversely proportional to the number of considered particles. This rate is parametrically much faster than previously expected. It is shown that this follows from the coherent addition of many small second order contributions to the energy of low-lying levels.

Random interactions naturally occur in various fields of physics. Assuming the symmetry of the probability distribution of the one-body Hamiltonian under unitary basis transformation in Hilbert space directly results in the randomness and a similar symmetry for the distribution of the Interaction Matrix Elements (IME). Typically, this symmetry is satisfied up to an energy scale E_c (the Thouless energy) so that models with random interactions may be expected to describe interacting systems provided one restricts oneself to energy scales of an order of magnitude given by E_c [1,2]. In condensed-matter systems, this corresponds to one-body excitation energies inside a window of width $E_c = g\Delta$ around the Fermi energy, hence containing a finite number of levels given by the conductance g (Δ is the mean level spacing).

Random Interaction Models (RIM) first appeared in nuclear physics and early investigations focused on the deviations from Random Matrix Theory introduced by considering interactions of finite order $k \ll n$ (n is the number of particles, for $k = n$ one recovers the Dyson ensembles of random matrices) [3]. The complexity of the excited spectrum of rare-earth atoms motivated the introduction of RIM in atomic physics[4], and RIM reproduced statistical features obtained in nuclear shell model calculations[5]. Last but not least, RIM were used in condensed matter physics to study the quasiparticle lifetime[6,7] and the conductance peak spacings and heights distributions [8] in quantum dots in the Coulomb blockade regime. More recently a lot of attention has been devoted to the properties of the ground-state of RIM[9,10,11] and several spectral features presented in these latter investigations indicate that RIM are realistic down to very low excitation energies. It is the purpose of the present letter to investigate in detail the ground-state structure of systems of few (n) fermions as the relative strength U/Δ of fluctuations of interaction increases. The main result of these investigations is a breakdown of perturbation theory for the ground-state at a critical value $U_c(n) \sim \Delta/n$. In particular, U_c is parametrically smaller by a factor $1/n$ than previously suggested [12]. Once this threshold is reached, the ground-state starts to be composed of an exponentially large number of Slater determinants, an occurrence which goes far beyond a simple renumbering of one-particle orbitals. We will see that this is due to the coherent addition of large numbers of small second order contributions for perturbation theory in the immediate vicinity of the ground-state.

We investigate a model for spin-1/2 fermions

$$H = \sum \epsilon_\alpha c^\dagger_{\alpha,s} c_{\alpha,s} + \sum U^{\gamma,\delta}_{\alpha,\beta} c^\dagger_{\alpha,s} c^\dagger_{\beta,s'} c_{\delta,s'} c_{\gamma,s} \qquad (1)$$

The greek indices label $m/2$ different one-body energies which are distributed as $\epsilon_\alpha \in [0; m/2]$ so that the mean spacing between spin-degenerate levels is $\Delta \equiv 1$ and $s^{(\prime)} = \uparrow, \downarrow$ are spin indices. The Hamiltonian is Spin Rotational Symmetric (SRS): the interaction commutes with both the total spin $|\vec{S}|$ and its projection S_z. The corresponding eigenvalues σ and σ_z are good quantum numbers and the Hamiltonian matrix acquires a block structure where blocks are labelled by σ_z

and σ. From now on we consider only the $\sigma = \sigma_z = 0$ (1/2) block for n even (odd). The results and arguments presented below can however be generalized to higher spin blocks or models of spinless fermions.

The Hamiltonian (1) can be viewed as a model of interacting fermions expressed in the basis of Slater determinants constructed from the set of one-particle eigenfunctions ψ_α of $H_0 \equiv \sum \epsilon_\alpha c^\dagger_{\alpha,s} c_{\alpha,s}$. In this basis, the IME are given by $U^{\gamma,\delta}_{\alpha,\beta} = \sum_{i,j} U(i-j)\psi^*_\alpha(i)\psi^*_\beta(j)\psi_\gamma(i)\psi_\delta(j)$, where $U(i-j)$ is the interaction potential in real space; i and j label sites on a lattice. Assuming that the presence of disorder or chaotic boundary scattering confers a random character to the ψ_α's directly leads to fluctuations of the $U^{\gamma,\delta}_{\alpha,\beta}$ around their average value. Only diagonal matrix elements have a nonzero average leading to mean-field charge-charge, spin-spin and BCS interactions [10] which we will neglect as they have at most a marginal influence on the object of interest here. We therefore take the IME in (1) to be randomly distributed inside a zero-centred Gaussian distribution of width U, $P(U^{\gamma,\delta}_{\alpha,\beta}) \propto e^{-(U^{\gamma,\delta}_{\alpha,\beta})^2/2U^2}$.

We start with a perturbative calculation of the ground-state energy up to the second order in the small parameter $U/\Delta \ll 1$. The first order correction vanishes on average, and the second order correction can be written

$$\Delta\mathcal{E}_0^{(2)} = \overline{\sum} \frac{(U^{\gamma,\delta}_{\alpha,\beta})^2}{\epsilon_\gamma + \epsilon_\delta - \epsilon_\alpha - \epsilon_\beta} \tag{2}$$

$\overline{\sum}$ indicates that the sum is taken over occupied levels γ and δ and unoccupied ones α and β (taking into account spin degeneracy), giving a total number of contributions $K \sim n^2(m-n)^2$. For the ground-state, one has $\epsilon_\gamma + \epsilon_\delta < \epsilon_\alpha + \epsilon_\beta$, and each term in the sum (2) is negative. The contributions from each scattering process therefore add coherently resulting in a strong reduction of the ground-state energy. The latter can be estimated for an equidistant spectrum by replacing sums by integrals in (2). This gives an homogeneous polynomial of order three in n and m, each term being multiplied by a logarithmic correction. In the dilute limit $1 \ll n \ll m$ the m^3 and $m^2 n$ terms drops out exactly so that the dominant contribution to the second order correction in the ground-state energy reads

$$\Delta\mathcal{E}_0^{(2)} \approx -A(U^2/\Delta) n^2 m \log(m) \tag{3}$$

The prefactor A can be estimated $A \approx 7$; details of the perturbative treatment are presented elsewhere [10].

In Fig.1 we show the behavior of the ground-state energy for $n = 2$, 4, 6 and 8. It is clearly seen that the average ground-state energy exhibits the quadratic dependence in U predicted by (2-3) at weak U, while at larger U, this dependence becomes linear. Most importantly, this crossover occurs at a weaker U for larger n. Both these features can be understood as one realizes that for dominant fluctuations of interaction $U/\Delta \gg 1$ the Hamiltonian depends linearly in U. In this regime, and for $n \gg 1$, the average many-body density of states is Gaussian with a width B well approximated by $B \sim nmU$ [13,14]. This width thus gives a good parametric estimate for the average ground-state energy in the asymptotic regime $\mathcal{E}_0^{(2)} \sim B \sim nmU$ [9] so that equating the asymptotic and perturbative expressions for the ground-state energy ($\Delta\mathcal{E}_0^{(2)} \sim nmU$) gives a critical value

$$U_c \sim \Delta/n \tag{4}$$

The crossover between the two regimes occurs at a rate given by U_c and is inversely proportional to the number of particles. As can be seen in Fig.1, below this threshold, the ground-state energy is well approximated by the second order perturbation expression (3), while above it, its U-dependence becomes lincar *which cannot be captured by any finite order of perturbation*

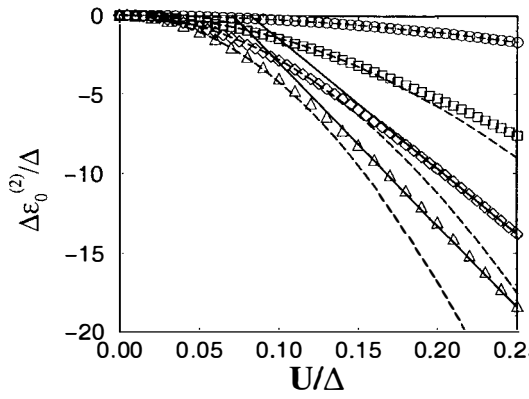


Figure 1: Average ground-state energies for 500 realizations of Hamiltonian (1) with $m = 16$ orbitals, $n = 2$ (circles), 4 (squares), 6 (diamonds) and 8 (triangles) compared to the second order perturbative result (3) (dashed lines) and to linear fits valid at large U (solid lines - see text).

theory, and we are forced to conclude that U_c gives the radius of convergence for perturbation theory in U.

For $U > U_c$, the ground-state starts to be mixed with higher excited states and the number of Slater determinants $|J\rangle$ necessary to construct it becomes much larger than one. A measure of this number is given by the Participation Ratio (PR), which, for a given many-body eigenstate $|\Psi_\lambda(U)\rangle$, is defined as $\xi_\lambda = (\sum_J |\langle J|\Psi_\lambda(U)\rangle|^2)^2 / \sum_J |\langle J|\Psi_\lambda(U)\rangle|^4$. If $|\Psi_\lambda(U)\rangle$ is made up of one single Slater determinant (as it is for $U = 0$), one has $\xi_\lambda = 1$ whereas when $|\Psi_\lambda(U)\rangle$ is homogeneously spread over the N Hilbert space basis states, $\xi_\lambda \sim N$. To check the above threshold (4), we numerically calculated the PR for the ground-state wavefunction $|\Psi_0(U)\rangle$. Results obtained from the exact diagonalization of small systems of $n \leq 8$ particles are shown in Fig.2. We first note a faster increase of ξ_0 with U at larger n which is not due to an increase of the Hilbert space size as it occurs before a significant portion of the Slater determinant basis starts to be occupied. Most importantly, this increase is exponential (note the vertical log-scale on Fig.2) : fixing e.g. $U/\Delta = 0.2$, one gets $\xi(n) \approx \exp(n/1.6)$. Since each order in perturbation theory gives only an algebraic number of contributions, this exponential increase of the PR cannot be captured by a finite, n-independent number of orders, and therefore indicates the divergence of the perturbation series as n increases. Another important feature of Fig.2 is the quite small value $U \ll \Delta$ at which ξ_0 starts to increase. This is quite surprising as Δ is the only energy scale close to the ground-state. When the PR increases beyond $\xi_0 \geq 2$, second (and higher) order terms become more and more important, until eventually perturbation theory breaks down. One can thus extract parametrically the radius of convergence of perturbation theory from the PR by defining a critical interaction strength U_c from the condition $\xi_0(U_c) = 2$. (This choice is arbitrary as long as one chooses a threshold value $\xi_0(U_c)$ much smaller than the total size of the Hilbert space as this would introduce an artificial n and m dependence in U_c.) The inset to Fig.2 shows a $n-$ (and absence of $m-$) dependence of U_c clearly confirming (4).

As yet another check of the threshold (4), we consider the onset of level repulsion for the spacing $s_1 = \mathcal{E}_1 - \mathcal{E}_0$ between the ground-state energy $\mathcal{E}_0$ and the first excited level $\mathcal{E}_1$. At $U = 0$, this spacing corresponds to a one-body excitation, and considering a randomly distributed one-body spectrum, it is Poisson distributed $P_P(s_1) = \exp(-s_1)$. Switching on U induces off-diagonal matrix elements connecting the two lowest levels and leads to repulsion between them. Making a two-level approximation incorrectly gives the onset of this repulsion at $U = \Delta$. A correct

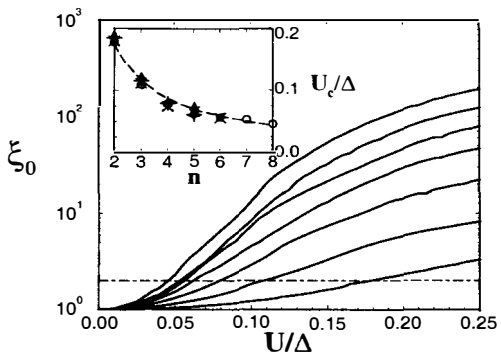


Figure 2: Ground-state PR ξ_0 vs. U/Δ averaged over 100 (for $n = 8$) to 2000 (for $n = 2$) realizations of Hamiltonian (1) for $m = 16$ and n=2, 3, ...8 (solid lines from bottom to top). The dotted dashed-line indicates the threshold $\xi_0 = 2$. Inset : Critical value of interaction U_c/Δ necessary to reach $\xi_0 = 2$ vs. n, for m=10 (triangles), 12 (+), 14 (×) and 16 (circles). The dashed line gives a decay $U_c/\Delta = 0.35/n$.

treatment goes as follows. Most terms in the second order contribution (2) are common to both the energies of the ground- and first excited states. The difference corresponds to scattering from or onto the $(n/2)^{\text{th}}$ and $(n/2+1)^{\text{th}}$ orbitals, giving a contribution to the energy difference between the lowest two levels

$$\overline{\sum} \frac{(U^{\gamma,\delta}_{\alpha,n/2})^2}{\epsilon_\alpha + \epsilon_{n/2} - \epsilon_\gamma - \epsilon_\delta} - \frac{(U^{\gamma,\delta+1}_{\alpha,n/2+1})^2}{\epsilon_\alpha + \epsilon_{n/2+1} - \epsilon_\gamma - \epsilon_{\delta+1}} \tag{5}$$

(There is an additional similar contribution arising from the scattering from the $n/2$ and $n/2+1$ orbitals.) We first make the substitution $\sigma((U^{\gamma,\delta}_{\alpha,n/2})^2 - (U^{\gamma,\delta+1}_{\alpha,n/2+1})^2) = U^2$ for IME fluctuations. Then, and considering an equidistant spacing, a simple counting shows that the number of contributions in the above expression corresponding to a given energy denominator $p\Delta$ grows as p^2 up to $p = n/2$ and decreases afterward. Neglecting logarithmic corrections, one gets an estimate for the contributions to the relative fluctuations given by $\sim (U^2/\Delta)n^2$. This estimate can also be obtained by replacing the sums in (5) with integrals. Once these fluctuations become of the order of the spacing between $\mathcal{E}_0$ and $\mathcal{E}_1$, $\sim (U^2/\Delta)n^2 \sim \Delta$, an avoided crossing occurs. This signals the onset of level repulsion which therefore occurs at the rate given by (4).

This reasoning is confirmed on Fig.3 (a,b,c) where we present the distribution $P(s_1)$ of the first level spacing for Hamiltonian (1) and different number of particles n at fixed interaction strength $U = \Delta/n$. The two main features that can be seen are : 1) $P(s_1)$ at fixed $U = U_c$ is n-independent, except that 2) $P(s_1)$ shows a clear even-odd dependence, in particular there is more level repulsion for odd n. This second fact is understood once one realizes that due to SRS, and within a given (σ_z, σ)-block, the first $U = 0$ excitation is doubly degenerate for n odd, while it is not degenerate for n even. This results in a stronger effect of the interaction in the former case and the even-odd effect seen on Fig.3 (a,b,c). It is to be stressed that this is purely a spin effect, this even-odd dependence does not appear for spinless fermions. On Fig.3 (d) we also show a plot of the low-lying part of the spectrum which shows an avoided crossing at a value $U/\Delta \approx 0.05$ much too small to be explained by a two-level approximation. We stress that in (d) the avoided crossing is not accompanied by an increase of the level spacing as would be the case in presence of non-fluctuating IME, and which would delay the breakdown of perturbation theory.

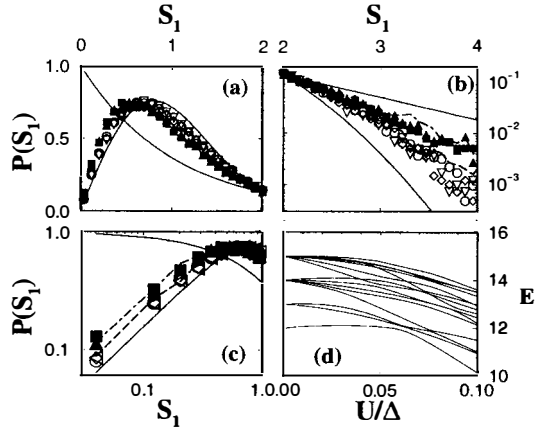


Figure 3: (a,b,c) Distribution $P(s_1)$ of the first level spacing for 50000 realizations of Hamiltonian (1) with a random distribution of orbitals ϵ_α, $m = 14$ (symbols) $n = 3, 4, \ldots 7$, at an interaction strength $U/\Delta = 1/n$. (a) Shows $P(s_1)$ on a normal scale, (b) its large s_1 tail on a semilogarithmic scale and (c) its small s_1 behavior on a log-log scale. Empty symbols correspond to odd n and full symbols to even n. Clearly, there is an even-odd dependence which is m-independent as shown by the superimposed values for $m = 18$ and $n = 3$ (dashed line) and $n = 4$ (dotted-dashed line) on (b) and (c). On (a,b,c) the solid lines show the Poisson and Wigner-Dyson distributions. (d) Shows one realization of the spectrum for Hamiltonian (1) with equidistant one-body spectrum. The spectrum correspond to the full sector $\sigma_z = 0$ so that level crossings occur between levels with different σ.

Equation (4) predicts a parametrically small radius of convergence for perturbation theory beyond which the ground-state is composed of exponentially many Slater determinants. It is somehow in opposition with earlier works [12] which, based on extrapolations from higher excitation energies, predicted a border $\sim \Delta$. The mechanism leading to the breakdown of perturbation theory at higher excitation energies is however due to mixing between two-body levels which are very close in energy, and thus give the dominant contribution in a second order approach. In the immediate vicinity of the ground-state these processes with small denominators do not exist as the lowest energy scale is Δ - the approaches used in [12] correspond then to a two-level approximation involving ground- and first excited states. The presented theory show that the correct procedure is to retain a large number of small second order contributions which have an enhanced effect close to the ground-state, as they acquire a well-defined sign and hence add coherently to give the small threshold (4). One has to conclude that the approach used in [12], while fully justified at a sufficient excitation energy, must break down somewhere close to the ground-state.

Random interaction models of the kind investigated here describe interacting systems restricted to energy differences of the order of the Thouless energy E_c [6]. In disordered diffusive systems one has $E_c = g\Delta$ (g is the conductance) and introducing a cut-off at E_c leads to m, $n \sim g$. From (4) one would expect the breakdown of perturbation theory to occur for $U_c \sim \Delta/g$, precisely at the amplitude of fluctuations of IME in these systems [6,15]. The studied model neglects however two ingredients which must be considered when dealing with more realistic systems. First, correlations between the two terms in (5) significantly reduce the value of this latter expression below the uncorrelated estimate $U^2 \sim (\Delta/g)^2$. Second, the mean-field charge-charge interaction (that we voluntarily neglected), when incorporated self-consistently into the one-body spectrum, leads to a strong reduction of the one-body density of states [16], hence an

increase of the level spacing at the Fermi level against which (5) must be weighted, and an increase of the denominators for the infrared contributions to second order perturbation theory. It is expectable that these two facts ensure the convergence of perturbation theory and the stability of the ground-state against off-diagonal fluctuations in diffusive metallic systems.

In summary, based on second order perturbation theory we predicted a fast reordering of the ground-state for systems of randomly interacting fermions which we confirmed numerically. While the influence of this reordering on the quasiparticle excitations is at present unclear, we found that it is accompanied by a change of statistics of the first energy excitation above the ground-state. Similar investigations in lattice models where this onset of level repulsion may influence the system's transport properties [17], and for which correlations between IME should play an important role (neglected in the presently studied model) are highly desirable.

Numerical computations were performed at the Swiss Center for Scientific Computing. Work supported by the Swiss National Science Foundation.

References

1. B.L. Altshuler and B.I. Shklovskii, Zh. Eksp. Teor. Fiz. **91**, 220 (1986).
2. R.A. Janik et. al., Phys. Rev. Lett. **81** 264 (1998); J.C. Osborn and J.J.M. Verbaarschot, Phys. Rev. Lett. **81**, 268 (1998).
3. J. B. French and S.S.M. Wong, Phys. Lett. **33B**, 447, (1970); **35B**, 5 (1971); O. Bohigas and J. Flores, Phys. Lett. **34B**, 261, (1971); **35B**, 383 (1971).
4. V.V. Flambaum et. al., Phys. Rev. A **50**, 267 (1994); V.V.Flambaum, F.M.Izrailev and G.Casati, Phys. Rev. E **54** (1996) 2136.
5. V. Zelevinsky et. al., Phys. Rep. **276**, 85 (1996).
6. B.L. Altshuler et. al., Phys. Rev. Lett. **78**, 2803 (1997).
7. A.D. Mirlin and Y.V. Fyodorov, Phys. Rev. B **56**, 13393 (1997); C. Mejia-Monasterio et. al., Phys. Rev. Lett. **81**, 5189 (1998); X. Leyronas, J. Tworzydlo and C.W.J. Beenakker, Phys. Rev. Lett. **82**, 4894 (1999).
8. Y. Alhassid, Ph. Jacquod and A. Wobst, Phys. Rev. B **61**, R13357 (2000); Y. Alhassid and A. Wobst, cond-mat/0003255.
9. Ph. Jacquod and A.D. Stone, Phys. Rev. Lett. **84**, 3938 (2000); Phys. Stat. Sol. **218**, 113 (2000).
10. Ph. Jacquod and A.D. Stone, cond-mat/0102100.
11. C.W. Johnson, G.F. Bertsch and D.J. Dean, Phys. Rev. Lett. **80**, 2749 (1998); R. Bijker, A. Frank and S. Pittel, Phys. Rev. C **60**, 021302 (1999); L. Kaplan and T. Papenbrock, Phys. Rev. Lett. **84**, 4553 (2000); S. Drozdz and M. Wójcik, nucl-th/0007045; D. Kusnezov, Phys. Rev. Lett. **85**, 3773 (2000).
12. S. Åberg, Phys. Rev. Lett. **64**, 3119 (1990); Ph. Jacquod and D. L. Shepelyansky, Phys. Rev. Lett. **79**, 1837, (1997); P.G. Silvestrov, Phys. Rev. Lett. **79**, 3994 (1997).
13. K.K. Mon and J.B. French, Ann. Phys. **95**, 90 (1975).
14. L. Benet, T. Rupp and H.A. Weidenmüller, cond-mat/0010426.
15. Ya.M. Blanter, Phys. Rev. B **54**, 12807 (1996).
16. B.L. Altshuler and A.G. Aronov in "*Electron-electron Interaction in Disordered Systems*", A.J. Efros and M. Pollak Eds, Elsevier (1985); P. Kopietz, Phys. Rev. Lett. **81**, 2120 (1998); Ya. M. Blanter and M.E. Raikh, Phys. Rev. B **63**, 075304 (2001).
17. W. Kohn, Phys. Rev. A **133**, 171 (1964); R. Berkovits and Y. Avishai, Phys. Rev. Lett. **76**, 291 (1996).

EXCITED STATES OF THE COOPER PROBLEM IN A THREE-DIMENSIONAL DISORDERED SYSTEM

JOSÉ LAGES
Laboratoire de Physique Quantique, UMR 5626 du CNRS, Université Paul Sabatier, F-31062 Toulouse Cedex 4, France

This work presents the study of the excited states of the Cooper problem in the three-dimensional Anderson model. It is shown that the excited pair states remain localized while their excitation energy ΔE is negative. For $\Delta E > 0$ the particles are delocalized over the three-dimensional lattice.

The Cooper problem [1] is the cornerstone of the well known BCS theory for superconductivity. Even if the Cooper problem deals with only two interacting particles (TIP) above a frozen Fermi sea, it nevertheless captures the essential physical features of the superconducting states. Indeed, in comparison with the BCS theory, the solution of the Cooper problem leads to the appearance of coupled states with a qualitatively correct coupling energy and pair size. Then it seems natural that the study of the Cooper problem with disorder could provide a useful step in the understanding of the superconductivity in presence of relatively strong disorder. The first studies on the Cooper problem with disorder were done for three-dimensional [2] and two dimensional [3] systems. These studies [2,3] were focused on the properties of the ground state of two particles above a frozen Fermi sea coupled via an on-site attractive Hubbard interaction. This interaction creates a phase of bi-particle localized states (BLS) in the regime of disorder where non-interacting states are delocalized. At the same time the mean-field solution of the Cooper problem (Cooper ansatz) gives delocalized pairs. This shows that the non-diagonal matrix elements of interaction play an important role in presence of disorder. These TIP results are in qualitative agreement with recent many-body investigations [4,5] of the ground state of the attractive Hubbard model with disorder.

Here the studies are concentrated on the properties of excited TIP states. For that purpose we introduce the Anderson Hamiltonian for one-particle,

$$H_1 = \sum_{\mathbf{n}} E_{\mathbf{n}} \left|\mathbf{n}\right\rangle \left\langle\mathbf{n}\right| + V \sum_{\langle \mathbf{n},\mathbf{m}\rangle} \left|\mathbf{n}\right\rangle \left\langle\mathbf{m}\right| \tag{1}$$

where $\mathbf{n}$ and $\mathbf{m}$ are the index vectors on the three-dimensional lattice with periodic conditions, $\langle , \rangle$ denotes nearest neighbor sites, V is the hopping term and the random on-site energies $E_{\mathbf{n}}$ are homogeneoulsy distributed in the energy interval $\left[-\frac{W}{2}, \frac{W}{2}\right]$, where W is the disorder strength. To study the effects of the attractive interaction ($U < 0$) on two particles near the Fermi sea we generalize the Cooper approach [1] for the disordered case. We write the TIP Hamiltonian in the basis of one-particle eigenstates of the Hamiltonian (1). In this basis the Schrödinger equation for TIP reads

$$(E_{m_1} + E_{m_2})\, \chi^{\lambda}_{m_1,m_2} + U \sum_{m_1',m_2'} Q_{m_1,m_2,m_1',m_2'}\, \chi^{\lambda}_{m_1',m_2'} = E_{\lambda}\, \chi^{\lambda}_{m_1,m_2}. \tag{2}$$

Here E_m are the one-particle eigenenergies corresponding to the one-particle eigenstates $|\phi_m\rangle$ of H_1 and $\chi^{\lambda}_{m_1,m_2}$ are the components in the non-interacting eigenbasis $|\phi_{m_1} \otimes \phi_{m_2}\rangle$ of the λ^{th} TIP eigenstate $\left|\chi^{\lambda}\right\rangle$ corresponding to the eigenenergy E_{λ}. The matrix elements $UQ_{m_1,m_2,m_1',m_2'}$ give the interaction induced transitions between non-interactive eigenstates $|\phi_{m_1} \otimes \phi_{m_2}\rangle$ and $\left|\phi_{m_1'} \otimes \phi_{m_2'}\right\rangle$. These matrix elements are obtained by writing the Hubbard interaction in the non-interactive eigenbasis of the model (1). In analogy with the original Cooper problem [1] the

summation in (2) is done over the non-interacting states above the Fermi level, in the labelling $E_{m'_{1,2}} > E_F$ corresponds to $m'_{1,2} > 0$. The Fermi energy is determined by a fixed filling factor $\nu = 1/2$. To keep similarity with the Cooper problem we restrict the summation on $m'_{1,2}$ by the condition $1 < m'_1 + m'_2 < M$. In this way the cut-off of M unperturbed orbitals introduces an effective phonon frequency $\omega_D \propto M/L^3 = 1/\alpha$ where L is the linear system size. When varying L we keep α fixed so that the phonon frequency is independent of the system size. All the data in this work are obtained with $\alpha = 30$ but we also checked that the results are not sensitive to the change of α.

In order to analyze the properties of the TIP excited states of the disordered Cooper problem we compute the energy level spacing distribution $P(s)$ obtained by the diagonalization of (2). From $P(s)$ we calculate

$$\eta = \frac{\int_0^{s_0} [P(s) - P_{WD}(s)]\, ds}{\int_0^{s_0} [P_P(s) - P_{WD}(s)]\, ds}. \tag{3}$$

Here $P_P(s) = \exp(-s)$ and $P_{WD}(s) = \frac{\pi s}{2} \exp\left(-\frac{\pi s^2}{4}\right)$ are respectively the Poisson and the Wigner-Dyson distributions, and $s_0 \simeq 0.4729$ is their intersection point. In this way, η varies from 1 $[P(s) = P_P(s)]$ to 0 $[P(s) = P_{WD}(s)]$ and thus characterizes a transition from localized to delocalized states. For example for the one-particle problem this method allows to detect efficiently the Anderson transition[6].

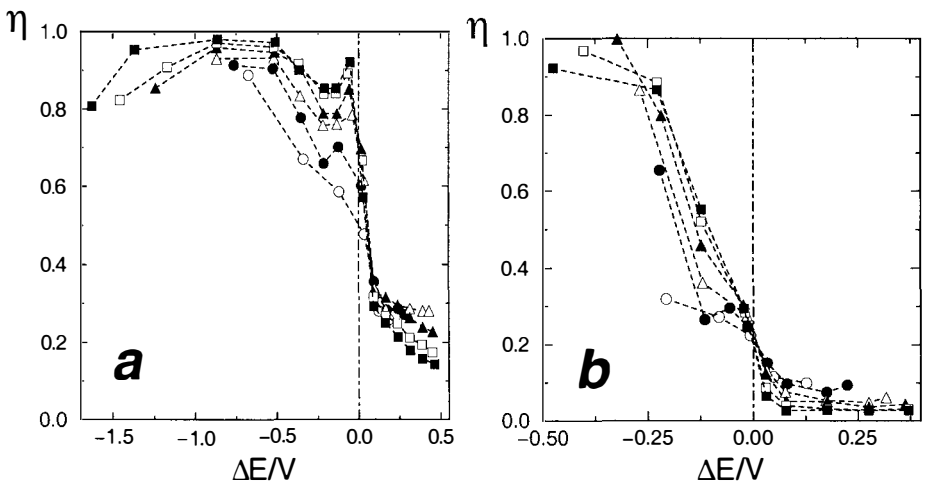


Figure 1: Dependence of η on the excitation energy ΔE for (**a**) $W = 18V > W_c \simeq 16.5V$ and (**b**) $W = 12V < W_c$. The interaction strength is $U = -4V$ and the linear lattice size is $L = 6$ (○), 7 (●), 8 (△), 10 (full triangle), 12 (square) and 14 (full square). The number of disorder realization used is $N_D = 3000$ and $\alpha = 30$.

In Fig. 1, η is shown for disorder strength $W = 18V$ (**a**) and $W = 12V$ (**b**), an interaction strength $U = -4V$ and for different linear lattice size, from $L = 6$ up to $L = 14$. η is presented versus the excitation energy $\Delta E = E - 2E_F$ where E is the energy of the two interacting particles. Without interaction for $W = 18V > W_c \simeq 16.5V$ [a] the one particle states are well localized (see Fig. 2a). When the on-site Hubbard attraction is switched on, coupled states appear below the Fermi energy of two non-interacting particles ($\Delta E < 0$). Fig. 1a clearly shows that at the thermodynamic limit the coupled states with $\Delta E < 0$ are localized ($\eta \to 1$). As

[a] At the band center $W_c \simeq 16.5V$ is the critical value of the disorder at which the Anderson transition occurs[6,7].

$W > W_c$ all the non-interacting orbitals are localized in the lattice basis. The on-site attractive interaction acts as an additional constraint forcing the two particles (with opposite spin) to stay together in the same well of potential (see Fig. 2b). Above the Fermi energy, η tends slowly to 0 indicating that these unbounded states ($\Delta E > 0$) are delocalized. This delocalization is due to the fact that an interaction (repulsive or attractive) between particles destroies single particle localization and leads to a propagation of pairs of size l_1 over a distance l_c much larger than l_1 [8,9]. The enhancement factor κ is then determined by the density ρ_2 of two-particle states coupled by the interaction and the interaction induced transition rate Γ_2 between noninteracting states, so that $\kappa = \Gamma_2 \rho_2$. For $\Delta E > 0$ the density ρ_2 grows with the excitation energy ($\rho_2 \propto \Delta E$)[9] that strongly enhances the delocalization of pairs (see Fig. 2c).

In Fig. 1b, η is shown for $W = 12V < W_c$. For this regime the non-interacting one-particle states are delocalized (see Fig. 2d). For the different linear lattice size L the ground state is still localized ($\eta \simeq 1$) in agreement with [2]. Indeed as $W/W_c \simeq 0.72 > W_s/W_c \simeq 0.35$ the TIP ground state is in the BLS phase, where W_s is the critical value of the disorder for the superconductor-insulator transition found in [2] for TIP pairs. In the region $-0.25V < \Delta E < 0$ although η drops from 0.9 to 0.25 a certain localization of TIP pairs still remains (see Fig. 2e). For $\Delta E > 0$, the TIP states become delocalized (see Fig. 2f).

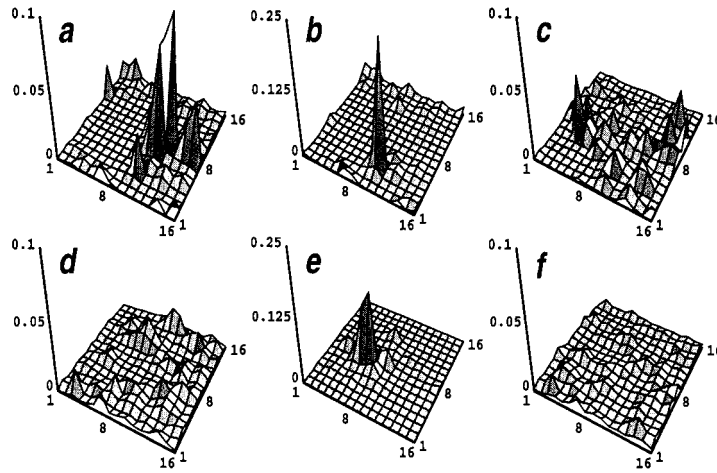


Figure 2: One-particle probability distribution $f_\lambda(\mathbf{n}_1) = \sum_{\mathbf{n}_2} \left| \chi^\lambda_{\mathbf{n}_1,\mathbf{n}_2} \right|^2$ extracted from TIP eigenstates $\left| \chi^\lambda \right\rangle$ and projected on a (x,y)-plane. The linear lattice size is $L = 16$. $f_\lambda(\mathbf{n}_1)$ is presented for $W = 18V$ [(a) ground state without interaction, (b) excited states $\lambda = 25$ with $\Delta E_\lambda \simeq -0.25V$ for $U = -4V$ and (c) excited states $\lambda = 758$ with $\Delta E_\lambda \simeq 0.25V$ for $U = -4V$] and for $W = 12V$ [(d) ground state without interaction, (e) excited states $\lambda = 83$ with $\Delta E_\lambda \simeq -0.05V$ for $U = -4V$ and (f) excited states $\lambda = 512$ with $\Delta E_\lambda \simeq 0.125V$ for $U = -4V$].

In order to characterize the wave function properties of the excited states of the disordered Cooper problem, we compute

$$\xi(E) = \left\langle \left(\sum_{m_1,m_2} \left| \chi^\lambda_{m_1,m_2} \right|^4 \right)^{-1} \right\rangle_{E_\lambda \in [E-\epsilon, E+\epsilon]} \tag{4}$$

where the brackets mark the averaging over $N_D = 400$ realizations of the disorder and over an energy interval 2ϵ centered on E. The inverse participation ratio (IPR) $\xi(E)$ counts the average number of non-interacting states $|\phi_{m_1} \otimes \phi_{m_2}\rangle$ occupied by the TIP wave functions belonging to

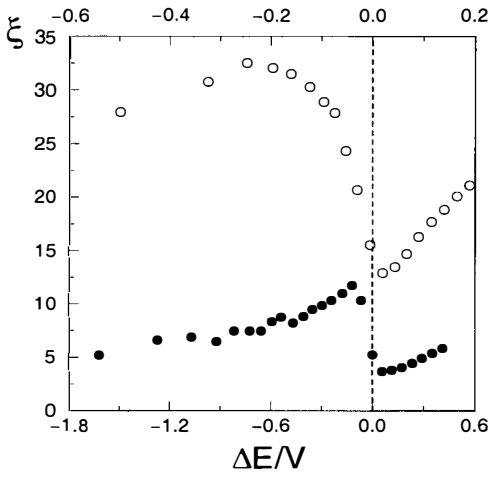


Figure 3: IPR ξ as a function of the coupling energy ΔE for a disorder strength $W = 12$ (○) [$\Delta E/V$ is then read on the upper horizontal axis] and $W = 18$ (●) [$\Delta E/V$ is then read on the lower horizontal axis]. The interaction strength is $U = -4V$ and the linear lattice size $L = 12$. $N_D = 300$ disorder realization are used, $\alpha = 30$, $2\epsilon \simeq 0.05$ for $W = 18$ and $2\epsilon \simeq 0.025$ for $W = 12V$.

energy interval $[E - \epsilon, E + \epsilon]$. Fig. 3 shows the IPR as a function of the coupling energy ΔE for $W > W_c$ and $W < W_c$. For $W = 18V$ as the one-particle noninteracting states are localized, only few of these states ($\xi \simeq 5 - 10$) are enough to build the TIP localized states with $\Delta E < 0$. On the contrary for $W = 12V$ the TIP localized states ($\Delta E < 0$) occupy more noninteracting states ($\xi \simeq 30$) than for $W = 18V$ (Fig. 3). Indeed, for $W < W_c$ the one-particle noninteracting states are delocalized and it is necessary to have a sufficient number of these states to see the TIP eigenstates localization induced by the quantum interferences.

In conclusion, the study of the excited states of the disordered Cooper problem shows that the BLS phase found in [2,3,4] exists for TIP eigenstates with energy $\Delta E < 0$. This phase is destroyed for TIP eigenstates above the Fermi level $\Delta E > 0$.

Acknowledgments

I thank D.L Shepelyansky for useful and stimulating discussions.

References

1. L.N. Cooper, *Phys. Rev.* **104**, 1189 (1956).
2. J. Lages and D.L. Shepelyansky, *Phys. Rev.* B **62**, 8665 (2000).
3. J. Lages and D.L. Shepelyansky, cond-mat/0104194.
4. B. Srinivasan and D.L. Shepelyansky, cond-mat/0102055.
5. J. Lages, G. Benenti, D.L. Shepelyansky, cond-mat/0101265, to appear in *Phys. Rev.* B.
6. B. I. Shklovskii, B. Shapiro, B. R. Sears, P. Lambrianides and H. B. Shore, *Phys. Rev.* B **47**, 11487 (1993).
7. T.Ohtsuki, K.Slevin, T.Kawarabayashi, *Ann. Physik* (Leipzig) **8**, 655 (1999).
8. D.L. Shepelyansky, *Phys. Rev. Lett.* **73**, 2607 (1994).
9. Y. Imry, *Europhys. Lett.* **30**, 405 (1995).

NON-EQUILIBRIUM TUNNELING EFFECTS OF INTERACTING HUBBARD-ANDERSON IMPURITIES

N.S.MASLOVA[1], P.I.ARSEEV[2], S.V.SAVINOV[1]
[1]*Moscow State University, 119899 Moscow, Russia*

[2]*P.N.Lebedev Physical Institute, 117924 Moscow, Russia*

Non-equilibrium interaction effects of two Hubbard-Anderson impurities have been experimentally studied by means of STM/STS methods and theoretically analyzed using self-consistent approach based on the Keldysh formalism.

In this work, the interaction of the localized impurity states formed by a pair of identical impurity Si $3nm$ apart at the (110) GaAs surface are studied by scanning tunneling microscopy and spectroscopy (STM/STS). In the experimentally observed spatial distribution of the local tunneling conductivity, one can recognize a two-fold switching on and off of each of atomic a and b states upon changing the tunneling bias. After switching on, the excess tunneling conductance occurs in the vicinity of each of these atoms in a bias range about $0.75eV$, which is much greater than the level width of localized state. At the same time, the transition from "dark" state to "light" one occurs within the range of bias changes $\simeq 0.15eV$, which is comparable to the energy level width of the localized state.

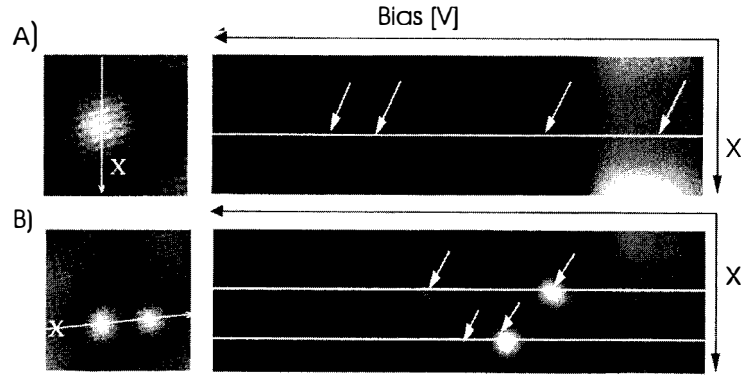


Figure 1: STM images (right panel) and map view of normalized tunneling conductivity measured along direction depicted on STM topography images(left panel). Specific features on STS images are marked by arrows. A) isolated Si impurity, scan area 5.8nm, bias range from +2.5V to -2V, B) two interacting Si impurities scan area 10nm, bias range from +2.9V to -2V

Electron transport through single Anderson impurity in the Coulomb blockade and the Kondo regime have been studied experimentally and is up till now under theoretical investigation [2,3,4,5]. But most of the authors concentrated on weak tunneling coupling, when tunnel junction is used only as a probe without affecting the impurity states [4]. So, usually tunneling conductivity through Anderson impurity is supposed to be determined by equilibrium impurity density of states. In the Coulomb blockade regime of tunneling through impurity or quantum dot the influence of tunneling current on impurity spectrum is neglected [5]. Thus, the impurity charge can acquire only discrete value; n_σ, $n_{-\sigma}$ can be equal only to 0 or 1. The width of tunneling conductivity peak in the Coulomb blockade regime are determined by the sum of relaxation

rates and can not achieve (without destroying this regime) experimentally observed anomalous large values $\simeq 0.75eV$ even at room temperatures. With increasing of tunneling coupling the discreteness of impurity charge is suppressed and one have to deal with impurity electron filling numbers which now are not integer determined from kinetic equations[1]. For the Kondo regime coupling to the leads modifies the impurity spectrum, but charge fluctuations are suppressed because initial impurity level lies deep below the Fermi level and is single occupied.

With increasing of applied bias nonequilibrium processes become to play significant role, especially at low temperatures. In the present work nonequilibrium charge distribution due to tunneling processes and the influence of tunneling bias voltage on the impurity states energy values is taken into account. Non-equilibrium electron filling numbers on Hubbard-Anderson impurities are obtained from self-consistent system of kinetic equations based on the Keldysh diagram technique [6]. The Coulomb interaction of localized electrons is treated self-consistently in mean-field approximation and is determined by these non-equilibrium filling numbers. It is shown that with increasing of tunneling bias two states with different energies for opposite spin electrons can appear on each impurity: the transition from "paramagnetic" regime to "magnetic" one and vice versa can occur. We have also determined the conditions for enhancement of transition to magnetic state by increasing of interaction between two Anderson impurities. We revealed that impurity interaction results in redistribution of localized non-equilibrium charges and can lead to pinning of impurity levels near the Fermi level of each electrode.

We consider theoretical model of two interacting Anderson impurities. STM tip is positioned above one of impurity atoms (atom "a"). Hamiltonian $\hat{H}$ of the model consists of the following parts:

$$\hat{H}_0 = \sum_{\mathbf{k},\sigma}(\varepsilon_k - \mu)c^+_{\mathbf{k},\sigma}c_{\mathbf{k},\sigma} + \sum_{\mathbf{p},\sigma}(\varepsilon_p - \mu - eV)c^+_{\mathbf{p},\sigma}c_{\mathbf{p},\sigma}, \tag{1}$$

describes non-interacting electrons in two electrodes: tip - $(\mathbf{k},\sigma)$, sample - $(\mathbf{p},\sigma)$

The part $\hat{H}_{imp}$ corresponds to the impurities states and takes into account the Hubbard repulsion:

$$\hat{H}_{imp} = \varepsilon_a \sum_\sigma a^+_\sigma a_\sigma + U_a/2 \sum_\sigma n^a_\sigma n^a_{-\sigma} + \varepsilon_b \sum_\sigma b^+_\sigma b_\sigma + U_b/2 \sum_\sigma n^b_\sigma n^b_{-\sigma} \tag{2}$$

$n^a_\sigma = a^+_\sigma a_\sigma$, a_σ - destroys an impurity electron with spin σ, $n^b_\sigma = b^+_\sigma b_\sigma$, b_σ - destroys an impurity electron with spin σ, ε_a, ε_b - the impurity energy levels (dependent on the bias V in general case).

The part $\hat{H}_{int}$ describes the interaction between the impurity states

$$\hat{H}_{int} = T \sum_\sigma (a^+_\sigma b_\sigma + h.c.) \tag{3}$$

$\hat{H}_{tun}$ is responsible for tunneling transitions from impurity states to each electrode (tip or substrate)

$$\hat{H}_{tun} = T_{\mathbf{p},a} \sum_{\mathbf{p},\sigma}(c^+_{\mathbf{p},\sigma}a_\sigma + h.c.) + T_{\mathbf{p},b} \sum_{\mathbf{p},\sigma}(c^+_{\mathbf{p},\sigma}b_\sigma + h.c.) + T_{\mathbf{k},b} \sum_{\mathbf{k},\sigma}(c^+_{\mathbf{k},\sigma}a_\sigma + h.c.) \tag{4}$$

Tunneling current and conductivity can be determined by self-consistent approach based on Keldysh diagram technique if we treat the on-site Coulomb interaction in the mean-field approximation.

Tunneling current is determined as

$$I(V) = \sum_{\mathbf{k},\sigma} \int d\omega T_{\mathbf{k}a}(G^{\sigma<}_{a\mathbf{k}} - G^{\sigma<}_{\mathbf{k}a}) \tag{5}$$

With the help of kinetic equation system this equation can be transformed to the following expression.

$$I_\sigma(V) = -4\gamma_k \int ImG^{R\sigma}_{a,a}(\omega)(n^\sigma_a(\omega) - n^0_k(\omega - eV))d\omega \tag{6}$$

$n^0_k(\omega)$ - equilibrium filling numbers of metallic tip, $G^R_{a,a}(\omega, V)$ - exact retarded Green function of impurity state. Tunneling rate γ_k is one of the set of kinetic coefficients determined as

$$\gamma_k(\omega) = |T_{ka}|^2\nu_{\mathbf{k}}(\omega), \qquad \gamma_b(\omega) = |T_{pb}|^2\nu_{\mathbf{p}}(\omega), \qquad \gamma_a(\omega) = |T_{pa}|^2\nu_{\mathbf{p}}(\omega), \qquad \Gamma = \gamma_a + \gamma_a + \gamma_k \tag{7}$$

where $\nu_{\mathbf{k}}(\omega) = -\frac{1}{\pi}\sum_k ImG^R(\boldsymbol{k}, \omega)$ is density of states in metallic tip, $\nu_{\mathbf{p}}(\omega) = -\frac{1}{\pi}\sum_p ImG^R(p, \omega)$ — substrate density of states.

Impurity energies in the mean-field approximation depend on applied bias V both directly due to external field in the contact area which changes the "bare" impurity level and indirectly due to the Coulomb interaction of nonequilibrium electron density.

$$\tilde{\varepsilon}^\sigma_a = \varepsilon_a + \alpha V + U_a < n^{-\sigma}_a >, \qquad \tilde{\varepsilon}^\sigma_b = \varepsilon_b + \beta V + U_b < n^{-\sigma}_b > \tag{8}$$

Now the main point is that non-equilibrium electron filling numbers for impurity atoms "a" and "b" should satisfy the self-consistency condition:

$$n^\sigma_a = \int d\omega n^\sigma_a(\omega) ImG^R_{aa}(\omega), \qquad n^\sigma_b = \int d\omega n^\sigma_b(\omega) ImG^R_{bb}(\omega), \tag{9}$$

where n^σ_a and n^σ_b are determined by the stationary equations. Using expression for n^σ_a and n^σ_b Eq. (6) for the tunneling current can be rewritten in the final form:

$$\begin{aligned} I_\sigma(V) &= \frac{\gamma_k(\gamma_b + \eta_\sigma)}{(\gamma_a + \gamma_k)(\gamma_b + \eta_\sigma) + \gamma_b\eta_\sigma} \\ &\times \int \left[\left(\gamma_a + \frac{\gamma_b\eta_\sigma}{\gamma_b + \eta_\sigma}\right) ImG^{R\sigma}_{a,a}(\omega, V) + T\frac{\gamma_b\gamma_k}{\gamma_b + \eta_\sigma} Im(R_{ab}G^{A\sigma}_{ab}(\omega, V))\right] \\ &\times \left(n^0_p(\omega) - n^0_k(\omega - eV)\right) d\omega \end{aligned} \tag{10}$$

where $n^0_p(\omega)$, $n^0_k(\omega - eV)$ are equilibrium filling numbers of substrate and metallic tip states respectively,

$$R^\sigma_{ab} = \frac{1}{(\tilde{\varepsilon}^\sigma_a - \tilde{\varepsilon}^\sigma_b) - i(\gamma_k + \gamma_a + \gamma_b)}, \qquad \eta^\sigma = T^2 ImR^\sigma_{ab} \tag{11}$$

and the self-consistent values of n^σ_a, n^σ_b are substituted in $G^R_{aa}, G^R_{ab}, R_{ab}$ for each value of the bias V. 1) Tunneling current depends only on the difference of electron distribution functions of the electrodes. 2) The first term of this expression for tunneling current describes the renormalization of relaxation rate by interaction of neighboring impurity atom b. If the interaction is absent $T = 0$, $\eta = 0$ one can obtain the usual form of tunneling current through impurity localized state. 3) The second term is responsible for charge redistribution between interacting impurity atoms. Tunneling conductivity is no more proportional to impurity density of states. It is an example of tunneling current through multi-channel system with interaction between different channels.

Enhancement of tunneling conductivity can be observed at such tunneling bias voltage, when $|\varepsilon^{\pm\sigma}_a(V) - E^t_F| < \Gamma$ or $|\varepsilon^{\pm\sigma}_a(V) - E^s_F| < \Gamma$ But it is very important to note that any increase of LDOS in the energy interval $E_F - eV < \varepsilon < E_F$ when changing applied bias V leads to enhancement of tunneling conductivity at eV. Analysis of suggested model allows to describe different regimes of tunneling conductivity behavior in the vicinity of impurity atoms with changes of tunneling bias.

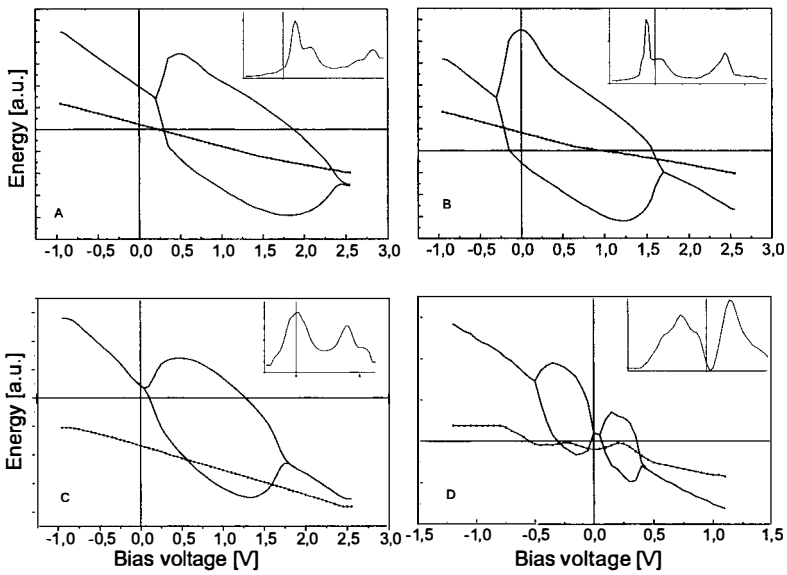


Figure 2: Behavior of atoms a and b energy levels vs. tunneling bias for different parameters of tunneling junction. Solid lines correspond to ε_a^{up} and ε_a^{down}, lines with squares — to ε_b^{up}. Two left graphs (A,C) correspond to weak coupling to STM tip. Upper right graph (B) corresponds to noninteracting impurity atoms, while lower one (D) - to strong coupling to STM tip. Inserts show corresponding calculated normalized differential tunneling conductivity for the same bias range

i) If $\gamma_k << \gamma_a, \gamma_b$ one of impurity atoms (atom "a") can be in "magnetic" state in certain range of tunneling bias. With changing of applied voltage transition from "paramagnetic" regime to "magnetic" one and vise versa can occur. This behavior leads to switching "ON" and "OFF" twice of "a" atom on spatially resolved local tunneling conductivity spectra (Fig.2 a-c). Besides, energy levels are pinned in vicinity of Fermi level of one of electrodes (tip or sample) while bias voltage changes in the range of order of U. In non-equilibrium case interaction between atoms "a" and "b" can enhance "magnetic" state and increase difference between energy values ε_σ and $\varepsilon_{-\sigma}$ of electrons with opposite spins localized on atom "a". Though in the equilibrium case interaction with paramagnetic atom "b" will result in suppression of "magnetic" state on atom "a" (compare Fig.2a and Fig.2b). Inserts in Figs.2a-d depicts the dependence of tunneling conductivity on applied bias in vicinity of "a" atom. Two wide peaks on tunneling conductivity spectra correspond to switching "ON" of "a" atom at $\varepsilon_a^\sigma(V, n_a^{-\sigma}) = E_F^t$ and $\varepsilon_a^{-\sigma}(V, n_a^\sigma) = E_F^s$

ii) For $\gamma_k >> \gamma_a, \gamma_b$ (sufficiently strong coupling to STM tip) the situation when "magnetic" state on a atom appears twice is possible. In Fig.2d the dependence of $\varepsilon_{a(b)}^{\pm\sigma}(V, n_{a(b)}^{\mp\sigma})$ on applied bias is shown. In the range of applied bias $|\varepsilon_a^\sigma(V, n_a^{-\sigma}) - E_F^s| < \Gamma$ atom "a" is in the "magnetic" state. But with increasing of tunneling bias, filling numbers quickly decrease and "magnetic" regime is suppressed, and atom "a" can be found in "paramagnetic" state. However at opposite polarity of applied bias atom "a" can again be found in "magnetic" state when $|\varepsilon_a^\sigma(V, n_a^{-\sigma})$ is close to the Fermi level of the tip $|\varepsilon_a^\sigma(V, n_a^{-\sigma}) - E_F^t| < \Gamma$. Interaction between a and b atom can enhance this transition. Tunneling conductivity vs bias voltage is shown in the insert of Fig.2d.

iii)And finally, when coupling to the STM tip is comparable with coupling of impurity atom to the substrate $\gamma_k \geq \gamma_a, \gamma_b$ increasing of tunneling bias usually leads to suppression of "magnetic" state because filling numbers decrease due tunneling processes.

Thus crucial role of nonequilibrium electron distribution in tunneling processes through coupled Anderson impurities is demonstrated. In particular, interaction between impurities with different value of the Coulomb repulsion can enhance magnetic regime of a single atom in nonequilibrium case at large applied bias. Suggested approach allows to explain recently obtained STS results and predicts some new interesting possible "switching" regimes.

1. P.I. Arseev, N.S. Maslova, S.I. Oreshkin, V.I. Panov and S.V. Savinov, JETP Lett **72**, 565 (2000).
2. Y. Goldin, Y. Avishai, PRB **61**, 16750 (2000).
3. A.-P. Jauho, N.S. Wingreen, Y.Meir, PRB **50**, 5528 (1994).
4. J. Konig, T. Pohjola, H.Schoeller, G. Schon, Physica E **6**, 371 (2000).
5. D.V. Averin, A.N. Korotkov, K.K. Likharev, PRB **44**, 6191 (1991).
6. P.I. Arseev, N.S. Maslova, S.V. Savinov, JETP Lett **68**, 320 (1998).

THEORY OF FANO RESONANCE IN STM SPECTROSCOPY OF KONDO IONS ON METAL SURFACES

O. Újsághy[1,2], J. Kroha[3], L. Szunyogh[1], A. Zawadowski[1,2,4]

[1]*Department of Theoretical Physics and* [2]*Research Group of the Hungarian Academy of Sciences, Technical University of Budapest, H-1521 Budapest, Hungary*

[3]*Institut für Theorie der Kondensierten Materie, Universität Karlsruhe, D-76128 Karlsruhe, Germany*

[4]*Solid State and Optical Research Institute of the Hungarian Academy of Sciences, H-1525 Budapest, Hungary*

The conduction electron density of states nearby a single magnetic impurity, as measured recently by scanning tunneling microscopy (STM), is calculated. It is shown that the Kondo effect induces a narrow Fano resonance as an intrinsic feature in the conduction electron density of states. The line shape varies with the distance between STM tip and impurity, in qualitative agreement with experiments, and is sensitive to details of the band structure. For a Co impurity the experimentally observed width and shift of the Kondo resonance are in accordance with those obtained from a combination of band structure and strongly correlated calculations.

It has been known for a long time that the local electron density of states has a specific structure due to the Kondo resonance [1], but due to the atomic resolution of scanning tunneling microscope (STM) only recent experiments [2,3,4] were able to study single, isolated Kondo impurities on metal surfaces. In these experiments a narrow, resonance-like structure was found in the measured $\frac{dI}{dV}$ characteristics of the tunneling current through the tip of an STM placed at a distance R from the impurity close to the surface (see Fig. 1). The line shape was either a dip (for Ce on Ag(111) [2]) or an asymmetric resonance (for Co on Au(111) [3] or Cu(111) [4]) near the Fermi energy (ε_F) resembling that of a Fano resonance [5] and it was observed only at low temperatures ($\sim 4-5$K). Changes of the line shape and decrease of the overall amplitude with increasing lateral distance from the impurity were also found [3,4] and the resonance was not observed for distances larger than $\sim 40\mathring{A}$ for Ce on Ag [2] and $\sim 10-12\mathring{A}$ for Co on Au [3] or Cu [4] surfaces. A "quantum mirage" experiment was also performed [4] by placing a Co impurity at one

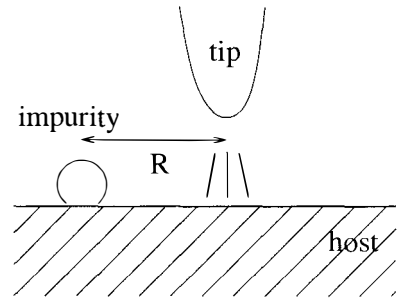


Figure 1: Schematic plot of the measurement's setting.

focus of a properly sized empty elliptical corral built from Co (or non-magnetic) adatoms where an attenuated resonance was also found in the opposite focus. Later a systematic study of the local electronic structure of individual transition-metal impurities on Au surfaces was performed [6] and showed that for elements near the end of the $3d$ row (Ti, Co, and Ni) the above mentioned narrow resonance structure appears, whereas for the elements around the center of the row (V,

Cr, Mn, Fe) the electronic structure is found to be featureless.

In these experiments the electron tunnels from the tip into the metal, travels to the impurity and, after scattering off it, goes back to the tip, resulting in an interference between the unperturbed and scattered electrons. There is also a possibility that the electrons tunnel from the tip directly to the magnetic impurity, more precisely into the d- or f-level of the atom. However, the tunneling rate for the latter process is probably very small, especially for f-levels, which are deeply inside the atom.

Here we summarize our calculation [7,8] where we have shown that the Fano resonance in the STM tunneling density of states can develop even if one neglects the direct tunneling to the impurity which greatly simplifies the theoretical treatment comparing to other studies [3,9,10]. This assumption is supported also by the quantum mirage experiment [4] where the opposite focus is spatially separated from the impurity level, thus the direct tunneling plays certainly negligible role there and justified for the experimental situation in the non-equilibrium theory of STM via adsorbate resonances performed by Plihal and Gadzuk [10]. In this case the STM measures the conduction electron local density of states (LDOS) which is modified due to the magnetic impurity.

For concreteness we focused on a Co atom on Au(111) and used the Anderson model [11] with a fivefold orbital degeneracy of the d-level [7]. First the self-consistent electronic structure of the Co atom on Au(111) was calculated by using the semi-relativistic Korringa-Kohn-Rostoker (KKR) method [12] in combination with local spin-density approximations (LSDA) [13] as was done previously [14] for similar problems. It turned out that mainly due to the $sp-d$ hybridization, the Co d-levels are somewhat shifted downward compared to the bulk Co, so that the average impurity occupation number is $n_d \simeq 8.8$ instead of $n_d = 7$ expected from the nuclear charge of Co, thus the system fluctuates only between the three charge states $z = 8, 9, 10$ which can be identified with the empty, singly and doubly occupied states of an effective non-degenerate Anderson model with new parameters $\overline{\varepsilon}_d = -0.84$eV and $\overline{U} = 2.84$eV [7]. Then the corresponding Co d-orbital spectral function was calculated at $T = 4$K using the non-crossing approximation (NCA) [15] from which we could estimate the Kondo temperature as $T_K \simeq 52$K and conclude that the narrow Kondo resonance is shifted somewhat upward from the Fermi level.

We performed a straightforward analytical calculation of the perturbed conduction electron LDOS measured by the STM [7] where the two basic ingredients are the unperturbed one-electron Green's function at the surface of the metal $\mathcal{G}_R^{(0)}(\omega - i\delta)$ (per spin) and the scattering amplitude $t(\omega - i\delta)$ due to the impurity. In the first, the spatial extent of the tip was taken into account as well, by introducing the smeared electronic field operators around the STM tip [7]. The latter, given by $\frac{\Delta}{\pi\rho_0} G_d(\omega - i\delta)$ in the Anderson model [7,11], according to our LSDA combined with NCA result and Nozières Fermi liquid theory [16] (for $T < T_K$ the Kondo resonance is a pure potential scatterer), can be approximated as

$$t(\omega - i\delta) = \frac{\Delta}{\pi\rho_0}\left(\frac{Z_d}{\omega - \overline{\varepsilon}_d - i\Delta} + \frac{Z_U}{\omega - \overline{\varepsilon}_d - \overline{U} - i\Delta} + \frac{Z_K}{\omega - \varepsilon_K - iT_K}\right), \tag{1}$$

where $G_d(\omega - i\delta)$ is the d-electron Green's function and ρ_0 is the bare conduction electron density of states per spin, Z_d, Z_U and Z_K are the appropriate strength of the poles, and Δ and ε_K are the broadening of the d-level, and the position of the Kondo resonance, respectively [7].

The final expression for the tunneling density of states reads [7]

$$\delta\rho_R(\omega) = \frac{[\mathrm{Im}\,\mathcal{G}_R^{(0)}(\omega - i\delta)]^2}{\pi\rho_0}\left\{\frac{(q_R + \varepsilon)^2}{\varepsilon^2 + 1} - 1 + C_R\right\} \tag{2}$$

where $\varepsilon = (\omega - \varepsilon_K)/T_K$ and

$$q_R = \frac{\mathrm{Re}\,\mathcal{G}_R^{(0)}(\omega - i\delta)}{\mathrm{Im}\,\mathcal{G}_R^{(0)}(\omega - i\delta)}. \tag{3}$$

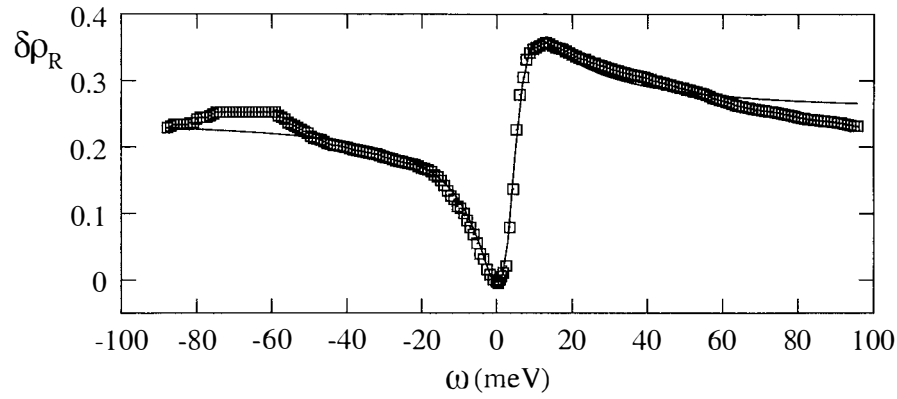


Figure 2: Fit of Eq. (2) (solid line) to the experimental data [3] (squares) at $R = 0$. The fit parameters are $q_{R=0} = 0.66$, $C_{R=0} = 0.95$ and $\varepsilon_K = 3.6$meV, $T_K = 5$meV$\sim$ 50K.

C_R, which depends on Z_d, $\bar{\varepsilon}_d$, Δ, and q_R [7], arises from potential scattering on the d-level and corresponds to a weakly energy dependent Friedel oscillation. The first part of Eq. (2) coming from the scattering by the Kondo resonance gives a Fano line shape in the tunneling LDOS, controlled by the parameter q_R.

The fit on the experimental data for a Co atom on a Au (111) surface [3] gave excellent agreement with fitting parameters being consistent with the predictions of an NCA calculation combined with band structure results [7] (see Fig. 2).

To calculate the distance dependence of q_R and C_R, i.e., of the line shape, the tunneling of electrons from the tip (1) into the 3-dimensional Au bulk states as well as (2) into the 2-dimensional Au(111) surface band [17] was considered. In both cases a free electron-like band structure was assumed [7]. Comparing the wave length of the oscillating line shape [3] with the known Fermi wave numbers of the Au bulk and the surface band [17] we can conclude that tunneling into the Au(111) surface band gives important contribution. Whereas the periodic changes of the line shape between Fano and Lorentzian ones and the decrease in the overall amplitude with increasing distance were demonstrated (see Fig. 3), the precise dependence of the line shape on R is not reproduced by our simplifying assumption of a free electron band structure [7]. That and as well as the precise understanding of the case of other transition metal elements will require taking into account the detailed band structure.

Summarizing, we have shown that the Kondo resonance in the magnetic impurity d-level density of states ($T < T_K$) causes a Fano line shape in the density of states measured by STM even if we take into account only the tunneling into the conduction electron states, therefore, the Fano line shape is an intrinsic property of the conduction electron LDOS and not an artifact of the STM measurement technique. From the fit to the experimental data for Co on Au(111) surfaces [3] we conclude that the Kondo resonance is shifted upward from the Fermi level, and T_K for Co on the surface is substantially reduced compared to the bulk value. By combining electronic structure calculations (LSDA) with methods for strong correlations (NCA) these findings are reproduced semi-quantitatively. In particular, the shift of the Kondo resonance is due to level repulsion between the d-level and the Kondo resonance. We demonstrated the dependence of the line shape on the distance of the tip from the impurity by using bulk as well as surface state Green's functions. We emphasize, however, that details of the band structure have to be taken into account in order to reproduce this distance dependence quantitatively.

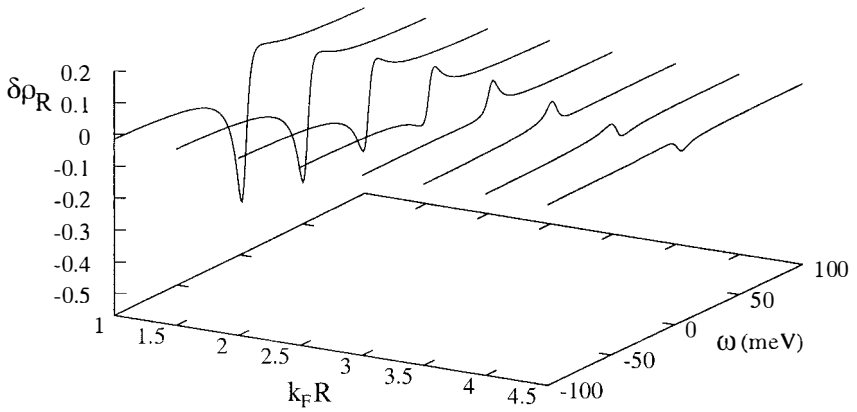


Figure 3: Qualitative dependence of the line shape of the tunneling DOS on the distance of the tip from the impurity using Eq. (2) and three-dimensional Au bulk states. The result obtained by using the two-dimensional free-electron like Au(111) surface band states [17] are quite similar.

Acknowledgments

We acknowledge useful discussions with R. Berndt, M. F. Crommie and W.-D. Schneider. This work was supported by the Humboldt foundation (A.Z.), by the OTKA Postdoctoral Fellowship D32819 (O.Ú.), by Hungarian grants OTKA T029813, T030240 and by DFG through SFB 195 (J.K.).

References

1. F. Mezei and A. Zawadowski, *Phys. Rev.* B **3**, 167 (1971), *Phys. Rev.* B **3**, 3127 (1971).
2. Jintao Li, W.-D. Schneider, R. Berndt and B. Delley, *Phys. Rev. Lett.* **80**, 2893 (1998); W.-D. Schneider, *Pramana, J. Phys.* **52**, 537 (1999).
3. V. Madhavan, W. Chen, T. Jamneala, M. F. Crommie, and N. S. Wingreen, *Science* **280**, 567 (1998).
4. H. C. Manoharan, C. P. Lutz and D. M. Eigler, *Nature* **403**, 512 (2000).
5. U. Fano, *Phys. Rev.* **124**, 1866 (1961)
6. T. Jamneala, V. Madhavan, W. Chen, and M. F. Crommie, *Phys. Rev.* B **61**, 9990 (2000).
7. O. Újsághy, J. Kroha, L. Szunyogh, and A. Zawadowski, *Phys. Rev. Lett.* **85**, 2557 (2000).
8. O. Újsághy, G. Zaránd, A. Zawadowski, *Solid State Commun.* **117**, 167 (2001).
9. A. Schiller, S. Hershfield, *Phys. Rev.* B **61**, 9036 (2000).
10. M. Plihal and J. W. Gadzuk, *Phys. Rev.* B **63**, 085404 (2001).
11. P. W. Anderson, *Phys. Rev.* **124**, 41 (1961).
12. L. Szunyogh, B. Újfalussy, P. Weinberger and J. Kollár, *Phys. Rev.* B **49**, 2721 (1994).
13. S.H. Vosko, L. Wilk and M. Nusair, *Can. J. Phys.* **58**, 1200 (1980).
14. M. Weissmann, A. Saúl, A. M. Llois and J. Guevara, *Phys. Rev.* B **59**, 8405 (1999).
15. N.E. Bickers, *Rev. Mod. Phys.* **59**, 845 (1987); T.A. Costi, J. Kroha and P. Wölfle, *Phys. Rev.* B **53**, 1850 (1996).
16. P. Nozières, *J. Low Temp. Phys.* **17**, 31 (1974).
17. W. Chen, V. Madhavan, T. Jamneala and M. F. Crommie, *Phys. Rev. Lett.* **80**, 1469 (1998).

DYNAMICS OF COULOMB–CORRELATED ELECTRON–HOLE PAIRS IN DISORDERED SEMICONDUCTOR NANOWIRES

I. VARGA[1,2], C. SCHLICHENMAIER[1], T. MEIER[1], K. MASCHKE[3], P. THOMAS[1] and S.W. KOCH[1]

[1] *Fachbereich Physik und Wissenschaftliches Zentrum für Materialwissenschaften, Philipps Universität, Marburg, D-35032 Marburg, Germany*

[2] *Elméleti Fizika Tanszék, Fizikai Intézet, Budapesti Műszaki és Gazdaságtudományi Egyetem, H-1521 Budapest, Hungary*

[3] *Institut de Physique Appliquée, École Polytechnique Fédérale de Lausanne, CH-1015 Lausanne, Switzerland*

The dynamics of optically generated electron-hole pairs is investigated in a disordered semiconductor nanowire. The particle pairs are generated by short laser pulses and their dynamics is followed using the Heisenberg equation of motion. Is is shown that Coulomb–correlation acts against localization in the case of the two–interacting particles (TIP) problem. Furthermore, currents are generated using a coherent combination of full-gap and half-gap pulses. The subsequent application of a full-gap pulse after time τ produces an intraband echo phenomenon 2τ time later. The echo current is shown to depend on the mass ratio between the electrons and the holes

1 Introduction

Optically generated carriers in a semiconductor environment produce an exciting scenario to study fast quantum coherent phenomena. The presence of disorder and the interaction between the carriers as well as with external fields produces a number of interesting phenomena [1]. The prospectives added by the recent fabrication of rings on a nanoscopic range [2] may add a further boost to the theoretical investigation of low–dimensional small semiconductor systems.

In this contribution we present two examples where the time evolution of the electron–hole pairs provides interesting insight into the combined effect of disorder and interaction. In the first one the spreading of initially localized electron–hole wave packets are shown to expand to considerably larger extent as compared to the size of single particle localization. In the second example we show how the phase coherent dynamics results in a new type of echo phenomenon discussed only recently.

2 The model and the equation of motion

The Hamiltonian of the two–band semiconductor subject to the external laser field represented by an electric field $E(t)$ reads

$$H = \sum_{\lambda=e,h} H_\lambda + H_I + H_C, \tag{1}$$

where the two bands, the conduction band with electrons, H_e, and the valence band with holes, H_h, are both written in the tight–binding approximation

$$H_\lambda = \sum_i \varepsilon_i^\lambda \sigma_{ii}^{\lambda\lambda} - J^\lambda \sum_i (\sigma_{i,i+1}^{\lambda\lambda} + \sigma_{i,i-1}^{\lambda\lambda}). \tag{2}$$

The interaction with the laser is kept within the dipole approximation

$$H_I = -E(t)d, \qquad \text{with} \qquad d = -e \sum_{\lambda\lambda' i} (R_i \delta_{\lambda\lambda'} + r_{\lambda\lambda'}) \sigma_{ii}^{\lambda\lambda'} \tag{3}$$

and the Coulomb interaction within the monopole–monopole approximation

$$H_C = \frac{1}{2}\sum_{ij}(\sigma_{ii}^{ee} - \sigma_{ii}^{hh})V_{ij}(\sigma_{jj}^{ee} - \sigma_{jj}^{hh}). \tag{4}$$

In the above equations we used $\sigma_{ij}^{\lambda\lambda'} = a_{\lambda i}^{\dagger}a_{\lambda' j}$, if $a_{\lambda i}^{\dagger}$ ($a_{\lambda i}$) creates (annihilates) a particle in the band λ (e or h) at site i. Hence in Eq. (4) the electron densities are described using $n_{ij}^{e} = \langle\sigma_{ij}^{ee}\rangle$ and the hole densities using $n_{ij}^{h} = \delta_{ji} - \langle\sigma_{ji}^{hh}\rangle$. The interband coherences (the pair amplitudes) are $p_{ij} = \langle\sigma_{ij}^{eh}\rangle$. The interaction between the carriers is assumed to have the regularized form of $V_{ij} = V_0\, a/(|i-j|a + a_0)$, where a is the lattice constant, a_0 and V_0 characterize the strength of the interaction ensuring a finite value for the excitonic binding energy. For both of our studies they were fixed in order to obtain an exciton binding energy typical for quasi–onedimensional GaAs quantum wires.

In our study disorder entered by choosing the on–site energies ε_i^{λ} from a flat distribution of width W. These random values at each site for different bands may be anti-correlated if the energy separations of the isolated sites are constant and correlated if the averages of the site energies coincide.

The time evolution of the various components of $\langle\sigma_{ij}^{\lambda\lambda'}\rangle$ are obtained via the solution of the Heisenberg equations of motion (using $\hbar = 1$)

$$i\partial_t\sigma_{ij}^{\lambda\lambda'} = \left[\sigma_{ij}^{\lambda\lambda'}, H\right] \tag{5}$$

In our first example we will simplify the equation assuming low excitation intensity. Thus linear response in the external laser field and henceforth the Hartree–Fock approximation for the particle–particle interaction are valid. This results for the interband coherences in

$$i\partial_t p_{ij} = \left(\epsilon_j^e + \epsilon_i^h - V_{ij}\right) - J^h\left(p_{i,j-1} + p_{i,j+1}\right) + J^e\left(p_{i-1,j} + p_{i+1,j}\right) - \mu_j E(t)\delta_{ij} \tag{6}$$

where μ_j is the polarizability at site j. The intraband coherences, in this case, are calculated using the sum rules, $n_{ij}^{e} = \sum_k p_{kj}p_{ki}^{*}$ and $n_{ij}^{h} = \sum_k p_{jk}p_{ik}^{*}$ valid in this low excitation limit.

The second problem requires the external field to be handled nonperturbatively. Therefore as a first step we have omitted the particle–particle interaction or only kept it at the level similar to that presented in Eq. (6). In this case the term containing the external field would be $eE(t)\left[(R_i - R_j)p_{ij} + r_{eh}(n_{ij}^{e} + n_{ji}^{h} - \delta_{ij})\right]$. The intraband amplitudes, n_{ij}^{e} and n_{ij}^{h} are obtained in a similar fashion and have to be solved simultaneously.

3 Two interacting particles

The time evolution of an initially localized excitation has been followed via the integration of the equations of motion (6) for the interband coherences, p_{ij}. The extension of the wave packet p_{ij} was characterized, among others, by the center of mass width, $R_{cm}^2 = \frac{1}{2}\sum_{ij}(i+j)^2|p_{ij}|^2$. A typical evolution of R_{cm} is given in Fig. 1. Here we used $N = 240$ sites, $J^e = -J^h = 20$meV and very strong disorder, $W^h = W^e = 4J^e$.

The case of anti-correlated disorder seems to be much more favorable in order to produce reduced localization of the wave packets as is shown in Fig. 1. The numerically obtained time functions may be fitted with high accuracy to a phenomenological form of $R(t) = ((Dt)^{-1/2} + \xi_{\infty}^{-1})^{-1}$ allowing a diffusion constant D and an extrapolated infinite time localization length ξ_{∞} to be obtained from the fitting procedure[4].

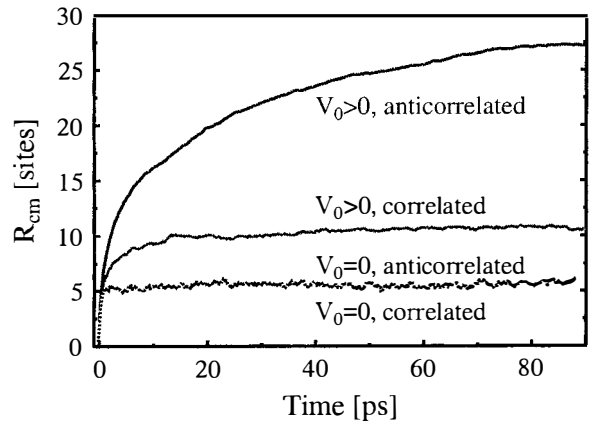


Figure 1: Center of mass width of a two–particle wave packet for correlated and anti-correlated disorder. $J^e = -J^h = 20$meV, $W^e = W^h = 4J^e$. The curves have been obtains after averaging over 20 samples.

4 Coherent control and current echo

In our other example we show how the rephasing process of *intra*band excitations after two subsequent laser pulses with a time delay of τ can be investigated. This is in contrast to the photon echo which is similarly seen in the *inter*band excitation. The observable showing such an echo phenomenon is the total intraband current.

The echo phenomenon has been first suggested using a voltage pump [8] for noninteracting particles. In the same scheme it has been shown that the many particle interaction reduces its height but does not destroy the current echo [6]. Recently the use of coherent control provides a further possibility to generate such an echo phenomenon [7].

A current in the system (1)–(4) may be generated using a special excitation in which the initial populations are produced via transitions that have different initial propagation into different spatial directions, i.e. a spontaneous current appears. This scheme is an example of coherent control [5]. It is realized using a pulse with mean frequency in resonance with transitions in the optical continuum and another pulse having only half that frequency, $E(t) = \mathrm{Re}\left\{E_1 e^{i\omega t+\phi_1} + E_2 e^{i\omega t/2+\phi_2}\right\}$. The resulting current can be calculated using the equation of motion, $\mathcal{J} = \dot{d} = i[H, d]$ which results in a sum of two terms, an intraband current, $\langle \mathcal{J}_{intra} \rangle$, and an interband current, $\langle \mathcal{J}_{inter} \rangle$. Here we give the former as $\langle \mathcal{J}_{intra} \rangle \sim J^e \sum_i \mathrm{Im}(n^e_{i+1,i}) - J^h \sum_i \mathrm{Im}(n^h_{i+1,i})$.

The renewed excitation of the system with a laser pulse after time τ causes phase conjugation. As it turns out we only need a light field with mean frequency ω for the second excitation. This phase conjugation leads to a collective rephasing of the electron and the hole intraband coherences, $n^{e,h}_{ij}$, at times [9]

$$T_e = \tau + \frac{J^h}{J^e}\tau \qquad \text{and} \qquad T_h = \tau + \frac{J^e}{J^h}\tau. \tag{7}$$

This is when the echo occurs in the conduction (valence) band for electrons (holes). Hence in the case when the holes are heavier than the electrons, $J^e > J^h$, the echo signal contains two peaks: one before $t = 2\tau$ for the electrons and another one after that for the holes.

In Fig. 2 we give an example when the second excitation at $t = 800$fs has been simplified for a full gap pulse instead of the combination present at $t = 0$. That is the reason why we see only

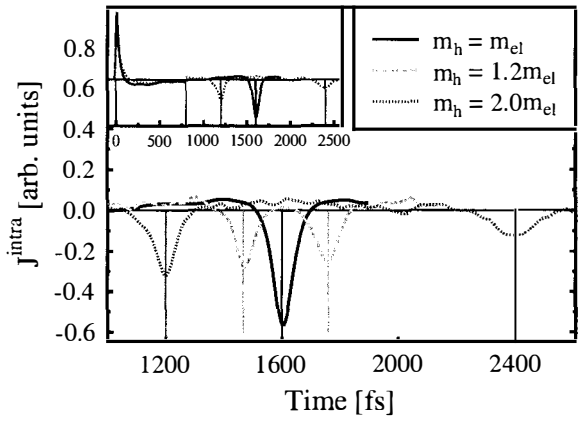


Figure 2: The echo time dependence on the effective mass of the particles. The inset shows the full time evolution with the first excitation at $t = 0$, the second excitation at $t = 800$fs using only a full gap pulse (producing a negligible response in the intraband current) and the spontaneous echo at $t = 1600$fs. In the main panel the variation of the echo peak is shown for various electron–hole mass ratios. The curves have been obtained as averages over 128 realizations of the disorder.

a minor change in the current response of the system at $t = \tau$. The double echo peak presented in Fig. 2 is obtained for a system consisting of $N = 71$ sites, with $m_e = 0.28m_0$, $W^{e,h} = 2J^{e,h}$ and correlated disorder.

Note that the present model shows a photon echo even in the absence of disorder, while in that case there is no current echo. This emphasizes the fundamental difference of these two echo phenomena.

Work is in progress to study the influence of the many–particle interaction on this phenomenon in the coherent–control scenario.

Acknowledgments

This work was supported by the Deutsche Forschunggemeinschaft (DFG) through the Quantenkohärenz Schwerpunkt, by the Max-Planck Research prize, the Leibniz prize and the Hungarian Research Fund (OTKA) under T029813, T032116 and T034832.

References

1. S. Weiser *et al.*, *Phys. Rev.* B **61**, 13088 (2000); C. Sieh *et al. Eur. Phys. J.* B **11**, 407 (1999); K. Maschke *et al.*, *Eur. Phys. J. B*, in press.
2. R.J. Warburton, *et al. Nature* **405**, 926 (2000).
3. D. Brinkmann, *et al. Eur. Phys. J.* B **10**, 145 (1999).
4. P. Thomas, *et al. phys. stat. sol.* (b) **218**, 125 (2000).
5. R. Atanasov, *et al. Phys. Rev. Lett.* **76**, 1703 (1996).
6. S. Sauter, *et al. Phys. Rev.* B **57**, 4299 (1998).
7. J. Stippler, *et al. phys. stat. sol.* (b) **221**, 379 (2000).
8. W. Niggenmeier, *et al. Phys. Rev. Lett.* **71**, 770 (1994).
9. C. Schlichenmaier, *Diploma Thesis* (Marburg, 2001), unpublished.

Ballistic Hall response

M. Long [1],F. Naef [2], P. Prelovšek [3,4],X. Zotos [2]

[1] *Department of Physics, University of Birmingham, Edgbaston, Birmingham B15 2TT, United Kingdom*

[2] *Institut Romand de Recherche Numérique en Physique des Matériaux (IRRMA), PPH-Ecublens, CH-1015 Lausanne, Switzerland*

[3] *Faculty of Mathematics and Physics, University of Ljubljana, 1000 Ljubljana, Slovenia*

[4] *J. Stefan Institute, 1001 Ljubljana, Slovenia*

The zero temperature Hall constant R_H, described by reactive (nondissipative) conductivities, is analyzed within linear response theory. It is found that in a certain limit (a finite system in the transverse direction), R_H is directly related to the density dependence of the Drude weight. This novel formulation implies a simple picture for the change of sign of charge carriers in the vicinity of a Mott-Hubbard transition. It is applied to the calculation of R_H in quasi-one dimensional prototype interacting electron models and compared to the semiclassical Boltzmann formulation for anisotropic tight binding systems.

1 Introduction

The Hall constant R_H is traditionally studied in the framework of the semiclassical Boltzmann approach or within linear response theory, the Kubo formulation. It characterizes the Hall response that can be considered as a generic phenomenon described by the set-up shown in Fig. 1; an (infinitesimal) magnetic field B is applied on the system in the $z-$direction with wavevector-q together with a uniform electric field of amplitude E^x and frequency ω that drives a current j^x along the $x-$direction. The combination of the two induces a j^y current along the transverse $y-$direction and the issue is, what electric field E^y must be applied as to cancel the induced j^y current. So the "Hall constant" $R_H = -\frac{1}{B}\frac{E^y}{j^x}$ can be studied at different (q,ω) and temperature T regimes.

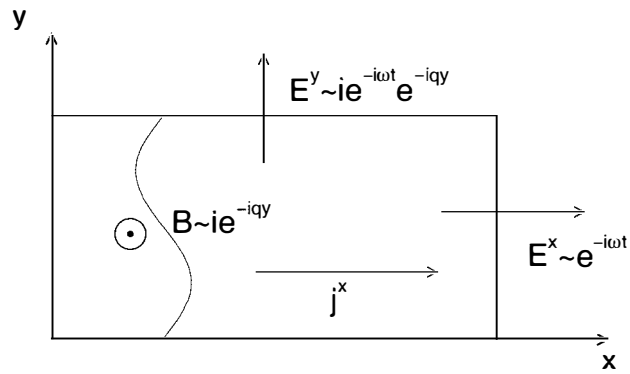


Figure 1: Hall response set-up.

In the usual case, the finite temperature - dissipative- response is analyzed in the limit of an infinite size system, by taking first the limit $q \to 0$ and then $\omega \to 0$. This is usually the most relevant experimental limit but also the most difficult to analyze theoretically for strongly

correlated electronic systems. Recently however, it was proposed [1,2,3] that valuable information on the Hall response can be obtained from the zero temperature ballistic regime, by analysis of the appropriate most diverging real (or imaginary) parts of the diagonal and off-diagonal conductivities (the phases of the fields as indicated in Fig. 1).

In particular, as we will present next, by considering the limit $\omega \to 0$ first and $q \to 0$ second, a simple relation exists between the Hall constant R_H and the Drude weight D characterizing ballistic transport at $T = 0$. These conditions, related to ballistic transport in a "mesoscopic" finite size system in the $y-$direction, provide a transparent picture of the density and interaction strength dependence of the Hall constant that is in accord with semiclassical arguments. This novel point of view naturally raises the question on the relation of the "Hall constant" between different (q, ω, T) regimes [4].

2 Drude weight and the Hall constant

A generic Hamiltonian describing interacting fermions on a lattice is given by a one band anisotropic tight binding model with sites labeled $l(m)$ along the $x(y)$-direction and periodic boundary conditions in both directions:

$$H = (-t_x)\sum_{l,m}(c^{\dagger}_{\sigma;l+1,m}c_{\sigma;l,m} + h.c.) + (-t_y)\sum_{l,m}(c^{\dagger}_{\sigma;l,m+1}c_{\sigma;l,m} + h.c.) + \hat{U}. \qquad (1)$$

For the (q, ω) limits described above and $T = 0$, it was shown [3] that:

$$R_H = -\frac{1}{D}\frac{\partial D}{\partial n}. \qquad (2)$$

Here D is the Drude weight [5] defined as the second order derivative of the ground state energy with respect to a fictitious flux ϕ piercing the system and modulating the hopping matrix element by $(-t) \to (-t)e^{i\phi}$; n is the carrier density.

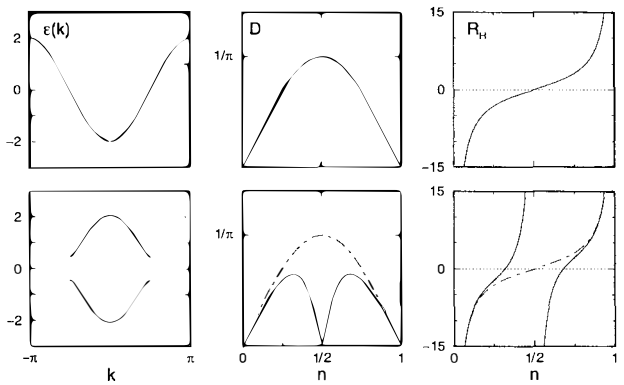


Figure 2: Comparison of dispersion ϵ_k, Drude weight D and Hall constant R_H for a metallic system (above) and a band insulator at half-filling (below)

From this formulation we readily recover the expected semiclassical behavior as indicated in Fig. 2: at low densities, $D \propto n$ so that $R_H = -1/n$. For an almost filled band of independent electrons (of one spin component) $D \propto \delta(= 1 - n)$ so that $D = +1/\delta$ for $n \preceq 1$. But for an

insulating system at half-filling ($n = 0.5$), with a charge gap due to band effects (semiconductor model) or correlations (Mott - Hubbard insulator), $D \propto \delta(= 0.5 - n)$, so $R_H = +1/\delta$ for $n \preceq 0.5$.

We should notice that the above formulation implies an anisotropic Hall constant for an anisotropic system as D depends on direction. This is shown explicitly in Fig. 3 for a free fermion tight binding model with anisotropic hoppings $t_x = 1, t_y$ and thus a dispersion $\epsilon_{\vec{k}} = -2t_x \cos k_x - 2t_y \cos k_y$. The curves are calculated from the Drude weights $D_x(D_y)$ along the $x-(y-)$ directions respectively. Notice that the effect of the flux ϕ is simply to displace $k \rightarrow k+\phi$.

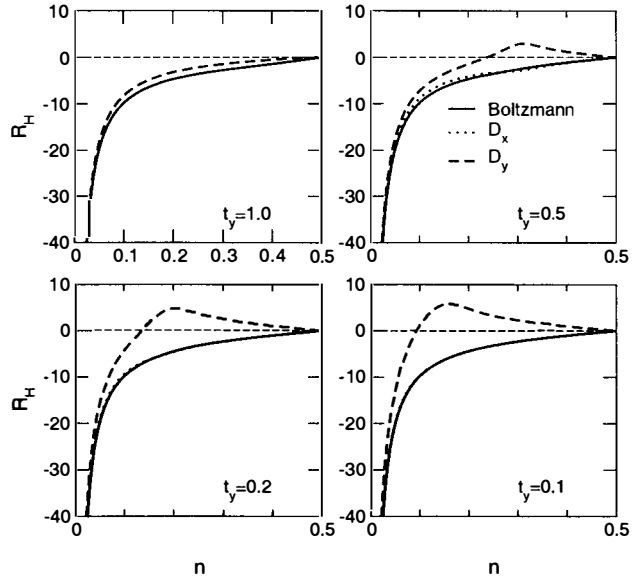


Figure 3: R_H from (2) for different anisotropies and Boltzmann approach.

In the Boltzmann formulation an independent particle band structure is implied; the Hall constant is by construction isotropic and given, within a single scattering time approximation, by:

$$R_H \propto (-1)\frac{\int d^d\mathbf{k} \int dq \frac{df}{dE}[(\frac{\partial E}{\partial q})^2 \frac{\partial^2 E}{\partial k_\parallel^2} - \frac{\partial E}{\partial k_\parallel}\frac{\partial E}{\partial q}\frac{\partial^2 E}{\partial k_\parallel \partial q}]}{\int d^d\mathbf{k} \int dq \frac{df}{dE}(\frac{\partial E}{\partial k_\parallel})^2 \int d^d\mathbf{k} \int dq \frac{df}{dE}(\frac{\partial E}{\partial q})^2} \tag{3}$$

Assuming a single particle dispersion of the form $E_{\mathbf{k},q} = \epsilon_{\mathbf{k}} - 2t_\perp \cos q$, with $\mathbf{k} = k_x$ and $q = k_y$, we find the behavior shown in Fig. 3. We notice that the discrepancy between the two formulations is minor in the isotropic case, while for the extreme anisotropic case $t_y = 0.1$ the two results agree in the large hopping direction while there is a qualitative difference in the small hopping one.

This agreement can be understood by considering the limit $t_\perp \rightarrow 0$ in (3) by noting that the Fermi surface becomes essentially uniform parallel to q so that, after some reductions:

$$R_H \propto (-1)\frac{\frac{\partial}{\partial n}\int d^d\mathbf{k}\frac{df}{d\epsilon}(\frac{\partial \epsilon}{\partial k_\parallel})^2}{\int d^d\mathbf{k}\frac{df}{d\epsilon}(\frac{\partial \epsilon}{\partial k_\parallel})^2} \tag{4}$$

Thus we recover expression (2) as $\int d^d\mathbf{k}\frac{df}{d\epsilon}(\frac{\partial \epsilon}{\partial k_\parallel})^2$ is equal to the Drude weight for independent fermions. The fact that the formulation (2) implies an anisotropic Hall constant is not surprising

as we are dealing with ballistic transport; finally, we should note that even if the dispersion is anisotropic but quadratic in the wavevector, R_H remains isotropic.

A case that can be further analyzed is that of quasi-one dimensional systems of independent or correlated electrons [3,6] by assuming that the Drude weight D along the easy-transport direction is the sum of $D's$ for each chain. For independent electrons we simply obtain,

$$D = \frac{2t}{\pi}\sin(\frac{\pi n}{2}), \quad R_H = -\frac{\pi}{2}\frac{1}{\tan(\frac{\pi n}{2})}, \tag{5}$$

a well known expression used for the Hall constant of quasi one-dimensional compounds [7]. Furthermore, for a one-dimensional system described by the prototype Hubbard model ($\hat{U} = U n_{\uparrow;l,m} n_{\downarrow;l,m}$) D can be calculated analytically by the Bethe ansatz method [8,9]. The resulting behavior, typical for a correlated system with a Mott-Hubbard insulating state at half-filling is shown in Fig. 4.

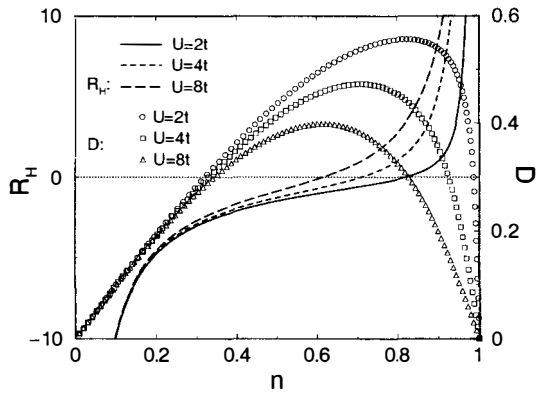


Figure 4: Drude weight and R_H from (2).

Acknowledgments

Part of this work was done during visits of (P.P.) and (M.L.) at IRRMA as academic guests of EPFL. X.Z. and F.N. acknowledge support by the Swiss National Foundation, the EPFL, the University of Fribourg and the University of Neuchâtel.

References

1. P. Prelovšek, *Phys. Rev.* B **55**, 9219 (1997).
2. P. Prelovšek, M. Long, T. Markež and X. Zotos, *Phys. Rev. Lett.* **83**, 2785 (1999).
3. X. Zotos, F. Naef, M. Long, and P. Prelovšek, *Phys. Rev. Lett.* **85**, 377 (2000).
4. P. Prelovšek, X.Zotos, *preprint.*
5. W. Kohn, Phys. Rev. **133**, A171 (1964). *Phys. Rev.* **133**, A171 (1964).
6. P. Prelovšek, T. Tohyama, S. Maekawa, *arXiv:cond-mat/0102418.*
7. J.R. Cooper *et al.*, *J. Phys (Paris)* **38**, 1097 (1997); K. Maki and A. Virosztek, *Phys. Rev.* B **41**, 557 (1990).
8. F.D.M. Haldane, *Phys. Lett.* **81A**, 153 (1981).
9. N. Kawakami and S-K. Yang, *Phys. Rev.* B **44**, 7844 (1991).

QUANTUM DOTS

Phase Evolution in a Kondo Correlated System[a]

Yang Ji, M. Heiblum,[b] D. Sprinzak, D. Mahalu and Hadas Shtrikman
Braun Center for Submicron Research, Dept. of Condensed Matter Physics
Weizmann Institute of Science, Rehovot 76100, Israel

We measured the phase evolution of electrons as they traverse a quantum dot (QD) formed in a two-dimensional electron gas that serves as a localized spin. The traversal phase, determined by embedding the QD in a double path electron interferometer and measuring the quantum interference of the electron wave functions manifested by conductance oscillation as a function of a weak magnetic field, evolved by radians, a range twice as large as theoretically predicted. As the correlation weakened, a gradual transition to the familiar phase evolution of a QD was observed. The specific phase evolution observed is highly sensitive to the onset of Kondo correlation, possibly serving as an alternative fingerprint of the Kondo effect.

The Kondo effect [1], a many body phenomenon, first discovered in metals slightly doped with magnetic impurities, has become one of the paradigms of strongly correlated systems. The effect, related to the Anderson model [2], results from an interaction of magnetic impurities with conduction electrons. In 1988 it was recognized [3,4] that the Kondo effect could also take place in a system of a spin polarized quantum dot (QD) [5], strongly coupled to an electron reservoir, thus forming a *spin singlet.* Indeed the effect was recently observed in a mesoscopic QD by Goldhaber-Gordon *et al.* [6], who were able to control *in situ* many relevant parameters that affect Kondo correlation. Even though the Kondo effect has been studied for some time, one of its most fundamental properties was never experimentally verified: a phase shift $\pi/2$ experienced by scattering electrons from the spin singlet [7,8]. Recently, such a calculation was applied to a Kondo correlated QD with similar predictions [9]. We address this issue experimentally by combining a mesoscopic, Kondo correlated QD with a *double path* Aharonov - Bohm (AB) interferometer [10,11]. After verifying the coherence, we proceeded to measuring the phase shift the traversing electrons through the dot experience. We find an unexpected behavior of the phase shift, which evolved in a range twice as large as that of the predicted one [9]. Moreover, we show that the phase evolution is extremely sensitive to the onset of Kondo correlation: while the conductance of the QD varies slightly and in a monotonous fashion with such onset, the phase behavior is radically different, serving as a distinct fingerprint of the Kondo effect.

The QD, serving here as a localized spin, is a small, confined, puddle of electrons, with two tunnel barriers coupling it to two electron reservoirs. The electrons in the puddle occupy a discrete ladder of energy levels, with level energy ε_d, and an average energy separation Δ between non spin degenerate levels. A capacitively coupled metallic gate (*plunger*) is used to tune the energy levels in the dot. Resonant tunneling between the two reservoirs (through the tunnel barrier – puddle – tunnel barrier system) takes place and current flows when an energy level is aligned with the Fermi level in the leads. When one of the electronic levels drops below the Fermi level in the leads, it gets occupied and the number of electrons in the dot increases by one. However, due to the small capacitance C of the QD and the discreteness of the electronic charge e, an additional, classical, *charging energy* $U_C = e^2/2C$, is needed in order to add a single electron into the dot. Effectively, the peak spacing is $U_C + \Delta$, where typically $U_C \gg \Delta$. At low temperature T ($k_BT \ll U_C$, with k_B the Boltzmann constant), when the Fermi surface in the leads lays in the gap between levels, there is a well-defined number of electrons in the QD and current does not flow. This is the well-known Coulomb Blockade phenomenon, where periodic

[a]Reprinted with permission from Science, **290**, 779(2000). Copyright ©2000 American Association for the Advancement of Science.

[b]To whom correspondence should be addressed.Email: Heiblum@wisemail.weizmann.ac.il

conductance peaks as a function of *plunger* voltage are separated by almost zero conductance valleys.

While Coulomb Blockade in QDs is a manifestation of the quantization of the electronic charge, the net spin of a QD is also quantized (in units $h/2$, with h the Plank constant). Generally, each energy state is spin degenerate, namely, it can host two electrons: one with *spin up* and one with *spin down*. Hence, the QD is *spin polarized* (with nonzero net spin) when it contains an odd number of electrons, thus acting as a 'magnetic impurity'. Furthermore, when the QD is strongly coupled to the leads and the temperature is sufficiently low, a spin singlet can form between the spin polarized dot and opposite spin electrons in the leads. This, so-called, Kondo correlation leads to an enhancement of the conductance of the valley between the spin degenerate peaks. The enhancement can be explained via an intuitive semi-classical approach. While the Coulomb Blockade is a first-order quantum mechanical effect the Kondo effect is a second-order effect, involving two electrons simultaneously. Having the top-most spin-degenerate energy level singly occupied with a spin up electron, this electron can tunnel out to the right lead while another electron, with spin down, simultaneously tunnels in from the left lead. This keeps the number of electrons in the dot constant but leads to a net spin flip in the dot. This process is followed by the return to the dot of the spin up electron in the right lead accompanied by a simultaneous jump of the spin down electron in to the right lead. The final result is a double-spin-flip of the dot and net transfer of a spin down electron from the left lead to the right one - leading to net current transfer [12,13]. In an alternative view, for a dot well coupled to the leads, the spin up electron's wavefunction leaks from the dot to the leads, keeping away the spin up electrons in the leads due to the Pauli exclusion principle. The spin down electrons, on the other hand, can get very close to the polarized dot. This can be modeled as an effective attractive potential for the spin down electrons near the dot, leading to the formation of a lower energy spin singlet (Fig. 1A). Due to this attractive potential, which turns out to be most effective for electrons at the Fermi energy, the impinging rate of spin down electrons on the dot increases, leading effectively to an increased current. The *effective transport density of states* develops a sharp peak at the Fermi energy (Fig. 1A), with a width reflecting the binding energy of the singlet. This small binding energy is customarily described by a *Kondo temperature*, T_K (some 1 K in our QDs). Hence, the Kondo enhanced valley conductance can be easily quenched by increasing the temperature, applying a finite DC bias across the QD, or reducing the coupling strength between the QD and the leads.

Ubiquitous conductance measurements in QDs have already demonstrated the Kondo effect [6]; however, they left the issue of coherence and phase evolution in such system open. To address this issue, we adopted our previously developed double-path electron interferometer with an embedded QD in one of its paths [11] tuned to the Kondo regime (Fig. 1B). In such system, smaller in overall dimensions than the *phase breaking length*, the current collected in the drain depends both on the magnitude, t_{QD}, and phase, ϕ_{QD}, of the transmission coefficient of the QD. Since the four base regions collect most of the back-scattered electrons, the net transmission of electrons going from source (S) to drain (D), t_{SD}, is a coherent sum of the transmissions via the two direct paths (dashed lines in Fig. 1B). With t_{ref}, ϕ_{ref}, belonging to the reference arm, $t_{SD} = t_{ref} + t_{QD}$ (assuming $t_{left} = t_{QD}$). The collected current in the drain, assuming a coherent system, is in turn $I_{SD} \propto |t_{SD}|^2 = |t_{left}|^2 + |t_{QD}|^2 + 2\,|t_{left}|\,|t_{QD}|\,cos(\phi_{ref} - \phi_{QD})$. Introducing a magnetic flux, Φ, in the area encompassed by the two paths, changes the relative phase of the reference arm via the AB effect [10], $\phi_{ref} \longrightarrow \phi_{ref} + 2\pi\Phi/\Phi_0$, with $\Phi_0 = h/e$ the *flux quantum*. This leads to an oscillating periodic component in the current as a function of magnetic field $\propto cos(\phi_{ref} - \phi_{QD} + 2\pi\Phi/\Phi_0)$. The phase evolution in the QD can then be directly deduced from the phase of the current oscillation in the drain. Such experiments, which have already been carried out with QDs in the Coulomb Blockade regime, lead to surprising results [11]. The measured phase of the QD was found to climb by π as each resonance swept through the Fermi

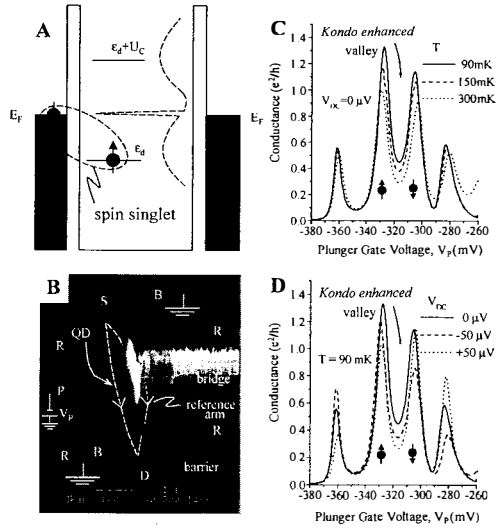


Figure 1: Kondo correlated spin singlet, sample description, and characterization of a Kondo pair. (**A**) Energy diagram of a quantum dot with Kondo correlation. The two spin-degenerate energy levels, ε_d and $\varepsilon_d + U_C$, are strongly coupled to the leads. At low temperature, a spin singlet is formed between the localized electron in the QD and an opposite spin electron in the leads, thus leading to a strong resonance in the *transport density of states* (dashed line) centered at the Fermi level in the leads. (**B**) A top-view scanning electron micrograph of the electronic double-path interferometer. The device is defined by negatively biased metallic gates (lightly gray areas) deposited on the surface of a GaAs-AlGaAs heterostructure with high mobility electrons 55 nm below the surface (density $n = 3 \times 10^{11} cm^{-2}$, mobility $\mu = 5 \times 10^5 cm^2 V^{-1} s^{-1}$, measured at 1.5 K). Three different regimes can be identified: source (S), drain (D), and base (B). The source and the drain openings support only one transverse mode, thus producing a planar electronic wavefront in the far field. The base regions collect back-scattered electrons to ensure that only the two forward-propagating paths (broken white lines) reach the collector. A metallic air bridge, formed by special lithographic techniques, is used to deplete the island between the two paths. A quantum dot (area $180nm \times 200nm$) is placed in the left arm, with both of its point contacts and the *plunger* gate (P) individually controlled. Reflectors R, confining the two paths, are used to deflect the electrons toward the drain. A *barrier* gate is used to cut off the reference (right) arm, in order to tune the bare dot to the Kondo regime. (**C**) The effect of increasing temperature on the conductance with $V_{DC} = 0\mu V$ across the QD. As the temperature increases, the (Kondo enhancemeant) of the central valley becomes smaller. (**D**) The effect of DC bias across the QD on the conductance at $T = 90$ mK. The central valley conductance decreases with increasing DC bias.

level in the leads, as expected. In the valley between the peaks, however, the phase experienced an unexpected abrupt $-\pi$ phase lapse — a phenomenon still not understood.

The double path interferometer is similar to that used in Ref. 11 (Fig. 1B). It is fabricated in a two dimensional electron gas (2DEG), embedded in a GaAs-AlGaAs heterostructure, with sub-micron metallic gates deposited on the surface. The QD is made smaller than usual ($180nm \times 200nm$) to allow large energy level spacing, hence allowing strong coupling of the dot to the leads, without overlapping of the energy levels. There are a few tens of electrons in the dot with average level spacing $\Delta \cong 0.5meV$ and a charging energy $U_C \cong 1.5meV$. Another *barrier* gate was added in order to shut off the reference arm and allow measuring the conductance of the bare QD. Measurements were done in a dilution refrigerator with base temperature $T_{lattice} < 50mK$ and an electron temperature $T_{electron} \sim 90mK$. Current collected in the drain was measured with standard lock-in techniques, with an excitation voltage $10\mu V$ at $7Hz$, applied between the source and the nearby base contacts. Four different samples, fabricated with different size QDs and in different 2DEG systems, were measured. All produced qualitatively similar results.

A *Kondo-enhanced* valley, confined between a pair of conductance peaks, is usually identified by its higher conductance and its quench either by an increased temperature, or by an applied finite DC bias across the QD, or by reducing the coupling to the leads [6]. Such an identification of the 'Kondo pair' was performed by measuring the conductance of the QD after pinching off the reference arm with the *barrier* gate. Four conductance peaks as a function of plunger gate (P) voltage are seen in Figs. 1C and 1D. At the lowest temperature and zero DC bias, the two center conductance peaks border a relatively high valley. These peaks are more closely spaced and have peak heights near the quantum conductance, e^2/h. As the temperature was increased ($90 \ldots 300$ mK, Fig. 1C) or the DC biased was raised ($0 \ldots \pm 50\mu V$, Fig. 1D), the central valley conductance decreased, the peak heights decreased, and the peak spacing increased — all characteristic of a Kondo correlated pair [6]. The conductance of the two outer valleys and peaks remained almost unchanged — characteristic of Coulomb Blockaded transport [5].

Having identified the Kondo pair, we removed the *barrier* gate voltage and formed the source and drain point contacts, thus allowing two paths interference. The drain current, as a function of the *plunger* gate voltage, is shown in Fig. 2A. It resembles the conductance of the bare QD (seen in Fig. 1C), but the peaks are shifted by some 80 mV in *plunger* gate voltage, their shape is distorted, and a large background appears. The obvious reason for the shift is the change in the electrostatic influence of the *barrier* gate and the two point contacts forming the source and drain. Shape distortion can be accounted for by the interference of the electron waves arriving from both of the interferometer arms. To perform interference, a controlled phase difference between the two direct paths from S to D was then induced by the application of a perpendicular magnetic field via the AB effect. The oscillation observed in the drain current (shown for example in five different points in Fig. 2A and 2B), with period 3.5 mT, immediately suggests coherency of transport in the QD current, when the dot is tuned to peaks or a valley of conductance. The high visibility ($5 - 25\%$), suggests that transport through the dot is highly coherent [10,11]. Assuming that the transmission of the reference arm remains unaffected by the *plunger* gate voltage, each trace of current oscillation (like in Fig. 2B) provides two data points: an average visibility and phase, leading to the magnitude and phase of the transmission coefficient of the QD. The visibility and the phase are shown as a function of *plunger* gate voltage in Fig. 2C. The visibility mimics quite well the conductance of the QD shown in Fig. 1C, suggesting that the coherent transmission and the total transmission are qualitatively similar in the entire energy range. While phase lapses, similar to those observed in Ref. 11, are observed between non-spin-degenerate levels (the outer valleys near $V_P = -280$ mV, -210 mV), the phase in the spin-degenerate levels **evolves continuously and monotonously, with no sign of phase lapse.** The phase climbs through the spin up peak and saturates at π in the valley, thereafter it continues and climbs by anohter 0.5π through the spin down peak. In

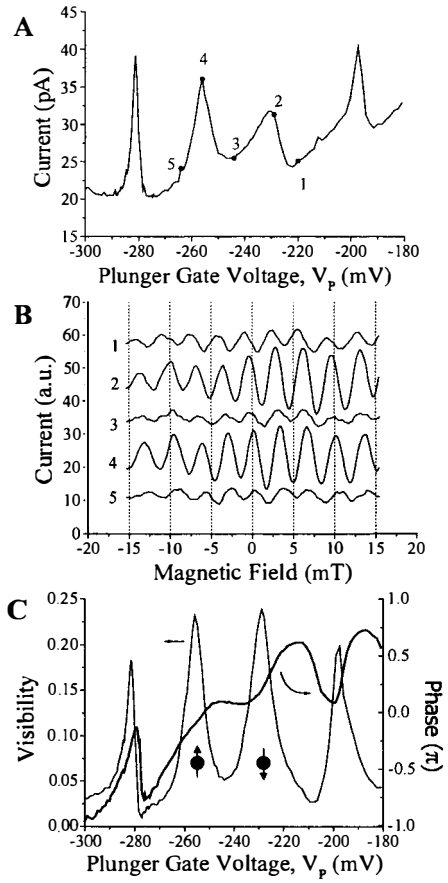


Figure 2: Complex transmission coefficient of the quantum dot in the Kondo regime measured via the Aharonov-Bohm (AB) effect. (**A**) Collector current as a function of *plunger* gate voltage at zero magnetic field. This current is very sensitive to magnetic field due to the AB effect, as shown in (**B**), when a series of interference patterns in the current collected by the drain (at specific points given in (A)), as a function of magnetic field (shifted vertically), taken at specific positions noted in (A). Trace 3, measured at center of the conductance valley between the Kondo pair, verifies coherency of electron transport in the Kondo valley. (**C**) Qualitative behavior of the magnitude (shown by the visibility of AB oscillation) and absolute value of the phase of the transmission coefficient of the QD — both obtained from the AB oscillations. Note that the phase evolves continuously through the Kondo pair while there is a phase lapse of $-\pi$ between the other consecutive peaks.

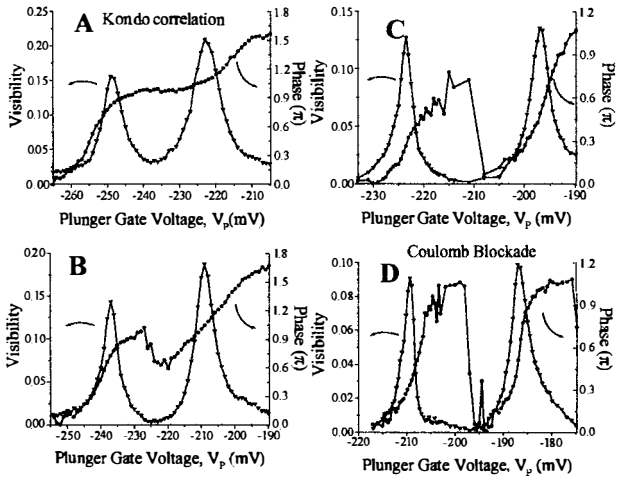


Figure 3: Phase lapse is formed as the coupling between the quantum dot and the leads is gradually reduced. When the coupling to the leads is strong (**A**), the phase evolution is continuous and the total phase change through the spin-degenerate pair is about 1.5π. As the coupling gets weaker (from (**A**) to (**D**)), and the QD enters the Coulomb Blockade regime, the familiar phase lapse [11] is recovered and a full phase evolution of π across each peak emerges. The peak position is shifting due to the influence of voltage applied to the gates that formed the two point contacts of the QD.

other samples, not shown here, we find the climb through the spin down peak to be also close to π. We believe that the total phase change across a Kondo pair varies from one sample to another because of peaks overlapping depending on their width and spacing. Hence, ideally, the phase seems to evolve by π into the *Kondo valley* and by 2π across the two spin degenerate levels. This is in contradiction with the prediction of Gerland et al. [9], who predicted a $\pi/2$ and π phase change, respectively. It is worth noting that in our device, due to the relatively high temperatures of the electrons, we could not reach the full Kondo enhancement, where the valley conductance reaches e^2/h [9,13,14]. Still, phase behavior is markedly distinct and different than the Coulomb Blockade regime. We believe it would stay invariant at lowest temperature.

Since the Coulomb Blockade regime can be easily approached by reducing the coupling strength between the QD and the leads, such a procedure was followed with results shown in Fig. 3. As the coupling strength becomes gradually weaker (from Fig. 3A to Fig. 3D), the phase evolves from a continuous increase across the two spin-degenerate levels to a sudden appearance of a small phase lapse in the valley (even though the Kondo correlation was still apparent in that condition), increasing eventually to a full $-\pi$ phase lapse — distinctive at Coulomb Blockade transport. As suggested before, the narrowing of the peaks, leading to reduced overlapping between them, indeed allowed a greater span of phase change, namely, a full accumulation of π across each peak.

Similarly, increasing the temperature to an order of T_K or applying a bias across the QD to an order of $k_B T_K$ destroys Kondo correlation (Fig. 1). Note, however, that as the temperature increases, the visibility tends to decrease because of the shorter dephasing length and phase smearing of the electrons in the interferometer. While the visibility follows the behavior of the conductance shown in Fig. 1C, the phase evolution, changes once again from that of a smooth and monotonic increase at low temperatures to that with a small phase lapse in the valley as

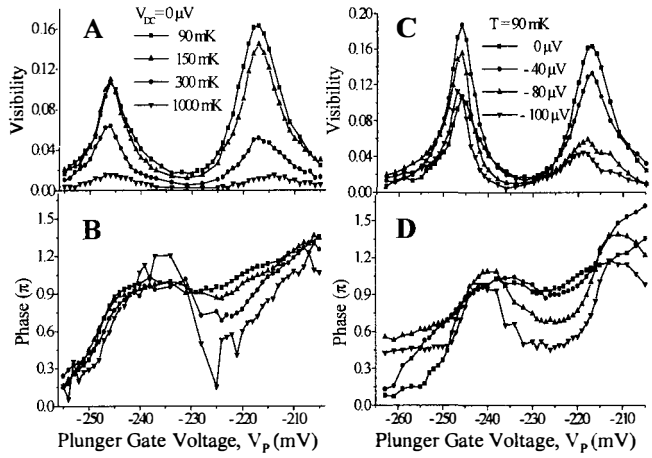


Figure 4: The effect of temperature and an applied DC bias on the phase evolution. (**A**) Qualitative behavior of the magnitude, and (**B**) phase evolution of the transmission coefficient as a function of *plunger* gate voltage, measured with increasing temperature. (**C**) qualitative behavior of the magnitude, and (**D**) phase evolution of the transmission coefficient as a function of *plunger* gate voltage, measured at 90 mK with increasing DC bias between source and base. In both cases, the monotonous phase evolution disappears at some point and a phase lapse is formed in the valley between the Kondo pair, as the QD approaches the Coulomb Blockade regime.

temperature increases. Phase lapse reaches a full $-\pi$ drop at temperature of about 1 K (Fig. 4B). Similarly, the application of a small DC bias across the QD leads to a similar change in the phase evolution, moving from a smooth increase to a phase lapse (Fig. 4D). In both cases Kondo correlation ceases to exist at $T \sim T_K \sim 1$ K and $eV_{DC} \sim k_B T_K \sim 100 \mu eV$.

The results presented here demonstrate a clear fingerprint of Kondo correlation in a QD with spin degenerate levels. As the correlation is being gradually suppressed, a gradual transition to the familiar behavior of the phase in the Coulomb Blockade regime emerges. The total phase change as the two spin-degenerate levels cross the Fermi energy in the leads is nearly 2π with a phase shift π in the conduction valley. This does not agree with the prediction by Gerland et al. [9] of π and $\pi/2$, respectively. Moreover, the phase evolution approaches to be highly sensitive to the onset of Kondo correlation. While the conductance is only a quantitative mark of the effect and has to be verified by changing temperature, voltage or coupling strength, the phase evolution has a distinctive behavior, which abruptly changes as one weakens the Kondo correlation while moving into the Coulomb Blockade regime.

1. J. Kondo, in *Solid state physics*, H. Ehrenreicht, F. Seitz, D. Turnbull, Eds. (Academic Press, New York, 1969), Vol. 23, pp. 183-281.
2. P. W. Anderson, *Phys. Rev.* **124**, 41(1961).
3. L. I. Glazman, M. E. Raikh, *JETP Lett.* **47**, 452(1988).
4. T. K. Ng, P. A. Lee, *Phys. Rev. Lett.* **61**, 1768(1988).
5. U. Meirav, E. B. Foxman, *Semicond. Sci. Technol.* **10**, 255 (1995).
6. D. Goldhaber-Gordon *et al.*, *Nature* **391**, 156 (1998).
7. D. C. Langreth, *Phys. Rev.* **150**, 516 (1966).
8. P. A. Nozieres, *J. Low Temp. Phys.* **17**, 31 (1974).

9. U. Gerland, J. von Delft, T. A. Costi, Y. Oreg, *Phys. Rev. Lett.* **84**, 3710 (2000).
10. A. Yacoby, M. Heiblum, D. Mahalu, H. Shtrikman, *Phys. Rev. Lett.* **74**, 4047 (1995).
11. R. Schuster *et al.*, *Nature* **385**, 417 (1997).
12. Y. Meir, N. S. Wingreen, P. A. Lee, *Phys. Rev. Lett.* **70**, 2601 (1993).
13. N. S. Wingreen, Y. Meir, *Phys. Rev.* **B49**, 11040 (1994).
14. J. Schmid, J. Weis, K. Eberl, K. v. Klitzing, *Phys. Rev. Lett.* **84**, 5824 (2000).
15. We thank D. Goldhaber-Gordon and E. Buks for valuable suggestions on the fabrication process and the measurement techniques. We also thank J. von Delft and Y. Oreg for helpful discussions prior to this work. The work was partly supported by the MINERVA foundation.

MULTI-LEVEL KONDO REGIMES IN A QUANTUM DOT

S. DE FRANCESCHI[1], W. G. VAN DER WIEL[1], T. FUJISAWA[2], J. M. ELZERMAN[1], W. IZUMIDA[2,3], S. TARUCHA[2,3], L. P. KOUWENHOVEN[1]

[1] *Department of Applied Physics, DIMES, and ERATO Mesoscopic Correlation Project, Delft University of Technology, PO Box 5046, 2600 GA Delft, The Netherlands*

[2] *NTT Basic Research Laboratories, Atsugi-shi, Kanagawa 243-0198, Japan*

[3] *ERATO Mesoscopic Correlation Project, University of Tokyo, Bunkyo-ku, Tokyo 113-0033, Japan*

In a recent work (van der Wiel *et al.*, Science **289**, 2105 (2000)) we studied the transport properties of a semiconductor quantum dot connected to one-dimensional leads. A strong Kondo effect was found under proper conditions, which followed the essential expectations from the Anderson impurity model, including the achievement of ideal conductance (i.e. $G = 2e^2/h$) at low temperatures (unitary limit). Here we push our analysis to a deeper level. We present a first attempt to fit the linear-response characteristics at different temperatures using the numerical-renormalisation-group technique. Although we obtain reasonable agreement for the lowest temperature, significant deviations appear at higher temperatures which may be due to the multi-level structure of the dot. Further signatures of multi-level physics emerge in the dependence of the tunnel conductance on a magnetic field perpendicular to the dot plane. In the range between 0 and 2 T, we find a rich variety of Kondo regimes that cannot be explained in terms of a single-level model.

The Kondo effect arises from the many-body interaction between conduction electrons and a localised spin, usually provided by a magnetic impurity embedded in a non-magnetic metal [1]. Recent developments in the field of nanotechnology have opened new perspectives for a deeper study of Kondo-related phenomena [2]. In 1988 it was pointed out that quantum dots could behave as artificial magnetic impurities and exhibit the Kondo effect [3]. Unlike the case of a metal containing magnetic impurities, the Kondo effect is expected to enhance the conductance, G, of a quantum dot device. This follows from the fact that electrons have to go through the quantum dot in order to contribute to transport. In this case the Kondo resonance facilitates mixing between the states belonging to the two opposite leads, resulting in an increased G. For the case of equal-trasmissivity barriers, G can reach $2e^2/h$ (unitary limit) at temperatures much smaller then the Kondo temperature, T_K.

The first observations of the Kondo effect in a quantum-dot device were reported in 1998, however without reaching the unitary limit [4]. The results of these experiments followed reasonably well the expectactions from the Anderson impurity model [5]. In this model the quantum dot has only one spin-degenerate level with energy ϵ_0 and line-width $\Gamma = \Gamma_l + \Gamma_r$, where Γ_l and Γ_r are the tunnel rates associated with the two tunnel barriers. The on-site Coulomb repulsion allows only one electron to sit on the dot so that the local spin, S, is equal to $1/2$. Following experiments [6,7,8] have brought up more data to be compared with theoretical predictions. Here we intend to address this issue and present some experimental results for which we haven't found a satisfactory explanation yet.

All of the measurements reported in this article were performed on the same quantum dot studied in Ref. 8. The device was fabricated from an AlGaAs/GaAs heterostructure grown by molecular beam epitaxy on semi-insulating GaAs. A modulation-doped AlGaAs/GaAs heterojuction was used to create a two-dimensional electron gas (2DEG) with a density of 2.6×10^{15} m^{-2}, 100 nm below the surface. The quantum dot was formed inside a one-dimensional wire defined in the 2DEG by dry etching (top-left inset to Fig. 1A). Quantum confinement was established by means of two transverse gates. We indicate by V_{gl} and V_{gr} the corresponding voltages. All measurements were performed in a dilution refrigerator with a base temperature

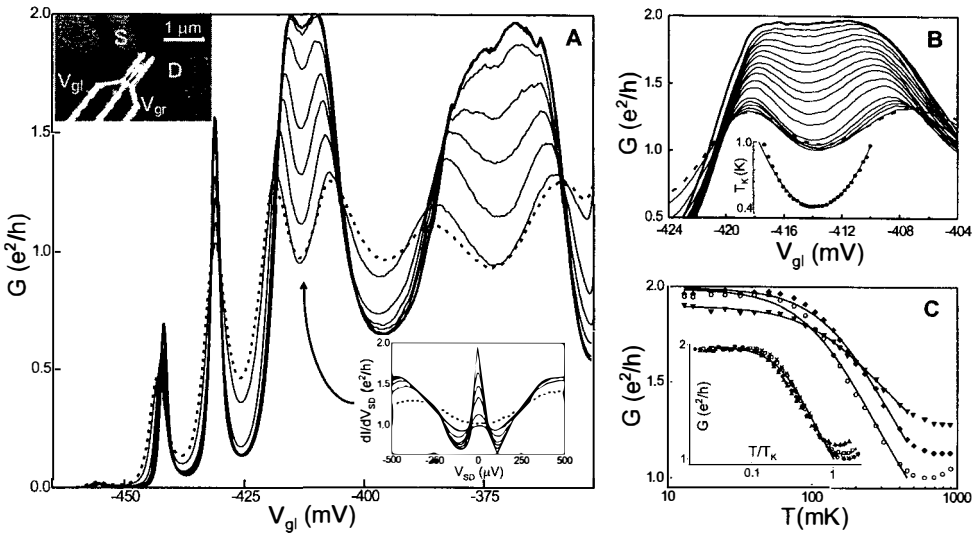


Figure 1: (A) Coulomb oscillations in G versus V_{gl} at $B = 0.4$ T for different temperatures. $T = 15$ mK (thick solid trace) up to 800 mK (thick dashed trace). V_{gr} is fixed at -448 mV. Top-left inset: atomic force microscope image of the device. Bottom-right inset: differential conductance, $\mathrm{d}I/\mathrm{d}V_{SD}$, versus dc bias voltage, V_{SD}, for $T = 15$ mK (thick solid trace) up to 900 mK (thick dashed trace), at $V_{gl} = -413$ mV and B = 0.4 T. The Kondo resonance manifests itself as a peak in $\mathrm{d}I/\mathrm{d}V_{SD}$ at zero bias. (B) $G(V_{gl})$ around the Kondo plateau in the case of optimised symmetric tunnel barriers. T ranges between 15 mK (thick solid trace) up to 800 mK (thick dashed trace). Inset: Kondo temperature, T_K, at the Kondo plateau as obtained from many fits as in (C); the solid line is a parabolic fit of $\mathrm{Log}(T_K)$ versus V_{gl}. (C) $G(T)$ at fixed gate voltage for $V_{gl} = -411$ (solid diamonds), -414 (open circles) and -418 (solid triangles) mV. The solid curves are fits as explained in the text. Inset: G versus normalised temperature, T/T_K, for six different gate voltages. All traces are fitted to a single curve (solid line).

$T = 15$ mK, using a standard lock-in technique with an ac voltage excitation between source and drain contacts of 3 μV.

Figure 1 contains some essential results from Ref. 8. In Fig. 1A the conductance, G, is plotted as a function of gate voltage V_{gl} for different temperatures. All traces were taken in a magnetic field $B = 0.4$ T perpendicular to the 2DEG. At base temperature, conductance in the valleys around $V_{gl} = -413$ mV and -372 mV reaches the value of $2e^2/h$. In fact, the valleys tend to disappear. When the temperature is increased, two separate Coulomb peaks develop with growing peak spacing. The adjacent Coulomb valleys show an opposite T-dependence. This even-odd asymmetry suggests a pairwise filling of the dot levels, i.e. an unpaired spin in a valley with N=odd, where we observe the Kondo effect, and a spin singlet for N=even. In the right inset to Fig. 1A we show the differential conductance, $\mathrm{d}I/\mathrm{d}V_{SD}$, versus source-drain bias, V_{SD}, for different T in the middle of the Kondo plateau at $V_{gl} = -413$ mV. The pronounced peak around $V_{SD} = 0$ reflects the Kondo resonance at the Fermi energy. We note that since the Zeeman splitting for $B = 0.4$ T is several times smaller than $k_B T_K$ the Kondo resonance is not split by the magnetic field. The peak height (i.e. the linear conductance) has a logarithmic T-dependence with a saturation at $2e^2/h$ for low T denoting the achievement of the unitary limit. The unitary limit implies that the transmission probability through the quantum dot is equal to one. Although U is an order of magnitude larger than $k_B T_K$, the Kondo effect completely determines electron tunneling at low energies (i.e. $T \ll T_K$ and $eV_{SD} \ll k_B T_K$).

These measurements were taken after optimizing the two barrier gate voltages, V_{gl} and V_{gr}, in order to obtain nearly equal tunnel barriers. However, sweeping V_{gl}, as in Fig. 1A,

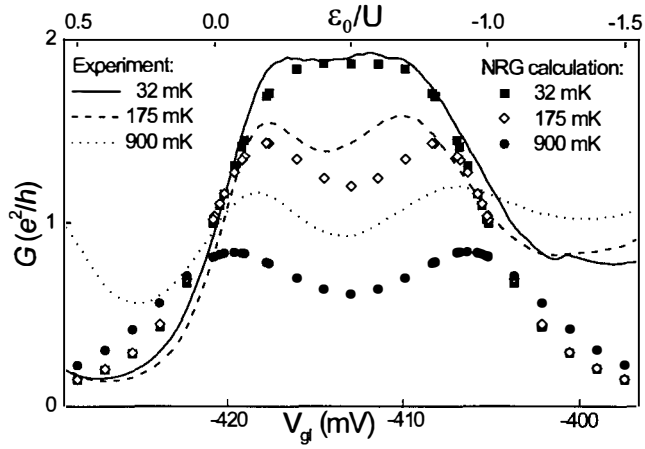


Figure 2: Comparison between linear-response measurements and numerical results obtained with the numerical renormalisation-group (NRG) method. The bottom scale (V_{gl}) is associated with the measured conductance traces (lines). The top scale (ϵ_0/U) refers to the numerical results (dots).

changes the left barrier much more effectively than the right one and hence the barriers cannot be symmetric over the whole V_{gl}-range. For a quantitative comparison to theory, we chose V_{gr} such that, upon sweeping V_{gl}, we could obtain a flat plateau close to $2e^2/h$ (Fig. 1B). The two discernable Coulomb oscillations at the highest temperatures have completely merged together at low T. In Fig. 1C we fit G versus T for different gate voltages to the empirical function $G(T) = G_0[T_K'^2/(T^2+T_K'^2)]^s$. This function is an analytical approximation to numerical renormalisation-group (NRG) results for the Anderson impurity model [9]. $T_K' = T_K/\sqrt{2^{1/s}-1}$ and s is a fit parameter that should be close to 0.2 for a spin-1/2 impurity. Indeed we find $s = 0.29$ and good agreement between experimental data and theoretical curves. The inset to Fig. 1B shows T_K versus V_{gl} as obtained from many fits as in Fig. 1C. Log(T_K) follows a quadratic dependence on V_{gl} (i.e., ϵ_0) with a minimum in the middle of the conductance plateau. From the parabolic fit we estimate $U = 0.5$ meV and $\Gamma = 0.23$ meV (see Ref. 8 for more details). All over the plateau, G is a universal function of the normalised temperature, T/T_K, regardless of the other energy scales, U, ϵ_0 and Γ (see inset to Fig. 1C).

The results presented so far follow quite well some essential expectations from the Anderson impurity model. These expectations include the unitary limit, the parabolic dependence of Log(T_K) on V_{gl}, and the scaling behavior in Fig. 1C. As we shall see below the Anderson model has also important limitations.

In Fig. 2 we compare some $G(V_{gl})$ curves measured at different temperatures with NRG results. The NRG data are plotted as a function of ϵ_0/U (top scale). All of the calculated traces are obtained using only one fitting parameter defined as $\Delta/\pi U$, where $\Delta = \Gamma/2$ (a detailed description of the numerical technique is given in Ref. 10). For a direct comparison with the experimental curves we used the linear relation $\epsilon_0 = \alpha V_{gl} + c$, where $\alpha = 45$ μeV/mV and c is an adjustable constant. The best agreement is obtained for $\Delta/\pi U$=0.05 and $U = 0.7$ meV, which is somewhat larger than the value reported above. With $\Gamma = 0.23$ meV we obtain $\Delta/\pi U = 0.052$ consistent with the value employed in the calculations. At the lowest temperature

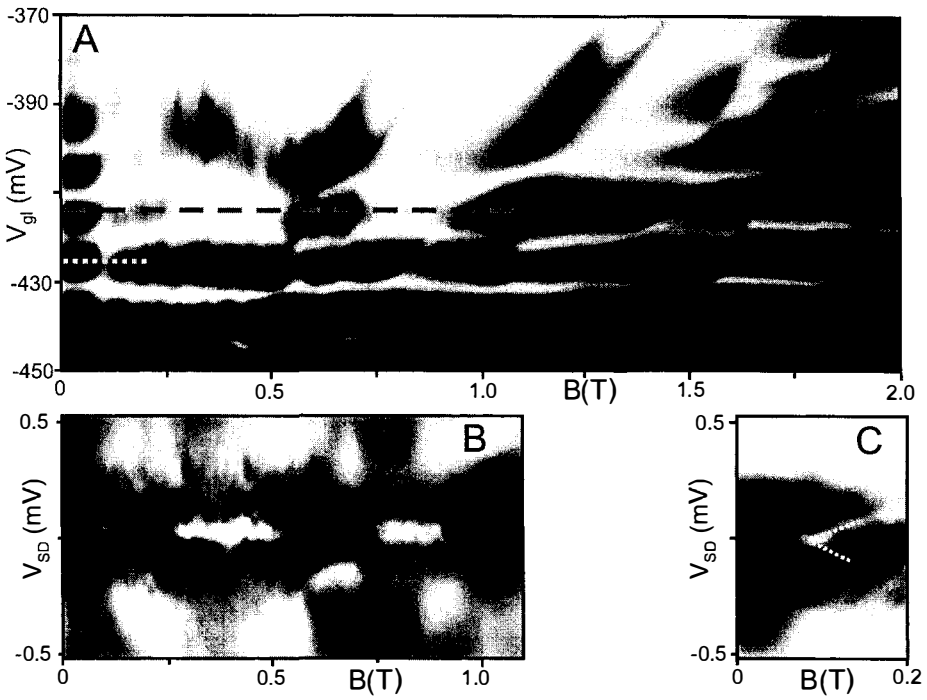


Figure 3: (A) Linear conductance G as a function of magnetic field, B, and gate voltage, V_{gl}. (B) Differential conductance, $\mathrm{d}I/\mathrm{d}V_{SD}$, versus B and dc bias voltage, V_{SD} at the dashed line in (A). (B) $\mathrm{d}I/\mathrm{d}V_{SD}(B, V_{SD})$ at the dotted line in (A). In (A), (B), and (C) light grey corresponds to values of order e^2/h.

(32 mK) NRG results reproduce fairly well the experimental conductance in the Kondo plateau and in the adjacent mixed-valence regimes. Away from this region, however, the numerical data deviate significantly from the experimental trace. This discrepancy is probably due to the V_{gl}-dependence of the tunnel rates Γ_r, and especially Γ_l. This effect is not taken into account in our NRG model which assumes $\Gamma_l = \Gamma_r = \Gamma/2 = constant$ over the shown energy range.

The agreement between theory and experiment is rather poor at higher temperatures. In the Kondo valley the NRG conductance decreases with T more rapidly than in the experiment. We seriously doubt that such a deviation could be cured by an improved control over the parameters involved in our calculation. Instead we suspect that the enhanced conductance denotes the contribution of excited states with energies close to the ground-state level. Increasing temperature may activate tunneling processes via these states.

We now discuss the effect of a magnetic field applied perpendicularly to the 2DEG plane. This will bring further evidence that multi-level effects can be very important.

In Fig. 3A G is plotted on grey scale as a function of V_{gl} and B. Dark regions have low conductance and correspond to the Coulomb blockade regimes. Light grey corresponds to $G \sim e^2/h$. The number of confined electrons increases with V_{gl}, but it is essentially independent of B. In spite of this fact, by varying B at a constant V_{gl} the linear conductance undergoes pronounced variations on a B-scale of 0.1 T. This unusual behaviour is most apparent in the middle part of the V_{gl}-range shown. In this regime the tunnel rates of the barriers are enhanced, however, without implying a substantial suppression of the Coulomb blockade effect. This is the condition for observing the strongest Kondo behaviour. We then ascribe the observed conductance

modulations to variations in the Kondo temperature. To prove this we have measured dI/dV_{SD} versus V_{SD} along the dashed and the dotted lines in Fig. 3A. The results are shown in Figs. 3B and 3C, respectively.

The dashed line is at $V_{gl} = -413$ mV. Along this line N is constant and presumably odd as argued in our analysis of Fig. 1. We find a strong Kondo resonance between 0.3 and 0.5 T (which explains our choice of $B = 0.4$ T for the measurements in Fig. 1); another Kondo resonance is found between 0.75 and 0.9 T. Here the field is strong enough to induce an appreciable splitting of the Kondo resonance, which is slightly visible in Fig. 3B.

Along the dotted line N is presumably even. We find a zero-bias resonance at $B = 0.1$ T. The resonance splits for $B > 0.1$ T as emphasised by the dotted lines in Fig. 3C. These features resemble those of the singlet-triplet Kondo effect observed in an integer-spin vertical quantum dot [6] (an extensive discussion of this effect can be found in Ref. 11). According to this interpretation, we believe that the ground state is a triplet for $B < 0.1$ T and becomes a singlet for $B > 0.1$ T. An enhanced Kondo effect takes place at the degeneracy point. The Kondo resonance splits at higher B following the singlet-triplet splitting (as in Ref. 6, the splitting of the Kondo peak is seen only for B larger than the degeneracy field).

Our analysis of Fig. 3 leads us to conclude that the pronounced B-dependence of the tunnel conductance arises from a variety of Kondo regimes occurring for both odd and even occupation numbers. We should like to stress that the anomalous B-dependence does not seem to be a peculiarity of the device studied. Similar features have been observed also in other quantum dot devices as reported in Refs. 7,13, and 14. In some of these experiments, conductance modulations were surprisingly regular with a clear anti-correlation between adjacent Coulomb valleys (i.e., $G(B, V_g)$ looked like a chess board when plotted on grey scale). Evidently, all these observations cannot be explained in terms of the Anderson model and a pairwise filling of the dot levels. Instead the non-trivial multi-level structure of the dot and local electron-electron interactions are likely to play a key role, as already pointed out in Refs. 7 and 13.

It has been shown that in small quantum dots, such as the one considered here, electron-electron interactions can have important consequences on the ground state properties. For instance, Tarucha *et al.* [12] have identified B-driven spin transitions in a vertical quantum dot, discriminating between the contributions from local Coulomb and exchange interactions. In that experiment, as well as in Refs. 7,13,14 and in the experiment discussed here, the magnetic field was applied perpendicularly to the dot. In such a configuration, the field couples to the orbital motion of the confined electrons resulting in a strong influence on the electronic properties of the dot. (Note that a 0.1-T field is sufficient to have one quantum flux through the dot and break for instance time-reversal symmetry.)

We believe that ground-state transitions induced by the magnetic field are responsible for the onset of the Kondo-dominated regimes observed in Fig. 3. However, the nature of these transitions and their relation to the Kondo effect is unclear.

In the case of N=even, we know that ground-state transitions between singlet and triplet states produce an enhancement of the Kondo temperature. Therefore, B-driven transitions between S=0 and S=1 would lead to enhanced conductance near the points of spin degeneracy. In the case of N=odd, it is not known if spin transitions, for instance between S=1/2 and S=3/2, would also occur in a similar fashion. The mechanism responsible for the fluctuation of the Kondo temperature is quite obscure.

A more satisfactory physical picture can be formulated for the case of high magnetic fields. In the quantum Hall regime confined electrons occupy concentric shells associated with Landau levels. The outer shell has the best tunnel coupling to the leads and hence dominates the Kondo effect. Changing the field while keeping N constant causes electrons to move from one shell to another. Therefore the occupation of the outer shell can change without a variation in the total number of confined electrons (note that N can be either even or odd). By sweeping the field

the Kondo effect turns on and off dependending on whether the occupation of the outer shell is odd or even, respectively. Starting from this simple picture, Tejedor and Martìn-Moreno [15] have recently proposed a more sophisticated model to explain the chess-board structure. Their analysis, however, applies only to the case of filling factors between 1 and 2. In our experiment this would correspond to $B > 2.5$ T, while conductance fluctuations are observed at much lower fields.

Finally, spin fluctuations could also be responsible for spin-blockade effects. Single-electron tunneling is suppressed whenever it involves two ground states differing in their spin by more than one unit. For instance, if two consecutive Coulomb valleys have $S = 0$ and $S = 3/2$ the conductance peak between them is suppressed. In Fig. 3A there are two narrow regions, one at $(B,V_{gl})\approx$(0.6 T,−410 mV) and one at $(B,V_{gl})\approx$(1.1 T,−420 mV), where the conductance peak may be suppressed due to spin blockade.

Acknowledgments

We acknowledge financial support from the Specially Promoted Research, Grant-in-Aid for Scientific Research, from the Ministry of Education, Science and Culture in Japan, from the Dutch Organisation for Fundamental Research on Matter (FOM), from the NEDO joint research program (NTDP-98), and from the EU via a TMR network.

References

1. A. C. Hewson, The Kondo Problem to Heavy Fermions (Cambridge University Press, Cambridge, 1993).
2. L. P. Kouwenhoven and L. I. Glazman, Phys. World **14**, 33 (2001).
3. L. I. Glazman and M. E. Raikh, JETP Lett. **47**, 452 (1988); T. K. Ng and P. A. Lee, Phys. Rev. Lett. **61**, 1768 (1988).
4. D. Goldhaber-Gordon *et al.*, Nature **391**, 156, (1998); Cronenwett *et al.*, Science **281**, 540 (1998); Schmid *et al.*, Physica B **256-258**, 182 (1998).
5. P. W. Anderson, Phys. Rev. **124**, 41 (1961).
6. S. Sasaki *et al.*, Nature **405**, 764 (2000).
7. J. Schmid *et al.*, Phys. Rev. Lett. **84**, 5824 (2000).
8. W. G. van der Wiel *et al.*, Science **289**, 2105 (2000).
9. D. Goldhaber-Gordon *et al.*, Phys. Rev. Lett. **81**, 5225 (1998); T. A. Costi *et al.*, J. Phys. Condens. Matter **6**, 2519 (1994).
10. W. Izumida, *et al.* J. Phys. Soc. Jpn. **70**, 1045 (2001).
11. M. Eto and Yu. Nazarov, Phys. Rev. Lett. **85**, 1306 (2000); M. Pustilnik *et al.*, cond-mat/0010336.
12. S. Tarucha *et al.*, Phys. Rev. Lett. **84**, 2485 (2000).
13. S. M. Maurer *et al.*, Phys. Rev. Lett. **83**, 1403 (1999).
14. M. Stopa, S. De Franceschi and L. P. Kouwenhoven, unpublished.
15. C. Tejedor and L. Martìn-Moreno, Phys. Rev. B **63**, 035319 (2001).

SPIN EFFECTS IN QUANTUM DOTS WITH STEEP POTENTIAL WALLS

S. LÜSCHER[1], A. FUHRER[1], T. HEINZEL[1], K. ENSSLIN[1], W. WEGSCHEIDER[2], and M. BICHLER[3]

[1] *Solid State Physics, ETH Zürich, 8093 Zürich, Switzerland*

[2] *Angewandte und Experimentelle Physik, Universität Regensburg, 93040 Regensburg, Germany*

[3] *Walter Schottky Institut, TU München, 85748 Garching, Germany*

Quantum dots are fabricated in AlGaAs heterostructures by means of a novel nanofabrication technique based on an atomic force microscope. Via suitable gate voltages the dots can be tuned into a regime where the electron transport is governed by an individual quantum state in the dot. By following the position and amplitude of several Coulomb peaks we can clearly identify neighboring pairs which evolve in parallel over a finite parameter range. This is interpreted in terms of electrons populating two quantum states with the same orbital but different spin quantum numbers. Our dots are different from conventional top gate defined quantum dots in the sense that the potential walls are much steeper and electron-electron interactions are weaker. This leads to an addition spectrum which can basically be described by carriers successively populating orbital states with spin-up and spin-down electrons. We discuss the consequences of this observation for the statistical analysis of quantum dot spectra.

1 Introduction

Electronic transport through semiconductor quantum dots has revealed a variety of novel and unexpected experimental observations. [1] The sequential addition of electrons on a conducting island and its experimental demonstration in terms of the Coulomb blockade oscillation of the conductance of quantum dots is well established in many groups worldwide. The question about the spin of the added electrons is less clear. In quantum dots with a symmetric confinement potential containing only a few electrons the occupation of the electronic states is governed by Hund's rules. [2,3] For quantum dots containing many electrons and having an irregular shape without symmetries the situation is less clear. Theoretically one expects that these quantum dots can be treated in the framework of quantum chaos. The energy spectrum is thought to be described by Random Matrix Theory (for a review see [4,5]).

High quality quantum dots are usually induced by top gate electrodes nanostructured by electron beam lithography. Here we proceed from a novel nanolithography approach based on an atomic force microscope (AFM). The surface of an AlGaAs heterostructure is locally oxidized via an electric field applied between the electron gas and a conductive AFM tip. [6,7] If the electron gas is located close enough to the surface (less than 40 nm in our case) it is depleted below the oxidized lines. In this way high-quality quantum wires [8] and dots [9] can be fabricated. The AFM-defined nanostructures are tuned by in-plane gate voltages applied across the laterally insulating lines. An additional homogeneous top gate electrode covering the entire sample leads to enhanced tunability of the potential details as well as screening of the interactions in the electron gas. We find that the potential walls of AFM nanostructures are unusually steep in wires [7] as well as in dots [10]. This effect results from a combination of the shallow electron gas, the high-electron density in our heterostructures ($N_s = 6 \cdot 10^{11} cm^{-2}$) as well as the special potential shape caused by the AFM-induced oxidation.

2 Coulomb blockade oscillations

Figure 1 (a) shows an AFM picture of an AFM-defined quantum dot. The picture is taken immediately after the patterning with an unbiased tip. The bright lines represent the oxide

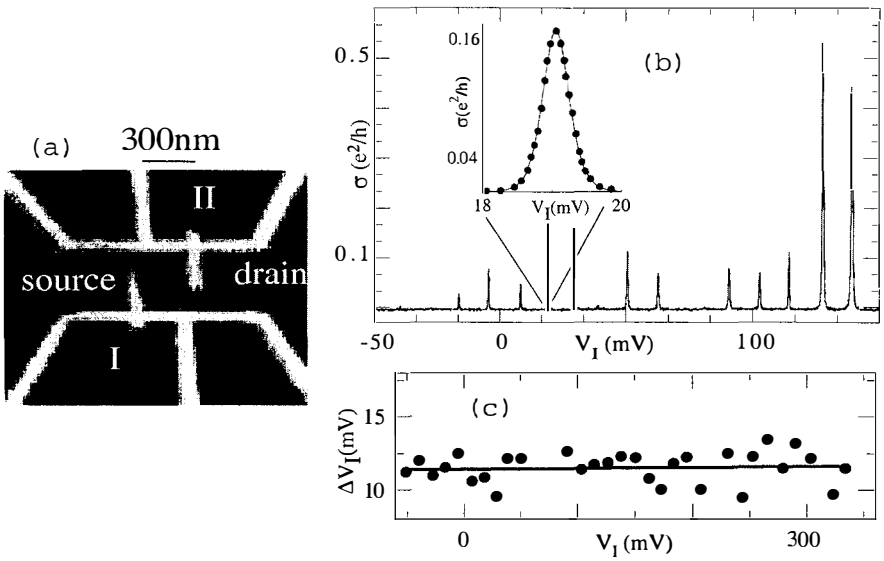


Figure 1: (a) AFM picture of a quantum dot. Areas I and II mark the plunger gates used to tune the electron occupancy of the dot. In-plane gates named QPCI and QPCII mark the lateral electrodes to tune the two quantum point contacts separating the quantum dot from source and drain. (b) Typical Coulomb blockade oscillations as a function of plunger gate voltage I. The inset shows a Coulomb peak at enlarged scale fitted to a thermally broadened line shape. (c) Linear fit (line) of a typical peak spacing ΔV_I as a function of V_I for a large range. The average peak spacing is almost constant, indicating small shape deformations.

lines below which the electron gas is depleted.

The sample was mounted in the mixing chamber of a $^3He/^4He$-dilution refrigerator with a base temperature of 90 mK. The mobility of the cooled 2DEG was 93 m^2/Vs. A DC bias voltage of $10\mu V$ was applied across the dot, and the current is measured with a resolution of 500 fA. The lithographic dot area is 280 nm x 280 nm. From capacitance measurements [18], we find an electronic dot area of 190 nm x 190 nm, a charging energy of $E_C = 1.25meV$, and a single particle level spacing of $\Delta = 200\mu eV$.

Figure 1 (b) shows typical Coulomb blockade oscillations in the regime where the quantum dot is only very weakly coupled to source and drain. The Coulomb peaks can be fitted with an expression characterizing thermal broadening [11]. We find an electronic temperature of 120 mK, slightly above the bath temperature of around 100 mK. From the measurement of Coulomb diamonds we extract the capacitance of the Coulomb island to its environment and therefore the lever arm converting the applied gate voltage into energy.

The electrons have to pass through the two laterally defined quantum point contacts on their way through the quantum dot. The transmission through each quantum dot can be adjusted by proper voltages to the in-plane gate electrodes QPC1 and QPC2. The electron occupancy on the quantum dot is tuned via plunger gates I and II. The overall potential is adjusted by the top gate covering the entire structure.

In order to reduce r_s, the ratio between Coulomb energy and Fermi energy, as much as possible, we chose a heterostructure with a high electron density, further increased by a top gate voltage of +100 mV to $N_s = 5.9 \cdot 10^{15} m^2$. This results in $r_s = 0.72$, which is smaller than in all previous experiments [14,15,16,17]. Additional screening is provided by the top gate.

Figure 1(c) shows typical peak spacings ΔV_I as a function of V_I. Compared to conventional dots defined by top gates[1], we find a much smaller variation of the average peak spacing as V_I is tuned, although the fluctuation of individual spacings is 15% of E_C. The capacitance between the dot and gate I varies only by 3% over the whole scan range, as compared to, for example, a factor of 3 in Ref. [15]. This indicates that tuning gate I or II predominantly changes the energy of the conduction band bottom, while the dot is only slightly deformed. By reconstructing the energy spectrum of the quantum dot in high magnetic fields [12] we find that the potential walls in our AFM-defined quantum dots can be up to 10 times steeper than in conventional top-gate defined quantum dots [13].

3 Evolution of the Coulomb peaks with magnetic field

The wave functions and energy levels are expected to depend on several external parameter, such as gate voltages and magnetic field. A magnetic field B applied perpendicular to the sample surface changes the flux enclosed by a corresponding semi-classical orbit and therefore has a characteristic influence on each energy level and its wave function. In Fig. 2(a), the evolution of five consecutive CB peaks is shown as a function of B . A pronounced pair correlation of both amplitude and peak position is observed (peak b correlates with peak c , and peak d with peak e , respectively). We interpret this parametric pair correlation in terms of a model recently developed by Baranger et al. [19]. The constant interaction model (see Ref. [1]) is used to subtract E_C from the peak spacings. The remaining individual energy separations equal $\Delta/2$ on average and reflect the fluctuating level separations inside the quantum dot, which consist of two parts. We assume that two paired peaks belong to the same spatial wave function, labeled by i, of opposite spin, and are split by an interaction energy ξ_i, while the energy of consecutive states with different orbital wave functions differs by $\Delta_i - \xi_i$. The Zeeman splitting is small compared to these energy scales for magnetic fields below 1T.

Since the separations between the two levels of equal spin of spin pair i and $(i+1)$, Δ_i , and possibly also ξ_i, vary as a function of B , levels may cross and the ground state of the dot can be either a singlet or a triplet state. Higher spin states are expected to be unlikely to occur [19,20]. At the singlet-triplet transitions, kinks in the parametric peak evolution occur and the pair correlation is interrupted [19]. We can identify such kinks in our data, among other features. Figure 2(b) shows the amplitudes of peaks c , d , and e . The correlation between peaks d and e is very strong around $B = 0$. For $0.4T < B < 0.6T$, this correlation is interrupted, while the amplitudes of peaks c and e are correlated instead. In this regime, correlated kinks in the evolution of peaks c and d are observed [Fig. 2(c)]. In Fig. 2(d), a possible corresponding scenario for the parametric dependence of energy levels is sketched: (left) two avoided crossings occur between level pair i and level pair $(i+1)$. This leads to the position of peaks c , d , and e as sketched in Fig. 2(d), right, corresponding to the difference in energy upon changing the electron number in the dot. Consequently, positions and amplitudes of peaks c and e should be correlated in $0.4T < B < 0.6T$, as observed. Note that this correlation is interrupted around $B = 0.5T$, possibly due to the influence of another energy level. possibly due to the influence of another energy level. We emphasize that this kink structure, i.e., a double-anti-crossing between two spin pairs, is the dominant one for all peak evolutions. This fact does not depend on the cooldown cycle.

From the data of Fig. 2, we estimate by averaging over all peak pairs in their correlated regions that the average interaction energy $\xi \approx 0.5\Delta$, i.e. about half as big as the single particle level spacing. Baranger et al. have estimated $\xi \approx 0.6\Delta$ for $r_s = 1$. Hence, our findings are in rough agreement with existing theory, while we are not aware of a theoretical prediction for the fluctuations in the spin splitting energy. From the above phenomenology, we conclude that for dots with stronger shape deformations, and hence more level crossings, or in dots with larger

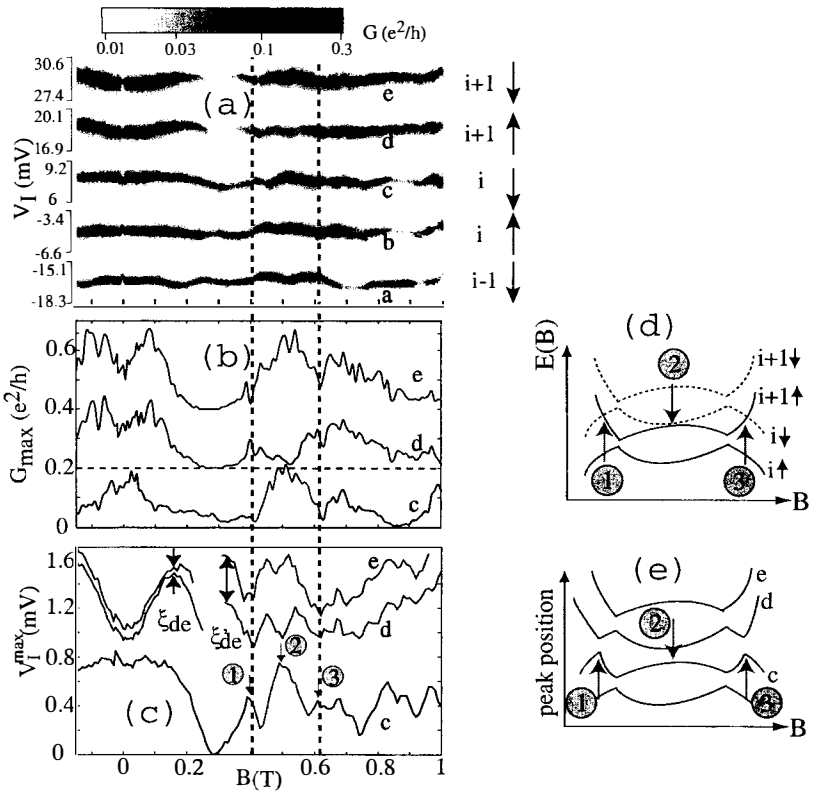


Figure 2: (a) Logarithmic grayscale plot of parametric variations in a magnetic field B for five consecutive CB peaks. A pair correlation in peak position amplitude is observed, which is interrupted in certain ranges of B , for example, in the re- gion between the dashed lines. (b) Parametric amplitudes for peaks c , d , and e , offset by $0.2e^2/h$ each. The correlation between peaks d and e is lost in $0.4T < B < 0.6T$, and e correlates with c instead. (c) The corresponding position of the peak maxima. The traces are offset for clarity. At magnetic fields labeled by 1 and 3, kinks in the peak position occur, while the separation between peaks d and e jumps across the region of suppressed amplitude from j de to j 0 de . (d) Scheme of a possible double anticrossing between spin-paired level i and $(1+i)$ (left, the black arrows indicate the spin), which could lead to the observed structure in the correlation for peaks c , d , and e (right). (e) Consequences of such level crossings for the magnetic field dependent positions of Coulomb peaks.

r_s (and thus larger ξ), the spin pairing is frequently interrupted and difficult to detect. This is possibly the reason why spin pairing has not been observed in the earlier experiments [14,15,16].

The quantum mechanical energy spectra of quantum dots with a classically chaotic geometry are expected to be described by random Matrix Theory (see introduction). Obviously one has to include spin phenomena as described in Fig. 2 in order to make a reasonable comparison between experiment and theory. Ref. [21] describes in more detail how such a scenario could look like.

4 Stadium shaped quantum dot

In order to substantiate our claims on the dot described in the previous section we present additional data on a completely different quantum dot. The dot is also fabricated by AFM lithography (see upper right in Fig. 3) but entry and exit point contact are situated face to face. In the first quantum dot there were no direct classical trajectories connecting source and drain. We expect that so-called bouncing ball orbits are more prominent in the second stadium shaped quantum dot. The coupling of the dot to source (S) and drain (D) is controlled by the lateral point contact electrodes pc1 and pc2. The dot occupancy is tuned by the plunger gates g as indicated in the figure.

The lower left part of Fig. 3 shows the evolution of the Coulomb peaks as a function of magnetic field. Even without subtracted charging energy E_C a pairwise evolution of neighboring peaks can be observed.

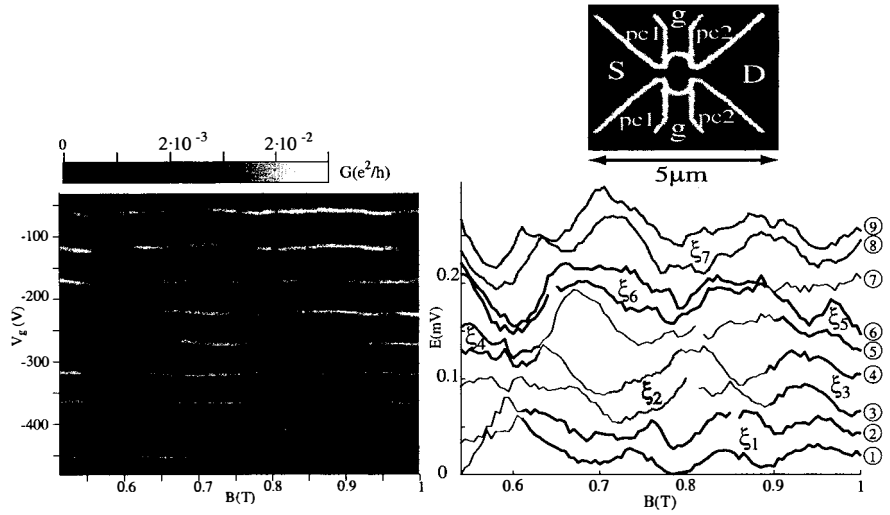


Figure 3: upper right: AFM image of a stadium shaped quantum dot. lower left: logarithmic grey scale plot of 9 consecutive Coulomb blockade resonance as a function of magnetic field. Pairing in peak amplitude and position is clearly visible. lower right: After subtraction of the charging energy the position of the Coulomb resonances is plotted on an energy scale.

The charging energy has been determined by gate voltage sweeps. The lever arm between applied gate voltage and dot energy follows from an analysis of carefully measured Coulomb diamonds. The lower right part of Fig. 3 shows the position of the same 9 Coulomb peaks on an energy scale related to the single particle level spacing Δ. In this plot it is straightforward to estimate the fluctuations in Δ. It is also possible to see the correlations between neighboring levels marked along the lines in various gray scales. As discussed for the previous dot level anti-crossings can be observed which border the regions of finite magnetic field over which levels evolve in parallel.

It is tempting to analyze the peaks in a statistical way using every second pair. In this way one could make a comparison to theoretical data which finds a separate statistics for spin split pairs (odd) separated on average by ξ_i and neighboring states separated by the energy difference $\Delta_i - \xi_i$ (even). In the experiment one has to average over many ensembles obtained by various sets of gate voltages or magnetic fields. Also possible rearrangements of the background charge

which can be clearly identified can influence such an analysis. In spite of the fact, that spin pairs can be clearly identified in various dot geometries, it remains difficult to extract statistical properties on odd and even states separately with satisfactory confidence.

In summary, we have observed spin pairing effects in a quantum dot with reduced electron-electron interactions and steeper side walls compared to dots investigated in earlier experiments. Spin pairing persists as a magnetic field is varied but is interrupted by kinks as well as other structures in the parametric evolution of the Coulomb blockade peaks. We have extracted the average interaction energy between states of identical spatial wave functions but opposite spin.

Acknowledgments

Financial support from the Schweizerischer Nationalfonds is gratefully acknowledged.

References

1. For a review, see L.P. Kouwenhoven, C.M. Marcus, P.L. McEuen, S. Tarucha, R.M. Westervelt, and N.S. Wingreen, in Mesoscopic Electron Transport, Proceedings of a NATO Advanced Study Institute, edited by L.P. Kouwenhoven, G. Schön and L. L. Sohn, (Kluwer, Dodrecht, Netherlands, 1997), ser. E, vol. 345, pp. 105-214.
2. S. Tarucha, D.G. Austing, T. Honda, R.J. van der Haage, and L.P. Kouwenhoven, Phys. Rev. Lett. **77**, 3613, (1996).
3. S. Tarucha, D.G. Austing, Y. Tokura, W.G. van der Wiel, and L.P. Kouwenhoven, Phys. Rev. Lett. **84**, 2485, (2000).
4. M. L. Mehta, Random Matrices (Academic Press, London, 1991).
5. C. W. J. Beenakker, Rev. Mod. Phys. 69, 731 (1997).
6. R. Held, T. Vancura, T. Heinzel, K. Ensslin, M. Holland, and W. Wegscheider, Appl. Phys. Lett. **73**, 262 (1998).
7. R. Held, S. Lüscher, T. Heinzel, K. Ensslin, and W. Wegscheider, Appl. Phys. Lett. **75**, 1134 (1999).
8. T. Heinzel, G. Salis, S. Lscher, R. Held, K. Ensslin, and W. Wegscheider Phys. Rev. B **61**, R13353 (2000).
9. S. Lüscher, A. Fuhrer, R. Held, T. Heinzel, K. Ensslin, and W. Wegscheider Appl. Phys. Lett. **75**, 2452 (1999).
10. A. Fuhrer, S. Lüscher, T. Heinzel, K. Ensslin, W. Wegscheider, and M. Bichler Phys. Rev. B **63**, 125309 (2001).
11. C. W. J. Beenakker, Phys. Rev. B **44**, 1646 (1991)
12. A. Fuhrer, S. Lüscher, T. Heinzel, K. Ensslin, W. Wegscheider, and M. Bichler Phys. Rev. B **63**, 125309 (2001).
13. P.L. McEuen, E.B. Foxman, U. Meirav, M.A. Kastner, Y. Meir, N.S. Wingreen, and J.S. Wind, Phys. Rev. Lett. **66**, 1926, (1991).
14. U. Sivan et al., Phys. Rev. Lett. **77**, 1123 (1996).
15. F. Simmel et al., Europhys. Lett. **38**, 123 (1997).
16. S. R. Patel et al., Phys. Rev. Lett. **80**, 4522 (1998).
17. F. Simmel et al., Phys. Rev. B **59**, R10 441 (1999).
18. M. A. Kastner, Rev. Mod. Phys. **64**, 849 (1992).
19. H. U. Baranger et al., Phys. Rev. B **61**, R2425 (2000).
20. R. Berkovits, Phys. Rev. Lett. **81**, 2128 (1998).
21. S. Lüscher, T. Heinzel, K. Ensslin, W. Wegscheider, and M. Bichler, Phys. Rev. Lett. **86**, 2118 (2001)

TIME-REVERSAL SYMMETRY BREAKING BY AC FIELD: EFFECT OF COMMENSURABILITY IN THE FREQUENCY DOMAIN

V.E. KRAVTSOV

The Abdus Salam International Centre for Theoretical Physics, P. O. Box 586, 34100 Trieste, Italy and Landau Institute for Theoretical Physics, 2 Kosygina Street, 117940 Moscow, Russia

It is shown that the variance of the linear dc conductance fluctuations in an open quantum dot under a high-frequency ac pumping depends significantly on the spectral content of the ac field. For a sufficiently strong ac field the dc conductance fluctuations are much stronger for the periodic pumping than in the case of the noise ac field of the same intensity. The reduction factor r in a static magnetic field takes the universal value of 2 only for the white–noise pumping. In general r may deviate from 2 thus signalling on the time-reversal breaking by the ac field. For the bi-harmonic ac field of the form $A(t) = A_0 [\cos(\omega_1 t) + \cos(\omega_2 t)]$ we predict the enchancement of effects of T-symmetry breaking at commensurate frequencies $\omega_2/\omega_1 = P/Q$. In the high-temperature limit there is also the parity effect: the enchancement is only present if either P or Q is even.

1 Introduction

Recently there has been a considerable interest in non-equilibrium mesoscopics. The effect of adiabatic charge pumping [1] has been experimentally observed [2] and analyzed theoretically [3,4]. Weak localization under ac pumping [5] and the photovoltaic effect [6] in a quantum dot have been theoretically studied. The non-equilibrium noise has been suggested [9] as a cause of both the low temperature dephasing saturation [7] and the anomalously large ensemble averaged persistent current [8].

Here we study the effect of the high-frequency ac field on the mesoscopic fluctuations of *linear* dc conductance when both the *weak dc voltage* and a *strong enough high-frequency pump field* are applied to the open quantum dot. We will study the dependence of the variance of the dc conductance fluctuations on the ac field intensity for the noiselike and an almost periodic ac field. In particular we focus on the reduction factor $r = 1 + \mathcal{C}/\mathcal{D}$ for the variance of conductance fluctuations after turning on a strong static magnetic field that kills the cooperon contribution to the variance $\langle \delta G^2 \rangle_C \equiv \mathcal{C}$ while leaving the diffuson one $\langle \delta G^2 \rangle_D \equiv \mathcal{D}$ unchanged.

This question is of the fundamental importance, since the universality of the reduction factor is related with the time-reversal invariance of the system without the static magnetic field. The external ac field certainly breaks the time-reversal invariance. However, if the characteristic frequency ω of the ac field is high it is intuitively clear that the effect of time-reversal symmetry breaking is observed only at special conditions.

Below we show that not only the power but also the spectral content of the ac field is important for an effective T-symmetry breaking. In particular, the white ac noise is shown to be the most effective way to diminish the conductance fluctuations by dephasing. Yet it does not lead to any deviations from the universal value of $r = 2$. The periodic ac field is least effective in dephasing but it produces the maximum possible (at a given ac power) effect of time-reversal breaking.

An interesting special case arises when the ac field is the superposition of two harmonic fields with different frequencies ω_1 and ω_2. We will show below that both the variance of conductance fluctuations and the inverse reduction factor $1/r$ have very sharp peaks as a function of the ratio $\alpha = \omega_2/\omega_1$ at any rational value of $\alpha = P/Q$ but the height of the peak decreases with increasing the denominator Q. Thus we conclude that the statistics of mesoscopic conductance fluctuations reveals *the effect of commensurability in the frequency domain* on the dephasing and the time-reversal breaking by the ac filed.

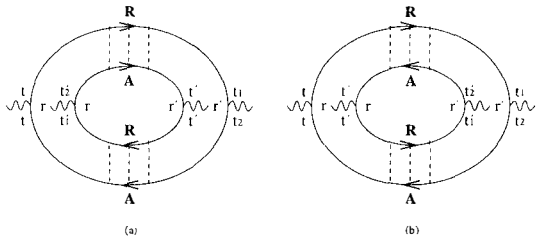


Figure 1: The cooperon (a) and the diffuson (b) contributions to the variance of conductance fluctuations.

2 The Landauer conductance in the time domain

The Landauer conductance $g = (\gamma V/4)^2\,[K(\mathbf{r},\mathbf{r}') + K(\mathbf{r}',\mathbf{r})]$ of a dot of the volume V with small contacts at $\mathbf{r}$ and $\mathbf{r}'$ and the electron escape rate γ, can be expressed in terms of the exact retarded and advanced electron Green's functions $G^{R,A}(\mathbf{r},\mathbf{r}';t,t')$ in the time domain[5,10,11]:

$$K(\mathbf{r},\mathbf{r}') = \int dt_1 dt_2\, \overline{G^R(\mathbf{r},\mathbf{r}';t,t_1) G^A(\mathbf{r}',\mathbf{r};t_2,t)}\, F_{t_1-t_2} \tag{1}$$

where $F_t = \pi T t \sinh^{-1}(\pi T t)$ is the Fourier-transform of the derivative of the Fermi distribution function for electrons in the leads and $\overline{f(t)} = \int_{-\mathcal{T}/2}^{\mathcal{T}/2} \frac{dt}{\mathcal{T}} f(t)$ denotes time averaging during the observation time $\mathcal{T}$. We consider a chaotic or disordered quantum dot with the number of open channels $M \gg 1$ and the electron escape rate $\Delta \ll \gamma = \Delta M \ll E_c$ where Δ is the mean level separation and the Thouless energy E_c is the inverse ergodic time. We also assume the dephasing rate $\gamma_{int}(T)$ caused by electron interaction to be smaller than the escape rate γ. In this situation the charging effects are negligible, the perturbative diagrammatic analysis (see Fig.1) is possible and the ergodic zero-dimensional approximation applies. In this approximation the diffuson and the cooperon contribution to the variance of conductance fluctuations is given by[11]:

$$\mathcal{D} \propto \int dt' dt'' \overline{D_\eta(t,t') D_{-\eta}(t,t'')}\; F^2_{t'-t''}. \tag{2}$$

$$\mathcal{C} \propto \int dt' d\eta' \overline{C_{t'+t}(-\eta' - 2t', -\eta + 2t') C_t(\eta,\eta')}\, F^2_{2t'}. \tag{3}$$

where averaging over t and η is assumed.

In Eqs.(2),(3) the time-dependent diffuson $D_\eta(t,t')$ and cooperon $C_t(\eta,\eta')$ are certain products of electron retarded (G^R) or advanced (G^A) Green's functions averaged over disorder:

$$\langle G^R(t_+,t'_+) G^A(t'_-,t_-)\rangle = \delta(\eta-\eta')\, D_\eta(t,t'),\quad \langle G^R(t_+,t'_+) G^A(t_-,t'_-)\rangle = \frac{1}{2}\,\delta(t-t')\, C_t(\eta,\eta'), \tag{4}$$

where $t_\pm = t \pm \eta/2, t'_\pm = t' \pm \eta'/2$.

In the ergodic regime they are independent of the coordinates and are given by [10,11]:

$$D_\eta(t,t') = \Theta_{\eta-\eta'} \exp\left[-\int_{t'}^{t} \Gamma_d(\eta,\xi)\, d\xi\right] \tag{5}$$

$$C_t(\eta,\eta') = \Theta_{t-t'} \exp\left[-\frac{1}{2}\int_{\eta'}^{\eta} \Gamma_c(t,\xi)\, d\xi\right], \tag{6}$$

where Θ_t is the step-function.

The functions $\Gamma_d(\eta,\xi)$ and $\Gamma_c(t,\xi)$ describe the dephasing caused by the ac field and by the electron escape into leads. For a ring with the diffusive electron motion and the circular electric field $E(t) = -\frac{\partial}{\partial t}A(t)$ cased by the time-dependent flux through it, these functions are given by [11,10]:

$$\Gamma_d(\eta,\xi) = \gamma + D\left(A(\xi+\eta/2) - A(\xi-\eta/2)\right)^2, \tag{7}$$

$$\Gamma_c(t,\xi) = \gamma + D\left(A(t+\xi/2) + A(t-\xi/2)\right)^2. \tag{8}$$

where γ is an electron escape rate, $A(t)$ is the vector-potential, and D is an electron diffusion coefficient.

The same expressions hold [10] for a single connected dot with a homogeneous longitudinal electric field $E(t)$ (the vector-potential $A(t)$ is unambiguously defined by the condition $\overline{A(t)} = \overline{E(t)} = 0$) but only in the high-frequency limit $\omega \gg E_c$. In the adiabatic limit $\omega \ll E_c$ one obtains [5,10]

$$\Gamma_d(\eta,\xi) = \gamma + C(E(\xi+\eta/2) - E(\xi-\eta/2))^2, \tag{9}$$

$$\Gamma_c(t,\xi) = \gamma + (C/4)(E(t+\xi/2) - E(t-\xi/2))^2 \tag{10}$$

where $C \sim L^2/E_c$, L being the dot size.

The existence of two different forms Eqs.(7),(8) and Eqs.(9),(10) is the manifestation of the fact [10] that there are two different *time-dependent* random matrix theories for each Dyson universality class.

3 The limit of high frequencies

Eqs.(2),(3) can be significantly simplified in the limit of high frequencies $\omega \gg \gamma$. At such a high-frequency pumping one can replace $\Gamma_d(\eta,\xi)$ and $\Gamma_c(t,\xi)$ in Eqs.(5,6) by the time averages $\Gamma_d(\eta) = \overline{\Gamma_d(\eta,\xi)}$ and $\Gamma_c(t) = \overline{\Gamma_c(t,\xi)}$. Then we obtain:

$$\frac{\mathcal{D}}{g_0^2} = \int_{-\mathcal{T}/2}^{\mathcal{T}/2} \frac{d\eta}{2\mathcal{T}} \left(\frac{\gamma^2}{\Gamma_d(\eta)}\right) \int_0^\infty e^{-t\Gamma_d(\eta)} F_t^2\, dt. \tag{11}$$

$$\frac{\mathcal{C}}{g_0^2} = \int_{-\mathcal{T}/2}^{\mathcal{T}/2} \frac{dt}{\mathcal{T}} \int_{-\infty}^{t} dt' \frac{\gamma^2 F_{2t-2t'}^2\, e^{-2(t-t')\Gamma_c(t')}}{\frac{1}{2}(\Gamma_c(t)+\Gamma_c(t'))}, \tag{12}$$

where $g_0 = \pi\gamma/4\Delta$ is the mean conductance, $\mathcal{T}$ is the observation time, and and $F_t = \pi T t \sinh^{-1}(\pi T t)$ is the Fourier-transform of the Fermi distribution function.

In Fig.2 we show the result of a direct numerical evaluation of integrals in Eqs.(2),(3) at $T = 0$. One can see how the high-frequency limit is reached for the inverse reduction factor in the case of harmonic pumping. Eqs.(11,12) can be further simplified in the limit of low temperatures $T \ll \gamma$ where $F_t \approx 1$ and in the limit of high temperatures $T \gg \omega(\gamma\tau_\varphi)^{-1/2}$ where $F_t^2 \approx (\pi/6T)\,\delta(t)$ and we have:

$$\frac{\langle \delta G^2\rangle_{D,C}}{g_0^2} = \frac{\pi\gamma^2}{12T} \int_{-\mathcal{T}/2}^{\mathcal{T}/2} \frac{dt}{\mathcal{T}} \frac{1}{\Gamma_{d,c}(t)}. \tag{13}$$

Below we consider only these limiting cases.

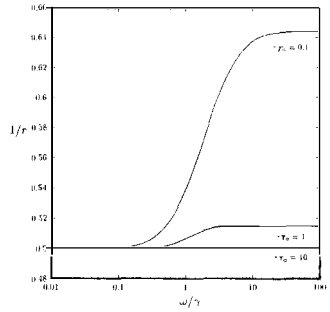


Figure 2: The frequency dependence of the inverse reduction factor for the harmonic pumping at different dimensionless intensities $I = 1/\gamma\tau_\varphi$ and low temperature $T \ll \gamma$.

4 Conductance fluctuations for the noise and harmonic ac pumping

There is a dramatic difference between the noiselike ac field with the short correlation time $\tau_0 \sim \omega^{-1} \ll \tau_\varphi$ and the harmonic ac field $A(t) = A_0 \cos(\omega t)$ with $\omega \gg \gamma$. In the case of the white-noise pumping the time-average of the cross-terms $\overline{A_{\xi+\eta/2}A_{\xi-\eta/2}}$ and $\overline{A_{t+\xi/2}A_{t-\xi/2}}$ in Eqs.(7,8) or Eqs.(9),(10) is zero and we obtain *the same, time-independent* dephasing rates $\Gamma_d = \Gamma_c = \gamma + 1/2\tau_\varphi$ for the cooperons and the diffusons with $\eta \neq 0$, where

$$\tau_\varphi^{-1} = \begin{cases} 4D\overline{A^2} & \omega \gg E_c \\ 4C\overline{E^2} & \omega \ll E_c \end{cases} \tag{14}$$

is proportional to the pumping intensity. For convenience of the further analysis we introduce the *dimensionless intensity* I:

$$I = \frac{1}{\tau_\varphi \gamma} \tag{15}$$

which for the harmonic pumping is equal to the number of absorbed/emitted field quanta $\hbar\omega$ for the time γ^{-1} electron spends inside the dot.

Then Eqs.(2),(3) give $\mathcal{C} = \mathcal{D}$, that is the diffuson and the cooperon contributions to the variance of conductance fluctuations are equal to each other. Hence *the time-reversal symmetry is effectively unbroken.*

The variance of conductance fluctuations in this case is given by:

$$\frac{\mathcal{D}}{g_0^2} = \frac{\mathcal{C}}{g_0^2} = \begin{cases} \frac{1}{2}\left(1+\frac{I}{2}\right)^{-2}, & T \ll \gamma + \frac{1}{2\tau_\varphi} \\ \frac{\pi\gamma}{12T}\left(1+\frac{I}{2}\right)^{-1}, & T \gg \gamma + \frac{1}{2\tau_\varphi} \end{cases} \tag{16}$$

For the harmonic pumping the dephasing rates are periodic functions of time:

$$\Gamma_d(\eta) \equiv \overline{\Gamma_d(\eta,\xi)} = \gamma + \tau_\varphi^{-1}\sin^2(\omega\eta/2), \quad \Gamma_c(t) \equiv \overline{\Gamma_c(t,\xi)} = \gamma + \tau_\varphi^{-1}\cos^2(\omega t), \tag{17}$$

and Eqs.(11,12) no longer lead to the same result.

For large pumping intensities $I = (\tau_\varphi\gamma)^{-1} \gg 1$ the dephasing functions Eq.(17) are small in the *'no-dephasing' windows* near zeros η_n and t_n of $\sin^2(\omega\eta/2)$ and $\cos^2(\omega t)$. It is these no-dephasing windows of the width $\omega^{-1}I^{-1/2}$ that make the dominant contribution to the magnitude of all phase-coherent effects at high pumping intensities $I \gg 1$.

In order to compute the diffuson and the cooperon contribution to the conductance fluctuations one can expand $\Gamma_d(\eta)$ and $\Gamma_c(t)$ in Eqs.(11),(12) near η_n, and t_n, perform integrations

from $-\infty$ to $+\infty$ over $\delta\eta = \eta - \eta_n$ and $\delta t = t - t_n$ and sum over all n. The result depends on the relation between the temperature of leads T and γ. For $T \ll \gamma \ll \tau_\varphi^{-1}$ we obtain:

$$\frac{\mathcal{D}}{g_0^2} \approx \frac{1}{4\sqrt{I}}, \qquad \frac{\mathcal{C}}{g_0^2} \approx \frac{1}{2I}, \qquad (I \gg 1). \tag{18}$$

One can see that the diffuson contribution $\mathcal{D}$ to the conductance fluctuations is parametrically larger than the cooperon one $\mathcal{C}$ even in the absence of a static magnetic field. This signals on the extremely strong T-breaking effect in this regime with the reduction factor $r = 1 + 2I^{-1/2}$ close to 1.

However, it is enough to raise the temperature of leads to make the T-breaking effect negligible. At high temperatures $T \gg \omega\sqrt{I}$ and strong pumping $I \gg 1$ Eq.(13) gives the same value

$$\frac{\mathcal{D}}{g_0^2} = \frac{\mathcal{C}}{g_0^2} = \frac{\pi\gamma}{12T}\,\frac{1}{\sqrt{I}}. \tag{19}$$

for the diffuson and the cooperon contribution to conductance fluctuations, and the reduction factor $r = 2$.

Comparing Eq.(16) with Eqs.(18),(19) we also conclude that at high intensities $I \gg 1$ the suppression of mesoscopic fluctuations by the noiselike ac field is always stronger than the suppression by a harmonic field of the same power. This is because the 'no dephasing' windows are absent in the case of noise.

5 Conductance fluctuations for an almost periodic ac field and statistics of zeros of the dephasing functions.

The idea of the 'no-dephasing windows' in the vicinity of zeros of the dephasing functions $\Gamma_d(\eta) - \gamma$ and $\Gamma_c(t) - \gamma$ can be applied to a general case of an almost periodic ac field. For such an ac filed the dephasing functions have a certain density of *complex* zeros $z_n = x_n + iy_n$ with a small complex part y_n:

$$\rho(y) = \sum_n \langle \delta(x - x_n)\delta(y - y_n)\rangle_x, \tag{20}$$

where $\langle ...\rangle_x = (\mathcal{T})^{-1}\int_{|x|<\mathcal{T}/2} dx...$ stands for the averaging over x.

Since only the time variables in the 'no dephasing windows' contribute to the variance of mesoscopic fluctuations at large pumping intensities, one can express the dependence of the variance on the dimensionless intensity I in terms of the density of zeros $\rho(y)$.

For an important example of the *bi-harmonic* ac field

$$A(t) = A_0\left[\cos(\omega t) + \cos(\alpha\omega t)\right] \tag{21}$$

one obtains in the high-temperature limit [11] $T \gg \omega\sqrt{I}$:

$$\frac{\langle \delta G^2\rangle_{D,C}}{g_0^2} = \frac{\pi^2\gamma}{3T\sqrt{2(1+\alpha^2)}}\, I^{-1}\int_{-\infty}^{+\infty} \frac{dy\,\rho_{d,c}(y)}{\left[I^{-1} + \frac{y^2}{8}(1+\alpha^2)\right]^{1/2}}, \tag{22}$$

where $\rho_{d,c}$ is the density of zeros that corresponds to the equation (the sign $\pm$ stands for the cooperon(diffuson) part):

$$\cos z + \cos(\alpha z) \pm 2 = 0. \tag{23}$$

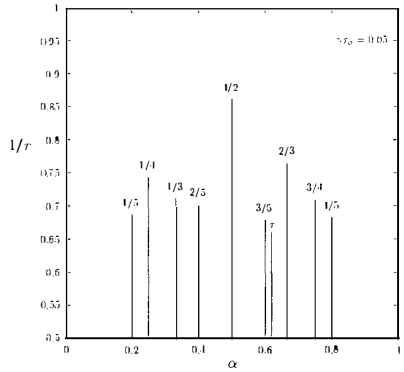


Figure 3: Reduction factor r vs the frequency ratio α in simple commensurate points $\alpha = P/Q$ for low temperatures $T \ll \gamma$ and pumping intensity $I = (\gamma\tau_\varphi)^{-1} = 20$. Also plotted is r for the golden mean $\alpha = \tau = \frac{\sqrt{5}-1}{2}$.

6 Effect of commensurability in the frequency domain

There is a drastic difference in the density of zeros $\rho_{d,c}(y)$ for the case of *commensurate* and *incommensurate* frequencies $\omega_1 = \omega$ and $\omega_2 = \alpha\omega$ in Eq.(21). For the case of commensurate frequencies $\alpha = P/Q < 1$ the density $\rho(y)$ is the set of δ-functions $(2\pi Q)^{-1}\sum\delta(y-y_n)$ separated by gaps $\Delta y_n \sim 1/Q$. In the limit of incommensurate frequencies $Q \to \infty$ the function $\rho(y)$ is continuous with no singularity at $y = 0$. This difference shows up in the dependence of the diffuson and the cooperon contribution to the variance of conductance fluctuations on the pumping intensity I.

Let us consider the case of commensurate frequencies $\alpha = P/Q$ with not very large denominator Q. At large dimensionless intensities $I \gg Q^2$ the gap $y_1 \sim 1/Q$ is large compared to $I^{-1/2}$, and one can neglect in Eq.(22) all complex roots with $y_n \neq 0$. Equation (23) with the sign minus has real roots at *any* α. Then one immediately concludes from Eq.(22) that for commensurate frequencies with $Q \ll \sqrt{I}$ the diffuson part of the variance of conductance fluctuations is proportional to $I^{-1/2}$. However, Eq.(23) with the sign plus (relevant for the cooperon contribution) has real solutions only if P and Q are *both odd.* In this case in the high-temperature limit we have $\mathcal{D} = \mathcal{C} \propto I^{-1/2}$ as for a strictly harmonic pumping. Thus the *symmetry between the diffuson and the cooperon contribution is unbroken.* One can see that the condition that both P and Q in $\alpha = P/Q$ in Eq.(21) are odd, is a particular case of a more general condition [12]

$$A(t+\tau^*) = -A(-t+\tau^*), \tag{24}$$

that is, by a certain shift τ^* (in our case τ^* is a quarter of the period) the vector-potenial $A(t)$ can be made an odd function of time. This is the natural definition for the time-reversal symmetry in the absence of a preferential time origin.

If either Q or P is even this condition is violated and the cooperon contribution is anomalously suppressed $\mathcal{C} \propto I^{-1}$. In this case the effective T-symmetry breaking is strong even in the high-temperature limit (see Fig.4. and Fig.5.). Such a *parity effect* is also present in the low-temperature limit $T \ll \gamma$ as it is seen from Fig.3 obtained by numerical integration of Eqs.(11,12). However, in this case it is much weaker and the symmetry Eq.(24) no longer implies $\mathcal{C} = \mathcal{D}$.

Now consider the case $Q \gg \sqrt{I}$. In this case the function $\rho_{d,c}(y)$ in Eq.(22)is effectively averaged over the interval $\delta y \sim I^{1/2}$ and can be replaced by a constant. As the result both the diffuson and the cooperon part of the variance is proportional to $I^{-1}\ln I$ and the effect

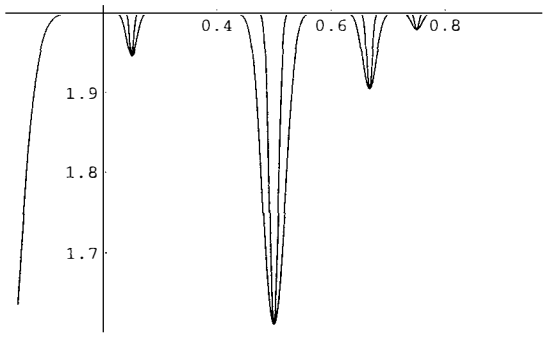


Figure 4: The reduction factor r as a function of the frequency ratio α in the high-temperature limit $T \gg \omega\sqrt{I}$ for $I = 4$ and $1/\mathcal{T}\omega = 0.05$ and 0.02. The dips at $\alpha = \frac{1}{2}, \frac{2}{3}, \frac{1}{4}$ and $\frac{3}{4}$ are seen while there is no dip for $\alpha = \frac{1}{3}$ where both P and Q are odd. The width of peaks is of the order of $1/\mathcal{T}\omega$.

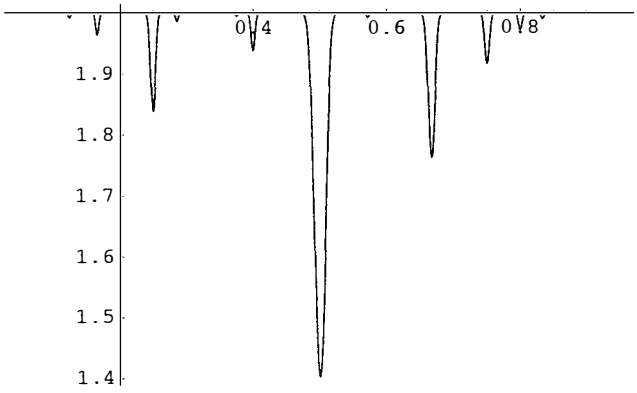


Figure 5: The reduction factor r as a function of the frequency ratio α in the high-temperature limit $T \gg \omega\sqrt{I}$ for $I = 8$ and $1/\mathcal{T}\omega = 0.02$. Small dips at $\alpha = P/Q$ with larger denominator Q (PQ is even) become visible.

of T-breaking drastically decreases. That is why the depth of dips in the reduction factor r at $\alpha = P/Q$ rapidly decrease with increasing the denominator Q at a given intensity I (see Fig.4 and Fig.5.). The same trend holds for the low-temperature regime too (Fig.3) but the reduction factor r does not reach its universal value even for the 'most irrational' frequency ratio $\alpha = (\sqrt{5}-1)/2$.

It is possible to obtain an explicit analytical expression for the cooperon and the diffuson contribution to the variance of conductance fluctuations in the high-temperature limit $T \gg \omega\sqrt{I}$:

$$\frac{\mathcal{D}}{g_0^2} \approx \frac{\gamma}{6T} \sum_{n,m=-\infty}^{+\infty} \tilde{\delta}(n-\alpha m) \begin{cases} I^{-1} K_0\left(2\sqrt{\frac{n^2+m^2}{I}}\right), & n^2+m^2>0 \\ I^{-1}\ln(2\sqrt{I}), & m=n=0 \end{cases}, \tag{25}$$

$$\frac{\mathcal{C}}{g_0^2} \approx \frac{\gamma}{6T} \sum_{n,m=-\infty}^{+\infty} (-1)^{n+m}\, \tilde{\delta}(n-\alpha m) \begin{cases} I^{-1} K_0\left(2\sqrt{\frac{n^2+m^2}{I}}\right), & n^2+m^2>0 \\ I^{-1}\ln(2\sqrt{I}), & m=n=0 \end{cases}, \tag{26}$$

where $K_0(x)$ is the Bessel function and $\tilde{\delta}(\omega x)$ is the spectral lineshape function of the harmonic component normalized so that $\tilde{\delta}(0) = 1$. Fig.4 and Fig.5 are obtained from Eqs.(25),(26) for

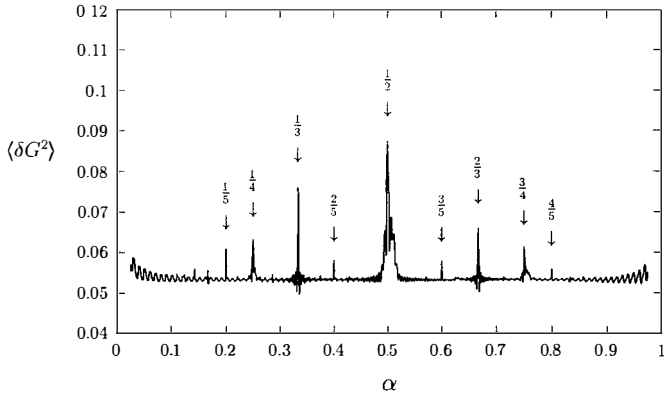


Figure 6: The total variance of conductance fluctuations (in units of the ensemble-average dc conductance) at $T \ll \gamma$ as a function of the frequency ratio α for $I = 20$ and $1/\mathcal{T}\omega = 0.01$. The width of peaks is of the order of $1/\mathcal{T}\omega$.

the Gaussian lineshape $\tilde{\delta}(x) = e^{-x^2\omega^2\mathcal{T}^2}$. Eqs.(25),(26) reveal an important and a bit counter-intuitive feature of the α dependences. The electron escape rate γ enters only in the dimensionless intensity I (see Eq.(15)) that controls the magnitude of peaks/dips in the α-dependences. The width of peaks/dips is determined by the spectral linewidth $\delta \simeq \mathcal{T}^{-1}$ of the harmonic components and can be much smaller than γ/ω.

The commensurability effect is present not only for the reduction factor r but also for the total variance of conductance fluctuations. In Fig.6. the total variance is plotted as a function of the frequency ratio α for the case of low temperatures $T \ll \gamma$.

In conclusion, the effect of ac pumping on the statistics of conductance fluctuations possesses an interesting dualism: the periodic ac fields that are least effective in suppressing of conductance fluctuations by dephasing, turn out to be the most effective in breaking the time-reversal symmetry. An important exception is the periodic ac field $A(t)$ that obeys the symmetry Eq.(24). At high temperatures its effect on the reduction factor r is negligible while the conductance fluctuations are much larger than for the white–noise of the same power.

I am grateful to X.-B. Wang, V.I.Yudson, E.Kanzieper and V.M.Akulin and O.M.Yevtushenko for a fruitful collaboration on the problem.

References

1. D. J. Thouless, Phys. Rev. B **27**, 6083 (1983).
2. M. Switkes, C. M. Marcus, K. Campman, A. C. Grossard, Science **283**, 1905 (1999).
3. P. W. Brouwer, Phys. Rev. B **58**, 10135 (1998).
4. T. A. Shutenko, I. L. Aleiner, and B. L. Altshuler, Phys. Rev. B **61**, 10366 (2000).
5. M. G. Vavilov and I. L. Aleiner, Phys. Rev. B, **60**, R16311 (1999).
6. M. G. Vavilov, V. Ambegaokar and I. Aleiner, cond-mat/0008469.
7. P. Mohanty, E. M. Q. Jariwala, and R. A. Webb, Phys. Rev. Lett. **78**, 3366(1997).
8. L. P. Levi, G. Dolan, J. Dunsmuir, and H. Bouchiat, Phys. Rev. Lett. **64**, 2074 (1990).
9. V. E. Kravtsov and B. L. Altshuler, Phys. Rev. Lett. **84**, 3394(2000).
10. V. I. Yudson, E. Kanzieper, and V. E. Kravtsov, cond-mat/0012200; Phys.Rev.B **64**(4).
11. X-B.Wang and V.E.Kravtsov, cond-mat/0008193; Phys.Rev.B **64**(5), (2001).
12. An equivalent symmetry is mentioned in: S.Flach, O.Yevtushenko and Y.Zolotaryuk, Phys.Rev.Lett.,**84**,2358 (2000).

Universal Scrambling Properties of Spectra and Wave functions in Disordered Interacting Systems

Frédéric Piéchon, Gilles Montambaux
Laboratoire de Physique des Solides Bât 510, CNRS, Université Paris-Sud, 91405 Orsay, France

Recent experiments on quantum dots in the Coulomb Blockade regime have shown how adding successive electrons into a dot modifies the energy spectrum and the wave functions of the electrons already present in the dot. Using a microscopic model, we study the importance of electron-electron interaction on these "scrambling" effects. We compute the Hartree-Fock single particle properties as function of the number p of added electrons. We define parametric correlation functions that characterize the scrambling properties of the Hartree-Fock wave functions and energy spectra. We find that each of these correlation functions exhibit a universal behavior in terms of the ratio p/p^* where p^* is a characteristic number that decreases with increasing either the interaction strength, the disorder strength or the system size.

1 Introduction

At very low temperature, by applying a gate voltage V_g to a Quantum Dot (QD) weakly connected to leads by tunnel contacts, one obtains a series of Coulomb blockade conductance peaks of height G_N at positions V_g^N. The peak positions V_g^N are directly related to difference $E_{N+1} - E_N$ between the ground state energies of the dot with N and $N+1$ electrons (in zero bias). The heights G_N are related to the overlap of the $|N>$ and $|N+1>$ ground state wave functions at the contacts [1]. During the last few years, many experiments [2,3] have shown that the statistical properties of the successive peak positions V_g^N could not be described within the framework of the random matrix theory (RMT). For the addition spectrum (e.g. statistical properties of the differences $\Delta_2 = V_g^{N+1} - V_g^N$), qualitative agreement with experimental results can only be obtained by taking into account fluctuations of the charging energy that originate from the spatial fluctuations of wave function amplitudes [2,4,5]. Although such fluctuations of wave functions already exist in RMT [4], the resulting charging energy fluctuations are parametrically to small if one ignores the reorganization or "scrambling" (of the wave functions and of the spectrum) induced by the addition of the successive electrons [2,5]. In fact, in a recent experimental study of the peak to peak heights correlation, Patel et *al.* [6] have unambiguously shown that this reorganization is important and could essentially be attributed to electron-electron interaction effects. Recently, Alhassid et *al.* [7] have confirmed the importance of scrambling using a phenomenological model based on Gaussian Random Matrix Process (GRMP)[8], and have obtained good agreement with Patel et *al.* experiment.

In the present work based on a microscopic model of a quantum dot, we present a detailed numerical study that shows directly the importance of the electron-electron interaction on the scrambling of the single particle properties obtained within a self consistent Hartree-Fock (SCHF) method.

2 Microscopic model

We model a two dimensional disordered dot of size $A = L_x \times L_y$ by the following Hamiltonian:

$$H = \sum_i w_i c_i^\dagger c_i - t \sum_{<ij>} [c_i^\dagger c_j + h.c.] + \frac{U}{2} \sum_{i,j=1}^{A} M_{ij} n_i n_j, \qquad (1)$$

where $< ij >$ denotes nearest neighbors on a square lattice of size $A = L_x \times L_y$ and $t = 1$. $c_i^\dagger$ and c_i are creation and annihilation operators for an electron (spinless) on site i and $n_i = c_i^\dagger c_i$.

The random on-site disorder potential w_i are uniformly distributed over $[-\frac{W}{2}, \frac{W}{2}]$. Because of the disorder, the electronic charge density exhibits fluctuations in space. We consider that the natural bare interaction between these charge fluctuations has a long range Coulomb form $M_{ij} = \frac{1}{|\mathbf{r}_i - \mathbf{r}_j|}$. We choose a torus geometry to prevent from electrostatic effects that tend to accumulate the charge on the surface. The distance $|\mathbf{r}_i - \mathbf{r}_j|$ is calculated from the shortest path relating the two sites i and j on the torus.

3 Hartree Fock picture of scrambling

We treat interaction effects in the self-consistent Hartree-Fock approximation. We thus assume that the ground state $|\Psi_0^N>$ of a dot with N particles is a Slater determinant of N effective single particle states $\psi_\alpha^N(\mathbf{r}_i)$ with associated quasi-energy ϵ_α^N. These states $\psi_\alpha^N(\mathbf{r}_i)$ are in fact the self-consistent eigenstates of an effective one–particle Hamiltonian $h^N = \sum_i w_i^{eff} c_i^\dagger c_i - \sum_{<ij>}[t_{ij}^{eff} c_i^\dagger c_j + h.c.]$. The effective onsite potential $w_i^{eff} = w_i + U\sum_j M_{ij} < \Psi_0^N|n_j|\Psi_0^N >$ is the sum of the disorder potential and the Hartree contribution. Similarly the effective hopping $t_{ij}^{eff} = t\delta_{<ij>} + UM_{ij} < \Psi_0^N|c_i^\dagger c_j|\Psi_0^N >$ includes the Fock exchange term. Self consistency is obtained with an iterative procedure.

The self consistent states $\psi_\alpha^N(\mathbf{r}_i)$ are linear combinations of the non interacting $\psi_\alpha^0(\mathbf{r}_i)$. However the $\psi_\alpha^N(\mathrm{r}_i)$ depend explicitly on interaction strength and particle number N and not only on disorder strength and system size as the $\psi_\alpha^0(\mathrm{r}_i)$. Therefore, by adding one by one p electrons into a dot with initially N particles, the effective one body Hamiltonian h^N is changed into another Hamiltonian h^{N+p} with the corresponding $\psi_\alpha^{N+p}(\mathbf{r}_i)$ and ϵ_α^{N+p}. In the Hartree-Fock approximation, one can always write $h^{N+p} = h^N + V^{N,N+p}$, such that the scrambling effects of the p additional electrons is described by an effective one body term $V^{N,N+p}$, that is neither diagonal in the position basis nor in the ψ_α^N basis of the dot with N particles. In fact this possibility of writing $h^{N+p} = h^N + V^{N,N+p}$ allows us to make a parallel with the phenomenological model of Alhassid and Malhotra[7]. In their work, the $N+p$ interacting particles system is described by an effective one body Hamiltonian $h^{N+p} = h_0 \cos(p\delta x) + h_1 \sin(p\delta x)$ in which h_0, h_1 are two random Gaussian matrices and δx is the parameter that control the scrambling strength. Their effective scrambling potential $V^{N,N+p}$ is thus given by $V^{N,N+p} \simeq h_0(\cos(p\delta x) - 1) + h_1 \sin(p\delta x)$.

4 Numerical results

4.1 Scrambling properties of SCHF single particle wave functions

In order to characterize the scrambling of the SCHF single particle wave functions, we have computed the following parametric correlation function:

$$C_\psi(p) = \overline{\left| \int d\mathbf{r}\ \psi_\alpha^{N+p}(\mathbf{r})\psi_\alpha^{N*}(\mathbf{r}) \right|^2} \qquad (2)$$

in which $\overline{...}$ means averaging on disorder configurations and on the N lowest single particle energy levels α. The scrambling of wavefunctions is characterized by a decrease of $C_\psi(p)$ with increasing p. A similar quantity has already been studied in the context of GRMP [8]. We have studied in detail the dependences of $C_\psi(p)$ on the disorder strength W (or conductance g), the interaction strength U and the system size A. The ranges of parameters considered are $W = 4 \to 10$; $U = 0.5 \to 3$, $A = 6\times 6 \to 11 \times 10$ sites. The initial values of N are chosen so that the band is quarter filled $\nu = N/A \simeq 1/4$. For each set of parameters we have averaged over 500 distinct disorder configurations. The results obtained for $C_\psi(p)$ are summarized on Figure 1a. This figure shows a quite interesting result, that the correlation function $C_\psi(p)$ can be recast

into a one parameter scaling form $C_\psi(p) = f_\psi(p/p_\psi)$ where p_ψ depends on the three parameters W, U, A. In the range of parameters studied we further obtain the following approximate fitting form:

$$\begin{aligned} C_\psi(p) &\simeq \frac{1}{[1+(\frac{p}{p_\psi})^{3/4}]^{1/2}} \\ 1/p_\psi &= c\ U^2 A^2 W^3 [1 + d_A\ U^2]. \end{aligned} \tag{3}$$

where $c \simeq 8.10^{-8}$ and $d_A = 0.03; 0.05; 0.1; 0.15; 0.2$ for $A = 6\times 6; 6\times 7; 7\times 8; 8\times 9; 9\times 10$ respectively. For a given p, $C_\psi(p)$ decreases when either W, U or A is increased. Thus the larger the system size, the stronger is the scrambling effect of a single additional electron. Let us compare the scaling (3) with the scaling obtained by Alhassid and Malhotra in the context of the GRMP model[7]. The behavior found in this model for the correlation function is $C_\psi^{GRMP}(p) \simeq [1+(\frac{p}{p_\psi})^2]^{-1}$ with $1/p_\psi \simeq \delta x\sqrt{M}$ for gaussian orthogonal matrices of size $M \times M$. The difference between the functional form $C_\psi(p)$ and $C_\psi^{GRMP}(p_{GRMP})$ seems to prevent any simple mapping between them. Nevertheless, if we consider only the tail of the two forms, we can identify the microscopic value p with $p_{GRMP}^{16/3}$. We then obtain the following relation between the microscopic parameters and the parameters of the GRMP model : $(\delta x\sqrt{M})^{16/3} \sim c\ U^2 A^2 W^3 (1 + d_A\ U^2)$.

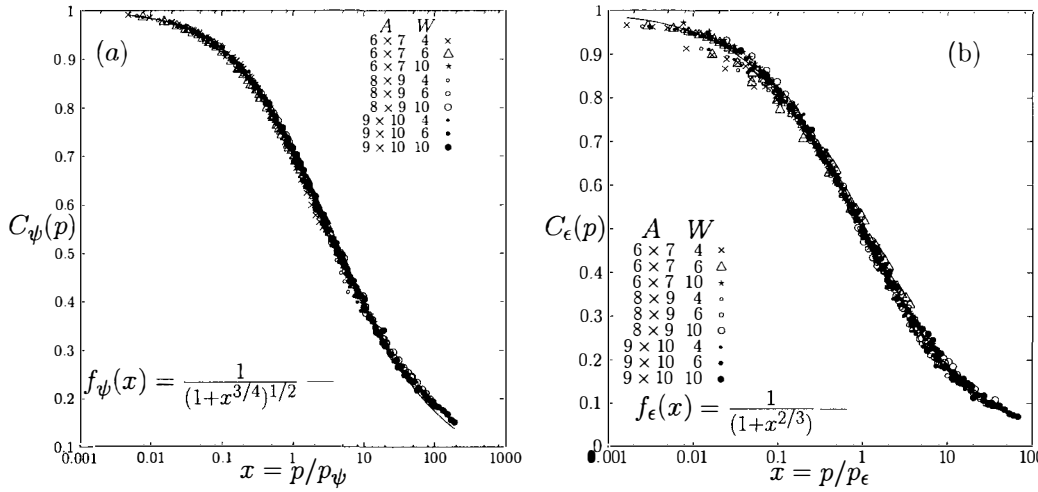


Figure 1: (a) $C_\psi(p)$ as a function of the scaling variable p/p_ψ. (b) $C_\epsilon(p)$ as a function of the scaling variable p/p_ϵ. For a given disorder W and system area A, we plot all the data points corresponding to the entire range $p = \{1, 2, .., 10\}$ and interaction range $U = \{0.5, 1, .., 3\}$.

4.2 Scrambling properties of SCHF single particle energy spectra

In order to characterize the scrambling of the SCHF single particle energy spectrum we have computed the following parametric correlation function:

$$C_\epsilon(p) = \frac{\overline{s_\alpha^{N+p} s_\alpha^N} - 1}{\overline{s_\alpha^N s_\alpha^N} - 1}, \tag{4}$$

where $s_\alpha^N = \epsilon_{\alpha+1}^N - \epsilon_\alpha^N$ is the spacing between two consecutive levels (s_α^N is normalized to the mean level spacing at this energy). Since the one particle density of state has a deep around the (average) Fermi level, we have used all α corresponding to energy levels (empty or occupied) neither in the this deep nor at the band edges. As it is illustrated on Figure 1b, we have found

that $C_\epsilon(p)$ can also be recast into a one parameter scaling form $C_\epsilon(p) = f_\epsilon(p/p_\epsilon)$ where p_ϵ depends on the parameters W, U, A. Quantitatively we obtain the following approximate fitting form:

$$\begin{aligned} C_\epsilon(p) &\simeq \frac{1}{1+(\frac{p}{p_\epsilon})^{2/3}}, \\ 1/p_\epsilon &\simeq cU^3A^2W^{2.75}, \end{aligned} \tag{5}$$

where $c \simeq 5.10^{-8}$. The quantitative behavior of p_ϵ, in terms of W, A, U, is different from that of p_ψ. This contrasts with GRMP-like models in which necessarily $p_\epsilon = p_\psi$. For the microscopic model, we believe that the difference found between p_ϵ and p_ψ reflects the distinct statistical behavior of the diagonal and the off-diagonal elements of $V^{N,N+p}$ in the ψ_α^N basis (within a perturbative approach, the SCHF single particle energy level position depends on both the diagonal and off-diagonal terms. In contrast the reorganization of SCHF wave functions depends only on the off-diagonal elements).

5 Conclusion

Based on a microscopic model of a disordered quantum dot, we have presented detailed numerical results that show the importance of electron-electron interaction on the scrambling of the single particle properties obtained within a self consistent Hartree-Fock method. As main result of this study, we have found one-parameter scaling properties for the two quantities $C_\psi(p), C_\epsilon(p)$ which describe respectively the reorganization of the one particle wave functions and of the energy spectrum when p particles are added to the system. The quantitative analysis of this one parameter scaling properties cannot be described by effective GRMP models considered until now [7,8]. This suggests that new specific random matrix models are necessary to describe microscopic disordered models of Coulomb interacting particles within the Hartree-Fock approximation.

References

1. L. P. Kouwenhoven et al., in *Mesoscopic Electron Transport*, Edited by L.L. Sohn, L.P. Kouwenhoven, and G. Schoen (NATO Series, Kluwer, Dordrecht, 1997)
2. U. Sivan et al, Phys. Rev. Lett. **77**, 1123 (1996),
3. F. Simmel, T. Heinzel and D. A. Wharam, EuroPhys. Lett. **38**, 123 (1997), S. R. Patel et al, Phys. Rev. Lett. **80**, 4522 (1998), F. Simmel et al, Phys. Rev. B **59**, 10441 (1999)
4. Ya. M. Blanter, A. D. Mirlin and B. A. Muzykantskii, Phys. Rev. Lett. **78**, 2449 (1997), R. O. Vallejos, C. H. Lewenkopf and E. R. Mucciolo, Phys. Rev. Lett. **81**, 677 (1998)
5. R. Berkovits, Phys. Rev. Lett. **81**, 2128 (1998), S. Levit and D. Orgad, Phys. Rev. B **60**, 5449 (1999), P. N. Walker, G. Montambaux and Y. Gefen, Phys. Rev. B **60**, 2541 (1999), A. Cohen, K. Richter and R. Berkovits, Phys. Rev. B **60**, 2535 (1999), L. Bonci and R. Berkovits, Europhys. Lett. **47**, 708 (1999), K-H Ahn, K. Richter and I-H Lee, Phys. Rev. Lett. **83**, 4144 (2000)
6. S. R. Patel et al, Phys. Rev. Lett. **81**, 5900 (1998),
7. Y. Alhassid and S. Malhotra, Phys. Rev. **B 60**, R16315 (1999)
8. Y. Alhassid and H. Attias, Phys. Rev. Lett. **74**, 4635 (1995), *ibid* Phys. Rev. **E 52**, 4776 (1995)

COMPARISON BETWEEN ONE- AND TWO-CHANNEL KONDO EFFECTS IN MESOSCOPIC SYSTEMS

A. Zawadowski
Department of Theoretical Physics and Research Group of the Hungarian Academy of Sciences, Technical University of Budapest, H-1521 Budapest, Hungary

Solid State and Optical Research Institute of the Hungarian Academy of Sciences, H-1525 Budapest, Hungary

There are strong recent indications that the Kondo phenomena play important role in the electronic transport and dephasing mechanism for some of the experimentally investigated metallic samples. The spin and the orbital Kondo problem with two-level systems provide very similar behavior above the Kondo temperature. Below the Kondo temperature the behavior is drastically different as in the latter case the entropy remains non zero. In the following several results derived earlier by different methods are simply reproduced by the time-ordered diagram technique in the leading logarithmic approximation valid above the Kondo temperature.

In the recent years the evidences have been fast growing that in many cases the low energy or low temperature electron transport in metals cannot be explained in terms of electron-electron and electron-phonon interactions. The anomalous behaviors occur e.g. in the electron dephasing rate [1] and mesoscopic transport [2,3]. The leading candidates to resolve those problems are the Kondo phenomena due to dynamical impurities. The one-channel Kondo problem (1CK) is dealing with magnetic impurities, the two-channel one (2CK) may describe the interaction between the electrons and the fast relaxing two-level systems (TLS). In the 1CK problem the characteristic Kondo temperatures T_K cover a very broad temperature range, while in the 2CK case the zero bias anomalies indicate the typical range around 5K [3]. In the second case the theoretical description of the Kondo temperature is still in debate [4,5] but the electron-hole symmetry breaking in the electronic band structure seems to explain the observed value.

While the high temperature Kondo phenomena ($T > T_K$) are not very different in the 1CK and 2CK cases, in the low temperature range their behaviors are drastically different. Lowering the temperature the impurity dynamics is largely enhanced around T_K. In the 1CK the ground state is singlet, thus the dynamics is gradually frozen out and Fermi liquid behavior is developing as the zero temperature is approached. On the other hand the 2CK ground state without low energy cutoff (e.g. level splitting) has a finite entropy, thus the enhanced dynamics can exist even at very low temperature. In the 1CK case the electron dephasing rate goes to zero as $T \to 0$, for the 2CK case a new energy scale is suggested [6], where the dephasing rate is slowly varying even well below the Kondo temperature. While the predictions are well confirmed for magnetic impurities, the role of TLS is still subject of intensive discussions which is partially due to the difficulties to identify the TLS-s in a real system. The non-universal behavior of dephasing rate at low temperature supports that in some cases the TLS may play a decisive role.

The recent experiments carried out by the Saclay group [2] in which the electronic transport in short wires is studied can be also very different for different metals, but also are very sensitive on impurities. The Ag and some of the Au samples show no anomalous behavior, closely following the predictions based on electron-electron interactions [7]. Some of the Au and the Cu samples show a fast electronic energy relaxation by smearing the electron distribution function around the Fermi energies corresponding to the left and right contacts. Recently, it became known that some of the Au samples contain fairly large amount of magnetic Fe impurities [2]. The observed anomalies were explained in a phenomenological way by assuming an anomalous electron-electron scattering rate which is singular in the energy transfer E like $1/E^2$.

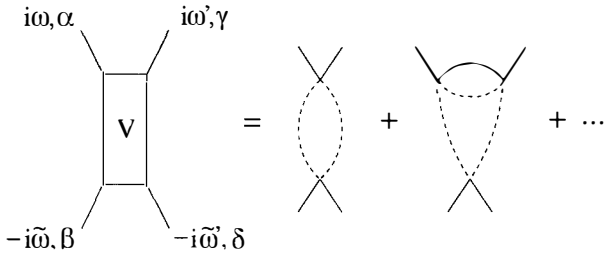


Figure 1: The effective magnetic impurity induced electron-electron interaction in the imaginary time technique. The diagrams contributing to lowest orders are also shown. The solid lines indicate the electrons, the dotted lines the Abrikosov's pseudofermions.

Such a behavior first derived by J. Kroha[8] in the framework of the 2CK problem for $T < T_K$. Recently, it has been pointed out by Kaminski and Glazman[9,10] that a similar behavior can be obtained for $T > T_K$ independently of the number of the channels. The result for $T < T_K$ in the 1CK case must be very different as in the framework of the Fermi liquid behavior no singular behavior can be expected.

The Kondo effect is due to the scattering of conduction electrons by a localized object (magnetic or substitutional impurity or some defects) with some internal degrees of freedom (e.g. spin, two close atomic positions). The typical Hamiltonian of Kondo-like problems is

$$H = \sum_{k\mu} \epsilon_k c^\dagger_{k\mu} c_{k\mu} + \sum_\alpha \epsilon_\alpha b^\dagger_\alpha b_\alpha + \sum_{k,k'} \sum_{\mu\nu\alpha\beta} V^{\alpha\beta}_{\mu\nu} c^\dagger_{k\mu} c_{k'\nu} b^\dagger_\alpha b_\beta \tag{1}$$

where ϵ_k is the electron kinetic energy with momentum k, $c^\dagger_{k\mu}$ creates an electron spherical wave with radial momentum k and internal quantum numbers μ and $b^\dagger_\alpha$ creates a heavy object with quantum number α (α being the spin, the position of the atom in the TLS, or a crystal field label of the impurity). Note that the internal indices μ and ν of the conduction electrons may also represent magnetic spin or orbital indices or a combination of these as well. $V^{\alpha\beta}_{\mu\nu}$ denotes the interaction coupling and a band cutoff D is applied.

That is obvious that a dynamical impurity with finite excitation energy can mediate energy transfer between the electrons as a localized phonon does. It was first pointed out in Refs.[11] that magnetic impurities also mediate energy transfer even in the absence of external magnetic field and crystalline field splitting in third order of the exchange coupling, while the second order contributes to the elastic scattering[12]. The result in the lowest orders of the perturbation for the electron-electron effective coupling for an electron pair of zero total energy ($\omega = \tilde{\omega}$) shown in Fig. 1 is

$$V_{\alpha\beta\gamma\delta}(\omega,\omega') = [V_{el}(\omega,\omega') + V_{inel}(\omega,\omega')]\boldsymbol{\sigma}_{\alpha\gamma}\boldsymbol{\sigma}_{\beta\delta}, \tag{2}$$

where the elastic and the inelastic parts are respectively

$$V_{el}(\omega,\omega') = \frac{1}{T}\frac{1}{3}S(S+1)J^2\left[1 + 4J\rho_0 \ln\frac{D}{|\omega|}\right]\delta_{\omega\omega'} \tag{3}$$

and

$$V_{inel}(\omega,\omega') = \frac{1}{3}S(S+1)J^2 4(J\rho_0)\frac{\pi}{\omega-\omega'}(\operatorname{sgn}\omega - \operatorname{sgn}\omega'), \tag{4}$$

where T is the temperature and $i(\omega - \omega')$ is the energy transfer in which the inelastic part is singular. That vertex was used to calculate the correction to the superconducting temperature in the presence of magnetic impurities[11]. In the analytic continuation to real energy variables these

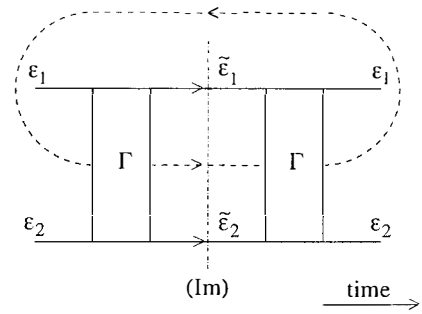


Figure 2: The two particle forward scattering amplitude $T(\omega)$ giving the decay rate is shown in time ordered representation, where the intermediate state providing the imaginary part is also shown.

contribute to the real part of the V_{inel} which is singular in the energy transfer E ($i(\omega-\omega') \to E$) as $1/E$.

Kaminski and Glazman [9] were the first to point out that the magnetic impurity induced electron-electron scattering rate is also singular in the energy transfer. In the fourth order of the perturbation theory that was proportional to $1/E^2$, as the energy dependence assumed by the Saclay group [2].

In the following the derivation of that result with logarithmic correction is presented in the non-vanishing leading logarithmic order. The Abrikosov's pseudofermion technique [13] is used, where the b operators in the Hamiltonian (1) create spin states and $V_{\mu\nu}^{\alpha\beta} \Longrightarrow J\boldsymbol{\sigma}_{\mu\nu}\mathbf{S}_{\alpha\beta}$ where J is the exchange coupling, $\boldsymbol{\sigma}$ is the Puli operator and $\mathbf{S}$ is the spin operator describing the localized spin. For simplicity the time ordered diagrams are used with real time. That technique can be applied starting with arbitrary states (e.g. non-equilibrium) and the transition amplitude between states $|i\rangle$ and $\langle f|$ is given as

$$\langle f|T|i\rangle_\omega = \sum_{n=1}^{\infty}\langle f|H_1\left(\frac{1}{\omega+i\delta-H_0}H_1\right)^n|i\rangle, \tag{5}$$

where ω is the energy of the initial state. In the Abrikosov's pseudofermion technique [13] the decay rate is calculated by taking the imaginary part of the forward scattering amplitude (using the optical theorem) thus

$$\frac{1}{\tau} \sim -\mathrm{Im}\{\langle i|T|i\rangle_\omega\}. \tag{6}$$

In that diagram technique the pseudofermion lines representing the spin states (dotted line) are closed and there is only one line running against the time insuring that at any moment only one spin state is present for a given magnetic impurity. The electrons are represented by solid lines.

A typical forward scattering diagram which gives the result of Kaminski and Glazman, e.g. in the electron-electron channel [9] in the leading logarithmic order is shown in Fig. 2, where the real part of vertex Γ is taken and the cut (dashed dotted line) represents the intermediate state where the imaginary part is taken. In the logarithmic approximation the vertex Γ is shown in Fig. 3, where the square boxes are parquet vertex correction $t(\bar{\omega})$ with energy $\bar{\omega}$ running through in the one particle channel and defined similarly to Eq. (5). The dotted line inside the one particle scattering amplitude runs in the direction of time.

Assuming that the total two-particle initial energy is ω and the energy transfer is e.g. $E = \varepsilon_1 - \tilde{\varepsilon}_1$, then the intermediate energy denominator e.g. in the diagram in Fig. 3 is $\omega - \tilde{\varepsilon}_1 - \varepsilon_2$, thus with $\omega = \varepsilon_1 + \varepsilon_2$ that is just the energy transfer. In this way the two-particle interaction rate is $\mathrm{Im}\,T \sim \frac{1}{E^2}$.

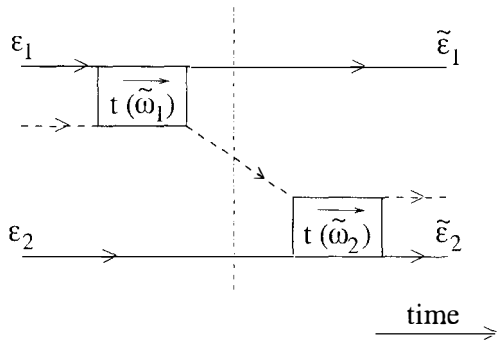


Figure 3: Typical time ordered diagram contributing to the vertex Γ in the leading logarithmic approximation is shown. The square boxes represent the electron-pseudofermion vertexes $t(\tilde{\omega})$ with total internal energy $\tilde{\omega}$. The dotted line represents the position of the energy denominator.

The one-electron scattering blocks $t(\tilde{\omega})$ are in logarithmic approximation ($|\tilde{\omega}| + kT > T_K$)

$$t(\tilde{\omega}) = \frac{J}{1 - 2J\rho_0 \ln \frac{D}{|\tilde{\omega}|+kT}} = \frac{1}{2\rho_0 \ln \frac{|\tilde{\omega}|+kT}{T_K}}. \tag{7}$$

where $T_K = D\exp\{-\frac{1}{2J\rho_0}\}$ is the Kondo temperature in the leading logarithmic approximation [14]. In the diagrams in Fig. 2 the one-particle vertex corrections represented by the square boxes are separated in time, thus their internal variables are $\tilde{\omega}_1 = \omega - \varepsilon_1$ and $\tilde{\omega}_2 = \omega - \tilde{\varepsilon}_1$, thus with $\omega = \varepsilon_1 + \varepsilon_2$, $\tilde{\omega}_1 = \varepsilon_1$ and $\tilde{\omega}_2 = \varepsilon_2 + E$. In this way the scattering rate is

$$\frac{1}{\tau(\omega)}\bigg|_{\omega=\varepsilon_1+\varepsilon_2} \sim \frac{1}{E^2}\int (t(\varepsilon_1)t(\varepsilon_2+E))^2(1-n(\tilde{\varepsilon}_1))(1-n(\tilde{\varepsilon}_2))\delta(\omega-\tilde{\varepsilon}_1-\tilde{\varepsilon}_2)d\tilde{\varepsilon}_1 d\tilde{\varepsilon}_2, \tag{8}$$

where $n(\varepsilon)$ are the occupation numbers of the electronic states in the actual non-equilibrium states. There are similar other terms contributing to the right hand side of Eq. (8), where the vertex correction terms are of fourth order in the one-particle vertices ($t(\varepsilon_1)$, $t(\varepsilon_2)$, $t(\varepsilon_1 + E)$, $t(\varepsilon_2 - E)$) with different combinations. That result is identical with Eq. (10) in Ref. [9] only the arguments of the vertex corrections are somewhat different. It is important to point out, that the vertex correction term cannot be factorized like $|\tau(\varepsilon_1)\tau(\varepsilon_2)|^2$ as it was suggested in Ref. [10]. See also Ref. [15] where the slave boson technique is applied.

The vertex $t(\tilde{\omega})$ can be easily calculated even for the non-equilibrium case. Considering a short wire with bias V, the Fermi energy for the contact 1(2) is denoted by $E_{F_1}(E_{F_1})$, then $E_{F_2} - E_{F_1} = eV > 0$. Assuming that the distance of the impurity from contact 2 is pL where L is the length of the sample and $0 < p < 1$. Then the non-interacting distribution of the electrons at the impurity is represented by the heavy line in Fig. 4. The scattering amplitude $t(\tilde{\omega})$ can be calculated by poor man's scaling by eliminating electron and hole states above and below the energy $\tilde{\omega}$ in equal distances.

The elimination of states both occupied and unoccupied does not give logarithmic contribution thus they do not contribute to the scaling. The elimination is in two steps I and II. Take e.g. ω such that $E_{F_2} - \omega > \omega - E_{F_1}$, then in the first step I the electron-hole states are eliminated for which $n = 0$ or $n = 1$. In the step II only those electron states are eliminated which have unoccupied counter hole states and $n \neq 0$, $n \neq 1$, thus only portion p of the states. In the step II the initial coupling is the result obtained by step I. Thus

$$t^I(\tilde{\omega}) = \frac{J}{1 - 2J\rho_0 \ln \frac{D}{|E_{F_2}-\tilde{\omega}|}} \tag{9}$$

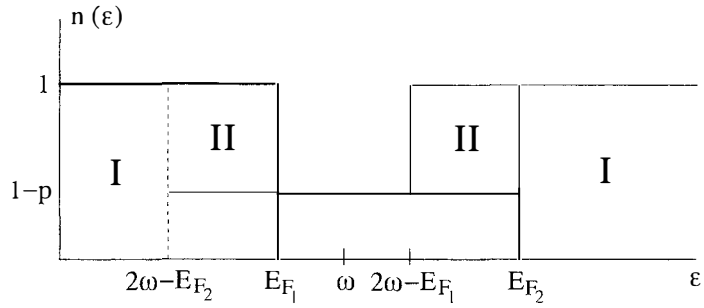


Figure 4: The electron distribution function in a wire at large bias eV is shown without the electron-electron interaction. The regions I and II are eliminated in the two steps, the heavy solid line separates the occupied and unoccupied regions.

and

$$t^{I+II}(\tilde{\omega}) = \frac{t^I(\tilde{\omega})}{1 - 2\rho_0 p t^I(E_{F_2} - \tilde{\omega}) \ln \frac{|E_{F_2} - \tilde{\omega}|}{\tilde{\omega} - E_{F_1}}}. \tag{10}$$

In Eq. (10) p occurs in the denominator. Here it is assumed that $|E_{F_2} - \tilde{\omega}| > \tilde{\omega} - E_{F_1} > T_K^0$, where T_K^0 is the bulk equilibrium Kondo temperature. In this case separate Kondo resonances are formed [8,15] at the two Fermi energies E_{F_1} and E_{F_2}, and e.g. the width of the resonance described by the separate Kondo temperature T_K^1 is defined by $\tilde{\omega}$ where $t^{I+II}(\tilde{\omega}) \to \infty$. Thus

$$T_K^1 = \frac{(T_K^0)^{\frac{1}{p}}}{(eV)^{\frac{1}{p}-1}}. \tag{11}$$

That reproduces the result of Ref. [16]. T_K^2 can be obtained by electron-hole transformation and $p \to 1 - p$.

The inclusion of the Korringa type of spin life-time is beyond the leading logarithmic approximation [17]. In the case of large bias V the temperature is replaced by eV and that can play a dominating role which is not discussed here, but smears the $1/E^2$ singularity [9,10,15].

According to the experiments [2] the scaling in the distribution in the wire with a large bias holds only for the larger biases. Above the Kondo temperature $n(E/eV)$ depends on only one dimensionless variable as far as the Kondo corrections containing T_K^0 (or in an other form D) are negligible. Recently J. Kroha extended his slave boson calculation [8] for $T > T_K$ and the entire problem is treated in Ref. [15].

Acknowledgments

I express my gratitude to J. Kroha as the main part of the work has been carried out in collaboration with him and I borrowed many of his ideas. I am especially grateful among many others to H. Pothier, N.O. Birge, M. Devoret, B. Altshuler, L.I. Glazman, J. von Delft, O. Újsághy and G. Zaránd for useful discussions. This work was supported by Hungarian Grants OTKA T024005, T029813, T034243 and by the A. v. Humboldt foundation.

References

1. See e.g. P. Mohanty, E.M.Q. Jariwala and R.A. Webb, *Phys. Rev. Lett.* **78**, 3366 (1997).
2. H. Pothier, S. Guéron, Norman O. Birge, D. Esteve and M.H. Devoret, *Z. Phys.* B **104**, 178 (1997), *Phys. Rev. Lett.* **79**, 3490 (1997); F. Pierre, H. Pothier, D. Esteve, M.H. Devoret, A.B. Gougam and N.O. Birge, in *Proceedings of the NATO ARW "Size Dependent Magnetic Scattering", 28 May - 1 June 2000, Pécs, Hungary*, (Kluwer Academic, Dordrecht, 2000), cond-mat/0012038, and the present volume.
3. See for a recent review O. Újsághy, G. Zaránd and A. Zawadowski, *Solid State Commun.* **117**, 167 (2001).
4. I.L. Aleiner, B.L. Altshuler, Y.M. Galperin, T.A. Shutenko, *Phys. Rev. Lett.* **86**, 2629 (2001).
5. A. Zawadowski and G. Zaránd, cond-mat/0009283.
6. A. Zawadowski, J. von Delft and D. Ralph, *Phys. Rev. Lett.* **83**, 2632 (1999).
7. For a review, see B.L. Altshuler and A.G. Aronov, in *Electron-Electron interactions in Disordered Systems*, ed. A.L. Efros and M. Pollak, (Elsevier Sience Publishers, B.V. 1985).
8. J. Kroha, *Adv. Solid State Phys.* **40**, 216 (2000).
9. A. Kaminski and L.I. Glazman, *Phys. Rev. Lett.* **86**, 2400 (2001).
10. See also Georg Göppert and Hermann Grabert, cond-mat/0102150.
11. J. Sólyom, A. Zawadowski, *Phys. Letters* A **25**, 91 (1967) and *Z. Physik* **226**, 116 (1969).
12. A.A. Abrikosov and L.P. Gorkov, *Zh. Eksperim. i. Theor. Fiz.* **39**, 1781 (1960), *Sov. Phys. JETP* **12**, 1243 (1961).
13. A.A. Abrikosov, *Physics* **2**, 5 (1965).
14. See e.g. G. Grüner, A. Zawadowski, *Reports on Progress in Physics* **37**, 1497 (1074).
15. J. Kroha and A. Zawadowski, cond-mat/0104151 and cond-mat/0105032.
16. P. Coleman, C. Hooley, O. Parcollet, *Phys. Rev. Lett.* **86**, 4088 (2001).
17. A. Zawadowski, P. Fazekas, *Z. Physik* **226**, 235 (1970).

COULOMB BLOCKADE AND ELECTRON SPIN IN QUANTUM DOTS

C. M. MARCUS[1], J. A. FOLK[1,2], R. M. POTOK[1], A. C. JOHNSON[1], L. P. KOUWENHOVEN[1,3], R. BERKOVITS[4,5,6], I. L .KURLAND[4], I. L. ALEINER[7], B. L. ALTSHULER[4,5]

[1] *Department of Physics, Harvard University, Cambridge, MA 02138*

[2] *Department of Physics, Stanford University, Stanford, CA 94305*

[3] *Department of Applied Physics and ERATO, Delft University of Technology, Box 5046, GA 2600 Delft, The Netherlands*

[4] *Physics Department, Princeton University, Princeton, NJ 08544*

[5] *NEC Research Institute, 4 Independence Way, Princeton, NJ 08540*

[6] *Minerva Center and Department of Physics, Bar-Ilan University, Ramat-Gan 52900, Israel*

[7] *Department of Physics, SUNY at Stony Brook, Stony Brook, NY 11794*

We investigate theoretically and experimentally the behavior of Coulomb blockade peaks in a magnetic field that couples principally to the ground-state spin (rather than the orbital moment) of a quantum dot. In the first part, we discuss numerically observed features in the magnetic field dependence of CB peak spacings that identify changes in spin of each ground state for successive numbers of electrons on the dot. We next evaluate the probability that the ground state of the dot has a particular spin as a function of the exchange strength and (Zeeman-only) magnetic field. We then describe experiments on gate-defined GaAs quantum dots in which Coulomb blockade peak positions and spacings are measured as a function of in-plane magnetic field, allowing changes in spin to be measured. Finally, we present recent experimental results on phase coherent transport through quantum dots embedded in the two arms of an Aharonov-Bohm ring, in the presence of large in-plane magnetic fields.

1 Introduction

In the absence of interactions, electrons populate states of a quantum dot in an alternating spin-up – spin-down sequence, such that the total spin of the dot, S, is zero when the number of electrons N on the dot is even, and $S = \frac{1}{2}$ when N is odd; higher spin states do not appear in the absence of large magnetic fields. Interaction can lead to deviations from even-odd filling, as described by the familiar Hund's rules in atomic physics. Hund's rules also apply in symmetric (e.g., circular) quantum dots [14] where interaction can lead to a build-up of ground state spin associated with states that are related by a symmetry of the system. When the quantum dot lacks symmetry or is disordered, degeneracies are not present and the connection between interaction and ground state spin is best described statistically, in terms of mesoscopic fluctuations of the relevant quantities.

By measuring electron transport through a weakly coupled quantum dot at low temperature and bias voltage (compared to the quantum level spacing) one can effectively study differences in ground state (GS) properties of the dot at successive electron number, providing a means of investigating the filling scheme. A standard experimental approach [1] is to measure conduction through the dot as a function of voltage, V_g, on a nearby capacitively coupled gate. Because the dot GS energy, E_N, at fixed electron number is influenced by V_g, the gate can be used to set the number of electrons on the dot. The fact that a large Coulomb energy is needed to add a single electron to the dot generally suppresses conduction through the dot in the tunneling regime, where whole charges must tunnel for conduction to occur. This effect is known as the Coulomb blockade (CB). At specific values of gate voltage, $V_g^{(N)}$, where $E_{N-1}(V_g) = E_N(V_g)$, conductance increases dramatically, marking this degeneracy condition in an experimental trace.

The position, $V_g^{(N)}$, of the N^{th} CB peak is proportional to the electrochemical potential, $\mu_N = E_N(0) - E_{N-1}(0)$. The distance between successive peaks then measures the difference between chemical potentials, $\Delta_2^N = \mu_N - \mu_{N-1}$, and so is a second derivative of GS energy. (We take the constant of proportionality converting gate voltage to dot energy to be unity for the theoretical discussion; experimentally, this constant can be readily measured, for instance, by comparing the influence of bias and gate voltages.)

In the last few years the GS spin of a variety of nanostructures, including metallic dots[2], semiconducting quantum dots[3,4,6], and carbon nanotubes[7,8], have been investigated using CB peak motion in a magnetic field. If the magnetic field coupling to the orbital degrees of freedom can be ignored, the field will manifest itself only through the Zeeman splitting, resulting in a shift of the GS energy by $g\mu_B SB$, where μ_B is the Bohr magneton. For 2D quantum dots, orbital coupling can be strongly suppressed—though not eliminated entirely[9,10]—by orienting the field strictly in the 2D plane. This is the experimental approach that will be described in Section III of this paper. On the other hand, for ultrasmall metallic dots and nanotubes, fields in any direction can be considered to act only through the Zeeman effect, since at experimentally reasonable fields the total flux through the structure is small on the scale of the quantum of flux.

For semiconducting quantum dots[3,4,5,6] the Zeeman splitting for $S = \frac{1}{2}$ becomes comparable to the mean single electron level spacing

$$\delta_1 = \langle s_i \rangle; \quad s_i = \varepsilon_i - \varepsilon_{i+1}, \tag{1}$$

(here ε_i denotes the orbital energy of the one-electron orbital state i, and $\langle \ldots \rangle$ stands for an average over different levels) at $B \sim 1T$ for the GaAs dots is Refs. [4,6] and $B \sim 10T$ for the Si dot in Ref. [3]. At lower fields, the splitting seldom exceeds s_i, and one might expect simple even/odd filling. In this case, CB peak positions would move with Zeeman field, B, (i.e., the magnetic field, ignoring orbital effects) as consecutive pairs, creating a pattern of alternating downward and upward sloped lines with slopes $g\mu_B/2$ and $-g\mu_B/2$ at low field, as seen in Fig. 1a. The peak spacings, Δ_2^N, would have a similar pattern of alternating lines, with slopes of $g\mu_B$ and $-g\mu_B$ as seen in Fig. 1b. Spin-orbit interaction can lead to fluctuations in the g factor, resulting in fluctuations in the slopes of the lines[11,12] but cannot change the pattern of alternating downward and upward lines. Once $g\mu_B B$ exceeds a particular spacing s_i, the peaks would cross as seen in Fig. 1a at higher fields.

Experimentally, simple even/odd filling is observed for the ultrasmall metallic dots[2], while for carbon nanotubes the situation is less clear. One published experiment finds simple even/odd filling[7], and one finds a more complicated scheme[8]. For multielectron semiconducting dots the data are also somewhat confusing, but appear to disagree with the simple even/odd filling scheme at low fields[3,4,5,13,25]. In symmetric, few-electron vertical dots[14] one may again recover relatively simple behavior for the first few electrons, with a well-understood appearance of Hund's rules. These conclusions are based on experiments where orbital magnetism dominates spin. However, for few electrons (i.e., $N <\sim 10$) the filling scheme can be readily interpreted, allowing the full spin structure to be mapped out as a function of N and B[14].

Figure 1 shows the theoretical CB peak motion and spacing as a function of Zeeman field for both noninteracting and interacting electrons (as discussed in Section II). The behavior of the interacting case (Fig. 1b) appears more similar to the experimentally observed behavior in semiconducting quantum dots (compare to Fig. 4). In some cases, adjacent peak positions (μ_N) move in the same direction and with the same slope, so that the corresponding spacings (Δ_2^N) are flat as a function of magnetic field. Moreover, not every change in the direction of the motion of a peak can be explained as a crossing of two orbital levels.

The build-up of GS spin in quantum dots has been considered theoretically in a number of different contexts previously[16,17,18,19,20,21,22,23], from providing an explanation[18] for the absence

of a bimodal distribution in CB peak spacings [24], to a prediction of kinks in the parametric motion of the peaks due to orbital effects of a perpendicular magnetic field [21], evidence for which is seen in recent experiments [25].

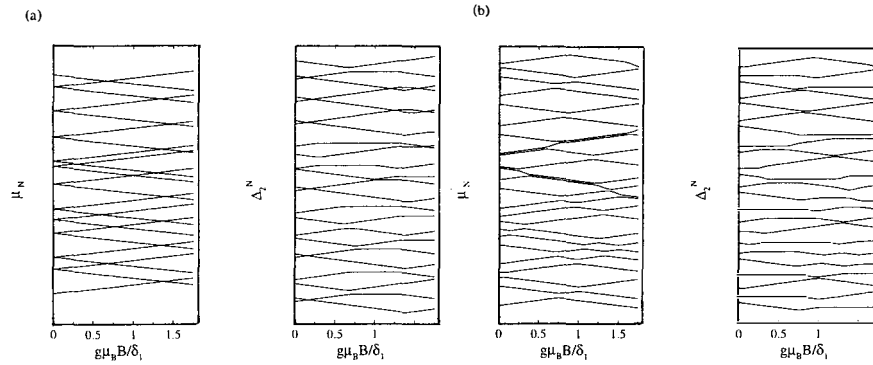


Figure 1: Typical conductance dependence on the gate voltage and magnetic field, B, with and without exchange interaction: (a) $J = 0$, (b) $J = 0.1\delta_1$. μ'_N is determined as $\mu'_N = \mu_N - e^2/C$ and taken in arbitrary units. Δ_2^N for each N is shifted arbitrarily by $N\times$constant to avoid overlapping.

2 Theory

The single electron spectrum ε_i in disordered or irregularly shaped quantum dots is characterized by the mean level spacing δ_1 and the Thouless energy $E_T \approx \hbar/t_{erg}$, where t_{erg} is the time it takes for a classical electron to cover the energy shell in the single-particle phase space. For either diffusive or ballistic-chaotic systems, t_{erg} is roughly given by the crossing time, L^2/D and L/v_F respectively, where v_F is the Fermi velocity, L is the system size, and D is the diffusion coefficient. The dimensionless conductance, $g_T = E_T/\delta_1$, in the metallic regime is large, $g_T \gg 1$. In this regime the statistics of the single electron spectrum on scales smaller than E_T are well described by random matrix theory (RMT) [26], which gives a quantitative description of the phenomenon of level repulsion. For an ensemble of $M \times M$ matrices ($M \to \infty$) with random and independent elements, the probability density of a realization of the spectrum ε_i is given by[26]:

$$P(\varepsilon_i) \propto \exp\left[\frac{\beta}{2}\sum_{i\neq j}\ln\left(\frac{|\varepsilon_i - \varepsilon_j|}{\delta_1}\right)\right], \tag{2}$$

where β is equal to 1, 2 or 4 for the orthogonal, unitary and symplectic ensembles respectively. The orthogonal (unitary) RM ensemble corresponds to preserved (violated) time reversal symmetry and negligible spin-orbit. The role of spin-orbit interaction in quantum dots has recently been considered experimentally and theoretically [5,15,27,10], and it has been shown [27] that the combination of spin-orbit interaction and Zeeman field produces new universality classes, generalizing the Dyson ensembles ($\beta = 1, 2, 4$).

Electron-electron interaction can be accounted for, in the simplest case of short-range interactions, by an interaction term in the Hamiltonian,

$$H_{int}(\vec{r}) = \lambda\delta_1 V\delta(\vec{r}), \tag{3}$$

where $V \propto L^d$ is the volume of the dot (in d dimensions) and λ is a dimensionless coupling constant characterizing the strength of the interaction. Matrix elements of this interaction, in

the basis of eigenstates $\varphi_i(\vec{r})$ of the noninteracting Hamiltonian, are given by

$$M_{kl}^{ij} = \lambda\delta_1 V \int d\vec{r}\varphi_i^*(\vec{r})\varphi_j^*(\vec{r})\varphi_k(\vec{r})\varphi_l(\vec{r}). \tag{4}$$

It is important to note that the statistical properties of the interaction matrix elements M_{kl}^{ij} are completely determined by the statistical properties of the single electron eigenstates $\varphi_i(\vec{r})$ and cannot be chosen in an arbitrary fashion as in the random interaction model[12]. In fact, in the limit $g_T \to \infty$ the diagonal matrix elements (i, j, k, l pairwise equal) are self-averaged by the space integration, Eq. (4), and thus show no level-to-level or sample-to-sample fluctuations[16]. In the same limit the off-diagonal matrix elements Eq. (3) turn out to be negligible.

Using the statistical properties of the interaction matrix elements it turns out that a large class of disordered metallic dots can, under very general conditions, be described by a remarkably simple Hamiltonian with only three system-dependent coupling constants, which do not fluctuate. In the limit of large g_T, the interaction part of the Hamiltonian corresponds to

$$H_{int} = E_c\hat{N}^2 - J(\vec{S})^2 + \lambda_{BCS}\hat{T}^\dagger\hat{T}, \tag{5}$$

(terms linear in $\hat{N}$ are allowed, but they can be included into the one-particle part of the Hamiltonian) where $\hat{N}$ is the number operator, $\vec{S}$ is the spin operator and $\hat{T} = \sum_i c_{i\uparrow}c_{i\downarrow}$ ($c_{i\uparrow}$ annihilates an electron in the i^{th} single electron orbital with spin $\uparrow$). In the simple model with short-range interaction and preserved time reversal ($\beta = 1$) the coupling constants have the following form:

$$E_c = \frac{1}{2}\lambda\delta_1; \quad J = 2\lambda\delta_1; \quad \lambda_{BCS} = \lambda\delta_1. \tag{6}$$

If time invariance is broken ($\beta = 2$), $\lambda_{BCS} = 0$ since the operator $\hat{T}$ is incompatible with the symmetry. Note that the interaction Hamiltonian Eq. (3) represents a particular model, and the expressions for the coupling constants Eq. (6) are valid only for this model. At the same time, the effective interaction Hamiltonian, Eq. (5), is more robust and depends only on the symmetries of the problem (for instance, on the absence of the spin-orbit scattering) and on the condition $g_T \gg 1$.

The first two terms in Eq. (5) represent the dependence of the energy of the dot on the total number of the electrons and on the total spin respectively. They commute with each other and with the single-particle part of the Hamiltonian. Therefore, all states of the dot can be classified by N and S. The term proportional to λ_{BCS} appears only in the orthogonal case ($\beta = 1$) and provided that $\lambda_{BCS} < 0$ this term leads to a superconducting instability. Superconducting correlations are suppressed by the magnetic field, and thus do not exist for $\beta = 2$.

Thus, the general form of the Hamiltonian describing electrons in a disordered or chaotic (non-superconducting) dot with $g_T \gg 1$ is given by

$$H = \sum_i \varepsilon_i n_i + E_c N^2 - JS(S+1) + g\mu_b SB. \tag{7}$$

Note that the only random component of the problem is the single-particle spectrum ε_i, while the exchange J and charging energy E_c do not fluctuate.

The conductance is calculated using the many-particle energies E_N and wave functions obtained numerically for random matrix realizations. An example of the peak positions and peak spacing evolution as functions of the magnetic field for a particular GOE realization is shown in Fig. 1 for (a) $J = 0$ and (b) $J = 0.1\delta_1$. For both cases we present $\mu'_N = \mu_N - E_c$. The noninteracting case, Fig. 1a, shows all the previously described features of the simple even/odd filling behavior. When a weak exchange interaction is included the behavior changes qualitatively. In particular, peak positions are not always paired. This occurs when two consecutive orbitals are

first filled with down spin electrons and only later they acquire up electrons. Note that the enhancement of the spin of the dot by S is indicated by a sequence of $2S$ peaks moving with the same slope. If the peak spacing Δ_2^N is plotted, two sets of $2S-1$ flat curves sandwiching a sloped one will appear.

Equation (7) can be used to estimate the probability distribution of GS spins. For weak exchange, $J \ll \delta_1$, the probability that the GS has spin S is simply the probability of finding $2S$ orbital levels sufficiently close that the reduction in energy due to exchange exceeds the excess kinetic energy needed fill the higher orbital levels,

$$\varepsilon_{i+2S} - \varepsilon_i < JS(S+1) + g\mu_B BS. \tag{8}$$

Using the random matrix distributions of level spacings, Eq. (2), one finds the probability of obtaining a ground state spin S can be written a function of the linear combination

$$X = \frac{J}{\delta_1} + \frac{g\mu_B B}{\lfloor S + \frac{3}{2} \rfloor \delta_1}, \tag{9}$$

giving a probability distribution for spin S,

$$P_{J,B}(S) = C_S^\beta X^{(\beta S+1)(2S-1)}(1 - K_S^\beta X^2), \tag{10}$$

where coefficients C_S^β and K_S^β depend on both β and S. Their values for $S = 1, 3/2$ are presented in table I.

	$\beta = 1$		$\beta = 2$	
	$S = 1$	$S = 3/2$	$S = 1$	$S = 3/2$
C	$\pi^2/3$	$9\pi^4/50$	$8\pi^2/9$	$81\pi^6/400$
K	$\pi^2/5$	$18\pi^2/49$	$8\pi^2/25$	$792\pi^2/1225$

Table 1: The factors C_S^β and K_S^β appearing in Eq. (10).

The important conclusion from RMT is that the combined influence of exchange and Zeeman field on the GS spin of a quantum dot can be expressed as a single scaling parameter that is a linear combination of J and B. Numerical simulations confirm this scaling and show, in fact, that it continues to holds for larger values of X than expected from the perturbative analysis leading to Eq. (10).

Whether these results continue to apply when $g_T \sim O(1)$ can be addressed numerically within a Hubbard model approach, described by the Hubbard Hamiltonian

$$H = \sum_{i,\sigma} \epsilon_i a_{i,\sigma}^\dagger a_{i,\sigma} - t \sum_{<i,j>,\sigma} (a_{i,\sigma}^\dagger a_{j,\sigma} + h.c) + U \sum_i a_{i,\uparrow}^\dagger a_{i,\uparrow} a_{i,\downarrow}^\dagger a_{i,\downarrow} + g\mu_B SB, \tag{11}$$

where $< i, j >$ denotes nearest neighbor lattice site, $a_{i,\sigma}^\dagger$ is an creation operator of an electron at site i with spin σ, ϵ_i is the site energy, chosen randomly between $-W/2$ and $W/2$ with uniform probability, and U is the interaction constant. Note that this problem becomes quite difficult numerically even for relatively small systems. For instance, a 4×4 lattice with 6 electrons for the $S = 0$ sector has a Hilbert space of 313,600 states. Using the Lanczos method we obtain the many-particle eigenvalues $E_N(S)$ for different values of interaction U, as shown in Fig. 2. For these data, disorder was fixed at $W = 8t$, which corresponds to the metallic regime although the value of the dimensionless conductance is quite low, $g_T \sim O(1)$.

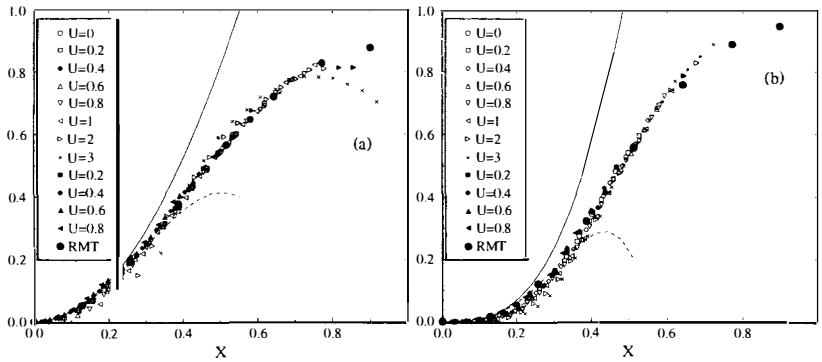


Figure 2: Probabilities of $S = 1$ for $J = 0.1\delta_1$ as functions of the magnetic field B for (a) the GOE and (b) GUE cases. The small symbols represent numerical results for the Hubbard model, the large filled symbols represent numerical results for the RMT model, while the curves (solid - first order, dashed - second order) represent Eq. (10).

We calculated the probability for the appearance of a specific value of GS spin S for different values of U and magnetic field B. In order to use the scaling parameter X we need to deduce the appropriate value of J for each value of U. This has been done by fitting the dependence of the average lowest energy in a given spin sector $\langle E(S)\rangle$ to

$$\langle E(S)\rangle = \delta_1 S^2 - JS(S+1). \tag{12}$$

The distribution $P_{J(U),B}(S)$ based on numerical results for 1000 different realizations of the Hubbard model, for different values of U and B for $\beta = 1$ and $\beta = 2$ is presented in Fig. 2 [28]. Although some deviations from Eq. 10 are seen, especially for the higher values of U, the overall form of the scaling function holds remarkably well.

3 Experiment: Ground State Measurement

In this section we describe experimental measurements of GS spin for a single gate-defined GaAs quantum dot containing roughly 400 electrons. The dot is coupled to electron reservoirs via tunnelling leads (i.e., $g < 2e^2/h$ for both leads) so transport is dominated by CB effects. Measurements were carried out at sufficiently low temperature and bias that the differences in GS energies between dots with $N-1$ and N electrons should be extractable from CB peak positions, $V_g^{(N)}$.

The dot is formed at the interface of a GaAs/AlGaAs heterostructure ($90\,nm$ below the wafer surface) by electrostatic depletion using surface gates. The two-dimensional electron gas (2DEG) has density $\sim 2.0 \times 10^{11}\,cm^{-2}$ and bulk mobility $\sim 1.4 \times 10^5\,cm^2/Vs$, yielding a transport mean free path $\sim 1.5\,\mu m$. The small dot area, $A \sim 0.25\,\mu m^2$, makes transport predominantly ballistic within the device. Characteristic energy scales for the measured device include the mean level spacing, $\Delta = 2\pi\hbar^2/m^* A \sim 30\,\mu eV$, the charging energy, $E_C \sim 400\mu eV$, and the Thouless energy $E_{th} = \hbar v_F A^{-\frac{1}{2}} \sim 340\mu eV$. Measurements were carried out in a dilution refrigerator using standard ac lock-in techniques with a source-drain bias voltage of $2\,\mu eV$. A base electron temperature of $T_e \sim 50\,mK$ was determined from CB peak widths.

To allow the magnetic field to couple predominantly to spin, the sample was oriented with the plane of the electron gas along the axis of the primary solenoid, aligned manually to within 0.5 degrees. In addition, a pair of coils attached to the vacuum can of the fridge, oriented

perpendicular to the plane of the sample, was used to null out any perpendicular field from misalignment as well as to explicitly break time-reversal symmetry [5]. The estimated uncertainty in $B_\perp$ is less than $\phi_o/4$ through the dot at $B_{||} = 5T$. Despite this precise field trimming capability, similar measurements [5] in larger dots indicate orbital coupling even from a perfectly aligned field (evident, for instance, in the complete disappearance of weak localization $B_\perp = 0$ at higher $B_{||}$). The estimated flux coupling due to an in-plane field appears consistent with recent theoretical estimates [9]; experiments to separate the influences of the spin-orbit coupling and in-plane flux coupling are now underway [10].

Conductance measurements across ten consecutive Coulomb blockade peaks, measured as a function of V_g and $B_{||}$ (i.e., *strictly* $B_{||}$, properly trimmed), are shown in grayscale in Fig. 3a. More positive gate voltage corresponds to higher energy, and can be calibrated from the CB "diamonds" using high source-drain bias measurements [1]. All data are taken with $B_\perp = 20mT$ in order to ensure that time-reversal symmetry is broken.

In addition to the linear motion of individual peaks, there is an overall parabolic shift of all peaks (see Fig. 3b), presumably due to the diamagnetic effect of the in-plane field on the effective well confinement potential. A paramagnetic shift is also visible at very low field, ($B_{||} < 0.2T$), and is not understood at present. In the analysis presented, the common curve (in Fig. 3b) has been subtracted from each peak position.

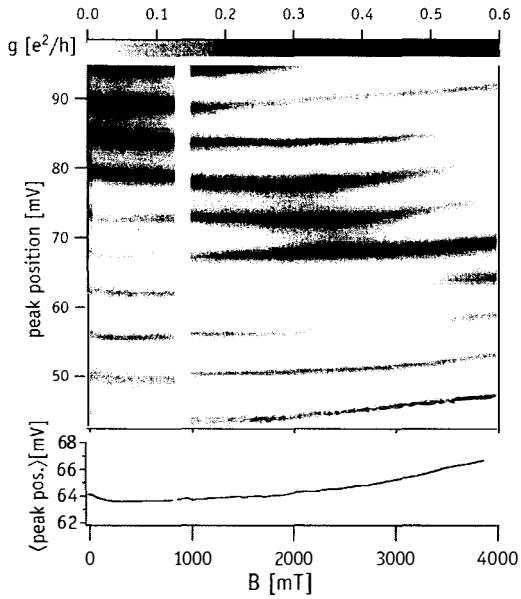


Figure 3: a) Nine consecutive Coulomb blockade peaks measured as a function of gate voltage V_g and parallel field B. Conductance is shown in grayscale, with black indicating high conductance and white low conductance. The field shown on the bottom axis is the field strictly parallel to the heterointerface; perpendicular field is held constant at $20mT$ as discussed in the text. Note that conductance in the valleys is low but not zero, due to strong tunnelling in the leads. b) Average peak position of the peaks in a), showing a diamagnetic shift to higher energies common to all peaks. This average is subtracted from all peak positions before further analysis.

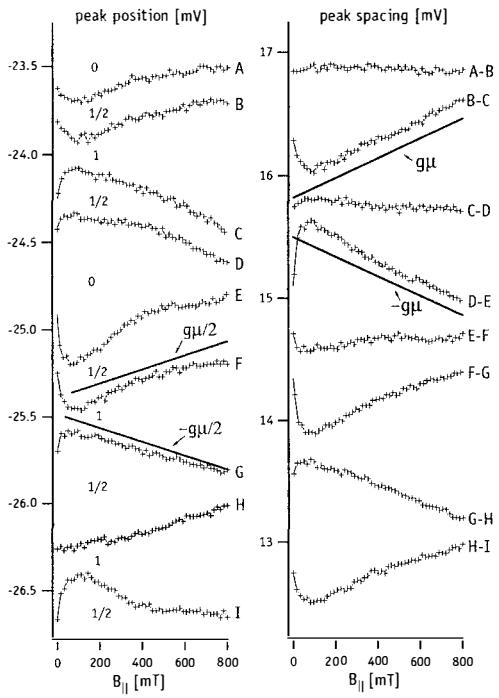


Figure 4: a) Peak positions (with average motion subtracted) as a function of parallel field for the nine peaks shown in Fig. 3a. Straight lines indicate expected peak motion for $\Delta S = \frac{1}{2}$ transitions using the g factor for bulk $GaAs$, $|g| = 0.44$. Positive slopes indicate transitions to lower spin states; negative slopes indicate transitions to higher spin states. Numbers indicate a possible ground-state spin structure for ten consecutive ground states. Peak position data are offset for clarity. b) Peak spacings for the position data shown in a), offset for clarity. Solid lines indicate expected motion of peak spacing for spin-$\frac{1}{2}$ transitions, using $|g| = 0.44$.

Positions and spacings from the peaks in Fig. 3 are shown in Fig. 4. The slopes of peak position as a function of $B_{||}$ are consistent with a Zeeman energy term $E_S = \pm\frac{1}{2}g\mu_B B_{||}$, using the g-factor for bulk $GaAs$, $|g| = 0.44$. As discussed in the Introduction, alternating slopes (as a function of $B_{||}$) of peak position would indicate GS spins alternating between $S = 0$ and $S = \frac{1}{2}$. The experimental data, on the other hand, shows several pairs of consequtive peaks moving with the same slope, implying the presence of higher-spin ground states. Proposed values for the eight consecutive GS spin states shown here are included in Fig. 4a. We emphasize, however, that these are only suggested values for the spin; it is not possible to unambiguously determine the GS spin from measurements of peak position, which reflect *changes* in spin from the N-1 to N ground states.

In the proposed spin labelling scheme, three out of the five even-N states have $S = 1$, i.e., $P(S = 1) \sim 0.6$. This fraction of $S = 1$ relative to the number of $S = 0$ states is greater than expected given reasonable estimates of J for $GaAs$ dots. Of course, with only five spin states considered, statistics are rather poor. Experiments currently in progress aim to greatly augment these statistics.

Figure 5 shows that the peak spacings (the same data as in Fig. 4) clearly separate into three branches, a top branch with slope $\sim g\mu_B$ (corresponding to a GS spin decrement followed by an increment) a bottom branch with slope $\sim -g\mu_B$ (corresponding to a GS spin increment followed

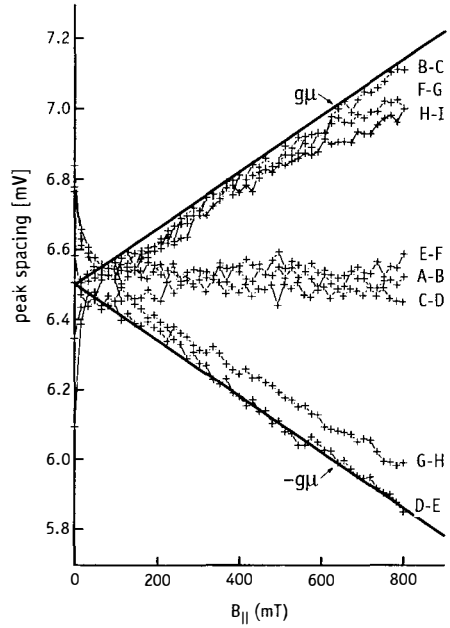


Figure 5: Peak spacings from Fig. 4b, offset to align spacings at $B_{||} = 0$. Slopes cluster in three branches, interpreted as a change from decreasing to increasing spin transitions (positive slope), two consecutive spin transitions in the same direction (zero slope), and a change from increasing to decreasing spin transitions (negative slope). Solid lines indicate expected motion of peak spacing for spin-$\frac{1}{2}$ transitions, using $|g| = 0.44$, with no adjustable parameters.

by a decrement) and a middle branch with slope near zero (corresponding to two consecutive increments or decrements). *The existence of this middle branch is the signature of higher GS spin states.* The good agreement between the slopes of the upper and lower branches and the expected slopes of $g\mu_B$, as well as the absence of a range of intermediate slopes suggest that the peak spacing reflects spin rather than orbital motion of levels. At higher fields, the directions of peak motion change, often abruptly and from one straight segment to another, as seen in Fig. 6. This behavior is qualitatively similar to the numerical data in Fig. 1b. The rounding of straight segments where the slope changes presumably results from spin-orbit interaction which mixes spins, and may provide a direct measure of spin-orbit interactions in dots. It is interesting to note that the peaks analyzed in Figs. 4 through 6 were measured in a regime of high tunneling conduction in the leads. This can be seen by noting the grayscale of Fig. 3. When the dot is more pinched off from the reservoirs, so that the CB peaks have a height of 0.1 e^2/h or less, peak motion is more difficult to interpret, and does not seem to follow the clear patterns illustrated. This is not understood at present, and will be investigated further.

4 Experiment: Coherent Transport of Spin and Charge

In a large in-plane magnetic field ($g\mu_B B_{||} \gg kT$) and low temperatures ($\Delta \gg kT$) transport on a CB peak marks a transition between ground states with well defined spin projections, m_S, along the direction of the applied field. Consider, for instance, the CB peak between $N-1$ and N electrons on the dot with $N-1$ even and GS spins $S^{(N-1)} = 0$ and $S^{(N)} = \frac{1}{2}$: Transport on the peak involves a spin *up* electron passing through the dot (for the sake of the argument, we

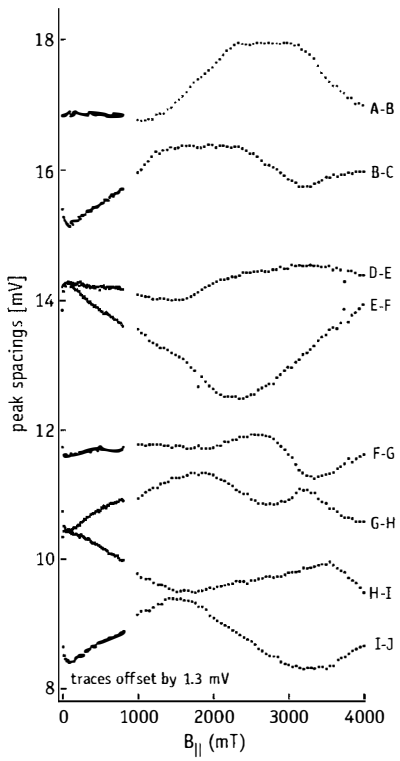


Figure 6: Peak spacings from Fig. 6b, shown over an extended range of parallel field, up to $B_{||} = 4T$. Slopes tend to change abruptly between linear segments, with rounding between the segments possibly providing a measure of spin-orbit or other spin-mixing interaction.

do not account for the negative g factor), involving the transition from $m_S = 0$ to $m_S = \frac{1}{2}$ when the electron enters, and from $m_S = \frac{1}{2}$ to $m_S = 0$ when the electron leaves. One may examine the coherence of this spin-selective transport process by embedding the quantum dot in the arm of an Aharonov-Bohm (AB) ring [29], as shown in Fig. 7.

In the experiment reported here, two gate-defined quantum dots are used, one in each arm of an AB ring (Fig. 7). This configuration allows a comparison of two situations of interest: (i) both dots have N even or N odd, which should allow an electron with a given m_S to pass through either arm and (ii) one dot has N even and one dot has N odd, which should allow a particular electron of a given m_S to only pass through one of the two arms. The latter situation is analogous to a two-slit interference experiment in classical optics, in which two polarizers oriented at 90 degrees are each placed in front of one of the slits. The expectation is that the situation (ii) will show a suppressed inference signal relative to situation (i). A detailed theoretical analysis of related configurations involving one or two dots embedded in AB rings, and the interplay between spin and coherence in such systems, is discussed in Ref. [30]. This paper also provides a useful guide to the rapidly growing literature surrounding dot-in-ring configurations. The present 'spin-filters-in-rings' set-up, i.e., dots in a ring in a large in-plane field, has not been considered experimentally or theoretically to our knowledge.

A micrograph of an AB ring device identical to the one measured is shown in Fig. 7b. The ring encloses an area of $\sim 3.5\mu m^2$, setting a perpendicular field of $\sim 1.2mT$ to thread one flux

quantum through the ring. The dots have an area of $\sim 0.04\mu m^2$, giving a quantum level spacing of $\sim 1K$. Measurements were carried out in a dilution refrigerator at an electron temperature of $\sim 80mK$.

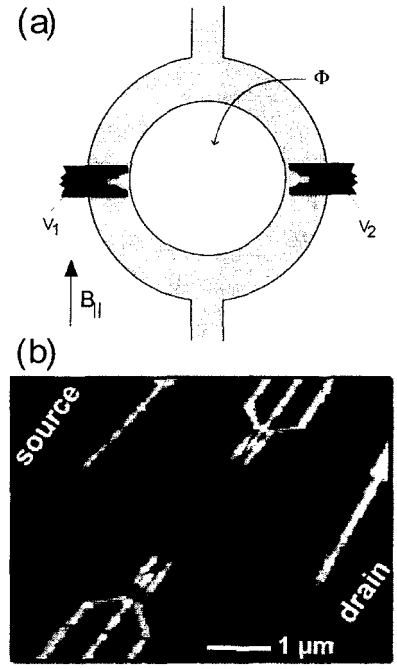


Figure 7: (a) Schematic set-up of quantum dot interferometer, comprising two quantum dots in the arms of a two-lead Aharonov-Bohm ring. An in-plane magnetic field $B_{\|}$ is used to polarize electrons while a small, independent perpendicular field is used to modulate the relative phase of electrons passing through the two arms of the interferometer. (b) An electron micrograph of a Delft interferometer, identical in size and design to the one in that was used in the measurement described in Section IV.

Differential conductance measured at finite source-drain bias is used to characterize spin transition between ground states of the $N-1$ and N electron dots ground states by looking at the evolution of excited-state features of the N^{th} CB peak as a function of in-plane field. Following the method used to deduce ground state spin transitions in nanotubes[7] (see also a related approach used in ultrasmall metal dots[2]), we find a Zeeman splitting either on the left side of the CB region (Fig. 8a), indicating a transition from S to $S+\frac{1}{2}$, or a Zeeman spit peak on the right side (Fig. 8b), indicating a transition from $S+\frac{1}{2}$ to S. A clear discussion of how spin transitions lead to these associated patterns of Zeeman splitting in nonlinear transport can be found in Ref.[7]. The fact that these patterns are observed in the present measurement means, for instance, that the temperature is sufficiently low that the Zeeman split levels can be resolved.

The initial experiments presented here have focussed on two questions in particular: first, is transport in this system with a large in-plane field—when the dots are expected to act as spin filters—phase coherent? And second, is quantum interference affected by changing N in one of the dots, which we expect to reverse the orientation of the filters in one of the arms, while N and hence the filter orientation in the other arm is held fixed.

Experimental results are shown in Fig. 9. On the left is a grayscale plot of conductance of

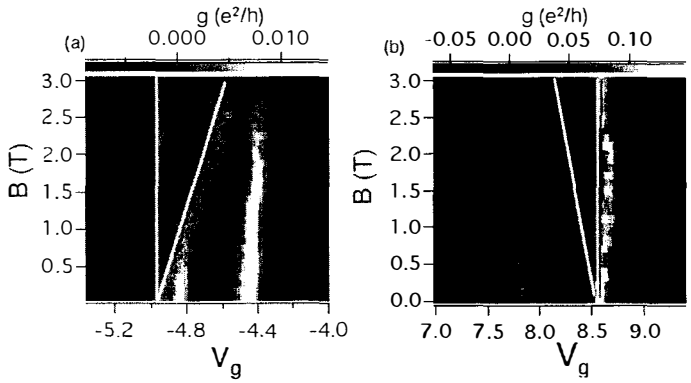


Figure 8: Grayscale plot of differential conductance across a broadened CB peak at finite source-drain voltage,(V_{sd} = 0.12 mV in (a) and 0.15 mV in (b)), as a function of in-plane magnetic field. Internal structure shows Zeeman splitting either on the left (a) or the right (b) edge of the peak, indicates a spin-increasing or spin-decreasing transition between $N-1$ and N [7]. The white lines are guides to the eye. (a) and (b) are for consecutive peaks in dot 2, with dot one fully pinched off, blocking arm 1 of the interferometer.

the full device as a function of gate voltages, V_1 and V_2, of the dots in the two arms, with an in-plane field $B_{||}$ = 6T. Clearly visible in this plot is one vertical stripe, marking a CB peak in dot 2, and several horizontal stripes, marking CB peaks in dot 1. The intersections of the stripes mark where both dots are on CB peaks. The intersection points of the two stripes are the points where we would expect independent spin filtering in each of the arms to occur. On the right of Fig. 9 are sweeps of perpendicular field (with $B_{||}$ = 6 T held constant) taken at each of the points of intersection of the CB stripes. AB oscillations are clearly visible in each of the traces, on a field scale consistent with one quantum of flux through the area enclosed by the ring. This answers the first question, posed above: Transport though the ring and the two quantum dots in a large in-plane field is at least partially coherent. The amplitude of the AB oscillations was $\sim$ 10% of the total conductance, and did not appear to depend on the value of in-plane field.

We did not observe a systematic dependence of AB amplitude upon changing N in dot 1, however. We do not think that this absence is explained by a lack of even/odd filling; over the several peaks examined, we would expect at least one upward and one downward spin transition in the set of five intersections. We do not know at this point why a clear signature of spin filtering in the arms was not observed. It is worth noting however, that few CB peaks could be resolved in these devices. Estimates of spin-orbit scattering rates in the arms of the ring do not make this a likely reason for the absence of a filtering effect, either. Fabrication is currently underway to build devices that would allow greater control of dot coupling parameters to continue to explore this interesting system.

5 Conclusions

In conclusion, we have investigated the interplay of interactions, spin, and (preliminarily) phase coherence in quantum dots the Coulomb blockade regime. In section II, we presented calculations of the probability that different values of ground state spin appear as a function of exchange interaction and magnetic field coupling to the spin. We find that the probability density is described by a one-parameter scaling law over a surprisingly wide range of magnetic fields and

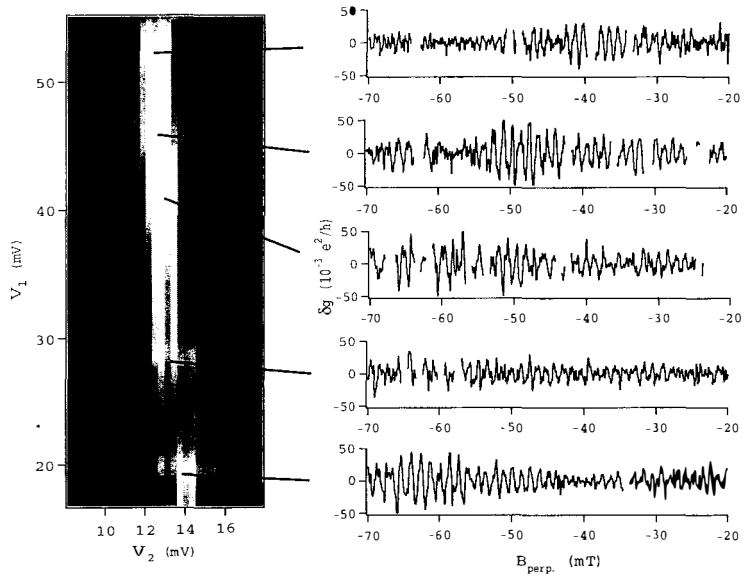


Figure 9: Left: Grayscale plot of two-lead conductance of AB ring as a function of center gate voltages on the dots in the two arms, in the CB regime. Vertical and horizontal stripes mark CB peaks in each of the arms. Right: AB conductance oscillations measured for a fixed CB peak for dot 2 and consecutive peaks in dot 1. No systematic dependence on electron number is observed in this small data set.

exchange interaction strengths.

We also described experiments investigating ground state spins of quantum dots using CB peak motion in a single gate-confined GaAs quantum dot. The experimental signature of non-minimal ground state spin is CB peak spacings with zero slope as a function of in-plane magnetic field. Such signatures are seen in several cases in the data. Further experiments are needed to obtain sufficient statistics to quantitatively test the predictions of theory.

Finally, we described preliminary experiments on phase coherent transport through quantum dots embedded in the two arms of an Aharonov-Bohm ring, in the presence of large in-plane fields. In this situation, the dots are expected to function as spin filters. Quantum interference is observed, in the form of periodic AB conductance oscillations as a function of perpendicular magnetic field. No systematic dependence on the number of electrons in dots is found, for reasons not presently understood. Further fabrication and experiments in this direction are underway.

6 Acknowledgements

Support from ARO-MURI DAAG55-98-1-0270 and the DARPA QuIST Program is gratefully acknowledged. JAF acknowledges support as a DoD Fellow; RMP acknowledges support as an ARO graduate fellow; ACJ acknowledges support as an NSF fellow. We thank P. W. Brouwer, B. I. Halperin and L. P. Rokhinson for many useful discussions, and S. M. Cronenwett for assistance with experiments and analysis. The device discussed in Section II was fabricated by S. R. Patel (Stanford) on material grown by C. I. Duruöz in the lab of J. S. Harris, Jr. (Stanford). The device discussed in Section III was fabricated by W.G. van der Wiel (T.U.Delft) and T. Fujisawa (N.T.T.).

1. M. A. Kastner, Rev. Mod. Phys. **64**, 849 (1992); R. C. Ashoori, Nature **379**, 413 (1996); Kouwenhoven *et al.*, in *Mesoscopic Electron Transport*, Ed. by L. L. Sohn, L. P. Kouwenhoven, and G. Schön (Kluwer, Dordecht, 1997).
2. D. C. Ralph, C. T. Black and M. Tinkham, Phys. Rev. Lett. **74**, 3241 (1995).
3. L. P. Rokhinson *et al.*, Phys. Rev. B 63 5321 (2001).
4. D. S. Duncan *et al.*, Appl. Phys. Lett. **77**, 2183 (2000).
5. J. A. Folk *et al.*, Phys. Rev. Lett. , in press, (2001), (also, cond-mat/0005066).
6. J. A. Folk *et al.*, Physica Scripta **T90**, 26 (2001), (also, cond-mat/0010441).
7. D. H. Cobden *et al.*, Phys. Rev. Lett. **81**, 681 (1998).
8. S. J. Tans *et al.*, Nature **393**, 49 (1998).
9. V. I. Falko and T. Jungwirth, cond-mat/0106019 (2001).
10. D. M. Zumbühl, J. B. Miller, C. M. Marcus, J. S. Harris, Jr., in preparation (2001).
11. K. A. Matveev, L. I. Glazman and A. I. Larkin, Phys. Rev. Lett. **85**, 2789 (2000).
12. P. W. Brouwer, X. Waintal and B. I. Halperin, Phys. Rev. Lett. **85**, 369 (2000).
13. D. R. Stewart *et al.*, Science **278**, 1784 (1998).
14. S. Tarucha *et al.*, Phys. Rev. Lett. **77**, 3613 (1996).
15. B. I. Halperin, *et. al*, Phys. Rev. Lett. **86**, 2106 (2001).
16. I. L. Kurland, I. L. Aleiner and B. L. Altshuler, Phys. Rev. B **62**, 14886 (2000).
17. A. V. Andreev and A. Kamenev, Phys. Rev. Lett. **81**, 3199 (1998).
18. R. Berkovits, Phys. Rev. Lett. **81**, 2128 (1998).
19. P. W. Brouwer, Y. Oreg and B.I. Halperin, Phys. Rev. B **60**, R13977 (1999).
20. E. Eisenberg and R. Berkovits, Phys. Rev. B **60**, 15261 (1999).
21. H.U. Baranger, D. Ullmo and L.I. Glazman, Phys. Rev. B **61**, R2425 (2000).
22. P. Jacquod and A. D. Stone, Phys. Rev. Lett. **84**, 3938 (2000).
23. Y. Oreg, P. W. Brouwer, X. Waintal, B. I. Halperin, cond-mat/0109541 (2001).
24. U. Sivan, *et al.*, Phys. Rev. Lett. **77**, 1123 (1996); F. Simmel, *et al.*, Europhys. Lett. **38**, 123 (1997); S.R. Patel, *et al.*, Phys. Rev. Lett. **80**, 4522 (1998); F. Simmel, *et al.*, Phys. Rev. B **59**, R10441 (2000).
25. S. Lüscher,*et al.* Phys. Rev. Lett. **86**, 2118 (2001).
26. M. L. Mehta *Random Matrices*, (Academic Press, NY, 1991).
27. I. L. Aleiner and V. I. Falko, cond-mat/0107385 (2001).
28. I. L. Kurland, R. Berkovits and B. L. Altshuler, Phys. Rev. Lett. **86**, 3380 (2001).
29. A. Yacoby, M. Heiblurn, D. Mahalu, and H. Shtrikman, Phys. Rev. Lett. **74**, 4047 (1995).
30. J. König and Y. Gefen, cond-mat/0107450 (2001).

THE g-FACTORS OF DISCRETE LEVELS IN NANOPARTICLES

K.A. Matveev[1], L.I. Glazman[2], and A.I. Larkin[2,3]
[1] *Department of Physics, Duke University, Durham, NC 27708-0305*
[2] *Theoretical Physics Institute, University of Minnesota, Minneapolis, MN 55455*
[3] *L.D. Landau Institute for Theoretical Physics, 117940 Moscow, Russia*

Spin-orbit scattering suppresses Zeeman splitting of individual energy levels in small metal particles. This suppression becomes significant when the spin-orbit scattering rate τ_{so}^{-1} is comparable to the quantum level spacing δ. At small $\delta\tau_{so}$ the g-factor exhibits strong mesoscopic fluctuations. We find the shape of their distribution function using the random matrix theory, and express its parameters in terms of physical characteristics: τ_{so}, δ, the electron mean free path l, and the particle size L. At $\delta\tau_{so} \to 0$ the average g-factor levels off at a small value $g \sim (l/L)^{1/2}$. On the contrary, in 2D quantum dots the g-factor is strongly enhanced by spin-orbit coupling.

1 Introduction

In bulk metals the spin-orbit interaction is known to result in relatively weak corrections to the g-factors of electrons [1]. For instance, in aluminum the g-factor is indistinguishable from the nominal value of 2, and in bulk gold $g = 2.1$. On the contrary, recent experiments with nanoparticles found much smaller values of g. Measurements of the level splitting induced by magnetic field in Al grains [2] yielded $g \approx 1.7$. Adding to these grains of only 4% of Au resulted in the drop of g down to ~ 0.7. In Au nanoparticles the value $g \approx 0.3$ was observed [3]. The lowest-order perturbation theory [1,4] in the strength of spin-orbit scattering enables one to analyze [2] small deviations of the g-factor in a nanoparticle from the nominal value $g = 2$. In this paper we develop a theory of the g-factor in the regime when it is strongly affected by spin-orbit scattering, which was the case in experiments [2,3].

In bulk materials the g-factor is conventionally determined from the electron spin resonance (ESR) data. ESR involves transitions between states of the electron continuum. On the contrary, the experiments with nanoparticles [2,3] study the Zeeman splitting of individual electron levels ϵ_i:

$$\epsilon_{i\sigma}(H) = \epsilon_i \pm \frac{1}{2} g_i \mu_B H. \tag{1}$$

Here H is the magnetic field, $\mu_B = e\hbar/2mc$ is Bohr magneton; m is the free electron mass. The splitting (1) is linear in H as long as it is small compared to the quantum level spacing δ. The g-factor determined by Eq. (1), in general, varies from level to level. In the absence of spin-orbit interaction $g_i = 2$. Evidently [2,3] the spin-orbit scattering affects the values of g_i.

Unlike its bulk value, the g-factor defined by Eq. (1) is very sensitive to even weak spin-orbit interaction. The reason is that the magnitude of the correction to $g = 2$ value measured by ESR in the bulk, is determined by the comparison of spin-orbit interaction to the typical electron band width, whereas the relevant energy scale for g-factors of individual levels is the quantum level spacing δ.

The spin-orbit interaction is usually described by the mean time of spin-orbit scattering τ_{so}. In order to assess the effect of spin-orbit interaction on the individual energy levels, this scattering time should be compared with the time $\sim 1/\delta$ that electron travels along a closed trajectory corresponding to a quantum level. At $\delta\tau_{so} \gg 1$ the electron spin flips very infrequently, and the effect of the spin-orbit scattering is weak. On the contrary, at $\delta\tau_{so} \ll 1$ the spin flips the average of $N = 1/\delta\tau_{so} \gg 1$ times during the electron motion along the closed trajectory. Thus the average spin in such a quantum state is significantly less than 1/2, and the response (1) to the magnetic field is strongly suppressed. Also, the value of average spin varies strongly from one

state to another; we present the corresponding distribution function in the next Section. The Random Matrix Theory (RMT) derivation of the distribution function is described in Section 3. The relation of the RMT parameter controlling the distribution function to the microscopic characteristics of the system is established in Section 4. The case of weak spin-orbit interaction and overall dependence of the g-factors on the strength of the spin-orbit interaction are discussed in Sections 5 and 6, respectively.

2 Main Results

If the number of spin flips during the electron motion along the closed trajectory corresponding to a quantum level is large, $N \gg 1$, then we can estimate the corresponding g-factor by applying the Central Limit Theorem. The flips occur at random moments in time; the root-mean-square value of the spin is $1/\sqrt{N}$, resulting in $g_i \sim g_0\sqrt{\delta\tau_{\rm so}}$. (Here g_0 is the bulk value of g-factor determined by the band structure of the material; $g_0 = 2$ for free electrons.)

The above estimate accounts only for the spin contribution to the g-factor. In fact, the level splitting in a magnetic field is determined by the total magnetic moment of the state

$$\langle M\rangle_i = \langle M_z^{\rm orb}\rangle_i + \langle M_z^{\rm sp}\rangle_i. \tag{2}$$

Here $\mathbf{M}^{\rm orb} = (e/2c)[\mathbf{r}\times\mathbf{v}]$ and $\mathbf{M}^{\rm sp} = g_0\mu_B\mathbf{s}$ are the orbital and spin magnetic moments; $\mathbf{r}$, $\mathbf{v}$, and $\mathbf{s}$ are the operators of position, velocity, and spin of the electron, respectively. The brackets $\langle\cdots\rangle_i$ denote the expectation value in i-th eigenstate of an electron confined to a nanoparticle in an infinitesimal magnetic field in z-direction. In a nanoparticle of a generic shape, the orbital levels are not degenerate. Then in the absence of the spin-orbit interaction the time reversal symmetry dictates $\langle[\mathbf{r}\times\mathbf{v}]_z\rangle_i = 0$ at $H \to 0$, although the variance $\langle[\mathbf{r}\times\mathbf{v}]_z^2\rangle_i \neq 0$. It is important to note that in the presence of spin-orbit interaction $\langle[\mathbf{r}\times\mathbf{v}]_z\rangle_i \neq 0$, and the orbital motion contributes to the splitting of levels by magnetic field[5].

In the presence of strong spin-orbit coupling, $\delta\tau_{\rm so} \ll 1$, one can estimate $\langle[\mathbf{r}\times\mathbf{v}]_z\rangle_i$ as the root-mean-square value $\sqrt{\langle[\mathbf{r}\times\mathbf{v}]_z^2\rangle_i} \sim |A|/\delta$ calculated without accounting for that coupling; here A is the (directed) area covered by a trajectory corresponding to level i. To find A we notice that during time $1/E_T$ the electron travels across the grain and, therefore, covers the area $\sim L^2$. (Here $E_T = D/L^2$ is the Thouless energy, L is the grain size, and D is the diffusion constant for electrons in the grain.) During the period of motion $1/\delta$ the electron bounces off the boundaries $\sim E_T/\delta$ times. Since the direction of motion after each bounce is random, the total directed area is $|A| \sim L^2\sqrt{E_T/\delta}$. Consequently, the orbital magnetic moment of a given state can be estimated as

$$\langle M_z^{\rm orb}\rangle_i \sim \frac{e\hbar}{c}L\sqrt{D\delta} \sim \frac{e\hbar}{cm^*}\times\begin{cases}\sqrt{l/L}, & \text{3D},\\ \sqrt{k_F l}, & \text{2D}.\end{cases} \tag{3}$$

Here l is the transport mean free path of electrons, and k_F is their Fermi wavevector, and m^* is of the order of the effective mass derived from the density of states of a bulk material.

One can also see from Eq. (3) that in a three-dimensional (3D) nanoparticle the orbital contribution to the g-factor is small $g_i^{\rm orb} \sim \sqrt{l/L} \ll 1$. However, in the case of strong spin-orbit scattering, $\delta\tau_{\rm so} \ll 1$, the above estimated spin contribution is also small, $g_i^{\rm sp}/g_0 \sim \sqrt{\delta\tau_{\rm so}} \ll 1$. Therefore in this regime both contributions may have to be taken into account.

We will show in Section 4 that at $\delta\tau_{\rm so} \ll 1$ the g-factor of a level is a random quantity with the distribution function

$$P(g) = 3\sqrt{\frac{6}{\pi}}\frac{g^2}{\langle\langle g^2\rangle\rangle^{3/2}}\exp\left(-\frac{3g^2}{2\langle\langle g^2\rangle\rangle}\right), \tag{4}$$

where the averaging $\langle\langle \cdots \rangle\rangle$ is performed either over an ensemble of 3D nanoparticles or over different levels in a single nanoparticle[6]. Furthermore, in Section 5 we express $\langle\langle g^2 \rangle\rangle$ in terms of two quantities, τ_{so} and l, which can be measured independently:

$$\langle\langle g^2 \rangle\rangle = \frac{3g_0^2}{2\pi\hbar}\delta\tau_{so} + \alpha\frac{l}{L}. \tag{5}$$

Here the dimensionless constant α is determined by the geometry of the nanoparticle; its exact value will be discussed in Section 5. Eqs. (4) and (5) are the main results of this paper.

3 Derivation of the Distribution Function of the g-Factors

We begin the study of the g-factors of individual levels by finding relation between g_i and the matrix elements of the operator of magnetic moment M. Due to the time-reversal symmetry, the levels in the nanoparticle are degenerate, with the wavefunctions $|\psi_i\rangle$ and $|T\psi_i\rangle$, where T stands for the time reversal operator. In a weak magnetic field H the levels are split by the perturbation MH. Using the standard method of degenerate perturbation theory, one can easily find the splitting in the form (1) with the g-factor

$$g_i = 2\frac{|\vec{\mu}|}{\mu_B}, \tag{6}$$

where the real vector $\vec{\mu}$ is defined as

$$\mu_x + i\mu_y = \langle T\psi_i|M|\psi_i\rangle, \quad \mu_z = \langle\psi_i|M|\psi_i\rangle. \tag{7}$$

The distribution function $p(\vec{\mu})$ is, by definition,

$$p(\vec{\mu}) = \int \frac{d^3\lambda}{(2\pi)^3} e^{i\vec{\lambda}\cdot\vec{\mu}} \langle\langle \exp(-i\lambda_x \mathrm{Re}\langle T\psi_i|M|\psi_i\rangle \\ -i\lambda_y \mathrm{Im}\langle T\psi_i|M|\psi_i\rangle - i\lambda_z\langle\psi_i|M|\psi_i\rangle)\rangle\rangle. \tag{8}$$

To perform the averaging in Eq. (8), we use the Random Matrix Theory (RMT) approach[7]. Instead of the ensemble of nanoparticles with strong spin-orbit scattering we will consider an ensemble of symplectic matrices of size $2N \times 2N$ with $N \gg 1$. Then the eigenfunctions $\langle\psi|$ and $\langle T\psi|$ of the Hamiltonian are N-component spinors:

$$\langle\psi| = (\{\phi_k^*, \chi_k^*\}), \quad \langle T\psi| = (\{-\chi_k, \phi_k\}). \tag{9}$$

The operator of magnetic moment M is a hermitian matrix, which due to its time-reversal properties can be diagonalized to the form $\mathrm{diag}\{M_1, -M_1, \ldots, M_k, -M_k, \ldots, M_N, -M_N\}$. In the basis of the eigenfunctions of M the matrix elements (7) take the form:

$$\langle\psi|M|\psi\rangle = \sum_{k=1}^{N} M_k(|\phi_k|^2 - |\chi_k|^2), \tag{10}$$

$$\langle T\psi|M|\psi\rangle = -2\sum_{k=1}^{N} M_k\phi_k\chi_k. \tag{11}$$

The advantage of the RMT approach is that the ensemble averaging in Eq. (8) is easily performed using the Porter-Thomas distribution[7] of the matrix elements:

$$\langle\langle \cdots \rangle\rangle = \int \prod_{k=1}^{N} \frac{d^2\phi_k d^2\chi_k}{(\pi/2N)^2} e^{-2N(|\phi_k|^2+|\chi_k|^2)} \ldots. \tag{12}$$

The averaging in Eq (8) with the help of (10)–(12) reduces to the calculation of N identical quadruple Gaussian integrals. The result has the form

$$p(\vec{\mu}) = \int \frac{d^3\lambda}{(2\pi)^3} e^{i\vec{\lambda}\cdot\vec{\mu}} \prod_{k=1}^{N} \left(1 + \frac{|\vec{\lambda}|^2 M_k^2}{(2N)^2}\right)^{-1}. \tag{13}$$

In the limit of large $N \gg 1$, this integral becomes Gaussian too, and we find

$$p(\vec{\mu}) = \left(\frac{2N^2}{\pi \mathrm{Tr} M^2}\right)^{3/2} \exp\left(-\frac{2N^2}{\mathrm{Tr} M^2}|\vec{\mu}|^2\right). \tag{14}$$

Taking into account the relation (6), we now immediately find the distribution function of the g-factor in the form (4) with the mean square g defined as

$$\langle\langle g^2 \rangle\rangle = \frac{3}{\mu_B^2} \frac{\mathrm{Tr} M^2}{N^2}. \tag{15}$$

As a phenomenological theory, RMT enabled us to find the functional form of the distribution function; however, the width of the distribution (15) is now expressed in terms of a phenomenological parameter $\mathrm{Tr} M^2/N^2$.

4 Relation of the RMT parameter to the Microscopic Properties of the System

The relation between the parameter $\langle\langle g^2 \rangle\rangle$ and the microscopic properties of the system cannot be established within the RMT. To do this, one has to find an observable quantity Q which can be evaluated within both the phenomenological RMT and a microscopic theory.

We choose Q to be the energy absorbed in unit time from a weak external ac magnetic field $H(t) = H_0 \cos \omega t$. Such a field induces transitions between quantum levels in the grain, leading to the absorption of the energy in the grain. Within the RMT, the absorption can be found with the help of the Fermi golden rule as

$$Q = \left\langle\!\!\left\langle 2\pi \sum_{k \le k_f < p} \left|\tfrac{1}{2} H_0 \langle \psi_k | M | \psi_p \rangle\right|^2 \delta(\omega + \epsilon_k - \epsilon_p) \right\rangle\!\!\right\rangle \omega. \tag{16}$$

The expression inside $\langle\langle \ldots \rangle\rangle$ is the rate of absorption of quanta of radiation interacting with the system. The absorption occurs due to the transitions from occupied states with $k \le k_f$ to the empty states, $p > k_f$, and are induced by the term $\frac{1}{2} H_0 M e^{-i\omega t}$ in the corresponding coupling Hamiltonian.

In RMT the energy levels and the eigenfunctions are uncorrelated, i.e., the averaging over the energy levels and matrix elements in Eq. (16) can be performed independently. Also, at $\omega \gg \delta$, one can neglect the correlations of the densities of states at energies separated by ω, and we find

$$Q = \frac{\pi \omega^2 H_0^2}{2\delta^2} \langle\langle |M_{kp}|^2 \rangle\rangle. \tag{17}$$

It is important to note that contrary to the above calculation of the g-factors of individual levels, Eqs. (6) and (7), here the matrix elements M_{kp} are between eigenstates with different energies. Upon averaging over the ensemble $\langle\langle |M_{kp}|^2 \rangle\rangle$ becomes independent of k and p. Its magnitude can be found by presenting the invariant $\mathrm{Tr} M^2$ as a sum of $\langle\langle |M_{kp}|^2 \rangle\rangle$ over all $2N$ values of k and p. Since the number of diagonal matrix elements $2N$ is small compared to the number of the off-diagonal ones, $4N^2 - 2N$, we conclude that $\langle\langle |M_{kp}|^2 \rangle\rangle = \mathrm{Tr} M^2/4N^2$ at $N \gg 1$. Combining this relation with Eqs. (17) and (15), we find

$$\langle\langle g^2 \rangle\rangle = \frac{24\,\delta^2}{\pi \hbar \omega^2 (\mu_B H_0)^2} Q. \tag{18}$$

It is noteworthy that this result, obtained within the RMT, contains no phenomenological parameters. It establishes a relation between the property of a single level, the g-factor, and a macroscopic quantity Q insensitive to the effects of discreteness of levels.

To evaluate the absorption rate Q for a given nanoparticle, it is convenient to express it as $Q = \frac{1}{2}\omega A'' H_0^2$ in terms of the imaginary part A'' of the zz-component of the tensor of magnetic polarizability [10] of the sample A_{ik}, defined as $M_i = A_{ik}H_k$. Then the result for the mean square g-factor takes the form

$$\langle\langle g^2 \rangle\rangle = \frac{12\,\delta^2}{\pi\hbar\mu_B^2}\,\frac{A''(\omega)}{\omega}. \tag{19}$$

It is well known [10] that at $\omega \to 0$ the imaginary part of the polarizability vanishes as $A''(\omega) \propto \omega$.

Since $M = M_z^{\rm orb} + M_z^{\rm sp}$, one can distinguish between the orbital and spin contributions to the magnetic polarizability of the nanoparticle. The spin contribution has the form

$$A_s(\omega) = \frac{\mu_B^2 g_0^2}{4\delta}\,\frac{1}{1 - i\omega\tau_{\rm so}/2}. \tag{20}$$

Here the first factor is the usual static Pauli susceptibility of the electron gas of the nanoparticle, and the second one accounts for the fact that spin correlations decay exponentially with the time constant $\tau_{\rm so}/2$. Substituting the imaginary part of the polarizability (20) into (19), we reproduce the first term of our main result (5).

The orbital contribution to the magnetic polarizability is due to the magnetic moment of the eddy currents generated in the sample by the ac magnetic field. For a particle of a shape symmetrical with respect to the rotations around the z-axis one can easily find

$$A'' = \frac{\omega\sigma}{4c^2}\,\overline{\rho_\perp^2}\,V, \quad \omega \to 0. \tag{21}$$

Here σ is the conductivity of the metal, V is the volume of the nanoparticle, and $\overline{\rho_\perp^2}$ is the "moment of inertia" of the grain, assuming unit density. For a spherical nanoparticle of radius L the combination of Eqs. (19) and (21) reproduces the second term in Eq. (5) with $\alpha = (6/5)(m/m^*)^2$.

For the thin ring geometry Eqs. (19) and (21) result in $\langle\langle g^2 \rangle\rangle = 3m^2L^2D\delta/\pi^3\hbar^3$, where L stands for the circumference of the ring. In the context of the persistent current problem the orbital effect of magnetic field on the splitting of the energy levels was studied earlier by Kravtsov and Zirnbauer [5]. They used the non-linear σ-model techniques [8] to solve the general problem of crossover from the symplectic ensemble to the unitary one. A special limiting case of that solution gave rise to a distribution function of level splittings, which reassuringly coincides with our result for the thin ring geometry. Phenomenologically the crossover problem was solved within RMT by Mehta and Pandey [9]. Our approach enables one to express their phenomenological crossover parameter to physical observables without resorting to σ-model calculations.

5 Correction to the g-Factor in the Case of Weak Spin-Orbit Interaction

In the case of weak spin-orbit interaction, $\delta\tau_{\rm so} \gg 1$, the correction to the average g-factor is small and can be found by perturbation theory. In the lowest order perturbation theory in spin-orbit coupling one finds [1]

$$g_i/g_0 = 1 - \frac{\hbar\delta}{\pi\tau_{\rm so}}\sum_{j\neq i}\frac{1}{(\epsilon_i - \epsilon_j)^2}. \tag{22}$$

Assuming that the energy levels ϵ_j are equidistant, the sum (22) was evaluated by Kawabata [4]. However, in a disordered system the Wigner-Dyson statistics of the energy levels is a more

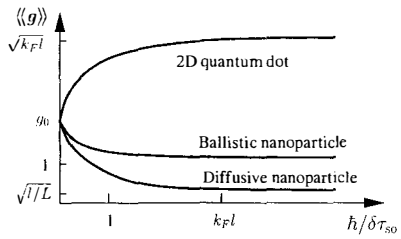


Figure 1: Sketch of the dependence of the average g-factor on the strength of spin-orbit scattering, see text. We assumed $m^*/m \simeq 1$ in this plot.

realistic assumption. In this case one of the levels j can be close to level i, resulting in a particularly large correction to the g-factor. Taking into consideration the fact that the level repulsion in the orthogonal ensemble suppresses the probability p_o of two levels being very close [7], $p_o(\epsilon_i - \epsilon_j) = \pi^2|\epsilon_i - \epsilon_j|/6\delta^2$, we find that the average value of the sum in Eq. (22) is logarithmically large:

$$\langle\langle g\rangle\rangle = g_0 - \frac{\pi g_0}{12}\frac{\hbar}{\delta\tau_{so}}\ln\frac{\delta\tau_{so}}{\hbar}. \qquad (23)$$

The logarithmic divergence in Eq. (23) was cut-off at the energy scale $|\epsilon_i - \epsilon_j| \sim \sqrt{\delta/\tau_{so}}$, because of the additional level repulsion caused by the weak spin-orbit coupling.

6 The Overall Dependence of the average g-Factor on the Strength of Spin-Orbit Interaction

Our results are summarized in Fig. 1. The lower curve shows the dependence of the average g-factor on the strength of the spin-orbit scattering in the case of a diffusive nanoparticle. In the regime of $1/\delta\tau_{so} \ll 1$ the behavior is described by Eq. (23), and at $1/\delta\tau_{so} \gg 1$ the average g-factor drops in agreement with Eq. (5). In the latter regime $\langle\langle g\rangle\rangle = (8/3\pi)^{1/2}\langle\langle g^2\rangle\rangle^{1/2}$, as one can easily see from the distribution function (4).

The middle curve in Fig. 1 shows schematically the behavior of a ballistic nanoparticle, where all the scattering of electrons is due to the reflection from the boundaries only. One can conduct a quantitative study in a simple model of a spherical ballistic nanoparticle of radius L with totally diffusive scattering off the boundaries. The result amounts to replacing $l \to 5L/8$ in Eq. (5) and keeping α the same as in the case of a diffusive sphere. Taking into consideration the rapid decrease of the distribution function (4) of the g-factor at $g^2 \ll \langle\langle g^2\rangle\rangle$, one should conclude that the nanoparticles showing the values of g^2 well below the ballistic value $\langle\langle g^2\rangle\rangle = (3/4)(m/m^*)^2$ are most likely in the diffusive regime. This is apparently the case in the experiment [3]: as it follows from Eq. (5), the measured $g = 0.3$ value yields the boundaries $l/L \leq 0.1$ and $\tau_{so}\delta/\hbar \leq 0.05$ for the mean free path and spin-orbit scattering rate.

The top curve in Fig. 1 shows the behavior of the g-factor in the case of a 2D quantum dot in a perpendicular magnetic field. In accordance with Eq. (3), in the strong spin-orbit scattering case, $1/\delta\tau_{so} \gg 1$, the orbital moment $\langle l_z\rangle$ reaches a very large value $\sim \sqrt{k_F l}$. In experiments with quantum dots in GaAs heterostructures the orbital effect should be further enhanced due to a small effective mass $m^* \approx 0.067m$ of electrons, so one can expect to find an independent of g_0 value, $\langle\langle g\rangle\rangle \sim (m/m^*)\sqrt{k_F l}$. At weaker spin-orbit scattering, $1/\delta\tau_{so} \leq 1$, the orbital enhancement of the g-factor is reduced.

7 Concluding Remarks

Our discussion of the effects of spin-orbit scattering on the g-factors of individual levels neglected electron-electron interactions. In the mean-field approximation we do not expect the interactions to affect our results. In particular, the well-known exchange enhancement of the g-factor occurs in the thermodynamic limit, and should not affect the g-factors of individual quantum levels defined by Eq. (1). On the other hand, in general the electron-electron correlations scramble the picture of single-electron levels used in this paper. However, for a few lowest energy levels usually observed in the experiment the single-electron picture is still valid [11], provided the conductance of the grain is large compared to $e^2/\hbar$.

Acknowledgments

This work was supported by NSF under Grants DMR-9974435, DMR-9731756, and DMR-9812340. KM also acknowledges support by A.P. Sloan Foundation and the kind hospitality of the TPI at the University of Minnesota. The authors acknowledge the hospitality of ICTP in Trieste, Italy and Centre for Advanced Study in Oslo, Norway, where part of this work was performed. We are grateful to B.L. Altshuler, K.B. Efetov, S. Guéron, V.E. Kravtsov, and D.C. Ralph for useful discussions.

References

1. W.P. Halperin, Rev. Mod. Phys. **58**, 533 (1986).
2. D.G. Salinas, S. Guéron, D.C. Ralph, C.T. Black, and M. Tinkham, Phys. Rev. B **60**, 6137 (1999).
3. D. Davidović and Tinkham, Phys. Rev. Lett. **83**, 1644 (1999).
4. A. Kawabata, J. Phys. Soc. Jpn. **29**, 902 (1970).
5. V.E. Kravtsov and M.R. Zirnbauer, Phys. Rev. B **46**, 4332, (1992).
6. The tensor properties of the g-factor and the corresponding joint distribution function for the tensor components were discussed in: P.W. Brouwer, X. Waintal, B.I. Halperin, Phys. Rev. Lett. **85**, 369 (2000).
7. See, e.g., *Statistical Theories of Spectra: Fluctuations,* ed. by C.E. Porter (Academic Press, New York, 1965).
8. K. Efetov, *Supersymmetry in Disorder and Chaos*, (Cambridge University Press, Cambridge, 1997).
9. M.L. Mehta and A. Pandey, J. Phys. A **16**, 2655 (1983).
10. L.D. Landau and E.M. Lifshits, *Electrodynamics of Continuous Media*, (Pergamon, New York, 1984).
11. B.L. Altshuler, Y. Gefen, A. Kamenev, and L.S. Levitov, Phys. Rev. Lett. **78**, 2803 (1997).

SHOT NOISE OF WEAK COTUNNELING CURRENT: NON-EQUILIBRIUM FLUCTUATION-DISSIPATION THEOREM

EUGENE V. SUKHORUKOV, DANIEL LOSS
University of Basel, Basel, Switzerland

We study the noise of the cotunneling current through one or several tunnel-coupled quantum dots in the Coulomb blockade regime. We consider the regime of weak (elastic and inelastic) cotunneling, and prove a non-equilibrium fluctuation-dissipation theorem which leads to a universal expression for the noise-to-current ratio (Fano factor).

1 Introduction

In recent years, there has been great interest in the shot noise in mesoscopic systems,[1] because it contains additional information about correlations, which is not contained, e.g., in the linear response conductance. The shot noise is characterized by the Fano factor $F = S/eI$, the dimensionless ratio of the zero-frequency noise power S to the average current I. While it assumes the Poissonian value $F = 1$ in the absence of correlations, it becomes suppressed or enhanced when correlations set in as e.g. imposed by the Pauli principle or due to interaction effects. In the present paper we study the shot noise of the cotunneling [2,3] current. We consider the transport through a quantum-dot system (QDS) in the Coulomb blockade (CB) regime, in which the quantization of charge on the QDS leads to a suppression of the sequential tunneling current except under certain resonant conditions. We consider the transport away from these resonances and study the next-order contribution to the current [a] (see Fig. 1). One might expect that the cotunneling, being a two-particle process, leads to strong correlations in the shot noise and to the deviation of the Fano factor from its Poissonian value $F = 1$. As it has been found recently,[5] this is indeed the case for the regime of strong cotunneling, i.e. when the cotunneling rate I/e is large compared to the intrinsic relaxation rate $w_{\rm in}$ of the QDS to its equilibrium state due to the coupling to the environment, $I/e \gg w_{\rm in}$. However we find here, that in the weak cotunneling regime, $I/e \ll w_{\rm in}$, the zero-frequency noise takes on its Poissonian value, as first obtained for a special case.[6] This result is generalized here, and we find a universal relation between noise and current for the QDS in the first nonvanishing order in the tunneling perturbation. Because of the universal character of this result (Eq. 12) we call it the nonequilibrium fluctuation-dissipation theorem (FDT)[7] in analogy with linear response theory.

2 Model system

In general, the QDS can contain several dots, which can be coupled by tunnel junctions, the double dot (DD) being a particular example.[6] The QDS is assumed to be weakly coupled to external metallic leads which are kept at equilibrium with their associated reservoirs at the chemical potentials μ_l, $l = 1, 2$, where the currents I_l can be measured and the average current I through the QDS is defined by Eq. 5. Using a standard tunneling Hamiltonian approach,[8] we write

$$H = H_0 + V\,, \quad H_0 = H_L + H_S + H_{\rm int}\,, \tag{1}$$

$$H_L = \sum_{l=1,2} \sum_k \varepsilon_k c_{lk}^\dagger c_{lk}\,, \quad H_S = \sum_p \varepsilon_p d_p^\dagger d_p\,, \tag{2}$$

[a] The majority of papers on the noise of quantum dots consider the sequential tunneling regime, where a classical description ("orthodox" theory) is applicable.[4] In this regime the noise is generally suppressed below its full Poissonian value $F = 1$. This suppression can be interpreted [5] as being a result of the natural correlations imposed by charge conservation.

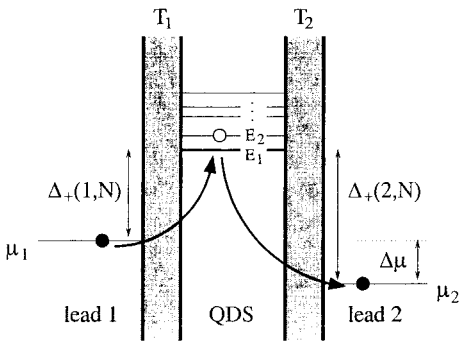


Figure 1: The quantum dot system (QDS) is coupled to two external leads $l = 1, 2$ via tunneling barriers. The tunneling between the QDS and the leads is parametrized by the tunneling amplitudes T_l, where the lead and QDS quantum numbers k and p have been dropped for simplicity. The leads are at the chemical potentials $\mu_{1,2}$, with an applied bias $\Delta\mu = \mu_1 - \mu_2$. The eigenstates of the QDS with one added electron ($N+1$ electrons in total) are indicated by their energies $E_1, E_2, \ldots$. In the cotunneling regime there is a finite energy cost $\Delta_\pm(l, N) > 0$ for the electron tunneling from the Fermi level of the lead l to the QDS $(+)$ and vice versa $(-)$, so that only processes of second order in V (visualized by two arrows) are allowed.

$$V = \sum_{l=1,2} (D_l + D_l^\dagger), \quad D_l = \sum_{k,p} T_{lkp} c_{lk}^\dagger d_p \,, \tag{3}$$

where the terms H_L and H_S describe the leads and QDS, respectively (with k and p from a complete set of quantum numbers),and tunneling between leads and QDS is described by the perturbation V. The interaction term $H_{\rm int}$ does not need to be specified for our proof of the universality of noise. The N-electron QDS is in the cotunneling regime where there is a finite energy cost $\Delta_\pm(l, N) > 0$ for the electron tunneling from the Fermi level of the lead l to the QDS $(+)$ and vice versa $(-)$, so that only processes of second order in V are allowed.

To describe the transport through the QDS we apply standard methods [8] and adiabatically switch on the perturbation V in the distant past, $t = t_0 \to -\infty$. The perturbed state of the system is described by the time-dependent density matrix $\rho(t) = e^{-iH(t-t_0)} \rho_0 e^{iH(t-t_0)}$, with ρ_0 being the grand canonical density matrix of the unperturbed system, $\rho_0 = Z^{-1} e^{-K/k_B T}$, where we set $K = H_0 - \sum_l \mu_l N_l$. Because of tunneling the total number of electrons in each lead $N_l = \sum_k c_{lk}^\dagger c_{lk}$ is no longer conserved. For the outgoing currents $\hat{I}_l = e\dot{N}_l$ we have

$$\hat{I}_l = ei\,[V, N_l] = ei(D_l^\dagger - D_l)\,. \tag{4}$$

The observables of interest are the average current $I \equiv I_2 = -I_1$ through the QDS, and the spectral density of the noise $S_{ll'}(\omega) = \int dt S_{ll'}(t) \exp(i\omega t)$,

$$I_l = {\rm Tr}\rho(0)\hat{I}_l, \quad S_{ll'}(t) = {\rm Re\,Tr}\,\rho(0)\delta I_l(t)\delta I_{l'}(0)\,, \tag{5}$$

where $\delta I_l = \hat{I}_l - I_l$. Below we will use the interaction representation where Eq. 5 can be rewritten by replacing $\rho(0) \to \rho_0$ and $\hat{I}_l(t) \to U^\dagger(t)\hat{I}_l(t)U(t)$, with

$$U(t) = T \exp\left[-i \int_{-\infty}^{t} dt'\, V(t')\right] . \tag{6}$$

In this representation, the time dependence of all operators is governed by the unperturbed Hamiltonian H_0.

3 Non-equilibrium fluctuation-dissipation theorem

We note that the two currents $\hat{I}_l$ are not independent, because $[\hat{I}_1, \hat{I}_2] \neq 0$, and thus all correlators $S_{ll'}$ are nontrivial. The charge accumulation on the QDS for a time of order $\Delta_\pm^{-1}$ leads to an additional contribution to the noise at finite frequency ω. Thus, we expect that for $\omega \sim \Delta_\pm$ the correlators $S_{ll'}$ cannot be expressed through the steady-state current I only and thus I has to be complemented by some other dissipative counterparts, such as differential conductances

$G_{ll'}$. On the other hand, at low enough frequency, $\omega \ll \Delta_\pm$, the charge conservation on the QDS requires $\delta I_s = (\delta I_2 + \delta I_1)/2 \approx 0$. Below we concentrate on the limit of low frequency and neglect contributions of order of $\omega/\Delta_\pm$ to the noise power. In the Appendix we prove that $S_{ss} \sim (\omega/\Delta_\pm)^2$ (see Eq. 20), and this allows us to redefine the current and the noise power as $I \equiv I_d = (I_2 - I_1)/2$ and $S(\omega) \equiv S_{dd}(\omega)$. [b] In addition we require that the QDS is in the cotunneling regime, i.e. the temperature is low enough, $k_B T \ll \Delta_\pm$, although the bias $\Delta\mu$ is arbitrary as soon as the sequential tunneling to the dot is forbidden, $\Delta_\pm > 0$. In this limit the current through a QDS arises due to the direct hopping of an electron from one lead to another (through a virtual state on the dot) with an amplitude which depends on the energy cost $\Delta_\pm$ of a virtual state. Although this process can change the state of the QDS (inelastic cotunneling), the fast energy relaxation in the weak cotunneling regime, $w_{\rm in} \gg I/e$, immediately returns it to the equilibrium state (for the opposite case, see Ref. [5]). This allows us to apply a perturbation expansion with respect to tunneling V and to keep only first nonvanishing contributions, which we do next.

It is convenient to introduce the notation $\bar{D}_l(t) \equiv \int_{-\infty}^{t} dt'\, D_l(t')$. We notice that all relevant matrix elements, $\langle N|D_l(t)|N+1\rangle \sim e^{-i\Delta_+ t}$, $\langle N-1|D_l(t)|N\rangle \sim e^{i\Delta_- t}$, are fast oscillating functions of time. Thus, under the above conditions we can write $\bar{D}_l(\infty) = 0$, and even more general, $\int_{-\infty}^{+\infty} dt\, D_l(t) e^{\pm i\omega t} = 0$ (note that we have assumed earlier that $\omega \ll \Delta_\pm$). Using these equalities and the cyclic property of the trace we obtain the following results (for details of the derivation, see Appendix),

$$I = e \int_{-\infty}^{\infty} dt\, \langle [A^\dagger(t), A(0)]\rangle, \qquad A = D_2 \bar{D}_1^\dagger + D_1^\dagger \bar{D}_2\,, \tag{7}$$

$$S(\omega) = e^2 \int_{-\infty}^{\infty} dt\, \cos(\omega t) \langle \{A^\dagger(t), A(0)\}\rangle\,, \tag{8}$$

where we have dropped a small contribution of order $\omega/\Delta_\pm$ and used the notation $\langle \ldots \rangle = {\rm Tr}\rho_0(\ldots)$.

Next we apply the spectral decomposition to the correlators Eqs. 7 and 8, a similar procedure to that which also leads to the equilibrium fluctuation-dissipation theorem. The crucial observation is that $[H_0, N_l] = 0$, $l = 1, 2$. Therefore, we are allowed to use for our spectral decomposition the basis $|\mathbf{n}\rangle = |E_{\mathbf{n}}, N_1, N_2\rangle$ of eigenstates of the operator $K = H_0 - \sum_l \mu_l N_l$, which also diagonalizes the grand-canonical density matrix ρ_0, $\rho_{\mathbf{n}} = \langle \mathbf{n}|\rho_0|\mathbf{n}\rangle = Z^{-1} \exp[-E_{\mathbf{n}}/k_B T]$. We introduce the spectral function,

$$\mathcal{A}(\omega) = 2\pi \sum_{\mathbf{n},\mathbf{m}} (\rho_{\mathbf{n}} + \rho_{\mathbf{m}}) |\langle \mathbf{m}|A|\mathbf{n}\rangle|^2 \delta(\omega + E_{\mathbf{n}} - E_{\mathbf{m}})\,, \tag{9}$$

and rewrite Eqs. 7 and 8 in the matrix form in the basis $|\mathbf{n}\rangle$ taking into account that the operator A, which plays the role of the effective cotunneling amplitude, creates (annihilates) an electron in the lead 2 (1) (see Eqs. 3 and 7). We obtain following expressions

$$I(\Delta\mu) = e \tanh\left[\frac{\Delta\mu}{2k_B T}\right] \mathcal{A}(\Delta\mu)\,, \tag{10}$$

$$S(\omega, \Delta\mu) = \frac{e^2}{2} \sum_{\pm} \mathcal{A}(\Delta\mu \pm \omega)\,. \tag{11}$$

[b] We note that charge fluctuations, $\delta Q(t) = 2\int_{-\infty}^{t} dt' \delta I_s(t')$, on a QDS are also relevant for device applications such as SET. [9] While we focus on current fluctuations in the present paper, we mention here that in the cotunneling regime the noise power $\langle \delta Q^2\rangle_\omega$ does not vanish at zero frequency, $\langle \delta Q^2\rangle_{\omega=0} = 4\omega^{-2} S_{ss}(\omega)|_{\omega\to 0} \neq 0$. Our formalism is also suitable for studying such charge fluctuations; this will be addressed elsewhere.

We note that because of additional integration over time t in the amplitude A (see Eq. 7), the spectral density $\mathcal{A}$ depends on μ_1 and μ_2 separately. However, away from the resonances, $\omega \ll \Delta_\pm$, only $\Delta\mu$-dependence is essential, and thus $\mathcal{A}$ can be regarded as being one-parameter function.[c] Comparing Eqs. 10 and 11, we obtain

$$S(\omega, \Delta\mu) = \frac{e}{2} \sum_{\pm} \coth\left[\frac{\Delta\mu \pm \omega}{2k_BT}\right] I(\Delta\mu \pm \omega) \tag{12}$$

up to small terms on the order of $\omega/\Delta_\pm$. This equation represents our nonequilibrium FDT for the transport through a QDS in the weak cotunneling regime. A special case with $T, \omega = 0$, giving $S = eI$, has been derived earlier.[6] To conclude this section we would like to list again the conditions used in the derivation. The universality of noise to current relation Eq. 12 proven here is valid in the regime in which it is sufficient to keep the first nonvanishing order in the tunneling V which contributes to transport and noise. This means that the QDS is in the weak cotunneling regime with $\omega, k_BT \ll \Delta_\pm$, and $I/e \ll w_{\rm in}$.

Acknowledgements

This work was supported by the Swiss NSF and by the DARPA program SPINS (DAAD19-01-0327).

Appendix

In this Appendix we present the derivation of Eqs. 7 and 8. In order to simplify the intermediate steps, we use the notation $\bar{O}(t) \equiv \int_{-\infty}^{t} dt' O(t')$ for any operator O, and $O(0) \equiv O$. We notice that, if an operator O is a linear function of operators D_l and $D_l^\dagger$, then $\bar{O}(\infty) = 0$ (see the discussion in Sec. 3). Next, the currents can be represented as the difference and the sum of $\hat{I}_1$ and $\hat{I}_2$,

$$\hat{I}_d = (\hat{I}_2 - \hat{I}_1)/2 = ie(X^\dagger - X)/2\,, \tag{13}$$

$$\hat{I}_s = (\hat{I}_1 + \hat{I}_2)/2 = ie(Y^\dagger - Y)/2\,, \tag{14}$$

where $X = D_2 + D_1^\dagger$, and $Y = D_1 + D_2$. While for the perturbation we have

$$V = X + X^\dagger = Y + Y^\dagger\,. \tag{15}$$

First we concentrate on the derivation of Eq. 7 and redefine the average current Eq. 5 as $I = I_d$ (which gives the same result anyway, because the average number of electrons on the QDS does not change $I_s = 0$).

To proceed with our derivation, we make use of Eq. 6 and expand the current up to fourth order in T_{lkp}:

$$I = i \int_{-\infty}^{0} dt \int_{-\infty}^{t} dt' \langle \hat{I}_d V(t) V(t') \bar{V}(t') \rangle - i \int_{-\infty}^{0} dt \langle \bar{V} \hat{I}_d V(t) \bar{V}(t) \rangle + \text{c.c.} \tag{16}$$

Next, we use the cyclic property of trace to shift the time dependence to $\hat{I}_d$. Then we complete the integral over time t and use $\bar{I}_d(\infty) = 0$. This procedure allows us to combine first and second term in Eq. 16,

$$I = -i \int_{-\infty}^{0} dt \langle [\bar{I}_d V + \bar{V} \hat{I}_d] V(t) \bar{V}(t) \rangle + \text{c.c.} \tag{17}$$

[c] To be more precise, we neglect small ω-shift of the energy denominators $\Delta_\pm$, which is equivalent to neglecting small terms of order $\omega/\Delta_\pm$ in Eq. 11.

Now, using Eqs. 13 and 15 we replace operators in Eq. 17 with X and $X^\dagger$ in two steps: $I = e\int_{-\infty}^{0} dt\langle[\bar{X}^\dagger X^\dagger - \bar{X}X]V(t)\bar{V}(t)\rangle$ + c.c., where some terms cancel exactly. Then we work with $V(t)\bar{V}(t)$ and notice that some terms cancel, because they are linear in c_{lk} and $c_{lk}^\dagger$. Thus we obtain $I = e\int_{-\infty}^{0} dt\langle[\bar{X}^\dagger X^\dagger - \bar{X}X][X^\dagger(t)\bar{X}^\dagger(t) + X(t)\bar{X}(t)]\rangle$ + c.c.. Two terms $\bar{X}XX\bar{X}$ and $\bar{X}^\dagger X^\dagger X^\dagger \bar{X}^\dagger$ describe tunneling of two electrons from the same lead, and therefore they do not contribute to the normal current. We then combine all other terms to extend the integral to $+\infty$,

$$I = e\int_{-\infty}^{\infty} dt\langle \bar{X}^\dagger(t)X^\dagger(t)X\bar{X} - \bar{X}XX^\dagger(t)\bar{X}^\dagger(t)\rangle \tag{18}$$

Finally, we use $\int_{-\infty}^{\infty} dtX(t)\bar{X}(t) = -\int_{-\infty}^{\infty} dt\bar{X}(t)X(t)$ (since $\bar{X}(\infty) = 0$) to get Eq. 7 with $A = X\bar{X}$. Here, again, we drop terms $D_1^\dagger \bar{D}_1^\dagger$ and $D_2\bar{D}_2$ responsible for tunneling of two electrons from the same lead, and obtain A as in Eq. 7.

Next, we derive Eq. 8 for the noise power. At small frequencies $\omega \ll \Delta_\pm$ fluctuations of I_s are suppressed because of charge conservation (see below), and we can replace $\hat{I}_2$ in the correlator Eq. 5 with $\hat{I}_d$. We expand $S(\omega)$ up to fourth order in T_{lkp}, use $\int_{-\infty}^{+\infty} dt\, \hat{I}_d(t)e^{\pm i\omega t} = 0$, and repeat the steps leading to Eq. 17. Doing this we obtain,

$$S(\omega) = -\int_{-\infty}^{\infty} dt\cos(\omega t)\langle[\bar{V}(t), \hat{I}_d(t)][\bar{V}, \hat{I}_d]\rangle\,. \tag{19}$$

Then, we replace V and $\hat{I}_d$ with X and $X^\dagger$. We again keep only terms relevant for cotunneling, and in addition we neglect terms of order $\omega/\Delta_\pm$ (applying same arguments as before, see Eq. 20). We then arrive at Eq. 8 with the operator A given by Eq. 7.

Finally, in order to show that fluctuations of I_s are suppressed, we replace $\hat{I}_d$ in Eq. 19 with $\hat{I}_s$, and then use the operators Y and $Y^\dagger$ instead of X and $X^\dagger$. In contrast to Eq. 18 terms such as $\bar{Y}^\dagger Y^\dagger Y\bar{Y}$ do not contribute, because they contain integrals of the form $\int_{-\infty}^{\infty} dt\cos(\omega t)D_l(t)\bar{D}_{l'}(t) = 0$. The only nonzero contribution can be written as

$$S_{ss}(\omega) = \frac{e^2\omega^2}{4}\int_{-\infty}^{\infty} dt\cos(\omega t)\langle[\bar{Y}^\dagger(t), \bar{Y}(t)][\bar{Y}^\dagger, \bar{Y}]\rangle\,, \tag{20}$$

where we have used integration by parts and the property $\bar{Y}(\infty) = 0$. Compared to Eq. 8 this expression contains an additional integration over t, and thereby it is of order $(\omega/\Delta_\pm)^2$.

References

1. For a recent review on shot noise, see: Ya. M. Blanter and M. Büttiker, *Shot Noise in Mesoscopic Conductors*, Phys. Rep. **336**, 1 (2000).
2. D. V. Averin and Yu. V. Nazarov, in *Single Charge Tunneling*, eds. H. Grabert and M. H. Devoret, NATO ASI Series B: Physics Vol. 294, (Plenum Press, New York, 1992).
3. D. C. Glattli *et al.*, Z. Phys. B **85**, 375 (1991).
4. For an review, see D. V. Averin and K. K. Likharev, in *Mesoscopic Phenomena in Solids*, edited by B. L. Al'tshuler, P. A. Lee, and R. A. Webb (North-Holland, Amsterdam, 1991).
5. E. V. Sukhorukov, G. Burkard, and D. Loss, Phys. Rev. B **63**, 125315 (2001).
6. D. Loss and E. V. Sukhorukov, Phys. Rev. Lett. **84**, 1035 (2000).
7. Such a non-equilibrium FDT was derived for single barrier junctions long ago by D. Rogovin, and D. J. Scalapino, Ann. Phys. (N. Y.) **86**, 1 (1974).
8. G. D. Mahan, *Many Particle Physics*, 2nd Ed. (Plenum, New York, 1993).
9. M. H. Devoret, and R. J. Schoelkopf, Nature **406**, 1039 (2000).

NANOTUBES

DOPING STATE OF MULTI-WALL CARBON NANOTUBE WIRES AND QUANTUM DOTS

Christian Schönenberger, Mark Buitelaar, Michael Krüger, Isabelle Widmer, Thomas Nussbaumer, and Mahdi Iqbal

Institute of Physics, University of Basel, Klingelbergstrasse 82, CH-4056 Basel, Switzerland

Employing strong electrostatic gating (liquid-ion gating), the position of the Fermi energy E_F (relative to the charge-neutrality point) was determined in multi-wall carbon nanotubes (MWNTs). E_F is negative (hole doping) and amounts to ≈ -0.3eV for MWNTs in air. Evidence that water, and not oxygen, is the main source of doping has been found. As a consequence, the number M of occupied 1d-modes (not counting spin) is > 2, i.e. $M \approx 10$. This is supported by the single-electron level spacing, deduced from observed single-electron charging effects (SET) at low temperature. The latter are dominated by co-tunneling processes, as we observe the Kondo effect. This provides evidence, that highly transmissive channels are present in MWNTs at low temperature, despite the 'disorder' observed before.

1 Introduction

Carbon nanotubes (CNTs) are ideal model systems for the exploration of electrical transport in low dimensions.[1] Two sorts of nanotubes (NTs) exist: Single-wall and multi-wall NTs. An ideal (undoped) SWNT can be either metallic or semiconducting, but here, we only focus on metallic NTs. In these tubes, the current is carried by two modes,[a] leading to a conductance of $4e^2/h$, provided backscattering is absent. Recent experiments have shown that scattering within metallic SWNT is weak. In a particular nice experiment the electrostatic potential drop along a voltage-biased NT was measured by using the tip of an atomic-force microscope as a probe.[2] For SWNTs, most of the potential drops at the contacts. In contrast, for MWNTs a considerable fraction of the potential drops along the tube, suggesting intrinsic scattering in MWNTs. A length dependent resistance was deduced before from electric resistance measurements on multiply contacted MWNTs.[3] The typical value for the resistance per unit length is $R' = 5 - 10\,\mathrm{k}\Omega/\mu m$. We mention, that there is one conflicting results: Frank *et al.*[4] came to the conclusion that MWNTs are ballistic conductors even at room temperature.[b] Seemingly compelling evidence for diffusive transport in MWNTs is provided by measurements of the magnetoresistance, both in parallel and perpendicular magnetic field.[3] For example, the resistance modulation in parallel magnetic field can be described very well by the Altshuler-Aronov-Spivak (AAS) theory (weak-localization in a cylindrical conductor), which relies on *diffusive* transport.[5] These experiments did also show that the electrical current is preferentially carried by the outermost tube, at least at low temperatures. Hence, a single nanotube is probed, albeit one with a large diameter of $d \approx 10 - 20\,\mathrm{nm}$, which is about ten times larger than that of prototype SWNTs. As emphasized before, a metallic SWNT is characterized by only $M = 2$ 1d-modes, a property that should be independent of the diameter. How can we than reconcile the availability of only 2 modes for an ideal NT with the observation of diffusive motion. Diffusive transport requires $M \gg 1$. May it be that MWNTs are doped to a such a degree that $M \gg 1$?

By using a new gating technique (electrochemical gating), we have recently shown that MWNTs are indeed (hole-) doped.[6] The number of 1d-modes is $\neq 2$, but rather $10 - 20$, see section 2. MWNTs are not single-mode, but rather few mode quasi-one-dimensional wires. Whether they are 1d diffusive, i.e. quasi-ballistic with a mean-free path l exceeding the circumference πd, or 2d diffusive ($l \leq \pi d$) is another question.

[a] If we refer to M modes, spin-degeneracy is not included.

[b] Note, that ballistic transport is not expected in MWNTs at room temperature, because the energy-separation between 1d subbands is comparable to kT.

Taking $R' = (2Me^2 l/\hbar)^{-1} = 5\,\mathrm{k}\Omega/\mu$ (L is tube length), yields $l \approx 100\,\mathrm{nm}$ which is of order of the circumference. This simple estimate is in good agreement with measurements of the energy-dependent tunneling DOS $\nu(E)$. $\nu(E)$ is not structureless, as would be expected if $l \ll \pi d$, but shows features reminiscent of quantization into 1d-modes, albeit with some broadening.[7]

Recently, we have studied gate-induced conductance fluctuations in MWNTs at low temperatures and tried to compare the measurements with UCF theory. In the regime of thermally-induced averaging, i.e. for tubes which are much longer than the phase-coherence length l_ϕ and/or the thermal length l_T, the functional dependence is in agreement with theory. These data allow to deduce l_ϕ, which follows Nyquist-dephasing below $\approx 4\,\mathrm{K}$. However, when we approach the universal limit, i.e. if $L \approx l_\phi$, the temperature dependence of conductance fluctuations markedly deviates from standard theories. This has led us to study shorter tubes in more detail by measuring the differential conductance $G_d = dI/dV$ as a function of transport voltage V and gate voltage U_g in the fully coherent regime, i.e. for $l_\phi \sim L$. Displaying $G_d(U_g, V)$ in a greyscale plot helps to recognize the underlying physics. This is in particular true for single-electron charging effects which might be present simultaneously to quantum interference effects, both modulating the equilibrium conductance.

Until now, however, no one has ever observed clear signatures of conventional Coulomb blockade in MWNTs. Single-electron tunneling (SET) effects, such a Coulomb blockade oscillations, were observed in SWNTs from the beginning.[8] The absence of SET effects in MWNTs is remarkable because the single-electron charging energy of MWNTs should be similar to that of SWNTs (the different tube diameters have only a minor effect on electrostatic capacitance). We have argued that contact resistances in MWNTs are so low that charging effects are absent.[3] Contact resistance can indeed be as low as $1\,\mathrm{k}\Omega$ at room temperature, which is low enough to suppress SET. At cryogenic temperature, however, contact resistances usually increase, so that SET may show up. In section 3 we present the first (and still rare) observation of SET in transport through a MWNT. Since the coupling to the contacts is rather strong, the conductance is dominated by higher-order co-tunneling processes. These new data allow to extract the single-particle level spacing δE of the MWNT quantum dot. Similar to the result from electrochemical gating, the measured δE suggests that ≈ 10 modes are occupied.

2 Doping state of multi-wall carbon nanotubes

In order to determine the degree of doping in MWNTs (or other nanotubes) the position of the Fermi energy need to be determined. One possible approach is to measure the conductance as a function of a gate voltage U_g, which shifts the Fermi energy E_F. If the conductance G increases (decreases) with increasing E_F, the NT is n-doped (p-doped), see Fig. 1a. At, or in the vicinity of the charge-neutrality point (CNP), the number of modes is minimal. It is 2 for a metallic tube and zero for a semiconducting one.[c] Hence, one expects to see a conductance minimum (or a resistance maximum) if E_F crosses the CNP. Ideally, for an undoped NT, E_F should lie at the CNP and the resistance maximum should appear at $U_g = 0$. If this maximum is observed at $U_g \neq 0$, the Fermi level is shifted due to some doping. In order to deduce E_F from the measured gate voltage, the electrochemical capacitance between gate and NT needs to be known. Conventional back gates (see Fig. 1b) have relatively low capacitance. Consequently Fermi-level shifts are small even for large applied gate voltages. In this case, the resistance maximum cannot be measured, and hence, the doping level cannot be determined. This problem is circumvented in our approach, in which the coupling capacitance is made very large. We immerse the nanotube into an electrolyte through which gating is achieved, see Fig 1c. For details, see Ref. 6. Very large gate capacitances are possible due to the large double-layer capacitance of the electrolyte

[c] At room temperature the 1d bandstructure in Fig. 1a is considerably smeared, so that no abrupt transitions are expected if E_F crosses a band onset.

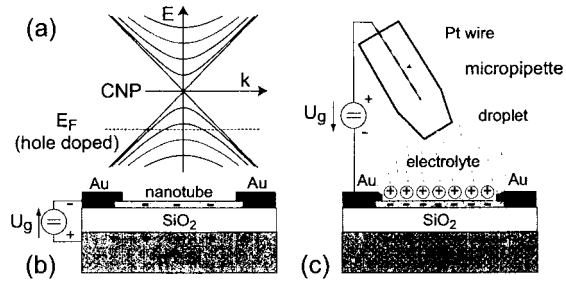


Figure 1: (a) Simplified 1d bandstructure of a metallic carbon nanotube. CNP, the charge neutrality point, refers to the position of the Fermi energy E_F of an undoped nanotube. The nanotube is hole (electron) doped if $E_F < CNP$ ($E_F > CNP$). E_F can be changed via the gate voltage U_g, conventionally applied to the substrate (backgate), as shown in (b). Much larger Fermi-energy shifts are possible through liquid-ion gating, (c). $LiClO_4$ ($1 - 500\,\mathrm{mM}$) was used as electrolyte.

NT interface. This has an important implication: Because the double-layer capacitance is much larger than the electrochemical capacitance of the NT, the total capacitance (series connection of the two) is determined by the nanotube alone. Hence, there is a one-to-one correspondence between gate-voltage change ΔU_g and Fermi level shift ΔE_F, i.e. $\Delta E_F \cong \Delta U_g$.

Electrochemical gating is studied at room temperature on single MWNTs with lithographically defined Au contacts evaporated over the NTs. The nanotube-contact structure is fabricated on degenerately doped Si with a 400 nm thick SiO_2 spacer layer. The subtsrate can be used as a conventional backgate, Fig 1b. If, as outlined in Fig. 1c, a positive gate voltage U_g is applied, the NT-electrolyte interface is polarized by the attraction of cations. Consequently, the Fermi level increases in the NT to maintain charge neutrality.

An example for the dependence of the nanotube resistance on (electrochemical) gate voltage is shown in Fig. 2. A pronounced resistance maximum is seen at $U_g = 1V$, which we identify as the CNP. In order to reach the CNP the Fermi energy must first be raised by ≈ 1 eV. This suggests that the NT is considerably hole-doped at $U_g = 0$. There is, however, a time dependence (not shown).[6] After immersion, the resistance maximum is observed at a smaller voltage of $\approx 0.3\,\mathrm{eV}$. The position of maximum R then gradually moves to larger voltages to finally stabilize at 1 V in this example. Hence, the doping level increases in the electrolyte. Typical Fermi-level shifts in air (before immersion) amount to $0.3 - 0.5$ eV.

Based on measurements of the electrical resistance of SWNTs in a controlled environment of different gases it was suggested that hole-doping is induced by by oxygen.[9] Our own experiments show that oxygen has an effect on the doping state of MWNTs. However, the effect is weak, as much larger doping shifts are seen in ambient air. An example is shown in Fig. 3. Here, we compare the evolution of the resistance of a MWNT at zero (back-) gate voltage when exposed to oxygen and air. Prior to exposure, the NT was annealed at 50 C° in vacuum. As a consequence of added hole doping the resistance is seen to decrease. The decrease is much more pronounced for air than for oxygen. The resistance increases again in vacuum, nicely demonstrating that the oxidizing species are only weakly adsorbed. The strongest source of doping is most likely due to water, as large Fermi-level shifts can be induced by water vapour alone.

For the interpretation of previous electrical measurements, the net doping concentration Q_d and the Fermi-level shift for a 'virgin' MWNT in air are important. Typical values for the latter are $0.3 - 0.5\,\mathrm{eV}$. Comparing this with the average 1d subband spacing $\hbar v_F/2d$ (≈ 33 meV for a 10 nm diameter NT), we conclude that $M = 9 - 15$ subbands may contribute to the conductance instead of 2 for an ideal metallic NT. A doping-induced $E_F = 0.3\,\mathrm{eV}$ corresponds to a doping

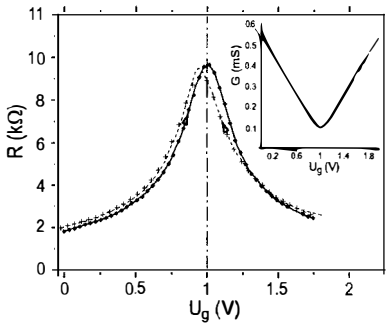


Figure 2: (Left) The typical evolution of the electrical resistance R of a single MWNT with gate voltage U_g measured in a 10 mM $LiClO_4$ electrolyte. Inset: Comparison of $G = 1/R$ (•) with theory (full curve), see Ref. 6.

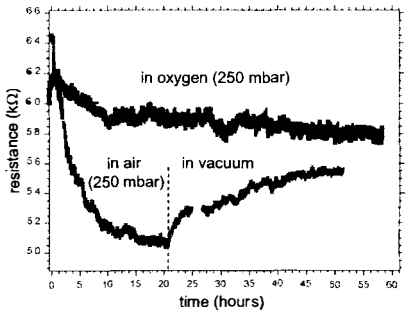


Figure 3: (Right) Doping induced change of the electrical resistance caused by the adsorption of (a) oxygen and (b) air. The nanotube was annealed before exposure. The resistance decrease is caused by increased hole-doping. Air (most likely water vapour) has a much bigger effect than pure oxygen.

concentration of $Q'_d/e \approx 2 \cdot 10^3\,\mu\mathrm{m}^{-1}$, or expressed per surface area to $Q_d/e \approx 0.7 \cdot 10^{13}\,\mathrm{cm}^{-2}$ giving approximately one elementary charge per 500 carbon atoms.

3 Multi-wall carbon nanotubes as quantum dots

As mentioned in the introduction, single-electron tunneling (SET), such as Coulomb oscillations, has not yet been observed in transport through MWNTs, most likely due to the relatively low contact resistances. As a function of gate voltage,[10] and also as a function of magnetic field,[3] pronounced conductance oscillations have been observed. Because these oscillations appear to be aperiodic, they were solely assigned to quantum interference of non-interacting quasi-particles, with the interference being caused by the presence of randomly distributed scatterers. It may be that this interpretation need to be reconsidered, since we have recently observed SET effects in MWNTs.

In order to entangle SET from quantum interference it is useful to measure dI/dV as a function of gate voltage U_g and transport voltage V. The obtained greyscale plots greatly helps to recognize the underlying physics.

In small (semi) isolated objects, like our MWNT devices, transport may be blocked by Coulomb interaction (Coulomb blockade). This is the case, if the energy for adding a single electron to the tube (the single-electron charging energy $e^2/2C$) is larger than the thermal energy kT and if the object is only weakly coupled to external leads (contact resistance $\gtrsim h/2e^2$). Coulomb blockade is suppressed if the energy of two charge states are degenerate. For example, if $E(N) = E(N+1)$, where $E(N)$ denotes the total ground-state energy of the NT with N electrons, an equilibrium current can flow via the sequence $N \rightarrow N+1 \rightarrow N$. Such degeneracies can be induced by the gate voltage U_g and appear in the simplest possible model (constant interaction model) periodic in U_g. In SWNTs Coulomb blockade has been observed by several groups before.[8] Until now, it was believed that MWNTs do not display Coulomb blockade because of low contact resistances. Recently, we have observed clear signatures of single-electron charging in a 300 nm long MWNT (distance between the contacts) with reasonably low-ohmic contacts (i.e. contact resistance $\lesssim h/2e^2$). An example is shown in Fig. 4 ($T = 270\,\mathrm{mK}$). In (a), measured for $B = 0$, a regular sequence is seen consisting of a large 'diamond' followed by three smaller

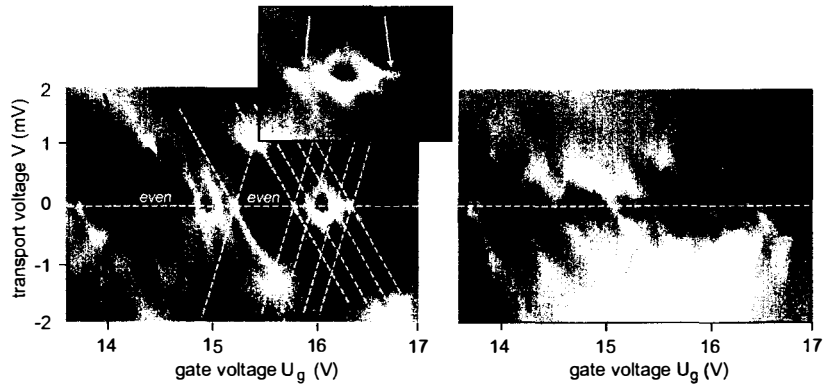


Figure 4: Differential conductance dI/dV as a function of transport voltage V (vertical) and gate voltage V_g (horizontal). White (black) corresponds to high (low) conductance. (a) was measured in zero magnetic field B and (b) in $B = 4\,\mathrm{T}$. The observed pattern is caused by single-electron charging effects. The inset shows a zoomed in portion of (a) in which two horizontal ridges (arrows) of high conductance are seen. These ridges are caused by the Kondo effect.

ones.[d] This pattern suggests a four-fold degeneracy of the single-electron states which we assign to spin degeneracy and an additional twofold orbital degeneracy. The latter may be caused by a peculiar degeneracy inherent to the graphite lattice, the so-called K, K′ degeneracy which originates from the presence of two identical carbon atoms per unit cell. If this interpretation is correct, this is quite amusing, because this basic feature has up to now not been seen in SWNTs.

Fig. 4b shows dI/dV measured at $B = 4\,\mathrm{T}$. Now, an irregular sequence is observed. It is well known that the K, K′ degeneracy is lifted in magnetic-field.

On the one hand, we do see clear signatures of Coulomb blockade suggesting low transparent contacts. On the other hand, the measured two-terminal resistance is low, of order of $h/2e^2$, suggesting highly (or intermediate) transparent contacts. Therefore, higher-order tunneling processes can play an important role in the electrical transport. A well known higher-order tunneling process is the Kondo effect, i.e. the dynamic screening of the spin on the dot due to exchange-correlation effects between the dot state and the electrodes. We observe the Kondo effect in a MWNT for the first time, see the features in Fig. 4., which are highlighted by arrows. At $V = 0$ and within the region of Coulomb blockade there are two 'ridges' of enhanced conductance. For the simplest filling scheme, i.e. $S = 0 \rightarrow 1/2 \rightarrow 0\ldots$, these ridges are expected to form in every second 'diamond' where the spin is $S = 1/2$. The Kondo effect has been observed before in SWNTs.[11]

The data in Fig. 4 allow to extract the single-particle level spacing δE. The large diamonds are large because an electron has to be added to a new level. The addition energy is therefore the sum of charging energy E_c and δE. Due to the fourfold degeneracy, the addition energy for the next three electrons is only E_c. Comparing the energies leads to a mean level spacing of $\delta E \approx 0.4\,\mathrm{meV}$. The 0d level spacing is predicted to be $\delta E = hv_F/2L$ for one mode, yielding $5.5\,\mathrm{meV}$ ($L = 300\,\mathrm{nm}$). The number of modes participating is therefore $M = 5.5/0.4 \approx 14$. Again we see that there are more than 2 modes occupied in MWNTs.[e]

Since the measured two-terminal conductance $G \sim 2e^2/h$,[f] the mean transmission probabil-

[d] For other gate voltages the pattern can look quite different, not resembling SET effects at all.

[e] Note, that we have taken $v_F = 8 \cdot 10^5\,\mathrm{m/s}$ to be constant in this estimate. This might be wrong because of the dispersion of higher subbands, lowering v_F.

[f] $G \approx 2e^2/h$ is a typical value for all our MWNT devices with contact separation $L \approx 300\,\mathrm{nm}$.

ity T per mode is only 0.1 (here, we have taken $M = 10$). If all modes would have $T = 0.1$, co-tunneling effects like the Kondo effects could safely be neglected. Hence, there must be a distribution of transmission eigenvalues similar to that in many-mode diffusive wires. For the latter, random-matrix shows that the distribution is bimodal. Although we are dealing with a very small ensemble (only 10 modes), the distribution of transmission values is most likely bimodal, too. Though there are ≈ 10 modes available to accommodate charge, charge transport to the contacts is determined by only one mode (or a very small number of modes). If the mode with highest transmission probability has the appropriate T (not too low, but also not too high), the Kondo effect will show up.[12] If T is larger, the observed conductance pattern can no longer be assigned to co-tunneling SET effects but rather reflects Fabry-Perot type interference.[13]

4 Conclusion

Multi-wall nanotubes in air are hole doped, most likely induced by the adsorption of water. Consequently, there are more than two 1d-modes occupied. A typical number is 10, not counting spin degeneracy. Estimates for the scattering mean-free path l vary widely in the literature and also among our own experiments. However, surprisingly many experiments suggests that the l is of order of the circumference of the tube. This may be a coincidence, but might also have a deeper reason: It was pointed out very early by White *et al.*[14] that the mean-free path should grow with tube diameter d according to $l \propto d$, provided the number of scatterers per unit length is constant. On the other hand, if we assume that the source of scattering is a direct consequence of doping, the scattering density is proportional to the doping density which for a given environment can be taken to be constant. Therefore, the number of dopants per unit length (or the number of scatterers) grows linearly with d. The combination of both effects results in a diameter independent mean-free path. Another argument for a diameter-independent mean-free path in MWNTs was put forward by Egger and Gogolin.[15]

At low temperature, single-electron tunneling (SET) effects have been observed in MWNTs for the first time. This has allowed to determine the single electron level spacing which appears to be consistent with the estimated number of occupied modes deduced from electrochemical gating. The presence of co-tunneling points to high transmission at the contacts. Even stronger: the prevailing absence of SET effects in MWNTs with $G \sim 2e^2/h$ suggests that at least one highly transmissive channel is present at low temperature.

References

1. for a review, see Physics World, Vol. 13, No. 6, June 2000.
2. A. Bachtold *et al.*, Phys. Rev. Lett. **84**, 6082 (2000).
3. C. Schönenberger *et al.*, Appl. Phys. **A 69**, 283 (1999).
4. S. Frank *et al.*, Science **280**, 1744 (1998).
5. A. Bachtold *et al.*, Nature **397**, 673 (1999).
6. M. Krüger *et al.*, Appl. Phys. Lett. **78**, 1291 (2001).
7. A. Bachtold *et al.*, cond-mat/0012262.
8. S. Tans *et al.*, Nature **386**, 474 (1997); M. Bockrath *et al.*, Science **275**, 1922 (1997).
9. J. Kong *et al.*, Science **287**, 622 (2000); P. G. Collins *et al.*, Science **287**, 1801 (2000).
10. M. Buitelaar *et al.*, to be published.
11. J. Nygard *et al.*, Nature **408**, 342 (2000).
12. J. Nygard and D. Cobden, cond-mat/0105289.
13. W. Liang *et al.*, Nature **411**, 665 (2001).
14. C.T. White and T.N. Todorov, Nature **393**, 240 (1998).
15. R. Egger and A.O. Gogolin, cond-mat/0101246.

ELECTROSTATIC FORCE MICROSCOPY OF ELECTRONIC TRANSPORT IN CARBON NANOTUBES

A. BACHTOLD[1], M.S. FUHRER[2], P.L. MCEUEN[3]

[1]*Department of Applied Physics and DIMES, Delft University of Technology, Lorentzweg 1, 2628 CJ Delft, The Netherlands*

[2]*Department of Physics, University of Maryland at College Park, College Park, MD 20742-4111, USA*

[3]*Laboratory of Atomic and State Physics, Cornell University, Ithaca NY 14853-2501, USA*

We use electrostatic force microscopy to probe the conducting properties of carbon nanotubes at room temperature. Multiwalled carbon nanotubes are shown to be diffusive conductors, while metallic single-walled carbon nanotubes are ballistic conductors over micron lengths.

1 Introduction

Carbon nanotubes are emerging as an excellent system for the investigation of electronic transport in one dimension. Two different classes of nanotubes exist: small diameter (≈1nm) single-wall nanotubes (SWNTs) and large diameter (≈10nm) multi-wall nanotubes (MWNTs). Most of what is known about the transport properties of nanotubes comes from dc electrical measurements of single nanotubes or bundles. These transport experiments suggest that metallic SWNTs are remarkably good conductors, with very long mean free paths [1,2,3]. Doped semiconducting SWNTs, on the other hand, have much higher resistances, and experiments suggest that transport is diffusive[4]. Various experiments on the transport properties of MWNTs have been performed. Experiments with low ohmic contacts attached to MWNTs show interference effects, like Aharonov-Bohm oscillations[5,6], weak localization[6,7] and universal conductance fluctuations[6,7]. These experiments indicate diffusive transport, while others under different experimental conditions show evidence for ballistic transport[8]. A complication for interpreting these experiments is the fact that the measured two-terminal transport characteristics do not uniquely identify the underlying device behavior. The two-terminal resistance is the sum of the contact resistance R_c and the intrinsic resistance R_i. It is unclear from previous experiments the degree to which each of these two contributions affects the measured conductance. Four-terminal measurements can, in principle, alleviate the effects of the contacts, but typical macroscopic electrodes act as invasive probes that influence the resistance of the object studied. Here we use electrostatic force microscopy (EFM)[9] to directly probe the nature of conduction in nanotubes and to compare the electronic properties of metallic SWNTs with those of MWNTs. By using an atomic force microscope (AFM) tip as a local voltmeter (EFM), we separately measure the intrinsic resistance and contact resistances of SWNTs and MWNTs. We show that in metallic SWNTs the measured resistance is due to contact resistance, i.e., electron transport is ballistic. Furthermore, measurements on MWNTs show that they are diffusive conductors with a typical resistance per length of 5-10 kOhm/μm.

2 Experimental methods

Samples are fabricated on a backgated substrate consisting of degenerately doped silicon capped with 1 μm SiO_2. SWNTs synthesized via laser ablation are suspended in dichloroethane, and the resulting suspension is placed on the substrate for approximately 15 seconds, then washed off with isopropanol. An array of structures, each consisting of two Cr/Au electrodes, is fabricated using electron beam lithography. Samples that have a measurable resistance between the electrodes are selected. An AFM is then used to choose samples that have only one nanotube rope

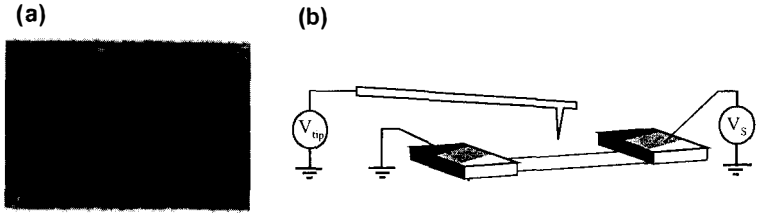


Figure 1: (a) Topographic AFM image of a 2.5 nm diameter bundle of SWNTs which is seen spanning between two gold electrodes. The separation between the electrodes is 1 μm. (b) Experimental setup for EFM. A conducting AFM cantilever is scanned above the device, which consists of a nanotube contacted by two gold electrodes.

between the electrodes. Objects whose height profile is consistent with single SWNTs (1-2 nm) are preferentially selected. An example of a SWNT rope contacted by two electrodes is shown in Fig. 1(a). Since the success of this contacting scheme works by chance, it is obvious that the yield is low. However, since a large array of structures can readily be fabricated, this scheme has turned out to be very convenient.

The MWNTs were synthesized by arc-discharge evaporation and deposited from a dispersion in chloroform onto an oxidized Si wafer. Nanotubes with diameter ranging from 8 to 17nm are selected and located using AFM. Gold contacts to the tube are then created using e-beam lithography.

We continue by reviewing the EFM technique [9]. An AFM tip with a voltage $V_{\rm tip}$ is scanned over a nanotube sample, see Fig. 1(b). The electrostatic force between the tip and the sample is given by

$$F = \frac{1}{2}\frac{dC}{dz}(V_{\rm tip} + \phi - V_s)^2 \,, \tag{1}$$

where V_s is the voltage within the sample, ϕ is the work function difference between the tip and sample, and C is the tip-sample capacitance. The tip is held at constant height above the surface by first making a line-scan of the topography of the surface using intermittent-contact AFM, and then making a second pass with the tip held at a fixed distance above the measured topographic features. In order to detect the electrostatic force, the cantilever is made to oscillate by an AC potential that is applied to the sample at the resonant frequency of the cantilever. This produces an AC force on the cantilever proportional to the local AC potential $V_s(w)$ beneath the tip:

$$F_{ac}(w) = \frac{dC}{dz}(V_{\rm tip} + \phi)\, V_s(w) \,. \tag{2}$$

The resulting oscillation amplitude is recorded using an external lock-in amplifier; the signal is proportional to $V_s(w)$. Calibration of this signal is made by applying a uniform $V_s(w)$ to the whole sample and measuring the response of the cantilever.

EFM yields a signal that is proportional to the local voltage within the nanotube circuit. However, the signal is also proportional to the derivative of the local capacitance. This will vary as the geometry changes, yielding e.g. different signals over a nanotube than over a contact at the same potential. However, dC/dz does not vary appreciably as a function of distance along the nanotube. The measured signal reflects accurately the local voltage within the nanotube.

In the EFM measurements, there is a background signal due to stray capacitive coupling of the tip to the large metal electrodes. We have developed a technique for subtraction of the background signal from the image, which is described in details in Ref. 10.

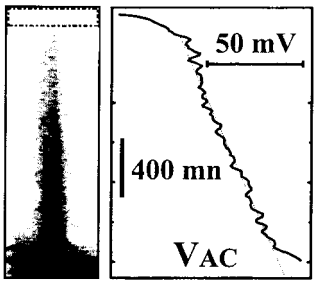


Figure 2: EFM image of a MWNT of diameter 9 nm. The resistance of the entire circuit is 30 kΩ . An ac bias of 100 mV is applied to the lower electrode; the IV characteristic verified that this bias was within linear response. A trace of the potential as a function of the nanotube length is also shown.

3 Results

Figure 2 shows an EFM measurement of a typical arc-produced MWNT with a diameter of 9 nm and a two-terminal resistance of 30 kΩ . The ac voltage is applied to the lower contact while the upper contact is grounded. The EFM signal drops uniformly along the MWNT length. This is verified in a line scan of the voltage along the tube length [shown in the right side of Fig. 2]. The linear voltage drop indicates that the tube behaves as a diffusive conductor with a well-defined resistance per unit length, $R_i = 10$ kOhm/μm. This confirms the results from previous transport[6] and scanned contact[11] measurements of MWNTs. The total contact resistances are measured to be approximately 15 kΩ. We note that the conductance of the tube has been controlled to not change when the tip scans over it. This indicates that the tip did not significantly perturb the conducting properties of the sample.

Next we discuss measurements of the metallic SWNT device shown in Fig. 1. The resistance of this 2.5 nm diameter bundle is 40 kΩ and has no significant gate voltage dependence. We have also measured the current at large biases – the current saturates at 50 μA. This is in agreement with the work by Yao, Kane and Dekker [12] where the current was observed to be limited to 25 μA per metallic nanotube due to optical or zone-boundary phonon scattering. We therefore conclude that the current is carried by two metallic SWNTs in the bundle.

Figure 3 shows the EFM image of this SWNT bundle, as well as a line trace along the backbone of the bundle. The potential is flat over its length, indicating that within our measurement accuracy there is no measurable intrinsic resistance. Taking into account the finite measurement resolution, we estimate that R_i of the bundle is at most 3 kΩ. The contact resistances are measured to be approximately 28 kΩ and 12 kΩ for the upper and lower contacts, respectively. The conductance of the tube has been controlled to no change when the tip scans over it.

Using the four-terminal Landauer formula, $R = (h/4e^2)(1 - T_i)/T_i$ per nanotube, where T_i is the transmission coefficient for electrons along the length of the nanotube, we find that T_i is larger than 0.5. This indicates that the majority of electrons are transported through the bundle with no scattering. Therefore transport is ballistic at room temperature over a length of $> 1\mu$m. This confirms the theoretical predictions of very weak scattering in metallic SWNTs [13,14]. This is also in agreement with previous low-temperature transport measurements which indicate that long metallic SWNTs may behave as single quantum dots[1,2], and room-temperature measurements of metallic SWNTs which sometimes exhibit low two-terminal resistance [3]. The dominant portion of the overall resistance of 40 kΩ thus comes from the contacts, indicating that the transmission coefficients for entering and leaving the bundle are significantly less than one and the contacts are not ideal.

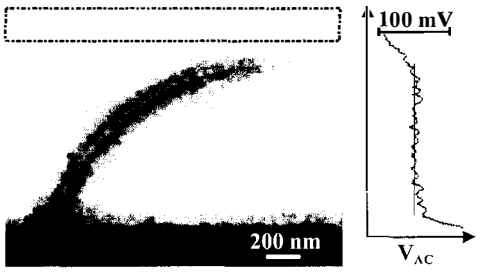


Figure 3: EFM image of the same bundle of SWNTs shown in Fig. 1. An AC potential of 100 mV is applied to the lower electrode. The upper electrode indicated by the box is grounded. The AC-EFM signal is flat along the length of the SWNT bundle, indicating that the potential drops occur at the contacts, and not along the bundle length. A trace of the potential as a function of vertical position in the image is also shown.

4 Conclusion

In conclusion, we have used electrostatic force microscopy to measure the properties of current-carrying nanotube circuits at room temperature. We can separately determine the contact resistances and intrinsic nanotube resistances. MWNTs are shown to be diffusive conductors, while metallic SWNTs are shown to be ballistic over micron lengths. In Ref[10], the transport properties of semiconducting SWNTs have been studied combining EFM with scanned gate microscopy. The conduction has been shown to be limited by a series of barriers that can be located along the tube.

Acknowledgments

We thank A. Rinzler and R. E. Smalley for supplying the nanotube materials. This work was supported by DOE (Basic Energy Sciences, Materials Sciences Division, the sp2 Materials Initiative) and by DARPA (Moletronics Initiative).

References

1. S.J. Tans, M.H. Devoret, H. Dai, A. Thess, R.E. Smalley, L.J. Geerligs, C. Dekker: Nature **386**, 474 (1997)
2. M. Bockrath, D. Cobden, P. McEuen, N. G. Chopra, A. Zettl, A. Thess, R.E. Smalley: Science **275**, 1922 (1997); D.H. Cobden, M. Bockrath, P.L. McEuen, A.G. Rinzler, R. Smalley: Phys. Rev. Lett. **81**, 681 (1998)
3. H.T. Soh, A.F. Morpurgo, J. Kong, C.M. Marcus, C.F. Quate, H. Dai: App. Phys. Lett. **75**, 627 (1999)
4. R. Martel, *et al.*, Appl. Phys. Lett. **73**, 2447 (1998).
5. A. Bachtold, *et al.*, Nature **397**, 673 (1999).
6. C. Schönenberger, *et al.*, Appl. Phys. **A 69**, 283 (1999).
7. L. Langer, *et al.*, Phys. Rev. Lett. **76**, 479 (1996).
8. S. Frank, P. Poncharal, Z.L. Wang, W.A. de Heer: Science **280**, 1744 (1998).
9. Y. Martin, D.W. Abraham, H.K. Wickramasinghe: Appl. Phys. Lett. **52**, 1103 (1988); J.E. Stern *et al.*: Appl. Phys. Lett. **53**, 2717 (1988); C. Schönenberger, S.F. Alvarado: Phys. Rev. Lett. **65**, 3162 (1990)
10. A. Bachtold, M. Fuhrer, S. Plyasunov, M. Forero, E.H. Anderson, A. Zettl, P.L. McEuen: Phys. Rev. Lett. **84**, 6082 (2000)

11. H. Dai, E. W. Wong, and C. M. Lieber, Science **272**, 523 (1996).
12. Z. Yao, C.L. Kane, C. Dekker: Phys. Rev. Lett. **84**, 2941 (2000)
13. C.T. White, T.N. Todorov: Nature **393**, 240 (1998)
14. M.P. Anantram, T.R. Govindan: Phys. Rev. B **58**, 4882 (1998); T. Ando, T. Nakanishi, R. Saito: J. Phys. Soc. Jpn. (Japan) **67**, 2857 (1998)

1/f NOISE IN CARBON NANOTUBES

Henk W.Ch. Postma, Tijs F. Teepen, Zhen Yao[a], Cees Dekker
Department of Applied Physics and DIMES, Delft University of Technology, Lorentzweg 1, 2628 CJ Delft, The Netherlands

The low-frequency electronic noise properties of individual single-wall metallic carbon nanotubes are investigated. The noise exhibits a $1/f$ frequency dependence and a V^2 voltage dependence. The noise power at 8 K appears to be three orders of magnitude smaller than at 300 K. As a demonstration of how these noise properties affect nanotube devices, a preliminary investigation of the noise characteristics of a fabricated intramolecular carbon nanotube single-electron transistor is presented.

The electronic properties of carbon nanotubes have attracted a lot of interest in both fundamental as well as application-driven studies.[1] Almost all of these studies focussed on the DC electronic properties, and little is known about the AC or noise properties. Only recently, the noise characteristics of carbon nanotubes have become the subject of investigation. The first measurements show that the low-frequency electronic noise is dominated by $1/f$ noise.[2,3] Many issues remain unclear, however, for example, how the noise power depends on temperature. Knowledge of the noise characteristics is important to characterize performance of nanotube devices. The study of the fluctuation phenomena will also enable one to examine, for instance correlation-induced reduced shot noise[4] in Luttinger liquids or bunching/anti-bunching-type phenomena that probe the quantum statistics[5,6] of electrons in nanotubes. Here, we report a characterization of the low-frequency electronic noise properties of individual metallic single-wall carbon nanotubes. The frequency dependence follows Hooge's law. Upon lowering temperature to 8 K, the noise power is reduced by three orders of magnitude. As an example of how this low-frequency noise affects the performance of nanotube devices, we study the charge sensitivity of an intramolecular carbon-nanotube single-electron transistor.

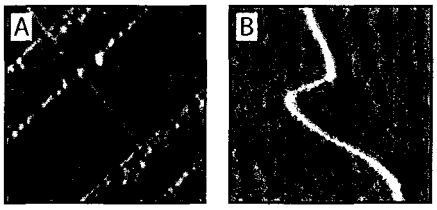


Figure 1: Atomic force microscope amplitude images of metallic carbon nanotubes. **a)** A straight nanotube connected by two Au electrodes lying on a SiO_2 surface. The image is 1 μm^2. **b)** A metallic nanotube with two buckles which have been induced with the atomic force microscope. The image size is 100×100 nm^2.

Individual carbon nanotube samples are fabricated as described before.[7] Figure 1a shows an example of a straight nanotube, connected by metallic electrodes. On such samples we have characterized the amount of $1/f$ noise present in nanotubes. In Fig. 1b, a double-buckle nanotube is shown. We recently reported that these devices act as room-temperature single-electron transistors.[8] Here we present a first analysis of its noise properties and discuss the charge sensitivity of such devices.

The noise power spectral density has been measured for individual nanotubes as a function of the DC current I_{DC} at room temperature (Fig. 2). At $I_{DC} = 0$, the voltage noise is

[a]Present address: Department of Physics, The University of Texas at Austin, Austin, TX 78712, USA

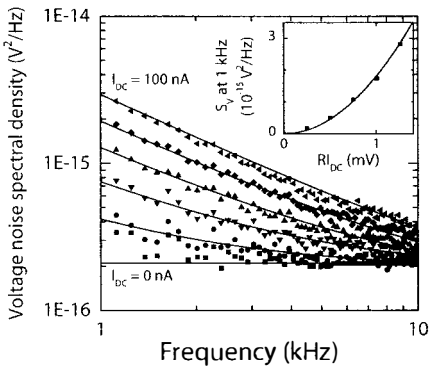


Figure 2: Noise spectra at $T = 300$ K for a nanotube with resistance $R = 12.6$ kΩ for various DC currents from 0 to 100 nA. The white noise visible at low I_{DC} is the expected thermal or Johnson-Nyquist noise of the sample $S_{V,JN} \equiv 4k_BTR = 2.1 \times 10^{-16}$ V^2/Hz, where k_B is Boltzmann's constant. The deviations from $1/f$ spectra at low current are due to $1/f$ noise from the amplifiers. The solid lines are fits with the function $S_V = S_{V,JN} + B/f$. The inset shows the excess $1/f$ noise at 1 kHz versus DC voltage $V_{DC} = RI_{DC}$. From the fit (solid line) we obtain $B = AV_{DC}^2 = 1.8 \times 10^{-6}V_{DC}^2$. The same value for A is found in voltage-biased measurements of the current noise $S_I = S_{I,JN} + AI_{DC}^2/f$, where $S_{I,JN} \equiv 4k_BT/R$.

white, i.e., it does not depend on frequency, and equals the expected value for thermal noise $4k_BTR = 2.1 \times 10^{-16}$ V^2/Hz of the nanotube, where $R = 12.6$ kΩ for this device. With increasing current, additional noise appears, which exhibits a $1/f$ frequency dependence. These two noise powers appear to add incoherently, i.e., $S_V = 4k_BTR + B/f$. The current dependence is studied in the inset to Fig. 2, where it is found that $B = AV_{DC}^2$.[9] The proportionality constant A thus found describes the full current and frequency dependence. All of these results are qualitatively consistent with the phenomenological dependence known as Hooge's law.[10]

As postulated by Hooge, A depends on the number of charge carriers in the conductor N through $A = \gamma/N$, where $\gamma \approx 2 \times 10^{-3}$.[11] Although it is now understood that the γ value is not universal, it is a good starting point to compare the magnitude of noise in nanotubes to that in bulk conductors described by Hooge's law. The nanotubes described here contain about 2000 conduction electrons.[12] Using the magnitude of A found above, we find $\gamma_{nanotubes} \approx 4 \times 10^{-3}$. Earlier, Collins *et al.* found that this number was about 2 orders of magnitude larger.[2] Our material, however, shows much less noise and is in fact quite a low-noise conductor.

The temperature dependence of the $1/f$ noise is displayed in Fig. 3. With the current and frequency dependence given above, it suffices to display the value of A. It appears that the noise is reduced in a monotonous way by three orders of magnitude upon lowering the temperature. This has been measured in many individual nanotube samples that we have studied.

In the commonly employed model for $1/f$ noise, it is assumed that fluctuating two-level systems in the surrounding give rise to a fluctuating potential profile, which leads to this low-frequency noise.[10] Within this model it is reasonable that a reduction of the temperature will lead to reduction of the noise, since at lower temperatures these two-level systems will freeze into local energy minima. The chemical stability, high degree of regularity and detailed knowledge of the electronic and mechanical structure of carbon nanotubes provide the right ingredients to study the origin of $1/f$ noise in detail. This, however, is beyond the scope of this brief report.

As an example of how the low-frequency noise affects the performance of a nanotube device, we have studied the noise properties of the double-buckle sample in Fig. 1b. In these samples, the addition of a single electron to the island between the two buckles costs a large energy due to the Coulomb charging of the island.[14] When the thermal energy k_BT is smaller than

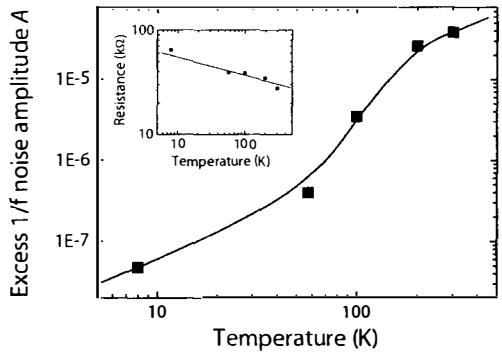


Figure 3: Excess $1/f$ noise power versus temperature for a single carbon nanotube. Plotted is the proportionality constant A of the $1/f$ noise spectral density $S_V = AV_{DC}^2/f$ as obtained from an analysis of the voltage and frequency dependence as is shown in Fig. 1. The inset shows the temperature dependence of the resistance of the nanotube. The lines are guides to the eye.

this charging energy, current is blocked. The blockade can be lifted, however, by increasing the electrostatic potential of the nanotube by means of a nearby conducting gate. Current can then flow. If the gate voltage is increased further, however, current is again blocked. This leads to a series of current peaks as a function of gate voltage, see Fig. 4a. The noise at 10 Hz has been measured versus gate voltage. Again peaked features are observed, see Fig. 4b. To characterize the performance of such a single-electron transistor, one determines how accurately charge on the gate can be measured. Thus, the measured current noise $\sqrt{S_I}$ is divided by the gate voltage sensitivity (dI/dV_g), and multiplied by the gate capacitance to obtain the so-called input equivalent charge noise $q_{noise} = C_g\sqrt{S_I}/(dI/dV_g)$, which is being displayed in Fig. 4c.[15] It diverges periodically (with a period twice as small as the distance between current peaks), every time the gate voltage sensitivity vanishes. In between, it reaches its optimum value of $2 \times 10^{-3}e/\sqrt{\text{Hz}}$ at the gate voltage indicated by the vertical dashed lines. This compares favorably to values $q_{noise} \approx 0.5 \times 10^{-3}$ e/$\sqrt{\text{Hz}}$ for conventional single-electron transistors which operate at mK temperatures,[16] because the data on the nanotube device are obtained at 60 K and the noise is reduced considerably as a function of temperature (see above).

We conclude with an estimate of the measurement bandwidth needed to observe shot noise $S_I = 2eI_{DC}$, which is a good approximation of the bandwidth needed to observe reduced shot noise or bunching/anti-bunching type effects. For this estimate we – optimistically – assume that samples may be fabricated with a 10 kΩ resistance and a $1/f$ noise power amplitude $A \approx 10^{-8}$ and we focus on the properties at 4 K. For simplicity we assume that all the amplifier noise can be reduced sufficiently such that only the thermal noise of the sample (2.2×10^{-26} A^2/Hz) dominates at low current. The total noise may then be written as $S_I = 4k_BT/R + 2eI_{DC} + AI_{DC}^2/f$. For the observation of shot noise, we obviously require that $\eta = (4k_BT/R + AI_{DC}^2/f)/2eI_{DC} < 1$, from which we deduce two boundary conditions for $I_- < I_{DC} < I_+$. At low current $I_{DC} < I_- \approx 4k_BT/\eta 2eR$, the thermal noise dominates, whereas at high current $I_{DC} > I_+ \approx 2ef\eta/A$ the $1/f$ noise dominates. Finally we require that $I_+ \gg I_-$ since one needs to observe the current dependence of the shot noise. If an experimental uncertainty of 10 % is sufficient ($\eta = 1/10$) and $I_+/I_- = 10$, we find $f > 2.2$ MHz. This frequency range is not accessible with our current setup, but is certainly accessible with a dedicated setup.

We thank R.E. Smalley and coworkers for the carbon nanotube material, A. Morpurgo for discussions, and B. van den Enden and R. Schouten for technical assistance. This work is supported by the Dutch Foundation for Fundamental Research on Matter (FOM) and the European

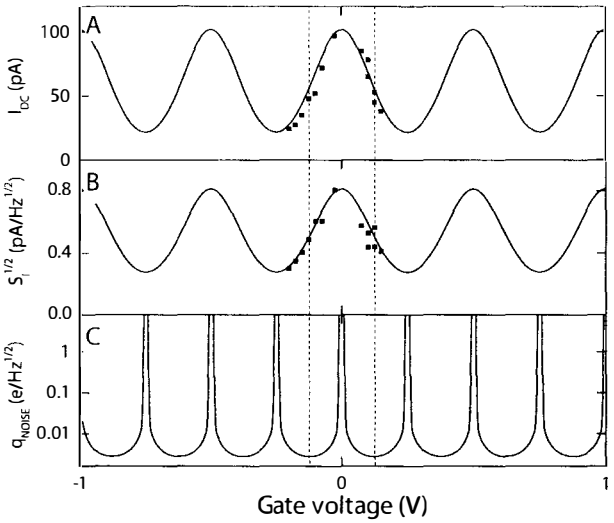


Figure 4: Noise characteristics of the carbon nanotube single-electron transistor shown in Fig. 1b at 60 K and 10 Hz. Both current and current noise depend on the gate voltage as is visible in *a* and *b*. Both are fit (solid lines) with a superposition of Coulomb conductance peaks.[13] In *c*, the results of these fits are used to determine the input equivalent charge noise of the device.

Community SATURN project.

References

1. C. Dekker, *Physics Today* **52 (5)**, 22 (1999).
2. P.G. Collins, M.S. Fuhrer, and A. Zettl, *Appl. Phys. Lett.* **76**, 894 (2000).
3. L. Roschier, R. Tarkiainen, M. Ahlskog, M. Paalanen, and P. Hakonen, *Appl. Phys. Lett* **78**, 3295 (2001).
4. R. De-Picciotto *et al.*, *Nature* **389**, 162 (1997).
5. M. Henny *et al.*, *Science* **284**, 296 (1999).
6. W.D. Oliver, J. Kim, R.C. Liu, and Y. Yamamoto, *Science* **284**, 299 (1999).
7. Z. Yao, H.W.Ch. Postma, L. Balents, and C. Dekker, *Nature* **402**, 273 (1999).
8. H.W.Ch. Postma, T.F. Teepen, Z. Yao, M. Grifoni, and C. Dekker, *Science* **293**, 76 (2001).
9. It is often convenient to assume that $S_{V,1/f} \propto V^2/f$ or $S_{I,1/f} \propto I^2/f$. In general, however, it is found that $S_{1/f} \propto V^{2+\alpha}/f^{1+\beta}$, where $|\alpha| \ll 1, |\beta| \ll 1$ are material dependent numbers. Here, we assume $\alpha = \beta = 0$.
10. P. Dutta and P.M. Horn, *Rev. Mod. Phys.* **53**, 497 (1981).
11. F.N. Hooge, *Phys. Lett. A* **29**, 139 (1969).
12. This estimate is for this nanotube with a length of 500 nm. We did not perform a systematic study of the $1/N$ dependence.
13. C.W..J. Beenakker, *Phys. Rev. B* **44**, 1646 (1991).
14. H. Grabert and M. Devoret (eds) in *Single Charge Tunneling* (Plenum, New York, 1992).
15. Please note that while $eV_{DC} \ll k_BT$, both the current noise and the DC current depend on bias voltage through the relations $I_{DC} \propto V_{DC}$ and $\sqrt{S_I} \propto V_{DC}$, so the bias voltage dependence of q_{noise} cancels.
16. A.B. Zorin *et al.*, *Phys. Rev. B* **53**, 13682 (1996).

TUNNELING INTO RESISTIVE MULTIWALLED CARBON NANOTUBES

R. TARKIAINEN, M. AHLSKOG, L. ROSCHIER, P. HAKONEN, and M. PAALANEN
Low Temperature Laboratory, Helsinki University of Technology, FIN-02015 HUT, Finland

We have studied electron tunneling between CVD-grown multiwalled carbon nanotube and gold contact in 2-lead and 4-lead measurement geometries with wide contact pads. We have compared the observed zero bias anomaly in tunneling conductance with the predictions of Luttinger liquid, 1D diffusion and coherent conductor models. We will discuss the validity of different models and the implications of their fitting parameters.

1 Introduction

Carbon nanotube is an interesting realization of one dimensional electrical conductor [1,2]. It is made out of long coaxial cylinders of graphene sheets which are decoupled from each other but conduct along their axis. The electrical properties of a single cylinder can be derived from the band structure of graphite and one finds both metallic and semiconducting behavior. As in ordinary semiconductors, one can also manipulate the conductivity of carbon nanotubes by doping.

In a truly one dimensional conductor electron backscattering, which requires a large momentum change, is a relatively rare event. In addition, one can apparently quite easily produce nearly defect free single walled nanotubes with low intrinsic impurity concentration. Consequently, one expects SWNTs to be exellent 1D conductors with nearly ballistic electron motion. Several experiments support this picture[3,4,5,6]. SWNTs are found to carry high current densities at higher voltages. Also, tunneling experiments with SWNTs can be explained with the Luttinger liquid model [7,8] which is valid for ballistic, strongly interacting electron gas [9,10,11]. The conductance of an ideal 1D conductor should also be quantized. For undoped metallic SWNTs, containing 4 independent conduction channels, the value of the quantized conductance is expected to be $4e^2/h$. However, accurate measurement of this value requires ideal low ohmic contacts, which have turned out to be difficult to make. A clean metal-nanotube interface acts as a tunneling barrier which, however, is useful for studying single electron density of states of the nanotubes[7].

Electrical properties of multiwalled nanotubes are somewhat less understood [12]. Role of inner layers, number of conducting channels, disorder strength, and carrier concentrations in these samples can vary over a wide range and are hard to control experimentally. The inner cylinders are capacitively coupled to the outer layer and participate only in the high frequency conductivity. Compared to single walled nanotubes, the larger diameter and screening by inner layers is expected to reduce electron-electron and presumably also electron-impurity scattering in the MWNTs. Otherwise, the electrical properties of MWNTs and SWNTs should be quite similar. Recent magnetoresistance measurements have confirmed that only the outermost graphene cylinder conducts but the mean free path of the electrons is quite short, less than 100 nm [13,14]. Presumable, high quality MWNTs are more difficult to produce than SWNTs and have a higher defect density per unit length. Also, the unmatched lattices of the inner layers may act as intrinsic scattering potential for electrons on the outermost layer. Due to large scattering the Luttinger liquid model is not expected to work well for MWNTs.

In this work we have studied tunneling density of states for CVD-grown multiwalled nanotubes by measuring the conductance of gold-nanotube tunnel junctions. After tunneling the electron has to penetrate Coulomb barrier, a time-dependent self energy which reduces the tunneling probability [15,16]. The self-energy has maximum value just after the tunneling and decreases as soon as the electron charge is redistributed in the nanotube. Thus, the tunneling density of states is a direct measure of the impedance of the nanotube. The impedance of ballis-

tic and diffusive nanotubes can be obtained from the impedance of inductive (LC) and resistive (RC) transmission lines, respectively.

2 Sample Preparation

We have prepared three over 2 μm long nanotube samples for the conductivity measurements. The nanotubes, grown by chemical vapour deposition (CVD), were multiwalled, with an initial diameter of about 18 nm. Compared to the arc discharge (AD) grown nanotubes, the CVD tubes have more curvature and bends, implicating a higher density of structural defects. These defects may act as scattering centers and increase the resistance of the tubes.

One of the nanotubes, later named as CVD sample, was deposited across two pre-evapored gold contacts. The two other samples, RIE1 and RIE2, were first deposited on the substrate and reactive ion etched down to a diameter of 10 nm, before the evaporation of the gold leads. Normally, one expects the RIE treatment to damage conducting samples and increase their resistance. The evaporation of contact metal on the top of the nanotube may have a similar effect. In addition, metals and nanotubes have usually different electron work functions which may lead to considerable doping of the nanotube by the contact metal. In case of gold, the contact doping is expected to be p-type.

The metal-nanotube contacts are tunnel junctions, whose microscopic structure is not well understood. However, our long junction may be parametrized by a distributed tunneling conductance and capacitance of the order of 100 μS/μm and 100 aF/μm, respectively. These values are valid for contacts formed on the top of the metal by the van der Waals force. A larger conductance and capacitance can be expected for junctions buried inside or under the metal. In case of single walled nanotubes, large differences have been detected between the top and buried contacts [7]. All our junctions were about 1 μm long and the gold electrodes were separated by a narrow gap (Fig. 1). Consequently, our resistance measurements are probing the properties of the nanotube in close contact with the gold.

3 Results

The samples were cooled down in a dilution refrigerator and their I *vs* V and conductance G *vs* V curves were measured from -100 to 100 mV from liquid He temperature down to 130 mK. In our 2-lead measurement geometry with wide contact pads, the resistance of the sample contains series resistance of the two long tunneling contacts. In the following analysis we will assume identical contacts, which dominate the resistance, and compare our data with the predictions of Luttinger liquid [17,18,19] and diffusive conductor models [20,21,22]. The resistance measured in 4-lead geometry is assumed to be dominated by the resistance of the nanotube, and these results will be compared with the coherent conductor model [23,24].

A clean interacting 1D electron gas is expected to behave like a Luttinger liquid (LL). A Fermi liquid has single electron excitations moving with the Fermi velocity v_F. In contrast, due to the repulsive e-e interaction, the low energy excitations of a LL are plasmawaves whose velocity $v_{pl} > v_F$. For our tunneling geometry, so called bulk tunneling geometry, the tunneling conductance is predicted to have a zero bias suppression $G \propto V^{\alpha}$ where $\alpha = (v_{pl}/v_F + v_F/v_{pl} - 2)/2M$, and M the number of independent conduction channels in the nanotube [10,11,7]. If the nanotube is modeled as an LC transmission line then $v_{pl} = 1/\sqrt{lc}$, where l and c are the kinetic inductance and effective capacitance per unit length, respectively [19]. Thus, the zero bias anomaly is a sensitive function of e-e interactions (v_{pl}), doping level of the nanotube (v_{pl}, M) and the capacitance of the junction (c).

In Figure 1 we have tested our low temperature ($eV >> k_BT$) conductance data against the LL model, which predicts a linear $\ln G$ *vs* $\ln V$ dependence. For a single tunnel junction in a finite

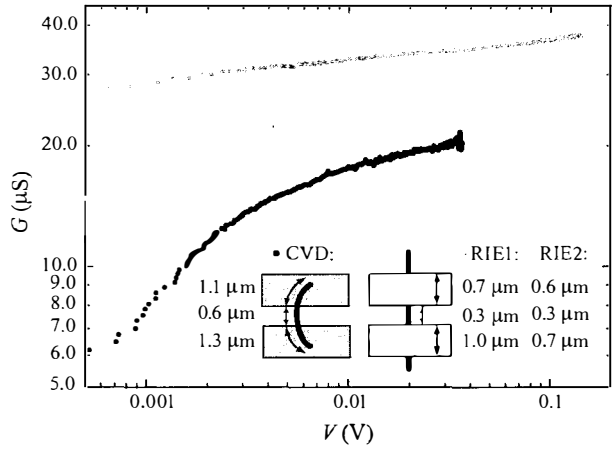


Figure 1: Test of Luttinger liquid model for three CVD-grown samples in low temperature limit $eV > k_BT$. According to the Luttinger liquid theory, $\ln G \propto \alpha \ln V$ above the plasmon energy at $eV \sim 2$ meV for two tunnel junctions in series. At higher voltages the model is limited by the lowest transverse mode of the nanotube at about 120 mV for RIE1 and RIE2 and 70 mV for the CVD-grown sample. Linear behavior is observed at higher voltages, but with unexpectedly small values of exponent α.

length nanotube, the LL model is expected to be valid over an energy interval from the plasmon energy $eV = \hbar v_{pl}/2L = 1$ meV to the lowest transverse mode energy $eV = \hbar v_F/\pi\phi = 60$ meV. These values are calculated for a tube whose lenght $L = 1$ μm, diameter $\phi = 10$ nm, $v_F = 8 \cdot 10^5$ m/s and $v_{pl} = 3 \cdot 10^6$ m/s. Our data is not linear over the predicted voltage window. If we, however, extract an exponent α at the highest voltages, it turns out to be 0.05 - 0.15, an unexpectedly small number. One might explain the small values of α by a high value of capacitance c of the gold-nanotube tunnel junction or by a high carrier concentration (large M) of the part of the nanotube which is in contact with the gold, *i.e.* by a strong doping effect of the gold. Also, strong tunneling effects may reduce the values of α. In contrast to the SWNT tunneling measurements[7], our α values are larger for the top contact than for the buried contact. Also, the increase of the α values with increasing tube diameter, *i.e.* with increasing number of conduction channels, is hard to understand.

Due to high anticipated resistance of the CVD tubes, it is natural to test our data against the predictions of the 1D diffusion model[20,22]. In this model, the leading low temperature correction to the tunneling conductance is proportional to $-\sqrt{V_o/V}$. This prediction is tested in Fig. 2 by plotting $\ln G(V)$ against $1/\sqrt{V}$. According to Fig. 2, $G(V) = G_o \exp(-\sqrt{V_o/V})$, which actually goes beyond the leading order prediction of the diffusion model and deviates from recent higher order predictions in Refs. 16 and 21. The parameter $V_o = (r/R_K)(e/\pi c)$ can be determined from the linear fits in Fig. 2[22]. In this formula the resistance quantum $R_K = h/e^2$. Assuming that $c = 100$ aF/μm for the top and and 300 aF/μm for the buried contact, we obtain quite reasonable values of 5 - 30 kΩ/μm for the line resistance r. Interestingly, the RIE treatment seems to reduce r which may indicate that the RIE is removing complete layers at once and the inner layers have less structural defects.

The demarcation line between 1D and 2D diffusion models is located at tunneling energy $eV = \hbar D^\star/(\pi\phi)^2 > 100$ meV for all our tubes[22]. The dimensionality of the sample is determined by $D^\star = 1/rc \sim .1{-}1$ m^2/s, the diffusion constant of the electric field rather than by D, the diffusion constant of single electrons. At lower voltages $eV < \hbar D^\star/(L/2)^2 \sim 3$ meV the diffusion

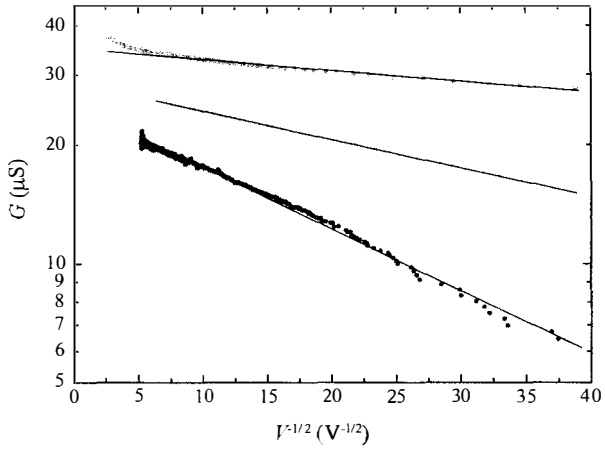


Figure 2: Test of 1D-diffusion model at low temperatures $eV >> k_BT$. The diffusion model fits the data of all three nanotubes over a wide voltage range with reasonable fitting parameters.

model breaks down and should be replaced by the coherent conductor model[23]. Except for the RIE1 sample at high voltages, the diffusion model gives an excellent fit to our data over a wide voltage range. The small upward curvature in the RIE1 data could be explained either by a V^3 correction to the tunneling probability or by the closeness of the lowest transverse mode at V = 120 mV (2 x 60 mV).

In an ideal 4-lead geometry one is measuring the resistance of a sample between narrow voltage contacts, *i.e.* without the contact resistances. The fact that the zero bias anomaly is also visible in our 4-lead measurement may result from the zero bias anomaly in the 1D conductivity of the nanotube[20,23] or, in our long contact geometry, from the tunneling of electrons through the low ohmic path, provided by the voltage leads. In the following we will assume the previous case and analyze our results with the coherent conductor model[23]. In this model the zero bias anomaly of a 1D conductor, containing several parallel conduction channels with transmission coefficients T_i and total resistance $R = h/e^2\Sigma T_i$, results from the e-e interactions. The interactions are parameterized by a phenomenological Coulomb energy E_c. This model has several restrictions which may not be fulfilled for our samples. The conductor is assumed to be shorter than the coherence length of diffusing electrons, and isolated from the voltage source by a shunt resistance R_s. The model works only in the high conductance limit of $g_0 = R_K/R + R_K/R_s >> 1$, and for max $(eV, k_BT) > g_0E_c\exp(-g_0/2)$. At the same time the measuring voltage cannot exceed the Thouless energy of $eV = \hbar D/L^2$.

The coherence length requirement can presumably be fulfilled at our lowest measurement temperatures. In our samples the tunneling resistors act as R_s, but unfortunately we cannot determine their values independently. Despite of these shortcomings, we have tested the model in Figure 3 for RIE2 sample in 4-lead geometry. A reasonable fit to our data is found with the parameters R = 34.5 kΩ, R_s = 5 kΩ, g_0 = 5.9, $\beta = \Sigma T_i(1 - T_i)/\Sigma T_i$ = 0.1 and E_c = 109 K. However, the fit is obtained in the low temperature and low voltage limit $(eV, k_BT) < g_0E_c\exp(-g_0/2)$, where the theory is not supposed to work. The parameters turn out to be quite reasonable except that the value of β is too small and the Coulomb energy far too large. For a diffusive 1D conductor β is expected to be 0.33.

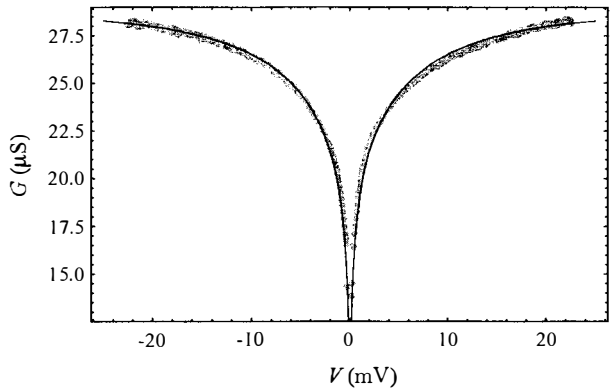


Figure 3: Test of coherent conductor model in RIE2 at $T = 130$ mK. This model fits the conductivity data quite well up to about 20 mV but fails, as expected, at higher voltages. However, the fitting parameters of this model turn out to be somewhat unphysical.

4 Summary

A nanotube can be modelled as an inner conductor of a transmission line whose outer conductor is formed by nearby metallic objects. In an usual measurement geometry, the ends of a nanotube are in short tunnelling contact with metallic pads while the long middle section rests on a semiconducting substrate, resulting in capacitance, electron density and ultimately impedance variations along the nanotube. The impedance and its variations can be studied by measuring the voltage dependent tunneling conductance of the contacts.

We have studied conductance of three CVD grown multiwalled nanotubes in 2-lead and 4-lead measurement geometries, with wide contact pads positioned close to each other. In the 2-lead geometry, the resistance of the sample is assumed to be essentially the series resistance of two identical tunneling contacts. We have compared our data with the two available theoretical models for electron motion in a transmission line: ballistic (LC transmission line) and diffusion model (RC transmission line). At high voltages, the tunneling current measures the impedance of the nanotube in intimate contact with gold contact while the impedance of the whole sample is probed at lower voltages. We find over a wide voltage range that the diffusion model explains our results with reasonable fitting parameters. The domination of the RC over the LC model may be justified by the large resistance R of the CVD grown nanotubes, and presumably by the reduced kinetic inductance L, *i.e.* enhanced carrier concentration of the nanotube in contact with gold. We obtain a rough estimate of 30 kΩ/μm for the resistance of the untreated CVD tube. Unexpectedly, reactive ion etching is found to reduce the resistance of the nanotube.

In our 4-lead measurements we have assumed to probe the resistance of the nanotube without contact resistances and have analyzed the results with the coherent conductor model. We have found a good fit to the data, but with somewhat unphysical values of the fitting parameters.

Acknowledgments

Fruitful discussions with Boris Altshuler, Leonid Glazman, Frank Hekking, Edouard Sonin, Boris Spivak and Andrei Zaikin are gratefully acknowledged. We also thank Dr. A. Fonseca and Prof. J.B. Nagy from the Universitaires Notre-Dame de la Paix à Namur, for providing us with the nanotubes in this work. This work was supported by the Academy of Finland and by ULTI III,

Access to Large Scale Facility Programme of the European Union (HPRI-1999-CT-00050).

References

1. See, *e.g.*, "Special Issue on Nanotubes" in Physics World, June 2000, p. 29.
2. C. Dekker, Physics Today, May 1999, p. 22.
3. S.J. Tans, M.H. Devoret, H. Dai, A. Thess, T.E. Smalley, L.J. Geerligs, and C. Dekker, Nature **386**, 474 (1997).
4. M. Bockrath, D.H. Cobden, P.L. McEuen, N.G. Chopra, A. Zettl, A. Thess, and R.E. Smalley, Science **275**, 1922 (1997).
5. J. Kong, C. Chou, A. Morpurgo, H.T. Soh, C.F. Quate, C. Marcus, and H. Dai, Appl. Phys. A **69**, 305 (1999).
6. A. Bachtold, M.S. Fuhrer, S. Plyasunov, M. Forero, E.H. Anderson, A. Zettl, and P.L. McEuen, Phys. Rev. Lett. **84**, 6082 (2000).
7. M. Bockrath, D.H. Cobden, J. Lu, A.G. Rinzler, R.E. Smalley, L. Balents, and P.L. McEuen, Nature **397**, 598 (1999).
8. Z. Yao, H. W. Ch. Postma, L. Balents, and C. Dekker, Nature **402**, 273 (1999).
9. See, *e.g.*, M.P.A. Fischer and L.I. Glazman in *Mesoscopic Electron Transport*, edited by L.L. Sohn, L.P. Kouwenhoven, and G. Schön (Kluwer Academic Publishers, Dordrecht, 1997) p. 331; J. Voigt, cond-mat/0005114.
10. R. Egger, and A. Gogolin, Phys. Rev. Lett.**79**, 5082 (1997)
11. C. Kane , L. Balents and M.P.A. Fisher, Phys. Rev. Lett.**79**, 5086 (1997).
12. R. Tarkiainen, M. Ahlskog, J. Penttiä L. Roschier, P. Hakonen, M. Paalanen, and E. Sonin, cond-mat/0104019.
13. L. Langer, V. Bayot, E. Grivei, J.-P. Issi. J.P. Heremans, C.H. Olk, L. Stockman, C.V. Haesendonck, and Y. Bruynseraede, Phys. Rev. Lett. **76**, 479 (1996).
14. C. Schönenberger, A. Bachtold, C. Strunk, J.-P. Salvetat, and L. Forro, Applied Physics A **69**, 283 (1999); A. Bachtold, C. Strunk, J.-P. Salvetat, J.-M. Bonard, L. Forro, T. Nussbaumer, and C. Schönenberger, Nature **397**, 673 (1999).
15. G.-L. Ingold and Yu.V. Nazarov, in: *Single Charge Tunneling*, ed. H. Grabert and M.H. Devoret, (Plenum Press, N.Y., 1992), pp. 21-107.
16. L.S. Levitov, A.V. Shytov, JEPT Lett. **66**, 215 (1997).
17. K.A. Matveev and L.I. Glazman, Phys. Rev. Lett. **70**, 990 (1993).
18. R. Egger, Phys. Rev. Lett. **83**, 5547 (1999); R. Egger and A.O. Gogolin, cond-mat/0101246
19. E.B. Sonin, to be published in JLTP July 2001.
20. B.L. Altshuler and A.G. Aronov, Zh. Eksp. Teor. Fiz. **77**, 2028 (1979) [Sov. Phys. JEPT. **50**, 968 (1979)]; B.L. Altshuler, and A.G. Aronov, in *Electron-Electron Interactions in Disordered Systems*, edited by A.L. Efros and M. Pollak (Elsevier Science Publishers B.V., Amsterdam, 1985).
21. E.G. Mishchenko, A.V. Andreev and L.I. Glazman, cond-mat/0106448.
22. F. Pierre, H. Pothier, P. Joyez, N.O. Birge, D. Esteve, and M.H. Devoret. Phys. Rev. Lett. **86**, 1590 (2001).
23. A.D. Zaikin, and D.S. Golubev, these proceedings.
24. D. Chouvaev, L.S. Kuzmin, D.S. Golubev and A.D. Zaikin, Phys. Rev. B**59**, 10599 (1999).

Proximity induced and intrinsic superconductivity in carbon nanotubes

M. Kociak[1], A.Kasumov[1,2], R. Deblock[1], S. Guéron[1], **B. Reulet**[1] and H. Bouchiat[1]
[1] *Laboratoire de Physique des Solides, Associé au CNRS, Bâtiment 510, Université Paris-Sud, 91405, Orsay, France.*

[2] *Institute of Microelectronics Technology and High Purity Materials,Russian Academy of Sciences, Chernogolovka 142432 Moscow Region,.*

We have developed a technique for measuring transport measurements on carbon nanotubes at very low temperature. Carbon nanotubes are connected through low contact resistance to metallic pads. When the contact pads are superconducting, nanotubes become superconducting due to proximity effect with surprising large values of supercurrent. It has also been recently possible to observe observe intrinsic superconductivity in ropes of single wall carbon nanotubes mounted on normal contacts provided that the distance between the normal electrodes is large enough, other wise superconductivity is destroyed by proximity effect. These experiments indicate the presence of attractive interactions in carbon nanotubes which overcome coulomb repulsive interactions at low temperature.

1 Introduction

Metallic carbon nanotubes are known to be model systems for the study of 1D electronic transport. Depending on diameter and helicity, single wall carbon nanotubes (SWNT) have at most 2 conducting channels with minimum resistance in the absence of disorder predicted to be $h/4e^2 = 6.5k\Omega$. [1,2,3] Electronic correlations are expected to lead to a breakdown of the Fermi liquid state. Nanotubes should then be described by Luttinger Liquids (LL) theories [4,5], with collective low energy excitations and no long range order. Proof of the validity of LL description with repulsive interactions in SWNT was given by the measurement of a resistance diverging as a power law with temperature down to 10 K [6]. The extrapolation of this behavior down to very low temperature would indicate an insulating state. However, this measurement was done on nanotubes separated from measuring leads by tunnel junctions. Because of Coulomb blockade [7], the low temperature and voltage regime were not explored. In contrast, we have developed a technique in which measuring pads are connected through low contact resistance to suspended nanotubes [8]. We first show that when the contact pads are superconducting, a large supercurrent can flow through nanotubes [9]. These experiments indicate that quantum coherent transport can take place on carbon nanotubes on micron scales. However the surprisingly high values found for critical currents in individual nanotubes rise the question of possible intrinsic superconductivity. Furthermore our experiments on ropes of SWNT connected to normal contacts show indeed evidence of such superconductivity below 0.5 K provided that the distance between normal electrodes is long enough.

2 Sample description and preparation

The SWNT are prepared by an electrical arc method with a mixture of nickel and yttrium as a catalyst [10,11]. SWNT with diameters of the order of 1.4 nm are obtained. They are purified by the cross-flow filtration method [11]. The tubes are usually assembled in ropes of a few hundred parallel tubes, but individual tubes can also be obtained after chemical treatment with a surfactant [12]. Isolation of an individual rope and connection to measuring pads are performed according to the following procedure. A focused laser beam releases a nanotube from a target onto the sample with a Si_3N_4 membrane coated with a metal film. A submicron width slit about $100\mu m$ in length has previously been cut in the membrane using a focused ion beam; the nanotube connects the edges of the slit and shorts the electric circuit whose resistance was over $1G\Omega$ before the nanotube

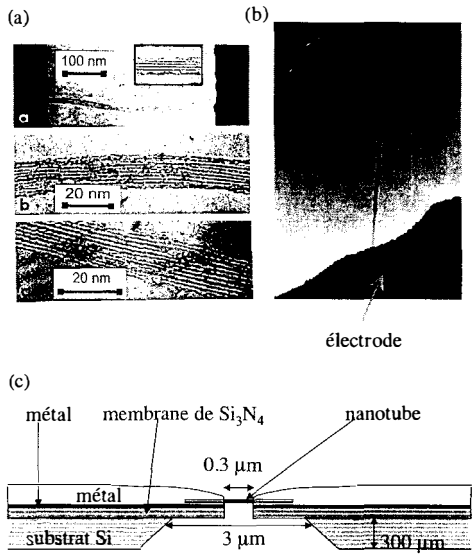


Figure 1: Transmission electronic micrograph of the nanotubes, suspended across a slit between 2 metallic pads. From these pictures it is possible to confirm that the metal of the contacts neither covers nor penetrates the tubes. A) Ropes. B) Sample Au_1, consists of a single SWNT $0.3\mu m$ long which is completely isolated at one end, on a length of 50 nm, but merges into a narrow rope of 7 tubes ($0.2\ \mu m$ long) on the other end. C)Schematic picture of a typical sample suspended across a slit and soldered to metallic pads.

was "shaken off". The resulting junctions have low resistivity ohmic contacts between the tube and the metal electrodes molten during the process, and can be characterized using transmission microscopy. The contact resistance is low and the tubes can be structurally and chemically characterized with a transmission electron microscope (TEM). The use of superconducting bilayer electrodes (Re/Au or Ta/Au) gives rise to the proximity effect. Re or Ta ensures good adhesion to the substrate and superconductivity of contacts; the imiscibility of the Re/Au and Ta/Au systems (both solid and liquid) and the very high melting temperature of Re and Ta prevents electrode damage during laser welding of the tubes to the top gold layer. Au is an ideal solder for nanotubes because it neither reacts with carbon, nor oxidizes. The samples were measured in a dilution refrigerator, at temperatures ranging from 300 K to 0.05 K, through filtered lines [13]. Magnetic fields up to 5 T could be applied perpendicularly to the contacts and the tubes. The resistance was measured by applying a small (1 nA to 10 nA, 30 Hz) a.c. current though the sample and measuring the a.c. voltage using lock-in detection.

The room temperature value R_0 of such junctions varies considerably from sample to sample, typically between 100Ω and $100k\Omega$. For ropes, when R_0 is of the order or larger than $10k\Omega$, a sharp divergence of the resistance is observed below $T = 50K$ corroborating experimental results obtained by other groups (12). This low-temperature insulating behavior has been attributed to the helicity of the tubes or to the existence of defects such as heptagon-pentagon pairs. It has also been theoretically shown (13) that Van der Waals interaction between individual nanotubes

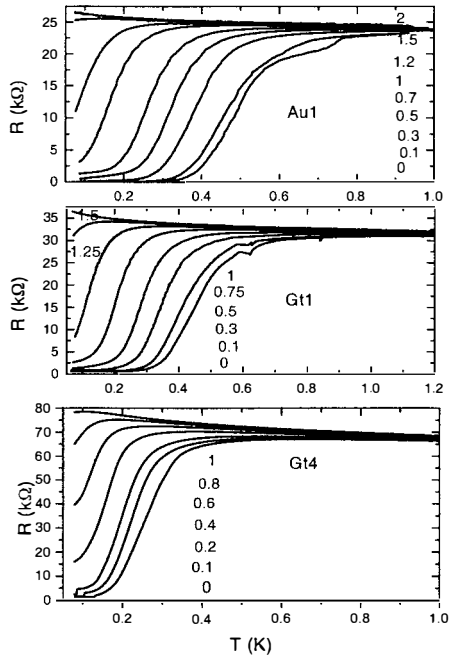


Figure 2: Temperature dependence of the resistance of individual single wall nanotubes mounted on Au/Ta measured for different values of the magnetic field perpendicular to the tube axis. (The labels on the curves correspond to the value of magnetic field in Tesla).

in a rope can induce a band gap of about 0.1 eV, making a rope consisting in individually metallic tubes semiconducting. We have found that it is also possible to obtain samples with resistance much lower than $6.5k\Omega$, indicating that a large fraction of the tubes participate in transport. Such low values of R_0 and metallic behavior down to low temperature indicate good metallic contacts. Moreover, intrinsic electronic transport properties of SWNT are more likely to be observed in suspended nanotubes than in deposited tubes where they could be altered by the substrate. Metallic behavior is observed for single SWNT when $R_0 < 30k\Omega$ and for ropes when $R_0 < 10k\Omega$.

3 Proximity induced superconductivity

A normal metal (N) in contact with a macroscopic superconductor (S) exhibits superconductivity on a characteristic length which is smaller than both the phase coherence length in the normal metal L_ϕ and the thermal length L_T, (in a clean metal $L_T = \hbar v_f / k_B T$ and in a dirty metal $L_T = \sqrt{\hbar D / k_B T}$ where D is the electron diffusion coefficient). Both lengths, of the order of a few μm, can be much longer than the superconducting coherence length. The superconducting transition temperature T_c and the gap Δ in the normal metal can be of the order of their values in S if the resistance of the SN interface is sufficiently small. This proximity effect has been extensively studied in multilayered planar SN junctions [14] and more recently in lithographically fabricated micron scale metallic wires made of normal noble metals between two macroscopic superconducting electrodes [15]. The maximum low temperature value of the supercurrent (critical

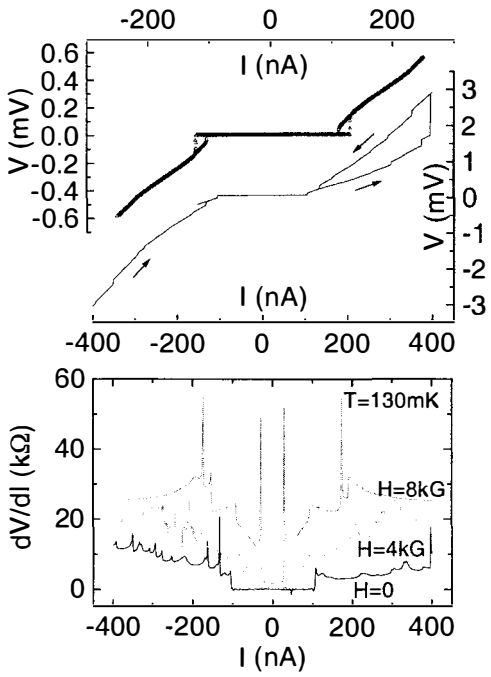


Figure 3: A) Upper curve, V(I) characteristics for the individual SWNT Au1 , from which the critical current is deduced. Lower curve, the same data on a wider current scale showing the existence of voltage steps for currents higher than i_c. B) Differential resistance measured with a small ac modulation of the current for various values of the magnetic field. It is clear from this data that the normal resistance $R_N = 25k\Omega$ is only recovered at currents much higher than i_c.

current) in such SNS junctions is $\pi\Delta/eR_N$, where R_N is the normal resistance of the junction [16]. We show that the supercurrent sustained by a single nanotube exceeds this prediction by a large factor.

We have observed proximity induced superconductivity in isolated SWNT samples like $Au1$ depicted in Fig.1 with $R_0 = 27k\Omega$. This value is of the order of the inverse quantum conductance $h/e^2 = 25.8k\Omega$, the maximum value for which one expects low temperature metallic behavior in a coherent 1D system. The tube is mounted on Ta/Au electrodes (5nm Ta, 100nm Au) and has a superconducting transition at $T_c = 0.4K$, close to the transition temperature of the contacts. The transition is shifted to lower temperature when a magnetic field is applied in the plane of the contacts (perpendicular to the tube axis). The critical field is surprisingly high (of the order of 1 Tesla) and is ten times larger than the measured critical field of the contact. Above 2 Tesla the resistance becomes field independent and a small increase is apparent when the temperature is lowered below $0.2K$ (Fig.2).

The most striking signature of induced superconductivity is the existence of Josephson supercurrents through the samples. The results of non-linear transport measurements performed on these superconducting samples are exemplified by the voltage vs. current characteristics on sample $Au1$ depicted in Fig.3. The transition between the superconducting state (zero voltage drop through the sample) and the dissipative state is quite abrupt and displays hysteresis at low temperature. It is characterized by a critical current i_c whose value at $T \sim 0$ is $i_0 = 0.104\mu A$ for

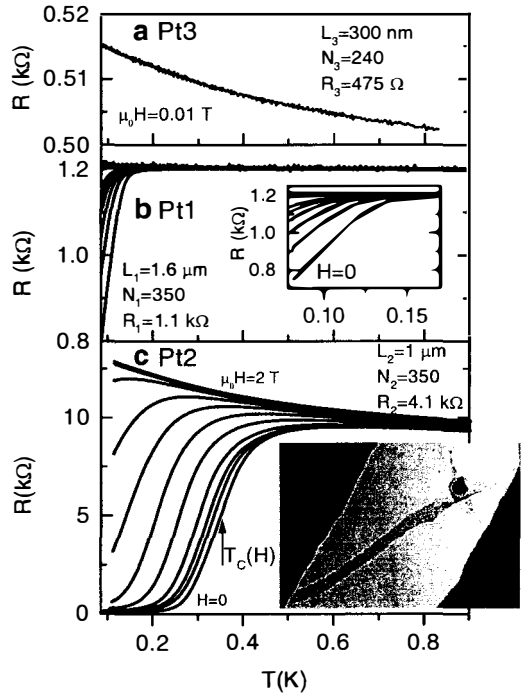


Figure 4: Resistance as a function of temperature for the three samples. The length L, number of tubes N and room temperature resistance R of each sample are given in the corresponding panel. a: Sample Pt3. b: Resistance of Pt1 in applied magnetic fields of $\mu_0 H$= 0, 0.02, 0.04, 0.06, 0.08, 0.1, 0.2, 0.4, 0.6, 0.8 and 1 T from bottom to top. Inset is a zoom of the low temperature region. c: Resistance of Pt2 at $\mu_0 H$=0, 0.05, 0.1, 0.2, 0.4, 0.6, 0.8, 1, 1.25, 1.5, 1.75, 2, 2.5 T from bottom to top. Inset: TEM micrograph of sample Pt2, from which we deduce L_2 and N_2. N_2 is estimated from the measured diameter D_2, through $N_2 = (D_2/(d+e))^2$, where d is the diameter of a single tube (d=1.4 nm), and e is the typical distance between tubes in a rope (e=0.2 nm). The dark spot is a Ni/Y catalyst particle.

$Au1$. We note that the junction does not recover its normal resistance above the critical current and the curve V(I) exhibits subsequent hysteretic jumps at higher currents. This behaviour is similar to that observed in long superconducting filaments (13), where above i_c, small normal regions (of size comparable to the inelastic length) appear located around defects in the sample (phase slip centers). However, the precise understanding of the physical mechanism involved in a SWNT with similar aspect ratio, but with dimensions 100 times smaller, requires further experimental and theoretical study.

It is very difficult to understand these results in the frame-work of conventional proximity induced superconductivity. The value of the product $R_N i_c$ at $T = 0$ is equal to 2.5 mV, 40 times larger than the expected value (0.06mV) assuming the gap is identical to its value in the superconducting electrodes (as estimated from T_c). More over signs of superconductivity persist for voltage drop through the sample much higher than the gap of pure tantalum. Similar results are found in similar individual SWNT samples with values of normal state resistance up to $70k\Omega$. Proximity induced superconductivity was also observed in ropes of SWNT with also suprisgly hifgh values of supercurrents.

An explanation of these phenomena is not straightforward. The problem of an SNS junction constituted of a Luttinger liquid between two superconducting reservoirs has been considered

theoretically by Fazio et al. [18] for weakly transmitting contacts and Maslov et al. [19] for perfectly transmitting contacts. In both cases, these authors show that it is indeed possible to induce superconductivity by a proximity effect. In the case of repulsive interactions and perfectly transmitting interfaces the zero temperature value of the critical current is not changed by the interactions. More recently it has been shown that the presence of attractive interactions in the Luttinger liquid can result in a significant increase of the critical current [20], [21].

Our data could indeed be explained by the existence of superconducting fluctuations intrinsic to SWNT. For an infinite nanotube, because of its 1D character, these fluctuations are not expected to give rise to a superconducting state at finite temperature. However, the superconducting state might be stabilized by the macroscopic superconductivity of the contacts. In such a situation, it is conceivable to expect that i_c could be enhanced compared to its value in a conventional SNS junction. The existence of superconducting fluctuations intrinsic to nanotubes may also explain the positive magneto-resistance (not shown) observed in all our samples where the normal state resistance is recovered at fields much higher than the critical field of the contacts. We see in the next section that these statements are corroborated by the observation of intrinsic superconductivity in ropes of SWNT.

4 Intrinsic superconductivity in ropes of SWNT on normal contacts

For these experiments the samples are ropes of SWNT suspended between normal metal contacts consisting of trilayers of sputtered $Al_2O_3/Pt/Au$ of respective thicknesses 5, 3 and 200 nm. This procedure insures that the tubes do not contain any chemical dopants such as alkalis or halogens. The contacts showed no sign of superconductivity down to 50 mK.

We select samples with a room temperature (RT) resistance less than 10 kΩ. As is generally observed, we find that the resistance increases as the temperature is lowered between 300 K and 1K . Things change however below 1K, as shown in Fig.4 for the three samples Pt1, Pt2, and Pt3, measured in magnetic fields ranging from 0 to 2.5 T. At zero field, the zero-bias resistance of Pt3 increases as T is reduced, whereas the resistances of Pt1 and Pt2 decrease drastically below $T_1^* = 140$ mK for Pt1 and $T_2^* = 550$ mK for Pt2. The resistance of Pt1 is reduced by 30% at 70 mK. That of Pt2 decreases by more than two orders of magnitude, and saturates below 100 mK at a value $R_r = 74\ \Omega$. We define a transition temperature T_{C_2} by the inflexion point of R(T). T_{C_2} is 370 mK at zero field, decreases at higher magnetic fields, and extrapolates to zero at 1.35 T (Fig 7c). At fields above 1.25 T, the resistance increases with decreasing temperature, similarly to Pt3, and becomes independent of magnetic field. The resistance of Pt1 follows qualitatively the same trend, but the full transition did not occur down to 70 mK. Figures 4 and 5 show that in the temperature and field range where the zero-bias resistance drops, the differential resistance is strongly bias-dependent, with lower resistance at low bias. These data suggest that the rope Pt2 (and, to a lesser extent, Pt1) is intrinsically superconducting. Although the experimental data of Pt2 seem similar to those of SWNT connected to superconducting contacts [9], there are major differences. In particular the $V(I), dV/dI(I)$ do not show any supercurrent because of the existence of a finite residual resistance.

We now analyse the superconductivity in these systems, taking into account several features: the large normal contacts, the coupling between tubes within the rope, the 1D character of each tube, and their finite length compared to relevant mesoscopic and superconducting scales. The resistance of any superconducting wire measured through normal contacts (an NSN junction) cannot be zero because the number of channels in the wire is much smaller than in the contacts [22]: a metallic SWNT, with 2 conducting channels, has a contact resistance of half the resistance quantum, $R_Q/2$ (where $R_Q = h/(2e^2)$=12.9 kΩ), even if it is superconducting. A rope of N_m parallel metallic SWNT will have a minimum resistance of $R_Q/(2N)$. Therefore we use the residual resistance $R_r = 74\ \Omega$ of Pt2 to deduce that Pt2 has at least $N_m = R_Q/2R_r \approx 90$

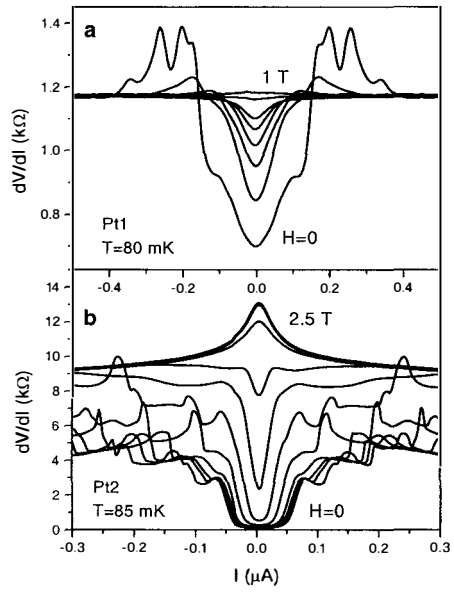


Figure 5: Differential resistance as a function of current for samples Pt1 and Pt2, in different applied fields. a: Sample Pt1. Fields are 0, 0.02, 0.04, 0.06, 0.08, 0.1, 0.2 and 1 T. b: Sample Pt2. Fields are 0, 0.2, 0.4, 0.6, 0.8, 1, 1.25, 1.5, 1.75, 2, and 2.5 T.

metallic tubes. This is approximately one quarter of the number of tubes in the rope, measured by TEM (Fig 4c). Similarly, R_Q is also the maximum resistance of any phase coherent metallic wire[23]. As a consequence, the high value (9.2 kΩ) of the resistance at 1K (which corresponds to an average resistance per metallic tube of 9.2 k$\Omega * N_m$ = 830 kΩ = 130 R_Q) cannot be understood if the nanotubes are independent, unless considering a very short (unphysical) phase coherence length $L_\varphi(1K) = L/130 = 8$ nm. On the other hand if the electrons are free to move from tube to tube[24], the resistance is simply explained by the presence of disorder. The mean free path is deduced from the RT resistance $R_2 = 4.1$ kΩ through[25] $l_{e2} \approx \frac{L}{R_2}\frac{R_Q}{N_m} \approx 18$ nm. We conclude that Pt2 is a diffusive conductor with a few hundred conduction channels.

With such a small number of channels, we expect the superconductivity to differ from 3D superconductivity. In particular, we expect to observe a broad resistance drop starting at the 3D transition temperature[26] T^* and going eventually to R_r at zero temperature. This is what is observed in Pt2 (see figure 4.c). We estimate the gap through the BCS relation $\Delta = 1.76\ k_B T^*$: $\Delta \approx 85\ \mu eV$ for Pt2. We can then deduce the superconducting coherence length along the tube in the diffusive limit $\xi_2 = \sqrt{\hbar v_f l_e/\Delta} \approx 0.3\ \mu$m where v_f is the longitudinal Fermi velocity 8×10^5 m/s[27]. Consistent with 1D superconductivity, ξ_2 is ten times larger than the diameter of the rope.

Finally, reminiscent of measurements of narrow superconducting metal wires[26], we find jumps in the differential resistance as the current is increased (Figures 5 and 6). For Pt2 the differential resistance at low currents remains equal to R_r up to 50 nA, where it strongly rises but does not recover its normal state value until 2.5 μA (fig 6a). The jump in resistance at the first

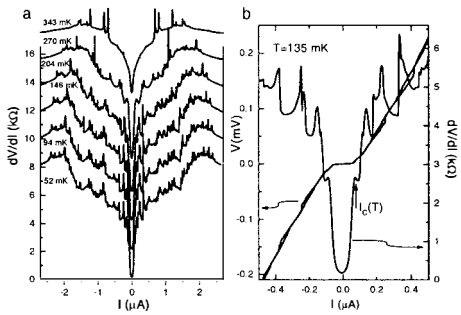


Figure 6: Left panel: Differential resistance of Pt2 vs. current for a larger current amplitude than in Fig.5, at different temperatures. Curves are offset vertically for clarity. Right panel: V(I) and $\frac{dV}{dI}(I)$ curves showing the hysteretic behavior in V(I) at each peak in the $\frac{dV}{dI}(I)$ curve.

step corresponds approximately to the normal state resistance of a length ξ_2 of Pt2. Each peak corresponds to a hysteretic feature in the V-I curve (fig 6b). Above 1 T the differential resistance is peaked at zero current. This is also the case for Pt3 (data not shown). The variations of the differential resistance of Pt1 are similar to those of Pt2 close to its transition temperature. These jumps are identified as phase slips [26,17,28], which are the occurrence of normal regions located around defects in the sample. Such phase slips can be thermally activated (TAPS), leading to an exponential decrease of the resistance instead of a sharp transition, in qualitative agreement with our experimental observation (fig 7a). At sufficiently low temperature, TAPS are replaced by quantum phase slips (QPS), which, when tunneling through the sample, contribute an additional resistance to the zero temperature resistance. Moreover, QPS are predicted to supress the transition when the normal state resistance of the sample on the phase coherence scale is larger than $R_Q/2$ [29](as confirmed by recent experiments [30]). Our data on Pt2 show no evidence of such an effect, even though the normal state resistance, measured above T*, is 40% larger than $R_Q/2$.

The current above which the jumps disappear, 2.5 μA, is close to the critical current $I_C = \Delta/R_r e \approx 1$ μA of a superconducting wire without disorder and with the same number of conducting channels[28]. This large value of critical current would also be the maximum supercurrent in a structure with this same wire placed between superconducting contacts (with gap Δ_S), and is much larger than the Ambegaokar-Baratoff prediction $R_N I_C = \Delta_S/e$. This might explain the anomalously large supercurrent measured in a previous experiment [9], where nanotubes were connected to superconducting contacts. We now discuss the effect of the magnetic field. The field at which the resistance saturates to its normal value and at which the critical current vanishes, 1.25 T, coincides with the field obtained by extrapolation of $T_C(H)$ to zero temperature (fig. 7b).

It is difficult to say what causes the disappearance of superconductivity. The value of Hc(0) should be compared to the depairing field in a confined geometry [31], and corresponds to a flux quantum Φ_0 through a length ξ of an individual SWNT of diameter d, $\mu_0 H_C = \Phi_0/(2\sqrt{\pi}d\xi) =$ 1.35 T. But $H_C(0)$is also close to the field $\mu_0 H_p = \Delta/\mu_B = 1.43$ T at which a paramagnetic state becomes more favorable than the superconducting state[32,33]. Note that this value is of the same order as the critical field that was measured on SWNT connected between superconducting contacts, i.e. much higher than the critical field of the contacts.

We now estimate the superconducting coherence length of the two other samples, to explain the extent or absence of observed transition. Indeed, investigation of the proximity effect at

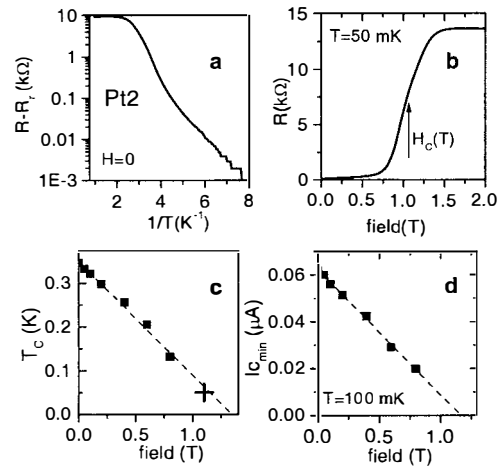


Figure 7: a Resistance of Pt2 plotted on a log scale as a function of the inverse temperature at H=0. We have subtracted the low temperature residual resistance (contact resistance). The slope yields an approximate activation energy of 0.8 K. b Magnetoresistance of Pt2 at 50 mK. We define the critical field as the inflection point of R(H): $\mu_0 H_C$(T= 50 mK)=1.1 T. c Transition line of Pt2 defined in the H,T plane by the inflection point of R(T) or equivalently by the inflection point of R(H). d Field dependence of the critical current of Pt2 defined as the current at which the first resistance jump occurs in the dV/dI curves of Fig.5. $I_C(H)$ extrapolates to a critical field of 1.2 T, in agreement with the linear extrapolation 1.3 T of $T_C(H)$.

high-transparency NS interfaces has shown that superconductivity resists the presence of normal contacts only if the length of the superconductor is much greater than ξ [34], i.e. if the wire contains a superconducting reservoir. This condition is nearly fulfilled in Pt2 ($\xi_2 \approx L_2/3$). Using the high temperature resistance values of Pt1 and Pt3, and assuming a gap Δ and number of metallic tubes equal to those of Pt2 we find $\xi_1 \approx L_1/2$ and $\xi_3 \approx 2L_3$. These values explain qualitatively a reduced transition temperature for Pt1 and the absence of a transition for Pt3. Moreover we can argue that the superconducting transitions we see are not due to a hidden proximity effect : if the $Al_2O_3/Pt/Au$ contacts were made superconducting by the laser pulse, the shortest nanotube (Pt3) would become superconducting at temperatures higher than the longer tubes (Pt1 and Pt2). The main result, i.e. no visible transition with a short rope, and a visible transition in a long rope, are confirmed by measurements on two other samples which are not presented here.

We now consider the possible mechanism of superconductivity. It has been suggested that coupling with low energy phonons can turn repulsive interactions in a Luttinger liquid into attractive ones and drive the system towards a superconducting phase [35]. Such low energy phonons have been experimentally observed in the form of mechanical bending modes of a suspended SWNT rope [36]. It was also shown that superconducting fluctuations can dominate at low temperature in ladders such as tubes [4]. In this case the system must be away from half-filling, a condition probably fulfilled in our experimental situation, due to hole doping from the contacts

[37,38]. Finally, the superconductivity reported here recalls that of graphite intercalated with alkalis (Cs,K), which also occurs between 0.2 and 0.5 K[39]. Much higher temperatures were observed in alkali doped fullerenes[40] because of the coupling to higher energy phonons. This suggests the possibility of increasing the transition temperature by chemically doping the nanotubes.

We have shown that ropes of carbon nanotubes are intrinsically superconducting. This is the first observation of superconductivity in a system with such a small number of conduction channels. The understanding of this superconductivity calls for future experimental and theoretical work and motivates in particular a search of superconducting fluctuations in a single SWNT.

A.K. thanks the Russian foundation for basic research and solid state nanostructures for financial support, and thanks CNRS for a visitor's position. We thank M. Devoret, N. Dupuis, T. Martin, D. Maslov, C. Pasquier for stimulating discussions.

1. M.S. Dresselhaus, G. Dresselhaus, and P.C. Eklund, *Science of Fullerenes and Carbon nanotubes* (Academic, San Diego, 1996).
2. N. Hamada, S. I. Sawada and A. Oshiyama, Phys. Rev. Lett. **68**, 1579 (1992).
3. J. W. G. Wildoer *et al.*, Nature **391**, 59 (1998).
4. R. Egger, A. Gogolin, Phys. Rev. Lett. **79**, 5082 (1997). R. Egger, Phys. Rev. Lett. **83**, 5547 (1999).
5. C. Kane, L. Balents, M. P. Fisher, Phys. Rev. Lett **79**, 5086 (1997).
6. M. Bockrath *et al.*, Nature **397**, 598 (1999).
7. H. Grabert and M. H. Devoret (eds), Single Charge Tunneling (Plenum, New-York, 1992); J. T. Tans *et al.*, Nature **386**, 474 (1997).
8. A.Yu. Kasumov, I.I. Khodos, P.M. Ajayan, C. Colliex, Europhys. Lett. **34**, 429 (1996); A.Yu. Kasumov *et al.*, Europhys. Lett. **43**, 89 (1998).
9. A.Yu. Kasumov *et al.*, Science **284**, 1508 (1999).
10. C. Journet, *et al.*, Nature **388**, 756 (1997).
11. L. Vaccarini, *et al.*, C.R.Acad.Sci.**327**, 925 (1999).
12. M. Burghard et al, *Electronic Properties of Novel Materials* (Eds H. Kuzmany et al,) AIP, New York (1998).
13. B. Reulet, H. Bouchiat, and D. Mailly, Europhys. Lett. **31**, 305 (1995).
14. G. Deutscher and P.G. de Gennes in *Superconductivity* (Ed. R.D. Parks) Marcel Dekker Inc. (1969).
15. R.B. van Dover, A. de Lozanne and M.R. Beasley *J.Appl. Phys.* **52**, 7327 (1981), H. Courtois, Ph. Gandit, B. Panetier, *Phys. Rev.* **B 52** 1162 (1995).
16. For a review of suppercurrents through superconducting junctions see: K. Likharev, *Rev. Mod. Phys.* **51**,101 (1979).
17. J. Meyer, G. V. Minnigerode, Physics Letters, **38A**, 7, 529 (1972)
18. R. Fazio, F.W.J Hekking and A.A. Odintsov, *Phys. Rev.*, **B 53**, 6653 (1995).
19. D. Maslov, M. Stone, P.M. Goldbart, D. Loss *Phys. Rev.*, **B 53,** 1548 (1995).
20. I. Affleck, J.B. Caux and A. Zagoskin *Phys. Rev.*, **B 62,** 1433 (2000).
21. J. Gonzalez, Phys. Rev. Lett. **87**, 136401 (2001).
22. R. Landauer, IBM Res. Dev. 1, 223 (1957).
23. D. J. Thouless, Phys. Rev. Lett. **39**, 1967 (1977).
24. Electronic transfer between tubes in a disordered rope is indeed suggested in: A. A. Maarouf, C. L. Kane, and E. J. Mele, Phys. Rev. B**61**, 11156 (2000); H.R. Shea, R. Martel and Ph. Avouris, Phys. Rev. Lett. **84**, 4441 (2000).
25. Y. Imry, Europhys. Lett. **1**, 249 (1986).
26. N. Giordano, Phys. Rev. B **50**, 160 (1991).
27. Note however that the transverse velocity is certainly much smaller, yielding a transverse coherence length $\xi_\perp$ smaller than the longitudinal one, but the 1D character of the tran-

sition depicted below indicates that $\xi_{\perp}$ is certainly larger than the diameter of the rope. Such anisotropic transport is observed in organic conductors where a very small coupling between 1D chains restores a 3D behavior of the electrons, and allows superconductivity in a macroscopic sample. (see e.g. C. Bourbonnais, D. Jérôme, in Advance in Synthetic Metals, eds P.Bernier, S. Lefrant and G. Bidan) 206 (1998).

28. Tinkham, M., Introduction to superconductivity, McGraw-Hill, 2d Ed. (Singapore, 1996).
29. A.D. Zaikin *et al.*, Phys. Rev. Lett. **78**, 1552 (1997).
30. A. Bezryadin, C. N. Lau and M. Tinkham Nature **404**, 971 (2000).
31. R. Meservey, P.M. Tedrow, Phys. Rep. **238**, no.4, 173 (1994).
32. A.M. Clogston, Phys. Rev. Lett. **9**, 266 (1962).
33. B.S. Chandrasekhar, Appl. Phys. Lett. **1**, 7 (1962).
34. W. Belzig, C. Bruder and G. Schön, Phys. Rev. B **54**, 9443 (1996).
35. D. Loss, and T. Martin, Phys. Rev. B **50**, 12160 (1994).
36. B. Reulet *et al.*, Phys. Rev. Lett **85**, 2829 (2000).
37. L. C. Venema *et al.*, Science **283**, 52 (1999).
38. A.A. Odintsov , Phys. Rev. Lett. **85**, 150 (2000).
39. N. B. Hannay *et al.*, Phys. Rev. Lett. **14**, 225 (1965).
40. O. Gunnarsson, Rev. Mod. Phys. **69**, 575 (1997).

TRANSPORT PHENOMENA IN NANOTUBE QUANTUM DOTS FROM STRONG TO WEAK CONFINEMENT

JESPER NYGÅRD[1], DAVID H. COBDEN[1,2]
[1]*Niels Bohr Institute, Ørsted Laboratory, Universitetsparken 5, DK-2100 Copenhagen, Denmark*

[2]*Department of Physics, University of Warwick, Coventry CV4 7AL, UK*

We report low-temperature transport experiments on single-wall nanotubes with metallic leads of varying contact quality, ranging from weak tunneling to almost perfect transmission. In the weak tunneling regime, where Coulomb blockade dominates, the nanotubes act as one-dimensional quantum dots. For stronger coupling to the leads the conductance can be strongly enhanced by inelastic cotunneling and the Kondo effect. For open contacts Coulomb blockade is completely suppressed, and the low-temperature conductance remains generally high, although we often see distinct dips in the conductance versus gate voltage which may result from resonant backscattering.

Experiments on single-wall carbon nanotubes have allowed the exploration of numerous quantum transport phenomena for the first time in a molecular system.[1] Until recently these phenomena were limited to the Coulomb blockade regime owing to the relatively poor (low-transmission) contacts achieved between the nanotubes and the metallic leads.[2,3] However, devices with good (high-transmission, or 'open') contacts can now be fabricated[4,5] by evaporating metals on top of nanotubes grown by either laser ablation or chemical vapor deposition. With improved contacts, cotunneling processes and the Kondo effect[6] become important, and indeed nanotube devices are a promising system for exploring new extensions of Kondo physics.[7] Further, once the transmission becomes very high we find behavior similar to that seen very recently by Liang *et al.*[5] Here *dips* appear in the conductance which are likely to be caused by resonances in the nanotube which acts as a cavity confined by the weakly reflecting contacts.

Our own devices are based on laser ablation grown single-wall nanotubes, deposited onto a SiO_2 substrate after sonication in dichloroethane. Pure gold leads are evaporated directly onto the tubes using electron-beam lithography and lift-off. A strongly doped silicon layer underneath the 300 nm thick SiO_2 layer is used as a gate electrode. A schematic device is shown in Fig. 1a, where the atomic force microscope (AFM) image reveals a nanotube bundle bridging two Au leads spaced by $L = 300$ nm.

Using this technique the two-terminal conductance at room temperature, $G_{\rm RT}$, is found to vary greatly between devices (for reasons uncertain at present). We select devices where $G_{\rm RT}$ is independent of gate voltage $V_{\rm g}$, implying that a metallic nanotube with little disorder[8] determines the conductance G. In these devices the conductance is limited mainly by the contacts.[9] Assuming for simplicity both contacts have transmission probability $P_{\rm C}$, one can show[10] that approximately $G_{\rm RT} \leq G_{\rm max} \times P_{\rm C}/(2 - P_{\rm C})$, and thus $P_{\rm C} \geq 2/(1 + G_{\rm max}/G_{\rm RT})$, where $G_{\rm max} = 4e^2/h$ is the maximum possible theoretical conductance of a tube.

In Fig. 1b we plot the average conductance $G_{\rm av}$ vs T for four devices with geometry and size similar to that in Fig. 1a, having $G_{\rm RT}$ ranging from 0.015 e^2/h ($P_{\rm C} < 0.01$) to 3.1 e^2/h ($P_{\rm C} \sim 0.9$). The two devices with $G_{\rm RT} < e^2/h$ (open symbols) show the strongest variation, their conductance decreasing roughly as a power law, $G \sim T^{0.7}$, below 100 K. This power law behavior, generic in low-conductance nanotube devices, can be consistently explained by the suppression of tunneling between the leads and the interacting one-dimensional electron system in the nanotube (thought to be a Luttinger liquid) at low energies.[11] The other two devices with higher $G_{\rm RT}$ (solid symbols) have much weaker T dependences and do not show such power laws.

At low T all the devices exhibit rapid, reproducible variations in the conductance G as a function of gate voltage $V_{\rm g}$. Figs. 1c–e show the behavior of three devices spanning a wide range

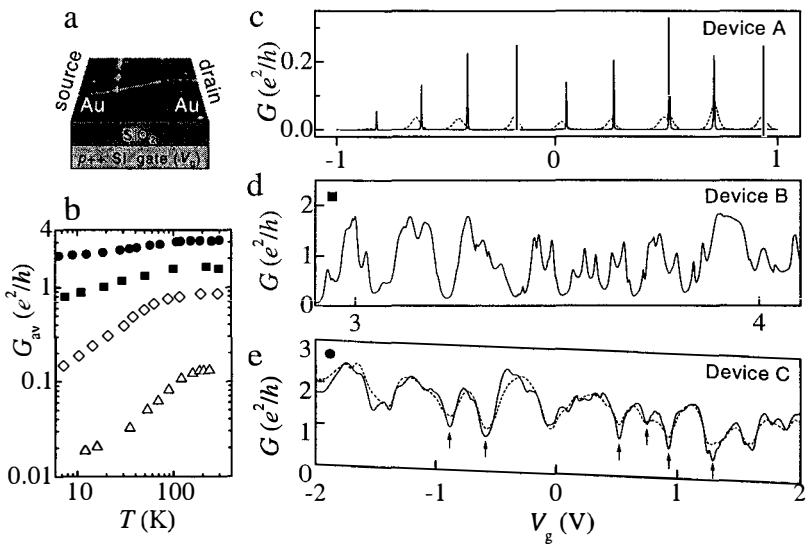


Figure 1: (a) AFM image of a device. (b) Average conductance G_{av} vs T for devices with different contact transparencies. (c)–(e) Conductance G vs gate voltage V_g. (c) Device A at 4 K (dotted) and 300 mK (solid). (d) Device B (squares in b) at 75 mK. (e) Device C (circles in b) at 4.2 K (dotted) and 1.2 K (solid).

of contact transmission. For the low-conductance device labeled A (Fig. 1c), with $G_{RT} = 0.3\ e^2/h$ ($P_C \sim 0.15$), Coulomb blockade[2] (CB) sets in thoroughly, producing a series of roughly periodic, isolated CB peaks. This is the norm for low-conductance devices. For device B (Fig. 1d), which has $G_{RT} = 1.6\ e^2/h$ ($P_C \sim 0.6$), the structure is still peak-like, but the peaks are less regular and G never vanishes between them even at 75 mK. For the highest conductance device, C, with $G_{RT} = 3.1\ e^2/h$ ($P_C \sim 0.9$), the fluctuations are weaker and no longer peak-like (Fig. 1e). In fact, in this case we can identify a series of well defined *dips* in G vs V_g which deepen as T is decreased from 4.2 K to 1.2 K, such as those indicated by arrows in Fig. 1e.

Nonlinear transport measurements reveal the key differences between these devices with different contact transmissions. In Fig. 2 the differential conductance dI/dV is plotted in greyscale vs source-drain bias V and V_g. For device A (Fig. 2a) the result is a standard Coulomb blockade diamond pattern, with zero conductance inside the diamonds.[2,3] The gate coupling $C_g/C \sim 0.13$ is typical for devices of this size (C_g is the capacitance to the gate and C the total capacitance). On the other hand, for both devices B and C, $C_g/C \leq 0.025$, implying that the potential in the nanotube is much less sensitive to the gate voltage when the contacts are more open, in spite of the similar geometry to device A. The mean level spacing in device A of $\Delta E \sim 2$ meV is about one sixth of the charging energy U and is consistent with the estimate[2] $\Delta E \approx \hbar v_F \pi / L$, where the separation L of the leads defines the effective length of the dot. This implies that the localization length in the tube is longer than L.

For device B (Fig. 2b), Coulomb diamonds can again be discerned, as indicated by the dotted lines, showing that CB is still effective enough to make the electron number N on the nanotube a well defined quantity. The diamonds are however much less distinct than in device A. This is explained by the increased level broadening and cotunneling resulting from the stronger lead coupling. What stands out most though is the presence of horizontal features of enhanced dI/dV at a certain V. In particular, there are ridges at $V = 0$ in the diamonds marked X (faint), Y,

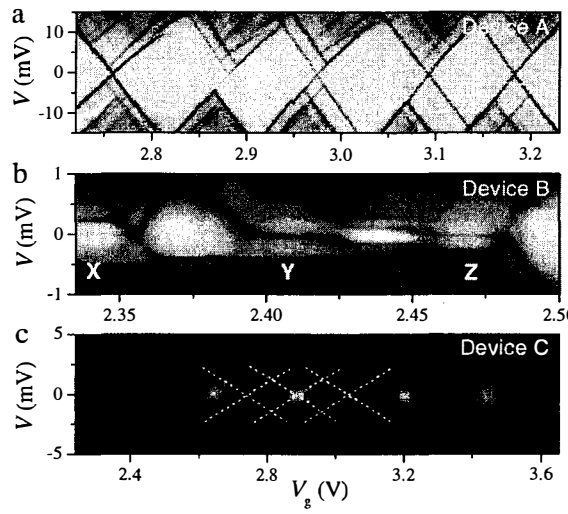


Figure 2: (a) Differential conductance dI/dV vs V_g and bias V for the same devices as in Fig. 1c–e. Measurements at 75 mK (a), 75 mK (b), and 1.2 K (c). Darker means higher conductance.

and Z. In Fig. 3a we show for the same V_g range the small-bias conductance G at a series of temperatures. At the highest T (dotted line) there are fairly regular CB oscillations. However, whereas for regular CB G decreases exponentially in the valleys as T is lowered, this is not the case in valleys X, Y and Z. In fact, for valley Y, which shows the strongest zero-bias ridge in Fig. 2b, G *increases* logarithmically with decreasing T as shown in Fig. 3b.

The zero-bias features and their anomalous T dependence are signatures of the Kondo effect in a quantum dot, which becomes significant along with cotunneling as the coupling to the leads increases.[6,7] When the electron number N is odd (valleys X,Y and Z), the total spin of the nanotube dot must be at least 1/2. In this case cotunneling processes can occur which flip the spin of the dot. These allow electrons in the two leads to become correlated, and a Kondo resonance appears at the Fermi energy resulting in enhanced transmission rates between the contacts when T is below the Kondo temperature T_K. On the other hand, in the even-N valleys, the ground state spin is usually zero [12] and no Kondo effect is seen at zero bias.

Finally, for device C (Fig. 2c) no Coulomb diamonds can be seen, as expected because the contacts are so transparent ($P_C \sim 0.9$) that there should be no Coulomb blockade. However, we notice that there do still exist crosses in this greyscale plot, as indicated by dotted lines, but that they are *white*, and are centered on the *dips* in G rather than the peaks. In the open regime, such patterns can be generated by Fano resonances, as reported in semiconductor quantum dots by Göres *et al.*[13] Such resonances must be formed from the interference between two transmitting modes, which in the case of nanotubes could be the K and K' points in the lowest 1D subband. The spacing of the dips in energy deduced from this plot is ~1–2 meV, which is roughly the same as the level spacing in device A. This is again consistent with the absence of CB, ie negligible charging effects, assuming these features are still related to electron states confined, however weakly, within the tube.

Very recently Liang *et al.* have seen similar, highly regular 'inverted diamond' patterns using devices with $G_{RT} \sim 1.5$–$2.5\ e^2/h$ based on nanotubes grown in-situ by chemical vapor deposition.[5] They explain the patterns as resulting from a clean metallic nanotube acting as an etalon-like resonant cavity with the contacts as weakly reflecting mirrors which scatter between

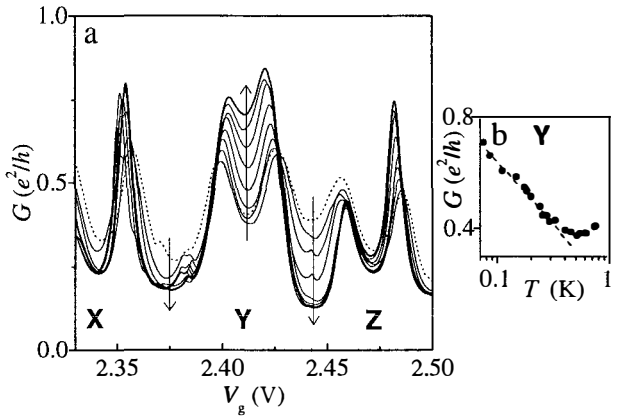


Figure 3: (a) G vs V_g for the device B (Fig. 2b), here at 75 (thick line), 85, 115, 175, 240, 295, 420, 590, and 730 mK (dotted). (b) G vs T for valley Y in a. The dotted line indicates $\log T$ behavior.

the K and K' modes. They find that the spacing of the dips varies with $1/L$, adding further weight to the idea that open metallic nanotubes are ballistic phase-coherent one-dimensional wires.

In summary, 1D transport can now be studied in single-wall nanotubes throughout the range from closed 1D quantum dots through the cotunneling and Kondo regime to the limit of open 1D channels with weak backscattering.

Acknowledgments

We thank M. Bockrath, H. Bruus, K. Flensberg, P.E. Lindelof for discussions, and R.E. Smalley and A. Rinzler for supplying the nanotube material. The work was carried out in the NBI Nanolab and supported the Danish Technical Research Council.

References

1. M.S. Dresselhaus *et al.* (eds). *Carbon Nanotubes - Synthesis, Structure, Properties, and Applications.* (Springer, Berlin, 2001).
2. S. Tans *et al. Nature* **386**, 474 (1997); M. Bockrath *et al. Science* **275**, 1922 (1997).
3. J. Nygård *et al. Appl. Phys. A* **69**, 297 (1999).
4. M.T. Soh *et al. Appl. Phys. Lett.* **75**, 627 (1999); Z. Yao *et al. Phys. Rev. Lett.* **84**, 2941 (2000).
5. W. Liang *et al. Nature* (in press).
6. L. Kouwenhoven and L. Glazman. *Physics World* **14**, 33 (2001).
7. J. Nygård *et al. Nature* **408**, 342 (2000).
8. M. Bockrath *et al. Science* **291**, 283 (2000).
9. A. Bachtold *et al. Phys. Rev. Lett.* **84**, 6082 (2000).
10. S. Datta, *Electronic Transport in Mesoscopic Systems* (Cambridge University Press, 1995).
11. M. Bockrath *et al. Nature* **397**, 598 (1999).
12. D.H. Cobden *et al. Phys. Rev. Lett.* **81**, 681 (1998).
13. J. Göres *et al. Phys. Rev.* **B 62**, 2188 (2000).

LOW-NOISE ELECTROMETER MADE OF MULTIWALLED CARBON NANOTUBE

L. ROSCHIER, R. TARKIAINEN, M. AHLSKOG, and P. HAKONEN
Low Temperature Laboratory, Helsinki University of Technology, FIN-02015 HUT, Finland

We investigate the possibility of using multiwalled carbon nanotubes for constructing low-noise single-electron transistors (SETs). We use free-standing structures where the carbon nanotube is positioned on top of two 20-nm-thick gold leads using AFM manipulation. A rapid, 10-30 sec, heat treatment at 1000 K after the manipulation results in contact resistances of 10-20 kΩ. The $1/f^{\alpha}$-noise is minimized in these free-standing constructions owing to the missing contact area with the SiO_2 substrate insulator that contains trapping centers of charge. The measured equivalent background charge noise is in the range $2{\cdot}10^{-5}$ ... $6 \cdot 10^{-6} e/\sqrt{Hz}$ at frequencies 10 ... 45 Hz. Good noise properties seem to be connected with the increase of conductance observed near zero bias.

1 Introduction

Multiwalled carbon nanotubes present a new, versatile class of building blocks for nanoelectronics [1,2,3]. Owing to their large kinetic inductance, MWNTs have been found to work as high impedance transmission lines with characteristic impedance $Z \sim 5$ kΩ [4]. Single electron transistors (SET) with regular gate modulation and charge-noise properties have been manufactured [5]. An additional feature that makes MWNT-SETs appealing is their small island capacitance, which makes it simple to produce devices working at a temperature of $T = 4.2$ K.

SETs are often characterized by their $1/f^{\alpha}$-noise. Typically, α varies between $1-2$ and the magnitude of the noise lies in the range $2{\cdot}10^{-3}$ ... $1{\cdot}10^{-4} e/\sqrt{Hz}$ at 10 Hz. Some Al- devices of stacked design have reached noise levels of $8{\cdot}10^{-6} e/\sqrt{Hz}$ [6]. The $1/f^{\alpha}$-noise in SETs is often caused by background charge variations in the dielectric substrate material [7].

The only known way to reduce this $1/f^{\alpha}$-noise in SETs is to avoid contact of the central island with any dielectric material [6]. In our devices, this is achieved by using a free-standing nanotube as an island. We use manipulation by atomic force microscope [8] to move a multiwalled carbon nanotube (MWNT) on top of two 20-nm-thick gold electrodes separated by 0.3 μm. For constructional details, we refer to Ref. 9.

When fabricating a SET-device with optimum charge sensitivity, current modulations should be maximized by using low impedance tunneling barriers such that they are on the order of quantum resistance $R_K = 26$ kΩ. In our samples low resistance is achieved by a rapid, 10 - 30 second heat treatment. Typically, contact resistances on the order of 10-20 kΩ are obtained, but substantial variation is observed. Owing to such a small contact resistance, our devices are already in the strong tunnelling regime, where the Coulomb-blockade in the IV-characteristics becomes slightly smoothened. In this paper we present results and analyze the conductance and noise properties of one particularly good sample manufactured of arc-discharge grown nanotube material. This sample exhibits low noise and good conductivity, both features of which we assign to the good purity of our samples

2 IV-characteristics and Noise Measurements

Fig. 1a illustrates the IV-curve of our sample measured at $T = 150$ mK. It shows a total resistance of $R \simeq 40$ kΩ at voltages $V > 10$ mV outside the Coulomb blockade regime. For the average junction capacitance we estimate $C_T = 40$ aF using the offset voltage in the IV-curve measured at $V > 10$ mV. Here we neglect the small asymmetry in the size of the Au-NT contact areas at the ends: 200/400 nm in length, respectively.

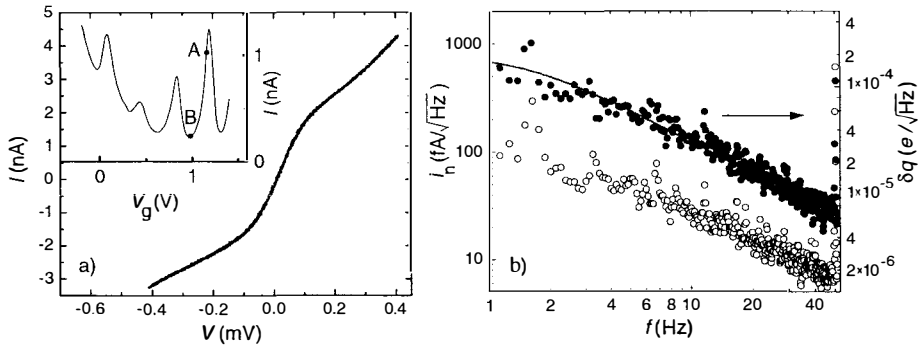


Figure 1: a) IV-curve of the device in Fig. 1 measured at $T = 150$ mK. In the middle of a rather weak Coulomb blockade there is an increase of conductance indicating resonant tunnelling over the multiwalled nanotube sample. The inset illustrates the gate modulation at a bias voltage of $V_{bias} = 70$ μV. Points marked by A and B denote biasing conditions for noise measurements at maximum and zero gain, respectively. b) Current noise i_n measured at minimum (lower) and maximum gain (upper trace). The right axis, obtained by scaling with the inverse of charge sensitivity $1/g_{ch} = 0.25$ e/nA, gives the equivalent charge noise δq for the upper trace.

In Fig 1a, there is an increase of conductance near zero bias voltage, contrary to the expected Coulomb blockade. We attribute this to resonant tunnelling which, however, leads to only two weakly quantized steps in the IV-curve. Thus, we regard our sample as semiballistic, *i.e.*, intermediate between ballistic and diffusive behavior. We believe that ballisticity of a free-standing tube is enhanced over a regular sample mostly for two reasons: 1) impurities on the substrate are further away and fluctuations induced by them become more unlikely, and 2) the amount of dirt on the surface of the nanotube is reduced during the AFM manipulation [10] and vacuum brazing.

Current modulation with respect to the gate voltage, shown in the inset of Fig. 1a, illustrates the sensitivity of our SET device. The modulation curve has been measured with voltage bias at $V_{bias} = 70$ μV which corresponds to a peak current of 1.2 nA. At the point marked by A in Fig. 1a, we have the maximum slope of $k = 11$ nA/V. The roundedness of the modulation curve is assigned to strong tunnelling effects since the tunnelling resistances, $10 - 20$ kΩ are below R_Q. Note that the gate modulation curve in the inset of Fig. 1a is not fully periodic: it does not show any effects related with even-odd number of electrons, which have been observed by Nygård *et al* in relation to the Kondo-effect in single-walled carbon nanotubes [11].

The noise current, measured both at maximum and minimum gain of the electrometer (points A and B in Fig. 1a, respectively), is displayed in Fig. 1b. As argued in Ref. 9, we interpret our current noise measurements in a similar fashion as in regular metallic devices. From the inset of Fig. 1a, we deduce a value for the charge sensitivity $g_{ch} = \frac{\Delta I}{\Delta q} = \frac{dI}{dV_g}\Delta V_{gate}/e = 4$ nA/e at point A. At the maximum gain, we obtain the minimum equivalent input charge noise of our device. The frequency dependence of this minimum noise power is close to $1/f^2$, a relationship that has occasionally been observed on metallic samples as well [6]. The observation of this kind of noise spectrum is an indication of a strong single fluctuator (random telegraph noise) which yields a Lorentzian spectrum [13] of the form

$$S_Q = \frac{B}{1 + 4\pi^2\tau^2 f^2} \qquad (1)$$

The solid curve in Fig. 1b illustrates the fitting of this formula using the parameters $A = 1.52 \cdot 10^{-9} e^2$, $B = 4.4 \cdot 10^{-8} e^2/Hz$ and $\tau = 0.11$ s. The agreement of Eq. (1) with data measured on other samples is found to be good as well. For further details of random telegraph noise in MWNTs, we refer to Ref. 12.

At a frequency of $f = 45$ Hz, we obtain a charge noise of $6 \cdot 10^{-6}$ e/$\sqrt{Hz}$, which is close in the performance to the best metallic devices with $8 \cdot 10^{-6}$ e/$\sqrt{Hz}$ at 10 Hz and ($\sim 4 \cdot 10^{-6}$ e/$\sqrt{Hz}$ at 45 Hz extrapolated using $1/f$ noise dependence) [6].

The minimum noise level for a SET is given by $\delta Q_{min} = \sqrt{\hbar C_\Sigma \Delta f R_Q / 4 R_T}$ where $C_\Sigma \sim 2C_T$ is the total island capacitance and Δf denotes the bandwidth of the measurement [14]. Taking $R_Q/4R_T \sim 1$ and assuming that the cotunneling rate is not large, we get for the minimum noise $1 \cdot 10^{-6}$ e/$\sqrt{Hz}$. This means that white noise will dominate over $1/f^2$-noise above 3 kHz in our device. Hence, the shot noise dominated region can in principle be reached using low-noise, high-band current preamplifiers. Recently, we have succeeded in measuring shot noise in MWNTs at $f = 10$ kHz using currents of 100 nA, *i.e.*, slightly above the Coulomb-blockade region [12].

3 Conductance vs. Gate Voltage

The general behavior of the sample described above is a bit exceptional when compared with our other samples. To elucidate its properties, we show the measured conductance for this sample at eight different gate voltages in Fig. 2. The conductance traces display clear peaks which are spaced apart by about 0.7 mV. According to length-quantized single-particle states , $eV = \hbar v_F / 2L$, the effective length L would be 350 nm. Note that these peaks in the $G(V)$ curves are rather wide, clearly broader than expected on the basis of temperature $T = 150$ mK.

Another possible explanation for the measured $G(V_g)$ is provided by Kondo-resonances, observed recently by Nygård *et al* [11] in single walled nanotubes. The observed shape and gate dependence of the peaks in Fig. 2 are similar to those reported in Ref. 11. However, since tuning of the gate voltage moves the peak off from the Fermi-level in our data, these results cannot be assigned to typical Kondo-resonance behavior in which the resonance stays always at the Fermi level. Nevertheless, we believe that our results are caused by the presence of some kind of resonance states which go hand in hand with the good quality (and small noise) of the present sample. A comprehensive theory for this must be worked out before our data can be explained properly.

4 Summary

We have shown that free-standing multi-walled carbon nanotubes provide excellent SET-devices for electrometer applications in nanoelectronics. The noise performance of our good-quality sample is dominated by random telegraph type of noise with Lorentzian spectrum. The background charge noise at small bias, $6 \cdot 10^{-6}$ e/$\sqrt{Hz}$ at $f = 45$ Hz, is close to that of the best state-of-the-art metallic devices. The reasons behind the good operation are the absence of contact with dielectric material and the probable nearly ballistic propagation in this system.

Acknowledgments

We wish to thank Catherine Journet and Patrick Bernier from the University of Montpellier for the high-quality, arc-discharge-grown nanotubes. Fruitful discussions with Frank Hekking, Edouard Sonin, and Andrei Zaikin are gratefully acknowledged. This work was supported by the Academy of Finland and by the Human Capital and Mobility Program ULTI of the European Union.

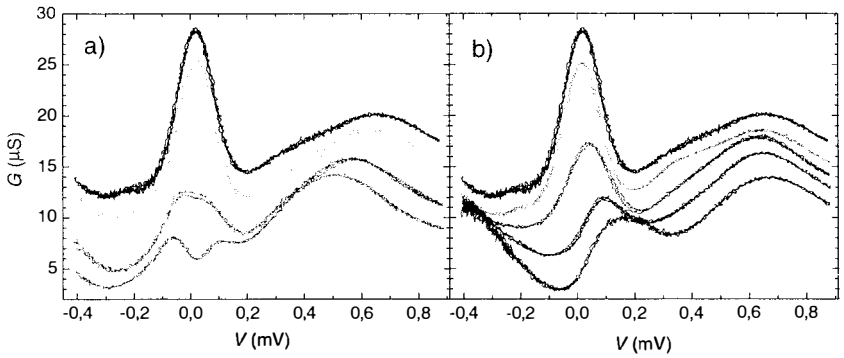


Figure 2: a) Conductance G vs. bias voltage V measured at $V_{gate} = -0.6, -0.65, -0.7, -0.75, -0.8$ V and (b) at $V_{gate} = -0.4, -0.45, -0.5, -0.55, -0.6$ V. $V_{gate} = -0.6$ V corresponds to the best conductance at small bias voltages.

References

1. See, *e.g.*, "Special Issue on Nanotubes" in Physics World, June 2000, p. 29, and also C. Dekker, Physics Today, May 1999, p. 22.
2. C. Schönenberger, A. Bachtold, C. Strunk, J.-P. Salvetat, and L. Forro, Applied Physics A **69**, 283 (1999).
3. M. Ahlskog, P. Hakonen, M. Paalanen, L. Roschier, and R. Tarkiainen, cond-mat/0104256.
4. R. Tarkiainen, M. Ahlskog, J. Penttilä, L. Roschier, P. Hakonen M. Paalanen, and E. Sonin, submitted to Phys. Rev. B.
5. M. Ahlskog, R. Tarkiainen, L. Roschier, and P. Hakonen Appl. Phys. Lett. **77**, 4037 (2000).
6. V.A. Krupenin, D.E. Presnov, M.N. Savvateev, H. Scherer, A.B. Zorin, and J. Niemeyer, J. Appl. Phys. **84**, 3212 (1998); V.A. Krupenin, D.E. Presnov, A.B. Zorin, and J. Niemeyer, J. Low Temp. Phys. **118**, 287 (2000).
7. See, *e.g.* B. Starmark, T. Henning, T. Claeson, P. Delsing, and A.N. Korotkov, J. Appl. Phys. **86**, 2132 (1999), and refrences therein.
8. L. Roschier, J. Penttilä, M. Martin, P. Hakonen, M. Paalanen, E. Kauppinen, U. Tapper, C. Journet, and P. Bernier, Appl. Phys. Lett. **75**, 728 (1999).
9. L. Roschier, R. Tarkiainen, M. Ahlskog, M. Paalanen, and P. Hakonen, Appl. Phys. Lett. **78**, 3297 (2001).
10. S. Frank, P. Poncharal, Z.L. Wang, W. A. de Heer, Science **280**, 1744 (1998).
11. J. Nygård, D.H. Cobden, and P.E. Lindelöf, Nature **408**, 342 (2000).
12. R. Tarkiainen *et al.*, to be published.
13. See *e.g.* Sh. Kogan, *Electronic Noise and Fluctuations in Solids* (Cambridge University Press, Cambridge, 1996), p. 31.
14. A.N. Korotkov, D.V. Averin, K.K. Likharev, and S.A. Vasenko, in *Single-Electron Tunneling and Mesoscopic Physics*, edited by H. Koch and H. Lubbig (Springer, Berlin, 1992), p.45; A. Korotkov, Phys. Rev. B **49**, 10381 (1994).

SPIN INJECTION AND MAGNETISM

TWO–COMPONENT INTERFERENCE EFFECT IN ONE– AND TWO–DIMENSIONAL SYSTEMS

PAVEL STŘEDA[1], PETR ŠEBA[1,2], ALEŠ VYHNAL[1]
[1] *Institute of Physics, Academy of Sciences of the Czech Republic, Cukrovarnická 10, 162 53 Praha*
[2] *Department of Physics, University of Hradec Králové, Víta Nejedlého 573, Hradec Králové*

Specific features of interference effects in two-component systems are described. It is argued that the arising additional interference between components strongly influences the partial conductances that are available e.g. in spin-polarized transport experiments.

1 Introduction

In the last years bilayer structures[1] composed of two coupled two-dimensional electron systems have been subject of the intensive studies. The current stage of the technology allows to attach electrical leads to each of the layers separately. The different conductivities could be thus measured in dependence on the position of current contacts. In the case of the symmetrical bilayer structure, there are two different conductances: $G_{11} = G_{22}$ for the source and drain attached to the same electron layer and $G_{12} = G_{21}$ if different layers are contacted. At low temperatures when the transport is fully coherent they are defined by partial transmission coefficients $T_{11} = T_{22}$ and $T_{12} = T_{21}$. Layer index, 1 and 2, is often called pseudo-spin and the above defined conductances have a similar meaning as that measured between ferromagnetic contacts with parallel and antiparallel orientation of the contact magnetization[2,3]. Both systems are thus expected to have similar basic transport properties.

The goal of this paper is to reveal those features of the transport properties which can be caused by the interference in weakly disordered systems. It can be expected that the standard weak localization have to be influenced by the existence of two components, subsystems of the same spin or pseudo-spin numbers. For simplicity the coupling between components is assumed to be associated with short-range scattering potentials only. In this case, sketched in Fig. 1, the exact solution, including fully the quantum coherence, can be found[4]. For example a double well structure in which the coupling is allowed only at holes in the barrier separating the electron layers can be modeled by this way.

It will be argued that in two-component systems an additional interference between components gives rise to oscillations of the difference between the partial transmission coefficients, $T_{11} - T_{12}$, in the dependence on model parameters. Its origin will be described in the simple case of a one-dimensional conductor, which leads to the same qualitative results.

2 One–dimensional case

The scattering of free electrons by short range scatterers located at points X_i $(i = 0, 1, .., n)$ is controlled by matching conditions for the wave function components $\Psi_1(x)$ and $\Psi_2(x)$. They have to be continuous and discontinuities of their derivatives from the right and from the left at X_i determine the strength of the interaction. The conditions have the following general form

$$\begin{aligned} \Psi_1(0) &= \frac{1}{A_i}\left[\Psi_1'(X_i)_+ - \Psi_1'(X_i)_-\right] + C_i\left[\Psi_2'(X_i)_+ - \Psi_2'(X_i)_-\right] , \\ \Psi_2(0) &= C_i\left[\Psi_1'(X_i)_+ - \Psi_1'(X_i)_-\right] + \frac{1}{A_i}\left[\Psi_2'(X_i)_+ - \Psi_2'(X_i)_-\right] , \end{aligned} \tag{1}$$

where A_i and C_i are real numbers if the system is supposed to be invariant to the pseudo-spin interchange and the time reversal symmetry is required. For zero values of C_i the subsystems are decoupled and scattering centers have the form of the potential $A_i\delta(x - X_i)$.

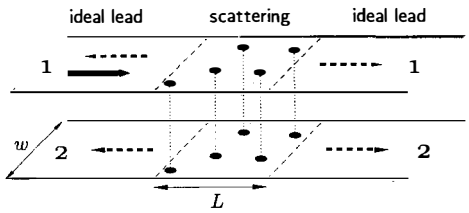


Figure 1: Scheme of the scattering process in a two-component system. Upper and lower strips of the width w represent the two-dimensional subsystems. Scatterers, black points, serve also as connection points between subsystems giving rise to a transition process.

In the case of a wave incoming from the left and belonging to the subsystem 1, the wave functions have the following form

$$\Psi_1(x_L) = e^{ikx_L} + \frac{1}{2}\left(r^{(+)} + r^{(-)}\right)e^{-ikx_L} \;;\; \Psi_1(x_R) = \frac{1}{2}\left(t^{(+)} + t^{(-)}\right)e^{ikx_R} ,$$
$$\Psi_2(x_L) = \frac{1}{2}\left(r^{(+)} - r^{(-)}\right)e^{-ikx_L} \;;\; \Psi_2(x_R) = \frac{1}{2}\left(t^{(+)} - t^{(-)}\right)e^{ikx_R} , \qquad (2)$$

where x_L and x_R denote coordinates within the asymptotic regions at the left or right of the scattering region, respectively. For a single scattering point X_0 we have

$$t_0^{(\pm)} = \frac{2k}{2k + i\Gamma_0^{(\pm)}} \;;\; r_0^{(\pm)} = t_0^{(\pm)} - 1 = -\frac{i\Gamma_0^{(\pm)}}{2k + i\Gamma_0^{(\pm)}} \;;\; \Gamma_0^{(\pm)} \equiv \frac{A_0}{1 \pm A_0 \cdot C_0} . \qquad (3)$$

Reflection and transmission amplitudes, $r^{(\pm)}$ and $t^{(\pm)}$, can be obtained by the following rotation of the pseudo-spin

$$\Psi^{(+)}(x) = \Psi_1(x) + \Psi_2(x) \quad ; \quad \Psi^{(-)}(x) = \Psi_1(x) - \Psi_2(x) . \qquad (4)$$

It can be shown that the wavefunctions $\Psi^{(+)}(x)$ and $\Psi^{(-)}(x)$ are solutions of the one-component one-dimensional scattering problem defined by positions of the scattering potential $\Gamma_i^{(+)}\delta(x - X_i)$ or $\Gamma_i^{(-)}\delta(x - X_i)$, respectively ($\Gamma_i^{(\pm)} \equiv A_i(1 \pm A_i \cdot C_i)^{-1}$). These two transformed subsystems are fully decoupled and there are no transitions between them. For large number of scatterers each of them has its own localization length, $\lambda^{(+)}$ or $\lambda^{(-)}$.

The total conductance G of the considered two-component system is given as the sum of the inverse resistances of newly defined parallel conductors

$$G = \frac{1}{1 + \left|\frac{r^{(+)}}{t^{(+)}}\right|^2} + \frac{1}{1 + \left|\frac{r^{(-)}}{t^{(-)}}\right|^2} = \left|t^{(+)}\right|^2 + \left|t^{(-)}\right|^2 \equiv 2(T_{11} + T_{12}) . \qquad (5)$$

Resulting localization length approaches the value $\lambda^{(+)}$, the larger one, in accord with the well known antilocalization effect [5].

The desired partial transmission coefficients are given as follows

$$T_{11} \equiv T_{22} = \frac{1}{4}|t^{(+)} + t^{(-)}|^2 = \frac{1}{4}|t^{(+)}|^2 + \frac{1}{4}|t^{(-)}|^2 + \frac{1}{2}|t^{(+)}||t^{(-)}|\cos\theta \qquad (6)$$
$$T_{12} \equiv T_{21} = \frac{1}{4}|t^{(+)} - t^{(-)}|^2 = \frac{1}{4}|t^{(+)}|^2 + \frac{1}{4}|t^{(-)}|^2 - \frac{1}{2}|t^{(+)}||t^{(-)}|\cos\theta , \qquad (7)$$

where θ denotes the difference of phase shifts gained during the transition through the decoupled subsystems identified by index $(+)$ and $(-)$. For small values of C_i $(0 < C_i << 1)$ the phase shift difference θ gradually increases with increasing number of scatterers resulting in oscillations of the difference $T_{11} - T_{12}$ surviving even for their configurationally averaged values.

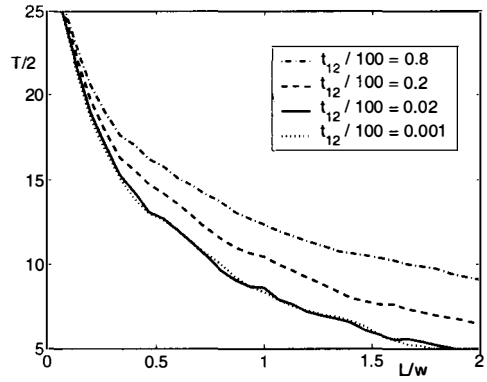


Figure 2: The total transmission coefficient T as function of the scattering region length L.

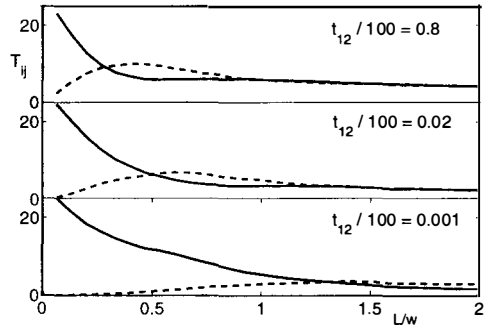


Figure 3: The partial transmission coefficients T_{11} (full line) and T_{12} (dashed line) as function of the scattering region length L for several values of the transition probability t_{12}.

3 Two–dimensional case

The results described in the previous section applies to many channel case as well, however, the derivation is not so straightforward. The scattering problem for a strip with a finite number of short-range scatterers, as sketched in Fig. 1, has been solved numerically. We assumed that all scatterers are identical, i.e. they give the same scattering cross-section σ_0 and transition probability t_{12} between subsystems if they would be placed alone within the two-dimensional space. To simplify the description by excluding the quantum fluctuations from our consideration the configurationally averaged values of the transmission coefficients will be discussed.

In Fig. 2 and Fig. 3 the dependence of transmission coefficients on the length L of the scattering region is shown. The used energy corresponds to 34 occupied subbands. Concentration of scatterers, $750/w^2$, and the total scattering cross-section $\sigma_0 = 0.1217$ where held fixed. Probability of an injected electron to cross scattering region increases with increasing transition probability t_{12} as shown in Fig. 2 where the total transmission coefficients $T = 2(T_{11} + T_{12})$ are plotted. This tendency is in agreement with expected antilocalization effect [5].

The more interesting is the dependence of partial transmission coefficients T_{ij}. For some values of the transition probability t_{12} and lengths L, partial transmission coefficients T_{11} become less than T_{12}, as can be seen in Fig. 3. We ascribe this unexpected result to the additional inter-

ference appearing in two-component systems described for the one-dimensional case. Predicted oscillations of the difference $T_{11} - T_{12}$ are strongly damped due to the localization effect.

4 Spin-orbit interaction

In the absence of magnetic impurities the natural candidate for spin dephasing and precession effects controlling spin-polarized transport is the spin-orbit coupling to impurity atoms or defects. The corresponding Hamiltonian has the following form

$$H = \frac{\vec{p}^2}{2m} + V(\vec{r}) + \frac{1}{4m^2c^2}\vec{\sigma} \times \nabla V(\vec{r}) \cdot \vec{p}\,, \tag{8}$$

where $\vec{\sigma}$ is the Pauli spin operator with components

$$\sigma_x \equiv \begin{pmatrix} 0 & 1 \\ 1 & 0 \end{pmatrix} \quad , \quad \sigma_y \equiv \begin{pmatrix} 0 & -i \\ i & 0 \end{pmatrix} \quad , \quad \sigma_z \equiv \begin{pmatrix} 1 & 0 \\ 0 & -1 \end{pmatrix} \quad . \tag{9}$$

In strictly two-dimensional case for which the potential $V(\vec{r})$ depends on x and y coordinates only the Hamiltonian commutes with σ_z and z component of the spin, $s_z = \pm\frac{1}{2}$, is a good quantum number. In this case eigenvalue problem requires to solve two independent Schrödinger equations for $\Psi^{(+)}$ and $\Psi^{(-)}$ representing states $s_z = +\frac{1}{2}$ and $s_z = -\frac{1}{2}$, respectively. As the results of the scattering problem the amplitudes, $r^{(\pm)}$ and $t^{(\pm)}$ can be obtained.

In the standard experimental setup the planar ferromagnetic contacts are used and their magnetic moments lie within the plane of studied two-dimensional systems. To model the corresponding spin polarized transport the results obtained in σ_z-representation have to be projected to the eigenfunctions of the spin operators σ_x or σ_y. In the one-channel case the transmission coefficients $T_{\uparrow\uparrow}$ and $T_{\uparrow\downarrow}$ have the same form as T_{11} and T_{12} given by Eqs.(6-7). It can be thus expected that the transmission coefficient for spin polarized transport in two-dimensional systems will show the same qualitative features as that presented in Fig. 3.

5 Concluding remarks

There is not a straightforward relation between partial conductances, G_{11} and G_{12}, and discussed transmission coefficients, T_{11} and T_{12}. However, it has been found that they have qualitatively the same features [6]. The above described analysis leads to the conclusion that the additional interference appearing in any two-component systems might be useful to understand some mysteries of the recent experimental observation. Especially, it might be responsible for the change of sign of the difference of two terminal conductances measured for parallel and antiparallel orientation of the contact magnetization [2,3].

References

1. A.Lorke, U.Merkt, F.Malcher, G.Weimann and W.Schlap, *Phys. Rev.* **B 42**, 1321 (1990).
2. C.M.Hu, J.Nitta, A.Jensen, J.B.Hansen and H.Takayanagi, *Phys. Rev.* **B 63**, 5333 (2001).
3. T. Matsuyama, G. Meier, D. Grundler, R. Kürsten and U. Merkt, *Proc. 25th Int. Conf. Semiconductor, Osaka 2000* (Springer, Heidelberg 2001).
4. P. Exner, R. Gawlista, P. Šeba and M. Tater, *Ann. Phys.* **252**, 133 (1996).
5. S. Hikami, A.I. Larkin and Y. Nagaoka, *Progr. Teor. Phys.* **63**, 707 (1980).
6. P.Šeba, P.Exner, K.N.Pichugin, A.Vyhnal and P.Středa, *Phys. Rev. Lett.* **86**, 1598 (2001).

DESIGN OF A SEMICONDUCTOR FERROMAGNET IN ARTIFICIAL CRYSTALS

Hideaki Takayanagi[1], Hiroyuki Tamura[1], Kenji Shiraishi[2], Takashi Kimura[1]

[1] *NTT Basic Research Laboratories, 3-1 Morinosato-Wakamiya, Atsugi 243-0198, Japan*

[2] *Department of Physics, Tsukuba University, Tsukuba 305-8271, Japan*

Possibility of flat-band ferromagnetism in quantum dot arrays is theoretically discussed. We consider dot arrays on Lieb and kagome lattices known to exhibit flat band ferromagnetism. By performing an exact diagonalization of the Hubbard Hamiltonian, the energy difference between the ferromagnetic ground state and the paramagnetic excited state is calculated. The dot-size dependence of the energy difference provides the estimation of the transition temperature of the ferromagnetic-paramagnetic transition. It is also shown that the flat-band ferromagnetism in the kagome lattice is broken as the flat band has finite dispersion in the magnetic field. A metal-insulator transition induced by the magnetic field is predicted. The calculations based on local density functional approximation show that the structure comprising the crossing InAs quantum wires works effectively as a kagome superlattice and has the ferromagnetic ground state when the flat band is half-filled.

1 Introduction

Recent progress in the fabrication technology in nano-scale has enabled us to make various types of small devices using semiconductor quantum dots. The present authors have proposed a new type of device forming a superlattice of quantum dots.[1] If we consider a quantum dot as a building block and put it on a site of the lattice, we can create an artificial crystal having interesting properties. In the dot lattice, we can design any type of lattice structure as we like regardless of number of electrons in it. Lieb [2] and kagome [3] lattices are interesting examples of such artificial lattices, because they have a dispersion-less subband (flat band) in their single-particle band structures. It has been proven that, in the repulsive Hubbard model of these lattices, ferromagnetism appears. However, there has been no clear evidence of the observation of flat-band ferromagnetism, because it is difficult to form these lattices using real materials since a lattice distortion effect would destabilize the ferromagnetism when the flat band is half-filled.

On the other hand, dot lattices do not have such a disadvantage. The dot lattice does not undergo structural deformations by electronic effects such as the Jahn-Teller distortion. Then, one can design lattice structures which do not exist in nature without worrying about the lattice instability. Moreover, the number of electrons in it can be changed in a controllable manner. By putting a gate electrode on the top of the electron gas, it is easy to modify the electron filling by changing the gate voltage.

In this paper, we discuss the possibility of realizing flat-band ferromagnetism in quantum dot superlattices. We consider two types of two dimensional dot lattices (Lieb and kagome lattices) and obtain single-particle band structures. Then we diagonalize a Hubbard Hamiltonian for these lattices and obtain the energy difference of the ferromagnetic ground state and the paramagnetic excited state. The exact diagonalization also provides interesting magnetic field effects on the kagome lattice, e.g., that the ferromagnetic-paramagnetic transition and the metal-insulator one occur simultaneously in the half-filled flat band. We also calculate the electronic characteristics of a structure comprising the crossing InAs quantum wires. The calculations based on local density functional approximation show that the structure works effectively as a kagome superlattice and has the ferromagnetic ground state when the flat band is half-filled.

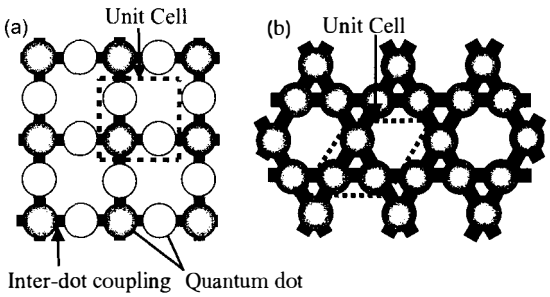


Figure 1: Lieb lattice (a) and kagome lattice (b). Solid lines represent the nearest neighbor transfer t.

2 Flat Band

We consider two types of dot arrays. Figure 1(a) is a two-dimensional Lieb lattice and Fig. 1(b) is a kagome lattice. Lieb lattice is a bipartite lattice which consists of two sublattices. Kagome lattice is a line graph of the hexagonal lattice. We consider a Hubbard model

$$H = -t \sum_{(i,j)\sigma} c^{+}_{i\sigma} c_{j\sigma} + U \sum_{i} n_{i\uparrow} n_{i\downarrow}, \tag{1}$$

where t is the transfer between a pair (i, j) of the nearest neighboring sites i and j, U is the on-site Coulomb energy on the site i, $c^{+}_{i\sigma}(c_{i\sigma})$ is the creation (annihilation) operator of an electron on the site i with spin $\sigma = \uparrow$ or $\downarrow$, and $n_\sigma = c^{+}_{i\sigma} c_{i\sigma}$. If the electrons are well localized near the dots but still can transfer between nearest-neighboring dots, the tight-binding approximation can be applied. By solving the tight-binding Hamiltonian (1) with $U = 0$ for the Lieb and the kagome lattices, we obtained a single-particle band structures shown in Fig. 2. In both cases, dispersionless flat bands are formed in the middle for the Lieb and in the top for the kagome lattice.

3 Exact Diagonalization[4]

We diagonalize the Hubbard Hamiltonian (1) for 2×2 unit cells of 12 dots. For the Lieb lattice, we use an anti-periodic boundary condition in the x direction and a periodic boundary condition in the y direction in order to avoid an unimportant finite-size effect of additional degeneracy at the cross point of the flat-band and dispersion band. For the kagome lattice, we use an ordinary periodic boundary condition.

3.1 High Spin States

The exact diagonalization provides the total spin of the ground state as a function of the number of electrons N. Figure 3 shows the total spin as a function of N for (a) the Lieb lattice and for (b) the kagome lattices. For any $U/t > 0$, high spin states appear at the half-filling ($N = 12$) for the Lieb lattice and $19 \leq N \leq 22$ for the Kagome lattice. This result is consistent with the theorems proved by Lieb [2] for the Lieb lattice and by Mielke [3] for the kagome lattice. The theorem by Lieb is that the repulsive Hubbard model with a half-filled flat-band in a bipartite lattice structure (i.e., there is one electron per dot) exhibits ferromagnetism with the total spin $S = |N_A - N_B|/2$ where N_A and N_B is the number of dots in sublattices A and B. Mielke also showed that the kagome lattice shows a ferromagnetic behavior for the electron filling of $5/3 \leq n < 11/6$. It is noted that the ferromagnetic state appears in a wide range of electron

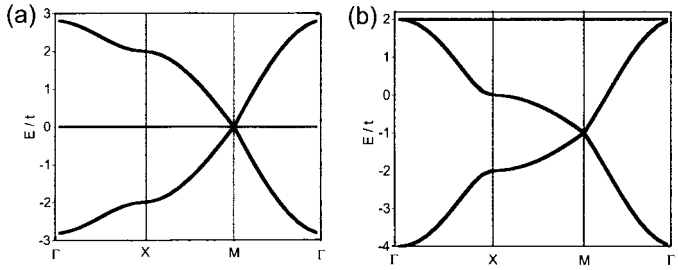


Figure 2: Single-particle band energy E for (a) Lieb and (b) kagome lattice calculated using the tight-binding approximation, where E is normalized in units of t.

filling in the kagome lattice, whereas ferromagnetism appears only at the half-filling for the Lieb lattice.

3.2 Transition Temperature

We can also calculate the energy difference ΔE between the ground state with spin $S = 2$ and the lowest excited state with spin $S = 0$ when the flat-band is half-filled, i.e., $N = 12$ for the Lieb and $N = 20$ for the kagome lattice. This energy difference can be regarded as a qualitative estimate of the transition temperature of ferromagnetic and paramagnetic transition in a macroscopic sample like a semiconductor quantum-dot array.

As Lieb has already pointed out, the high spin state in the Lieb lattice is caused by the antiferromagnetic ordering at the half-filling. The high spin state in the kagome lattice is caused by an effective exchange interaction of the third-order process cycling and exchanging two electrons with the opposite spins within the triangular lattice of three sites. When $U/t \gg 1$, one can deduce $\Delta E \simeq 4.3t^2/U$ for the Lieb lattice and $\Delta E \simeq 0.26t$ for the kagome lattice.

When U/t is small, the energy difference is proportional to U in both cases, i.e., $\Delta E \simeq 0.16U$ for the Lieb lattice and $\Delta E \simeq 0.05U$ for the kagome lattice. This is because the Coulomb repulsion raises the energy of the order of U when electrons on the flat band have the opposite spins in the lowest spin state, whereas, by the Pauli principle, it does not when electrons on the flat band have the same spins in the high spin state.

To evaluate t and U for quantum dot arrays, we assume that the electrons are confined in a two-dimensional confinement potential given by $V(r) = m^*\omega^2(r^2 - a^2)/2$, where m^* is the effective mass of an electron, ω is the confining oscillator frequency, and a is the inter-dot spacing. The atomic wavefunction localized in the potential $V(r)$ is given in a good approximation by $\phi(r) = (2/\sqrt{\pi}d)\exp(-2r^2/d^2)$, where $d = 2\sqrt{\hbar/m^*\omega}$ is the dot-diameter. The transfer and on-site Coulomb energies are given by

$$t = \hbar\omega\left(1 - \frac{7a^2}{2d^2}\right)\exp\left(-\frac{a^2}{d^2}\right), \quad U = \frac{\sqrt{2\pi}}{4\pi\varepsilon d}, \tag{2}$$

where ε is the dielectric constant. In realistic dot arrays formed by a negatively biased gate electrode depleting the underneath two-dimensional electron gas, the inter-dot spacing is usually fixed and cannot be changed. By mofying the gate voltage, the dot-diameter can be changed. To simulate this, we evaluate t and U from Eq. (2) for a fixed inter-dot spacing and calculate ΔE as a function of dot diameter. The energy difference is appreciable for $0.3 \leq d/a \leq 0.7$. We estimate ΔE for dot arrays of various sizes. We consider GaAs, InAs, and Si dots and assume $a = 2d$. For dots with a spacing of 100 nm which is available within the present fabrication technology, ΔE is of the order of several hundreds mK and we can expect that ferromagnetism

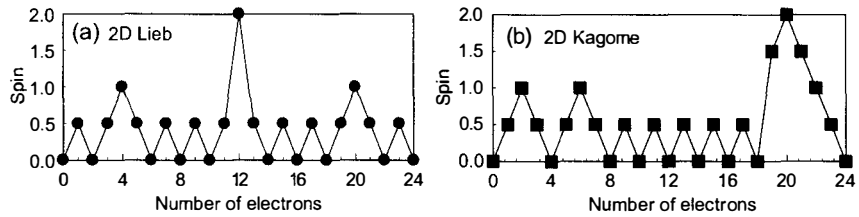


Figure 3: Total spin as a function of the number of electrons $0 \leq N \leq 24$ for (a) $U/t = 10$ in the Lieb lattice and for (b) $U/t = 4$ in the kagome lattice.

is observable in the dilution teperature region. For dots of spacing 5 nm, ΔE is as high as a few tens of K.

3.3 Magnetic Field Effect [5]

We study the magnetic field effects on the kagome lattice. We assume a tight-binding model again. The magnetic field is incorporated in hopping integral t_{ij} in the usual manner through the Peierls phase for a gauge field as $t_{ij}(\boldsymbol{A}) \equiv t\exp(i\theta_{ij})$, $\theta_{ij} = -(2\pi/\Phi_0)\int_{\boldsymbol{r}_i}^{\boldsymbol{r}_j} \boldsymbol{A}\cdot d\boldsymbol{r}$, where $\boldsymbol{A}$ is a vector potential for the magnetic field Φ, $\Phi_0 \equiv h/e$ is the magnetic flux quantum. We obtain the Hofstadter butterfly (the single-particle energy spectrum) of the kagome lattice. The magnetic field changes the phase of the wave function and the interference between the electron wave functions. As a result, the magnetic field breaks the interference-oriented flat band in the kagome lattice. It is noted that the flat band is not always broken by a magnetic field for other lattice structures. For example, the flat band of the Lieb lattice is preserved even in a magnetic field. This is because that the flat band in the Lieb lattice originates not from the interference but from the lattice topology.

In order to discuss the magnetoresistance in the kagome lattice, let us come back to the exact diaginalization of the Hubbard Hamiltonian (1) with $t_{ij}(\boldsymbol{A})$ instead of t. We calculate the Drude weight D of the ground states for the kagome lattice with 2 unit cells. In the bulk limit, generally speaking, if $D = 0$, the system is insulating, while if $D > 0$ it is metallic (or superconducting). Let us start from the case when the filling is away from half-filled on the flat band. All data of the Drude weight are overlapped at $D = 0$, indicating the insulating behavior at zero magnetic field, and become finite, indicating the metallic behavior when the magnetic field is applied. The metal-insulator transition induced by the magnetic field leads to the giant negative magnetoresistance (GNMR) of the kagome lattice. The GNMR is clearly understood within a single-particle picture. The group velocity of electrons is zero without the magnetic field and the system is insulating. In magnetic field the flat band has a finite curvature and the group velocity becomes finite, resulting in a matallic system.

We also calculate the Drude weights at the half filled flat band. For small $U/t < 3.8$ the magnetic field dependence is qualitatively the same as that for the case away from half filling. However, for large U/t, we find the metal-insulator transition occurs simultaneously with the ferromagnetic-paramagnetic one for a magnetic field ($\Phi = 1/8$). We can see for large U/t that the high-spin st ($S = 2$) and insulating states with neglibible Drude weights below $\Phi = 1/8$ turn into the low-spin ($S = 0$) and metallic states with finite Drude weights above $\Phi = 1/4$.

Let us consider the physical picture for these simultaneous transitions. The electrons on the flat band for the high-spin state have the same spin direction. We should remember that the number of $k-$points and and that of the electrons are exactly the same at half filling. Thus, all the up-spin states for the high-spin states are completely occupied at the half-filling, while all the down-spin states are unoccupied. Thus, the up-spin electrons on the flat band cannot

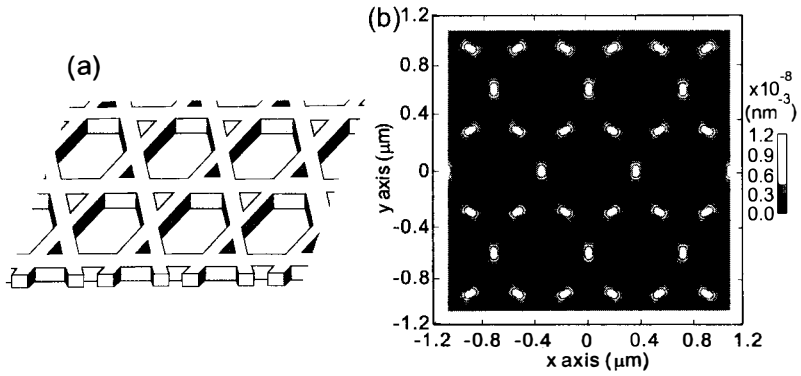


Figure 4: The effective kagome crystal we examined. (a) The crossing quantum wire is InAs. The cross section of each wire is square shaped. The cross point is identical to a kagome crystal. (b) A cross-sectional view of LSDA-calculated spin density of ferromagnetic states.

move there because of the Pauli principle and the absence of any spin-flipping processes in the present Hamiltonian. There are the reasons the high-spin states are insulating at half filling. Above $\Phi = 1/4$, the metallic states appear because there the ground states turn to low-spin ones where both unoccupied and occupied states co-exist for both up and down spins and electrons can now move, resulting in the simultaneous ferromagnetic-paramagnetic and metal-insulator transitions.

There is an important advantage of a mesoscopic system when we study magnetic field effects discussed here. In bulk systems the magnetic field that is needed in order to input a magnetic-flux quantum within a unit cell, which has a lattice constant of few angstroms, is of the order of 10^4 T, but in quantum dot superlattices, the magnetic field needed is very small and realistic. For example, in the kagome dot superlattice proposed in the next section, the magnetic field needed is of the order of 0.1 T.

4 Local Spin Density Functional Approximation [6]

We finally examine the structure which contains crossing quantum wires with square cross sections as shown in Fig. 4(a). The width of each quantum wire is 0.104 μm. and the lateral size of each two-dimensional unit cell is 0.72 μm. We assume that the quantum wire is InAs surrounded by $In_{0.72}Ga_{0.28}As$ barrier regions with barrier height of 0.21 eV. Since the effective width of quantum wires at the cross points is larger than the normal width of the wire, the cross points can act as qunatum dot aritificial atoms. Accordingly, we expect that this artificial structure would prove to be effectively identical to a kagome superlattice, for which flat-band ferromagnetism is predicted.

We investigate the electronic strutures of paramagnetic states, and examine whether a kagome superlattice is truly formed. To calculate the electronic structure, we perfome first-principles electronic structure calculation based on the local spin density functional approximation (LSDA) with the Perdew-Zunger exchange-correlation potential. In the calculations, wave functions are expanded by a plane wave basis set. The band structure of the paramagnetic configuration when five electrons are contained in each unit cell shows that the third lowest band is dispersionless and half-filled. This flat-band characteristics is well reproduced by the tight-binding Hamiltonian of the kagome lattice discussed in the previous section. This indicates that the quantum-wire based structure acts as a kagome superlattice. This is also confirmed

by the calculated total charge density. The calculated total charge density has maxima at the rectangularly shaped cross points, thus forming a kagome superlattice.

Next, we examine the ferromagnetic state of this kagome superlattice. The calculated spin density has maximums at the cross points, forming a kagome superlattice as shown in Fig. 4(b). This figure clearly indicates the appearrance of ferromagnetism. The calculated band structures show that the Fermi level is located between up- and down-spin flat-bands, reflecting the ferromagnetism. The energy separation between up- and down-spin bands is 0.05 meV. The total energy of the ferromagnetic state is lower than that of the paramagnetic state by about 130 mK. These results indicate that the ground state of this kagome superlattice is ferromagnetic. It is surprising that whether non-magnetic semiconductor changes into ferromagnetic material solely depends on the shape of the array of quantum dots.

We also find that the ground state is still ferromagnetic when the flat band is partly filled other than half-filled, and becomes paramagnetic when the flat band is empty or fully filled. Therefore, the ferromagnetic and the paramagnetic states can be freely switched when the electron filling in the flat band is modulated by applying a gate voltage. We also find that the structures with smaller wire width enhance the stability of ferromagnetic states; the energy difference between para- and ferromagnetic states in the effective kagome superlattice with 10 nm-wide InAs becomes 2.3 K.

5 Conclusions

Flat-band ferromagnetism in quantum dot arrays has been theoretically discused. We considered dot arrays on the Lieb and kagome lattices which are known to exhibit flat-band ferromagnetism. We performed the exact diagonalization of the Hubbard Hamiltonian and calculated the energy difference or the transition temperature of ferromagnetic and paramagnetic states in the Lieb and the kagome superlattices. The exact diagonalization also showed the flat-band ferromagnetism in the kagome lattice is broken in the magnetic field. A metal-insulator transition induced by the magnetic field was predicted in this system. We also performed the calculations based on local spin density functional approximation for the structure comprising the crossing InAs quantum wires. The result showed that the examined structure works effectively as a kagome superlattice and has the ferromagnetic ground state when the flat band is half-filled. It is noted that the flat-band ferromagnetism as well as interesting phenomena discussed in this paper can be observable in dot arrays fabricated using the present technology.

Acknowledgments

We would like to thank Prof. K. Kuroki and Prof. K. Kusakabe for valuable discussions. We also thank Dr. S. Ishihara for his support of the present work. This work was partly supported by NEDO International Joint Research Grant.

References

1. H. Tamura, K. Shiraishi, and H. Takayanagi, *Jpn. J. Appl. Phys.* **39**, L241 (2000).
2. E. H. Lieb, *Phys. Rev. Lett.* **62**, 1201 (1989).
3. A. Mielke, *J. Phy. A: Math. Gen.* **24**, L73 (1991).
4. H. Tamura, K. Shiraishi, T. Kimura, and H. Takayanagi, *cond-mat/0105021.*
5. T. Kimura, H. Tamura, K. Shiraishi, and H. Takayanagi, *cond-mat 0104043.*
6. K. Shiraishi, H. Tamura, and H. Takayanagi, to be published in *Appl. Phys. Lett.* May, (2001).

SPIN TRANSPORT AND SPIN INJECTION IN MESOSCOPIC METAL AND SEMICONDUCTOR DEVICES

B.J. VAN WEES, F.J. JEDEMA, A.T. FILIP
Department of Applied Physics and Materials Science Centre, Nijenborgh 4.13, University of Groningen, The Netherlands

We present our recent experiments on spin dependent transport in mesoscopic systems. First we give a basic theoretical description of spin transport in multiterminal devices. It is shown that multiterminal measurements make it possible to fully isolate the spin valve signal from other spurious (magnetoresistance) effects. Experiments on spin transport in metal and low-dimensional semiconductors are discussed. Spin accumulation and spin transport are observed in permalloy/copper spin valves, allowing a determination of the spin flip lengths in copper strips($\approx 1\mu m$ at 4.2 K and $\approx 350nm$ at room temperature). It is shown that the failure to observe spin transport in ferromagnet/semiconductor devices might be explained by "conductivity mismatch" arguments.

1 Introduction

Spintronics is a rapidly emerging field in which one tries to study, or make explicit use of, the spin degree of freedom of the electron. Sofar the most well known examples of spintronics are the tunneling magnetoresistance (TMR) of magnetic tunnel junctions, and the giant magneto resistance (GMR) of multilayers. A new direction is emerging, where one actually attempts to inject spin currents, transfer and manipulate the spin information, and detect the resulting spin polarization. Most of the efforts have focussed sofar at generating or detecting spin accumulation in semiconductors with (circularly) polarized light [1,2,3] However, from a device point of view, as well as a for studying the fundamental properties of spin transport, it is desirable to have fully electrical injection and detection, preferably at room temperature. For this it is necessary to study spin transport on mesoscopic scales (typically 1 μm). This contribution describes our recent studies of spin transport, where we have used conventional ferromagnets as injectors and detectors. They are connected to either a two-dimensional electron gas (2DEG) present in InAs/Al(Ga)Sb heterojunctions, or a non-magnetic metal.

2 Basic model for spin transport in diffusive systems

We first give a review of the basic model for spin transport,which we will call the "standard model". We focus on the diffusive transport regime, which applies when the mean free path l is shorter than the device dimensions. The description of electrical transport in a ferromagnet in terms of a two-current (spin-up and spin-down) model dates back to Fert and Campbell [4]. Van Son et al.[5] have extended the model to describe transport through ferromagnet-normal metal interfaces. A firm theoretical underpinning, based on a Boltzmann transport equation, has been given by Valet and Fert [6]. They have applied the model to describe the effects of spin accumulation and spin dependent scattering on the giant magneto resistance (GMR) effect in magnetic multilayers [9,10]. The "standard" model allows for a detailed quantitative analysis of the experimental results.

An alternative model, based on thermodynamic considerations, has been put forward and applied by Johnson [7,8]. In principle both models describe the same physics, and should therefore be equivalent. However, the Johnson model has a drawback in that it does not allow a direct calculation of the spin polarization of the current (η in refs.[7,8]), whereas in the standard model all measurable quantities can be directly related to the parameters of the experimental system.

In the model the transport in a ferromagnet is described by spin dependent conductivities:

$$\sigma_\uparrow = N_\uparrow e^2 D_\uparrow \quad with \quad D_\uparrow = 1/3 v_{F\uparrow} l_\uparrow, \tag{1}$$

$$\sigma_\downarrow = N_\downarrow e^2 D_\downarrow \quad with \quad D_\downarrow = 1/3 v_{F\downarrow} l_\downarrow \tag{2}$$

Here $N_{\uparrow,\downarrow}$ denotes the spin dependent density of states (DOS) at the Fermi energy, and $D_{\uparrow,\downarrow}$ the spin dependent diffusion constants, expressed in the spin dependent Fermi velocities $v_{F\uparrow,\downarrow}$, and electron mean free paths $l_{\uparrow,\downarrow}$. Note that the spin dependence of the conductivities is determined by *both* density of states and diffusion constants. This should be contrasted with magnetic F/F or F/N *tunnel* junctions, where the spin polarization of the tunneling electrons is determined by the spin-dependent DOS only. Also in a typical ferromagnet several bands (which generally have different spin-dependent densities of states) contribute to the transport. However, provided that the elastic scattering time and the interband scattering times are shorter than the spin-flip times (which is usually the case) the transport can still be described in terms of spin-up and spin-down conductivities.

According to eqs.1,2 in a bulk ferromagnet the current is spin polarized, with a polarization given by:

$$\alpha_F = \frac{\sigma_\uparrow - \sigma_\downarrow}{\sigma_\uparrow + \sigma_\downarrow} \tag{3}$$

The next step is the introduction of spin flip processes, described by a spin flip time $\tau_{\uparrow\downarrow}$ for the average time to flip an up-spin to a down-spin, and $\tau_{\downarrow\uparrow}$ for the reverse process. The detailed balance principle imposes that $N_\uparrow/\tau_{\uparrow\downarrow} = N_\downarrow/\tau_{\downarrow\uparrow}$, so that in equilibrium no net spin scattering takes place. As pointed out already, usually these spin-flip times are larger than the momentum scattering time $\tau = l/v_F$. The transport can then be described in terms of the parallel diffusion of the two spin species, where the difference in densities is controlled by spin-flip processes. It should be noted however that in particular in ferromagnets (e.g.permalloy[11])the spin flip times may become comparable to the momentum scattering time. In this case an (additional) spin-mixing resistance arises[9], which we will not discuss further here.

The effect of the spin-flip processes can now be described by the following equation (assuming for simplicity diffusion in one dimension only):

$$D\frac{\partial^2(\mu_\uparrow - \mu_\downarrow)}{\partial x^2} = \frac{(\mu_\uparrow - \mu_\downarrow)}{\tau_{sf}} \tag{4}$$

Here $D = D_\uparrow D_\downarrow (N_\uparrow + N_\downarrow)/(N_\uparrow D_\downarrow + N_\downarrow D_\uparrow)$ is the spin averaged diffusion constant, and the spin-relaxation time τ_{sf} is given by: $1/\tau_{sf} = 1/\tau_{\uparrow\downarrow} + 1/\tau_{\downarrow\uparrow}$. The general solution of eqs. 1 and 3. for a uniform ferromagnet or non-magnetic wire is now given by:

$$\mu_\uparrow = a + bx + \frac{c}{\sigma_\uparrow} exp(-x/\lambda_{sf}) + \frac{d}{\sigma_\uparrow} exp(x/\lambda_{sf}) \tag{5}$$

$$\mu_\downarrow = a + bx - \frac{c}{\sigma_\downarrow} exp(-x/\lambda_{sf}) - \frac{d}{\sigma_\downarrow} exp(x/\lambda_{sf}) \tag{6}$$

Here the spin diffusion length $\lambda_{sf} = \sqrt{D\tau_{sf}}$. The coefficients a,b,c, and d are determined by the boundary conditions imposed at the junctions where the wires are coupled to other wires etc. In the absence of spin flip scattering at the interfaces the boundary conditions are: 1) continuity of $\mu_\uparrow, \mu_\downarrow$ at the interface, and 2) conservation of spin-up and spin-down currents $j_\uparrow, j_\downarrow$ across the interface.

As remarked already, the physics of spin injection/detection with an F/N tunnel junction is different. The most important difference between a F/N tunnel junction and a F/N clean contact is that in the first case the spin polarization of the current is determined by the composition of and properties of the first atomic layers next to the tunnel barrier. A non-magnetic

("magnetically dead") region of only a few atoms thick can already fully suppress the spin polarization (of the density of states). In contrast, as will be shown in the next section, for clean contacts the spin polarization is determined by a region of thickness λ_F away from the interface. Since usually $\lambda_F \gg l$, this can be considered as a "bulk" property of the ferromagnet. In this case a non-magnetic interface layer has no effect on the spin polarization, as long as its length is shorter than the spin-flip length.

3 The F/N interface

Van Son et al.[5] applied eqs.1 to 3 describe the spin accumulation and spin-coupled resistance of an F/N interface. Fig.1 shows how the spin-polarized current in the (bulk) ferromagnet is converted into a non-polarized current in the paramagnetic region (a non-magnetic metal or semiconductor) away from the interface. As can be seen in fig.1 two phenomena occur. First a

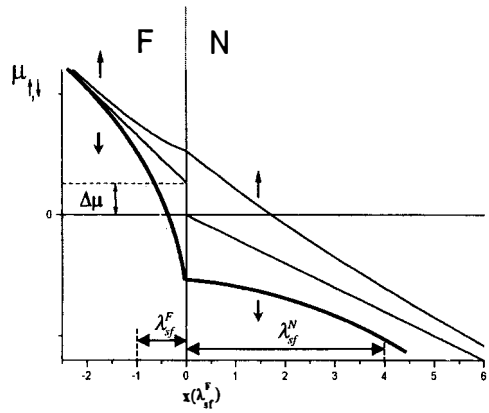


Figure 1: Electrochemical potentials (or densities) of spin-up and spin-down electrons as a function of position x relative to the F/N interface, with a current I through the interface. Both spin accumulation as well as spin coupled resistance can be observed (see text) The figure corresponds to $\lambda_N = 5.\lambda_F$.

"spin-coupled" interface resistance arises given by:

$$\Delta R = \frac{\Delta\mu}{eI} = \frac{\alpha_F^2 \lambda_N \lambda_F}{\sigma_N \lambda_F + (1-\alpha_F^2)\sigma_F \lambda_N} \tag{7}$$

The second phenomenon is that at the interface the electrochemical potentials $\mu_\uparrow, \mu_\downarrow$ of spin-up and spin-down electrons diverge. This implies that spin accumulation occurs, which has a maximum value at the interface:

$$\mu_\uparrow - \mu_\downarrow = \frac{2\Delta\mu}{\alpha_F} \tag{8}$$

with $\Delta\mu$ given by eq.7. In addition the expression for the spin polarization P of the current at the interface is:

$$P = \frac{I_\uparrow - I_\downarrow}{I_\uparrow + I_\downarrow} = \frac{\alpha_F \sigma_N \lambda_F}{\sigma_N \lambda_F + (1-\alpha_F^2)\sigma_F \lambda_N} \tag{9}$$

For conventional ferromagnets α_F is expected to be in the range $0.1 < \alpha_F < 0.7$. The above then shows that the magnitude of spin-coupled resistance, spin accumulation, and polarization of the current is essentially limited by $\sigma_N^{-1}\lambda_N$ or $\sigma_F^{-1}\lambda_F$, which ever is the smallest. Since in almost all cases $\lambda_F \ll \lambda_N$ for metallic systems, this implies that the spin flip length in a ferromagnet is the

limiting factor. This problem becomes progressively worse when (high conductivity) metallic ferromagnets are used to inject spin polarized electrons in(low conductivity)semiconductors. We will discuss this "conductivity mismatch" problem in section 9.

4 Spin accumulation in multiterminal spin valve structures

The elementary way to study spin accumulation effects is to use spin valves. These can be F/F, F/N/F, or ../F/N/F/N/.. multilayer structures. Spin accumulation effects play an important role in these systems (for reviews see [9,10]). However, the effects of spin accumulation are often difficult to separate from the magnetoresistance of the ferromagnets, such as anisotropic magnetoresistance (AMR), spin dependent interface scattering, (anomalous) Hall effects etc. The solution is provided by using a multiterminal geometry, where separate current and voltage leads are used. This technique was pioneered by Johnson and Silsbee [8], who studied spin injection in a single crystal Al bar at low temperatures. Due to the relatively large size of their samples, and consequently extremely low resistances (in the $n\Omega$ range), SQUID based measurements were required to measure the small signals. A second experimental system is the Johnson spin transistor [8], which we will discuss in more detail in section 5.

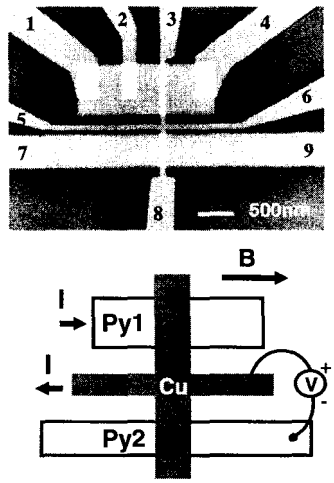


Figure 2: Sample layout (a) Scanning electron microscope image of the mesoscopic spin valve junction. The two wide strips are the ferromagnetic electrodes Py1 and Py2. The vertical arms of the Cu cross (with contacts 3 and 8) lay on top of the Py strips, the horizontal arms of the Cu cross form contacts 5 and 6. Contacts 1,2,4,7, and 9 are attached to Py1 and Py 2 to allow four-terminal AMR measurements of the Py electrodes. (b) Schematic representation of the non-local measurement geometry. Current is entering from contact 1 and extracted at contact 5. The voltage is measured between contacts 6 and 9.

We will illustrate this technique by experiments of Jedema et al.[12], who fabricated and studied mesoscopic spin valve structures for the study of spin accumulation in metal systems (see fig. 2) Two 50 nm thick ferromagnetic permalloy (NiFe) strips are deposited on a substrate. Their geometry (length/width ratio) is chosen differently in order to obtain different coercive fields. In a second evaporation step a Cu cross is deposited. Care is taken that the interface between the Py and the Cu is clean, by using Kaufmann sputter cleaning to remove any oxide or contamination.

In the "potentiometric" [7], or (equivalently) "non-local" [12]geometry current is send from 1 to 5

and the voltage is measured between 6 and 9. In this configuration the voltage drop in the injector ferromagnet is not measured, whereas there is no net charge current, and therefore no voltage drop in the ferromagnetic electrode which measures the voltage. Therefore all magnetoresistance effects of the ferromagnets themselves are eliminated from the measurements. By matching solution of eq. 4 at the F/N interfaces and the centre of the Cu cross, one obtains the following expression for the measured resistance in parallel: $R_{\uparrow\uparrow}$ and in anti parallel: $R_{\uparrow\downarrow}$ configuration

$$R_{\uparrow\uparrow,\uparrow\downarrow} = \pm\frac{\Delta R}{2} = \pm\frac{1}{2}\frac{\alpha_F^2 \lambda_N exp(-L/2\lambda_N)}{\sigma_N A(M+1)[Msinh(L/2\lambda_N)+cosh(L/2\lambda_N)]} \tag{10}$$

with A: cross sectional area of the Cu wires, and $M = (1-\alpha_F^2)\lambda_N\sigma_F/\lambda_F\sigma_N$. In the experiments one expects $\lambda_N \gg \lambda_F$. Then eq.10 has two limits : For $\lambda_F \ll$ L $\ll \lambda_N$ the spin signal scales as: $\Delta R \propto 1/L$, whereas for $L \gg \lambda_N$ the signal is attenuated exponentially: $\Delta R \propto exp(-L/\lambda_N)$. Also, depending on the ratio of spin flip lengths and conductivities in the ferromagnet and nonmagnetic regions, the signal can be attenuated, even in the absence of spin-flip scattering. We will discuss this conductivity mismatch in section 9.

For comparison, in the "conventional" spin valve measurement, current is send from electrode 1 to 7, and the voltage is measured between 4 and 9. The following expression is obtained:

$$R_{\uparrow\uparrow,\uparrow\downarrow} = R_{series} \pm \Delta R \tag{11}$$

with ΔR given by eq.10. The magnitude of the spin signal is twice that in the other geometry. However, as pointed out already, this geometry suffers from the fact that a resistance R_{series} of the ferromagnet is measured. The AMR contribution is given by : $\Delta R/R = Ccos(\varphi)$, where φ is the angle between the magnetization direction and the current direction, and C is of the order of 0.01. This shows that in the case of imperfect switching, when the magnetization does not switch through 180^o at the coercive field, a problem arises, as has been indeed observed by the authors of ref.[12].

5 Observation of spin injection and spin accumulation in an all metal spin valve

Jedema et al.[12] succeeded in using the above principle to demonstrate spin injection and detection in an all metal spin valve structure. Measurements are shown in fig.3. When the applied field is swept from negative to positive, an increase in the resistance is obtained when the ferromagnetic strip with the smallest coercive field switches, and an anti-parallel magnetization is obtained. When the coercive field of the second strip is exceeded, a drop in the resistance is observed, corresponding to the magnetization being parallel again. The hysteresis behavior observed in figs. 3c,d corresponds to the situation when the direction of the magnetic field is reversed, while the second strip has not switched yet. As can be seen in fig. 3, the spin valve signal is increased when the temperature is reduced to 4.2K. Eq.10 shows that there are three unknowns in the experiment: $\alpha_F, \lambda_F, \lambda_N$. In order to determine these, a series of measurements was performed with increasing electrode spacing L, ranging from 250 nm to 2 μm. By fitting the measured ΔR to eq.10 the spin flip length could be extracted. At room temperature $\lambda_N \approx 350nm$, and $\lambda_N \approx 1000nm$ at $4.2K$ It was concluded that the fitting procedure was not sensitive enough to obtain α_F and λ_F separately. It was found that $\alpha_F\lambda_F \approx 1nm$, which, using an estimated $\lambda_F \approx 5nm$ from literature yields $\alpha_F \approx 0.22$.

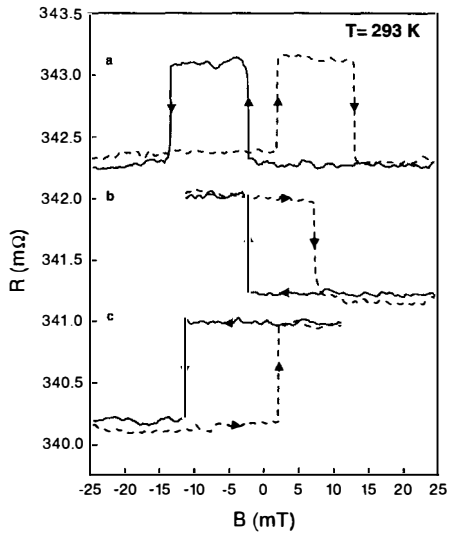


Figure 3: Spin valve effect at T=4.2K (a), and room temperature (b) in the multiterminal geometry for a sample with 250 nm Py electrode spacing. An increase in resistance is observed, when the magnetization configuration is changed from parallel to anti parallel. The solid (dashed) lines correspond to the negative (positive) sweep direction (c), (d) illustrate the "memory effect". For clarity (c) and (d) are offset downwards. The sizes of the Py1 and Py 2 electrodes are $2.0x0.5\mu m^2$ and $14x0.1\mu m^2$

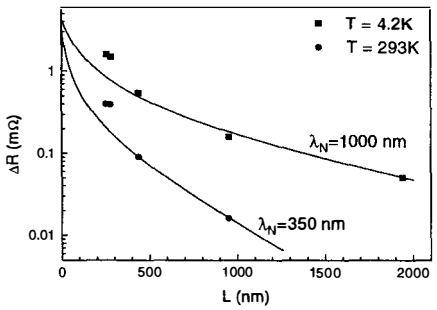


Figure 4: Dependence of the magnitude of the spin signal ΔR on the Py electrode distance L. The solid squares represent data taken at 4.2K; the solid circles represent data taken at room temperature. The solid lines represent the best fits based on equation 10

6 Comparison with the Johnson spin transistor

When scaled to the device cross section, the signals observed by Jedema et al.[12] are about 10^4 times smaller than those obtained in the sandwich geometry of ref.[8] (known as the Johnson spin transistor) This is consistent with the fact that a current spin polarization $\alpha_F \approx 1$ is required to explain the results of ref.[8] in terms of spin accumulation. In contrast, the results of ref.[12] correspond to a spin polarization of about 0.01-0.02. (Note that the amplitude of the signal scales with the square of the spin polarization). In our opinion this means that the results of ref.[8] cannot be due to spin transport and spin accumulation. In this respect it should be noticed that in the sandwich structure of the current does not only flow perpendicular, but also parallel to the F/N/F layers. Therefore the magnetoresistance (in particular the AMR) can contribute to the measured signal, in the case that the magnetic switching of the layers is not perfect (e.g. when a multidomain structure is formed before or during the switching) The data of [8] indeed show that the switching of the layers is not abrupt. In this respect it should be noticed that in "conventional" spin valve measurements a contribution of the AMR to the signal was also observed by the authors of ref.[12], which in unfavorable cases fully overwhelmed the spin accumulation signals.

7 Future prospects for spin accumulation and spin transport in all metal devices

It was found in ref.[12] that the average time for spin relaxation is about 10^3 times the momentum relaxation time. Similar ratios have also been found from conduction electron spin resonance (CESR) experiments[16], which allow the determination of the spin flip time T_1 from the width of the observed resonance. The spin-orbit interaction was found to be the dominant mechanism for spin flip in non-magnetic metals. It can be induced by phonon scattering, or by scattering from static imperfections, such as impurities, dislocations, and surface scattering. This implies that the spin-diffusion length $l_{sf} = \sqrt{D\tau_{sf}}$ scales proportional to the electron mean free path. We believe that by reducing the scattering it should be possible to extend the spin-flip length to several micrometers. This will make it possible to study the effects of spin accumulation in more complicated devices, such as the "spin flip" transistor proposed by Bauer et al.[17].

8 Spin injection in a two-dimensional electron gas

The above shows that the spin accumulation results on metal systems can be understood within the framework of the standard model, and that the parameters obtained are in reasonable agreement with those obtained from CESR experiments, as well as the analysis of magneto transport in multilayers. This raises the question whether spin injection in (low-dimensional) semiconductors can also be achieved in a similar way, by using direct injection from ferromagnetic electrodes. One interesting "application" is the spin field effect transistor proposed by Datta and Das [18]. In addition to the action of the gate voltage on the electron density, they proposed to use the electric field generated by the gate to tune the spin-orbit interaction in the system, and thus control the spin precession.

Several authors have made an attempt to study spin injection using this principle [22,20,19,21]. The geometry used by Filip et al.[13]is shown in fig. 5. The starting material is 15 nm InAs quantum well, sandwiched in between Al(Ga)Sb barrier layers, in which a 2-dimensional electron gas is present. First the 2DEG is patterned into a $1\mu m$ wide mesa structure. After removing the top barrier layers, and removing possible oxide, ferromagnetic contacts are made across the mesa structure. Similar to the all-metal case discussed above, different widths were chosen to obtain different coercive fields. Fig. 5 shows the results at 4.2K. Fig 5a,b, show the measurements of the AMR of the two ferromagnetic electrodes. The show two different coercive fields, which

implies that in between the magnetization should be antiparallel. However fig. 5c shows that no spin signal could be detected.

9 Conductivity mismatch

For the geometry of fig.5 the expected signal is given by :

$$R_{\uparrow\uparrow,\downarrow\uparrow} = \pm\frac{\Delta R}{2} = \pm\frac{\alpha_F^2\lambda_N}{\sigma_N A[(M^2+1)sinh(L/\lambda_N)+2Mcosh(L/\lambda_N)]} \tag{12}$$

with M given by eq. 4. The crucial point to be noted here is that in this experiment the ratio of conductivities of the metal ferromagnetic electrodes and the 2DEG is about 10^3, and therefore one finds $M \approx 10^4$. As seen from eq.12, this leads to a large attenuation of the spin signal, even when $L \ll \lambda_N$, and no spin flip takes place in the 2DEG. Although it cannot be excluded that there are additional reasons for the absence of the spin signal (such as random precession induced by the spin orbit interaction in the InAs) it follows that the "conductivity mismatch" has major consequences for this system. The conductivity mismatch problem has been described in detail by Schmidt et al.[24]. The fundamental reason is that the ratio of spin-up and spin-down currents is determined by the total resistance encountered in a region of the length $\lambda_F + \lambda_N$. In the above case the spin-independent resistance dominates, leading to an equalization of both currents. In our opinion the "conductivity mismatch" also applied to ballistic semiconductors coupled to ferromagnetic electrodes, or to alternative methods to inject or detect spin polarized electrons in semiconductors coupled to metallic ferromagnets by means of transparent contacts.

Two solutions present themselves for the circumvention of the conductivity mismatch problem; The first is to use injectors/detectors which have α_F close to 1, e.g. due to the giant Zeeman effect in semiconductors [1] However this is restricted so far to low temperatures. The

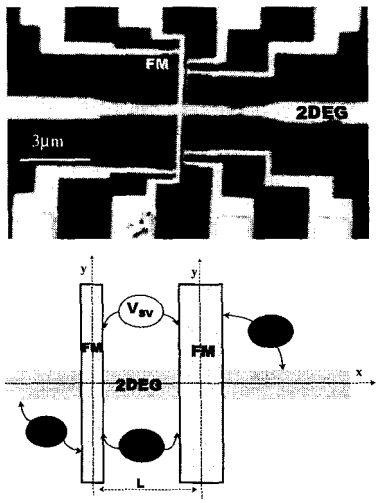


Figure 5: a) SEM micrograph of a sample. The $1\mu m$ wide 2DEG channel is horizontal, and two ferromagnetic electrodes are vertical. b) Sketch of the two measurement configurations. The indices 'SV' and 'NL' refer to the classic spin-valve and, respectively, to the non-local geometry. In the latter there is no current flow between injector and detector.

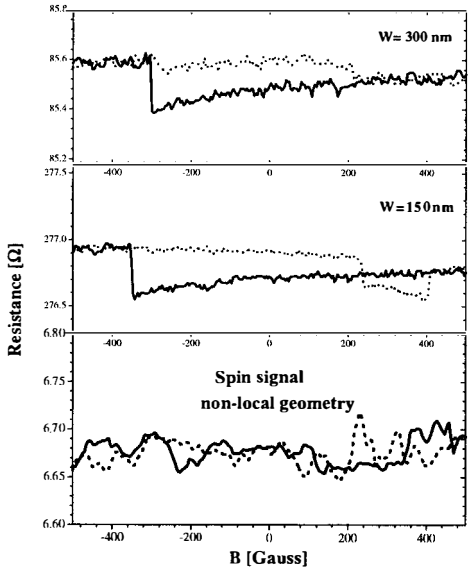


Figure 6: Spin valve measurements for Py/2DEG/Py device. Top two curves give the AMR traces for the two ferromagnetic electrodes, showing different coercive fields in one sweep direction. No spin signal is observed in any of the geometries. The dashed lines correspond to a sweep of the magnetic field towards positive fields.

other can be applied to the case where non fully spin polarized ferromagnets are used. By using tunnel barriers the resistance of the injector/detector can be made comparable to that of the semiconductor. However, as pointed out already, the mechanism for spin injection changes, which will impose more stringent conditions on the fabrication.

Acknowledgments

The authors acknowledge the Stichting Fundamenteel Onderzoek der Materie (F.O.M.) for financial support

References

1. R. Fiederling *et al.* Nature 402, 787 (2000)
2. Y. Ohno *et al.* Nature 402, 790 (2000)
3. I. Malajovich *et al.* Phys. Rev. Lett. 84, 1015 (2000)
4. A. Fert, and I.A. Campbell, J. de Physique, Colloques 32, C1-46 (1971)
5. P.C. van Son, H. van Kempen, and P. Wyder, Phys. Rev. Lett. 58, 2271 (1987)
6. T. Valet and A. fert, Phys. Rev. B48, 7099 (1993)
7. M. Johnson, and R.H. Silsbee, Phys. Rev. Lett. 55, 1790 (1985); M. Johnson and R.H. Silsbee, Phys. Rev. B

8. M. Johnson, Phys. Rev. Lett. 70, 2142 (1993)
9. M.A.M. Gijs and G.E.W. Bauer, Advances in Physics 46, 285 (1997)
10. J-Ph. Ansermet, J. Phys.:Condens. Matter 10, 6027 (1998)
11. S. Dubois et al. Phys. Rev. B60, 477 (1999);S.D. Steenwijk et al., J. Mag. Magn. Mat. 170 L1 (1997)
12. F.J. Jedema, A.T. Filip, and B.J. van Wees, Nature (2001)
13. A.T. Filip, B.H. Hoving, F.J. Jedema, and B.J. van Wees, Phys. Rev. B62, 9996 (2000)
14. A. Fert and S. Lee, Phys. Rev. B53, 6554 (1996)
15. S. Herschfield and H.L. Zhao, Phys Rev. B56, 3296 (1997)
16. F. Beuneu and P. Monod, Physica 86-888B, 265 (1977)
17. A. Brataas, Yu. V. Nazarov, and G.E.W. Bauer, Phys. Rev. Lett. 84, 2481 (2000)
18. S. Datta, and B. Das, Appl. Phys. Lett. 56, 665 (1990)
19. Meier *et al.* unpublished
20. S. Gardelis, C.G. Smith, C.H.W. Barnes, E.H. Linfield, and D.A. Ritchie, Phys. Rev. B60, 7764 (1999)
21. C.M. Hu, J. Nitta, A. Jensen, J.B. Hansen, and H. Takayanagi, Phys. rev. B (to be published)
22. P.R. Hammar, B.R. Bennett, M.J. Yang, and M. Johnson, Phys. Rev. Lett. 79, 1750 (1999)
23. B.J. van Wees, Phys. Rev. Lett. 84, 5023 (2000)
24. G. Schmidt, D. Ferrand, L. Molenkamp, A.T. Filip, and B.J. van Wees, Phys. Rev. B62, R4790 (2000)

CHANNEL BLOCKING BY A THIN DOMAIN WALL IN BALLISTIC FERROMAGNETIC QUANTUM WIRES

DIETMAR WEINMANN[1], ROBERT L. STAMPS[2], RODOLFO A. JALABERT[1]

[1] *IPCMS-GEMME, UMR 7504, CNRS-ULP, 23 rue du Loess, 67037 Strasbourg Cedex, France*
[2] *Department of Physics, University of Western Australia, Nedlands WA 6907, Australia*

The magneto-conductance of ferromagnetic quantum wires is dominated by the effect of the magnetic field dependent domain structure on the conducting electrons. In ballistic ferromagnetic quantum wires, the electrical conduction is dominated by reflection and transmission of channels through the domain walls. We find that the effect of a domain wall on the resistance is mainly due to the blockade of majority spin transport channels with large transverse quantization energy. The resistance is calculated analytically in the limit of thin walls, including the contribution of transmission processes through the wall with spin-flip.

1 Introduction

Spin-dependent electronic magneto-transport in low dimensional structures is a fundamental problem in transport theory, being particularly rich in the case of transition metals due to the interplay between conduction states and local magnetic moments. The giant magneto-resistance in artificially structured magnetic multilayers [1] and granular mixtures of magnetic and non-magnetic metals [2] are examples of how spin-dependent scattering of conduction electrons can affect the electronic conductivity. The spin-dependent scattering at a single magnetic domain wall in a ferromagnetic wire, and its effect on the conductance of the wire, represents a generic problem which is situated at the basis of this subject.

Transport through single domain walls is realized in recent magneto-conductance experiments in submicron-diameter ferromagnetic wires[3,4], whose parameters are close to the ballistic mesoscopic regime. In this paper we present a theory of quantum transport in ballistic ferromagnetic wires containing a single domain wall. We consider the case of magnetization along the axis of the wire, suppose weak localization effects can be ignored, and calculate the magneto-conductance with and without a magnetic domain wall in the wire. In contrast to previous calculations of transport through wires in the diffusive and the ballistic regime,[5,6,7] we do not assume that spins of the conduction electrons follow the magnetization direction through the wall, but calculate analytically the transmission through the domain wall with and without spin-flip.

2 Model and method

2.1 Electrons in a ferromagnetic material

In order to simplify the problem, we assume that the electrons which are responsible for the magnetic structure of the wire do not contribute to its transport properties, and we restrict ourselves to the limit of small currents. Furthermore, we approximate the conduction states as free electron like, where spin up and spin down electrons at the same energy in the conduction band have different momenta.[8,9,10] This corresponds to a spin-dependent potential for the conduction electrons determined by the magnetic structure of the wire. The Hamiltonian for the current carrying conduction electrons reads

$$H = -\frac{h^2}{2m}\nabla^2 + \frac{\Delta}{2}\vec{f}(\vec{r})\cdot\vec{\sigma}\,, \tag{1}$$

where Δ is the magnitude of the exchange energy difference between the up and down electrons associated with the local moments, $\vec{f}(\vec{r})$ is the position-dependent magnetization direction, and

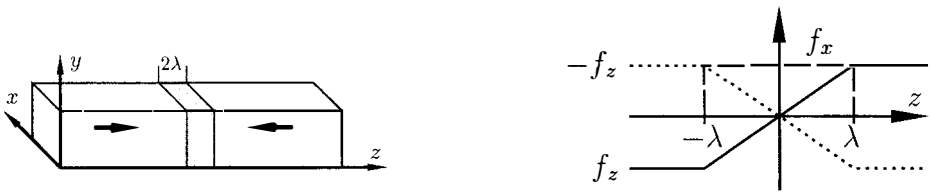


Figure 1: Left: The geometry and orientation of the wire and the magnetization. Right: The z-dependence of the projections f_x and f_z of the magnetization onto the corresponding coordinate axes.

$\vec{\sigma}$ is the vector of the Pauli matrices. We assume the magnetization varies only along the wire axis z, and have $\vec{f}(\vec{r}) = \vec{f}(z)$, rendering the Hamiltonian separable. A domain wall represents a deformation of the spin-dependent potential over a length 2λ, corresponding to its thickness. In a wire containing a single domain wall, there are three regions with different potentials: two regions with spatially uniform spin-dependent potentials separated by the wall region wherein the potentials vary spatially. A sketch of the wire and the spin-dependent potentials associated with the domain wall is shown in Figure 1.

2.2 Landauer-Büttiker formalism

Assuming a 180° wall with a magnetization parallel to the wire (Fig. 1 left), the states outside the wall are plane waves, propagating in the z-direction with spin up (down) energies

$$E_{\uparrow(\downarrow)} = \frac{\hbar^2}{2m}\left[\left(\frac{\pi n_x}{W}\right)^2 + \left(\frac{\pi n_y}{W}\right)^2 + k_z^2\right] \pm \frac{\Delta}{2}\,. \tag{2}$$

We have taken a square cross section of side W, and the quantum numbers n_x and n_y enumerate the modes in the transverse directions. The detailed shape of the cross section is not important because we always consider a large number of channels. The density of channels or transverse states is $\rho = 2\pi m A/h^2$, where $A = W^2$ is the cross section area.

Using the Landauer formula, the dimensionless conductance g can be expressed in terms of the transmission of the conduction electrons through the domain wall, yielding

$$g = \frac{G}{e^2/h} = \sum_{n_x,n_y}\sum_{\sigma,\sigma'} T_{\sigma\sigma'}(n_x,n_y)\,, \tag{3}$$

where $T_{\sigma\sigma'}$ is the transmission probability between the asymptotic states (channels) (n_x, n_y, σ) and (n_x, n_y, σ') at the Fermi energy E_F. The channel quantum numbers n_x and n_y are conserved because of the separability of H. Angular momentum conservation implies that if a conduction electron suffers a spin-flip, a spin imbalance will build up at the wall. We assume that the relaxation of the localized spins towards the lattice is fast enough and the current low enough that this modification of the wall can be neglected.

2.3 The domain wall

The spinors $(\phi_\uparrow, \phi_\downarrow)$, describing an electron at the Fermi energy, satisfy

$$\left[\frac{\hbar^2}{2m}\frac{\partial^2}{\partial z^2} + \epsilon - \frac{\Delta}{2}\left(f_x(z)\sigma_x + f_y(z)\sigma_y + f_z(z)\sigma_z\right)\right]\begin{pmatrix}\phi_\uparrow\\ \phi_\downarrow\end{pmatrix} = 0\,, \tag{4}$$

where $\epsilon = E_F - 1/(2m)(\hbar\pi/W)^2(n_x^2 + n_y^2)$ is the longitudinal kinetic energy of an electron with transverse quantum numbers n_x and n_y. The functions $f_\bullet$ are projections of the magnetization onto the coordinate axes corresponding to the Pauli spin matrices $\sigma_\bullet$. For a Bloch wall with typical width 2λ we have [11] $f_x(z) = \mathrm{sech}(z/\lambda)$, $f_y(z) = 0$, and $f_z(z) = \tanh(z/\lambda)$. The solution of Eq. (4) is a difficult problem that has been tackled using numerical techniques, analytically using perturbation expansions [8] or the WKB approximation [12], and approximations for the magnetic Bloch wall profile using trigonometric functions [7]. In our treatment, we approximate the magnetic wall profile by a linearly varying potential (see Fig. 1 right), with the characteristic scale λ:

$$\begin{array}{llll} f_x(z) = 0\ , & f_z(z) = \mathrm{sgn}(z)\ , & \text{for } |z| \geq \lambda \\ f_x(z) = 1\ , & f_z(z) = z/\lambda\ , & \text{for } |z| < \lambda\ . \end{array} \tag{5}$$

3 Conductance change due to a domain wall

The magneto-conductance δg is calculated from Eq. (3) as the difference between the conductances without and with a domain wall. Due to the splitting Δ, the number of spin down(up) channels is $N_{\downarrow(\uparrow)} = \rho(E_F \pm \Delta/2)$. Without a domain wall, the magnetization is uniform and all incident channels are transmitted. The dimensionless conductance in this case is $g = 2\rho E_F$.

The effect of the domain wall on the conduction electrons is twofold. First, the z-component of the magnetization corresponds to a potential step. Second, the non-zero x-component allows for spin-flip processes. This only slightly modifies the transmission coefficients for higher longitudinal kinetic energy.[8] More strongly affected are the electrons in the incident spin down channels with longitudinal kinetic energy $\epsilon < \Delta/2$, since these cannot overcome the potential step of height Δ and are completely blocked, provided the spin-flip processes can be neglected. This reduces the number of transmitted channels by $\rho\Delta$, leading to a relative change of the conductance due to the domain wall of

$$\frac{\delta g}{g} = -\frac{\Delta}{2E_F}\ . \tag{6}$$

Note that in the ideal case of an abrupt domain wall of zero thickness $\lambda = 0$, there is no spin-flip and Eq. (6) accounts for all of the magneto-conductance.

3.1 Finite thickness

Spin-flip processes are possible due to mixing of spin channels if the domain walls have finite thickness λ. The effect is to reduce the blockade effect of the potential step associated with the magnetic wall. We now calculate the transmission probability of an incoming plane wave with longitudinal energy $-\Delta/2 \leq \epsilon < \Delta/2$ and momentum $k_+ = \sqrt{2m(\epsilon - \Delta/2)}/\hbar$ including spin-flip.

Because of the linear potential of Eq. (5), it is convenient to express the wave-functions in terms of the Airy functions Ai and Bi.[13] The solution without spin-flip can be written as

$$\phi_\downarrow^0(z) = \begin{cases} \exp\left(ik_+(z+\lambda)\right) + b\exp\left(-ik_+(z+\lambda)\right)\ , & \text{for } z \leq -\lambda \\ \alpha_\downarrow Ai(c(z-a)) + \beta_\downarrow Bi(c(z-a))\ , & \text{for } |z| \leq \lambda \\ d\exp\left(-\kappa(z-\lambda)\right)\ , & \text{for } z \geq \lambda \end{cases} \tag{7}$$

with $\kappa = \sqrt{2m(\epsilon + \Delta/2)}/\hbar$, $c = (m\Delta/\hbar^2\lambda)^{1/3}$, and $a = 2\lambda\epsilon/\Delta$ being the classical turning point. The amplitudes b, $\alpha_\downarrow$, $\beta_\downarrow$ and d are obtained from the matching conditions for the wave function at $z = \pm\lambda$.

For an incoming plane wave with spin down ($\phi_\uparrow^0 = 0$), the coupling of the two spin-components in the wall region leads to a non-homogeneous equation for $\phi_\uparrow$. With a particular

solution $\delta\phi_\uparrow$ of the latter, the spin up component $\phi^1_\uparrow$, induced by $\phi^0_\downarrow$ in lowest order in the coupling strength, is given by

$$\phi^1_\uparrow(z) = \begin{cases} f\exp\left(\kappa(z+\lambda)\right), & \text{for } z \le -\lambda \\ \alpha_\uparrow Ai(-c(z+a)) + \beta_\uparrow Bi(-c(z+a)) + \delta\phi_\uparrow(z), & \text{for } |z| \le \lambda \\ t\exp\left(ik_+(z-\lambda)\right), & \text{for } z \ge \lambda \end{cases} . \tag{8}$$

The matching conditions for the wave-function at $z = \pm\lambda$ allow us to obtain analytic expressions for $T_{\downarrow\uparrow} = |t|^2$ in the limit of very thin walls using an expansion of the Airy functions for small arguments. The width of the wall is given by the dimensionless parameter $p = (c\lambda)^{3/2} = (\Delta/2E_\mathrm{F})^{3/2}(k_F\lambda)^3$. Introducing $r = 2\epsilon/\Delta$, for $p \ll 1$, we obtain $T_{\downarrow\uparrow}(\epsilon) = 4p^2(1+r)$. These spin-flip contributions to the conductivity modify the $\lambda{=}0$ result of Eq. 6 to

$$\frac{\delta g}{g} \approx (-1+4p^2)\,\frac{\Delta}{2E_\mathrm{F}}. \tag{9}$$

4 Conclusions and Outlook

We have considered the effect of a single domain wall on the ballistic transport through a ferromagnetic quantum wire. Such a domain wall can be induced by an external magnetic field, and magneto-conductance appears through a blocking of transport channels having low longitudinal kinetic energy. Finite size domain walls allow spin-flip processes that increase transmission through the wall, and we have calculated this effect analytically in the case of thin walls. However, in order to address the magneto-conductance in experimental situations[4], thick domain walls need to be considered [14] as well as the effects of impurity scattering and phase breaking processes occuring throughout the total length of the wire measured in experiment.

Acknowledgments

Helpful discussions with F. Gautier and U. Ebels are acknowledged. We thank the ARC for support. RLS acknowledges support under a CNRS visiting fellowship. RAJ and DW acknowledge financial support from the European Union within the TMR program.

References

1. M.N. Baibich *et al., Phys. Rev. Lett.* **61**, 2472 (1988); G. Binach *et al., Phys. Rev.* B **39**, 4828 (1989).
2. A.E. Berkowitz *et al., Phys. Rev. Lett.* **68**, 3745 (1992).
3. Y. Otani *et al., IEEE Trans. Magn.* **34**, 1096 (1998).
4. U. Ebels *et al., Phys. Rev. Lett.* **84**, 983 (2000).
5. J.B.A.N. van Hoof *et al., J. Magn. Magn. Mat.* **177**, 188 (1998); J.B.A.N. van Hoof *et al., Phys. Rev.* B **59**, 138 (1999).
6. G. Tatara, *Phys. Rev. Lett.* **78**, 3773 (1997).
7. H. Imamura *et al., Phys. Rev. Lett.* **84**, 1003 (2000).
8. G.G. Cabrera and L.M. Falicov, *Phys. Stat. Sol. (b)* **61**, 539 (1974); *ibid* **62**, 217 (1974).
9. P.M. Levy and S. Zhang, *Phys. Rev. Lett.* **79**, 5110 (1997).
10. D.M. Edwards *et al., J. Phys.: Cond. Mat.* **3**, 4941 (1991).
11. W.F. Brown, *J. Appl. Phys.* **36**, 1380 (1965).
12. K. Nakanishi and Y.O. Nakamura, *Phys. Rev.* B **61**, 11278 (2000).
13. M. Abramowitz and C.A. Stegun, *Handbook of Mathematical Functions* (Dover, New York, 1972).
14. R.A. Jalabert, R.L. Stamps and D. Weinmann, to be published.

A phenomenological two-subband model for quantum point contacts: the 0.7 conductance anomaly and the associated thermopower

Henrik Bruus[1], Vadim Cheianov[2], Karsten Flensberg[1]
[1] *Ørsted Laboratory, Niels Bohr Institute, Universitetsparken 5, DK-2100 Copenhagen, Denmark*
[2] *NORDITA, Blegdamsvej 15, DK-2100 Copenhagen,Denmark*

A recently proposed phenomenological two-subband model for transport through quantum point contacts is used to study the 0.7 conductance anomaly in quantum point contacts (QPC). The model utilizes the Landauer-Büttiker formalism and involves thermal depopulation of the two subbands. In particular we can account for the anomalous conductance plateau value 0.7 and the unusual temperature dependence of this plateau. Moreover, the model can explain a puzzle related to newly published thermopower experiments on QPCs.

1 Introduction

It has been known and well understood since 1988 [1,2] that the dc-conductance g (measured in units of $2\,e^2/h$) of narrow quantum point contacts and quantum wires (both referred to as QPCs below) exhibits integer quantization. During the past five years an increasing part of the experimental and theoretical work on QPCs has been devoted to studies of the so-called 0.7 conductance anomaly,[3–12] a particular deviation from integer quantization appearing on the first conductance plateau. This anomaly is a narrow plateau, or in some cases just a plateau-like feature appearing in scans of g versus gate voltage V_g at a value of g which is reduced by a factor 0.7 relative to the ideal value. Related anomalies also show up in experiments on thermopower [6] and noise. [7]

An explanation of the 0.7 anomaly has to involve the many different experimental findings listed below. Previous theoretical works [10,11] have addressed only one of these findings. However, we show in this paper that the many different aspects of the 0.7 anomaly can be consistently interpreted by invoking the model of enhanced spin correlations in the QPC, which we previously put forward to explain the 0.7 plateau. [12] In the following we focus only on the case of zero-bias and zero magnetic field. The main experimental features of the 0.7 anomaly are:

(e1) The anomalous plateau is observed in a large variety of QPCs at a value $g \simeq 0.7$. [3,4,5]

(e2) The temperature dependence is qualitatively the same for all samples: the anomalous plateau is most strongly developed in some (device dependent) temperature range typically above 2 K. With increasing temperature both the anomalous and the integer plateaus vanish by thermal smearing, while with decreasing temperature the width of the anomalous plateau shrinks and the conductance approaches the usual integer value. [3,4,5]

(e3) A detailed study of the temperature dependence of g shows that in the low temperature regime the conductance suppression has an activated behavior: $1 - g(T) \propto \exp(-T_a/T)$. [5]

(e4) The activation temperature T_a is a function of V_g is well approximated by the power law $T_a \propto (V_g - V_g^0)^2$, where V_g^0 is a threshold voltage. [5]

(e5) At a fixed temperature corresponding to a well developed 0.7 plateau, g shows a strong dependence on an in-plane magnetic field. [3,4,6] With increasing magnetic field the anomalous plateau smoothly decreases from $g \simeq 0.7$ at $B = 0$ T to $g \simeq 0.5$ at $B = 13$ T.

(e6) The value of g on the 0.7 plateau depends on the source-drain bias. It increases smoothly from $g \simeq 0.7$ at zero bias to $g \simeq 0.9$ at large bias (~ 2 mV). [5]

(e7) Even at zero bias the 0.7 plateau may appear closer to $g \simeq 0.5$ than to 0.7. [3,8,9]

(e8) An anomalous plateau appears in thermopower experiments on the 0.7 plateau. [6]

(e9) An anomalous suppression of shot noise occurs on the 0.7 plateau. [7]

2 The phenomenological model in the simple case of adiabatic transmission

Based on experiments[3] and local density functional theory[10,12] it has been suggested that at the low electron densities in the QPC near pinch-off, spontaneous spin polarization arises. However, a rigorous microscopic theory justifying this conclusion is still lacking. As a starting point for our phenomenological analysis we simply assume the existence of a finite spin polarization expressed by a general spin-density functional, as we explained in our earlier work. [12]

We stress that the spin polarization is not necessarily permanent. Due to a coupling to reservoirs of electrons it should exhibit mesoscopic fluctuations. The fluctuating polarization may, however, be indistinguishable from a static one in a transport experiment if the dynamics of the spin degrees of freedom in the constriction is adiabatic (slow) as compared to both the length of the QPC and the time of passage of electrons through the QPC. Thus for simplicity we just treat the case of a stationary polarization. We assume the existence of a critical chemical potential μ_c, at which the cross-over from full to partial polarization occurs. For $\mu < \mu_c$ the densities are $n_\uparrow = n_\uparrow^0$ and $n_\downarrow = 0$, while for $\mu > \mu_c$ a non-zero $n_\downarrow$ develops, i.e. two spin subbands appear with different subband edges ε_σ^s.

All the phenomenology of the 0.7 anomaly is contained in the μ dependence of the position of the subband edges. The (normal) majority band edge is independent of μ, while the (special) minority band edge $\varepsilon_\downarrow^s(\mu)$ depends on μ through the μ-dependent minority Fermi energy $\Delta(\mu)$:

$$\varepsilon_\uparrow \equiv 0, \qquad \varepsilon_\downarrow^s(\mu) = \mu - \Delta(\mu). \tag{1}$$

Based on some general assumptions about the spin density functional of the electron system in the constriction we have previously determined the functional form of $\Delta(\mu)$. [12] The result for $\mu_c = 0$ is

$$\Delta(\mu) = \begin{cases} C\,\mu^2, & \text{for } \mu > 0 \\ \mu, & \text{for } \mu < 0. \end{cases} \tag{2}$$

Given these subband edges and using the Landauer-Büttiker formula, we can determine the conductance analytically at finite temperature T in the case of adiabatic transmission coefficients:

$$g(\mu, T) = \frac{1}{2} \sum_{\sigma=\uparrow,\downarrow} \int_{-\infty}^{\infty} d\varepsilon\, \Theta[\varepsilon - \varepsilon_\sigma^s(\mu)] \left(-f'\left[\frac{\varepsilon - \mu}{k_B T}\right] \right). \tag{3}$$

Here f' is the derivative of the Fermi-Dirac distribution $f[x/k_BT] = [\exp(x/k_BT) + 1]^{-1}$ and $\Theta[x]$ is the step function. Eqs. (1)-(3) lead to the conductance (in units of $2e^2/h$)

$$g(\mu, T) = \frac{1}{2} \left(\frac{1}{e^{-\mu/k_BT} + 1} + \frac{1}{e^{-\Delta(\mu)/k_BT} + 1} \right). \tag{4}$$

3 Experimental implications of the simple model with adiabatic transmission

We can explain **(e1)-(e4)** by inserting Eq. (2) into Eq. (4). Consider first the low temperature case of partial polarization: $k_BT \ll \Delta(\mu) \ll \varepsilon_\downarrow^s(\mu) - \varepsilon_\uparrow^s(\mu)$. In this case both fractions in Eq. (4) are 1 and the conductance is the usual 1. An expansion in $\Delta(\mu)$ yields $g \approx 1 - \frac{1}{2}\exp[\Delta(\mu)/k_BT]$, which by the identification $\Delta(\mu) = T_A$ explains **(e3)** and **(e4)**.

In the temperature range $\Delta(\mu) \ll k_BT \ll \mu - \varepsilon_\uparrow^s(\mu)$ the first (majority) fraction remains 1 while the second becomes 1/2 yielding $g = 0.75$. Since $\Delta(\mu) = C\,\mu^2$ for $\mu > 0$ (which in a sense expresses a pinning of $\varepsilon_\downarrow^s$ to μ), the temperature range inequality is in fact fulfilled for a sufficiently broad range of μ (in experiments $\mu \propto V_g$), thus giving rise to a 0.7 quasi-plateau. This explains **(e1)** and **(e2)**, which is also illustrated in Fig. 1(a).

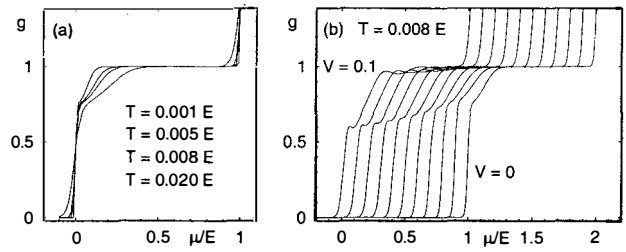


Figure 1: (a) The conductance g from Eqs. (2) and (4) with $C = 0.5$. E is the energy spacing of the ordinary subbands. The 0.7 anomaly gets stronger as T increases. (b) The effect of adding a non-adiabatic square box potential of increasing strength V to the adiabatic QPC-potential. The anomalous plateau is lowered from 0.7.

A preliminary analysis of **(e5)** within our model by adding an in-plane magnetic is presented in our previous work. [12] Likewise, an explanation of the finite bias observation **(e6)** requires an extension of our model, which we presented in another paper. [5] The experimental results **(e7)** and **(e8)** will be treated below, while an analysis of **(e9)** is postponed to future work.

4 Non-adiabatic transmission: the lowering of the 0.7 plateau toward 0.5

In our simple adiabatic model we used a step-function transmission coefficient for electrons traversing the QPC. Non-adiabatic transmission is easily taken into account by replacing the theta function in Eq. (3) by a transmission coefficient $\mathcal{T}_\sigma(\varepsilon)$:

$$g(\mu,T) = \frac{1}{2}\sum_{\sigma=\uparrow,\downarrow}\int_{-\infty}^{\infty} d\varepsilon\, \mathcal{T}_\sigma(\varepsilon)\left(-f'\left[\frac{\varepsilon-\mu}{k_BT}\right]\right). \tag{5}$$

Through the transmission coefficient $\mathcal{T}_\sigma(\varepsilon)$ the conductance now depends on the geometry of the QPC and is no more universal. However, some qualitative predictions can still be made without a knowledge of the exact transmission properties of the QPC. First of all, since as in the adiabatic case the condition $\Delta(\mu) \ll k_BT \ll \mu - \varepsilon_\uparrow^s(\mu)$ can still be fulfilled, the quasi-plateau will persist. Secondly, mainly the transmission coefficient of minority spin band is affected which results in a suppression of the anomalous plateau while the integer plateau remains close to 1.

As a specific model of the measurements of Reilly *et al.* [9] we add a non-adiabatic square-well potential of height V and length L (we use $L = 10$) to the adiabatic QPC potential. For $\varepsilon < 0$ we thus set $\mathcal{T}(\varepsilon) = 0$, while for $\varepsilon > 0$, we have $\mathcal{T}(\varepsilon) = 1/|\cosh(\kappa L) + i\gamma\sinh(\kappa L)|^2$, where $k = \sqrt{\varepsilon}$, $\kappa = \sqrt{V-\varepsilon}$, and $\gamma = (\kappa/k - k/\kappa)/2$. The result displayed in Fig. 1(b) shows that in our non-adiabatic model the anomalous 0.7 plateau may be suppressed to values of $g \simeq 0.6$ or lower without being destroyed. Fig. 1(b) looks like the results presented by Reilly *et al.* [9] in their Fig. 2, where the tuning of the non-adiabaticity is controled experimentally by simultanous tuning of top- and side-gates. Thus in our model **(e7)** can be explained by non-adiabaticity.

5 Thermopower in the adiabatic model: the anomalous thermopower plateau

Additional information about the 0.7 anomaly has come from the thermopower measurements on QPCs by Appleyard *et al.* [6] They analyzed their results in terms of the standard Mott expression valid for the degenerate electron gas, and reported a strong deviation in the conductance region $0 < g < 1$. In particular the Mott expression predicts a zero in the thermopower at the 0.7 plateau, but instead a plateau was found as they showed in their Fig. 3. We now demonstrate how our model is in agreement with the experiment. In thermopower measurements the current

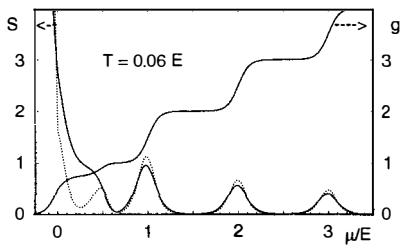


Figure 2: The thermopower S in units of k_B/e calculated from our model Eq. (7), full line, compared to the Mott expression Eq. (8), dotted line. Our model compares well with experiment, Figs. 2 and 3 in Appleyard *al.* [6]

due to a voltage difference δV across the QPC is exactly cancelled by the current due to an opposed temperature difference δT. In the Landauer-Büttiker formalism we can express this as

$$I = \frac{e}{h}\int d\varepsilon\, \mathcal{T}(\varepsilon)\left[f\Big(\frac{\varepsilon-\mu-e\delta V/2}{k_B(T+\delta T/2)}\Big) - f\Big(\frac{\varepsilon-\mu+e\delta V/2}{k_B(T-\delta T/2)}\Big)\right] \equiv 0. \tag{6}$$

Expansion in δV and δT leads to the linear response thermopower $S(\mu,T)$,

$$S(\mu,T) \equiv -\frac{\delta V}{\delta T} = \frac{1}{egT}\int d\varepsilon\, \mathcal{T}(\varepsilon)\,(\varepsilon-\mu)\Big(-\frac{\partial f}{\partial \varepsilon}\Big). \tag{7}$$

For a degenerate gas, i.e. $k_BT \ll |\mu - \varepsilon_\sigma^s|$, we recover from Eq. (7) the Mott relation

$$S(\mu,T) = -\frac{\pi^2 k_B^2 T}{3e}\frac{1}{g}\frac{\partial g}{\partial \mu}. \tag{8}$$

It is now straightforward to insert Eqs. (2) and (4) into either Eq. (7) or Eq. (8) to obtain the thermopower expected in our model versus the one expected form the Mott model. The result is plotted in Fig. 2. Our model is in agreement with the experiment and differs from the Mott result due to the breakdown of the degeneracy condition in the minority band at the 0.7 plateau.

Acknowledgments

This work was supported by the Danish Natural Science Research Council, Grant No. 9600548.

References

1. B.J. van Wees *et al.*, Phys.Rev.Lett. **B 60**, 848 (1988).
2. D.A. Wharam *et al.*, J.Phys.C **21**, L209 (1988).
3. K.J. Thomas *et al.*, Phys. Rev. Lett. **77**, 135 (1996); Phys. Rev. B **58**, 4846 (1998); Phys. Rev. B **61**, R13365 (2000).
4. C.-T. Liang *et al.*, Phys. Rev. B **60**, 10687 (1999).
5. A. Kristensen *et al.*, J. Appl. Phys. **83**, 607 (1998). Physica B **249-251**, 180 (1998). Phys. Rev. B **62**, 10950 (2000).
6. N. J. Appleyard *et al.*, Phys. Rev. B **62**, R16275 (2000).
7. T.G. Griffiths et al., Proceedings ICPS-25 (2000).
8. S. Nuttinck *et al.*, Jpn. J. Appl. Phys. **39**, L655 (2000).
9. D. J. Reilly *et al.*, Phys. Rev. B **63**, R121311 (2001).
10. C.-K. Wang and K.-F. Berggren, Phys. Rev. B **54**, R14257 (1996); **57**, 4552 (1998).
11. B. Spivak and F. Zhou, Phys. Rev. B **61**, 16730 (2000).
12. H. Bruus, V. Cheianov, K. Flensberg, Physica E, in press (2001), cond-mat/0002338.

TMR IN NANOSCALE F-N-F SYSTEMS: MESOSCOPIC FLUCTUATIONS

GONZALO USAJ, HAROLD U. BARANGER
Department of Physics, Duke University, Box 90305, Durham NC 27708-0305, USA

We study spin-dependent transport through ferromagnet/normal-metal/ferromagnet double tunnel junctions in the mesoscopic Coulomb blockade (CB) regime. We calculate the conductance for arbitrary orientation of the lead magnetizations. The tunneling magnetoresistance (TMR), defined at the CB conductance peaks, is calculated and its probability distribution presented. We show that mesoscopic fluctuations can lead to the optimal value of the TMR.

1 Introduction

The Coulomb blockade (CB) of electron tunneling has been extensively investigated during the last decades. [1] Nevertheless, the presence of ferromagnets has not been considered to date.

On the other hand, spin-polarized electron tunneling has become a very active area of research, motivated by its potential role in new electronic devices [2] as well as by the possibility of observing novel effects. [3,4,5] Paradigmatic examples are the ferromagnet/normal-metal/ferromagnet (F-N-F) double tunnel junctions. These systems consist of two ferromagnetic leads separated by a metallic grain. Their main feature is that the resistance depends on the relative orientation of the magnetization in the ferromagnets. This is characterized by the tunneling magnetoresistance (TMR), defined as the relative change of the resistance when the magnetizations of the ferromagnets rotate from being parallel to anti-parallel. When the thermal energy k_BT is smaller than the charging energy E_C, the CB occurs. How this charging effect modifies the TMR has been the subject of recent experimental [4] and theoretical [6,7] work. The effects of quantum interference within the CB have not been considered in these systems as of yet.[7]

Quantum interference in these structures necessarily entails mesoscopic fluctuations as the detailed shape of the grains cannot be controlled. Such effects become important for sufficiently low temperature or, at room temperature, for sufficiently small systems. Here we study quantum effects in the TMR at the CB peaks—the *mesoscopic tunneling magnetoresistance*—in F-N-F systems. We show that there are CB peaks with the *maximum* possible value of TMR; in contrast to the classical case, no special tuning is required. Since in such regime, the CB conductance peak height, G_{peak}, fluctuates as a function of the gate voltage, [8,1] the mesoscopic TMR is characterized by a probability distribution rather than by a single number. We obtain this distribution. For non-collinear configurations, we calculate G_{peak} as a function of the angle between the magnetizations in the two leads. Here, the usual description in terms of a rate-equation is not possible, and a more general equation for the conductance is presented.

2 Collinear magnetizations

Let us consider a normal metal grain weakly coupled to two ferromagnetic reservoirs by tunnel junctions (Fig. 1). The potential of the grain is controlled by gate voltage V_g. We assume that $\Gamma \ll k_BT \ll \Delta \ll E_C$, where Γ is the total width of the resonant levels in the grain and Δ their mean spacing. Then, only a single (spin-degenerate [a]) energy level, m, contributes to the conductance at each CB peak. The mesoscopic tunneling magnetoresistance is defined as

$$\eta = \frac{G_P - G_{AP}}{G_{AP}} \tag{1}$$

where $G_{P(AP)}$ is the conductance at the CB peak in the parallel (antiparallel) configuration.

[a] Assuming the Zeeman energy associated with any magnetic field present is much smaller than k_BT and the absence of spin-orbit (SO) coupling.

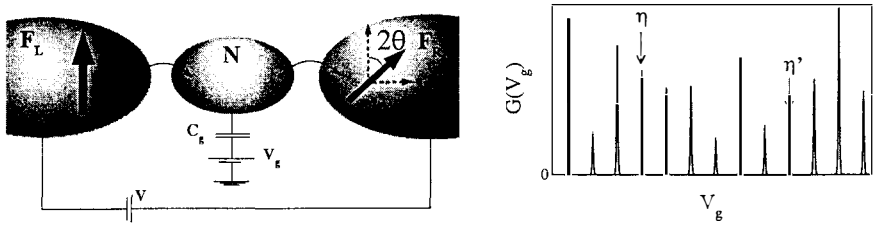


Figure 1: Left: F-N-F double junction. Right: Conductance as a function of the gate voltage.

Linear-response theory yields for the conductance [9]

$$G_{\rm peak} = \frac{e^2\,\lambda}{\hbar\,k_BT}\sum_{\sigma=\uparrow,\downarrow}\frac{\Gamma^L_\sigma\,\Gamma^R_\sigma}{\Gamma^L_\sigma+\Gamma^R_\sigma}\,, \tag{2}$$

where λ is a numerical factor (see Sec. 3). The partial width Γ^q_σ, $q=L(R)$, due to tunneling to the left (right) electrode is $\Gamma^q_\sigma = 2\pi\,\sum_\alpha \rho^q_\alpha |V^q_{\alpha\sigma}|^2$ with $V^q_{\alpha\sigma}$ the matrix element between $|m,\sigma\rangle$ in the grain and the channels $\alpha=\uparrow,\downarrow$ in lead q, and ρ^q_α the local density of states of those channels. For point-contact leads, $\Gamma^q_{\uparrow(\downarrow)} = |\phi_q|^2\,t^q_{\uparrow(\downarrow)}$ where $|\phi_q|^2$ is the wave function [b] of the resonant level at the contact point $\mathbf{r}_q$ and t^q_α is a factor which depends on both ρ^q_α and the tunnel barrier. Notice we assume that the tunneling through the barriers conserves spin. Since metallic grains are generally irregular in shape, one expects random matrix statistics for the wave functions. Following Ref. [8], we use the GOE ensemble to describe the fluctuations of $|\phi_q|^2$ and assume no correlation between $|\phi_L|^2$ and $|\phi_R|^2$. We obtain

$$\mathcal{P}_{\rm GOE}(\eta) = \frac{a}{\pi|\eta_{\rm m}|}\,\frac{\Theta(1-\eta/\eta_{\rm m})}{\sqrt{1-\eta/\eta_{\rm m}}\sqrt{\eta/\eta_{\rm m}}\,[1+\eta/\eta_{\rm m}(a^2-1)]}\,, \tag{3}$$

with

$$\begin{aligned} a &= (\zeta^{1/4}+\zeta^{-1/4})/(\delta^{1/4}+\delta^{-1/4})\,, \qquad \zeta = D_R d_R/D_L d_L\,, \qquad \delta = D_R d_L/D_L d_R\,, \\ \eta_{\rm m} &= 2P_LP_R/\{1-P_LP_R+[(1-P_L^2)(1-P_R^2)]^{1/2}\}\,, \qquad P_q = (D_q-d_q)/(D_q+d_q)\,. \end{aligned} \tag{4}$$

Here P_q is the spin-polarization of the electrons coming from the leads [10] and D_q (d_q) denote t^q_α for the majority (minority) spins. The maximum value of the TMR, $\eta_{\rm m}$, is also the upper limit for the TMR when $k_BT \gg E_C$. In that regime, it is reached when $\zeta=1$ (optimal asymmetry) while in our case the condition is $|\phi_L|^2/|\phi_R|^2 = \zeta$. If the two leads are made of different materials, the former condition requires that the tunneling barriers be expressly designed while in the mesoscopic regime there are always fluctuations that satisfy the latter condition. Indeed, the probability of the TMR being close to the maximum value is not small. In this case, then, *the mesoscopic fluctuations lead to the optimal value of the TMR.* This is also the case in the presence of spin-orbit coupling. [11]

3 Non-Collinear Magnetizations

If the magnetizations of the two ferromagnetic leads are not collinear, Eq. 2 *does not* apply. Since the quantization axes in the leads are *fixed* by the bulk magnetization of the ferromagnets, the natural axis of quantization in the left lead is not the same as in the right lead. Then, the electrons tunnel into a superposition of "up" and "down" states. This *coherence* cannot

[b] Within a Hartree-Fock treatment of the electron-electron interactions, the transport is described in terms of the self-consistent single electron wave functions.

be included in a simple rate equation—a more general approach is required. Technically, this means that Γ^L and Γ^R, which in the general case are matrices, cannot be diagonalized in the same basis. The current through an arbitrary system connected to two leads is [12]

$$J=\frac{e}{2h}\int \mathrm{d}\varepsilon\,\mathrm{Tr}\left\{\left(\mathbf{\Gamma}^L-\mathbf{\Gamma}^R\right)\mathrm{i}\mathbf{G}^<+\left(\mathbf{\Gamma}^L f_L-\mathbf{\Gamma}^R f_R\right)\mathbf{A}\right\}\ , \tag{5}$$

where $\Gamma^q_{nm}=2\pi\sum_\alpha \rho^q_\alpha V^{q*}_{\alpha n}V^q_{\alpha m}$ and α labels the channels in the leads, $\mathbf{A}=\mathrm{i}(\mathbf{G}^r-\mathbf{G}^a)$ is the spectral function, $\mathbf{G}^{r(a)}$ is the retarded (advanced) many-body Green function of the full system, and $f_{L(R)}$ is the Fermi distribution on the left (right) lead. The indices n and m label the single electron states used for describing the interacting Hamiltonian $H_{\mathrm{grain}}=H_{\mathrm{grain}}(\{d_n\};\{d_n^\dagger\})$ of the grain. It is convenient to express $\mathbf{G}^<$, the lesser Green function, in terms of the operators $\mathbf{I}^q\equiv\mathbf{\Gamma}^q(\mathbf{G}^<-\mathrm{i}f_q\mathbf{A})$: $\mathbf{G}^<=(\mathbf{\Gamma}^L+\mathbf{\Gamma}^R)^{-1}(\mathbf{I}^L+\mathbf{I}^R+\mathrm{i}(\mathbf{\Gamma}^L f_L+\mathbf{\Gamma}^R f_R)\mathbf{A})$. For elastic transport $(\mathbf{I}^L+\mathbf{I}^R)_{nn}=0$, so that Eq. 5 becomes

$$J=\frac{e}{h}\int \mathrm{d}\varepsilon\,\mathrm{Tr}\left\{\mathbf{\Gamma}^R\left(\mathbf{\Gamma}^L+\mathbf{\Gamma}^R\right)^{-1}\mathbf{\Gamma}^L\mathbf{A}\right\}(f_L-f_R)\ , \tag{6}$$

which generalizes previous results to the case $\left[\mathbf{\Gamma}^L,\mathbf{\Gamma}^R\right]\neq 0$. In the linear-response and weak coupling ($\Gamma\ll k_BT$) regime, the conductance is given by

$$G=\frac{e^2}{\hbar}\mathrm{Tr}\left\{\mathbf{\Gamma}^R\left(\mathbf{\Gamma}^L+\mathbf{\Gamma}^R\right)^{-1}\mathbf{\Gamma}^L\mathbf{A}^*_{\mathrm{eq}}\right\} \tag{7}$$

with

$$(A^*_{\mathrm{eq}})_{m,n}=\sum_{i,j}(P_i+P_j)\,\langle\Psi_i|\,d_m\,|\Psi_j\rangle\,\langle\Psi_j|\,d_n^\dagger\,|\Psi_i\rangle\,\left[-f'(e_j-e_i)\right], \tag{8}$$

$H_{\mathrm{grain}}\,|\Psi_i\rangle=e_i\,|\Psi_i\rangle$, P_i is the *equilibrium* probability of $|\Psi_i\rangle$ and $f(x)=1/(\exp[x/k_BT]+1)$. For a given CB peak, only two states with spin $|S'-S|=1/2$ are at resonance[c] (P_S is negligible for other values of S). Then

$$(A^*_{\mathrm{eq}})_{m,n}=\delta_{n,m}\,\frac{F(S,S')}{2S+1+2(S'-S)f(e_{S'}-e_S)}\,\left[-f'(e_{S'}-e_S)\right]\ , \tag{9}$$

where we have used $P_{S,S_z}=P_S/(2S+1)$ [S_z degeneracy], $P_S+P_{S'}=1$ [$E_C\gg k_BT$], $f\,P_{S,S_z}=(1-f)P_{S',S'_z}$ [detailed balance] and defined $F(S,S')=\sum_{S_z,S'_z}|\,\langle\Psi_{S',S'_z}|\,d_n^\dagger\,|\Psi_{S,S_z}\rangle\,|^2$. The function $[2S+1+2(S'-S)f(x)]^{-1}[-f'(x)]$ reachs its maximum at $x_M=\frac{1}{2}k_BT\ln([1+2S']/[1+2S])$. The conductance at the peak turns out to be

$$G_{\mathrm{peak}}=\frac{e^2}{\hbar k_BT}\,\lambda_{S,S'}\,\mathrm{Tr}\left\{\mathbf{\Gamma}^R\left(\mathbf{\Gamma}^L+\mathbf{\Gamma}^R\right)^{-1}\mathbf{\Gamma}^L\right\} \tag{10}$$

with $\lambda_{S,S'}=2\left(1+S+S'-\sqrt{1+2S}\sqrt{1+2S'}\right)F(S,S')$. Note that $F(0,\frac{1}{2})=1$ and then $\lambda_{0,\frac{1}{2}}=(3-2\sqrt{2})$ in agreement with previous results.[9,13] Notice that Eq. 10 contains Eq. 2 as a special limit. With different prefactors it is also valid in the presence of spin-orbit.[11] All these prefactors are irrelevant for the TMR since they do not depend on the polarization in the leads. It is worth mentioning that the temperature dependence of the CB peak position (x_M) might be used to measure the total spin of the grain—a very active subject.[14,15]

With the help of Eq. 10 we now calculate the conductance in the non-collinear configuration. Let us assume the magnetization on the left lead points in the z-direction while on the right lead it is tilted by an angle 2θ (Fig. 1). The spin channels on the right lead are then given

[c]We assume the total spin S of the grain is a good quantum number

by $|\hat{n},\uparrow\rangle = (\cos\theta, \sin\theta)^{\mathrm{T}}$, $|\hat{n},\downarrow\rangle = (-\sin\theta, \cos\theta)^{\mathrm{T}}$. Writing the state of the grain at the right contact in this basis, e.g. $\Psi_{\uparrow}(\mathbf{r}_R) = \phi_R(\cos\theta\,|\hat{n},\uparrow\rangle - \sin\theta\,|\hat{n},\downarrow\rangle)$, we readily obtain $\mathbf{\Gamma}^R$ and then the conductance. For symmetric leads and barriers ($P_q = P$, $\zeta = 1$)

$$G_{\mathrm{peak}}(2\theta) = G_{\mathrm{peak}}(0)\frac{(1-P^2)(1+\xi)}{1+(1-P^2)\xi - P^2\cos 2\theta} \tag{11}$$

with $\xi = \frac{|\phi_L|^4+|\phi_R|^4}{2\,|\phi_L|^2|\phi_R|^2}$. The maximum (minimum) conductance occurs at $2\theta = 0$ (π). Note that the maximum becomes narrowed as $P \to 1$. It is important to point out that Eq. 11 is different from the result obtained in the classical regime.[16] In particular, $G_{\mathrm{peak}}(2\theta)$ can be smaller than the universal lower-bound found in Ref. [16]. We think this difference arises from the resonant character of the transport considered here. Finally, it can be shown [11] that in the presence of SO coupling the extremal values of $G_{\mathrm{peak}}(2\theta)$ are shifted the amount the spin of the electron rotates while in the grain.

Acknowledgments

We appreciate helpful conversations with I. L. Aleiner, M. Johnson, K. A. Matveev and D. C. Ralph. GU acknowledges financial support from CONICET (Argentina).

References

1. For review see L. P. Kouwenhoven, *et al.*, in *Mesoscopic Electron Transport*, edited by L. L. Sohn, L. P. Kouwenhoven, and G. Schön (Kluwer, Dordrecht, 1997) pp. 158-176
2. For recent reviews see G. A. Prinz, *Science* **282**, 1660 (1998); M. Johnson, *IEEE Spectrum*, **37(2)**, 33 (2000).
3. M. Johnson, *Phys. Rev. Lett.* **70**, 2142 (1993).
4. K. Ono *et al*, *Phys. Soc. Jpn.* **65**, 3449 (1996); *ibid.* **66**, 1261 (1997); L. F. Schelp *et al*, *Phys. Rev.* B **56**, R5747 (1997).
5. S. Guéron *et al*, *Phys. Rev. Lett.* **83**, 4148 (1999).
6. J. Barnas and A. Fert, *Phys. Rev. Lett.* **80**, 1058 (1998); S. Takahashi and S. Maekawa, *ibid.* **80**, 1758 (1998); X. H. Wang and A. Brataas, *ibid.* **83**, 5138 (1999); H. Imamura, S. Takahashi and S. Maekawa, *Phys. Rev.* B **59**, 6017 (1999); A. Brataas and X. H. Wang, cond-mat/0004082.
7. The effect of a discrete energy spectrum has been considered recently by J. Barnas *et al*, *Phys. Rev.* B, **62**, 12363 (2000)
8. R. A. Jalabert, A. D. Stone, and Y. Alhassid, *Phys. Rev. Lett.* **68**, 3468 (1992).
9. C. W. J. Beenakker, *Phys. Rev.* B **44**, 1646 (1991).
10. Since P_q is a property of the "lead + tunnel-barrier", it can be significantly different from the bulk spin-polarization; J. M. De Teresa *et al Phys. Rev. Lett* **82**, 4288 (1999).
11. G. Usaj and H. U. Baranger, *Phys. Rev* B, **63**, 184418, (2001)
12. Y. M. Meir and N. S. Wingreen, *Phys. Rev. Lett.* **68**, 2512(1992); H. M. Pastawski, *Phys. Rev.* B **46**, 4053 (1992); J. H. Davies *et al ibid.* B **47**, 4603 (1993).
13. L. I. Glazman and K. A Matveev, Pis'ma Zh. Eksp. Teor. Fiz. **48**, 403 (1988) [JETP Lett. **48**, 445 (1988)]; H. Akera, *Phys. Rev.* B **59**, 9802 (1999); **60**, 10683 (1999).
14. P. W. Brouwer, Y. Oreg and B. I. Halperin, *Phys. Rev.* B **60**, R13977 (1999); H. U. Baranger, D. Ullmo and L. Glazman, *ibid.* **61**, R2425 (2000); I. L. Kurland, I. L. Aleiner and B. L. Altshuler, *ibid.* **62**, 14886 (2000).
15. J. Folk *et al*, cond-mat/0010441
16. A. Brataas, Yu. V. Nazarov and G. E. W. Bauer, *Phys. Rev. Lett.* **84**, 2481 (2000) and cond-mat/0006174.

SPIN TORQUE IN A MAGNETIC TRILAYER COUPLED TO A SUPERCONDUCTOR

XAVIER WAINTAL[1], PIET W. BROUWER[1]
[1]*Laboratory of Atomic and Solid State Physics, Cornell University, Ithaca, NY 14853-2501*

A ferromagnet–normal-metal–ferromagnet trilayer does not conserve spin current and as a result, the conduction electrons can create a torque on the magnetic moments. When the trilayer is connected to a superconducting electrode, the spin torque created by a current flowing perpendicularly to the trilayer can drive the system to a configuration where the two magnetic moments are perpendicular to each other. Here we argue that in contrast to the non-equilibrium torque, the equilibrium torque (or magnetic exchange interaction) does not single out the perpendicular configuration. We calculate the equilibrium torque for a one-dimensional lattice model and find that it is sensitive to the presence of the superconductivity.

1 Introduction

Spin current is a useful concept to describe the effect of the conduction electrons on the dynamics of the magnetic moments in a ferromagnet–normal-metal–ferromagnet trilayer.[1,2,3,4] The interaction with the local exchange field causes the potential felt by the conduction electrons to be spin dependent. In the presence of a spin-dependent potential, the spin current carried by the conduction electrons is not conserved in the ferromagnetic layers. Since the total spin of the system is conserved, the missing spin current must be accounted for as a torque acting on the magnetic moments of the ferromagnets.[1] The torque from non-conservation of the equilibrium spin currents is known as the magnetic exchange (or RKKY) interaction.[2] (There is a direct analogy between the equilibrium spin current flowing in presence of an non zero angle between the two magnetic moments and the persistent current flowing through a mesoscopic ring in presence of an Aharonov-Bohm flux.) An additional torque is exerted out of equilibrium when a current is passed through the system. Experimentally, this non-equilibrium torque has been shown to be large enough to switch the relative orientation of the two magnetic moments of the two magnetic layers from parallel to antiparallel to each other.[5] In this paper, we report on our investigation of these torques when the trilayer is connected to a superconducting electrode. The non-equilibrium torque has been considered in Ref. 6 where it is shown that the torque can drive the system to a configuration where the two magnetic moments are perpendicular to each other. Here, we address the question whether a similar effect can be expected for the (equilibrium) magnetic exchange interaction.

2 Definition of the spin torque

Following Ref. 6, we consider a trilayer system consisting of two ferromagnetic layers F_a and F_b with a normal metal (N) spacer and one superconducting contact (S), see Fig. 1. The magnetic moment of the layer F_b adjacent to S is considered fixed, e.g., by anisotropy forces. In a lattice formulation, the trilayer is described by the the Bogoliubov-De Gennes (BdG) equation[7]

$$H_i \Psi_i + t \sum_{\langle ij \rangle} \Psi_j = \epsilon \Psi_i. \tag{1}$$

Here Ψ_i is the quasiparticle wavefunction amplitude on site $i = (i_x, i_y, i_z)$, which has an electron-hole as well as a spin index, $\Psi_i = (\psi_i^{e\uparrow}, \psi_i^{e\downarrow}, \psi_i^{h\uparrow}, \psi_i^{h\downarrow})^T$. Further, t is the hopping amplitude,

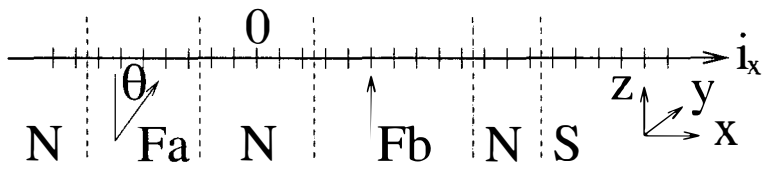


Figure 1: Schematic of the Ferromagnet-Normal-metal-Ferromagnet (FNF) trilayer under consideration. Two ferromagnetic layers, F_a and F_b, separated by a normal metal spacer (N), are connected to one normal-metal contact (left), and one superconducting contact (S, right). (A normal-metal spacer is added between F_b and S.) The arrows indicate the directions of the local exchange fields, $\vec{h}_a$ ($\theta_i = \theta$ for $i \in F_a$) and $\vec{h}_b$ ($\theta_i = 0$ for $i \in F_b$).

$\sum_{\langle ij \rangle}$ stands for the sum over nearest neighbors and,

$$H_i = \begin{pmatrix} v_i - \epsilon_F + h_i \cos\theta_i & h_i \sin\theta_i & 0 & \Delta_i \\ h_i \sin\theta_i & v_i - \epsilon_F - h_i \cos\theta_i & -\Delta_i & 0 \\ 0 & -\Delta_i^* & -v_i + \epsilon_F - h_i \cos\theta_i & -h_i \sin\theta_i \\ \Delta_i^* & 0 & -h_i \sin\theta_i & -v_i + \epsilon_F + h_i \cos\theta_i \end{pmatrix}, \tag{2}$$

where v_i is an on-site potential, ϵ_F the Fermi energy, $\vec{h}_i$ the local exchange field which we take in the xz plane. and θ_i the angle between $\vec{h}_i$ and the z axis. The superconducting gap $\Delta_i = \Delta_0$ in S and $\Delta_i = 0$ elsewhere. (This is appropriate if S is coupled to the trilayer by a point contact.)

The spin current $\vec{J}_{i_x}$ is the current associated with the time derivative of the spin density. The spin current $J_{i_x,\varepsilon}$ carried by a quasi-particle at energy ε and with wavefunction Ψ reads

$$\vec{J}_{i_x,\epsilon} = -t \ \mathrm{Im} \sum_{i_y,i_z} (\psi^{e\dagger}_{i+d} \vec{\sigma} \psi^e_i - \psi^{hT}_{i+d} \vec{\sigma} \psi^{h*}_i), \tag{3}$$

with $d = (1,0,0)$, while the equilibrium spin current $J^{\mathrm{eq}}_{i_x}$ is

$$\vec{J}^{\mathrm{eq}}_{i_x} = -\frac{1}{2} \sum_{\epsilon>0} \vec{J}_{i_x,\epsilon}. \tag{4}$$

Here, $\vec{\sigma} = (\sigma_x, \sigma_y, \sigma_z)^T$ is a vector of Pauli matrices acting on the spin index. Non-conservation of the spin current in F_a and F_b results in a torque $\vec{\tau}_a$ ($\vec{\tau}_b$) exerted on the magnetic moment of F_a (F_b) (the origin is chosen in the normal metal spacer separating F_a and F_b),

$$\vec{\tau}_a = \vec{J}_{-\infty} - \vec{J}_0 \quad , \quad \vec{\tau}_a = \vec{J}_0 - \vec{J}_{+\infty}. \tag{5}$$

3 Non-equilibrium torque

For a wide trilayer with a diffusive spacer layer, the main contribution to the non-equilibrium torque lies in the plane spanned by the two magnetic moments ($\vec{h}_a, \vec{h}_b$) (the xz plane in Fig. 1).[6] In the absence of the superconducting contact, the non-equilibrium torque $\tau^{\mathrm{ne}}_{a(b)}$ induced by a current I changes of sign at $\theta = 0, \pi$, thus stabilizing the configurations $\theta = 0$ or $\theta = \pi$ depending of the direction of the current.[1] The presence of the superconductor, however, gives a geometric constraint that allows one to find a relation between τ^{ne}_a and τ^{ne}_b, from which it follows that τ^{ne}_a also vanishes at $\theta = \pi/2$. To find this relation, note that the spin current vanishes inside S (for bias voltage $eV < \Delta_0$). Although the ferromagnetic layers do not conserve spin current, they do conserve the majority and minority currents parallel to their exchange fields $\vec{h}_{a(b)}$, hence

$$\vec{\tau}_a \perp \vec{h}_a \quad , \quad \vec{\tau}_b \perp \vec{h}_b. \tag{6}$$

Since $\vec{J}_{+\infty} = 0$ and $\vec{h}_b$ points along the z-axis, we find from Eq. (6),

$$\vec{J}_0 = J_0 \ \vec{x} \tag{7}$$

Finally, we use that, for wide trilayers, $\vec{J}_{-\infty}$ is polarized along $\vec{h}_a$ and therefore, by Eq. (6) gives no contribution to the torque.* The torque $\vec{\tau}_a$ is thus given by the projection of $\vec{J}_0$ to the unit vector perpendicular to $\vec{h}_a$ and hence,

$$\tau_a^{\rm ne} = \tau_b^{\rm ne} \cos\theta. \tag{8}$$

Equation (8) shows that the non-equilibrium torque $\tau_a^{\rm ne}$ can stabilize the $\theta = \pi/2$ configuration. (Note, however, that the presence of the S contact creates an asymmetry between the torques τ_a and τ_b, so that it is necessary for this effect that the magnetic moment of F_b is held fixed.)

4 Equilibrium torque

The previous section dealt with the non-equilibrium torque, which lies in the plane spanned by the two magnetic moments $\vec{h}_a$ and $\vec{h}_b$. It was found that $\tau_a^{\rm ne} = 0$ for $\theta = \pi/2$. We now ask whether the equilibrium torque has the same property.

The answer is negative. Again, we can see this by a geometrical argument. In equilibrium, no spin current flows outside the trilayer on either side, and thus $\vec{\tau}_b^{\rm eq} = -\vec{\tau}_a^{\rm eq} = \vec{J}_0$. In combination with Eq. (6), one then finds that $\vec{\tau}_b^{\rm eq}$ and $\vec{\tau}_a^{\rm eq}$ point out of the plane spanned by $\vec{h}_a$ and $\vec{h}_b$. There is no relation as simple as Eq. (8) for the out-of-plane component of the torque, hence no special behavior at $\theta = \pi/2$ is expected.

There are two ways to compute the equilibrium torque: either by a direct calculation of the equilibrium spin currents in the trilayer, cf. Eq. (4), or from the derivative of the ground state energy with respect to the angle θ,

$$\tau_a^{\rm eq} = \frac{\partial E}{\partial \theta}. \tag{9}$$

It should be emphasized that the equilibrium torque involves contributions from energies in the entire conduction band, as opposed to the non-equilibrium torque where only quasiparticle states near the Fermi level play a role.

To illustrate the θ dependence of $\tau_a^{\rm eq}$, we have performed a numerical exact diagonalization of the BdG equation (1). We have considered the special case of a one-dimensional trilayer, $i = i_x$ in Eq. (1). In Fig. 2, $\tau_a^{\rm eq}$ is plotted as a function of θ. We notice that the equilibrium torque (exchange interaction) depends strongly on the value of the superconducting gap Δ_0. This implies that both the direct spin exchange between the two magnets and other contributions that involve the superconductor play a role. For a very large gap $\Delta_0 \gg t$, where $2t$ is the width of the conduction band in N, the superconductor acts as a hard wall and the results are qualitatively the same as without superconductivity. However, an interesting regime appear for relatively small values of the gap $\Delta_0 < t$ where the equilibrium torque depends strongly on Δ_0, although the actual θ-dependence of $\tau_a^{\rm eq}$ is very sensitive to the particular choice of parameters and, for a realistic calculation, would require knowledge of the detailed band structure of the different materials. In the particular example shown in Fig. 2, for $\Delta_0 = 0.1t$ the biquadratic harmonic dominates the exchange coupling [8], showing that, after eventual fine tuning of parameters, nontrivial values of θ can be stabilized. (A similar effect may also occur without a superconducting contact, see, e.g., Ref. 8.)

*This is the case if the majority and minority spins are incoherently transmitted or reflected by the ferromagnetic layers, which is a good assumption for a wide trilayer with many propagating channels at the Fermi level. However, the conclusion (8) also holds for coherent transmission or reflection Ref. 6.

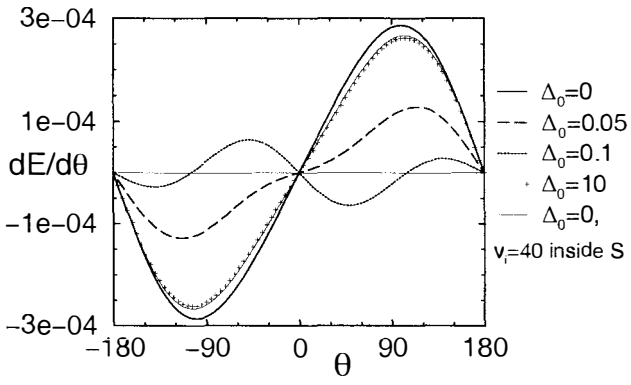


Figure 2: Equilibrium torque τ^{eq} for a one-dimensional FNF trilayer with one superconducting contact. Torque is shown as a function of the angle θ between the moments of the two ferromagnetic layers, and for various values the superconducting gap Δ_0, or without superconducting contact, see figure. The system consists of 80 sites, the relative sizes of the different layers being respectively for N, F_a, N, F_b, N and S: 9, 11, 9, 11, 4 and 36. We set $v_i = \epsilon_F = 0$ and $h_i = 0.8$. All energies are measured in units of t.

Acknowledgments

We thank P. Chalsani, A. A. Clerk, E. B. Myers, and D. C. Ralph for useful discussions. This work was supported by the NSF under grant no. DMR 0086509 and by the Sloan foundation.

References

1. J. Slonczewski, *J. Magn. Magn. Mater.* **159**, L1 (1996).
2. J. Slonczewski, *Phys. Rev.* B **39**, 6995 (1989).
3. A. Brataas, Y. V. Nazarov, and G. E. W. Bauer, *Phys. Rev. Lett.* **84**, 2481 (2000).
4. X. Waintal, E. B. Myers, P. W. Brouwer, and D. C. Ralph *Phys. Rev.* B **62**, 12317 (2000).
5. E. B. Myers, D. C. Ralph, J. A Katine, R. N. Louie, and R. A. Buhrman , *Science* **285**, 867 (1999). J. A. Katine, F. J. Albert, R. A. Buhrman, E. B. Myers, and D. C. Ralph, *Phys. Rev. Lett.* **84**, 3129 (2000).
6. X. Waintal and P. W. Brouwer, *Phys. Rev.* B, **63**, 220407(R) (2001).
7. P.G. de Gennes, *Superconductivity of metals and alloys*, (Benjamin, New York 1966).
8. J. Slonczewski, *J. Magn. Magn. Mater.* **150**, 13 (1995).

QUANTUM COMPUTING

RESONANT COOPER PAIR TUNNELING THROUGH A DOUBLE SUPERCONDUCTING ISLAND QUBIT

P. LAFARGE[1,2], E. BIBOW[1], L. P. LEVY[1,3]

[1] *Grenoble High Magnetic Field Laboratory, CNRS and MPI-FKF, B.P.166, F-38042 Grenoble Cedex 9, France*

[2] *Université Joseph Fourier, B.P. 53, F-38401 Grenoble Cedex 9, France*

[3] *Institut Universitaire de France and Université Joseph Fourier, B.P. 53, F-38401 Grenoble Cedex 9, France*

We have measured transport in the Coulomb blockade regime through a quantum system consisting of two superconducting islands coupled by a Josephson junction. The double-island is a model for a charge qubit and is weakly connected to leads by small superconducting tunnel junctions. At low bias voltages, a new resonant transport process for Cooper pairs is observed which can be used as a probe of the macroscopic energy levels of the double-island.

The first implementation of a quantum bit in a solid state device has been recently achieved in a Cooper pair box, a circuit where a single superconducting island is coupled to a reservoir by a low capacitance tunnel junction [1]. In this circuit, the competition between Coulomb blockade and Josephson effect allows the coherent superposition and manipulation of charge states [2]. The class of circuits based on small Josephson junctions, has been proposed for implementing quantum bits (qubits) in solid state devices [3,4,5,6]. They offer the possibility of a large scale integration. However, the processes leading to decoherence are more difficult to control than in microscopic systems such as trapped ions, quantum optical systems or spin systems. For this reason, it is important to understand the interactions of qubits with the other macroscopic degrees of freedom of the circuit. This interaction determines the decoherence time τ_φ and the relaxation time τ_r between the eigenstates of the qubit. The question is crucial to improve the coupling between two qubits or between a qubit and a measurement device. For charge qubits, former experiments have demonstrated the superposition of charge states [2] and measured the spectrum of the eigenstates [7]. However, despite the lower bound for the decoherence time $\tau_\varphi \sim$ 5 ns determined by Nakamura et al.[1], very little is known quantitatively about the intrisic properties of the macroscopic eigenstates of a charge qubit.

We have measured transport through a quantum system consisting of two superconducting islands coupled by a small Josephson junction. This double-island is a model of a charge qubit since, under suitable bias conditions, it can be described as a controllable two level system. The control is achieved with gate voltages capacitively coupled to each island and transport measurements are made possible by means of two weak tunnel junctions connecting the double-island to reservoirs. A schematic of the whole circuit is shown on Fig. 1. Each junction is characterized by the charging energy $E_c = e^2/2C$, where C is the junction capacitance and the Josephson energy $E_J = h\Delta/(8e^2R_t)$, where Δ is the superconducting gap and R_t is the tunnel resistance. In our circuit, the three junctions have the same charging energy E_c but the two external junctions have a Josephson energy E'_J much smaller than E_c while the middle junction has E_J comparable to E_c. The two islands are thus weakly coupled to the leads but strongly coupled to each other making the device comparable to a double quantum dot with strong interdot coupling [8,9]. A convenient basis of states for describing the double-island is thus given by the states $|n_1, n_2\rangle$, where n_1 and n_2 are the number of excess Cooper pairs on the first and the second island respectively. The conditions $E'_J \ll E_c$ and $E_J \sim E_c$ ensures that significant mixing of charge states will only occur through the central junction. If two charge states $|n_1, n_2\rangle$ and $|n_1 - 1, n_2 + 1\rangle$ differing by the tunneling of one Cooper pair charge across

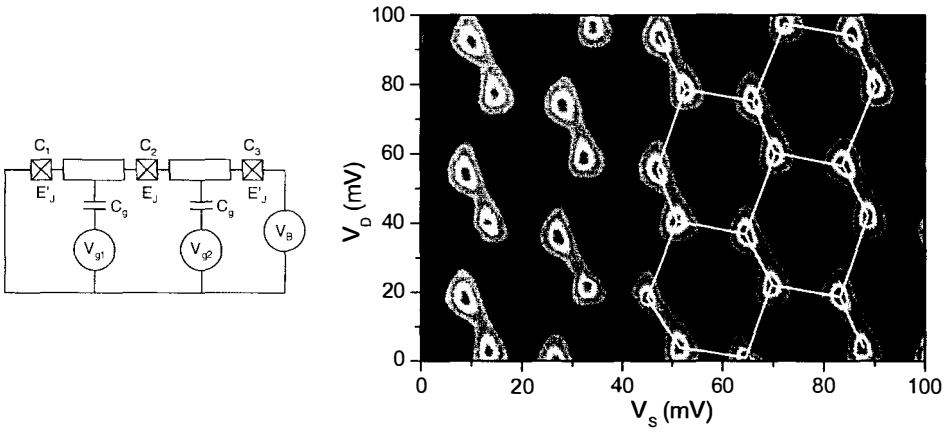


Figure 1: Schematic of the double-island qubit device and gray scale plot of the current as a function of V_s and V_d in the normal state. The black and gray areas correspond to zero and finite current respectively. The maximum current is 37 pA. The sample is taken in the normal state by applying a 1 T magnetic field and the bias voltage is 50 μV. The solid lines forming an hexagonal lattice are guides for the eyes.

the middle junction are close to a degeneracy point, the Josephson coupling across the middle junction can mix them and the circuit is placed in a controlled superposition. The control is achieved by tuning the difference $V_d = V_{g2} - V_{g1}$ in applied gate voltages. At the degeneracy point, the new eigenstates of the system are quantum superposition of the unperturbed charge states ($|\pm\rangle = \frac{1}{\sqrt{2}}(|n_1, n_2\rangle \pm |n_1 - 1, n_2 + 1\rangle)$) and their splitting is equal to E_J.

The circuit is fabricated by electron beam lithography followed by shadow evaporation of Al on a Si substrate covered by a 500 nm thick Si oxide layer. The three junctions have identical nominal size. The difference in Josephson energies between the external junctions and the central junction is obtained by using different oxidation pressure when growing the oxide barrier of the junctions. The sample is thermally anchored to the mixing chamber of a dilution refrigerator and the measurement leads are carefully filtered using distributed RC filters. All the measurements are performed at $T = 50$ mK. The device is voltage biased and the current is measured by means of a battery powered current amplifier. The normal state resistance of the three junctions in series is 448 kΩ. The superconducting gap $\Delta = 200$ μeV is extracted from the large scale I-V characteristic of the sample. When investigating transport properties, the sum $V_s = V_{g1} + V_{g2}$ and the difference $V_d = V_{g2} - V_{g1}$ in the two gate voltages are the natural parameters acting respectively on the total charge of the islands and on their difference. Figure 1 shows a two-dimensional plot of the current as a function of V_s and V_d at a fixed value of the bias voltage in the normal state. Transport is periodic in the gate voltages V_{g1} and V_{g2} with period e/C_g and so periodic in V_s and V_d with period $2e/C_g$. The gate capacitance deduced from the period is $C_g = 8.5$ aF. The current peaks in the V_s-V_d plane are centered on the vertices of an hexagonal lattice which is a well-known fingerprint of Coulomb blockade in double island [12] or double quantum dot circuits [9]. We estimate the junction capacitances and resistances by comparing the current versus gate voltage curves with simulations made using thermally activated sequential electron tunneling. The best fit gives $C_1 = 0.51$ fF, $C_2 = 0.69$ fF, $C_3 = 0.78$ fF, $R_1 = 225$ kΩ, $R_2 = 15$ kΩ, $R_3 = 205$ kΩ. Using the Ambegaokar-Baratoff relation, the estimated Josephson energies are $E_J = 43$ μeV and $E'_J \approx 3$ μeV.

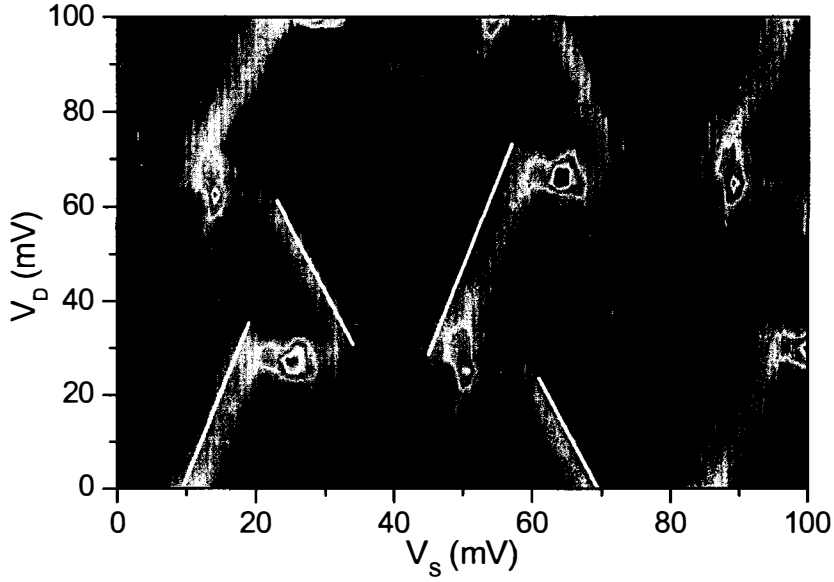


Figure 2: Current as a function of V_s and V_d in the 2e-periodic regime. The sample is in the superconducting state and the bias voltage is -125 μV. The maximum current is 0.7 pA. The solid lines result from calculation of the resonance peak positions using the values of capacitances previously obtained.

In the superconducting state, three transport regimes can be identified as a fonction of the bias voltage V_b. For bias voltages larger than $\Delta/e = 200$ μV, the Coulomb blockade modulation of the current is e-periodic with the gate induced charges $C_g V_{g1}$ and $C_g V_{g2}$. In this regime, quasiparticles are present in the circuit. At bias voltages lower than Δ/e, the modulation becomes 2e-periodic without any remaining e-periodic signal. Therefore, we assume that, in this regime, transport only involves Cooper pairs. Note that our device does not include quasiparticle traps in the measurement leads. For bias voltages between 125 μV and 200 μV, the current peaks form lines in the V_s-V_d plane as shown on Fig. 2. At lower bias voltages, the system enters a third regime where the current peaks are only observed at isolated points in the parameter space spanned by V_b, V_s and V_d (Fig. 4). These peaks appear already as dots on Fig. 2. Their position in the V_s-V_d plane is independent of the bias voltage and their amplitude is maximum at $V_b =$ 65 μV.

We now focus on the two lower bias regimes. The patterns observed in the transport properties can be understood by considering transitions between the charge states of the double-island. Because of the periodicity of the current with gate voltages, we can restrict, in our analysis, V_d between $-e/C_g$ and e/C_g and V_s between 0 and $2e/C_g$. At temperature much lower than E_c, only three charge states are relevant for the double-island: $|0,0\rangle$, $|1,0\rangle$ and $|0,1\rangle$. When considering transitions, we have also to take into account the number k of Cooper pairs having passed through the whole circuit. The energies of the charge states are given by the electrostatic energy of the whole circuit $E(n_1, n_2, k)$ which depends on V_s and V_d. The difference V_d sets $\Delta E = E(1,0,k) - E(0,1,k)$, and the sum V_s controls the mean value $(E(1,0,k) + E(0,1,k))/2$ with respect to $E(0,0,k)$ or $E(0,0,k+1)$. However, the three

states mentionned above play different roles. The $|1,0\rangle$ and $|0,1\rangle$ states are strongly coupled by Josephson tunneling. They form the basis of states of the double-island qubit whose eigenstates have the form $|\psi\rangle = \alpha|1,0\rangle + \beta|0,1\rangle$. The $|0,0\rangle$ state, hereafter referred to as the probe state, is only weakly coupled to the two others and is always an eigenstate. As a consequence, the probability for tunneling into or out of the double-island and so the current is greatly enhanced when the probe state is in resonance with another state of the system.

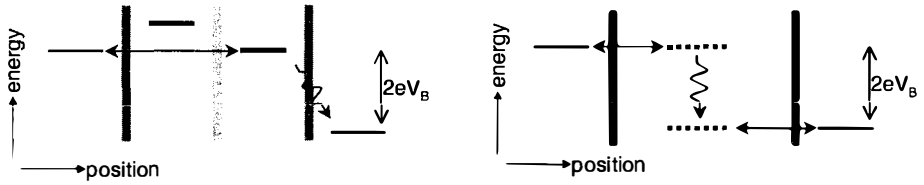


Figure 3: Left : energy diagram for the case that the probe state is in resonance with the $|0,1\rangle$ state. Right : energy diagram illustrating the double resonance between the probe state and the eigenstates of the double-island which are indicated by dotted lines.

In the 2e-periodic regime, the transport current arises only via Cooper pair tunneling. Transferring a charge $2e$ across the whole sample lowers the energy by $2eV_b$ and, since it is not possible to dissipate energy by creation of quasiparticles, Cooper pair tunneling should vanish. However, as shown on Fig. 2, at a certain set of gate voltages, Cooper pair tunneling can take place which results in a finite current through the device. Such a process, known as resonant Cooper pair tunneling, has been studied theoretically [13] and experimentally [14,15] in superconducting single electron transistors. In our circuit, at resonance, a Cooper pair enters or leaves the double island with zero electrostatic energy difference, thereby charging the qubit with a charge $\pm 2e$. It creates a dc current if the double-island can discharge and the resonant process can start all over. During the discharge of the double-island, a Cooper pair tunnels across one junction and transfers its energy to the electromagnetic environment.

Among the possible resonant tunneling processes, the most probables are the following. As illustrated on Fig 3, one resonance occurs between the probe state $|0,0\rangle$ and the $|0,1\rangle$ state by a second order tunneling event across two junctions with k unchanged. The second possible resonance is a similar process between $|1,0\rangle$ and the probe state $|0,0\rangle$ with k changed into $k+1$. Since the energy difference between the charge states depends on V_s and V_d, at fixed value of V_b, the resonance condition yields a relation between V_s and V_d and the current peaks show up as lines in the plots. The two possible processes produce two resonance lines per period in V_d. The expected peak positions, calculated using the expression of the electrostatic energy of the whole circuit, are in good agreement with the experimental current lines (see Fig. 2). According to the theory of resonant Cooper pair tunneling, the amplitude of the current is proportional to ${E'_J}^2$ and to the impedance of the electromagnetic environment which is not controlled in our experiment. Taking into account the values of the tunnel resistances, the observed current $I \sim 0.2$ pA is in agreement with former measurements of Cooper pairs resonant tunneling in SET transistors [14]

The low bias resonant peaks shown on Fig. 4 are clearly of different kind. They are sharper than the ones at higher bias voltage and have larger amplitude. The fact that they occur at single points in the V_s-V_d plane indicates that two resonance conditions are involved simultaneously. Moreover, these peaks are located on a line where the two states $|1,0\rangle$ and $|0,1\rangle$ are degenerate. At degeneracy, the ground state and excited state of the qubit are respectively the symmetric and antisymmetric superposition of the $|1,0\rangle$ and $|0,1\rangle$ states. During a transport process, two resonances occur: between the probe state and the excited state when a Cooper pair enters

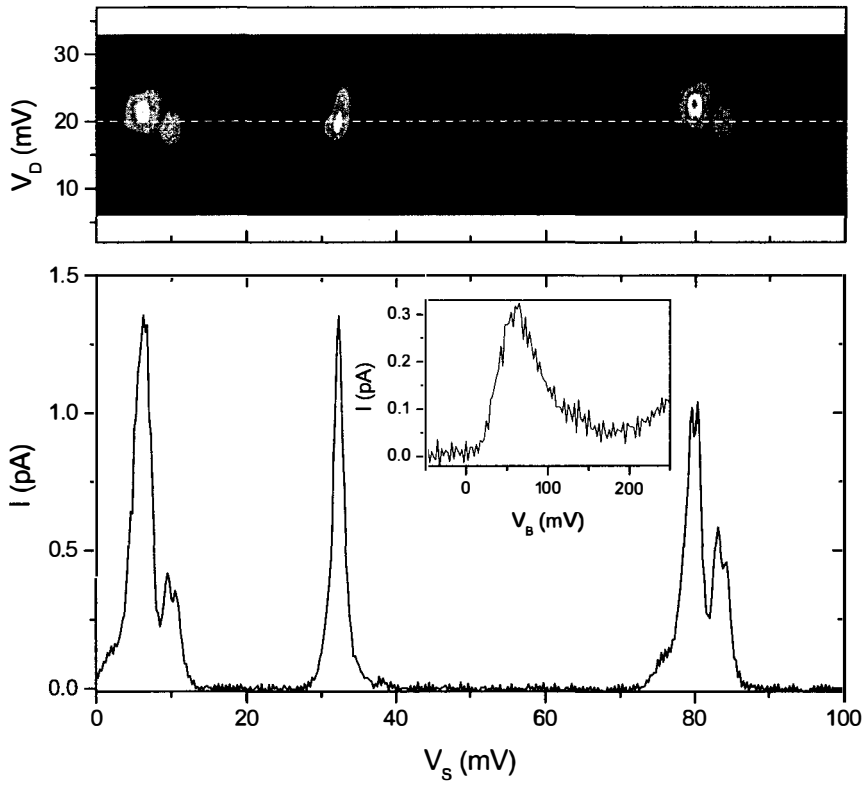


Figure 4: Top: contour plot of the current versus V_s and V_d at $V_b = -75$ μV. Bottom: current as a function of V_s measured along the dashed line of the top panel ($V_d = 20$ μV). Inset: current versus V_b for V_s and V_d in the vicinity of a resonant peak.

the double-island and between the ground state and the probe state when leaving the double-island (Fig. 3). Within this hypothesis [16], the energy gain $2eV_b$ equals the energy gap between the eigenstates which is E_J at degeneracy. The amplitude of the current is determined by the time scale of the transition between the excited and ground state. The transition can be inelastic with dissipation provided by the electromagnetic environment or taking place in the double-island itself. In this case, the relaxation from the excited to the ground state acts as a bottleneck to the transport current. The observed current intensity sets an upper bound for the excited state lifetime of the order of 200 ns. But the transition can also be elastic if the qubit is coherently coupled to another macroscopic degree of freedom of the circuit. From the peak position as a function of V_b, we obtain $E_J = 130$ μV, a larger value than our first estimate. A quantitative analysis shows that the peaks are very well fitted with a Lorentzian line-shape. Using the expression of the electrostatic energy as a function of V_s, we deduce the width w of the peak in energy units $w = 10$ μeV. Assuming that the width is determined by the coupling to the measurement leads [7], the expected value is 3 μ eV, of the same order as the observed peak

width. The external couplings limit here the coherence time of the qubit, and further studies will be required to determine which process ultimatly limit the coherence in a charge qubit.

In conclusion, the transport properties of a double-island qubit as a function of the applied gate voltages display novel resonant current peaks in the Cooper pair tunneling regime. We have shown that resonant tunneling of Cooper pair can be used as a new technique to investigate the physics of coupled discrete states in a charge qubit.

Acknowledgments

We thank T. Crozes, T. Fournier, P. van der Linden, B. Pannetier for help with fabrication and measurement and P. Joyez and A. Shnirman for stimulating discussions.

References

1. Y. Nakamura, Yu. A. Pashkin, J. S. Tsai, *Nature* **398**, 786 (1999).
2. V. Bouchiat, D. Vion, P. Joyez, D. Esteve, M. H. Devoret, *Phys. Scripta* T **76**, 165 (1998).
3. A. Shnirman, G. Schön, Z. Hermon, *Phys. Rev. Lett.* **79**, 2371 (1997).
4. D. V. Averin, *Solid State Commun.* **105**, 659 (1998).
5. Y. Makhlin, G. Schön, A. Shnirman, *Nature* **398**, 305 (1999).
6. J. E. Mooij *et al.*, *Science* **285**, 1036 (1999).
7. Y. Nakamura, C. D. Chen, and J. S. Tsai, *Phys. Rev. Lett.* **79**, 2328 (1997).
8. N .C. van der Vaart *et al.*, *Phys. Rev. Lett.* **74**, 4702 (1995).
9. C. Livermore, C. H. Crouch, R. M. Westervelt, K. L. Campman, A. C. Gossard, *Science* **274**, 1332 (1996).
10. M. T. Tuominen, J. M. Hergenrother, T. S. Tighe, M. Tinkham, *Phys. Rev. Lett.* **69**, 1997 (1992).
11. P. Lafarge, P. Joyez, D. Esteve, C. Urbina, M. H. Devoret, *Nature* **365**, 422 (1993).
12. H. Pothier, P. Lafarge, C. Urbina, D. Esteve, M. H. Devoret, *Europhys. Lett.* **17**, 249 (1992).
13. A. Maassen v.d. Brink, A. A. Odintsov, P. A. Bobbert, G. Schön, *Z. Phys. B* **85**, 459 (1991).
14. D. B. Haviland, Y. Harada, P. Delsing, C. D. Chen, T. Claeson, *Phys. Rev. Lett.* **73**, 1541 (1994).
15. P. Joyez, Ph.D. thesis, Université Paris 6, 1994.
16. A. Shnirman (private communication).

Engineering entanglement with Josephson qubits

Rosario Fazio[1,3], G. Massimo Palma[2,3], Francesco Plastina[2,3], Jens Siewert[1,3]
[1] *Dipartimento di Metodologie Fisiche e Chimiche (DMFCI), Università di Catania, viale A.Doria 6, I-95125 Catania, Italy*

[2] *Dipartimento di Scienze Fisiche e Astronomiche (DSFA) Università di Palermo, via Archirafi 36, I-90123 Palermo*

[3] *Istituto Nazionale di Fisica della Materia, Unità di Catania e Palermo*

In this contribution we discuss two aspects related to the possibility to use Josephson nanocircuits for the implementation of a quantum computer.We propose a scheme to generate and detect entanglement between charge states. Furthermore we analyze possible implementations of the Deutsch algorithm with up to three qubits.

1 Introduction

In the past decade it has become clear that the laws of quantum mechanics allow of ways of performing computation which are exponentially more efficient than classical computers. The origin of the exponential efficiency can be ascribed to the intrinsic parallelism of quantum time evolution and can be understood by viewing quantum computers as programmable quantum interferometers. The design of any quantum computing device must therefore give prescriptions to prepare superpositions of states of a suitable physical system, to produce the desired phase difference among the various possible computational paths and to measure the output state. The phenomenon of entanglement, by itself one of the most striking features of quantum mechanics [1], seems the main ingredient in many known examples of quantum speed-up in quantum computation and communication [2]. Quantum computers are described in terms of quantum bits of information - or "qubits" - and gates. In particular, two-bit gates are essential to introduce entanglement between two entries of the computational register. In recent years, considerable progress has been made in the field of "quantum hardware", namely to find those physical systems to implement quantum computers. Parallel to this activity it is important to develop implementations of "quantum software". Quantum algorithms have been implemented in a variety of systems [3]. A solid-state implementation of Grover's algorithm has been proposed theoretically [4].

The quest for large scale integrability has stimulated an increasing interest in superconducting nanocircuits [5] as possible candidates for the implementation of a quantum computer. The recent experimental breakthrough for Josephson qubits [6,7,8] is the first important step towards a solid-state quantum computer. Together with the investigation of the "quantum hardware", it is important to devise ways to perform simple logic gates with a given implementation and, in a further step, to realize complete quantum algorithms.

In this contribution we report[9,10] on our recent activity on the two aspects just mentioned, i.e. the possibility to detect entanglement and implement quantum algorithms in superconducting nanocircuits.

2 Entanglement

As sketched in Fig.1, we consider two superconducting single electron tunneling (SET) transistors (labeled by a, b) coupled by a small Josephson junction. By choosing appropriately the working point of the device as in the experiment of Nakamura *et al.* [6], coherent Cooper-pair tunneling takes place only across the left and the coupling junctions, while quasi-particle tun-

neling is important across the right junctions. Therefore, the coherent part of the Hamiltonian describing the system can be written as

$$H = \sum_{i=a,b} \left[E_{ch}(n_i - n_{x,i})^2 - E_J \cos 2\varphi_i \right] + E_c^{(ab)}(n_a - n_{x,a})(n_b - n_{x,b}) + E_J^{(ab)}(\Phi) \cos 2(\varphi_a - \varphi_b) \quad (1)$$

where E_{ch} and E_J are the charging and Josephson energy, while $n_{x,i}$ are the offset charges. The phases φ_i and the number of charges on the islands n_i (measured in units of the elementary charge e) are conjugate variables $[\varphi_i, n_j] = i\ \delta_{ij}$. The state of each individual SET can be manipulated by varying n_x, thus providing the necessary single-bit gates. However, in order to produce entanglement, we must also be able to perform non-local transformations. This can be achieved by using a switchable Josephson coupling $E_J^{(ab)}(\Phi)$, provided by a SQUID pierced by an external flux Φ. Note that the SQUID capacitance gives also rise to an electrostatic coupling $E_c^{(ab)}$.

By fixing the transport voltage $|eV| \simeq 2\Delta + E_{ch}$ and due to the Coulomb blockade $E_{ch} \gg E_J$, it suffices to consider only the three charge states with $n = 0, 1, 2$. The states $|0\rangle$ and $|2\rangle$ of the two SETs (constituting the computational basis) will be involved in the entanglement generation, while quasiparticle transitions through the state $|1\rangle$ will allow to perform the quantum measurement. To describe these incoherent transitions, only the tunneling rates related to transitions across the right junction, $\Gamma_2^{a/b}$ and $\Gamma_1^{a/b}$, are relevant (in the regime we consider, $\Gamma_2^{(a/b)} \sim \Gamma_1^{(a/b)} \sim \Gamma$), the other rates are exponentially small[11].

Ideally the detection of entanglement goes through the following steps: *i)* prepare the entangled state; *ii)* switch off the coupling between the two qubits; *iii)* perform the measurement. The first task can be achieved by sending a suitable sequence of voltage pulses to the two islands while keeping the coupling energy $E_J^{(ab)} \neq 0$. For appropriate pulse durations, the system can be prepared in the singlet state, $|\Psi^{(-)}\rangle = (|02\rangle - |20\rangle)/\sqrt{2}$. After the preparation, the coupling between the two SETs should be switched off. As for the third (and more important) step, we discuss below two possible detection schemes.

Whether the preparation of the state $|\Psi^{(-)}\rangle$ was successful (despite the presence of decoherence) can be tested by measuring the correlation between the integrated quasiparticle current signals, following the proposal to detect entanglement from noise [12] of the two SETs, $\tilde{I}_{a/b} = \int_0^{t_m} I_{a/b}(t)\, dt$. Here t_m is the integration time which is chosen to be much larger than Γ^{-1}. The correlator is given by

$$\mathcal{C} = e^{-2}\langle \tilde{I}_a \tilde{I}_b \rangle = e^{-2} \int_0^{t_m} dt_1 \int_0^{t_m} dt_2 \, \langle I_a(t_1) I_b(t_2) \rangle \ . \quad (2)$$

The experiment can be performed by means of repeated preparations of the initial state and measurements of the correlator. A value of $\mathcal{C}$ different from zero would indicate that current is flowing in both channels, which cannot happen if the system is in state $|\Psi^{(-)}\rangle$. However, complete anticorrelation between the two currents is not enough to infer that the charge state of the two islands is entangled. In fact, any statistical mixture of the form $\rho_p = p\rho_{mix} + (1-p)|\Psi^{(-)}\rangle\langle\Psi^{(-)}|$, with $\rho_{mix} = \frac{1}{2}(|02\rangle\langle 02| + |20\rangle\langle 20|)$, also leads to $\mathcal{C} = 0$.

In order to discriminate between quantum vs. classical correlations we note that if the system is in state $|\Psi^{(-)}\rangle$, the result $\mathcal{C} = 0$ is obtained also if one carries out a bi-local rotation before the detection stage. Indeed, bringing both islands to degeneracy for a time interval $\Delta t = 2\theta/E_J$, one can rotate the state of the two qubits by the same angle θ leaving $|\Psi^{(-)}\rangle$ unaffected. On the contrary, when the system is in state ρ_{mix}, a non-zero population of $|22\rangle$ is produced, giving rise to a non-zero $\mathcal{C}$.

This proposal is found to be robust against the presence of residual couplings (which cannot be avoided in the experiment). Indeed, even in realistic situations, the singlet and the statistical mixture give rise to very different correlation signals. In Figs.2,3, $\mathcal{C}$ is shown for $t_m = 3\Gamma^{-1}$, for both $p = 0$ and $p = 1$, and for different values of the charging energy of the SETs and $E_J^{(ab)}$, respectively. Their analysis indicates that, during the measurement, the Cooper pair states $n = 0, 2$ should be kept off degeneracy, otherwise the coherent oscillations in the two SETs may significantly alter the state. Differences between the pure and mixed state in Fig.2 can be detected down to values of $E_{ch}/E_J \geq 1$ while for $E_{ch}/E_J < 1$, it is impossible to discriminate between $p = 0$ and $p = 1$ because of the extra Cooper pair tunneling. On the contrary, the signal does not vary substantially with increasing $E_J^{(ab)}$ (see Fig.3).

A different approach, which does not require the technologically demanding current correlation measurement can be designed as well. The basic requirement will be the ability to implement a two–qubit gate, used to disentangle the state and to "transfer" the initial entanglement into coherence of the state of one of the qubits. There are many possibilities to achieve this goal. By applying the gate

$$\mathcal{G} = \begin{pmatrix} 1 & 0 & 0 & 0 \\ 0 & 1 & 0 & 0 \\ 0 & 0 & 0 & -i \\ 0 & 0 & i & 0 \end{pmatrix} , \tag{3}$$

we obtain

$$\mathcal{G}|\Psi^{(-)}\rangle\langle\Psi^{(-)}|\mathcal{G} \longrightarrow \frac{1}{2}(|0\rangle - i|2\rangle)(\langle 0| + i\langle 2|) \otimes |2\rangle\langle 2| , \tag{4}$$

$$\mathcal{G}\rho_{mix}\mathcal{G} \longrightarrow \frac{1}{2}\boldsymbol{I} \otimes |2\rangle\langle 2| . \tag{5}$$

The final state is separable with the b qubit always in the state $|2\rangle\langle 2|$, while a is either in a coherent or in a completely incoherent superposition of the basis states, depending on the initial presence of entanglement. One can reveal the coherence of the state of the control qubit by performing a current measurement as in[6]. If the excess current shows oscillations with respect to a varying rotation angle, the state is coherent and therefore the initial state was a singlet. On the other hand, if the excess current coming from a is constant, one can infer that the initial state was not entangled.

3 Deutsch algorithm

In the previous section we have discussed how to create and detect entanglement by means of simple one-qubit and two-qubit operations. In the following we sketch briefly that by extending the two-qubit setup and by applying sequences of similar operations, the complete three-qubit Deutsch algorithm can be implemented.

Consider the subset of Boolean functions $f : \{0,1\}^N \to \{0,1\}$ with the property that f is either constant or balanced (that is, it has an equal number of 0 outputs as 1s). The Deutsch-Josza algorithm[13] determines whether the function f is constant or balanced. With a classical algorithm, this problem would, in the worst case, require $2^{N-1}+1$ evaluations of f whereas the quantum algorithm solves it with a single evaluation by means of the following steps (here we focus on the refined version by Collins *et al.*[14]):

(i) All qubits are prepared in the initial state $|0\rangle$, therefore the N-qubit register is in the state $|00\ldots0\rangle$.

(ii) Perform an N-qubit Hadamard transformation $\mathcal{H}$

$$|x\rangle \xrightarrow{\mathcal{H}} \sum_{y\in\{0,1\}^N} (-1)^{x\cdot y} |y\rangle , \quad (x \in \{0,1\}^N), \tag{6}$$

where $x \cdot y = (x_1 \wedge y_1) \oplus \ldots \oplus (x_N \wedge y_N)$ is the scalar product modulo two. This is equivalent to performing a one-bit Hadamard transformation to each qubit individually.

(iii) Apply the f-controlled phase shift U_f

$$|x\rangle \xrightarrow{U_f} (-1)^{f(x)} |x\rangle \ , \quad (x \in \{0,1\}^N) \ . \tag{7}$$

(iv) Perform another Hadamard transformation $\mathcal{H}$.

(v) Measure the final state of the register. If the result is $|00\ldots0\rangle$ the function f is constant; if, however, the amplitude $a_{|00\ldots0\rangle}$ of the state $|00\ldots0\rangle$ is zero the function f is balanced. This is because

$$a_{|00\ldots0\rangle} = \frac{1}{2^N} \sum_{x\in\{0,1\}^N} (-1)^{f(x)} \ . \tag{8}$$

In order to implement the algorithm it is necessary to show that each individual step (preparation of the state, gate operations, measurement) can be realized in a given system. Since we know how to prepare and to measure the states of charge qubits, our task is to demonstrate that the gate operations corresponding to *all* possible functions f can be performed with a single device. An important aspect of our proposal is that the gate operations are represented in a basis of superpositions of charge states.

As discussed in Ref. [10], it is possible to implement the one, two and three bit algorithm by means of Josephson qubits. In the one-bit case there are two constant functions and two balanced functions f. The gates U_f implementing the constant functions are given by $(-1)^{f(0)} I_1$ where I_1 is the identity operator. The balanced functions can be represented (with respect to the computational basis) by $(-1)^{f(0)}\sigma_z$ where σ_i denote the Pauli matrices. The problem can be simplified by identifying functions f which lead to final states differing only by a global phase factor. We use the convention $f(00\ldots0) = 0$.

The key point for our implementation of the Deutsch algorithm is the observation that the algorithm and Nakamura's experiment have the same structure. First the systems are prepared in a symmetric superposition of states. The Rabi oscillation in the experiment corresponds to the action of the controlled phase shift U_f. Finally the system is measured. If we identify the time evolution $\exp(i(E_J t/2\hbar)\sigma_z) \leftrightarrow U_f$ for the one-bit case, the different functions f can be implemented by choosing the time t appropriately. Note that in the scheme of Deutsch's algorithm, the gate U_f acts on the same basis states which then are measured; the Hadamard transformation produces the appropriate superpositions. In contrast to this, the measurement in the experiment is done in the charge basis while the "gate" acts in the basis $\{|+\rangle, |-\rangle\}$ which is related to the charge basis by a Hadamard transformation.

While the two-qubit algorithm can be implemented by using two uncoupled qubits [14] the three-bit case involves gates U_f which produce entangled final states and require coupled qubits. The appropriate circuit is presented in Fig.4. Note that the algorithm can be realized in a pulsed experiment analogously to the discussion in the previous section if the Cooper-pair boxes are replaced by SETs.

Apart from the constant function 35 balanced functions need to be implemented. The goal is to proceed along the same lines as above, that is, preparation of the state $|000\rangle$, sudden sweep of $n_x^{(j)}$ etc. The action of the gates U_f takes place in the basis $\{|++\!+\rangle, |++\!-\rangle, \ldots, |--\!-\rangle\}$. That is, the gates operate at the degeneracy point $n_x^{(j)} = 1/2$ of the charge qubits.

By analyzing the functions f and the corresponding gates U_f we have found that, apart from the constant function and its gate there are 7 balanced functions for which the gates are separable. Further there are 12 balanced functions for which the gates factorize into a one-qubit part and a two-qubit part. The other gates entangle all three qubits. The sequences of operations and the device parameters necessary to represent each of these gates have been

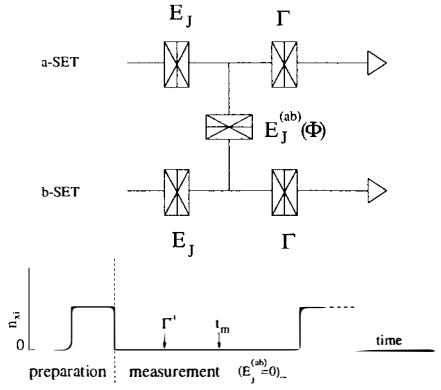


Figure 1: (Top) Schematic representation of the proposed setup. The left junctions and the SQUID allow for the coherent manipulations to prepare the state. The right junctions provide the measurement setup. (Bottom) Procedure to prepare and detect the entanglement. The procedure in repeated as in the experiment in Ref[6]

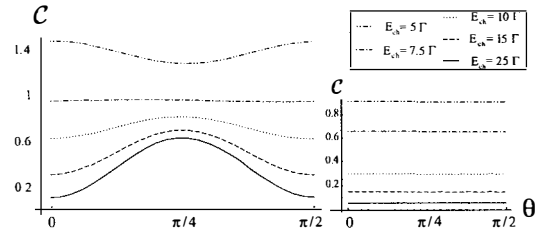


Figure 2: Time Average of the current correlation function over the time interval $\Delta t = 3\Gamma^{-1}$ as a function of the rotating angle θ for the case of the mixture (left) and the singlet (right). The parameters in both figures are $E_J^{(ab)} = 10\Gamma$, $E_J = 20\Gamma$, $E_c^{(ab)} = 0.1\Gamma$ and the indicated values for E_{ch}.

discussed in Ref. [10]. In particular it turns out that, for all functions f, it is realistic to expect a high fidelity of the gate operation: since the error for the balanced functions can simply be measured by the coefficient $|a_{|00\ldots0\rangle}|$ (see Eq. (8)) the error is found to be less than 10^{-3} in all possible cases.

Acknowledgments

The authors would like to thank L. Amico, D.V. Averin, M.-S. Choi, G. Falci, Y. Makhlin, G Schön, A. Shnirman, V. Vedral and C. v.d. Wal for helpful discussions. This works has been supported by the EU under IST-FET contracts EQUIP and SQUBIT, by INFM under contract PRA-SSQI.

4 References

1. J.S. Bell, *Speakable and unspeakable in Quantum Mechanics*, Cambridge University Press (1987).
2. A.K. Ekert and R. Jozsa, Phil. Trans. R. Soc. London A, **356**,1715, (1998).
3. N.A. Gershenfeld and I.L. Chuang, Science, **275**, 350 (1997); J. Ahn, T.C. Weinacht, and P.H. Bucksbaum, Science **287**, 463 (2000); P.G. Kwiat *et al.*, quant-ph/9905086 (1999).

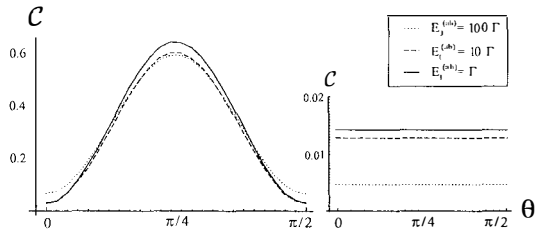


Figure 3. The same as in the previous figure, for different values of the Josephson coupling of the SQUID $E_J^{(ab)}$ ($E_{ch} = 25\Gamma$, $E_J = 10\Gamma$, $E_c^{(ab)} = 0.1\Gamma$). The correlator in both cases is almost insesitive to $E_J^{(ab)}$

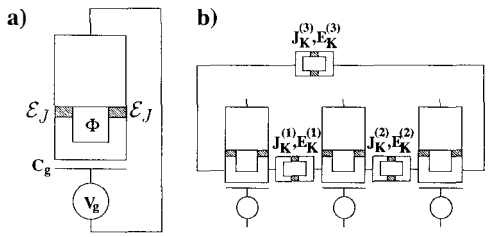


Figure 4: a) A charge qubit. The Josephson energy of the junction can be controlled by the magnetic flux Φ: $E_J(\Phi) = 2\mathcal{E}_J \cos(\pi\Phi/\Phi_0)$, where $\mathcal{E}_J$ is the Josephson energy of the junctions of the symmetric SQUID and $\Phi_0 = \hbar/(2e)$ is the flux quantum [Y.Makhlin, G.Schön and A.Shnirman, Nature **398**, 305 (1999)]. b) A possible realization of coupled charge qubits.

4. M.N. Leuenberger and D. Loss, quant-ph/0011415 (2000).
5. A. Shnirman, G. Schön, and Z. Hermon, Phys. Rev. Lett. **79**, 2371 (1997); Y.Makhlin, G.Schön and A.Shnirman, Nature **398**, 305 (1999); D.A. Averin, Sol. State Comm. **105** 659 (1998); J.E. Mooij, T.P. Orlando, L. Levitov, L. Tian, C. van der Wal, and S. Lloyd, Science **285**, 1036 (1999); L.B. Ioffe, , V.B. Geshkenbein, M.V.Feigel'man, A.L. Fauchere, and G. Blatter,Nature **398**, 679 (1999); G. Falci, R. Fazio, G.M. Palma, J. Siewert, and V. Vedral, Nature **407**, 355 (2000).
6. Y. Nakamura, Yu.A. Pashkin, J.S. Tsai, Nature **398**, 786 (1999).
7. J.R. Friedman *et al.*, Nature **406**, 43 (2000).
8. C. v.d. Wal *et al.*, Science **290**, 773 (2000).
9. F. Plastina, R. Fazio, G.M. Palma, cond-mat/0105029.
10. J. Siewert, R. Fazio, cond-mat/0105169.
11. D. V. Averin and V. Y. Aleshkin, JETP Lett. **50 (7)**, 367 (1989).
12. G. Burkard, D. Loss, E.V. Sukhorukov Phys. Rev. **B** 61, R16303 (2000).
13. D. Deutsch, Proc. R. Soc. London A **400**, 97 (1985); D. Deutsch and R. Josza, Proc. R. Soc. London A **439**, 553 (1992).
14. D. Collins, K.W. Kim, and W.C. Holton, Phys. Rev. A. **58**, R1633 (1998).

COOPER PAIR BOX COUPLED TO A CURRENT-BIASED JOSEPHSON JUNCTION

F.W.J. HEKKING[1], O. BUISSON[2], F. BALESTRO[2] AND M.G. VERGNIORY[1]
[1] *Laboratoire de Physique et Modélisation des Milieux Condensés & Université Joseph Fourier, C.N.R.S., BP 166, 38042 Grenoble-cedex 9, France*

[2] *Centre de Recherches sur les Très Basses Températures, laboratoire associé à l'Université Joseph Fourier, C.N.R.S., BP 166, 38042 Grenoble-cedex 9, France*

We study the dynamics of a quantum superconducting circuit which consists of a Josephson charge qubit, coupled capacitively to a current biased Josephson junction. Under certain conditions, the eigenstates of the qubit and the junction become entangled. We obtain the time evolution of these states in the limit of weak coupling. Rabi oscillations occur, as a result of the spontaneous emission and re-absorption of a single oscillation quantum in the junction. We discuss a possible way to experimentally determine the quantum state of the junction and hence observe the Rabi oscillations.

1 Introduction

Advances in quantum information theory [1] are at the origin of the recent search for quantum mechanical two-level systems that can be used as quantum bits (qubits). In order to process quantum information in a useful way, certain operations on systems which consist of many qubits must be performed, such as the preparation and manipulation of, as well as a measurement on, entangled quantum states of coupled qubits. In this context, superconducting devices using small Josephson junctions are of particular interest. It has been experimentally demonstrated that a single Cooper pair box constitutes a two-level system which can be coherently controlled [2,3,4]. Moreover, the use of a Cooper pair box as a qubit in the context of quantum computers was studied theoretically [5,6,7]. But as of yet, the existence of entangled states, which are at the heart of quantum information processing, has not been demonstrated experimentally.

In this article we study one of the simplest superconducting circuits in which entangled states can be realized [8]. It consists of a Cooper pair box coupled to a current-biased Josephson junction. Theoretically, this quantum circuit can be described by a two-level system coupled to a harmonic oscillator. After a description of the quantum circuit in the next Section, we discuss the time evolution of its eigenstates in Sec. 3. In particular, we demonstrate the existence of entanglement, very similar to the entanglement found for an atom in an electromagnetic cavity [9]. In Sec. 4 we discuss a possible way to measure the Rabi oscillations, associated with the dynamics of the entangled states. The last Section contains a discussion of the feasibility of our proposal.

2 Superconducting circuit

The circuit that we will study is depicted in Fig. 1. It contains a superconducting quantum circuit connected to an electrodynamic environment. The quantum circuit itself consists of three elements, which we will discuss in some detail below.

2.1 Cooper pair box

The Cooper pair box consists of a small superconducting island, coupled capacitively to a gate voltage V_g (gate capacitance C_g). The island is furthermore connected capacitively to a superconducting electrode via a Josephson junction (capacitance C_j, Josephson energy E_j). Using the basis states $|n\rangle$, where n corresponds to the number of excess Cooper pairs on the island,

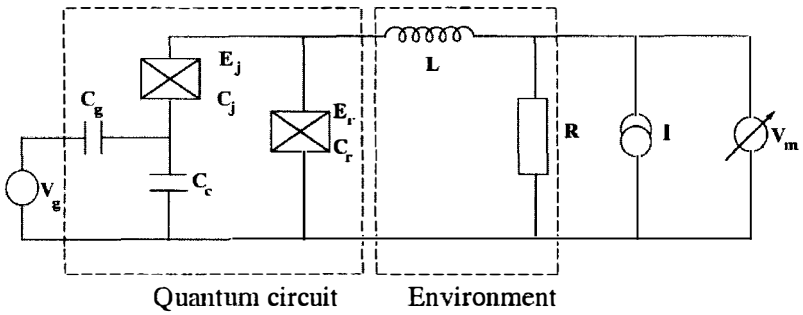


Figure 1: Superconducting quantum circuit connected to an electrodynamic environment.

we can write the Hamiltonian for the box as

$$\hat{H}_{\rm box} = E_{C,j} \sum_n (2n - N_g)^2 |n\rangle\langle n| - \frac{E_j}{2} \sum_n \left(|n+1\rangle\langle n| + |n-1\rangle\langle n| \right). \tag{1}$$

Here, $E_{C,j} = e^2/2C_{j,\rm eff}$ is the total charging energy of the box ($C_{j,\rm eff} = C_j + [1/C_r + 1/(C_c + C_g)]^{-1}$) and $N_g = -C_g V_g/e$. The first term of this Hamiltonian corresponds to the electrostatic energy of the box. Generally, this energy is minimal if the number n of excess Cooper pairs on the island is an integer. However, if the dimensionless gate-voltage N_g is an odd integer, $N_g = 2m + 1$, a degeneracy occurs, and the number n of Cooper pairs fluctuates between m and $m + 1$. The second term of the Hamiltonian, corresponding to the Josephson coupling between the island and the electrode, lifts this degeneracy. As a result, close to odd integer values of N_g, a gap opens up of order E_j and the relevant charge states are superpositions of the charge states $|m\rangle$ and $|m + 1\rangle$. In particular, if the gate-voltage is such that $N_g \simeq 1$, the states with $n = 0$ and $n = 1$ are almost degenerate. At low energies, the Hamiltonian $\hat{H}_{\rm box}$ involves only these two states, and thus can be written as a matrix

$$\hat{H}_{\rm box} \simeq \begin{pmatrix} E_{C,j} N_g^2 & -E_j/2 \\ -E_j/2 & E_{C,j}(2 - N_g)^2 \end{pmatrix}. \tag{2}$$

The two eigenstates $|-\rangle$ and $|+\rangle$ are superpositions of the charge states $|0\rangle$ and $|1\rangle$,

$$|-\rangle = \alpha|0\rangle + \beta|1\rangle \tag{3}$$

$$|+\rangle = \beta|0\rangle - \alpha|1\rangle, \tag{4}$$

where $\alpha^2 = 1 - \beta^2 = [1 + \delta E_g/\sqrt{(\delta E_g)^2 + E_j^2}]/2$ with $\delta E_g = -4E_{C,j}\delta N_g$ and $\delta N_g = N_g - 1$. The corresponding eigenenergies are

$$E_{\mp} = E_{C,j}[1 + (\delta N_g)^2] \mp \frac{1}{2}\sqrt{(\delta E_g)^2 + E_j^2}. \tag{5}$$

We see that the Cooper pair box behaves as a quantum mechanical two-level system, usually referred to as a Josephson charge qubit

2.2 Current biased Josephson junction

A current biased Josephson junction can be characterized by two conjugate variables: the charge $\hat{Q}$ on the junction and the phase difference ϕ across it. Ignoring effects related to the presence

of the environment, we can write the Hamiltonian as

$$\hat{H}_r = \frac{\hat{Q}^2}{2C_{r,\mathrm{eff}}} + U(\phi), \tag{6}$$

where $C_{r,\mathrm{eff}}$ is the effective capacitance of the junction in the circuit, $C_{r,\mathrm{eff}} = C_r + [1/C_j + 1/(C_c + C_g)]^{-1}$, and $U(\phi) = -E_r \cos\phi - (\Phi_0/2\pi)I\phi$ is the well-known tilted washboard potential ($\Phi_0 = h/2e$ is the superconducting flux quantum). It depends on the Josephson energy E_r and the bias current I. For bias currents below the Josephson critical current $I_c = 2\pi E_r/\Phi_0$, the potential $U(\phi)$ contains local periodic minima as a function of ϕ. These minima are quadratic with characteristic frequency $\omega_r = (\sqrt{8E_r E_{C,r}}/\hbar)(1 - (I/I_c)^2)^{1/4}$, where $E_{C,r} = e^2/2C_{r,\mathrm{eff}}$.

For very low bias currents ($I \ll I_c$), the minima are separated by large potential barriers $\Delta U \sim 2E_r - \Phi_0 I/2$. As a result, in the quantum limit, various low-lying states can be found in each minimum if $E_r \gg E_{C,r}$; the broadening of the energies of these states due to tunneling between neighboring minima can be ignored. Hence these states are well approximated by harmonic oscillator eigenstates, *i.e.*, we can approximate $\hat{H}_r \simeq \hbar\omega_r(a^\dagger a + 1/2)$, where the operator $a^\dagger$ (a) creates (destroys) an oscillation quantum in the junction. The eigenstates are denoted $|\chi_k\rangle$, corresponding to the presence of $k = 0, 1, 2, \ldots$ oscillation quanta in the junction. Thus, at low bias current, the junction behaves as a quantum mechanical superconducting resonator. Since in this limit the phase is localized in a well-defined minimum of the potential $U(\phi)$, the time-averaged voltage V_m across the junction remains zero.

If the bias current is increased to values close to I_c such that $I \lesssim I_c$, the potential $U(\phi)$ is well approximated by a cubic potential with a barrier height given by $\Delta U \simeq (4\sqrt{2}/3)E_r(1 - I/I_c)^{3/2}$. Both ΔU and $\hbar\omega_r$ decrease with increasing I; they vanish when $I = I_c$. The number of localized states in a given well decreases as $\Delta U/\hbar\omega_r \sim (1 - I/I_c)^{5/4}$. Moreover, the remaining levels broaden due to quantum tunneling out of the minima of the potential $U(\phi)$. A tunneling event changes the state of the junction [10], thereby leading to a finite voltage V_m across it that can be detected. The broadening of the ground state energy is given by the tunneling rate $\Gamma_0 \sim \hbar\omega_r \exp(-\Delta U/\hbar\omega_r)$. Since the excited states are located closer to the top of the barrier, the tunneling rates increase with increasing level index k: $\Gamma_k/\Gamma_0 \sim (432\Delta U/\hbar\omega_r)^k$ [11]. The tunneling rates for the first two states $|\chi_0\rangle$ and $|\chi_1\rangle$ are therefore very different. We will see in Section 4 how this property can be used in order to distinguish these two quantum states.

2.3 Coupling capacitance

The capacitance C_c plays a crucial role in the circuit of Fig. 1 since it couples the charge qubit and the current-biased junction to each other. As a result, these two circuits are no longer independent and the system must be considered in its totality. Physically, the capacitance C_c couples the charge $2n - N_g$ on the qubit to the charge Q on the junction. Using the relation $\hat{Q} = \sqrt{\hbar\omega_r C_{r,\mathrm{eff}}/2}(a - a^\dagger)/i$, the coupling Hamiltonian can be written as

$$\hat{H}_c = -iE_{\mathrm{coupl}}(2n - N_g)(a^\dagger - a). \tag{7}$$

Here we introduced the characteristic coupling energy $E_{\mathrm{coupl}} = \sqrt{\hbar\omega_r/E_{C,r}}E_{C,c}/2$, where $E_{C,c} = e^2/2C_{c,\mathrm{eff}}$, with $C_{c,\mathrm{eff}} = C_c + C_g + (1/C_j + 1/C_r)^{-1}$. We will see in the next section how this coupling energy leads to entanglement between the states of the qubit and the junction.

3 Operation at low bias current: entanglement

In this section we discuss the behaviour of the circuit for values of the bias current away from the critical current, $I \ll I_c$. In this limit, the system can be considered as a two-level system

(the qubit) coupled to a harmonic oscillator (the current biased junction). The dynamics of such a system has been discussed in the past [12]. More recent applications are concerned with quantum optics [9] or Josephson junctions [13]. Here we will show how entangled states can be obtained which involve both the qubit and the junction [8].

Throughout this section we will be interested in the situation $N_g \simeq 1$, such that we have to consider the qubit states $|-\rangle$ and $|+\rangle$ only. Furthermore, as far as the junction is concerned, we will limit the discussion to the ground state $|\chi_0\rangle$ and the first excited state $|\chi_1\rangle$. Hence, in the absence of coupling, $E_{\rm coupl} = 0$, the four lowest energy eigenstates are $|-,\chi_0\rangle, |-,\chi_1\rangle, |+,\chi_0\rangle$, and $|+,\chi_1\rangle$. Let us now consider the special case $\hbar\omega_r = E_j = \bar{E}$, *i.e.*, the states $|-,\chi_1\rangle$ and $|+,\chi_0\rangle$ are degenerate for $N_g = 1$. Their energy is $\bar{E}$ with respect to the energy of the ground state $|-,\chi_0\rangle$. In the limit of weak coupling, $E_{\rm coupl} \ll \bar{E}$, this degeneracy is lifted: the states $|-,\chi_1\rangle$ and $|+,\chi_0\rangle$ get mixed and hence give rise to the two entangled states $|\psi_1\rangle$ and $|\psi_2\rangle$,

$$\begin{aligned} |\psi_1\rangle &= [|-,\chi_1\rangle + i|+,\chi_0\rangle]/\sqrt{2}, \\ |\psi_2\rangle &= [|-,\chi_1\rangle - i|+,\chi_0\rangle]/\sqrt{2}, \end{aligned}$$

corresponding to the energies $\bar{E} - E_{\rm coupl}$ and $\bar{E} + E_{\rm coupl}$, respectively.

Suppose that the system has been prepared in the state $|\psi(t=0)\rangle = |+,\chi_0\rangle$ at time $t = 0$. This can be achieved by a suitable manipulation of the gate voltage V_g at times prior to $t = 0$ [4]. If we keep V_g fixed such that $N_g = 1$ at times $t > 0$, the time evolution of $|\psi(t)\rangle$ is given by

$$|\psi(t)\rangle = \frac{1}{\sqrt{2}i}\left[e^{-i(\bar{E}-E_{\rm coupl})t/\hbar}|\psi_1\rangle - e^{-i(\bar{E}+E_{\rm coupl})t/\hbar}|\psi_2\rangle\right]. \tag{8}$$

We see that the state $|\psi(t)\rangle$ oscillates coherently between $|-,\chi_1\rangle$ and $|+,\chi_0\rangle$. In fact, these so-called quantum Rabi oscillations can be interpreted as the spontaneous emission and re-absorption of one oscillation quantum by the junction. An interesting quantity is the probability $P_{\chi_0}(t)$ to find the junction in the state $|\chi_0\rangle$ (no oscillation quanta) after a certain time t. This probability shows Rabi oscillations as a function of t with frequency $2E_{\rm coupl}/\hbar$,

$$P_{\chi_0}(t) = |\langle +,\chi_0|\psi(t)\rangle|^2 = \frac{1}{2}[1 + \cos(2E_{\rm coupl}t/\hbar)]. \tag{9}$$

Since these Rabi oscillations are characteristic for the entanglement realized in the circuit, their measurement would provide direct evidence of the presence of the entangled states $|\psi_1\rangle$ and $|\psi_2\rangle$. We will discuss the possibility to perform such a measurement in the next Section.

4 Operation at bias current close to I_c: quantum measurement

In order to measure the probability $P_{\chi_0}(t)$ to find the junction in the state $|\chi_0\rangle$ at time t, it is necessary to perform a series of measurements. Each of these measurements consists of the preparation of the state $|\psi(t=0)\rangle = |+,\chi_0\rangle$ at time $t = 0$ and the subsequent coherent evolution until the time t, when the actual measurement of the state of the junction is performed. The statistics of the ensemble of measurements then yields $P_{\chi_0}(t)$.

The proposed measurement procedure consists in transforming the two distinct quantum states $|\chi_0\rangle$ and $|\chi_1\rangle$ into two different stable classical states which are easily measurable: the zero-voltage and the finite voltage state of the current-biased junction. This measurement is a one shot method which gives binary information on the initial quantum state of the junction.

In order to measure the state of the junction at a certain time t, we propose to proceed as follows. Starting at time t, the bias current I is increased during a short ramping time δt to a value I_m close to I_c. The bias current is kept at I_m for a time Δt and then switched back to a low value away from I_c. Finally, the DC-voltage across the junction is measured.

The increase of the bias current to I_m drastically increases the tunneling rates Γ_0 and Γ_1 of the two possible states of the junction. During the time Δt, the junction can transit into a finite voltage state as a result of a tunneling process. However, as we have seen, the escape time depends strongly on the initial quantum state. For instance, $\Gamma_1 \sim 1000\Gamma_0$ if $\Delta U/\hbar\omega_r > 3$. Therefore, if the junction is in the state $|\chi_1\rangle$, a DC voltage starts to develop after a time $1/\Gamma_1$, whereas this will happen after a much longer time $1/\Gamma_0 \gg 1/\Gamma_1$ if the junction is in the state $|\chi_0\rangle$. Hence if we switch the bias current I back to a value away from I_c after a time Δt such that $1/\Gamma_1 \ll \Delta t \ll 1/\Gamma_0$, the junction remains in the zero-voltage state *if and only if the junction is in the state* $|\chi_0\rangle$. It is during the time Δt that the two quantum states bifurcate into two different voltage states, hence we refer to this time as a measuring time. After Δt, the current is switched back to a lower value. Since the $I-V$ characteristics of the junction are hysteretic, the zero voltage and finite voltage states remain dynamically stable. Thus we have a relatively long time to perform the actual voltage measurements and distinguish the two junction states.

5 Discussion

The functioning of the quantum circuit presented in this paper relies on various assumptions. Below we will discuss these assumptions for each part of the circuit in some detail.

Josephson charge qubit. One of the main assumptions concerning the qubit is the absence of quasiparticles. If a quasiparticle tunnels onto the island, the state of the Cooper pair box changes: it no longer behaves as a quantum mechanical two-level system. Thus we need the superconducting gap to be sufficiently large, $\Delta > E_{C,j} + E_j/2$. We furthermore need the box to be quantum mechanically coherent during the experiment. This is one more reason to impose the absence of quasiparticles. But in addition it means that the coupling to the outside world must be sufficiently weak. Generally, the main source of decoherence is formed by time-dependent fluctuations of the effective gate charge N_g, either induced by fluctuations of the gate-voltage V_g, or by residual dynamics of charged impurities close to the qubit. However, if the qubit is operated close to the degeneracy point $N_g = 1$, the effect of this noise will be weak, since the energies $E_\pm$ depend only quadratically on the amplitude of the fluctuations.

Current biased Josephson junction. When using the current biased Josephson junction as a quantum mechanical resonator, it is essential for the states $|\chi_0\rangle$ and $|\chi_1\rangle$ to be well-defined, *i.e.*, the broadening $\Gamma_{0,1}$ of the corresponding energy levels must be small compared to E_{coupl}. For this reason we need to work at low bias current, such that $\Gamma_1 \sim 1000\Gamma_0 \sim 1000\sqrt{E_r E_{C,r}}\exp\sqrt{E_r/E_{C,r}} \ll E_{\text{coupl}}$. In addition, decoherence to the external circuit should not occur on a time scale of the order of $\hbar/E_{\text{coupl}}$. This means that the impedance should be sufficiently high. For a purely resistive environment for instance (R finite and $L = 0$ in Fig. 1), the typical relaxation time is RC_r. We do require this time to exceed the Rabi period $\hbar/E_{\text{coupl}}$.

When using the junction as a detector it is important that it changes its state before relaxation processes induced by the environment occur. Thus we need to increase the current I sufficiently close to I_c such that $1/\Gamma_1$ is much smaller than the relaxation time.

Apart from increasing the tunneling rates Γ_k, an increase of the bias current I has another important effect. Since the frequency ω_r depends on I, the resonance condition $\hbar\omega_r = E_j$ is no longer satisfied after the increase. As soon as the difference $|\hbar\omega_r - E_j|$ exceeds E_{coupl}, the qubit and the junction are no longer entangled and the states $|-,\chi_1\rangle$ and $|+,\chi_0\rangle$ become again eigenstates of the system. The probability to be in either of these states $|\chi_0\rangle$ or $|\chi_1\rangle$ ceases to evolve in time. This way, the probability P_{χ_0} remains "frozen" into its value at the time t of the measurement (as long as relaxation phenomena can be neglected). In order for t to be well-defined, the ramping time δt must be short compared to the period $\hbar/E_{\text{coupl}}$ of the Rabi oscillations. On the other hand, the ramping itself should not induce transitions in the junction, thus we need to impose the condition $\omega_r \delta t \gg 1$.

In most experiments [10,14], the environment is dominated by a resistor R. On the one hand, R should be large in order for the relaxation time to be long. On the other hand, R should be low enough to avoid heating at low temperature due to the bias current flowing through the resistor. In order to avoid these conflicting conditions, we propose to use a large on-chip inductor in series with the junction (see Fig. 1). To minimize the effect of the environment, the inductor has to be much larger than R/ω_r and $1/(C\omega_r^2)$. Then the relaxation time is given by $(L\omega_r)^2 C/R$, which can be much larger than typical RC_r-times [10]; the characteristic frequency of the junction is not affected by the environment. Moreover, if the temperature T of the environment satisfies the condition $R/L \ll 2kT/\hbar \ll \omega_r$, the escape rate is given by $\ln(\Gamma_0(T)/\Gamma_0) = (9/\pi\sqrt{2})(h/e^3)(C_r/LI_c)(1-I_m/I_c)^{1/2}kT$, where Γ_0 is the zero-temperature rate for quantum tunneling. The excess escape rate due to thermal fluctuations in the resistor is, surprisingly, independent of the resistance R of the environment.

For the numerical estimates presented below we will consider parameters of typical superconducting circuits [10,4]. For the Josephson charge qubit we have chosen $E_j = 26.1\mu$eV and $E_{C,j} = 70\mu$eV. The coupling capacitance is chosen to be of the order of C_j, $C_c = 0.5$fF, yielding $E_c = 256$neV. For a Josephson junction with a capacitance of 6.35pF and a critical current of 10μA, the characteristic frequency is about 13GHz at zero bias current.

The resonant condition $\hbar\omega_r = E_j$ for the charge qubit and the Josephson resonator is obtained at a bias current of 9.4μA. The period of the Rabi oscillations is given by $T_{\rm Rabi} \approx 8$ ns. Taking into account the environment of Fig. 1 with $R = 8\Omega$ and L=10nH, the relaxation time is about 136ns and thus longer than the period of the Rabi oscillations.

During the measurement process, the bias current is chosen to be $I_m = 9.91\mu$A, corresponding to a characteristic frequency of 4GHz. The relaxation time is 51ns. For $T = 20$mK, we estimate the escape time to the voltage state to be $6\mu s$ from the state $|\chi_0\rangle$ and $7ns$ from the state $|\chi_1\rangle$. Taking $\Delta t = 50ns$, we expect the junction to bifurcate into the voltage state with a probability larger than 99.9% for the state $|\chi_1\rangle$ and smaller than 0.1% for the state $|\chi_0\rangle$.

In conclusion, we proposed an efficient procedure for single-shot quantum measurements of entangled states in a Cooper pair box coupled to a current-biased Josephson junction.

Acknowledgments

We thank G. Falci, R. Fazio, and E. Paladino for interesting discussions.

References

1. See, *e.g.*, A. Steane, Rep. Prog. Phys. **61**, 117 (1998).
2. V. Bouchiat *et al.*, Physica Scripta T**76**, 165 (1998).
3. Y. Nakamura, C. D. Chen, and J. S. Tsai, Phys. Rev. Lett. **79**, 2328 (1997).
4. Y. Nakamura, Yu. A. Pashkin, and J. S. Tsai, Nature **398**, 786 (1999).
5. A. Shnirman, G. Schön, and Z. Hermon, Phys. Rev. Lett. **79**, 2371 (1997).
6. Y. Makhlin, G. Schön, and A. Shnirman, Nature **398**, 305 (1999).
7. Y. Makhlin, G. Schön, and A. Shnirman, cond-mat/0011269.
8. O. Buisson and F.W.J. Hekking, proceedings of MQC2 (Naples, Italy, 2000); cond-mat/0008275.
9. M. Brune *et al.*, Phys. Rev. Lett. **76**, 1800 (1996).
10. J.M. Martinis, M.H. Devoret and J. Clarke, Phys. Rev. Lett. **55**, 1543 (1985).
11. U. Weiss, *Quantum dissipative systems* (World Scientific, Singapore, 1999).
12. E. Jaynes and F. Cummings, Proc. IEEE **51**, 89 (1963).
13. F. Marquardt and C. Bruder, Phys. Rev. B **63**, 54514 (2001).
14. P. Silvestrini *et al.*, Phys. Rev. Lett. **79**, 3046 (1997).

DYNAMICS OF ANDREEV LEVEL QUBITS

V.S. SHUMEIKO[1], E.N. BRATUS'[2], G. WENDIN[1]
[1] *Chalmers University of Technology and Göteborg University, 41296 Göteborg, Sweden*
[2] *B. Verkin Institute for Low Temperature Physics and Engineering, Kharkov, Ukraine*

The dynamics of an rf SQUID with a one-mode point contact is analyzed. The state of Andreev levels in the contact can be measured by measuring flux oscillations through the SQUID.

Introduction

In a search for electronic realizations of qubits, a superconducting ring (rf SQUID) interrupted by a quantum point contact (QPC) presents interesting possibilities. It is theoretically well established that the current through short superconducting contacts is solely carried by Andreev bound states.[1,2] These states are formed in the contact due to Andreev reflections by the large gradient of the superconducting phase across the contact. In a QPC, the number of conducting electronic modes is limited, each conducting mode containing only one pair of Andreev bound states. Thus a superconducting QPC may be viewed as a kind of quantum dot where the quantization effect is achieved due the combination of normal and Andreev reflections. The simplest system, which consists of two Andreev levels in a one-mode QPC, can then be considered as a qubit (Andreev level qubit). In highly transmissive contacts, the Andeev levels lie deep within the superconducting gap and are well decoupled from the continuum states. At the same time, Andreev levels are coherently coupled to the supercurrent, which makes them accessible for manipulations and measurements. By ramping external flux or by applying properly designed rf flux pulses, one can drive Andreev two-level system (TLS) from the ground state to a certain excited state; this state can then be measured by monitoring the flux through the SQUID. If the state of the Andreev TLS is not an eigenstate of the Hamiltonian of the contact, one has to expect quantum fluctuations of the flux.

Several types of persistent current qubits based on rf SQUIDs have been suggested in the literature; see for example.[3] In these qubits, macroscopic tunnel junction(s) are used as the Josephson element, and the quantum fluctuation of flux are due to the charge fluctuations at the junction capacitor. The macroscopic quantum tunneling between degenerate flux states of the SQUID was recently observed in the experiments.[4,5] In our case, the mechanism of flux fluctuation is different: the junction capacitance does not play any significant role, and the quantum fluctuations result from the coupling of the flux to the true microscopic degree of freedom, the Andreev TLS.

The ground state properties of an rf SQUID with an atomic-size QPC have been experimentally tested by Koops et al.[6] In this experiment, the Josephson current-phase relation was determined by measuring the total flux through the SQUID by an inductively coupled SQUID magnetometer as a function of the applied flux. The contact was fabricated by means of the controllable break-junction technique,[7] and a current of the order of few current quanta,[8] $I_q = e\Delta/2\hbar$, was achieved ($I_q \approx 0.37$ mkA for Nb). In the present paper we will discuss the properties of excited states of Andreev TLS and the dynamics of Andreev level qubits.

Circuit parameters

In this section, we discuss the rf SQUID parameters suitable for the operation of Andreev level qubits. Let us consider an almost perfect atomic-size one-mode constriction with a very small reflectivity in the normal state $R = 1 - D \ll 1$. The electrodes of the constriction form a loop of length $\mathcal{L}$; to be able to neglect the non-homogeneity of the current density, we

assume the loop cross section to be comparable to the screening length, $S \sim \lambda_L^2$. To avoid creation of real excitations, the qubit must operate at low frequencies, $\omega \ll \Delta \ll E_F$; at these frequencies the current is constant along the superconducting loop and obeys the bulk relation, $I = enSv_s$, where n is the electron density, and v_s is the superfluid velocity. Integration over the loop yields a relation between the current and the superconducting phase difference across the contact ϕ, $(2\pi L_s/c\Phi_0)I = (\phi - \phi_t)$, where $\phi_t = 2\pi\Phi_t/\Phi_0$ is the normalized total flux through the ring, $\Phi_0 = ch/2e$. The inductance, $L_s = mc\mathcal{L}/e^2nS$, appearing in this equation can be estimated as $L_s \sim (k_F\lambda_L)^2\mathcal{L}/\mathcal{N}$, where $N = Sk_F^2 \sim 10^4$ is the number of conducting electronic modes in the loop. The total flux through the loop is the sum of external flux, ϕ_e, and flux induced by the current, $\phi_t = \phi_e + (2\pi L/c\Phi_0)I$. The current through the contact consists of the Josephson current, $I_J\{\Psi\}$, which depends on the state Ψ of Andreev TLS, and the dissipative and displacement currents, $I = I_J\{\Psi\} - (\Phi_0/2\pi c)(G\dot{\phi} + C\ddot{\phi})$, where $G \approx G_q = 2e^2/h$ is the junction conductance, and C is the junction capacitance.

The derived equations present part of the full dynamic description of the qubit: they describe the dynamics of the superconducting loop which plays the role of environment for the contact, and they must be completed by the dynamical equation for Andreev TLS. To simplify the analysis, we decouple the contact dynamics from the environment by assuming the non-hysteretic regime for the SQUID, i.e., we assume $\beta \equiv 2\pi(L_s + L)I_q/c\Phi_0 \ll 1$, or $L_s, L \ll \xi_0(k_F\lambda_L)^2$, where $\xi_0 = \hbar v_F/\Delta$ is the superconducting coherence length. In this regime, the contribution of the Josephson current to the loop dynamics is small, and the current oscillations in the superconducting loop are characterized by the resonant frequency $\omega_p = c/\sqrt{LC}$ and the damping rate $\nu = G/C$. To avoid creation of real excitations by these current oscillations, the frequencies must be small compared to the superconducting energy gap, $\hbar\nu, \hbar\omega_p \ll \Delta$. We note that the first assumption is equivalent to the requirement of small charging energy compared to the Josephson coupling energy, which is of order Δ in our case, $e^2/C \ll \Delta$, or $C \ll \xi_0$. Furthermore, we assume that the frequency of intrinsic evolution of the Andreev TLS is small compared to the frequency characteristics of the loop, $\omega \ll \nu, \omega_p$. Then the current in the loop adiabatically follows the evolution of the Andreev TLS, and the relation between the Josephson current and the phase difference has the quasistatic form

$$\beta I_J\{\Psi\} = I_q(\phi - \phi_e). \tag{1}$$

Andreev two-level system

Now we turn to a discussion of the dynamics of the Andreev TLS and the relation between the current and the Andreev TLS wave function Ψ. Andreev TLS in atomic-size superconducting QPCs is well discussed in literature.[2,9] The contact is modeled by the quasiclassical 1D Bogoliubov-de Gennes equation, $i\partial_t\hat{\psi} = \hat{H}\hat{\psi}$, (here we assume $\hbar = 1$), written for 4-component vectors $\hat{\psi} = (\psi^+, \psi^-)$, where $\psi^\pm$ are the quasiclassical amplitudes of the two-component Nambu wave function Ψ,

$$\Psi = \psi^+ e^{ik_0x} + \psi^- e^{-ik_0x}. \tag{2}$$

k_0 is the Fermi wave vector of the conducting mode. The Hamiltonian has the form $\hat{H} = \tau_z\sigma_z v_0\hat{p} + \hat{\Delta}(x,t)$, where τ_i and σ_i are Pauli matrices in the $\{\psi^\pm\}$ space and the Nambu space respectively.

The matching equation at the junction is, $\hat{\psi}(-0,t) = \hat{T}e^{i\sigma_z\phi(t)}\hat{\psi}(+0,t)$, where $\hat{T} = (1-\tau_y r)/t$ is the transfer matrix of the junction, t, r being (real) scattering amplitudes.

The eigenvectors of the stationary problem, ϕ=const, for the energy levels lying within the superconducting gap, $|E < \Delta|$, are given by equations,

$$\hat{\psi}_{L,R}(x,t) = \hat{\psi}_{L,R}e^{\pm\zeta x/v_0}e^{-iEt}, \quad E^2 = \Delta^2 - \zeta^2, \tag{3}$$

where $\hat{\psi}_L = (Au^-, Bu^+)$, and $\hat{\psi}_R = (Cu^+, Fu^-)$, and $u^\pm = e^{\pm i\gamma/2}$ for $E > 0$ ($\gamma \to \pi - \gamma$ for $E < 0$), $e^{i\gamma} = (E + i\zeta)/\Delta$. The discrete spectrum is then given by the equation $\sin^2\gamma = D\sin^2(\phi/2)$, consisting of two levels with energies $E_\pm = \pm E_A$, $E_A = \Delta\sqrt{1 - D\sin^2(\phi/2)}$. Explicit expressions for the coefficients A, B, F through C are $A/C = -\mathrm{sgn}\sin(\phi/2)$, $B/C = r|\sin(\phi/2)|/\sin\gamma_-$, $F/C = \sin\gamma_-/r|\sin(\phi/2)|$, while the coefficient C, resulting from the normalization condition, has the form, $|C|^2 = (\zeta/v_0)(1 - \sin\gamma_-/\sin\gamma_+)^{-1}$, $\gamma_\pm = \gamma \pm \phi/2$.

The current calculated at the junction ($x = 0$) for a pure state of Andreev TLS is given by the equation $I_J\{\Psi\} = Tr\ \tau_z\hat{\psi}(0)\hat{\psi}^\dagger(0)$. For the levels $E_\pm$ the current is $I_\pm = \mp I_q D\sin\phi(\Delta/2E_A)$. In the equilibrium at zero temperature, only the lower Andreev level is populated, and the Josephson current is solely produced by this level, $I_J = I_-$. For any nonequilibrium mixed state of the Andreev TLS with population numbers $n_\pm$, the current is $I_J = I_-(n_- - n_+)$. However, if the Andreev TLS is in a coherent superposition of the eigenstates,

$$\hat{\psi}(t) = a\hat{\psi}_+ e^{-iE_A t} + b\hat{\psi}_- e^{+iE_A t}, \tag{4}$$

(here we explicitly showed time-dependent factors of the eigenvectors) then, in addition to a dc current, $I_{dc} = I_-(|b|^2 - |a|^2)$, there is also an ac current,

$$I_{ac} = I_\sim \mathcal{R}(a^* b e^{2iE_A t}), \quad I_\sim = 8I_q D\sqrt{R}\sin^2(\phi/2)(\Delta/E_A). \tag{5}$$

This non-stationary current, substituted into Eq. (1), will lead to a time dependence in the phase difference, which will destroy the stationary state and lead to dynamical behavior of the whole system.

Rabi oscillations

To discuss the dynamics of Andreev TLS, we first assume that external flux is modulated by a small rf signal, $\delta\phi_e(t) = \phi_\omega e^{i\omega t} + \phi_\omega^* e^{-i\omega t}$, whose frequency is close to the interlevel distance $2E_A$. In this, resonant, case the state of the Andreev TLS is described by a superposition in Eq. (4) with the coefficients slowly varying with time, $a(t), b(t)$. To derive the dynamical equations for these coefficients, we gauge out the time dependent part of the phase difference from the matching condition using the transformation $\psi_R \to e^{-i\sigma_z\delta\phi(t)}\psi_R$. This will lead to an additional term in the Hamiltonian,

$$\delta\hat{H} = \theta(x)[-(1/2)\sigma_z\delta\dot{\phi}(t) + \frac{\partial\hat{\Delta}}{\partial\phi}\delta\phi(t)] \tag{6}$$

Then the standard procedure of averaging over rapid ($\sim \omega$) oscillations in the wave equation gives

$$i\dot{a} = \lambda\phi_\omega^* e^{i(2E_A - \omega)t} b, \quad i\dot{b} = \lambda\phi_\omega e^{-i(2E_A - \omega)t} a. \tag{7}$$

where λ is the matrix element between the states $\pm E_A$,[2]

$$\lambda = (\hat{\psi}_+\delta\hat{H}\hat{\psi}_-) = \frac{\sqrt{R}D\Delta^2\sin^2(\phi/2)}{E_A}. \tag{8}$$

Exactly at the resonance, $\omega = 2E_A$, the instant switching-on of the rf field (in practice, the switching time should be $\sim 1/\omega$) will excite the Andreev TLS from the ground state to the state with $a(t) = i\sin\lambda|\phi_\omega|t$, $b(t) = \cos\lambda|\phi_\omega|t$. In terms of the Bloch vector $\mathbf{M} = (2\mathcal{R}(ab^*), 2\mathcal{I}(ab^*), |a|^2 - |b|^2)$, this corresponds to a slow rotation of the Bloch vector in a vertical plane (nutation) with the Rabi frequency, $\Omega = 2\lambda|\phi_\omega|$, in addition to the fast rotation in a

horizontal plane, and leads to the current oscillations, $I_J = I_- \cos\Omega t + I_\sim \sin\Omega t \sin(2E_A t + \delta)$, δ is the phase of ϕ_ω. By applying rf pulses with a certain duration, one is able to obtain any coherent state of the qubit. After switching off the rf signal, the Bloch vector will continue to rotate in a horizontal plane (precession) with the frequency $2E_A$, and this state will persist until dephasing and relaxation converts it into the ground state.

Applicability of the resonant approximation requires $\Omega \ll 2E_A$. Furthermore, to maintain the adiabatic behavior of the superconducting loop assumed above, we have to require $2E_A \ll \hbar\nu, \hbar\omega_p \ll \Delta$, which implies that the SQUID must be biased at $\phi \approx \pi$: in this case, the Andreev levels lie deep inside the superconducting energy gap, $E_A \approx \Delta\sqrt{R + \bar{\phi}^2/4}$ ($R, \bar{\phi} = \phi - \pi \ll 1$), and the precession frequency is small. The Rabi frequency is estimated in this case as $\Omega \approx \Delta\phi_\omega\sqrt{R/(R + \bar{\phi}^2/4)}$, which yields the condition of small Rabi frequency, $\phi_\omega \ll \sqrt{R}$.

The relaxation and dephasing mechanisms for the Andreev qubit are similar to the ones for persistent current qubits [10,11] (fluctuation of the bias, electromagnetic emission). However, there is an additional relaxation mechanism which is specific for the Andreev level qubit and which involves microscopic interactions with the quasiparticles in the electrodes, primarily with phonons. The electron-phonon relaxation of Andreev levels has been analyzed in literature [12], and the corresponding rate was estimated as $\nu_{ph} \sim R\sqrt{(R + \bar{\phi}^2/4)}\,(\Delta^3/\theta_D^2)$. The condition of small relaxation rate compared to the Rabi frequency, which is necessary for the coherent qubit dynamics, can be fulfilled under the condition $R^{3/2}(\Delta/\theta_D)^2 \ll \phi_\omega \ll \sqrt{R}$. In atomic-size break junctions, a reflectivity as small as $R \sim 0.01$ can be achieved.

Now we are able to discuss the nonlinear effect of self-induced oscillations of the phase difference due to the ac current in Eq. (5). This current oscillates with the resonant frequency and may strongly affect the Andreev TLS. It follows from Eqs. (1), (5) that the current oscillations will modulate the phase difference with the amplitude $\phi_\omega = \mu a^* b$, $\mu = 8\lambda\beta/\Delta$. This gives the following modification of the dynamic equation (7),

$$i\dot{a} = \lambda\phi_\omega^* b + \lambda\mu|b|^2 a, \quad i\dot{b} = \lambda\phi_\omega a + \lambda\mu|a|^2 b. \tag{9}$$

In the absence of external rf field, this nonlinear equation is easily solved, giving $a(t) = ae^{i\lambda\mu b^2 t}$ and $b(t) = be^{i\lambda\mu a^2 t}$. This solution corresponds to the precession of the Bloch vector with frequency $\lambda\mu(a^2 - b^2)$. Thus, the self-induced oscillations do not influence the level populations but only shift the precession frequency by the magnitude $\sim \beta\Delta$.

References

1. A. Furusaki and M. Tsukada, Phys. Rev. B **43**, 10164 (1991).
2. V.S. Shumeiko, E.N. Bratus', and G. Wendin, Phys. Rev. B **48**, 13129 (1993).
3. T.P. Orlando et al., Phys. Rev. B **60**, 15398 (1999).
4. J.R. Friedman, V.P.W. Chen, S.K. Tolpygo, and J.E. Lukens, Nature **406**, 43 (2000).
5. H. Caspar, et al., Science **290**, 1039 (2000).
6. M.C. Koops, G.V. van Duyneveldt, and R. De Bruyn Ouboter, Phys. Rev. Lett. **77**, 2542 (1996).
7. C.J. Muller, J.M. van Ruitenbeek, and L.J. de Jongh, Physica **190C**, 485 (1992).
8. C.W. Beenakker and H. Van Houten, Phys. Rev. Lett. **66**, 3056 (1991).
9. L.Y. Gorelik, V. S. Shumeiko, R. I. Shekhter, G. Wendin and M. Jonson, Phys. Rev. Lett. **75**, 1162 (1995).
10. Lin Tian et al., cond-mat/9910062.
11. D.V. Averin, J.R. Friedman, and J.E. Lukens, Phys. Rev. B **62**, 11802 (2000).
12. D.A. Ivanov and M.V. Feigel'man, JETP Lett. **68**, 890 (1998).

Electron spins for spintronics and quantum communication in quantum dots and wires

DANIEL LOSS, PATRIK RECHER, HANS-ANDREAS ENGEL
Department of Physics and Astronomy, University of Basel, Klingelbergstrasse 82, CH-4056 Basel, Switzerland

Electron spins in nanostructures such as quantum dots and wires have promising applications for spintronics, quantum computing and quantum communication. We give a brief introduction to the quantum computing proposal using electron spins in quantum dots. A quantum dot in the Coulomb blockade regime, attached to leads and in the presence of a magnetic field is used to study single-spin effects. With an ESR source, the spin can be coherently controlled, leading to Rabi-oscillations of the dot spin. It is shown that the intrinsic single-spin decoherence time T_2 is directly accessible via a stationary charge current through the dot. In addition, we show that the quantum dot acts as an efficient spin filter, single-spin read-out device or as a spin pump. Finally, we consider mobile non-local spin entangled electrons as needed for quantum communication. We propose how to create such EPR pairs by means of Andreev tunneling at a superconductor-normal junction and discuss experimental setups in which spin entanglement and non-locality may be detected via transport measurements.

1 Introduction

The control of charge is well established for electronics, while the enormous application potential for spin in electronic devices were recognized only recently. [1] Electron spin effects allow for fundamental improvements of conventional devices, e.g. in magnetic read-out heads for computer hard drives based on the GMR effect, non-volatile memories, memories based on single spins, or in spin transistors. Further, electron spins in quantum-confined structures such as semiconductor quantum dots, atoms, or molecules can be used as a quantum bit (qubit) [2] for quantum computing [3,4] and, as EPR pairs in wires, [4] for quantum communication. [5] This concept of using the spin of the electron as a qubit, is supported by various experiments, demonstrating the injection of spin-polarized currents from a magnetic- to a non-magnetic semiconductor, [6,7] showing unusually long spin dephasing times T_2^* in semiconductors (approaching microseconds) as well as phase-coherent spin transport over distances of up to $100\,\mu$m [8], and long spin relaxation times T_1 exceeding microseconds. [9] Quantum dots have many tunable parameters like geometry, energy spectrum, coupling between dots etc., and thus allow for various techniques for controlling and manipulating the electronic states of the dots, in particular the spin state. The electronic dot-orbitals are further very sensitive to external magnetic and electric fields. [10] Small dots have charging energies in the meV range, resulting in quantization of charge on the dot (Coulomb blockade). This allows the precise control of the number of electrons, and of the spin ground state, on the dot. Controlling the number of electrons down to zero has been achieved in GaAs heterostructures. [11] Together with an ESR source, single electron spins in quantum dots are also accessible for coherent manipulations. We have shown that the stationary charge current passing through a quantum dot probes the dot spin (i.e. read-out of a single spin) and can be used to measure the intrinsic spin relaxation time T_1 as well as the spin decoherence time T_2 of a single spin on the dot. [12,13]

An array of coupled quantum dots, see Fig. 1, each dot containing a top most spin 1/2, was found to be a promising candidate for a scalable quantum computer [2] where the quantum bit (qubit) is defined by the spin 1/2 on the dot. Quantum algorithms can then be implemented using local single-spin rotations and the exchange coupling between nearby spins, see Fig. 1. This proposal is supported by experiments where, e.g., Coulomb blockade effects, [14] tunneling between neighboring dots, [10,14] and magnetization [15] have been observed as well as the formation of a delocalized single-particle state in coupled dots. [16] For a detailed review of quantum computing

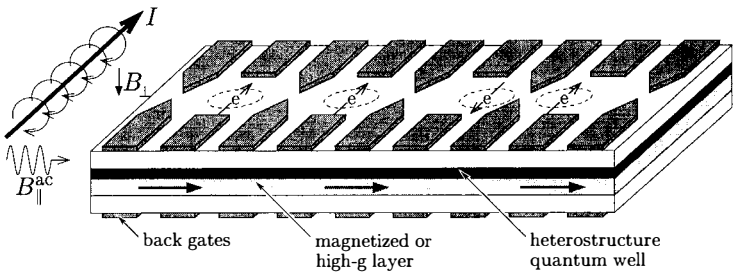


Figure 1: Quantum dot array, controlled by electrical gating. The electrodes (dark gray) define quantum dots (circles) by confining electrons. These electrons can be moved by electrical gating into the magnetized or high-g layer, producing locally different Zeeman splittings. Alternatively, magnetic field gradients can be applied, as e.g. produced by a current wire (indicated on the left of the dot-array). Then, since every dot-spin is subjected to a different Zeeman splitting, the spins can be addressed individually, e.g. through ESR pulses of an additional in-plane magnetic ac field with the corresponding Larmor frequency $\omega_L = g\mu_B B_\perp/\hbar$. Such mechanisms can be used for single-spin rotations and the initialization step. The exchange coupling between the quantum dots can be controlled by lowering the tunnel barrier between the dots. In this figure, the two rightmost dots are drawn schematically as tunnel-coupled.

with electron spins in quantum dots see Ref. [17].

The charge of the electron can further be used to transport a spin-qubit along conducting wires. [18] This allows one to use using spin-entangled electrons as Einstein-Podolsky-Rosen (EPR) [19] pairs, which can be created (e.g. in coupled quantum dots or near a superconductor-normal interface), transported, and detected. [18,20,21] Such EPR pairs represent the fundamental resources for quantum communication. [5]

2 General considerations for Quantum Computing with Electron Spins

The electron spin is a natural candidate for a qubit since its spin state in a given direction, $|\uparrow\rangle$ or $|\downarrow\rangle$, can be identified with the classical bits $|0\rangle$ and $|1\rangle$, while an arbitrary superposition $\alpha|\uparrow\rangle + \beta|\downarrow\rangle$ defines a qubit. In principle, any quantum two-level system can be used to define a qubit. However, one must be able to control coherent superpositions of the basis states of the quantum computer, i.e. no transition from quantum to classical behavior should occur. Thus, the coupling of the environment to the qubit should be small, resulting in a sufficiently large decoherence time T_2 (the time over which the phase of a superposition of $|0\rangle$ and $|1\rangle$ is well-defined). Assuming weak spin-orbit effects, the spin decoherence time T_2 can be completely different from the charge decoherence time (a few nanoseconds), and in fact it is known [8] that T_2 can be orders of magnitude longer than nanoseconds. Time-resolved optical measurements were used to determine T_2^*, the decoherence time of an ensemble of spins, with T_2^* exceeding 100 ns in bulk GaAs. [8] More recently, the single spin relaxation time T_1 (generally $T_1 \geq T_2$) of a single quantum dot attached to leads was measured via transport to be longer than a few μs, [9] consistent with calculations. [32] In Sec. 3.1 we propose a setup to extract the single spin decoherence time T_2 of an electron confined in a quantum dot from transport measurements.

For implementing realistic calculations on a quantum computer, a large number of qubits will be necessary (on the order of 10^5). For this it is essential that the underlying concept of implementation is consistent with a large number of qubits, which can be operated in parallel, which is required in known error correction schemes. Spin-based qubits in quantum dots statisfy this scaling requirement since arrays of quantum dots [4,33] (see Fig. 1) can be produced with state-of-the-art techniques of defining nanostructures in semiconductors.

As an input for quantum algorithms and for error correcting schemes, initialized qubits are

required, say in state $|\uparrow\rangle$. Single spins can be polarized by exposing them to a large magnetic field $g\mu_B B \gg kT$ and letting them relax to the ground state. Such a magnetic field could be applied locally or realized by forcing the electrons (via external gates) into a magnetized layer, into a layer with a different effective g factor [2,4] or with polarized nuclear spins (Overhauser effect) [34] etc., see also Fig. 1. Single-spin operations alone are not sufficient for quantum computing, one also needs two-qubit gates. Thus one has to allow for the spins to interact with each other. In coupled quantum dots, the exchange interaction is tunable by raising or lowering the tunnel barrier or by external parameters like magnetic or electric fields. [2,34,35,17] At the end of each computation (typically a sequence of classical bits) the spin state of each dot has to be measured. This can be done by e.g. using a spin-selective tunnel barrier and an additional (empty) dot where the charge of the electron is detected by an electrometer depending on the state of the qubit. [2] Alternatively, spin filtering and also spin-state measurements can be achieved by tunneling through a quantum dot [12] as we discuss in detail in Sec. 3.3 and Sec. 3.4.

3 Coherent Manipulation of Electron Spins

We consider a quantum dot attached to leads in the Coulomb blockade regime with spin $\frac{1}{2}$ ground state. We have shown that, by applying continuous or pulsed ESR fields to the dot spin, the single spin decoherence time T_2 (Sec. 3.1) and the Rabi oscillations (Sec. 3.5) of the spin can be observed via the current.[13] Further, a quantum dot can be operated as a spin filter (Sec. 3.3), or as a single spin read-out device (Sec. 3.4).[12]

The dot shall be coupled to two Fermi leads $l = 1, 2$ at chemical potentials μ_l. The coupling to the leads is described by a standard tunneling Hamiltonian H_T.[10] We consider small dots where the energy-level distance δ on the dot is large compared to bias $\Delta\mu = \mu_1 - \mu_2 > 0$ and temperature, $\delta > \Delta\mu,\ kT$. A Zeeman splitting $\Delta_z = g\mu_B B_z$ lifts the spin-degeneracy on the dot. An oscillating magnetic ESR field in x direction, $B_x^0 \cos(\omega t)$, produces Rabi spin flips at $\omega = \Delta_z$ on the dot. We assume different Zeeman splittings for the dot and the leads, $\Delta_z \not\approx \Delta_z^{\text{leads}}$ such that the effect of the ESR field on the leads is negligible. Different Zeeman splittings can be achieved by using materials with different g factors [6,7] and/or local magnetic fields. We have then derived and studied the master equation for the reduced density matrix ρ of the dot. Thereby, we have treated the tunneling Hamiltonian H_T pertubatively and evaluated the diagonal transition rates up to 2nd order "golden-rule" [12] and the off-diagonal rates up to 1st order.[13] The current contribution in first order of H_T is the sequential tunneling current I_s [10] where the electron number on the dot fluctuates. The second-order contribution is the cotunneling current I_c [37] where the number of electrons on the dot only changes in virtual intermediate states.

3.1 Detection of Single-Spin Decoherence

We have proposed a setup, see Fig. 2(a), where, by applying an ESR field to the dot-spin, the stationary current in the sequential tunneling regime exhibits a new resonance peak whose linewidth is determined by the single spin decoherence time T_2.[13] In this setup, the Zeeman splitting on the dot is large, $\Delta_z > \Delta\mu,\ kT$. Then, the energy levels can be tuned such that no sequential tunneling current flows through the dot when it is in its ground state $|\uparrow\rangle$, see Fig. 2(a). However, if an ESR field is present and produces Rabi-flips on the dot, current flows through the dot involving state $|\downarrow\rangle$. We have calculated the stationary current I through the dot by solving the master equation within the rotating wave approximation and find

$$I(\omega) \propto \frac{V_{\downarrow\uparrow}}{(\omega - \Delta_z)^2 + V_{\downarrow\uparrow}^2}. \tag{1}$$

Equation (1) shows that the current as a function of the ESR frequency ω has a resonant peak at $\omega = \Delta_z$ and width $2V_{\downarrow\uparrow}$, which is given by the total spin decoherence time on the dot,

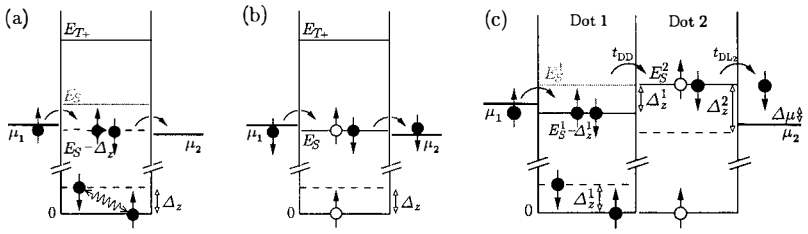


Figure 2: (a) By shifting the energy levels such that $E_S > \mu_1 > E_S - \Delta_z > \mu_2$, the setup can be used to measure the single spin decoherence time T_2, see Sec. 3.1. If initially the spin-state on the dot is $|\uparrow\rangle$, sequential tunneling is blocked by energy conservation. Exciting the dot-spin via ESR (Rabi flip, draws as wavy line) the dot becomes unblocked for spin up electrons from lead 1. Finally, from the singlet, spin up or down can tunnel into lead 2. (b) Implementation of a spin filter with a quantum dot coupled to unpolarized leads with chemical potentials $\mu_{1,2}$. The dot is in the sequential tunneling regime, $\mu_1 > E_S > \mu_2 > E_S - \Delta_z$, with the singlet/triplet levels E_S/E_{T_+} (counting from $E_\uparrow = 0$) and Zeeman splitting $\Delta_z = g\mu_B B_z$. (c) Combined setup, "spin inverter", where the spin state of dot 1 switches the current as in (b) and where dot 2 acts as a spin filter, in the regime $E_S^1 \approx E_S^2$; $E_S^1 > \mu_1 > E_S^1 - \Delta_z^1$; $E_S^2 > \mu_2 > E_S^1 - \Delta_z^2$; $|t_{DD}| < |t_{DL_2}|$; and $\Delta_z^1 \not\approx \Delta_z^2$. This allows the transition sequence $\uparrow(\uparrow)_1(\uparrow)_2 \xrightarrow{\text{ESR}} \uparrow(\downarrow)_1(\uparrow)_2 \to (\uparrow\downarrow)_1(\uparrow)_2 \to (\uparrow)_1(\uparrow\downarrow)_2 \to (\uparrow)_1(\uparrow)_2\downarrow$.

$V_{\downarrow\uparrow} = (W_{S\uparrow} + W_{S\downarrow})/2 + 1/T_2$, see Fig. 3. Here, $W_{S\sigma}$ denotes the rate for an electron to tunnel from a lead into the dot which was initially in state $|\sigma\rangle = |\uparrow\rangle, |\downarrow\rangle$. Thus, the line width of the current provides a lower bound on the intrinsic single-spin decoherence time T_2. [13] For weak tunneling $W_{S\sigma} < 2/T_2$, this bound saturates, i.e. the width of the peak becomes $2/T_2$.

Finally, we point out that if this setup is operated at zero bias $\Delta\mu = 0$, only electrons with spin $\uparrow$ can tunnel onto the dot and only with spin $\downarrow$ off the dot. Thus, the leads become locally spin-polarized. This concentration gradient in the leads acts as effective spin-dependent chemical potential, leading to a finite spin-current while there is no charge current. Such spin-currents can be detected e.g. via the (finite) noise of the charge current.[18]

3.2 Pumping

The setup described in the previous section can be used as an electron *pump* if one allows for spin-dependent tunneling rates $\gamma_l^\uparrow \neq \gamma_l^\downarrow$ for lead l. [13] The current at zero bias $\Delta\mu = 0$ is driven with an externally applied ESR source and is proportional to $\gamma_1^\uparrow\gamma_2^\downarrow - \gamma_1^\downarrow\gamma_2^\uparrow$. Spin-dependent tunneling rates are produced by spin-polarized leads, [12] by spin-dependent tunneling barriers or by the combined setup shown in Fig. 2(c). This setup uses an additional quantum dot as spin filter and acts as a "spin inverter" which takes spin up electrons as input and produces spin down electrons as output. [13]

3.3 Spin Filter

We consider a system where the Zeeman splitting in the leads is negligible while on the dot it is given as $\Delta_z = \mu_B |gB|$, see Fig. 2(b). For an odd number of electrons on the dot with total spin 1/2, the topmost electron is in the spin ground state $|\uparrow\rangle$. In the sequential tunneling regime only the spin singlet state can be occupied, thus only electrons with spin $\downarrow$ can tunnel onto and off the dot, thus I_s is spin-$\downarrow$ polarized, as shown in Fig. 2(b). However, the cotunneling contribution to the current I_c contains a spin-$\uparrow$ component which potentially reduces the efficiency of the spin-filtering effect. The degree of spin-polarization is [12]

$$I_s(\downarrow)/I_c(\uparrow) \sim \frac{\min\{\Delta_z^2, (E_{T_+} - E_S)^2\}}{\gamma \max\{kT, \Delta\mu\}}, \tag{2}$$

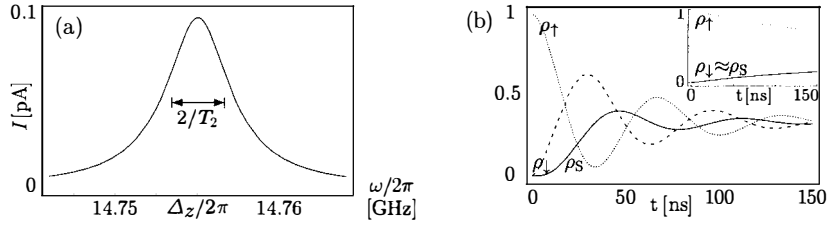


Figure 3: (a) The stationary current as a function of the ESR frequency ω for $B_z = 0.5\,\mathrm{T}$, $B_x^0 = 0.45\,\mathrm{G}$, $T_1 = 1\,\mu\mathrm{s}$, $T_2 = 100\,\mathrm{ns}$, $\gamma_1 = 5 \times 10^6\,\mathrm{s}^{-1}$, and $\gamma_2 = 5\gamma_1$. Here, the linewidth gives a lower bound for the intrinsic spin decoherence time T_2 (shown schematically by arrow, see Sec. 3.1), while it becomes equal to $2/T_2$ for $B_x^0 = 0.08\,\mathrm{G}$ and $\gamma_1 = 5 \times 10^5\,\mathrm{s}^{-1} \ll 2/T_2$, where $I(\omega = \Delta_z) \approx 1.5\,\mathrm{fA}$. (b) Rabi oscillations visible in the time evolution of the density matrix $\rho_\uparrow$ (dotted), $\rho_\downarrow$ (dashed) and ρ_S (full line) for spin polarized leads and $\gamma_l^\uparrow = 4 \times 10^7\,\mathrm{s}^{-1}$, $T_1 = 1\,\mu\mathrm{s}$, $T_2 = 300\,\mathrm{ns}$, $\Delta_x = 5W_{S\downarrow}$ $B_x^0 = 10\,\mathrm{G}$, and $g = 2$ with $\rho_\uparrow = 1$ at $t = 0$. The spin decoherence is here dominated by the measurement process, $W_{S\downarrow} = \gamma_1 \gg 1/T_2$; however, for weaker measurement, it will be determined by T_2. In the inset we show the case of a strong measurement, $\gamma_l^\uparrow = 10^9\,\mathrm{s}^{-1}$. Such a continuous strong measurement on the dot-spin suppresses the coherent oscillations, which is known as the Zeno effect.[38]

where we assume $\gamma_1 = \gamma_2 = \gamma$ for simplicity, with the tunneling rate γ_l between lead l and the dot. In the sequential tunneling regime we have $\gamma < kT, \Delta\mu$, thus, for $kT, \Delta\mu < \Delta_z, |E_{T_+} - E_S|$ the ratio Eq. (2) is large and the spin-filter is very efficient. Such a spin filter has a broad range of applications, since most spintronics devices require spin-polarized currents.[1]

3.4 Spin Read-out

We have shown that a quantum dot connected to fully spin polarized leads, $\Delta_z^{\mathrm{leads}} > \Delta_z$, can be used for reading the spin state of the quantum dot via the charge current[12]. Such a situation can be realized with magnetic semiconductors[6] or in the quantum Hall regime where spin-polarized edge states are coupled to a quantum dot[39]. If the spin polarization in both leads is $\uparrow$, and the dot is in state $|\downarrow\rangle$, electrons with spin $\uparrow$ can tunnel onto the dot, forming a singlet, and then tunnel into the other lead and thus $I_s \neq 0$. Since the leads can only absorb spin-up electrons, these are the only allowed sequential tunneling transitions, i.e. $\uparrow(\downarrow) \rightarrow (\uparrow\downarrow) \rightarrow (\downarrow)\uparrow$. However, if the dot is in state $|\uparrow\rangle$, no electron can tunnel onto the dot because the formation of the triplet is forbidden by energy conservation, i.e. $I_s = 0$. Again, there is a small cotunneling leakage current for the dot-state $|\uparrow\rangle$, with a ratio of the two currents given by Eq. (2), but where the numerator becomes $(E_{T_+} - E_S + \Delta_z)^2$, since here only the cotunneling process with an intermediate triplet state is possible. Therefore, the initial spin state of the quantum dot can be detected by measuring the current through the dot. Combining this with the initialization techniques from Sec. 2 and using ESR pulses for switching the spin state, a *spin read-in/read-out device* at the ultimate single-spin limit can be produced.[12] The lifetime of classical information stored in such a device is given by the spin relaxation time T_1, which would thus be directly measurable.

A detailled analysis of the read-out procedure allows to quantify the measurement efficiency. If the spin on the dot is $|\downarrow\rangle$, then the probability for no electron being transmitted after time t is $P_\downarrow(t) = \exp(-Wt)(1 + Wt)$, where $W = 2I/e$ is the rate of tunneling from one of the leads to the dot. For example, after time $2e/I$ the spin state can be determined with more than 90% probability.[13] For a typical sequential tunneling current on the order of $0.1 - 1\,\mathrm{nA}$,[10] this measuring time is $0.3 - 3\,\mathrm{ns}$, which is well below achievable spin relaxation times T_1.

3.5 Rabi Oscillations and ESR pulses

The ESR field produces coherent Rabi oscillations of the dot spin, see Fig. 3. These oscillations are described by the density matrix $\rho(t)$ and the master equation of the dot. Since the current in lead 2 is proportional to the population ρ_S of the state $|S\rangle$, measuring the time-dependent current allows to observe the density matrix and thus the Rabi oscillations of the dot spin. For $kT < \Delta\mu$ and spin-polarized leads, see Sec. 3.4, the current in lead 2 is $I_2(t) = e\gamma_2^{\uparrow}\rho_S(t)$. Note that the electrons tunneling onto the dot perform a projective (strong) measurement of the dot-spin, see Sec. 3.1. Thus, to observe Rabi oscillations in I_2 experimentally, the Rabi frequency must be larger than the coupling to the leads, otherwise the continuous measurement suppresses the Rabi oscillations [Zeno effect, see inset of Fig. 3(b)]. In order to have a sufficiently strong current signal, an ensemble average is required, e.g by using an array of independent dots arranged in parallel or by time series measurement over a single dot. From the coherent current oscillations due to the Rabi oscillations of the dot-spin, T_2 can be deduced in the time domain.[13]

An alternative method for measuring T_2 is pulsed ESR. An initial spin state, say, $|\downarrow\rangle$, is rotated with a $\pi/2$ pulse into the xy-plane and starts to precess with frequency Δ_z. After a delay τ, the remaining coherent part of the spin is rotated by another $\pi/2$ pulse and finally $\rho_\downarrow$ is measured via the current, e.g. by using the read-out technique explained in Sec. 3.4. Since the final spin direction, and thus $\rho_\downarrow$, depends on the precession angle, the measured current is an oscillating function of τ with frequency Δ_z, which decays on a timescale T_2.[13]

4 Creation and detection of mobile spin-entangled electrons

The spin singlet $|S\rangle = (|\uparrow\downarrow\rangle - |\downarrow\uparrow\rangle)/\sqrt{2}$ is a prominent example of a maximally entangled state. If the two spins are spatially separated the singlet acts as an Einstein-Podolsky-Rosen (EPR) pair. [19] The intrinsic correlation provided by the singlet allows two parties ("Alice and Bob") e.g. to communicate in an absolute secure way (which is not possible using classical communication only). This observation led to several quantum communication tasks such as dense coding, quantum cryptography or quantum teleportation. [5] Study of entanglement per se is interesting since it is responsible for fundamental predictions of quantum mechanics such as violation of Bell's inequality or genuine two-particle interference effects. [21] The non-locality of EPR pairs has been tested experimentally for photons but not yet for *massive* particles like electrons let alone in a solid state environment. Here we propose a setup that creates *mobile* non-local spin entanglement by making use of Andreev tunneling at a biased superconductor-normal junction. [20] We show that the Aharonov-Bohm oscillations produced by the interference of the entangled electrons consist of h/e- and $h/2e$-periods which could be used to test the non-locality of the EPR pair. In turn we discuss an experimental detection scheme for spin-entangled electrons in mesoscopic nanostructures based on current-noise measurement. [18]

4.1 Andreev Entangler

In s-wave superconductors (SC), the electrons form Cooper pairs with singlet spin-wavefunctions.[40] These Cooper pairs serve as a natural source of spin-entangled electrons as pointed out in Ref.[41]. Here we propose a biased device setup where a SC is weakly coupled to two separate quantum dots which are coupled in addition to normal outgoing Fermi-liquid leads, see Fig. 4 [20]. Single-electron tunneling from a SC to a normal region is suppressed in the sub-gap regime $0 < \Delta\mu = \mu_S - \mu_l, kT < \Delta$ where Δ is the SC energy gap. [42] Thus, only coherent transport of two electrons of opposite spin is allowed (Andreev tunneling). The two intermediate quantum dots in the Coulomb blockade regime [10] force the two electrons to tunnel into *separate* leads, since tunneling of two electrons via the same dot into the same lead is suppressed by the on-site Coulomb repulsion U of the dots.

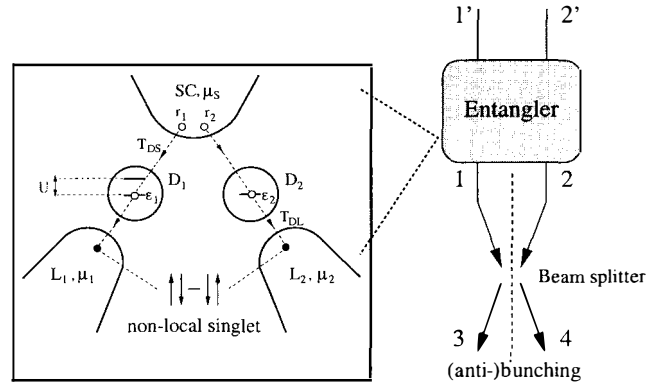


Figure 4: In the box on the left the Andreev Entangler is sketched. The two electrons of a Cooper pair tunnel with amplitude T_{DS} from two points $\mathbf{r}_1$,$\mathbf{r}_2$ of the superconductor, SC, to two dots $D_{1,2}$ by means of Andreev tunneling. The dots are coupled to normal leads $L_{1,2}$ with tunneling amplitude T_{DL}. The chemical potentials of the SC and leads are μ_S and $\mu_1 = \mu_2$, resp. For efficient operation, $|T_{DL}| > |T_{DS}|$ and large Coulomb repulsion U is required. On the right the experimental setup for measuring noise of entangled electrons (see Sec. 4.2) is drawn. The entangler takes uncorrelated electrons from the Fermi leads $1'$ and $2'$. Pairs of entangled electrons (singlet or triplet) are produced in the entangler (e.g. singlets in the Andreev Entangler) and then injected into the leads 1 and 2, one electron per lead. The currents of these two leads are mixed with a beam splitter (to induce scattering interference). Then, the noise is measured in leads 3 and 4: no noise for triplets (antibunching), whereas we get enhanced noise for singlets (bunching).

The current for tunneling of two electrons via different dots into different leads shows a two-particle Breit-Wigner resonance peaked at $\epsilon_1 + \epsilon_2 = 0$, with ϵ_n the chemical potential of dot $n = 1, 2$ counted from the chemical potential μ_S of the SC. In particular, if $\epsilon_n = 0$, the two electrons are injected into the leads at the *same* orbital energy. This turns out to be crucial for the detection of entanglement via noise measurements proposed in Sec. 4.2. The spin-singlet is maintained during the tunneling processes if the dots contain an even number of electrons each with a total spin zero in the ground state and in addition the regime $\Delta, U, \delta\epsilon > \Delta\mu > \gamma_l, kT$, and $\gamma_l > \gamma_S$ is realized. [20] Here, $\delta\epsilon$ denotes the energy level spacing of the dots and $\gamma_{S(l)} = 2\pi\nu_{S(l)}|T_{DS(l)}|^2$ is the tunneling rate to the dots from the SC and the leads, respectively, with $\nu_{S(l)}$ being the normal DOS per spin at the chemical potentials $\mu_{S(l)}$. Quantum dots made out of semiconducting heterostructures satisfy the stated regime of interest. [10] Further, Andreev tunneling through a SC/semiconductor junction was achieved experimentally. [43,44] Other promising materials are carbon nanotubes which also show Coulomb blockade behavior with U and $\delta\epsilon$ in the regime of our interest. [45]

We have calculated the stationary charge current using a T-matrix approach and find for the ratio of the current for injecting two entangled electrons into *different* leads (current I_1) with the current for injecting the two electrons into the *same* lead (current I_2) [20]

$$\frac{I_1}{I_2} = \frac{2\mathcal{E}^2}{\gamma^2}\left[\frac{\sin(k_F\delta r)}{k_F\delta r}\right]^2 e^{-2\delta r/\pi\xi}, \qquad \frac{1}{\mathcal{E}} = \frac{1}{\pi\Delta} + \frac{1}{U}, \tag{3}$$

where $\gamma = \gamma_1 + \gamma_2$ and k_F is the Fermi wavevector in the SC. The current I_1 becomes exponentially suppressed with increasing distance $\delta r = |\mathbf{r}_1 - \mathbf{r}_2|$ between the tunneling points on the SC, the scale given by the superconducting coherence length ξ. In the important case $\delta r \lesssim \xi$ the suppression is only polynomial $\propto 1/(k_F\delta r)^2$. On the other hand, we see that the effect of the dots appears in the suppression factor $(\gamma/\mathcal{E})^2$ for tunneling into the same lead. Thus, the entangler is efficient if $k_F\delta r < \mathcal{E}/\gamma \sim 10 - 100$, typically. Note that the Andreev Entangler produces two electrons in a singlet state which are separated in orbital space, i.e. it creates

mobile EPR pairs.

The non-locality of the desired singlet-state could be tested in an Aharonov-Bohm type of experiment. We consider a setup where the two leads 1 and 2 are connected such that they form an Aharonov-Bohm loop, where the electrons are injected from above via the superconductor, traversing the left (lead 1) and/or right (lead 2) arm of the loop before they rejoin to interfere and then exit into the same lead, where the current is then measured as a function of varying flux ϕ through the loop. For simplicity we assume that the entire phase is acquired when the electron hops from the dot into the leads, so that the process dot-lead-dot gives basically the full Aharonov-Bohm phase factor $e^{\pm i\phi/\phi_0}$ of the loop. The total current in this setup is $I = I_1 + I_2 + I_{AB}$ with the flux-dependent contribution [20]

$$I_{AB} = \sqrt{8I_1I_2}F(\epsilon_l)\cos(\phi/\phi_0) + I_2\cos(2\phi/\phi_0). \tag{4}$$

For simplicity, we used $\epsilon_1 = \epsilon_2 = \epsilon_l$, and $\gamma_1 = \gamma_2 = \gamma_L$. Here, the first term is periodic in ϕ_0 like for single-electron Aharonov-Bohm interference effects and results from the interference between a contribution where the two electrons travel through different arms with contributions where the two electrons travel through the same arm. The second one is periodic in *half* the flux quantum $\phi_0/2$, describing thus the interference of two coherent electrons traveling through the same arm. The factor $F(\epsilon_l) = \epsilon_l/\sqrt{\epsilon_l^2 + (\gamma_L/2)^2}$ in (4) counts for the fact that I_1 shows a two-particle resonance where I_2 has only a single-particle resonance due to the Coulomb blockade effect. Both Aharonov-Bohm oscillations with periods h/e, and $h/2e$, vanish with decreasing I_2, i.e. with increasing on-site repulsion U and/or gap Δ. However, their relative weight is given by $\sqrt{I_1/I_2}$, for $|\epsilon_l| \sim \gamma_L$, implying that the $h/2e$ oscillations vanish faster than the h/e ones if the separation of the two electrons is efficient ($I_1 > I_2$).

4.2 Noise of Entangled Electrons

Here we address the question of how one can detect entangled electrons that are injected into current leads using noise measurements. Suppose an entangler generates pairs of entangled electrons which are then injected into leads 1 and 2, one electron each, as shown in Fig. 4. An actual realization of such an entangler was presented in Sec. 4.1. Another possibility would be to use coupled quantum dots where the ground state of a two-electron system (one (excess) electron in each dot) is entangled. [34] By changing the gate voltages applied to the dots the electrons can then escape to separate leads. Before the electrons are measured they have to pass a beam splitter that induces two-particle interference effects in the sense that there is an equal probability amplitude for incoming electrons (from lead 1 or 2) to leave into lead 3 or 4. The quantity of interest is then the noise, i.e. the current-current correlations, measured in leads 3 and/or 4. Since the entanglement of an injected entangled electron pair gets only partially reduced by the Coulomb interaction with the Fermi sea, [18] we can use standard scattering theory for non interacting quasiparticles in a Fermi liquid. [46] The injected EPR pair can either be a triplet (+) or a singlet (−) with wavefunction $|\pm\rangle = 1/(\sqrt{2})(a^\dagger_{\mathbf{1}\uparrow}a^\dagger_{\mathbf{2}\downarrow} \pm a^\dagger_{\mathbf{1}\downarrow}a^\dagger_{\mathbf{2}\uparrow})|\psi_0\rangle$ where $\mathbf{n} = (\epsilon_n, n)$, ϵ_n being the energy of the electron injected into lead n, and $|\psi_0\rangle$ is the filled Fermi sea. We assume that the leads consist of one quantum channel and have DOS ν. For the spectral densities at zero frequency, $S_{\alpha\beta} = \lim_{T\to\infty}\frac{h\nu}{T}\int_0^T \mathrm{dtRe}\langle\pm|\delta I_\alpha(t)\delta I_\beta(0)|\pm\rangle$, of the current fluctuations $\delta I_\alpha = I_\alpha - \langle I_\alpha\rangle$ between the leads α and β we find in the absence of backscattering [18]

$$S_{33} = S_{44} = -S_{34} = 2\frac{e^2}{h\nu}T(1-T)(1 \mp \delta_{\varepsilon_1\varepsilon_2}). \tag{5}$$

Here, the minus (plus) sign refers to the spin triplet (singlet) and T is the transmission coefficient of the beam splitter. If two electrons with the same energies, $\varepsilon_1 = \varepsilon_2$, in the singlet state are injected into the leads 1 and 2, the shot noise is enhanced by a factor of two compared to

$2e^2T(1-T)/h\nu$, the value for uncorrelated particles. [46,47] This *bunching* of the electrons is due to their symmetric orbital wavefunction, such that the electrons preferably appear in the same outgoing leads. For the triplet, an *antibunching* effect appears, completely suppressing the noise, i.e. $S(\omega=0)=0$. Since bunching appears only for a state with a symmetric orbital wave function, which cannot occur for unentangled states, measuring noise enhancement in the outgoing arms of the beamsplitter provides therefore a *unique* evidence for entanglement.

5 Conclusions

We briefly reviewed some general considerations for quantum computing using electron spins in quantum dots. Further, we have studied quantum dots in the Coulomb blockade regime and attached to leads. By breaking the spin degeneracy by a magnetic field, a broad range of devices such as spin-filter, single spin read-out, and spin inverter becomes feasible. Using ESR, the Rabi oscillations of the dot-spin are observable via time dependent charge currents. In addition, the stationary charge current as a function of the ESR frequency shows a resonance and a linewidth which gives a lower bound for the T_2 time. As a resource for quantum communication, mobile EPR pairs can be produced by means of Andreev tunneling from a superconductor via quantum dots to outgoing leads. In turn, the entanglement and the non-locality character of the EPR pair can be tested in transport measurements via the noise and the Aharonov-Bohm oscillations.

1. G.A. Prinz, *Phys. Today* **45**(4), 58 (1995); *Science* **282**, 1660 (1998).
2. D. Loss and D.P. DiVincenzo, *Phys. Rev.* A **57**, 120 (1998); cond-mat/9701055.
3. A. Steane, *Rep. Prog. Phys.* **61**, 117 (1998).
4. D.P. DiVincenzo and D. Loss, *J. Magn. Magn. Mater.* **200**, 202 (1999); cond-mat/9901137.
5. C. H. Bennett and D. P. DiVincenzo, *Nature* **404**, 247 (2000).
6. R. Fiederling *et al.*, *Nature* **402**, 787 (1999).
7. Y. Ohno *et al.*, *Nature* **402**, 790 (1999).
8. J.M. Kikkawa, I.P. Smorchkova, N. Samarth, and D.D. Awschalom, *Science* **277**, 1284 (1997); J.M. Kikkawa and D.D. Awschalom, *Phys. Rev. Lett.* **80**, 4313 (1998); D.D. Awschalom and J.M. Kikkawa, *Phys. Today* **52**(6), 33 (1999).
9. T. Fujisawa, Y. Tokura, Y. Hirayama, *Phys. Rev.* B **63** 081304 (2001)
10. L.P. Kouwenhoven, G. Schön, and L. L. Sohn, *Mesoscopic Electron Transport*, NATO ASI Series E, Vol. 345, (Kluwer Academic Publishers, Dordrecht, 1997).
11. S. Tarucha *et al.*, *Phys. Rev. Lett.* **77**, 3613 (1996).
12. P. Recher, E.V. Sukhorukov, and D. Loss, *Phys. Rev. Lett.* **85**, 1962 (2000).
13. H.-A. Engel and D. Loss, Phys. Rev. Lett. **86**, 4648 (2001) and cond-mat/0011193.
14. F.R. Waugh *et al.*, *Phys. Rev. Lett.* **75**, 705 (1995);
    C. Livermore *et al.*, *Science* **274**, 1332 (1996).
15. T.H. Oosterkamp *et al.*, *Phys. Rev. Lett.* **80**, 4951 (1998).
16. R.H. Blick *et al.*, *Phys. Rev. Lett.* **80**, 4032 (1998); *ibid.* **81**, 689 (1998).
    T.H. Oosterkamp *et al.*, *Nature* **395**, 873 (1998);
    I.J. Maasilta and V.J. Goldman, *Phys. Rev. Lett.* **84**, 1776 (2000).
17. G. Burkard, H.-A. Engel, D. Loss, *Fortschr. Phys.* **48**, 965 (2000).
18. G. Burkard, D. Loss, and E.V. Sukhorukov, *Phys. Rev.* B **61**, R16303 (2000).
19. A. Einstein, B. Podolsky, N. Rosen, *Phys. Rev.* **47**, 777 (1935).
20. P. Recher, E.V. Sukhorukov, and D. Loss, *Phys. Rev.* B **63**, 165314 (2001).
21. D. Loss and E.V. Sukhorukov, *Phys. Rev. Lett.* **84**, 1035 (2000).
22. P.W. Shor, in *Proc. 35th Symposium on the Foundations of Computer Science*, ed. S. Goldwasser (IEEE Computer Society Press), 124 (1994).

23. L.K. Grover, *Phys. Rev. Lett.* **79**, 325 (1997).
24. J.I. Cirac and P. Zoller, *Phys. Rev. Lett.* **74**, 4091 (1995); C. Monroe *et al.*, *ibid.* **75**, 4714 (1995).
25. Q.A. Turchette *et al.*, *Phys. Rev. Lett.* **75**, 4710 (1995).
26. D. Cory, A. Fahmy, and T. Havel, *Proc. Nat. Acad. Sci. U.S.A.* **94**, 1634 (1997); N.A. Gershenfeld and I.L. Chuang, *Science* **275**, 350 (1997).
27. B. Kane, *Nature* **393**, 133 (1998).
28. A. Shnirman, G. Schön, and Z. Hermon, *Phys. Rev. Lett.* **79**, 2371 (1997).
29. D.V. Averin, *Solid State Commun.* **105**, 659 (1998).
30. L.B. Ioffe *et al.*, *Nature* **398**, 679 (1999).
31. T.P. Orlando *et al.*, *Phys. Rev.* B **60**, 15398 (1999).
32. A.V. Khaetskii and Y.V. Nazarov, *Phys. Rev.* B **61**, 12639 (2000); cond-mat/0003513.
33. D.P. DiVincenzo, G. Burkard, D. Loss, and E. Sukhorukov, in *Quantum Mesoscopic Phenomena and Mesoscopic Devices in Microelectronics*, eds. I.O. Kulik and R. Ellialtoglu (NATO ASI), p. 399 (2000); see cond-mat/99112445.
34. G. Burkard, D. Loss, and D. P. DiVincenzo, *Phys. Rev.* B **59**, 2070 (1999).
35. G. Burkard, G. Seelig, and D. Loss, *Phys. Rev.* B **62**, 2581 (2000).
36. M. Devoret, D. Estève, and Ch. Urbina, Nature (London) **360**, 547 (1992).
37. D.V. Averin and Yu.V. Nazarov, in *Single Charge Tunneling*, eds. H. Grabert, M.H. Devoret, NATO ASI Series B, Vol. 294, Plenum Press, New York, 1992.
38. A. Peres, *Quantum Theory* (Kluwer, Amsterdam, 1993).
39. M. Ciorga *et al.*, *Phys. Rev.* B **61**, R16315 (2000).
40. J.R. Schrieffer *Theory of Superconductivity* (Benjamin/Cummings, NY, 1964)
41. M.-S. Choi, C. Bruder, and D. Loss, *Phys. Rev.* B **62**, 13569 (2000).
42. F.W.J. Hekking, L.I. Glazman, K.A. Matveev, and R.I. Shekhter, *Phys. Rev. Lett.* **70**, 4138 (1993).
43. H. Takayanagi *et al.*, *Phys. Rev. Lett.* **75**, 3533 (1995).
44. S. De Franceschi, F. Giazotto, F. Beltram, L. Sorba, M. Lazzarino, and A. Franciosi, *Appl. Phys. Lett.* **73**, 3890 (1998).
45. L.C. Venema, J.V.G. Wildöer, J.W. Janssen, S.J. Tans, H.L.J. Temminck Tuinstra, L.P. Kouwenhoven, and C. Dekker, *Science* **283**, 52 (1999).
46. M. Büttiker, *Phys. Rev. Lett.* **65**, 2901 (1990); *Phys. Rev.* B **46**, 12485 (1992).
47. V.A. Khlus, *Zh. Eksp. Teor. Fiz.* **93**, 2179 (1987).

CORRELATED TRANSPORT AT MULTIPLE SUPERCONDUCTOR-FERROMAGNET INTERFACES

DENIS FEINBERG[1], GUY DEUTSCHER[2], GIUSEPPE FALCI[3], FRANK HEKKING[4]
[1]*LEPES, CNRS, BP 166, 38042 Grenoble, FRANCE*

[2]*Department of Physics, University of Tel Aviv, Tel Aviv, ISRAEL*

[3]*DMFCI, University of Catania, and INFM, ITALY*

[4]*LPMMC, CNRS and University J. Fourier, Grenoble, FRANCE*

We consider hybrid structures made of two superconducting-normal (or ferromagnetic) contacts. At short distances, reflexion processes across the superconductor, from one contact to the other, can lead to new physical effects. Normal reflexion involves cotunneling, which is spin-conserving, while Andreev reflexions converting an electron into a hole reverse the spin. Here we investigate the transport properties of the structure and emphasize its sensitivity to spin polarizations. An application is given in terms of a principle for a spin-STM.

Superconductor-ferromagnet (S/F) contacts are currently the focus of lively interest. One basic reason is that, most superconductors possessing a singlet ($S = 0$) order parameter, the physics at a S/F interface is expected to be very rich. Besides the work done in the past on tunnel junctions, recently the possibility of Andreev reflexions[1] at transparent contacts has been considered[2]. Such a process converts a, say, electron into a hole with opposite spin. As a result, it is strongly hindered in a ferromagnet, owing to the exchange energy, usually much larger than the superconducting gap below which Andreev reflexion occurs. This reduction has been measured [3] and used as a way to measure the spin polarization thanks to a superconducting point contact [4]. On the other hand, it has been proposed [5,6] that such processes may also occur, although weaker, *between* neighbouring interfaces. Then, Andreev reflexion might be restored if the two ferromagnets facing the same region (of size ξ, the superconducting coherence length) have opposite spin polarizations (SP). Moreover, the transport properties in such a multi-terminal hybrid structure also involves cotunneling between the two electrodes, which, contrarily to Andreev reflexion, conserves the spin.

Let us denote by A and B the two ferromagnetic electrodes, biased at voltages V_A and V_B with respect to the superconductor. We shall assume $V_A, V_B << \Delta$ in what follows. The electron transfer processes occuring at the interfaces, at energies below the superconducting gap Δ, are of three kinds (Figure 1). First, one has the Andreev reflexions at each interface, which result into currents $I_A = G_{2A}V_A$ and $I_B = G_{2B}V_B$. Second, "crossed" Andreev reflexions connect A and B, with (equal) currents $I_A = I_B = G_{CA}(V_A + V_B)$. Finally, cotunneling processes result in opposite currents $I_A = -I_B = G_{EC}(V_B - V_A)$ (Figure 2). Combining these currents, one obtains in matrix form

$$\begin{pmatrix} I_A \\ I_B \end{pmatrix} = \begin{pmatrix} G_{2A} + G_{CA} + G_{EC} & G_{CA} - G_{EC} \\ G_{CA} - G_{EC} & G_{2B} + G_{CA} + G_{EC} \end{pmatrix} \begin{pmatrix} V_A \\ V_B \end{pmatrix} \quad (1)$$

Notice that all Andreev processes involve a (non spin polarized) pair current flowing in the superconductor. On the other hand, cotunneling implies no current into S but a current from one contact to the other. The conductances can be obtained in a tunneling model for each interface. In lowest order in perturbations, each process involves coherent tunneling of two quasiparticles, through virtual excitation of quasiparticle states (QP) in the superconductor. In particular, the amplitudes for crossed Andreev processes are proportionnal to spectral functions involving creation of a, say, spin-up electron-like QP in S, in the vicinity of contact A, and destruction of a

spin-down hole-like QP in S, in the vicinity of B. They are thus related to the anomalous Green's function, which decays on ξ. On the other hand, the amplitudes for cotunneling processes involve creation of a, say, spin-up electron-like QP in S, in the vicinity of contact A, and destruction of a spin-up electron-like QP in S, in the vicinity of B. They are thus related to the normal Green's function, which also decays on ξ. Notice that both processes are phase coherent, involving a phase change which depends only on the energy, the superconducting phase and the distance between contacts. Using Fermi's golden rule, and assuming nor impurity neither spin scattering in S, following [7] for a single interface, one obtains the "crossed" conductances

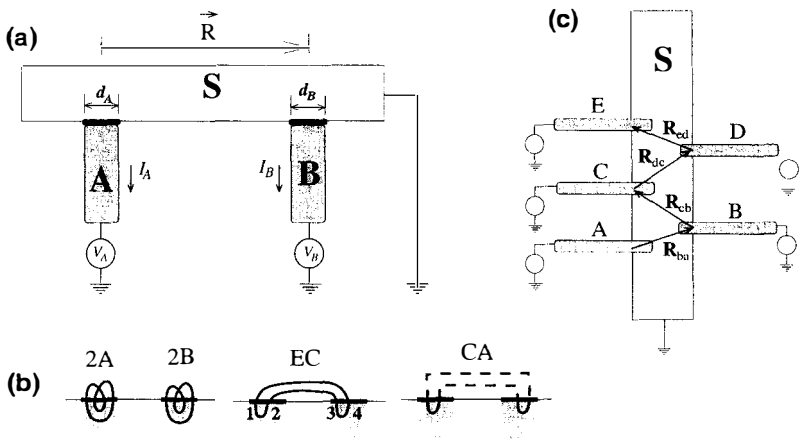


Figure 1: (a) Schematics of the three-terminal A/S/B device; (b) diagrammatic representation of the processes leading to subgap conductance: single-contact two-particle tunneling ($2A$ and $2B$), elastic cotunneling (EC). which probes the normal Green's function (full lines) of S and "crossed Andreev" (CA), which probes the anomalous propagator (dashed line); (c) a simple experimental design for measuring the excess EC and CA currents: various electrodes (A,B,C,D,E) allow to probe different distances $\vec{R}_{ij}$.

$$G^{\sigma}_{EC} \approx \frac{\pi^2 h}{16e^2}\, \mathcal{G}^{\sigma}_{A}\, \mathcal{G}^{\sigma}_{B}\, F_{EC}(A,B) \tag{2}$$

$$G^{\sigma}_{CA} \approx \frac{\pi^2 h}{16e^2}\, \mathcal{G}^{\sigma}_{A}\, \mathcal{G}^{-\sigma}_{B}\, F_{CA}(A,B) \tag{3}$$

where $\mathcal{G}^{\sigma}_{A}, \mathcal{G}^{\sigma}_{B}$ are the single electron conductances of each contact for a given spin σ. The factors $F_{EC}(A,B)$, $F_{CA}(A,B)$ are geometrical functions of : the contact sizes (or number of channels), the geometry, and the Fermi wavevector mismatch at the interfaces. The spin correlation involved by each of these processes is apparent on Eqs. (2,3). Let us consider a few particular cases. First, for ideal point contacts separated by a distance R, one has $F_{EC}(A,B) \sim \frac{e^{-2R/\pi\xi}}{(k_S R)^2} cos^2(k_S R)$, $F_{CA}(A,B) \sim \frac{e^{-2R/\pi\xi}}{(k_S R)^2} sin^2(k_S R)$ where k_S is the Fermi number in S. An exponential decay appears on the length ξ which can be as large as a fraction of μm, a scale below which metallic contacts can be made with lithographic techniques. Nevertheless, the algebraic interference factor is detrimental to the observation of a crossed conductance [8], at least in the geometry of two small contacts. Notice that the EC and CA geometrical factors differ only by the Fermi oscillations. On the other hand, if each contact carries many channels, one can show [6] that interferences of Fermi oscillations make $F_{EC}(A,B) = F_{CA}(A,B)$. In this case, the conductances G_{EC} and G_{CA} differ only through the possible spin dependence of the single electron conductances. This important result is robust in that it is not restricted to the range of validity of

perturbation theory. A recent investigation of the tunneling model by the Keldysh technique shows that it holds for any energy and contact transparency, provided that at least one contact is wide compared to the Fermi length k_F^{-1} [9].

A glance to Eq. (1) shows that this property has an important consequence : unless both electrodes A and B are spin polarized, then the two (CA and EC) channels compensate in the crossed conductance dI_A/dV_B. This is due to the fact that for each spin orientation, electron-electron and electron-hole reflexions are equally probable so that no current is induced in one electrode by biasing the other. On the opposite, if both electrodes are spin polarized, one finds that the crossed conductance is (under simplifying assumptions concerning the Fermi vector mismatch at the interfaces) proportionnal to the product $-P_A P_B$ of the spin polarizations of A and B (notice the minus sign). For instance (Figure 2), if A and B are maximally polarized, no Andreev process is possible inside any contact. However,

i) If A and B have parallel SP's, cotunnelling occurs, with spin polarized current flowing from A to B (B to A).

ii) If A and B have antiparallel SP's, the only process is Andreev-like between the contacts, with Cooper pairs entering or exiting the superconductor, each electron of the pair coming from a *different* electrode.

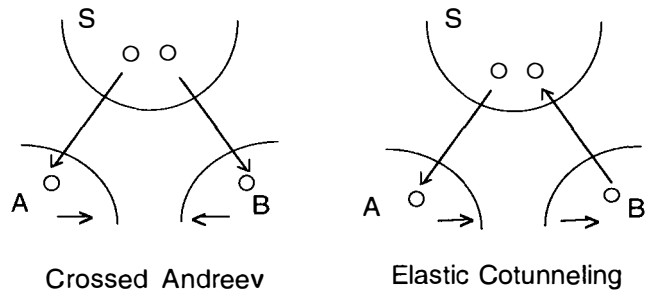


Figure 2: Sketch of the two basic crossed processes : elastic cotunneling (spin-conserving) and crossed Andreev, with decay of a Cooper pair in A and B (opposite spins).

In the general case, both processes combine and join to the Andreev reflexion occurring at each contact. It is interesting to notice that if only one of the electrode only, say A, is spin-polarized, the total current flowing through B is zero. It is made of contributions from crossed Andreev and cotunneling currents which are equal but carry different spins. As a result, a *spin current* (but no charge current) flows through B.

Let us show how such properties can be used to measure the spin polarization of a magnetic material, say A. The idea is to use the sensitivity of the above crossed conductance (in amplitude *and* sign) to the relative SP of A and a reference material B. The simplest configuration is to set $V_B = 0$ and $V_A = V$, such as

$$\begin{aligned} I_A &= (G_{2A} + G_{CA} + G_{EC})V \\ I_B &= (G_{CA} - G_{EC})V \end{aligned} \tag{4}$$

If in addition contact A involves a tunnel barrier, G_{2A} can be neglected, and one is left with two currents induced by the voltage V : one "direct" current I_A, insensitive to the spin

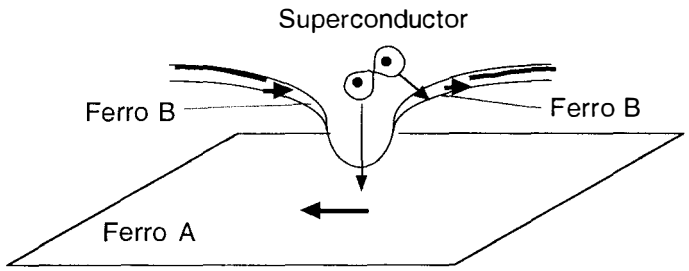


Figure 3: Enlarged view of the tip end, where one of the crossed process (CA) is represented.

polarizations (as can be checked from equations (2,3)), and a "crossed" or induced current I_B, which directly reflects the relative SP's of A and B. This principle could be implemented in a STM geometry [10] (Figure 3) : a superconducting tip is coated by a magnetic layer B, apart from its extreme end through which electrons tunnel into a magnetic surface A. The whole tip (S plus ferromagnet B) is biased at the voltage V with respect to A. The direct current flowing through the tip is not sensitive to the orientation of SP at the surface A and allows topographic imaging. On the other hand, the induced current flowing between S and B changes sign as the spin polarization at surface A below the tip changes with respect to that of B. Therefore it allows domain imaging, with a resolution limited only by the tunneling current (atomic scale) rather by the coherence length ξ. A detailed study shows that a number of conditions are required to observe this effect [10]. First, the "free" superconducting tip end should be smaller than ξ. Second, the magnetization of B should be robust, still not perturbing the magnetic sample [11]. Third, to avoid spurious noise across the interface S/B, the latter should be transparent only close to the tip end and tunnel elsewhere. It is interesting to notice that the configuration of the two contacts S/A and S/B is here concentric : radial symmetry ensures that quasiparticle propagation through S between the two contacts occurs in any direction, thus strongly enhancing the sensitivity with respect to two small contacts situated at a distance R. For instance, taking the tunnel conductance $G_A \sim 10^{-7}$S, $V \sim 10^{-4}$V and a good interface S/B, the expected currents are in the picoAmpere range.

In conclusion, we have shown how correlated transport can occur through a superconducting region of size smaller than ξ. It can be considered as a new active circuit element, with new functionalities (spin polarization measurement) at the level of principles. Further work is concerned with the proximity effect in the superconductor, which is expected to weaken (but cannot suppress) the above phenomena, and to diffusive systems.

References

1. G. E. Blonder, M. Tinkham and T. M. Klapwijk, Phys. Rev. **B25**, 4515 (1982)
2. M. J. M. de Jong and C. W. J. Beenakker, Phys. Rev. Lett. **74**, 1657 (1995).
3. S. K. Upadhyay, A. Palanisami, R. N. Louie and R. A. Buhrman, Phys. Rev. Lett. **81**, 3247 (1998).
4. R. J. Soulen Jr, J. M. Byers, M. S. Osofsky, B. Nadgorny, T. Ambrose, S. F. Cheng, P. R. Broussard, C. T. Tanaka, J. Nowak, J. S. Moodera, A. Barry and J. M. D. Coey, Science **282**, 85 (1998).
5. G. Deutscher and D. Feinberg, Appl. Phys. Lett. **76**, 487 (2000).
6. G. Falci, D. Feinberg and F. W. J. Hekking, Europhys. Lett., **54**, 255 (2001).

7. F.W.J. Hekking and Yu.V. Nazarov, Phys. Rev. **B49**, 6847 (1994).
8. M. S. Choi, C. Bruder and D. Loss, Phys. Rev. B**62**, 13569 (2000).
9. R. Mélin and D. Feinberg, preprint Cond-Mat/0106329.
10. D. Feinberg and G. Deutscher, preprint.
11. Yet, here the distance between A and B is increased (several tenths of nm) compared to the usual magnetic STM configuration (a few Angstroems) thus stray field effects should be much weaker, at least for parallel magnetizations.

GENERATING ENTANGLED ELECTRON PAIRS FROM A SUPERCONDUCTOR

G. LESOVIK[1], T. MARTIN[2], G. BLATTER[3]

[1] *L.D. Landau Institute for Theoretical Physics, Russian Academy of Sciences, Kosygina Str. 2, 117940, Moscow*

[2] *Centre de Physique Théorique et Université de la Méditerranée, Case 907, 13288 Marseille, France*

[3] *Theoretische Physik, ETH-Hönggerberg, CH-8093 Zürich, Switzerland*

A weakly biased normal-metal–superconductor junction is considered as a potential device injecting entangled pairs of quasi-particles into a normal-metal lead. The two-particle states arise from Cooper pairs decaying into the normal lead and are characterized by entangled spin- and orbital degrees of freedom. The separation of the entangled quasi-particles is achieved with a fork geometry and normal leads containing spin- or energy-selective filters. Measuring the current–current cross-correlator between the two normal leads allows to probe the efficiency of the entanglement.

1 Introduction

Einstein, Podolsky and Rosen[1] showed several decades ago that quantum mechanics is a non local theory, were the degrees of freedom of dissociated pairs of particles, originating from the same physical process, are correlated. Recently, potential applications of this EPR entanglement have been found in quantum cryptography[2], in quantum teleportation[3], and in quantum computing[4]. It is thus necessary to search for practical ways to produce such pairs given a specific interaction between particles. While past experiments have focused on pairs of photons[5] propagating in vacuum, attention is now turning to electronic systems[6], where this entanglement interaction can be stronger while coherence can still be maintained over appreciable distances in mesoscopic conductors. A scheme was recently presented[7] which discussed the entanglement of electrons via the exchange interaction in pairs of quantum dots. Here, we propose a rather robust electronic entanglement scheme based on the Andreev reflection of electrons and holes at the boundary between a normal metal and a superconductor.

The basic concept underlying the microscopic description of superconductivity is the formation of Cooper pairs. A normal metal in vicinity to a superconductor bears the trace of this phenomenon through the presence of Bogoliubov quasi-particles, or through the non-vanishing of the Gor'kov Green function[8] $F = \langle c_{\mathbf{k}\uparrow} c_{-\mathbf{k}\downarrow} \rangle$ ($c_{\mathbf{k}\sigma}$ denote the usual electron annihilation operators). While in a superconductor $F = \Delta/\lambda$ is a consequence of a nonzero gap parameter Δ (λ is the pairing potential), the coherence surviving in the adjacent normal metal can be understood through the presence of evanescent Cooper pairs. These involve two electrons with entangled spin- and orbital degrees of freedom, carrying opposite spins in the case of usual s-wave pairing and with kinetic energies above and below the superconductor chemical potential. This proximity effect has been illustrated in several recent experiments[9].

In order to detect this entanglement and implement it for applications, it is necessary to achieve a spatial separation between the two constituent electrons. The entanglement apparatus which is proposed here consists of a mesoscopic normal-metal–superconductor (NS) junction with normal leads arranged in a fork geometry (see Fig. 1). Using appropriate spin- or energy-selective filters in the two normal leads the quasi-particle pairs are properly separated and their entanglement can be quantified through a comparison of the intra- and inter- lead noise.

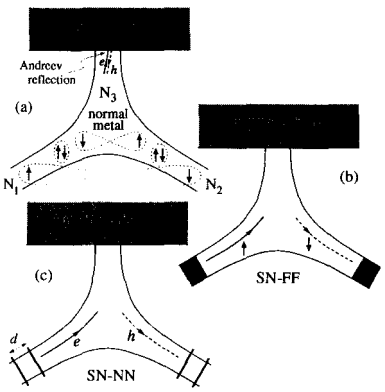


Figure 1: Normal-metal–superconductor (NS) junction with the normal-metal lead arranged in a fork geometry. (a) Without filters, entangled pairs of quasi-particles (Cooper pairs) injected into the lead N_3 propagate into leads N_1 or N_2 either as a whole or one by one. The ferromagnetic filters in setup (b) enforce the separation of the entangled spins, while the Fabry-Perot type interferometers in the setup (c) separate electron- and hole type quasi-particles.

2 Noise, correlations, and entanglement

We start by noting that for a *single* channel NS wire the zero frequency fluctuations of the currents carried by electrons with different spins are completely correlated,

$$\langle\langle I_\sigma I_{-\sigma}\rangle\rangle_{\omega=0} \equiv \int dt\, \langle\langle I_\sigma(t) I_{-\sigma}(0)\rangle\rangle = \langle\langle I_\sigma^2\rangle\rangle_{\omega=0}, \tag{1}$$

hence $\langle\langle (I_\sigma - I_{-\sigma})^2\rangle\rangle_{\omega=0} = 0$ ($\langle\langle ... \rangle\rangle$ implies the subtraction of the average currents). This perfect correlation in the (subgap) motion of the quasi-particles with different spins is a consequence of the entanglement of the Cooper pairs injected into the normal wire.

Next, recall that the current noise cross-correlations in a SN-NN fork geometry – without filters on the normal probes – are positive when the transmission between the superconductor and the normal leads is low [10]. The unusual sign (for fermions) of these correlations is due to paired electrons penetrating the two normal leads separately, c.f., Fig. 1(a). The positive correlations are further enhanced when the competing channel (with paired electrons entering the leads jointly) is suppressed through the addition of appropriate spin- or energy selective filters to the normal leads, see Figs. 1(b) and (c). The wave function of the entangled states generated with ideal spin/energy filters then is of the type

$$|\Phi^{\rm ent}_{\varepsilon,\sigma}\rangle = \alpha|\varepsilon,\sigma;-\varepsilon,-\sigma\rangle + \beta|\mp\varepsilon\pm\sigma;\pm\varepsilon\mp\sigma\rangle, \tag{2}$$

where the first (second) argument in $|\phi_1;\phi_2\rangle$ refers to the quasi-particle state in lead 1 (2) evaluated behind the filters and the upper (lower) signs refer to the setup projecting the spin (energy); the coefficients α and β can be tuned by external parameters, e.g., a magnetic field. In such a multi-terminal device, the measurement of the zero frequency noise cross-correlator $\langle\langle I_{\sigma 1} I_{-\sigma 2}\rangle\rangle_{\omega=0}$ then serves to detect electron entanglement, in analogy with the above single channel NS wire.

A step like dependence of the gap parameter at the NS interface is assumed, subgap transport is specified, while the normal leads are single-channel and ballistic. Using the scattering

formulation of NS transport[11], the current operator per spin in normal lead n is defined as

$$\begin{aligned} I_{\sigma n}(t) &= \frac{ie\hbar}{2m}\sum_{\alpha,\alpha'}\int_0^\infty d\varepsilon d\varepsilon' \{[u^*_{\varepsilon\alpha}(x)\overleftrightarrow{\partial}_x u_{\varepsilon'\alpha'}(x)]\gamma^\dagger_{\varepsilon\alpha}\gamma_{\varepsilon'\alpha'} \\ &- [v^*_{\varepsilon\alpha}(x)\overleftrightarrow{\partial}_x v_{\varepsilon'\alpha'}(x)]\gamma_{\varepsilon'\alpha'}\gamma^\dagger_{\varepsilon\alpha}\}\exp[i(\varepsilon-\varepsilon')t], \end{aligned} \tag{3}$$

where the operators $\gamma_{\varepsilon\alpha}$ describe electron and hole Bogoliubov quasiparticles (with positive energies ε) on the normal side with $\alpha = \{p,\sigma,n\}$ a multi-index characterizing the 'charge' $p\,(=e,h)$, spin $\sigma\,(=\pm 1/2)$, and incidence (lead n); $f\overleftrightarrow{\partial}_x g \equiv f\partial_x g - g\partial_x f$. The associated wave functions ($u_{\varepsilon\alpha}(x)$ and $v_{\varepsilon\alpha}(x)$) are expressed in terms of the scattering matrix $s_{\alpha,\alpha'}$; e.g., for an electron with spin σ incident from lead n and observed in lead m at x_m

$$\begin{aligned} u_{e\sigma n}(x_m) &\simeq \left[\delta_{nm}e^{ik_+x_n} + s_{e\sigma n,e\sigma m}e^{-ik_+x_m}\right]/\sqrt{hv_+}, \\ v_{\varepsilon e\sigma n}(x_m) &\simeq \left[s_{e\sigma n,h-\sigma m}e^{ik_-x_m}\right]/\sqrt{hv_-}, \end{aligned} \tag{4}$$

with wave numbers $k_\pm = \sqrt{2m(\mu_S \pm \varepsilon)}$ and the quasi-particle velocities $v_\pm = \hbar k_\pm/m$ (μ_S is the chemical potential in the superconductor). The difference between the two wave numbers $k_\pm$ will be neglected ($\mu_S \gg \Delta$).

3 Device "engineering" from scattering elements

Let us now turn to the fork geometry of Fig. 1: the current leads N_1 and N_2 are connected to N_3, which itself is terminated with the NS interface. We discuss two schemes: a) two ferromagnetic metal contacts (with magnetizations in opposite directions) in leads N_1 and N_2 block the propagation of the opposite spin, see Fig. 1(b), b) two energy filters in N_1 and N_2 (coherent quantum dots) select the kinetic energies of electrons and holes symmetrically above and below the superconducting chemical potential (Fig. 1(c)). In both proposals, the penetration of a Cooper pair into a given lead is prohibited, while allowing the split pair to pass the filters. E.g., one electron propagates through N_1 with spin 'up', while simultaneously the other electron (with opposite kinetic energy) propagates through N_2 with spin 'down'.

The scattering matrix $s_{\alpha,\alpha'}$ has to account for all multiple scattering processes: the Andreev reflection at the N_3S interface can be specified in terms of the transmission and reflection amplitudes t_{13}, t_{23}, and r_{ii} ($i = 1,2$) describing the normal-metal part of the device[12]. The latter include the scattering by the 'beam splitter' $N_3 \longleftrightarrow N_1, N_2$, and account for the presence of spin or energy filters in leads N_1 and N_2. The corresponding transmission and reflection amplitudes are found iteratively following the scheme sketched in Fig. 2 and accounting for all interference processes in the device.

Beam Splitter: Time reversal invariance is assumed for simplicity. It is then possible to express the transmission probability, say, between leads N_1 and N_2 in terms of the other two transmissions:

$$T^{(2)}_{12} = T^{(2)}_{13}T^{(2)}_{23}[2 - T^{(2)}_\Sigma \pm 2(1-T^{(2)}_\Sigma)^{1/2}]/{T^{(2)}_\Sigma}^2, \tag{5}$$

where $T^{(2)}_\Sigma \equiv T^{(2)}_{13} + T^{(2)}_{23}$, and $T^{(2)}_{ij} = |t^{(2)}_{ij}|^2$. For a fully symmetric beam splitter $T^{(2)}_{ij} = 4/9$. A partially symmetric setup (with respect to the leads N_1, N_2) with small transmissions $T^{(2)}_{23} = T^{(2)}_{13}$ has been studied in Ref. [13]. The choice of the lower sign in (5) allows us to consider also the case when all three transmissions are small, so this parametrization covers the whole range of splitter transmission. Using the unitarity of the scattering matrix, the reflection amplitudes of the splitter are

$$r^{(2)}_{ii} = t^{(2)*}_{jk}t^{(2)}_{ij}t^{(2)}_{ik}[{T^{(2)}_{jk}}^{-1} - {T^{(2)}_{ij}}^{-1} - {T^{(2)}_{ik}}^{-1}]/2. \tag{6}$$

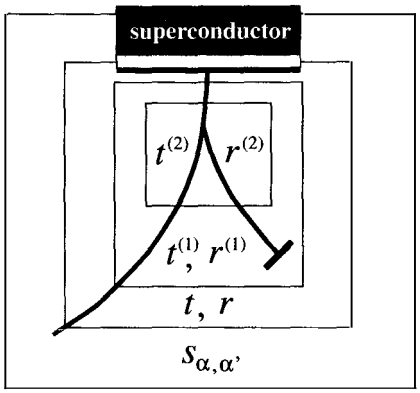


Figure 2: The scattering matrix $s_{\alpha,\alpha'}$ determining the noise correlator (12) incorporates all the internal scattering features of the fork, the beam splitter ($\to t^{(2)}$, $r^{(2)}$), the stubs ($\to t^{(1)}$, $r^{(1)}$), and the normal scattering at the NS interface ($\to t$, r).

The phases of the reflection and transmission amplitudes, in addition to describing the intrinsic properties of the links between the three wires, account for the choice of the origin in each lead. Practical choices for these origins are: a) the position of the NS interface in lead N_3 and b) that of the filters in N_1 and N_2. Typical phases accumulated during free propagation are $\exp(\pm ik_{\pm}b)$ with b a typical length in the beam splitter.

Stubs: When blocking the propagation through N_2 with an ideal filter, the transmission and reflection amplitudes $t_{13}^{(1)}$, $r_{33}^{(1)}$, and $r_{11}^{(1)}$ follow from the transmission and reflection amplitudes $t_{12}^{(2)}$, $t_{13}^{(2)}$, $t_{23}^{(2)}$, $r_{11}^{(2)}$, and $r_{22}^{(2)}$ of the three bare leads via

$$t_{13}^{(1)} = \frac{t_{13}^{(2)} - t_{12}^{(2)}t_{23}^{(2)} + t_{13}^{(2)}r_{22}^{(2)}}{1 + r_{22}^{(2)}}, \tag{7}$$

$$r_{33}^{(1)} = -\frac{t_{23}^{(2)}}{1 + r_{22}^{(2)}}, \quad r_{11}^{(1)} = r_{11}^{(2)} - \frac{t_{23}^{(2)\,2}}{1 + r_{22}^{(2)}}. \tag{8}$$

When blocking occurs at N_1, the amplitudes are obtained by exchanging the lead indices in (7) and (8).

NS boundary: We formally split the NS boundary into two parts describing normal and Andreev scattering, see Fig. 2. In order to include the normal scattering component we combine the two scatterers $\{t_{13}^{(1)}, r_{33}^{(1)}, r_{11}^{(1)}\}$ and $\{t_{\rm NS}, r_{\rm NS}, r'_{\rm NS}\}$ in series and obtain the amplitudes at the next level,

$$t_{13} = \frac{t_{13}^{(1)}t_{\rm NS}}{1 - r_{33}^{(1)}r'_{\rm NS}}, \tag{9}$$

$$r_{33} = r_{\rm NS} + \frac{t_{\rm NS}^2 r_{33}^{(1)}}{1 - r_{33}^{(1)}r'_{\rm NS}}, \quad r_{11} = r_{11}^{(1)} + \frac{t_{13}^{(1)\,2}r'_{\rm NS}}{1 - r_{33}^{(1)}r'_{\rm NS}}, \tag{10}$$

where the primed reflection amplitude $r'_{\rm NS}$ is associated with the particle incident from the superconductor. Finally, we account for perfect Andreev reflection at the NS interface; for an electron incident from N_1 the scattering amplitude reads

$$|s_{e\sigma 1, h-\sigma 2}|^2 = \frac{|t_{13+}|^2|t_{23-}|^2}{1 + |r_{11+}|^2|r_{22-}|^2 + 2\mathrm{Re}(r_{33+}r_{33-}^*)}, \tag{11}$$

where the indices $\pm$ indicate that the energy dependent scattering amplitudes have to be evaluated at the positive(negative) value of the quasi particle energy $\varepsilon(-\varepsilon)$. For each energy ε only one of the two leads, N_1 or N_2, is open, resulting in a two-terminal device, thus the relations $|r_{ii}|^2 = 1 - |t_{i3}|^2 = |r_{33}|^2$ hold. The main feature contained in Eq. (11) are the Andreev type resonances building up within the normal-metal leads. These resonances are determined through the sign changes in $\mathrm{Re}(r_{33+}r^*_{33-})$ and their distance $\sim \hbar v_F/L$ is determined via the Fermi velocity v_F and the characteristic size L of the region. In addition, zeros appear in the spectral density which are a consequence of a vanishing transmission for electrons or holes in this three lead geometry.

The above scheme fully specifies the scattering matrix $s_{\alpha,\alpha'}$ for the case with ideal filters. For non-ideal filters the stub should be replaced with a proper description of the lead N_2 including its non-ideal filter; in addition, the normal scatterer described through the amplitudes $\{t_{13}, r_{33}, r_{11}\}$ above has to be combined with an additional scatterer describing the non-ideal filter in the lead N_1. E.g., an energy filter requires inclusion of a Fabry-Perot interferometer characterized through the scattering amplitudes t_1, t_2, r_1', r_2 and the separation d of the double barrier system and producing a transmission $t_{FP} = t_1 t_2 \exp(ikd)/[1 - r_1 r_2' \exp(2ikd)]$. The resonance spacing should be larger than the applied bias for a proper device operation as a filter. The initial resonance lines produced by the quantum dot will then be decorated by Andreev-type resonances and zeros originating from the NS-fork structure.

The above entangler is essentially a two terminal device where electrons with, say, a given spin from lead 1 are converted into holes with an opposite spin in lead 2. The current correlations between 1 and 2 are positive and can be obtained using the definition of the noise in combination with (3), at $T = 0$,

$$\langle\langle I_{\sigma 1} I_{-\sigma 2}\rangle\rangle = \frac{e^2}{h} \sum_{\alpha,\alpha'} \int_0^{eV_1} d\varepsilon \, |s_{\alpha,\alpha'}|^2 (1 - |s_{\alpha,\alpha'}|^2), \tag{12}$$

where a voltage eV_1 is applied between the lead N_1 and the superconductor while keeping the lead N_2 unbiased. For the case of ferromagnetic filters, the chemical potential which enters the (sharp) electron and hole distribution functions depends also on the spin index. The multi-indices α and α' to be summed over in (12) depend on the type of filters in the normal leads N_1 and N_2: For ferromagnetic filters (SN-FF) with the spin in $F_{1(2)}$ pointing up (down) $\alpha = \{e(h) \uparrow 1\}$ and $\alpha' = \{h(e) \downarrow 2\}$ (the propagation of other states is blocked by the filters). On the other hand, for the setup selecting a definite quasi particle energy via Fabry-Perot type filters we have to sum over spins with $\alpha = \{e \uparrow (\downarrow) 1\}$ and $\alpha' = \{h \downarrow (\uparrow) 2\}$ (we assume filters selecting quasi particles and quasi holes in leads N_1 and N_2, respectively). Applying the same voltage to the lead N_2 as well does not change the answer in the normal fork (SN-NN) but renders the result for the ferromagnetic filters (SN-FF) twice larger. The current fluctuations (12) are straightforwardly converted into "counting" correlations as known from quantum optics: with $en_{\sigma n}(t) = \int_0^t dt' I_{\sigma n}(t')$ we find $\langle\langle n_{\sigma 1}(t)\, n_{-\sigma 2}(t)\rangle\rangle|_{t\to\infty} \approx (t/e^2)\langle\langle I_{\sigma 1}\, I_{-\sigma 2}\rangle\rangle_{\omega=0}$ and hence $\langle\langle (n_{\sigma 1} - n_{-\sigma 2})^2\rangle\rangle / \langle\langle n_{\sigma 1}^2\rangle\rangle \approx 0$. The result (12) together with the fact that the two currents $I_{\sigma 1}$ and $I_{-\sigma 2}$ are necessarily correlated constitutes the main justification for the proposed entanglement device: Eq. (12) corresponds precisely to the current noise in lead 1.

4 Conclusion

This electronic entanglement apparatus can now be completed with a detection apparatus in order to test non-local correlations (Bell inequalities). For an entangler based on ferro/energy filters, the detection apparatus involves filters of opposite type (energy/ferro). Concentrating on energy filters, a positive energy particle emerging in lead N_1 can have either spin orientation,

which can be "measured" by connecting this lead to, say, a magnetic contact with known spin orientation. In the opposite arm one should have a similar contact but with a magnetization axis rotated by $\pi/2$ in order to achieve the analog of the spin correlation experiments of Ref. [5].

Summarizing, we have proposed an electronic entanglement device based on the proximity effect and have shown how to probe the resulting non-local electronic correlations in an emphatic way through a measurement of the current cross-correlator. Using a special fork geometry with, say, Fabry-Perot filters one arrives at a natural source of spin-entangled electron pairs, a device with potential applications in quantum computing architectures based on spintronics[16]. This device presents the advantage – as compared to its ferromagnetic cousin – that it can be realized with nowadays splitters[17] and quantum dot technology, e.g., using semiconductor-superconductor heterostructures[18]. The formation of sharp resonances in the conductance of the dots is sufficient to achieve this entanglement without additional coupling between the dots. Moreover, this SN-NN device appears to be more promising regarding potential applications for quantum information processing: the insertion of Fabry-Perot filters destroys only the orbital entanglement of the electrons, while the (most valuable) spin entanglement persists, contrary to the situation in the SN-FF device where the filters project the spin.

References

1. A. Einstein, B. Podolsky, and N. Rosen, Phys. Rev. **47**, 777 (1935).
2. A. Ekert, Phys. Rev. Lett. **67**, 661 (1991).
3. C.H. Bennett *et al.*, Phys. Rev. Lett. **70**, 1895 (1993).
4. A. Steane, Rep. Prog. Phys. **61**, 117 (1998).
5. J.F. Glauser and A. Shimony, Rep. Prog. Phys. **41**, 1981 (1978), and references therein; A. Aspect, P. Grangier, and G. Roger, Phys. Rev. Lett. **47**, 460 (1981); see P.G. Kwiat *et al.*, *ibid.* **75**, 4337 (1995) for modern sources of entangled photon pairs.
6. G. Burkard, D. Loss, and E. Sukhorukov, Phys. Rev. B **61**, R16303 (2000).
7. D. Loss and E.V. Sukhorukov, Phys. Rev. Lett. **84**, 1035 (2000); P. Recher, E.V. Sukhorukov, and D. Loss, cond-mat/0009452.
8. A.A. Abrikosov, L.P. Gor'kov, and I.E. Dzyaloshinski, *Methods of Quantum Field Theory in Statistical Physics* (Prentice-Hall, Englewood Cliffs, N.J., 1963).
9. V.T. Petrashov *et al.*, Phys. Rev. Lett. **70**, 347 (1993); *ibid.* **74**, 5268 (1995); A. Dimoulas *et al.*, *ibid.* **74**, 602 (1995); H. Courtois *et al.*, *ibid.* **76**, 130 (1996); F.B. Müller-Allinger *et al.*, *ibid.* **84**, 3161 (2000).
10. J. Torrès and T. Martin, Europhys. J. B **12**, 319 (1999).
11. M.J.M. de Jong and C.W.J. Beenakker, Phys. Rev. B **49**, 16070 (1994); B.A. Muzykantskii and D.E. Khmelnitskii, *ibid.* **50**, 3982 (1994); M.P. Anantram and S. Datta, *ibid.* **53**, 16 390 (1996); G. Lesovik, T. Martin, and J. Torrès, *ibid.* **60**, 11935 (1999).
12. G. B. Lesovik, A.L. Fauchère, and G. Blatter, Phys. Rev. B **55**, 3146 (1997); A.L. Fauchère, G.B. Lesovik, and G. Blatter, *ibid.* **58**, 11177 (1998).
13. Y. Gefen, J. Imry, and R. Landauer, Phys. Rev. Lett. **52**, 139 (1984); M. Büttiker, Y. Imry, and M. Ya. Azbel, Phys. Rev. A **30**, 1982 (1984).
14. S.I. Bozhko, V.S. Tsoi and S.E. Yakovlev, Pis'ma Zh. Eksp. Teor. Fiz. **36**, 123 (1982) [JETP Lett. **36**, 153 (1982)]; P.A.M. Benistant, H. van Kampen and P. Wyder, Phys. Rev. Lett. **51**, 817 (1983).
15. G. Deutscher and D. Feinberg, App. Phys. Lett. **76**, 487 (2000).
16. D. Loss and D.P. di Vincenzo, Phys. Rev. A **57**, 120 (1998).
17. M. Henny *et al.*, Science **284**, 296 (1999); W. Oliver *et al.*, *ibid.*, 299 (1999).
18. H. Takayanagi *et al.*, Phys. Rev. Lett. **75**, 3533 (1995).

ELECTRONIC EPR-LIKE EXPERIMENTS WITH SUPERCONDUCTORS

R. MÉLIN
Centre de Recherches sur les Très Basses Températures (CRTBT)
CNRS, BP 166 X, 38042 Grenoble Cedex, France

We discuss a few situations related to non separable correlations in multiterminal hybrid structures. We show that the existence of such correlations can modify the strength of the gap of the superconductor. We discuss linear combinations of non local Cooper pairs. We discuss a possible transport experiment intended to probe non separable correlations. The models are worked out at the heuristic level of effective single site Green's functions.

1 Introduction

Non locality and non separable correlations are one of the deepest features of quantum mechanics. The presence of non separable correlations in quantum mechanics was identified by Einstein, Podolsky and Rosen [1] (EPR) in 1935. One of the possible alternatives to quantum theory could have been hidden variable theories. Bell has shown in 1964 that there exists a basic difference between hidden variable theories and quantum mechanics [2]. A. Aspect has shown experimentally in 1981 that Bell inequalities were violated with photons [3]. This constitutes the ultimate test of quantum mechanics, which is a non local theory without hidden variables.

Our goal is to describe the physics of heterostructures in which a superconductor is connected to several electrodes, and discuss the consequences for electronic EPR-like experiments. In these systems, non separable correlations are due to superconducting pairs correlations [6,7]. The approach is heuristic in the sense that it contains the correct phenomenology but does not rely on full mathematical rigor. We use a single site Green's function toy-model in which charge conservation is enforced "by hand" [5]. This approach is complementary to lowest order perturbation theory [8]. We already worked out part of the rigorous formulation of microscopic transport theory which will be presented elsewhere [9].

2 Implications for thermodynamics

Let us start to discuss a model in which a superconductor x is connected to N ferromagnetic electrodes α_k, $k = 1, ..., N$ [4]. Each of these elements is represented by an effective single site Green's function [10]. We calculate the Gorkov function $\left[\hat{G}^{+,-}(\omega)\right]_{1,2}$ of the superconducting site connected to the ferromagnetic electrodes [4]. The hopping matrix elements can be arbitrarily large. The gap should satisfy the self-consistent equation $\Delta = U \int_{-\infty}^{+\infty} d\omega/(2i\pi) \left[\hat{G}^{+,-}(\omega)\right]_{1,2}$, where U is the microscopic attractive interaction. This leads to the modified BCS relation

$$\Delta = D \exp\left[-\frac{1}{\rho_N U}\left(1 + \pi\rho_N\Gamma_\uparrow\right)\left(1 + \pi\rho_N\Gamma_\downarrow\right)\right], \tag{1}$$

where D is the bandwidth, ρ_N is the normal state density of states and Γ_σ is the spectral linewidth of spin-σ electron: $\Gamma_\sigma = \sum_{k=1}^{N} \Gamma_{k,\sigma}$, where $\Gamma_{k,\sigma} = |t_{x,\alpha_k}|^2 \rho_{k,\sigma}$. The spectral linewidths measure the coupling between the superconductor and the ferromagnetic electrodes. With two electrodes only, one has $\Gamma_\uparrow = 2\gamma$, $\Gamma_\downarrow = 0$ in the parallel alignment. In the antiparallel alignment, one has $\Gamma_\uparrow = \Gamma_\downarrow = \gamma$. We deduce from Eq. 1 the value of the ratio of the gaps:

$$\frac{\Delta_{AP}}{\Delta_P} = \exp\left(-\frac{\pi^2\rho_N\gamma^2}{U}\right).$$

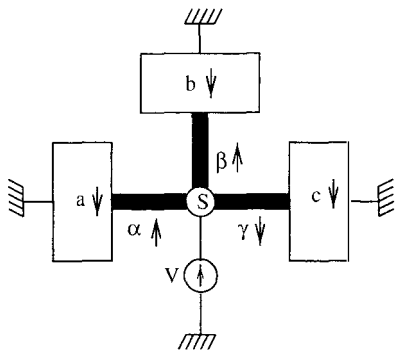


Figure 1: Representation of a device in which three ballistic ferromagnetic regions α, β, γ are connected to a superconductor. The additional electrodes a, b, c are used to to perform a measurement of the linear superposition.

The gap is stronger if the electrodes are in a parallel alignment. This is because the proximity effect is stronger in the antiparallel alignment. This behavior coincides with a diffusive model solved recently [11].

3 Linear superpositions of correlated pairs of electrons

Now we consider a system in which a superconductor is connected to three ferromagnetic ballistic regions by high transparency contacts. The three ferromagnetic ballistic regions are connected to three ferromagnetic reservoirs by low transparency contacts (see Fig. 1). We want to show that transport in this system can be interpreted in terms of projections of a BCS-like wave function, which is a linear superposition of correlated pairs [5].

Transport formula: We assume that a voltage V is applied on the superconductor. The Andreev current is found to be the sum of all Cooper pair transmissions [5]:

$$I^A_{n,\sigma} = 4\pi^2 \int d\omega \left[n_F(\omega - eV) - n_F(\omega) \right] \sum_m \hat{Q} \left[u_{n,\sigma,\sigma'} u_{m,-\sigma,\sigma'} \right] |G^A_{x,x,1,2}|^2, \tag{2}$$

where $u_{n,\sigma,\sigma'} = \pi^2 |t_{x,a_n}|^2 |t_{a_n,\alpha_n}|^2 \rho^2_{\alpha_n,\sigma} \rho_{a_n,\sigma} / (1 + \pi^2 |t_{a_n,\alpha'_n}|^2 \rho_{a_n,\sigma} \rho_{a_n,\sigma})^2$. The operator $\hat{Q}$ is used to enforce charge conservation [5].

BCS-like wave function: It is tempting to look for a BCS-like wave function associated to the situation on Fig. 1. For instance in the presence of only two electrodes α and β having a spin orientation $\sigma_a = \uparrow$ and $\sigma_\beta = \downarrow$, the superconducting wave function is the product of two contributions: (i) Local Cooper pairs (residing in S); (ii) Non local Cooper pairs (residing in the ferromagnets α and β). We drop out the contribution of local Cooper pairs and write the wave function under the form $|\psi\rangle = c^+_{\alpha,\uparrow} c^+_{\beta,\downarrow} |0\rangle$. In the presence of three ballistic regions α, β, γ, the BCS-like wave function takes the form

$$|\psi\rangle = c^+_{a,\uparrow} \left[\sqrt{\frac{t_\beta \rho_{\beta,\downarrow}}{t_\beta \rho_{\beta,\downarrow} + t_\gamma \rho_{\gamma,\downarrow}}} c^+_{\beta,\downarrow} + \sqrt{\frac{t_\gamma \rho_{\gamma,\downarrow}}{t_\beta \rho_{\beta,\downarrow} + t_\gamma \rho_{\gamma,\downarrow}}} c^+_{\gamma,\downarrow} \right] |0\rangle, \tag{3}$$

where we assume that α, β and γ are three fully spin polarized ferromagnets with spin orientations $\sigma_\alpha = \uparrow$, $\sigma_\beta = \sigma_\gamma = \downarrow$ (see Fig. 1).

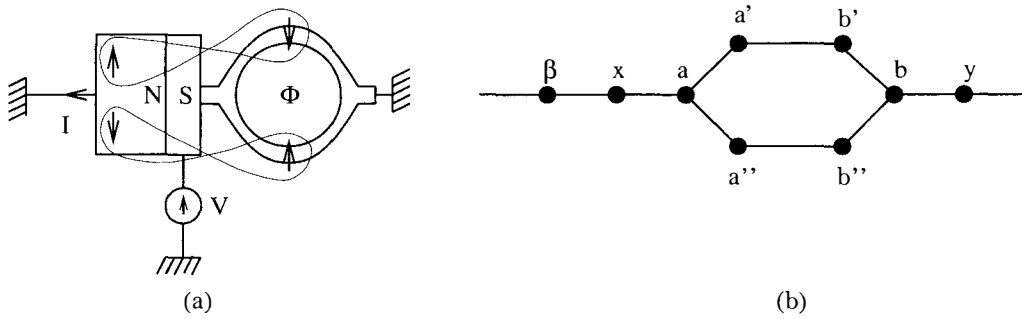


Figure 2: (a) Geometry of the Aharonov-Bohm experiment. The current I flowing into the left electrode is modulated by the flux enclosed by the other electron making the correlated pair. (b) The circuit used in the single site version of Keldysh formalism. Site x is superconducting.

Interpretation of the transport formula: In the presence of an arbitrary number of electrodes, the BCS-like wave function is a superposition of all possible Cooper pairs:

$$|\psi\rangle = \mathcal{N}^{-1/2} \sum_{p,q} \sqrt{t_{\alpha_p} t_{\alpha_q} \rho_{\alpha_p,\uparrow} \rho_{\alpha_q,\downarrow}}\, c^+_{\alpha_p,\uparrow} c^+_{\alpha_q,\downarrow} |0\rangle,$$

where the normalization coefficient is $\mathcal{N} = \sum_p t_{\alpha_p} \rho_{\alpha_p,\uparrow} \sum_q t_{\alpha_q} \rho_{\alpha_q,\downarrow}$. One can define a projection operator associated to the Cooper pair (p,q): $\hat{\mathcal{P}}_{p,q} = c^+_{\alpha_p,\uparrow} c^+_{\alpha_q,\downarrow} c_{\alpha_p,\uparrow} c_{\alpha_q,\downarrow}$. The spin-up current through electrode a_p is found to be

$$I_p = 4\pi^2 \mathcal{N}^2 \sum_q \int d\omega \left[n_F(\omega - eV) - n_F(\omega) \right] \gamma_{a_p,\uparrow} \gamma_{a_q,\downarrow} \left| \langle \psi | \hat{\mathcal{P}}_{p,q} | \psi \rangle \right|^2 |G^A_{x,x,1,2}|^2, \qquad (4)$$

where $\gamma_{a_{p(q)},\uparrow} = \pi^2 |t_{a_{p(q)}}|^2 \rho_{a_{p(q)},\uparrow(\downarrow)}$. We interpret the transport formula (4) as follows: (i) *Before the tunneling event*, the Cooper pairs are described by the BCS-like wave function. (ii) *Short after the tunneling event*, there is one Cooper pair transfered in electrodes (a_p, a_q). (iii) *Long after the tunneling event*, there is a spin-up electron in electrode p and a spin-down electron in electrode q without phase coherence between the two.

The situation in which S is replaced by a normal metal is already non trivial. In this case, the wave function is a linear superposition of single electron states while we pointed out here the existence of a linear superposition of two-electron states.

4 Experiment proposal

Geometry: Now we discuss a more realistic experiment that can be made without ferromagnets. The idea is to connect two electrodes to a superconductor. One of these electrodes contains an Aharonov-Bohm loop (see Fig. 2).

Physical picture: Let us assume that the Aharonov-Bohm loop is weakly connected to the rest of the circuit. In the tunnel regime, there are discrete energy levels $\epsilon_n(\phi)$ on the Aharonov-Bohm loop, which are periodic functions of ϕ. One-electron conduction is maximal when one level is resonant. The Aharonov-Bohm loop can be represented by an effective transmission amplitude $T(\phi)$. The Cooper pair current is proportional to $|t_{x,\beta}|^2 |T(\phi)|^2$, which oscillates with ϕ. As a consequence, the current through the left electrode on Fig. 2 oscillates as a function of the flux enclosed in the right electrode.

Single site calculation: The non local contribution to the current through the left electrode on Fig. 2 takes the form [5]:

$$I^{A,n.l.}_{\beta,\sigma} = \int \hat{Q} \left[\frac{4\pi^2 |t_{x,\beta}|^2 |t_{x,a}|^2 \rho_{\beta,\sigma} \rho^2_{a,-\sigma} \rho_{b,-\sigma} \left[(\gamma'_{-\sigma} + \gamma''_{-\sigma})^2 + 2\gamma'_{-\sigma}\gamma''_{-\sigma}[1 - \cos(2\pi\phi/\phi_0)] \right]}{\left[1 + (\rho_{a,-\sigma} + \rho_{b,-\sigma})(\gamma'_{-\sigma} + \gamma''_{-\sigma}) + 2\gamma'_{-\sigma}\gamma''_{-\sigma}\rho_{a,-\sigma}\rho_{b,-\sigma}[1 - \cos(2\pi\phi/\phi_0)] \right]^2} \right] \times \left[n_F(\omega - eV) - n_F(\omega) \right] |G^A_{x,x,1,2}|^2 d\omega. \quad (5)$$

The current (5) oscillates with a period $\phi_0 = h/e$, which is in agreement with the tunnel limit behavior. The magnitude of the oscillatory component is of order $|t_{x,\beta}|^2 |t_{x,a}|^2$. Note that the local current

$$I^A_{\beta,\mathrm{local}} = 4\pi^2 |t_{x,\beta}|^4 \rho_{\beta,\uparrow} \rho_{\beta,\downarrow} \int d\omega \left[n_F(\omega - eV) - n_F(\omega) \right] |G^A_{x,x,1,2}|^2, \quad (6)$$

also oscillates with ϕ because of the renormalization of the Green's function $G^A_{x,x,1,2}$. These oscillations in the local contribution correspond to processes in which a Cooper pair is extracted from the superconductor and is transferred into the right reservoir. The Cooper pair couples to the Aharonov-Bohm flux, comes back in the superconductor and is transferred into the left electrode. This process appears at order $|t_{x,\beta}|^4 |t_{x,a}|^8$ while the current due to non separable correlations appears at order $|t_{x,\beta}|^2 |t_{x,a}|^2$. If at least one of the interfaces has a low transparency, it would be possible to retain mostly the current due to non separable correlations.

5 Conclusions

To summarize, we have pointed out a few situations intended to probe non separable correlations in electronic systems. The dependence of the superconducting gap upon the spin orientation of a ferromagnetic environment may be tested in experiments. It would be harder to test the linear superposition of correlated pairs of electrons. The Aharonov-Bohm effect can be probed in experiments because phase coherence can propagate over sufficiently large distances in normal metals. Finally, we note that an electronic EPR experiment based on ballistic electrons in semiconductors has been proposed recently [12].

Acknowledgments

The author wishes to thank fruitful discussions with P. Degiovanni, D. Feinberg and S. Peysson.

References

1. A. Einstein, B. Podolsky and N. Rosen, Phys. Rev. **47**, 777 (1935).
2. J.S. Bell, Physics **1**, 195 (1964).
3. A. Aspect, P. Grangier, and G. Roger, Phys. Rev. Lett. **47**, 460 (1981).
4. R. Mélin, arXiv:cond-mat/0010490, submitted to J. Phys Cond. Matt. (2001).
5. R. Mélin, arXiv:cond-mat/0011364, submitted to Eur. Phys. J. B. (2001).
6. D. Loss and E.V. Sukhorukov, Phys. Rev. Lett. **84**, 1035 (2000).
7. G.B. Lesovik, T. Martin, and G. Blatter, arXiv:cond-mat/0009193.
8. G. Falci, D. Feinberg, and F.W.J. Hekking, arXiv:cond-mat/0011339, submitted to Europhysics Letters (2001).
9. R. Mélin and D. Feinberg, in preparation (2001).
10. J.C. Cuevas, A. Martin-Rodero and A. Levy Yeyati, Phys. Rev. B **54**, 7366 (1996).
11. I. Baladie, A. Buzdin, N. Ryzhanova, A. Vedyayev, Phys. Rev. B **63**, 054518 (2001).
12. R. Ionicioiu, P. Zanardi, and F. Rossi, Phys. Rev. A **63**, 050101 (2001).

QUANTUM COMPUTATION WITH FQHE QUASIPARTICLES

D.V. AVERIN and V.J. GOLDMAN
Department of Physics and Astronomy, SUNY, Stony Brook, NY 11794-3800, U.S.A.

We propose an approach to implementing anyonic quantum computation in systems of antidots in the two-dimensional electron liquid in the FQHE regime. The approach is based on the adiabatic transfer of FQHE quasiparticles in the antidot systems, and uses their fractional statistics to perform quantum logic. Advantages of our scheme over other semiconductor-based proposals of quantum computation include the energy gap in the FQHE liquid that suppresses decoherence, and the topological nature of quasiparticle statistics that makes it possible to entangle two quasiparticles without their direct dynamic interaction.

1 Introduction

"Topological" quantum computation with anyons has been suggested as a way of implementing intrinsically fault-tolerant quantum computation [1,2,3,4]. Intertwining of anyons, quasiparticles of two-dimensional electron system (2DES) with non-trivial exchange statistics, induces unitary transformations of the system wavefunction that depend only on the topological order of the underlying 2DES. These transformations can be used to perform quantum logic, the topological nature of which is expected to make it more robust against environmental decoherence. The aim of this work is to propose specific and experimentally feasible approach for implementation of basic elements of the anyonic quantum computation using adiabatic transport of the fractional quantum Hall effect (FQHE) quasiparticles in systems of quantum antidots [5].

An antidot is a small hole in the 2DES produced by electron depletion, which localizes FQHE quasiparticles at its boundary due to combined action of the magnetic field and the electric field created in the depleted region. If the antidot is sufficiently small, the energy spectrum of the antidot-bound quasiparticle states is discrete, with finite excitation energy Δ. When Δ is larger than the temperature T, modulation of external gate voltage can be used to attract quasiparticles one by one to the antidot [5,6]. In this regime, adiabatic transport of individual quasiparticles in the multi-antidot systems can be used to perform quantum logic, in close analogy to adiabatic transport of individual Cooper pairs in systems of small superconducting islands in the Coulomb blockade regime [7]. In what follows, we describe specific designs of such logic gates, and discuss parameters of the FQHE qubits and mechnisms of decoherence in antidot systems.

2 FQHE qubits and logic gates

In analogy to Cooper-pair qubits [7,8,9], information in the FQHE qubits can be encoded by the position of a quasiparticle in the system of two antidots. In this case, the FQHE qubit (Fig. 1) is the double-antidot system gate-voltage tuned near the resonance, where the energy difference ε between the quasiparticle states localized at the two antidots is small, $\varepsilon \ll \Delta$. At energies smaller than Δ, dynamics of such double-antidot system is equivalent to the dynamics of a common two-state system (qubit). The quasiparticle states localized at the two antidots are the $|0\rangle$ and $|1\rangle$ states of the computational basis of this qubit. The gate electrodes of the structure can be designed to control separately the energy difference ε and the tunnel coupling Ω of the resonant quasiparticle states.

The most natural approach to construction of the *two-qubit gates* with the FQHE qubits is to use fractional statistics [10,11] of the FQHE quasiparticles. Due to this statistics, intertwining of the two quasiparticle trajectories in the course of time evolution of the two qubits realizes controlled-phase transformation with non-trivial value of the phase. Precise result of this operation depends on the nature of the FQHE state. In this work, we discuss the most basic and robust Laughlin

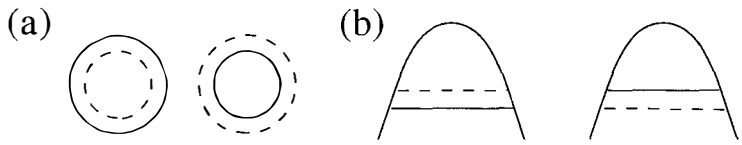


Figure 1: Schematic structure (a) and energy profile (b) of the double-antidot FQHE qubit. Solid (dashed) lines (in (b), only the horizontal lines) indicate the edges of the incompressible electron liquid when the quasiparticle is localized at the right (left) antidot. Displacement of the electron liquid is quantized due to quantization of the single-particle states circling the antidots.

state with the filling factor $\nu = 1/m = 1/3$, where the quasiparticles have abelian statistics and intertwining of trajectories leads to multiplication of the state wavefunction by the phase factor $e^{\pm 2\pi i/3}$. The sign of the phase depends on the direction of the magnetic field and the direction of rotation of one quasiparticle trajectory around another.

A possible structure of the controlled-phase gate is shown in Fig. 2. Each of the columns of four antidots contains two qubits, and arrows denote trajectory of quasiparticle transfer through the system. The transfer leads to transformation of the quantum state of the two qubits and its shift from the gate input (left column in Fig. 2) to the output (right column). The quasiparticle transfer can be achieved by the standard adiabatic level-crossing dynamics. If a pair of antidots is coupled by the tunnel amplitude Ω, a gate-voltage induced variation of the energy difference ε through the value $\varepsilon =$ ● (slow on the time scale Ω^{-1}) leads to the transfer of a quasiparticle between these antidots. Correct operation of the controlled-phase gate in Fig. 2 requires that the gate voltage pulses applied to the antidots are timed so that the state of the upper qubit is propagated at first halfway through the gate, then the state of the lower qubit is propagated through the whole gate, and finally the state of the upper qubit is transferred to the output. In this case, if the quasiparticle of the upper qubit is in the state $|1\rangle$, trajectories of the quasiparticle propagation in the lower qubit encircle this quasiparticle, and the two states of the lower qubit acquire an additional phase difference $\pm 2\pi/3$, conditioned on the state of the upper qubit. We take the direction of magnetic field to be such that the state $|1\rangle$ of the lower qubit acquires a positive extra phase $2\pi/3$. Assuming that parameters of the driving pulses are adjusted in such a way that the dynamic phases accumulated by the qubit states are the multiple integers of 2π, the transformation matrix P of the gate can be written as

$$P = \mathrm{diag}\,[1, 1, 1, e^{2\pi i/3}] \tag{1}$$

in the basis of the four gate states $|00\rangle$, $|$●$1\rangle$, $|10\rangle$, $|11\rangle$.

Controlled-phase gate (1) combined with the possibility of performing arbitrary singe-qubit transformations is sufficient for universal quantum computation. To demonstrate this explicitly, we construct a combination of the gate (1) with single-qubit gates that reproduces the usual controlled-NOT (C-NOT) gate C. The C-NOT gate is known to be sufficient for universal quantum computation [12]. Since the gates P and C are not equivalent with respect to single-qubit transformations, two applications of P are required to reproduce C [13]. To find appropriate single-qubit transformations that should complement the two P's, it is convenient to first reduce P to the conditional z-rotation R of the second qubit through angle $-\pi/3$, $R = \mathrm{diag}\,[1, 1, e^{-i\pi/3}, e^{i\pi/3}]$. We notice that $R = S(-\pi/3)P$, where $S(\alpha)$ is an unconditional shift of the phase of the state $|1\rangle$ of the first qubit by α. After this reduction, it is straightforward to find the necessary single-qubit transformations from the requirements that the state of the first qubit is unchanged by C, while the conditional action of C on the second qubit is given by the Pauli matrix σ_x. These two requirements do not specify the necessary transformations uniquely. One possible choice is to use the transformations that correspond physically to modulation of the tunnel coupling

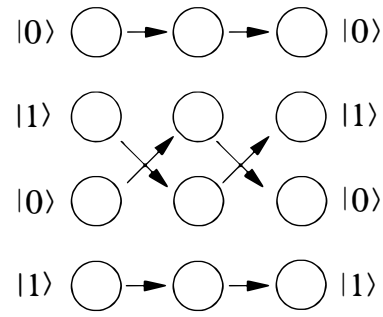


Figure 2: Antidot implementation of the two-qubit controlled-phase gate. The states $|0\rangle$ and $|1\rangle$ are the computational basis states of the two qubits. The arrows show the quasiparticle transfer processes for each basis state during the gate operation.

between the states of the second qubit (i.e., involve only matrices σ_x, σ_y). In this case, we obtain

$$C = S(\pi/2)U_-^\dagger S(-\pi/3)PU_-U_+S(-\pi/3)PU_+^\dagger\,, \tag{2}$$

where $U_\pm = [\hat{1}]_1 \otimes [\exp\{-i\varphi(\sigma_x \pm \sigma_y)/\sqrt{2}\}]_2$. Here the subscripts $1,2$ denote the part of the transformation acting on the first and the second qubit, respectively, and the rotation angle φ is given by the condition $\cos 2\varphi = 1/\sqrt{3}$, $\varphi \in [0,\, \pi/2]$. Physically, the transformations S can be implemented as pulses of the gate voltage applied to the antidot $|1\rangle$ of the first qubit, while Us represent pulsed modulation of the amplitude of the tunnel coupling betweeen the two antidots of the second qubit that keeps the phase of this coupling fixed.

3 Mechnisms of decoherence

At low temperatures, the energy gap in the FQHE liquid exponentially suppresses quasiparticle excitations in the bulk of the sample. Due to this suppression, only sample edges and external metallic gate electrodes support low-energy excitations that can give rise to dissipation and decoherence in the antidot qubits. Qubit is coupled to both the gate electrodes and the edges by the Coulomb interaction. The charge q of the qubit quasiparticle (for the primary Laughlin FQHE liquids, $q = e/m$, where m is an odd integer) induces a charge on the gate electrodes that oscillates in the course of qubit time evolution. The current induced in this way in the electrodes with finite resistance R leads to energy dissipation and decoherence. This decoherence mechanism associated with "electromagnetic environment" of the structure (see, e.g., [14]) is generic for most of the solid-state qubits. In the FQHE qubits, its strength should be lower than in other charge-based qubits, due to the smaller charge of the FQHE quasiparticles. Indeed, if the gate electrode is close to an antidot (on the scale of the distance d between the two qubit antidots), the amplitude of the variations of the induced charge is roughly equal to the quasiparticle charge q. In this "worst-case" scenario, the limitation on the quality factor of qubit dynamics introduced by the gate electrode is equal to $e^2R/\hbar m^2$ and is on the order of 10^{-3} for realistic values of the resitance R and $m = 3$ qubits considered in this work. Optimization of the gate structure of the qubit should further reduce the strength of this type of decoherence by reducing electrostatic gate-qubit coupling.

Coulomb interaction also couples qubit dynamics to edge excitations of the FQHE liquid. The edge supports one-dimesional (1D) chiral plasmon modes [15] propagating with velocity v. In the situation of interest here, when the qubit-edge distance L is much larger than the qubit size d, the coupling operator V can be expressed directly in terms of the 1D density $\rho(x)$ of charge

carried by plasmon modes: $V = \sigma_z \int dx U(x)\rho(x)$. In this expression, σ_z represents the position of the quasiparticle on one or the other antidot of the qubit, and $U(x)$ is the variation (with the quasiparticle position) of the electrostatic potential created by the qubit at point x along the edge. A representative estimate of dissipation/decoherence rate introduced by this coupling is given by the decay rate Γ of the excited antisymmetric superposition of the antidot states. Assuming that the qubit dipole is perpendicular to a straight edge, and that the electric field is not screened between the edge and the qubit, we can find Γ directly:

$$\Gamma = \left(\frac{d}{L}\right)^2 \left(\frac{e^2}{4\epsilon\epsilon_0\hbar v}\right)^2 \frac{\Omega}{2\pi\hbar m^3} e^{-L\Omega/\hbar v} . \tag{3}$$

Here ϵ is the material dielectric constant. This equation shows that the edge-related limitation $\hbar\Gamma/\Omega$ on the qubit quality factor can vary widely depending on the system geometry and qubit energy parameters. For a realistic set of numbers, $\epsilon \simeq 10$, $v \simeq 10^5$ m/s, $\Omega \simeq 0.1$K, $d \simeq 100$nm (see the discussion below), we have $\hbar\Gamma/\Omega \simeq 10^{-3}$ for the edge that is $L \simeq 3$ μm away from the qubit.

4 Estimates and discussion

The basic set of conditions necessary for correct operation of the FQHE qubits and gates described above can be summarized as $T \ll \varepsilon, \Omega \ll \Delta$. The antidot excitation energy Δ is estimated as $\Delta \simeq \hbar u/r$, where r is the antidot radius and $u \simeq 10^4 \div 10^5$ m/s [16] is the velocity of quasiparticle motion around the antidot. This means that at a temperature $T \simeq 0.05$K the radius r should be smaller than 100 nm. Since the tunnel coupling Ω decreases rapidly with the tunneling distance s between the antidots, $\Omega \propto \exp\{-eBs^2/12\hbar\}$ [17], the fact that it should remain at least larger than T means that the distance between the tunnel-coupled antidots should not exceed few magnetic lengths $l = (eB/\hbar)^{1/2}$, where $l \simeq 10$ nm for typical values of the magnetic field B. Although these requirements on the radius r and antidot spacing s can be satisfied with the present-day fabrication technology, they present a formidable challenge. It should be noted that these requirements are not specific to our FQHE scheme, but characterize all semiconductor solid-state qubits based directly on the quantum dynamics of individual quasiparticles, and not collective degrees of freedom (used, e.g., in the case of superconductors).

We believe that the challenges in fabrication of the FQHE qubits are well compensated for by the advantages of the FQHE approach. First of them is the energy gap of the FQHE liquid that suppresses quasiparticle excitations and associated decoherence in the bulk of the 2DES, and allows to control the remaining sources of decoherence through the system layout – see the discussion above. The second advantage is the topological nature of statistical phase that makes it possible to entangle qubits without their direct dynamic interaction. This should lead to a simpler design of the FQHE quantum logic circuit in comparison to other solid-state qubits, where control of the qubit-qubit interaction typically presents a difficult problem.

Acknowledgments

This work was supported by the NSA and ARDA under the ARO contract.

References

1. A.Yu. Kitaev, quant-ph/9707021.
2. J. Preskill, in: *Introduction to quantum computation and information*, Eds. H.-K. Lo, S. Papesku, and T. Spiller, (World Scientific, 1998), p. 213.

3. S. Lloyd, quant-ph/0004010.
4. M.H. Freedman, A.Yu. Kitaev, M.J. Larsen, and Z. Wang, quant-ph/0101025.
5. V.J. Goldman and B. Su, *Science* **267**, 1010 (1995).
6. I.J. Maasilta and V.J. Goldman, *Phys. Rev. Lett.* **84**, 1776 (2000).
7. D.V. Averin, *Solid State Commun.* **105**, 657 (1998).
8. Yu. Makhlin, G. Schön, and A. Shnirman, *Nature* **398**, 305 (1999).
9. Y. Nakamura, Yu.A. Pashkin, and J.S. Tsai, *Nature* **398**, 786 (1999).
10. B.I. Halperin, *Phys. Rev. Lett.* **52**, 1583 (1984).
11. D. Arovas, J.R. Schrieffer, and F. Wilczek, *Phys. Rev. Lett.* **53**, 722 (1984).
12. A. Barenco *et al. Phys. Rev. A* **52**, 1583 (1995).
13. Yu. Makhlin, quant-ph/0002045.
14. G.-L. Ingold and Yu.V. Nazarov, in: *Single Charge Tunneling*, Eds. H. Grabert and M. Devoret (Plenum, NY, 1992), p. 21.
15. X.G. Wen, *Int. J. Mod. Phys. B* **6**, 1711 (1992).
16. I.J. Maasilta and V.J. Goldman, *Phys. Rev. B* **57**, R4273 (1998).
17. A. Auerbach, *Phys. Rev. Lett.* **80**, 817 (1998).

EFFICIENT QUANTUM COMPUTING INSENSITIVE TO PHASE ERRORS

B. GEORGEOT, D. L. SHEPELYANSKY
Laboratoire de Physique Quantique, UMR 5626 du CNRS, Université Paul Sabatier, F-31062 Toulouse Cedex 4, France

We show that certain computational algorithms can be simulated on a quantum computer with exponential efficiency and be insensitive to phase errors. Our explicit algorithm simulates accurately the classical chaotic dynamics for exponentially many orbits even when the quantum fidelity drops to zero. Such phase-insensitive algorithms open new possibilities for computation on realistic quantum computers.

1 Introduction

The problem of quantum computation has attracted recently a great deal of attention [1,2,3]. This interest stems from the fact that the massive parallelism permitted by quantum mechanics enables to reach exponential efficiency of computation in certain quantum algorithms. The most famous example is the Shor algorithm which allows to factor large numbers exponentially faster than any known classical algorithm [4]. Recently, other types of exponentially efficient algorithms has been developed for the simulation of various physical systems [5,6,7]. The exponential gain in computation is related to the exponentially large Hilbert space of the quantum computer which is composed of multi-qubit states operating in parallel (each qubit is a two-level quantum system). Usually the algorithms are constructed for ideal quantum computers operating free of noise and imperfections. In reality, any physical realization of such a computer involves a certain level of imperfections, noise in gate operations and decoherence. First investigations showed that quantum computation can tolerate a sufficiently low level of errors [8,9]. More recently, it has been found that quantum computation is tolerant to quantum errors when simulating classical chaotic dynamics for which classical computer errors grow exponentially with time [7]. However in general the quantum errors grow with the number of gate operations and any realistic quantum computer is faced with this problem. To deal with this problem of fault-tolerant computation, quantum error-correcting codes were recently developed [10,11,12]. They allow to reduce the level of errors in a systematic way, but require the introduction of many redundant qubits and additional gates, which significantly complicates the computational process. The complexity of these codes depends strongly on the type of errors they should correct. Indeed, while simpler classical codes need to correct only bit errors, the quantum ones should in addition simultaneously correct the quantum phase errors. The quantum phase errors seem to be of primary importance since the massive parallelism of quantum computing is related to entanglement in the Hilbert space which is directly based on phase coherence. Therefore, according to this common lore it seems impossible to perform efficient and accurate quantum computations in presence of uncontrolled strong phase errors. In this paper we show on an explicit example that it is not always the case, and that there are algorithms insensitive to phase errors which perform accurate and efficient computation. Our example is based on the simulation of classical chaotic dynamics, which is very hard to simulate accurately on classical computers since this dynamics is unstable and round-off errors grow exponentially with time. In spite of this, our quantum algorithm, including measurement, remains insensitive to phase errors for arbitrary time.

2 The Arnold-Schrödinger cat quantum algorithm

To illustrate this phenomenon, we choose an algorithm which simulates the classical chaotic dynamics of the well-known Arnold cat map [13,14]. It was recently shown [7] that quantum computers can simulate this dynamics with exponential efficiency. In addition it was shown that a small

level of quantum errors in the gate operations of order ϵ allows to simulate accurately this map on times of order $O(1/\epsilon^2)$. Thus quantum computers can face classical exponential instability and chaos.

The dynamics of the map we are studying is given by:

$$\bar{y} = y + x \pmod 1 \ , \ \bar{x} = y + 2x \pmod 1 \ , \qquad (1)$$

where bars denote the new values of the variables after one iteration. This is an area-preserving map, in which x can be considered as the space variable and y as the momentum. A discretized version on a $N \times N$ square lattice is also described by this map. In [7], a quantum algorithm called Arnold-Schrödinger cat map was introduced, and it was shown to simulate this dynamics on the lattice with exponential efficiency. In this paper, we modify this algorithm in such a way that exponential efficiency is preserved and in addition it becomes insensitive to phase errors. This is obtained by the introduction of a new measurement procedure.

The quantum algorithm introduced in [7] simulates the discrete classical dynamics given by (1) and operates with $3n_q - 1$ qubits. These qubits are organized in three registers. Two of them describe the classical phase space with N^2 points and $N = 2^{n_q}$. The third register with $n_q - 1$ qubits is used as workspace. In this way, an initial classical phase space density can be represented by a quantum state $\sum_{i,j} a_{ij}|x_i > |y_j > |0 >$, with $x_i = i/N$, $i = 0, ..., N-1$ and $y_j = j/N$, $j = 0, ..., N-1$, written in binary representation, and we choose initially $a_{ij} = 0$ or $1/\sqrt{N_d}$ where N_d is the number of points in the classical distribution. Then, iterations of the map (1) are performed with the help of additions of integers modulo (N) (modular additions). The quantum algorithm we use for this operation is similar to the one described in [15] (see also [7]). First we compute all the carries of the addition, using two Toffoli gates and one controlled-not (CNOT) gate per qubit. Then we perform the addition starting from the last qubit and erasing the carries by running the inverse of the preceding step. This needs two CNOT gates per qubit addition and the same gates as above to erase the carries. The result is taken modulo (N) by eliminating the last carry. After these operations, the amplitudes $|a_{ij}|$ describe the classical phase space distribution function after iteration of (1). In total, one needs $16n_q - 22$ Toffoli and CNOT gates per map iteration. On the contrary, a classical computer will require $O(2^{2n_q})$ operations per iteration for $N_d = O(N^2)$ orbits.

It is important to stress that during the whole process the classical distribution function is determined only by the probabilities $|a_{ij}|^2$ of the quantum computer wavefunction expanded on the Hilbert space basis of register states $|x_i > |y_j >$ (after each map iteration the third register is always in the state $|0 >$). Thus, the information about the classical distribution function is stored in these probabilities, and is not sensitive to the relative quantum phases of a_{ij}. This suggests that the phase errors accumulated during gate operations will not affect the quantum computer simulation of this classical chaotic dynamics.

3 Effect of phase errors

To study the effects of quantum errors, one usually uses the fidelity [9], defined as: $f(t) = | < \psi_\epsilon(t)|\psi_0(t) > |^2 = |\sum_{i,j} a_{ij}^{(\epsilon)}(t) a_{ij}^{*(0)}(t)|^2$. Here $|\psi_0(t) >= \sum_{i,j} a_{ij}^{(0)}(t)|x_i > |y_j >$ is the quantum state after t perfect iterations, while $|\psi_\epsilon(t) >= \sum_{i,j} a_{ij}^{(\epsilon)}(t)|x_i > |y_j >$ is the quantum state after t imperfect iterations. Obviously, this quantity is very sensitive to the relative phases of a_{ij}. Since the classical phase space density is not sensitive to these phases, we introduce another characteristic which is related only to the amplitudes $|a_{ij}|$. We call it *faithfulness* and define it by: $f_a(t) = (\sum_{i,j} |a_{ij}^{(\epsilon)}(t) a_{ij}^{(0)}(t)|)^2$. This quantity can be considered as a generalization of the usual fidelity. As well as $f(t)$, the faithfulness $f_a(t)$ is always ≤ 1, and it determines the deviation from the exact amplitudes (the value 1 is reached only for $|a_{ij}^{(\epsilon)}(t)| = |a_{ij}^{(0)}(t)|$ for all

i,j). In addition, one has always $f_a(t) \geq f(t)$. Contrary to the usual fidelity, the faithfulness measures only amplitude errors, being insensitive to the quantum phases. We note that its definition is related to the preferential basis chosen initially in the Hilbert space.

To study the dependence of fidelity and faithfulness on phase errors, the nondiagonal part of each Toffoli and CNOT gate used in the algorithm was multiplied by a diagonal matrix with elements $\exp(i\theta_m)$, with random phases θ_m homogeneously distributed in $[-\epsilon_\phi, \epsilon_\phi]$. The results are shown in Fig. 1 (Left). Here the initial state was chosen in the form of a cat's smile (see Fig. 1 of [7] and the coarse-grained version in Fig. 2). In the presence of phase errors only, the fidelity f decreases with the number of map iterations and drops almost to zero for sufficiently strong phase noise. At the same time, the faithfulness f_a is not affected even by the maximal possible phase noise. We also checked that $f_a = 1$ is not affected if each a_{ij} is multiplied after each gate by a random phase $\exp(i\theta_m)$ with θ_m distributed in $[-\pi, \pi]$, although in this case the fidelity is almost zero after one map iteration.

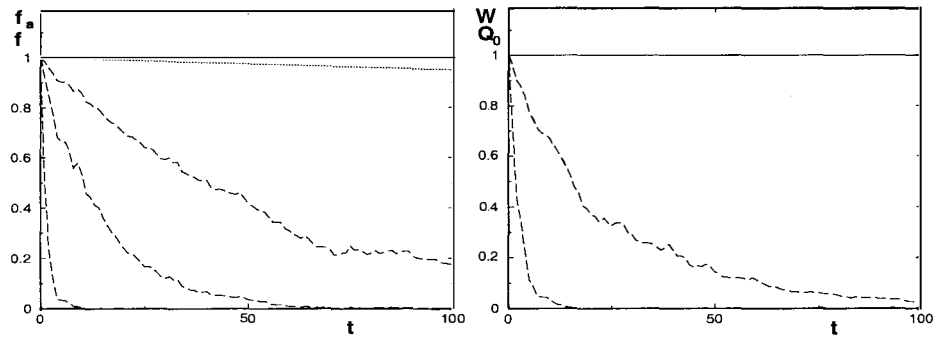


Figure 1: LEFT: Quantum fidelity f of Arnold-Schrödinger cat as a function of time t for quantum phase errors of strength $\epsilon_\phi = 0.05, 0.1, 0.3$ (dashed curves from top to bottom). Faithfulness f_a is shown for the maximal phase errors with $\epsilon_\phi = \pi$ (full line). The dotted line shows $f_a(t)$ when in addition to maximal phase errors there are small amplitudes errors of strength $\epsilon = 0.01$. Initial state is chosen in the form of a cat's smile on a 128×128 lattice (see text and Fig. 2), and $n_q = 7$. In total, 20 qubits are used for the computation.
RIGHT: Zero harmonic Q_0 of Arnold-Schrödinger cat normalized by its value in absence of errors as a function of time t for quantum phase errors of strength $\epsilon_\phi = 0.07, 0.2$ (dashed curves from top to bottom). Full line shows the total probability W inside one cell (i'_g, j'_g) (see text) normalized in the same way for the maximal phase errors with $\epsilon_\phi = \pi$. Initial condition is chosen as for Left, $n_q = 7$ and $n_g = 5$.

To show the difference between phase and amplitude (bit) errors, we computed the faithfulness in presence of a small unitary noise in the gates. For that, in addition to large phase errors, for each gate the nondiagonal part was diagonalized, and each eigenvalue was multiplied by a random phase $\exp(i\eta)$, with $-\epsilon < \eta < \epsilon$. This introduces both phase and amplitude errors, and Fig. 1 (Left) shows that the faithfulness starts to drop slowly with time. Hence despite the presence of strong phase errors the faithfulness is sensitive only to the amplitude errors.

Thus the information stored in the amplitudes is not sensitive to phase decoherence. Still, one should find a way to retrieve a part of this exponentially large information. Usually one performs a quantum Fourier transform (QFT) and measures the maximal harmonics of the distribution, as was suggested in [7]. However, the QFT is extremely sensitive to the quantum phases of a_{ij}, as is illustrated in Fig. 1 (Right). The zero harmonic $Q_0(t) = \sum_{i,j} a_{ij}(t)/N = \sqrt{N_d}/N$ is time-independent in the absence of errors, but drops rapidly with t if phase errors are present. To avoid the effects of phase errors, one can measure only the first n_g qubits from the n_q qubits present in the register $|x>$ and the same for the register $|y>$. This procedure introduces a coarse-graining of the phase space (x, y), with the number of cells $N_g = 2^{2n_g}$. The result of such a measurement is determined by the total probability inside each cell $W_{i_g j_g} = \sum_{<i,j>} |a_{ij}|^2$

where the summation is performed over all (i, j) inside the cell (i_g, j_g). This probability is not sensitive to phase errors, and can be extracted by a number of measurements which is polynomial in N_g. Fig. 1 (Right) shows that the probability in a chosen cell (i'_g, j'_g) is indeed insensitive to phase errors. We note that this coarse-grained probability is a very natural quantity for the dynamical system under investigation. One is not interested in the exponential amount of information present in all a_{ij} since one cannot even store it classically, and therefore it is better to operate with coarse-grained characteristics as is usually done in chaotic dynamical systems. The number of cells N_g can be kept constant while the number of iterated classical orbits increases exponentially with n_q. All these orbits are iterated accurately and with exponential efficiency during quantum computation, and the constant number of cells N_g is used only to extract the essential information generated by this chaotic dynamics.

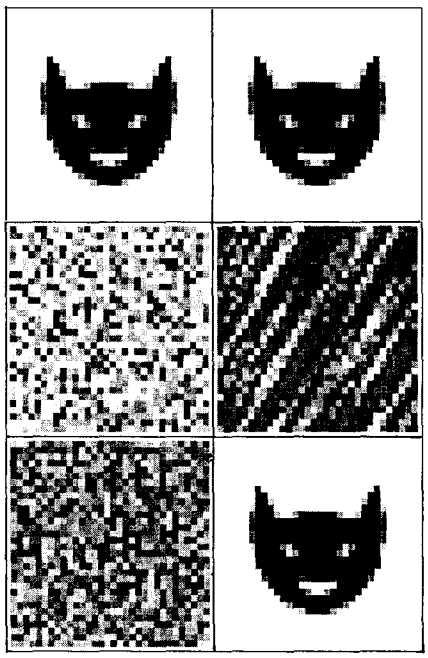


Figure 2: Coarse-grained image of Arnold-Schrödinger cat measured through the probabilities $W_{i_g j_g}$ at different moments of time $t = 0$(upper panels), $t = 50$ (middle panels), $t = 100$ (lower panels). Grayness is proportional to $W_{i_g j_g}$, from white (minimum) to black (maximum). Time inversion is done at $t = 50$. The quantum computation is done with phase errors of amplitude $\epsilon_\phi = \pi$ for both columns. In addition, for the left column the computation includes also amplitude errors of strength $\epsilon = 0.3$. The initial state is as in Fig.1, and $n_q = 7$. The coarse-graining corresponds to measuring the first five qubits ($n_g = 5$) in the $|x>$ and $|y>$ registers. A color figure is available at http://xyz.lanl.gov/abs/quant-ph/0102082.

Another test of the effects induced by phase and amplitude errors can be performed on the basis of time-inversion. Indeed, the exact map (1) is exactly time-invertible. However, in presence of imperfections this reversibility can be destroyed. In the régime of classical chaos, the classical round-off errors grow exponentially with time and destroys time-reversibility in a logarithmically short time. For quantum simulations, it was shown in [7] that quantum errors grow only polynomially with time. Due to that, time-reversibility is preserved in quantum computation of (1) for relatively small errors. However, it is naturally expected to be destroyed

in the case of strong errors. Contrary to this expectation, Fig.2 (Right) shows that time-reversibility is exactly preserved in the presence of phase errors of maximal amplitude, and the classical distribution is exactly reproduced for all t. In the right column, the difference between the two images at $t = 0$ and $t = 100$ is on the level of classical computer precision. On the contrary, strong enough amplitude errors completely destroy time-reversibility, as is shown on Fig.2 (Left).

4 Discussion

Thus, all the data clearly show that our quantum algorithm simulating (1) is insensitive to phase errors. This result can be understood in the following way. All nondiagonal parts of the gates used in the algorithm are represented by the operator σ^x, while the noncommuting part of phase errors is represented by σ^z. Of course, σ^x and σ^z do not commute. However, the action of σ^x, $\sigma^z\sigma^x$ and $\sigma^x\sigma^z$ on a two-component spinor gives the same amplitudes of the components (with different relative phases). Thus any quantity encoded in the amplitudes, in our case the classical distribution function, remains invariant in presence of σ^z (phase) errors. On the contrary, it is sensitive to σ^x (amplitude) errors. Another way of understanding this insensitivity to phase errors is to remark that all used gates belong to a very specific subgroup among unitary transformations of the Hilbert space, that is the group of permutations of the basis formed by the states where each qubit is polarized in the z direction (each qubit is either $|0>$ or $|1>$). The amplitudes in this basis are insensitive to phase errors if only such transformations are present in the algorithm. Indeed, any permutation can be written as a product of transpositions which exchange only two states. By the same argument as for $\sigma^x\sigma^z$ given above, such a transformation is immune to phase errors, and hence any permutation. We stress again that phase errors do affect the final state through the relative phases, but do not affect the measurement which gives the cell probabilities $W_{i_g j_g}$.

The above mathematical argument explains the insensitivity to phase errors. In a more physical way, we can say that the map (1) describes the classical dynamics of the Arnold cat map, which naturally should not be sensitive to quantum phases. Of course, one can imagine other quantum algorithms which will simulate this classical dynamics using both phases and amplitudes of the wave function, and therefore will be sensitive to phase errors. However, on the basis of the Arnold-Schrödinger cat algorithm discussed in this paper, we make the conjecture that classical Hamiltonian dynamics of generic systems can always be simulated on a quantum computer in a way insensitive to phase errors. Indeed, for such a dynamics the classical information can be naturally encoded in the amplitudes only [16]. It is rather likely that such a situation can appear in quantum computations which are not connected with classical mechanics, for example probing the range of values of a function.

The implementation of such algorithms insensitive to phase errors can be enormously simpler than in the case of other algorithms sensitive to quantum phases. Indeed, the necessity to correct both phase and amplitude errors significantly complicates quantum error-correcting codes [10,11,12]. If only amplitude errors are to be corrected, one can use much simpler codes close to the classical ones. Also, in some physical systems phase errors can be naturally much stronger than amplitude ones. For example, recent studies of the emergence of quantum chaos in a quantum computer [17] showed that for sufficiently strong residual inter-qubit interaction, exponentially many states are mixed and amplitude errors become enormously strong. On the contrary, below the quantum chaos border, amplitude errors are very small whereas phase errors are still important. In spite of that, a quantum computer in this régime can efficiently simulate algorithms of the type discussed here.

We note that while the algorithm presented above is exponentially faster than any deterministic classical algorithm iterating the map (1) nevertheless one can try to compete with it with

the help of classical Monte Carlo simulation with a polynomial number of trajectories. Such an approach does not produce the exact density distribution with an exponential number of orbits which is hidden in the quantum wavefunction. However, the statistical accuracy of both methods can be comparable since one makes a polynomial number of measurements of the quantum final state. At the same time one should keep in mind that such a Monte Carlo simulation is based on the statistical assumption that a polynomial number of trajectories can correctly describe the fine structure of classical phase space. In contrast, the quantum simulation takes exactly into account the dynamics on *all* scales. We also stress that without large phase errors the QFT gives access to information which is unaccessible even for classical Monte Carlo algorithms.

In conclusion, we have shown the existence of quantum algorithms which can simulate efficiently certain computational problems and at the same time are insensitive to phase errors. Our explicit example is related to the simulation of classical motion and we make the conjecture that classical Hamiltonian dynamics can always be simulated in a way immune to phase decoherence. The existence of such efficient quantum algorithms insensitive to the relative phases shows that contrary to the common lore, the massive parallelism of quantum computing is not necessarily related to quantum interference. Actually, quantum mechanics allows to follow in parallel exponentially many computational paths in a way insensitive to phase decoherence.

Acknowledgments

We thank C. W. J. Beenakker for discussions and the IDRIS in Orsay and the CalMiP in Toulouse for access to their supercomputers. This work was supported in part by the EC RTN contract HPRN-CT-2000-0156.

References

1. D. P. Di Vincenzo, Science **270**, 255 (1995).
2. A. Ekert and R. Josza, Rev. Mod. Phys. **68**, 733 (1996).
3. A. Steane, Rep. Progr. Phys. **61**, 117 (1998).
4. P. W. Shor, in Proc. 35th Annu. Symp. Foundations of Computer Science (ed. Goldwasser, S.), 124 (IEEE Computer Society, Los Alamitos, CA, 1994).
5. S. Lloyd, Science **273**, 1073 (1996); D. S. Abrams and S. Lloyd, Phys. Rev. Lett. **79**, 2586 (1997).
6. B. Georgeot and D. L. Shepelyansky, Phys. Rev. Lett. **86**, 2890 (2001).
7. B. Georgeot and D. L. Shepelyansky, quant-ph/0101004, to appear in Phys. Rev. Lett.
8. J. I. Cirac and P. Zoller, Phys. Rev. Lett. **74**, 4091 (1995).
9. C. Miquel, J. P. Paz and R. Perazzo, Phys. Rev. A **54**, 2605 (1996); C. Miquel, J. P. Paz and W. H. Zurek, Phys. Rev. Lett. **78**, 3971 (1997).
10. A. R. Calderbank and P. W. Shor, Phys. Rev. A **54**, 1098 (1996).
11. A. Steane, Proc. Roy. Soc. Lond. A **452**, 2551 (1996).
12. J. Preskill, Physics Today, **52**, No. 6, 24 (1999); and lecture notes http://theory.caltech.edu/people/preskill.
13. V. I. Arnold and A. Avez, *Ergodic Problems of Classical Mechanics*, Benjamin, N. Y. (1968).
14. A. Lichtenberg and M. Lieberman, *Regular and Chaotic Dynamics*, Springer, N.Y. (1992).
15. V. Vedral, A. Barrenco and A. Ekert, Phys. Rev. A **54**, 147 (1996).
16. This is the case for the algorithm proposed in [6] to simulate the classical Chirikov standard map.
17. B. Georgeot and D. L. Shepelyansky, Phys. Rev. E **62**, 3504 (2000); *ibid.* **62**, 6366 (2000); D. L. Shepelyansky, Physica Scripta **T90**, 112 (2001).

List of Participants

Boris Altshuler

Princeton Univ.
Dept. of Phys.
305 Jadwin Hall
NJ 08545 Princeton
USA
bla@feynman.princeton.edu

Anne Anthore

CEA-DRECAM-SPEC
Groupe quantronique
CE de Saclay
91191 Gif/Yvettes cedex
France
anthore@drecam.saclay.cea.fr

Dmitri Averin

SUNY
Dept. of Phys. and Astro.
NY 11794 Stony Brook
USA

daverin@qcom.physics.sunysb.edu

Yshai Avishai

Ben Gurion Univ.
Phys. Dept;
Ilze Katz Ctr for Nanoscale Science
Beer Sheva
yshai@bgumail.bgu.ac.il

Adrian Bachtold

Univ. of Tech.
Dept. of Applied Phys.
Lorentzweg 1
2628 CJ Delft
Netherlands
bachtold@qt.tn.tudelft.nl

Harold Baranger

Duke Univ.
Dept. of Phys.
Box 90305
NC 27708-0305 Durham
USA
baranger@phy.duke.edu

Carlo Beenakker

Leiden Univ.
Inst. Lorentz
PO Box 9506
2300 RA Leiden
Netherlands
beenakker@lorentz.leidenuniv.nl

Jean-Marc Berroir

ENS/LPMC
24, rue Lhomond
75231 Paris cedex 5 Paris cedex 5
France
berroir@lpmc.ens.fr

Gianni Blatter

ETH Hoenggerberg
Theor. Phys.
CH-8093 Zuerich
Switzerland

blatter@itp.phys.ethz.ch

Laszlo Borda

Univ. of Tech. and Eco.
Dept. of Theor. Phys.
Budafoki ut 8
HIIII Budapest
Hungary
borda@mott.phy.bme.hu

Serguei Brazovski

Univ. Paris Sud/LPTMS
Bât. 100
91405 Orsay cedex
France

brazov@ipno.in2p3.fr

Christoph Bruder

Univ. of Basel
Dept. Phys. and Astro.
Klingelbergstrasse 82
CH-4056 Basel
Switzerland
christoph.bruder@unibas.ch

Henrik Bruus

Niels Bohr Inst.
Oersted Lab.
Univsitetsparken 5
DK-2100 Copenhagen
Denmark
bruus@nbi.dk

Hans Peter Buchler

ETH Hoenggerberg
Inst. fur Theor. Phys.
8097 Zuerich
Switzerland

buechler@itp.phys.ethz.ch

Evgeni Buchstab

Technion
Solid State Inst.
32000 Haifa
Israel

phr32eb@tx.technion.ac.il

Jerome Buerki

Harvard Univ.
Phys. Dept.
17, Oxford street
MA 02138 Cambridge
USA
buerki@fas.harvard.edu

Olivier Buisson

CNRS/CRTBT
BP 166 X
38042 Grenoble cedex
France

buisson@labs.polycnrs-gre.fr

Eyal Buks

Caltech
Condensed Matter Phys.
103 Sloan Annex
CA 91125 Pasadena
USA
eyal@caltech.edu

Markus Büttiker

Univ. of Geneva
Dept Theor. Phys.
24 quai E. Ansermet
1211 Geneva
Switzerland
buttiker@serifos.unige.ch

Jerome Cayssol

Univ. Paris Sud/LPS
Labo. de phys. des solides
Bât. 510
91405 Orsay cedex
France
cayssol@lps.u-psud.fr

Albert M. Chang

Purdue Univ.
Dept. of Phys.
IN 47907-1396 West Lafayette
USA
yingshe@physics.purdue.edu

Nikolai Chtchelkatchev

Landau Inst of Theor. Phys.
Kosygin str. 2
142432 Moscow
Russia

nms@landau.ac.ru

Hervé Courtois

CNRS/CRTBT
25, ave. des Martyrs
38042 Grenoble cedex 9
France

herve.courtois@labs.polycnrs-gre.fr

Silvano de Franceschi

Univ. of Tech.
Dept. of Applied Phys.
Lorentzweg 1
2628 CJ Delft
Netherlands
silvano@qt1.tn.tudelft.nl

Richard Deblock

Univ. Paris Sud/LPS
Labo. de phys. des solides
Bât. 510
91405 Orsay cedex
France
deblock@lps.u-psud.fr

Pascal Degiovanni

ENS/Labo de Phys.
46 allée d'Italie
69007 Lyon
France

pascal.degiovanni@ens-lyon.fr

Pierre Devillard

CNRS/CPT
Case 907
Luminy
13288 Marseille cedex 9
France
devillar@cpt.univ-mrs.fr

Konstantin Efetov

Ruhr Univ.
Theor. Phys. III
Univ. str. 150
44780 Bochum
Germany
efetov@tp3.ruhr-univ-bochum.de

Klaus Ensslin

ETH Hoenggerberg
Solid State Inst.
8093 Zuerich
Switzerland

ensslin@solid.phys.ethz.ch

Daniel Esteve

CEA-DRECAM-SPEC
Quantronics Group
91191 Gif/Yvettes cedex
France

desteve@cea.fr

Giancarlo Faini

CNRS/L2M
196, ave. Henri Ravera
BP 107
9225 Bagneux cedex
France
giancarlo.faini@l2m.cnrs.fr

Vladimir Falko

Lancaster Univ.
Dept. of Phys.
LA1 4YB Lancaster
UK

v.falko@lancaster.ac.uk

Rosario Fazio

Univ. di Catania
Dipt. di Meto. Fis. e Chim.
Viale A. Doria 6
I-95125 Catania
Italy
fazio@dmfci.ing.unict.it

Nikolai Fedorov

RAS/Lebedev Inst.
RAS
Leninsky Prospect 53
117924 Moscow
Russia
fedorov@td.lpi.ru

Mikhail Feigelman

Landau Inst of Theor. Phys.
Kosygin str. 2
117940 Moscow
Russia

feigel@landau.ac.ru

Denis Feinberg

CNRS/LEPES
BP 166
38042 Grenoble cedex 9
France

feinberg@lepes.polycnrs-gre.fr

Alexander Finkelstein

Weizmann Inst. of Phys.
Dept. of Cond. Matter
Phys.
76100 Rehovot
Israel
lwalfn@wisemail.weizmann.ac.il

Klaus Frahm

Univ. Paul Sabatier
Labo. de phys. quant.
118, route de Narbonne
31062 Toulouse cedex
France
frahm@irsamc2.ups-tlse.fr

Valentin Freilikher

Bar-Ilan Univ.
Dept. of Phys.
52900 Ramat-Gan
Israel

freili@mail.biu.ac.il

Yuval Gefen

Wiezmann Inst.
Dept. of Cond. Matter
Phys.
76100 Rehovot
Israel
fngefen@wicc.weizmann.ac.il

Ulf Gennser

CNRS/L2M
196, ave. Henri Ravera
BP 107
9225 Bagneux cedex
France
ulf.gennser@l2M.cnrs.fr

Bertrand Georgeot

IRSAMC/Univ. P. Sabatier
Labo. de phys. quant.
118, route de Narbonne
31062 Toulouse cedex 04
France
georgeot@irsamc2.ups-tlse.fr

Christian Glattli

CEA/ENS
DRECAM/SPEC
Orme des Merisiers
91191 Gif/Yvettes cedex
France
dglattli@cea.fr

Leonid Glazman

Univ. of Minnesota
Teor. Phys. Inst.
Physics 148, 116 church st.
MN 55455 NE Minneapolis
USA
glazman@tc.umn.edu

Vladimir Goldman

SUNY
Dept. of Phys.
NY11794-3800 Stony Brook
USA

goldman@insti.physics.sunysb.edu

Gabriel Gomila

Univ. di Lecce
Dipt. de Ing. delle innov
Via Arnesa s/n
73100 Lecce
Italy
gabriel.gomila@unile.it

Leonid Gorelik

Chalmers Univ. of Techn.
Göteborg Univ.
S-41296 Goteborg
Sweden

gorelik@fy.chalmers.se

Moty Heiblum

Weizmann Inst. of Phys.
Sub Micron Semicond. Ctr.
76100 Rehovot
Israel

heiblum@wisemail.weizmann.ac.il

Pieter Heij

Univ. of Tech.
Physics/VS-QT
Lorentzweg 1
2628 CJ Delft
Netherlands
heij@qt.tn.tudelft.nl

Frank Hekking

Magistere-CNRS
BP 166
38042 Grenoble cedex 9
France

hekking@belledonne.polycnrs-gre.fr

Joseph Imry

Weizmann Inst. of Phys.
CM Phys.
76100 Rehovot
Israel

fnimry@wicc.weizmann.ac.il

Ken Ichiro Imura

Univ. Paris Sud/LPS
Bât 510
ou LPTMS - Bât. 100
91405 Orsay cedex
France
imura@ipno.in2p3.fr

Dmitri Ivanov

ETH Hoenggerberg
Theor. Phys.
CH-8093 Zuerich
Switzerland

ivanov@itp.phys.ethz.ch

Philippe Jacquod

Leiden Univ.
Inst. Lorentz
PO Box 9506
2300 RA Leiden
Netherlands
pjacquod@lorentz.leidenuniv.nl

Philippe Joyez

CEA-DRECAM-SPEC
Grupe Quantronique
CE de Saclay
91191 Gif/Yvettes cedex
France
joyez@cea.fr

Eugene Kanzieper

Hitachi Cambride lab.
Madingley Road
CB3 0HE Cambridge
UK

kanzieper@phy.cam.ac.uk

Jens Koenemann

Univ. Hannover
Inst. fur Festkernphys;
Appelstrasse 2
30167 Hannover
Germany
konemann@nano.uni-hannover.de

Vladimir Kravtsov

ICTP
PO Box 586
34100 Trieste
Italy

kravtsov@ictp.trieste.it

Philippe Lafarge

CNRS - MPI/FKF
Labo. des champs magn.
intenses
BP 166
38042 Grenoble cedex 9
lafarge@polycnrs-gre.fr

Jose Lages

Univ. P. Sabatier
IRSAMC
Groupe de Phys. Théor
31062 Toulouse
France
lages@irsamc2.ups-tlse.fr

Mireille Lavagna

CEA/DRFMC/SPSMS
17, rue des Martyrs
38054 Grenoble cedex
France

lavagna@cea.fr

François Lefloch

CEA/DRFMC/SPSMS
17, ave. des Martyrs
38054 Grenoble cedex 9
France

flefloch@cea.fr

Konrad Lehnert

Yale Univ.
Dept. of Appl. Phys.
Room 405 Becjon Ctr
CT 06511 New Haven
France
konrad.lehnert@yale.edu

Laurent Levy

CNRS/LCMI
BP 166
38042 Grenoble cedex 9
France

levy@grenet.fr

Alfredo Levy Yeyati

Univ. Autonoma
Dpt. de Fis. Téor. de la
Mat. Cond. CV
28049 Madrid
Spain
aly@uamcal.fmc.uam.es

Rene Lindell

Univ. of Techno.
Low Temp. Lab.
PO Box 2200
FIN-02015 HUT Otakaari
3A Espoo
rene.lindell@hut.fi

Daniel Loss

Univ. of Basel
Dept. of Phys
Klingelbergstrasse 82
CH-4056 Basel
Switzerland
daniel.loss@unibas.ch

Dominique Mailly

CNRS/L2M
196, ave. Henri Ravera
BP 107
9225 Bagneux cedex
France
dominique.mailly@l2M.cnrs.fr

Charles Marcus

Harvard Univ.
Dept. of Phys.
17, Oxford street
MA 02138 Cambridge
USA
marcus@harvard.edu

Thierry Martin

CNRS/CPT
Case 907
Luminy
13288 Marseille cedex 9
France
martin@cpt.univ-mrs.fr

Cécile Naud

CNRS/L2M
196, ave. H. Ravera
BP 107
9225 Bagneux cedex
France
cecile.naud@l2M.cnrs.fr

Mikko Paalanen

Univ. of Tech.
Low Temp. Lab.
PO Box 2200
Fin-02015 HUT Helsinki
Finland
paalanen@neuro.hut.fi

Natalia Maslova

Moscow State Univ.
Phys. Dept
Chair of Quantum
Radiophys.
119899 Moscow
spm@simlab.ilc.msu.su

Yuli Nazarov

Univ. of Tech.
Dept. of Applied Phys.
Lorentzweg 1
2628 CJ Delft
Netherlands
y.v.nazarov@tn.tudelft.nl

Bernard Pannetier

CNRS/CRTBT
25, ave. des Martyrs
BP 166
38042 Grenoble cedex 9
France
pannetier@labs.polycnrs-gre.fr

Yigal Meir

Ben Gurion Univ.
Dept. of Phys.
84105 Beer Sheva
Israel

ymeir@bgumail.bgu.ac.il

Hervé Ness

Univ. College
Dept. of Phys. and Astro.
Gower str.
WC1 6BT London
UK
h.ness@ucl.ac.uk

Stéphane Peysson

Inst. of Theor. Phys.
Valckenierstraat 65
1013XE Amsterdam
Netherlands

speysson@wins.uva.nl

Régis Melin

CNRS/CRTBT
BP 166 X
38042 Grenoble cedex
France

melin@polycnrs-gre.fr

Nguyen Van Lien

NCNST
Inst. of Phys.
46 Nguyen Uan Ngoc st.
Cong Vi Ba Dinh, Hanoi
Vietnam
nvlien@bohr.ac.vn

Jean-Louis Pichard

CEA-DRECAM-SPEC

91191 Gif/Yvettes cedex
France

pichard@drecam.saclay.cea.fr

Julia Meyer

Ruhr Univ.
Theor. Phys. III
D-44780 Bochum
Germany

jm@tp3.ruhr-uni-bochum.de

Jesper Nygard

Niels Bohr Inst.
Oersted Lab.
Univsitetsparken 5
DK-2100 Copenhagen
Denmark
nygard@nbi.dk

Frédéric Piechon

Univ. Paris Sud/LPS
LPS
Bât. 510
91405 Orsay cedex
France
piechon@lps.u-psud.fr

Alejandro Monastra

Univ. Paris XI/LPTMS
Bât. 100
91405 Orsay cedex
France

monastra@ipno.in2p3.fr

Stefan Oberholzer

Univ. of Basel
Inst. of Phys.
Klingelbergstrasse 82
CH-4056 Basel
Switzerland
stefan.oberholzer@unibas.ch

Bernard Plaçais

ENS/LPMC
24, rue Lhomond
75231 Paris cedex 5
France

placais@lpmc.ens.fr

Gilles Montambaux

Univ. Paris Sud/LPS
LPS
Bât. 510
91405 Orsay cedex
France
montambaux@lps.u-psud.fr

Yuval Oreg

Weizmann Inst. of Phys.
Dept. of Cond. Matter
Phys.
76100 Rehovot
Israel
oreg@wicc.weizmann.ac.il

Henk Postma

Univ. of Tech.
Applied Phys.
Lorentzweg 1
2628 CJ Delft
Netherlands
henk@qt.tn.tudelft.nl

Tatsuro Nagano

Washington State Univ.
Dept. of Phys.
WA 99164-2814 Pullman
USA

tnagano@wsu.edu

Stéphane Ouvry

Univ. Paris Xl/LPTMS
LPTMS
Bât. 100
91405 Orsay cedex
France
ouvry@inpo.in2p3.fr

Hugues Pothier

CEA-DRECAM-SPEC
Bât. 772
Orme des Merisiers
91191 Gif/Yvettes cedex
France
hpothier@cea.fr

Oleg Prus

Technion
Solid State Inst.
Haifa
Israel

prus@ssrc.technion.ac.il

Wilfried Rabaud

CNRS/CRTBT
25, ave. des Martyrs
BP 166X
38042 Grenoble cedex 9
France
rabaud@polycnrs-gre.fr

Bertrand Reulet

Univ. Paris Sud/LPS
Bât. 510
91405 Orsay cedex
France

reulet@lps.u-psud.fr

Michael Reznikov

Technion
Solid State Inst.
32000 Haifa
Israel

ssmisha@tx.technion.ac.il

Patrice Roche

CEA-DRECAM-SPEC
DRECAM
Orme des Merisiers
91191 Gif/Yvettes cedex
France
roche@spec.saclay.cea.fr

Valentin Rodriguez

CEA-DRECAM-SPEC
DRECAM
Orme des Merisiers
91191 Gif/Yvettes cedex
France
vrodrig@spec.saclay.cea.fr

Leif Roschier

Univ. of Tech.
Low Temp. Lab.
PL 2200
02015 TKK Helsinki
Finland
leif.roschier@hut.fi

Michael Roukes

Caltech
Cond. Matt. Phys.
114-36
CA 91125 Pasadena
USA
roukes@caltech.edu

Valery Ryazanov

RAS
Inst. of Solid State Phys.
Moscow District
142432 Chernogolovka
Russia
ryazanov@issp.ac.ru

Ines Safi

CNRS/CPT
Case 907
Luminy
13288 Marseille cedex 9
France
safi@cpt.univ-mrs.fr

Sergey Safonov

Univ. of Exeter
School of Phys.
Stocker Road
EX4 4QL Exeter
UK
s.safonov@ex.ac.uk

Laurent Saminadayar

CNRS/CRTBT
BP 166 X
38042 Grenoble cedex 9
France

saminadayar@polycnrs-gre.fr

Marc Sanquer

CEA/DRFMC/SPSMS
LCP - Bât.C1
17, ave. des Martyrs
38054 Grenoble cedex
France
msanquer@cea.fr

Alexander Savchenko

Univ. of Exeter
School of Phys.
Stocker Road
EX4 4QL Exeter
UK
a.k.savchenko@exeter.ac.uk

Georg Schmidt

Univ. Wuerzburg
Phys. Inst.
97074 Am Hubland
Germany

georg.schmidt@physik.uni-wuerzbu

Rob Schoelkopf

Yale Univ.
Dept. of Applied Phys. and Phys.
PO Box 208284
CT 06520-8284 New Haven
rob.schoelkopf.yale.edu

Christian Schoenenberger

Univ. of Basel
Inst. of Phys.
Klingelbergstrasse 82
CH-4056 Basel
Switzerland
christian.schoenenberger@unibas.c

Vitaly Shumeiko

Chalmers Univ. of Techn.
School of Phys.
MINA
S-41296 Gothenburg
Sweden
vitaly@fy.chalmers.se

Jens Siewert

Univ. di Catania
Dipt. di Meto. Fis. e Chim.
Viale A. Doria 6
I-95125 Catania
Italy
jsiewert@dmfci.ing.unict.it

Peter G. Silvestrov

Leiden Univ.
Inst. Lorentz
PO Box 9506
2300 RA Leiden
Netherlands
silvestr@lorentz.leidenuniv.nl

Uri Sivan

Technion
Dept. of Phys
32000 Haifa
Israel

phsivan@tx.technion.ac.il

Pavel Streda

Acad. of Sciences
Inst. of Phys.
Na Slovance 2
CA 182 21 Praha 8
Czech Republic
streda@fzu.cz

Eugene Sukhorukov

Univ. of Basel
Dept. of Phys. and Astro.
Klingelbergstrasse 82
CH-4056 Basel
Switzerland
e.sukhorukov@unibas.ch

Hideaki Takayanagi

NTT Basic Res. Lab.
3-1 Morinosoto-Wakamiya,
Atsugi-shi
243-0198 Kanagawa
Japan
takayan@will.brl.ntt.co.jp

Christophe Texier

Univ. Paris Sud/LPTMS
Bât. 100
91405 Orsay cedex
France

texier@ipno.in2p3.fr

Julien Torres

CNRS/CPT
Case 907
Luminy
13288 Marseille cedex 9
France
torres@cpt.univ-mrs.fr

Orsolya Ujsaghy

Tech. Univ.
Inst. of Phys.
Budafoki ut 8
H-1581 Budapest
Hungary
ujsaghy@born.phy.bme.hu

Denis Ullmo

Univ. Paris Sud/LPTMS

91405 Orsay cedex
France

ullmo@ipno.in2p3.fr

Gonzalo Usaj

Duke Univ.
Dept. of Phys.
PO Box 90305
NC 27708-0305 Durham
USA
usaj@phy.duke.edu

Jan van Ruitenbeek

Leiden Univ.
Kamerlingh Onnes Lab.
Niels Bohrweg 2
NL-2333 RA Leiden
Netherlands
ruitenbe@phys.leidenuniv.nl

Bart van Wees

Univ. of Groningen
Vakgroed FDL
Dept. of Applied Phys.
9747AG Groningen
Netherlands
wees@phys.rug.nl

Imre Varga

Philipps Univ. Marburg
Fachbereich Physik
Renthof 5
D-35032 Marburg and der
Lahn

Julien Vidal

Gr. de Phys. des sol.
Tour 23-24, 5ème étage
2 place Jussieu
75251 Paris cedex 05
France
vidal@gps.jussieu.fr

Maud Vinet

CEA/DRFMC/SPSMS
17, ave. des Martyrs
38054 Grenoble
France

mvinet@cea.fr

Felix von Oppen

Freie Univ. at Berlin
Inst. fur Theor. Phys.
Arnimallee 14
14195 Berlin
Germany
vonoppen@physik.fu-berlin.de

Xavier Waintal

Cornell Univ.
Phys. Dept.
NY 14850 Ithaca
USA

waintal@ccmr.cornell.edu

Dietmar Weinmann

IPCMS-GEMME
CNS/UMR 7504
23, rue du Loess
67037 Strasbourg cedex
France
weinmann@ipcms.u-strasbg.fr

Goran Wendin

Chalmers Univ. of Techn.
Dept. of Microelec. and
Nanosc.
MC2
SE-41296 Goteborg
wendin@fy.chalmers.se

Robert Whitney

Weizmann Inst. of Phys.
Cond. Matt. Phys.
76100 Rehovot
Israel

whitney@wicc.weizmann.ac.il

Amir Yacoby

Weizmann Inst. of Phys.
Dept. of Cond. Matter
Phys.
76100 Rehovot
Israel

Victor Yakovenko

Univ. of Maryland
Dept. of Phys.
MD-20742-4111 College
Park
USA
yakoven@physics.umd.edu

Andrei Zaikin

Forschungszentrum
Inst. for Nanotechnology
D-76021 Karlsruhe
Germany

zaikin@tfp.physik.uni-karlsruhe.de

Alfred Zawadowski

Tech. Univ.
Inst. of Phys.
PO Box 1521
I. Budafoki ut 8 Budapest
Hungary
zawa@phy.bme.hu

Xenophon Zotos

IRRMA (EPFL-PPH)

1015 Ecublens Lausanne
Switzerland

xenophon.zotos@epfl.ch

INDEX OF AUTHORS

Aarts J., 143,
Ahlskog M., 437, 459,
Aleiner I.L., 391,
Altland A., 309,
Altshuler B.L., 391,
Anthore A., 301,
Arseev P.I., 333,
Averin D.V., 551,
Avishai Y., 11,

Bachtold A., 427,
Balestro F., 515,
Baranger H.U., 493,
Beloborodov I.S., 309,
Belzig W., 93,
Ben Yoseph G., 181,
Benoit A., 263,
Bergère M., 319,
Berkovits R., 391,
Berthier C., 59,
Bibow E., 503,
Bichler M., 367,
Blatter G., 167, 267, 541,
Bouchiat H., 273, 443,
Bratus E.N., 521,
Brazovskii S., 315,
Brouwer P.W., 497,
Bruder C., 137,
Bruus H., 489,
Büchler H.P., 267,
Buchstab E., 181,
Buisson O., 127, 515,
Buitelaar M., 421,
Bürki J., 27,
Büttiker M., 107, 263,

Calemczuk R., 121,
Chandrasekhar V., 159,
Chang A.M., 41,
Chapelier C., 175,
Cheianov V., 489,
Chtchelkatchev N.M., 153,
Cobden D., 455,
Courtois H., 127, 159,
Cron R., 17,

Das Sarma S., 39,
David G., 207,
De Franceschi S., 361,
Deblock R., 273, 443,
Dehlinger G., 207,
Dekker C., 433,
Delsing P., 117,
Demler E., 133,
Deutscher G., 535,
Devillard P., 67,
Devoret M.H., 17, 301,
Dötsch U., 207,
Douçot B., 255,
Dubos P., 127,

Efetov K.B., 309,
Elzerman J.M., 361,
Engel H.A., 525,
Ensslin K., 207, 367,
Esteve D., 17, 301,
Etienne B., 73, 263,

Faini G., 255,
Falci G., 535,
Fal'ko V.I., 147, 283,
Fazio R., 509,
Feinberg D., 535,
Filip A.T., 475,
Finkel'stein A., 225,
Fisher A.J., 23,
Flensberg K., 489,
Folk J.A., 391,
Frahm K.M., 279,
Freytag N., 59,
Fuhrer A., 367,
Fuhrer M.S., 427,
Fujisawa T., 361,
Gavish U., 243,

Gefen Y., 85, 291,
Gennser U., 207,
Georgeot B., 557,
Geshkenbein V.B., 167, 267,
Glattli D.C., 73,
Glazman L.I., 405,
Goldman V.J., 51, 551,
Golubev D.S., 237,
Golubov A.A., 143,
Gomila G. , 111,
Grützmacher D., 207,
Guéron S., 443,
Gutman D.B., 85,
Guyon R., 171,

Hakonen P., 437, 459,
Hasselbach K., 263,
Haug R.J., 283,
Heiblum M., 353,
Heinzel T., 207, 367,
Hekking F.W.J., 309, 515, 535,
Hoffmann C., 163,
Horvatic M., 59,

Ihn T., 207,
Ilani S., 187,
Imry Y., 243,
Imura K.I., 319,
Ioffe L.B., 167,
Iqbal M., 421,
Ivanov D.A., 167,
Izumida W., 361,

Jacquod P., 323,
Jalabert R.A., 485,
Jedema F.J., 475,
Jehl X., 121,
Ji Y., 353,
Jin Y., 73,
Johnson A.C., 391,
Joyez P., 17,

Kanzieper E., 251,
Kasumov A., 443,
Katomeris G., 217,
Kikoin K., 11,
Kimura T., 469,
Koch S.W., 343,
Kociak M., 443,
Könemann J., 283,
König P., 283,
Kouwenhoven L.P., 361, 391,
Kravtsov V.E., 251, 373,
Kroha J., 339,
Krüger M., 421,
Kurland I.L., 391,
Kvon Z.D., 195,
Kwon H.J., 39,

Lafarge P., 503,
Lages J., 329,
Larkin A.I., 405,
Leboeuf P., 287,
Lefloch F., 163, 175,
Lehnert K.W., 117,
Lesovik G., 171, 541,
Levinson Y., 243,
Lévy L.P., 59, 503,
Levy Yeyati A., 17,
Linfield E.H., 213,
Long M., 347,
Loss D., 413, 525,
Lüscher S., 207, 367,

Mahalu D., 187, 353,
Mailly D., 121, 255, 263, 273
Marcus C.M., 391,
Marquardt F., 137,
Martin T., 67, 103, 171, 541
Martin-Rodero A., 17,
Maschke K., 343,
Maslova N.S., 333,
Matveev K.A., 405,
McCann E., 147, 283,
McEuen P.L., 427,
Meier T., 343,
Meir Y., 221,
Mélin R. , 547,

Monastra A.G., 287,
Montambaux G., 255, 381,
Moussy N., 159,

Naef F., 347,
Naud C., 255,
Nazarov Yu.V., 93,
Ness H., 23,
Noat Y., 273,
Nussbaumer T., 421,
Nygard J., 455,

Oberholzer S., 99,
Oboznov V.A., 143,
Oreg Y., 133,
Ouvry S., 319,

Paalanen M., 437,
Palma G.M., 509,
Pannetier B., 127, 159,
Pepper M., 195,
Pichard J.L., 217,
Piéchon F., 381,
Pierre F., 301,
Plastina F., 509,
Pogosov A.G., 195,
Postma H.W.C., 433,
Pothier H., 301,
Potok R.M., 391,
Prelovsek P., 347,
Proskuryakov Y.Y., 195,
Prus O., 181, 201,
Pudalov V., 201,
Punnoose A., 225,

Rabaud W., 263,
Recher P., 525,
Reggiani L., 111,
Reulet B., 273, 443,
Reuter D., 255, 263,
Reznikov M., 201,
Ritchie D.A., 195,
Roche P., 73,
Rodriguez V., 73,
Roschier L., 437, 459,
Roshko S.H., 195,
Rusanov A.Yu., 143,
Ryazanov V.Y., 143,

Safi I., 67,
Safonov S.S., 195, 213,
Saminadayar L., 263,
Sanquer M., 121, 163,
Savchenko A.K., 195, 213,
Savinov S.V., 333,
Scheidl S., 33,
Schlichenmaier C., 343,
Schmidt T., 283,
Schoelkopf R.J., 117,
Schönenberger C., 99, 421,
Seba P., 465,
Selva F., 217,
Sengupta K., 39,
Senz V., 207,
Shapira S., 181,
Shayegan M., 59,
Shepelyansky D.L., 557,
Shiraishi K., 469,
Shtrikman H., 187, 353,
Shumeiko V.S., 521,
Siewert J., 509,
Simmons M.Y., 195,
Sivan U., 181, 201,
Sprinzak D., 353,
Stafford C.A., 27,
Stamps R.L., 485,
Stern A., 181,
Streda P., 465,
Strunk C., 99,
Sukhorukov E.V., 99, 413,
Szunyogh L., 339,

Takayanagi H., 469,
Tamura H., 469,
Tarkiainen R., 437, 459,
Tarucha S., 361,
Teepen T.F., 433,
Texier C., 107,

Thomas P., 343,
Tkachov G., 147,
Tokunaga Y., 59,
Torrès J., 103,
Tribe W.R., 213,

Ujsaghy O., 339,
Urbina C., 17,
Usaj G., 493,
Ussishkin I., 181,

Van der Wiel W.G., 361,
Van Ruitenbeek J.M., 3,
Van Wees B.J., 475,
Varga I., 343,
Vecino E., 17,
Veretennikov A.V., 143,
Vergniory M.G., 515,
Vidal J., 255,
Vinet M., 175,
Von Oppen F., 33,
Vyhnal A., 465,

Wahlgren P., 117,
Waintal X., 497,
Wegscheider W., 367,
Weinmann D., 485,
Wendin G., 521,
Whitney R.S., 291,
Widmer I., 421,
Wieck A., 255, 263,

Yacoby A., 187,
Yaish Y., 181, 201,
Yakovenko V.M., 39,
Yanson A.I., 3,
Yanson I.K., 3,
Yao Z., 433,
Yudson V.I., 251,

Zaikin A.D., 237,
Zawadowski A., 339, 385,
Zotos X., 347,
Zutic I., 39,

Achevé d'imprimer sur les presses de l'Imprimerie BARNÉOUD